ICCSA 2014

Fourth International Conference on Complex Systems and Applications

June 23-26, 2014
Le Havre, Normandie, France

Editors
M.A. Aziz-Alaoui, Cyrille Bertelle,
Xinzhi Liu and Damien Olivier

Preface

The previous International Conference "Complex Systems and Applications (ICCSA)" was held in Le Havre during June 29 - July 2, 2009. It was an historical event, many of the most famous names in this topic have attended. This fourth ICCSA will be held again in France, Normandy, Le Havre on the Seine river estuary, during June 23 - 26, 2014.
This conference will provide a unique international forum, where exciting interactions and communications take place among researchers, and it will bring fruitful cooperation and collaborations to the world community. The fourth ICCSA will focus on recent advances in complex systems and applications in all fields of science and engineering. There will be several invited expository addresses covering recent trends and many invited lectures on problems of current interest and important applications in various disciplines.

Le Havre, France & Waterloo, Canada
June 10th 2014

M.A. Aziz-Alaoui
Cyrille Bertelle
Xinzhi Liu
Damien Olivier

Contents

Keynote Speakers

The Origin of Complexity: Local Activity and the Third Law of Thermodynamics

Leon CHUA

University of California
Berkeley, USA

The first two laws of thermodynamics cannot be used to explain numerous complex phenomena that had puzzled many luminaries, including Boltzmann, Schrodinger, Prigogine, Eigen, Gellman, Turing, Smale, etc. This 2-hour lecture introduces the new "principle of local activity" which resolves the above conundrum by providing a mathematical foundation for the current hot albeit disarrayed research area dubbed "complexity". The principle of local activity asserts that "complexity is impossible without local activity". This mathematically rigorous, yet simple and constructive theory can be applied by anyone with a basic background in ordinary differential equation and linear algebra. The concept of local activity and its pearl, called the "edge of chaos", provides the essential tool for explaining and predicting all sorts of hitherto unresolved complex phenomena from both natural and social sciences. The secret behind the principle of local activity is that it implies a non-monotonically increasing "entropy function", thereby providing the missing complement of the second law of thermodynamics.

The "Local Activity Principle" and its gem, the "Edge of Chaos", are the rigorous mathematical foundation for building a scientific theory of "Complexity". For "reaction diffusion systems", a simple explicit procedure requiring only elementary linear algebra and theory of complex numbers is presented with detailed illustrations, including the FitzHugh-Nagumo equations, the Brusselator equations, the Gierer-Meinhardt equations, the Oregonator equations and the Hodgkin-Huxley equations, in the following publication: Klaus Mainzer and Leon Chua, Local Activity Principle, Imperial College Press, 2013.

The single most significant aspect of the "local activity principle", henceforth dubbed the "third law of thermodynamics", that distinguishes it from numerous other jargons, e.g., *emergence, self-organization dissipative structure, slaving principle, synergetics,* etc. is that it is a "constructive" mathematical theory that allows researchers to calculate and identify a tiny subset of the parameter space where complex phenomena can occur. Finally, we remark that although there exists already a third law of thermodynamics, based on Nernst's 1912 postulate, and which had been debated by Einstein and Planck, this law is seldom taught in Physics courses not only because it has few practical applications *unlike the second law*, but also because it has at least 3 "different" versions where none are equivalent, and where no version is sufficiently general, and no version can avoid unresolved issues.

Climate Networks and Extreme Events

Juergen Kurths

Potsdam Institute for Climate Impact Research & Humboldt University,
Berlin & King´s College, University of Aberdeen, UK

We analyse some climate dynamics from a complex network approach. This leads to an inverse problem: Is there a backbone-like structure underlying the climate system? For this we propose a method to reconstruct and analyze a complex network from data generated by a spatio-temporal dynamical system. This approach enables us to uncover relations to global circulation patterns in oceans and atmosphere. The global scale view on climate networks offers promising new perspectives for detecting dynamical structures based on nonlinear physical processes in the climate system. Moreover, we evaluate different regional climate models from this aspect.

This concept is also applied to Monsoon data in order to characterize the regional occurrence of extreme rain events and its impact on predictability. Changing climatic conditions have led to a significant increase in magnitude and frequency of spatially extensive extreme rainfall events in the eastern Central Andes of South America. These events impose substantial natural hazards for population, economy, and ecology by floods and landslides. For example, heavy floods in Bolivia in early 2007 affected more than 133.000 households and produced estimated costs of 443 Mio. USD.

Here, we develop a general framework to predict extreme events by combining a non-linear synchronization technique with complex networks. We apply our method to real-time satellite-derived rainfall data and are able to predict a large amount of extreme rainfall events. Alongside with the societal benefits of predicting natural hazards associated with extreme rainfall, our study reveals a linkage between polar and subtropical regimes as responsible mechanism: Extreme rainfall in the eastern Central Andes is caused by the interplay of northward migrating frontal systems and a low-level wind channel from the western Amazon to the subtropics, providing additional moisture. Frontal systems from the Antarctic thus play a key role for sub-seasonal variability of the South American Monsoon System.

References

Arenas, A., A. Diaz-Guilera, J. Kurths, Y. Moreno, and C. Zhou, Phys. Reports 469, 93 (2008).
Donges, J., Y. Zou, N. Marwan, and J. Kurths, Europhys. Lett. 87, 48007 (2009).
Donner, R., Y. Zou, J. Donges, N. Marwan, and J. Kurths, Phys. Rev. E 81, 015101(R) (2010).
Mokhov, I. I., D. A. Smirnov, P. I. Nakonechny, S. S. Kozlenko, E. P. Seleznev, and J. Kurths, Geophys. Res. Lett. 38, L00F04 (2011).
Malik, N., B. Bookhagen, N. Marwan, and J. Kurths, Climate Dynamics, 39, 971 (2012).

Donges, J., H. Schultz, N. Marwan, Y. Zou, J. Kurths, Eur. J. Phys. B 84, 635-651 (2011).
Donges, J., R. Donner, M. Trauth, N. Marwan, H.J. Schellnhuber, and J. Kurths, PNAS 108, 20422-20427 (2011).
Rehfeld, K., N. Marwan, S. F. M. Breitenbach, J. Kurths, Climate Dynamics 41, 3-19 (2013).
Runge, J. , J. Heitzig, V. Petoukhov, J. Kurths, Phys. Rev. Lett. 108, 258701 (2012).
Menck, P., J. Heitzig, N. Marwan, J. Kurths, Nature Physics 9, 89-92 (2013).Boers, N., B. Bookhagen, N. Marwan, J. Kurths, and J. Marengo, Geophys. Res. Lett. 40, 4386 (2013)Mheen, M., H. A. Dijkstra, A. Gozolchiani, M. Toom,Q. Feng, J. Kurths, and E. Hernandez-Garcia, Geophys. Res. Lett. 40, 2714 (2014)
Feldhoff, J., S. Lange, J. Volkholz, J. F. Donges, J. Kurths, F. Gerstengarbe, Climate Dynamics DOI 10.1007/s00382-014-2182-9 (2014)

TIME-SERIES BASED PREDICTION OF COMPLEX DYNAMICS AND COMPLEX NETWORKS

Celso Grebogi

Institute for Complex Systems and Mathematical Biology
King's College, University of Aberdeen
Aberdeen AB24 3UE, UK

http://www.abdn.ac.uk/icsmb/people/details/grebogi

In the fields of complex dynamics and complex networks, the reverse engineering, systems identification, or inverse problem is generally regarded as hard and extremely challenging mathematically as complex dynamical systems and networks consists of a large number of interacting units. However, our ideas based on compressive sensing, in combination with innovative approaches, generates a new paradigm that offers the possibility to address the fundamental inverse problem in complex dynamics and networks. In particular, in this talk, I will argue that evolutionary games model a common type of interactions in a variety of complex, networked, natural systems and social systems. Given such a system, uncovering the interacting structure of the underlying network is key to understanding its collective dynamics. Based on compressive sensing, we develop an efficient approach to reconstructing complex networks under game-based interactions from small amounts of data. The method is validated by using a variety of model networks and by conducting an actual experiment to reconstruct a social network. While most existing methods in this area assume oscillator networks that generate continuous-time data, our work successfully demonstrates that the extremely challenging problem of reverse engineering of complex networks can also be addressed even when the underlying dynamical processes are governed by realistic, evolutionary-game type of interactions in discrete time.

Network reconstruction based on evolutionary-game data via compressive sensing, W.-X. Wang, Y.-C. Lai, C. Grebogi, and J. Ye, Phys. Rev. X **1**, 021021 (2011)

Predicting catastrophe in nonlinear dynamical systems by compressive sensing, W.-X. Wang, R. Yang, Y.-C. Lai, V. Kovanis, and C. Grebogi, Phys. Rev. Lett. **106**, 154101 (2011)

Forecasting the future: Is it possible for adiabatically time-varying nonlinear dynamical systems? R. Yang, Y.-C. Lai, and C. Grebogi, Chaos **22**, 033119 (2012)

Optimizing controllability of complex networks by minimum structural perturbations, W.-X. Wang, X. Ni, Y.-C. Lai, and C. Grebogi, Phys. Rev. E **85**, 026115 (2012)

Unstable Dimension Variability: When an attractor has both a saddle and a repellor

Jim Yorke[1]
In collaboration with S. Das[1] and Yoshitaka Saiki[2] ,

[1] University of Maryland
[2] Graduate School of Commerce and Management, Hitotsubashi University, Tokyo

The hyperbolicity or nonhyperbolicity of a chaotic set has profound implications for the dynamics. Here we investigate one mechanism that can lead to nonhyperbolicity in common invertible (respectively, noninvertible) maps of dimension 3 (respectively, 2) and higher. In particular, we investigate a situation (first considered by Abraham and Smale in 1970 for different purposes) in which the dimension of the unstable (and stable) tangent spaces are not constant over a chaotic set; we call this "unstable dimension variability". In such circumstances, as a parameter is varied, there can be collisions between pairs of such periodic orbits resulting in annihilation analogous to saddle node bifurcations – but with rather different statistical behavior. A simple two-dimensional map that displays behavior typical of this phenomenon is presented and analyzed – with surprising results.

Related papers with preliminary results:

E. Kostelich, I. Kan, C. Grebogi, E. Ott And J. A. Yorke, Unstable dimension variability: a source of nonhyperbolicity in chaotic systems, Physica D 109 (1997), 81-90.

C. Grebogi, E. Ott and J. A. Yorke, Super persistent chaotic transients, Ergodic Theory and Dyn. Sys. 5 (1985), 341-372.

Control of complex systems

R.S.MacKay[1]

1. Mathematics Institute and Centre for Complexity Science, University of Warwick, Coventry CV4 7AL, UK

We propose that for many complex systems, e.g. economy, it is more important to control the statistical behaviour than the precise trajectory. Thus we present the beginnings of a theory for control of probability distributions for complex systems. We work in the class of probabilistic cellular automata (PCA), though results generalise easily to continuous-time interacting particle systems and some to coupled map lattices. For "weakly dependent" PCA, the effect on the statistical behaviour of time-dependent control is unique and we give a formula for it. For strongly dependent PCA, we demonstrate numerically that the effects of small parameter changes and small nudges can be large, leading to tipping from one phase to another. This work was supported by the Alfred P. Sloan Foundation New York.

Proceedings of ICCSA 2014
Normandie University, Le Havre, France – June 23-26, 2014

DYNAMICS OF CONTAGIOUS SOCIAL DISEASES: EXAMPLE OF OBESITY

J. Demongeot, O. Hansen and C. Taramasco[1][2][3]

Abstract. Modelling contagious diseases needs to incorporate information about social networks through which the disease spreads out as well as data about demographic and genetic changes in the susceptible population. In this paper, we propose a theoretical framework (conceptualization and formalization) which seeks to model obesity as a process of transformation of one's own body determined by individual (physical and psychological), inter-individual (relational, *i.e.*, relative to the relationship between the individual and others) and socio-cultural (environmental, *i.e.*, relative to the relationship between the individual and his milieu) factors. Individual and inter-individual factors are tied to each other in a socio-cultural context whose impact is notably related to the visibility of any body being exposed on the public stage in a non-contingent way. The question we are dealing with in this article is whether such kind of social diseases, *i.e.*, depending upon socio-environmental exposure, can be considered as "contagious". In other words, can obesity be propagated from individuals to individuals or from environmental sources over a whole population?
Keywords. social networks; contagious social diseases; obesity; homophilic rule

1 Introduction

Social and socio-infectious diseases (like Sexually Transmitted Diseases, SMD's) are numerous and obesity can be considered as one of the most characteristic of what could be identified as a social "contagious" disease. Both stigmatization and mimicking [1] constitute the way of dissemination of obesity into a family or a social network. Obesity is defined as an abnormal or excessive accumulation of fat in adipose tissue (Body Mass Index or BMI≥30, where BMI=Weight (kg)/Size^2 (m^2)) leading to more or less important health problems at the individual level.

Currently, obesity would reach an pandemic development everywhere in the world: according to the latest world estimates of WHO (World Health Organization), obesity rate would have tripled between 1980 and 2005 [2,3]. This rate of development suggests that this pathology involves a socio-cultural problem grafted into a predisposition at the individual level. All specialists agree now that, for decades, we are witnessing an increase in worldwide obesity prevalence. This is true in developed as well as in developing countries. No society seems to be immunized against this pandemic. Data from MONICA (WHO) project [2] show that obesity prevalence in the majority of the European countries increased in 10 years (1992-2002), going from 10 to 20% in men and from 10 to 25% amongst women. In France, between 1980 and 2006, obesity prevalence went from 6.4% to 16% in men and from 6.3% to 17.6% amongst women [3,4]. Based on these facts, several studies have been performed to identify risk factors associated with this affection as well as to contain the pandemic, which became a real public health problem [5]. It is well known that obesity has a genetic component as a familiar predisposition towards this affection testifies. However, this genetic component does not explain the increasing (spectacular) progression in disease prevalence. Additional behavioral, psycho-social, and economic factors must be considered [6-8]. In this context, Christakis et al. showed the possibility of person to person obesity contagion in a social network [9].

[1] J. Demongeot and O. Hansen are with University J. Fourier of Grenoble, Lab. AGIM, CNRS FRE 3405, Faculty of Medicine, 38700 La Tronche, France. E-mails: Jacques.Demongeot@agim.eu, Olivier.Hansen@agim.eu
[2] C. Taramasco is with Escuela de Ingeniería Civil en Informática, Universidad de Valparaiso, Chile. E-mail: carla.taramasco@polytechnique.edu
[3] Manuscript received April 19, 2014; revised May 14, 2014.

Moreover, Cohen et al. suggested that obesity diffusion could occur via a common exogenous source applied to a set of individuals [10].

Realistic models of contagious diseases incorporate information about the social networks through which the disease spreads out as well as data about demographic and genetic changes in the susceptible population. They also include all the possible knowledge about the contacts between susceptible and sick individuals. In Section 2, we present the mathematical framework necessary to take into account at a microscopic level the dynamics of contacts between susceptible and sick individuals. Then we introduce the description of the obesity dynamics in Section 3, a social pathology partly caused by collective behaviours mimicking some dominant habits of nutrition transmitted through social networks, modelled here by using the notion of homophilic graphs.

To investigate obesity in a multi-factorial manner, we take into account inseparable factors to analyze the impact through time that obese individual transformation may have on the social structure. With this aim, we develop a network model in which individual interactions are in part due to homophilic selection/deselection, *i.e.,* a process of preferential attachment and detachment of inter-individual links according to characteristics of the individuals involved. Homophily is here defined as the tendency of an individual to create links with other individuals sharing similar attributes with him and to cut links with other dissimilar individuals. Homophily suggests that individuals tend to interact with those who resemble them. Second, and reciprocally, we study if obesity can be considered as a "contagious" social disease. So we study the role which could be played by the structure of the social fabric in the increase and current development of obesity. We evaluate the impact of relations between individuals (micro-level) as well as the impact of relations between districts (meso-level) and between countries (macro-level). This approach highlights the necessity to integrate the dynamics of each scale to better understand the evolution of the pathology. It is proposed two stochastic models: i) an epidemiological compartmental model and ii) an individual centered network model, considering three influences: exogenous heterogeneous (individual-cultural), exogenous homogeneous (individual-social) and endogenous (individual-individual). All together, this research study on obesity will allow to investigate the social and cultural dimension involved in being and transforming one's body. In Section 4, we present elements of demographic dynamics to add to the social contagion dynamics. Eventually, we present in Section 5 a proposal of an obesity preventive policy and in Section 6 we propose some perspectives about a new more realistic modelling of the contact dynamics.

2 Social networks and obesity

2.1 General graph framework

Given that each individual is immersed in a social system, linked together with other individuals through diverse and complex interactions, each individual i can then be characterized, in a first approach, by their number of neighbors k_i, whereas the overall system is characterized by the connection structure between individuals. To study the role played by social interactions in obesity spreading, five simple network topologies are considered to describe inter-individual connections: random (Erdös-Renyi type), scale-free, small-world and two empirical network topologies. Empirical networks are built from degree distributions found by Christakis et al. [8] in real networks. On Figure 1, we can find examples of architecture simulated following the above topologies. We will use these architectures for starting from initial configurations of the *a priori* network, before applying the homophilic rule and converging to an "attractor" of its dynamics, *i.e.*, a stable configuration of links and node states of the interaction graph related to the social network involved in the obesity contagion spread.

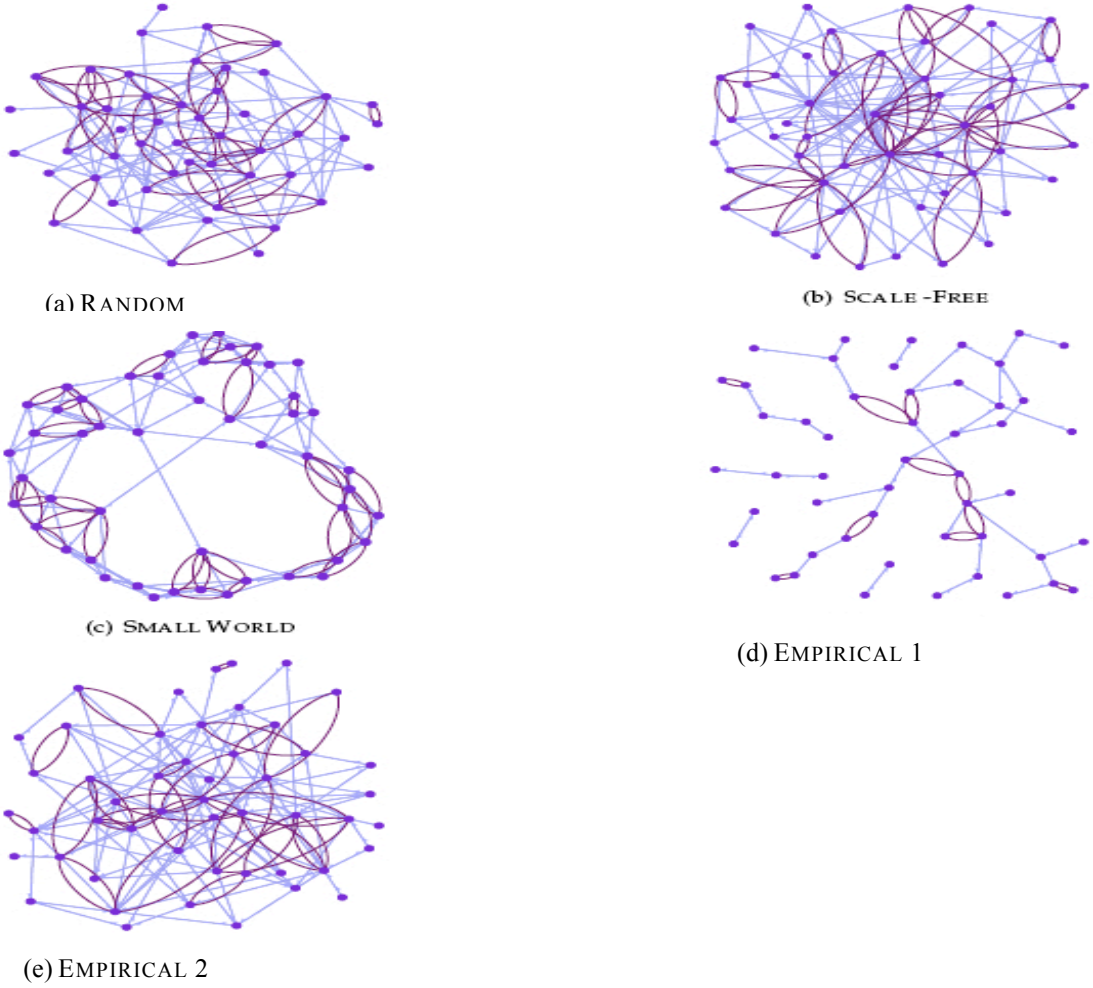

Figure 1: Simulation of various initial architectures: random, scale-free, small world, empirical (1 and 2)

2.2 Social contagion

We have modeled the social contagion mechanisms through which the disease can propagate from individuals to individuals or from environmental sources over populations, individuals changing of state like in biological regulatory networks for which many theoretical and numerical tools have been recently developed [13-16].

On Figure 2, each individual is represented in its social neighborhood: he can influence (orange and red arrows) the narrow context to which he belongs. Hence, each individual in a given social sub-network will receive direct influences from his neighbors (inter-individual factors) as well as influences from his environment (social factors) depending on his own context. Under theses influences, some individual (in blue on Figure 2) can become obese and other not (in green on Figure 2).

3 Obesity dynamics of links and states

3.1 Homophilic graphs

The function homophily (resp. heterophily) will be defined as the tendency of an individual to create (resp. cancel) links with other individuals sharing similar (resp. dissimilar) attributes, by playing with probability agents involved in an infectious contact having a given state (*e.g.*, for obesity, susceptible *S*, overweight *W* and obese *O*) before contact. Tendency an agent or node *i* has to create or cut a link with another agent *j* in a contagion graph *G* with *N* agents, depends on similarity distances *d(i,j)* in graph.

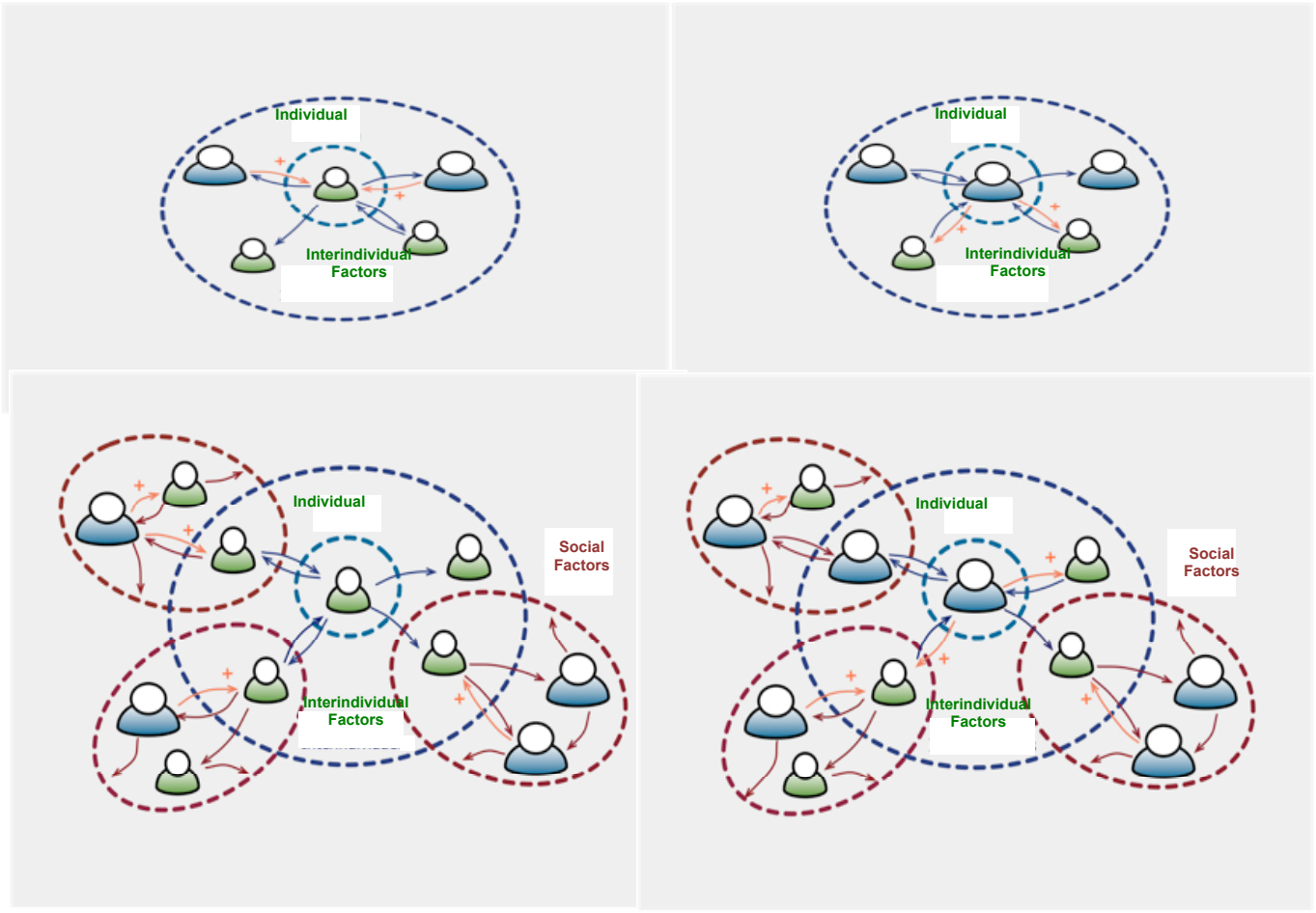

Figure 2: Inter-individual relationships between obese and non obese individuals in a social context

Let us suppose that there are two possible states x and y for the nodes of G and denote at time t by $L_{x,y}(t)$ (resp. $L_{x,x}(t)$) the number of heterophilic (resp. homophilic) links of type x, $L_x(t)$ the number of links coming from type x nodes and $L(t)$ the total number of links, and by τ the relaxation time. We suppose in each time lapse of duration τ, a certain proportion of nodes (agents) creates (resp. cancel) links toward nodes being in same (resp. different) state, with a certain tolerance threshold. Then the simulation follows the successive steps:

1. At $t = t_0$, generate the random value τ from an exponential distribution of parameter $1/\beta$

2. At $t = t_0 + \tau$,

- choose a fraction ϕ of nodes in G. Let M = ϕN.

- for each node i of these M nodes (i=1,…,M), define its state $x(i)$ (known initial conditions), its out-degree $k_i \in \mathbb{N}$ (equal to the number of links exiting from i), generate its tolerance to the difference, a real number h_i, $0 \leq h_i \leq 1$, from a probability distribution $g(h)$ and do the following operations:

  – for $k_i = 0$, connection from i to j:
  - choose a node j by chance among N–1 other nodes
  - create a link from i to j with probability $h_i^{d(i,j)}$, where $d(i,j)$ is the direct distance between i and j, with 3 levels: 0, 1 and 2, defined as follows:

$$d(i,j)=0, \text{ if } x(i) = x(j)$$

=1, if $x(i)=S$, $x(j)=W$ and vice versa

=1, if $x(i)=W$, $x(j)=O$ and vice versa

=2, if $x(i)=S$, $x(j)=O$ and vice versa

– for $k_i \geq 1$, connection or disconnection from i to j:

- if V_i denotes the set of neighbours of i, let choose a node j among the $|Vi|=k_i$ neighbours of i with the probability $1/k_i$. We will denote by V_j^i the set of the neighbours of j, minus i

- let $\delta(i,j)$ be the total similarity distance between nodes i and j. The link between i and j will be cut with the probability $1-h_i^{\delta(i,j)}$, where the total distance δ is defined by:

$$\delta(i,j) = d(i,j), \text{ if } c(i,j) = 0$$
$$= \alpha d(i,j) + (1-\alpha)c(i,j), \text{ if } c(i,j) \neq 0,$$

where the indirect distance $c(i,j) = \Sigma_{k \in Vj}\, i\ d(i,k)/(k_j-1)$

$= 0$, if $k_j=1$

- if the link between i and j has been cut, we choose by chance a new node k in $G \setminus V_i \setminus V_j^i$ and we create a link from i to k with the probability:

$$\text{Prob}(i \rightarrow k) = f(d(i,k))n_{x(k)}h_i^{d(i,k)}/[\Sigma_{l \in G \setminus Vi \setminus Vj} i\ n_{x(l)}h_i^{d(i,l)}],$$

where $n_{x(k)}$ is the number of nodes in $G \setminus V_i \setminus V_j^i$ having the same state as k, *i.e.*, $n_{x(k)}= n_S$ (resp. n_W, n_O) if k is susceptible (resp. overweight, obese). We will consider in the simulations 3 versions for the function f:

- Version 1: $f(d(i,w))=1$, if $d(i,w)=0$; =0 elsewhere

- Version 2: $f(d(i,w))=1$, if $d(i,w)=0$ or 1; =0 elsewhere

- Version 3: $f(d(i,w))=1$, if $d(i,w)=0$, 1 or 2,

these versions being used in the individual centred network for representing three types of progressively increasing influence: exogenous heterogeneous (individual-cultural, Version 1), exogenous homogeneous (individual-social, Version 2), endogenous (individual-individual, Version 3)

3. Change the states $x(j)$, for all j at the end of links created, by increasing their obesity weight of one level (S to W, W to O, O to O)

4. Generate a new τ and go to **2**

5. Stop when the graph G is no more changing.

3.2 Homophilic dynamics simulations

On Figure 2, we have fixed the corporal states (obese, overweight and normal) following the distribution of the BMI in the French population [11] in 2009: obese (14,5%), overweight (31.9%,) and normal (53,6%) individuals. The tolerance has been taken at the level 0.25 and the connection probability has been chosen following the Version 1. Directed networks with 1000 nodes each have been simulated, with a probability to have forward directional (resp. bidirectional) links equal to a=0.6 (resp. b=0.2). The node positioning has been done following the attraction-repulsion Fruchterman-Reingold algorithm [12].

3.3 Equilibrium configurations

Under the homophilic rule, the networks are converging until an equilibrium configuration of both links of the undirected graph architecture and node states, independently of the initial architecture and initial state distribution. By using a simulation engine of the social network, we can study the speed of convergence to this equilibrium for all the initial topologies proposed in Section 2. The Figure 4 shows that the relaxation time to the steady state (related to the speed of convergence to equilibrium) depends on the network topology. The shape of the initial and final "in-degree" distributions are about the same after applying the homophilic dynamics (Figures 4 and 5), but we can show that paradoxically in the small-word initial

topology, the mean clustering coefficient diminishes, but the marginal clustering coefficient C_s calculated for each state s increases (this phenomenon being due to the modification of the state distribution): $C_s = \langle X_s \rangle / N$, where $\langle X_s \rangle$ is the expectation of the random variable equal to the number of nodes in state s linked to a node in the same state s. The global clustering coefficient C is defined by: $C = \langle X \rangle / N$, where $\langle X \rangle$ is the expectation of the random variable equal to the number of couples of linked nodes having the same state. The final value of the homophily depends weakly on the topology (Figure 6). The final configuration of the network has always the homophily maximum, the segregation into 3 groups depending on the topology (Figures 6 and 7).

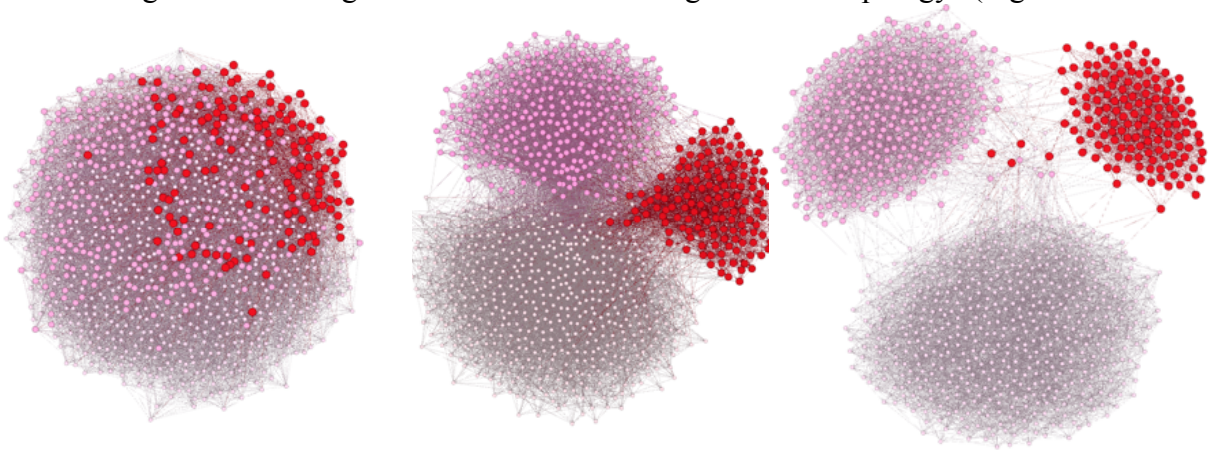

Figure 3: Dynamics with a progressive clustering (from left to right) inside a small-world directed network with initial proportion of obese individuals in red (14,5%), overweight in pink (31.9%,) and normal in white (53,6%), with 0.25 tolerance and connection probability of the Version 1

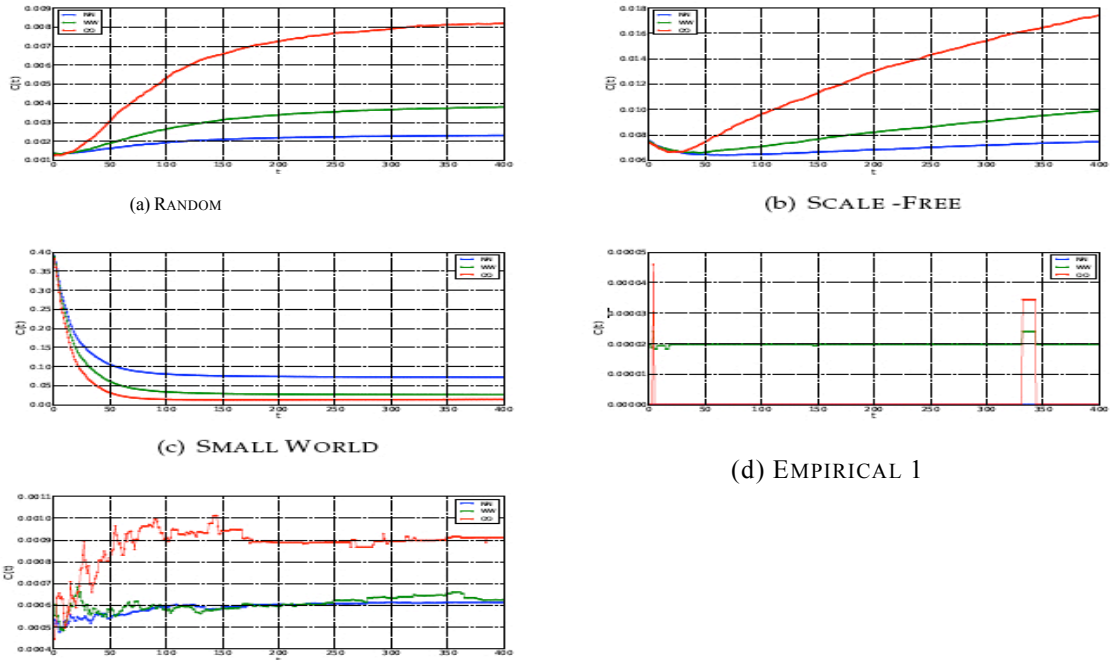

(a) RANDOM

(b) SCALE -FREE

(c) SMALL WORLD

(d) EMPIRICAL 1

(e) EMPIRICAL 2

Figure 4: Evolution of the marginal clustering coefficient C_s for each state s and for the architectures and initial distribution of states (normal in blue, overweight in green and obese in red) of Section 2, with tolerance h equal to 0.25 and connection probability of the Version 3

In order to improve this study, a theoretical estimation of the speed of convergence to the equilibrium configuration could be made, as well as the consideration of the robustness of the process: do exist more than one equilibrium state, and if yes, are other "attractors" only fixed states or possibly periodic configurations? Which network parameters are critical, *i.e.*, at which parameter perturbation (provoking a change in number or nature of attractors) is sensitive the dynamics? Which perturbation of the initial configuration of the social network changes attraction (stability) basins? All these problems will be addressed in a future work.

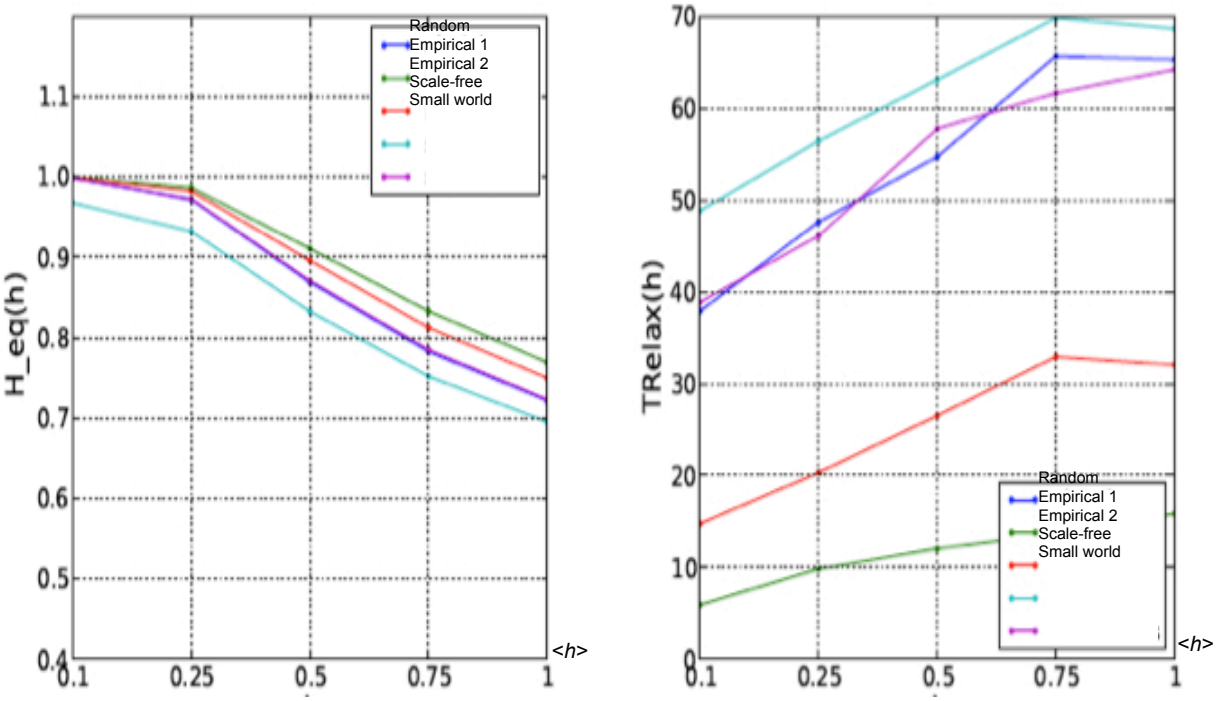

Figure 5: Left: with connection probability of the Version 3, evolution of the global connectivity *C* coefficient at equilibrium as function of the mean tolerance <*h*>. Right: evolution of the relaxation time to equilibrium as function of the mean tolerance <*h*>

3.4 Examples of dynamics of obesity

Homophily defined as above suggests that individuals tend to interact with those who resemble them in terms of alimentary behaviour and the structure of the social fabric is involved in the increase and current development of obesity [17-29]. By using the simulation rules of Section 3.1., we compare the simulated graphs with real data in case of obesity. Four situations have been tested: the pure random graph (links chosen by chance), the free scale graph (the distribution of out-degrees follows a power law), the small world graph (links around hub nodes are reinforced) and homophilic graphs, with different versions of probability of linking. The approach described above has highlighted the necessity to integrate a random dynamics at each scale to better understand the evolution of the obesity pathology, *e.g.*, in Figure 7, the connectivity of the real social network representing the obesity spread is better taken into account in the homophilic network Version 1 (the qualitative differences between versions being small) than in the other versions: random, scale-free or small world ones.

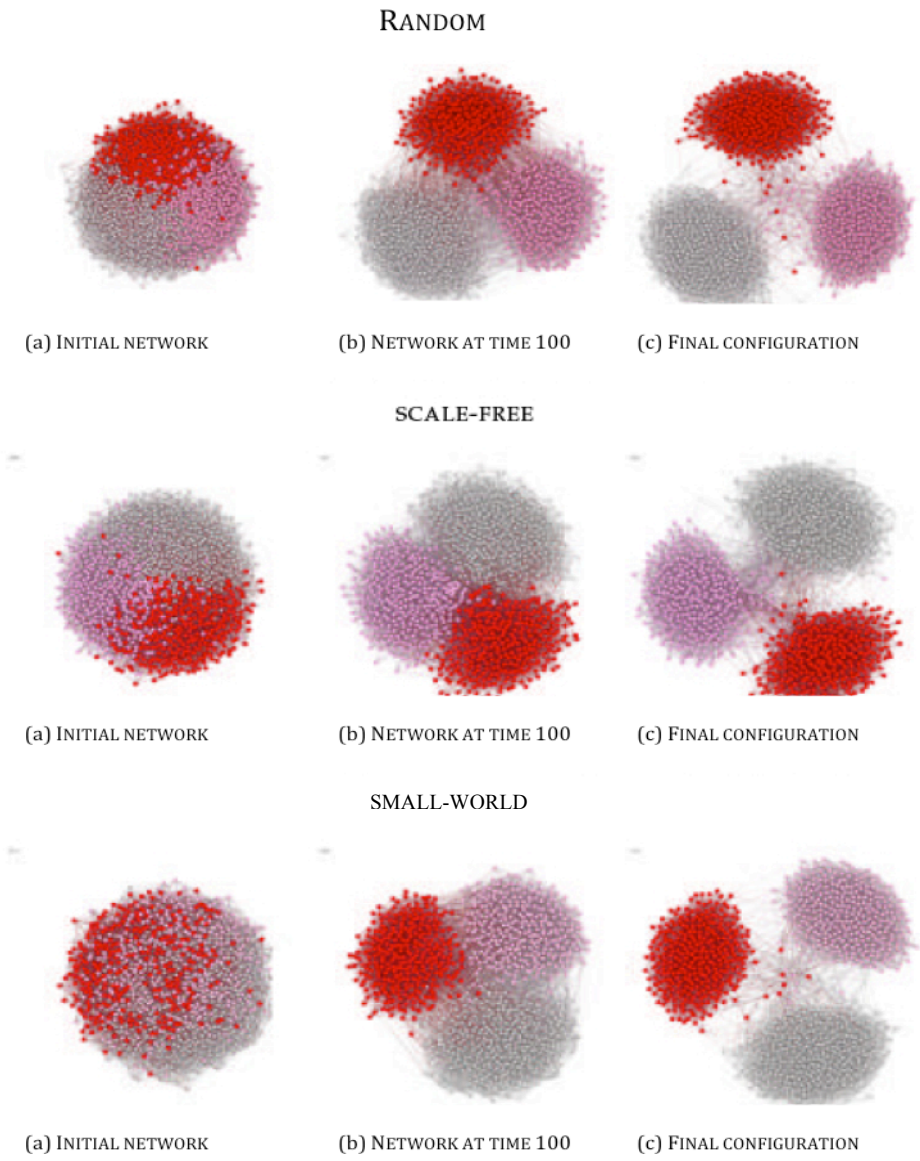

Figure 6: Homophilic dynamics for the architectures and initial distributions of states of Figure 5, with tolerance *t* equal to 0.25 and connection probability of Version 3

4 Demographic dynamics

For evaluating the number of suceptibles and to define them by age and sex (which are important factors in the occurrence of obesity), we need to develop a dynamic projection model by using key socio-demographic indicators of the studied population. The lack of documented data often not allows to use performant tools of Individual Based Model (IBM) demographic simulation as FELICIE, DESTINIE, OMPHALE, MOGDEN, LIFEPATH,… [17-19]. So we proposed the model DOPAMID which requires less raw data for its dynamic projection method.

4.1 DOPAMID model overview

The objective of the model is to make evolve a population in function of statistics based on its composition in age classes. This evolution allows to express patterns in the composition of the population. Statistics used are the distribution of the population according to the age and sex of the individuals, mortality, fertility, composition of families as well as the dependency of individuals. Starting from a population

respecting these statistics, the model advances in time over a period of up to 90 years. Population members will therefore age, reproduce, die…

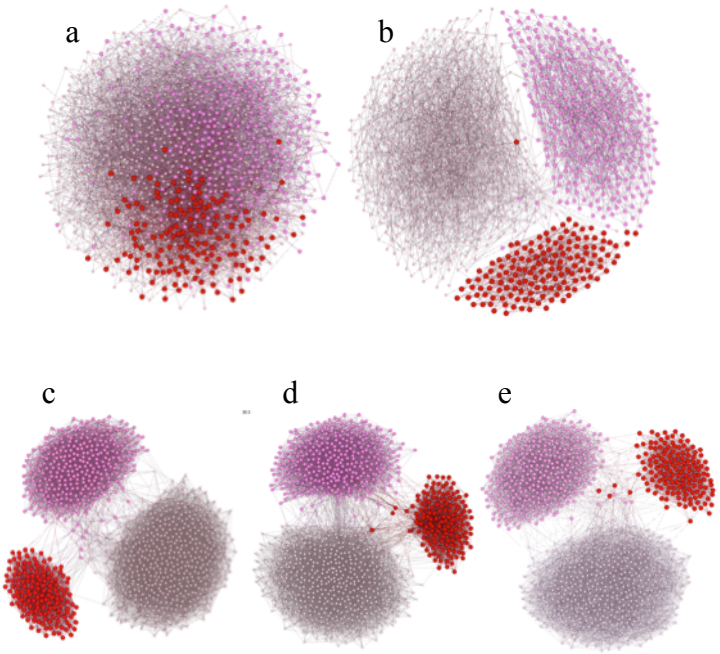

Figure 7: Simulation of social graphs representing obesity network: initial conditions (a), asymptotic state in case of an homophilic graph Version 1 (b), random graph (c), scale free graph (d) and small world graph (e)

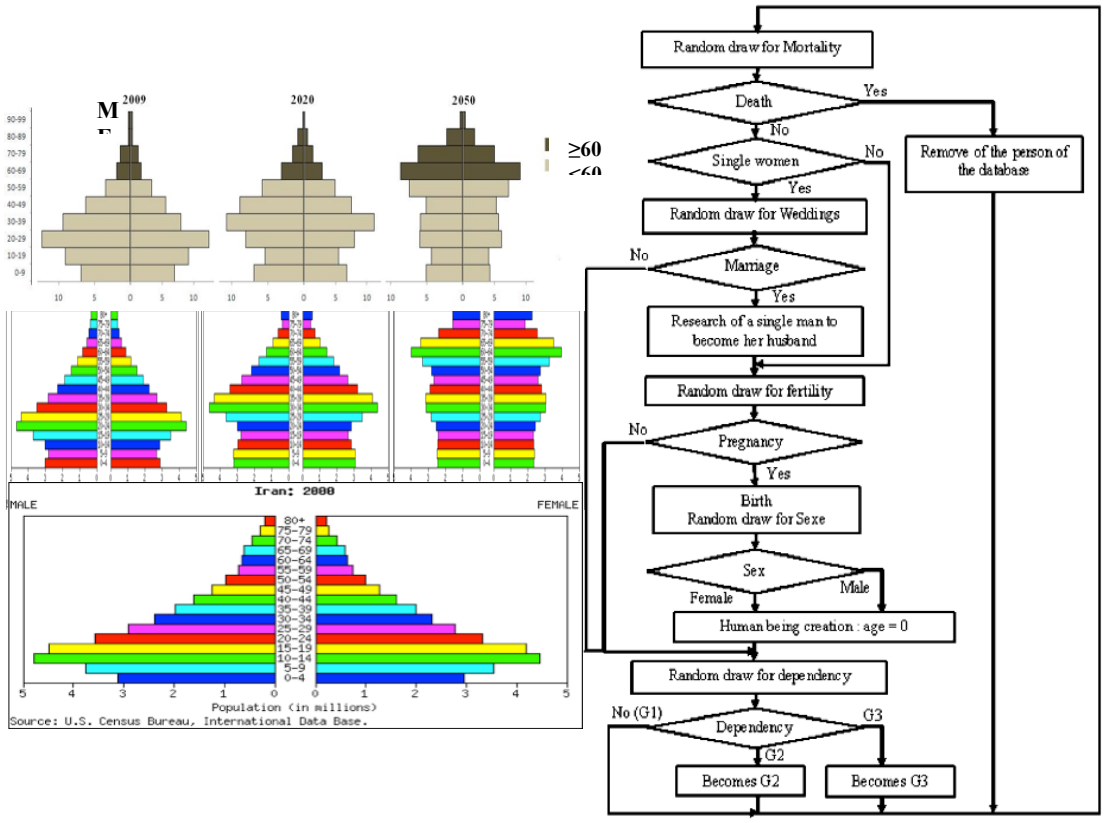

Figure 8: Left: top: simulation made by our DOPAMID model of the evolution of Iranian demography between 2009 and 2050, middle: same simulation by using the simulation algorithm of the US Census Bureau, bottom: real data in 2000. Right: ageing algorithm applied each year for each human being (http://www.census.gov/population/international/)

4.2 The model algorithm

The decision taking is based on the generation of random numbers. For example, for sex at birth, statistics are: 51,35 % of males and 48,65 % of females. A random number between 0 and 1 is generated, and if it is less than 0,5135, the child will be a boy and a girl, if it exceeds. The initial number of human beings is supposed to be equal to 10,000. Each year and for each person, the scenario described in Figure 10 is applied.

We have for example simulated the evolution of the Iranian population between 2009 and 2050 (cf. Figure 8), for validating our model from real data and simulated projections coming from the US Bureau of Census [20]. A study of an important pathology associated to obesity, the type 2 diabetes [21], shows that the proportion of diabetic is equal to 3.5% in normal weight Iranian population, and 6.4% and 14.3% respectively in overweight and obese population, representing an Odd ratio of respectively 1.7 (the 95%-confidence interval being equal to [1.1, 2.5]) and 4 (the 95%-confidence interval being equal to [2.7, 5.8]). The demographic modelling allows calculating for each age class the proportion of obese and the risk of type 2 diabetes: here for example, the Odd ratio per 10 years is equal to 1.2 (the 95%-confidence interval being equal to [1.1-1.4]). A precise distribution with respect to gender and age class can be found in [22].

The connection between the demographic dynamics and the social networks has to be carefully made in the future: it needs a deep knowledge (presently absent) on the structure by age class into the social networks, as well as on the rules of transmission and intergenerational inheritance of the alimentation and adapted physical activity habits. Nevertheless, the evolution of the size of the whole population has to be already introduced in order to fix the number of nodes and interaction links for calibrating our social networks models.

5 Towards the proposal of an obesity preventive policy

The BMI has been defined about two centuries ago by a Belgian physician (A. Quételet) and it represents the basic tool for doing the obesity diagnosis and therapeutic surveillance New policies are now needed to contain this world pandemic and we suggest the following ways in order to watch and cure the obesity:

1) defining new optimal threshold for defining obesity states and associated risks from the classical BMI [23]
2) using a new index called the Body Adiposity Index (DAI) allowing differentiating muscular, skeletal and adipose masses [24]
3) elucidating all genetic factors involved in the obesity genesis (endogenous individual factors) [25]
4) searching for all metabolic factors implied in the development of the disease (nutrition, as well as predisposition to use glycolytic pathway more than oxidative phosphorylation in order to produce energy, like in the Warburg effect [26,27]
5) identifying all social factors favouring the present epidemic in particular exogenous environmental factors, in social networks involving young individuals (educative, sportive, familial, social,…) in order to prevent actively the disease before the adult age (for example, cf. www.repop.fr) at school or during the hospital sojourns [28]
6) studying all psycho-social factors leading to obesity stigmatization in relation to mental body image and self-esteem [29].

6 The dynamics of contacts

6.1 Influence of the contact duration

Let introduce now a contact duration τ and a contagion coefficient β possibly depending on τ [30]. It is possible to retrieve the quad-

ratic term of interaction already present in all the classical models of contagion [30-40] by using a stochastic approach coming from the random chemistry of contacts [41-57] for interpreting the rules of Section 3.1. developed in [58]. We have, if the demographic dynamics is neglected as well as the overweight transition:

$$P(S(t+dt)=k,\ O(t+dt)=N-k) - P(S(t)=k,\ O(t)=N-k) = -\beta k(N-k)dt \int_0^T P(S(t-\tau)=k,\ O(t-\tau)=N-k)d\tau + \beta(k+1)(N-k-1)dt \int_0^T P(S(t-\tau)=k+1,\ O(t-\tau)=N-k-1)d\tau,$$

where $S(t)$ (resp. $O(t)$) is the size of the susceptible (resp. obese) population at time t.

The microscopic equation above leads to the mean differential equation ruling the expectations of the random variables S and I:

$$dE(S(t))/dt = -\beta \int_0^T E(S(t-\tau))E(I(t-\tau))d\tau$$

and to the macroscopic equation:

$$dS/d = -\beta \int_0^T S(t-\tau)I(t-\tau)d\tau,$$

in which we found the quadratic term of the classical models of contagion. This quadratic term is also present in the interaction potential of Hopfield like networks in which the study of the robustness with respect to the contagion parameter change has been performed [59-69] as well as in recent studies taking into account the spatial character of the disease spread [70-79].

6.2 Confinement and Saturation

The localisation of contamination has been treated by different authors [80, 81]. When contagion occurs in confined locations (like professional, educational or residence buildings), we can use saturation dynamics terms coming from the enzymatic kinetics (cf. for example [82, 83]) for expressing all the possibilities to have together k from the S susceptible population and i from the O obese population in n contagion sites located in B buildings. We call this quantity the partition function $P(S,0)$ and $B(\partial^2 \mathrm{Log}P/\partial \mathrm{Log}S\partial \mathrm{Log}O)/n$ is the total mean number of occupied sites, considered as proportional to the infection rate, and we have:

$$dS(t)/dt = -\beta B(\partial^2 \mathrm{Log}P/\partial \mathrm{Log}S\partial \mathrm{Log}O)/n + fS - \mu S + \rho O$$
$$dO(t)/dt = \beta B(\partial^2 \mathrm{Log}P/\partial \mathrm{Log}S\partial \mathrm{Log}O)/n + f'O - \mu'O - \rho O,$$

where the demographic parameters f (fecundity) and μ (mortality) are taken into account for the susceptible as well as for the obese population (f' and μ') and where ρ denotes the recovering rate at which an obese recovers an healthy weight.

An example of such a dynamics is the saturation Michaëlian one, if there is only one contagion site:

$$P(S,O) = (1 + v_{C,S}S)(1 + v_{C,O}O),$$

where $v_{C,S}$ (resp. $v_{C,I}$) is the probability for a susceptible (resp. obese) to access a contagion site. If $v_{C,S} = 1$ and $v_{C,O} << 1$, then the infection rate equals about $\beta SO/(1+S)$ and the equations of the dynamics are:

$$dS(t) = -\beta S(t)O(t)/(1+S(t)) + (f - \mu + \rho)S(t)$$
$$dO(t) = \beta S(t)O(t)/(1+S(t)) + (f' - \mu' - \rho)O(t)$$

6.3 Non-linear interactions and complex dynamics

Threshold interactions used in classical Hopfield like models [59-69] are already non-linear ones, but take into account only pair contacts, neglecting possible additional effects due to the presence and mutual interaction of more than two individuals in the contagion process. It is now possible to introduce for modelling this possible potentialization a formalism for being able to define non-linear n-uples interactions [84] and simulate the model in a spatial Markovian context like in the present study or in certain case of remote spatial influence (due to the new social networking on the web) in a renewal context [85], as well as different time scales modelling complex dynamics, for separating the local dynamics from the global trend of the obesity epidemic [86].

7 Conclusion

Results shown in this paper about social networks involved in obesity have been obtained by modeling and simulating networks with various initial architecture (random, scale-free, small-world, empirical) evolving under the so-called social homophilic constraint. The computed evolution of these networks seems to be similar to the real one observed in developed countries for a socially "contagious" disease, the obesity. Complementary studies are now required allowing from large samples estimating the unobservable parameters linked both to initial network architecture (taking into account the specificity of the sub-populations of susceptibles, *e.g.*, differences between the schoolchildren, professional and elderly people networks) and to their weights evolution, as well as incorporating the demographic dynamics [87], a more accurate model of social contacts through which the disease can spread out and some elements about the psychogenesis of the homophilic dynamics [88-90] and their surveillance at home [91,92] or on Twitter [93,94].

Acknowledgment

The research for this work was supported, in part, by the PHC Maghreb SCIM.

References

[1] A. Myers, and J.C. Rosen, "Obesity stigmatization and coping: relation to mental health symptoms, body image, and self-esteem," Int. J. Obesity Relat. Metab. Disord., vol. 23, pp. 221–230, 1999.

[2] H. Tunstall-Pedoe, MONICA Project. World's largest study of heart disease, stroke, risk factors, and population trends 1979-2002", WHO, Geneva, 2003.

[3] International Association for the Study of Obesity Obesity: preventing and managing the global epidemic, International Obesity Task Force Prevalence Data, TRS 894, WHO, Geneva, 2000.

[4] G. Maillard, M.A. Charles, N. Thibault, A. Forhan, C. Sermet, A. Basdevant, and E. Eschwege, "Trends in the prevalence of obesity in the french adult population between 1980 and 1991," Int. J. Obesity Relat. Metab. Disord., vol. 23 , pp. 389-394, 1999.

[5] J. Barth, "What should we do about the obesity epidemic?," Pract. Diab. Int., vol. 19, pp. 119-122, 2002.

[6] T. de Saint-Pol, "Obésité et milieux sociaux en France : les inégalités augmentent," Bulletin Epidemiologique Hebdomadair, vol. 20, pp. 175-179, 2008.

[7] J. Laitinen, C. Power, and M.R Jarvelin, "Family social class, maternal body mass index, childhood body mass index, and age at menarche as predictors of adult obesity," Am. J. Clin. Nutrition, vol. 74, pp. 287-294, 2001.

[8] M. Scharoun-Lee, L.S. Adair, J.S. Kaufman, and P. Gordon-Larsen, "Obesity, race/ethnicity and the multiple dimensions of socio-economic status during the transition to adulthood: A factor analysis approach," Social Science and Medicine, vol. 6, pp. 708-716, 2009.

[9] N. Christakis, and J. Fowler, "The spread of obesity in a large social network over 32 years," The New England Journal of Medicine, vol. 17, pp. 77-82, 2006.

[10] E. Cohen-Cole, and J.M. Fletcher, "Is obesity contagious? Social networks vs. environmental factors in the obesity epidemic," Journal of Health Economics, vol. 27, pp. 1382-1387, 2008.

[11] ObEpi-Roche, Enquête épidémiologique nationale sur le surpoids et l'obésité, Roche, Paris, 2009.

[12] T. Fruchterman, and E. Reingold, "Graph drawing by force-directed placement," Software: Practice and Experience, vol. 21, pp. 1129–1164, 1991.

[13] J. Demongeot, H. Ben Amor, A. Elena, P. Gillois, M. Noual, and S. Sené, "Robustness of regulatory networks. A generic approach with applications at different levels: physiologic, metabolic and genetic," International Journal of Molecular Sciences, vol. 10, pp. 4437–4473, 2009.

[14] J. Demongeot, A. Elena, M. Noual, S. Sené, and F. Thuderoz, "«Immunetworks», intersecting circuits and dynamics," Journal of Theoretical Biology, vol. 280, pp. 19-33, 2011.

[15] J. Demongeot, E. Goles, M. Morvan, M. Noual, and S. Sené, "Attraction basins as gauges of environmental robustness in biological complex systems," PloS ONE, vol. 5, 8, 2010.

[16] J. Demongeot, M. Noual, and S. Sené, "Combinatorics of Boolean automata circuits dynamics," Discrete Applied Mathematics, vol. 160, pp. 398-415, 2012.

[17] J. Gaymu, P. Festy, M. Poulain, and G. Beets, "From elderly population projections to policy implications, in: Future elderly living conditions in Europe (Felicie)," Les cahiers de l'INED, vol. 162, pp. 267-290, 2008.

[18] M. Duée, and C. Rebillard, La dépendance des personnes âgées: une projection en 2040, Données sociales - La société française, INSEE, Paris, 2006.

[19] J. Légaré, Y. Décarie, Using Statistics Canada Life-Paths Microsimulation Model to Project the Health Status of Canadian Elderly, SEDAP Research Paper 227, SEDAP, Hamilton, 2008.

[20] http://www.census.gov/population/international/

[21] H. Harati, F. Hadaegh, N. Saadat, and F. Azizi, "Population-based incidence of Type 2 diabetes and its associated risk factors: results from a six-year cohort study in Iran," BMC Public Health, vol. 9, 186, 2009.

[22] F. Hosseinpanah, M. Barzin, P.S. Eskandary, P. Mirmiran, and F. Azizi, "Trends of obesity and abdominal obesity in Tehranian adults: a cohort study," BMC Public Health, vol. 9, 426, 2009.

[23] V. Dauphinot, H. Wolff, F. Naudin, R. Gueguen, C. Sermet, J.M. Gaspoz, and M.P. Kossovsky, "New obesity body mass index threshold for self-reported data," J. Epidemiology Com. Health, vol. 63, pp. 128-132, 2009.

[24] R.N., Bergman, D. Stefanovski, T.A. Buchanan, A.E. Sumner, J.C. Reynolds, N.C. Sebring, A.H. Xiang, and R.M. Watanabe, "A Better Index of Body Adiposity," Obesity, vol. 19, pp. 1083-1089, 2011.

[25] A. Baranova, R. Collantes, S.J. Gowder, H. Elariny, K. Schlauch, A. Younoszai, S. King, M. Randhawa, S. Pusulury, T. Alsheddi, J.P. Ong, L.M. Martin, V. Chandhoke, Z.M. Zobair, and M.D. Younossi, "Obesity-related Differential Gene Expression in the Visceral Adipose Tissue," Obesity Surgery, vol. 15, pp. 758-765, 2005.

[26] L. Demetrius, J. Coy, and J. Tuszynski, "Cancer proliferation and therapy: the Warburg effect and quantum metabolism," Theoretical Biology and Medical Modelling, vol. 7, 2, 2010.

[27] L. Demetrius, and J. Tuszynski, "Quantum metabolism explains the allometric scaling of metabolic rates," J. Royal Soc. Interface, vol. 7, pp. 507-514, 2010.

[28] C. Delhumeau, J. Demongeot, F. Langlois, and C. Taramasco, "Modelling the hospital length of stay in Diagnosis Related Groups Data Bases," in: IEEE ARES-CISIS' 09 & BT' 09, IEEE Press, Piscataway, pp. 955-960, 2009.

[29] A. Myers, and J.C. Rosen, "Obesity stigmatization and coping: relation to mental health symptoms, body image, and self-esteem," Int. J. Obes. Relat. Metab. Disord., vol. 23, pp. 221–230, 1999.

[30] J. Demongeot, O. Hansen, H. Hessami, A.S. Jannot, J. Mintsa, M. Rachdi, and C. Taramasco, "Random modelling of contagious diseases," Acta Biotheoretica, vol. 61, pp. 141-172, 2013.

[31] D. Bernoulli, Essai d'une nouvelle analyse de la mortalité causée par la petite vérole, et des avantages de l'inoculation pour la prévenir, Mém. Acad. Roy. Sci., Paris, 1760.

[32] J. d'Alembert, Onzième Mémoire : sur l'application du calcul des probabilités à l'inoculation de la petite vérole ; notes sur le mémoire précédent ; théorie mathématique de l'inoculation, *in:* Opuscules mathématiques, David, Paris, 1761, pp. 26-95, 1761.

[33] W.H. Hamer, The Milroy lectures on epidemic disease in England: the evidence of variability and persistency of type, Bedford Press, London, pp. 733-739, 1906.

[34] R. Ross, Prevention of Malaria, John Murray, London, 1910.

[35] J. Brownlee, "On the Curve of the Epidemic," The British Medical Journal, vol. 1, pp. 799-800, 1915.

[36] R. Ross, "Some a priori pathometric equations," The British Medical Journal, vol. 1, pp. 546-547, 1915.

[37] R. Ross, "An Application of the Theory of Probabilities to the Study of a priori Pathometry. Part I," Proceedings Royal Soc. London Series A, vol. 92, pp. 204-230, 1916.

[38] M.E Gibson, "Sir Ronald Ross and his contemporaries," J. Royal Society of Medicine, vol. 71, pp. 611-618, 1978.

[39] W.O. Kermack, and AG. McKendrick, "A contribution to the mathematical theory of epidemics," Proceedings Royal Soc. London Series A, vol. 115, pp. 700-721, 1927.

[40] W.O. Kermack, and A.G. McKendrick, "Contributions to the mathematical theory of epidemics. III. Further studies of the problem of endemicity," Proceedings Royal Soc. London Series A, vol. 121, pp. 141-194, 1933.

[41] M. Delbrück, "Statistical fluctuations in autocatalytic reactions," J. Chem. Phys., vol. 8, pp. 120-124, 1940.

[42] A.F. Bartholomay, "On the Linear Birth and Death Processes of Biology as Markoff Chains," Bull. Math. Biophys., vol. 20, pp. 97-118, 1958.

[43] A.F. Bartholomay, "Stochastic models for chemical reactions: I. Theory of the unimolecular reaction process," Bull. Math. Biophys., vol. 20, pp. 175-190, 1958.

[44] A.F. Bartholomay, "Stochastic models for chemical reactions: II. The unimolecular rate constant," Bull. Math. Biophys., vol. 21, pp. 363-373, 1959.

[45] D.A. McQuarrie, "Kinetics of small systems," J. Chem. Phys., vol. 38, pp. 433–436, 1963.

[46] D.A. McQuarrie, C.J. Jachimowski, and M.E. Russell, "Kinetics of small systems. II," J. Chem. Phys., vol. 40 pp. 2914-2921, 1964.

[47] C.J. Jachimowski, D.A. McQuarrie, and M.E. Russell, "A Stochastic Approach to Enzyme-Substrate Reactions," Biochemistry, vol. 3, pp. 1732-1736, 1964.

[48] D.A. McQuarrie, "Stochastic approach to chemical kinetics," J. Appl. Probab., vol. 4, pp. 413-478, 1967.

[49] M.R. Hoare, "Molecular Markov Processes," Nature, vol. 226, pp. 599-603, 1970.

[50] N.T.J. Bailey, "The simple stochastic epidemic: A complete solution in terms of known functions," Biometrika, vol. 50, pp. 235-240, 1963.

[51] K. Dietz, "Epidemics and Rumours: A Survey," Journal of the Royal Statistical Society Series A, vol. 130, pp. 505-528, 1967.

[52] J. Demongeot, "A stochastic model for the cellular metabolism," in: Recent Development in Stats, North Holland, Amsterdam, pp. 655-662, 1977.

[53] L. Allen, "An Introduction to Stochastic *Epidemic* Models," Mathematical Epidemiology, vol. 1945, pp. 81-130, 2008.

[54] C.J. Rhodes, L. Demetrius, Evolutionary Entropy Determines Invasion Success in Emergent Epidemics, PLoS ONE 5 (2010) e12951.

[55] T. Britton, Stochastic epidemic models: a Survey, Mathematical Biosciences 225 (2010) 24-35.

[56] D.T. Gillespie, A General Method for Numerically Simulating the Stochastic Time Evolution of Coupled Chemical Reactions, Journal of Computational Physics 22 (1970) 403–434.

[57] P. Magal, and S. Ruan, "Susceptible-Infectious -Recovered Models Revisited: From the Individual Level to the Population Level," Bulletin of Mathematical Biology (Submitted).

[58] C. Taramasco, "Impact de l'obésité sur les structures sociales et impact des structures sociales sur l'obésité ? Facteurs individuels et environnementaux," PhD thesis, Ecole Polytechnique, Paris, 2011.

[59] M. Aldana, and P. Cluzel, "A natural class of robust networks," Proc. Natl. Acad. Sci. USA, vol. 100, pp. 8710-8714, 2003.

[60] J. Demongeot, A. Elena, and S. Sené, “Robustness in neural and genetic networks,” Acta Biotheoretica, vol. 56 pp. 27-49, 2008.
[61] H. Ben Amor, J. Demongeot, A. Elena, and S. Sené, “Structural Sensitivity of Neural and Genetic Networks,” Lecture Notes in Computer Science, vol. 5317, pp. 973-986, 2008.
[62] A. Elena, and J. Demongeot, “Interaction motifs in regulatory networks and structural robustness,” in: IEEE ARES-CISIS' 08, IEEE Press, Piscataway, pp. 682-686, 2008.
[63] A. Elena, H. Ben-Amor, N. Glade, and J. Demongeot, “Motifs in regulatory networks and their structural robustness,” in: IEEE BIBE' 08, IEEE Press, Piscataway, pp. 234-242, 2008.
[64] A. Elena, Robustesse des réseaux d’automates à seuil, University J. Fourier, Grenoble, 2009.
[65] J. Demongeot, A. Elena, M. Noual, and S. Sené, “Random Boolean Networks and Attractors of their Intersecting Circuits,” in: Proceedings IEEE AINA' 11, IEEE Proceedings, Piscataway, pp. 483-487, 2011.
[66] N. Glade, A. Elena, N. Fanchon, J. Demongeot, and H. Ben Amor, “Determination, optimization and taxonomy of regulatory networks. The example of Arabidopsis thaliana flower morphogenesis,” in: IEEE AINA' 11, IEEE Press, Piscataway, pp. 488-494, 2011.
[67] J. Demongeot, and J. Waku, “Robustness in genetic regulatory networks, II Application to genetic threshold Boolean random regulatory networks (getBren),” Comptes Rendus Mathématique, vol. 350, pp. 225-228, 2012.
[68] J. Demongeot, and J. Waku, “Robustness in genetic regulatory networks, IV Application to genetic networks controlling the cell cycle,” Comptes Rendus Mathématique, vol. 350, pp. 293-298, 2012.
[69] J. Demongeot, E. Drouet, A. Moreira, Y. Rechoum, and S. Sené, “Micro-RNAs: viral genome and robustness of the genes expression in host,” Phil. Trans. Royal Soc. A, vol. 367, pp. 4941-4965, 2009.
[70] J.S. Koopman, and I.M. Longini, “The Ecological Effects of Individual Exposures and Nonlinear Disease Dynamics in Populations,” Am. J. Public Health, vol. 84, pp. 836-842, 1994.
[71] M. Kretzschmar, “Measures of concurrency in networks and the spread of infectious disease,” Mathematical Biosciences, vol. 133, pp. 165-195, 1996.
[72] M.M. Sathik, and A.A. Rasheed, “Social Network Analysis in an Online Blogosphere,” International Journal of Engineering Science and Technology, vol. 3, pp. 117-121, 2011.
[74] J. Gaudart, R. Giorgi, B. Poudiougou, S. Ranque, O. Doumbo, and J. Demongeot, “Spatial cluster detection: principle and application of different general methods,” Rev. Epid. Santé Pub., vol. 55, pp. 297-306, 2007.
[75] J. Gaudart, O. Touré, N. Dessay, A.L. Dicko, S. Ranque, L. Forest, J. Demongeot, and O.K. Doumbo, “Modelling malaria incidence with environmental dependency in a locality of Sudanese savannah area, Mali,” Malaria Journal, vol. 8, e61, 2009.
[76] J. Gaudart, M. Ghassani, J. Mintsa, M. Rachdi, J. Waku, and J. Demongeot, “Demography and Diffusion in epidemics: Malaria and Black Death spread,” Acta Biotheoretica, vol. 58, pp. 277-305, 2010.
[77] J. Demongeot, J. Gaudart, J. Mintsa, and M. Rachdi, “Demography in epidemics modelling,” Com. Pure & Appl. Analysis, vol. 11, pp. 61-82, 2012.
[78] J. Demongeot, J. Gaudart, A. Lontos, E. Promayon, J. Mintsa, and M. Rachdi, “Least diffusion zones in morphogenesis and epidemiology,” Int. J. Bifurcation and Chaos, vol. 22, 50028, 2012.
[79] J. Demongeot, M. Ghassani, M. Rachdi, I. Ouassou, and C. Taramasco, “Archimedean Copula and Contagion Modelling in Epidemiology,” Networks & Heterogeneous Media, vol. 8, pp. 149-170, 2013.
[80] P. Amarasekare, “Interactions between local dynamics and dispersal: insights from single species models,” Theor. Population Biology, vol. 53, pp. 44-59, 1998.
[81] J.A.N. Filipe, and G.J. Gibson, “Comparing approximations to spatio-temporal models for Epidemics with local Spread,” Bull. Math. Biol., vol. 63, pp. 603-624, 2001.
[82] J. Demongeot, and M. Laurent, “Sigmoidicity in allosteric models,” Math. Biosci., vol. 67, pp. 1-17, 1983.
[83] J. Demongeot, and N. Kellershohn, “Glycolytic oscillations: an attempt to an "in vitro" reconstitution of the higher part of glycolysis,” Lectures Notes in Biomaths, vol. 49, pp. 17-31, 1983.
[84] J. Demongeot, and S. Sené, “The singular power of the environment on nonlinear Hopfield networks,” in: CMSB’11, ACM Proc., New York, pp. 55-64, 2011.
[85] J. Demongeot, and J. Fricot, “Random fields and renewal potentials,” NATO ASI Serie F 20, pp. 71–84, 1986.
[86] M. Barthélemy, J.P. Nadal, and H. Berestycki, “Disentangling collective trends from local dynamics,” P. Natl. Acad. Sci. USA, vol. 107, pp. 7629–7634, 2010.
[87] J. Demongeot, O. Hansen, H. Hessami, A.S. Jannot, J. Mintsa, M. Rachdi, and C. Taramasco, “Random modelling of contagious diseases,”Acta Biotheoretica, vol. 61, pp. 141-172, 2013.
[88] B. Trojaola-Zapirain, F. Carminati, A. Gonzales Torres, E. Gonzales de Mendivil, C. Fouassier, M. Gex-Fabry, F. Martin, J. Labarere, J. Demongeot, E.N. Lorincz, and G. Galli Carminati, “Group unconscious common orientation: exploratory study in OMIE group training for therapists,” Neuroquantology, vol. 12, pp. 139-150, 2014.
[89] S.A. Cunningham, E. Vaquera, C.C. Maturo, and K.M. Venkat Narayan, “Is there evidence that friends influence body weight? A systematic review of empirical research,” Social Science and Medicine, vol. 75, pp. 1175-1183, 2012.
[90] W.A. Brechwald, and M.J. Prinstein, “Beyond homophily: a decade of advances in understanding peer influence processes,” Journal of Research on Adolescence, vol. 21, 166e179, 2011.
[91] G. Virone, N. Vuillerme, M. Mokhtari, and J. Demongeot, “Persistent Behaviour in Healthcare Facilities: from actimetric tele-surveillance to therapy education,” Lect. Notes Comp. Sci., vol. 8458, pp. 297-311, 2014.
[92] J. Demongeot, H. Ben Amor, H. Hazgui, and J. Waku, “Robustness in Neural and Genetic Regulatory Networks: Mathematical Approach and Biological Applications,” Acta Biotheoretica, vol. 62 , 2014.

[93] E. Aramaki, S. Maskawa, and M. Morita, "Twitter catches the flu: detecting influenza epidemics using Twitter," in: EMNLP'11, ACL, Stroudsburg, PA, USA, pp. 1568-1576, 2011.
[94] T. Sakaki, M. Okazaki, and Y. Matsuo, "Earthquake shakes Twitter users: real-time event detection by social sensors," in: WWW'10, ACM, New York, pp. 851-860, 2010.

Fractal geometry and urban patterns – from exploring morphology to applications in planning

Pierre Frankhauser (University of Besançon)

Fractal geometry turned out to be a powerful approach in many domains for describing complex structures which have multiscale properties. In particular, fractal analysis allows making evident scaling properties and hence underlying structural order principles which cannot be discovered by other measuring approaches like densities which refer to one unique scale. We present here how this approach helps to analyze the distribution of build-up surface in urban patterns and how it can be used to link these morphologiocal properties to specific contexts of urbanization. Indeed, contemporary urban patterns have usually an irregular shape reminding rather deposits on surfaces or corrosive phenomena. This can be explained by the fact that urban growth is nowadays often a weakly controlled process where a couple of agents interact on different scales. Hence urbanization can be seen as self-organization process. Nevertheless it can be surprising that these interactions generate structures which follow obviously underlying order principle. In contrast there exist, too, urban planning concepts, which follow scaling principles by definition, what allows reflecting on elements to what extend such patterns correspond to optimization principles. We start by introducing fractal models which illustrate how fractals can be linked to urban patterns. Then we introduce the measuring methods used and we discuss the results obtained. In a last part we show a possible link to the order parameter concept used in synergetics and we finish by giving an outlook how the fractal approach can be useful for developing planning concepts in the sense of optimization.

Hamiltonian Chaos: Two-temperature Equilibrium in Hot Plasmas predicted

Otto E. Rossler

Faculty of Mathematics and Science, University of Tübingen, Auf der Morgenstelle 8, 72076 Tübingen, Germany

Abstract

Deterministic Hamiltonian chaos, as discovered by Poincaré, remains good for surprises. It not only explains equilibrium thermodynamics as shown by Sinai in 1970, with a recent extension to far-from-equilibrium thermodynamics. It in addition also implies cryodynamics, sister discipline to thermodynamics, which governs globular star clusters and the cosmos at large. It is proposed that Hamiltonian chaos thirdly entails a new mixed theory, "thermocryodynamics." The latter describes hot plasmas in the electrostatic approximation. The thermal equilibrium of a confined plasma predictably combines two sub-equilibria of differing temperatures – and this even in two ways. The new chaos-based paradigm is bound to have technological consequences.

Key words: Poincaré, classical chaos, plasma, croydynamics, thermocryodynamics, multiple equilibria (April 18, 2014)

Introduction

Poincaré [1] invented Hamiltonian chaos theory. The latter can deterministically explain thermodynamics, both in its equilibrium features as shown by Sinai [2,3] and in its far-from-equilibrium features [4]. Hereby repulsive, either hard-disk or short-range, potentials are in charge. A switch to attractive infinite-range Newtonian potentials yields the new science of "cryodynamics", sister discipline to thermodynamics [5]. This new discipline at the same time is the oldest since it could have been founded by Newton himself. In cryodynamics, the deterministic equilibrium state is not stable as in thermodynamics, but unstable.

In the following, a new third chaos-based fundamental classical Newtonian theory is offered: "deterministic thermocryodynamics." It deals with mixed – both repulsion and attraction based – Hamiltonian systems – that is, with hot plasmas in the electrostatic approximation.

Hot Plasmas form a Third Fundamental Paradigm

Hot plasmas are more complicated than pure-repulsion or pure-attraction based chaotic gases. The latter gases are at the root of multi-particle celestial mechanics [5]. In contrast to these two pure cases, a hot plasma is a hybrid. While involving reciprocal attraction between its two components, it in addition is characterized by repulsion between the members of either particle class; electrons and protons are both repulsive among their own kind. This two-tiered effect makes the theory much more complicated. If one assumes the simplified case that the two forces were pure Newtonian and anti-Newtonian, respectively, to avoid the complications caused by electromagnetism, then a third chaos-based theory applies which can be called "thermocryodynamics."

The finite-number-of-degrees-of-freedom characteristic of both the Newtonian and the anti-Newtonian (smooth Boltzmannian) paradigm is, strictly speaking, no longer valid in plasma theory because the infinitely many degrees of freedom of Maxwell's field equations enter as well, more or less mitigated by quantum

mechanics. This formal complication can be heuristically neglected in a first discussion under the assumption of "not too high" densities and temperatures.

Towards a Description of the Equilibrium Structure of Hot Plasmas

A first prediction is that the equipartition-type equilibrium of hot plasmas is, like that of pure cryodynamical systems (a gas of gravitating particles), unstable regarding the two different particle classes that mutually attract each other. This means that the ions and the electrons must get disproportioned in their kinetic energies. Whereas in a gravitating gas the disproportioning of the kinetic energies of two mass classes goes on without limit [4], it in the present case is "braked." For the electrostatic repulsion within each charge class has an energy-homogenizing effect just as in ordinary repulsive statistical-mechanics. The fact that the repulsion is long-range Newtonian rather than of the hard-potential type makes no difference regarding equipartition [4].

Therefore a new overall stable equilibrium is bound to form. What is unusual is only that the two particle classes that rach form a constant equilibrium temperature among their own kind, must at the same time disequilibrate energy-wise (owing to the pseudo-gravitational attraction acting between them). Hence as a "compromise" the equilibrium temperatures of the two components of the plasma become unequal – while taken together maintaining the constant overall equilibrium temperature of the plasma as a whole. Thus we have a new phenomenon: a constant-temperature equilibrium structure in hot plasmas that at the same time possesses unequal "subtemperatures" in its two components.

If this appears strange, it becomes even more so given the fact that there must exist *two* such alternatives: either the electrons, or the ions can be the hotter species within the overall equilibrium temperature in principle.

The two-subtemperatures prediction applies as mentioned at not too high densities so that the perturbing complications of electrodynamics can be neglected. It represents if true a previously unknown qualitatively new phenomenon of nature: "bistability within equilibrium thermocryodynamics." This conclusion is very surprising because in statistical thermodynamics taken alone, bistability of equilibria is an impossibility under closed-system conditions as is well known.

The degree of unfamiliarity of this combined Newtonian-anti-Newtonian proposal goes even further: The "dissociated equilibrium" is also non-unique. If it is true that such a foreign two-tiered equilibrium exists in our idealized "Maxwell-free" plasma, a *second* equilibrium in which the ratio of subtemperatures is inverted qualitatively is bound to exist as well. The latter arises when the disproportioning two subtemperatures had, starting out from different initial conditions, disproportioned the other way. Then it is not the electrons that have the higher average kinetic energy at equilibrium at the expense of the ions but rather the ions are hotter than the electrons.

Nevertheless it is unlikely that under realistic conditions, both "dissociations" have the same probability to occur. Only one of the two "double-temperature equilibria" can be expected to become manifest at a given overall equilibrium temperature. Nevertheless this "meta-bistability" – bistability between two individually bistable regimes – comes as another startling possibility.

The present theory of a "mixed Newtonian-anti-Newtonian" gas (or, if you prefer, of a gas of "two types of frictionless magnetic monopoles of differing mass") is so unfamiliar that the skeptical response that the disproportioning-type prediction cannot be correct, is hard to refute. Is there an empirical fact which can be adduced in favor of the present theory?

An Empirical Question

The proposed "disproportioning of kinetic energies" with two sub-temperatures, one for each particle class, can be sharpened into an empirically meaningful question. It reads: "The *lighter* particle class (electrons) owing to their faster equilibration predictably possesses a – say – three times higher sub-temperature at equilibrium than the heavier particles."

This suggestion rings a bell. There exist many papers in the literature in which "two-temperature plasmas" are empirically and theoretically described (cf. [7]). Hereby, invariably the electrons have the higher temperature by a factor of up to three. These empirical results were always obtained under open-system conditions, however, because thermodynamics by definition forbids dissociated equilibrium temperatures. Thermodynamics was was the only eligible statistical-mechanical theory.

Now – with cryothermodynamics existing – the guess can be ventured that one or another of these empirical results may actually remain valid closer to equilibrium than the experimentalist authors thought, so that perhaps such measured temperatures may in a rare case have persisted closer to equilibrium – and even may have represented a local equilibrium temperature distribution once.

The both qualitative and exact proposal made above – that a new phase diagram with more than one equilibrium sub-temperature can exist – could stimulate experimentalists to venture an attempt at falsification: Can there really exist a phase diagram at equilibrium that features bistability? And: Could the bistable equilibrium be itself bistable again in a "meta-bistable" manner? Further theoretical and numerical work appears to be necessary.

Discussion

Hamiltonian chaos theory still represents a powerful challenge to date. Whole disciplines – some of them new – can be based on it. The traditional – purely statistical – approach to thermodynamics would then lose its privileged status after more than a century because it was unable to arrive at the new phenomena spotted here which if true entail whole new subfields of statistical mechanics. Sinai's deterministic-chaos approach to statistical mechanics [2,3] would then prove to be the superior alternative. It was found to be applicable (with "soft disks") to both close-to and far-from equilibrium conditions potentials in the ballparl of the "breathing plane-tree alley problem" [4]. And it then proved to remain just as powerful after inversion of all potentials into a Newtonian gas [4]. This deterministic methodology gives cryodynamics [5] the same solid basis as Sinai-type thermodynamics. Many mathematical details still wait to be harvested.

The deterministic-chaos theory of two statistical-mechanical sister theories has been added a further strand under the name "thermocryodynamics." This third discipline, if blessed with acceptance, will be much more difficult than were its two predecessors. Most worrisome is the eventually necessary addition of the infinitely many degrees of freedom of electrodynamics. Later, or in parallel, also new qualitative phenomena in the low-temperature domain governed by quantum mechanics will call for consideration, and later also analogs or polar opposites may arise in the subnuclear domain.

Thus chaos theory almost looks like being still in its infancy when it comes to a fuller understanding of many-particle Hamiltonian systems. Both Cryodynamics and Thermocryodynamics could in principle have been invented one-and-a-half century ago. The field is still a "hot" terrain on which one has to take off one's shoes. The best techniques wait to be developed. For example, many of the equilibrium phenomena envisioned above are numerically inaccessible with currently available methods, cf. [8]. Poincaré introduced transfinitely exact chaos theory into the Newton's paradigm in his unique "quantitative qualitative" fashion.

To conclude, Hamiltonian chaos applies to gases ("gas" means "chaos"). Gases can be made up from mutually attractive particles – as in cosmology, in galaxy theory and in globular-cluster theory – and gases can be made up from two polar classes of particles – as in a soup of two kinds of magnetic monopoles or else in plasma theory. Both these multi-particle domains, the gravitational and the electrostatic one, are still almost uninvestigated from a chaos-theoretic perspective. Hot plasmas offer an exciting "virgin territory" in this context. The multistable phase diagram predicted to exist is a total mystery to the extent of looking like – or perhaps being – a mirage. Glasses can be complicated – but gases? The oldest domain of deterministic science founded by Newton in the footsteps of Descartes is as young as ever in the spirit of the great Poincaré.

Acknowledgments

I thank Aziz Alaoui, Christophe Letellier, Bob Gilmore, Marc Lefranc, René Lozi, Leon Chua and Ron Chen for stimulation. For J.O.R.

References

[1] H. Poincaré, Sur le problème des trois corps et les équations de la dynamique. Acta Mathematica **13**, 1-270 (1890); see: J. Barrow-Greene, Poincaré and the Three Body Problem. American Mathematical Society, Providence 1997, pp. 89-90.

[2] Ya.G. Sinai, *Properties of spectra of ergodic dynamical systems.* Sov. Math., Dokl. **4**, 875-877 (1963).

[3] Ya.G. Sinai, *Dynamical systems with elastic reflections.* Russ. Math. Surv. **25**, 137–189 (1970).

[4] O.E. Rossler, Rolling ball in breathing plane-tree alley paragigm. European Scientific Journal **9**(27), 1-7 (2013).

[5] O.E. Rössler, The new science of Cryodynamics and its connection to cosmology. *Complex Systems* **20**, 105-113 (2011).

[6] O.E. Rossler and F. Kuske, Thermocryodynamics: a new theory for hot plasmas. (Submitted.)

[7] P. André, J. Aubreton, M.F. Elchinger, V. Rat, P. Fauchais, A. Lefortand and A.B. Murphy, A statistical mechanical view of the determination of the composition of multi-temperature plasmas. *Plasma Chemistry and Plasma Processing* **24**, 435-446 (2004).

[8] K. Sonnleitner, StV4: A symplectic time-reversible Störmer-Verlet algorithm of the 4th order for Hamiltonian multi-particle systems, with two applied examples (a gas and a T-tube configuration) [in German]. PhD dissertation, University of Tubingen 2010. http://de.scribd.com/doc/89182284/Sonnleitner-Dissertation

Secrets of swarm architecture: deciphering construction rules in ant colonies

Guy Theraulaz

Centre de Recherches sur la Cognition Animale, CNRS, UMR 5169, Université Paul Sabatier, 118 route de Narbonne, 31062 Toulouse, France

Email: guy.theraulaz@univ-tlse3.fr
Webpage: http://cognition.ups-tlse.fr/_guyt/index.html

Abstract: The amazing ability of social insects to solve everyday-life problems, also known as «swarm intelligence» has received a considerable attention the past twenty years. One of the most famous feats of insect societies is their ability to build impressive nest architectures. Not only their characteristic scale is typically much larger than the size of individual insects but some of these nests can also be highly complex. The amazing evolution of construction techniques used by ants, wasps, bees and termites has provided a whole set of innovations in terms of architectural designs that proved to be efficient to solve problems as various as controlling nest temperature, ensuring gas exchanges with the outside environment or adapting nest architecture to growing colony size. The big question is: how these efficient designs emerge from the combination of millions of local building actions performed by individual workers? And how do insects interact with each other to coordinate their building actions? To investigate these issues, we focused on the early stages of nest construction in the garden ant Lasius niger. This experimental paradigm was used to disentangle the coordinating mechanisms at work and characterize individual behaviors (transport and assemblage of construction material) and the stigmergic interactions involved in the coordination of building actions. We then developed a 3D model implementing the mechanisms detected on the individual level and showed that they correctly explain the construction dynamics and the spatial patterns observed at the collective level for various conditions. Our model showed that the evaporation rate of a building pheromone was a highly influential parameter on the shape transition of the resulting structures. The model also revealed that complex helicoidal structures connecting nearby chambers emerge from a constant remodeling process of the nest architecture.

Short bio: Guy Theraulaz is a senior research fellow at the National Center for Scientific Research CNRS) and an expert in the study of collective animal behaviors. He is also a leading researcher in the field of swarm intelligence, primarily studying social insects but also distributed algorithms, e.g. for collective robotics, directly inspired by nature. His research focuses on the understanding of a broad spectrum of collective behaviors in animal societies by quantifying and then modeling the individual level behaviors and interactions, thereby elucidating the mechanisms generating the emergent, group-level properties. He was one of the main characters of the development of quantitative social ethology and collective intelligence in France. He

published many papers on nest construction in ant and wasp colonies, collective decision in ants and cockroaches, and collective motion in fish schools and pedestrian crowds. He has also coauthored five books, among which Swarm Intelligence: From Natural to Artificial Systems (Oxford University Press, 1999) and Self-organization in biological systems (Princeton University Press, 2001) that are now considered as reference textbooks.

Constructing a Simple Chaotic System with an Arbitrary Number of Equilibrium Points or an Arbitrary Number of Scrolls

Guanrong (Ron) Chen
City University of Hong Kong

In a typical 3D autonomous chaotic system, such as the Lorenz and the Rossler systems, the number of equilibrium points is three or less and the number of visible scrolls in their attractors is two or one. Today, we are able to construct a relatively simple 3D autonomous chaotic system that can have any desired number of equilibrium points or any desired number of visible scrolls in their chaotic attractors. This talk will briefly introduce the basic ideas and outline the design methodologies.

Reduction of complexity of dynamical systems : Applications to fishery modelling

Pierre Auger

UMI IRD 209 UMMISCO
Centre IRD de l'île de France, Bondy, France
Centre UMMISCO de Dakar, Sénégal
e-mail : pierre.auger@ird.fr

Abstract: Population and community models are complex in the sense that they usually take into account many variables and parameters. We present methods allowing the reduction of the dimension of the system which may become, in this way, mathematically more tractable. The reduction of the proposed system is undertaken with the help of aggregation methods which aim at studying the relationships between a large class of complex systems, in which many variables are involved, and their corresponding reduced or aggregated systems, governed by a few variables. The kind of aggregation methods that we consider is based on time scale separation methods. In order to illustrate the methods in population and community dynamics, we present an application of these aggregation methods in the context of fishery modelling. We consider a spatial stock-fishing effort model with several fishing sites. We study the effects of fast price variation as a result of demand and supply on the global dynamics of the fishery. We study cases of a linear as well as a non-linear demand function of price. We focus on a commercial species, the "thiof" in Senegal, showing decreasing catch with a booming market price.

General Session 1
PDE, Control, Observability

Proceedings of ICCSA 2014
Normandie University, Le Havre, France - June 23-26, 2014

BOUNDARY CONSTRAINED CONTROLLABILIY PROBLEM

Ali Boutoulout, Hamid bourray and Layla Ezzahri *†

Abstract. The aim of this paper is to characterize the minimum energy control that steers a hyperbolic system to a final state between two prescribed functions only on a boundary subregion Γ of the system evolution domain Ω. We give some definitions and properties of this new concept, and then we concentrate on the determination of the control which would realize a given final state with output constraints on Γ with minimum energy. This problem is solved using two approachs the first is the Subdifferntial approach and the second one is base on the Lagrangian multipliers which leads to an algorithm for the computation of the optimal control. The obtained results are illustrated by numerical simulations which lead to some conjectures.

Keywords. Minimum energy, hyperbolic systems, optimal control, subdifferential approach, Lagrangian multipliers.

1 Introduction

In the field of analysis and control of these systems, several notions have been developed particularly controllability, stability and by duality observability and detectability, etc. These various concepts have been widely studied and leads to a vast and disparate literature [1], [2].
The concept of controllability is one of the most important concepts in the analysis of distributed systems. This notion can be done in an abstract way by considering various types of functional spaces and operators to introduce some definitions and establish various characterization and properties.
The term of regional controllability has been used to refer to control problems in which the target of our interest is not fully specified as a state, but refers only to a smaller region (which can be internal or boundary) of the system domain. This concept has been widely developed and interesting results have been obtained, in particular, the possibility to reach a state only on an internal subregion [3] or on a part of the boundary [4].
The mathematical model of a real system is obtained from measurements or from the approximation techniques and is often affected by disturbances [5], and the solution of such a system is approximately known. For these reasons we are here interested in introducing the concept of controllability with constraints, which the aim is to steer a system from an initial state to a final one between two prescribed functions given only on a part of a subregion ω of the geometric area Ω where the system is considered.
This work is a contribution to the enlargement of the regional analysis of distributed systems, representing a new concept of controllability with constraints [6], limited mainly to systems described by hyperbolic partial differential equations.

*Ali Boutoulout, Hamid bourray and Layla Ezzahri are with department of Mathematics and Informatics of Faculty of Sciences at the University Moulay Ismail of Meknes in Morocco. E-mails: boutouloutali@yahoo.fr, hbourray@yahoo.fr, lailaezzahri@gmail.com

†Manuscript received April 19, 2009; revised January 11, 2010.

2 Problem statement and preliminaries

2.1 Formulation

Let Ω be an open bounded and regular subset of $\mathbb{R}^n$ with a boundary $\partial\Omega$. For $T > 0$, let $Q = \Omega\times]0,T[$ and $\Sigma = \partial\Omega\times]0,T[$, we consider the following hyperbolic system

$$\begin{cases} \dfrac{\partial^2 y}{\partial t^2}(x,t) - Ay(x,t) = Bu(t) & Q \\ y(x,0) = y_0(x), \dfrac{\partial y}{\partial t}(x,0) = y_1(x) & \Omega \\ \dfrac{\partial y}{\partial \nu_A}(\xi,t) = 0 & \Sigma \end{cases} \tag{1}$$

Where A is a second-order elliptic linear symmetric operator, which generates a strongly continuous semi-group $(S(t))_{t\geq 0}$, $\dfrac{\partial y}{\partial \nu_A}(\xi,t)$ denotes the co-normal with respect to A, $B \in \mathcal{L}(\mathbb{R}^p, H^1(\Omega))$, $u \in U = L^2(0,T,\mathbb{R}^p)$ (p depends on the number of the considered actuators) and (y_0, y_1) in the state space $\mathcal{X} = H^2(\Omega) \times H^1(\Omega)$. We design by $Z_u(T) = (y_u(T), \dfrac{\partial y_u}{\partial t}(T)) \in \mathcal{X}$ the solution of (1).

For $\Gamma \subseteq \partial\Omega$ let consider

$$\begin{aligned} \chi_\Gamma : H^{\frac{3}{2}}(\partial\Omega) \times H^{\frac{1}{2}}(\partial\Omega) &\to H^{\frac{3}{2}}(\Gamma) \times H^{\frac{1}{2}}(\Gamma) \\ (z, z') &\mapsto \chi_\Gamma(z,z') = (\bar{\chi}_\Gamma z, \tilde{\chi}_\Gamma z') \end{aligned}$$

with

$$\begin{aligned} \tilde{\chi}_\Gamma : H^{\frac{1}{2}}(\partial\Omega) &\to H^{\frac{1}{2}}(\Gamma) \\ z &\mapsto \tilde{\chi}_\Gamma z = z_{|\Gamma} \end{aligned}$$

$$\begin{aligned}\bar{\chi}_\Gamma : H^{\frac{3}{2}}(\partial\Omega) &\to H^{\frac{3}{2}}(\Gamma)\\ z' &\mapsto \bar{\chi}_\Gamma z' = z'_{|_\Gamma}\end{aligned}$$

While χ_Γ^* (resp. $\tilde{\chi}_\Gamma^*$ and $\bar{\chi}_\Gamma^*$) is the adjoint operator of χ_Γ (resp. $\tilde{\chi}_\Gamma$ and $\bar{\chi}_\Gamma$) which is the restriction operator.

Let's consider the trace operator

$$\begin{aligned}\gamma : H^2(\Omega)\times H^1(\Omega) &\to H^{\frac{3}{2}}(\partial\Omega)\times H^{\frac{1}{2}}(\partial\Omega)\\ (z_1,z_2) &\mapsto \gamma(z_1,z_2)=(\gamma_0 z_1,\gamma_0 z_2)\end{aligned}$$

with $\gamma_0 : H^m(\Omega)\to H^{m-\frac{1}{2}}(\partial\Omega)$ $(m=1,2)$ denotes the trace operator of order zero which is linear, continuous, and surjective, while γ^* (resp. γ_0^*) is the adjoint operator of γ (resp. γ_0). Let $\alpha_1(.)$ and $\beta_1(.)$(resp. $\alpha_2(.)$ and $\beta_2(.)$) two given functions from $H^{\frac{3}{2}}(\partial\Omega)$ (resp. $H^{\frac{1}{2}}(\partial\Omega)$) such that $\alpha_1(.)\le\beta_1(.)$ (resp. $\alpha_2(.)\le\beta_2(.)$) a.e on Γ.
Throughout the paper we set

$$[\alpha_i(.),\beta_i(.)]=\{y_i\in H^{\frac{1}{2}}(\Gamma)\mid \alpha_i(.)\le y_i(.)\le\beta_i(.)\ a.e\ on\ \Gamma\},$$

Let H be the operator from $U\to H^2(\Omega)\times H^1(\Omega)$, for $u\in U$, defined by:

$$Hu=\int_0^T S(T-s)Bu(s)ds$$

We recall that an actuator is conventionally defined by a couple (D,f), Where $D\subset\overline{\Omega}$ is the geometric support of the actuator and f is the spatial distribution of the action on the support D.
In the case of a pointwise actuator (internal or boundary) $D=\{b\}$ and $f=\delta(b-.)$, where δ is the Dirac mass concentrated in b, and the actuator is then denoted by (b,δ_b). For definitions and the properties of strategic actuators we refer to [4,6].

2.2 Definitions and properties

Definition 2.1.
We say that the system (1) is $\Gamma-[\alpha_1(.),\beta_1(.)]\times[\alpha_2(.),\beta_2(.)]$- Controllable if

$$(Im\chi_\Gamma\gamma H)\cap([\alpha_1(.),\beta_1(.)]\times[\alpha_2(.),\beta_2(.)])\neq\emptyset$$

Remark 2.1.
The above definition is equivalent to say that:
The system (1) is $\Gamma-[\alpha_1(.),\beta_1(.)]\times[\alpha_2(.),\beta_2(.)]$- Controllable at the time T if
there exists $u\in U$ such that:

$$\alpha_1(.)\le\bar{\chi}_\Gamma\gamma_0 y_u(T)\le\beta_1(.)$$

and

$$\alpha_2(.)\le\tilde{\chi}_\Gamma\gamma_0\frac{\partial y_u}{\partial t}(T)\le\beta_2(.)a.eon\Gamma$$

Remark 2.2.

1. The above definition means that we are interested only in the transfer of system (1) to a state between $\alpha_i(.)$ and $\beta_i(.)$ on Γ

2. A system which is controllable on Γ is $[\alpha_1(.),\beta_1(.)]\times[\alpha_2(.),\beta_2(.)]-$controllable on Γ

3. A system (1) which is $[\alpha_1(.),\beta_1(.)]\times[\alpha_2(.),\beta_2(.)]$-Controllable on Γ_1 is $[\alpha_1(.),\beta_1(.)]\times[\alpha_2(.),\beta_2(.)]$-Controllable for any $\Gamma_2\subseteq\Gamma_1$.

4. The control u depends on the time variable, but it also implicitly depends on Γ

The $\Gamma-[\alpha_1(.),\beta_1(.)]\times[\alpha_2(.),\beta_2(.)]$-controllability may be characterized by the following result:

Proposition 2.1.
The system (1) is $\Gamma-[\alpha_1(.),\beta_1(.)]\times[\alpha_2(.),\beta_2(.)]$- *Controllable if and only if*

$$(Ker\chi_\Gamma+Im\gamma H)\cap([\alpha_1(.),\beta_1(.)]\times[\alpha_2(.),\beta_2(.)])\neq\emptyset$$

Remark 2.3. The above definitions do not allow pointwise or boundary controls, since for such systems B is not bounded.

3 Minimum energy control

The purpose of this section is to explore two approachs the first is the Subdifferntial approach [9] and the second one is base on the Lagrangian multipliers devoted to the computation of the optimal control problem for the hyperbolic equation excited by an internal zone actuator which steers the system (1) from $(y_0,y_1)\in H^2(\Omega)\times H^1(\Omega)$ to a final state (p^d,v^d) such that $\alpha_1(.)\le\ \bar{\chi}_\Gamma\gamma_0 p^d\le\beta_1(.)$ and $\alpha_2(.)\le\tilde{\chi}_\Gamma\gamma_0 v^d\le\beta_2(.)$ on a subregion Γ.
More precisely we are interested to the following minimization problem

$$\begin{cases}\inf\mathcal{J}(u)=\int_0^T||u(t)||^2_{I\!R^p}dt\\ u\in U_{ad}^\Gamma\end{cases}\qquad(2)$$

where

$$\begin{aligned}U_{ad}^\Gamma=\{u\in U\mid\ &\alpha_1(.)\le\bar{\chi}_\Gamma\gamma_0 y_u(T)\le\beta_1(.)\text{ and}\\ &\alpha_2(.)\le\tilde{\chi}_\Gamma\gamma_0\frac{\partial y_u}{\partial t}(T)\le\beta_2(.)\},\end{aligned}$$

is the set of admissible controls.
The following result ensure the existence and the uniqueness of the solution of the problem (2).

Proposition 3.1.
If the system (1) is $[\alpha_1(.),\beta_1(.)]\times[\alpha_2(.),\beta_2(.)]$- *Controllable on* Γ *then the problem (2) has a unique solution* u^*.

3.1 Subdifferential approach

Let denote by $\Gamma_0(U)$ the set of functions $f : U \to \tilde{I\!R} =]-\infty, +\infty]$ proper semi-continuous and convex on U.
For $f \in \Gamma_0(U)$

$$dom(f) = \{u \in U | f(u) < \infty\}$$

and f^* the polar function of f given by

$$f^*(v^*) = \sup_{u \in dom(f)} \{\langle v^*, u\rangle - f(u)\} \qquad \forall v^* \in U$$

For $v_0 \in dom(f)$ the set

$$\partial f(v_0) = \{u^* \in U | f(u) \geq f(v_0) + \langle u^*, u - v_0\rangle \ \ \forall u \in U\}$$

denotes the subdifferential of f at v_0
For G a nonempty subset of U

$$\psi_G(u) = \begin{array}{ll} 0 & if\ u\ \in G, \\ +\infty & otherwise; \end{array}$$

denotes the indicator functional of G
Let $f_\sigma(u) = \frac{1}{2} \parallel u \parallel^2$ a self-polar function defined on U. For all $\lambda > 0$ and $f \in \Gamma_0(U)$, it is known that the mapping $g_\lambda : x \to (f_\sigma + \lambda f)^*(x)$ is Frechet differentiable with gradient $\nabla_{g_\lambda} = \dfrac{x - J_f(x)}{\lambda}$, where J_f is the unique solution of the problem

$$\inf_{y \in U} \{\frac{1}{2\lambda} \parallel y - x \parallel^2 + f(y)\}$$

with these notations (2) is equivalent to the problem

$$\left\{ \begin{array}{l} \inf(\frac{1}{2} \parallel u \parallel^2 + \psi_{U^\Gamma_{ad}}(u)) \\ u \in U^\Gamma_{ad} \end{array} \right. \tag{3}$$

And the solution of problem (3) may be characterized by the following result.

Proposition 3.2.
If the system (1) is $[\alpha_1(.), \beta_1(.)] \times [\alpha_2(.), \beta_2(.)]$- *Controllable on* Γ *then* u^* *is the solution of (3) if and only if*

$$u^* \in U^\Gamma_{ad} \quad and \quad \psi^*_{U^\Gamma_{ad}}(-u^*) = - \parallel u^* \parallel^2 \tag{4}$$

Let us set $a(.) = (\alpha_1(.), \alpha_2(.)) - \chi_\Gamma \gamma S(T)(y_0, y_1)$ and $b(.) = (\beta_1(.), \beta_2(.)) - \chi_\Gamma \gamma S(T)(y_0, y_1)$, then

$$U^\Gamma_{ad} = \{u \in U | \chi_\Gamma \gamma H u \in [a(.), b(.)]\}$$

and we have the result:

Proposition 3.3.
If the system (1) is $[\alpha_1(.), \beta_1(.)] \times [\alpha_2(.), \beta_2(.)]$ *controllable on* Γ *then* u^* *is the solution of (3) if and only if:*

$$\min\{\langle (\chi_\Gamma \gamma H)^\dagger a(.), u^*\rangle, \langle (\chi_\Gamma \gamma H)^\dagger b(.), u^*\rangle\} = \parallel u^* \parallel^2 \tag{5}$$

where $(\chi_\Gamma \gamma H)^\dagger = (\chi_\Gamma \gamma H)^*((\chi_\Gamma \gamma H)(\chi_\Gamma \gamma H))^{-1}$ *is the generalized inverse of* $(\chi_\Gamma \gamma H)$

Remark 3.1.

- If $\alpha_1(.) = \beta_1(.) = \{p_d\}$ and $\alpha_2(.) = \beta_2(.) = \{v_d\}$ we find the notion of regional controllability [8], then $a(.) = b(.) = (p_d(.), v_d(.)) - \chi_\Gamma \gamma S(T)(y_0, y_1)$ and $U^\Gamma_{ad} = (\chi_\Gamma \gamma H)^\dagger((p_d, v_d) - \chi_\Gamma \gamma S(T)(y_0, y_1))$ and the solution of (2) is given by

$$u^*(t) = (\chi_\Gamma \gamma H)^\dagger((p_d, v_d) - \chi_\Gamma \gamma S(T)(y_0, y_1))$$

- The numerical simulations of the subdifferentiel approach cannot be carried without difficulties, to overcome them, we will give in what follows an approach based on the Lagrangian multiplier

3.2 Lagrangian Approach

We consider the problem (2), when the system is excited by one zone actuator (D, f). The following result gives a useful characterisation of the problem (2):

Proposition 3.4.

If the actuator (D, f) *is* $[\alpha_1(.), \beta_1(.)] \times [\alpha_2(.), \beta_2(.)]$-*strategic on* Γ *then the solution of (2) is given by :*

$$u^* = -(\chi_\Gamma \gamma H)^*(\lambda^*_1, \lambda^*_2) \tag{6}$$

Where $(\lambda^*_1, \lambda^*_2)$ *is the solution of:*

$$\left\{ \begin{array}{ll} (p^{d^*}, v^{d^*}) = & P_{[\alpha_1(.), \beta_1(.)] \times [\alpha_2(.), \beta_2(.)]}[\rho(\lambda^*_1, \lambda^*_2) + (p^{d^*}, v^{d^*})] \\ (p^{d^*}, v^{d^*}) + & R_\Gamma(\lambda^*_1, \lambda^*_2) = \chi_\Gamma \gamma S(T)(y_0, y_1) \end{array} \right. \tag{7}$$

While $P_{[\alpha_1(.), \beta_1(.)] \times [\alpha_2(.), \beta_2(.)]} : H^{3/2}(\Gamma) \times H^{1/2}(\Gamma) \longrightarrow [\alpha_1(.), \beta_1(.)] \times [\alpha_2(.), \beta_2(.)]$ *denotes the projection operator,* $\rho > 0$ *and* $R_\Gamma = (\chi_\Gamma \gamma H)(\chi_\Gamma \gamma H)^*$.

Corollary 3.1.
If the system (1) is controllable on Γ, *and* ρ *convenably chosen, then the system (7) has only one solution* $(\lambda^*_1, \lambda^*_2, p^{d^*}, v^{d*})$.

Remark 3.2.
If $\alpha_1(.) = \beta_1(.)$ and $\alpha_2(.) = \beta_2(.)$ we find the notion of exact regional controllability and the solution of (2) is given by

$$u^*(.) = (\chi_\Gamma \gamma H)^* R^\dagger_\Gamma(\alpha_1(.), \alpha_2(.))$$

Remark 3.3.
Similar results can be obtained in pointwise actuator case.

4 Application

In this subsection we describe a numerical scheme which allows the determination of the desired state between $\alpha_i(.)$ and $\beta_i(.)$ on the subregion Γ.
To achieve this we shall use the following algorithm which is based on Uzawa one

1. Choose:
   - The subregion Γ, the actuator (D, f) and a precision threshold ϵ small enough.
   - Functions $(p_0^d, v_0^d) \in [\alpha_1(.),\ \beta_1(.)] \times [\alpha_2(.), \beta_2(.)]$, $(\lambda_1^1, \lambda_2^1) \in H^{3/2}(\Gamma) \times\ H^{1/2}(\Gamma)$
2. $(p_{n-1}^d, v_{n-1}^d, \lambda_1^n, \lambda_2^n)$ known, we determine u_n,p_n^d,v_n^d with the formula
   - $u_n = -(\chi_\Gamma \gamma H)^*(\lambda_1^n, \lambda_2^n)$,
   - $(p_n^d, v_n^d) = P_{[\alpha_1(.),\beta_1(.)]\times[\alpha_2(.),\beta_2(.)]}(\rho(\lambda_1^n, \lambda_2^n) + (p_{n-1}^d, v_{n-1}^d))$,
3. $(\lambda_1^{n+1}, \lambda_2^{n+1}) = (\lambda_1^n, \lambda_2^n) + \chi_\Gamma \gamma(y_{u_n}(T), \dfrac{\partial y_u}{\partial t}(T)) - (p_n^d, v_n^d)$
4. If $\parallel\ (p_{n+1}^d, v_{n+1}^d) - (p_n^d, v_n^d)\ \parallel \leq\ \epsilon$ we stop, else we return to 2.

Conclusion

We have developed an extension of the notion of controllability for hyperbolic systems with constraints in the boundary case, we characterized the optimal control using two approaches and interesting results are obtained and will be illustrated with numerical example and simulations. Future works aim to extend this notion of regional controllability with constrained to the case of the gradient.

References

[1] R.F. Curtain, and H. Zwart,An introduction to infinite dimentional linear systems theory, Springer Verlag, NewYyork, 1995.

[2] R. F. Curtain and A. J. Pritchard, Infinite Dimensional Linear Systems Theory, Springer-Verlag, Berlin, 1978.

[3] A. El Jai, A.J. Pritchard, M.C. Simon and E. Zerrik, Regional Controlability of distributed system, Int. J. Control, 62,(6) (1995), 1351–1365.

[4] A. El Jai and A.J. Pritchard, Sensors and actuators in distributed systems analysis, Wiley, 1988.

[5] D.Q. Mayne, J.B. Rawlings, C.V. Rao and P.O.M. Scokaert, Constrained model predictive control: Stability and optimality, Automatica J., 36,(6) (2000), 789–814.

[6] E. Zerrik, A. El Jai and A. Boutoulout, Actuators and regional boundary controllability of parabolic system, Int. J. Sys. Sci, 31,(1) (2000), 73–82.

[7] E. Zerrik and F. Ghafrani, M. Raissouli An extended controllability problem with minimum energy. Journal of Mathematical Sciences, Vol. 161, No. 2009, 344-353

[8] E. Zerrik and R. Larhrissi, Regional boundary controllability of hyperbolic systems. Numerical approach, Journal of dynamical and control systems, Vol 8, N 3, (2002), 293–312.

[9] J.-P. Aubin, S. Wilson. Optima and Equilibria: An Introduction to Nonlinear Analysis, Springer (2002).

[10] K. Yoshida, Functional analysis Springer-Verlag,New York, 1980.

[11] A. Pazy, Semigroups of Linear Operators and Applications to Partial Dif-ferential Equations, Springer-Verlag, New York (1990).

[12] J. L. Lions, Controlabilité exacte. Perturbation et Stabilisation des systèmes distribués, Masson (1988).

Proceedings of ICCSA 2014
Normandie University, Le Havre, France - June 23-26, 2014

BOUNDARY FLUX CONTROLLABILITY PROBLEM: APPROACH AND SIMULATION

Imad El Harraki, Ali Boutoulout and Hamid Bouray *†

Abstract. The purpose of this paper is to show how one can steers a hyperbolic system to a final desired gradient on a part of the boundary of the evolution system domain with interior actuators and boundary control using HUM approach. The developed approach leads to find the link between the boundary and the interior control, it also helps to open out a numerical approach for constructing the desired controls.

Keywords. hyperbolic systems, gradient controllability, strategic actuator, HUM approach.

1 Introduction

Distributed parameter systems are dynamical systems whose states depend not only on time but also on spatial coordinates. Many real systems are purely of distributed nature, and many of the systems conceived by humans are naturally very complex. Indeed, every complex problem always necessitates a complex solution. In spite of the fact that the most elaborated mathematical methods have been developed, a lot is to be done to bridge the gap between applied mathematics and the industrial world. The system theory contributed to fulfill this objective, and thus, obtain exploitable results in different domains. Particularly, controllability is one of the most interesting branches of the system theory. For a given distributed parameter system, the regional controllability concept refers to control problems in which the target is not fully specified as a state, but refers only to a region ω, a portion of the spacial domain Ω on which the governing partial differential equations(S) is considered. Many interesting results have been developed [[6],[3]]. These results have been extended to the case where ω is a part of the boundary $\partial\Omega$ this concept find applications in various industrial problems, for example, of particular interest in problems of elastic membrane, where the idea would be to stabilize a flux in a part of its boundary .We are interested in the system gradient evolution on a boundary subregion $\Gamma \subset \partial\omega$. This paper is organized as follows. Section 2 present a definitions and the link between boundary and regional gradient controllability of hyperbolic systems. Section 3 focuses on the approach devoted to the computation of the control that permits to attain gradient in a subregion Γ of $\partial\Omega$.Section 4 elaborates on its relationship with regional gradient controllability and actuators.

*Ali Boutoulout Hamid bourray and Imad El harraki are with department of Mathematics and Informatics of Faculty of Sciences at the University Moulay Ismail of Meknes in Morocco. E-mails: boutouloutali@yahoo.fr, hbourray@yahoo.fr, imadharraki@gmail.com

†Manuscript received April 19, 2009; revised January 11, 2010.

2 Boundary gradient controllability

2.1 Definitions and preliminary

Let Ω be an open bounded subset of $\mathbb{R}^n$ with regular boundary $\partial\Omega$. For $T > 0$ we denote by $Q = \Omega\times]0,T[$,$\Sigma = \partial\Omega\times]0,T[$ and we consider a hyperbolic system defined by

$$\begin{cases} \dfrac{\partial^2 y(x,t)}{\partial t^2} - Ay(x,t) = Bu(t) & in \quad Q \\ y(x,0) = y_0(x), \dfrac{\partial y}{\partial t}(x,0) = y_1(x) & in \quad \Omega \\ y(\xi,t) = \eta(\xi,t) & on \quad \Sigma \end{cases} \tag{1}$$

where A is a second-order elliptic linear symmetric operator given by:

$$\begin{cases} A = -\sum_{i,j=1}^{n} \partial_i(a_{ij}\partial_j) \text{ with } a_{ij} = a_{ji} \in \mathcal{C}^1(\Omega) \text{ and there exists } \alpha \\ \text{such that } \sum_{i,j=1}^{n} a_{ij}\xi_i\xi_j \geq \alpha \sum_{i=1}^{n} \mid \xi_i \mid^2 \quad \forall \xi = (\xi_1,...,\xi_n) \in \mathbb{R}^n \end{cases} \tag{2}$$

$B \in \mathcal{L}(U, H^1(\Omega))$ where $U = L^2(0,T;\mathbb{R}^p)$ and p is the number of actuators, $V = L^2(]0,T[\times\partial\Omega)$ for $(y_0,y_1) \in H^3(\Omega)\times H^2(\Omega)$ We denote $(y_\nu(t), y'_\nu(t))$ the solution of the equation (1), and $\nu \in \tilde{U}$ with
$\tilde{U}= \{\nu \in U \times V \text{such that}(y_\nu(T), y'_\nu(T)) \in H^3(\Omega) \times H^2(\Omega)\}$

For $\omega \subset \Omega$ an open subregion of Ω with positive Lesbegue measure let χ_ω be the restriction function defined by

$$\begin{array}{rcl} \chi_\omega : (L^2(\Omega))^n \times (L^2(\Omega))^n & \longrightarrow & (L^2(\omega))^n \times (L^2(\omega))^n \\ (z_1,z_2) & \longrightarrow & \chi_\omega(z_1,z_2) = (z_1,z_2)|_\omega \end{array}$$

and χ_ω^* denotes the adjoint operator, given by

$$\begin{array}{rcl}\chi_\omega^* : (L^2(\omega))^n \times (L^2(\omega))^n & \longrightarrow & (L^2(\Omega))^n \times (L^2(\Omega))^n \\ (z_1, z_2) & \longrightarrow & \chi_\omega^*(z_1, z_2) = \left\{ \begin{array}{ll} (z_1, z_2) & in \quad \omega \\ 0 & in \quad \Omega \setminus \omega \end{array} \right.\end{array}$$

Consider the operator ∇ given by the formula

$$\begin{array}{rcl}\nabla : H^2(\Omega) & \longrightarrow & (H^1(\Omega))^n \\ y & \longrightarrow & \nabla y = (\dfrac{\partial y}{\partial x_1}, ..., \dfrac{\partial y}{\partial x_n})\end{array}$$

Let's consider the trace operator

$$\begin{array}{rcl}\gamma : (H^2(\Omega))^n \times (H^1(\Omega))^n & \longrightarrow & (H^{\frac{3}{2}}(\partial\Omega))^n \times (H^{\frac{1}{2}}(\partial\Omega))^n \\ (y^1, y^2) & \longmapsto & \gamma(y^1, y^2) = (\bar{\gamma}y^1, \bar{\gamma}y^2)\end{array}$$

with

$$\begin{array}{rcl}\bar{\gamma} : (H^i(\Omega))^n & \longrightarrow & (H^{i-\frac{1}{2}}(\partial\Omega))^n \\ z & \longmapsto & \bar{\gamma}z = (\gamma_0 z_1, .., \gamma_0 z_n)\end{array}$$

and $\gamma_{i_0} : H^i(\Omega) \longrightarrow H^{i-\frac{1}{2}}(\partial\Omega)$ are the trace operators of order zero which are linear, continuous, and surjective. γ^* (resp. γ_0^*) denote the adjoint of operator γ (resp. γ_0) For $\Gamma \subset \partial\Omega$, consider

$$\begin{array}{rcl}\chi_\Gamma : (H^{\frac{1}{2}}(\partial\Omega))^n \times (H^{\frac{1}{2}}(\partial\Omega))^n & \to (H^{\frac{1}{2}}(\Gamma))^n \times (H^{\frac{1}{2}}(\Gamma))^n \\ (\xi, \xi^{'}) & \mapsto \chi_\Gamma(\xi, \xi^{'}) = (\xi, \xi^{'})|_\Gamma\end{array}$$

Let us give some definitions about the regional controllability of the gradient.

Definition 2.1. • The system (1) is said to be ω-exactly gradient controllable if for all $(g_p^d, g_s^d) \in (H^2(\omega))^n \times (H^1(\omega))^n$ there exists $(u, \eta) \in U \times V$ such that

$$\chi_\omega(\nabla y_\nu(T), \nabla y_\nu^{'}(T)) = (g_p^d, g_s^d)$$

- The system (1) is said to be ω-weakly gradient controllable if for all $\varepsilon > 0$ for all $(g_p^d, g_s^d) \in (H^2(\omega))^n \times (H^1(\omega))^n$ there exists$(u, \eta) \in U \times V$ such that

$$\| \chi_\omega(\nabla y_\nu(T), \nabla y_{nu}^{'}(T)) - (g_p^d, g_s^d) \|_{(H^2(\omega))^n \times (H^1(\omega))^n} \leq \varepsilon$$

Definition 2.2.

- The system (1) is said to be ω-exactly gradient controllable if for all $(g_p^{d_\Gamma}, g_s^{d_\Gamma}) \in (H^{\frac{3}{2}}(\Gamma))^n \times (H^{\frac{1}{2}}(\Gamma))^n$ there exists $(u, \eta) \in U \times V$ such that

$$\chi_\Gamma(\gamma\nabla y_\nu(T), \gamma\nabla y_\nu^{'}(T)) = (g_p^{d_\Gamma}, g_s^{d_\Gamma})$$

- The system (1) is said to be Γ-weakly gradient controllable if for all $\varepsilon > 0$ for all $(g_p^{d_\Gamma}, g_s^{d_\Gamma}) \in (H^{\frac{3}{2}}(\Gamma))^n \times (H^{\frac{1}{2}}(\Gamma))^n$ there exists $(u, \eta) \in U \times V$ such that

$$\| \chi_\Gamma(\gamma\nabla y_\nu(T), \gamma\nabla y_\nu^{'}(T)) - (g_p^{d_\Gamma}, g_s^{d_\Gamma}) \|_{(H^{\frac{3}{2}}(\Gamma))^n \times (H^{\frac{1}{2}}(\Gamma))^n} \leq \varepsilon$$

Consider the operator for $\nu = (u, v)$ and $y_0 = y_1 = 0$

$$\begin{array}{rcl}H : & U \times V \longrightarrow H^2(\Omega) \times H^1(\Omega) & \\ & (u, \eta) \mapsto (y_\nu(T), y_\nu^{'}(T)) & \end{array} \quad \begin{array}{ll} in & \omega \\ in & \Omega \setminus \omega \end{array} \tag{3}$$

Definition 2.3.

It is clear that the system (1) is $\Gamma-$exactly (resp. Γ-weakly) gradient controllable if

$$\begin{array}{c} Im\chi_\Gamma\gamma\nabla H = (H^{\frac{3}{2}}(\Gamma))^n \times (H^{\frac{1}{2}}(\Gamma))^n \\ (resp. \quad \overline{Im\chi_\Gamma\gamma\nabla H} = (H^{\frac{3}{2}}(\Gamma))^n \times (H^{\frac{1}{2}}(\Gamma))^n.) \end{array} \tag{4}$$

Remark 2.1. :

1. The above definitions mean that we are only interested in the transfer of the system gradient to a desired function on the subregion $\Gamma \subset \partial\Omega$.
2. If the system (1) is exactly gradient controllable in Γ then it is weakly gradient controllable in Γ.
3. For $\Gamma_2 \subset \Gamma_1$ the system (1) is exactly (resp. weakly) gradient controllable in Γ_1 then it is exactly (resp. weakly) gradient controllable in Γ_2.

2.2 The Link between regional internal gradient controllability and regional boundary gradient controllability

In what follows, we give properties and a link between the internal and the boundary regional controllability. Let $\omega \subset \Omega$ such that $\Gamma \subseteq \partial\Omega \bigcap \partial\omega$. and

$$R_i : (H^{i-\frac{1}{2}}(\partial\Omega)) \longrightarrow (H^i(\Omega))$$

such that $\gamma_{i_0} R_i g = g$ for all $g \in H^{i-\frac{1}{2}}(\partial\Omega)$.

Proposition 2.1. *If the system (1) is exactly (respectively weakly) gradient controllable in ω then it is exactly (respectively weakly) gradient controllable on Γ.*

3 Regional target control with internal actuators and boundary control

Consider the system (1) excited by n zone actuators (D_i, f_i) where $D_i \subset \Omega$ and $f_i \in L^2(D_i)$ and a boundary control $\eta \in V$.

$$\left\{ \begin{array}{ll} \dfrac{\partial^2 y(x,t)}{\partial t^2} - \triangle y(x,t) = \sum_{i=1}^{n} (\chi_{D_i} f_i)(x) u_i(t) & in \quad Q \\ y(x,0) = y_0(x), y_\nu^{'} = y_1(x) & in \quad \Omega \\ y(\xi,t) = \eta(\xi,t) & on \quad \Sigma \end{array} \right. \tag{5}$$

The propose of this section is to explore an approach devoted to the calculation of the control which steers the system (5) to a given gradient in the subregion Γ of $\partial\Omega$. Suppose that $(g_p^{d_\Gamma}, g_s^{d_\Gamma}) \in (H^{\frac{1}{2}}(\Gamma))^n \times (H^{\frac{1}{2}}(\Gamma))^n$ is given. and we set

$$\bar{G} = \{(\phi_0, \phi_1) \in C^\infty(\bar{\Omega}) \times C^\infty(\bar{\Omega}) \mid \phi_0 = \phi_1 = 0 \quad \text{sur} \quad \Omega\backslash\omega\} \tag{6}$$

Let ω a subregion of Ω such that $\Gamma \subseteq \partial\Omega \bigcap \partial\omega$. For ω, consider the internal controllability problem: Find $(u, \eta) \in U \times V$ such that

$$\chi_\omega(\nabla y(T), \nabla \frac{\partial y}{\partial t}(T)) = (g_p^d, g_s^d) \text{ on } \omega \tag{7}$$

Where $((g_p^d, g_s^d) \in (H^1(\omega))^n \times (H^1(\omega))^n) \cap (Im(\nabla) \times Im(\nabla))$ is given with

$$\begin{cases} \Delta g_{p_i}^d = 0 & \Omega \\ g_{p_i}^d = g_{p_i}^{d_\Gamma} & \partial\Omega \end{cases} \tag{8}$$

$$\begin{cases} \Delta g_{p_i}^s = 0 & \Omega \\ g_{p_i}^s = g_{p_i}^{s_\Gamma} & \partial\Omega \end{cases} \tag{9}$$

3.1 HUM approach

The approach developed here is an extension of the Hilbert uniqueness method (HUM) developed by Lions (see[6])
For $(\phi_{i_0}, -\phi_{i_0}) \in \bar{G}$, the system

$$\begin{cases} \frac{\partial^2 \phi_i(x,t)}{\partial t^2} - \triangle\phi_i(x,t) = 0 & in \quad Q \\ \phi_i(x,T) = \phi_{i_0}, \frac{\partial \phi^i}{\partial t}(x,T) = \phi_{i_1} & in \quad \Omega \\ \phi_i(\xi,t) = 0 & on \quad \Sigma \end{cases} \tag{10}$$

Has a unique solution (see[6]).
In $\bar{G}$ we define the following semi-norm :

$$\|(\phi_{i_1}, -\phi_{i_0})\|_{\bar{G}} = \left(\int_0^T \left(\langle \frac{\partial \tilde{\phi_i}}{\partial x_i}, f \rangle_{L^2(D_i)} \right)^2 dt \right)^{\frac{1}{2}} \tag{11}$$

$$\tilde{\phi} = \begin{pmatrix} \tilde{\phi}_1 \\ . \\ . \\ . \\ \tilde{\phi}_n \end{pmatrix}$$

with

$$\tilde{\phi_i} = \begin{cases} \phi_i & in \quad D_i \cup \Gamma_i \\ 0 & in \quad (D_i \cup \Gamma_i)^c \end{cases}$$

and $(D_i \cup \Gamma_i) \cap (D_j \cup \Gamma_j) = \emptyset$ for all $i \neq j$ and we consider the system :

$$\begin{cases} \frac{\partial^2 \psi(x,t)}{\partial t^2} - \triangle\psi(x,t) = \sum_{i=1}^n \langle \frac{\partial \tilde{\phi_i}(t)}{\partial x_i}, f_i \rangle_{L^2(D)} (\chi_{D_i} f_i)(x) & in \quad Q \\ \psi(x,0) = y_0(x), \frac{\partial \psi}{\partial t}(x,0) = y_1(x) & in \quad \Omega \\ \psi(\xi,t) = div(\tilde{\phi}(\xi,t)) & on \quad \Sigma \end{cases} \tag{12}$$

which has a unique solution such that $(\psi(T), \frac{\partial \psi}{\partial t}(T)) \in H^2(\Omega) \times H^1(\Omega)$(see[10]).
but $(\psi(T), \frac{\partial \psi}{\partial t}(T)) = (\psi_0(T), \frac{\partial \psi_0}{\partial t}(T)) + (\psi_1(T), \frac{\partial \psi_1}{\partial t}(T))$, where ψ_0 and ψ_1 are solutions of the systems

$$\begin{cases} \frac{\partial^2 \psi_0(x,t)}{\partial t^2} - \triangle\psi_0(x,t) = 0 & in \quad Q \\ \psi_0(x,0) = y_0(x), \frac{\partial \psi_0}{\partial t}(x,0) = y_1(x) & in \quad \Omega \\ \psi_0(\xi,t) = 0 & on \quad \Sigma \end{cases} \tag{13}$$

and

$$\begin{cases} \frac{\partial^2 \psi_1(x,t)}{\partial t^2} - \triangle\psi_1(x,t) = \sum_{i=1}^n \langle \frac{\partial \tilde{\phi_i}(t)}{\partial x_i}, f_i \rangle_{L^2(D_i)} (\chi_{D_i} f_i)(x) \\ \psi_1(x,0) = 0, \frac{\partial \psi_1}{\partial t}(x,0) = 0 \\ \psi_1(\xi,t) = div(\tilde{\phi}(\xi,t)) \end{cases} \tag{14}$$

We consider the operator

$$\Lambda_i(\tilde{\phi_{i_1}}, -\tilde{\phi}_{i_0}) = \mathcal{P}(\frac{\partial \psi_1}{\partial x_i}(T), \frac{\partial \psi_1}{\partial x_i}'(T))$$

is a symmetric and bounded operator where $\mathcal{P} = \chi_\omega^* \chi_\omega$. Then the regional gradient controllability problem on ω turns up to solve the equation :

$$\Lambda_i(\tilde{\phi_{i_1}}, -\tilde{\phi}_{i_0}) = -\mathcal{P}(\frac{\partial \psi_0}{\partial x_i}(T), \frac{\partial \psi_1}{\partial x_i}(T)) + \chi_\omega^*(g_{p_i}^d, g_{s_i}^d) \tag{15}$$

and we have the following result:

Theorem 3.1. *If $\langle \frac{\partial w_j}{\partial x_i}, f_i \rangle_{L^2(D_i)} \neq 0$ then the semi norm (11) is a norm. Moreover, if*

$$-\mathcal{P}(\frac{\partial \psi_0}{\partial x_i}(T), \frac{\partial \psi_1}{\partial x_i}(T)) + \chi_\omega^*(g_{p_i}^d, g_s^{d_i}) \in \bar{G}_i^*$$

where $\bar{G}_i^*$ is the dual of the completion of $\bar{G}$ with the respect to norm (11), then Eq. (15) has a unique solution (ϕ_{i_1}, ϕ_{i_0}) and the control $(u^*, div(\tilde{\phi}))$ where $u^*(t) = \sum_{i=1}^n \langle \frac{\partial \phi_i(t)}{\partial x_i}, f_i \rangle_{L^2(D_i)}$ is the solution of problem (7) and drives the system (5) to (g_p^d, g_s^d) on Γ at time T.

3.2 Numerical approach

In this section we give approach which gives explicit formula for $\tilde{\phi_{i_0}}$, $\tilde{\phi_{i_1}}$ and the optimal control solution of (5). We have seen that the problem (5) can be used to solve (15), which is equivalent to solving the minimization problem

$$\inf_{(\tilde{\phi_{i_1}}, \tilde{\phi_{i_0}}) \in \widehat{G}} R(\tilde{\phi_{i_1}}, \tilde{\phi}_{i_0}) \tag{16}$$

where R is given by

$$\begin{aligned} R(\tilde{\phi_{i_1}}, \tilde{\phi_{i_0}}) &= \frac{1}{2} \int_0^T \left(\langle \frac{\partial \tilde{\phi_i}}{\partial x_i}, f_i \rangle_{L^2(D_i)} \right)^2 dt + \langle \frac{\partial \psi_0}{\partial x_i}(T), \tilde{\phi_{i_1}} \rangle \\ &- \langle \frac{\partial \psi_0'}{\partial x_i}(T), \tilde{\phi}_{i_0} \rangle - \langle g_{p_i}^d, \tilde{\phi_{i_1}} \rangle + \langle g_{s_i}^d, \tilde{\phi}_{i_0} \rangle \end{aligned}$$

which

$$\begin{cases} \langle \tilde{\phi}_{i_0}, w_j \rangle_\omega = \frac{2}{T} \frac{(\langle \frac{\partial \psi_0'}{\partial x_i}(T), w_j \rangle - \langle g_{s_i}^d, w_j \rangle)}{(\langle f_i, \frac{\partial w_j}{\partial x_i} \rangle_{L^2(D_i)})^2} \\ \langle \tilde{\phi}_{i_1}, w_j \rangle_\omega = \frac{2\lambda_j}{T} \frac{(\langle \frac{\partial \psi_0}{\partial x_i}(T), w_j \rangle - \langle g_{p_i}^d, w_j \rangle)}{(\langle f_i, \frac{\partial w_j}{\partial x_i} \rangle_{L^2(D_i)})^2} \end{cases} \tag{17}$$

Then we obtain

$$\tilde{\phi}_{i_0} = \begin{cases} \sum_{j=1}^{\infty} \frac{2}{T} \frac{(\langle \frac{\partial \psi_0'}{\partial x_i}(T), w_j\rangle \quad - \quad \langle g_{s_i}^d, w_j\rangle)}{(\langle f_i, \frac{\partial w_j}{\partial x_i}\rangle_{L^2(D_i)})^2} w_j(x) & x \in \omega \\ 0 & x \in \Omega \backslash \omega \end{cases} \tag{18}$$

and

$$\tilde{\phi_{i_1}} = \begin{cases} \sum_{j=1}^{\infty} \frac{2}{T} \lambda_j \frac{(\langle \frac{\partial \psi_0'}{\partial x_i}(T), w_j\rangle \quad - \quad \langle g_{p_i}^d, w_j\rangle)}{(\langle f_i, \frac{\partial w_j}{\partial x_i}\rangle_{L^2(D_i)})^2} w_j(x) & x \in \omega \\ 0 & x \in \Omega \backslash \omega \end{cases} \tag{19}$$

We define a final error (depending on the subregion ω and the location of the actuator) by considering $\mathcal{E} = \|\nabla y_u(T) - g_p^d\|^2_{(L^2(\omega))^n} + \|\nabla y_u'(T) - g_s^d\|^2_{(L^2(\omega))^n}$.
The general algorithm for computing the optimal control for (5) is as follows.

3.2.1 Algorithm

1. Choose actuator location: $D_i \subset \Omega$, the subregion ω and precision ε.
2. Choose approximation order M.
3. Calculation of $\tilde{\phi}_{i_0}$ and $\tilde{\phi}_{i_1}$ using (18), (19) .
4. Solve (10) and obtaining $\nabla y_u(T)$ and $\nabla y_u'(T)$.
5. If $\mathcal{E} \leq \varepsilon$ stop, else $M \leftarrow M + 1$ and return to step 3.

4 Simulation results

Here we consider tow-dimensional system excited by 2 zone actuators (D_1, f_1) and (D_2, f_2) where $D_1 \subset \Omega$,$f_1 \in L^2(D_1)$ and $D_2 \subset \Omega$, $f_2 \in L^2(D_2)$

$$\begin{cases} \frac{\partial^2 y(x,t)}{\partial t^2} - \frac{\partial^2 y(x,t)}{\partial x^2} = f_1(x)u_1(t) + f_2(x)u_2(t)) & in \quad Q \\ y(x,0) = y_0(x), \quad \frac{\partial y}{\partial t}(x,0) = y_1(x) & in \quad \Omega \\ y(0,t) = y(1,t) = 0 & on \quad \Sigma. \end{cases} \tag{20}$$

We take
$y_0(x) = y_1(x) = 0$.
For $T = 3$ and $f1 = 1_{D_1}, f2 = 1_{D_2}$, with

$$\begin{cases} D_1 = [0, 0.15] \times [0, 0.15] \cup [0.85, 1] \times [0.85, 1] \\ D_2 = [0.15, 0.5] \times [0.15, 0.5] \cup [0.5, 0.85] \times [0.5, 0.85] \end{cases}$$

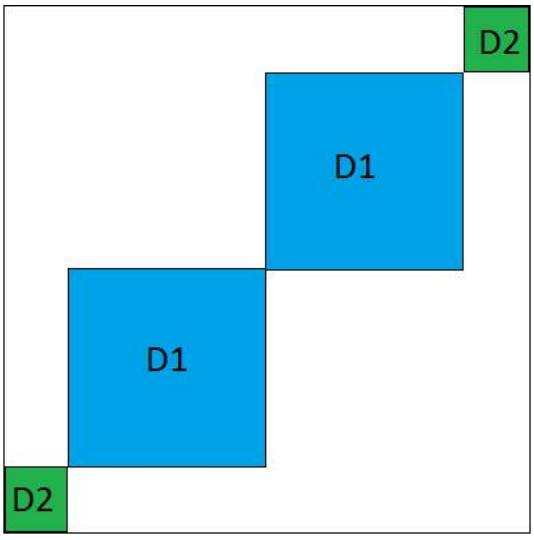

Figure 1: The domains D_1 and D_2

we have the following results:

4.1 Example1

Here we test the previous algorithm with the desired gradient position and speed gradient given by

$$\begin{cases} g_{p_x}^d(x,y) = 9\cos(\pi x)\sin(piy) \\ g_{p_y}^d(x,y) = 9\sin(\pi x)\cos(piy) \end{cases}$$

$$\begin{cases} g_{s_x}^d(x,y) = 6\cos(\pi x)\sin(\pi y) \\ g_{s_y}^d(x,y) = 6\sin(\pi x)\cos(\pi y) \end{cases}$$

For $\omega =]0,1[\times]0,1[$ we have the figures:

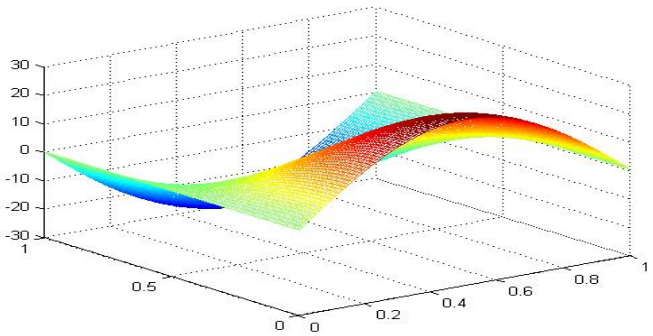

Figure 1: The desired position gradient $g_{p_x}^d$

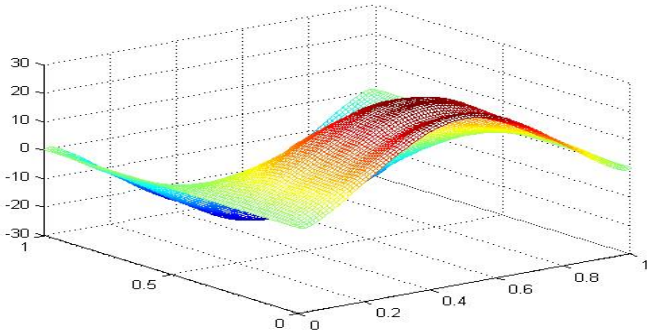

Figure 2: The reachad position gradient $g^d_{p_x}$ in ω.

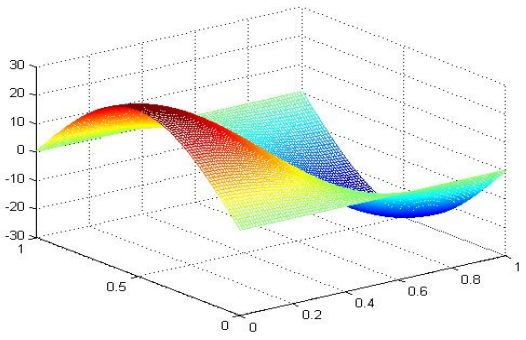

Figure 3: The desired position gradient $g^d_{p_y}$

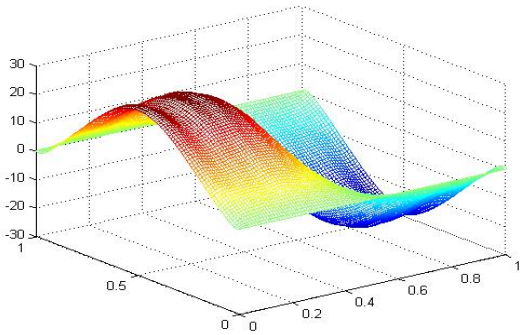

Figure 4: The reachad position gradient $g^d_{p_y}$ in ω.

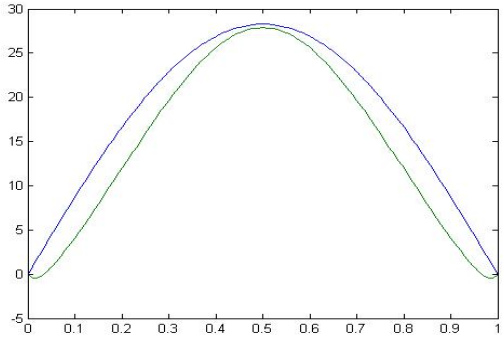

Figure 11:The desired position gradient g^d_p (dashed line) and its reached (solid line) in Γ

5 Weak gradient controllability and actuators

In this section we show that there exist a link between the weak gradient controllability and the actuators structure. Consider system (1) excited by p zone actuators (D_i, f_i) where $D_i \subset \Omega$ and $f_i \in L^2(D_i)$

$$\begin{cases} \dfrac{\partial^2 y(x,t)}{\partial t^2} - Ay(x,t) = \sum_{i=1}^{p} (\chi_D f_i)(x) u_i(t) & in \quad Q \\ y(x,0) = y_0, \dfrac{\partial y}{\partial t}(x,0) = y_1 & in \quad \Omega \\ y(\xi,t) = \eta(\xi,t) & on \quad \Sigma \end{cases} \tag{21}$$

and the boundary control $\eta = \sum_{i=1}^{n} \dfrac{\partial \phi}{\partial x_i}$ where ϕ is the solution of as follow system:

$$\begin{cases} \dfrac{\partial^2 \varphi(x,t)}{\partial t^2} - A^* \varphi(x,t) = 0 & in \quad Q \\ \varphi(x,T) = -h_0; \varphi'(x,T) = h_0 & in \quad \Omega \\ \varphi(\xi,t) = 0 & on \quad \Sigma \end{cases} \tag{22}$$

Proposition 5.1.
If the system (21) exited by the sequence of the actuator $(f_i, D_i)_{1\le i\le p}$ is weakly gradient controllable on Ω. Then

1. $p \ge \sup(r_n)$.
2. *$Rank(G_m) = r_m$, for all $m \ge 1$ where (G_m) is the matrix of order (p, r_m) given by*

$$(G_m)_{i,j} = \begin{cases} \sum_{k=1}^{n} \langle \dfrac{\partial \omega_{m_j}}{\partial x_k}, f_i \rangle_{D_i} & zonal\ case \\ \sum_{k=1}^{n} \dfrac{\partial \omega_{m_j}}{\partial x_k}(b_i) & pointwise\ case \end{cases}$$

References

[1] A. Boutoulout, H. Bourray and F. El Alaoui, 2013 *Boundary gradient observability for semilinear parabolic systems: Sectorial approach*, math. Sci. Lett. 2, No.1, 45-53.

[2] A. Boutoulout, H. Bourray and F. El Alaoui, 2012 *Boundary flux reconstruction for semilinear parabolic systems: HUM Approach*, International Review of Automatic Control (I.RE.A.CO.), Vol, 5, No.5, 652-659.

[3] R. F. Curtain and H. Zwart, 1995, *An introduction to infinite dimentional linear systems theory*, Springer Verlag, NewYork.

[4] A. El Jai and A.J Prichard, 1988, *Sensors and actuators in distributed systems analysis, Ellis Horwood series in applied mathematics, J. Wiley.*

[5] A. Kamal, A. Boutoulout and S. A Ould Beinane, 2010 *Regianl boundary controllabiity of semilinear distributed parabolic systems*, International Review of Automatic Control(I.RE.A.CO.), 3(4): 378-387.

[6] J. L. Lions, 1988, *Contrôlabilité éxacte perturbation et stabilisation des systèmes distribués* non homognes et applications. Tome 1, Masson.

[7] J. L. Lions, E. Magenes 1968, Problèmes aux limites non homogénes et applications. Vol. 1. et 2. Dunod.

[8] A. Pazy, 1983 *Semigroups of linear operators and applications to partial differential equations*, Springer-Verlag, New-York.

[9] E. Zerrik and A. Boutoulout and A. Kamal, 1999, *Regional gradient controllability of parabolic systems*, Int. J. appl. Math and Comp. Sci, Vol. 9, No. 4, 767-787.

[10] E. Zerrik, H. Bourray and S. Ben Hadid, 2010 Sensors and boundary state reconstruction of hyperbolic systems, Int. J. Appl. Math. Comput. Sci., 2010, Vol. 20, No. 2, 227-238.

[11] E. Zerrik and R. Larhrissi,2001, *Regional target control of the wave equation*, Int. J. Systems Science, Vol. 32, No. 10, 1233-1242.

Proceedings of ICCSA 2014
Normandie University, Le Havre, France - June 23-26, 2014

REGIONAL GRADIENT OBSERVABILITY : SECTORIAL APPROACH

A. Khazari, A. Boutoulout, H. Bourray and I. El harraki *

Abstract. The aim of this talk is to study the notion of the gradient observability on a subregion ω of the evolution domain Ω for the class of semilinear hyperbolic systems that is the intermediary between the linear and nonlinear classes. We show, under some hypotheses, that the gradient reconstruction is guaranteed by means of the sectorial approach combined with fixed point techniques. This leads to several interesting results which are performed through numerical examples and simulations.

Keywords. Distributed systems; hyperbolic systems; gradient reconstruction; regional gradient observability; fixed point; sectorial operator.

1 Introduction

The aim if this paper is to study the regional gradient observability of an important class of semilineair hyperbolic systems between linear and non linear systems. We will focus our attention on the case where yhe dynamics of the systems is a linear operator of the sectoriel case and the generation of an analytic semi group $(S(t)_{t\geq 0})$in the Hilbert space. For observability problem when one is confronted with the question of reconstructing the gradient state and the gradient speed, it is important to take into account the effects of non linearity. For example, approximate controllability of semilinear can be obtained when the non linearity satisfies some conditions (see[11] and [12]), and the techniques used combine a variational approach to controllability problem for linear equation and fixed point method. The techniques are also based on linear infinite dimensional observability theory together with a variety of fixed point theorems.

2 Problem statement

Let Ω be an open bounded subset of $\mathbb{R}^n (n = 1, 2, 3)$.
For $T > 0$, we denote $Q = \Omega\times]0, T[$, $\Sigma = \partial\Omega\times]0, T[$ and we Consider the following semi linear hyperbolic system

$$\begin{cases} \dfrac{\partial^2 y}{\partial t^2}(x,t) = \mathcal{A}y(x,t) + \mathcal{N}y(x,t) & \text{in} \quad Q \\ y(x,0) = y^0(x), \dfrac{\partial y}{\partial t}(x,0) = y^1(x) & \text{in} \quad \Omega \\ y(\xi,t) = 0 & \text{on} \quad \Sigma \end{cases} \tag{1}$$

where $(y^0, y^1) \in H_0^1(\Omega) \times L^2(\Omega)$.
where $\mathcal{A}$ is a second order elliptic linear operator, symmetric generating a strongly continuous semigroup $(S(t))_{t\geq 0}$ and N $\mathcal{N}$ is a nonlinear operator assumed to be locally lipshitzian.
Let $(y, \dfrac{\partial y}{\partial t})$ denotes the solution of the equation (1) and assume that $(y, \dfrac{\partial y}{\partial t}) \in \mathcal{F} = H_0^1(\Omega) \times H_0^1(\Omega)$ and the function of measurements is given by the output function

$$z(x,t) = Cy(x,t) \tag{2}$$

where C is a linear operator from $\mathcal{F}$ to the space $\mathbb{R}^q$.
For a basis of eigenfuctions of the operator $\mathcal{A}$, with the condition of Dirichlet, which is noted by Φ_{mj}, and the associated eigenvalues λ_m of multiplicity r_m, the semigroup $(S(t))_{t\geq 0}$ is given by
For any $(y_1, y_2) \in E = L^2(\Omega) \times L^2(\Omega)$

$$\bar{S}(t)\begin{pmatrix} y_1 \\ y_2 \end{pmatrix} = \begin{pmatrix} \sum_{m}^{\infty}\sum_{j=1}^{r_m}\Big[\langle y_1, \Phi_{mj}\rangle \cos(-\lambda_m)^{\frac{1}{2}}t \\ +(-\lambda_m)^{-\frac{1}{2}}\langle y_2, \Phi_{mj}\rangle \sin(-\lambda_m)^{\frac{1}{2}}t\Big]\Phi_{mj}(.) \\ \sum_{m}^{\infty}\sum_{j=1}^{r_m}\Big[-(-\lambda_m)^{\frac{1}{2}}\langle y_1, \Phi_{mj}\rangle \sin(-\lambda_m)^{\frac{1}{2}}t \\ +\langle y_2, \Phi_{mj}\rangle \cos(-\lambda_m)^{\frac{1}{2}}t\Big]\Phi_{mj}(.) \end{pmatrix}$$

Without loss of generality we note: $y(t) := y(x;t)$ and we associate to the system (1) the linear system

$$\begin{cases} \dfrac{\partial^2 y}{\partial t^2}(t) = \mathcal{A}y(t) & \text{in} \quad Q \\ y(0) = y^0, \dfrac{\partial y}{\partial t}(0) = y^1 & \text{in} \quad \Omega \\ y(t) = 0 & \text{on} \quad \Sigma \end{cases} \tag{3}$$

System (3) admits a unique solution
$y \in C(0;T;H_0^1(\Omega)) \cap C^1(0;T;L^2(\Omega))$ (see [[1]]).

*A. Khazari, A. Boutoulout, H. Bourray and I. El harraki are with Departement of Mathematics & Computer Science, Moulay ismail University, Meknes, Morocco.
E-mails: adil0974@gmail.com, boutouloutali@yahoo.fr, hbourrayh@yahoo.fr and imadharraki@gmail.com

Let denote $\bar{y} = (y, \frac{\partial y}{\partial t}), \bar{\mathcal{A}}(y_1, y_2) = (y_2, \mathcal{A}y_1)$
for all $(y_1, y_2) \in D(\bar{\mathcal{A}}) = (H_0^1(\Omega) \cap H^2(\Omega)) \times L^2(\Omega)$,
$\bar{\mathcal{N}}(y_1, y_2) = (0, \mathcal{N}y_1)$ and $\bar{y}^0 = (y^0, \frac{\partial y^0}{\partial t} = y^1)$.
The system (1) may be written as

$$\begin{cases} \frac{\partial \bar{y}}{\partial t}(t) = \bar{\mathcal{A}}\bar{y}(t) + \bar{\mathcal{N}}\bar{y}(t) & 0 < t < T \\ \bar{y}(0) = \bar{y}^0 \end{cases} \tag{4}$$

and the system (3) is equivalent to

$$\begin{cases} \frac{\partial \bar{y}}{\partial t}(t) = \bar{\mathcal{A}}\bar{y}(t) & 0 < t < T \\ \bar{y}(0) = \bar{y}^0 \end{cases} \tag{5}$$

the systems ((4), (5)) are augmented with the output function

$$\bar{z}(t) = \bar{C}\bar{y}(t) \tag{6}$$

with $\bar{C} = (C, 0)$
System (1) can be interpreted in the mild sense as follows

$$\begin{cases} \bar{y}(t) = \bar{S}(t)\bar{y}^0 + \int_0^t \bar{S}(t-\tau)\bar{\mathcal{N}}\bar{y}(\tau)d\tau \\ \bar{y}(0) = \bar{y}^0 \end{cases} \tag{7}$$

and the output equation can be expressed by

$$\bar{z}(t) = \bar{C}\bar{S}(t)\bar{y}^0 = \bar{K}(t)\bar{y}^0, \quad t \in]0, T[$$

Let $\bar{K}$ be the observation operator defined by

$$\begin{array}{rcl} \bar{K} : \mathcal{F} & \longrightarrow & \mathcal{O} = L^2(0, T; I\!R^q) \times L^2(0, T; I\!R^q) \\ \bar{z} & \longrightarrow & \bar{C}\bar{S}(.)\bar{z} \end{array}$$

which is linear and bounded with the adjoint $\bar{K}^*$ given by

$$\begin{array}{rcl} \bar{K}^* : \mathcal{O} & \longrightarrow & \mathcal{F} \\ \bar{z}^* & \longrightarrow & \int_0^T \bar{S}^*(t)\bar{C}^*\bar{z}^*(t)dt \end{array}$$

Consider the operator $\overline{\nabla}$ given by the formula

$$\begin{array}{rcl} \overline{\nabla} : H_0^1(\Omega) \times H_0^1(\Omega) & \longrightarrow & (L^2(\Omega))^n \times (L^2(\Omega))^n \\ (y_1, y_2) & \longrightarrow & \overline{\nabla}(y_1, y_2) = (\nabla y_1, \nabla y_2)) \end{array}$$

where

$$\begin{array}{rcl} \nabla : H_0^1(\Omega) & \longrightarrow & (L^2(\Omega))^n \\ y & \longrightarrow & \nabla y = (\frac{\partial y}{\partial x_1}, ..., \frac{\partial y}{\partial x_n}) \end{array}$$

$\overline{\nabla}^*$ is the adjoint of $\overline{\nabla}$.
The initial state $\bar{y}^0$ and $\overline{\nabla}\bar{y}^0$ its gradient are assumed unknown.
For $\omega \subset \Omega$ an open subregion of Ω and has positive Lebesgue measure, let $\overline{\chi}_\omega$ be the restriction operator defined by

$$\begin{array}{rcl} \overline{\chi}_\omega : (L^2(\Omega))^n \times (L^2(\Omega))^n & \longrightarrow & (L^2(\omega))^n \times (L^2(\omega))^n \\ (y_1, y_2) & \longmapsto & \overline{\chi}_\omega(y_1, y_2) = (\chi_\omega y_1, \chi_\omega y_2) \end{array}$$

where

$$\begin{array}{rcl} \chi_\omega : (L^2(\Omega))^n & \to & (L^2(\omega))^n \\ \xi & \mapsto & \chi_\omega \xi = \xi|_\omega \end{array}$$

and $\overline{\chi}_\omega^*$ (resp χ_ω^*) is the adjoint of $\overline{\chi}_\omega$ (resp χ_ω), and we consider the operator

$$\bar{H} = \overline{\chi}_\omega \overline{\nabla} \bar{K}^*$$

Let the gradient $\overline{\nabla}\bar{y}^0 = (\nabla y^0, \nabla y^1)$ of the initial state $\bar{y}^0 = (y^0, y^1)$ be decomposed as follows:

$$\overline{\nabla}\bar{y}^0 = \begin{cases} \bar{y}_1^0 & \text{in} \quad \omega \\ \bar{y}_2^0 & \text{in} \quad \Omega\backslash\omega \end{cases} \tag{8}$$

where $\bar{y}_1^0 = (y_1^0, \frac{\partial y_1^0}{\partial t} = y_1^1)$, $\bar{y}_2^0 = (y_2^0, \frac{\partial y_2^0}{\partial t} = y_2^1)$ and

$$\nabla y^0 = \begin{cases} y_1^0 & \text{in} \quad \omega \\ y_2^0 & \text{in} \quad \Omega\backslash\omega \end{cases}, \qquad \nabla y^1 = \begin{cases} y_1^1 & \text{in} \quad \omega \\ y_2^1 & \text{in} \quad \Omega\backslash\omega \end{cases}$$

Since ω is an open set of Ω and $\bar{y}_0 \in H_0^1(\Omega) \times H_0^1(\Omega)$, we have

$$\begin{array}{l} \exists \bar{y}_1^0 \in \ker(I - \overline{\chi}_\omega \overline{\nabla\nabla}^* \overline{\chi}_\omega^*) \\ \text{such that} \quad \bar{y}_0 = \overline{\nabla}^* \overline{\chi}_\omega^* \bar{y}_1^0 + \overline{\nabla}^* \overline{\chi}_{\Omega\backslash\omega}^* \bar{y}_2^0 \end{array} \tag{9}$$

Definition 2.1. The semilinear system (1) augmented with output (2) is said to be regionally gradient observable on Ω or regionally G-observable if we can reconstruct the gradient of its state and the gradient of its speed in a subregion ω of Ω at any time t.

The study of regional gradient observability amounts to solving the following problem:

Problem 2.2.
Given the semilinear system (1) and output (2) on $[0, T]$, is it possible to reconstruct $\overline{\nabla}\bar{y}^0 = (\nabla y^0, \nabla y^1)$ which is the gradient of initial state and the gradient of initial speed of (1) on Ω ?

3 Sectorial case

In this section, we study Problem 2.2 under some supplementary hypothesis on $\mathcal{A}$ and the nonlinear operator $\mathcal{N}$. With the same notations as in the previous case, we reconsider the semilinear system described by the equations (4) and (6)where one suppose that the operator $\bar{\mathcal{A}}$ generates an analytic semigroup $(\bar{S}(t))_{t\geq 0}$ in the state space E.
Let's consider $\bar{\mathcal{A}}_1 = \bar{\mathcal{A}} + aI$ such that $Re(\sigma(\bar{\mathcal{A}}_1)) > \delta > 0$ with a is a positive real number and $Re(\sigma(\bar{\mathcal{A}}_1))$ denotes the real part of spectrum of $\bar{\mathcal{A}}_1$. Then for $0 \leq \alpha < 1$, we define the fractional power $(\bar{\mathcal{A}}_1)^\alpha$ as a closed operator with domain $E^\alpha = D(\bar{\mathcal{A}}_1^\alpha)$ which is a dense Banach space on E endowed with the graph norm

$$\| \, . \, \|_{E^\alpha} = \| \, \bar{\mathcal{A}}_1^\alpha(.) \, \|_E$$

Let us consider $V = Im(\overline{\chi}_\omega \overline{\nabla} \bar{K}^*)$ then the objective is to study the Problem 2.2 in V endowed with the norm

$$\| \, . \, \|_V = \| \, \bar{H}^*(.) \, \|_Y \tag{10}$$

we have

$$\| \, \bar{S}(t) \, \|_{\mathcal{L}(E,E^\alpha)} \leq ct^{-\alpha} \exp(a-\alpha)t = g_1(t)$$

where c is a constant. For more details, see([2], [4], [10]) For $r, s > 1$, assume that

$$\left\{ \begin{array}{l} \dfrac{1}{r} + \dfrac{1}{s} = 1 \\ g_1 \in L^{r}(0,T) \end{array} \right. \tag{11}$$

and the operator $\bar{\mathcal{N}} : L^r(0,T;E^\alpha) \longrightarrow L^s(0,T;E)$ is well defined and satisfies the following conditions :

$$\left\{ \begin{array}{l} \| \, \bar{\mathcal{N}}x - \bar{\mathcal{N}}y \, \|_{L^s(0,T;E)} \leq k(\| \, x \, \|, \| \, y \, \|) \, \| \, x - y \, \|_{L^r(0,T;E^\alpha)} \\ \forall x, y \in L^{r}(0,T;E^\alpha) \\ \\ \bar{\mathcal{N}}(0) = 0 \quad \text{with} \quad k : I\!R^+ \times I\!R^+ \longrightarrow I\!R^+ \\ \\ \text{such that} \quad \lim\limits_{(\theta_1,\theta_2)\to(0,0)} k(\theta_1,\theta_2) = 0 \end{array} \right. \tag{12}$$

This hypothesis are verified by many important class of semi linear hyperbolic systems. For example the equation governing the flow of neutrons in a nuclear reactor

$$\left\{ \begin{array}{ll} y^{'} - ky^{''} - ay = -by^2 & \\ y(t) = 0 & \text{in} \quad [0,1] \\ y(0) = 0 & \end{array} \right.$$

whith $y(t) \in L^2([0,1]), 0 \leq t \leq T, k, a, b > 0$. The operators $\mathcal{A}$ and $\mathcal{N}$ corresponding are

$$\begin{array}{rrcl} \mathcal{A} : & H_0^1([0,1]) \cap H^2([0,1]) & \to & L^2([0,1]) \\ & y & \to & \dfrac{1}{k}y^{'} - \dfrac{a}{k}y \\ \\ \mathcal{N} : & H_0^1([0,1]) & \to & L^2([0,1]) \\ & y & \to & \dfrac{by^2}{k} \end{array}$$

The assumption is satisfied with $r = 2, s = 1$ and $k(\theta_1, \theta_2) = \dfrac{b}{k}(\theta_1 + \theta_2)$. Various examples are given and discussed in ([2], [9]).

We show that there exists a set of admissible initial gradient states and admissible initial gradient speed, admissible in the sense that allows to obtain system (3) weakly G-observable.

Let's consider

$$\varphi(\bar{y}_1^0, .) : L^r(0,T;E^\alpha) \to L^r(0,T;E^\alpha)$$

given by

$$\varphi(\bar{y}_1^0, \bar{y})(t) = \bar{S}(t)\overline{\nabla}^* \bar{\chi}_\omega^* \bar{y}_1^0 + \bar{S}(t)\bar{\chi}_{\Omega\setminus\omega}^* \bar{y}_2^0 + L(t)\bar{N}\bar{y} \quad t \in [0,T]$$

where $\bar{y}_1^0, \bar{y}_2^0$ are respectively the restriction in ω and in $\Omega\setminus\omega$ of the initial gradient condition $\overline{\nabla}\bar{y}^0$ given by (8). we assume that

$$\| \, \bar{S}(t)\overline{\nabla}^* \bar{\chi}_\omega^* \, \|_{\mathcal{L}(V,E^\alpha)} \leq g_2(t) \quad \text{with} \quad g_2 \in L^2(0,T) \tag{13}$$

then we have the following result

Proposition 3.1. *Suppose that the system (3) is weakly G-observable in ω, and (11), (12) and (13) satisfied, then the following assertion hold:*

- *There exists $a_1 > 0$ and $m > 0$ such that for all $\bar{y}_1^0 \in B(0,m) \subset V$ the function $\varphi(\bar{y}_1^0, .)$ has a unique fixed point $\bar{y}$ in the ball $B(0,a_1) \subset L^r(0,T;E^\alpha)$ solution of the system (4).*
- *There exist $m = m(a_1)$ and $m_1 = m_1(a_1)$ such that $\| \, \overline{\nabla}^* \bar{\chi}_{\Omega\setminus\omega}^* \bar{y}_2^0 \, \|_E \leq m_1$ the mapping f is lipschitzien where :*

$$\begin{array}{rcl} f : B(0,m) & \longrightarrow & B(0,a_1) \\ \bar{y}_1^0 & \longmapsto & \bar{y} \end{array}$$

Remark 3.1. The given results show that there exists a set of admissible gradient initial state. If the gradient initial state is taken in $B(0,m)$, with a bounded residual part then the system (4) has only one solution in $B(0,a_1)$.

Here we show that if the measurements are in $B(0,\rho)$, with ρ is suitably chosen then the gradient initial state can be obtained as a solution of a fixed point problem. Let us consider the mapping

$$\varphi_1(\bar{z}, \bar{y}_1^0) = (\bar{K}\overline{\nabla}^*\overline{\chi}_\omega^*)^\dagger \Big(\bar{z} - \bar{C}\bar{S}(.)\overline{\nabla}^*\overline{\chi}_{\Omega\setminus\omega}^* \bar{y}_2^0 - \bar{C}L(.)\bar{N}f(\bar{y}_1^0) \Big) \tag{14}$$

and assume that $\forall \bar{y}_1^0 \in V$, $\bar{C}L(.)\bar{N}f(\bar{y}_1^0) \in \mathrm{Im}(\bar{K}\overline{\nabla}^*\overline{\chi}_\omega^*)$ Then we have the following result.

Proposition 3.2. *Assume that*

$$\exists c_1 > 0 \quad \textit{such that} \quad \| \, \bar{C}L(.)\bar{y} \, \|_Y \leq c_1 \, \| \, \bar{y} \, \|_{L^s(0,T;E)} \quad \forall \bar{y} \in L^s(0,T;E) \tag{15}$$

$$\textit{and} \quad \exists c_2 > 0 \quad \textit{such that} \quad \| \, \bar{C}\bar{S}(.)\bar{y} \, \|_Y \leq c_2 \, \| \, \bar{y} \, \|_E \quad \forall \bar{y} \in E \tag{16}$$

and if the system linear (5) is weakly G-observable in ω and (12) holds, then there exists $a_2 > 0$ and $\rho = \rho(a_2) > 0$, such that for all $\bar{z} \in B(0,\rho) \subset Y$, the function (14) admit a unique fixed point in $B(0,m)$ which correspond to the gradient initial condition $\bar{y}_0^1$ observed in ω. Furthermore, the function h is Lipschitzian where :

$$\begin{array}{rcl} h : B(0,\rho) & \longrightarrow & B(0,m) \\ \bar{z} & \longmapsto & \bar{y}_1^0 \end{array}$$

4 Numerical approach

We show the existence of a sequence of the initial gradient states and initial gradient speed which converges respectively to the regional initial gradient states and initial gradient speed to be observed in ω.

Proposition 4.1. *We suppose that the hypothesis of the prop (3.2) are verified, then for $\bar{z} \in B(0,\rho)$, the sequence of the initial gradient condition defined in $B(0,m) \subset V$ by*

$$\left\{ \begin{array}{ll} \bar{y}_{1,0}^0 & = 0 \\ \bar{y}_{1,n+1}^0 & = (\bar{H}^*)^\dagger \Big(\bar{z} - \bar{C}\bar{S}(.)\overline{\nabla}^*\bar{\chi}_{\Omega\setminus\omega}^* \bar{y}_2^0 - \bar{C}L(.)\bar{N}f(\bar{y}_{1,n}^0) \Big) \end{array} \right. \tag{17}$$

converges to $\bar{y}_1^0$ the regional initial gradient condition (the regional initial gradient state y_1^0 and the regional initial gradient speed y_1^1) to be observed in ω. where $\bar{y}_2^0$ is the residual part of the initial gradient condition in $\Omega\setminus\omega$.

4.1 Algorithm

Let's consider $r_{n+1} = \bar{z} - \bar{C}\bar{S}(.)\overline{\nabla}^* \bar{\chi}^*_{\Omega\setminus\omega}\bar{y}^0_2 - \bar{C}L(.)\bar{N}f(\tilde{y}^0_{1,n})$, then we have $\tilde{y}^0_{1,n+1} = (\bar{H}^*)^\dagger r_{n+1}$
and $\bar{z}_n = \bar{H}^*\tilde{y}^0_{1,n} + \bar{z} - r_{n+1} = r_n + \bar{z} - r_{n+1}$
Thus we obtain the following algorithm:
Algorithm:

Step 1 : The initial condition $\bar{y}^0_1 = (y^0, y^1)$,
the region ω, The domain D
and the function of distribution f
and the accuracy threshold ε,
$r_1 = \bar{z} - \bar{C}\bar{S}(.)\overline{\nabla}^* \bar{\chi}^*_{\Omega\setminus\omega}\bar{y}^0_2 - \bar{C}L(.)\bar{N}f(\tilde{y}^0_{1,0})$

Step 2 : Repeat

$\ominus\ \tilde{y}^0_{1,n} = (\bar{H}^*)^\dagger r_n$

$\ominus$

$$\begin{cases} \dfrac{\partial \bar{y}_n(t)}{\partial t} & = \bar{\mathcal{A}}\bar{y}_n(t) + \bar{\mathcal{N}}\bar{y}_n(t) \\ \bar{y}_n(0) & = \bar{\chi}^*_\omega \tilde{y}^0_{1,n} + \bar{\chi}^*_{\Omega\setminus\omega}\bar{y}^0_2 \end{cases}$$

$\ominus\ \bar{z}_n = \bar{C}\bar{y}_n$

Until $\| \bar{z} - \bar{z}_n \|_Y \leq \varepsilon$.

Step 3 : $\tilde{y}^0_{1,n}$ which corresponds to the initial gradient condition to be observed $\bar{y}^0_1$ in ω.

else $r_{n+1} = r_n + \bar{z} - r_{n+1}$ go to step 2.

References

[1] J. L. Lions and E. Magenes, "Problèmes aux limites non homogènes et applications," *Dunod. Paris,* vols. 1 et 2, 1968.

[2] D. Henry, "Geometric theory of semilinear parabolic systems," *Lect. Notes Math. 840, Springer-Verlag Berlin Heidelberg New York,* 1981.

[3] A. El Jai, M. C. Simon and E. Zerrik, "Regional observability and sensor structures," *Sensors and Actuators Journal,* vol. 39, pp. 95-102, 1993.

[4] E. Zerrik, H. Bourray, and A. El Jai, "Regional observability for semilinear distributed parabolic systems," *Journal of Dynamical and Control Systems,* vol.10, No. 3, pp. 413-430, 2004.

[5] A. Boutoulout, H. Bourray, and F-Z. El Alaoui, "Boundary gradient observability for semilinear parabolic systems: Sectorial approach," *Math. Sci. Lett,* vol. 2, pp. 45-54,2013.

[6] A. Boutoulout, H. Bourray, F.Z. El Alaoui and S. Benhadid, "Regional observability for distributed semilinear hyperbolic systems," *International Journal of Control,* pp. 1-13, 2014.

[7] A. Boutoulout, H. Bourray and A. Khazari, "Gradient observability for hyperbolic system," *International Review of Automatic Control (I.RE.A.CO),* vol 6, pp. 274-263, 2013.

[8] E. Zerrik, H. Bourray and S. Benhadid, "Sensors and Regional observability of the wave equation," *Sensors and Actuators Journal,* vol. 138, pp. 313-328, 2007.

[9] K. Kassara and A. El Jai, "Algorithme pour la commande d'une classe de systmes paramtre rpartis non linaires," *Rev. Mar. d'Aut. et de Trait. de signal,* vol. 1, pp. 3-24, 1983.

[10] E. Zeidler, "Nonlinear functional analysis and its applications II/A linear applied functional analysis," *Springer,* 1990.

[11] E. Zuazua, "Exact Controllability for Semilinear Wave Equations in One Space Dimension, " *Annales de lInstitut Henri Poincaré : Analyse Non Linéaire,* vol. 10, pp. 109-129, 1993.

[12] E. Zuazua, "Exact Controllability for the Semilinear Wave Equations, " *Journal de Mathématiques Pures et Appliquées,* vol. 59, pp. 1-31, 1990.

General Session 2
Fractal Analysis, Social Systems

Proceedings of ICCSA 2014
Normandie University, Le Havre, France - June 23-26, 2014

A Hybrid Network/Grid Model of Urban Morphogenesis and Optimization

Juste Raimbault [*], Arnaud Banos [†], and René Doursat [‡]

Abstract. We describe a hybrid agent-based model and simulation of urban morphogenesis. It consists of a cellular automata grid coupled to a dynamic network topology. The inherently *heterogeneous* properties of urban structure and function are taken into account in the dynamics of the system. We propose various layout and performance measures to categorize and explore the generated configurations. An *economic evaluation* metric was also designed using the sensitivity of segregation models to spatial configuration. Our model is applied to a real-world case, offering a means to optimize the distribution of activities in a zoning context.

Keywords. Agent-based modeling, cellular automata, bi-objective Pareto optimization, evidence-based urbanism, urban morphogenesis.

1 Introduction

Recent progress in many disciplines related to urban planning can be interpreted as the rise of a "new urban science" according to Batty [7]. From agent-based models in quantitative geography [17], in particular the successful Simpop series by Pumain et al. [30], to other approaches termed "complexity theories of cities" by Portugali [28], involving physicists of information theory such as Haken [15] or architects of "space syntax theory" such as Hillier [18], the field is very broad and diverse. Yet, all these works share the view that urban systems are quintessentially *complex systems*, i.e. large sets of elements interacting locally with one another and the environment, and collectively creating a emergent structure and behavior. Taking into account the intrinsic *heterogeneity* of geographical and urban systems, this view lends itself naturally to an agent-based modeling and simulation (ABMS) approach.

[*]Graduate School, École Polytechnique, Palaiseau, France; and LVMT, École Nationale des Ponts et Chaussées, Paris, France. E-mail: juste.raimbault@polytechnique.edu

[†]Géographie-cités, CNRS UMR8504, Paris, France. E-mail: arnaud.banos@parisgeo.cnrs.fr

[‡]Complex Systems Institute, Paris Île-de-France (ISC-PIF), CNRS UPS3611. E-mail: rene.doursat@iscpif.fr

Among the most popular ABMS methods are cellular automata (CA), in which agents are cells that have fixed locations on a grid and evolve according to the state of their neighbors. CA models of urban planning, in particular the reproduction of existing urban forms and land-use patterns, have been widely studied, notably by White and Engelen [39], then analyzed [5, 9] and synthesized [6] by Batty. A recent review by Iltanen [19] of CA in urban spatial modeling shows a great variety of possible system types and applications. They include, for example, "microeconomic" CA for the simulation of urban sprawl [11], "linguistic" CA (including real-time rule update via feedback from the population) for the measure of sustainable development in a fast growing region of China [41], and one-dimensional CA [26] showing discontinuities and strong path-dependence in settlement patterns.

In this context, we propose a *hybrid* model of urban growth that combines a CA approach with a graph topology containing long-range edges. It is inspired by Moreno et al.'s work [24, 25], which integrates a network dynamics in a CA model of urban morphology. Its goal was to test the effects of physical proximity on urban development by introducing urban mobility in a network whose evolution was coupled with the evolution of urban shape. We generalize this type of model to take into account *heterogeneous urban activities* and the *functional properties* that they create in the urban environment. This idea was introduced by White [38] and explored by van Vliet et al. [36] but, to our knowledge, never considered from the perspective of *physical accessibility* and its impact on sprawl patterns.

The rest of the paper is organized as follows. The model and indicator functions used to quantify the generated patterns are explained in Section 2. Next, Section 3 presents the results of internal and external validations of the model by sensitivity analysis and reproduction of typical urban patterns. It is followed by an application to a concrete case, proposing a bi-objective optimization heuristic of functional configuration based on the relevant objective functions from the validation study. We end with a discussion and conclusion in Sections 4 and 5.

2 Model description

2.1 Agents and rules

The world is represented by a square lattice $(L_{i,j})_{1\leq i,j\leq N}$ composed of cells that are empty or occupied (Fig. 1). This is denoted by a function $\delta(i,j,t) \in \{0,1\}$, where time t follows an iterative sequence $t \in \mathbb{T} = \tau\mathbb{N} = \{0,\tau,2\tau,...\}$ [14] with a regular time step τ. Another evolving structure is laid out on top of the lattice: a Euclidean network $G(t) = (V(t), E(t))$ whose vertices V are a finite subset of the world and edges E (its agents) represent *roads*. In the beginning, the lattice is empty: $\delta(i,j,0) = 0$, and the network is either initialized randomly (e.g. uniformly) or set to a user-specified configuration $G(0) = (V_0, E_0)$. In order to translate functional mechanisms into the growth of a city, we assume that the initial vertices include a subset formed by *city centers*, $C_0 \subset V_0$, which have integer *activities*, denoted by $a : C_0 \to \{1,\dots,a_{\max}\}$.

To characterize the urban structures emerging in this world, we define in general a set of k functions of the lattice, $(d_k(i,j,t))_{1\leq k\leq K}$, called *explicative variables*. These variables are here: d_1, the *density*, i.e. the average δ around a cell (i,j) in a circular neighborhood of radius ρ; d_2, the Euclidean *distance* of a cell to the nearest road; d_3 the *network-distance* of a cell to the nearest city center, i.e. the sum of d_2 and edge lengths; and d_4, the *accessibility* of activities (or rather difficulty thereof), written

$$d_4(i,j,t) = \left(\frac{1}{a_{\max}} \sum_{a=1}^{a_{\max}} d_3(i,j,t;a)^{p_4} \right)^{1/p_4} \qquad (1)$$

where $d_3(i,j,t;a)$ is the network-distance of the cell to the nearest center with an activity a, and $p_4 \geq 1$ (typically 3) defines a p-norm.

A set of weights $(\alpha_k)_{1\leq k\leq K} \in [0,1]^K$ is assigned to these variables to tune their respective influence on what we define as the net *land value* of a cell, as follows:

$$v(i,j,t) = \frac{1}{\sum_k \alpha_k} \sum_{k=1}^{K} \alpha_k \frac{d_{k,\max}(t) - d_k(i,j,t)}{d_{k,\max}(t) - d_{k,\min}(t)}. \qquad (2)$$

Houses are preferentially built where v is high, i.e. d_k's are low. Thus the evolution of the system proceeds in three phases at each time step: (a) all values $v(i,j)$ are updated, (b) among the cells that have the best values, n new cells are randomly chosen and "built" (set to $\delta = 1$); (c) for each built cell, if d_2 is greater than a threshold θ_2 (maximum isolation distance), then that cell is directly connected to the network by creating a new road branching out orthogonally from the nearest edge.

Network initialization is random (see details in 3.1), and the selection of new cells is also random among identical values of v. A sensitivity analysis and model exploration is conducted in the next section to determine the relative effect of parameters with respect to these sources of randomness. In any case, growth is halted after a constant amount of time T, evaluated from experiments, so that the final structure is neither "unfinished" nor filling out the world (see 3.1). Fig. 2 displays the core ABMS flowchart with feedback interactions between agents.

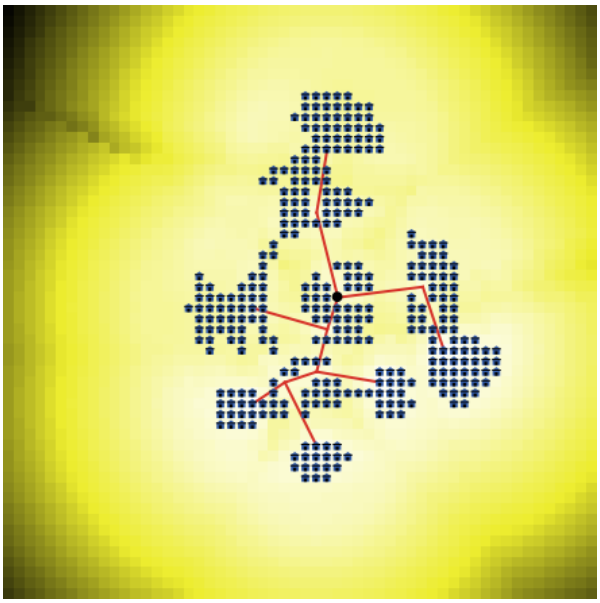

Figure 1: Example of urban morphology generated by the model. Houses (blue squares) were built in some cells of a 56×56 lattice. City centers and roads (red edges) compose the added network. Cell shades (yellow) represent distances to the built cells (the brighter, the closer).

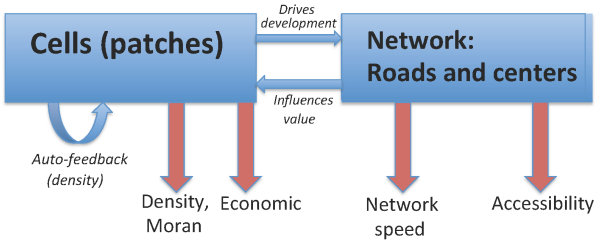

Figure 2: The hybrid network/grid model. *Blue arrows*: feedback interactions. *Red arrows*: output evaluation functions.

2.2 Evaluation functions

Once a structure is generated, its properties need to be quantified so that it can be categorized or compared to other structures for optimization purposes. To this goal, we define various *evaluation functions*, both objective quantification measures and structural fitness values. The measures described in this section take into account all the explicative variables, whose distributions over the grid are emergent properties that cannot be known in advance and are therefore essential to monitor.

Morphology To assess the morphological structure of an urban configuration, we map it onto a 2D metric space

defined by a pair of global indicators (D, I) called the *integrated density* and the *Moran index* (Fig. 4). The density $D \in [0,1]$ is calculated by taking the p-norm (with exponent $p_D \geq 1$, typically 3) of the local densities d_1:

$$D(t) = \left(\frac{1}{\sum_{i,j} \delta(i,j,t)} \sum_{\substack{i,j=1 \\ \delta(i,j,t)\neq 0}}^{N} d_1(i,j,t)^{p_D} \right)^{1/p_D} \quad (3)$$

Moran's I, an index of spatial autocorrelation, is widely used in quantitative geography [35, 20] to evaluate the "polycentric" character of a distribution of populated cells. It is defined by

$$I(t) = \frac{M^2}{\sum_{\mu\neq\nu} 1/d_{\mu\nu}} \frac{\sum_{\mu\neq\nu}(P_\mu - \overline{P})(P_\nu - \overline{P})/d_{\mu\nu}}{\sum_{\mu=1}^{M^2}(P_\mu - \overline{P})^2} \quad (4)$$

where the lattice is partitioned into $M \times M$ square areas, at an intermediate scale between cell size and world size ($1 \ll M \ll N$), $d_{\mu\nu}$ is the distance between the centroids of areas μ and ν, $(P_\mu)_{1\leq\mu\leq M^2}$ denotes the number of occupied cells in each area, and $\overline{P}$ is their global average. We can recognize in this formula the normalized ratio of a modified covariance (pairwise correlations divided by distances) and the variance of the distribution. Moran's I belongs by construction to the interval $[-1, 1]$, where values near 1 correspond to a strong monocentric distribution, values around 0 to a random distribution, and values near -1 to a checkered pattern (every other cell occupied). Usually, polycentric distributions have relatively small positive I values, depending on the size and distance between centers.

Network performance Due to the branching nature of the growth algorithm, the network of roads G cannot contain any other loops than the ones initially present in G_0. Therefore, notions of "clustering coefficient" or "robustness" (with respect to node removal) are not relevant here. On the other hand, since G is intended to simulate a *mobility* network, we can evaluate its performance by defining a *relative speed* [4] S, representing the "detours" imposed by G with respect to direct, straight travels:

$$S(t) = \left(\frac{1}{\sum_{i,j} \delta(i,j,t)} \sum_{\substack{i,j=1 \\ \delta(i,j,t)\neq 0}}^{N} \left(\frac{d_3(i,j,t)}{e_3(i,j,t)} \right)^{p_S} \right)^{1/p_S} \quad (5)$$

where $p_S \geq 1$ (also 3), and $e_3(i,j,t)$ is the direct Euclidean distance between cell (i,j) and the nearest city center over the network, i.e. the one that realizes the value of $d_3(i,j,t)$. Note that $S \geq 1$ and is actually higher for more convoluted networks (thus it is a measure of "slowness", but we still employ "speed").

Functional accessibility The global functional accessibility A to city centers is another p-norm (also 3), based on the relative local accessibility from each cell, which is d_4 over its maximum:

$$A(t) = \left(\frac{1}{\sum_{i,j} \delta(i,j,t)} \sum_{\substack{i,j=1 \\ \delta(i,j,t)\neq 0}}^{N} \left(\frac{d_4(i,j,t)}{d_{4,\max}(t)} \right)^{p_A} \right)^{1/p_A} \quad (6)$$

This normalization puts A in $[0,1]$ and allows comparing configurations of different sizes. Like S, "better" urban configurations are characterized by a lower A.

Economic performance It was shown by Banos [2] that the Schelling segregation model, a standard ABM of socio-economic dynamics [33], was highly sensitive to the spatial structures in which it could be embedded, since segregation rules depended on proximity. This justifies the use of this model as an evaluation of *economic performance* of our urban configurations, measuring how much structure influences segregation. To this aim, we implemented a model of residential dynamics based on the work of Benenson et al. [10]. The output function is a segregation index $H(t)$ calculated on the residential patterns that emerge inside a distribution of built patches. For urban structures produced in a practical case (Section 3.3), we obtained densities of mobile agents between 0.1 and 0.2. Following Gauvin et al. [13], the phase diagram of the Schelling model indicates that in such a density range, tolerance thresholds of 0.4 to 0.8 lead to clustered frozen states, where the calculation of a spatial segregation index is indeed relevant. The detailed description of this economic model is out of the scope of this paper.

3 Results

Our hybrid network/grid model was implemented in NetLogo [40]. Plots and charts were created in R [32] from exported data. Processing of GIS Data (for vectorization by hand of simple raster data) was done in QGIS [31]. Exploration of the 4D space of explicative variables' weights α_k was conducted inside the $[0,1]^4$ hypercube with a linear increment of 0.2. This created $6^4 - 1 = 1295$ points, from $(0,0,0,0)$ excluded to $(1,1,1,1)$ included, via $(0.2,0,0,0)$, etc. Unless otherwise noted, the output values of the evaluation functions were averaged over 5 simulations for each combination of the α_k's.

3.1 Generation of urban patterns: external validation of the model

Typical patterns We ran the model on different initial configurations, in which a few city centers C_0 (typically 4) were randomly positioned on a 56×56 lattice, and their activity values drawn in $[1, a_{\max}]$ (both uniformly). The initial network G_0 was built progressively and quasi deterministically over increasing distances, by

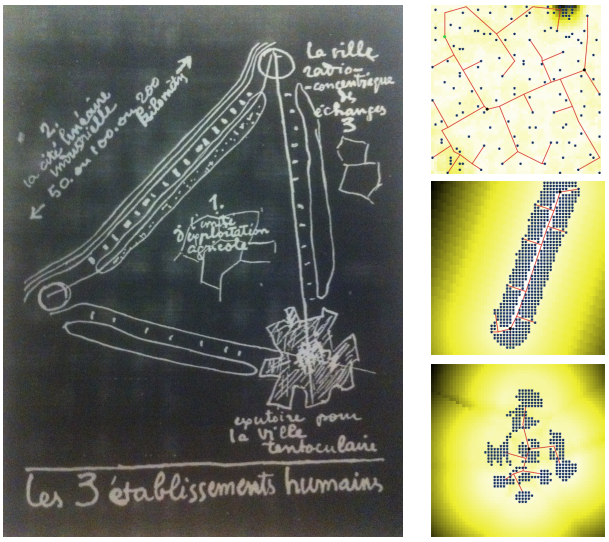

Figure 3: Typical patterns obtained from our model, reproducing Le Corbusier's analysis of "human settlements". In his 1945 attempt to theorize urban planning, Le Corbusier analyzed the form of cities by hand and outlined three types of settlements: radial-concentric cities, linear cities along communication roads, and rural communities. We were able to reproduce this typology by setting the weights of the explicative variables of our model to corner values: *Top-right*: $(\alpha_k) = (1, 0, 0, 0)$, i.e. density-based only. *Middle*: $(0, 1, 0, 0)$, i.e. distance-to-road only. *Bottom*: $(0.2, 0, 1, 0)$, i.e. network-distance combined with a little density. *Left*: source [22].

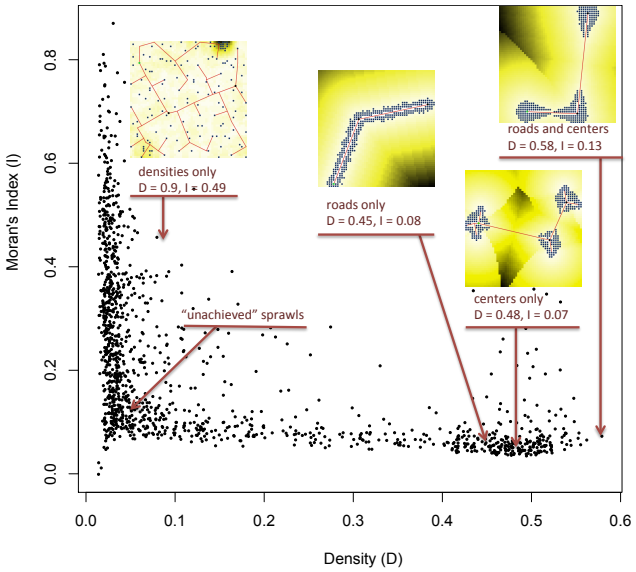

Figure 4: Morphological classification of urban patterns. Scatterplot in the (D, I) evaluation plane with four typical structures highlighted. Three of them, despite visual differences, are relatively close to each other in this space, indicating that two metrics are not sufficient for a full classification. The area near the origin corresponds to unfinished patterns, i.e. which occupy only a small part of the world and cannot be compared with larger ones. Almost all I values were positive.

creating isolated clusters and linking them until they percolated into one component. The initial grid was empty ($\delta = 0$ everywhere). Simulations were cut off at 30 iterations ($T = 30\tau$), before the sprawl of urban settlements reached the square boundaries of the world and started "reverberating". Since this artifact occurred the fastest in a density-driven model, $\alpha_k = (1, 0, 0, 0)$, we empirically assessed T in that case and applied it everywhere.

Different parameter settings generated very diverse structures. In particular, we observed striking similarities between the patterns obtained for binary values of α_k's in some "corners" of the hypercube (one or two measures d_k with weight 1, the others 0), and the fundamental urban configurations that Le Corbusier had identified in his 1945 analysis of human settlements [22] (Fig. 3).

Classification of structures Using the pair of morphological indicators (D, I) defined above, and by varying the α_k's, we constructed a 2D map of the dynamical regimes of our system (Figs. 4-5), in which qualitatively different morphological "classes" could be distinguished. The projected locations of urban configurations in this plane allowed a better understanding and comparison of their features and growth process. Again, for certain corner parameter values (all of them 0 except one or two at 1), the results ended up in distinct locations on the map,

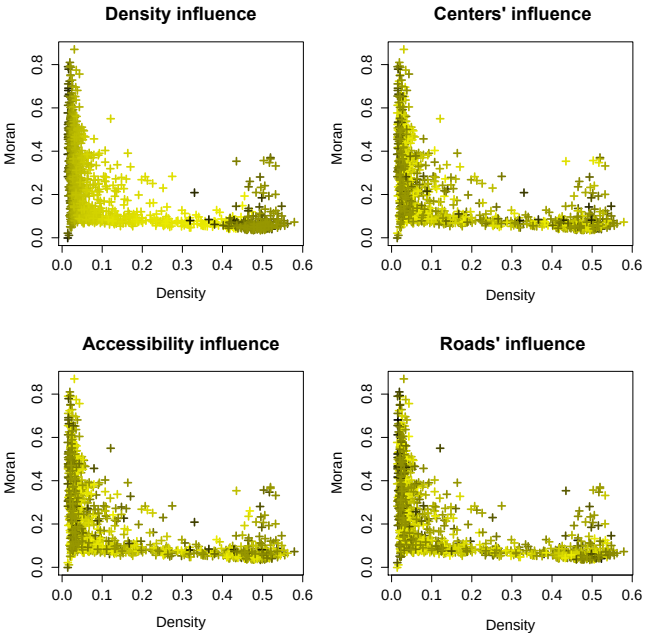

Figure 5: Influence of each explicative variable d_k on urban morphogenesis. Color darkness corresponds to the relative value of weight α_k used during the growth of mapped structures. Whereas Figs. 4-5 showed distinct classes at expected locations, this plot displays a rather uniform and chaotic distribution of high weights for d_2, d_3, and d_4, revealing a pervasive role of roads, city centers, and accessibility. Only density d_1 correlates better with its own evaluation function D (a high influence of density results in low-density patterns), except for the low-I cluster on the right.

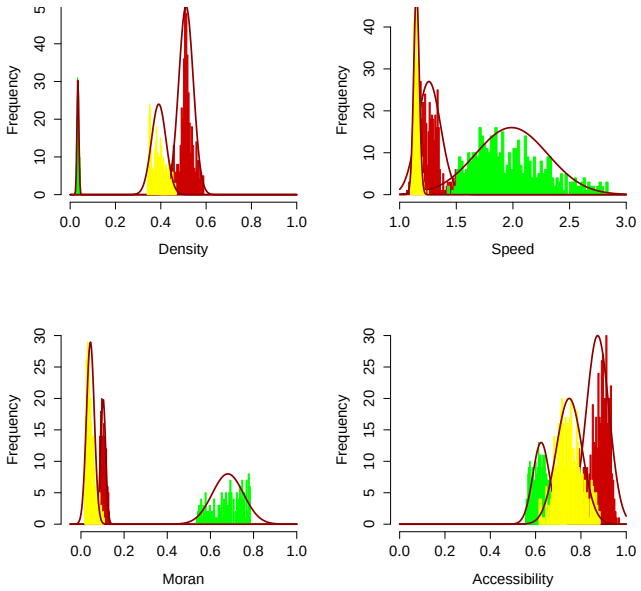

Figure 6: Statistical distribution of the output evaluations. For each of the 15 corner points of the 4D hypercube of α_k's (excluding the origin), we ran 500 simulations from random initializations of 4 city centers C_0. Three resulting distributions out of these 15 are displayed, each in the form of a histogram of evaluation function values, D, S, I, and A, fitted with a Gaussian curve. *Green*: $(\alpha_k) = (1, 0, 0, 0)$, i.e. a simulation taking into account only the density d_1. *Yellow*: $(0, 1, 0, 0)$, i.e. Euclidean distance d_2 only. *Red*: $(0, 0, 0, 1)$, i.e. accessibility d_4 only. These three histograms were chosen for their minimum overlap and clarity of display; the other 17 are similar. The narrow peaks (except one), spread about the mean by $\pm 10\%$, attest to the low sensitivity of the model with respect to the spatial initialization, and validates its internal consistency. This also allowed us to rely on a smaller number of runs in our experiments.

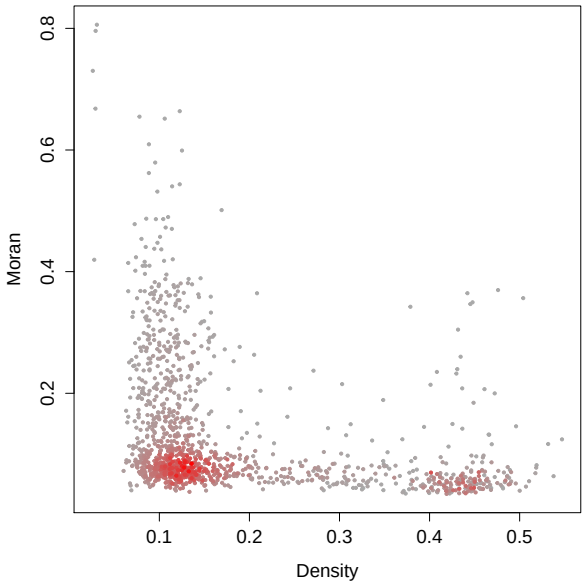

Figure 7: Assessing the influence of the update scheme on the morphologies. In the (D, I) classification plane, each point corresponds to 3 runs of a given combination of α_k parameters, repeated under a sequential ($n = 1$) and under a parallel ($n = 20$) update scheme. For each run, the symmetric difference Δ between the two patterns is computed and its average over the 3 runs is projected on the map. The color of a point highlights its "significance", defined as the product of its local density (clustered points represent more frequent configurations) and its pattern size, $|\Delta|$ (large patterns are more significant). The scattered points indicate that the model is sensitive to the update scheme for certain parameters. On the other hand, the concentration of significant points near the origin and $D = 0.5$ means that corner cases, such as $(1, 0, 0, 0)$, are more robust.

which could be relatively well explained. Intermediate combinations of parameters, however, seemed to project the structures quite literally "all over the map", which might be interpreted as the emergence of chaos in the system.

3.2 Sensitivity analysis and parameter space exploration: internal validation

Sensitivity to initial conditions To ensure the validity of the results, we investigated the sensitivity of the model to the spatial conditions, the initial set of nodes C_0, estimating in particular the number of repetitions necessary to obtain statistically meaningful values for the evaluation functions. If conclusions drawn from one case were highly susceptible to small changes in the initial layout, then the model would obviously have less significance than if there was some invariance with respect to abstract topological features (in particular the distribution of centers' activities). The optimization heuristics would have to be designed very differently in these two cases.

Toward this assessment, we ran a large number of simulations under the same parameter values but starting from different initial C_0 configurations, and collected statistics on the output. For each of the 15 binary combinations of α_k's (excluding all zero), standard deviations were calculated over 500 runs. We obtained narrow peak distributions in most cases, with Gaussian widths typically at 10% of the mean function value (Fig. 6). In order to ensure that these were typical widths across the whole parameter space and not only at the extreme binary points, we also explored the 80-point grid $\{0, 0.5, 1\}^4$ with 100 runs per point (except the origin), to assess the relative spread of distributions in a more representative subspace. Both studies confirmed that the evaluation functions were significantly less sensitive to the exact spatial locations than the parameters and overall topology, and justified our use of a smaller number of trials in subsequent experiments. Typically, assuming a normal distribution of width $\sigma = 0.1$, we needed $n = (2\sigma \cdot 1.96/0.05)^2 \simeq 60$ trials to reach a 95% confidence interval of length 0.05, and 5 trials for a length 0.17. For practical reasons of computing speed, we chose the latter.

Sensitivity to update scheme On the other hand, the emergent urban patterns depended on the number n of cells filled at every iteration, before land values were recalculated at the next iteration, i.e. whether the update scheme was a sequential ($n = 1$) or parallel ($n > 1$). Building several houses "simultaneously" between two market reevaluations is consistent with the view that real-world functions have a response delay, here of the order of τ. There must be a limit, however, and an intermediate n must be found to obtain reasonable simulations.

To this aim, we explored the 4D parameter space of the α_k's as in Figs. 4-5 and ran one sequential update scheme and one parallel update scheme with $n = 20$ in each case. At the end of the simulation, $t = T$, the two corresponding output patterns δ_{seq} and δ_{par} were compared by calculating their symmetric difference, i.e. the subset of lattice cells that were built either in one or the other but not in both: $\Delta = \{(i,j);\ \delta_{\text{seq}}(i,j,T) \neq \delta_{\text{par}}(i,j,T)\}$. Then, these difference patterns Δ were projected on the same classification map (D, I) used previously (Fig. 7). The results showed that for many combinations of parameters, the model's behavior could be noticeably influenced by the update scheme, as many difference patterns exhibited a nontrivial structure with high density or high Moran's index or both. On the other hand, it exhibited a stronger invariance for the corner quadruplets of α_k's: in these cases the Δ's clustered near the origin and $D = 0.5$. Based on this study, we decided to adopt a parallel update scheme with $n = 15$ built cells per time step in the remainder of the experiments.

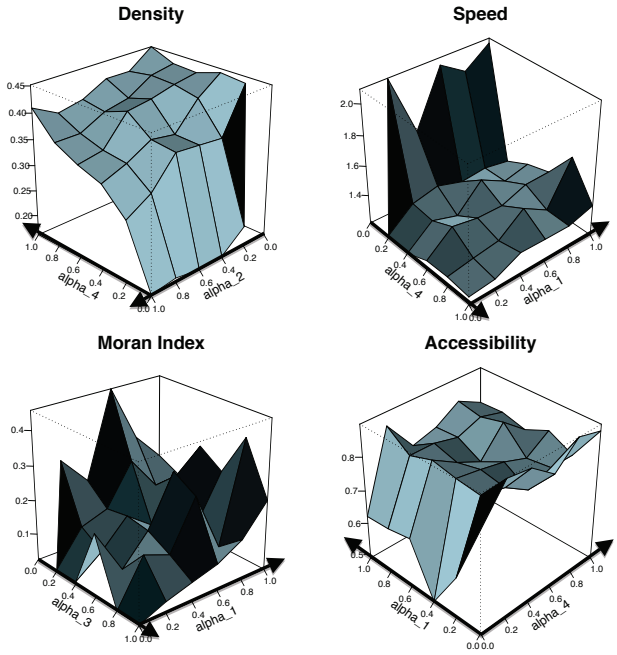

Figure 8: Sample surface plots of the evaluation functions. For each 4D field of evaluation values in the hypercube, we select two out of four parameters and display the 2D slice corresponding to the other two parameters set to $(0, 0)$. Horizontal axes are reoriented in each case to minimize visual clutter. This exhaustive exploration has an intrinsic explanatory value (see text), and allows us to predict with some level of confidence how the model responds to certain input parameters.

Exploration of parameter space The above two preliminary studies validated the robustness of the model with respect to the initialization and update scheme, and helped us choose a reasonable number of runs (about 5) for each parameter combination, and a adequate degree of parallelism in the simulations ($n = 15$). Next, we revisited the α_k hypercube (same 1295 points in the partition of step 0.2), this time calculating the complete charts of all evaluation functions. Other parameters with a direct correspondence to the real-world, depending on the scale adopted, were set to fixed values. For example, the neighborhood radius ρ or the road-triggering distance θ_2 were both equal to 5 cells: this number could represent 50m, characteristic of a block at the scale of a district, or 500m for a district in a city, or 5km between cities in a region.

Examples of evaluation surfaces in 2D projection spaces are shown in Fig. 8. Each function, D, I, S, and A, was plotted against two parameters out of four, chosen for their higher "influence" (variations in amplitude) on the function. The economic index H was not calculated here (see 3.3). This exhaustive exploration of parameter space was necessary to gain deeper insight into the behavior of the model. It also represents a crucial step toward making computational simulations more rigorous [3].

Altogether, we observed that outputs varied for the most part smoothly, except Moran's index which appeared more chaotic. Variations were greater in cases where one parameter was dominant. For example, the measures of density D, speed S and (global) accessibility A all exhibited a significant jump when including the effect of (local) accessibility d_4 in the simulations, i.e. when transitioning from $\alpha_4 = 0$ to $\alpha_4 > 0$. In particular, the more activities were influent, the denser the city became—a nonintuitive emergent effect, compared to top-down planning alternatives that would try to optimize accessibility while keeping density low. Speed, or rather "sluggishness", exploded when density was the only influence on urban sprawl: this confirmed that pure density-driven dynamics creates anarchic growth, without concern for network performance.

As for global accessibility, or rather the difficulty thereof, it was minimal for $\alpha_4 = 0$: an interesting paradoxical effect suggesting that when individual agents took into account local accessibility ($\alpha_4 > 0$), a few of them might have occupied the "best spots" too quickly, significantly diminishing the others' prospects. Therefore, at the collective level, it would be better for everyone to ignore that dimension—an example where competition at the individual level does not produce the most efficient system for all. Finally, no meaningful conclusion could be formulated about the chaotic variations of Moran's index, except for its extreme sensitivity to spatial structure.

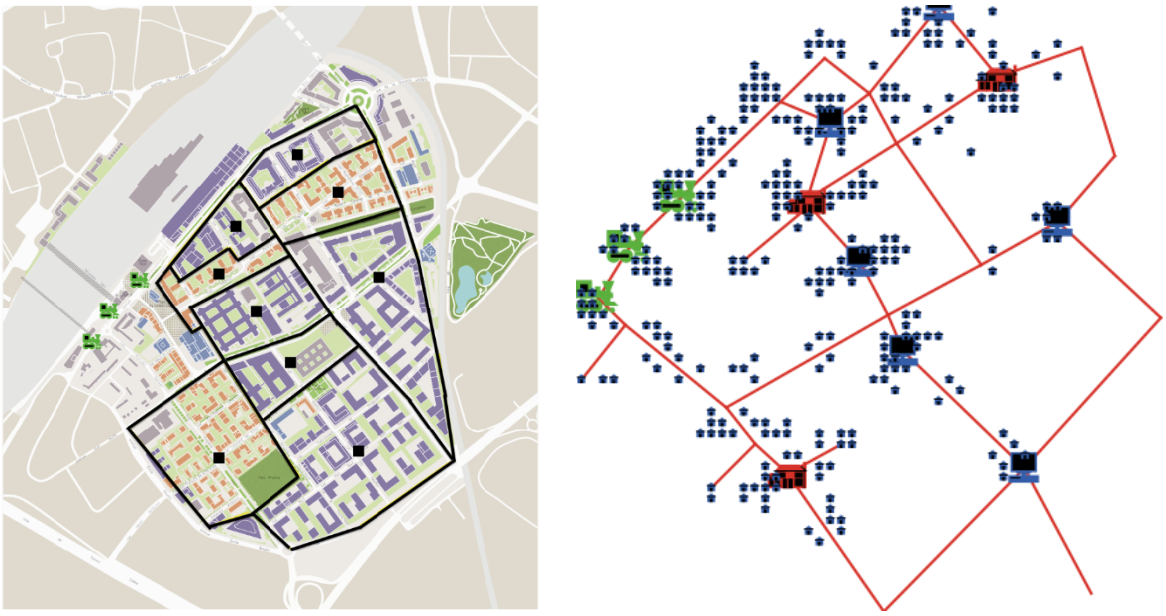

Figure 9: Practical application: optimizing the distribution of activities over urban centers. *Left*: existing master plan of the Massy Atlantis district: 9 building areas are identified by their centers (black squares). Buildings are color-coded by type of activity (orange: residential, blue: tertiary). Railroad tracks traverse the upper left corner (light blue strip) and three train transportation hubs are also represented (green locomotive icons): these are part of the fixed environment. *Right*: example of housing configuration obtained after a simulation in which the 9 centers' activities were initialized to the same values as their real-world counterpart (red house icons: residential, blue computer icons: tertiary; one of 510 possible distributions). The evaluation functions of the outcome are $(H, A) = (0.067, 0.76)$, a point close to the Pareto front of Fig. 10 (blue circle).

3.3 Practical example

In this section, we apply our model to the optimization of activities on top of a real-world urban structure obtained from a geographic file, as opposed to an randomly generated, artificial configuration. This type of scenario occurs in a planning problem where one must decide about the possible land use of predefined zones.

The practical example under study here concerns the planning of a new district. It is based on a real-world neighborhood, Massy Atlantis (Paris metropolitan area), built in 2012 (Fig. 9). We would like to investigate whether a more efficient planning could have been achieved. The goal of this exercise is to find an optimal assignment of two types of activities, "residential" (apartments) or "tertiary" (offices), to the centers of 9 areas located on a map. The transportation infrastructure is already in place and the train station is also considered a center with a fixed, third type of activity. A network of avenues is laid out and passes through the 9 centers. The district is initially empty (unbuilt). The particular spatial configuration was automatically imported from a GIS shapefile, so the computation could be readily applied to other cases.

Parameters of the model were set as follows: high influence of activities, $\alpha_4 = 1$, reflecting the fact that accessibility to home, workplace, and train station are of special importance to the agents of this district; medium influence of density, $\alpha_1 = 0.7$, because, not far from Paris, housing must reasonably fill the available areas; no influence of road proximity, $\alpha_2 = 0$, since the initial network is already built and the scale is relatively small; and no influence of network-distance, $\alpha_3 = 0$, because centers in this problem are abstract entities representing areas.

For every possible distribution of binary activities over the 9 areas, excluding the two uniform cases (all residential or all tertiary), the model was simulated 5 times, producing a total of $(2^9 - 2) \times 5 = 2550$ runs. The resulting configurations were examined here via a morphological projection in the (H, A) plane, instead of (D, I) used in the previous sections, as we judged it to be a more meaningful measure of fitness in this application. The calculation of the economic segregation index H involved a secondary agent-based simulation on top of the main urban development model (details not provided here).

Results are shown in Fig. 10. We obtained a Pareto front of "optimal solutions" trying to minimize both H and A, while observing that the actual configuration is not far from being optimal itself, and appears to be a compromise between accessibility and economic performance. After closer examination of the Pareto front and its vicinity, we found that the distribution of activities was highly mixed in these points. More precisely, we defined a spatial heterogeneity index of center activities by

$$\lambda = a_{\max} \frac{\sum_{\substack{c \neq c' \\ a(c) \neq a(c')}} d(c, c')^{-1}}{\sum_{c \neq c'} d(c, c')^{-1}} \tag{7}$$

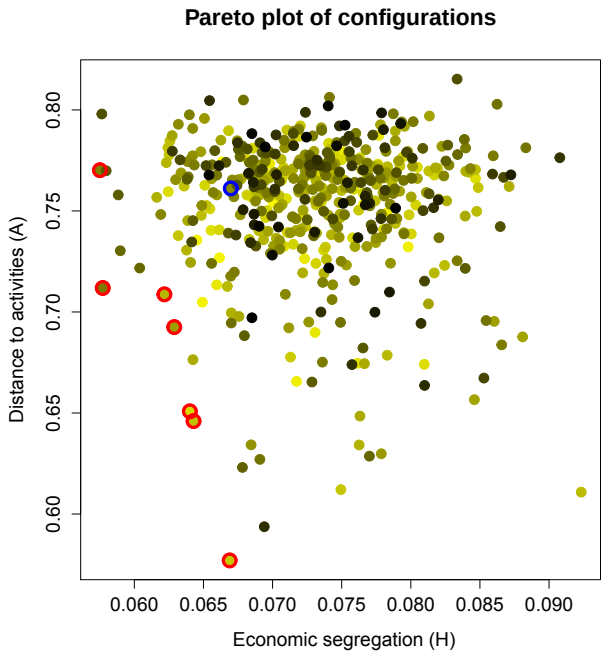

Figure 10: Scatterplot of all configurations in the (H, A) morphological plane. A Pareto front (red circles) is apparent in the bottom left part of the plot: it corresponds to "optimal" configurations trying to minimize both H and A objectives. The real situation (blue circle in $H = 0.067, A = 0.76$) corresponds to Fig. 9 and is not far from this front. Points are colored according to their level of heterogeneity λ, from low (black) to high (yellow). More homogeneous configurations are concentrated in the central cluster, whereas Pareto points and their neighbors have higher heterogeneity levels. This lends support to the principle of "functional diversity", which is often adopted by city planners today but has never been backed up by computational simulations.

where $c = (i, j)$ and $c' = (i', j')$ are two centers, $d(c, c')$ their Euclidean distance, and $a(c)$, $a(c')$ their activities. Points in the scatterplot were colored according to their level of λ. Highly heterogeneous configurations appeared in regions of the plot distinct from homogeneous configurations, which were for the most part located in the central cluster. Optimal solutions and their neighbors all corresponded to high heterogeneity. This interesting result is a step toward evidence-based justification of mixed land use in planning—a principle often invoked by city planners but never quantitatively demonstrated.

In conclusion, this case study is encouraging as it proposes a concrete methodology of optimal planning with respect to criteria that are relevant to a particular situation. It could be used in a generic way by city planners for similar challenges, while remaining cautious on the conditions of its applicability. We discuss this point next.

4 Discussion

The reproduction of typical urban morphologies and the possible application to a real-world problem shown in the previous sections indicate that a model like ours can be useful for evidence-based decision-making in urban planning. Several questions remain open, however, and would need further investigation.

Scale of the model One ambiguity of the model is that it can be applied at different scales, therefore there is no unique correspondence between its agents and the real world. As the above results illustrate, the simulated urban configurations may represent a system of cities at the macroscopic scale, the neighborhoods of one city at the mesoscopic scale, or the buildings of one district at the microscopic scale. Without engaging in an ontological debate over levels of abstraction, this could still be pointed out as a potential issue.

We wish to argue, however, that the multiscale applicability of our model is legitimate as a great number of urban systems and associated dynamics have been shown to be "scale-free", in particular by Pumain [29], and even to possess fractal properties, by Batty [8]. It means that scaling laws may also operate in our model, therefore qualitative results should remained unchanged while the quantitative evolution of variables and relations should only depend on the underlying power law's exponent.

Barthélemy [21] warns that most multiagent urban models fail because they do not focus on the "dominating" physical process but, instead, integrate too many aspects that bear no relevance to the emergent properties of the system. Following up on this advice, we believe that we have successfully identified "good" proxies for the dominating processes of urban morphogenesis, namely: urban density, accessibility to road network, and accessibility to main functionalities.

Local scope When the model is considered at a mesoscopic or microscopic scale, another objection could be that it seems to limit itself to an artificially "closed" urban system, neglecting important contextual phenomena such as economic exchanges. Yet, although input and output flows are greatly simplified here, they are still present in implicit form. Our simulated world is not truly closed, since newly built houses are associated with a net influx of resources. Moreover, despite the absence of a direct economic force in the growth dynamics (the H index is only a post-hoc metric), the attractiveness of centers constitutes a proxy for underlying activity, and a form of interdependence among urban processes. Finally, other models that have taken into account the global complex network of cities [1] have reproduced well-known patterns of urban systems much like ours.

Therefore, here too, local or global approaches appear to be equivalent and the modeling decisions and compromises made in each case must be compared. This question also ties in with the fundamental issue, contained in the previous point, of the existence of a "minimal dimension" for a generalized representation of urban systems.

The challenge is to understand how universal the dependence between a system and its dimension may be, and if a generalized minimalist formulation can be constructed. Speculations toward that ambitious goal have been formulated by Haken [15] through a notion of "semantic information" linked to properties of attractors in dynamical systems. This theory, however, has not been quantified, i.e. neither confirmed nor falsified.

Quantitative calibration The question of the validity of the model is also linked to the need for a finer quantitative calibration based on real patterns, which creates a dilemma: on the one hand, calibration on the errors of output function proxies does not influence the formation of spatial patterns; on the other hand, calibration on the spatial patterns themselves is too constraining and may preclude the emergence of other, similar patterns. Previous works addressing the issue of calibration [23] have not been conclusive so far.

To revisit this question, we would need to apply our model at a finer grain of spatial resolution, i.e. a very large world in terms of data size. In this scenario, it would be particularly important to keep processing time under control by reducing computational complexity, for example through a cache of the network's shortest paths. The potential increase in size can also create methodological hurdles, not just computational, as a huge amount of details in the resulting patterns might contribute to more noise than signal and significantly bias the indicators. One solution would be to create a new operator extracting the morphological envelope of the generated pattern, along the lines of an original method proposed by Frankhauser et al. [12, 34]. Other ways to deal with noise may involve Gaussian smoothing.

Complex coupling with economic model Our method of economic evaluation consists of "simple coupling", i.e. running a secondary agent-based model (the basis of H's calculation, not described here) after the primary urban growth simulation has finished. Another important direction of research would implement a "complex coupling" between the two models in the sense proposed by Varenne [37]: the study of urban sprawl on other time scales would require the *simultaneous* and mutually interacting evolutions of the population, the building rents, and the terrain values. Obviously, this would lead to a more sophisticated model oriented toward a whole new set questions, such as the evaluation of long-term rent policies to foster social diversity.

5 Conclusion

We have proposed a hybrid network/grid model of urban growth structures, and studied their morphological and functional properties by simulation. Results showed that it could reproduce the characteristic urban facts of a classical typology of "human settlements", and was also applicable to a concrete scenario by calculating "optimal" solutions (in the Pareto sense) to a planning challenge in an existing zoning context. Our work provide evidence in favor of the "mixed-use city", a topic on which literature is still scarce and future work is needed. This paradigm is now commonly advocated by city planners, such as Mangin [22] through his concept of *"ville passante"* (a pun on "evolving/flowing/pedestrian city"), and would require more validation through quantitative results.

Finally, beyond its technical achievements and potential usefulness as a decision-making tool, our work also fuels a contemporary debate on the state-of-the-art in "quantitative urbanism". Siding with Portugali [27], we certainly agree that the conception and application of computational models is a delicate matter, which can lead to more confusion than explanation if not properly handled and validated. Depending on the scale, a careless choice of parameter values can produce dubious results. Yet, we support the idea that *quantitative* insights are paramount for a better understanding of urban and social systems. With the recent explosion in data size and computing power, evidence-based analysis and solutions are becoming a real alternative to older attitudes, such as Lefebvre's [16], which doubted that scientific approaches could ever translate or predict the mechanisms of a city.

References

[1] C. Andersson, A. Hellervik, K. Lindgren, A. Hagson, and J. Tornberg. Urban economy as a scale-free network. *Physical Review E*, 68(3):036124, 2003.

[2] A. Banos. Network effects in schelling's model of segregation: new evidences from agent-based simulation. *Environment and Planning B: Planning and Design*, 39(2):393–405, 2012.

[3] A. Banos. *Pour des pratiques de modélisation et de simulation libérées en Géographie et SHS*. PhD thesis, UMR CNRS Géographie-Cités, ISCPIF, Décembre 2013.

[4] A. Banos and C. Genre-Grandpierre. Towards new metrics for urban road networks: Some preliminary evidence from agent-based simulations. In *Agent-based models of geographical systems*, pages 627–641. Springer, 2012.

[5] M. Batty. Cellular automata and urban form: a primer. *Journal of the American Planning Association*, 63(2):266–274, 1997.

[6] M. Batty. *Cities and Complexity: Understanding Cities with Cellular Automata, Agent-based Models, and Fractals*. MIT Press, 2007.

[7] M. Batty. *The New Science of Cities*. MIT Press, 2013.

[8] M. Batty and P. Longley. *Fractal Cities: A Geometry of Form and Function*. Academic Press, London, 1994.

[9] M. Batty and Y. Xie. Possible urban automata. *Environment and Planning B*, 24:175–192, 1997.

[10] I. Benenson. Multi-agent simulations of residential dynamics in the city. *Computers, Environment and Urban Systems*, 22(1):25–42, 1998.

[11] G. Caruso, G. Vuidel, J. Cavailhes, P. Frankhauser, D. Peeters, and I. Thomas. Morphological similarities between dbm and a microeconomic model of sprawl. *Journal of Geographical Systems*, 13:31–48, 2011.

[12] P. Frankhauser and C. Tannier. A multi-scale morphological approach for delimiting urban areas. In *9th Computers in Urban Planning and Urban Management conference (CUPUM'05), University College London*, 2005.

[13] L. Gauvin, J. Vannimenus, and J.-P. Nadal. Phase diagram of a schelling segregation model. *The European Physical Journal B*, 70(2):293–304, 2009.

[14] B. Golden, M. Aiguier, and D. Krob. Modeling of complex systems ii: A minimalist and unified semantics for heterogeneous integrated systems. *Applied Mathematics and Computation*, 218(16):8039–8055, 2012.

[15] H. Haken and J. Portugali. The face of the city is its information. *Journal of Environmental Psychology*, 23(4):385–408, 2003.

[16] L. Henri. Le droit à la ville. *Anthropos*, 1968.

[17] A. J. Heppenstall, A. T. Crooks, and L. M. See. *Agent-based models of geographical systems*. Springer, 2012.

[18] B. Hillier, A. Leaman, P. Stansall, and M. Bedford. Space syntax. *Environment and Planning B: Planning and Design*, 3(2):147–185, 1976.

[19] S. Iltanen. Cellular automata in urban spatial modelling. In *Agent-based models of geographical systems*, pages 69–84. Springer, 2012.

[20] F. Le Néchet and A. Aguilera. Déterminants spatiaux et sociaux de la mobilité domicile-travail dans 13 aires urbains françaises : une approche par la forme urbaine, à deux échelles géographiques. In *ASRDLF 2011*, SCHOELCHER, Martinique, July 2011. http://asrdlf2011.com/.

[21] R. Louf and M. Barthelemy. Modeling the polycentric transition of cities. *ArXiv e-prints*, Sept. 2013.

[22] D. Mangin. *La ville franchisée: formes et structures de la ville contemporaine*. Éditions de la Villette Paris, 2004.

[23] C. Maria de Almeida, M. Batty, A. M. Vieira Monteiro, G. Câmara, B. S. Soares-Filho, G. C. Cerqueira, and C. L. Pennachin. Stochastic cellular automata modeling of urban land use dynamics: empirical development and estimation. *Computers, Environment and Urban Systems*, 27(5):481–509, 2003.

[24] D. Moreno, D. Badariotti, and A. Banos. Un automate cellulaire pour expérimenter les effets de la proximité dans le processus d'étalement urbain : le modèle raumulus. *Cybergeo : European Journal of Geography*, 2009.

[25] D. Moreno, A. Banos, and D. Badariotti. Conception d'un automate cellulaire non stationnaire à base de graphe pour modéliser la structure spatiale urbaine: le modèle remus. *Cybergeo: European Journal of Geography*, 2007.

[26] D. Peeters and M. Rounsevell. Space time patterns of urban sprawl, a 1d cellular automata and microeconomic approach. *Environment and Planning B: Planning and Design*, 36:968–988, 2009.

[27] J. Portugali. Complexity theories of cities: Achievements, criticism and potentials. In *Complexity Theories of Cities Have Come of Age*, pages 47–62. Springer, 2012.

[28] J. Portugali, H. Meyer, E. Stolk, and E. Tan. *Complexity theories of cities have come of age: an overview with implications to urban planning and design*. Springer, 2012.

[29] D. Pumain. Scaling laws and urban systems. *Santa Fe Institute, Working Paper n 04-02*, 2:26, 2004.

[30] D. Pumain. Multi-agent system modelling for urban systems: The series of simpop models. In *Agent-based models of geographical systems*, pages 721–738. Springer, 2012.

[31] QGIS Development Team. *QGIS Geographic Information System*. Open Source Geospatial Foundation, 2009.

[32] R Core Team. *R: A Language and Environment for Statistical Computing*. R Foundation for Statistical Computing, Vienna, Austria, 2013.

[33] T. C. Schelling. Models of segregation. *The American Economic Review*, 59(2):488–493, 1969.

[34] C. Tannier, G. Vuidel, and P. Frankhauser. Délimitation d'ensembles morphologiques par une approche multi-échelle. In J.-C. Foltête, editor, *Actes des huitièmes Rencontres de Théo Quant*, page 14, Besançon, France, 2008. http://thema.univ-fcomte.fr/theoq/.

[35] Y.-H. Tsai. Quantifying urban form: compactness versus' sprawl'. *Urban Studies*, 42(1):141–161, 2005.

[36] J. van Vliet, J. Hurkens, R. White, and H. van Delden. An activity-based cellular automaton model to simulate land-use dynamics. *Environment and Planning-Part B*, 39(2):198, 2012.

[37] F. Varenne, M. Silberstein, et al. *Modéliser & simuler. Epistémologies et pratiques de la modélisation et de la simulation, tome 1*. 2013.

[38] R. White. Modeling multi-scale processes in a cellular automata framework. In *Complex artificial environments*, pages 165–177. Springer, 2006.

[39] R. White and G. Engelen. Cellular automata and fractal urban form: a cellular modelling approach to the evolution of urban land-use patterns. *Environment and planning A*, 25(8):1175–1199, 1993.

[40] U. Wilensky. Netlogo. Center for Connected Learning and Computer-Based Modeling, Northwestern University, Evanston, IL., 1999.

[41] F. Wu. A linguistic cellular automata simulation approach for sustainable land development in a fast growing region. *Computers, Environment and Urban Systems*, 20:367–87, 1996.

Proceedings of ICCSA 2014
Normandie University, Le Havre, France - June 23-26, 2014

GAMAGRAM: GRAPHICAL MODELING WITH THE GAMA PLATFORM

Patrick Taillandier *†

Abstract. These last years have seen the multiplication of platforms dedicated to the conception and simulation of agent-based models for studying complex systems. If these platforms allowed to democratize this modeling approach, they are often complex to use by non-computer scientists as most of them require to define models by writing numerous code lines. In this paper, we present GAMAGraM, a new graphical modeling plug-in integrated into the GAMA platform. This plug-in allows users to define models from a graphical interface. Defining a model with the GAMAGraM plugin means first defining the structure of the model by a conceptual entity-relationship diagram, then defining the properties of entities through dedicated dialog boxes. The graphical editor provides autocompilation tools allowing to ease the work of the modelers.
Keywords. Complex System, Agent-based Modeling, Graphical Modeling, GAMA Platform

1 Introduction

Nowadays, agent-based modeling is more and more used to study complex systems, in particular by researchers coming from other fields than computer sciences (geography, environmental sciences). Unfortunately, the use of such modeling approach requires to have skill in programming, in particular when the system to model integrates social and spatial aspects. This issue has for consequence that most of the models are still developed by computer scientists and not directly by domain experts, which slows the diffusion of this modeling approach and the transfer of knowledge to the decision-makers.

In order to tackle this issue, some agent-based modeling platforms have proposed to let the user define his/her models thanks to a graphical interface allowing to minimize the quantity of lines of code to write. However, these platforms are often complex to use or very limited in terms of models they allow to build.

The GAMAGraM plugin has for ambition to be simple to use and at the same time very powerful. It is based on the GAMA platform [12] that allows to define large-scale models integrating rich spatial and social dynamics (e.g. MAELIA [19, 11], MIRO [4]).

*Patrick Taillandier is with UMR CNRS IDEES, University of Rouen, France. E-mail: patrick.taillandier@univ-rouen.fr
†Manuscript received April 19, 2009; revised January 11, 2010.

The paper is organized as follows: Section 2 presents the context of this work, in particular the existing agent-based modeling platforms and the graphical modeling languages. Section 3 is dedicated to the presentation of the GAMAGraM plugin. At last, Section 4 concludes and presents perspectives.

2 Context

2.1 existing platforms

Nowadays, there are numerous platforms dedicated to the agent-based modeling of complex systems. These platforms can be divided in 3 - non-exclusive - groups according to the type of programing language used to define models.

The first group is composed of the platforms that require to define models through a high-level generic programming language (Java, C++, Python...). These platforms are most of the time intended to computer scientists and are the most adapted to the development of large-scale models. Repast Symphony [17], MASON [15] and SWARM [16] belong to this category.

The second group is composed of the platforms that provide a dedicated modeling language. These platforms are most of the time easier to use than the ones of the first group. There are intended to a wider range of users. However, they require some skills in algorithmic. Netlogo [20] and GAMA [12] belong to this group.

The last group is composed of the platforms that allow to define a model through a graphical modeling language. These platforms require less skills in computer science than the platforms belonging to the two other groups. Moreover, they offer the advantage to ease the discussion between modelers and domain-experts/stakeholders and are thus particularly adapted to be used in a participatory modeling context.

StarLogo [18] and Modelling4All [13] belong to this group. These tools that can be used by all types of users are mostly pedagogical tools and are limited to the development of simple models.

Another platform that belongs to this group is Repast Symphony. It proposes to define models through three ways: by using Java, using the ReLogo language or

through a graphical modeling language [17]. If for simple models (or rapid prototyping) the ReLogo language and the graphical modeling tools can be used, developing a complex model with this platform requires to have knowledge in Java.

In its last version, the Cormas platform [8] provides as well some graphical modeling tools (definition of activity diagram). However, this platform, specialized for participatory modeling, does not offer the same richness as GAMA or Repast Symphony in terms of model development, in particular for the development of models based on vector geographical - GIS - data.

At last, the MAGeo platform [14] allows to simply define a model through a dedicated graphic interface. It proposes to formalize the agent behavior as an aggregation of basic behaviors with a simple grammar. This grammar is perfectly adapted to the definition of simple agents, but does not allow (or not directly) to define more complex agents.

To conclude on the existing platforms allowing to develop models through a graphical interface, they are either too complex to use for non-computer scientists (e.g. Repast Symphony) or too limited to develop large-scale models (e.g. StarLogo, Modelling4All, Cormas, MAGeo).

2.2 graphical modeling

Numerous graphical languages were proposed for modeling purpose. The most famous and used one is UML. In the context of agent-based modeling, some works have shown the interest of using such graphical language for communication [6]. However, some authors have point out that the use of UML as an agent-oriented modeling language is inappropriate [7].

Other graphical language based on UML and dedicated to multi-agent systems have been proposed: the most famous ones are AUML [5] and AML [9]. These languages allow to introduce some specific features linked to the agent paradigm. However, their scope goes beyond the agent-based modeling and covers all the multi-agent aspects, which can make these languages difficult to apprehend by non-computer scientists.

A last modeling language to cite is the one proposed by the MAGeo platform. This language is based on the AOC (Actor - Organization - Behavior) meta-model [10]. This graphical language is close to the UML one and respects most of the properties of the OOP (Objected-Oriented Programming). In addition, it allows to natively define multi-level models. However, this language does not allows to define complex behaviors for the agents. In particular, no difference is made between what an agent can do and what it is going to do (capabilities versus behavior).

For the GAMAGraM plugin, our goal is to propose a modeling language simple to manipulate (with a very small number of concepts) and that allows to develop large-scale models. In order to achieve this objective, we identified several properties that our modeling language should respect:

- Properties of the OOP
- Differentiate what an agent can do and what it is going to do (capabilities versus behavior)
- Native handling of multi-level modeling
- Possibility to define elements related to the simulation visualization

To conclude, if numerous graphical modeling languages exist, none of them covers all the properties that we have identified. Moreover, generic languages such as UML, A-UML and AML can be more complex to use as they propose many features that are not useful for agent-based modeling and lack of specific features that can help modelers.

3 Modeling with GAMAGraM

3.1 General properties of GAMAGraM

GAMAGraM has for objective to fill the need in platforms accessible to the highest number and at the same time allowing the definition of large-scale models. We chose to develop GAMAGraM as a plugin of GAMA, because this open-source platform provides already numerous features to develop models, in particular concerning the management of GIS data. Moreover, GAMA is easily extensible.

GAMAGraM allows GAMA users to graphically define their models and eventually to translate them to the GAML language (GAMA Modeling Language). In addition, GAMAGraM allows to translate a GAML model into a graphical one. This feature aims at facilitating the discussions (and communication) about a model. GAMAGraM is based on the Graphiti plugin of Eclipse [3].

3.2 Definition of the model structure

The modeling process with GAMAGraM consists first in defining a conceptual model consisting in a entity-relationship diagram, then to fill all the defined entities through dialog boxes.

We chose to base the conception of the conceptual model on a new modeling language based on the GAMA meta-model. Indeed, if many agent-oriented meta-models were proposed in the literature (see [7] for a presentation of the most famous ones), most of them are not directly dedicated to simulation purpose and very difficult to grasp for non-computer scientists. Another advantage of using the GAMA meta-model is to limit the gap between the conceptual model and the final implemented GAMA model.

Figure 1 presents the meta-model of GAMA. The main component of this meta-model is the **Species**. A **Species**, like a class in OOP, defines the common characteristics to all the agents of a population. In particular,

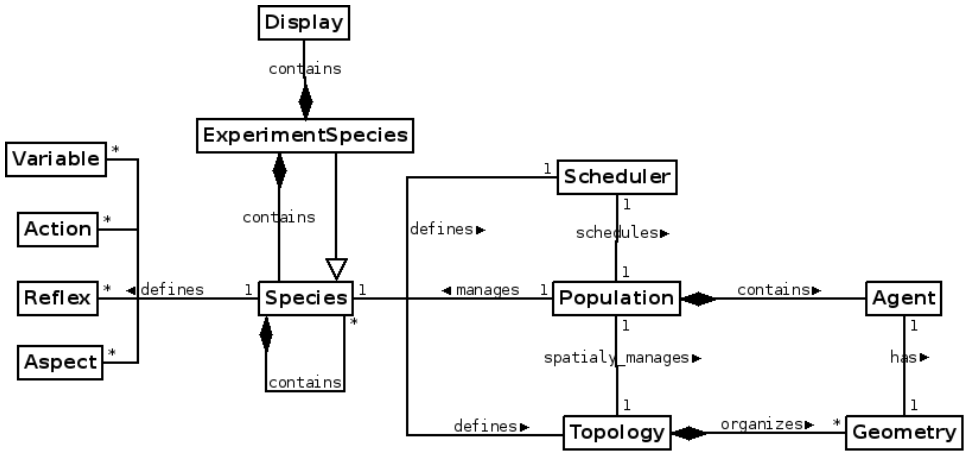

Figure 1: Meta-model of GAMA

it defines their variables, their actions, their reflexes and their aspects. An **Action** is a capabilities that the agents of the population have, i.e. something that the agents can do. A **Reflex** is a behavior, i.e something that the agents of the population are going to do (if some conditions are respected). An **Aspect** represents a possible display of the agents. Note that a species can specifies several actions, reflexes and aspects. In addition, a species specifies the spatial topology and scheduling of the agent population. A containment relationship between species allows to describe the hierarchical levels of agency. At last, a specialization relationship between species allows to define inheriting links between them. An **ExperimentSpecies** represents a context of execution of a model. It is a particular species that contains a set of species (the one defined in the model) and a set of displays.

More details about the meta-model of GAMA can be found in [21]. The use of this meta-model allows to respect the 4 properties defined in Section 3. Note that this meta-model is close to the AOC one, but offers more freedom in terms of agent behavior definition.

Figure 2 presents the modeling graphical framework of GAMAGraM. The right palette allows to select the type of elements to add to the diagram. This framework proposes all the classic features of graphical editors (undo, drag and drop....).

Table 1 presents all the elements that can be added to the conceptual diagram.

When a graphical model is created, a first species of agents is automatically created: the world species. The world species corresponds to the first level of agency that describes the global spatial topology of the model, its basic scheduling, its parameters and global behaviors, and is the host of the populations of agents described by the species written by the modeler.

Thus, the development of the conceptual model consists in defining all the species (with their chosen topology: continuous, grid) living in the world, their capabilities (actions), their behavior (reflexes) and possible displays (aspects). Note that the inheriting relation can be used between species. In addition, the definition of the conceptual model consists in defining the possible contexts of execution of the simulation (experiments) and for each of them the corresponding outputs (displays). Each time the user modifies the diagram, this one is validated: if there is no error in the diagram, all its components appear with green borders, and buttons corresponding to each defined experiments appear in the top of the editor (for example, see the *my_GUI_xp* button in Figure 2). But clicking on one of the experiment buttons, the user can load it (and run the corresponding simulation(s)). If there are errors in the diagram, the problematic components appears with red borders.

As an example, Figure 3 presents the conceptual model of a simple predator prey model. In this model, 4 species of agents live in the world:

- *vegetation_cell*: species with a grid topology that will be used as spatial environment for the other agents. This species has only one behavior (reflex): *grows*.
- *animal*: species with a continuous topology that will be used as the generic species to define the predators and preys. This species has 4 behaviors (reflex): *eats*, *moves*, *reproduces* and *dies*. It also has one action called *eating* and one aspect called *circle*.
- *prey*: species with a continuous topology that inherits from the *animal* species. This species overrides the *eating* action.
- *predator*: species with a continuous topology that inherits from the *animal* species. This species overrides the *eating* action.

In addition, we define one GUI experiment called *main_xp* that has a display called *map* and a display called *charts*. A tutorial describing how to build this diagram can be found on the GAMA website [2].

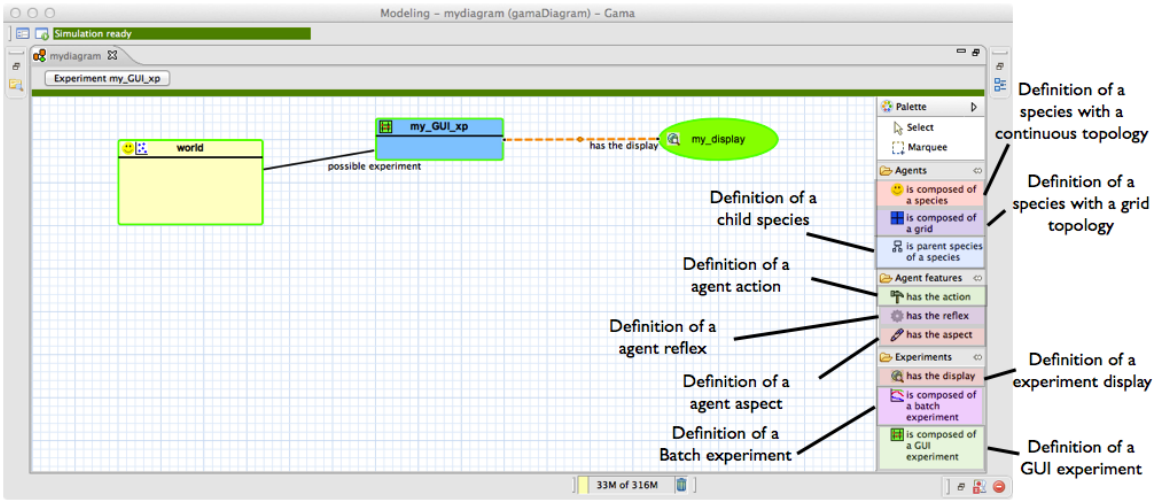

Figure 2: Graphical User Interface of the GAMAGraM plug-in

Table 1: Entities of the graphical modeling language

Symbol	Source	Description
my_species	A species	**Species**: A species of agents with a continuous topology.
my_cell	A species	**Grid**: A species of agents with a grid topology
world	-	**World**: the first level of agency. It contains all other species of agents.
my_action	A species	**Action**: A capability that the agents have.
my_reflex	A species	**Reflex**: A behavior that will be activated at each simulation step (according to a given condition).
my_aspect	A species	**Aspect**: A possible display for the agents.
my_GUI_xp	The world	**GUI Experiment**: load only one simulation with the graphical user interface
my_batch_xp	The world	**Batch Experiment**: load a set of simulations without the graphical user interface
my_display	A GUI Experiment	**Display**: frame allowing to display outputs (map, charts...)

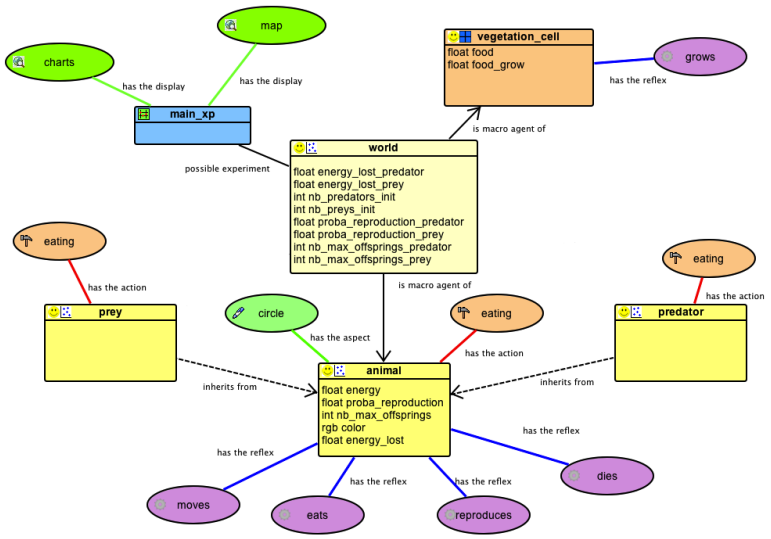

Figure 3: Conceptual model of the predator-prey model

3.3 Definition of the properties of each entity

Once the conceptual model defined, the next step consists in describing the properties of each defined entities.

When the user clicks on an entity, a new dialog box allowing to parameterize it appears. It is through these dialog boxes that the modeler will be able to transform his/her conceptual model into a simulation. Most of the time, the parameterization will just consist in making a choice between different options, but sometimes it will consist in writing GAML instructions. Note that a complete description of the GAML language can be found in the GAMA documentation [1].

The most important entity to parameterize is the species one. The species dialog box allows to define many properties of the species without having to write code (see Figure 4). In particular, it allows to define the geometry of the agents (point, line, or polygons) and variables. For each variable the modeler has to define its name and its type (among many types such as integer, float number, string, list, matrix, map, point, geometry, graph, path...). In addition, the modeler can define optional facets for each variable such as its initial value, a minimum, a maximum, an expression that will be used to re-compute the variable at each simulation step or a function that defined how the variable will be computed each time it is called. In addition, the modeler can give skills to the species. A skill is a predefined set of variables and actions coded in Java. For instance, the moving skill gives to the species the variables *speed*, *heading* and *destination* and the actions *move*,*goto*,*wander* and *follow*. At last, the modeler can define an *init* block that represents the constructor of the species, i.e. define what will happen at the creation of the agents.

Note that the dialog boxes for the world species and the grid definition are very similar. For the grid, the

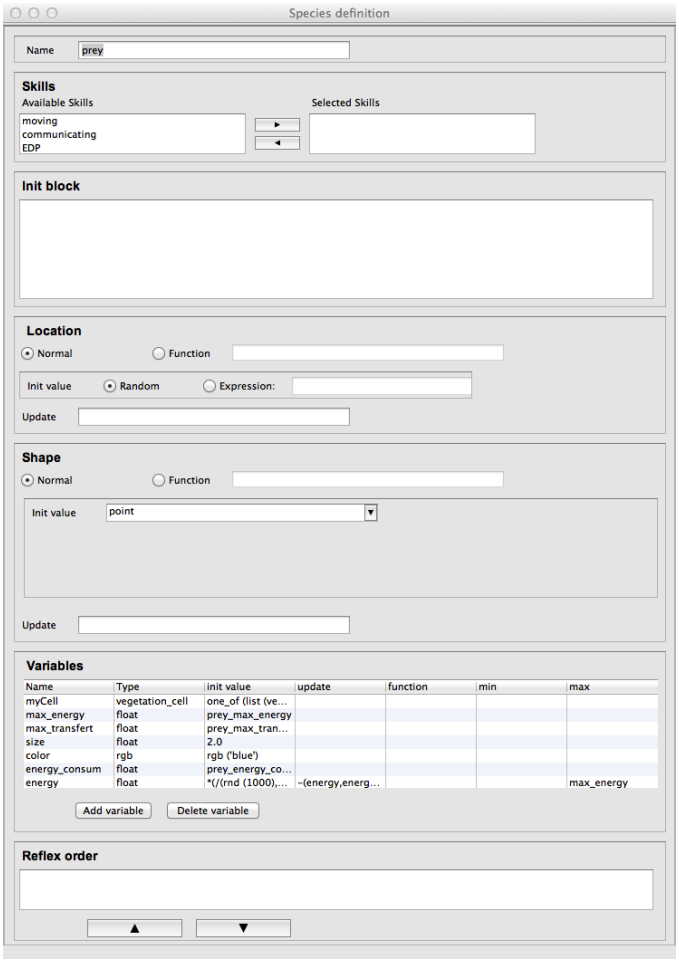

Figure 4: Dialog box for Species definition

dialog box allows just to additionally define the number of cells in the rows and in the columns, and the type of neighborhood: Moore, van Neumann or Hexagonal. For the world species , the dialog box allows to additionally define if the environment is torus or not.

Concerning the parameterization of reflexes, the dialog box allows to choose the condition of the reflex activation and its effect. The activation condition and the effect are described using the GAML language. The action dialog box is very similar to the reflex one. The only difference is that no condition can be defined.

For the aspect definition, the dialog box allows to define the layers (and their order) that will compose the aspect. These layers are defined through a dialog box, in which the modeler can choose the shape to display (a simple shape such as a circle, a square, a rectangle..., an icon, a text or a complex geometry such as a polyline or a polygon), its color, and some specific properties (rotation, fill/empty shape...).

The experiment definition dialog box allows to define the parameters that the user will be able to modify through the simulation interface.

At last, concerning the display definition, the dialog box allows to define the layers that will compose the display (and their order), to choose a color for the background and the refreshing rate. The layers are defined through a dialog box, in which the modeler can choose the elements to display (a list of agents, a chart, an image, a text...), the level of transparency of the layer, its size and its position.

The complete description of these dialog boxes can be found on the game website [2].

4 Conclusion

In this paper, we presented the GAMAGraM plugin that allows to define agent-based models through a graphical interface. This plug-in, which is under GPL license, is available from the GAMA website [2].

In order to validate our claims concerning the ease of use of our plugin and its powerfulness in comparison to others platforms, we plan to carry out tests with end-users (in particular geographers).

In addition, we plan numerous improvements for the plugin. A first one will consist in adding tools to define the reflexes and actions of agents directly through a graphical interface. We plan for that to add the possibility to define these elements thanks to an activity diagram. At last, we plan to add a WYSIWYG interface for the display definition.

References

[1] Gama modeling guide 1.6: https://code.google.com/p/gama-platform/wiki/modelingguide16, January 2014.

[2] Gama website: https://code.google.com/p/gama-platform, January 2014.

[3] Graphiti: http://www.eclipse.org/graphiti/, 2013 October.

[4] A. Banos, N. Marilleau, and M. Team. Improving individual accessibility to the city: an agent-based modelling approach. In *ECSS*, 2012.

[5] B. Bauer, J. Müller, J. Odell, and A. Arbor. Agent uml: A formalism for specifying multiagent interaction. *Agentoriented software engineering*, 1957:91–103, 2001.

[6] H. Bersini. Uml for abm. *JASSS*, 15(1):9, 2012.

[7] G. Beydoun, G. Low, B. Henderson-Sellers, H. Mouratidis, J. J. Gomez-Sanz, J. Pavon, and C. Gonzalez-Perez. Faml: a generic metamodel for mas development. *Software Engineering, IEEE Transactions on*, 35(6):841–863, 2009.

[8] F. Bousquet, I. Bakam, H. Proton, and C. Le Page. Cormas: Common-pool resources and multi-agent systems. In *Tasks and Methods in Applied Artificial Intelligence*, pages 826–837. Springer Berlin Heidelberg, 1998.

[9] R. Cervenka, I. Trencansky, and C. M. Modeling social aspects of multiagent systems: the aml approach. In *AOSE*, 2005.

[10] E. Daudé, P. Langlois, B. Blanpain, E. Sapin, et al. Aoc, une ontologie formelle pour la modélisation de systèmes complexes en géographie. In *Outils, méthodes et modèles en géomatique pour la production de connaissances sur les territoires et le paysage*, 2010.

[11] B. Gaudou, C. Sibertin-Blanc, O. Therond, F. Amblard, J. Arcangeli, M. Balestrat, M. Charron-Moirez, E. Gondet, Y. Hong, T. Louail, E. Mayor, D. Panzoli, S. Sauvage, J. Sanchez-Perez, P. Taillandier, V. Nguyen, M. Vavasseur, and P. Mazzega. The maelia multi-agent platform for integrated assessment of low-water management issues. In *MABS*, 2013.

[12] A. Grignard, P. Taillandier, B. Gaudou, D. Vo, N. Huynh, and A. Drogoul. Gama 1.6: Advancing the art of complex agent-based modeling and simulation. In *PRIMA 2013: Principles and Practice of Multi-Agent Systems*, volume 8291 of *Lecture Notes in Computer Science*, pages 117–131, 2013.

[13] K. Kahn and H. Noble. The modelling4all project a web- based modelling tool embedded in web 2.0. In *International Conference on Simulation Tools and Techniques*, 2009.

[14] P. Langlois, B. Blanpain, and E. Daudé. Magéo, une plateforme de simulation multi-agents pour tous. In *SimTools*, 2013.

[15] S. Luke, C. Cioffi-Revilla, L. Panait, and K. Sullivan. Mason: A new multi-agent simulation toolkit. In *SwarmFest Workshop*, volume 8, 2004.

[16] N. Minar, R. B. Y, and C. L. Z. The swarm simulation system: A toolkit for building multi-agent simulations. Technical report, Santa Fe Institute, 1996.

[17] M. North, N. Collier, J. Ozik, E. Tatara, C. Macal, M. Bragen, and P. Sydelko. Complex adaptive systems modeling with repast simphony. *Complex Adaptive Systems Modeling*, 1(1):3, 2013.

[18] M. Resnick. Starlogo: an environment for decentralized modeling and decentralized thinking. In *Conference companion on Human factors in computing systems*, pages 11–12, 1996.

[19] P. Taillandier, O. Therond, B. Gaudou, et al. A new bdi agent architecture based on the belief theory. application to the modelling of cropping plan decision-making. In *IEMSs*, 2012.

[20] S. Tisue and U. Wilensky. Netlogo: A simple environment for modeling complexity. In *International Conference on Complex Systems*, pages 16–21, 2004.

[21] D.-A. Vo, A. Drogoul, and J. Zucker. An operational metamodel for handling multiple scales in agent-based simulations. In *RIVF*, pages 1–6. IEEE, 2012.

Proceedings of ICCSA 2014
Normandie University, Le Havre, France - June 23-26, 2014

MATHEMATICAL MODELING OF HUMAN BEHAVIORS DURING CATASTROPHIC EVENTS.

N. Verdière, V. Lanza, R. Charrier, D. Provitolo, E. Dubos-Paillard,
C. Bertelle, M.A. Aziz-Alaoui *

Abstract. In this paper, we introduce a new approach for modeling the human collective behaviors in the specific scenario of a sudden catastrophe, this catastrophe can be natural (i.e. earthquake, tsunami) or technological (nuclear event). The novelty of our work is to propose a mathematical model taking into account different concurrent behaviors in such situation and to include the processes of transition from one behavior to the other during the event. Thus, in this multidisciplinary research included mathematicians, computer scientists and geographers, we take into account the psychological reactions of the population in situations of disasters, and study their propagation mode. We propose a SIR-based model, where three types of collective reactions occur in catastrophe situations: reflex, panic and controlled behaviors. Moreover, we suppose that the interactions among these classes of population can be realized through imitation and emotional contagion processes. Some simulations will attest the relevance of the proposed model.
Keywords. Modeling, catastrophic event, human behavior

1 Introduction

Nowadays, management of disasters has become a major issue, due to their huge financial and human costs. In fact, our societies, independently from their development level, are still not sufficiently prepared to a natural or anthropic catastrophe and to possible domino effects. However, there is an increasing trend concerning the number of disasters, ranking from a hundred in 1960 to over 800 in 2000, and the trend is not expected to be inverted in the future, due to the population growth and densification in the risk zones [1].

A fundamental lever for reducing human vulnerability in the face of such events is definitely the population training, in order to adapt their behaviors to extreme situations. In fact, during several catastrophic events, controlled and uncontrolled behaviors in either individuals, small groups or crowds have been observed. These reactions depend not only on the event and its temporality (nature, unexpectedness, presence of alert), but also on the population characteristics (density, composition, preparation level) [5].

In this paper, our aim is to model the collective behaviors that take place in a crowd during a catastrophe, in order to better apprehend and handle the collective reactions. In the literature, several models at different scales have been proposed for modeling crowd dynamics, also in extreme scenarios as in a panic situation [3]. At microscopic level we encounter cellular automata or agent based models [14], where each individual of the population is modeled as single entity. Moreover, especially for the study of pedestrian flows, some microscopic models consider the pedestrians as particles subject to a mixture of socio-psychologically and physical forces [11]. This approach permits to take into account the heterogeneity of the population but this means also high computational requirements and sometimes a difficulty in transferring the microscopic properties at a macroscopic level [16]. At macroscopic level, the models of crowd dynamics consist in partial differential equations that describe the evolution in time and space of the density and mean velocity of the crowd flow. In particular, interactions of crowds and structures in panic situations have been considered [2, 9]. Finally, at mesoscopic level, between the microscopic and the macroscopic ones, we have the models that exploit the approach of the kinetic theory, through the Boltzmann or Vlasov equations, depending on the different range of interactions [3].

However, these mathematical models consider only the panic reaction, and do not take into account what is well-known by now in human sciences [7, 15]: in a catastrophe, the population can

*N. Verdière, V. Lanza, R. Charrier, C. Bertelle and M.A. Aziz-Alaoui are with Université du Havre; 25 rue Philippe Lebon; BP 540; 76058 Le Havre Cedex, France. E-mail: verdiern@univ-lehavre.fr, D. Provitolo is with UMR Geoazur, 250 rue A. Einstein, 06560 Vallone, France, E. Dubos-Paillard is with UMR Geographie Cités, 13 rue du Four, 75006 Paris, France.

exhibit different concurrent reactions, not only the panic one, and each individual does not keep the same behavior during all the event. It is what we propose to do in this paper in exploiting the potential of SIR models [13] that are widely used in epidemics. Indeed, in these models, one can decompose the population in several subpopulations categorized in compartments. Furthermore, different types of transition between these compartments can be easily considered.
In this paper, we omit the spatial dynamics in order to focus first of all on the different psychological behaviors in a crowd, and the processes of transition from one behavior to an other during a disaster.

The collective behaviors that have been observed in the impact and in the destruction zone [5] can be classified in two main categories:

- the instinctive behaviors, managed by the reptilian zone of the brain, that handle with the impulsive and urged behaviors [12]

- the controlled behaviors, where the pre-frontal cortex adapts in a more reflexive way the reactions to an external perturbation [8].

In particular, in the first group we have all the behaviors of instinctive escape and fight, the panic, but also the behaviors as a sort of automaton [17], while in the second one we have all the persons that keep calm and self-control.

In our case, we have subdivided the population in situation of catastrophe in three groups corresponding to the three following collective reactions: reflex behaviors except the panic one, panic and controlled behaviors. Indeed, according to the specific status of the panic, this reaction has been differentiated from the others reflex behaviors. Moreover, according to [10], we suppose that the interactions among these classes of population can be realized through imitation and emotional contagion processes. In fact, it is well-known that in a crowd the perception of an emotional state causes in an observer an automatic imitation of this expression.

The paper is structured as follows. In part 2, our choice of the thee groups of compartmental reactions is discussed and from this discussion, the mathematical model is deduced. In part 3, the available data present in the literature are presented and our strategy for calibrating the model is given. In part 4, numerical simulations attest the relevance of our suggested approach.

2 The mathematical model

2.1 Choice of three groups of compartmental reactions

In this paper, we consider the human behaviors in the impact zone of a catastrophe, with a fast dynamic and no alert to the population. We suppose that the effect of surprise is total and there are no precursor signs or warnings that allow the population to adopt preventive behaviors. To give an example, there may be an earthquake or a local tsunami. We have distinguished three different types of behaviors in such situation.

The first type consists in the reflex behaviors and concerns the reptilian brain. In our case, it corresponds to the set of instinctive behaviors except panic. This mechanism permits to react quickly, either by running away as fast as possible or by being flabbergasted and being physically unable to move in space. It can take the form of sideration and automate behaviors for example [5]. In our model, we have decided to globalize all these reflex behaviors, despite their diversity.

The second one corresponds the panic behavior. Panic has a particular status since, even if it is not always adopted (as, for example, during an earthquake in prepared regions as Japan), this behavior is the most feared. Indeed, this mechanism is difficult to stop once started [6] and can provoke dangerous situations in a crowd, due to trampling and crushing. Moreover, the extinction of collective panic is more linked to internal dynamics than to the remoteness of the danger [5]. Thus, even if it belongs to reflex behaviors, we consider it apart due to its particular nature. Furthermore, in our model, the collective panic can propagate via imitation and contagion mechanisms [10].

Finally, the third type includes all the controlled behaviors. They are governed by the prefrontal cortex, which takes over the reptilian brain. Thus, reflex reactions are substituted by controlled, intelligent and reasoned reactions. They can take different forms in a catastrophe, as, for example, evacuation, leak, containment, sheltering, research for help, pillage, theft... As for the first type, we have decided to globalize all these controlled behaviors, despite their variety.

It is worth noting that the three previous behaviors do not all occur at the same time and respect a certain order. Indeed, the first behavior of an individual in the face of danger is a reflex one followed,

in a second step, by controlled or panic behavior [8].

2.2 Formalization of the human behavior

In this paper, we propose a SIR-based mathematical model composed of four classes, one constitutes daily behaviors, and the three others correspond to the three previous behaviors described at Section 2.1. Thus, first of all, we suppose to have a class named Q composed of individuals in a daily behavior and that, during the event, no death nor birth takes place. Hence, globally the population is constant and composed by N individuals. Moreover, during the catastrophe, Q is the sum of two subpopulations:

- $Q_1(t)$: it designs the number of individuals with routine behaviors. Clearly, just before the catastrophic event occurs, all the population is in this state, therefore $Q_1(0) = N$,
- $Q_2(t)$: it designs the number of individuals who come back to normal lifestyle after the outbreak of the disaster. We expect that at the end of the event, all the individuals will be in this state, thus $Q_2(t_{end}) = N$.

According to Section 2.1, the population during the catastrophe is decomposed into 3 subpopulations who are represented by the following variables:

- $x(t)$ = number of persons with reflex behaviors,
- $y(t)$ = number of persons with controlled behaviors,
- $z(t)$ = number of persons with panic behaviors.

Since we suppose to be in presence of a sudden and unpredictable event, all the involved population will have firstly a reflex reaction, corresponding to instinctive comportments. Thus, the routine behaviors, represented here with the variable $Q_1(t)$, can only be transformed in reflex behaviors, that is in $x(t)$. Hereafter, reflex behaviors can become controlled or panic behaviors. Since $Q_2(t)$ represents the number of individuals who come back to normal lifestyle, it can be alimented only by the controlled behaviors $y(t)$. In fact, an individual needs to recover self-control in order to regain the everyday routine. Moreover, we suppose that, once they have come back to normality, they maintain their habitual behaviors. Thus, the individuals in Q_2 cannot pass in Q_1 and re-enter in the loop.

Furthermore, according to our psychological and geographical references [7, 10, 6, 4], during catastrophic events we have interactions and transitions between the different behaviors, as represented in Figure 1. The exterior event, that is the catastrophe onset, is represented by a forcing function γ which can be discrete or continuous, depending on the type of the event under study. For example, an event such as a local tsunami can be modeled by a discrete function, whereas an inundation can be modeled by a continuous function since it can be announced fewer hours before its start. In our case, we suppose to be in the first situation and the brutality and the speed of the catastrophic event is modeled through a logistic function.

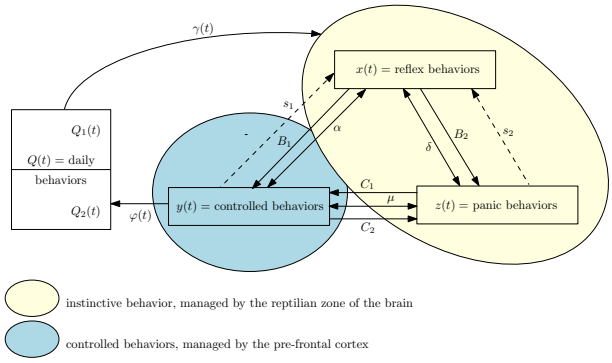

Figure 1: Graphic modeling of three types of human behaviors in context of disasters

For taking into account the possible continuation or repetition of the catastrophe perception stress, the arrows labeled s_1 and s_2 are added, where s_1 and s_2 are supposed to be constant parameters. Once the population is in a reflex behavior, they can evolve in a controlled or panic one according to the parameters B_1 and B_2, respectively. In the same way, a part of the controlled population can evolve to a panic behavior and reciprocally according to the coefficients C_1 and C_2, respectively.
All the previous transitions are causality links. However, some processes of imitation and contagion exist and are modeled by the arrows labeled α, μ, δ. In the graphic, α transposes the process of imitation between x and y which is realized in both directions. This process is modeled as an epidemiological propagation and has the following form: $\alpha \cdot f_1(x(t)) \cdot y(t)$. This modeling permits to favor the imitation in one direction, in particular from x to y. Indeed, in our numerical tests, we have assumed that there must be at least 55% of reflex behaviors for that controlled individual behaviors imitate reflex ones.
In the same manner, the constant δ traduces the imitation processes between x and z and is mod-

eled by the function $\delta \cdot f_2(x(t)) \cdot z(t)$. Finally, the constant μ traduces the imitation processes between controlled and panic individuals behavior, knowing that the imitation is essentially in the sens panic towards controlled individuals behavior. It is modeled by the term $\mu \cdot g(y(t)) \cdot z(t)$.
From the graphical modeling in Figure 1, the mathematical model is deduced:

$$\begin{cases} \frac{dx}{dt} = \gamma(t)Q_1(t)\left(1-\frac{x(t)}{x_m}\right) - (B_1+B_2)x(t) \\ +\alpha f_1(x(t))y(t) + \delta f_2(x(t))z(t) + s_1 y(t) + s_2 z(t), \\ \\ \frac{dy}{dt} = B_1 x(t) - \alpha f_1(x(t))y(t) + C_1 z(t) - s_1 y(t) \\ \quad -C_2 y(t) - \varphi(t)y(t)\left(1-\frac{Q_2(t)}{Q_2 m}\right) + \mu g(y(t))z, \\ \\ \frac{dz}{dt} = B_2 x(t) - s_2 z(t) - \delta f_2(x(t))z(t) - C_1 z(t) \\ \quad +C_2 y(t) - \mu g(y) z, \\ \\ \frac{dQ_1}{dt} = -\gamma(t)Q_1(t)\left(1-\frac{x(t)}{x_m}\right), \\ \\ \frac{dQ_2}{dt} = \varphi(t)y(t)\left(1-\frac{Q_2(t)}{Q_{2m}}\right) \end{cases} \tag{1}$$

Since the concerned population is supposed to be constant, that is the equality $Q_1(t)+Q_2(t)+x(t)+y(t)+z(t) = N$ for all $t \in [0,T]$ is verified, system (1) can be reduced to four equations and rewritten as:

$$\begin{cases} \frac{dx}{dt} = \gamma(t)Q_1(t)\left(1-\frac{x(t)}{x_m}\right) - (B_1+B_2)x(t) \\ +\alpha f_1(x(t))y(t) + \delta f_2(x(t))z(t) + s_1 y(t) + s_2 z(t), \\ \\ \frac{dy}{dt} = B_1 x(t) - \alpha f_1(x(t))y(t) + C_1 z(t) - s_1 y(t) \\ \quad -C_2 y(t) - \varphi(t)y(t)\left(1-\frac{N-Q_1(t)-x(t)}{Q_2 m}\right. \\ \quad \left.\frac{-y(t)-z(t)}{}\right) + \mu g(y(t))z(t), \\ \\ \frac{dz}{dt} = B_2 x(t) - s_2 z(t) - \delta f_2(x(t))z(t) - C_1 z(t) \\ \quad +C_2 y(t) - \mu g(y) z(t), \\ \\ \frac{dQ_1}{dt} = -\gamma(t)Q_1(t)\left(1-\frac{x(t)}{x_m}\right). \end{cases} \tag{2}$$

3 Calibration of the model

Unfortunately, in the literature, the available data to calibrate the model are scarce. However, one can distinguish two groups of quantitative data. The first one concerns the percentages of the population adopting a certain type of behavior and the second one relates on the duration of such behaviors.

3.1 The percentages of population adopting a certain type of behavior

The different types of human behaviors described previously can manifest in variable proportions, in function of the considered catastrophe, the suddenness of the threat, the composition of the group, the individual aptitudes for understanding the danger and the knowledge of the environment. Moreover, [4] considers that in most of the catastrophes, "15% of individuals manifest obvious pathological reactions, 15% keep their cool and 70% manifest an apparently calm behavior but answer in fact to a certain degree of emotional sideration and lost of initiative which reports to a pathological register". These percentage have to be modulated according to the different parameters of our model, which leads us to consider:

- $x(t) = 50$ to 75% of the population
- $y(t) = 12$ to 25% of the population
- $z(t) = 12$ to 25% of the population

At our knowledge, no data are available for quantifying transition mechanisms from one state to an other.

3.2 The duration of the behavior

The three different reactions have different duration [17]. The duration of the reflex and panic behaviors varies from few minutes to one hour. Most of the time, these two types of behavior do not exceed 15 minutes. However, for the first one, it may take longer especially if it corresponds to a delay of evacuation in a disaster area. In this case, support and research behaviors for relatives and victims gradually appears [5]. For the second one, the collective panic behaviors resolves generally spontaneously. However, sometimes, an external intervention permits to the panic population $z(t)$ to come back to an automate behavior $x(t)$, before adopting a controlled behavior $y(t)$.
In general, the duration of the uncontrolled behavior $x(t) + z(t)$ does not last more than 1h30. In this model, we suppose that an individual cannot stay 1 hour in a reflex behavior and another hour in a panic state. The duration of the controlled behavior $y(t)$ varies from few minutes to fewer hours,

according to the intervention of the emergency response.
The choice of the parameters will be done in order to find these data.

4 Numerical examples

For the numerical simulations, we have transformed the model in a dimensionless form, that is, population numbers correspond to fractions of the total population. In the following subsection, the functions intervening in the dimensionless model are specified.

4.1 The functions γ, φ, f_1, f_2, f_3

In the case of a sudden catastrophe, as a local tsunami, modeled by the function γ, we suppose that the population begins to be rapidly informed that is to say after 1 minute, and that all the concerned population is informed in the 3 following minutes, hence, the shape of the function γ in Figure 2. Clearly, the return to the normality, corresponding to the function φ, can not be immediate. We have supposed that it is done after 5 minutes from the outbreak and this return is done very slowly, which leads us to consider the function φ as in Figure 2. As we have said before, the form of the curves has to be modulated according to the type of catastrophe event (depending if it is announced or not).

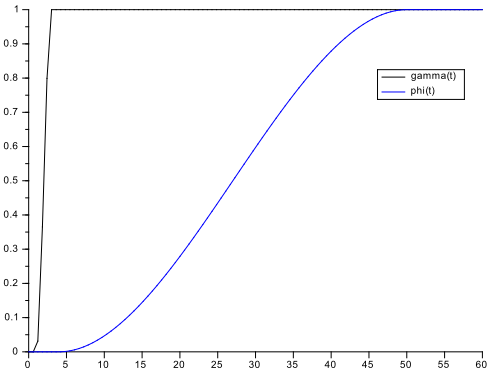

Figure 2: Functions φ and γ

The terms $\alpha f_1(x(t))y(t)$ and $\delta f_2(x(t))z(t)$ are the terms of imitation between $x(t)$ and $y(t)$, and $x(t)$ and $z(t)$, respectively. We promote the imitation from $x(t)$ to $y(t)$ in assuming that there must be at least 55% of reflex behaviors for that controlled individuals imitate reflex behavior (see Figure 3).

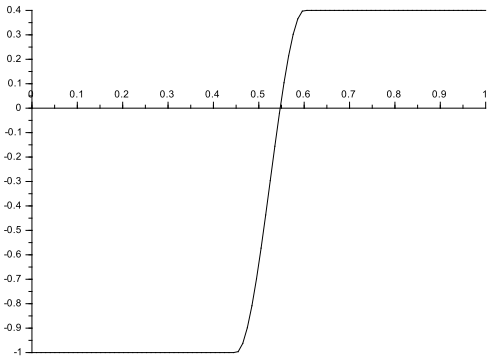

Figure 3: Function f_1 and f_2

For the imitation term $\mu g(y(t))z$, we suppose that the imitation is essentially in the sense from $z(t)$ to $y(t)$ (see Figure 4).

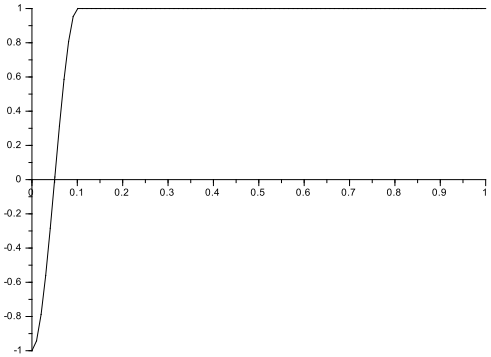

Figure 4: Function g

Functions f_1, f_2, g, φ and γ are modelised through the function

$$h(s) = \begin{cases} h_{min} \text{ for } s < s_{min} \\ h_{max} \text{ for } s > s_{max} \\ -\dfrac{h_{max} - h_{min}}{2} \cos\left(\dfrac{s - s_{min}}{s_{max} - s_{min}}\pi\right) \\ +\dfrac{h_{min} + h_{max}}{2} \text{ else} \end{cases} \tag{3}$$

where $[s_{min}, s_{max}]$ is the support of the function h and h_{min} (resp. h_{max}) is its minimum value (resp. maximum value).

4.2 Numerical simulations

Different scenarios were made and correspond to different values of parameters.

4.2.1 Simulation 1

The first one corresponds to Figure 5. The chosen values of the parameters permit to find the calibration data presented at Section 3. The areas between each curve and the horizontal axis gives the global percentage of the corresponding population. The global percentage of reflex behaviors ($x(t)$) equal to 61,41% is included between 50 and 75% otherwise the global percentages of panics and controlled behaviors respectively equal to 18,42% and 20,17% are included between 12% and 25%. Furthermore, the model gives the evolution of these global behaviors distributions.

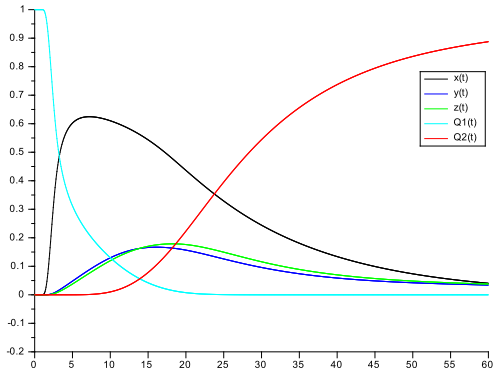

Figure 5: Simulation of the model with the parameters values: $x_m = 0.75$, $Q_{2m} = 1$, $B_1 = 0.04$, $B_2 = 0.02$, $s_1 = 0.01$, $s_2 = 0.01$, $C_1 = 0.5$, $C_2 = 0.5$, $\alpha = \delta = \mu = 0.01$.

4.2.2 Simulation 2

In this section, we are interested in the evolution of the model when the parameter B_2 varies, in particular, the possibility to evolve from reflex to panic behaviors. The numerical simulations at Figure 6 shows that for a low value of B_2, the density of population having a reflex behavior remains important during all the simulation. However, for a high value of this parameter (Figure 7), the density of this population decreases to extinguish rapidly. Furthermore, the densities of panic and controlled populations grow significantly between Figure 6 and 7.

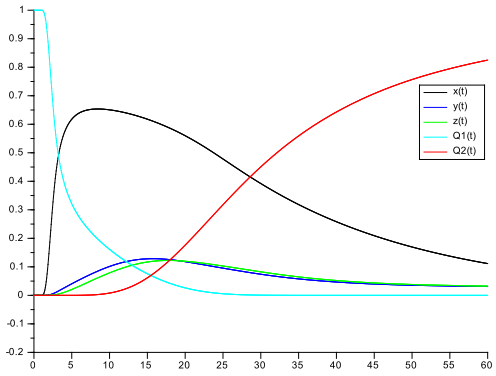

Figure 6: Simulation of the model with the parameters values: $x_m = 0.75$, $Q_{2m} = 1$, $B_1 = 0.04$, $B_2 = 0.002$, $s_1 = 0.01$, $s_2 = 0.01$, $C_1 = 0.5$, $C_2 = 0.5$, $\alpha = \delta = \mu = 0.01$.

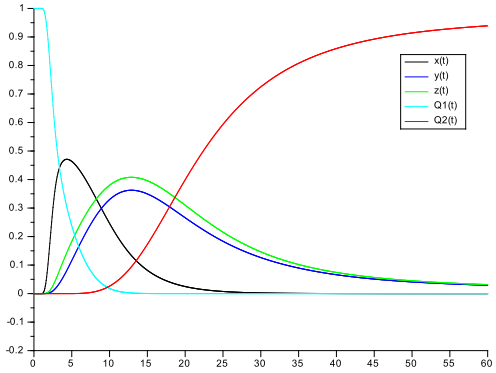

Figure 7: Simulation of the model with the parameters values: $x_m = 0.75$, $Q_{2m} = 1$, $B_1 = 0.04$, $B_2 = 0.2$, $s_1 = 0.01$, $s_2 = 0.01$, $C_1 = 0.5$, $C_2 = 0.5$, $\alpha = \delta = \mu = 0.01$.

4.2.3 Simulation 3

In the following simulations, we force the emergence of panic and controlled behaviors in acting on the parameters B_1, B_2, C_1 and C_2. Figure 8 shows that the return from controlled to daily behavior can be furthered, while Figure 9 induces a high proportion of panic behaviors and a return more difficult to normality as remarked by [6].

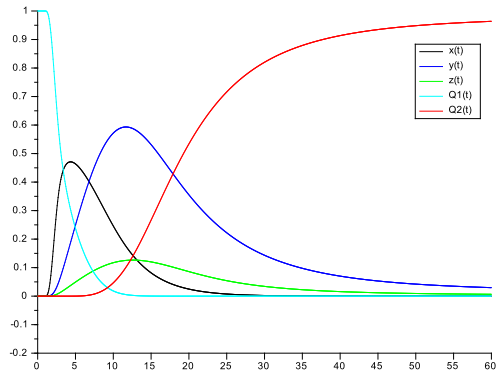

Figure 8: Simulation of the model with the parameters values: $x_m = 0.75$, $Q_{2m} = 1$, $B_1 = 0.2$, $B_2 = 0.04$, $s_1 = 0.01$, $s_2 = 0.01$, $C_1 = 0.5$, $C_2 = 0.1$, $\alpha = \delta = \mu = 0.01$.

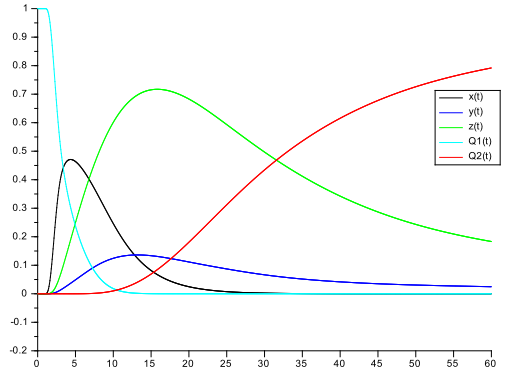

Figure 9: Simulation of the model with the parameters values: $x_m = 0.75$, $Q_{2m} = 1$, $B_1 = 0.04$, $B_2 = 0.2$, $s_1 = 0.01$, $s_2 = 0.01$, $C_1 = 0.1$, $C_2 = 0.5$, $\alpha = \delta = \mu = 0.01$.

5 Conclusion

This paper introduces a new step in the modeling of the crowd dynamics in catastrophic events. Indeed, it considers three concurrent behaviors and includes the processes of transition from one behavior to the other. Up to now, the main models consist in modeling the panic which is a fear behavior but it is not always adopted. Furthermore, panic does not necessarily lasts during all the event and, on the contrary, the global behavior of the crowd can change. In this work, two other behaviors have been integrated in the modeling: the reflex one and the controlled one. As seen in human sciences, our simulations show that they can influence the crowd behavior and a return to normality. The next step of this work will consist in doing a mathematical study of this model and integrating it in a diffusion process.

References

[1] D. Provitolo A. Dauphiné. *Risques et catastrophes. Observer, spatialiser, comprendre, gérer.* Paris : Armand Colin, 2013.

[2] J. Venel B. Maury. A mathematical framework for a crowd motion model. *C.R. Acad. Sci. Paris*, 346:1245–1250, 2008.

[3] N. Bellomo and C. Dogbé. On the modeling of traffic and crowds: A survey of models, speculations, and perspectives. *SIAM review*, 53(3):409–463, 2011.

[4] S.T. Boyd. Réactions psychologiques des victimes de catastrophes. *South african Medicine Jal*, 60:744–748, 1981.

[5] L. Crocq. *La psychologie des catastrophes et les blessés psychiques.* Noto R. Médecine de catastrophe, Paris, Milan, Barcelone, Masson, 1994.

[6] L. Crocq. *Les paniques collectives.* Paris : Odile Jacob, 2013.

[7] E. Dubos-Paillard D. Provitolo and J.P. Müller. Emergent human behaviour during a disaster: thematic versus complex systems approaches. In *EPNACS 2011 within European Conference of Complex System*, Septembre 2011.

[8] N. George and L. Gamond. Premières impressions. *L'essentiel Cerveaux et Psycho: Les émotions au pouvoir Science*, 7, 2011.

[9] P. Goatin, R.M. Colombo, and M.D. Rosini. A macroscopic model for pedestrian flows in panic situations. In *GAKUTO International Series Mathematical Sciences and Applications*, volume 32, pages 255–272, 2010.

[10] E. Hatfield, J.T. Cacioppo, and R.L.Rapson. *Emotional Contagion.* Cambridge, Cambridge University Press, 1994.

[11] D. Helbing, I. Farkas, and T. Vicsek. Simulating dynamical features of escape panic. *Nature*, 407(6803):487–490, 2000.

[12] H. Laborit. *La légende des comportements.* Paris: Flammarion, 1994.

[13] James D Murray. *Mathematical Biology I: An Introduction*. Springer, New York, NY, USA,, 2002.

[14] X. Pan, C. S. Han, K. Dauber, and K.H. Law. A multi-agent based framework for the simulation of human and social behaviors during emergency evacuations. *AI & Society*, 22(2):113–132, 2007.

[15] D. Provitolo. *Structural and dynamical complexities of risk and catastrophe systems: an approach by System Dynamics Modelling*. Springer (Ed.), 2009.

[16] H. Rahmandad and J. Sterman. Heterogeneity and network structure in the dynamics of diffusion: Comparing agent-based and differential equation models. *Management Science*, 54(5):998–1014, 2008.

[17] E. Vermeiren. *Psychologie des foules : éléments de compréhension et de prévention en situation de catastrophe collective*. Urgences, 2007.

Proceedings of ICCSA 2014
Normandie University, Le Havre, France - June 23-26, 2014

Service Regularity Loss in High-Frequency Feeder Bus Lines: Causes and Self-Driven Remedies

Jorge González [*], René Doursat [†], and Arnaud Banos [‡]

Abstract. An agent-based model of a single bus line is designed to assess quality of service in terms of regularity and occupancy. Agents represent buses moving on a linear network of stops, where passengers (summarized by counts) get on and off. Three performance-loss factors are considered: distances between stops, drivers' behavior, and influx of users along the line. We show that service regularity is less impacted by section lengths and bus speeds than by demand. Two solutions are tried: increasing the number of buses through a higher departure frequency, and improving the exchange of passengers with all-door boarding instead of the usual one-door scheme. These solutions are self-driven since no central supervision is required. We defined a measure of regularity based on the distribution of "headways" (time intervals) betwen buses. According to our model, higher frequencies do not improve regularity, whereas all-door boarding does for large numbers of incoming passengers. We describe a case study based on real data collected from a "feeder" service of the Parisian regional train network. It is highly unbalanced, as it serves opposite commuting directions during the morning and evening peaks, making it an especially interesting example.

Keywords. Public transportation network, bus, reliability, delay, agent-based modeling, boarding.

1 Introduction

Every transportation system in the world relies on buses due to their numerous advantages. A bus network does not need a huge infrastructure investment because it can use existing streets and roads [4, 7], making it more economical than other public transportation systems. It is resilient, in the sense that if a bus encounters a problem, other buses can overtake it or be rerouted as needed [1, 6]. At relatively low operating costs, it is also a profitable enterprise [4, 8]. On the other hand, buses are often perceived by the public as uncomfortable and unreliable because of highly variable travel and waiting times, which depend on the traffic conditions over the shared road network [1, 2].

Nowadays, priority at crossroads and exclusive lanes are recognized to greatly improve the efficiency of bus transportation systems, in particular commercial speed [6, 5]. Yet, even high-standard systems suffer a loss of regularity as consecutive buses inevitably start "clumping" together after a while, something that can be observed in every city around the world. There can be long empty periods followed by the arrival of two or more buses at the same time. Not many explanatory models of this phenomenon have been proposed, most of the research work focusing on the supervision of bus operation, the fast detection of perturbations, and optimal strategies to restore service after a disturbance [3].

We explore here two self-regulatory approaches toward improving the quality of service of a bus line. The first approach increases supply through the number of buses and frequency of departure. The second approach facilitates demand by implementing *all-door boarding* instead of one-door boarding. It allows passengers to board the bus through any door by installing fare collectors at every entrance or at every bus stop. Our study is based on the agent-based modeling and simulation (ABMS) of a single bus line, applied to real data collected from Nr. 91.06C (*Massy-Palaiseau: Gare RER – Saclay: Christ*) in the greater Paris area. This line is a "feeder" service providing the main connection between the Plateau de Saclay, an academic and industrial hub, and the regional suburban train network (RER). During the morning and evening rush hours, it has a high frequency of one bus every five minutes, as the great majority of commuters work at the facilities located in Saclay. This particularity is also the reason for a highly asymmetrical schedule, with a morning peak in the outbound direction, and an evening peak heading inbound. Moreover, as the region is also experiencing a recent development boom, customer demand has increased rapidly in the last few years and this growth is expected to continue. For all these reasons, this case study is an interesting object of application, both from a scientific and a practical perspective.

2 Methodology

We propose an agent-based model whose main agents are the buses running on one line. Individual passengers are

[*]SystemX Technological Research Institute; and Graduate School, École Polytechnique, Palaiseau, France. E-mail: jorge.gonzalez-suitt@polytechnique.edu

[†]Complex Systems Institute, Paris Île-de-France (ISC-PIF), CNRS UPS3611. E-mail: rene.doursat@iscpif.fr

[‡]Géographie-cités, CNRS UMR8504, Paris, France. E-mail: arnaud.banos@parisgeo.cnrs.fr

not differentiated, but grouped by destination. To build the network, bus stops are connected by edges, called "sections", forming a 1D pathway from one terminal to the other. Bus stops and sections are also considered agents with attributes and indexed accordingly. On each section, between two consecutive stops, a bus moves at its own constant speed. We assume that a bus driver has a *preferred* speed and each section has both a *recommended* and a *maximum* speed. The preferred speed of a bus is the speed that its driver tends to. The recommended speed of a section is the speed that buses tend to over that section, and may reflect geographical constraints, traffic flow, or some degree of central regulation. These origins are not taken into account, however, only the effect of this quantity is factored in by assigning it equally to all buses. In sum, the actual speed of a bus depends on the recommended and maximum speeds of a section and the preferred speed of the driver. When a bus arrives at a station, it stops if passengers want to board or exit the bus, and stays there as long as needed. Then, it moves over to the next section and so on, until the last stop.

2.1 Model

The parameters of the model are the following: there are M sections and $M+1$ bus stops. The path-like graph representing the bus line is denoted by $G = (V, A)$, where V is the set of bus stops and A the set of sections. The elements of V are indexed by $i = 0, 1, \ldots, M$, corresponding to their position along the line, with the first stop at $i = 0$ and the last stop at $i = M$. Let d_a be the length of section $a \in A$, and v_a^{rec} and $v_a^{\max}$ the recommended and maximum speeds on this section. The first two values are uniformly drawn in intervals $[d_-, d_+]$ and $[v_-^{\text{rec}}, v_+^{\text{rec}}]$, respectively. We denote by $p^{i,j}$ the rate of passenger influx going from origin i to destination j, with $(i, j) \in V^2$, by $P^i = \sum_{j \in V} p^{i,j}$ the total influx rate at stop i, and by $P = \sum_{i \in V} P^i$ the global influx rate. The p's are drawn from a power-law distribution in $[P_-, P_+]$ with exponent α. Let $D^{i,j}$ be the fraction of influx at stop i heading for j, so that $0 \leq D^{i,j} \leq 1$ and $\sum_j D^{i,j} = 1$. Another index, $b \in B = \{1, 2, \ldots, N\}$ denotes the b-th bus to leave from stop 0: its departure time is T_b, and its capacity C_b. The scheduled headway between consecutive buses is H_0, and its standard deviation σ_H. The preferred speed of bus driver is denoted by v_b^{pref}, and is drawn from a normal distribution of mean μ_v^{pref} and width σ_v^{pref}. Finally, Δt represents the time-step of our discrete model.

Next, we introduce the variables of the dynamics (omitting the time-dependency notation "...(t)" for greater readability). Let $r^{i,j}$ be the actual number of passengers waiting at stop i who want to go to j, o_b^j the number of passengers on bus b whose destination is also j, and $o_b = \sum_{j \in V} o_b^j$ the current occupancy of the bus. Additionally, v_b^{com} denotes the commercial speed, and v_b the actual speed of bus b. Finally, $t^i(b)$ represents the arrival time of bus b at stop i.

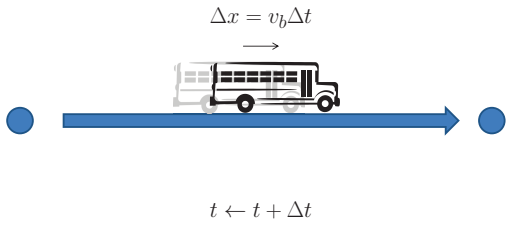

(a) Bus $b \in B$ going ahead.

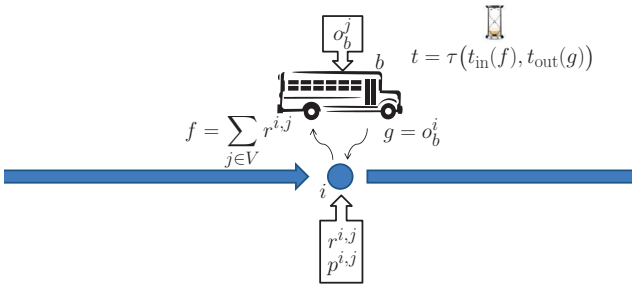

(b) Bus $b \in B$ is stopped at $j \in V$.

Figure 1: Schematic representation of the agent rules.

2.2 Initialization

Given M, we build the graph $G = (V, A)$ of our model as follows. Each bus stop $i \in V$ is assigned a total passenger influx rate $P^i \sim \mathcal{PL}(\alpha, P_-, P_+)$, which is a power-law distribution $\mathcal{PL}(p) \sim p^{-\alpha}$ restricted to $[P_-, P_+]$, and per-destination influx rates $p^{i,j} = P^i D^{i,j}$ for all $j > i$. When using real data, we may set one or more of these values to actual measurements. Each bus $b \in B$ leaves stop 0 according to a randomly perturbed timetable with a departure at $T_b \sim \mathcal{N}(bH_0, \sigma_H^2)$, where $\mathcal{N}(\mu, \sigma^2)$ is the normal distribution of mean μ and variance σ^2, and is also given a preferred speed $v_b^{\text{pref}} \sim \mathcal{N}(\mu_v^{\text{pref}}, {\sigma_v^{\text{pref}}}^2)$ and capacity C_b. There are no users at the beginning of the simulation: $r^{i,j} = 0$ and $o_b^j = 0$ for all $i, j \in V, b \in B$.

2.3 Microscopic rules

At each time step, variables are updated according to the following rules (Fig. 1):

1. "Waiting" rule: passengers come to bus stops at constant rates that depend on their itinerary, thus we write: $r^{i,j} \leftarrow \mathcal{P}(p^{i,j} \Delta t) + r^{i,j}$ for all $j > i$, where $\mathcal{P}(\lambda)$ is the Poisson law of mean λ.

2. "Exiting" rule: when bus b arrives at stop i, the o_b^i passengers inside who wanted this destination exit the bus, therefore: $o_b^i \leftarrow 0$.

3. "Boarding" rule: at this point, we use the following temporary variables: $f = \sum_{j \in V} r^{i,j}$ for the number of passengers waiting at stop i, $g = o_b^i$ for the passengers who just left the bus, $c = C_b - o_b + g$ for the

remaining capacity on the bus, and n for the passengers who are boarding the bus. Two cases arise:

- "Undercapacity boarding" rule: if $f \leq c$, then all $n = f$ passengers are able to take the bus, hence: $o_b^j \leftarrow o_b^j + r^{i,j}$, and $r^{i,j} \leftarrow 0$ for all $j > i$ (Fig. 1b).
- "Overcapacity boarding" rule: if $f > c$, only $n = c$ passengers can take the bus and $n' = f - c$ must stay out. In this case, we draw an n-combination of destinations from the set of f passengers: let $s^{i,j}$, with $0 \leq s^{i,j} \leq r^{i,j}$ and $\sum_{j \in V} s^{i,j} = n$, denote the number of passengers with destination j who boarded the bus. Then we apply: $o_b^j \leftarrow o_b^j + s^{i,j}$ and $r^{i,j} \leftarrow r^{i,j} - s^{i,j}$ for all $j > i$. Finally: $o_b \leftarrow C_b$.

4. "Stopping" rule: bus b stays at stop i for a duration $\tau(t_{\text{in}}(f), t_{\text{out}}(g))$, where $\tau(t, t')$ can represent either a maximum, if the entrance and exit doors are separated: $\tau = t_0 + \max\{t_{\text{in}}(f), t_{\text{out}}(g)\}$, or a sum, if inward and outward passenger flows are mixed: $\tau = t_0 + t_{\text{in}}(f) + t_{\text{out}}(g)$. In both cases there is a fixed stopping overhead t_0, including the time to open the doors. The arguments, t_{in} and t_{out} represent the time taken by passengers who are boarding and exiting the bus, respectively. Generally, they are nonnegative logistic functions but we adopt here a simple linear scheme: $t_{\text{in}}(f) = \rho_{\text{in}} f$ and $t_{\text{out}}(g) = \rho_{\text{out}} g$, where the ρ's are time-per-person rates.

5. "Lingering" rule: when bus b is about to leave stop i after a time t, and if it is still under capacity, the simulation verifies if other passengers have arrived in the meantime: if $f = \sum_{j \in V} r^{i,j} > 0$ at this instant, then the bus stays longer to allow the additional passengers to board, otherwise it leaves. This process may occur several times as long as new passengers are showing up. However, if the boarding rate is less than the average time between two incoming passengers, $\rho_{\text{in}} < 1/P^i$, the likelihood of repeating this process decreases with successive iterations.

6. "Moving" rule: when bus b leaves a stop, its speed is set to $v_b = (v_a^{\text{rec}} + v_b^{\text{pref}})/2$ on the whole section $a \in A$ that lies ahead. From there, at each iteration, if $\Delta x = v_b \Delta t$ is greater than the remaining distance to the next stop, the bus arrives at that stop; otherwise, its location is simply increased by Δx (Fig. 1a).

2.4 Output values

Let $\mathcal{B}^i$ denote the set of buses $l = 1, \ldots, |B|$ sorted by increasing arrival time $t^i(b)$ at stop i. For all $b_l^i \in \mathcal{B}^i$ with $l < |B|$, we have by construction: $t^i(b_l^i) \leq t^i(b_{l+1}^i)$, therefore we can calculate the headways between buses observed at stop i as follows: $h^i(b_l^i) = t^i(b_{l+1}^i) - t^i(b_l^i)$. This allows us to define a bus group $K = \{k, k+1, \ldots, k'\}$ for a given time threshold $\theta > 0$ such that, for all $l \in K \setminus \{k'\}$, we get $h^i(b_l^i) \leq \theta$, but $h^i(b_{k-1}^i) > \theta$ and $h^i(b_{k'}^i) > \theta$.

At every time step, the following quantities are measured: occupancies o_b, headways $h^i(b)$, bus group sizes $|K|$ and commercial speeds v_b^{com}. The latter are the ratio of the total length of the line to the total time spent by each bus on this line. We also define the average headway at stop i: $\mu_h^i = \langle h^i(b) \rangle_{b \in B}$, its standard deviation $\sigma_h^i = \sqrt{\langle h^i(b)^2 \rangle_{b \in B} - (\mu_h^i)^2}$, and its maximum $h_+^i = \max_{b \in B}(h^i(b))$.

3 Main Results

Several parameters have been introduced in Section 2.1. In order to analyze their impact on the dynamics and the outcome of the model, we conduct different tests in which only one of them is modified at a time. With the goal of applying this methodology to practical situations, we use real data from the bus line 91.06C described above. Most of the parameters can be set or estimated on the basis of the available data. Since this line is mainly used by commuters coming from the RER train system in the morning and returning there in the evening, buses generally start full and empty themselves in the morning, whereas they start empty and fill up in the evening. This important asymmetry, typical of feeder lines, is taken into account in our work. We choose two datasets to test our hypotheses: one covering the morning rush hour in the direction RER → Saclay, the other covering the evening rush hour in the opposite direction, Saclay → RER. These datasets provide the values used in the tests of Section 3.1, excluding a different parameter every time, which is arbitrarily varied to assess its effect on the system.

The physical properties of the line, its size M and section lengths $\{d_a\}_{a \in A}$, are known. The normal distribution of preferred speeds is estimated at $\mu_v^{\text{pref}} = 50$km/h and $\sigma_v^{\text{pref}} = 2$km/h, which is a reasonable assumption since the line in part uses bus-only lanes and has priority at crossroads. User influx profiles originate from the data and, as expected, are widely different in the morning and evening. Buses are articulated three-door with a capacity of $C = 120$. The planned headway is $H_0 = 5$mn, and departure times are not randomly perturbed in these simulations, i.e. $\sigma_H = 0$. The uniform distribution interval of recommended speeds is given by $v_-^{\text{rec}} = 40$km/h and $v_+^{\text{rec}} = 60$km/h. The boarding and exiting rates are $\rho_{\text{in}} = 3$s/passenger and $\rho_{\text{out}} = 1$s/passenger, and we use the maximum-function variant of τ with a fixed stopping overhead of $t_0 = 5$s. This reflects the fact that boarding takes on average three times longer than exiting, as it is allowed only through one door, where passengers need to pay, whereas there are two other doors for immediate exit. The time step Δt is set to 1s and every run lasts 14,400 iterations, i.e. 4 hours, which is enough to cover each of the two rush periods between 7-10am and 4-7pm. Each test consists of 100 runs for statistical purposes.

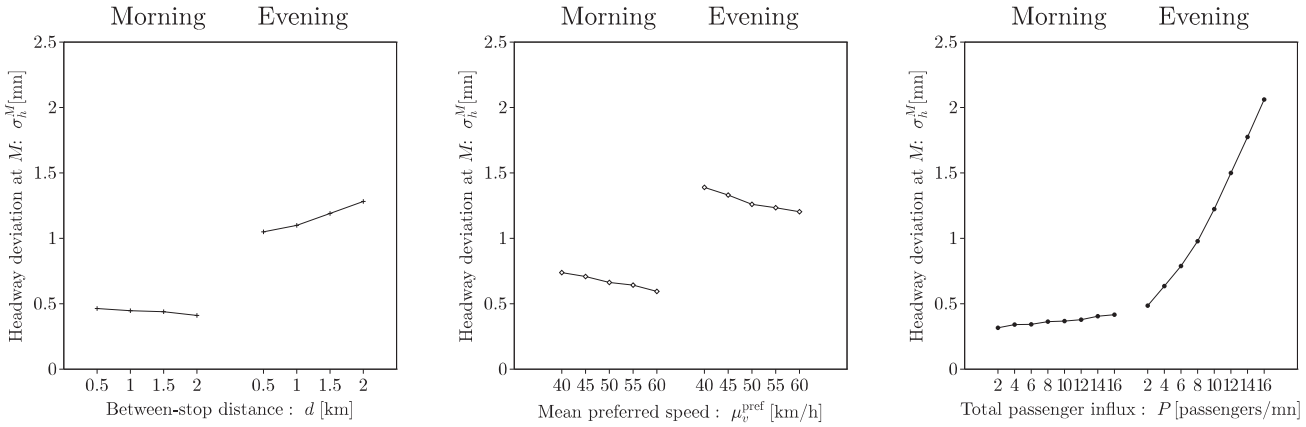

(a) Test 1: section length. (b) Test 2: preferred speed. (c) Test 3: passenger influx.

Figure 2: Assessing amplitude effects: (a) Section lengths and (b) speed levels have little effect on headways, while (c) higher demand can lead to greater disturbance in the evening. See Section 3.1.1 for details.

3.1 Assessing disturbance factors

In a first step, we want to explore parameter space to find out how different factors may either encourage or control disturbances in the planned schedule. In a next part, we will propose preventive measures to alleviate these fluctuations. The quantities of interest are:

- the uniform distribution of section lengths d, parameterized by d_- and d_+
- the normal distribution of preferred speeds v_b^{pref}, parameterized by μ_v^{pref} and σ_v^{pref}
- the power-law distribution of incoming users P^i, parameterized by P_-, P_+ and α, and normalized by P.

Six tests were performed: three to study *amplitude effects* and three for *heterogeneity effects*. Each test consists in varying only one of the parameters and running the model 100 times for each value to obtain a more reliable average for the output and reduce stochastic bias. In 3.1.1, we focus on the effect of amplitude, thus we set lengths, speeds, and influx rates to the same values for all agents. In 3.1.2, we focus on the effect of heterogeneity, thus we set the mean of each distribution and try out different standard deviations. In both cases, the mean and the standard deviation of all outputs are calculated.

3.1.1 Assessing amplitude effects

In the first batch of three tests, the effect of input amplitude is assessed by giving homogeneous values to all the parameters:

- Test 1: section lengths are all equal to $d = d_- = d_+$, which can be 500, 1000, 1500, or 2000m
- Test 2: preferred speeds are all equal to μ_v^{pref}, which can be 40, 45, 50, 55, or 60km/h, while $\sigma_v^{\text{pref}} = 0$
- Test 3: passenger influx profiles are given by the data (users were polled about their planned itineraries, recorded in $D^{i,j}$), then renormalized by dividing by their sum and multiplying by total rate P, which can be 2, 4, 6, 8, 10, 12, 14, or 16 p/mn.

Among the output values described in Section 2.4, the results obtained for the headway standard deviation at the last bus stop, σ_h^M, are plotted in Fig. 2. Note that stops are renumbered according to direction, therefore the morning's last stop is the evening's first stop, and vice-versa. Headway standard deviation provides the best benchmark quantity, as it is not directly impacted by the varied inputs—in contrast to commercial speed, for example, which depends directly on preferred speed.

Headways are most disturbed by higher passenger demand In Figs. 2a, 2b (lengths and speeds), we observe that regularity is always better in the morning than the evening. However, comparing to Fig. 2c (passenger influx), the effect of increasing lengths and speeds on headways appears much weaker than the effect of increasing demand in the evening. Headway standard deviation increases quickly with demand along the evening profile of passenger influx. This stands in contrast to the morning profile, where this effect is much less pronounced. This stark discrepancy can be explained by the fact that the timetable is assumed to be respected at the departure point in the model, hence a higher demand in the morning should not affect it very much. But whereas passengers take a little time to exit buses, the time needed to board was estimated to be three times as high. Therefore, it is only natural that evening buses, which gradually fill up, experience more delays than morning buses, which are generally full at once. In conclusion, depending on the time of the day, increasing demand can have the strongest effect on regularity, essentially correlated with the time that buses spend at stops.

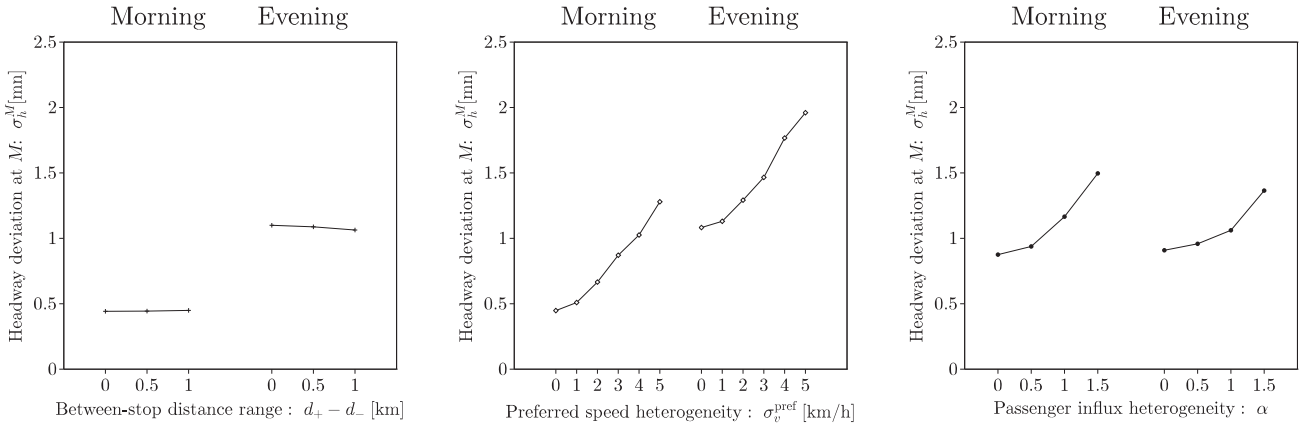

(a) Test 4: section length interval. (b) Test 5: preferred speed deviation. (c) Test 6: passenger influx exponent.

Figure 3: Assessing heterogeneity effects: (a) Heterogeneity in section lengths does not disturb planning. (b) Heterogeneity in preferred speeds can disturb planning, but not in a realistic range (which should remain below ±4km/h). (c) Heterogeneity in demand along stops is a clear cause of planning disturbance. See Section 3.1.2 for details.

3.1.2 Assessing heterogeneity effects

In the second batch of three tests, the effect of heterogeneity on the quality of service is studied by varying the standard deviation of the parameters' distribution laws under constant mean:

- Test 4: distance dispersion $[d_-, d_+]$ is set to three ranges, $[1000, 1000]$, $[750, 1250]$, and $[500, 1500]$, keeping the mean at $(d_- + d_+)/2 = 1000$m
- Test 5: preferred speed dispersion σ_v^{pref} is set to 0, 1, 2, 3, 4, and 5km/h, while $\mu_v^{\text{pref}} = 50$km/h
- Test 6: passenger influx is increasingly diversified by setting α to 0, 0.5, 1, 1.5, and $[P_-, P_+]$ to $[1, 1]$, $[0.1, 2.5]$, $[0.01, 8]$, and $[0.001, 20]$, respectively, then in each case renormalizing the P^i's by $P = 8$p/mn and multiplying them by the $D^{i,j}$'s from the data.

As in the previous assessment, only the final headway standard deviation is examined (Fig. 3). Our observations follow.

Heterogeneity in section lengths does not disturb planning Fig. 3a shows that there is pratically no difference in the headway distribution when section lengths are diversified. Altogether, combined with Fig. 2a, we can conclude that section lengths do not have any significant effect on headways.

Heterogeneity in preferred speeds can disturb planning, but not in a realistic range It can be seen in Fig. 3b that a higher dispersion among the preferred speeds of bus drivers is a clear factor of variability in headways, as one could expect. Compared to the default levels of Fig. 3a, however, this effect becomes noticeable only for $\sigma_v^{\text{pref}} \geq 4$km/h, which is unlikely to be the case in practice.

Heterogeneity in demand along stops is a clear cause of planning disturbance In Fig. 3c, an increase of the exponent α in the power-law distribution of passenger influx rates also creates more variable headways. Therefore, we conclude that more heterogeneity in passenger influx rates leads to less regularity.

3.2 Assessing preventive measures

In this section, we use our model to test self-driven measures, i.e. without the need for online central intervention, that may improve the quality of service on line 91.06C. We consider two main possibilities: *increasing the frequency* of bus departure on the line, and implementing *all-door boarding* in buses. The former is easily achieved in our model by reducing the value of parameter H_0. The latter can be simulated through a drop in boarding time ρ_{in} down to 1.5s/p, i.e. half the level of the current one-door boarding scheme. Theoretically, it should be one third, since the articulated buses have three doors. Therefore, 1.5s/p is a reasonable upper bound of the actual time per passenger. We look again at the effect on the final headway distribution via its standard deviation σ_h^M. We also consider here its maximum h_+^M, i.e. the maximum time interval without passing buses.

Increasing the departure frequency reduces the maximum headway but not the dispersion Fig. 4a shows that smaller H_0 values provoke a sharp decrease in maximum headway, but hardly modify headway variability. It means that this measure would not be effective: despite adding more buses to the line, the target frequency could still be missed. Moreover, supply was increased unilaterally in this virtual test, whereas in real life, economic considerations would condition it by an increase in user demand—which could eventually worsen the situation.

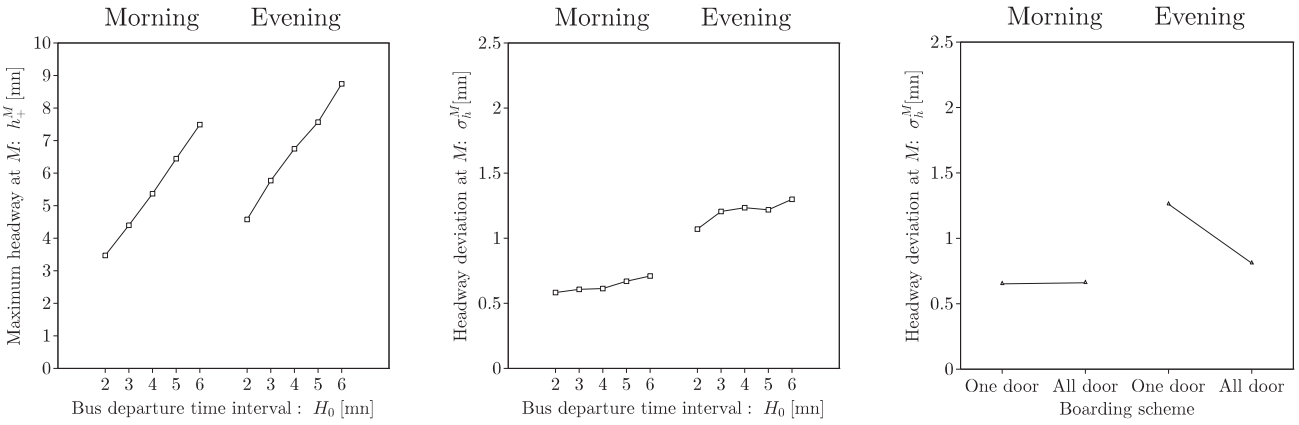

(a) Varying time intervals at departure.

(b) All-door vs. one-door boarding.

Figure 4: Comparing an increase in the frequency of the line to the implementation of all-door boarding as palliative measures against loss of regularity.

All-door boarding can improve service during the evening peak In Fig. 4b we see that the effect on headway dispersion is significant in the evening, but inexistant in the morning. Implementing all-door boarding also slightly increases the average speed of buses in the evening. Therefore, this measure seems an effective way of combatting irregularity in the case where there are many boarding passengers. These results suggest that opening all doors can alleviate the inherent loss of performance due to boarding, and restore some balance.

4 Discussion

We have proposed an agent-based model and simulation of bus transportation, focusing on the regularity of transit and avoidance of "clumping" as an essential criterion of quality of service. We studied the influence of various factors on this quantity, including distances between stops, preferred speeds of drivers, and planned frequency of bus departures. Based on real data, our statistical results indicate that *user demand*, represented by the influx of passengers at the bus stops, was the parameter with the most significant effect on the variability of time intervals, or "headways", between vehicles at the final stop on the line. By contrast, section lengths or driving styles showed little to no impact on regularity.

Similar to ongoing research in this domain [6], we applied this model to a simulation of real-world behavior and the evaluation of self-regulation measures, in the sense that no central supervision or control were needed in real time. We identified *all-door boarding* to be the most helpful in minimizing the loss of regularity. The great advantage of this measure is its low-cost implementation, as it only involves installing fare-collector equipment at the bus doors and/or bus stops. One drawback, however, could be an increase in "free riders", as the absence of direct control might give users an incentive to bend the rules. A cost-benefit analysis would need to be conducted to assess the weight of this potential issue. On the other hand, increasing the frequency of departure at the start of the line does not appear to be effective. It is also not economically feasible as it would need to be justified by an overall increase in demand volume, therefore probably cancelling any advantage it might bring.

The available data from line 91.06C allowed us to set most of the parameters of our model to realistic values. The hypotheses we made about speed levels are in accordance with the features of this particular line. Bus 91.06C partially runs on bus-only lanes, specially constructed for that purpose, and wherever it shares the road with other vehicles, traffic is never heavy in the directions and times of day that we considered here, therefore it could be neglected. It also seemed a reasonable assumption to model driving styles by a normal distribution, as it is a characteristic law of human behavioral diversity. In that case, we observed that the average preferred speed had no effect on regularity, while the width of its dispersion was only moderately influential. We also assumed that passengers flowed in at independent times, so they could be modeled via a Poisson process. Although it was verified by the data on this line, it may not always be a faithful representation of other types of discrete events, in particular the sudden and simultaneous appearance of dozens of users from the same location (such as an office building at closing time). Finally, other possible external factors were not taken into account in this model and should be the focus of future work: for example, more realistic interference from concurrent traffic on the roads and at intersections, through a bias applied on the average section speeds, or by using a secondary agent-based model to simulate the cars.

Acknowledgments

This research work was conducted under the leadership of the Technological Research Institute SystemX, supported by public funds within the scope of the French Program "Investissements d'Avenir". It is part of the MIC project on Multimodal Transportation Systems in the context of the Systems of Systems program. Simulations were carried out with software by The CoSMo Company. We thank the Communauté d'agglomération du Plateau de Saclay (CAPS) and Albatrans (bus operator) for the provided data.

References

[1] X. Chen, L. Yu, Y. Zhang, and J. Guo. Analyzing urban bus service reliability at the stop, route, and network levels. *Transportation Research Part A: Policy and Practice*, 43(8):722 – 734, 2009.

[2] C. F. Daganzo. How to improve bus service, 2008.

[3] E. Diab and A. El-Geneidy. Variation in bus transit service: Understanding the impacts of various improvement strategies on transit service reliability. *Public Transport: Planning and Operations*, 4(3):209 – 231, 2013.

[4] D. A. Hensher. Sustainable public transport systems: Moving towards a value for money and network-based approach and away from blind commitment. *Transport Policy*, 14(1):98 – 102, 2007.

[5] A. X. Horbury. Using non-real-time automatic vehicle location data to improve bus services. *Transportation Research Part B: Methodological*, 33(8):559 – 579, 1999.

[6] C. Pangilinan, W.-S. Chan, A. Moore, and N. Wilson. Bus supervision deployment strategies and the use of real-time avl for improved bus service reliability. *Transportation Research Board*, 2063:28 – 33, 2008.

[7] A. Tirachini, D. A. Hensher, and S. R. Jara-Díaz. Comparing operator and users costs of light rail, heavy rail and bus rapid transit over a radial public transport network. *Research in Transportation Economics*, 29(1):231 – 242, 2010. Reforming Public Transport throughout the World.

[8] A. Weinstock, W. Hook, M. Replogle, and R. Cruz. Recapturing global leadership in bus rapid transit, 2011.

Proceedings of ICCSA 2014
Normandie University, Le Havre, France - June 23-26, 2014

INTERMITTENCY, MULTIFRACTAL VECTOR FIELDS, LIE CASCADES AND STOCHASTIC CLIFFORD ALGEBRA

D. Schertzer, I. Tchiguirinskaia

Abstract.

We show in this paper that stochastic Clifford algebra defines a convenient framework to generate multifractal vector fields. They in fact define a generic case of Lie cascades. .

1 Intermittency and cascades

Intermittency is a key issue in statistical physics. A major breakthrough occurred with multifractals in the 1980s: intermittency became understood as resulting from an infinite hierarchy of fractal supports of the field singularities. However this was mostly done for scalar fields, whereas the fields of interest, e.g. the velocity for turbulence, are generally vector fields. This gap has prevented many developments.

Some time ago, "Lie cascades" were introduced [2], [4] to deal with multifractal vector fields. This was done by first considering a scalar multiplicative cascade as a non trivial limit for a vanishing inner scale of the exponentiation of a generator, defined as an additive stochastic process with a logarithmic divergence with the inner scale. Although non trivial, this limit is by noway limited to scalar processes.

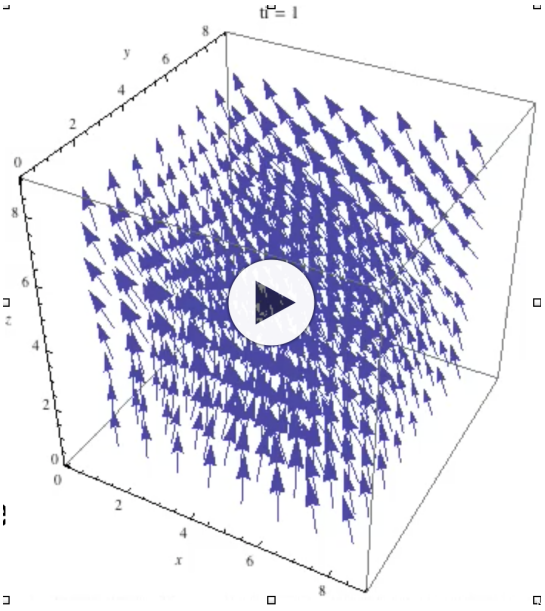

Figure 1: Snapshot of a multifractal simulation of a 3D+1 intermittent vector field.

2 Lie cascades and Clifford algebra

Indeed, the exponentiation of an additive stochastic process is only the simplest case of an exponentiation from a stochastic element of a Lie algebra to its Lie group of transformations. The concerned transformation corresponds to the fine graining/downscaling of the field to higher and higher resolution [3].

However, the theoretical efforts were mostly concentrated on the Levi decomposition of this algebra into its radical and a semi-simple algebra. Developments were again paused, this time due to the possible large number of degrees of freedom of the latter, in particular with respect to the information that can be easily extracted from a d-dimensional vector field. In short, some physics was missing.

Although Clifford algebra $Cl_{p,q}$ have been mentioned at once for rather straightforward generalisations of complex cascades, they were no more than mentioned for a while. This has been in sharp contrast with the rather frequent use of the "pseudo-quaternions" $l(2,R) = Cl_{2,0} = Cl_{1,1}$, back to [1], to generate generalised scales to analyse and simulate anistropic scaling (scalar) fields. This was not done by chance: $Cl_{p,q}$ has a basis whose vectors anticommute and square to the identity or its opposite, and is generated by a quadratic form Q of signature (p,q). These properties being physically meaningful are convenient to understand, analyse and simulate intermittent vector fields. The applications of the corresponding Lie cascades will be illustrated with the help of simulations of geophysical processes (see Fig.1). We will discuss in particular the case of fractional vorticity equations that generate a 23/9-dimensional turbulence that broadly generalize the so-called quasi-geostrophic turbulence [5].

*D. Schertzer and I. Tchiguirinskaia are with LEESU, University Paris-Est, Ecole des Ponts ParisTech, France. E-mails: Daniel.Schertzer@enpc.fr, Ioulia.Tchiguirinskaia@enpc.fr

†Manuscript received April 17, 2014; revised April 17, 2014.

Acknowledgements

The research for this work was partially supported by the Chair "Hydrology for Resilient Cities" (supported by Veolia).

References

[1] D Schertzer and S Lovejoy. Generalised scale invariance in turbulent phenomena. *Physico-Chemical Hydrodynamics Journal*, 6:623–635, 1985.

[2] D Schertzer and S Lovejoy. From scalar cascades to Lie cascades: joint multifractal analysis of rain and cloud processes. In R A Feddes, editor, *Space/time Variability and Interdependance for various hydrological processes*, pages 153–173. Cambridge University Press, Cambridge U.K., 1995.

[3] D Schertzer and S Lovejoy. Mulitfractals, generalized scale invariance and complexity in geophysics. *International Journal of Bifurcation and Chaos*, 21(12):3417–3456, 2011.

[4] D Schertzer, S Lovejoy, F Schmitt, I Tchiguirinskaia, and D Marsan. Multifractal cascade dynamics and turbulent intermittency. *Fractals*, 5(3):427–471, 1997.

[5] D Schertzer, I Tchiguirinskaia, S Lovejoy, and A F Tuck. Quasi-geostrophic turbulence and generalized scale invariance, a theoretical reply. *Atmos. Chem. Phys.*, 12:327–336, 2012.

Proceedings of ICCSA 2014
Normandie University, Le Havre, France – June 23-26, 2014

ABOUT THE DETECTION OF PANIC IN INDIVIDUAL AND COLLECTIVE HUMAN BEHAVIORS

Brethé Jean François[1], Campo Mickael[2], Charrier Rodolphe[3], Corson Nathalie[4], Druaux Fabrice[1], Harik El Housssein Chouaib[3], Guerin François[1], Guinand Frédéric[3], Rabai Haifa[3], Leclercq Edouard[1], Lefebvre Dimitri[1], Olivier Damien[3], Saad Ali[1], Thouvarecq Régis[2]

Abstract. This short contribution concerns the measurement and analysis of weak signals for panic issued from the attitudes of people and movements of crowds. For this purpose, the use of drones and mobile robots is proposed to monitor groups of people for detecting collective emotional stress. In addition, motion and physiological sensors can be used to capture the stress of isolated individuals. Using artificial intelligence tools, the aim of the project MASPAN is to correlate individual and collectives behaviors and to propose a better understanding of panic phenomena.

Keywords. Panic, change detection, sensoring, artificial intelligence.

1 Introduction

Many terrible crowd disasters have occurred during pilgrimage, sports events, or other mass gatherings due to individual and collective panic. The Loveparade in 2010 (Figure 1) or the Mecque pilgrimage in 2006 (Figure 2) are two famous examples with numerous injurious and dead people. [14].

Figure 1: Loveparade in 2010.

Figure 2: Mecque pilgrimage in 2006.

The public policies have the responsibility to organize and coordinate efficient response when such incidents occur due to human, natural or industrial causes. Thus, a better understanding is useful to anticipate panic phenomena and to coordinate more effective interventions. Automatic vision systems, signal processing methods, artificial intelligence and other methods that detect congestions and dangerous crowd turbulences in real world settings can collaborate with individual motion and physiological sensors to improve the analysis of panic behaviors. This is the context of the proposed paper and the aim of the MASPAN project. Section 2 is about the state of the art. Section 3 presents the experimental platform used in MASPAN project, it introduces some methods for changes detection and analysis. Finally the conclusion proposes a new paradigm for panic understanding.

2 Detection of panic behaviors

The development of machine vision, artificial intelligence and pattern recognition techniques is inspiring many real world applications and these applications, in turn, are promoting new technological developments. The aim of this section is to present some innovative methods that are applied to detect panic in groups of persons and in individual behaviors.

[1] with GREAH Normandy University, Le Havre.
[2] with CETAPS Normandy University, Rouen.
[3] with LITIS Normandy University, Le Havre.
[4] with LMAH Normandy University, Le Havre.

2.1 Panic in collective behaviors

Collective motions are one of the most common and spectacular manifestation of coordinated behaviors. Such behaviors include systems consisting of units ranging from elementary particles to groups of animals and people [27]. In this contribution we focus on groups of persons as a whole (holistic paradigm). The study of collective movements is important during emergencies such as natural or technological disasters or also during terrorist attacks.

Quantitative theories and mathematical models of the collective dynamics of pedestrians have been recently derived from collective animal dynamics (Figure 3) [24]. This approach is motivated due to the lack of complementary data to develop and validate the explanatory model. Thus, some investigations concern non-human model organisms and emphasize the behavioral similarities and dissimilarities between humans and animals [25]. The major drawback with the use of such observations is the correlation with human behaviors.

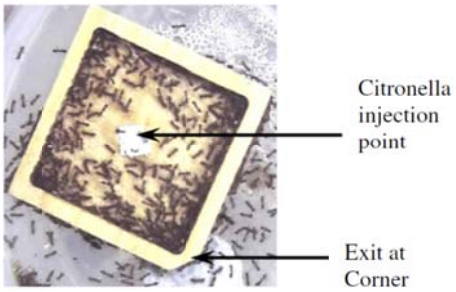

Figure 3: Panic in a population of ants [25]

Simulation-based crowd video has been also investigated. For example, AGORASET, is proposed including ground-truth and metrics ready for use for pattern recognition purposes (Figure 4) [4]. One should take care of the range of validity and limitations of the use of such synthetic datasets in the context of panic understanding.

Figure 4: Simulation with AGORASET [4]

[6] uses data produced by AGORASET and introduces an unsupervised method for the detection and location of dense crowds in images without context-awareness (Figure 5). After retrieving multiscale texture-related feature vectors from the image, a binary classification determines which parts of the image belong to the crowd and which to the background.

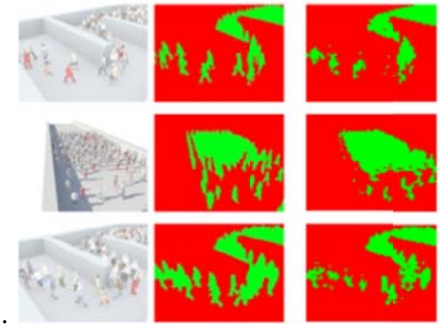

Figure 5: Crowd detection (right) according to [6] and compared with true detection (centre) and original simulation images (left)

Some other approaches rely on optical flow computations. Such methods run in real-time and preserve the privacy of the people being monitored. Such methods have been applied to actual video sequence with promise full results [14].

Considering each individual separately is another approach (atomistic paradigm) that has the advantage to be suitable to detect subtle anomalies in a heterogeneous surveillance scene. Such methods required image segmentation and pattern recognition tools (Figure 6) [15].

Figure 6: Identification and tracking of individuals in a crowd [15]

2.2 Panic in individual behaviors

Fear, worry, anxiety, horror, (…), from an atomistic perspective, many terms has been used to understand what is individual panic. Considered broadly as an affective distress similar to an intense fear or discomfort,

panic is mainly experienced in anticipation of a harmful event, such as waiting a "vital" competition, expecting to receive a punishment, facing a predator, or waiting an inevitable death.

Figure 7: Facial expression of fear [5]

Emotions are considered to have multiple components. Accordingly, panic is associated with specific behaviors (i.e. action tendencies) and physiological responses (i.e., neural responses and peripheral activations), which could help to detect the emergence of such affective troubles. Thus, an imminent threat would lead individuals to adopt avoidance behaviors [8] and to increase their respiration and heart rate due to a noradrenergic activity [3]. In this case, fear and anxiety, two emotions usually associated with panic, may be observed and measured objectively, supporting thus the bottom-up paradigm of emotional contagion [2]. This approach of the study of emotion propagation with group contexts could thus help to a better understanding of panic in crowds, which is one of the two research axes of the present MASPAN project.

Different tools are used to appreciate the intensity of an emotional distress episode through a continuum based on the degree of subjective inference required from the experimenter or the participants. On one hand, subjective tools are often used in psychology studies consisting mainly in completing self-assessment questionnaires or in using observational grids for non-verbal behaviors (Figure 8) [17].

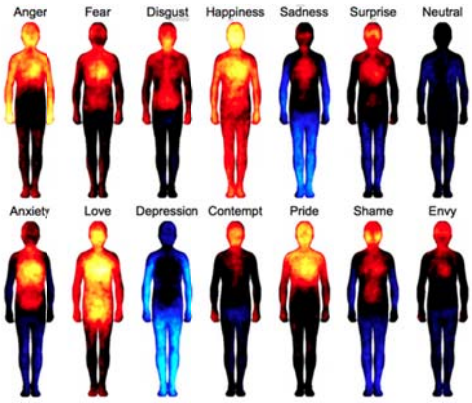

Figure 8: Bodily maps of regions activated by emotions [17]

These studies provide interesting findings but they did not allow to be sure that what has been measured was not biased by self-inferences or poor assessment capacities. Pertinent to answer some research question, validated subjective tools are not appropriate to measure weak and brief signals associated with dynamic emotional experience such as panic.

On the other hand, one finds techniques that directly measure affective responses through the production process at the physiological level. Based on biological and neurophysiological approaches of emotions, scientific literature showed the use of tools adapted to the study of emotional networks in the brain as electroencephalography (EEG) or functional magnetic resonance imaging (fMRI) (Figure 9).

Figure 9: An EEG recording at Dalhousie University

Vocal and facial expressions of emotions as facial-EMG, or acoustic measurements can be also be used. Finally the emotion influence on autonomic system has been investigated with EMG, heart rate monitor, thermometer, blood sampling, electrodermal activity measures, vascular activity.

Finally, while panic leads individuals to flee, some other instruments of objective measures used in movement studies could be used such as motion tracking systems (accelerometers, motion and gait analysis tools, video-based automatic tracking). Such instruments have already been successfully used in the area of affective computing but, as the other objective techniques that are mentioned above, they often require a very controlled environment and may be obtrusive, often limiting behavioral freedom, and consequently the ecological validity of research in the field of emotions. By also studying panic through an atomistic paradigm, the MASPAN project proposes to challenge this difficulty to contribute to objectively understand what is panic via ecological protocols.

3 Sensoring and analyzing the panic

The aim of this section is to present the sensoring platform proposed for MASPAN project and to introduce

some methods that are investigated to extract significant information about panic.

3.1 An effective experimental platform

In order to collect measurements about individual and collective behaviors the project MASPAN uses some specific sensors. In particular land and flying robots have been equipped with video cameras (Figures 10 and 11) .

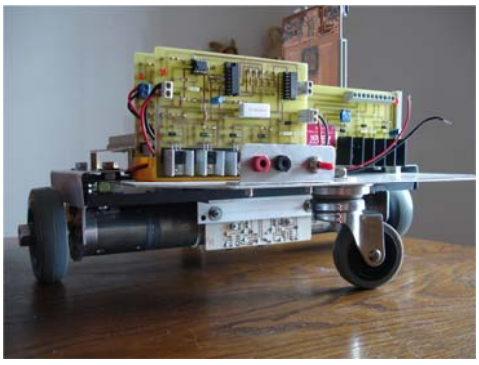

Figure 10: Land mobile robot (GREAH)

Figure 11: Flying robots (GREAH and LITIS)

Motion sensors (acceleration board, telemeters and goniometers) have been also developed to collect and analyse the walk and run of individuals [20] (Figure 12).

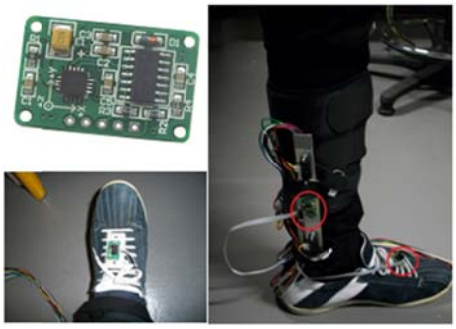

Figure 12: Acceleration board (GREAH)

Another class of sensors is arising with the massive development of intelligent and connected wearables. Many sensors are embedded in such a product touching the skin of individuals. For instance intelligent T-shirts are now proposed on the market. They can capture the hart and respiratory frequency in real time (Figure 13). These physiological data lead to individual measures of emotional levels of the monitored people. Then data may be sent by the mobile phone network or stored on a mobile device. These kind of products may open many perspectives on panic studies and risk prevention.

Figure 13: Hexoskin t-shirt
(extracted from http://www.hexoskin.com/)

3.2 Change detection in signal processing

Raw signals measured with individual or collective behaviors must be analyzed. For these purpose it is necessary

- To extract the significant features,
- To detect the changes with statistical or artificial intelligence approaches.

Feature selection attempts to select or extract significant attributes in the original data which contain useful information for pattern classification [9]. In any fault diagnosis problems, feature extraction from the raw signals is a very critical step because these extracted features not only characterize the information relevant to the considered behavior, but also affects the final classification results. This step is typically required due to the high dimensionality of the problem. The number of features used will usually be much less than the number of original measurements. The commonly used techniques for selection of features are based on binary logical tools as decision tree [22], principal component analysis [7] and genetic algorithms [13].

The objective of the statistical approaches is to decide if the data characterizing the history of a process (for example collective or individual human behaviors) are generated by the same model. The aim is to decide between two hypotheses: the data set results from the same distribution F0 or there is a time for change and the data

set is divided into two subsets described by F0 and F1 probability density functions. For example, in our previous study [21], x-axis shin acceleration extracted from the accelerometer presented has been proved to be suitable to detect the freeze of gaits for Parkinson's disease patients (Figure 14).

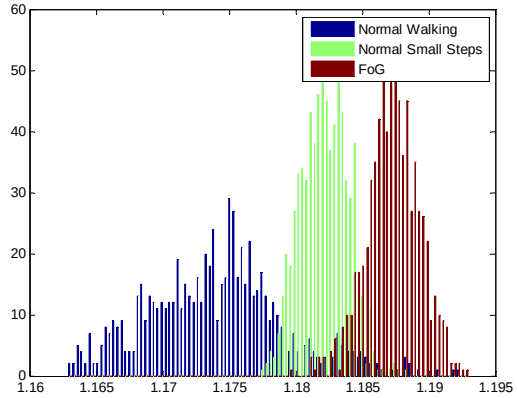

Figure 14: Mean histogram of x-axis shin acceleration data [21]

Methods for mono variable and multivariable approaches are generally separated [26]. The pioneer algorithm proposed in [23] computes the mean of the samples. Roberts (1959) [19] proposed the algorithm of the Exponentially Weighted Moving Average (EWMA) for detecting low amplitude changes. The algorithm of the Cumulative Sum (CUSUM) has also been also proposed to improve detection for low amplitude changes. In its basic form, CUSUM is a hypothesis test that detects a change in the probability density function of the observations [18] (Figure 15). Numerous works based on CUCUM and Dynamical CUSUM (DCS) have been proposed to detect changes in various domains [16].

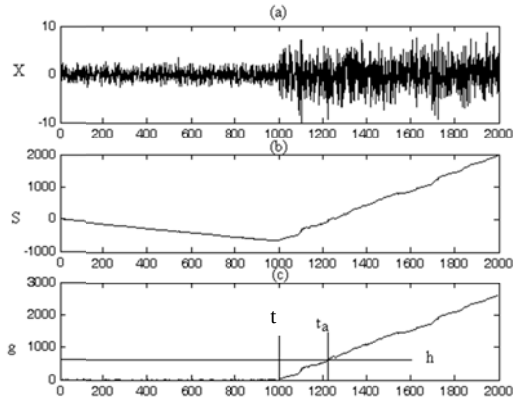

Figure 15: CUSUM algorithm (a) raw data (b) CUSUM (c) detection function [16]

In signal processing, Artificial Neural Networks (ANNs) stand for an interesting and valuable alternative to the statistical methods, because they can deal with complex situations [11]. Fixed sized neural networks are a popular technique for the pattern classification and diagnosis of non-linear behaviors. Multi-layer perceptrons, Gaussian networks and radial basis functions are the most commonly supervised networks used for detection and diagnosis tasks [28]. However, they suffer from serious limitations, such as the moving target problem which is the interference between old and new learned knowledge. Also the structure of the networks may become so large that it could not learn all fault patterns with an acceptable performance. In addition when network expands or topology changes, ANNs have to be totally retrained and so the adaptation capability becomes the adequate solution in neural network applications. To overcome these problems adaptive growing ANNs have been investigated [1].

4 Conclusion

The literature about panic is clearly separate into two categories of works. The ones that consider and study panic as a collective behaviors and the other that consider panic as the result of individual fear. The project MASPAN aims to propose a global understanding of the panic phenomena by connecting individual and collective behaviors (Figure 16).

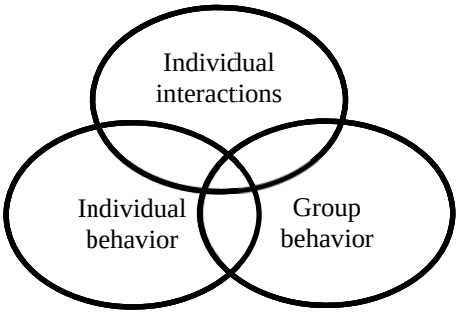

Figure 16: A global understanding of the panic phenomena

We propose to adopt a thermodynamically point of view of the panic that explains individual and collective behaviors with similar indicators based on entropy notion. Note that for video frames, entropy has been already introduced as the degree of randomness of both directions and displacements. Consequently, entropy can measure the disorder/randomness [10]. To continue in that sense, we will use an analogy with physical and traffic systems to give a better understanding of the individual and collective panic behaviors. The basic idea is to consider a crowd as a physical system and the individuals that constitute the group as the energy of this system. Note that a similar comparison has been already developed to study some traffic networks [12]. In this context, the density of the speed flow will play the role of the temperature. In

comparison with physical systems the maximal order is related to an uniform density whereas disorder and panic arise when the density becomes heterogeneous.

Physic	Energy	Temperature (homogenous for thermodynamical equilibrium when disorder is maximal)
Traffic	Vehicles	Occupation rate (homogenous for traffic equilibrium when order is maximal)
Crowd	Individuals	Speed flow density (homogenous for normal situations and heterogeneous when panic occurs)

Acknowledgment

The research for this work was supported, in part, by the PEPS MASPAN

.

References

[1]. Barakat M., Lefebvre D., Khalil M., Druaux F., Mustapha M., Parameter selection algorithm with self adaptive growing neural network classifier for diagnosis issues, *Int. J. Mach. Learn. & Cyber*. (JMLC), Vol. 4, pp. 217-233,Springer-Verlag, 2013.

[2]. Barsade, S. G., & Gibson, D. E. (1998). Group emotion: A view from top and bottom. In D. H. Gruenfeld, M. Neale, & E. Mannix (Eds.), *Research on managing groups and teams*, Vol. 1, pp. 81-102. Greenwich, CT: JAI Press.

[3]. Charney, D.S. (2004). Psychobiological mechanisms of resilience and vulnerability: Implications for successful adaptation to extreme stress. *American Journal of Psychiatry, 161,* 195-216.

[4]. Courty N. Allain P. Creusot C., Corpetti T., Using the AGORASET dataset: Assessing for the quality of crowd video analysismethods, Pattern Recognition Lett., http://dx.doi.org/10.1016/j.patrec.2014.01.004, 2014

[5]. Duchenne G., Mécanisme de la physionomie humaine, ou Analyse électro-physiologique de l'expression des passions applicable à la pratique des arts plastiques, Paris, 1862.

[6]. Fagette, A., Courty N. Racoceanu D. Dufour J.Y., Unsupervised dense crowd detection by multiscale texture analysis. *Pattern Recognition Lett*., 2013.

[7]. Fernández S., Jesús Manuel., & Murakami S., A comparison of two learning mechanisms for the automatic design of fuzzy diagnosis systems for rotating machinery. Applied Soft Computing, 4, 413–422, 2004.

[8]. Frijda, N. H. (1986). *The Emotions.* Cambridge: Cambridge University Press.

[9]. Fukunaga, K. Introduction to Statistical Pattern Recognition. Purdue University, Lafayette, IN, Academic Press, London, 1972.

[10]. Haidar Sharif, Chabane Djeraba, An entropy approach for abnormal activities detection in video streams, *Pattern Recognition* 45, 2543–2561, 2012.

[11]. Haykin. S., Neural Networks, A Comprehensive Foundation, 2nd ed. New York, NY: Macmillan, 1999.

[12]. Huide Zhou, Rachid Bouyekhf, Abdellah El Moudni. Modeling and entropy based control of urban transportation network. *Control Engineering Practice*, Vol. 21, Issue 10, pp. 1369-1376, 2013.

[13]. Jack, L.B., Nandi, A.K., Genetic algorithms for feature extraction in machine condition monitoring with vibration signals. IEE Proceedings of Vision & Image Signal Processing 147, 205–212, 2000.

[14]. Krausz B., Bauckhage C., Loveparade 2010: Automatic video analysis of a crowd disaster, *Computer Vision and Image Understanding* 116, 307–319, 2012

[15]. Leach, M.J.V., Sparks E.P, Robertson N.M, Contextual anomaly detection in crowded surveillance scenes. Pattern Recognition Lett.,, http://dx.doi.org/10.1016/j.patrec.2013.11.018, 2014.

[16]. Mustapha O, Khalil M., Hoblos G, Chafouk H., Lefebvre D., Fault detection algorithm using DCS method combined with filters bank derived from the wavelet transform, *International Journal of Innovative Computing, Information and Control ICIC*, ISSN 1313-1327, Vol. 5, no.5, 2009.

[17]. Nummenmaa L., Glerean E., Hari R., Hietanen J.K., Bodily maps of emotions, *Psychological and cognitive sciences*, *PNAS*, 2013.

[18]. Page, E. S. (1954). Continuous Inspection Schemes. *Biometrika*, Vol. 41(1/2), 100-115.

[19]. Roberts, S. W. (1959). Control Chart Tests Based on Geometric Moving Averages. *Technometrics*, 1(3), 239-250.

[20]. Saad A., Guerin F., Zaarour I., Ayache M., Lefebvre D., Sensoring and Features Extraction for the Detection of Freeze of Gait in Parkinson Disease, Proc. IEEE SSD, Barcelona, Spain, february 2014.

[21]. Saad A., Zeinedine A., Zaarour I., Ayache M., Guerin F., Lefebvre D., A preliminary study of the causality of freezing of gait for Parkinson's disease patients: Bayesian Belief Network approach, *IJCSI* Vol. 10, Issue 2, March 2013.

[22]. Samanta, B., & Al-Baulshi, K. R., Artificial neural network based fault diagnostics of rolling element bearings using time domain features. *Mechanical Systems and Signal Processing*, 17(2), 317–328, 2003.

[23]. Shewhart, W. A. (1925). The Application of Statistics as an Aid in Maintaining Quality of a Manufactured Product. *Journal of the American Statistical Association*, 20(152), 546-548.

[24]. Shiwakoti N. Sarvi M. Rose G. Burd M., Animal dynamics based approach for modeling pedestrian crowd egress under panic conditions, *Transportation Research Part B* 45, 1433–1449, 2011.

[25]. Shiwakoti N. Sarvi M., Understanding pedestrian crowd panic: a review on model organisms approach, *Journal of Transport Geography* 26, 12–17, 2013.

[26]. Verron S., Li J. et Tiplica T.. Fault detection and isolation of faults in a multivariate process with Bayesian network. *Journal of Process Control*, Vol. 20, Issue 8, Pages 902-911, September 2010.

[27]. Vicsek T., Zafeiris A., Collective motion, *Physics Reports* 517, 71–140, 2012.

[28]. Wasserman., Advanced Methods in Neural Computing, Van Nostrand Reinhold, New York, USA, 1995.

Proceedings of ICCSA 2014
Normandie University, Le Havre, France – June 23-26, 2014

URBAN EVENTS AND EMERGING PHENOMENA

B. Elissalde, F. Lucchini, L. Grassot and Y. Salamand[1]

Abstract. Starting from two examples of great free outdoor events ("Armada de Rouen" and "Braderie de Lille"), we aimed to capture the trends of change of urban life from mobile phone data, leading to test the hypothesis that self-organization phenomena are likely to emerge in the movements of the crowd within the different parts of a city. To tackle the issue of uncertainty and randomness, we conducted three types of calculations: formulation of indices, probabilistic calculations using chains of Markov, and simulation platform. Despite the various numbers of individual behaviors during the events, some unusual mobile phone uses can be selected, but they do not allow deducting an understanding of changes in the overall city life. The results of this experiment lead to the question in Geography of transition and feedbacks between the individual and the collective level.

Keywords. Mobile phone network, events, urban rhythms, emerging phenomena.

1 Introduction

This spatio-temporal analysis attempts to approach the phenomena of emergence in temporary urban situations such as those encountered in the context of major cultural and sporting events. These events are identifiable in time that fall within a specific urban space by introducing the existence of discontinuity in a time continuum of the city and variability in the intra- urban spatial attractiveness. Are questioned bothly the way we identify the traces of an event in a set of data, and the threshold (s) of space or time (s) from which emerging phenomena arise. In the specific case of two examples of great free outdoor events ("Armada de Rouen" and "Braderie de Lille"), it seeks to capture the trends of change of urban life from data that can provide a spatio-temporal sequencing rhythm, studying the phenomena of emergence from the behavior of mobile phones users. These behaviors are deployed in an urban environment with mobility constraints and availability, but including, at the time of events, a more or less strong accentuation of uncertainty on the move. The hypothesis that self-organization phenomena are likely to emerge in the movements of the crowd within the different parts of a city is one of our ways of working.

2 A global emerging model: cellphone calls punctuate urban rhythms

Starting from the sociological fact that the mobile phone has become a technological tool widely distributed in the population, it is assumed here that its use comes quite naturally in the professional and private lives of the inhabitants, thus reproducing relatively faithfully the rhythms of urban life [1], [6]. The outcome is that we can consider information from the mobile phone as a real descriptor of urban life.

In the case of events "Armada de Rouen" and "Braderie de Lille" data made from the past through the Orange operator calls appear from one day to the next, with a large effect number, a beautiful pattern in the daily rhythm of cell phone calls. Although potentially subject to strong variations, the number of calls of residents, who work on-site or passers remains relatively stable at the same days and times. Thus dealing with the day to day of neighborhood life those volumes are fairly predictable phenomenon if no new event changes the calendar. However, this overall order is upset by urban events including the ephemeral nature may, in some cases, change the functions or the perception of neighborhoods.

Questioned in terms of emergence, synthesis produced by the records of all Orange relay aerial detecting the call can be highly variable if other units of time were retained? Then secondary events appear in the main event: showers and thunderstorms, free rock concerts in evening for the Armada, fireworks, jogging, parade crew ... And by expanding the question, at what time interval the features of standardized daily rhythms of activity gives way to a stochastic configuration?

3 Complex systems and collective behavior revealing the complexity of urban space

[1] B. Elissalde, F. Lucchini, L. Grassot and Y. Salamand are with Department of Geography, Normandie University, Rouen, France. E-mails: bernard.elissalde@univ-rouen.fr, francoise.lucchini@univ-rouen.fr, l.grassot@gmail.com, yves.salamand@univ-rouen.fr

In the context of an unusual event as those involving big crowds, the uncertainty comes from the linking of data taking into account the time of day, depending on the area of the town, according to the status of the user (resident or visitor / tourist), according to the intensity of the use of mobile phones and mobility in urban space. We aim to demonstrate two combos of ideas. Initially the idea of M. Batty [2] that "*Behavior is not simply a product of intentions. It is as much a product of uncertainty*" is related to the multiplicity of individual attitudes, from the routine to the strategic ones. However, although agreeing that collective behavior generally does not adhere to everyday rules, some investigators emphasize the emergence of rules and patterns within the collectivity that are related to the group. Participants in collective behavior behave alike, not because of an established rule or of the force of authority, and not because as individuals they have the same attitudes, but because of a distinctive group process. They have some main behaviors, because of a distinctive group process. The issue is to detect these group processes.

4 Detecting group processes

To solve this dilemma, we conducted three types of calculations: formulation of indices, probabilistic calculations using chains of Markov, and simulation platform.

4.1 Formulation of indices

We calculated indices that measure the concentration of several categories of users of mobile, organized according to their nationality, the intensity of their phone use, and according to their degree of mobility in the city. These indices (all built by the same method) measures the ratio between the share of this category in a given location (eg the French in the city center) and in a given time with respect to all of this category throughout the city, first ratio is then compared to the weight of this place in the total registrations for the entire city. These indices therefore reflect both the weight of each category of users, but they also take into account the weight of each place in a given category.

Indices are well aware of the phenomena of over-or under-spatial concentration by hours and in different locations [3]. The contrast is striking between the under-representation of metropolitan on the docks, in comparison with the number of subscribers in the city and the other over-representation of foreign clients on the docks and in the city center. Thus draw between urban practices ubiquity of the inhabitants of the urban area tropism docks and town center for foreign visitors.

4.2 Probabilistic calculations using Markov chains

We performed calculations using Markov chains [7], that is to say the probability of occurrence of a particular category, under this schedule, according to that part of the urban space. Beyond the variability of urban occupation one day to another, our interest is focused on the issue of displacement of the intensity of urban activity by hours. From the perspective of urban space, if we change our look from the level of spatial information of the entity "whole city" to an entity consists of one of the neighborhoods, we observed that the rhythm changes, and this new rhythm is not a reduced representation of the main figure.

About the "Armada de Rouen", the results allow for their simplicity to make some simple observations and propose a line of work. They suggest the idea of certain constancy in the amount of people that are on the docks beyond an hour, as it is during the first hour of attendance that the decrease is the strongest. The same applies to those who leave the docks to the city center, the flow does not occur in the same way as time slots observed.

Putting themselves in the perspective of Markov, we can calculate an average probability of duration of stay or exit from the dock area (for some days and all days of the event). It would obviously be interesting from there to find deviations from the mean probability in order to highlight situations of "abnormality" which appear according to certain time steps.

Which areas will stand out from the general pattern if these general time frames are crossed with cutting agglomeration in multiple areas? From thence we deduce the question of the possible specificity of the area where the events take place. The data provided by the mobile phone could they identify a specific urban rhythm-driven event of mass phenomena stations in a zone and inter-zone transfers?

4.3 Platform of simulation for urban events

We are elaborating a simulation platform available to highlight the appearance of stochastic disturbances by urban events. Do mobile phone user practices present in Rouen during the Armada allow identifying specific patterns of behavior in the public space? It appears from the records of telephone events as the direct link between the general phenomena and individual behavior keeps a light opacity. Indeed it appears that the moments and the degree of variation of telephone activity taking any rhythmic regularity, if not to say that non-European persons rather communicate during the night (or festive practices jetlag?). Whatever the angle of vision adopted, even if the overall level has a retroactive impact on individual behavior, it appears that the observation of in-

dividual mechanisms of the system (ie here the behavior of groups of users of mobile telephony) allows not deduct an understanding of its overall behavior.

The results of this experiment in Geography ask the question of transition and feedbacks between the individual and the collective level. More generally, the rhythms of the city, the variable intensity of urban life, and more generally the spatio-temporal approach uses the city, are a challenge for urban studies [5], [6]. We propose to break with a static approach to urban space, from data that come as close as pulsations of the city.

Acknowledgment

In the context of the Institute of Complex Systems of Normandy, the research for this work was supported, in part, by the Region of Haute Normandie, by the Orange company and by ERDF RISC project.

.

References

[1] Aguiton C., Cardon D., Smoreda Z., 2009, « Living Maps ». *Proceedings of the First international Forum of application and Management of Personal Electronic Information*, MIT, Cambridge, MA, US.

[2] M. Batty**,** Agent-Based Pedestrian Modelling, CASA, Working papers series Paper 61 - Jan 2003

[3] Crang M ., 2001, « Rhythms of the city ». May J., Thrift N., 2001, *Timespace, Geographies of Temporality*, London, Routledge.

[4] Elissalde B., Lucchini F., Freire-Diaz S., 2011, Mesurer la ville éphémère. *Données Urbaines*, 6, Pumain D., Mattei M-F. (eds), Anthropos, Economica, 105-122.

[5] Lucchini F., Elissalde B., Freiré-Diaz S., 2013, Caractériser l'attractivité des quartiers urbains par les données de la téléphonie mobile. *Information Géographique*, 1, 2013, 44-62.

[6] Ratti C., Sevtsuk, Huang, Pailer, 2005, « Mobile Landscapes: Graz in Real Time ». *Proceedings of the 3rd Symposium on LBS & TeleCartography*

[7] Xin Lu, Erik Wetter Nita Bharti, Andrew J. Tatem7& Linus Bengtsson, "Approaching the Limit of Predictability in Human Mobility », Nature.com SCIENTIFIC REPORTS| 3 : 2923 | DOI: 10.1038/srep02923

General Session 3
Networks and Complex Systems

Proceedings of ICCSA 2014
Normandie University, Le Havre, France - June 23-26, 2014

LEVERAGING SUCCESS FACTORS OF SOFTWARE PROJECTS: SCRUM IS A COMPLEX SYSTEM

Pierre Parrend, Pierre Collet *†‡

Abstract. Agility for IT project management, especially the SCRUM framework, lays on a systemic approach to management. We strongly believe that a thorough understanding of complex system concepts behind SCRUM will highlight success factors, thereby empowering practitioners with a comprehensive framework for leading their projects to full achievement. We depict how SCRUM embodies a cognitive loop typical of complex systems, and how the framework complies with the properties of complex systems: non-reversibility; the 3 rules of preservation, evolution, control; multi-scale. Two empirical experiments underline the correlation between these properties and the actual efficiency of project management. One bases on a series of software development projects, which are analyzed a posteriori; the second one bases on a controlled experiment implying 8 parallel student groups working on the same development project.

Keywords. Information and communication technologies; software project organisation; agility; SCRUM; success factor; empirical studies.

*Pierre Parrend is with ECAM Strasbourg-Europe, Schiltigheim, France, as well as with ICube Laboratory, Strasbourg University, France; ECCE, CS-DC UNESCO UniTwin. Email: pierre.parrend@ecam-strasbourg.eu

†Pierre Collet is with ICube Laboratory, Strasbourg University, France; ECCE, CS-DC UNESCO UniTwin. Email: pierre.collet@unistra.fr

‡Manuscript received March 27, 2014

Proceedings of ICCSA 2014
Normandie University, Le Havre, France - June 23-26, 2014

DETECTING THE SOURCE OF CHAOS IN AN INTERACTION NETWORK

Haifa Rabai, Rodolphe Charrier and Cyrille Bertelle *

Abstract.

We study the spread of chaos generated by one node in an interaction network modeled by a Coupled Map Network (CMN). This graph is formed by nodes characterized by a measurable state variable that may exhibit chaotic time series. The interaction is modeled by a coupling process that may propagate the node states in the network.

We aim to study how to identify how to detect the set of nodes becoming disturbed by the spread of chaos in the graph as well as the node which is the source of this propagation.

In this paper, we propose to use some measures to quantify the dynamic complexity of the nodes in order to identify the group of chaotic nodes and to detect the chaotic influence of the source of the spread of chaos in the graph. We show by some simulations on random graphs that the Shannon entropy computed on the close returns plots enables to detect chaotic series from a node. The extension of close returns plots to joint recurrence plots enables to identify the source chaos in the graph.

Keywords. Interaction network, Coupled Map Networks, Close returns plots, Chaos, Shannon entropy.

1 Introduction

Coupled Map Network[7] is a dynamic system composed of many interacting nonlinear elements coupled in a way that leads them to share information about each other's state. This coupling process can propagate the node states in the network leading to a synchronization phenomenon which is defined as a correlation among time series.

Our research work is part of this context. We are interested in studying the spread of one chaotic state in an interaction network whose structure is unknown. Each node of this interaction network has a dynamic measurable state variable that may exhibit potentially chaotic time series. The arcs of this graph define the interaction between nodes that is modeled by coupling in the Coupled Map Network.

We assume that at a given time t, one node can have a chaotic internal state that can spread in the network through interaction leading to disturbing the behavior of other nodes that may become chaotic in their turn.

We aim to detect the set of nodes impacted by the spread of chaos and to identify the node which is the source of the disturbance in the interaction network.

We propose then to use respectively the Shannon entropy and the mean conditional probabilities of recurrence proposed by Kurths et al. [6] to quantify the dynamic complexity of the nodes and to identify the origin of the spread of chaos in the graph.

The paper is organized as follows. First, we give the model for our Coupled Map Network. After that, we present the Shannon entropy computed on the close returns plots and we give an overview of the mean conditional probabilities of recurrence computed on the joint recurrence plots. The last section presents our simulations and the results obtained for each measure. Finally, we summarize the main ideas presented in this paper and present some perspectives.

2 Coupled Map networks

Coupled Map Network (CMN) [1] is a dynamic system with a discrete time step and continuous states space. The dynamic nodes of the model are distributed in space and interact with each other by coupling. As a result of interacting dynamic elements, we can observe in the CMN an interesting synchronized behavior [3].

To obtain a chaotic state variable, we use the logistic map [4]. This nonlinear application enables to define the state variable of the nodes thanks to its control parameter and to couple many state variables.

A node's state x generated by this nonlinear application is given by:

$$x^{t+1} = f(x^t, a) = 4\ a\ x^t(1 - x^t) \tag{1}$$

where a is the control parameter of this application and t is the time step. When a is equal to 1, we have a "chaotic state". On the other hand, when this parameter is inferior to about 0.89, we only have periodic or fixed point behaviors. The dynamics for the nodes are given by the following global equation:

$$X^{t+1} = ((1 - \epsilon)I + \epsilon CG)F(X^t) \tag{2}$$

*Haifa Rabai,Rodolphe Charrier and Cyrille Bertelle are with Department of Computer Sciences, Universit du Havre, France. E-mails: haifa.rabai@univ-lehavre.fr, rodolphe.charrier.rabai@univ-lehavre.fr, cyrille.bertelle@univ-lehavre.fr

where X is the vector of dynamical variables of all nodes, ϵ is the coupling parameter, it also may be a matrix if each node has its own interaction strength. I is the identity matrix, $F(X) = [f(x_1^t), f(x_2^t), ..., f(x_n^t)]^T$ the nonlinear function applied to each node state and G the adjacency matrix with elements taking value 1 if node X_l interacts with node X_k and 0 otherwise. C is a diagonal matrix that represents the coupling between one node and the other nodes.
In the following, we present the measures selected to identify the chaotic nodes and the source of the spread of chaos.

3 Detecting chaotic nodes

In order to characterize the dynamical properties of the nodes time series, we propose to use the Shannon entropy computed on the close returns plots [2].
Close returns plot is an array matrix $N \times N$ that is build as follows. Let x_k be the time series of a given node X_k and N is the number of samples needed to build the close returns plots.
The principle consists in comparing this time series at each time step i to itself with a delay j. It is noted that for the sake of clarity, the time step will be denoted i to fit the matrix notation below.

$$R_{X_k}(i,j) = \theta(\left\| x_k^i - x_k^{i+j} \right\| - \delta_k) \tag{3}$$

where $\theta(x_i)$ is the Heaviside function.
If the difference is less than a certain threshold δ_k, they are considered as recurrent and represented by 1 in the matrix. Otherwise, they are said to be non-recurrent and 0 is placed at (i,j). It is given by:

$$S = -\sum_{n=1}^{H} P_n log(P_n) \tag{4}$$

where P_n is the probability to observe non-recurrent segments in a close return plot, that is the number of non-recurrent horizontal segments with length $n > 0$ divided by the total number of non-recurrent segments [5]. H is the longest sequence of recurrent elements.

4 Detecting the source of chaos

In order to detect the interactions between the chaotic nodes, we propose to use a method based on the recurrence properties and developed by Kurths et al. This method aims to infer coupling directions between dynamical systems based on their recurrence properties. It hinges on the recurrence plots and their extension to joint recurrence plots.
The second step consists in computing the joint recurrence plots between each couple of nodes X_l and X_k which gives the following matrix:

$$JR_{X_l X_k}(i,j) = R_{X_k}(i,j) \times R_{X_l}(i,j) \tag{5}$$

The next step consists in computing the mean conditional probabilities of recurrence (MCR) between a couple of chaotic nodes. This measure is defined as follows:

$$\text{MCR}(X_l|X_k) = \frac{1}{N}\sum_{j=1}^{N} p(\mathbf{x_l^j}|\mathbf{x_k^j}) \tag{6}$$

$$= \frac{1}{N}\sum_{j=1}^{N} \frac{\sum_{i=1}^{N} JR_{X_k,X_l}(i,j)}{\sum_{i=1}^{N} R_{X_k}(i,j)} \tag{7}$$

where $p(\mathbf{x_l^j}|\mathbf{x_k^j})$ estimates the probability that the trajectory of X_l recurs to the neighborhood of x_l^j under the condition that the trajectory of X_k recurs to the neighborhood of x_k^j.
If X_k drives X_l, we have $MCR(X_l|X_k) < MCR(X_k|X_l)$ and we write $\Delta MCR(X_l|X_k) = MCR(X_l|X_k) - MCR(X_k|X_l)$. The process of finding the source of chaos in the interaction network is described as follows.

1. Choose an initial node among the chaotic nodes.
2. Search the lowest MCR between this node and all the other chaotic nodes.
3. This MCR gives us the next node to be processed. Return by starting from this node to step 2.
4. The previous loop ends when we come back to a node already visited: this node is considered as the source of chaos spread.

5 Simulations

In order to evaluate the efficiency of the measures presented previously, we simulated a random graph formed by 50 nodes with only one chaotic node chosen randomly. We used our CMN to generate the interaction network and obtained then a directed and dynamic graph.
To generate the time series of the chaotic node, we set the value of the parameter a to 1. On the other hand, we initialized the control parameter of the other nodes with random values between 0 and 0.89.
Figure 1 below shows an example of a coupled map network formed by 50 nodes. The source of chaos that we aim to identify in the interaction network is colored in green. The red nodes are those that we expect to be influenced by the spread of chaos as they are directly and indirectly related to the chaotic node.

5.1 Results

We computed the Shannon entropy related to each node. The values obtained are either positive or equal to zero.

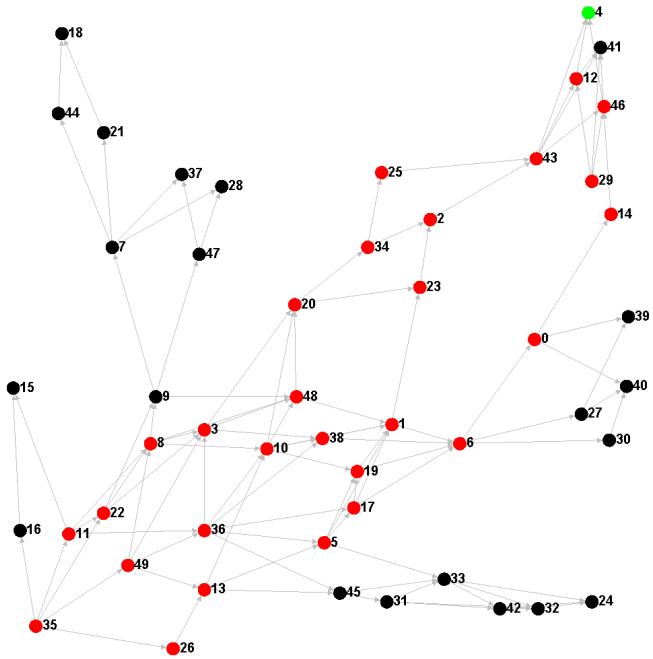

Figure 1: Coupled map network formed by 50 nodes having identifiers from 0 to 49. The green node is the source of the spread of chaos. The red nodes are those who are expected to be influenced by the propagation of chaos in the interaction network.

The nodes that have a positive Shannon entropy, are those who have chaotic time series and thus are impacted by the spread of chaos.
With regard to the origin of chaos spread, we computed the recurrence rates related to the nodes identified as chaotic by the Shannon entropy. The increase of the coupling parameter leads to a decrease of the nodes recurrence rate. This phenomenon is explained by the increase of the non-recurrent points due to the appearance of chaotic time series. Therefore, we don't expect to have necessarily the same inequality of the mean conditional probabilities of recurrence between the driver and the response as proposed by Kurths et al. Rather, this inequality is based on the difference between the recurrence rate of the driver and the response. Suppose X_k is the driver and X_l is the response, we may have $RR^{X_k} < RR^{X_l}$ and therefore, $MCR(X_k|X_l) < MCR(X_l|X_k)$.
We computed the mean conditional probabilities of recurrence between every couple of chaotic nodes. Following the algorithm presented previously, if we consider any node in the set of chaotic nodes, we can trace a set of paths that lead to the source of chaos.

5.2 Discussion

The use of the Shannon entropy has been successful in detecting the chaotic nodes. However, this measure is insufficient to quantify how the nodes are impacted by the spread of chaos in the network. The mean conditional probability of recurrence computed on the joint recurrence plots enables to deal with this issue. In fact, computing this measure depends partly on the recurrence rate of the nodes which indicates the effect of the spread of chaos on the nodes dynamics. Thus, the nodes who are more impacted by the spread of chaos, has a smaller recurrence rate.
Based on this inequality, we succeeded in tracing paths that lead to the source of chaos.

6 Conclusion

In this paper, we presented our research work which consists in studying the spread of one chaotic state in an interaction network as a result of the interaction between the nodes. We used the Shannon entropy computed on the close returns plots as a measure for detecting the sub group of chaotic nodes in the graph. The chaotic influence between this set of chaotic nodes is detected by the mean conditional probability of recurrence computed on the joint recurrence plots. This measure was successful in inferring the chaotic influence directions between nodes. By comparing the mean conditional probabilities related to each couple of chaotic nodes, we were able to identify the source of the disturbance in the network.

References

[1] J. Koiller and L.-S. Young. Coupled map networks. *Nonlinearity*, 23(5):1121, 2010.

[2] G. B. Mindlin and R. Gilmore. Topological analysis and synthesis of chaotic time series. *Phys. D*, 58(1-4):229–242, Sept. 1992.

[3] L. M. Pecora, T. L. Carroll, G. A. Johnson, D. J. Mar, and J. F. Heagy. Fundamentals of synchronization in chaotic systems, concepts, and applications. *Chaos: An Interdisciplinary Journal of Nonlinear Science*, 7(4):520–543, 1997.

[4] S. C. Phatak and S. S. Rao. Logistic map: A possible random-number generator. *Phys. Rev. E*, 51:3670–3678, Apr 1995.

[5] H. Rabarimanantsoa, L. Achour, C. Letellier, a. Cuvelier, and J.-F. Muir. Recurrence plots and Shannon entropy for a dynamical analysis of asynchronisms in noninvasive mechanical ventilation. *Chaos (Woodbury, N.Y.)*, 17(1):013115, Mar. 2007.

[6] M. C. Romano, M. Thiel, J. Kurths, and C. Grebogi. Estimation of the direction of the coupling by conditional probabilities of recurrence. *Phys. Rev. E*, 76(3):036211, 2007.

[7] T. Shibata and K. Kaneko. Coupled map gas: structure formation and dynamics of interacting motile elements with internal dynamics. *Physica D: Nonlinear Phenomena*, 181(3-4):197–214, July 2003.

Proceedings of ICCSA 2014
Normandie University, Le Havre, France – June 23-26, 2014

Estimation of Total Sediment Load Transport into Madani Dam Reservoir

Kiyoumars Roushangar, Saeid Sadaghian[1][2]

Abstract. Although accurate sediment load prediction is very important in planning, designing, operating and maintenance of water resources structures but the modelsmechanism is complex, and the deterministic transport models are based on simplifying assumptions often lead to large prediction errors. In this research, firstly, two intelligent ANN methods, Radial Basis and General Regression Neural Networks, are adopted to model of total sediment load transport into Madani dam reservoir (north of Iran) using the measured data and then applicability of the sediment transport methods developed by Engelund and Hansen, Ackers and White, Yang, and Toffaleti for predicting of sediment load discharge are evaluated. Based on comparison of the results, it is found that the GRNN model gives better estimates than the sediment rating curve and mentioned classic methods.

Keywords: Sediment transport, Dam reservoir, RBF, GRNN, Prediction

1 INTRODUCTION

An estimate of sediment transport rates in alluvial rivers is important in the context of erosion, sedimentation, flood control, long-term morphological assessment, etc. Extensive research during the last decades has produced a plethora of sediment transport models. Unfortunately, the predictive accuracy of these models is often questionable, and in many practical situations prediction errors of these models are observed to be unacceptably high.

The adequacy of these models has been critically examined and reported (see [1 to 5]) From these studies it can be concluded that sediment transport is an immensely complex process, and expressing it through a deterministic mathematical framework may not be possible. The approach of artificial neural networks are universal approximators and have the advantages of using field recorded data directly without simplification and is not like regression analysis, which needs to make an assumption of equation in advance. ANNs provide an analytical alternative to conventional techniques, which are often limited by strict assumptions of normality, linearity, variable independence, etc. The neural networks approach has been applied to many branches of engineering sciences.

This approach is becoming a valuable tool for providing civil and hydraulic (river) engineers with sufficient details for design purposes and river-management practices. ANNs have also provided promising results in the field of hydrology and water resources such as stream flow prediction (see [6, 7]), rainfall-runoff modeling (see [8, 9]), and energy dissipater structures (see [10]

The main purpose of this study is the prediction of sediment discharge into Madani dam reservoir located in Ajichai River (in the northwest part of Iran as the case study area) and comparison between rating curve, total-load transport equations and ANN intelligent approaches.

2 Study area: Madani (Vanyar) Dam of Tabriz (IRAN)

Ajichay River is the longest river in the state of eastern Azerbayjan of Iran. The Ajichay River basin is approximately 13700 km2 and is situated in the eastern part of the Lake Urmieh in the north west of Iran. This river originates from the southern foothills of Sabalan Mountain and after joining the various branches from Bozgoosh, Ghooshedagh, Kasbe and northern foothills of Sahand and passing Sarab Planes and Tabriz, joins Urmieh Lake in 90 km from Tabriz. Madani dam was constructed near Tabriz city and old vanyar station is located in entrance of reservoir of Madani dam (10km from dam structure).

[1] Faculty of Civil Eng., University of Tabriz, Iran. E-mail: roshangari@tabrizu.ac.ir

[2] M.S student,Azad University of Ahar,Ahar,Iran. E-mail: sadaghiansaeid@yahoo.com

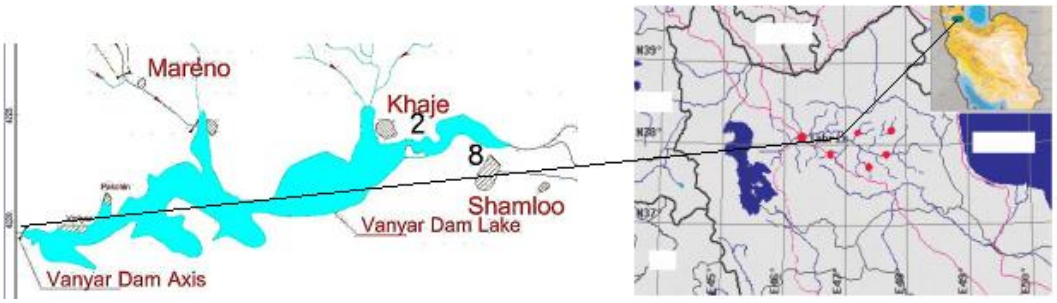

Figure1. Study area

The data set used in this study was obtained from Iran water resource organization from 1970 to 2008 and consist of monthly sediment concentration, water discharge and flow depth at gauging station (Vanyar station) in entrance of reservoir of Madani dam (See Fig1.) located on the Ajichay River. These data were divided into two partitions, i.e. one for training and the other for testing.

3 ANN

3.1 Generalized Regression Neural Networks

A Generalized Regression Neural Networks (GRNN) is a variation of the Radial Basis Neural Networks, which is based on kernel regression networks (see [11]). A GRNN doesn't require an iterative training procedure as back propagation networks. A GRNN consists of four layers: input layer, pattern layer, summation layer and output layer as shown in Fig. 2.The number of input units in input layer depends on the total number of the observation parameters. The first layer is connected to the pattern layer and in this layer each neuron presents a training pattern and its output. The pattern layer is connected to the summation layer. The summation layer has two different types of summation, which are a single division unit and summation units. The summation and output layer together perform a normalization of output set. In training of network, radial basis and linear activation functions are used in hidden and output layers. Each pattern layer unit is connected to the two neurons in the summation layer, S and D summation neurons.

S-summation neuron computes the sum of weighted responses of the pattern layer. On the other hand, D summation neuron is used to calculate unweight outputs of pattern neurons.

The output layer merely divides the output of each S-summation neuron that of each D-summation neuron, yielding the predicted value to an unknown input vector x as

$$Y_i^{'} = \frac{\sum_{i=1}^{n} y_i \exp[-D(x, x_i)]}{\sum_{i=1}^{n} \exp[-D(x, x_i)]} \qquad (1)$$

$$D(x, x_i) = \sum_{k=1}^{m} \left(\frac{x - x_{ik}}{\sigma}\right)^2 \qquad (2)$$

Yi is the weight connection between the *i*th neuron in the pattern layer and the Summation neuron, *n* is the number of the training patterns, *D* is the Gaussian function, *m* is the number of elements of an input vector, x_k and x_{ik} are the *j*th element of *x* and *xi*, respectively, σ is the spread parameter, whose optimal value is determined experimentally.

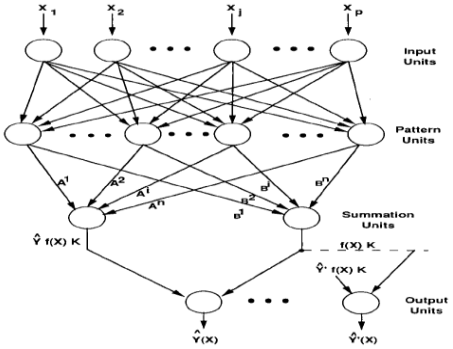

Figure 2. The GRNN structure

3.2 Radial basis network (RBF)

The RBF network is similar in topology to the MLP network (see [12]). Fig. 3 shows a schematic diagram of a general RBF network with *N*, *L*, and *M* nodes in the input, hidden and output layers, respectively. It shows the N-dimensional input patterns [*X*] is being mapped to *M*-dimensional outputs [*Z*], with nodes in the adjacent layers exhaustively connected. The nodes in the hidden layer are each specified by a transfer function *f*, which transforms the incoming signals. For the *j*th input pattern X_{Jp} , the response of the *j*th hidden node Y_j is of the form:

$$y_j = f\{\frac{\left\|X^p - U_j\right\| u_*^n}{2\sigma_j^2}\} \qquad (3)$$

Where ||.|| is the Euclidian norm; *Uj* the center of the *j*th radial basis function *f*; and *S* the spread of the RBF that is indicative of the radial basis from the RBF center within which the function value is significantly different from zero. The network output is given by a linear weighted summation of the hidden node responses at each node in the output layer. The output for *k*th node on the output layer Z_{pk} is computed as

$$Z_p k = \sum_{j=1}^{L} y_j w_{kj} \qquad (4)$$

Where w_{kj} is the weight connection between hidden and output nodes. From several possible radial basis functions,the most common choice is the Gaussian. The Gaussian RBF center of the *j*th hidden node can be specified by the mean U_j and the deviation s_j. Training an RBF involves two stages: (1) determining the basis functions on the hidden layer nodes and (2) the output layer weights. Fitting the RBF function involves finding suitable RBF centers and spreads. A variety of techniques have been evolved to optimize the number of RBF centers. The present study employed the minimum description length algorithm (Leonardis and Bischof, 1998) to optimize the parameters of the RBF networks.

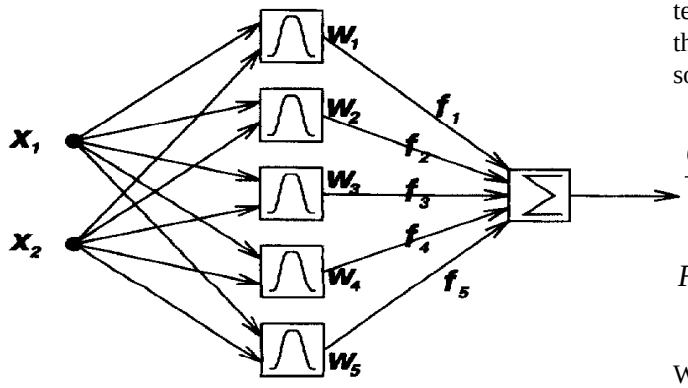

Figure 3. The RBNN structure

4 SEDIMENT TRANSPORT

A large number of sediment transport equations have been developed by investigators using different approaches to investigate sediment transport functions or formulas. The transportation of sediment particles is governed by several interrelated parameters that contribute to the complexity of the phenomena, and it is often subject to semi empirical or empirical treatments because theoretical studies can only be performed in simplified cases. Therefore, sediment transport is primarily studied through laboratory measurements. However, because laboratory conditions are controlled (i.e., certain parameters are kept constant and are not necessarily similar to natural channels), the derived equations, obtained from different approaches when tested on field data, may predict values for the total sediment concentration that are drastically different from each other and from the measured datasets in natural channels

4.1 REVIEW OF SEDIMENT TRANSPORT MODELS

The rate of sediment transport in rivers depends on many variables such as water discharge, average flow depth, flow velocity, energy slope, shear stress, stream power, particle size and gradation as well as temperature. It is very difficult to simultaneously incorporate all these variables and to develop one sediment transport function. A number of such transport functions has been put forward and details can be found in the literature. In the following, the four equations tested (in this study) are briefly presented.

Ackers &White equation. Ackers & White (see [13]) applied the advantages of dimensional analysis technique, but used the physical arguments to express the mobility and transport rate of sediment in terms of some dimensionless parameters.

$$\frac{Q_t}{Q} = C\frac{D_m}{R}\left(\frac{V}{u_*}\right)^n\left(\frac{F_{1g}}{A} - 1\right)^m \qquad (5)$$

$$F_{gr} = \frac{u_*^n}{\sqrt{[gD_m(\rho_s/\rho - 1)]}}\left[\frac{V}{\sqrt{32Log(10R/D_m)}}\right]^{1-n}$$

Where V = average flow velocity, *n*=sediment size–related transition exponent, *m*=sediment transport function exponent, $F1_g$= sediment mobility number, C= coefficient related to sediment size, u_* =shear velocity, *A*=initial motion parameter, ρ_s and ρ =sediment and water density, D_m= overall D_{50} =median diameter particle and R=hydraulic radius.

Toffaleti Formula. The procedure to determine bed-material discharge developed by Toffaleti (see [14])

is based on the concepts of Einstein (see [15]) with three modifications:

1. Velocity distribution in the vertical is obtained from an expression different from that used by Einstein;

2. Several of Einstein's correction factors are adjusted and combined; and Toffaleti defines his bed-material discharge as total river sand discharge, even though he defines the range of bed-size material from 0.062 to 16 mm.

$$q_T = \frac{0.6\, p_i}{\left(T_\tau A_1 K_4 / V^2\right)^{5/3} (D_{si}/0.0058)^{5/3}} \quad (6)$$

Where A_1 and K_4=tofalleti coefficient, P_i=fraction of total sediment, T_T= temperature coefficient, D_{si}=median diameter particle

Yang's Method. The theory of minimum rate of energy dissipation (see [16]) states that when a dynamic system reaches its equilibrium condition, its rate of energy dissipation is a minimum. The minimum value depends on the constraints applied to the system. Yang proposed a sediment transport formula based on the concept of unit stream power, which can be utilized for the prediction of total bed material concentration transported in sand bed flumes and rivers. The formula is as follows:

$$Log C_T = 6.681 - 0.63 Log \frac{\omega_s D_s}{\nu} - 4.816 Log \frac{u_*}{\omega s} + (2.784 - 0.305 Log \frac{\omega_s D_s}{\nu} - 0.282 Log \frac{u_*}{\omega_s}) Log\left(\frac{VS}{\omega_s} - \frac{V_c S}{\omega_s}\right) \quad (7)$$

Where C_T= concentration ppm, D_{si}=median diameter particle, ω_S=fall velocity, and s= energy slope.

Engelund and Hansen. Engelund-Hansen'(see [17]) equation is based on the shear stress approach. The equation can be written as:

$$q_t = 0.05 \gamma_s V^2 \sqrt{\frac{D_{50}}{g(G_s - 1)}} \left[\frac{\tau_0}{(\gamma_s - \gamma) D_{50}}\right]^{\frac{3}{2}} \quad (8)$$

Where τ_0 =flow shear stress, G_s =specific gravity and γ_s and γ = specific weights of sediment and water, respectively

Regression approach. A Sediment Rating Curve (SRC) describes a unique functional relationship between sediment yield and discharge; therefore, it is obtained as a smooth and continuous curve with reasonable degree of sensitivity. The sediment yield–discharge relation used in the standard SRC is represented by the equation of the form

$Q_s = a Q_w^{\,b}$ (9)

Where Q_S is suspended sediment discharge, Q_W is flow discharge, and a and b are the coefficients determined by regression analysis.

5 Models application and Results

The parameters governing sediment transport process can be described by:

$$Q_S = f(Y, Q, V, R, D_{50}) \quad (10)$$

Where Q_S=total transport load, V=average velocity, Q=flow discharge, Y=flow depth, R=hydraulic radius, and D50= mean diameter of bed particles.

Nondimensional hydraulic parameters governing sediment transport process can be described by:

$$Fr = \frac{V}{\sqrt{gY}} \text{ =Froude number,} \quad (11)$$

$$S_f = \frac{n^2 V^2}{R^{4/3}} \quad (12)$$

$$\mathrm{Re} = \frac{\rho V Y}{\mu} \text{ =Reynolds number,} \quad (13)$$

Where S_f=energy slope. n=Manning's roughness coefficient. S=bed slope. μ = dynamic viscosity

One of the most important steps in developing a satisfactory forecasting model is the selection of the input variables. Because, these variables determine the structure of the ANN model and influence the weighted coefficient and the results of the model. The structures of models for predicting of sediment transport in Ajichai River showed in Tables 2. The whole data set was divided into two parts randomly: a training set consisting of 70% data points and a validation or testing set consisting of 30% data points. Before applying the ANN to the data, the training input and output values are normalized using the equation

$$X' = 0.05 + 0.95 \frac{X - X_{\min}}{X_{\max} - X_{\min}} \quad (14)$$

Where X' is the normalized value of variable i, X is the original value, and X_{max} and X_{min} are the maximum and minimum of variable i, respectively.

Multi-layer ANN can have more than one hidden layer; however theoretical works have shown that a single hidden layer is sufficient for ANNs to

Table1. The structure of sediment transport models

Model output	Number	Input	Number of records
Qs	1	$(Q)_t$	931
Qs	2	$(Q,Fr)_t$	931
Qs	3	$(Q,Re,)_t$	931
Qs	4	$(Q,R/D_{50},)_t$	931
Qs	5	$(Q,Re,R/D_{50},Fr)_t$	931
Qs	6	$(Q,Re,S_f)_t$	931

approximate any complex nonlinear function. Therefore, in this study, one hidden layered ANN is used. A difficult task with ANNs involves choosing parameters such as the number of hidden nodes and the learning rate. Determining an appropriate architecture of a neural network for a particular problem is an important issue, since the network topology directly affects its computational complexity and its generalization capability. The performance of all ANN configurations was assessed based on three error measures namely, correlation coefficient, R, which presents the degree of association between predicted and true values; root mean square error, RMSE, which is preferred in many iterative prediction, optimization schemes; and mean absolute error, MAE, which is a parameter commonly understood in engineering applications, and mean absolute relative error, MARE, Expressions for these measures are given as follows.

$$RMSE = \sqrt{[\sum_{i=1}^{N} \frac{(Qs_M - \overline{Q}s_p)}{N}^2}$$

$$R = \frac{\sum_{i=1}^{N} (Qs_M - \overline{Q}s_M).(Qs_p - \overline{Q}s_p)}{\sqrt{\sum_{i=1}^{N} (Qs_M - \overline{Q}s_M)^2 \ (Qs_p - \overline{Q}s_p)^2}}$$

$$RMSE = \sqrt{[\sum_{i=1}^{N} \frac{(Qs_M - \overline{Q}s_p)}{N}^2}$$

$$MAE = \frac{1}{N} \sum_{i=1}^{N} |Qs_M - Qs_p|$$

$$MARE = \frac{1}{N} \sum_{i=1}^{N} \left| \frac{(Qs_M - Qs_p}{Qs_M} \right| \times 100$$

Where, Qs_p is the predicted total load, Qs_m is the observed sediment discharge, Qs_m is the average of the predicted total load, Qs_p is the average of the observed total load records and N is the total number of events considered. Here, the hidden layer node numbers of each model are determined after trying various network structures since there is no theory yet to tell how many hidden units are needed to approximate any given function. The optimal architecture was determined by varying the number of hidden neurons (from 2 to 12), and the best structure was selected. The tangent sigmoid and pure linear functions are found appropriate for the hidden and output node activation functions, respectively. The training of the ANN models was stopped when either the acceptable level of error was achieved or when the number of iterations exceeded a prescribed maximum of 2000.

The learning rate of 0.04 was also used. In the RBF and GRNN models, the center selection process found an appropriate tolerance value of 0 and the radial basis spread of 1.

Comparing between ANN, sediment rating curve and classic methods are shown by Table 2.According to this Table, best results were obtained by model(3) and GRNN performance (Test: MARE=22.83%, R=0.90). The input layer consisted of (*Q, Re, Sf)* whereas the output layer node corresponded to the unique total sediment load. Sediment rating curve and plot of observed and predicted total load using GRNN model are showed in Fig4 to Fig6. The total sediment loads simulated by GRNN and the RBF are reported in Table 2.

It can be seen from this table that the RBF performances is unsatisfactory in prediction of total sediment load in comparison with the GRNN model. The GRNN model has smaller RMSE, MAE and MARE values than the RBF model. Also, among the R values of the models, GRNN has the highest. In Table 2 the accuracy of the GRNN and RBF models are compared to that of the models of Ackers and White, Yang, Engelund and Hansen, Toffaleti and sediment rating curve. It can be seen that the accuracy of the ANN models are higher than that of the existing models. For the ANN model the RMSE, MAE and MARE are low and the coefficient of correlation (R) is high. It shows that the Ackers and White approach is more accurate than other equations and sediment rating curve for estimating total sediment transport in rivers compared in this study. As a result, the results of training and testing of models demonstrate that GRNN method is superior to other models in forecasting of total sediment load.

Table2. Comparing between ANN, sediment rating curve and classic methods

Model	Training				Testing			
	MARE (%)	RMSE	MAE	R	MARE (%)	RMSE	MAE	R
GRNN	8.72	0.0015	0.0065	0.99	22.83	0.1004	0.0408	0.90
RBF	9.30	0.00104	0.0060	0.99	35.4	0.0883	0.0403	0.81
SRC	-	-	-	-	70.38	0.2043	0.0875	0.70
Ackers & White Formula	-	-	-	-	49.2	0.1201	0.0560	0.70
Yang Formula	-	-	-	-	56.103	0.1269	0.0689	0.61
Toffaleti Formula	-	-	-	-	71.36	0.1445	0.0705	0.45
Engelund – Hunsen Formula	-	-	-	-	91.36	0.1568	0.0920	0.30

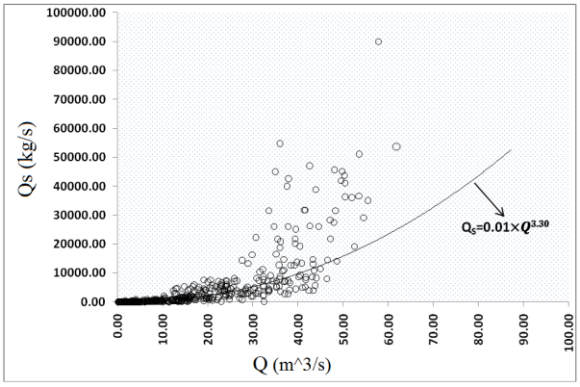

Figure4. Sediment rating curve

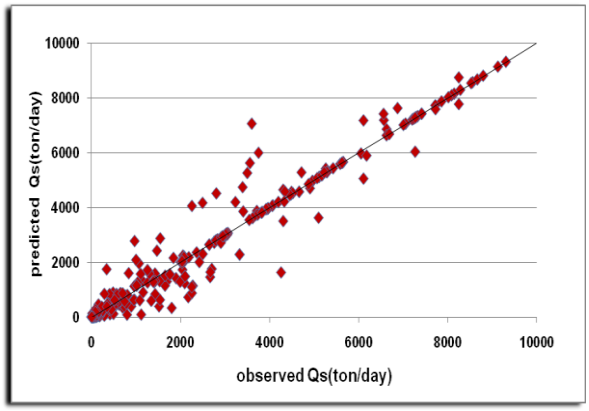

Figure 5. Plot of observed and predicted total load using GRNN model

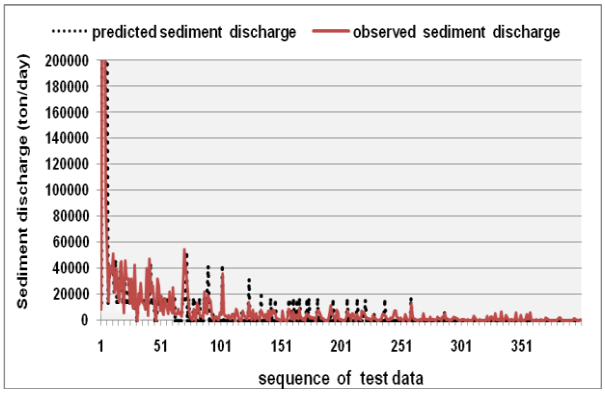

Figure 6. Plot of observed and predicted total load using GRNN model

Moreover, it is said that GRNN method can be successfully applied for total sediment load forecasting according to performance criteria.

In summary, the GRNN model trained using three important parameters (Q, Re, Sf) can be used to estimate total bed material load in lack of sediment data. However, it should be pointed out that the accuracy of an ANN model is data sensitive, and should not be applied to the conditions outside of the data range used in training the ANN model without verification. In other words, for other cases with data range out of this study, an appropriate ANN should be trained using data set of that case study to estimate total sediment load.

6 Conclusions

In this research, for predicting of sediment discharge input to reservoir of Madani dam, in one hand sediment rating curve and classic methods are used and in other hand the applicability of data driven approaches like Radial Basis and General Regression Neural Networks are evaluated.

Models having various input variables were trained and tested for station before dam input. The performance of the GRNN and RBF models was compared to the rating curve sediment and Ackers and White, Yang, Engelund and Hansen, and Toffaleti methods. Results showed that, the GRNN

and RBF models performed better than the existing models. For the input parameters, GRNN model having (*Q, Re, Sf)* variables was selected as the best fit total load forecasting model according to criteria of performance evaluation. Results confirmed that, GRNN method is superior to other models in forecasting of total sediment load and Ackers and White approach is more accurate than other equations and sediment rating curve for estimating of total sediment transport input to Madani dam reservoir. Finally it should be noted that, the transport mechanism is complex, and the deterministic transport models are based on simplifying assumptions that often lead to large prediction errors. Artificial Intelligence techniques models go someway towards incorporating this additional unknown physics and thereby improve the predictive accuracy. However, due to the black-box nature of ANN models the learned relationship between the inputs and output is not revealed and can only be tested with a new instance. This requires cautious usage of the new model, and it should not be used beyond the ranges of the data for which it was trained.

References

[1] ASCE Task Committee, Sediment transportation Mechanics: "Sediment Discharge Formulas", Journal of Hydraulic Engineering, ASCE. 97(HY4) 523-567 , 1971

[2] M. S.Yalin, "Mechanics of Sediment Transport, 2nd edn. Pergamon Press, Oxford,1977.

[3] L. C. Van Rijn, "Sediment transport, Part I: Bed-load transport", J. Hydraul. Eng. 11010 1431–1456, 1984.

[4] L. C. Van Rijn, "Sediment transport". Part II: Suspended-load transport, J. Hydraul. Eng. 11011 1613–1641, 1984.

[5] K. Roushngar, Y. Hassanzadrh, A. Keynejad, M .T. Alami, V. Nourani, D. Mouaze, "Studying of flow model and bed load transport in a coarse bed river: case study – Aland River Iran", Journal of Hydroinformatics. 13 (4) 850–866, 2011.

[6] L.C. Chang, F.J. Chang, Y.M. Chiang, "A two-step-ahead recurrent neural network for stream-flow forecasting", Hydrological Processes. 18 81–92, 2004.

[7] L.C. Chang, F.J. Chang, "intelligent control for modeling of real-time reservoir operation". Hydrological Processes. 15 1621–1634, 2001.

[8] Lin G. Chen L., "A non-linear rainfall-runoff model using radial basis function network". Journal of Hydrology. 289 1–8,2004.

[9] A.S. Tokar, P.A. Johnson, "Rainfall runoff modeling using artificial neural network", Journal of Hydrologic Engineering. ASCE. 4(3) 232–239, 1999.

[10] K. Roushangar, S. Akhgar, F. Salmasi, J. Shiri, "Modeling energy dissipation over stepped spillways using machine learning approaches". Journal of Hydrology, 504, 254-265, 2014.

[11] H.K. Cigizoglu, O.,Kisi" Methods to improve the neural network performance in suspended sediment estimation", J. Hydrol. 312 221–238,2006

[12] D.A.K. Fernando, A.W. Jayawardena, "Runoff forecasting using RBF network with OLS algorithm", Journal of Hydraulic Engineering. 3 (3) 203–209, 1998.

[13] P. Ackers, W. R. White," Sediment transport: new approach and analysis". *Proc. ASCE* 99(11), 2041-2060, 1973.

[14] F. B. TOFFALETI, "A Procedure for Computation of the Total River Sand Discharge and Detailed Distribution, Bed to Surface." Committee on Channel Stabilization, U. S. Army Corps of Engineers Waterways Experiment Station, Vicksburg,Technical Report No. 5, 1968.

[15] H.A. Einstein, "The Bedload Function for Sediment Transport in Open Channel Flow", U.S.Department of Agriculture Soil Conservation Technical Bulletin No. 1026. 1950.

[16] C. T. Yang, "Incipient motion and sediment transport". Proc. ASCE 99(11), 1679-1704, 1973.

[17] F. Engelund, E. Hansen, "A Monograph on Sediment Transport in Alluvial Stream", 1-63. Teknisk Forlag,Copenhagen V, Denmark ,1967.

Proceedings of ICCSA 2014
Normandie University, Le Havre, France - June 23-26, 2014

MOTIF-BASED TOPOLOGY FORMATION FOR PEER-TO-PEER VIDEO STREAMING NETWORKS

Venus Marza *, Mehdi Dehghan †and Behzad Akbari ‡

Abstract. A new wave of live streaming networks labeled Peer-to-Peer (P2P) networks attracts more researchers and rapidly becomes one of the most popular applications. In order to achieve the main attractive properties of peer-to-peer streaming networks such as low delay, less overhead, high reliability and fault tolerantly, we introduce a novel topology formation strategy based on motif structures that can handle P2P requirements. From an each P2P characteristic perspective, the best motifs for setting up P2P topology are presented and finally all features have been taken into account for this purpose. The experimental results shows that one of motifs among thirteen 3-motif structures has moderate behavior in all quality metric's domain.

Keywords. Network Motifs, Live Video Streaming, Peer-to-Peer Topology, Site Percolation, Band Percolation

1 Introduction

R. Milo *et.al* (see [8]) defined "network Motifs", patterns of interconnections that occure in complex networks at numbers that are significantly higher than those in randomized networks. Network motifs provide a valuable contribution to both network analysis (see [2]) and optimization (see [7, 6, 3, 5]).

L.Krumov *et.al* (see [7]) propose an approach that uses network motifs (a local, stochastic metric) for distributed topology optimization. They constructed sample optimal topologies for two structural P2P overlays, CAN and Kademlia, with the aim of load balancing. Motif-based optimization (MBO) approach (see [6]) is suited for any network in which the nodes have a certain degree of freedom to choose the set of other nodes they communicate with. They have shown how to improve the load balancing of two common peer-to-peer protocols, CAN and KAD, by optimizing their local structure with the help of motifs and the effects on network performance (see [7]).

In addition, Krumov *et.al* (see [5]) introduce an approach for constructing streaming topologies that are resilient to node failures and DoS (denial-of-service) attacks. D.Conway in 2011 (see [3]) describes a new method for modeling network growth and evolution that relies on graph motifs to generate simulated network data with particular structural characteristic. However, the model appears sensitive to the size and structure of the initial base graph.

Some studies have been done to analyze the concept of modularity, for example: A. Arenas *et.al* in 2008 (see [2]) use a modularity-based framework only as a illustrative example of how motifs could be defined to detect general node classes in networks.

The contribution of this paper is to find suitable network's motif for live video streaming in peer-to-peer topologies in which P2P requirements such as end-to-end delay, overhead, robustness against failures and attacks either in peers or their connections have been met.
In the other word, the idea is to use network Motifs to characterize the local environment of node and decide which directional communication need to be followed that all requirements of live video streaming in P2P topologies are satisfied. Therefore, peers can join to the network topology according to special structure and formed final desirable topology without any complexity.

The rest of this work is organized as follows. Section 2 briefly introduces the network's motif and shows how 3-node directed sub-graph formed Motif structure. In Section 3 we describe P2P topology requirements in live video streaming applications and it followed by how these characteristics are satisfied with each motif's structure in Section 4. Finally, Section 5 concludes the paper and discusses future works.

2 Network Motifs

In general, network Motifs are a well-defined intermediate scale for characterizing the local structure of networks. In our P2P topology, 3-node sub-graphs have been selected because they are the smallest sub-graph in networks. Since live video streaming networks should be directed, from source to participants, directed sub-graphs has been chosen. Therefore, 3-node directed sub-graphs

*Venus Marza is with Department of Computer Engineering, West Tehran Branch, Islamic Azad University, Tehran, Iran. E-mail: v.marza@srbiau.ac.ir

†Mehdi Dehghan is with Department of Computer Engineering and Information Technology, Amirkabir University of Technology. E-mail: dehghan@aut.ac.ir

‡Behzad Akbari is with Department of Electrical and Computer Engineering, Tarbiat Modares University. E-mail: b.akbari@modares.ac.ir

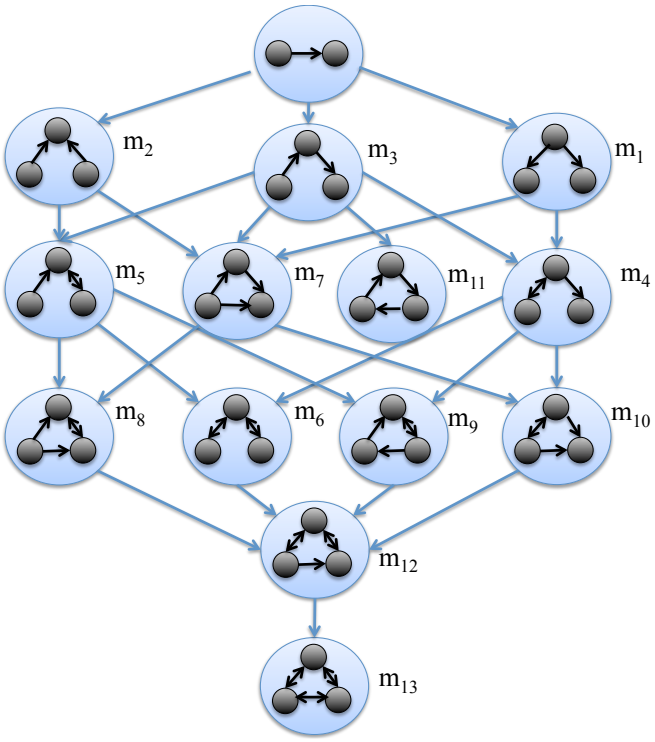

Figure 1: Motif formation tree: all possible directed subgraph of 3-node

are utilized and 13 different motifs that consist of three nodes are appeared. As Shown in Figure 1, the first three motifs, m_1, m_2 and m_3, are shaped by adding a new node to level 1 and the other motifs are organized in hierarchical order just by appending a new edge in each level.

2.1 Frequency Pattern of Motifs

The frequency of a pattern in a target graph is the maximum number of different matches of that pattern. Three different frequency methods are used for motifs [9]. Frequency concept F_1 counts every match of special pattern and gives a complete overview of all possible occurrences of it. Frequency concepts F_2 and F_3 restrict the reuse of graph elements: concept F_2 only allows edge disjoint matches and concept F_3 is even more restrictive and all matches have to be vertex and edge disjoint. In our studies concept F_1 has been used.

2.2 Significance Value of Motifs

For a given network, two different values, the $P-Value$ and the $Z-Score$, are usually calculated by using frequency concept F_1. A motif is considered to be significant [8] if the probability that the motif occurs in a single random graph is below than $p = 0.01$ or if the $z-score$ of it is higher than 2. The $Z-Score$, $Z(m)$, for a motif m, takes the average frequency in randomized networks into account and it is defined as [4]:

$$Z(m) = \frac{F_1(m) - \overline{F_{1,r}(m)}}{\sigma_r(m)} \quad (1)$$

Where $\sigma_r(m)$ denotes the standard deviation of the considered motif in the random graphs, and $\overline{F_{1,r}(m)}$ is the average frequency in the randomized networks, by utilizing the frequency concept F_1.

Besides, Different tools have been developed for the detection and analysis of network motifs (see [10]). FANMOD that has been used in this article, is a relatively recent tool that calculates both the statistics of the motifs given by $z-scores$ and the relative frequency for all detected motifs of a particular size. The respective $z-score$ of all motifs in networks that was used for measuring P2P parameters (such as delay, overhead, site percolation and bond percolation) are around 400 and their p-values are almost zero. It means that identified motifs appear more often than in the according random graph model, so their topology are suitable for evaluation motif's role.

3 Essential Requirements of P2P Live Streaming Networks

The following key requirements are addressed for P2P topologies [1] and we have customized them for live streaming applications:

- **Scalability**: Very large numbers of participating peers can join to network without any significant performance degradation.
- **Efficiency**: Routing should incur a minimum number of overlay hops and minimal end-to-end delay should be guaranteed.
- **Fault Tolerance**: Participating nodes in P2P networks can be added or removed as members can join or leave social networks. Network's links may also fail at any time. In this situation still all resources should be accessible from all peers.
- **Reliability**: Any single point of failure should be removed. Moreover, in any malicious attack or undesirable failures, which cease operations, the overlay network should provide an acceptable service.
- **Decentralized**: Lack of centralized control in the overlay network.
- **Self-organization**: In the presence of churn, the overlay network should reconfigure itself towards stable configurations.

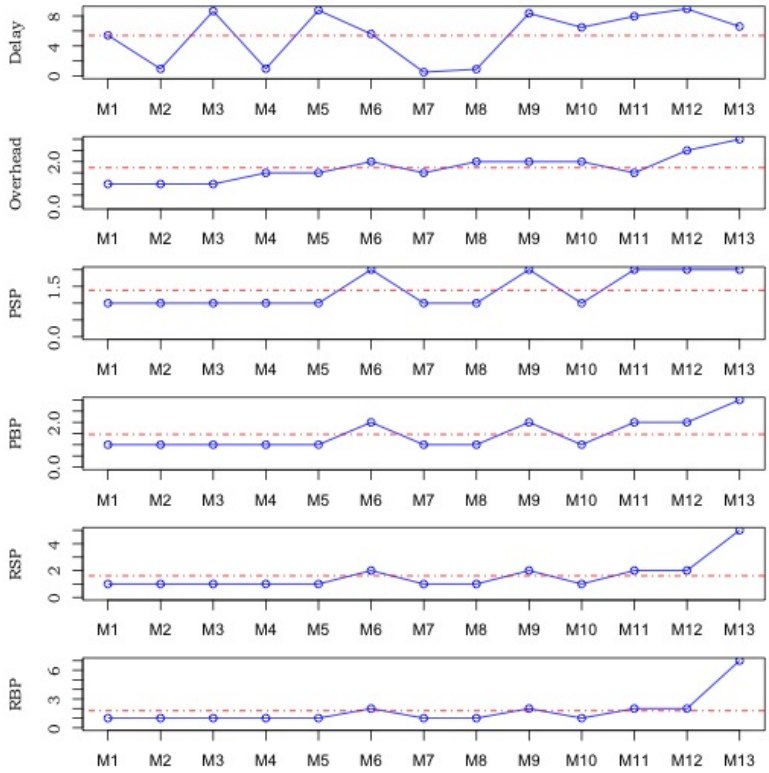

Figure 2: (a) Average delay of motifs, (b) Average overhead of motifs, (c) Preferential Site Percolation of motifs, (d) Preferential Bond Percolation of motifs, (e) Random Site Percolation of motifs, (f) Random Bond Percolation of motifs, in live video streaming networks.

4 Matching P2P Live Streaming Network's Requirements with Motif Characteristics

In the following subsections, we have shown that how P2P live streaming requirements can be handled by each of thirteen predefined motifs. In subsection 4.1, scalability and efficiency should be satisfied. subsection 4.2 is noticed about decentralization and self-organization and at the end, subsection 4.3 focuses on fault-tolerant and reliability of P2P networks.

4.1 Delay

Delay has been measured as number of hops that video chunks passed away from source to each peer. If video chunks can be received in minimum hops, efficiency will be handled. In addition, maximum number of peers has been scheduled to access their desirable video chunks on time when peers connect to each other (with respect to their predefined bandwidth constraint) in minimum number of hops; for this reason, scalability will be satisfied too.

Experiment 1. Whenever all peers received their first chunk, their delay was submitted and overall average delay was calculated as well. As shown in Figure 2 (a), motifs m_2, m_4, m_7 and m_8 are the best motifs for scalability and efficiency improvement in video streaming from delay's point of view.

4.2 Overhead

Without loss of generality, we assumed that push-based strategy has been used for video streaming and peers in P2P topology haven't any previous knowledge about chunk's availability of their neighbors. Therefore, peers may receive redundant video chunks and their bandwidth waste as well. Overhead in these types of topologies have been measured based on redundant chunks that each peer has detected. P2P topology is decentralized because peers have decided independently and based on their bandwidth's constraint for streaming available chunks to their neighbors. Moreover, reconfiguration in these P2P topologies is based on peer's detection, *i.e.* peers identify whether their necessary chunks has been provided or not to change their community.

Experiment 2. since peers don't have any knowledge about available chunks of their neighbors and push-based strategy has been utilized in whole of topology, it's obvious that bidirectional edges have led to receiving useless chunks and increasing overhead. Figure 2 (b) presented that m_1, m_2 and m_3 are the best motifs in topology formation when just overhead is considerable matter.

Table 1: Best motifs in each domain (PSP: Preferential Site Percolation) (PBP: Preferential Bond Percolation) (RSP: Random Site Percolation) (RBP: Random Bond Percolation)

	Delay	*Overhead*	*PSP*	*PBP*	*RSP*	*RBP*
Delay	m_2 , m_4 , m_7 , m_8	m_2	m_6	m_6	m_6	m_6
Overhead	*	m_1 , m_2 , m_3	m_{11}	m_{11}	m_{11}	m_{11}
PSP	*	*	m_6 , m_{11} , m_{12} , m_{13}	m_{13}	m_{13}	m_{13}
PBP	*	*	*	m_{13}	m_{13}	m_{13}
RSP	*	*	*	*	m_{13}	m_{13}
RBP	*	*	*	*	*	m_{13}

4.3 Site & Bond Percolation

With vulnerability perspective, we can categorize attacks and failures in four types of procedures from a complex network standpoint: 1) Preferential Site Percolation which remove nodes with highest degree until the network is partitioned; 2) Random Site Percolation which randomly eliminate nodes one by one until the network becomes unconnected; 3) Preferential Bond Percolation that edges with highest Betweeness will be deleted till the network takes apart; and finally 4) Random Bond Percolation which has repeated to omit edges randomly until the network is partitioned into components.

As defined in Section 3, reliability has been achieved if any single point of failure would have taken away from topology. It means that P2P live streaming topologies should endure malicious attacks. So, reliability can be mapped to Preferential Site / Bond Percolation. Besides, peers join and leave P2P streaming networks unexpectedly and topology must manage it during its configuration; Random Site Percolation has noticed about this kind of behavior. Moreover, if peers can't communicate with each other properly, their connection would be damaged and this issue can be handled by Random Bond Percolation metric.

Experiment 3. The results of running these four procedures on our motif-based topologies are summarized in Figure 2 (c), (d), (e) & (f). Each number in y-axis shows that in how many steps the network was not partitioned (the greater-the better); it has been shown that not only m_1, m_2, m_3, m_4, m_5, m_7, m_8, and m_{10} are more sensitive to malicious attacks on their nodes but also they are more fragile to malicious attacks on their edges. In contrast, Motifs m_6, m_9, m_{11}, m_{12}, and m_{13} are more robust in both malicious attack's domains. Besides, networks that have been built based on those motifs endure node and edge's failures much better than the others.

Note that m_{13} is the best motif for attacks and failures. However, m_6, m_9, m_{11} and m_{12} also have an acceptable level for reliability and fault tolerantly.

5 Main results

We considered that if a particular characteristic is the main purpose for topology formation, which motifs will be the best ones (Experiments 1, 2, 3). In addition, Table 1 is summarized the best motifs by analyzing two metrics in 2-D matrix. Here, by taking all quality metrics into consideration, we plan to instate trade-off between these desirable but incompatible features for setting-up P2P streaming topology.

As shown in Figure 2, by red dashed lines: (a) Motifs m_3, m_5, m_9, m_{11}, and m_{12} are un-acceptable ones for delay; (b) Motifs m_{12} and m_{13} aren't satisfactory from overhead's point of view; (c) Motifs m_1, m_2, m_3, m_4, m_5, m_7, m_8, and m_{10} are not appropriate for reliability. Therefore, just motif m_6 has moderate behavior in all domains, *i.e.* It means that m_6 is the best motif for topology formation in situation that all P2P live streaming requirements are our concern simultaneously.

In conclusion, whenever we pay attention to special attribute then Experiment 1, 2, or 3 will be followed. For inspection of two features, Table 1 shows helpful information; for example, in reliable environments if we ensure that malicious attacks and unexpected failures will never be happened then using motif m_2 is reasonable choice and we just take care of delay & overhead in these circumstances. However, by analyzing all P2P characteristics in live streaming, motif m_6 is the best candidate for topology formation.

6 Conclusion & Future Works

This research provides a novel perspective on the construction and evolution of P2P video streaming networks. Our contributions are listed as following: Firstly, we have gathered the key features of P2P live streaming. Secondly, we have mapped these requirements on complex network's metrics such as closeness (delay), degree centrality (overhead), hubs and authorities (Preferential Site Percolation), betweeness (Preferential Bond Percolation), Random Site Percolation, Random Bond Percolation. In the next step, the smallest directed sub-graph (3-node motif) has been utilized for establishing P2P topologies

and the most appropriate motifs in each domain have been introduced. Finally, since there is a trade-off between these features, by analyzing and combining all P2P requirements, we shows that motif m_6 has moderate style for arranging peers in P2P live streaming networks.

To the best of our knowledge, our work is the first one that addresses how to form P2P live streaming topology based on motif's structure by covering all requirements. In future work, we plan to apply this procedure on other applications.

References

[1] K. Aberer, L. O. Alima, A. Ghodsi, S. Girdzijauskas, S. Haridi, M. Hauswirth, "The essence of P2P: a reference architecture for overlay networks", *Fifth IEEE International Conference on Peer-to-Peer Computing*, 2005.

[2] A. Arenas, A. Fernandez, S. Fortunato, S. Gomez, "Motif-based communities in complex networks", *Journal of physics A: Mathematical and Theoretical*, 2008.

[3] D. Conway, "Modeling Network Evolution Using Graph Motifs", *CoRR*, 2011

[4] Lachezar Krumov, "MOPS: Optimizing Structured Peer-to-Peer Networks Based on their Local Motif-Signature", *Technical Report*, TUD-CS-2009-0022, 2009.

[5] Lachezar Krumov, Adriana Andreeva, Thorsten Strufe, "Resilient Peer-to-Peer Live-streaming using Motifs", *International Symposium on a World of Wireless Mobile and Multimedia Networks (WoWMoM), 2010 IEEE* , pages 1-8, June 2010.

[6] Lachezar Krumov, "Local Structures Determine Performance within Complex Networks", *PhD Thesis*, Technical University Darmstadt, November 2010.

[7] L. Krumov, I. Schweizer, D. Bradler, T. Strufe, "Leveraging Network Motifs for the Adaptation of Structured Peer-to-Peer-Networks", *Global Telecommunications Conference (GLOBECOM 2010), 2010 IEEE*, pages 1-5, Dec. 2010.

[8] R. Milo,S. Shen-Orr, S. Itzkovitz, N. Kashtan, D. Chklovskii, U. Alon, "Network motifs: simple building blocks of complex networks", *Science (New York)* 298(5594): p. 824-7, 2002.

[9] F. Schreiber, H. Schwobbermeyer, "Towards Motif Detection in Networks: Frequency Concepts and Flexible Search", *Proc. Intl. Workshop Network Tools and Applications*, 2004.

[10] E. A. Wong, B. Baur, "On Network Tools for Network Motif Finding: A Survey Study", 2010.

Proceedings of ICCSA 2014
Normandie University, Le Havre, France – June 23-26, 2014

A NETWORK SCIENCE APPROACH TO INTER-ORGANIZATIONAL INNOVATION NETWORKS: THE CASE STUDY OF ENTERPRISE EUROPE NETWORK

Giovanna Ferraro and Antonio Iovanella[1, 2]

Abstract. The paper introduces an analysis of a real inter-organizational innovation network with a network science approach. The study is integrated with a Social Network Analysis referring to the EEN.
Keywords. Network science, social network analysis, choreography, inter-organizational networks, innovation.

1 Introduction

Network Science is an emerging, interdisciplinary research field aiming to understand the structure, development and weaknesses of networks through different methods attained to different disciplines as mathematics, statistics, physics and computer science. It is "*an attempt to understand networks emerging in nature, technology and society using a unified set of tools and principles. Despite apparent differences, many networks emerge and evolve, driven by a fundamental set of laws and mechanisms and these are the provinces of network science*" [3].

The purpose of this paper is to consider the Network Science paradigm as a tool to study inter-organizational innovation networks by means of graph theory as mathematical abstraction and other multidisciplinary approaches to infer behaviors of various phenomena.

Innovation networks are defined as: "*a basic institutional arrangement to cope with systemic innovation. Networks can be viewed as an inter-penetrated form of market and organization* [...]. *They include joint ventures, licensing arrangements, management contracts, sub-contracting, production sharing and R&D collaboration*" ([14], [16]).

Among them, inter-organizational innovation networks are characterized by recurring exchange interactions between members that retain residual control of their individual resources yet periodically jointly decide over their use [11]. Members of such systems can be firms, organizations or research centers, located in different regions and specialized in particular sectors, linked by common interests, technologies and skills and networked by the decision to collaborate according to specific rules. Technological districts, business incubators and consortia created by international initiatives financed by the European Commission are some examples of such kind of networks.

Herein by means of the Enterprise Europe Network (EEN), a real case study, we model an inter-organizational innovation network as a complex network and infer the main properties that characterize the structure and behavior of the system selecting an appropriate set of tools to measure them.

Although real networks may appear very different from each other with respect to their functions and attributes, the analysis of their structure shows the ubiquity of several asymptotic features and reveals the emergence of general and common self-organizing rules.

Such systems, denoted by a significant number of nodes, are characterized by a structure that is irregular, complex and dynamically evolving in time. The study thereof, focused on the network topology, identifies a series of principles and statistical properties common to the majority of real systems. The networks' structure has relevant consequences on systems' robustness and reaction to external perturbations. The topology is likewise important in determining the emergence of collective dynamical behavior, such as synchronization [21], or in managing the most important features of relevant processes [22].

Network science includes the Social Network Analysis (SNA) as a tool to conceptualize and investigate interactions among social entities. In general terms, SNA can be considered as an archetype that abstracts social life in terms of structures of relationships among actors [19].

SNA concerns issues of centrality, meaning the individuals which are best connected to others or have most influences, connectivity, showing how individuals are connected to one another through the network and

[1] Giovanna Ferraro and Antonio Iovanella are with Department of Enterprise Engineering, University of Rome Tor Vergata, Italy. E-mails: giovanna.ferraro@uniroma2.it, antonio.iovanella @uniroma2.it.
[2] Manuscript received April 17, 2014; revised May 21, 2014.

community, indicating the nodes that are highly and tightly linked.

The paper is organized as follows: section 2 describes the case study and the network modelization, section 3 introduces the analysis of the network structure, section 4 presents the case study in terms of a scale-free network, section 5 describes the emergence of the network choreography, section 6 reports the final thoughts and the key issues that require further research.

2 EEN as a case study

Here, we deem as case study, the Enterprise Europe Network (EEN) that was launched in 2008 by the European Commission's Directorate-General for Enterprise and Industry. It builds on the former Euro Info Centre (EIC) and Innovation Relay Centre (IRC) Networks, established in 1987 and 1995 respectively.

EEN can be considered a key instrument in the European Union's strategy to boost growth and jobs. The network brings together as members, more than 600 different and independent organizations as chambers of commerce, technology centers, universities, research institutes and development agencies, from 54 countries. EEN's mission is helping small companies make the most of the business opportunities in the European Union by offering combined services according to the principle of one-stop shop for small business. The services offered concern technology transfer, access to finance, advice on EU law and standards, intellectual property rights, research funding and internationalization.

Partners of the networks are independent organizations organized in consortia at country level. We consider the collaborations among partners through the analysis of the Partnership Agreements (PAs). The aim of the partnership process is to get clients to sign-up a long-term collaboration with companies or researchers that match their needs and expectations. Therefore, PAs represent important performance indicators for measuring the effectiveness and efficiency of the activities undertaken by the Network. PAs comprise different services such as technological and commercial cooperation and collaborative research.

The examined data have been collected by the Executive Agency of the EEN – EASME – and concern 54 members countries and 4940 PAs signed during the period from 1st January 2011 to 31st December 2012 - 1910 PAs in 2011 and 3030 in 2012.

The data processing and the network analysis are conducted using the software R[3] with the *igraph*[4] package.

[3] http://www.r-project.org
[4] http://igraph.sourceforge.net

2.1 Modelization

The classical mathematical abstraction of the network is a graph G. A graph $G = (V, E)$ is composed of a set V of n nodes and a set E of m links defining a relationship among these nodes. We refer to a member by an index i meaning that we allow a one-to-one correspondence between an index and a member.

Each member of EEN represents a node of a graph: two members, says i and j, are adjacent through a link if and only if there is a connection between i and j and a weight w_{ij} equal to the number of PAs signed between two members.

The granularity of the available data being at country level, the network is composed as follows: each node is a centroid that represents a country inside which there are independent organizations, as network partners, while links exist if two countries share at least one PA.

To the graph G is associated an adjacency matrix A, where its elements are defined as $a_{ij} = w_{ij}$ if nodes i, j of G are connected, $a_{ij} = 0$ otherwise. Since the said graph represents reciprocal relationships, the matrix is symmetric (i.e. $a_{ij} = a_{ji}$) with zero elements on the main diagonal.

In this work, we are interested on the structure of the connections among members rather than on their intensity. Therefore we focus the analysis on EEN as an unweighted network where the links between nodes are either present or not and the network can be denoted by (0, 1), 1 if i and j are connected, 0 otherwise - or binary matrices. The study of EEN weighted graph representation and the relative evidences will be presented in a forthcoming paper.

3 Analysis of the network structure

Most of real networks, despite intrinsic differences, are described by similar structural features, as for instance relatively small path lengths, high clustering coefficients, fat tailed shapes in degree distributions and degree correlations. Such properties make real networks different from the traditional models studied in the graph theory like regular lattices and random graphs. Indeed, real networks meet the scale-free structure and the evidence comes from the convergence between empirical data and analytical models that foresee the network structure [7].

In this section, we describe some structural properties observed in the topology of the EEN.

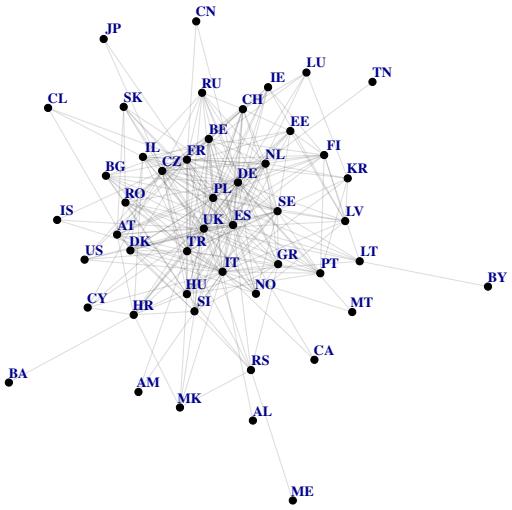

Figure 1: The 2011 EEN graph (G_{2011}).

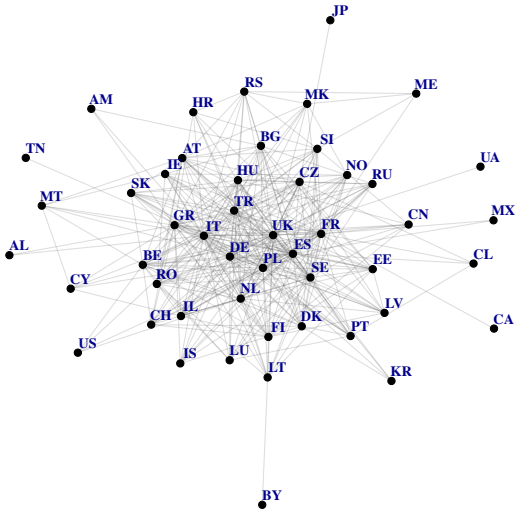

Figure 2: The 2012 EEN graph (G_{2012}).

3.1 Network parameters

We set two different graphs for each year, namely G_{2011} and G_{2012} where the nodes n_{2011} and n_{2012} are, respectively, the countries with at least one PA signed and where links m_{2011} and m_{2012} reflect interactions among countries, rather than the entire set of 4940 PAs, thus decreasing the number to m_{2011} = 285 and m_{2012} = 357. After this pre-processing, the network graph configuration is composed by n_{2011} = 48 and n_{2012} = 49 and it is illustrated in Figure 1 and 2 where node labels are the official country codes.

The EEN countries that have not signed any PA in the period 2011-2012 are not considered in the analysis.

One of the basic characteristics of a graph G is its density d that measures the portion of links in the set E compared to the maximum possible number of links between nodes in set V (equal to $n_x(n_x - 1)/2$, x = {2011, 2012}) and assumes values from 0 to 1. Density indicates how the communication paths in the system are able to get information out to the members. In EEN graphs, the value of the density is low (0.25 and 0.30) denoting that the network is sparse. Such sparsely connected networks show the typical power-law node-degree distribution in which most nodes have only few links while some few nodes are extremely connected.

Table 1 gives some basic information about EEN in the two different years. The reported network measures will be explained throughout the paper.

The diameter D is the length of the shortest path between the most distanced nodes measuring the extent of a graph and the topological length between two nodes. It characterizes the ability of two nodes to communicate with each other. The smaller is D, the shorter is the expected path between them as the hubs act as bridges between the many small nodes. In EEN graphs the value of D is 4, i.e. the path among farthest nodes is very short; in consequence all nodes appear strongly connected due also to EEN modest size in terms of number of nodes.

Table 1: EEN graph parameters

Network measures	2011	2012
Nodes (n)	48	49
Links (m)	285	357
Density (d)	0.25	0.30
Diameter (D)	4	4
Clique number (χ)	12	12
Average shortest path (L)	1.91	1.78
Cluster coefficient (C)	0.65	0.67
Degree exponent (γ)	2.82	2.69
Second eigenvalue (λ_2)	0.84	0.92

3.2 Community, clique and dendrograms

In a network a *community* is a sub-graph whose nodes are tightly connected. The requirement that all pairs of community members choose each other leads to the definition of a clique. A *clique* is a maximal complete sub-graph of three or more nodes, i.e. a subset of nodes all of which are adjacent to each other, and such that no other nodes exist adjacent to all of them. The cardinality of the maximal clique is indicated with χ and in EEN the value is 12 for both years. Table 2 resumes the membership in each clique.

From the analysis it results that in 2011 the EEN has only one clique of 12 members while in 2012 the network contains 6 cliques each having 12 members. There is a relevant overlapping represented by 8 countries,

namely IT, UK, DE, ES, PL, TR, NL and BE constant overtime; in 2012 the overlapping is extended to IL. In the system there is indeed, a group of countries strictly inter-connected surrounded by partners having different level of membership in terms of clique. Figure 3 shows all cliques for 2012.

Table 2: Clique compositions in years 2011 and 2012.

2011											
IT	UK	DE	ES	PL	FR	TR	NL	BE	SE	CZ	CH
2012											
IT	UK	DE	ES	PL	FR	TR	NL	BE	SE	IL	FI
IT	UK	DE	ES	PL	FR	TR	NL	BE	SE	IL	CZ
IT	UK	DE	ES	PL	FR	TR	NL	BE	GR	IL	FI
IT	UK	DE	ES	PL	FR	TR	NL	BE	GR	IL	CZ
IT	UK	DE	ES	PL	HU	TR	NL	BE	SE	IL	CZ
IT	UK	DE	ES	PL	HU	TR	NL	BE	GR	IL	CZ

The hierarchy of communities in the network is usually represented by a *dendrogram* that graphically denotes through splitting in a tree. The horizontal position of the split indicates the distance at which communities were connected.

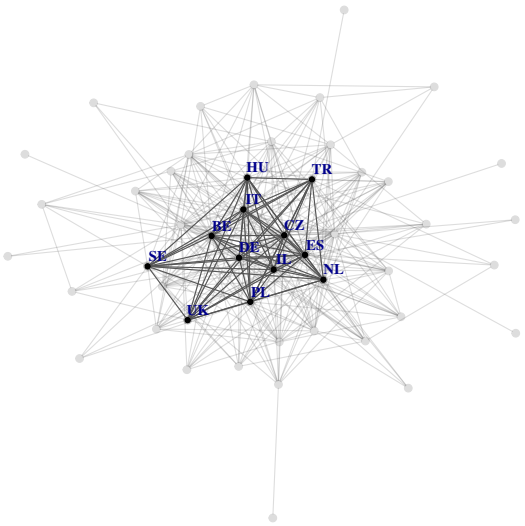

Figure 3: The highlighted links for 2012 EEN cliques.

Figure 4 reports the dendrogram for the year 2012, where communities are detected by means of the edge shortest path betweenness measure [18], which iteratively extract community from the graphs considering at each step geodesic network paths.

The dendrogram reveals information concerning which countries are grouped together at various levels of dissimilarity and at the right of the dendrogram each country forms its own cluster.

The dendrogram confirms what we reported in Table 2, i.e. the presence of a core of countries closely connected in one community while the others follow at different level of the hierarchy.

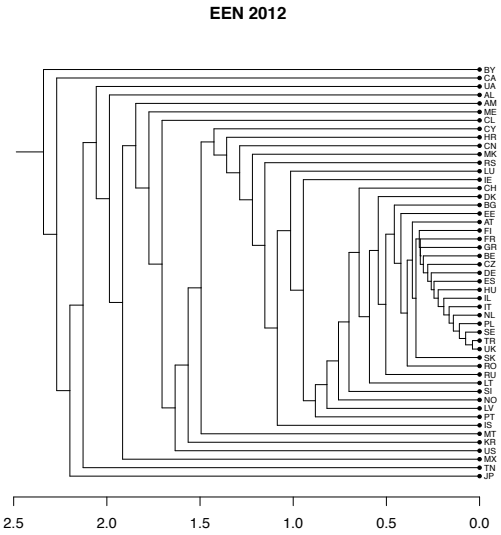

Figure 4: The EEN dendrogram for 2012.

3.3 Centrality measures

The topology of several real networks is related to the possibility of identifying the properties of every node. Usually, nodes with similar characteristics tend to link to each other. They have features that carry relevant information regarding their role in the network. Specifically, we refer to centrality value that represents the node's relative importance within a graph, the higher is the centrality index of a node, the higher is its perceived centrality in the graph. Moreover, centrality measures assess the nodes involvement in or contribution to the cohesiveness of the network [6].

The concept of centrality has an inherent ambiguity; there is no point in including all measures in one method. The best ones are related to the applications depending on the degrees of the local and overall structures. There is a similarity in certain measures indeed a node rank can depend on the status to which, it is connected to. Centrality measures in some cases provide considerably various results. The choice of them requires the consideration of the specificity of the measures and the requirements of different applications.

There are several measures describing the centrality; the most commonly used are the degree centrality, the closeness, the betweenness, the eigenvector centrality and the Bonacich index.

The *degree centrality* of a node is the number of links incident upon a node and can be interpreted in terms of the size of members' neighborhoods within the network. The degree defines the immediate risk of a member to catch whatever is flowing through the network. It quantifies how well it is connected to the other elements of the graph.

Table 3: Centrality measures for the EEN in 2012.

Country	*ID*	*Degree*	*Closeness*	*Betweenness*	*Eigenvector*	*Bonacich Index*
Italy	IT	40	0.857	173.795	1.000	1.110
United Kingdom	UK	37	0.814	112.440	0.981	0.627
France	FR	35	0.787	143.730	0.914	-1.740
Spain	ES	34	0.762	77.512	0.927	-1.112
Germany	DE	32	0.750	36.406	0.928	-0.690
Poland	PL	31	0.738	44.689	0.891	-0.529
Greece	GR	29	0.716	62.175	0.792	-1.750
Sweden	SE	28	0.706	22.489	0.838	-0.784
Turkey	TR	28	0.696	20.339	0.850	-0.567
The Netherlands	NL	26	0.686	21.366	0.800	-0.920
Hungary	HU	22	0.632	10.199	0.698	-0.952
Czech Republic	CZ	21	0.632	56.780	0.672	1.162
Belgium	BE	21	0.632	14.168	0.682	-0.449
Austria	AT	19	0.615	9.657	0.612	-0.140
Denmark	DK	18	0.608	9.910	0.587	-0.042
Finland	FI	18	0.608	5.252	0.610	-1.140
Bulgaria	BG	17	0.593	10.612	0.559	-1.494
Romania	RO	16	0.600	3.620	0.577	-0.732
Slovenia	SI	16	0.585	10.423	0.526	-1.458
Estonia	EE	15	0.593	1.906	0.552	0.269
Israel	IL	15	0.585	2.803	0.559	-1.108
Lithuania	LT	13	0.571	47.563	0.450	0.103
Slovakia	SK	13	0.571	0.455	0.500	-0.300
Norway	NO	13	0.565	1.389	0.482	-0.249
Russia	RU	12	0.565	0.380	0.474	-1.653
Ireland	IE	12	0.558	2.769	0.432	-1.717
Portugal	PT	12	0.558	4.189	0.437	0.149
Switzerland	CH	12	0.558	0.454	0.459	-1.395
Serbia	RS	12	0.552	6.381	0.363	0.010
Latvia	LV	11	0.558	0.133	0.432	1.220
Macedonia	MK	10	0.545	4.340	0.322	1.197
Luxembourg	LU	10	0.545	0.458	0.378	-0.057
Iceland	IS	9	0.527	0.114	0.365	-0.065
Croatia	HR	8	0.533	0.282	0.300	-0.685
China	CN	8	0.533	0.272	0.306	-1.253
Malta	MT	7	0.495	1.203	0.221	-0.623
Cyprus	CY	6	0.511	0.840	0.212	-0.147
Chile	CL	4	0.485	0.200	0.140	0.266
U.S.A.	US	4	0.485	0.000	0.160	1.019
South Korea	KR	4	0.480	0.000	0.161	0.750
Montenegro	ME	4	0.466	0.307	0.101	-0.185
Armenia	AM	3	0.475	0.000	0.111	-0.780
Mexico	MX	2	0.471	0.000	0.087	-1.948
Albania	AL	2	0.471	0.000	0.085	0.263
Tunisia	TN	1	0.466	0.000	0.047	1.561
Ukraine	UA	1	0.453	0.000	0.047	1.078
Canada	CA	1	0.444	0.000	0.043	-1.288
Japan	JP	1	0.390	0.000	0.032	1.613
Belarus	BY	1	0.366	0.000	0.021	0.554

The *closeness centrality* refers to a natural distance between all pairs of nodes defined by the length of their shortest paths. Thus, the more central a node is, the lower is its distance to all other nodes. This value measures how long it will take to spread information from a member to all others sequentially.

The *betweenness centrality* determines the number of times a node acts as bridge along the shortest path between two other nodes. This measure reveals the members that are essential for connecting different regions of the network.

The *Eigenvector centrality* measures the node's influence in a network according to the number and the quality of its connections. Indeed a member with a smaller number of high quality links has more power than one with a larger number of mediocre contacts.

The *Bonacich index* refers to the notion that the power of a node is recursively defined by the sum of the power of its alters. Positive values imply that members become more powerful as their the alter (neighbor) comes to be more powerful, while negative values imply that members are more powerful only as their alters become weaker, as occurs in competitive or antagonistic relations.

Table 3 reports the centrality measures referred to EEN members in 2012.

The crosscheck between degree and centrality scores clearly shows the presence of the three classes of members, i.e. hubs, semi-peripherals and peripherals.

The Table highlights the presence of more than one hub since nodes as IT, UK, DE, ES, FR and PL have a neighbor value greater than 30 meaning that they are well connected to the other countries due to the high number of links. These countries have also a high rank of closeness signifying their relevant involvement in the network and their contribution to spread more easily information within the system even if they connect different regions of the graph due to the higher betweenness values. Indeed, hubs act as bridges between the many small nodes.

DE, PL, SE, TR and NL show a low value of betweenness maintaining a high rank of eigenvector centrality meaning a relevant influence of these nodes in the network even without acting as a bridge in connecting the different region of the graph.

There are some interesting cases as for CZ and LT where a high score in betweenness corresponds to relatively small values in eigenvector centrality, intending that these countries lay on many shortest paths but they are connected mostly to low score members.

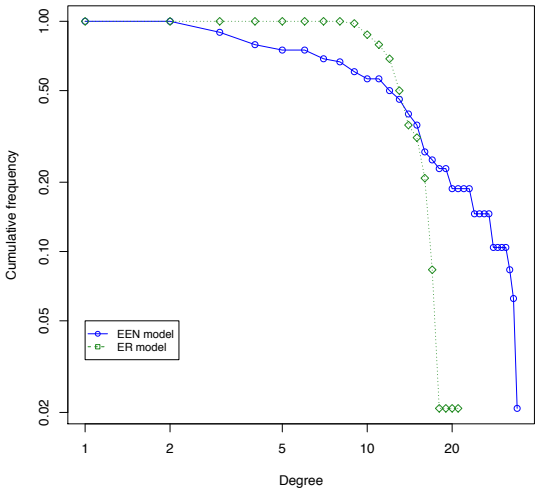

Figure 5: Degree distribution for the 2011 EEN and the Erdös and Rényi model.

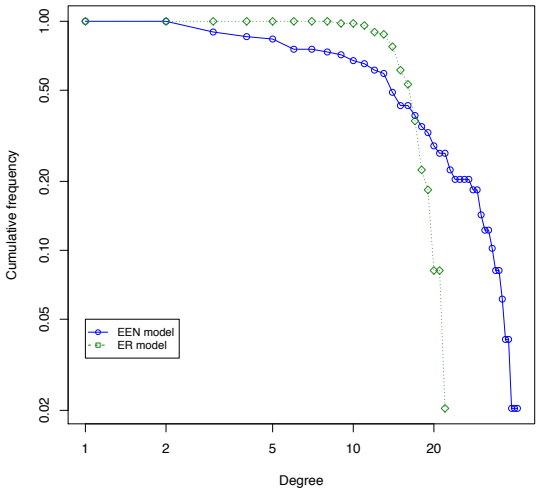

Figure 6: Degree distribution for the 2012 EEN and the Erdös and Rényi model.

Regarding the Bonacich index, some countries as IT, UK, CZ, LV, MK, US, SK, JP, TN and UA have positive and high values denoting that these nodes become more influent as their neighbors come to be more powerful. The majority of negative scores means that nodes are more powerful only if their neighbours become weaker as in competitive relations.

4 EEN as a scale-free network

We propose complex networks with the scale-free feature ([22] and references therein) an adequate framework within which to represent EEN. We refer mainly to the Barabási-Albert (BA) scale-free network model [4], [2],[13]. BA networks are open and dynamically formed by continuous addition of new nodes that represent members, while links mimic collaborative agreements. Links' inhomogeneity reflects the degree of members' involvement in the network and the difference among hubs, semi-peripheral and peripheral nodes.

Scale-free networks emerge in real situations in which the kind of inhomogeneity in the degree distribution represents few nodes having many links whereas the majority of them has few connections. Therefore, a single node or hub cannot be considered representative since these networks are held together by a different, although limited, number of highly connected hubs while the majority of nodes has smaller connection degree than the average. All nodes are linked with a rather short path due to the small world characteristic [22] even in case of large and sparse systems.

Scale-free networks are mainly identifiable by three characteristics: the average path length, the clustering coefficient and the degree distribution.

The average shortest path in EEN is 1.91 in 2011 and 1.78 in 2012 meaning that in the time period considered, the distance among members decreases shaping the small world characteristic of the network.

Clustering is introduced by structural embeddedness that is the existence of dense ties among nodes. In innovation networks, members sharing common partners have knowledge about each other's trustworthiness, capabilities, competences, and reputation and thus mitigating the effects of power asymmetries [9]. In the case study this value is $C_{2011} = 0.65$ and $C_{2012} = 0.67$ indicating the presence of dense local subgroups of interconnected nodes.

Regarding the degree distribution, the degree k_i of a node i represents the number of its links; the larger the degree, the more significant the node is in a network. The average of k_i over all i is the network average degree and the spread of node degrees over a network is characterized by a distribution function $P(k)$ that represents the probability that a randomly selected node has exactly k links.

The BA model asserts that growth and preferential attachments determine the self-organization of a network with scale-free structure. Actually, real networks constantly grow by adding new nodes that at each time-step join the network and link to other nodes already present in the system. New nodes tie preferentially to those that are more highly connected, following a "rich get richer" phenomenon [4].

The probability $\prod(k_i)$ that a new node will be connected to an already existing node i depends on the degree k_i for the property of the preferential attachments:

$$\Pi(k_i) = \frac{k_i}{\sum_{j=1}^{N} k_j}$$

In BA model, the connectivity distribution follows a power law function, i.e. the probability $P(k)$ that a node

in the network interacts with k other vertices decays with the law $P(k) \sim k^{-\gamma}$ with slope γ as the scaling exponent.

The values of the average path length, the cluster coefficient and γ reported in Table 1 meet the three scale-free properties required and they are comparable with the values of other real networks as reported in [22]. As a consequence, EEN exhibits the scale-free properties and is represented by the BA model.

The power law degree distribution is tested by comparing the slope of the degree distribution of the EEN and that of a classic random graph having the same number of nodes and links, and generated using the Erdös and Rényi model. Figures 5 and 6 depict the comparison between the two distributions. The power law slope of the EEN clearly decays less quickly than that of the random graph.

4.1 Network robustness

Network robustness permits to understand the behavior of certain systems under failures and attacks and allows to protect them against assaults or to exploit their weaknesses.

In the BA model, the network is robust if it contains a giant cluster comprised of most of the nodes even after a fraction of its nodes is removed.

Robustness refers to the capacity of the network to perform its basic functions even in case of nodes and links missing. Related to robustness, the resilience is the dynamical feature that entails a change in the network's essential activities. Resilience is the capacity of the network to adapt to internal and external errors by altering its processes while continuing to perform [5].

Real networks exhibit an unexpected degree of tolerance to the random deletion of their nodes due to their heterogeneity. Indeed, such breakdowns affect mainly the various small nodes that play a limited role in maintaining the networks' integrity and their removal has limited impact on their structure.

The random failure or *error* is the capacity of the network to uphold its connectivity features even in case of casual deletion of a portion of its nodes or links.

Scale-free networks with $\gamma \leq 3$ show a high robustness to random failure meaning that to break such networks apart, virtually all nodes should be removed.

In general, once a small fraction of nodes is removed, the distance among the remaining nodes increases, since some paths that contribute to the network connectivity are eliminated. Thus, for the remaining nodes, it is more difficult to communicate with each other.

In scale-free networks the diameter remains unchanged under an increasing level of errors, even when more than 5% of the nodes fail. The connections among the remaining nodes are unaffected due to the inhomogeneous connectivity distribution. Indeed, scale-free networks are characterized by the majority of nodes having few links, therefore nodes with small connectivity will be selected with much higher probability than hubs and their removal does not alter the path structure and has no influence on the overall network structure [1].

The *attack* refers to a removal process targeted to specific nodes i.e. the highly connected. In real networks, the deletion of a single hub does not fragment the system as the remaining hubs can still hold the system's integrity. However if the number of removed nodes reaches a critical threshold, the network suddenly breaks in disconnected components.

To simulate a *deliberate attack*, the most connected nodes are eliminated and, in sequence, the others in decreasing order of connectivity. In scale-free networks, when the most linked nodes are removed, the diameter increases rapidly doubling its original value if 5% of hubs are eliminated [1]. This vulnerability to attacks is due to the inhomogeneity of the connectivity distribution. Indeed, the removal of the few highly linked nodes alters the network topology and decreases the capacity of the remaining nodes to communicate with each other.

Hence, the structural robustness is not valid against a deliberate attack, as the simultaneous removal of the most connected nodes will destroy any system showing its fragility or its own *Achilles' Heel* [1]: the network behind is robust to random failures but vulnerable toward attacks.

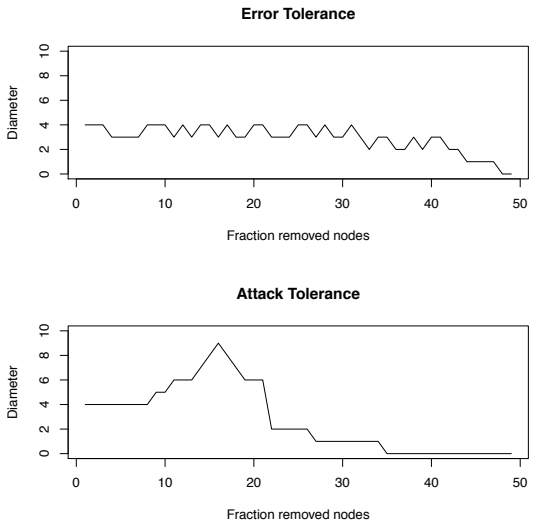

Figure 7: The effects on EEN diameter of error tolerance and attack tolerance in 2012.

Despite in the observed network we do not expect a random failure or a deliberate attack due to the fact that the nodes of the graph represent countries, we have implemented a double analysis – the Error Tolerance and the Attack Tolerance – and its effects on the network's diameter to detect the general features.

Due to modest size of the graph, EEN tends to retain its diameter at each time step a random node is removed, as in the case of error, almost at 70% oscillations notwithstanding.

The attack tolerance analysis is carried out removing at each time step the node with the highest degree, simulating an attack to the most connected nodes. The EEN diameter increases for growing percentage of nodes' removals and it suddenly decreases when almost 50% of the nodes are erased. Figure 7 shows the effects on EEN diameter of error tolerance and attack tolerance.

5 Network choreography

The network choreography is the system's capacity to address collaboration among multiple members. Choreography is focused on inter-organization coordination for external perspectives while collaboration is addressed by self-organizing interactions.

It requires some structural hypothesis on network topology and some membership characteristics and involves the accomplishment of certain activities among network members to reach the innovation outcome.

We refer to [13] for a complete description of network choreography.

5.1 Synchronization

Scale-free networks exhibit several interesting dynamical phenomena; in particular, we focus on the synchronization motion of their dynamical elements [21] and on a qualitative and paradigmatic correspondence between the emergence of synchronization in a network and the establishment of the choreography phenomenon.

In complex networks, nodes are characterized by a collection of variables that identifies a state. Such variables tend to synchronize in an equilibrium point that represents the state of choreography and the synchronization enables the homogeneity of state variables of the members involved in choreography. Moreover, due to the self-organization process of scale-free networks, their syncronizability holds even when new nodes are constantly added.

The study of the synchronization can not be detailedly performed because not all state variables of each member are known. Nevertheless, in [21] it is sustained that if we contemplate the Laplacian matrix $L = A - D$ where A is the adjacency matrix and D is the diagonal degree element matrix with $d_{ii} = k_i$ and 0 elsewhere, its largest eigenvalue is $\lambda_1 = 0$ and if the second eigenvalue λ_2 is positive and not close to λ_1, then the synchronization state is exponentially stable.

In the case study, the EEN adjacency matrixes for the years 2011 and 2012 have $\lambda_1 = 0$ in both cases and, respectively, $\lambda_2 = 0.84$ and $\lambda_2 = 0.92$. Therefore the synchronization is a stable state and, consequently, the choreography is a stable state for the EEN during the years under evaluation.

5.2 Network membership

Inter-organizational innovation networks require peculiar membership characteristics for the potential members that are attracted to join networks to get some benefits. Network membership characteristics are expressed by means of ontology and homophily properties.

5.2.1 Ontology

The term ontology is relevant in many fields as knowledge engineering and artificial intelligence. Several definitions and a wide range of applications are considered in different topics (e.g. see [8] and references therein).

We consider the definition of ontology provided in [20]: "*An ontology is a formal explicit specification of a shared conceptualization*". Ontology is therefore:

- *Formal*: it communicates the intended meaning of defined terms, independent on social or computational context. Formalism is a complete set of definitions express as logical axioms and documented in natural languages [15].
- *Explicit*: it defines the design of decisions, concepts and constrains.
- *Shared*: it regards a knowledge accepted by a group in which the members agree about the objects and the relations of such knowledge.
- *Conceptualized*: it concerns an abstract, simplified view of the world that we wish to represent. Every knowledge base, knowledge-based system or knowledge-level agent is committed to some conceptualization [15].

Table 4: EEN ontology.

Ontology features	EEN
Formal	Network members are grouped in Consortia and are legally bound with the network executive agency by Framework Partnership Agreements.
Explicit	Operational manual and guidelines contain all the key information regarding the working practices. These documents contain the obligations and formalities that members should follow.
Shared	All rules and procedures are shared. A common language is accepted and used among members. The exchange of good practices is encouraged to spread knowledge, enhance excellence and professionalism across the network.
Conceptualized	Rules and guidelines are conceptualized. Members sign a "code of conduct".

In this way, the state variables given for every member and the matrix A above mentioned are parts of the conceptualization, are formal since they respect a mathematical modelization, are explicit because every member knows its composition and shared since each member commits to have a state variable identically composed following the coupling rules.

In EEN the set of rules, guidelines and common language are formalized, explicit, shared and conceptualized among network members. The features remain valid also for the mathematical model given by the adjacency matrix A, while it is worthwhile to mention that for the complexity of a real case it is virtually impossible to explicit the state variables and the matrix Γ.

5.2.2 Homophily

Homophily is the tendency of nodes to link with others that are similar to them or, in other words, the members' attitude to associate and connect with similar [17]. Individuals in homophily relationships share common characteristics that make communication and relationships easier. Inter-organizational networks foresee similar interests among members that share innovation attitude, goals and believes.

In the literature, homophily in scale-free network is related to network topological aspects in terms of node similitude related to preferential attachment. It represents a relevant aspect leading the growth of networks. In particular, homophily refers to how the preferential attachment privileges the bond between new nodes and those having high number of nearest neighbors and high similitude jointly [10].

Concerning the homophily, in this case study nodes represent countries, therefore, this property is not particular meaningful as they are similar by definition. Nevertheless, in all the other general cases is important to consider.

6 Conclusions

This paper shows the use of network science paradigm as a tool to study inter-organizational innovation networks. The real case study is modeled by means of graph theory and other multidisciplinary tools to gather behavior of various phenomena.

We perform a network analysis of the case study aiming to generate a descriptive model that explain and describe EEN basic features and a network modeling that permits to design process models that reproduce the collected data but can also be utilized to infer predictions.

We suggest the BA model as an adequate framework to represent real inter-organizational innovation networks as in this model the network structure and its evolution are strictly correlated.

Further research should be conducted to extend the analysis in a broader range of contexts and networks, especially for macroeconomics considerations. Nevertheless, some essential characteristics have been studied. In particular, network topology influences connections among members; scale-free networks are able to spread and uphold interactions among nodes; robustness concerns the network capacity to face changes in the economic environment; ontology provides a shared common vision of the network and homophily enables cohesive relationships among members.

The network topology allows affirming the existence of a synchronizations state and its similarity to the phenomenon of choreography. Although this similarity is only paradigmatic, it permits to give some hints about the state stability as showed in the case study. The analysis of the data shows the presence of such stable state of choreography, which ensures members to profit from the value-added of the network according to their connections: members join EEN to get benefits from the network itself and from the networking processes to improve their competitiveness and innovation capability.

Acknowledgment

Authors would like to thank the Executive Agency for Small and Medium-sized Enterprises and the Evaluation and Monitoring Unit for the support to data retrieving.

References

[1] R. Albert, H. Jeong, A.-L. Barabási, "Error and attack tolerance of complex networks", Nature, 406, pp. 378–382, 2000.

[2] R. Albert, A.-L. Barabási, "Statistical Mechanics of Complex Networks", Reviews of Modern Physics, vol. 74, nr. 1, pp. 47-97, 2002.

[3] A.-L. Barabási, "Network science", Philosophical Transaction of The Royal Society A, 371, 2013.

[4] A.-L. Barabási and R. Albert, "Emergence of scaling in random networks", Science, 286, pp. 509-512, 1999.

[5] A.-L. Barabási, Network Science, available from http://barabasilab.neu.edu/networksciencebook/, 2014.

[6] S.P. Borgatti, M.G. Everett, "A Graph-theoretic perspective on centrality", Social Networks, SON 499, pp. 1-19, 2005.

[7] G. Caldarelli, Scale-Free Networks, Oxford Univ. Press, Oxford, 2007.

[8] B. Chandrasekaran, J.R. Josephson, V.R. Benjamins, "What are ontologies and why do we need them?", IEEE Intelligent Systems, 14(1), pp. 20-26, 1999.

[9] R. Cowan, N. Jonard, "Knowledge portfolios and the organization of innovation networks", Academy of Management Review, 34 (2), pp. 320-342, 2009.

[10] M.L. de Almeida, G.A. Mendes, G.M. Viswanathan, L. R. da Silva, "Scale-free homophilic network", The European Physical Journal B, 86:38, 2013.

[11] M. Ebers, Explaining Inter-Organizational Network Formation in M. Ebers (ed), The Formation of Inter-Organizational Networks, 1997.

[12] P. Erdös, A. Rényi, "On random graphs", Publicationes Mathematicae, 6, pp. 290-297, 1959.
[13] G. Ferraro, A. Iovanella, "Choreography in inter-organizational innovation networks", arXiv:1311. 6609v2, 2013.
[14] C. Freeman, "Networks of innovator: A synthesis of research issue", Research Policy, 20, pp. 499-514, 1991.
[15] T.R. Gruber, "Toward principles for the design of ontologies used for knowledge sharing?", International Journal of Human-Computer Studies, 43, (5–6), pp. 907–928, 1995.
[16] K. Imai, Y. Baba, "Systemic Innovation and Cross-border Networks: Transcendent Markets and hierarchies to create a new techno-economic system", International Seminar on Contributions of Science and Technology to Economic Growth, OECD, Paris, 1989.
[17] M. McPherson, L. Smith-Lovin, J.M. Cook, "Birds of a Feather: Homophily in Social Networks", Annual Review of Sociology 27, pp. 415–444, 2001.
[18] M. E. J. Newman, M. Girvan, "Finding and evaluating community structure in networks", Physical Review E, 69, 026113, 2004.
[19] J. Scott, P.J. Carrington eds. The SAGE Handbook of Social Network Analysis, SAGE Publications, London, 2012.
[20] R. Studer, V. Richard Benjamins, D. Fensel, "Knowledge Engineering: Principles and methods", Data & Knowledge Engineering, 25, pp. 161-197, 2006.
[21] X.F. Wang, G. Chen, "Synchronization in scale-free dynamical networks: robustness and fragility", IEEE Transactions on Circuits and Systems I: Fundamental Theory and Applications, 49 (1), pp. 54-62, 2002.
[22] X.F. Wang, G. Chen, "Complex networks: small-world, scale-free and beyond", Circuits and Systems Magazine, IEEE Circuit and System Magazine, 3 (1), pp. 6-20, 2003.

General Session 4
Multi-agents Systems, Heuristics

Proceedings of ICCSA 2014
Normandie University, Le Havre, France - June 23-26, 2014

KINETIC WEALTH-EXCHANGE MODELS: A SHORT REVIEW

Marco Patriarca and Els Heinsalu*†

Abstract. We present an updated review of kinetic wealth-exchange models, that are minimal economy models in which interacting economic units exchange wealth. Despite their simplicity, they can describe and predict realistic shapes of wealth distribution. We start from the models of Angle, introduced in the social sciences already in the 80's, then we proceed through the models of Bennati, Drăgulescu and Yakovenko, and Chakraborti and Chakrabarti, and finally we focus on the immediate-exchange versions introduced recently. We also consider the influence of heterogeneity in the units parameters and discuss how it provides a simple and effective mechanism for the production of a fat tail in the wealth distribution.
Keywords. Kinetic Exchange models; wealth distribution; Boltzmann distribution; power law distribution; many-agent models.

1 Introduction

There is a link that has connected statistical mechanics and social sciences since their birth, lying in the fact that both of them have as study subject systems with an explicit statistical character [1, 2]. Year after year this link has become stronger as more and more scientist have underlined the importance of a quantitative approach in social sciences, see e.g. Refs. [3, 4, 5, 6, 7, 8, 9, 10].

In fact, many discoveries first made in the field of social sciences introduced new key concepts for statistical mechanics and later for the science of complex systems, such as the *fat tails* found by V. Pareto in the distribution of wealth [11, 12], the first formulation of the *random walk model* and of the associated *diffusion equation* made by L. Bachelier in his study of financial time series [13, 14, 15], and the *large fluctuations* observed by Mandelbrot in the time series of cotton price [16]. At the same time, for economists physics has often represented a prototype for modeling economic systems while economics relies more and more on the theory of stochastic processes and the science of complex systems [17].

There is a family of mathematical models of economy systems, that are the subject of the present contribution, in which the mentioned link is most clear. Namely, the *kinetic wealth exchange models*, introduced independently in different fields such as social sciences, economics, and physics. They provide a description of wealth flow in terms of stochastic wealth exchange between *units*, resembling the energy transfer between the molecules of a fluid [4, 18, 19]. The goal of this contribution is to provide an overview of such models discussing their general features.

We also consider the heterogeneous version, in order to illustrate how such simple models can generate realistic wealth distributions over a wide range of wealth, from small and intermediate values of wealth, where the wealth distributions are well fitted by a Γ-distribution [20, 21, 22, 23], up to the high-wealth region where the Pareto power-law is observed if suitably *diversified* units are introduced [24, 4, 19]. These results have opened the way to a simple, quantitative complex systems approach in modeling real wealth distributions, as the outcome of the wealth exchanges among economical units.

2 General structure of kinetic exchange models

Kinetic exchange models provide a minimal description of wealth exchange between economic units (representing, e.g., individuals, families, or companies) in a way formally similar to that in which energy is transferred between molecules of a fluid due to collisions [25, 26]. Such models were introduced independently in different fields such as social sciences [20, 27, 28], economics [29, 30, 31], and physics [32, 21, 22, 2, 33, 34]. John Angle [20, 27] originally introduced this type of models basing them on the surplus theory, with the goal of describing the origin of wealth inequalities.

Compared with other agent-based models of financial markets [35], the structure of kinetic exchange models is extremely simple, since they describe a market only in terms of wealth flows between economic units. No other elements of a market dynamics, such as price formation or the production-consumption processes, are considered explicitly. Even within such a simple framework, kinetic exchange models predict quite realistic shapes of wealth distributions [4] in all the ranges of wealth.

Kinetic exchange models assume that the total wealth of the system is conserved. This follows from wealth conservation during each single unit-unit interaction. The

*National Institute of Chemical Physics and Biophysics, Rävala 10, Tallinn 15042, Estonia. E-mails: marco.patriarca@kbfi.ee, els.heinsalu@kbfi.ee
†Manuscript received April 17, 2014

general dynamics can be formulated through the following update rule at a generic time iteration t,

$$x_j^{'} = x_j + \Delta x_{jk}\,, \qquad x_k^{'} = x_k - \Delta x_{jk}\,, \tag{1}$$

where j and k are the labels of the two interacting units chosen randomly among the N units of the system ($j,k = 1,\ldots,N$), x_j and x_k ($x_j^{'}$ and $x_k^{'}$) are the wealths of the trading units j and k before (after) the exchange, and $\Delta x_{jk} = -\Delta x_{kj}$ the exchanged amount of wealth. Without loss of generality, in Eqs. (1) the minus (plus) sign has been chosen for j (k). What is the unit whose wealth increases or decreases depends on the sign of Δx_{jk}.

Many numerical works have shown that the equilibrium wealth distribution coincides formally with the Gibbs energy distribution of a system of particles. In fact, this is just what is expected theoretically from the conservation of the total wealth of the system, analogously to mechanical systems in which energy is conserved.

The dynamics of most of the kinetic exchange models can be formulated in a unified way through an amount of exchanged wealth in Eqs. (1) given by $\Delta x_{jk} = \tilde{\omega}_{jk}\, x_k - \tilde{\omega}_{kj}\, x_j$, as discussed in Ref. [25], where $\tilde{\omega}_{jk}$ and $\tilde{\omega}_{kj}$ are two suitable stochastic variables extracted independently at each trade and limited in the interval $(0,1)$. A more general formulation basically including all kinetic exchange models is through an exchanged wealth given by

$$\Delta x_{jk} = \tilde{\omega}_{jk}\, x_k - \tilde{\omega}_{kj}\, x_j + \tilde{\xi}_{jk}\,, \tag{2}$$

where $\tilde{\xi}_{jk}$ is another stochastic variable. In this way, the total exchanged amount of wealth Δx_{jk} receives a contribution from the random variable $\tilde{\xi}_{jk}$, representing an additive contribution (the only constraint on the value of $\tilde{\xi}_{jk}$ is imposed by the available wealth), and another contribution proportional to the units wealths through the terms $\tilde{\omega}_{jk}\, x_k$ and $-\tilde{\omega}_{kj}\, x_j$. As discussed below, the models studied so far consider either the absolute contribution $\tilde{\xi}_{jk}$ or the multiplicative contributions proportional to the units wealth, while, to the best of our knowledge, no models studies both types of contribution together.

The stochastic variable $\tilde{\omega}_j$ represents the fraction of wealth given by agent j to k during the transaction, and vice versa for $\tilde{\omega}_k$.

Further generalizations of kinetic exchange models can be easily expressed in terms of the properties of the stochastic variables $\tilde{\omega}_i$, while maintaining the same formulation of the exchange law.

3 Models

3.1 The models of Angle

Here we consider the model introduced by John Angle in 1983 in Refs. [36, 20]. The other model of Angle, i.e., the OPIP *One-Parameter Inequality Process*, is illustrated below. The Angle model is inspired by the surplus theory of social stratification and describe how a non-uniform wealth distribution arises from wealth exchanges between individuals. The dynamical evolution is determined by Eqs. (1) with

$$\Delta x_{jk} = \epsilon\, \omega\, [\eta_{j,k}\, x_j - (1-\eta_{j,k})\, x_k]\,. \tag{3}$$

Here ϵ and $\eta_{j,k}$ are random variables: ϵ is a random number in the interval $(0,1)$, which can be distributed either uniformly or with a certain probability distribution $g(\epsilon)$, as in some generalizations of the basic model [36]; $\eta_{j,k}$ is a random dichotomous variable responsible for the unidirectionality of the wealth flow as well as for the nonlinear character of the dynamics. It is a function of the difference between the wealths of the interacting agents j and k, $\eta_{j,k} \equiv \phi(x_k - x_j)$, assuming the value $\eta_{j,k} = 1$ with probability p_0 for $x_j > x_k$ or the value $\eta_{j,k} = 0$ with probability $1 - p_0$ for $x_k > x_j$. The value $\eta_{j,k} = 1$ produces a wealth transfer $|\Delta x_{jk}| = \epsilon\, \omega\, x_j$ from agent j to k, while the value $\eta_{j,k} = 0$ corresponds to a wealth transfer $|\Delta x_{jk}| = \epsilon\, \omega\, x_k$ from k to j.

A special case of this model is that with symmetrical interaction, obtained for $p_0 = 1/2$. Notice that for this value of p_0 the random variable $\eta_{j,k} \equiv \eta$ becomes independent of x_j and x_k. The equilibrium wealth distribution for a generic value of λ is found to be described by a Γ-distribution,

$$f_{\alpha,\beta}(x) = \frac{\beta}{\Gamma(\alpha)} (\beta x)^{\alpha-1} \exp(-\beta x)\,, \tag{4}$$

with equal shape and rate parameters [37]

$$\alpha = \beta = \frac{1+2\lambda}{2(1-\lambda)}\,. \tag{5}$$

The fact that $\beta = \alpha$ is determined by the average wealth $\langle X\rangle = \alpha/\beta = 1$, that in turn follows from the assumed initial conditions $x_i = 1$, $i = 1,\ldots,N$.

This expression provides a value of α and β that is just half of that of the Chakraborti and Chakrabarti model considered below, see Eq.(11). Since $\lambda = 1 - \omega \in [0,1)$, the parameter α is a real number in the interval $[1/2,\infty)$. Notice the divergence at $x \to 0$ that will persist as long as $\alpha < 1$, meaning saving propensities $\lambda < 1/4$ (this is visible in Fig. 1 for the cases $\lambda = 0$, $\lambda = 0.1$, and $\lambda = 0.2$). At $\lambda = 1/4$ the exponential distribution is obtained, while for $\lambda > 1/4$ the distribution assumes a bell shape with mode $\bar{x} > 0$. In all the simulations the average wealth is $\langle x\rangle = 1$.

The Angle model has a simple mechanical analogue if the quantity $D = 2\alpha$ defined is interpreted as an effective dimension for the system. In fact, it can be checked that the distribution $f_{\alpha,\alpha}(x)$ is the equilibrium distribution for the kinetic energy of a perfect gas in D dimensions as well as for the potential energy of a D-dimensional harmonic oscillator or a general harmonic system with D degrees of freedom. This definition of effective dimension

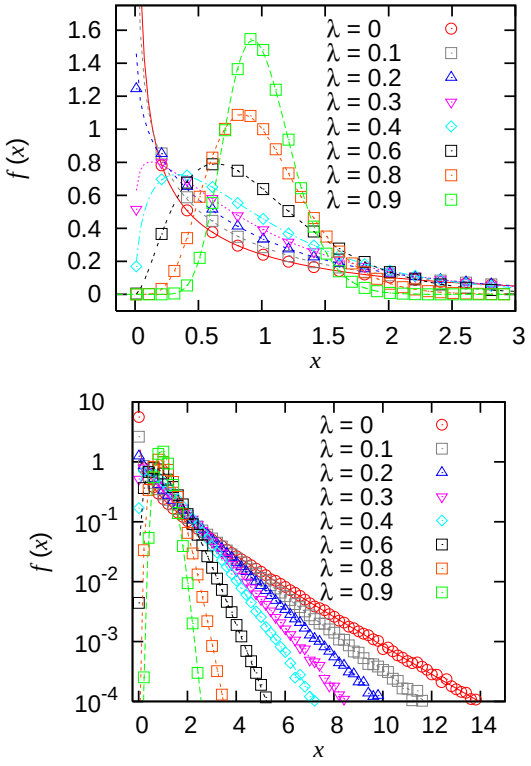

Figure 1: Equilibrium wealth distribution for the version of the Angle model defined by Eqs. (3) with $p_0 = 1/2$: results of numerical simulations (symbols) are compared with the fitting using a Γ-distribution (curves) for different values of the saving parameter $\lambda = 1 - \omega$ in linear (above) and semi-log (below) scale. The value of α is given by Eq. (5). See text for further details.

is consistent with the equipartition theorem, see Ref. [38] for details.

The OPIP model is described in detail in Refs. [39, 28]. It differs from the previous Angle model in that it only employs a stochastic dichotomic variable η_{jk}, which can assume randomly the values $\eta_{jk} = 0$ or $\eta_{jk} = 1$. The model is defined by Eqs. (1) with

$$\Delta x_{jk} = -\eta_{jk}\omega x_k + (1 - \eta_{jk})\omega x_j \,. \tag{6}$$

The model describes a unidirectional flow of wealth from agent k toward agent j for $\eta_{jk} = 1$ or vice versa for $\eta_{jk} = 0$. For the particular case in which the two values of η_{jk} are always equiprobable, one can rewrite the process, without loss of generality, with a $\Delta x_{jk} = \omega x_k$ in Eqs. (1). As found in Refs. [39, 28], for small enough ω the stationary wealth distribution is well fitted by a Γ-distribution with $\alpha \approx 1/\omega - 1 = \lambda/(1 - \lambda)$. We find that this fitting (not shown) is very good at least up to $\lambda \approx 0.7$.

3.2 The model of Bennati

Another model was introduced in 1988 by Eleonora Bennati [29, 30]. Its basic version, that we discuss here, is a simple unidirectional model where units exchange constant amounts Δx_0 of wealth [29, 30, 31]. In principle, in the Bennati model a situation where the wealths of the agents would become negative could occur and this is prevented allowing the transaction to take place only if the condition $x'_j, x'_k \geq 0$ is fulfilled: the process is described by Eq. (1) with $\Delta x_{jk} = \Delta x_0$ if $x'_j, x'_k \geq 0$ and with $\Delta x_{jk} = 0$ otherwise. Since the wealth can vary only by a constant amount Δx_0, the model reminds a set of particles exchanging energy by emitting and re-absorbing light quanta of equal energy. Analytically the equilibrium state of the model is well described by an exponential distribution. The main difference respect to the other models considered here is that in the Bennati model the amount of wealth exchanged between the two agents is independent of x_i, while in the other models represents a multiplicative random process, since $\Delta x_{jk} \propto x_i$.

3.3 The model of Yakovenko

The models introduced in 2000 by A. Dragulescu and V. M. Yakovenko [32] were conceived to describe flow and distribution of money. They have a sound interpretation both of the conservation law $x'_j + x'_k = x_j + x_k$, since money is measured in the same unit and conserved during transactions, and of the stochasticity of the update rule, representing a randomly chosen realization of trade. Various models were considered in Ref. [32], with a $\Delta_{jk}x$ either constant (similarly to the Bennati model discussed above) or dependent on the values x_i of the agents; also more realistic models, in which e.g. firms were introduced or debts were allowed. For simplicity, we consider among them the model which probably best represents

the random character of kinetic wealth exchange models, in which the total initial amount $x_j + x_k$ is reshuffled randomly between the two interacting units,

$$\begin{aligned} x'_j &= \epsilon\,(x_j + x_k)\,, \\ x'_k &= \bar{\epsilon}\,(x_j + x_k)\,. \end{aligned} \tag{7}$$

Equivalently, the dynamics can be described by Eqs. (1), with

$$\Delta x_{jk} = \bar{\epsilon}\,x_j - \epsilon\,x_k\,. \tag{8}$$

The equilibrium distribution is well fitted by the exponential distribution $f_{2,2}(x)$. A mechanical analogue is a gas, in which particles undergo pair collisions in which some energy is exchanged [40].

3.4 The model of Chakraborti and Chakrabarti

In the model introduced in 2000 by A. Chakraborti and B. Chakrabarti [33] the general exchange rule reads,

$$\begin{aligned} x'_j &= \lambda x_j + \epsilon\,(1-\lambda)(x_j + x_k)\,, \\ x'_k &= \lambda x_k + \bar{\epsilon}\,(1-\lambda)(x_j + x_k)\,, \end{aligned} \tag{9}$$

where $\bar{\epsilon} = 1 - \epsilon$. Here the new wealth x'_j (x'_k) is expressed as a sum of the saved fraction $\lambda x'_j$ ($\lambda x'_k$) of the initial wealth and a random fraction ϵ ($\bar{\epsilon}$) of the total remaining wealth, obtained summing the respective contributions of agents j and k. Equations (9) are equivalent to Eqs. (1), with

$$\Delta x_{jk} = \omega(\bar{\epsilon}\,x_j - \epsilon\,x_k) = (1-\lambda)(\bar{\epsilon}\,x_j - \epsilon\,x_k)\,. \tag{10}$$

Like in the Angle model, at equilibrium the system is well described by a Γ-distribution (4) but with a parameter α given by [38, 41]

$$\alpha \equiv \frac{D}{2} = \frac{1+2\lambda}{1-\lambda} = \frac{3}{\omega} - 2\,, \tag{11}$$

which is twice the value of the corresponding parameter of the Angle model with $p_0 = 1/2$, discussed above.

In Fig. 2 numerical results are compared with the fitting based on Eq. (11). In this case the probability density is always finite for $x \to 0$, since for $\lambda = 0$ ($\omega = 1$) one has $\alpha = 1$ and the distribution does not diverge but is equal to the exponential function.

3.5 Models of immediate exchange

In this section we consider a version of kinetic exchange model introduced recently [42] describing a market where encounters between units are accompanied by immediate exchanges. By "immediate exchange" it is meant here for example the type of interchanges that characterize barter, where goods are directly exchanged without using a medium of exchange, such as money, or market

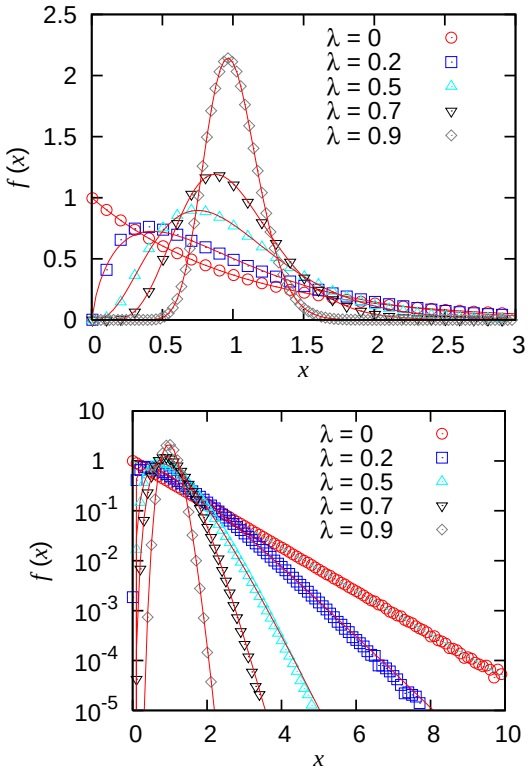

Figure 2: Equilibrium wealth distributions of the model of Chakraborti and Chakrabarti in linear and semi-log scale for different values of the saving parameter λ in the closed economy model defined by Eqs. (9). The continuous curves are the fitting functions, i.e. a Γ-distribution of the form Eq. (4) just as for the Angle model, but with the value of $\alpha(\lambda)$ is given by Eq. (11).

economies where goods are exchanged with money immediately or according to some agreed time schedule. Immediate exchanges are to be contrasted with the "delayed exchanges", characterizing e.g. gift economies, where for cultural reasons valuables are given without an explicit agreement for immediate or future rewards. In the latter case one has unidirectional transfers of wealth from one unit to another one.

In the barter interpretation, each unit i ($i = 1, 2, \ldots, N$) has some items to exchange for something else; the total value of the items is x_i. In the time evolution two units j and k are extracted randomly at every time iteration and interchange something with value $\epsilon_j x_j$ and $\epsilon_k x_k$, respectively, where ϵ_j and ϵ_k are two independent uniform random numbers in the interval $(0, 1]$, different at each iteration. The random nature of these quantities describes the situation in which each time when somebody is trying to do a trade it can be of a different object among all the things he owns and is willing to exchange for something else. The model does not distinguish between different types of goods and focuses on the amounts of wealth exchanged between the units. Therefore one of the goods can be possibly understood as the currency in use and the model can be reinterpreted as one of a currency-based market. In the latter case the random numbers describe intrinsic fluctuations of prices and currency values. Correspondingly, the delayed exchanges can describe payments of services without immediate reward, e.g., insurance business.

The dynamics of the proposed model can be defined by the following equations:

$$\begin{aligned} x_j^{'} &= (1-\epsilon_j)x_j + \epsilon_k x_k \,, \\ x_k^{'} &= (1-\epsilon_k)x_k + \epsilon_j x_j \,, \end{aligned} \tag{12}$$

which can be rewritten in the same form of Eqs. (1) with

$$\Delta x_{jk} = \epsilon_k x_k - \epsilon_j x_j \,. \tag{13}$$

Because $\epsilon_j, \epsilon_k > 0$ then from Eqs. (1) together with (13) it is clear that a situation where $x_i = X$ (i.e., a unit i owns all the wealth of the system) or $x_i = 0$ (i.e., a unit i is totally poor) is not possible at any moment of time. Numerical simulations show that the equilibrium distribution $f(x)$ of wealth is a Γ-distribution (4) with $\alpha = \beta = 2$, i.e., $f(x) = f_{2,2}(x) = 4x\exp(-2x)$. Thus, $f(0) = f_{2,2}(0) = 0$ and $f(x)$ decays exponentially at large x.

The dynamics described by Eqs. (12) is closer than other kinetic exchange models to inter-molecular energy exchanges, in which, according to kinetic theory, the energy exchanged in a collision between two molecules j and k has the form given by Eq. (13) with ϵ_j and ϵ_k depending on the initial directions of the molecular velocities and to be considered *independent random numbers* in the hypothesis of molecular chaos [43].

The immediate-exchange model introduced above is formally very similar to the model introduced by Drăgulescu and Yakovenko [32] described above, in which, however, only one random number ϵ is present, and that can be re-obtained from the model introduced above setting $\epsilon = \epsilon_k$ and $\epsilon_j = 1 - \epsilon_k$. However, in the context of wealth exchanges such a strong correlation between ϵ_j and ϵ_k is difficult to understand. In fact, the dynamics of the Drăgulescu and Yakovenko model can be better understood if rewriting it as a random reshuffling in a single time of the total initial amount $x_j + x_k$ between the two interacting units, see Eq. (7).

The presence of two independent random numbers ϵ_j and ϵ_k (instead of the single random number ϵ) implies basically different interpretations of the models. In fact, the model of Drăgulescu and Yakovenko leads to the exponential equilibrium wealth distribution describing a society where most of the people are really poor and the distribution mode is $\bar{x} = 0$. Instead, the model proposed leads to the Γ-distribution with shape and rate parameters $\alpha = \beta = 2$, which corresponds to a society where most of the people have the wealth around the average value $\langle X \rangle = 1$ (assuming that initially each unit has a wealth $x = 1$), with a mode $\bar{x} = 1/2$ and actually there is nobody with $x = 0$, $f(x{=}0) = 0$.

Thus, the exponential shape of the equilibrium wealth distribution of the Drăgulescu and Yakovenko model arises from the possibility that during a given interaction a unit can in principle lose *all* wealth that will go to some other unit. Considering Eq. (8) this will happen to unit j whenever the extracted value of the random number ϵ is close enough to zero. The model of Chakraborti and Chakrabarti [33] is in this respect illuminating, since it shows that due to the introduction of saving (through a saving propensity $\lambda > 0$) such a situation never occurs and there are no units for $x \to 0$, leading not to the exponential but to a Γ-distribution (4) with shape parameter (10). Therefore, units carrying out immediate exchanges can be formally seen as equivalent to units with a saving propensity. More precisely the immediate exchange model leads to the same equilibrium wealth distribution as the model of Chakraborti and Chakrabarti with $\lambda = 1/4$. The fundamental difference is that in the model proposed here, the situation with $x_i = 0$ is excluded naturally without further assumptions solely by the fact that even if during an (actual) exchange a unit j gives away everything, he always receives something in exchange from the other unit k and thus, after the transaction always $x_i > 0$ for each i. Considering Eqs. (12), the probability that unit j loses all wealth during a single interaction is definitely smaller, respect to the analogous one, e.g., in the Drăgulescu-Yakovenko model, since here this will happen only if ϵ_j is close enough to one *and* ϵ_k to zero.

It is worth comparing this model with the first model introduced by Angle [36, 20] that assumes a unidirectional flow in which with probability p_0 a random fraction ϵ of the wealth x_j of unit j is transferred to unit k, while with probability $1 - p_0$ a random fraction ϵ of the wealth x_k

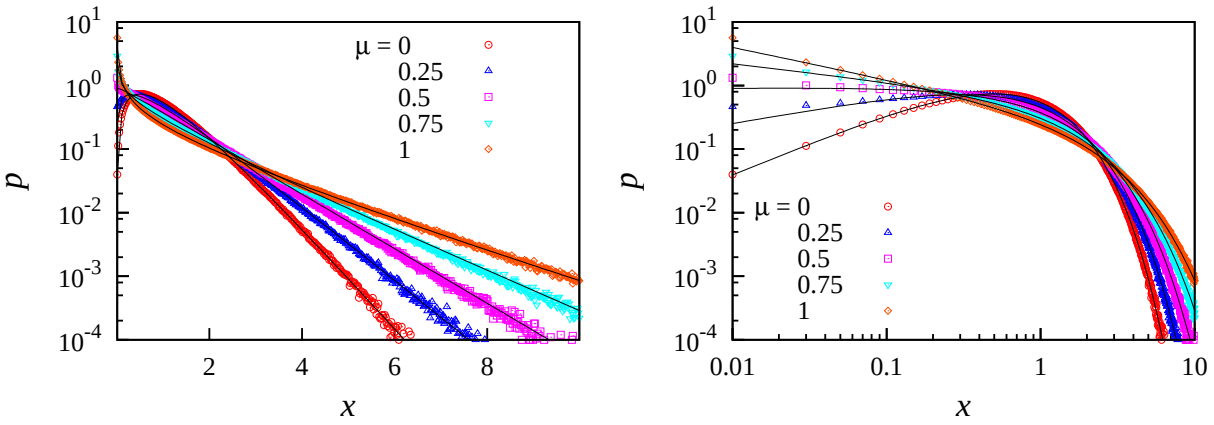

Figure 3: Log-Log (left) and Log (right) plot of the equilibrium distribution $p(x)$ of wealth x for different values of μ, i.e., for different fractions of unidirectional interactions. The value $\mu = 0$ corresponds to immediate exchanges only and $\mu = 1$ to the situation when all the interactions are unidirectional. Dots represent results from numerical simulations, while lines are a fitting using the Γ-distribution (4) with $\alpha = \beta$ and the values of α given by Eq. (14) for different values of μ.

of unit k is transferred to unit j, and for the sake of simplicity the particular the case of symmetrical interaction $p_0 = 1/2$, see Eq. (3) above. In this case the growth of the fraction of poor units with wealth close to zero is even more dramatic than in the Drăgulescu-Yakovenko reshuffling dynamics considered above: in fact, the resulting equilibrium wealth distribution of this model is found to *diverge* at $x \to 0$, signaling a wealth accumulation in the hands of a very few units.

The value $\alpha = 2$ of the immediate exchange model introduced above is recovered for $\lambda = 1/2$.

One could expect that (at least in the case of symmetrical interactions) that the series of unidirectional wealth flows of the Angle model provides results equivalent to those produced by a superposition of immediate (bidirectional) exchanges. However, the basically distinct shapes of the equilibrium wealth distributions at $x \to 0$ in the model of Angle and in the immediate-exchange model proposed here, reveal that this is not the case.

To better understand this issue, one can study a system where a fraction μ of the interactions are unidirectional flows while the remaining fraction $1 - \mu$ are immediate exchanges. Namely, at each time iteration the pair of units extracted for a trade will carry out with probability μ the unidirectional transaction and with probability $1-\mu$ the immediate exchange defined by Eq. (13).

If $\mu = 0$, i.e., all interactions are immediate exchanges, the equilibrium wealth distribution is a Γ-distribution with $\alpha = 2$. For any $\mu > 0$ the equilibrium distributions are still well described for sufficiently large x by a Γ-distribution, see Fig. 3. The dependence of α on μ is given by

$$\alpha(\mu) = 2\exp[-\ln(4)\mu] \ = 2^{1-2\mu}\,. \qquad (14)$$

For $\mu = 1/2$, i.e., when half of the interactions are unidirectional and half are immediate exchanges, $\alpha = 1$ and the equilibrium wealth distribution is exponential, $f(x) = \exp(-x)$. For $x < 0.05$ the distributions deviate from the Γ-distributions, see Fig. 3 for $x \to 0$; the deviation is the larger the larger is the fraction of unidirectional interactions, μ. For $\mu = 1$ the model of Angle is recovered. Also in this case, one can think of the effect of immediate exchanges in terms of an effective saving $\lambda > 0$. Putting together Eqs. (5) and (14) one can find that

$$\lambda(\mu) = \frac{2^{2(1-\mu)} - 1}{2^{2(1-\mu)} + 2}\,. \qquad (15)$$

From here we can see that to $\mu 1$ corresponds $\lambda = 0$, i.e., the units can lose everything. Instead, $\mu = 1/2$ leads to the same equilibrium distribution as the model of Angle with saving propensity $\lambda = 1/4$, and $\mu = 0$ to the equilibrium distribution with saving propensity $\lambda = 1/2$. Distributions corresponding to values of $\lambda > 1/2$ cannot be obtained, since they would correspond to negative values of μ.

4 Heterogeneous models

Here heterogeneity in kinetic exchange models is considered. For the sake of clarity we limit ourselves to consider an example the generalization of the Chakraborti-Chakrabarti model considered above. Heterogeneity is introduced by assigning different values for each unit i to the only system parameter, that is ω_i (λ_i). The formulation of the heterogeneous model is obtained straightforwardly from that of the corresponding homogeneous ones by replacing the generic term $\omega\, x_i$ (λx_i) with $\omega_i x_i$ ($\lambda_i x_i$) in the evolution law. Therefore Eqs. (9) become

$$\begin{aligned} x'_j &= \lambda_j x_j + \epsilon\,[(1-\lambda_j)x_j + (1-\lambda_k)x_k]\,, \\ x'_k &= \lambda_k x_k + \bar{\epsilon}\,[(1-\lambda_j)x_j + (1-\lambda_k)x_k]\,, \end{aligned} \qquad (16)$$

and the exchanged amount of wealth in Eqs. (10) is now

$$\Delta x = \bar{\epsilon}\,\omega_j\,x_j - \epsilon\,\omega_k\,x_k = \bar{\epsilon}(1-\lambda_j)x_j - \epsilon(1-\lambda_k)x_k\,. \quad (17)$$

The set of parameters $\{\omega_i\}$ ($\{\lambda_i\}$) is constant in time and specifies the profiles of the agents. The values $\{\omega_i\}$ ($\{\lambda_i\}$) are assumed to be distributed in the interval between 0 and 1 with probabilities h_i (g_i) and $\sum_i h_i = 1$ ($\sum_i g_i = 1$). In the limit of an infinite number of agents, one can introduce a probability distribution $h(\omega)$ [$g(\lambda)$], with $\int_0^1 d\omega\, h(\omega) = 1$ [$\int_0^1 d\lambda\, g(\lambda) = 1$].

Various analytical and numerical studies of this model have been carried out [4, 19, 39, 24, 44, 45, 46, 47, 48, 49, 50, 51] and as a main result it has been found that the exponential law remains limited to intermediate x-values, while a Pareto power law appears at larger values of x. Such a shape is prototypical for real wealth distributions.

A most interesting feature of the equilibrium state is that the shape of the wealth distribution $f_i(x)$ of agent i maintains the shape of a Γ-distribution, despite the sum of the wealth distributions of the single agents, $f(x) = \sum_i f_i(x)$, produces a power law tail. Vice versa, one could say that the global wealth distribution $f(x)$ can be resolved as a mixture of partial wealth probability densities $f_i(x)$ with exponential tail, with different parameters. For instance, the corresponding average wealth depends on the saving parameter as $\langle x\rangle_i \propto 1/(1-\lambda_i) = 1/\omega_i$; see Refs. [52, 50, 53] for details.

5 Conclusions

We have briefly reviewed the kinetic wealth-exchange models of closed economy systems.

The homogeneous models can describe realistically wealth distributions at a small wealth scale, especially within the immediate-exchange versions, as well as the intermediate wealth region. The corresponding Γ-distribution is known to be just the canonical energy distribution of a general statistical many-particle system, where the number of degrees of freedom is related to the shape parameter of the Γ-distribution. This suggests that it is the same simple mechanism of exchange of a certain quantity and the conservation of such exchanged quantity is at the origin of the observed Γ-distribution both in condensed matter and in economics.

The heterogeneous kinetic wealth exchange models turn out to be particularly relevant in the study of real wealth distributions in the large-wealth region, where the Pareto power law tail is located. The reason s that in a heterogeneous kinetic wealth exchange model an overlap of the wealth distributions of all the single agents takes place, that produces a power law tail. This mechanism seems to be a quite general one and is completely within the framework of canonical statistical mechanics.

Acknowledgements

This work has been supported by the Estonian Science Foundation via grant no. 9462 (M.P., E.H.).

References

[1] P. Ball. "The physical modelling of society: a historical perspective." *Physica A*, vol. 314, p. 1, 2002.

[2] V. Yakovenko, J. J. Barkley Rosser. "Statistical Mechanics of Money, Wealth, and Income." *Rev. Mod. Phys.*, vol. 81, pp. 1703–1725, 2009.

[3] J.-P. Bouchaud. "The subtle nature of financial random walks." *CHAOS*, vol. 15, p. 026104, 2005.

[4] A. Chatterjee, S. Yarlagadda, B. K. Chakrabarti (editors). *Econophysics of Wealth Distributions - Econophys-Kolkata I.* Springer, 2005.

[5] J. Feigenbaum. "Financial physics." *Rep. Prog. Phys.*, vol. 66, p. 1611, 2003.

[6] R. N. Mantegna, H. E. Stanley. *An Introduction to Econophysics.* Cambridge University Press, Cambridge, 2000.

[7] D. Stauffer, C. Schulze. "Microscopic and macroscopic simulation of competition between languages." *Phys. Life Rev.*, vol. 2, p. 89, 2005.

[8] D. Stauffer, S. M. de Oliveira, P. M. C. de Oliveira, J. S. de Sa Martins. *Biology, Sociology, Geology by Computational Physicists.* Elsevier Science, 2006.

[9] B. K. Chakrabarti, A. Chakraborti, A. Chatterjee (editors) *Econophysics and Sociophysics: Trends and Perspectives.* Wiley - VCH, Berlin, 1 edn., 2006.

[10] R. Taagepera. *Making social sciences more scientific. The need for predictive models.* Oxford University Press, Oxford, 2008.

[11] V. Pareto. *Cours d'economie politique.* Rouge, Lausanne, 1897.

[12] V. Pareto. *Manual of political economy.* Kellag, New York, 1971.

[13] L. Bachelier. "Theorie de la Speculation." *Annales Scientifiques de l'Ecole Normale Superieure*, vol. III-17, p. 21, 1900.

[14] "English Translation of: L. Bachelier, Theorie de la Speculation, Annales Scientifiques de l'École Normale Superieure (1900) III -17." In S. Haberman, T. A. Sibbett (editors) "History of Actuarial Science," vol. 7, p. 15. Pickering and Chatto Publishers, London, 1995.

[15] A. J. Boness. "English Translation of: L. Bachelier, Theorie de la Speculation, Annales de l'Ecole Normale Superieure III-17 (1900), pp. 21-86." In P. H. Cootner (editor) "The Random Character of Stock Market Prices," p. 17. MIT, Cambridge, MA, 1967.

[16] B. B. Mandelbrot. "The variation of certain speculative prices." *J. Business*, vol. 36, p. 394, 1963.

[17] W. B. Arthur. *Science*, vol. 284, p. 107, 1999.

[18] B. Hayes. "Follow the Money." *Am. Sci.*, vol. 90, p. 400, 2002.

[19] A. Chatterjee, B. Chakrabarti. "Kinetic exchange models for income and wealth distributions." *Eur. Phys. J. B*, vol. 60, p. 135, 2007.

[20] J. Angle. "The surplus theory of social stratification and the size distribution of personal wealth." *Social Forces*, vol. 65, pp. 293–326, 1986.

[21] A. Dragulescu, V. M. Yakovenko. "Exponential and power-law probability distributions of wealth and income in the United Kingdom and the United States." *Physica A*, vol. 299, p. 213, 2001.

[22] A. Dragulescu, V. M. Yakovenko. "Evidence for the exponential distribution of income in the USA." *Eur. Phys. J. B*, vol. 20, p. 585, 2001.

[23] J. C. Ferrero. "The statistical distribution of money and the rate of money transference." *Physica A*, vol. 341, p. 575, 2004.

[24] J. R. Iglesias, S. Goncalves, G. Abramsonb, J. L. Vega. "Correlation between risk aversion and wealth distribution." *Physica A*, vol. 342, p. 186, 2004.

[25] M. Patriarca, E. Heinsalu, A. Chakraborti. "Basic kinetic wealth-exchange models: common features and open problems." *Eur. Phys. J. B*, vol. 73, pp. 145–153, 2010.

[26] M. Patriarca, A. Chakraborti. "Kinetic exchange models: From molecular physics to social science." *Am. J. Phys.*, vol. 81, pp. 618–623, 2013.

[27] J. Angle. "The Inequality Process and the distribution of income to blacks and whites." *J. Math. Sociol.*, vol. 17, p. 77, 1992.

[28] J. Angle. "The inequality process as a wealth maximizing process." *Physica A*, vol. 367, pp. 388–414, 2006.

[29] E. Bennati. *La simulazione statistica nell'analisi della distribuzione del reddito: modelli realistici e metodo di Monte Carlo.* ETS Editrice, Pisa, 1988.

[30] E. Bennati. "Un metodo di simulazione statistica nell'analisi della distribuzione del reddito." *Rivista Internazionale di Scienze Economiche e Commerciali*, vol. 35, p. 735, 1988.

[31] E. Bennati. "Il metodo Monte Carlo nell'analisi economica." *Rassegna di lavori dell'ISCO*, vol. X, p. 31, 1993.

[32] A. Dragulescu, V. M. Yakovenko. "Statistical mechanics of money." *Eur. Phys. J. B*, vol. 17, pp. 723–729, 2000.

[33] A. Chakraborti, B. K. Chakrabarti. "Statistical mechanics of money: How saving propensity affects its distribution." *Eur. Phys. J. B*, vol. 17, pp. 167–170, 2000.

[34] A. Chakraborti. "Distribution of money in model markets of economy." *Int. J. Mod. Phys. C*, vol. 13, pp. 1315–1321, 2002.

[35] E. Samanidou, E. Zschischang, D. Stauffer, T. Lux. "Agent-based models of financial markets." *Rep. Prog. Phys.*, vol. 70, pp. 409–450, (2007.

[36] J. Angle. "The surplus theory of social stratification and the size distribution of personal wealth." In "Proceedings of the American Social Statistical Association, Social Statistics Section," pp. 395–400. Alexandria, VA, 1983.

[37] M. Patriarca, E. Heinsalu, R. Kitt, J. Kalda. "Econophysics studies in Estonia." *Science&Culture*, vol. 76, pp. 374–379, 2010.

[38] M. Patriarca, A. Chakraborti, K. Kaski. "Statistical model with a standard gamma distribution." *Phys. Rev. E*, vol. 70, p. 016104, 2004.

[39] J. Angle. "The statistical signature of pervasive competition on wage and salary incomes." *J. Math. Sociol.*, vol. 26, pp. 217–270, 2002.

[40] C. A. Whitney. *Random processes in physical systems. An introduction to probability-based computer simulations.* Wiley Interscience, NY, 1990.

[41] M. Patriarca, A. Chakraborti, K. Kaski. "Gibbs versus non-Gibbs distributions in money dynamics." *Physica A*, vol. 340, p. 334, 2004.

[42] E. Heinsalu, M. Patriarca. "Uni- versus bi-directional kinetic exchange models." *Int. J. Comp. Economics and Econometrics, in press*, 2013.

[43] A. Chakraborti, M. Patriarca. "Gamma-distribution and Wealth inequality." *Pramana J. Phys.*, vol. 71, p. 233, 2008.

[44] P. Repetowicz, S. Hutzler, P. Richmond. "Dynamics of Money and Income Distributions." *Physica A*, vol. 356, p. 641, 2005.

[45] A. Chatterjee, B. K. Chakrabarti, S. S. Manna. "Money in Gas-Like Markets: Gibbs and Pareto Laws." *Physica Scripta T*, vol. 106, p. 367, 2003.

[46] A. Das, S. Yarlagadda. "A distribution function analysis of wealth distribution." *arxiv.org:cond-mat/0310343*, 2003.

[47] A. Chatterjee, B. K. Chakrabarti, S. S. Manna. "Pareto law in a kinetic model of market with random saving propensity." *Physica A*, vol. 335, p. 155, 2004.

[48] A. Chatterjee, B. K. Chakrabarti, R. B. Stinchcombe. "Master equation for a kinetic model of trading market and its analytic solution." *Phys. Rev. E*, vol. 72, p. 026126, 2005.

[49] A. Das, S. Yarlagadda. "An analytic treatment of the Gibbs–Pareto behavior in wealth distribution." *Physica A*, vol. 353, p. 529, 2005.

[50] M. Patriarca, A. Chakraborti, K. Kaski, G. Germano. "Kinetic theory models for the distribution of wealth: Power law from overlap of exponentials." In A. Chatterjee, S.Yarlagadda, B. K. Chakrabarti (editors) "Econophysics of Wealth Distributions," p. 93. Springer, 2005.

[51] A. Silva, V. Yakovenko. "Temporal evolution of the thermal and superthermal income classes in the USA during 1983-2001." *Europhys. Lett.*, vol. 69, pp. 304–310, 2005.

[52] A. Chatterjee, S. Yarlagadda, B. K. Chakrabarti (editors) *Econophysics of Wealth Distributions.* Springer, 2005.

[53] M. Patriarca, A. Chakraborti, G. Germano. "Influence of saving propensity on the power law tail of wealth distribution." *Physica A*, vol. 369, p. 723, 2006.

Proceedings of ICCSA 2014
Normandie University, Le Havre, France - June 23-26, 2014

SCALING LAWS IN CHENNAI BUS NETWORK

Atanu Chatterjee and Gitakrishnan Ramadurai *

Abstract. In this paper, we study the structural properties of the complex bus network of Chennai. We formulate this extensive network structure by identifying each bus stop as a node, and a bus which stops at any two adjacent bus stops as an edge connecting the nodes. Rigorous statistical analysis of this data shows that the Chennai bus network displays small-world properties and a scale-free degree distribution with the power-law exponent, $\gamma > 3$.

Keywords. Chennai bus network, Scaling laws, Transportation network

1 Introduction

1.1 Chennai Bus Network

Chennai is one of the metropolitan cities in India with a structured and a close-knit bus transport network. The Chennai bus network (CBN) is operated by the Metropolitan Transport Corporation (MTC), a state government undertaking. Spanning an area of 3,929 sq. km and with over 800 routes sprawling across entire Chennai, this extensive network also boasts of the largest bus terminus in Asia. With the population of the city being the sixth largest in the country, this medium of transport is most widely used for day-to-day commutation.

The reason that the bus network, in general, achieves this favourable status lies primarily in two factors: (i) *cost*, and (ii) *penetration*. With high volume of commuters flowing through this network each day, the cost of travel per day, per person becomes significantly low. Although, this is a parameter which is usually met by every other public transport system, the penetration factor is the one which significantly makes bus networks the prime mode of transportation in cities. A high penetration effect exhibited by a bus network enables a person to travel between any two points in the city very easily which is in contrast to other public modes of transportation, where geographical constraints associated with the network layout are much higher in number. Thus, bus transportation allows flexibility in travel. A natural question arises here; what is the least number of buses one should change to go from one place to another? Or more precisely, why do we require changing buses at all? To answer these questions, we need to look at a more abstract and networked structure of the bus routes, and argue based on its various statistical properties.

*Both the authors are affiliated with the Department of Civil Engineering, Transportation Engineering Division, Indian Institute of Technology Madras, Chennai 600036, India. E-mails: atanu@smail.iitm.ac.in, gitakrishnan@iitm.ac.in

1.2 Complex Networks: overview

The recent surge of interest in the field of network science has caused researchers to formulate almost every physical system as an interacting network (see [1 - 8]). We define a network as a graph, $\mathscr{G}$, consisting of links, L, and nodes, N, in a tuple, $\mathscr{G} = (N, L)$ where, $N = (n_1, n_2, ...) \in \Re$ and $L = N \times N \in \Re^2$. When such a network shows non-trivial properties like the patterns in which the wiring between the nodes occur, then such a network is usually termed as a complex network [3 - 4]. The non-triviality in the properties arises primarily from the varying degrees of the strength of interaction between a pair of nodes, which is non-uniform and irregular. In the light of the success of recent investigations using a network science approach, we formulate the CBN as a complex network, and analyze its various statistical properties (see [9]).

The irregularity in the interaction patterns of nodes have been found in many social, biological and technological systems. Two prominent network models have been proposed in order to understand these systems: (a) *small-world network model*, and (b) *scale-free network model*. Both the models are categorized by certain network metrics, which are many, namely degree-distribution, clustering coefficient, network diameter, average path length, betweenness centrality, etc. The small-world network model was proposed by Watts and Strogatz in 1998 (see [10]) and included a novel modification of the Erdos-Renyi random graph model which was proposed in 1959 (see [11]). The small-world network is an interesting model that captures our social interactions in a very promising way. The two major characteristics of this model are: (i) *short average path length* between any pair of nodes, and (ii) *high clustering effect* denoting strong-knit communities (see [8, 12]). Small-world effects have been found in electric power grids (see [7]), road maps (see [13]), protein-yeast (metabolite) interaction networks (see [14]), etc. Also, it is interesting to note that the Indian railway network (IRN) shows small-world characteristics (see [5]). The other model was proposed by Barabasi and Albert in 1999 when they mapped the topology of a portion of

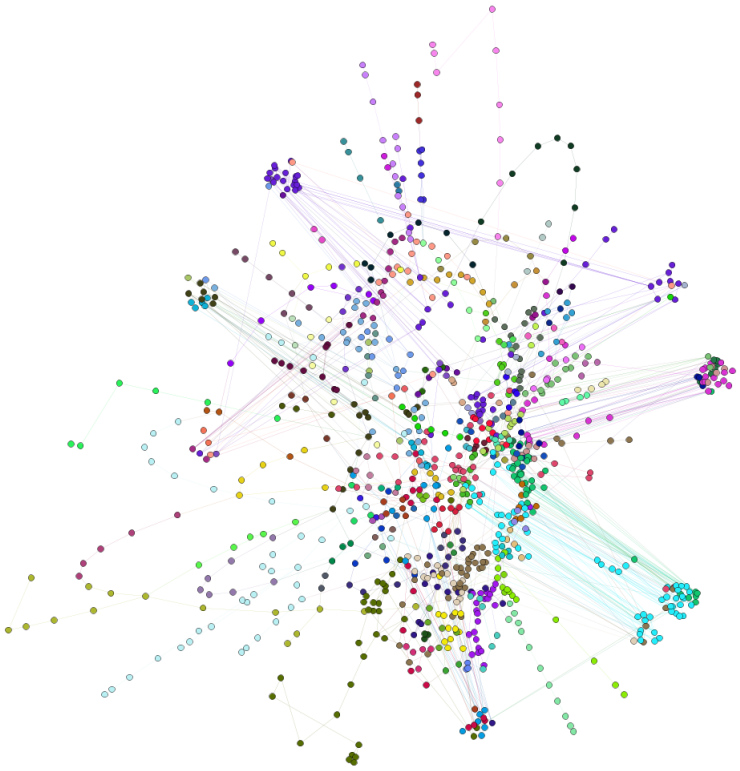

Figure 1: The Chennai Bus Network is plotted with nodes, $N = 1009$ and links, $L = 1610$. The layout is obtained using force-directed algorithm with complexity $\mathcal{O}(n^2)$

the World Wide Web (see [2]). An interesting aspect of their model is the *scale-free degree distribution* of the nodes, marked by the presence of *hubs* (see [1, 2]). Social networks (see [15]), movie actors collaboration networks (see [16]), authors citation networks (see [17]), the World Wide Web (see [2]), protein-protein interaction networks (see [18]), mobile communication networks (see [19]) etc. have been shown to follow a scale-free growth. With respect to transportation networks, airline networks and some subway networks have been observed to obey the Barabasi-Albert scale-free model (see [9, 20, 28, 29, 31]). However, it is worthwhile to note that the network topologies are not the absolute metrics that define strict classes of physical systems, e.g., some researchers have proposed a scale-free model for the rail-network of China (see [20]).

2 Methodology

Before creating an abstract model of the bus transport network, one needs to clearly distinguish between the geographical placing of the actual bus stops and the placing of the analogous nodes in a complex connected network. We define a connected network as a graph, in which a path traversal is possible between any pair of nodes. We also define the two analogous spaces: the *geographical space* and its topological equivalent, *network space*. In the network space, every node pair $(i - j)$ is separated by a distance, l_{ij} of one unit. The actual significance of defining an equivalent network space lies in the value of this distance metric, l_{ij}. If $l_{ij} = 1$, there exists a bus that takes a commuter from i to j directly whereas, if $l_{ij} > 1$, then a person has to change buses at least once at some intermediate stop between i and j.

The MTC website maintains a database of the entire bus route of Chennai. In order to create our network model, we identify every bus stop as a node and a bus connecting any two adjacent bus stops as a link between them. At this point, we assume that the bus network is bi-directional in nature hence, the links connecting a pair of nodes are undirected. In order to analyze this extensive network, a node-node adjacency matrix, $\mathscr{A}(N, L)$ is generated. An element of this matrix, a_{ij} is either zero, one, or some quantity greater than one. If two nodes,$i - j$ are not connected directly then, $a_{ij} = 0$. Since parallel edges are possible, a_{ij} can take any integer positive value; note that $a_{ii} = 0$. The summation of the row, i.e., for all i and a fixed j, we have the total degree of the j^{th} node. The degree of a node implies the total number of links that pass through a node. For a node signifying a bus stop, as in this case, the degree of a bus stop will signify the strategic importance that bus stop manifests on the network. A bus stop with a high de-

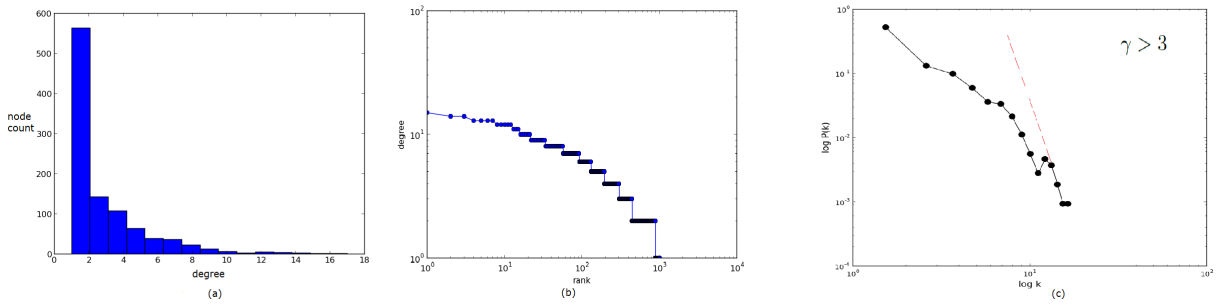

Figure 2: (a) A histogram plot showing the degree distribution and node count; (b) Rank-degree correlation plot on a log-log scale showing weak *Zipfian* distribution; (c) Plot of *log p(k)* vs. *log k*, and the corresponding straight line fit for the tail with slope $\gamma > 3$

gree will have a high number of routes crossing it. Nodes with very high degrees in a network are often termed as *hubs*. Since our network is undirected, we do not distinguish between out-degree and in-degree for a node thus, $deg(j) = outdeg(j) + indeg(j)$. In order to analyze various properties of this complex network, we identify the metric such as the clustering coefficient, which is a measure of the degree to which the nodes have the tendency to cluster together. For an undirected network, the local clustering coefficient of node i is given by, $C_i = 2 \times l_{ij}/k_i \times (k_i - 1)$ where, l_{ij} is a link connecting i to j, and k_i are the neighbours of node i. The neighbourhood, N_i, for a node, i is defined the set of its immediately connected neighbours as, $N_i = \{n_j : l_{ij} \in L \wedge l_{ji} \in L\}$. For the complete network, Watts and Strogatz defined a global clustering coefficient, $\mathscr{C} = \sum_i C_i/n$. The other important metric of particular interest is the degree-distribution function, $p(k_i)$, where $p(k_i)$ is the probability of degree, i, having a degree count, k. It is a measure of the degree distribution of nodes varying across the entire network. The shortest path between any pair of nodes is computed using *Dijkstra's algorithm.*

3 Results

We construct the network from the MTC database with the number of nodes, $N = 1009$ and the number of edges, $L = 1610$. The layout of the CBN in Figure 1 is obtained by using force-directed algorithm, assuming every node is connected by a spring. The prime idea is to minimize the energy of the system as every node tends to repel every other node (to which it is not connected directly) while being attracted by the elastic force of the spring-like edge. Using clustering algorithm, *Chinese whispers* (see [21]) we find that the CBN has close-knit clusters. Although few in number, they are located in those places of Chennai where mostly residential areas and business centres have conglomerated with time. Clusters represent a structure of the node set such that node traversal is possible from any one node to every other node in that set. Clusters in social networks represent high density ties between groups of people. In a transportation network, clusters represent the density of inter-dependency between the nodes, e.g., commercial areas like market places will tend to cluster with residential areas. But it is interesting to note that the clustering coefficient, $\mathscr{C} = 0.068$ for the CBN is significantly higher than a random network generated on the same edge set.

Another important metric that quantifies the topological structure of a network is the degree distribution function, $p(k)$. Figure 2(a) represents the degree distribution of the CBN as a function of the number of nodes. It can be clearly seen that the histogram decays very rapidly initially, for all degrees, $d_i \leq 2$, but afterwards, the decay is uniform for degrees, $2 < d_i \leq 6$. Henceforth, the decay is again rapid for all degree, $d_i > 6$. It is also observed that the majority of the nodes have a very low degree while a very few nodes have significantly high degrees. The average degree, $\bar{d}_i$ for the nodes in the CBN is found to be 3.19 with the median degree, $\bar{D}_i$ being 2. The maximum and minimum degrees for the CBN are $d_{max} = 15$ and $d_{min} = 1$. When the degree-rank correlation is plotted on a log-log scale, we get a weak *Zipfian* distribution, as seen in Figure 2(b) (see [22]). From Figure 2(a) and 2(b), it is evident that the degree and rank of a node are inversely related. Therefore, the CBN shows evidence for a $power - law$ degree distribution, $p(k) \sim k^{-\gamma}$. In order to find the power law exponent, γ, the probability distribution function for a degree, $p(k_i)$, is plotted with respect to the degrees of nodes, k_i, on a log-log scale. Since it is presumed that the distribution follows a power-law curve, the $k - p(k)$ plot on a log-log scale should be a straight line. Figure 2(c) shows a linear trend in the scatter of points on the log-log plane. Although the trend is linear, the slope initially follows the points smoothly, however, towards the end it decays rather rapidly. It is also worth noting that the distribution of the points is clustered at the tail end of the line in the log-log plane. The slope of the straight line that captures the fat-tail of the degree distribution is the power-law exponent, γ. The slope of

the straight line is found to be greater than 3 (see [30]).

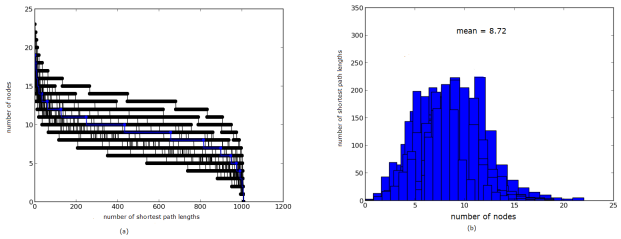

Figure 3: (a) Figure showing the variation of shortest path length for a single node to every other node with the number of nodes encountered; (b) skewed Gaussian distribution of the path length and number of nodes with mean, $\bar{l}_{ij} = 8.72$

It is quite natural for a traveller to search for the shortest path from his point of origin to his destination. The shortest path between a pair of nodes is the one that minimizes the number of node traversals between them. In order to answer the above question, the shortest path from a single source to every other node is plotted in Figure 3(a). The curve resembles a S-pattern. An interesting point to observe here is that more than 80% of the paths require 8 or less nodes, and only about 20% of the remaining paths require more than 8 nodes. This process is repeated for all the $\binom{N}{2}$ node pairs in the network, and the sigmoid distribution is found to be similar in all the cases. In Figure 3(b), we plot the normalized sigmoid curves. It essentially reveals a skewed Gaussian distribution of the shortest path lengths with the mean path length $\bar{l}_{ij} = 8.72$, which implies that on an average, any random pair of nodes can be visited by at most nine hops across this extensive bus network. Also, observe that the number of nodes steeply rises till 26 for the remaining 20% nodes, accounting for the large diameter of the CBN. Also, it is worth noting that the average path length varies with number of nodes as $\bar{l}_{ij} \sim ln(N)$, which is a characteristic feature of a small-world network (see [23]).

4 Discussion

The diffusion of structural and statistical concepts of network science has not been uniform in understanding transportation networks in general. While networks such as airlines, railways, and public transit networks have been extensively studied (see [6, 24 - 28]), the quantum of work done in understanding road transportation, and in particular, the bus networks, has been relatively less (see [29]). In this paper, we have rigorously analyzed the topological structure of the bus network of Chennai. It is quite interesting to see that the CBN shows various remarkable characteristic properties.

The density of this extensive network is surprisingly low, $\rho \sim 0.003$, which gives us an idea of the spatial flow of the network across the entire city from the core to the extremities. As the CBN shows a scale-free degree distribution, there are a significantly large numbers of nodes that have a low degree when compared to the mean. On the contrary, majority of the links are held by a very few number of nodes, as we can see from Figure 2(a, b, c). These set of nodes, which contribute towards majority of the connections in the network are often termed as hubs. Thus the CBN shows existence of hubs, which is again an interesting result for a transportation network. The core of the network, inclusive of the hubs, would often tend to cluster around the regions in the city which experience maximum flow of commuters. Also note that the existence of bus depots, where buses from all routes eventually converge to, can also be considered as hubs.

Another characteristic feature of this network that requires focus is the power-law exponent, γ. The value of γ is found to be greater than three, with the *cutoff* being at $k = 7$. We do not claim an accurate value of gamma as its determination demands a weighted plot that would naturally evoke a heavier-tailed distribution than in Figure 2(c), with a much accurate straight line fit (see [30]). We understand the dependence of γ on the topological structure of the network, and correlate networks with similar characteristics. A critical observation of the histogram plot in Figure 2(a) reveals before us the uniformity in the degree distribution towards the end of the tail. A high value of γ represents more spread in the degrees amongst nodes, which is contrary to many real networks where $2 < \gamma < 3$, like the internet, power grids, social networks, etc., which have numerous hubs. In case of transportation networks, the value of γ has been found to vary from 2 to 5.5 (see [28]) for some metro networks, and $2 < \gamma < 3$ for public transit networks. A special thing to note here is that the networks for which $2 < \gamma < 3$, have been found to show ultra small-world characteristics, $\bar{l}_{ij} \sim ln((ln(N))$ whereas for $\gamma > 3$, the dependence of the average path length on the number of nodes follows as, $\bar{l}_{ij} \sim ln(N)$, resembling small-world phenomenon (see [23]). Some earlier works in bus networks of China show linear to exponential degree distribution (see [29]). For a public transport system, it is of immense importance that the travel times are reduced and people can efficiently commute from one place to another by changing minimum number of buses.

In the Indian context, people have shown that the Indian railway network is a small-world network (see [5]). However, they found that the degree distribution is not scale-free. With respect to airline networks, some earlier works have claimed that the Indian airline network follows a scale-free growth with $\gamma = 2.2$ (see [31]). All of these results claim universality in the structure of transportation networks. Being scale-free induces an additional advantage to the network by making it more robust and resilient to random failures (see [1 - 3, 7 - 8, 32]). It is indeed good to have scale-free, small-world transportation systems that would effectively reduce travelling time in

cities, and preserve network connectivity in critical situations.

5 Conclusion

Although various concepts of network science are being increasingly used as a tool for studying the underlying topology of networks, it still remains an elusive tool to visualize road transportation networks. In this paper, we have formulated a network model for the sixth largest city in India and understand its various structural attributes. The remarkable features of this extensive network include *scale-free degree distribution*, *short average path length* and *high clustering coefficient*. It is being claimed that it would require at most nine hops to traverse any pair of random nodes in this network. Thus, the CBN exhibits small-world phenomenon and a scale-free growth with $\gamma > 3$. Based on the above attributes, it can be claimed that the CBN is essentially an efficient and a robust network.

Acknowledgements

The authors acknowledge the support from Center of Excellence in Urban Transport at Indian Institute of Technology, Madras sponsored by Ministry of Urban Development, Government of India and the Information Technology Research Academy, a Division of Media Labs Asia, a non-profit organization of the Department of Electronics and Information Technology funded by the Ministry of Communications and Information Technology, Government of India. The authors also thank Sushmitha Penta and Madhav Ch, for their help with data collection.

References

[1] A. L. Barabasi and R. Abert, "Emergence of Scaling in Random Networks," *Science*, vol. 286, pp. 509 - 512, 1999.

[2] R. Albert, H. Jeong and Barabsi A. L., "Internet: Diameter of the world-wide web," *Nature*, vol. 401, pp. 130 - 131, 1999.

[3] M. E. J. Newman, "The structure and function of complex networks," *SIAM Review*, vol. 45, pp. 167 - 256, 2003.

[4] S. H. Strogatz, "Exploring complex networks," *Nature*, vol. 410, pp. 268 276, 2001.

[5] P. Sen et al, "Small-world properties of the Indian Railway Network," *Phys. Rev. E*, vol. 67, pp. 036106-1 - 036106-5, 2003.

[6] J. Sienkiewicz and J. Holyst, "Statistical analysis of 22 public transport networks in Poland," *Phys. Rev. E*, vol. 72, pp. 046127-1 - 046127-11, 2005.

[7] G. L. Nakarado, A. Istvan and R. Albert, "Structural vulnerability of the North American power grid," *Phys. Rev. E*, vol. 69, pp. 025103-1 - 025103-4, 2004.

[8] D. Easley and J. Kleinberg, *Networks, Crowds, and Markets: Reasoning about a Highly Connected World*, Cambridge University Press, 2010.

[9] A. L. Barabasi and R. Albert, "Statistical Mechanics of Complex Networks", *Rev. of Mod. Phy.*, vol. 74, pp. 47 - 97, 2002.

[10] D. J. Watts and S. H. Strogatz, "Collective dynamics of 'small-world' networks," *Nature*, vol. 393, pp. 440 - 442, 1998.

[11] P. Erdos and A. Renyi, "On the evolution of random graphs," *Publicationes Mathematicae*, vol. 6, pp. 290 - 297, 1959.

[12] M. S. Granovetter, "The Strength of Weak Ties," *The Am. J. of Sociology*, vol. 78, pp. 1360 - 1380, 1973.

[13] X. S. Yang, "Small - world networks in geophysics," *Geophys. Res. Lett.*, vol. 28, pp. 2549 2552, 2001.

[14] P. Bork et al, "Protein interaction networks from yeast to human," vol. 14, pp. 292 - 299, 2004.

[15] N. R. Onody and P. A. de Castro, "Complex network study of Brazilian soccer players," *Phys. Rev. E*, vol. 70, pp. 037103-1 - 037103-4, 2004.

[16] L. A. N. Amaral, A. Scala, M. Barthelemy, and H. E. Stanley, "Classes of small-world networks," *Proc. of the Nat. Acad. of Sci.*, vol. 97, pp. 11149 - 11152, 2000.

[17] H. Small, "Co-citation in the scientific literature: A new measure of the relationship between two documents," *J. Am. Soc. Inf. Sci.*, vol. 24, pp. 265 - 269, 2007.

[18] H. Jeong, S. P. Mason, A. L. Barabasi and Z. N. Oltvai, "Lethality and centrality in protein networks", *Nature*, vol. 411, pp. 41 - 42, 2001.

[19] J. P. Onnela, J. Saramki, A. L. Barabasi et al, "Structure and tie strengths in mobile communication networks", *Proc. of the Nat. Acad. Sci.*, vol. 104, pp. 7332 - 7336, 2006.

[20] F. Feng and L. Wang, "Robustness Measure of Chinas Railway Network Topology Using Relative Entropy," *Discrete Dynamics in Nature and Society*, vol. 2013, pp. 1 - 8, 2013.

[21] C. Biemann, "Chinese whispers: an efficient graph clustering algorithm and its application to natural language processing problems," *Proceedings of the First Workshop on Graph Based Methods for Natural Language Processing*, pp. 73 - 76, 2006.

[22] R. Ferrer i Cancho and R.V. Sol, "Least effort and the origins of scaling in human language," *Proc. of the Nat. Acad. of Sci.*, vol. 100, pp. 788 - 791, 2002.

[23] R. Cohen and S. Havlin, "Scale-Free Networks Are Ultrasmall," *Phys. Rev. Lett.*, vol. 90, pp. 058701-1 - 058701-4, 2003.

[24] J. Wu et al, "Urban transit system as a scale-free network," *Mod. Phys. Lett. B*, vol. 18, 2004.

[25] R. Guimera, S. Mossa, A. Turtschi and L. A. N. Amaral, "The worldwide air transportation network: Anomalous centrality, community structure, and cities' global roles," *Proc. of the Nat. Acad. of Sci.*, vol. 102, pp. 7794 - 7799, 2004.

[26] S. Melonia, A. Arenasb and Y. Morenoc, "Traffic-driven epidemic spreading in finite-size scale-free networks," *Proc. of the Nat. Acad. of Sci.*, vol. 106, 16897 - 16902, 2009.

[27] C. von Ferber, T. Holovatch, Yu. Holovatch, V. Palchykov, "Public transport networks: empirical analysis and modeling," *The Eur. Phy. J. B*, vol. 68, pp. 261 -275, 2009.

[28] S. Derrible and C. Kennedy, "The complexity and robustness of metro networks," *Physica A: Statistical Mechanics and its Applications*, vol. 398, pp. 3678 - 3691, 2010.

[29] X. Xua, J. Hub, F. Liua and L. Liua, "Scaling and correlations in three bus-transport networks of China," *Physica A: Statistical Mechanics and its Applications*, vol. 374, pp. 441 - 448, 2007.

[30] A. Clauset, C. R. Shalizi and M. E. J. Newman, "Power-Law Distributions in Empirical Data," *SIAM Review*, vol. 51, pp. 661- 703, 2009.

[31] G. Bagler, "Analysis of the airport network of India as a complex weighted network," *Physica A: Statistical Mechanics and its Applications*, vol. 387, pp. 2972 - 2980, 2008.

[32] R. Pastor-Satorras and A. Vespignani, "Epidemic Spreading in Scale-Free Networks," *Phys. Rev. Lett.*, vol. 86, pp. 3200 - 3203, 2001.

Proceedings of ICCSA 2014
Normandie University, Le Havre, France - June 23-26, 2014

A NEW LOAD BALANCING STRATEGY FOR DISTRIBUTED COMPUTING SYSTEMS

Mahdi Abed Salman, Cyrille Bertelle and Eric Sanlaville *†

Abstract. Load balancing strategies determine when and how jobs are migrated. The objective is to keep the system in an equilibrium state, with the lowest overhead. In most DCS's, load balancing takes place only among a few neighbor nodes and, gradually, a global equilibrium is reached. A new load balancing strategy is proposed, tested and compared with two well known strategies. The proposed strategy outperforms both others.

Keywords. Distributed System, Balancing strategy, Sandpile, Small world, Multiagent Simulation.

1 Introduction

A distributed computing system DCS is a set of computing nodes connected by a communication network. They are working together to carry out users tasks.

In a DCS, load balancing aims at enhancing the resource utilization. It tries to distribute load (that is, jobs to process) evenly between system nodes and to minimize the mean tasks response time. However, load balancing methods add some overhead to the global system.

Load balancing strategies determine when and how jobs are migrated. The objective is to keep the system in an equilibrium state, with the lowest overhead. In most DCS's, load balancing takes place only among a few neighbor nodes and, gradually, a global equilibrium is reached.

The efficiency of load balancing depends on the amount and accuracy of available information at each node. Some information is acquired either by directly querying the some partner node during the load balancing process or provided by a more sophisticated knowledge discovery method. Of course, acquiring some information adds more overhead to the system, proportionally to the amount of knowledge required, the size of the network and its topology. Some algorithms require complete knowledge of the network state while others perform well depending on a few entries inside local repositories.

The accuracy of the available information depends on several parameters like update frequency or system changing rate (arrival and departure of jobs). The network topology is also playing an important role when propagating valid information inside the network.

The main contribution of this study is to present a new load balancing strategy and to compare its performances with some other strategies from the literature.

The document is organized as follow: In section 2, a short review of related works is given. Selected strategies of load balancing are explained in section3 (knowledge discovery is just sketched in this extended abstract). In section 4, a simulation is made to validate our claims. Section 5 provides some conclusions.

2 Related Works

Load balancing in DCS's depends on many parameters which make it a complex problem. It is difficult (if not impossible) to take all parameters into account when designing an algorithm for load balancing for a DCS.

Researchers are mainly taking two directions: resource discovery and load movement (job migration). Literature investigates both problems extensively, but resource discovery is not detailed here. Many job migration strategies exist, some of the most popular are presented below.

Willebeek-LeMair and Reeves [5] proposed five load balancing schemes. However only Receiver Initiated Diffusion RID and Sender Initiated Diffusion SID schemes are using local knowledge that is global load balance is obtained through local knowledge and decisions. In SID, nodes frequently broadcast their current load status to all of their direct neighbors. A node initiates a migration towards another node whose load is below a threshold. In RID, a node whose load drops below a threshold T_{low}, requests a migration from all its direct neighbors which are overloaded.

Cao et al.[2] presented a load-balancing framework called Mobile Agent based LoaD balancing (MALD) that uses stationary agents that monitor the workload on local servers and mobile agent to carry loads to under-loaded server. Hence this is an SID scheme but controlled by agents.

J.L.J Laredo et. al.[3] presented an on-line and decentralized scheduler based on a Self-organized Criticality

*Mahdi Abed Salman is a PhD student at LITIS-University of Le Havre, from the Department of Computer Science, University of Babylon, Iraq. E-mail: mahdi4it@gmail.com

†Cyrille Bertelle and Eric Sanlaville are with Faculty of Science and techniques, University of Le Havre, France. E-mails: cyrille.bertelle@univ-lehavre.fr, eric.sanlaville@univ-lehavre.fr

model classically called *sandpile*. The authors show that a sandpile model[1] could yield a better performance if the nodes are arranged as a small world network rather than a lattice 2D grid.

Other models that are used to perform load balancing depending on local available information are also applicable.

We propose a new load balancing strategy based on RID scheme(but that selects the migration source node). A comparison of performances is made between the SID model proposed in [5], the sandpile scheduler proposed in [3], and the one proposed in this paper. The latter outperforms the two other strategies for a given DCS model. More precise descriptions for the three strategies are given in section 3.

3 Chosen models and tested load balancing strategies

Three main elements are important in a DCS load balancing model: network structure, load information, and balancing strategy. The network is the base and it affects everything else. It determines how information is broadcasted and jobs are migrated. Network could be physical or logical (depending on how a link is defined) static or dynamic (depending on links stability).

Whatever resource discovery method is used, a sufficient knowledge is considered present after several iterations of system life. Usually, nodes cache information about other nodes to use it for future communication. An entry in a local cache can be defined as a link to another node. Knowledge creates an *overlay* network above the *initial network*. In peer-to-peer networks, an overlay network is a logical network which is built from the information exchanged between peers using some diffusion method. An overlay network is dynamic in term of local knowledge content. It is modeled by a directed graph, where an arc (i, j) means that node i has some knowledge about node j (here about its load).

A balancing strategy is defined by an algorithm and by the parameters that are used to take a migration decision. Parameters include, but are not limited to, load metrics for each node (especially for potential source and destination), bandwidth for the links between these nodes. *In this paper, the load is measured by the remaining time of jobs being executed, plus the execution times of waiting jobs.*

Three strategies are tested in this paper. Note that neighborhood is relative to the overlay network.

1. SID Strategy: some load is moved from current node if it is overloaded to the under-loaded node that is chosen from neighborhood uniformly at random[5].
2. SandPile strategy: The load of current node is avalanched (dropped) down to the neighbor nodes, if some criteria are met. For example in [**?**] load of a node is avalanched, if it is greater than the summation of loads of two neighbor nodes selected at random. Extra load is distributed among the three nodes.
3. Proposed strategy: load is demanded by the current node if it is under-loaded, and from a maximum loaded node in its neighborhood.

A node is said to be overloaded or under-loaded according to the load of neighbor nodes. A selected method used to check the state of a node is given below:

- Let l_j be the length (its execution time) of job j.
- Let L_v be the load of node v.
- Let L_{max} be the maximum load in the neighborhood.
- Let L_{min} be the minimum load in the neighborhood.
- $L_{interval} \leftarrow (Lmax - Lmin)$.
- Let $\alpha \in (0, 0.5)$.
- $T_{under} \leftarrow L_{min} + L_{interval} \times \alpha$.
- $T_{over} \leftarrow L_{min} + L_{interval} \times (1 - \alpha)$.
- A node v is overloaded if $L_v > T_{over}$, under-loaded if $L_v < T_{under}$.

A job j is migrated from overloaded node v to under-loaded node u if and only if: v has more than one job and migration of j does not change load inequality between u and v i.e $(L_u + l_j) < (L_v - l_j)$, where L_v and L_u are computed before the migration.

4 Simulation

4.1 Parameter settings

A simulation program has been designed based on the GraphStream package [4], to create a destination platform. A node class has been extended to facilitate agents' accommodation. Agents are autonomous objects that take decisions according to their internal state and/or environment state. Environment may be represented by the state of accommodating node in addition to available information about neighbor nodes. An agent interacts with other agents to accomplish assigned tasks.

Several graphs are generated to reflect topology of different initial networks. Each graph is stored in a file.

Jobs are arriving according to local arrival rates (that is, rates differ from one node to another). Arrival rates are generated uniformly at random with respect to the total network capacity. A job set contains a number of jobs proportional to the network size and duration of simulation. Each job is characterized by its length and the node it is submitted to.

An experiment needs many parameters to be specified, for example: Initial network file, job set file, knowledge (cache) size, load balancing strategy and a maximum duration for running simulation program.

Many initial networks have been generated. They are of different size and typologies like Complete, Grid, Random etc. Only small world network(see [**?**]) of order 1000 is presented here. Table 1 shows the features of the network that has been tested on a laptop. Average clustering coefficient of a graph is the mean value of the clustering coefficient of all nodes in the graph. Clustering coefficient of the vertex v is the density of a sub-graph that is composed only from v neighbors. Density is the rate of number of edges to possible number of edges in a graph. i.e. $\frac{|E|}{N(N-1)}$. E is the edges sets. N is the number of nodes in the graph(network).

Table 1: Features of initial network graph

feature	value
Generation Method	Small World
Connected Components	1
Diameter	5.0
Density	0.016
Average clustering coefficient	0.3
Graph Order	1000
Edges Count	8000
Maximum node degree	26
Minimum node degree	11
Average Node degree	17

Two sets of jobs are used. One set contains identical job lengths (5 units of time) while the other has different job lengths (uniformly distributed $\in [1, 9]$). Features of the two sets are shown in table 2.

All runs have duration of 1000 units of time. Migration of one job from one node to another takes one unite of time. All strategies are applied on the overlay network that has been created by some resource discovery method using mobile agents. 0.4 is chosen for α. The cache size is 20, we obtained 20 is sufficient to do load balancing efficiently.

Table 2: Features of sets of jobs

	A	B
Number of jobs	199431	199867
Job length	identical	Variable
Average job length(ms)	5.0	4.98
Average arrival rate	0.199	0.199
Total load per node		
Mean	997.0	996.0
Standard deviation	565.79	568.90
Maximum	2050	2084
Minimum	0	0

4.2 Results

Table 3 shows features of a snapshot of overlay network taken when system has reached the steady state. Figures 1 and 2 show the mean response time and the maximum response time respectively calculated for each of the three strategies on two job sets A and B. Response time is the duration of time from job submission until the completion of its execution. Maximum and mean response time at time t is the maximum and mean response time of jobs that have finished their execution in time t.

Table 3: Features of overlay network graph

feature	graph 1
Type	Small World
Connected Components	1
Diameter	4.0
Density	0.038
Average clustering coefficient	0.295
Graph Order	1000
Edges Count	19054
Maximum in-degree	192
Minimum in-degree	0
Average in-degree	19
Maximum out-degree	20
Minimum out-degree	19
Average out-degree	19

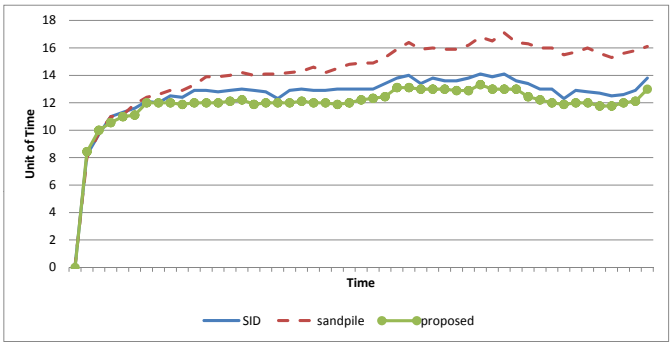

(a) Set A:Mean Response Time

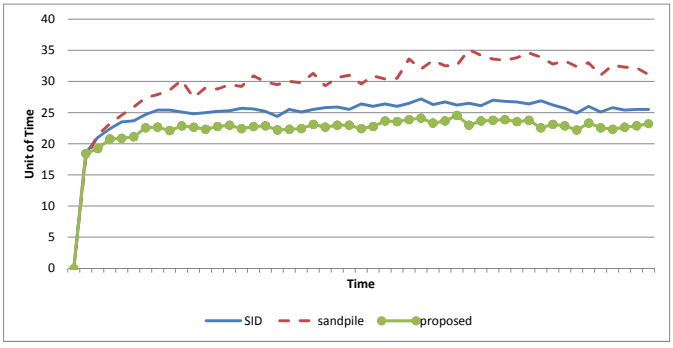

(b) Set A:Maximum Response Time

Figure 1: Balancing strategies with job set A

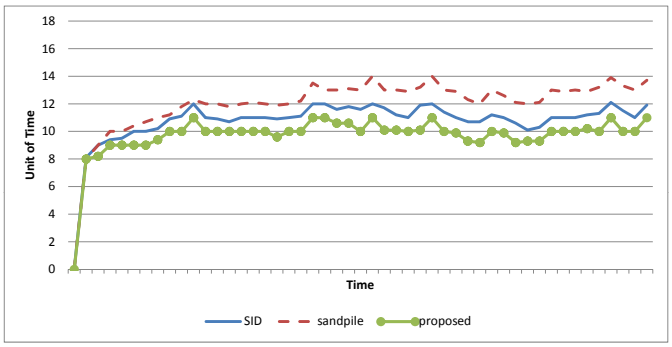

(a) Set B:Mean Response Time

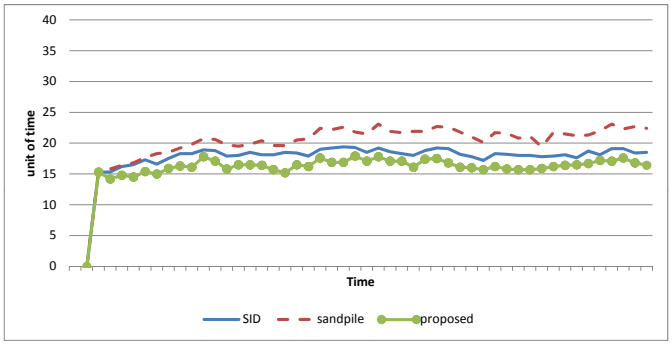

(b) Set B:Maximum Response Time

Figure 2: Balancing strategies with job set B

All Strategies reach steady state at same time. Steady state is reached even with high average load near the maximum load capacity. The difference of maximum response time between two sets is a result of the difference in maximum job size.

5 Conclusion

Dynamic Load balancing in distributed systems can be achieved efficiently by local strategies, if the overlay network obtained from resources discovery has small world structure, and an average degree between 16 and 32. Our strategy aims to eliminate any peak node (having a high load with regards to its neighbors). Domain overlapping feature of a small world network helps in rapid spreading of peaks reduction procedure in the whole network. Many nodes in their neighborhood try to decrease the load of a peak node. After that the role of source node may be relocated to another one. Proposed strategy outperforms other two strategies in such type of networks. A sandpile strategy is the worst in performance if the communication cost is disregarded. Both, the SID strategy and the proposed one add same overheads with regard to the information acquired in case of static networks. Sandpile is more sensitive to job granularity.

References

[1] P. Bak, C. Tang, and K. Wiesenfeld. Self-organized criticality: An explanation of the 1/f noise. *Phys. Rev. Lett.*, 59:381–384, Jul 1987.

[2] J. Cao, Y. Sun, X. Wang, and S. Das. Scalable load balancing on distributed web servers using mobile agents. *Journal of Parallel and Distributed computing*, 63:996–1005, 2003.

[3] J. Laredo, P. Bouvry, F. Guinand, B. Dorronsoro, and C. Fernandes. The sandpile scheduler. *Cluster Computing*, pages 1–14, 2014.

[4] Y. Pigné, A. Dutot, F. Guinand, and D. Olivier. Graphstream: A tool for bridging the gap between complex systems and dynamic graphs. *arXiv preprint arXiv:0803.2093*, 2008.

[5] M. H. Willebeek-LeMair and A. P. Reeves. Strategies for dynamic load balancing on highly parallel computers. *IEEE Trans. Parallel Distrib. Syst.*, 4(9):979–993, Sept. 1993.

Proceedings of ICCSA 2014
Normandie University, Le Havre, France - June 23-26, 2014

DOES YOUR TRADING STRATEGY BEATS MINE ?
AN AGENT-BASED APPROACH TO EVALUATE TRADING EFFICIENCY

Philippe MATHIEU and Yann SECQ *

Abstract. Stock markets are complex systems whose price dynamics are driven strictly by traders behaviours. In such dynamic context, how is it possible to evaluate concretely a trading strategy ? This paper is a first step to define several evaluation methods that can be used to assess the performance of a trading strategy in a heterogeneous context. We propose an evaluation hierarchy, ranging from a simple approach to more complex settings involving bio-inspired concepts like ecological competitions.

Keywords. agent-based computational economy, multi-agent system, artificial stock markets, trading strategies, ecological competitions.

1 Introduction

In this paper, we are concerned with the problematic of the evaluation of a trading strategy in an order-based market like EURONEXT-NYSE. More precisely, we identify several evaluation strategies that can be used in order to compare trading behaviours in a dynamic environment close to real stock markets mechanisms.

The section 2 introduces main concepts of order-based markets and briefly presents the simulation platform that we have used for our experimentations. The section 3 details previous works done to evaluate trading strategies and emphasizes missing aspects of some studies. The section 4 is the main contribution of this paper: a hierarchy of evaluations defined in order to benchmark trading strategies performances in a stock market. The section 5 describes experimentations that have been done in order to validate the proposed hierarchy. Finally, section 6 synthesizes the contribution of our work.

2 Artificial stock markets

Within the agent-based computational economy (ACE) community several works ([1], [6]) have focused more specifically on artificial stock markets to simulate different aspects of real markets. Nevertheless, as detailed in [6], even with an agent-based approach, market models can be rather abstract and not so close to the actual rules of real markets. More recently, some simulators like `JASA` [10] or `ATOM` [8] have been developed to closely reproduce existing market rules. In this section, we introduce the main concepts of such frameworks that are particularly fitted to study market micro-structures, individual performances or even social welfares.

2.1 Orders and Prices

An order is the expression of an interest from a market actor to buy or sell an asset. Real life markets have developed numerous kind of orders, some of them for really specific purposes. In artificial markets, the more commonly found orders types are *limit orders* and *market orders*. The simplest order is the *market order* which just stipulates the quantity that the actor is willing to buy or sell. It is called *market order* because the price used will be the one currently holding when the order will be processed. The *limit order* is more prudential as the actor states both the quantity and the maximum (resp. minimum) price that he is willing to concede in order to buy (resp. sell). In this paper, we use only these two kind of orders but our platform, `ATOM`, provides also more exotic orders like *update*, *cancel* or even *iceberg* orders.

An order is thus a 4-tuple of: {`Actor, Asset, Price, Qty`}, where `Actor` is the sender of this order, `Asset` is the name of the traded asset, `Price` is the price the actor is willing to sell or buy (infinity for a *market order*) and `Quantity` is expected number of assets that should be exchanged. From an implementation point of view, orders carry more information, for example, each order is uniquely identified and prices reference orders that have been involved in their creation, allowing to study finely which actors have been trading together.

2.2 Traders

Traders are market actors that observe the market and interact through the emission of orders to buy or sell assets. Depending on market conditions and their own trading behaviour, they send orders to the market to trade assets in order to maximize their returns. The main criteria used to assess the performance of a trader is the notion of *wealth*. This criteria, when used in an individual context, is defined through an evaluation of the trader portfolio and available cash. More precisely, a trader's wealth is

*Laboratoire d'Informatique Fondamentale de Lille (CNRS UMR 8022), Université Lille 1. E-mails: philippe.mathieu@univ-lille1.fr, yann.secq@univ-lille1.fr

generally defined by its available cash and the valuation of its portfolio under current market prices.

2.3 Marketplace

The marketplace is the container allowing the aggregation of orders and the pricing mechanism defines how the offer and demand match. We are focused here on *Continuous Double Auction* (CDA) markets. With the main stock markets, a trading journey is structured in 3 periods: a pre-opening period and a closing period that use a fix pricing mechanism and the main period running throughout the journey that use a continuous pricing mechanism. This continuous pricing algorithm implies that every time a new order enter the market for a given asset, the fixing mechanism is executed and one or several prices can be generated. This particular aspect is a distinctive feature of CDA simulation platforms as prices are computed exactly as they are in a real market like NYSE Euronext.

2.4 ATOM: an artificial stock market simulator

The platform we use for our experimentations is a multi-agent platform called `ATOM`[1] [3]. This simulator implements an order-driven market that reproduce the main features of the microstructure of marketplaces like *NYSE Euronext*, including its system of double book of orders for each asset. In `ATOM`, agents rely on their own strategies to send orders on different assets. Thus, unlike macroscopic market models, agents do not emit a simple signal to buy or sell but can send *real* orders consistent with those presented in the previous subsection.

`ATOM` is built on classic agent design-patterns [7] to allow the enforcement of equity between agents and to conduct experimentations at several scales: from an intraday level (intraday) by reasoning on each fixed price to multi-day scale (extraday) by reasoning only on the closing prices. Although `ATOM` supports multi-assets negotiation, this article focuses on the usage of a single order book. Finally, `ATOM` can scale, for example 1000 agents sending 1000 orders during 1000 trading days (thus 1 million orders) can be evaluated in less than one hour on a commodity computer.

2.5 Using the ATOM API

The aim of this section is not to provide a complete technical documentation of ATOM or even a survey of its capabilities but to illustrate through two small code snippets how to easily define an agent and an experimentation.

The figure 1 describes how to define a new trading strategy. Because ATOM is developed in *Java*, an object-oriented language, the user has to specialize the `Agent` class and to override the method `decide` to define what the agent should do at a given point of the trading `Day` on a given order book. The simple strategy implemented in table 1 is just the alternance of an ASK then BID limit orders with a fixed quantity (500) and a fixed price (14000). Prices are specified in cents in order to use integers to represent prices which less problematic than the use of real numbers.

```
import v13.*;
import v13.agents.*;
class MyAgent extends Agent {
  public MyAgent(String name) {
    super(name);
  }
  public Order decide(String obName, Day day) {
    // Alterning ASK and BID orders
    if (day.currentTick() % 2 == 0) {
      // Log a message in the generated log file
      market.log.info("ASK@"+day.currentTick());
      return new LimitOrder(obName, "nop",
        LimitOrder.ASK, 500, (long) 14000);
    }
    market.log.info("BID@"+day.currentTick());
    return new LimitOrder(obName, "nop",
      LimitOrder.BID, 500, (long) 14000);
  }
}
```

Figure 1: Definition of a new trading strategy with ATOM

When trading strategies are defined, the user can describe the market by specifying assets that will be traded (which are represented as `OrderBook` and by defining a specific day structure or using a predefined one. Once the market is ready a `Simulation` can be launched as illustrated in figure 2.

```
import v13.*;
import v13.agents.*;
public class SimpleSimulation {
  public static void main(String[] args) {
    Simulation sim = new MonothreadedSimulation();
    // Sending all logs to standard output
    sim.setLogger(new Logger(System.out));
    sim.addNewOrderBook("AAPL");
    sim.addNewAgent(new SimpleAgent("Alan"));
    sim.run(Day.createSinglePeriod(
      MarketPlace.CONTINUOUS, 10), 1);
    sim.market.printState();
  }
}
```

Figure 2: A simple simulation with ATOM

[1] `ATOM` can be tried and downloaded: `http://atom.univ-lille1.fr`

```
Map<String, String> param = new HashMap<>();
// Trading day structure
param.put(Form.OPENING, "0");
param.put(Form.CONTINUOUS, "1000");
param.put(Form.CLOSING, "0");
// Trading strategies configuration (partial)
Agent a = new ZIT("Toto");
// Add a ZIT strategy, with 100 agents that talk
// at each turn (speed)
param.put(Form.FAMILY_NAME + idx, a.name);
param.put(Form.FAMILY_POPULATION + idx, "100");
param.put(Form.FAMILY_SPEED + idx, "1");
...
// Experimentation configuration
param.put(Form.COMPETITION_TYPE,
                  Form.ECOLOGICAL_COMPETITION);
param.put(Form.NB_DAYS, "3");
param.put(Form.NB_SIMULATIONS, "" + 10);
// Launching the simulation
Evaluation e = Evaluation.runEvaluation(params);
```

Figure 3: Configuration and execution of an experimentation with ATOM

For experimentations presented in this paper, we have developed the `Evaluation` class to ease the configuration and execution of complex settings. The figure 3 illustrates how experimentations done in section 5. One static method is provided in order to launch with only one line an experimentation that is configured through a dictionary (or a CSV file). The parameters describe all elements linked to the day structure, the trading strategies involved and finally experimentation parameters on the number of days, the number of iteration and the kind of evaluation method.

3 State of the art

Lots of references can be found in the literature on trading strategies evaluation but mainly in the context of *back testing* approaches. Within non academic context, several commercial products are available specifically to back test trading strategies before using them on real markets[2].

The principle of back testing consists in using static prices series in order to estimate the return that would have generated a given strategy within this context. Back testing is a first approach that is useful but it generally do not handle constraints like liquidity, slippage or fees. Another important aspect is linked to the principle itself of back testing: the evaluated strategy do not influences prices dynamic because prices are statically fixed from historical data.

An interesting and critical perspective of this approach and its abuse is detailed in *Pseudo-Mathematics and Financial Charlatanism: The Effects of Backtest Overfitting on Out-of-Sample Performance*[2]. To borrow one citation of their conclusion that capture the main idea of their paper: "*I remember my friend John von Neumann used to say, with four parameters I can fit an elephant, and with five I can make him wiggle his trunk*".

Given the fact that we do not trust back testing evaluations, we have found few relevant works in the context of trading strategies evaluation. Nevertheless, two papers provides interesting studies on this subject and are detailed below.

In *Evaluation of automated-trading strategies using an artificial market*, K. Izumi, F. Toriumi and H. Matsui have developed an artificial stock market to evaluate automated trading strategies in the context of the Kaburobo competition [12]. After showing that back testing evaluations lead to different ranking with the same strategies tested on two datasets from consecutive years (overfitting issue), they use their simulator to compare trading strategies in a dynamical context (ie. where prices are the consequence of order emission and not fixed from static series).

Experiments have been done from the following setup:

- 8 trading strategies[3] with 3 variations for each (short/long and narrow/wide), so a total of 24 agents,
- trading days were defined with 100 time steps,
- each simulation has been repeated 10 times and results were averaged.

The authors have ranked trading strategies against their final returns and have produced an interesting visualization through a 2D-graph showing strategies relative positions against average final returns and risk.

Despite an interesting setting, it remains unclear if these results still holds with a higher number of agents or if the initial proportion of strategies is not uniform. This question is crucial because the definition of initial configurations in such a complex system is not easy: there is the number of trading strategies that are involved, for each strategy, there is the number of agents that use it in the simulation, and finally, there is the total number of agents in the simulation. It should be stressed that this problematic of the "right" number of agents to be used in a given simulation in order to reach the intended macroscopic emergent behaviour is an open question.

The second work that sparked our interest is titled *Using Evolutionnary Game-Theory to analyze the performance of trading strategies in a continuous double auction market* by Kai Cai, Jinzhong Niu and Simon Parsons. Authors are interested in the evaluation of heterogenous

[2]For example, the open source testbed: CATSBF

[3]*GoldenCross*, *HLBand*, *MACD*, *Enveloppe*, *PsychologicalLine*, *RSI*, *TechnicalKun* and *Bayesian* whose definitions are given in their annexes

trading strategies and rely on an interesting evolutionary game theory approach. As detailed by the authors, most studies that have been done on CDA markets were focused on market efficiency. The focus being on the global market efficiency and not on trading strategies efficiency, experimentations mainly involve only one strategy (ZI-U, ZI-C, ZIP ...).This paper also identifies the fact that lots of experiments are done on a *one-to-many* context, i.e. two trading strategies are confronted with one instance of the first strategy against n instances of the second strategy [11]. This approach can be seen as stability analysis in an homogenous traders population.

In their study, the authors have selected 6 classical strategies: *Zero-Intelligence with Constraint*, *Zero-Intelligence Plus*, *Truth-Telling*, *Pure-Simple*, *Roth-Erev* [4] and *Gjerstad-Dickhaut* [5]. They add two variations to this set: *Linear Gjerstad-Dickhaut*, a faster implementation of GD, and *Estimated Equilibrium Price*. The experiments have been done with the JASA Simulator[4] with a more complex setting than the previous paper:

- 20 agents splitted in 10 buyers and 10 sellers,
- a trading session defined on 5 days made of 300 time steps,
- each simulation has been repeated 100 times.

One important hypothesis, that we also share, is that an agent during the simulation cannot change its strategy. It does not mean that trading strategies are not adaptative, but it means that we do not study meta strategies that would select different trading strategies during a day.

For their first experiment, the authors use a *one-to-many* method where there is only *one* buyer and the others agents share the same strategy and act as sellers. The criteria used to ranked these two strategies is the average profit. A extensive table synthesizes the tournament between the 8 strategies where each cell hold the average profit of the seller versus the average profit of buyers and also the standard deviation of profit. Then, authors do a game theory analysis to identify dominant strategies. Their conclusion is that even if some strategies are effectively dominated, for the dominant strategies it is not clear to determine which one is the best.

To further their study the authors use an *heuristic strategy analysis* first proposed by Walsh [14]. This model is used to analyze complex games with repeated interactions, for which a full game-theoretic analysis is intractable. This approach treats exogenously specified heuristic strategies as primitive, rather than the atomic actions, and computes a heuristic-payoff table specifying the expected payoffs of the joint heuristic strategy space.

Even with their approach, authors conclude that results are of course highly dependent on the set of strategies that are used during simulations ...

[4] http://jasa.sourceforge.net

4 Towards a taxonomy of trading strategies evaluations

In this section, we introduce a set of evaluation mechanisms that can be used to rank the relative efficiency of trading strategies in a *many-to-many* context. These evaluation mechanisms range from the simplest approach which is similar to the one used by K. Izumi (iterated simulation), to more complex mechanisms close to the evolutionary approach from K. Cai. Before detailing each mechanism, we introduce the main concepts that we use to build our evaluation methods.

4.1 How to aggregate traders scores ?

Even if this question seems to be obvious, we want to address it because lots of papers make a distinction between homogenous and heterogenous agent populations. The issue that we have with this dichotomy is how to classify a parametrized strategy ? Let's take for example a simple periodical strategy that alternate buy and sell orders on a given period (every turn, every 5 turns ...). Should we consider that `Periodic(1)` is the same strategy as `Periodic(100)` ? If we have an existing set of n strategies and that we introduce a new strategy that just use successively each strategies every n turn, is it a new strategy or should it be considered as a variation of the n initial strategies ?

This question is not rhetorical and has to be taken into account. Indeed, evaluating a strategy involving several instances induces a choice on the aggregation of the score of strategies based on the same algorithm but using different initial parameters. In the Kai Cai study detailed in section 3, this issue do not appears as their strategies are not parametrized and so it is clear that GD and RE are distinct strategies. But in the study of K. Izumi, for each strategy we have 3 different parametrization based on the temporal window used to generate aggregated market criteria. From an intensional point of view these three variations are the same strategy but from an extensionality[5] point of view they must be distinct because their observable properties differs.

To tackle this question of the definition of a strategy, we propose to define the notion of strategy from an intensional point of view. Thus parametrized strategies are considered as a single strategy. We also exclude the use of *meta* strategies, ie. a strategy built from other strategies that are dynamically selected during the simulation. Or to be more precise, one can use a meta-strategy in a simulation, but this strategy's score cannot be merged with the strategies that constitutes it. For example, a meta-strategy that switch between two periodical strategies which sends alternatively a sell and a buy order every n ticks, with $n = 2$ and $n = 6$ will not be merged with the equivalent strategy $Periodic(2)$. These assumptions are

[5] `http://en.wikipedia.org/wiki/Extensionality`

necessary in order to clearly define the population update mechanism that is involved with ecological competition evaluations.

4.2 Generic evaluation algorithm

As we want to appreciate the relative efficiency of trading strategies, we have to define some efficiency criteria to quantify their performances. The classical criteria is generally the wealth (as defined before) or sometime more simply the rank of strategies.

We define an evaluation as a 5-tuple $\{S, I, C, P, T\}$ where:

- S is the set of trading strategies,
- I is the population initialization mechanism,
- C is the set of efficiency criteria,
- P is the population update mechanism.
- T is the evaluation termination condition,

With these characteristics the general evaluation algorithm can be sketched as follows:

```
while(T is not satisfied) {
  instantiate a new population with I
  launch a simulation for n days
  evaluate all evaluation criteria from C
  update population families with P
  save prices history for all order books
}
```

This algorithm allows us to instantiate the two evaluation mechanisms that defines our initial evaluation taxonomy: iterated simulations and ecological competitions. A third transversal aspect that can be used by both evaluations is subclasses computations that are linked with the population initialization stage. This aspect is not detailed in this paper, but some elements on its importance to avoid some kind of cheating are presented below.

4.3 Iterated simulations

This approach repeats a simulation for a given number of times and averages the scores obtained on all criteria. Rankings are then based on sorted set on criteria values. This approach is highly dependent on the initial configuration of the simulation in terms of strategies that are present and in their repartition amongst traders (ie. initial numbers of instances for each strategy).

More precisely, with iterated simulations evaluation method, the evaluation tuple is instantiated as:

- S is the set of all strategies involved in the simulation,
- I, the population initialization mechanism, is an instanciation of each strategies with a given number $nbAgents$ of instances ,
- C, the set of efficiency criteria, is made of the wealth criteria and the rank criteria,
- P, the population update mechanism, is the identify function,
- T, the termination criteria, is the number of iterations, ie. how many times should a simulation be repeated.

4.4 Ecological competitions

This approach is also based on iterated simulations but at the end of each simulation the proportion of each strategy within the agent population is re-evaluated with respect to its performance during the simulation. Thus, from simulation to simulation, proportions between strategies evolve and can lead after several iterations to stable (ie. little variations in strategies repartition) or cyclic situations [13].

4.4.1 Direct ecological competition

This approach is interesting but can lead to the extinction of some strategies if they perform too poorly. One could think it should not be critical, but if the disappearing strategies are those that act as liquidity providers (typically *Zero Intelligence* strategies), then the simulation dynamic can be deeply affected. Indeed, if all adaptive agents are waiting for their orders to be matched while no new orders are emitted to add some liquidity, no more activity happens in the market. Thus, it can be interesting to exclude some strategies from the population evolution update mechanism.

More precisely, with direct ecological competition evaluation method, the evaluation tuple is instantiated as:

- S is the set of all strategies involved in the simulation,
- I, the population initialization mechanism, is an instanciation of each strategies with a given number $nbAgents$ of instances that evolves in function of the strategy performance in the previous simulation. In our experimentations, the criteria used to determine $nbAgents$ is the aggregated wealth of all agents using the same trading strategy and their relative proportion with respect to the global wealth of all strategies.
- C, the set of efficiency criteria, is made of the wealth criteria and the rank criteria,
- P, the population update mechanism,
- T, the termination criteria, is the number of iterations, ie. how many times should a simulation be repeated. Another criteria could be used by detecting stable or cyclic outcomes but it has not been implemented yet. With this criteria, computation costs could be lowered by stopping the experimentation as soon as the population evolution has stabilized.

4.4.2 Ecological competition with fixed subset

As hinted before, when using direct ecological simulation, all trading strategies population evolves and some strategies can be totally removed from the simulation. If liquidity providers are excluded, we could reach a market where no more trading activity exist. The variation that we propose defines a subset of the initial trading strategies that should not be involved in the population update mechanism P. Thus, these *preserved* strategies keeps a constant number of instances during all simulations and their scores are not taken into account. Generally, strategies that are *preserved* act as liquidity providers (ZIT in our experimentations).

4.5 Subclasses

When evaluating a set of strategies, one can find situations were one strategy exploits another one. These situations are generally referred as master-slave contexts where one strategy (the slave) sacrifices itself to favorise another strategy (the master). In order to detect this situation that can be assimilated to a kind of cheating, the notion of subclasses has been developed.

Subclasses are used to change the initial choice of strategies that are allowed to participate in a tournament. Thus, instead of selecting the whole set of strategies, only subsets (ie. subclasses) are selected. More precisely, the principle is to explore all possible strategy selection by excluding n strategies.

For example, if we suppose that we have n strategies, there are $n-1$ initial configurations where 1 strategy is excluded. If we compute subclasses with 2 strategies, we then have $(n-1)*(n-2)$ initial configurations. If we have 30 strategies, computing subclasses becomes rapidly intractable. Nevertheless, subclasses initializations are interesting because they allow the detection of master-slave situations.

Even if it is not straightforward to build such master-slave strategies in the context of a stock market where agent scheduling is stochastic, subclasses are useful to detect this kind of biases.

5 Experimentations

This section illustrates the evaluation of some classical trading strategies and demonstrates the significant differences obtained with respect to the evaluation method that is used. It should be noted that the results presented below do not integrate subclasses as their computations are high with 13 families[6].

[6] And the set of trading strategies do not contain strategies that have been designed to induce a master-slave scheme.

5.1 Trading strategies

The trading strategies that we have used for these experiments are based on simple behaviours:

- chartist agents (moving average, RSI, momentum, variation, indicators and mixed moving average): these agents use simple conditions on the prices to forecast their future variation and decide to buy or sell
- periodic agents : periodically buy and sell
- Zero Intelligence Traders (ZIT) : these agents send orders in a random direction with a random limit price

Two more complex trading strategies are also added to this pool whose principle is based on learning classifiers that focus on information based on prices (`PriceLCS`) or on order book information (`OrderLCS`). A detailed presentation of these strategies can be found in [9].

5.1.1 Evaluation of these strategies

To evaluate this set of strategies, we have executed several experimentations with both iterated simulations and ecological competitions without preservation. As the number of agents for each trading strategy is high (one hundred), we do not have included here the results for ecological competitions excluding liquidity providers. For all these experiments, we used thirteen trading strategies instantiated through one hundred agents and a day structure with only one continuous session of 1000 ticks. This setting imply that each trading day involve $13*100*1000 = 1.300.000$ orders.

5.1.2 Iterated simulations

This first experiment consists in the comparison of the same initial configuration (13 families, 100 agents per family) with a varying number of iterations (respectively 10, 20 and 30). The two criteria used to sort families are the cumulated wealth of agents using the same strategy, and the rank achieved by a family based on its cumulated wealth.

Even if stochasticity is present in trading strategies and also in the scheduler that execute the round of talks between agents, results are very stable and are independent from the number of iterations as illustrated by table 1.

When two trading days instead of one are used, some permutations in the middle of the ranking are observed, but the four best and worst strategies are stable.

One interesting observation from this experimentation is that complex strategies that involve learning from prices ($PriceLCS$) or from orders within the order book ($OrderLCS$) have the best results.

	Rank	Wealth
1	OrderLCS	OrderLCS
2	PriceLCS	PriceLCS
3	Momentum1	Momentum1
4	MixedMA1	MixedMA1
5	MinorityAgent	MinorityAgent
6	MajorityAgent	MajorityAgent
7	Variation1	Variation1
8	MovingAv1	MovingAv1
9	Indic1	Indic1
10	Periodic1	Periodic1
11	Zit1	Zit1
12	Rsi1	Rsi1
13	BBand	BBand

Table 1: Iterated simulations with 10, 20 and 30 iterations

5.1.3 Ecological competitions with fixed subset

This second experimentation use the same initial configuration as iterated simulations but a reconfiguration of the initial population is done after each iteration by taking into account the family cumulated wealth. The *ZIT* strategy is excluded from this evolution process in order to always keep liquidity providers in the market.

	Rank	Wealth
1	Momentum1	OrderLCS
2	PriceLCS	Zit1
3	MixedMA1	Variation1
4	OrderLCS	Periodic1
5	MinorityAgent	Rsi1
6	MajorityAgent	MinorityAgent
7	MovingAv1	MajorityAgent
8	Indic1	BBand
9	BBand	Indic1
10	Periodic1	MixedMA1
11	Variation1	MovingAv1
12	Rsi1	PriceLCS
13	Zit1	Momentum1

Table 2: Ecological competitions with 30 iterations

As illustrated by tables 2 and 3 results are less stable than iterated simulations. One explanation is that small differences in the first rankings can rapidly lead to a significant advantage or disadvantage in agent instances.

The figures 4, 5, 6, 7, and 8 illustrate that when the number of agents for each trading strategy evolve from 5 to 1000, the best strategies change. This aspect is deceiving but could be fixed by executing each competitions several times. Nevertheless, others populations update algorithms could be used to limit population growth between two generations. Thus, population evolution would be more interesting in the first generations.

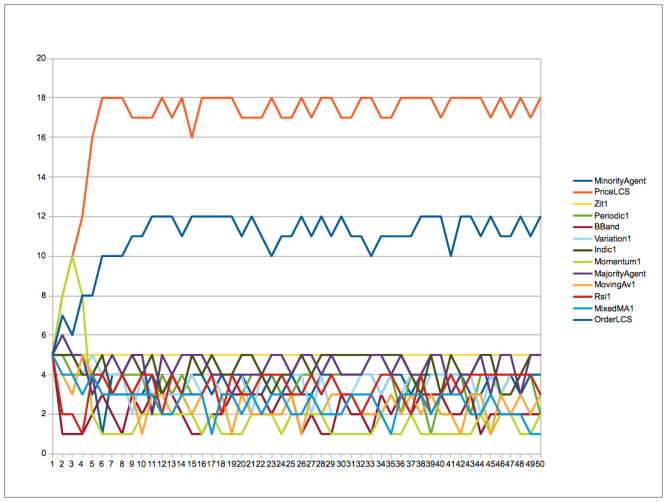

Figure 4: Ecological competition with 5 agents per family

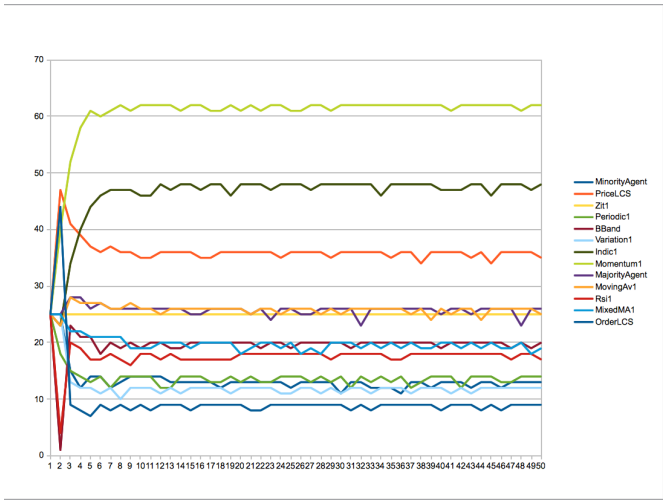

Figure 5: Ecological competition with 25 agents per family

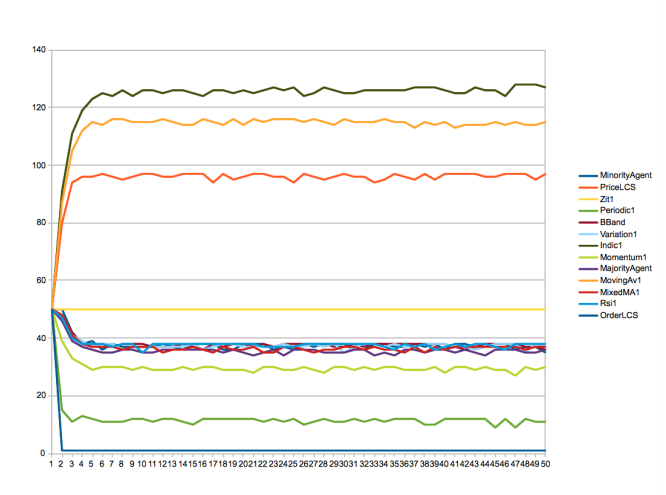

Figure 6: Ecological competition with 50 agents per family

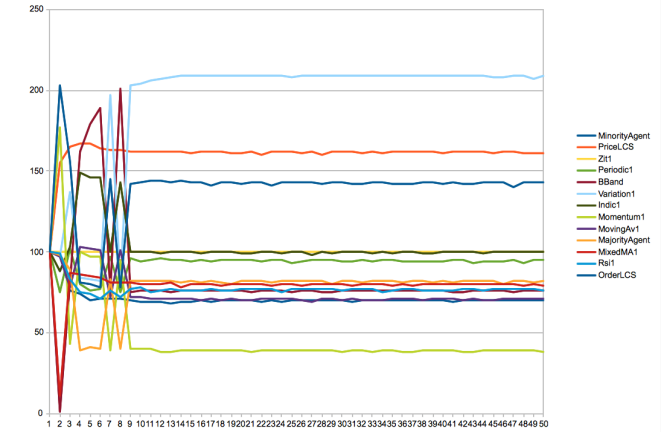

Figure 7: Ecological competition with 100 agents per family

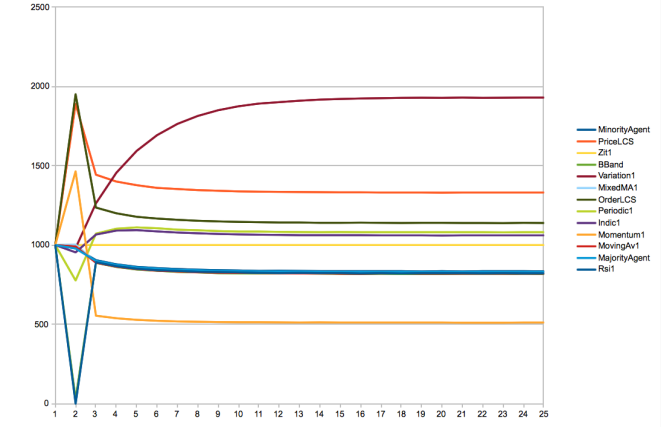

Figure 8: Ecological competition with 1000 agents per family

	Rank	Wealth
1	Momentum1	OrderLCS
2	BBand	PriceLCS
3	MinorityAgent	Zit1
4	MajorityAgent	Indic1
5	MixedMA1	MixedMA1
6	MovingAv1	Variation1
7	Variation1	MinorityAgent
8	Indic1	Periodic1
9	Periodic1	Rsi1
10	Rsi1	MajorityAgent
11	Zit1	MovingAv1
12	OrderLCS	BBand
13	PriceLCS	Momentum1

Table 3: Ecological competitions with 50 iterations

6 Conclusion

Comparing trading strategies efficiency in a stock market is not an easy task. In this paper, we focused our problematic to the evaluation of trading strategies in an order-based stock market simulator implemented in an agent-based approach. We also assume the fact that a trader activity has a direct impact on the price curve (thanks to the agent-based implementation), which is generally not the case in classical evaluation models like back-testing methods.

To assess the performance of a given trading strategy, we propose in this paper to use a taxonomy of evaluations models, ranging from simple iterated simulations with aggregated and averaged results to a more complex approach that computes a large space of possible initial populations configurations. This initial taxonomy proposes some pertinent evaluation models, but should of course be augmented and refined.

This evaluation taxonomy has been used to evaluate some classical trading strategies to illustrate the fact that depending on the evaluation method used, results can be significantly different. These examples demonstrate that one can always find a context which are favorable to a given trading strategy (as clearly demonstrated in [2]). Thus, great care should be taken before claiming that a given strategy outperforms another one.

It should be noted that in this paper, constraints linked to computational equity between agents have not been taken into account. That is to say that agents whose behaviour implies higher computing costs than simpler agents are not penalized. This orthogonal aspects should be further studied to take into account the intuitive idea that reactive agents (rule-based) can be faster on the market than more cognitive agents (learning agents) and so they should be able to interact more regularly with the market.

This notion can also be linked to the trading frequency that should be integrated to the evaluation framework

in order to be able to assess the performance of trading strategies with significative trading frequencies differences (for examples high frequency trading vs. extra day trading). One way to take into account this aspect could be to define a new evaluation criteria that divide the wealth by the number of orders executed to achieve this wealth. Another way could be to introduce fees on orders that are sent, thus agent that flood the market with a small percentage of orders executed would be penalized directly on their wealth.

References

[1] W. B. Arthur, J. Holland, B. LeBaron, R. Palmer, and P. Tayler. *The Economy as an Evolving Complex System II*, pages 15–44. Addison-Wesley, Reading, MA, 1997.

[2] David H. Bailey, Jonathan M. Borwein, Marcos Lopez de Prado, and Qiji Jim Zhu. Pseudo-mathematics and financial charlatanism: The effects of backtest overfitting on out-of-sample performance. *Notices of the American Mathematical Society*, 61(5):458–471, 2014.

[3] O. Brandouy and P. Mathieu. A generic architecture for realistic simulations of complex financial dynamics. In *PAAMS'2010*.

[4] Ido Erev and Alvin E. Roth. Predicting how people play games: Reinforcement learning ... *American Economic Review*, 88:848–881, 1998.

[5] Steven Gjerstad and John Dickhaut. Price formation in double auctions. *Games and Economic Behavior*, 22:1–29, 1998.

[6] B. LeBaron. Building the santa fe artificial stock market. *Brandeis University*, 2002.

[7] P. Mathieu and Y. Secq. Environment updating and agent scheduling policies in agent-based simulators. In *ICAART'2012*.

[8] Philippe Mathieu and Olivier Brandouy. Introducing atom. In *Proceedings of the 10th International conference on Practical Applications of Agents and Multi-Agents Systems (PAAMS'2012)*, Practical Advances in Intelligent and soft computing, pages 269–272. Springer, 2012. Short paper, Best Demo award.

[9] Philippe Mathieu and Matthis Gaciarz. Improving classifier agents with order books information. In Yves Demazeau, Toru Ishida, Juan M. Corchado, and Javier Bajo, editors, *Advances on Practical Applications of Agents and Multi-Agents Systems (PAAMS'2013)*, volume 7879 of *Lecture Notes in Computer Science*, pages 205–215. Springer, 2013.

[10] Imon Palit, Steve Phelps, and Wing Lon Ng. Can a zero-intelligence plus model explain the stylized facts of financial time series data? In *Proceedings of the 11th International Conference on Autonomous Agents and Multiagent Systems - Volume 2*, AAMAS '12, pages 653–660, Richland, SC, 2012. International Foundation for Autonomous Agents and Multiagent Systems.

[11] Gerald Tesauro and Rajarshi Das. High-performance bidding agents for the continuous double auction. In *Proceedings of the 3rd ACM Conference on Electronic Commerce*, EC '01, pages 206–209, New York, NY, USA, 2001. ACM.

[12] Nachi Ueno, Motohiro Shamoto, Koichi Kato, and Yoichi Muraoka. The kaburobo contest. In *Software Engineering Research and Practice*, pages 606–610, 2005.

[13] V. Volterra. Variations and fluctuations of the number of individuals in animal species living together. *Animal Ecology*, 1926.

[14] William E. Walsh, Rajarshi Das, Gerald Tesauro, and Jeffrey O. Kephart. Analyzing complex strategic interactions in multi-agent systems. In *In AAAI-03 Workshop on Game Theoretic and Decision Theoretic Agents*, pages 109–118, 2002.

Proceedings of ICCSA 2014
Normandie University, Le Havre, France - June 23-26, 2014

INTERACTION CAPTURING MODEL IN A DISTRIBUTED COMPUTING SYSTEM

Mahdi Abed Salman, Cyrille Bertelle and Eric Sanlaville *†

Abstract. A model for the representations of interaction in distributed computing systems is proposed, simulated and discussed.
Keywords. Distributed System, Complex System, Load balancing, Multi-agents, Interaction modeling

1 Introduction

A distributed computing system DCS is a set of computing nodes connected by a communication network. They are working together to carry out user tasks. In fully distributed systems, where there is no central point, communications between nodes are made through message passing i.e. there is no shared memory.

A node may host many agents that have been designed to do specific tasks. An agent is an autonomous software entity. It has a working environment. It is able to take decisions depending on its internal state or/and environments state. It communicates with other local or remote agents to request or report information. An agent changes its state or responds to a request depending on receiving information.

Building a DCS needs to consider many parameters. The list starts from network topology. For each topology a suitable information broadcasting method should be specified. Then, comes the size of local knowledge that makes load balancing methods perform effectively. A load balancing scheme and for each scheme a suitable load balancing strategy that determines when and how an extra load is transferred are also needed, and the list does not end.

Dealing with many parameters makes the study of a DCS difficult. Furthermore DCS's may be considered as complex system. In complex system theory[3], a system is composed of many subsystems. Relations between subsystems and inside subsystems are present. The global behavior of a complex system emerges from the interaction between agents that reside the different subsystems and can never be expressed by the features of single individuals.

Some kind of long term relations may be created between agents according to frequent request-respond communication[2]. A relation may combine more than two agents that are hosted in different nodes.

In this study, we try to investigate how relations are created in some realistic model of a distributed system. A description is given for these relations and the role of its participants.

The remaining of this document is organized as follow: In section 2, a description of the selected model of a distributed computing system is given. In section 3, a model of interaction between agents is presented. Then, in section 4, experiments and discussion of results are given. Section 5 concludes the study.

2 DCS model

A distributed system is modeled by a graph. The type of the graph is usually small world[8] or scale free[1] network.

The undirected graph is denoted by $G = (V, E)$ where V is the set of vertices (nodes) and E is the set of links (edges). Information flows in the network according to those graphs structure. We call them *Initial* graphs.

A node is capable of receiving jobs from users, scheduling jobs for execution, sending/receiving information to/from its neighbors, and moving jobs to/from other nodes to balance load in the system. Most of nowadays computers are multitasks and equipped with multi-core processors which allow them to run many programs simultaneously. It is preferable to have some agents to manage some of these tasks independently.

In our model, each node v is occupied by two stationary agents: information agent and balancing agent. The information agent, denoted by I, is responsible to communicate with neighbor nodes and exchanges load information with them. The load is measured (*In this paper*) by the remaining time of jobs being executed, plus the execution times of waiting jobs. Cached information at nodes forms what is called "overlay" network. In peer-to-peer networks, an overlay network is a logical network which is built from the information exchanged between peers using some diffusion method. An overlay network is dynamic in term of local knowledge content. It is mod-

*Mahdi Abed Salman is a PhD student at LITIS-University of Le Havre, from the Department of Computer Science, University of Babylon, Iraq. E-mail: mahdi4it@gmail.com

†Cyrille Bertelle and Eric Sanlaville are with Faculty of Science and Techniques, University of Le Havre, France. E-mails: cyrille.bertelle@univ-lehavre.fr, eric.sanlaville@univ-lehavre.fr

eled by a directed graph, where an arc (i, j) means that node i has some knowledge about node j (here about its load).

The balancing agent, denoted by B, is responsible to keep load level of its node near the average of load levels of the known set of nodes called "node view". This view represents a partial knowledge of global system state. I maintains the partial view.

Many methods of information diffusion could be used for this purpose, for example: mobile agent or rumor spreading. If mobile agent is used, I communicates with visiting mobile agents[4][6] to exchange available up to date load information.

If rumor spreading[7][5] is selected, I chooses one of neighbor nodes at random and exchanges information with that node.

Mobile agent based information diffusion is used in this study because it uses less communication bandwidth. Whatever the selected method of information diffusion is, a balancing agent should have "enough" information to do its assigned task correctly.

A node looks at its view. Using one of possible load balancing strategies[9], It determines its role as sender or receiver initiator of load balancing. It searches for source or destination of load migration according to its specified role. In this study, a new load balancing strategy is used. The strategy is summarized as follow.

For a node u, balancing agent B_u searches inside its view for the maximum loaded node v, compares its load level $L_u$with that of L_v, if $L_u \leq \frac{L_v}{2}$ then B_u contacts the corresponding balancing agent B_v to send it a job.

A job j is migrated from overloaded node v to under-loaded node u if and only if: v has more than one job and migration of j does not change load inequality between u and v i.e $(L_u + l_j) < (L_v - l_j)$, where L_v and L_u are computed before the migration and l_j is the length (its execution time) of job j.

3 Interaction model

To capture interaction in a distributed system, the model below is proposed. In this model three elements must be specified. They are:

1. *Event*: Interactions mean exchanging messages between actors that may concern many events or subjects. For clarity, it is better to focus on one type and omit non related messages. An event may be a simple message passing or a job migration.

2. *An indicator*: To determine how to sense or calculate traffic rate of an event on a selected connection. In this study, the simplest indicator is a counter of the number of events concerning a given arc. The counter is incremented by one for each occurrence of the event (job migration) through a given arc.

3. *The threshold*: During running of the model, a node creates many relations (arcs) with other nodes. Accordingly, a highly connected high density graph is expected to appear. To investigate the behavior of the system, only arcs that have their indicator values satisfying specific criteria are kept. All other arcs are removed. In this study, two type of threshold are tested.

   - local threshold: for each node, only one out arcs with maximum weight value is kept. All other arcs are removed.
   - global threshold: All arcs that have weight value less than T are removed, where T is global threshold and computed from weight distribution vector.

The resulting graph is considered as a representation of the event under investigation.

4 The implementation

4.1 Parameters and configuration

A simplified model is simulated and the simulation runs for a specific duration. During running of the simulation, A directed graph $G' = (V, A)$ is maintained, where A is the set of arcs that represent job flows from overloaded to under-loaded nodes in the network. We call this graph the *migration* graph. It is initialized as $V(G') = V(G)$ and $A(G') = \phi$.

The *event* here is the migration process. For each migration, if arc $(v, u) \notin A$ then it is added $A \leftarrow A \cup (v, u)$.

(v, u) has an attribute called "weight". $w(v, u)$ equals the number of jobs migrated from v to u. Weight is the *indicator* of migration event.

A node $v \in G'(V)$ has an attribute called energy e. $e \leftarrow (J_{in} - J_{out})$, where J_{in} is the number of jobs brought to v and J_{out} is number of jobs taken from v.

When the experiment is terminated, each node $v \in V(G')$ is called :

- ⊡ *source* and shaped by a rectangle: if $e_v \leq p1$,
- △ *bridge* and shaped by a triangle: if $p1 < e_v \leq p2$,
- ◯ *sink* and shaped by a circle: if $e_v > p2$.

  where:
  $p1 \leftarrow min_e + \frac{1}{3}(max_e - min_e)$,
  $p2 \leftarrow max_e - \frac{1}{3}(max_e - min_e)$,
  max_e, min_e are the maximum and minimum energy values respectively.

A *threshold* is applied on G' as explained before. Global threshold T is computed by the following formula:
$T \leftarrow w_{high} + \frac{1}{3}(w_{max} - w_{high})$,
where w_{high} is the highest frequent weight, w_{max} is the maximum weight. This is empirically chosen to break migration graph into a significant number of components.

Common features of resulting components are calculated , for example: number of nodes, number of arcs, average node degree, diameter, number of loops, strongly connected components, weakly connected components etc. A component is a set of nodes (graph or sub-graph) and it is called connected when there exists a path (without considering the direction of the edges) between any two nodes belong to that set. In a directed graph, a component is called weakly connected if a connected (undirected) graph is resulting from replacing all of its directed edges with undirected edges. A component is strongly connected SCC if there is a path in each direction between each pair of nodes of the component.

4.2 Tests and results

Many initial networks are generated and tested. They are of different size. For simplicity reasons, one small size network is presented here. It is generated according to Watts-Strogatz[8] algorithm. A submitted study showed that it is sufficient to do load balancing effectively using knowledge size between 16 and 32 entries for this network type. In this study, size of 16 entries is used. Table 2 shows the features of the network that has been tested on laptop.

Two sets of jobs are used. One set contains identical job lengths (5 units of time) while the other has different job lengths (uniformly distributed in $[1, 9]$). Features of the two sets are shown in table 1.

All runs have duration of 1000 units of time. A job is migrated if unbalance of load is detected between two nodes that are neighbors in term of knowledge representation graph(overlay network). Job movements form the migration graph. Table 2 shows graph features of initial network, a snapshot of overlay network and resulting migration graph (before applying a threshold). The snapshot of overly network is taken when the network reaches the steady state.

Migration graph is updated as mentioned above. Results are similar for both job sets. Results of only one set are presented here. Weight values are ranged from 1 to 13. The mean weight value is 1.33. The most frequent weight is 1 repeated 39527. For energy: the maximum and minimum values are 180 and -197 respectively. All resulting components are weakly connected, however, one small strongly connected component appears in the results of local threshold only. Details of obtained results are summarized in tables 3 and 4.

Table 1: Features of sets of jobs

	A	B
Number of jobs	199431	199867
Job length	identical	Variable
Average job length(ms)	5.0	4.98
Average arrival rate	0.199	0.199
Total load per node		
Mean	997.0	996.0
Standard deviation	565.79	568.90
Maximum	2050	2084
Minimum	0	0

Table 2: Features of graphs

Feature	Initial	Overlay	Migration
Components Count	1	1	1
Diameter	5	5	8
Density	0.016	0.030	0.106
Ave. clustering coeff.	0.5	0.11	0.070
Graph Order	1000	1000	1000
Edges count	8000	15294	60250
Maximum (out) degree	21	16	151
Minimum (out) degree	12	15	0
Average (out) degree	16	15	53
Maximum in degree	-	35	143
Minimum in degree	-	3	3
Average in degree	-	15	53

Table 3: Local Threshold: all resulting components

C.	Nodes	Arcs	Diameter	Sources	Bridges	Sinks	SCC count	max Size
0	387	387	15	229	144	14	1	2
1	181	181	19	97	73	11	1	5
2	162	162	9	90	63	9	0	0
3	127	127	17	73	50	4	0	0
4	119	119	13	76	36	7	1	4
5	16	15	3	11	3	2	0	0
6	6	5	2	4	1	1	0	0
7	2	2	1	0	2	0	1	2

Table 4: Global Threshold: largest 10 out of 62 connected components

C.	Nodes	Arcs	Diameter	Sources	Bridges	Sinks
1	57	72	1	31	0	26
2	28	29	2	10	1	17
3	24	34	1	13	0	11
4	23	24	1	10	0	13
5	23	25	1	9	0	14
6	20	21	1	9	0	11
7	19	19	1	8	0	11
8	18	19	1	8	0	10
9	17	19	1	9	0	8
10	16	16	1	8	0	8

4.3 Discussion

In the migration graph, an arc between two nodes is a sign of occurrence of interaction event. High weight value of an arc means frequent communication. Energy value expresses impact of a node in load balancing process. The large difference between maximum weight value and maximum energy value is due to high out degree of nodes.

The large average of out-degree and in-degree in migration graph belongs to the dynamicity of the overlay network and the variation in job arrival rates.

A node with very high job arrival rate acts as source of jobs. In migration graph, it has high out-degree and zero in-degree.

A node with very low arrival rate acts as sink for jobs. It has high in-degree and zero out-degree.

Nodes with arrival rate near the average play *bridges* role. They have in-degree and out-degree near the average also. These nodes make the migration graph strongly connected. Hence, it has small diameter, see table 2. Nodes are classified as source, bridge or sink before applying a threshold.

Local threshold produces few components. Keeping one out-edge of nodes makes components have large diameter. Most components take tree structure. Some of resulting components have one strongly connected component. See table 3.

Global threshold breaks migration graph into many small components. A node in these components is either a source or a sink and rarely a bridge. Bridges in these components may result from sharp classification of nodes i.e. they are more likely sources or sinks. No strongly connected component is noticed, Hence, last two columns are dropped from table 4 because they are all zeros.

5 Conclusion

In this study, a simple model of agent based distributed computing system is built, simulated and interaction among thousands of agents is analyzed.

Setting an indicator to count occurrence of an event is an important step in interaction modeling. The value of an indicator is updated for each occurrence of the event. Weighting edge between nodes according to number of communications made over it is an example of an indicator.

Threshold is used to emphasize "hot" edges in the graph or hide interactions that seldom occur. A more thorough study is mandatory for a deeper understanding of the system behavior. Further work will be made to see the effect of selected load balancing strategy on structure of the obtained interaction.

References

[1] A.-L. Barabási and R. Albert. Emergence of scaling in random networks. *Science*, 286(5439):509–512, Oct. 1999.

[2] C. Bertelle, A. Dutot, F. Guinand, and D. Olivier. Organization detection for dynamic load balancing in individual-based simulations. *Multiagent and Grid Systems*, pages 1–40, 2007.

[3] N. Boccara. *Modeling complex systems*. Springer, 2004.

[4] M. Charpentier. Cooperative mobile agents to gather global information. *Network Computing and Applications*, pages 271–274, 2005.

[5] A. E. F. Clementi, P. Crescenzi, C. Doerr, P. Fraigniaud, M. Isopi, A. Panconesi, F. Pasquale, and R. Silvestri. Rumor spreading in random evolving graphs. *CoRR*, abs/1302.3828, 2013.

[6] D. Gavalas, G. E. Tsekouras, and C. Anagnostopoulos. A mobile agent platform for distributed network and systems management. *The Journal of Systems & Software*, 82(2):355–371, 2009.

[7] G. Giakkoupis. Tight bounds for rumor spreading in graphs of a given conductance. In T. Schwentick and C. Dürr, editors, *STACS*, volume 9 of *LIPIcs*, pages 57–68. Schloss Dagstuhl - Leibniz-Zentrum fuer Informatik, 2011.

[8] D. J. Watts and S. H. Strogatz. Collective dynamics of 'small-world' networks. *Nature*, 393(6684):440–442, June 1998.

[9] M. H. Willebeek-LeMair and A. P. Reeves. Strategies for dynamic load balancing on highly parallel computers. *IEEE Trans. Parallel Distrib. Syst.*, 4(9):979–993, Sept. 1993.

General Session 5
Bio-Systems

Proceedings of ICCSA 2014
Normandie University, Le Havre, France - June 23-26, 2014

COLORED NOISE EFFECTS ON GHOST STOCHASTIC RESONANCE

M. Bordet*†, S. Morfu*‡ and M. Rossé *

Abstract. We analyze the Ghost Stochastic Resonance (GSR) effect in an electronic circuit exactly ruled by the FitzHugh-Nagumo (FHN) equations, both numerically and experimentally. When the circuit is excited with a bichromatic driving with two close frequencies, we show that for an appropriate noise intensity the circuit response exhibits a ghost frequency which is not present in the biharmonic input signal. In this paper, we highlight the effects of colored noise on GSR.

Keywords. Ghost stochastic resonance - nonlinear dynamics - FitzHugh-Nagumo - electronic circuit - colored noise.

1 Introduction

During the past decades, the investigation of nonlinear systems have attracted a large amount of work taking into account different input excitations. These studies have revealed various nonlinear effects in numerous assorted fields, such as electronics, optics, biology and neuroscience [1, 2, 3, 4]. Note that these examples constitute a non exhaustive list of concerned domains where nonlinear signatures have allowed to account for the behavior of natural systems.

Among the highlighted nonlinear phenomena, Coherence Resonance (CR) which may occur under certain conditions when the system is only excited by noise, shows that the system response can achieve a maximum of regularity for an optimum noise intensity [5]. CR has provided a better understanding of neurons activity in the absence of stimuli [6]. Moreover, CR has also been studied in electronic circuits for both white and colored noises [1, 7, 8, 9].

Beside this CR effect, the interaction between a deterministic signal and a random fluctuation has led to another phenomenon, called Stochastic Resonance (SR). SR results in a system response enhancement to an applied stimulus for an optimum noise intensity [10]. Like CR, SR brings natural phenomena comprehension in biology and neuroscience. For instance, thanks to SR, climate dynamics and the neurons response to subthreshold stimuli are now better known [3, 11]. Likewise in the CR case, a great deal of work have been devoted to SR in electronic circuits [12, 13].

Next, considering two-frequency driving has revealed two major phenomena. On the first hand, Landa and McClintock have shown the occurrence of Vibrational Resonance (VR) in nonlinear systems [14]. On the other hand, Chialvo & al. have found a resonance at a frequency missing in the input excitation [15]. Since this ghost frequency is not sent at the system input and since noise is essential to reveal the resonance, this effect is now better known as Ghost Stochastic Resonance (GSR) in literature. Although similarities exist between VR and GSR, note that some differences remain. First, two conditions which are not necessary to exhibit VR are required to reveal GSR: (1) a linear interference of the individual tones, which naturally leads to signal peaks at the fundamental frequency and (2) a nonlinear threshold that detects these peaks thanks to the noisy term. Second, for GSR the two considered frequencies need to be of the same order, whereas for VR the two frequencies could be very distinct. Among the other differences, VR is studied when the high frequency component amplitude is tuned in order to observe the resonant behavior, while GSR is inspected by tuning the noise intensity. The last but not least difference appears in the analyse of the system responses which are respectively estimated at the low frequency component and at the ghost frequency in the VR and GSR cases. GSR has been introduced first to explain the missing fundamental illusion in pitch perception [4, 16] and next has been used for modelling Dansgaard-Oeschger events in climatic changes [17, 18]. Other studies have been carried out in optics [19, 20, 21] and visual perception [22]. Furthermore, as we have previously seen in the cases of CR, SR and VR which have been widely studied in electronics and neuroscience [1, 6, 7, 8, 9, 11, 12, 13, 23, 24, 25, 26], GSR have also motivated a great deal of work in these domains [27, 28, 29, 30, 31, 32, 33]. The intensive interest devoted to GSR in electronics and neuroscience can be explained with two main reasons. In a first time by the issues due to the biophysical aspect of GSR with the pitch perception of complex sounds by the auditory system [34] and in a second time with the significance of electronic circuits in the development of new bio-inspired applications [35, 36, 37].

*M. Bordet, S. Morfu and M. Rossé are with Laboratoire Electronique Informatique et Image (LE2I) UMR CNRS 6306, université de Bourgogne, France. E-mails: † maxime.bordet@u-bourgogne.fr and ‡ smorfu@u-bourgogne.fr

In this paper, we propose to study GSR in presence of colored noise in an electronic neural circuit exactly ruled by the FHN equations. To that end, we analyse the circuit output magnitude spectrum and the rate of spike firing in the circuit voltage output. The paper is organized as follows: in the next section, we present our experimental setup. The third section is devoted to the white and colored noise effects on GSR in the harmonic case. The last section provides concluding remarks.

2 Experimental system and methods

2.1 The nonlinear circuit

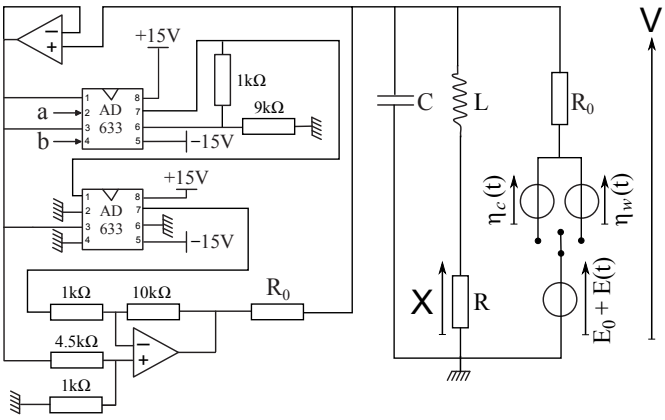

Figure 1: The FitzHugh-Nagumo circuit excited by a stimulus consisting of an offset voltage E_0, a signal $E(t)$ obtained by adding two sine waves with close frequencies and either an additive white noise source $\eta_w(t)$ or an additive colored noise source $\eta_c(t)$. a and b are two external voltage sources which tune the roots of the cubic nonlinearity. The voltage V constitutes the circuit output. AD633JN and TL081CN are analog multipliers and classical operational amplifiers.

To carry out our experiments on GSR, we use an electronic circuit which has already exhibited CR, VR and GSR in presence of a white noise source exclusively [9, 25, 26, 33]. This electronic system is exactly ruled by the FHN equations. Indeed, by applying the Kirchhoff's laws to the device of Figure 1, it can be shown that the dynamics of the voltage V is governed by the following set of normalized equations:

$$\begin{aligned} \frac{dV}{dt} &= -V(V-a)(V-b) - W + E_0 + E(t) + \eta_{w,c}(t), \\ \frac{dW}{dt} &= \varepsilon(V - \gamma W). \end{aligned} \quad (1)$$

In Eq. (1), t and W which represent the normalized time and the slow variable of the FHN model respectively depend on the experimental time t_{exp} and the voltage X according to the transformation:

$$t = \frac{t_{exp}}{R_0.C} \ , \ W = \frac{R_0.X}{R}. \quad (2)$$

Moreover, the two normalized parameters ε and γ are set with the components values as follows:

$$\varepsilon = \frac{{R_0}^2.C}{L} \ , \ \gamma = \frac{R}{R_0}, \quad (3)$$

where R_0, R, C and L have been chosen such that $\varepsilon = 3.6358$ and $\gamma = 0.2367$. Two external DC generators tune the roots of the cubic nonlinearity to $a = 2\ V$ and $b = -2.6\ V$. The offset voltage E_0 has been set to -1V such that without noise, and when there is no excitation, namely $E(t_{exp}) = 0\ V$ and $\eta_{w,c}(t_{exp}) = 0\ V$, the voltage V doesn't trigger spikes. The input forcing $E(t_{exp})$ has been obtained by adding two sine waves with the same amplitude A but with different frequencies f_1 and f_2 which obey to:

$$\begin{aligned} f_1 &= 2.f_0 + \Delta f, \\ f_2 &= 3.f_0 + \Delta f. \end{aligned} \quad (4)$$

In Eq. (4), f_0 represents the *ghost* frequency and is set to 300 Hz in the whole article, whereas Δf corresponds to a frequency shift. $\Delta f = 0$ refers to the harmonic case and $\Delta f \neq 0$ denotes the inharmonic case. Throughout this paper, $\Delta f = 0$ since we focus our study on the harmonic case. Lastly, either the additive white noise source $\eta_w(t_{exp})$ or the additive Ornstein-Uhlenbeck random fluctuation $\eta_c(t_{exp})$ will be subsequently added to the deterministic excitation $E(t_{exp})$. Their respective correlation functions fulfill:

$$< \eta_w(t_{exp}), \eta_w(t_{exp} - t'_{exp}) > = \ \sigma^2 \delta(t_{exp} - t'_{exp}), \quad (5)$$

$$< \eta_c(t_{exp}), \eta_c(t_{exp} - t'_{exp}) >= \frac{\sigma^2}{2.\tau}.\exp^{-\frac{|t_{exp}-t'_{exp}|}{\tau}}. \quad (6)$$

In Eq. (5), σ denotes the Root Mean Square (RMS) amplitude of the gaussian white noise. The colored noise of correlation function provided by Eq. (6) is obtained with the following Ornstein-Uhlenbeck process:

$$\frac{d\eta_c(t_{exp})}{dt_{exp}} = \frac{\psi(t_{exp})}{\tau} - \frac{\eta_c(t_{exp})}{\tau}, \quad (7)$$

where τ represents the correlation time, while $\psi(t_{exp})$ is a gaussian white noise with a RMS amplitude equal to σ and a correlation function defined by:

$$< \psi(t_{exp}), \psi(t_{exp} - t'_{exp}) > = \ \sigma^2 \delta(t_{exp} - t'_{exp}). \quad (8)$$

2.2 Modus operandi

The white random fluctuations $\eta_w(t_{exp})$ and $\psi(t_{exp})$ are generated by executing a Matlab routine which in a first

time generates random samples with a gaussian distribution and then converts them in an analog signal available on the computer audio output [26, 28, 38, 39]. Whereas the colored noise $\eta_c(t_{exp})$ is experimentally obtained by filtering the white noise $\psi(t_{exp})$ with a classical first-order low-pass filter as represented in Figure 2 [26]. The cutoff frequency is adjusted with a fixed capacitor C′ and a potentiometer P which allows to adjust the correlation time to τ=P.C′ and so, to more or less color the random fluctuation $\eta_c(t_{exp})$. It is worth noting that the white noise limit is achieved when τ tends towards 0.

Note that in the whole article, the acquisitions of our experimental data have been performed by means of a LeCroy Waverunner oscilloscope by averaging the results on 200 realizations. Note also that to obtain our numerical data, we have computed Eq. (1) with a fourth-order Runge-Kutta algorithm with 2^{20} samples and an integration time $dt = 100/[2^{20}(f \times R_0 \times C)]$.

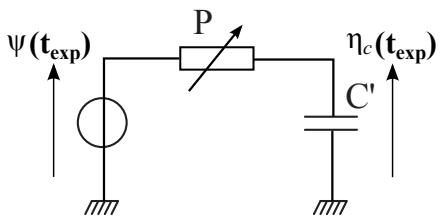

Figure 2: First-order low-pass filter used to color the white noise $\psi(t_{exp})$. With C′ = 2.2 nF and P is a potentiometer which set the correlation time of the colored noise $\eta_c(t_{exp})$ to τ=PC′.

3 Noise effects in the harmonic case

In this section we propose to investigate GSR in the harmonic case, that is when $\Delta f = 0$. Therefore, according to Eq. (4) the two frequencies f_1 and f_2 are set to 600 Hz and 900 Hz respectively.

3.1 Frequency analysis

To appraise the GSR phenomenon, we have computed the magnitude spectrum of the voltage $V(t_{exp})$ against the noise RMS value σ. The amplitudes obtained at the frequencies f_0, f_1 and f_2 are noted Q_0, Q_1 and Q_2. Numerical and experimental results are respectively plotted on the left and on the right in Figure 3 for both the white (solid lines) and colored noise cases. Note that four correlation times have been considered: $\tau = 20\ \mu s$ (dashed lines), $\tau = 72\ \mu s$ (dash-dotted lines), $\tau = 145\ \mu s$ (dotted lines), $\tau = 218\ \mu s$ (vertical dashed lines). The spectrum has displayed resonances at the two input components f_1 and f_2, but it has also revealed a convex-shaped curve at the ghost frequency f_0. Whatever the correlation time, both our simulations and our experimentations show resonant curves versus the noise RMS intensity σ. So, there exists an optimum amount of noise which can provide an enhancement for the ghost frequency detection. Based upon the results presented in Figure 3, white noise allows to reach higher amplitudes for Q_0, Q_1 and Q_2 than the colored noise. Moreover, it can be raised that a stronger noise intensity is required to optimize the detection of the three frequencies f_0, f_1 and f_2 when the correlation time τ of the colored noise $\eta_c(t_{exp})$ increases.

3.2 Statistical study of the voltage output time series

Another way to highlight the presence of the ghost frequency f_0 consists in studying the time series of the voltage $V(t_{exp})$ and to analyse the rate of spikes firing. In our case, a spike is considered when the voltage output $V(t_{exp})$ crosses a fixed threshold V_{th} set to 0V [33]. To characterize this effect in the FHN circuit, we have taken into account three specific probabilities P_0, P_1 and P_2. These quantities stand for the respective probabilities that the output voltage V triggers spikes within the ranges given by f_0±5%, f_1±5% and f_2±5%. Figure 4 displays our numerical data (left) and our experimental data (right) when the probabilities are plotted versus the noise amplitude σ. The white noise case (solid lines) but also the four previous correlation times in the colored noise case have been considered: that is $\tau = 20\ \mu s$ (dashed lines), $\tau = 72\ \mu s$ (dash-dotted lines), $\tau = 145\ \mu s$ (dotted lines), $\tau = 218\ \mu s$ (vertical dashed lines). Analogously to the study of the output magnitude spectrum operation, we have obtained a resonant behavior versus the RMS noise intensity σ. Once again, both our simulations and our experiments show that whatever the correlation time studied, there exists an appropriate noise amplitude which provides an enhancement for the detection of the frequencies f_0, f_1 and f_2. Note that when the probability P_0 reaches its maximum, the probability that the voltage V responds with a frequency present in the input excitation is null. Moreover, the impact of the correlation time on the results is the same that in the study of the magnitude spectrum behavior. Indeed, the white noise provides the higher values in the estimation of P_0, P_1 and P_2. Afterwards, as τ grows, an higher RMS noise intensity is necessary to attain the maximum probabilities that the system triggers spikes with frequencies approximatively equal to f_0, f_1 or f_2. This effect can be explained by the properties of the Ornstein-Uhlenbeck process described in Eq. (6). In fact, the total noise power intensity according to Eq. (6) is equal to $\sigma^2/(2.\tau)$. It involves that increasing τ for a fixed white noise intensity σ^2 leads to a diminution of the total noise power supplied in the circuit.

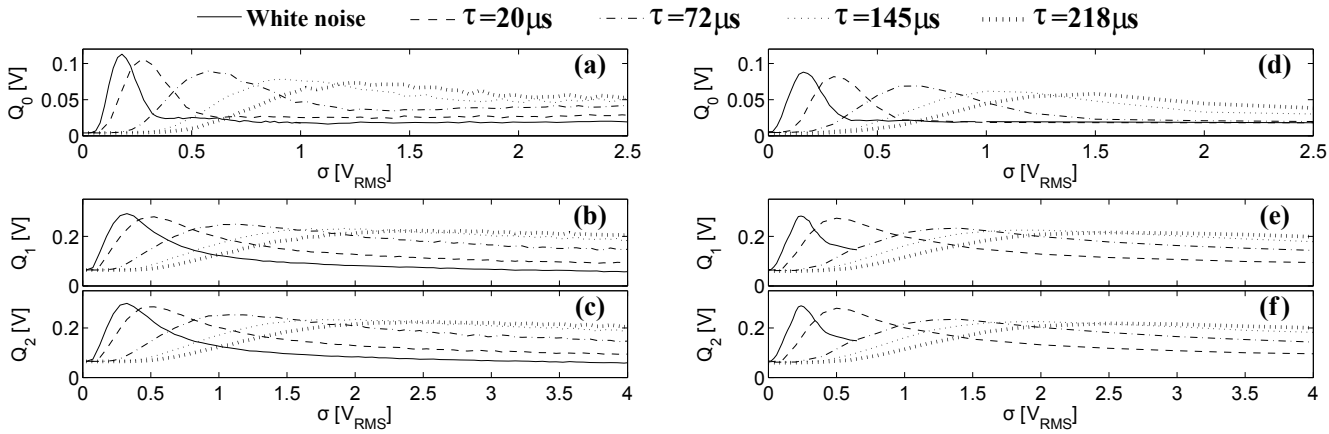

Figure 3: Effect of the noise correlation time τ on the magnitude spectrum of the voltage V estimated for the three frequencies: f_0 (a and d), f_1 (b and e) and f_2 (c and f). The simulation results are presented on the left (a, b and c) while the experimental data are available on the right (d, e and f). Circuit parameters: $a = 2\ V$, $b = -2.6\ V$, $E = -1\ V$, $\epsilon = 3.6358$, $\gamma = 0.2367$, $A = 0.3\ V$, $f_0 = 300\ Hz$, $f_1 = 600\ Hz$, $f_2 = 900\ Hz$, $\Delta f = 0\ Hz$ and $V_{th} = 0\ V$.

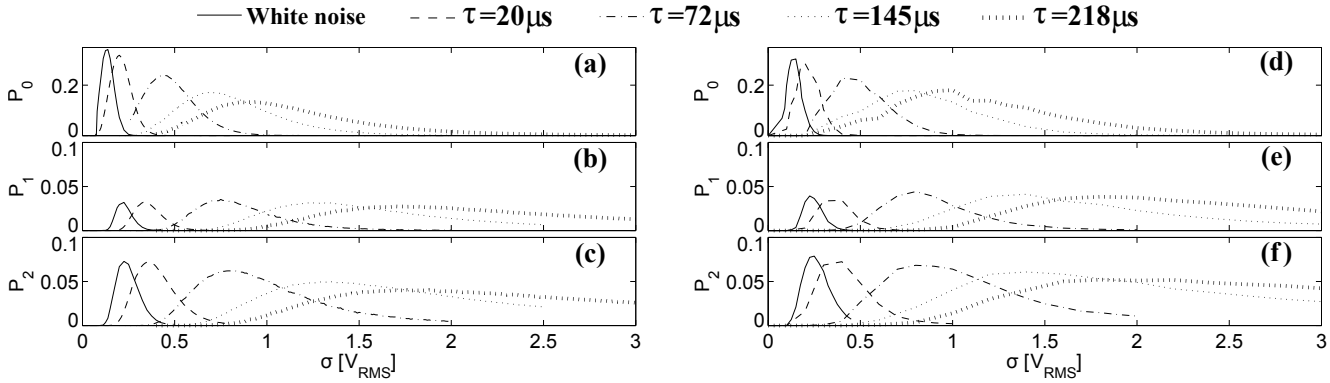

Figure 4: Effect of the noise correlation time τ on the probability that the voltage V triggers spikes with a rate in the ranges defined by $f_0 \pm 5\%$ (a and d), $f_1 \pm 5\%$ (b and e) and $f_2 \pm 5\%$ (c and f). The simulation results are plotted on the left (a, b and c) while the experimental results are provided on the right (d, e and f). Circuit parameters: $a = 2\ V$, $b = -2.6\ V$, $E = -1\ V$, $\epsilon = 3.6358$, $\gamma = 0.2367$, $A = 0.3\ V$, $f_0 = 300\ Hz$, $f_1 = 600\ Hz$, $f_2 = 900\ Hz$ and $\Delta f = 0\ Hz$. The threshold to detect spikes triggering in the time series is set to $V_{th} = 0\ V$.

4 Conclusion and discussions

We have analyzed both experimentally and numerically the response of an electronic circuit governed by the set of FitzHugh-Nagumo equations. This circuit has been excited with a stimulus composed by the second- and third-order harmonics of a given fundamental frequency and subsequently corrupted by either a white or colored noise source. Two different studies have been carried out to show that the circuit response exhibits resonant behaviors at distinct frequencies. The first one takes into consideration the magnitude spectrum of the circuit output signal and the second one is based on the statistical analysis of the voltage output time series.

First, the magnitude spectrum of the circuit voltage output V has presented bell-shaped response at the two frequencies applied in the circuit (f_1 and f_2) when it was plotted against the noise RMS amplitude σ. In a counterintuitive manner, the magnitude spectrum has also revealed a nonlinear signature with a resonant behavior at a frequency absent of the input excitation (f_0). That is another way to retrieve the ghost frequency in the circuit. We have shown that the resonant behaviors of the magnitude spectrum at the three frequencies f_0, f_1 and f_2, exist in the white and colored noise cases. Even if the bell-shaped responses subsist in a colored noisy medium at the three distinct frequencies, it is worth noting that when the correlation time grows, the detection of these frequencies is reduced.

Second, as it is common in literature the statistical analysis of the voltage output time series have also displayed resonances at the three frequencies f_0, f_1 and f_2. Moreover, in this paper, we have taken into account the noise correlation time. Indeed, we have shown that for

each rate of spikes firing within the ranges $f_0 \pm 5\%$, $f_1 \pm 5\%$ and $f_2 \pm 5\%$ an optimum noise intensity allows to reach a maximum for the probabilities P_0, P_1 and P_2 whatever the correlation time considered. Based upon the results presented in this paper, it is clear that the white noise provides a better detection of the frequencies f_0, f_1 and f_2 than the colored noise.

To conclude, considering the close link between biophysical and engineering aspects of GSR, we expect that our work on an electronic device could be of significance for new potential bio-inspired applications in the human auditory system. Some others aspects of GSR could be studied in presence of colored noises in order to better know the phenomenon. For instance, the harmonic case when more than two frequencies composed the input stimulus, the inharmonic case, that is when $\Delta f \neq 0$ or also GSR in coupled structures of such elementary circuits.

Acknowledgements

The research for this work was supported, in part, by the Regional Council of Burgundy.

References

[1] D. E. Postnov, S. K. Han, T. G. Yim and O. V. Sosnovtseva, "Experimental observation of coherence resonance in cascaded excitable systems," *Phys. Rev. E*, vol. 59, R3791, 1999.

[2] V. N. Chizhevsky, E. Smeu and G. Giacomelli, "Experimental evidence of Vibrational Resonance in an optical system," *Phys. Rev. Lett.*, vol. 91, 220602, 2003.

[3] C. Nicolis and G. Nicolis, "Stochastic aspects of climatic transitions-Additive fluctuations," *Tellus*, vol. 33, pp. 225-234, 1981.

[4] D. R. Chialvo, "How we hear what is not there: A neural mechanism for the missing fundamental illusion," *Chaos*, vol. 13, 1226, 2003.

[5] A. S. Pikovsky and J. Kurths, "Coherence resonance in a noise-driven excitable system," *Phys. Rev. Lett.*, vol. 78, pp. 775-778, 1997.

[6] B. Lindner, J. García-Ojalvo, A. Neiman and L. Schimansky-Geier, "Effects of noise in excitable systems," *Phys. Rep.*, vol. 392, pp. 321-424, 2004.

[7] Y. Horikawa, "Coherence resonance with multiple peaks in a coupled FitzHugh-Nagumo model," *Phys. Rev. E*, vol. 64, 031905, 2001.

[8] S. Brugioni, D. -U. Hwang, R. Meucci and S. Boccaletti, "Coherence resonance in excitable electronic circuits in the presence of colored noise," *Phys. Rev. E*, vol. 71, 062101, 2005.

[9] G. Lassere, S. Morfu and P. Marquié, "Coherence resonance in Bonhoeffer-Van der Pol circuit," *Electron. Lett.*, vol. 45, pp. 669-670, 2009.

[10] L. Gammaitoni, P. Hänggi, P. Jung, and F. Marchesoni, "Stochastic Resonance," *Rev. Mod. Phys.*, vol. 70, pp. 223-287, 1998.

[11] D. Nozaki, D. J. Mar, P. Grigg and J. J. Collins, "Effects of Colored Noise on Stochastic Resonance in Sensory Neurons," *Phys. Rev. Lett.*, vol. 82, pp. 2402-2405, 1999.

[12] G. P. Harmer and D. Abbott, "Simulation of circuits demonstrating stochastic resonance," *Microelec. J.*, vol. 31, pp.553-559, 2000.

[13] W. Korneta, I. Gomes, C. R. Mirasso and R. Toral, "Experimental study of stochastic resonance in a Chuas circuit operating in a chaotic regime," *Physica D*, vol. 219, pp. 93-100, 2006.

[14] P. S. Landa and P. V. E. McClintock, "Vibrational resonance," *J. Phys. A: Math. Gen.*, vol. 33, pp. 433-438, 2000.

[15] D. R. Chialvo, O. Calvo, D. L. Gonzalez, O. Piro and G. V. Savino, "Subharmonic stochastic synchronization and resonance in neuronal systems," *Phys. Rev. E*, vol. 65, 050902(R), 2002.

[16] P. Balenzuela and J. García-Ojalvo, "Neural mechanism for binaural pitch perception via ghost stochastic resonance," *Chaos*, vol. 15, 023903, 2005.

[17] H. Braun, A. Ganopolski, M. Christl and D. R. Chialvo, "A simple conceptual model of abrupt glacial climate events," *Nonlin. Processes Geophys.*, vol. 14, pp. 709-721, 2007.

[18] H. Braun, P. Ditlevsen and J. Kurths, "New measures of multimodality for the detection of a ghost stochastic resonance," *Chaos*, vol. 19, 043132, 2009.

[19] J. M. Buldú, D. R. Chialvo, C. R. Mirasso, M. C. Torrent and J. García-Ojalvo, "Ghost resonance in a semiconductor laser with optical feedback," *Europhys. Lett.*, vol. 64(2), pp. 178-184, 2003.

[20] G. Van der Sande, G. Verschaffelt and J. Danckaert, "Ghost stochastic resonance in vertical-cavity surface-emitting lasers: Experiment and theory," *Phys. Rev. E*, vol. 72, 016113, 2005.

[21] J. M. Buldú, C. M. González, J. Trull, M. C. Torrent and J. García-Ojalvo, "Coupling-mediated ghost resonance in mutually injected lasers," *Chaos*, vol. 15, 013103, 2005.

[22] K. Fujii, S. Kita, T. Matsushima and Y. Ando, "The missing fundamental phenomenon in temporal vision," *Psycological Research*, vol. 64, pp. 149-154, 2000.

[23] E. Ullner, A. Zaikin, J. García-Ojalvo, R. Báscones and J. Kurths, "Vibrational resonance and vibrational propagation in excitable systems," *Phys. Lett. A*, vol. 312, pp. 348-354, 2003.

[24] B. N. S. Medeiros, V. Minces, G. B. Mindlin, M. Copelli and J. R. R. Leite, "An excitable electronic circuit as a sensory neuron model," *Int. J. Bifurcation Chaos*, vol. 22, 1250244, 2012.

[25] M. Bordet and S. Morfu, "Experimental and numerical study of noise effects in a FitzHughNagumo system driven by a biharmonic signal," *Chaos, Solitons and Fractals*, vol. 54, pp. 82-89, 2013.

[26] M. Bordet and S. Morfu, "Experimental and numerical enhancement of vibrational resonance in neural circuit," *Electron. Lett.*, vol. 48, pp. 903-905, 2012.

[27] A. Lopera, J. M. Buldú, M. C. Torrent, D. R. Chialvo and J. García-Ojalvo, "Ghost stochastic resonance with distributed inputs in pulse-coupled electronic neurons," *Phys. Rev. E*, vol. 73, 021101, 2006.

[28] O. Calvo and D. R. Chialvo, "Ghost stochastic resonance in an electronic circuit," *Int. J. Bifurcation Chaos*, vol. 16, pp. 731-735, 2006.

[29] I. Gomes, M. V. D. Vermelho and M. L. Lyra, "Ghost resonance in the chaotic Chuas circuit," *Phys. Rev. E*, vol. 85, 056201, 2012.

[30] P. Balenzuela, J. García-Ojalvo, E. Manjarrez, L. Martínez and C. R. Mirasso, "Ghost resonance in a pool of heterogeneous neurons," *BioSystems*, vol. 89, pp. 166-172, 2007.

[31] T. Noguchi and H. Torikai, "Ghost Stochastic Resonance From an Asynchronous Cellular Automaton Neuron Model," *Circuits & Systems II: Express Briefs, Transactions on*, vol. 60, pp. 111-115, 2013.

[32] S. Martignoli, F. Gomez and R. Stoop, "Pitch sensation involves stochastic resonance," *Sci. Rep.*, vol. 3, 2676, 2013.

[33] M. Bordet, S. Morfu and P. Marquié, "Ghost Stochastic Resonance in a neural circuit," *Electron. Lett.*, vol. 50, Issue 12, 2014.

[34] J. F. Schouten, R. J. Ritsma and B. L. Cardozo, "Pitch of the residue," *Acoust. Soc. Am.*, vol. 34, pp. 1418-1424, 1962.

[35] P. Hasler, P. D. Smith, R. Ellis, D. Graham and D. Anderson, "Biologically inspired auditory sensing system interfaces on a chip," *Sensors*, proceedings of IEEE, 2002.

[36] C. Posch, "Bio-inspired vision," *J. Inst.*, vol. 7, C01054, 2012.

[37] S. Morfu, P. Marquié, B. Nofiele and D. Ginhac, "Nonlinear systems for image processing," *Advances in Imaging and Electron Physics*, vol. 152, pp. 79-151, 2008.

[38] S. Morfu, J. C. Comte and J. M. Bilbault, "Digital information receiver based on Stochastic Resonance," *Int. J. Bifurcation Chaos*, vol. 13, pp. 233-236, 2003.

[39] S. Morfu and J. C. Comte, "Stochastic Resonance: another way to retrieve subthreshold digital data," *Phys. Lett. A*, vol. 309, pp. 39-43, 2003.

Proceedings of ICCSA 2014
Normandie University, Le Havre, France - June 23-26, 2014

A COMPARATIVE STUDY OF NOISE EFFECTS IN A FITZHUGH-NAGUMO CIRCUIT

S. Morfu* †, P. Marquié*, G. Lassere* and M. Bordet* ‡ *

Abstract. This paper focuses on the behaviour of a nonlinear FitzHugh-Nagumo circuit in the stochastic case that is in presence of noise and without deterministic driving. When the circuit is tuned below the Andronov-Hopf bifurcation, classical coherence resonance signature is revealed. We compare the stochastic response of the system when the noise acts on two different parameters of the system. It is experimentally shown that an enhancement of the system response can be achieved when the noise is directly added into the nonlinearity.

Keywords. Coherence resonance - nonlinear circuit- white noise - nonlinear dynamics - neural circuit.

1 Introduction

In linear systems, it is commonly admitted that noise has a negative effect since the signal to noise ratio at the system output monotonously decreases. As engineers use linear approximation, noise is usually removed rather than added in the system. However, if the nonlinearity is taken into account, the behavior of the system in presence of noise is completely different. Indeed, it has been shown that noise can enhance the response of a nonlinear system to a deterministic signal via the well known Stochastic Resonance effect (*S.R.*). Since the introduction of *S.R.* to explain the recurrence of ice ages in the context of climate dynamics [1], this paradoxical effect has been reported in different fields such as physics [2], chemistry [3], signal processing [4, 5, 6, 7] and electrical engineering [8]. Even if some limitations of the applications of the *S.R.* effect in the information processing area have been discussed [9], it has been clearly shown that noise enhances the detection of weak amplitude signals through nonlinear circuits [10, 11, 12].

At the same time, these electronic elements exhibiting *S.R.* have been coupled in lattices of stochastic resonators to reveal that noise also assists the propagation of a deterministic signal [13, 14, 15, 16]. For instance, in the context of neural sciences, it has been demonstrated that noise can sustain action potential propagation in myelinated neurons [17, 18].

*S. Morfu, P. Marquié, G. Lassere and M. Bordet are with Laboratoire Electronique Informatique et Image (LE2I) UMR CNRS 6306, université de Bourgogne, France. E-mails: † smorfu@u-bourgogne.fr and ‡ maxime.bordet@u-bourgogne.fr

More specifically, the *S.R.* effect was introduced to explain how noise can improve the detection of weak stimuli by mechanoreceptors such those of the crayfish [19]. However, neurons also respond even in absence of external stimuli via another effect known as Coherence Resonance (*C.R.*) [20, 21]. *C.R.* usually occurs without external forcing when the parameters of the system are set near a Hopf-bifurcation [22]. Without noise, the system does not display a limit cycle and remains in the rest state, whereas noise can induce a stochastic limit cycle. Therefore, there exists an optimum value of noise for which the regularity of the system response is the best. It means that the coherence of the system response achieve an optimum for a critical noise value.

This *C.R.* phenomenon allows to account for the activity of neurons even in absence of external stimuli and could provide insight into disturbance in control mechanisms that cause apnea in clinical diseases states [23]. Therefore, like *S.R.*, *C.R.* has rapidly become an interdisciplinary paradigm which has been widely investigated both numerically and theoretically.

Experimental evidence of this nonlinear effect has been observed in excitable optical system [24], in chemical media and in electronic circuits [25, 26].

Concerning electronic devices exhibiting Coherence Resonance, very few experimental realizations have been proposed. For instance, Chua circuits in a chaotic regime have revealed a *C.R.* signature in presence of noise [25]. Moreover, in most studies, noise often appears to be additive and directly added to one hand of the equation that rules the system response [26]. One might wonder how noise can affect the system response if it is directly included in the nonlinearity. This paper experimentally addresses this question. Indeed, we consider the effects of these two kinds of noise in a nonlinear circuit ruled by the set of FitzHugh-Nagumo equations.
We first detail the nonlinear circuit and briefly establish its deterministic response. In the third section, two noise sources are considered and their effects on the systems response is compared. The last section is devoted to concluding remarks.

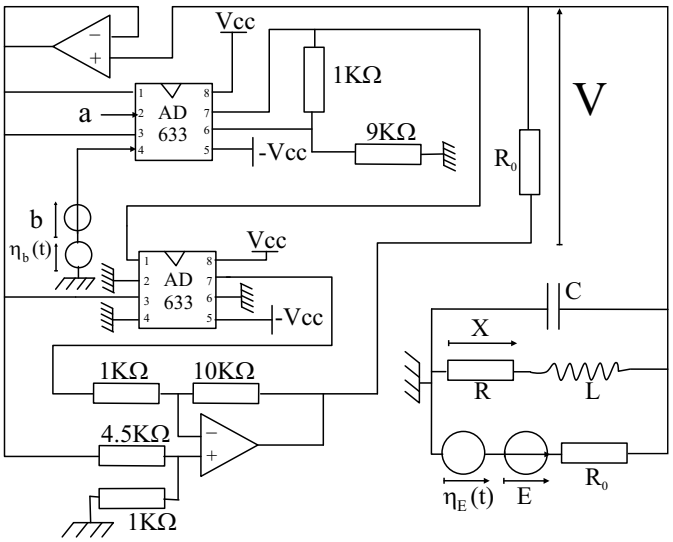

Figure 1: The nonlinear circuit. E is delivered by a DC generator while $\eta_E(t)$ and $\eta_b(t)$ correspond to additive noise sources. AD633JNZ are analog multipliers, while TL081CN operational amplifiers are used. $R = 320\Omega$, $R_0 = 1.33k\Omega$, $L = 10mH$, $C = 22nF$, $a = 2.0V$, $b = -2.6V$.

2 The nonlinear circuit

Our experiments are carried out using the circuit of Fig. 1 which includes classical TL081 operational amplifiers, AD633JNZ analog multipliers, additional constant voltage sources a, b, E and two noise sources $\eta_E(t)$, $\eta_b(t)$. L is a linear inductor, R and R_0 represent linear resistors. In the whole article, we focus on the analysis of the voltage V. Using the datasheet of analog multipliers and expressing the current through each branch of the circuit of Fig. 1, the voltages V and X are ruled by:

$$\begin{aligned} R_0 C \frac{dV}{dt_{exp}} &= -V\big(V-a\big)\big(V-b-\eta_b(t_{exp})\big) \\ &\quad -\frac{R_0 X}{R} + E + \eta_E(t_{exp}) \\ \frac{L}{R}\frac{dX}{dt_{exp}} &= V - X. \end{aligned} \tag{1}$$

Next, introducing the transformations

$$\gamma = \frac{R}{R_0}, \quad W = \frac{R_0 X}{R}, \quad \epsilon = \frac{R_0^2 C}{L}, \quad t = \frac{t_{exp}}{R_0 C}, \tag{2}$$

yields the following set of equations in normalized time units:

$$\begin{aligned} \frac{dV}{dt} &= -V\big(V-a\big)\big(V-b-\eta_b(t)\big) \\ &\quad -W + E + \eta_E(t) \\ \frac{dW}{dt} &= \epsilon(V - \gamma W). \end{aligned} \tag{3}$$

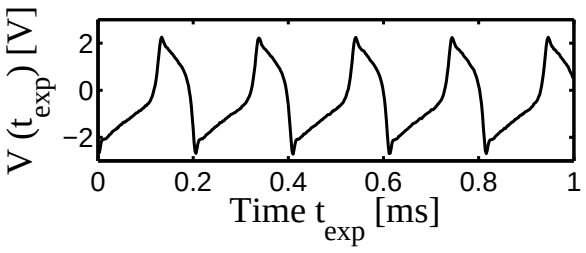

Figure 2: Response of the nonlinear circuit without noise. the voltage V has been recorded when $E = -0.24V > E_{inf}$. Parameters of the experimental system: $a = 2V$, $b = -2.6V$, $\gamma = 0.24$, $\epsilon = 3.9$, $R_0 = 1.33k\Omega$, $C = 22nF$, $R = 320\Omega$, $L = 10mH$.

Therefore, our circuit corresponds to a FitzHugh-Nagumo system submitted to noise. The components values have been adjusted to $R = 320\Omega$, $R_0 = 1.33k\Omega$, $L = 10mH$, $C = 22nF$ to set the parameters γ and ϵ to:

$$\gamma = 0.24 \text{ and } \epsilon = 3.9. \tag{4}$$

Moreover, in the whole article, the external voltage sources a and b will remain constant and equal to $a = 2V$ and $b = -2.6V$.

The deterministic response of the circuit is obtained in absence of noise, that is when $\eta_E(t) = 0$ and $\eta_b(t) = 0$. In this case, the behaviour of system (3) can be interpreted with its nullclines. Indeed, when the derivative of eqs. (3) are set to 0, we deduce the equations of the system nullclines under the following form

$$W = -V(V-a)(V-b) + E \quad \text{and} \quad W = \frac{V}{\gamma}. \tag{5}$$

The first nullcline corresponds to a cubic function vertically shifted by the external DC voltage source E, while the second one is a straight line which intersects the first nullcline. A limit cycle occurs when the parameter E is such that the linear nullcline intersects the cubic one between its two extrema [22].

In our case, this situation occurs if the voltage E is set in a range defined by two critical values E_{inf} and E_{sup}, namely $[E_{inf} = -0.25\ V;\ E_{sup} = 0.60\ V]$. The behaviour of the circuit is then oscillatory and the voltage V corresponds to a periodic train of spikes. (see Fig. 2 obtained for $E = -0.24V > E_{inf}$) In this article, we consider the case where the parameter E is chosen below the Andronov-Hopf bifurcation, that is $E < E_{inf}$. Namely, we choose $E = -0.3V$ which involves that no oscillation occurs without noise.

3 Influence of noise

In all the following, we investigate the behaviour of our experimental device versus the Root Mean Square

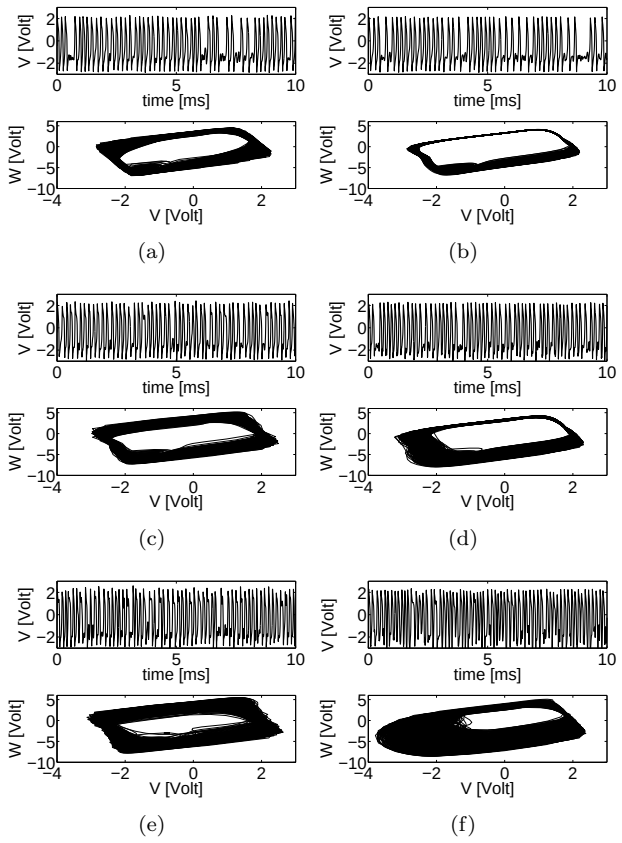

Figure 3: Experimental evidence of C.R. for two different noise sources. The time series and the corresponding phase portraits are presented for three different noise amplitudes. At the left, an additive noise corrupting the parameter E is used, while at the right, noise acts in the nonlinearity. Noise level added in parameter E: (a) $\sigma = 350mV_{rms}$, (c) $\sigma = 700mV_{rms}$, (e) $\sigma = 1050mV_{rms}$. Noise amplitude considered in the nonlinearity: (b) $\sigma = 50mV_{rms}$, (d) $\sigma = 200mV_{rms}$, (f) $\sigma = 660mV_{rms}$. Parameters of the experimental system: $a = 2V$, $b = -2.6V$, $\gamma = 0.24$, $\epsilon = 3.9$, $E = -0.3V$, $R_0 = 1.33k\Omega$, $C = 22nF$, $R = 320\Omega$, $L = 10mH$.

($R.M.S.$) amplitude σ of the gaussian noise sources $\eta_E(t)$ and $\eta_b(t)$ when the system is tuned below the Andronov-hopf bifurcation, namely when $E = -0.3\ V$.

Typical chronograms of the fast variable are available in Fig. 3 with the corresponding phase portraits. At the left of Fig. 3, noise was only added on the parameter E, while at the right, noise was only considered on the nonlinearity root b, which will be refered as a nonlinearity noise in the following.

For both noise sources, weak noise amplitudes induce an irregular response of the system. Indeed, as represented in Fig. 3 (a) and (b), very few spikes are produced. For strong RMS noise amplitudes, like in Fig. 3 (e) and (f), even if more spikes are induced by noise, the regularity of the system is not the best since the spike triggering is mainly ruled by noise. In fact, as shown in Fig. 3 (c) and (d), it is for an intermediate value of noise that the system regularity seems enhanced.

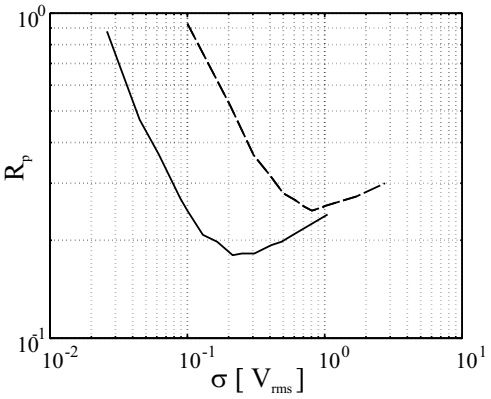

Figure 4: Coefficient of variation R_p versus the noise $R.M.S.$ amplitude σ. The curve in solid line is obtained for a noise included in the nonlinearity while the dashed line corresponds to a noise corrupting the parameter E. Parameters of the experimental system: $a = 2.0V$, $b = -2.6V$, $\gamma = 0.24$, $\epsilon = 3.9$, $E = -0.3V$, $R_0 = 1.33K\Omega$, $C = 22nF$, $R = 320\Omega$, $L = 10mH$.

For each of the two noise sources, there exists an optimum value of noise which enhances the coherence of the system response. In the case of a noise source directly added to the nonlinearity root b, the optimum value is 200 mV_{RMS}, whereas for a noise corrupting the parameter E, the optimum value is 700 mV_{RMS}. It shows that a weaker intensity of noise is required to enhance the system response when noise directly interacts into the nonlinearity.

Concerning the phase portraits, note that a noise included in the nonlinearity involves a phase portrait with a thinner trajectory in the upper right corner than in the bottom left corner. This means that the nonlinearity noise mainly acts when the system is near its rest state, that is before a pulse is triggered. Moreover, as shown by the chronograms of Fig. 3 (c) and (d), another consequence is that the peak amplitude and the temporal length of the triggered pulse is less affected by a nonlinearity noise. Therefore, we can expect a better regularity when noise acts on the nonlinearity.

To show this gain of efficiency, a relevant quantity usually computed in $C.R.$ context is the time between two consecutive pulses. Owing to the addition of noise, this spike timing t_p is a random variable with a given mean $\langle t_p \rangle$ and a standard deviation $\sqrt{\text{var}(t_p)}$. Therefore, the variability of spike timing can be quantified by the coefficient of variation defined by [20, 22]:

$$R_p = \frac{\sqrt{\text{var}(t_p)}}{\langle t_p \rangle}. \tag{6}$$

Noting that a null coefficient of variation R_p would correspond to a strictly periodic spiking, a good coherence in the system involves a weak value of R_p and vice versa.

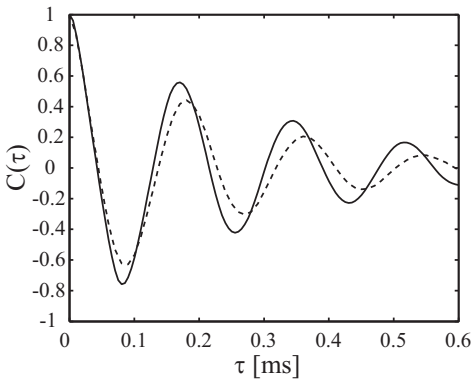

Figure 5: Normalized autocorrelations of the fast variable for each of the two noise source when the optimum of regularity is achieved. Solid line: nonlinearity noise of intensity $\sigma = 200mV_{RMS}$. Dashed line: noise corrupting the parameter E with intensity $\sigma = 700mV_{RMS}$

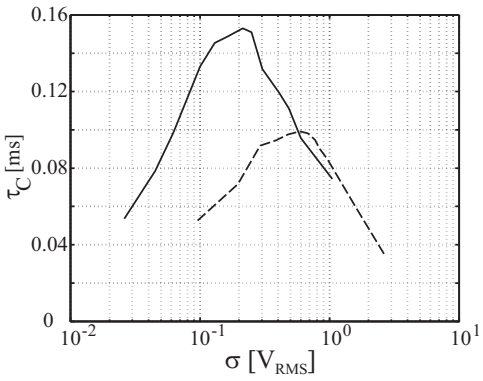

Figure 6: Correlation time τ_C versus the noise $R.M.S.$ amplitude σ. The solid line corresponds to a noise included in the nonlinearity while the dashed line is obtain with an additive noise corrupting the parameter E. Parameters of the experimental device: $a = 2V$, $b = -2.6V$, $\gamma = 0.24$, $\epsilon = 3.9$, $E = -0.3V$.

Hence, this quantity can be also interpreted as a noise to signal ratio in stochastic resonance context [22]. To determine the spike timing t_p, we consider that a pulse in the temporal sequence of the fast variable $V(t)$ is defined when $V(t)$ exceeds the threshold value $V_{th} = 0V$.
Under these conditions, as shown in Fig. 4, for each of the two additive noise sources, there exists an appropriate amount of noise which minimizes the coefficient of variation. Note that the best performance is achieved with a noise source included in the nonlinearity. Indeed, the minimum achieved in this case is weaker than in the more classical case where noise corrupts the parameter E. Moreover, the minimum of R_p is reached for $\sigma = 200\ mV_{RMS}$ when noise is included in the nonlinearity, whereas the noise intensity must be increased up to $\sigma = 700\ mV_{RMS}$ in the other case. Therefore, we can conclude that it is advantageous to consider noise into the nonlinearity since a weaker RMS amplitude of noise is required to optimize the system regularity.

Owing to the fact that neurons encode information in the time interval between two consecutive pulses, the coefficient of variation seems suitable in neural context. However, this quantity is defined with a threshold crossing which does not take into account the shape of the system response. From a signal processing point of view, it is more appropriate to consider the following normalized autocorrelation

$$C(\tau) = \frac{\langle \widetilde{V}(t_{exp})\widetilde{V}(t_{exp}+\tau)\rangle}{\langle \widetilde{V}(t_{exp})^2\rangle}, \qquad (7)$$

where $\widetilde{V}(t_{exp}) = V(t_{exp}) - \langle V(t_{exp})\rangle$ and where the brackets $\langle . \rangle$ denote a standard averaging. This normalized autocorrelation allows to compute the correlation time defined by [22]

$$\tau_C = \int_0^\infty C^2(t_{exp})dt_{exp}. \qquad (8)$$

The normalized autocorrelation corresponding to the optimum value of noise which provides the maximum of regularity is plotted at Fig. 5 for each of the two noise sources. The decrease of the extrema reached by the autocorrelation is much more pronounced when noise acts on the parameters E. It results that the correlation time defined by expression (8) will be greater when noise is included in the nonlinearity. As shown in Fig. 6, this correlation time exhibits a resonant behaviour versus the RMS noise amplitude σ for both noise sources. As expected by the autocorrelations presented in Fig. 5, the optimum of regularity in the systems response is better when noise acts in the nonlinearity. Indeed, the maximum reached by the correlation time is 0.152, that is much more than in the standard scenario of $C.R.$ which provides a correlation time around 0.1.

4 Conclusion

In this paper, we have used a nonlinear circuit to compare the effects of two additive noise sources in a FitzHugh-Nagumo oscillator. Especially, we have shown that classical Coherence Resonance can be observed when the system is perturbed by a noise directly added in the first equation ruling the system. Beside this well known effect, we have shown that a greater benefit of noise can be achieved if noise interacts in the nonlinearity. This result suggests that systems ruled by the set of FitzHugh-Nagumo equations, such as neurons, could adopt a strategy to enhance their response. Moreover, this work on nonlinearity noise could be of crucial interest to better understand how noise may enhance information propagation in lattices of coupled circuits modeling for instance myelinated nerve fibers [17, 18, 27].

Acknowledgements

The research for this work was supported, in part, by the Regional Council of Burgundy.

References

[1] R. Benzi, G. Parisi, A. Sutera and A. Vulpiani, "Stochastic resonance in climate changes," *Tellus*, vol. 34, pp. 10-16, 1982.

[2] L. Gammaitoni, P. Hänggi, P. Jung and F. Marchesoni, "Stochastic resonance," *Rev. Mod. Phys.*, vol. 70, pp. 223-282, 1998.

[3] F. Sagués, J. M. Sancho and J. García-Ojalvo, "Spatiotemporal order out of noise," *Rev. Mod. Phys.*, vol. 79, pp. 829-882, 2007.

[4] S. Zozor and P. O. Amblard, "Stochastic resonance in discrete time nonlinear AR(1) models," *IEEE Trans. on Signal Processing*, vol. 49, pp. 109-120, 1999.

[5] S. Zozor and P. O. Amblard, "Stochastic resonance in locally optimal detectors," *IEEE Trans. on Signal Processing*, vol. 51, pp. 3177-3181, 2003.

[6] S. Zozor and P. O. Amblard, "Noise aidded processing: revisiting dithering in a Sigma-Delta quantizer," *IEEE Trans. on Signal Processing*, vol. 53, pp. 3202-3210, 2005.

[7] S. Morfu, P. Marquié, B. Nofiele and D. Ginhac, "Nonlinear systems for image processing," *Advances in imaging and electronic physics*, vol. 152, pp. 79-153, 2008.

[8] S. Fauve and F. Heslot, "Stochastic resonance in a bistable system," *Phys. Lett. A*, vol. 97, pp. 5-7, 1983.

[9] M. D. Mc Donnell, N. G. Stocks, C. E. M. Pearce and D. Abbott, "Stochastic resonance and the data processing inequality," *Electron. Lett.*, vol. 39, Issue 17, pp. 1287-1288, 2003.

[10] X. Godivier, J. Rojas-Varela and F. Chapeau-Blondeau, "Noise-assisted signal transmission via stochastic resonance in a diode nonlinearity," *Electron. Lett.*, vol. 33, Issue 20, pp. 1666-1668, 1997.

[11] J. C. Comte and S. Morfu, "Stochastic resonance: another way to retrieve subthreshold digital data," *Phys. Lett. A*, vol. 309, pp. 39-43, 2003.

[12] F. Chapeau-Blondeau and D. Rousseau, "Injecting noise to improve performance of optimal detector," *Electron. Lett.*, vol. 43, Issue 16, pp. 897-898, 2007.

[13] F. Chapeau-Blondeau, "Noise-assisted propagation over a nonlinear line of threshold elements," *Electron. Lett.*, vol. 35, Issue 13, pp. 1055-1056, 1999.

[14] S. Morfu, J. C. Comte, J. M. Bilbault and P. Marquié, "Noise enhanced propagation in a dissipative chain of triggers," *Int. J. Bifurc. and Chaos*, vol. 12, pp. 629-633, 2002.

[15] F. Duan, F. Chapeau-Blondeau and D. Abott, "Noise-enhanced SNR gain in a parallel array of bistable oscillators," *Electron. Lett.*, vol. 42, Issue 17, pp. 1008-1009, 2006.

[16] S. B. Yamgoué, S. Morfu and P. Marquié, "Noise effects on gap wave propagation in a nonlinear discrete LC transmission line," *Phys. Rev. E*, vol. 75, pp. 036211, 2007.

[17] S. Morfu, "Propagation failure reduction in a Nagumo chain," *Phys. Lett. A*, vol. 317, pp. 73-79, 2003.

[18] A. Ochab-Marcinek, G. Schmid, I. Goychuk and P. Hänggi, "Noise-assisted spike propagation in myelinated neurons," *Phys. Rev. E*, vol. 79, 011904, 2009.

[19] J. K. Douglass, L. Wilkens, E. Pantazelou and F. Moss, "Noise enhancement of information transfert in crayfish mechanoreceptor by stochastic resonance," *Nature*, vol. 365, pp. 337-340, 1993.

[20] B. Lindner, J. Garcia-Ojalvo, A. Neiman, L. Schimansky-Geier, "Effect of noise in excitable systems," *Phys. Rep.*, vol. 392, pp. 321-424, 2004.

[21] G. Schmid and P. Hänggi, "Intrinsic coherence resonance in excitable membrane patches," *Mathematical Biosciences*, vol. 207, pp. 235-245, 2007.

[22] S. Pikovsky and J. Kurths, "Coherence resonance in a noise-driven excitable system," *Phys. Rev. Lett.*, vol. 78, pp. 775-778, 1997.

[23] D. Paydarfar and D. M. Buerkel, "Dysrhythmias of the respiratory oscillator," *Chaos*, vol. 5, pp. 18-29, 1995.

[24] G. Giacomelli, M. Giudici, S. Balle and J. Tredicce, "Experimental Evidence of Coherence Resonance in an Optical System," *Phys. Rev. Lett.*, vol. 84, 3298, 2000.

[25] O. Calvo, S. R. Mirasso and R. Toral, "Coherence resonance in chaotic electronic circuits," *Electron. Lett.*, vol. 37, Issue 17, pp. 1062-1063, 2001.

[26] G. Lassere, S. Morfu and P. Marquié, "Coherence resonance in a Bonhoeffer Van der Pol circuit," *Electron. Lett.*, vol. 45, Issue 13, pp. 669-670, 2009.

[27] P. Marquié, J. C. Comte and S. Morfu, "Analog simulation of neural information propagation using an electrical FitzHugh-Nagumo lattice," *Chaos, Solitons and Fractals*, vol. 19, pp. 27-30, 2004.

Proceedings of ICCSA 2014
Normandie University, Le Havre, France - June 23-26, 2014

HermaDEB AN EVOLUTIONARY INDIVIDUAL BASED MODEL FOR THE ENERGY ALLOCATION IN HERMAPHRODITE

Dorra Louati Maâroufi Slimane Ben Miled Narjès Bellamine Ben Saoud *†‡§¶

Abstract.

Sex change in hermaphrodite species is one of the most interesting phenomenon from an evolutionary perspective. In this work, we model the energetic and sexual behaviour of hermaphrodite species to determine the optimal size of sex change in this hermaphrodite species. We developed an evolutionary model that couples two theories, Dynamic Energy Budget (DEB) and Sexual Allocation theory, dealing with the use of energy (food uptake) for the physiological organization of an organism. Our approach is based on the study of the optimal sex change size as an emergent parameter from individuals behaviour. We develop an evolutionary individual-based model implementing these two theories with a simple genetic algorithm to determine the optimal sex change size. The model description follows the ODD (Overview, Design concepts, Details) protocol, it is simulated with NetLogo platform and it is parametrized for Dusky grouper (*Epinephelus marginatus*). For this hermaphrodite species, both growth and maturation predicted by the model fit well with field observations.

Keywords. modelling, evolutionary IBM, DEB, sex-ratio, simulation, ABM, sex change.

1 Introduction

Sequential hermaphrodites are species able to produce sequentially male and female gametes. We call it protandrous if the transition is from male to female, and protogynous if it is from female to male. One of the major evolutionary questions about sequential hermaphrodite is to determine where the direction and the timing of sex change are viewed as responses to demographic and environmental parameters [3].

The first answer was provided with Size Advantage Hypothesis models introduced by [8, 33, 21, 35]. Their models are based on direct relationships between individual fitness and both, sexual resource allocation (to either male or female role) and absolute [8, 33, 3] or relative [28] individual size. Size advantage is generally caused by a direct effect - mating preferences - or caused by an indirect effect or budget effect [17] - larger individuals will generally have more resources allocated to reproduction and produce more gametes. The size of sex change appears as an evolutionary stable strategy, ESS, of the population dynamics [14, 35].

However, these models are unable to describe the time of sex change when resource fluctuates and especially in case of starvation. This gap can be filled by coupling sex allocation models with models describing the use of food resources for metabolic and physiological processes as Dynamic Energy Budget (DEB) theory [20].

DEB theory presents simple mechanistic rules that describe the uptake and use of energy and nutriments (substrates, food, light) and the consequences for physiological organization throughout an organism's life cycle, including the relationships of energetic with ageing [20]. This theory attempts to put in equations quantitative aspects of metabolism at the individual level [18, 19, 20, 29].

Although, knowing the properties and behaviour of isolated individual is insufficient to predict the entire population behaviour (needed to introduce sex allocation models). Individual based models [13, 11, 30] are developed and used in order to account the variability of phenotype (e.g. fitness) and behavioural characteristics (e.g foraging efficiency), and the interactions between individuals [5].

The main objective of this study is to introduce an individual based model (IBM) as a generic modelling approach that represents the physiological complexities of these species and that will be used for investigating the effect of social control on population dynamics. Our motivations is, first, to investigate the energy fluctuation effect on the optimal size of sex change by comparing observed dynamics for different scenarios and, second to analyse the Evolutionarily Stable Strategies (ESS).

Our model uses data linked to the sequential protogynous hermaphrodite dusky grouper, (*Epinephelus marginatus*). This fish is a sequential hermaphrodite in which sex allocation is sensitive to the immediate social environment, such as the size of an individual relative to others in the social group [22], the sex-ratio of the social group [31, 27] and local density [22, 23]. Moreover, the grouper occupies an important position in fish lineages because of their population size, the large number of different species, and their geographical distribution. Although, it should be noted that the dusky grouper was indexed in the red list of The World Conservation Union (IUCN) as

*D. Louati Maâroufi and N. Bellamine Ben Saoud are with Laboratoire RIADI, Ecole Nationale des Sciences de l'Informatique, Université de la Manouba, Tunisie. e-mail: dorra.louati@gmail.com

†D. Louati Maâroufi and S. Ben Miled are with Groupe de Bioinformatique et Modélisation, Institut Pasteur de Tunis, Université de Tunis El Manar, Tunisie.

‡S. Ben Miled is with ENIT-LAMSIN, Université de Tunis El Manar, Tunisie. e-mail: slimane.benmiled@pasteur.rns.tn

§N. Bellamine Ben Saoud is with Institut Suprieur d'Informatique, Université de Tunis El Manar, Tunisie. e-mail: narjesbbs@gmail.com

¶Manuscript received April 2014;

endangered species (http://www.iucn.org).

The model description follows the ODD protocol for describing individual and agent based models [11, 12] and consists of seven elements. The first three elements provide an overview, the fourth element explains general concepts underlying the model's design, and the remaining three elements provide details.

2 Materials and Methods

2.1 Overview of used Models and model coupling

The goal of DEB theory is the study of the metabolism organization described by the mass and energy flows (see figure 1) inside the organisms. This theory attempts to put in equations quantitative aspects of metabolism at the individual scale. It also allows to connect different organization scales, from the cell to the ecosystem [18, 19, 20] and [29]. Our model is based on the DEB standard model, which considers an isomorphic organism, with one reserve and one structure feeding on one type of food and for which only food is limiting. This model is assumed to be appropriate for animals [20].

DEB theory does not take into account the issues of sexual allocation, all individuals are modelled in the same way, producing eggs, this choice is due to DEB generic formulation. To consider issues of sex change in hermaphrodite, we need to couple it with, assumptions and models from theory of sex allocation.

By models coupling, we mean models interoperation. The coupling may be weak, in this case the models remain independent, and interact via an interface. Coupling can also be strong, in this case the designer must write a super model and modify integrated models to adapt them to each other [7]. In our model, we have extended the standard model of DEB theory, incorporating a simple model of sex allocation. This strong coupling has lead to HermaDEB model.

The sex allocation theory explains for successive hermaphrodite species, the optimal time when individuals change sex. In summary, the change of sex in successive hermaphrodites, occurs when the reproductive value is related to the age or size and when this relationship is not the same for both sexes [3, 35].

Sex allocation theory and size-advantage models, assumes that sex change occurs at a fixed size [34]. The size at which individual should change sex S_{change}corresponds to the intersection of males and females reproductive success curves. S_{change} is estimated, in several works [4], by optimizing reproductive success.

Our approach consists in modelling the energy allocation by DEB theory model and S_{change} optimization by a simple genetic algorithm [26]. In this genetic algorithm, we consider the size of sex change as "'genotype"' and reproductive success as "'fitness"' function.

We check if by the energetic behaviour described by DEB theory and sex allocation's assumptions, we can find an invariant sex change size and whether the relationship between the size of sex change and the maximum size, predicted by [4, 1], remains true.

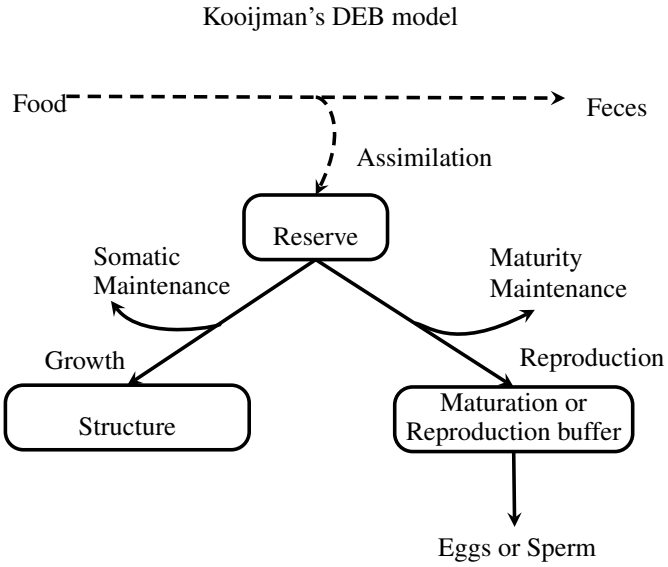

Figure 1: Energy fluxes in the standard deb model. A fraction κ of the mobilised reserve is used for somatic maintenance plus growth, the rest $1-\kappa$ for maturity maintenance plus maturation (in juveniles) or reproduction (in adults). Somatic maintenance has priority over growth and maturity maintenance has priority over maturation or reproduction. Reserve that is allocated to reproduction is first collected in a buffer; the reproduction buffer has species-specific handling rules for transformation into eggs. The birth is marked by the beginning of feeding (the dashed line corresponds to juvenile and adult stages) before birth, the embryo relies on its reserves to satisfy its energy needs. (figure from http://www.cein.ucla.edu/new/p156.php?pageID=367)

2.2 Model Description

2.2.1 Overview

Purpose We develop an agent based model which simulates the hermaphrodites behaviour as they use uptake food from the environment using and extending the DEB-IBM implementation realized by (Martin et al.) [25]. We use the standard DEB theory model with the ageing module [20] for the energy allocation and we extend it to describe the sexual allocation in the hermaphrodite case. Our main goal is to understand the emergent first change size for this species.

Entities, state variables, and scales In our model, we have two types of agents, (1) individuals : fishes from the dusky grouper species and (2) environment.

the environment is characterized by a constant food density X, in time and space, (see table (1) for entire state variables and table (2) for entire DEB parameters).

Symbol	Dimension	Description
V	L^3	Structural volume of the individual.
X	e	Available food density.
E	e	Non-allocated energy in reserve
E_H	e	Accumulated energy invested into maturation.
$\dot{h}$	t^{-1}	Specific death probability rate.
$\ddot{q}$	t^{-2}	Damage inducing compounds
sex	-	Individual sex-role
age	years	Individual age
l^{change}	-	Sex change size

Table 1: Model state variables with definitions. In the description of the dimension the following symbols are used, $-$ stand for no dimension, t for time, L for length and e for energy.

From DEB theory view, the state of an organism is completely described by : the structural volume, V, (or the structural length, $L = V^{1/3}$) of the individual, reserve energy E and maturity E_H seen as a cumulative energy allocated to the maturation. Two additional state variables : damage inducing compounds (acceleration) ($\ddot{q}$) and damage (hazard)($\dot{h}$) are specific to the ageing process [20]. As we are interested by the individual sexual choice and the population sex-ratio, we add supplementary state variables : sex, age and sex change size.

Process overview and scheduling Each time step, individuals feed and use this uptake energy to run their metabolic processes (somatic maintenance, growth, maturity maintenance, maturity or reproduction).

The individual DEB state variables (V,E,E_H) are then updated following the DEB standard model differential equations. If the individual can no longer pay maintenance somatic costs he dies [25]. If the individual survives and if he reaches a maturity level that allows him to move to the next life stage, he goes (see fig: 3).

During adulthood, the individuals accumulate energy in the reproduction buffer until the pre-reproduction period. During this period each individual checks if he can change sex depending on his size. Breeding season lasts about four months (from June to September) [24]. Males try to mate with as many females as possible. Females mate only once during the entire breeding period and all their eggs are fertilized by a single male. Thus, females are more selective in choosing partners and mate only with males of their size or bigger.

To simulate the reproductive pattern, a year is divided into three periods, breeding period (mating season), pre-reproductive period and free period (period without reproduction). To follow the evolution of our individual we choose a time step of one week.

During the free period individuals do not interact and share only food resources, which are abundant and constant.

During the pre-reproductive Individuals, asexual before puberty, become first females until reaching the sex change size and then play the males role.

For each time step, the following algorithm is run.

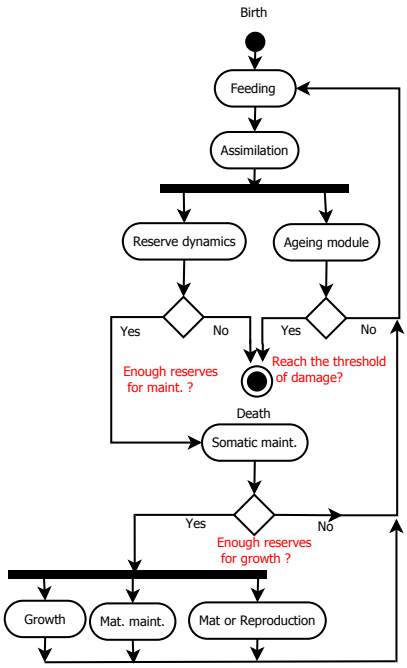

Figure 2: Energy behaviour of an individual : juvenile individual manages its energy budget as following: at each timestep he feeds, then the energy is stored in the reserve by the assimilation process.Damages related to assimilation is estimated. These damages result from oxidation which is supposed, in DEB model, to cause the age-related physiological decline. If the damages reach the value which leads the death either if the reserves do not any more cover the somatic maintenance costs, the individual dies. If he survives the other processes are supplied with energy according to their priorities. At the juvenile stage, the individual accumulates energy in the maturity buffer. This accumulated energy will be redirected to the reproduction at puberty.

```
For each individual
    [
Calculate processes rates
Update DEB state variables
if (mobilized energy <
maintenance energy)
[Die]
  if (random number <
probability of ageing related death)
[Die]
```

```
randomly move
if (female or asexual adult ) and
(pre-reproduction period)
[Choose a sexual role
 update sex state variable]
if (female) and (reproduction period)
[if (Find partner)
lay-eggs
ask partner [lay sperm]
  Become sexually inactive
]
]
```

2.2.2 Design Concepts

Basic principles We implement an individual-based model, in which individuals are governed by the previous theoretical model (coupling DEB theory and the theory of sex allocation). This is done on NetLogo [36, 32] using and extending the DEB-IBM implementation realized by (Martin et al.)[25]. Each individual perceives the sex and $size$ (L) of individuals in the surrounding area.

Emergence In our model, individuals sex change size, population dynamics, population structure and sex-ratio emerge from the individual metabolic organization and from individuals interaction via meeting.

Adaptation The model does not include adaptation processes.

Fitness We define the fitness of an individual, i, as the per capita birth rate of i. It depends on the produced gametes quantity and on the probability to be fertilized or to fertilize. Thus, for an individual, i:

$$f(i) = \dot{e}_i^{\gamma} F(i,j) \tag{1}$$

with $\dot{e}_i^{\gamma}$ is the produced gametes number per unit of mating, (if we consider the female gametes $\dot{e}_i^{\gamma}$ becomes $\dot{e}_i^{\square}$ otherwise $\dot{e}_i^{\square}$ for males) and $F(i,j)$ the fitness return the probability for a gamete produced by i to be or to fertilized and to gives an offspring with individual j. Some authors call F marriage function [16].

This probability, F, takes also into account the probability to meet the partner j and to accept to reproduce with it. This implies that sexual competition acts via F. So, the fitness return of a mating of two individuals of the same sex is equals to 0. I our case we suppose that for female, matting occur only with larger male.

This hypothesis was introduced by several authors [34], it assumes harem type reproduction due to sexual competition, where large individuals are males. This hypothesis is verified in some groupers [37, 22].

In this case, if a female meets a bigger male than her, they will reproduce with probability 1, if not they will not reproduce and probability is 0.

We note that, we suppose for the individual i, the produced gametes quantity depends only on individual reserve energy allocated to reproduction and not on the partner.

The male's fitness, of a mating, is equal to the number of eggs produced by its partner. While for female, fitness is equal to its own produced eggs.

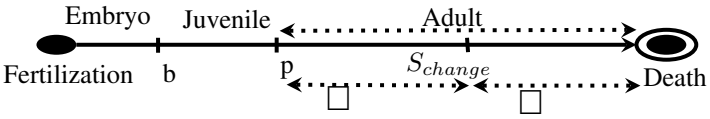

Figure 3: For DEB theory the transition from one life stage to another is related to the maturity, birth (b) marks the transition from embryo to juvenile stage and happens when the maturity U_H reached maturity birth $U_H = U_h^b$. Likewise puberty (p) that occurs when the maturity reached maturity puberty $U_H = U_H^p$. In our model, we add two other stages, female (□) and male (□).The switch from female to male, happens if the individual's length L corresponds to sex change size $L = S_{changes}$. This size also corresponds to maturity and sex change could be seen as a second puberty.

Interaction Individuals interact only during the breeding season to give birth to offspring. A female chooses (see 2.2.3) the male with which she mates during a time-step. The female invests all her eggs during this encounter and becomes sexually inactive until the next breeding season. Male manages to re-create his sperm capital, sperm is of low energy cost compared to the eggs, and then continues to fertilize available females .

Stochasticity In the DEB Standard model there is no stochasticity : DEB parameters are defined for the entire species and individual are all of the same sex. The variation between individuals in the DEB model, depends on the environment and mortality. We add a random deviation from DEB parameters for each individual.

Observations At the individual level: individuals annually report the following data : age, size (L), size at the sexual change , age at the sexual change and the annual offspring count.

At the population level: a monitor for sex-ratio observation, in the graphical interface, as a world grid where individuals move.

2.2.3 Details

Initialization At the beginning of the year, 100 individual are introduced in the models in the embryo stage, with DEB parameters state variables with some deviation. Indeed DEB

S	D	Description	Value
κ	$-$	fraction of mobilized energy allocated to soma.	0.8
κ_R	$-$	fraction of reproduction energy fixed in eggs.	0.8
$\dot{k}_M$	t^{-1}	somatic maintenance rate coefficient: $\frac{[\dot{p}_S]}{[E_G]}$	0.0029
$\dot{k}_J$	t^{-1}	maturity maintenance rate coefficient: $\frac{[\dot{p}_J]}{[E_R]}$	0.0025
g	$-$	energy investment ratio: $[E_G]/\kappa[E_m]$	2.89
$\dot{v}$	Lt^{-1}	energy conductance (velocity).	0.0178
u_E^0	$-$	initial scaled reserve	0.001
u_E^p	$-$	scaled maturity at puberty	4.4
u_E^b	$-$	scaled maturity at birth	$5.22E-7$
h_a	$1/d^2$	Weibull aging acceleration	$1.0E-7$
s_G	$-$	Gompertz stress coefficient	$2.0E-4$
$s-cost$	$-$	the cost of a sperm clutch, a proportion of the egg energetic cost.	0.1

Table 2: Model inputs, Model DEB parameters with definitions. In the description of the dimension the following symbols are used, $-$ stands for no dimension, t for time, L for length and e for energy.

parameters are multiplied by a log-Normally distributed random number (lower than 0.1) specific to each individual in order to provide inter-individual variability.

Inputs The model is parametrised for *Epinephelus marginatus* species, and the input parameters are those of the DEB model parameters estimated using the freely available package DEBtool http://www.bio.vu.nl/thb/deb/deblab/debtool/ (see table 2).

Submodels

DEB theory model The model, represented in the figure (fig: 1) describes the allocation of energy to various body function: the different processes (powers) are described by the following equations : The organism assimilates the intake food. Free energy is then fixed into reserves, $\dot{p}_A = \{\dot{p}_{Am}\} f L^2$ with scaled functional response $f = \frac{X}{K+X}$ with X is food density and K is saturation constant. The reserve change is written as difference between assimilation rate and mobilization rate $\dot{p}_C$: $\frac{d}{dt}E = \dot{p}_A - \dot{p}_C$. A fraction κ of the mobilized energy is used for somatic maintenance and growth $\kappa\dot{p}_C = \dot{p}_S + \dot{p}_G$, the rest $1-\kappa$ is allocated to maturity maintenance of maturity and maturity (before puberty) or reproduction (after puberty) $(1-\kappa)\dot{p}_C = \dot{p}_R + \dot{p}_J$. We keep the same dimensionless formulation is used in model of (Martin et al.) [25] in order to simplify the equations. For more details on the implementation please see http://cream-itn.eu/projects/wp-1/daphnia-2/deb-ibm. The scaled formulation of DEB standard model is used in our model, (see table 3). The equations governing the dynamics of the scaled length and scaled reserve are : $\frac{d}{dt}e = \frac{f-e}{l}\dot{K}_M g$ and $\frac{d}{dt}l = \frac{e-l-l_T}{l+e/g}\frac{\dot{K}_M}{3}$ with g stands for investment ratio and $\dot{K}_M$.

P	embryo	juvenile	adult
$\dot{p}_A$	0	fl^2	fl^2
$\dot{p}_C$	$el^2\frac{g+l}{g+e}$	$el^2\frac{g+l}{g+e}$	$el^2\frac{g+l}{g+e}$
$\dot{p}_S$	κl^3	κl^3	κl^3
$\dot{p}_G$	$\kappa l^2\frac{e-l}{1+e/g}$	$\kappa l^2\frac{e-l}{1+e/g}$	$\kappa l^2\frac{e-l}{1+e/g}$
$\dot{p}_R^{M.}$	$(1-\kappa)l^2\frac{e-l}{1+e/g}$	$(1-\kappa)l^2\frac{e-l}{1+e/g}$	0
$\dot{p}_R^{R.}$	0	0	$(1-\kappa)(l^2\frac{e-l}{1+e/g}+l^3-l_p^3)$

Table 3: The scaled powers expressions $\dot{p}_*/\{\dot{p}_{Am}\}L_m^2$ as specified by the standard deb model.This dimensionless formulation uses scaled length l and scaled reserve density e at scaled functional response $f = \frac{X}{K+X}$ with food density X and K saturation constant. κ stands for allocation fraction, g stands for investment ratio and $\dot{K}_M$. The dot "˙" stands for a rate : $\frac{1}{t}$.

Find partner At each time step during the mating period, a no fertilized female, seeks for a bigger male than her for breeding. As she has information on the individual group around her ,she randomly takes a male among those who fulfil the size criteria and who is not engaged with another female at the same time step. Once chosen, the male and female reproduce. The female becomes sexually inactive, as a female, and the male continues to seek opportunities for reproduction at the next time step till the end of the reproduction period.

Reproduce Reproduction involves the slope of eggs and their fertilization by sperm. We assume that all the eggs of a female are fertilized by the same male and that a cloud of sperm is necessary for the egg fertilization. This is because the probability of encounter between one sperm and one egg differs from 1.

2.3 Simulation experiments

Our simulation was carried out as a simple genetic algorithm [26] , applying the process of natural selection to find the sex change size that is more likely to persist throughout the generations. This algorithm considers the size of sex change as genotype and reproductive success as fitness function.

The first generation (of 100 individual) was introduced in the simulation with a random distribution of size change of sex, the average size of between puberty and the maximum size. Then individuals feed and manage their energy using DEB model equations. During the breeding season, individuals reproduce by reproduction module (see 2.2.3). The offspring inherit the average sex change size from both parents and have the DEB parameters with a statistical variation as that of the first generation. This reproductive cycle was simulated for 355 years. We then run the simulations so designed 100

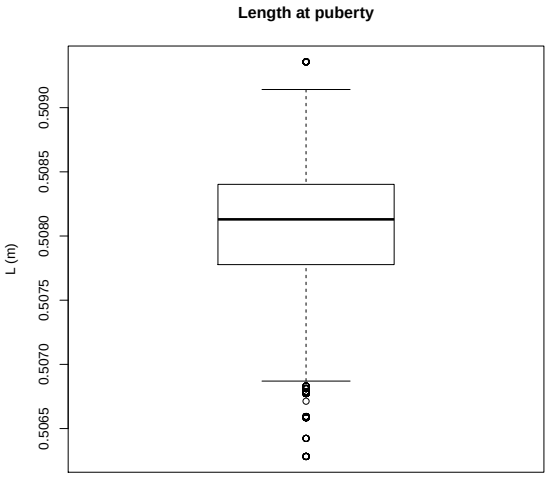

Figure 4: The average size at puberty of individuals (in 100 simulation) is represented in this box-plot. The figure, shows that the average puberty size is 0.5081 cm with a standard deviation of 0.00045 cm.

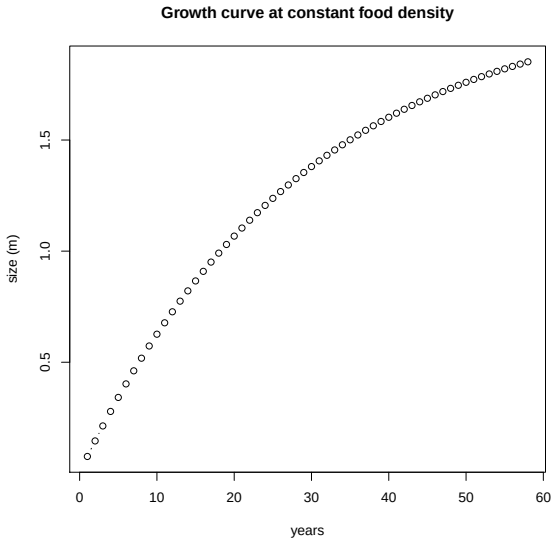

Figure 5: At constant food density, grouper growth curve follows the curve of Bertalanffy, the implementation of DEB-IBM [25] with the parameters calculated with DEBTool are consistent with the of Bertalanffy growth curve.

times. The simulation time was chosen to ensure that the average size of sex change $S_{changes}$ has stabilized. In fact we performed 10 simulation for 1200 years. We then calculated for each year j the following ratio: $r_j = \frac{S^{max}_{changes} - S^{max}_{changes}}{L_m - L_p}$, with $S^{max}_{changes}$, $S^{min}_{changes}$, respectively, the maximum sex change size and the minimum sex change size, L_m the maximum individual length and L_p the length at puberty. Then we take the simulation time as year j for witch $r_j = 0.05$, thus $j = 355$ years .

Each year, to avoid problems of population density in the fixed environment, individuals are randomly removed from the adults class and juvenile class to ensure a constant population of 100 adults and 100 Juveniles.

3 Results and discussion

3.1 Results

3.1.1 Growth and maturation fit well with field observations

The grouper is a protogynous species relatively long-lived (50 years) and can reach a length (1.5 m) [15]. In our simulations, Grouper reaches puberty at about 50 cm (fig: 4). Individuals have a maximum size (average of 100 simulation), between 1.93 and 2 meters (fig: 5).

In the litterature, according to the data of fishbase http://www.fishbase.org/summary/6470, the grouper reaches the puberty around 47 cms.

These results are rather close to the reality what proves that model DEB is effective for the prediction of the growth and the maturity.

3.1.2 Constant relative age and size at sex change

Our model predicts a constant proportion of S_{change}/L_m. Indeed, the ratio of the average size of sex change and the maximum average size of 100 simulation varies between 0.78 and 0.81, with size sex change average = 1.56 m.

Statistical analysis of the data of 52 species hermaphrodite fish suggest that fish change sex at a constant proportion (0.79) of their maximum size [1].

3.2 Discussion

In our work, we fill up the gap between sex allocation and environmental resources by coupling standard DEB model [20] with sex allocation ones [3]. In one side, our approach, describes the energy budget allocation of a hermaphrodite, taking into account the male and female gametes energy, which is not considered in the standard DEB model. In the other side, our model links food availability to sexual allocation and thus explicitly expresses sex change to environmental resources. This link, enable us to explore the effects of fluctuating food on the sex change in hermaphrodites and to predict optimal sex change size. We were able to confirm the predicted -done by theoretical model [4] and by statistical observations [1]- that ratio between size at sex change and the maximum size remains constant across species. This result shows that our approach could be a good method to answer sex change issues.

Although, DEB and sex allocation models act at different time and population scales [9]. Similarly to [6], we distinguish two main states : individual states (*e.g.*individual size or sex) and population states (*e.g.*population age or size distribution, population sex-ratio). Generally, population states are seen as an emergent phenomenon of individual states through inter-

individual models (ecological interactions) acting at ecological or population time scale. However, individual variables are the result of intra-individual physiological mechanism (modelled by DEB theory) at their own time scale.

This multi-level coupling, leads to the following difficulty: from the evolutionary point of view, life history characteristics are traits that affect organism life table, as reproduction, and survivor-ship. These characters are individual characters changing by mutations (at individual time scale) and selections (emergence phenomenons due to, among other, ecological mechanisms). However at the physiological scale life history traits are equilibrium point of physiological process. One way to solve this difficulty is to consider DEB parameters as an evolutionary parameters and that life history traits are observers (*i.e.*an easy accessed values that measure the system evolution). In the particular case of sex allocation model, age/size at sex change or individual gamete sex-ratio should no longer be seen as a life history traits, but a measure of strategy success related to physiological mechanism of energy allocation. The evolution acting on fraction of catabolic energy powers spent on maintenance and growth ,κ, or on the reproduction energy fraction fixed in gametes, κ_R.

Our model leads to a discussion on the relationship between complex system levels. Nevertheless it stays at experiment stage, and should be completed by population dynamics analysis tools. Indeed, according to the Grimm classification [10] our model is based on a bottom-up approach, which starts from the individual to understand the mechanisms and emergent properties in population level. Our approach, must be complemented by top-down approach that defines the properties at the population level [10, 2].

Thus, according to Grimm [10], it is imperative *to refer to framework of theoretical ecology*, and to analyse the IBM with tools that offered by variable states models. Resilience, Persistence and Stability of our model should be analysed to understand the emergent population dynamics that emerge in our model . Without this effort further analysis , simulations of our models will remain as experiments without leading to general theories on the dynamics of hermaphrodite populations.

Acknowledgements

We wish to thank Prof. Kooijman and his team. Prof. Kooijman, helped us to find the DEB parameters for groupers, his online course on DEB theory http://www.bio.vu.nl/thb/deb/course/ was of great support for the use of DEB theory.

References

[1] D J Allsop and S a West. Constant relative age and size at sex change for sequentially hermaphroditic fish. *Journal of evolutionary biology*, 16(5):921–9, September 2003.

[2] François Bousquet, Christophe Le Page, and Jean-Pierre Müller. Modélisation et simulation multi-agent. *deuxiemes assises du GDRI3*, 2002.

[3] E.L. Charnov. *The theory of sex allocation.* Princeton University Press, 1982.

[4] Eric Charnov and Unnur Skúladóttir. Dimensionless invariants for the optimal size (age) of sex change. *Evolutionary Ecology Research*, 2:1067–1071, 2000.

[5] D L DeAngelis and L J Gross. *Individual-Based Models and Approaches in Ecology: Populations, Communities, and Ecosystems*. Chapman and Hall, New York, 1992.

[6] Odo Diekmann, Hans Heesterbeek, and Tom Britton. *Mathematical tools for understanding infectious disease dynamics*. Princeton University Press, 2012.

[7] Yawa Edem Fianyo. Couplage de modèles à l'aide d'agents: le système osiris. *These de Doctorat, Université Paris IX-Dauphine*, 2001.

[8] M T Ghiselin. The evolution of hermaphroditism among animals. *The Quarterly Review. of Biology*, 44:189–208, 1969.

[9] J Gil-Quijano, G Hutzler, and T Louail. Accroche-toi au niveau, j'enlève l'échelle. *Revue d'intelligence artificielle*, 24(5):625–648, 2010.

[10] Volker Grimm. Ten years of individual-based modelling in ecology: what have we learned and what could we learn in the future? *Ecological modelling*, 115(2):129–148, 1999.

[11] Volker Grimm, Uta Berger, Finn Bastiansen, Sigrunn Eliassen, Vincent Ginot, Jarl Giske, John Goss-Custard, Tamara Grand, Simone K Heinz, Geir Huse, et al. A standard protocol for describing individual-based and agent-based models. *Ecological modelling*, 198(1):115–126, 2006.

[12] Volker Grimm, Uta Berger, Donald L DeAngelis, J Gary Polhill, Jarl Giske, and Steven F Railsback. The odd protocol: a review and first update. *Ecological Modelling*, 221(23):2760–2768, 2010.

[13] Steven F Grimm, Volker and Railsback. *Individual based modeling and ecology*. Princeton university press, 2005.

[14] Ian C W Hardy, I Pen, and F J Weissing. Sex ratios : Concepts and research methods edited. chapter Optimal se, pages 26–45. Cambridge University Press, 2002.

[15] Phillip C Heemstra and John E Randall. Fao species catalogue. vol. 16. groupers of the world (family serranidae, subfamily epinephelinae). an annotated and illustrated catalogue of the grouper, rockcod, hind, coral grouper and lyretall species. 1993.

[16] Mimmo Iannelli, Maia Martcheva, and F Fabio Augusto Milner. *Gender-structured population modeling: mathematical methods, numerics, and simulations*. Siam, 2005.

[17] Peter GL Klinkhamer, Tom J De Jong, and Hans Metz. Sex and size in cosexual plants. *Trends in Ecology & Evolution*, 12(7):260–265, 1997.

[18] S.A.L.M. Kooijman. *Dynamic Energy and Mass Budgets in Biological Systems*. Cambridge University Press, 2000.

[19] S.A.L.M. Kooijman. Quantitative aspects of metabolic organization; a discussion of concepts. *Phil. Trans. R. Soc. B*, 356:331–349, 2001.

[20] S.A.L.M. Kooijman. *Dynamic Energy Budget theory for metabolic organisation*. Cambridge University Press, 2010.

[21] E G Leigh, E L Charnov, and R R Warner. Sex ratio, sex change, and natural selection. *Proc. Natl. Acad. Sci. USA*, 73(10):3656–3660, October 1976.

[22] Min Liu and Yvonne Sadovy. The influence of social factors on adult sex change and juvenile sexual differentiation in a diandric, protogynous epinepheline, Cephalopholis boenak (Pisces, Serranidae). *Journal of Zoology*, 264(3):239–248, 2004.

[23] M M F Lutenesky. Density-dependent protogynous sex change in territorial-haremic fishes: models and evidence. *Behav. Ecol.*, \bf 5:375–383, 1994.

[24] G Marino, E Azzurro, MG Finoia, MT Messina, A Massari, A Mandich, et al. Recent advances in induced breeding of the dusky grouper epinephelus marginatus (lowe, 1834). In *Recent Advances in Mediterranean Aquaculture Finfish Species Diversification. Proceedings of the Seminar of the CIHEAM Network on Technology of Aquaculture in the Mediterranean (TECAM), jointly organized by CIHEAM and FAO*, volume 24, pages 215–225, 2000.

[25] Benjamin T. Martin, Elke I. Zimmer, Volker Grimm, and Tjalling Jager. Dynamic energy budget theory meets individual-based modelling: a generic and accessible implementation. *Methods in Ecology and Evolution*, 3(2):445–449, 2012.

[26] Melanie Mitchell and Charles E Taylor. Evolutionary computation: an overview. *Annual Review of Ecology and Systematics*, 30(1):593–616, 1999.

[27] P L Munday. Bi-directional sex change: testing the growth-rate advantage model. *Behav. Ecol. Sociobiol.*, \bf 52:247–254, 2002.

[28] Roldan C Munoz and Robert R Warner. A New Version of the Size-Advantage Hypothesis for Sex Change: Incorporating Sperm Competition and Size-Fecundity Skew. *American Naturalist*, 161(5):749–761, 2003.

[29] RM Nisbet, EB Muller, K Lika, and SALM Kooijman. From molecules to ecosystems through dynamic energy budget models. *Journal of animal ecology*, 69(6):913–926, 2000.

[30] Amelie Schmolke, Pernille Thorbek, Donald L. DeAngelis, and Volker Grimm. Ecological models supporting environmental decision making: a strategy for the future. *Trends in Ecology & Evolution*, 25(8):7, June 2010.

[31] D Y Shapiro, G W Potts, and R J Wooton. Sex reversal and sociodemographic processes in coral reef fishes. In Fish Reproduction: Strategies and Tactics. *Academic Press*, pages 103–118, 1984.

[32] Seth Tisue and Uri Wilensky. Netlogo: A simple environment for modeling complexity. In *International Conference on Complex Systems*, pages 16–21, 2004.

[33] Robert R Warner, The American Naturalist, and No Jan Feb. The Adaptive Significance of Sequential Hermaphroditism in Animals. *The American Naturalist*, 109(965):61–82, 1975.

[34] RR Robert R Warner. Sex change and the size-advantage model. *Trends in Ecology & Evolution*, 3(6):133–136, 1988.

[35] Stuart West. *Sex allocation*. Princeton University Press, 2009.

[36] Uri Wilensky. {NetLogo}. 1999.

[37] Garcia-Rubies A. Louisy P. Zabala, M. and E. Sala. Spawning behaviour of the mediterranean dusky grouper (lowe, 1834) (pisces, serranidae) in the medes islands marine reserve (nw mediterranean, spain). *Scientia Marina*, 61:65–77, 1997.

Proceedings of ICCSA 2014
Normandie University, Le Havre, France – June 23-26, 2014

MODELING THE OBESITY : A SHORT REVIEW OF LITERATURE

Mariem Jelassi, Slimane Ben Miled, Narjes Bellamine and Jacques Demongeot

Abstract. Modeling has become one key approach to better understand and respond complex problems in many fields including public health. For this reason, different modeling approaches exist which handle on different facets of a problem's complexity. One of the most important problems of latest decades is the obesity disease and its implications in public health. Many research tend to understand this phenomena using mathematical, statistical and simulation models. The purpose of this paper is to present an overview of some of these models using ODD (Overview, Design concepts, Detail) protocol.
Keywords. Obesity, simulation models, ODD, literature review

1. Introduction

In 1997, World Health Organization (WHO) declared obesity as a global epidemic thereby becoming the first non infectious disease categorized as an epidemic. Many research have been conducted using different modeling ways (mathematical, statistical, simulations,...) [1], in order to understand the obesity spread and to find out best prevention policies. The purpose of this paper is to present an overview of some models using ODD [2] (Overview, Design concepts, Detail) protocol. The choice of these models was made according to the scale studied (population, individuals, multi-scale), the kind of model (mathematical, statistical, network-based, agent-based) and the state variables used. There is a lot of research on obesity [1] depending on the question that researchers want to answer (economic consequence, trends in BMI, intervention policy...). In our case, we are interested in the social and environmental determinants of obesity. For this reason, the selected models presented here deal with various state variables (obesity state, age, sex, ethnicity, income, eating habits,…) at different scales. A background section will introduce ODD protocol. We then present the different models, summarize and compare them. At the end of the paper we suggest a direction for our future works.

2. Background: ODD

The 'ODD' (Overview, Design concepts, and Details) protocol was published in 2006 to standardize the descriptions of individual-based and agent-based models (ABMs) [2].

ODD protocol (see Fig.1) aims to make model descriptions more understandable and complete, thereby making ABMs easy to duplicate. We will generalize the use of ODD protocol for all these models in order to present the different mathematical, statistical, network and individual-based models studied to highlight the environmental contributors to obesity.

Overview	Purpose
	State variables and scales
	Process overview and scheduling
Design concepts	Design concepts
Details	Initialization
	Input
	Submodels

Fig. 1 – The seven elements of the ODD protocol, which can be grouped into the three blocks: Overview, Design concepts, and Details.(from Grimm [3])

3. Review of some current obesity models

We selected to review papers [4-15] published or presented at international conferences. We will classify them according to their scale (population, individual or both) to emphasize similarities and differences between them (see Fig.2).

3.1 Population scale

A scale represents a level in which phenomena happens. At population level, interactions represent average of individuals' interactions.

3.1.1 Ordinary Differential Equations

Evangelista et al. [4] studied the effect of peer-pressure in fast food consumtion and its effects on an individual's weight. They used an epidemiological deterministic ODE structured by BMI (body mass index). They showed that demographic age, race, education and income variables are positively correlated to the weight while sex is not. It appears that social pressure induced by fast food eaters has more effect on obesity than media, social and economic status. Therefore, they deduce that policies should focus on incrementing the peer pressure to stop eating at fast food.

Ejima et al. [5] have created an age structured deterministic epidemiological model to describe the risk of obesity and to compare the interventions effectiveness of primary (never obese individual) and secondary (obese and ex-obese individuals) interventions. They conclude that the optimality of intervention programs depends on the contagiousness of obesity.

González-Parra et al. [6] realized a stochastic ODE to investigate the dynamics of a mathematical obesity model within fluctuating social environment due to factors as advertising and educative compaigns. They found that there is a close relationship between amplitude of social environment parameters fluctuation and variability of forecasts for the incidence of obesity in the population.

3.1.2 Partial Differential Equations

González-Parra et al. [7] constructed an age structured PDE to predict the dynamic of the correlation between the development of obesity in a population and age in Valencia.
They found that an increasing trend of obesity in the following years in well accordance with the trend observed in several countries.

3.2 Individual scale

In this section, we present some statistical, network and agent-based models of obesity spread.

3.2.1 Statistical model

Christakis et al. [8] used a longitudinal statistical models to examine whether individual weight gain is associated to weight gain of a person's environment (friends, siblings, spouse or neighbors). This study was performed on data from the multigenerational Framingham over 32 years. Results showed that the probability of becoming obese increase by 57% if a friend become obese, by 40% in the case of one adult siblings and 37% in the case of spouse.

This study also showed that the immediate geographic location, ie corpulence neighbors, has no effect on this probability, and a person of the same sex have relatively more influence on obesity that a person of the opposite sex. They found also that smoking cessation and obesity are not correlated. [8] justified their results by three explanations : homophily, induction and confounding.

3.2.1. Network-based model

Bahr et al. [9] realized network-based interaction models, using different topologies, to simulate obesity spread along social networks and predict effective weight management interventions. They showed that regardless of the network topology and the interaction rule, individuals are grouped according to their BMI and social forces drive these groups towards increasing obesity.

3.2.2. Agent-based model

Hammond et al. [10] realized an agent-based model (ABM) on which they analyze of two non-price mechanisms for obesity: the physiology of dieting, and socially influenced weight changes.
They found that the concept of ideal weight norms alone can increase the incidence of overweight and obesity, even if the initial population is predominantly of healthy weight.

Burke et al. [11] constructed an agent-based model to explore factors that could explain the increase of obesity prevalence. They considered falling food prices and metabolic heterogeneity, and they deduced that changing food prices have greater effects on heavier individuals.

Bourisly [12] used also an agent-based model with agents for individuals (obese or not) and agents for environment (food healthy or not, health advocate and antagonist and exercise facilities) dispatched randomly in the space. He found that managing food prices is the most effective strategy to reduce obesity, which seems consistent with the explanation of [11], which define falling food prices as a reason for obesity.

3.3 Multi-scale

Taramasco [13] studied the obesity spread in a social structure considering endogenous forces defined as the co-influence individual-individual and exogenous forces defined as the co-influence individual-environment, and she found that individuals are divided into groups according the their obesity state.
In her approach, Taramasco studied the population scale by using a compartmental mathematical model and individual scale by using network-based model to represent the influence of individuals on each others.

1. Discussion and conclusion

Many studies were conducted to understand which environmental elements or individual states are the most important in the obesity spread. At the population scale, EDO and PDE enable us to prove the main role of age and sex. But these models are based on the assumption that all individuals behave the same when they are exposed to a same external force and reject the existence of behavior diversity inside population.

Models presented in this paper, except [8], considered social influences as static effects and relationships type independent. But social effects can be divided into endogenous (inductive effects or social network effects) and contextual (exogenous/ environmental) effects [15]. In this context, Christakis et al.[8] consider that individuals have different effects depending on relationship types (friends, siblings, spouse or neighbors). For that, they introduce multi-edges network representing the relationships. The idea is that network topology, as data, can inform us about obesity's spread. A main point is the topological measure definition of social effect considered in [8] as the degree centrality index- representing how connected a node is- and do not his degree of influence. Its seems to us that a more powerful approach reflecting the influence of a node instead of its connectivity could be done using eigenvector centrality. We have to note that [9] and [13] introduced dynamics into network but they considered just static endogenous effects.

We conclude by thinking that a model mixing [8] and [13] is a good way to evaluate the spread of the disease into a population.

.

[15], but like [8] we will consider the fact that endogenous forces are heterogenous. And a second point that we want to study is the sensibility of results to the choice we make to analyze a network, especially the choice of centrality to model obesity spread.

References

[1] Grimm, Volker, et al. "The ODD protocol : a review and first update." Ecological Modelling 221.23 (2010): 2760-2768.

[2] Levy, D. T., et al. "Simulation models of obesity: a review of the literature and implications for research and policy." *Obesity reviews* 12.5 (2011): 378-394.

[3] Grimm, Volker, et al. "A standard protocol for describing individual-based and agent-based models." Ecological modelling 198.1 (2006): 115-126.

[4] Evangelista, Arlene M., et al. "USA the fast food nation: obesity as an epidemic." *T-7, MS B* 284 (2004).

[5] Ejima, Keisuke, Kazuyuki Aihara, and Hiroshi Nishiura. "Modeling the obesity epidemic: social contagion and its implications for control." *Theor Biol Med Model* 10 (2013): 17.

[6] Gonzalez-Parra, Gilberto, ARENAS, Abraham J., et SANTONJA, F.-J. "Stochastic modeling with Monte Carlo of obesity population." *Journal of Biological Systems*, 2010, vol. 18, no 01, p. 93-108.

[7] González-Parra, Gilberto, Rafael J. Villanueva, and Abraham J. Arenas. "An age structured model for obesity prevalence dynamics in populations." *Revista MVZ Córdoba* 15.2 (2010).

[8] Christakis, N., Fowler, J. "The spread of obesity in a large social network over 32 years." New England Journal of Medicine 357(4), 370–379. (2007)

[9] Bahr, David B., et al. "Exploiting social networks to mitigate the obesity epidemic." *Obesity* 17.4 (2009): 723-728.

[10] Hammond, Ross A., and Joshua M. Epstein. "Exploring price-independent mechanisms in the obesity epidemic." Brookings Institution Center on Social and Economic Dynamics, 2007.

[11] Burke, Mary; Heiland, Frank Social dynamics of obesity, Public policy Discussion Papers, Federal Reserve Bank of Boston, No. 06,5. (2006).

[12] Bourisly, Ali K. "An Obesity Agent Based Model: A New Decision Support System for the Obesity Epidemic." *AsiaSim 2013*. Springer Berlin Heidelberg, 2013. 37-48.

[13] C. Taramasco - "Impact de l'obésité sur les structures sociales et impact des structures sociales sur l'obésité". Thèse, Ecole Polytechnique X (2011).

[14] Bourisly, Ali K. "An Obesity Agent Based Model: A New Decision Support System for the Obesity Epidemic." *AsiaSim 2013*. Springer Berlin Heidelberg, 2013. 37-48.

[15] Cohen-Cole, E., Fletcher, J., 2008. "Is obesity contagious? social networks vs. environmental factors in the obesity epidemic." Journal of Health Economics 27(5),1382–1387.

Fig.2 Obesity Models

Description \ Model			Evangelista (2004)[1]	Christakis (2007)[2]	González- Parra (2010)[3]
	Type of Model		Deterministic ordinary differential equations	Statistical study of a static network	Stochastic ordinary differential equation model
Overview	Purpose		Study the role of peer pressure on becoming fast food eater and its effect on the weight of an individual	Study whether weight gain of an individual is associated with weight gain of a person's environment (friends, siblings, spouse or neighbors).	Investigate the dynamics of a mathematical model of obesity population within fluctuating social environment.
	State variables and scale	State variables	Sex, age, race / ethnicity, education, income	Age, sex, education and body mass of all individuals of the different generations and their friends, families and neighbors who are also part of the study.	Unhealthy eating habits
		Scales	Population	Individuals	Population
	Process overview and scheduling		Several Epidemiological models based on the BMI (Body Mass Index) have been discussed in this article by considering the following compartments: * N : individuals with normal weight (BMI between 18.5 and 24.5) * O_1 : overweight individuals (BMI between 24.5 and 29.9) * O_2 : obese individuals (BMI greater than 29.9) * Q_1 : individuals from O_1 who stop eating at fast food * Q_2 : individuals from O_2 who stop eating at fast food	Christakis et al. conducted a longitudinal statistical analysis by drawing the social network formed by the data in a general undirected graph, then analyzing it.	The basic model of Jodar et al[4]. is divided in six subpopulations: * N(t) :children with normal weight; * L(t) : latent children ; children with habit of BFS consumption but still normal weight; * S(t) : children with overweight; * O(t) : obese children; * DS (t) : overweight children on diet; * DO (t) : obese children on diet. Based on this model, a stochastic differential equation model is constructed by perturbing two of its social related parameters with white noise terms characterized by Gaussian distribution having zero mean and unit spectral density.

1 Evangelista, Arlene M., et al. "USA the fast food nation: obesity as an epidemic." *T-7, MS B* 284 (2004).
2 Christakis, N., Fowler, J. The spread of obesity in a large social network over 32 years. New England Journal of Medicine 357(4), 370–379. (2007)
3 Gonzalez-Parra, Gilberto, ARENAS, Abraham J., et SANTONJA, F.-J. Stochastic modeling with Monte Carlo of obesity population. *Journal of Biological Systems*, 2010, vol. 18, no 01, p. 93-108.
4 Jodar L, Santonja F, Gonz´lez-Parra G, Modeling dynamics of infant obesity in the region of Valencia, Spain, Comp Math Appl 56(3):679–689, 2008.

	Design concepts	Basic principles : * The weight of individual eating in fast food increases. * The time it takes for an overweight individual to become obese is de7.5 months. Interaction: peers[5] of an individual can interact with him and get him to eat in fast food. Collective : individuals of the population are grouped according to their class membership (N, O_1, O_2, Q_1, Q_2).	Interaction: Different relationships are defines between individuals in the population (friends, siblings, spouse or neighbors). Observation : the likelihood of becoming obese increase by 57% if a friend become obese, by 40% in the case of one adult siblings and 37% in the case of spouse.	Basic principles : * Unhealthy eating habits is positively correlated to obesity. * Social environment has fluctuations over the time due to factors as advertising and educative campaigns, and this affects the social peer pressure to unhealthy eating habits.
Details	**Input**	* Population of the United States(about 300 million people): 33% of normal weight, 34% overweight and 30% obese. * 33% of the population is on diet, of which 16.5% break the diet .	Framingham[6] multigenerational epidemiological study : 12,067 individuals evaluated in 32 years, from 1971 to 2003.	Children population (3-5 years old) in the Spanish region of Valencia
	Submodels	Once an individual begins to eat in fast food, he becomes a fast food eater and starts progress towards the state "overweight" $O_1(t)$ due to its high consumption. And if he continues to eat fast food, then he may become obese $O_2(t)$. An individual in one of these two states can stop eating fast food and going on a diet and therefore proceed to state $Q_i(t)$, for i = 1 , 2 for O_1 and O_2 respectively. Evangelista made three models: * Model (N, O_1, O_2, Q_1, Q_2) with a non-linear probability of moving to Q_1, Q_2. * Model (N, O_1, O_2, Q_1, Q_2) with a linear probability to move to Q_1, Q_2. * Model (N, O_1, O_2, Q) with a non-linear probability ti move to Q passage but without probability to return from Q to O_1, O_2.	* Graphical representation of the network using the Kamada-Kawai algorithm in Pajek software. * Generating video network by means of the Social Network Image Animator (known as Sonia). * Checking if the data are conformed to theoretical network models such as small-world networks, scale-free, hierarchical, etc.	The basic model is divided in six subpopulations: * N(t) :children with normal weight; * L(t) : latent children ; children with habit of BFS consumption but still normal weight; * S(t) : children with overweight; * O(t) : obese children; * DS (t) : overweight children on diet; * DO (t) : obese children on diet. Three models are introduced using stochastic perturbations : * The first one considers perturbations on the transmission parameter (social transmission rate to unhealthy eating habits due to social environment pressure) * The second one on the rate at which a latent children become overweighted child * The third one considers the two previous parameters jointly by a two-dimensional Wiener process. - Confidence intervals for the stochastic solutions for overweight and obese populations are given using Monte Carlo method . Then they applied Euler-Maruyama stochastic numerical scheme to those three stochastic differential systems.

5 Set of people with common elements with an individual (age, social background, concerns, aspirations, etc..) and may influence him (source: Dictionary of Psychiatry of CILF editions).

6 Long-term study, whose initial purpose was cardiovascular disease. Dawber TR. The Framingham Study: the epidemiology of atherosclerotic disease. Cambridge, MA: Harvard University Press, 1980.

Description \ Model		González-Parra (2010)[7]	Taramasco (2011)[8]	Bourisly (2013)[9]
	Type of Model	Partial differential equation model	Individual-based model (IBM)	Agent-based model (ABM)
Overview	Purpose	Model the correlation between the development of obesity in a population and age and time to predict its dynamics.	Study the spread of obesity in a given static or dynamic social structure considering the co-influence individual-individual (endogenous forces) and the co-influence individual-environment (exogenous forces).	Model for the obesity epidemic and create a decision support system to reduce obesity in a given population.
	State variables and scale – State Variables	Age	Obesity state, tolerance	Obesity state
	State variables and scale – Scales	Population	Population & individuals	individuals
	Process overview and scheduling	González-Parra constructed an age structured mathematical model to describe the future dynamics of obesity prevalence for different ages considering only overweight and obese populations	Carla's work is based on 2 parallel stochastic models : - The first one is an epidemiological compartment model based on the obesity state : * S : susceptible, normal individual who may be exposed to risk behaviors. * E : exposed, normal individual with risk behaviors. * W: overweight individual, who can reduce or increase its dietary imbalance. * O: obese individual. - The second model is an individual-based model (IBM) that takes into account the co-influence individual-individual (endogenous forces) and the co-influence individual-environment (exogenous forces).	Using Netlogo tool, Bourisly created an agent based model containing different agents including individuals (obese or not), food (healthy or not), health advocate and antagonist, exercise facilities. All these agents are distributed randomly in the grid, and depending on the neighborhood of an individual * Obese individual * Non-obese individual * Healthy food * Non-healthy food * Health advocate * Health antagonist * Fee-based exercise facility * Free exercise facility

7 González-Parra, Gilberto, Rafael J. Villanueva, and Abraham J. Arenas. "An age structured model for obesity prevalence dynamics in populations." *Revista MVZ Córdoba* 15.2 (2010).

8 C. Taramasco - Impact de l'obésité sur les structures sociales et impact des structures sociales sur l'obésité. Thèse, Ecole Polytechnique X (2011).

9 Bourisly, Ali K. "An Obesity Agent Based Model: A New Decision Support System for the Obesity Epidemic." *AsiaSim 2013*. Springer Berlin Heidelberg, 2013. 37-48.

	Design concepts	*Interaction* : individuals of different ages can interact with each others and contribute in the peer pressure. *Observation* : this model is considered as suitable to forecast the obesity in each age group for different countries.	*Basic principles* : individuals can influence each other to become obese. *Emergence* : individuals are divided into groups according to their obesity state. *Sensing* : individuals sense the obesity state of others according to their own homophily variable to create/break links in the network. *Interaction* : direct interaction exists between individuals to reprensent the influence between them. *Stochasticity* : the transition between the different compartments (N, E, W, O) is partly random. *Collectives* : as a result of individuals behavior, collectives appear according to the obesity state of individuals. *Observation* : the tolerance of individuals is important to the social collectives creation.	*Basic principles* : individuals are sorrounded by different environmental parameters including healthy and non-healthy food, health advocate and health antagonist agents, free and fee-based exercise facilities, and connections to obese and non-obese individuals. *Sensing* : individuals sense the other agents and depending on that, they can change their obesity status. *Stochasticity*: all agents are placed randomly in the space. *Interaction* :obese and non-obese agents (individuals) interact with each other and with other environmental agents. *Observation* : managing food prices is an effective strategy to reduce obesity compared to exercise, individual encounter, number of food source allocations, and advertisements.
Details	**Input**	Health Survey of the Region of Valencia 2000 (4.319 interviews) and Health Survey of the Region of Valencia 2005 (4.012 interviews) considering only overweight and obese populations.	From the 2009 ObEpi survey (France), Taramasco considered 1000 individuals whose 14,5% obeses and 31,9% overweight.	In-silico population with 35.7% obese individuals.
	Submodels	This model is structured in age and time and contains two compartments : * S (a, t) : the number of overweight individuals at the age of 'a' and 't' time. * O (a, t) : the number of obese individuals at the age of 'a' and 't' time.	Carla's model contains two different processes : * The first one is related to the network dynamic, which means that it manages the creation/breaking links within the network, based on individuals' tolerance. * The second one is related to the transition between the different obesity states that individuals can have.	- A non-obese agent can become obese if he is in close proximity to other obese agents, non-healthy food, health antagonist, and with limited exposure to exercise facilities. - An obese agent can become non-obese if he is in close proximity to other non-obese agents, healthy food, health advocates, and exercise facilities.

Description \ Model			Bahr (2009)[10]	Burke (2007)[11]	Hammond (2007)[12]
	Type of Model		Network-based interaction models	Agent-based model (ABM)	Agent-based model (ABM)
Overview	Purpose		Simulate obesity spread along social networks and predict effective weight management interventions.	Explore factors that could explain the increase of obesity prevalence by considering falling food prices and metabolic heterogeneity.	show how a few simple, individual-based, non-price mechanisms (including norms, social influences, and physiology) can provide insight into the obesity epidemic.
	State variables and scale	State Variables	Obesity state	Obesity state	Obesity state, gender, physical activity, dietery decision
		Scales	Individuals	Individuals	Individuals
	Process overview and scheduling		Bahr et al used network simulation, with individuals can have four possible states: underweight, normal, overweight and obese. The model updates all individuals BMI simultaneously.	Burke et al. considered the effect of reducing food prices in the context of a model involving endogenous body weight norms and an explicit, empirically grounded description of human metabolism.	Hammond and al. combined the Harris-Benedict equations which explain core facts of individual obesity and dieting (such as the familiar pattern of recidivism), and the simple "follow the average" social adjustment mechanism which produces a powerful, and counter-intuitive upward BMI dynamic in the population.

10 González-Parra, Gilberto, Rafael J. Villanueva, and Abraham J. Arenas. "An age structured model for obesity prevalence dynamics in populations." *Revista MVZ Córdoba* 15.2 (2010).

11 Burke, Mary; Heiland, Frank (2006) : Social dynamics of obesity, Public policy Discussion Papers, Federal Reserve Bank of Boston, No. 06,5

12 Hammond, Ross A., and Joshua M. Epstein. *Exploring price-independent mechanisms in the obesity epidemic*. Brookings Institution Center on Social and Economic Dynamics, 2007.

Design concepts		*Interaction* : individuals interact with each others inside the social network. *Observation* : * Collectives are created according to BMI individuals. And social forces drive these collectives towards increasing obesity. * interventions should target well-connected and/or normal weight individuals at the edges of a cluster which may quickly halt the spread of obesity. *Collectives* : In all simulations, regardless of the network topology and the interaction rule, individuals are grouped according to their BMI *Stochasticity* : each individual can react to the same stimuli in different ways even if every individual used the same rule.	*Basic principles* : * Thinness (up to a point) is prized * Individuals assess themselves in relation to others rather than against an absolute scale. *Sensing* : individuals sense the norm weight and the environmental features as food prices. *Observation* : changing food prices have greater effects on heavier individuals because of the shape of the metabolic rate curve.	*Sensing* : individuals sense the norm weight and price-independant environmental features as media, public health mechanisms... *Observation* : core equations reflecting the physiology of weight change could reproduce many observed phenomena. *Emergence* : There is a Social conformity toward the group ideal weight.
Details	**Input**	Simulations count 1000 to 1000000 individuals with different topologies : Square lattices, Random Networks, Small-world networks, Scale free Networks, and empirical one based on Framingham study.	NHANES surveys spanning (intermittently) the period from 1976 through 2000	U.S. obesity data
	Submodels	In the beginning, individuals are initialized with a state of BMI. they identified four possible states: underweight, normal, overweight, obese. At each time step, the model updates all BMI of individuals simultaneously.	There is a group's commonly-held norm or "desired" weight that each individual wants to have and compares her own weight to that value. Each individual tends to maximize a myopic utility function over short-term food and nonfood consumption, taking the reference weight and prices into account.	They started with core equations known to govern the physiology of human energy balance (weight loss and weight gain). Then they explored a model of social influence in decision-making about eating and weight, and demonstrate a mechanism through which ideal weight norms alone can drive a sharp increase in incidence of overweight and obesity—even beginning in a population which is predominantly of healthy weight. They considered different types of diet. Then they showed the BMI trajectories; the Temptation trajectories, broken out by gender.

Proceedings of ICCSA 2014
Normandie University, Le Havre, France - June 23-26, 2014

QUALITATIVE PROPERTIES IN TWO-PATCHES OF PREDATOR-PREY SYSTEM WITH UNIDIRECTIONAL MIGRATION OF PREY AND EFFECT OF MIGRATED POPULATION

Radouane Yafia, M. A. Aziz Alaoui *†‡

Abstract. In this paper, we consider a model describing the dynamics of predator-prey populations living in two patches. The two patches follow the Lotka-Volterra type and are coupled through prey migration. Our purpose in this work is to study the effect of migration rate on the behavior of the coupled systems. We prove the positivity of solutions and find the upper and lower bounds with respect to the migration rate of prey. Also we show the stability/instability of the possible steady states and we establish the global stability of the positive steady state by giving a candidate lyapunov function.

Keywords. Predator-prey model, boundedness, coupled system, ordinary differential equations, local and global stability.

1 Introduction

In the current paper we consider two symmetric (identical) patch given by Lotka-Volterra system as follows (before migration):

$$\begin{cases} \frac{dx_i}{dt} = ax_i(1-x_i) - bx_iy_i \\ \frac{dy_i}{dt} = cx_iy_i - dy_i \\ \qquad i \in \{1,2\} \end{cases} \tag{1}$$

and we take into account the migration of the prey population from the first patch to the second patch only (in one direction only) with a migration rate k and we consider the contribution of the migrated (refuged) prey population in the growth of the predator population of the refuge patch (second patch). The model is given by a system of four ordinary differential equations as follows:

$$\begin{cases} \frac{dx_1}{dt} = ax_1(1-x_1) - bx_1y_1 - \underbrace{kx_1}_{migrated\ prey\ population} \\ \frac{dy_1}{dt} = cx_1y_1 - dy_1 \\ \frac{dx_2}{dt} = ax_2(1-x_2) - bx_2y_2 + \underbrace{kx_1}_{refuged\ prey\ population} \\ \frac{dy_2}{dt} = c(x_2 + \underbrace{kx_1}_{contribution\ in\ the\ growth})y_2 - dy_2 \end{cases} \tag{2}$$

Where $x_i(t)$ and $y_i(t)$ are the total numbers of prey and predator at time t respectively and all the constants a, b, c and d are nonnegative and the rate $\frac{c}{d}$ is related to the conversion of prey biomass into predator biomass.

The Lotka-Volterra model have been studied in various forms by many authors (see,[4, 5, 6]) by changing the functional response, by taking into account the effect of diffusion terms or by including the time delay in order to better understanding the dynamics of population interaction or studying the model with different form of functional response (see, [1, 2, 3, 18, 19]. Other authors consider some models which describing the interaction between two patches or more by taking into account the effect of the migration of one or two species from one patch to another (see, [8, 9, 10, 11, 14, 15]) and references therein.

In [13], Kuang et al. introduce a model in which a single specie disperse between two patches of a heterogenous environment with barriers between patches and a predator for which the dispersal between patches involve a barrier. In [12], the author introduced a two diffusively coupled predator prey populations. The coupled system is composed of four differential equations that is modelling the interaction of two identical patches in which dynamics are coupled through the migration of individuals of predator population only. This interaction between the predator and prey populations takes the form given by Rosenzweig-MacArthur (1963) [16] in which the prey population grows logistically and the predator has a Holling type II functional response. In [7], Feng et al. consider the same model by taking into account the migration of

*Université Ibn Zohr, Faculté Polydisciplinaire de Ouarzazate, B.P:638, Ouarzazate, Morocco. yafia1@yahoo.fr

†Laboratoire de Mathmatiques Appliques du Havre 25 rue Philippe Lebon, 76600 Le Havre, France, aziz.alaoui@univ-lehavre.fr

‡Manuscript received ; revised January .

both prey and predator population and studied the stability/instability of the possible steady states.
Recently, Quaglia et al. (2012) [17] consider a model of two patches coupling by the migration of both species. The model given by two identical patch with the same reproduction rate and different carrying capacities in each patch. The authors studied the existence and stability of the possible equilibrium points.
At now all the presented coupled patches of predator prey models take into account the migration of one species in one direction (from one patch to another patch only) or in the two directions (mutual migration) and the migration of both species in one direction or in two directions without considering the effect of the migrated (refuged) population on the refuge patch.
In this work, we take into account the migration of the prey population from the first patch to the second patch only (in one direction only) with a migration rate k and we consider the contribution of the migrated (refuged) prey population in the growth of the predator population of the refuge patch (second patch). We study the positivity and boundedness of solutions. Therefore we give the conditions of the existence of possible steady states and their local and global stability with respect to the migration rate.

2 Positivity an boundedness

Consider now the uncoupled systems (1) which correspond to the case when $k = 0$. By integrating from 0 to t, from the equation $(1)_1$ and for any initial data $x_{i0} > 0, i = 1, 2$ and $y_{i0} > 0, i = 1, 2$, we have

$$x_i(t) = x_{i0} e^{\int_0^t (a(1-x_i(s))-by_i(s))ds} > 0, i = 1, 2 \quad (3)$$

From the equation $(1)_2$, we have

$$y_i(t) = y_{i0} e^{\int_0^t (cx_i(s)-d)ds} > 0, i = 1, 2 \quad (4)$$

Then we deduce that for $k = 0$ the uncoupled systems has a positive solution for any positive initial data.
Let us now consider the case when the migration rate is positive ($k > 0$) which corresponds to the coupled system (2). From equations $(2)_1$ and $(2)_2$, we have

$$x_1(t) = x_{10} e^{\int_0^t (a(1-x_1(s))-by_1(s)-k)ds} > 0 \quad (5)$$

and

$$y_1(t) = y_{10} e^{\int_0^t (cx_1(s)-d)ds} > 0$$

From equation $(2)_3$,

$$\begin{aligned} x_2(t) &= x_{20} e^{\int_0^t (a(1-x_2(s))-by_2(s))ds} \\ &\quad + k \int_0^t e^{\int_s^t (a(1-x_2(u))-by_2(u))du} x_1(s) ds \end{aligned}$$

from equation (5), we have $x_1(t) > 0$, $\forall t > 0$. Then we deduce that $x_2(t) > 0$, $\forall t > 0$.
From equation $(2)_4$,

Theorem 2.1. *Let $X(t) = x_1(t) + x_2(t)$ the total number of the prey population of the two patches and $X_0 = x_{10} + x_{20}$. $X(t)$ satisfies the following inequality*

$$0 \leq X(t) \leq \left(\left(\frac{1}{X_0} - \frac{1}{2} \right) e^{-at} + \frac{1}{2} \right)^{-1}$$

and

$$\limsup_{t \longrightarrow +\infty} X(t) \leq 2, \forall t \in]0, +\infty[$$

for $X_0 < 2$.

Theorem 2.2. *Let $Y(t) = y_1(t) + y_2(t)$ the total population of the predator specie of the two patches. Then, we have*

$$Y_0 e^{-dt} \leq Y(t) \leq \left(Y_0 - \frac{2ck}{2c-d} \right) e^{-(2c-d)t} + \frac{2ck}{2c-d}$$

and for $2c > d$ and for $Y_0 \geq \frac{2ck}{2c-d}$ we have

$$\limsup_{t \longrightarrow +\infty} Y(t) \leq \frac{2ck}{2c-d}$$

Where $Y_0 = y_{10} + y_{20}$.

3 Steady states and stability

Proposition 3.1. *Under some conditions, system (2) has seven equilibrium points.*
The following table summarize the existence of the steady states : Where $D = a^2 + am$ and $D_1 = a^2 + 4ak\frac{d}{c}$ and $m = k(1 - \frac{k}{a})$.

Definition 3.1. Let $Pr_1(x_1, y_1, x_2, y_2) = (x_1, y_1)$ the projection of the point (x_1, y_1, x_2, y_2) on the equations $(2)_1$-$(2)_2$ describing the first patch (x_1, y_1) and $Pr_2(x_1, y_1, x_2, y_2) = (x_2, y_2)$ the projection of the point (x_1, y_1, x_2, y_2) on the equations $(2)_3$-$(2)_4$ describing the second patch (x_2, y_2)

Theorem 3.1. *Consider that $E_* = (x_1^*, y_1^*, x_2^*, y_2^*)$ is a steady state of system (2). The stability of E_* is deduced from the stability of $Pr_1E_* = (x_1^*, y_1^*)$ and $Pr_2E_* = (x_2^*, y_2^*)$.*
1)- If Pr_1E_* and Pr_2E_* are asymptotically stable, then E_* is also asymptotically stable.
2)- If Pr_1E_* or Pr_2E_* is unstable, then E_* is also unstable

Let V_i the lyapunov function associated to the patch i with $i = 1, 2$ defined by:

$$V_i(x_i, y_i) = (x_i - x_i^*) - \frac{d}{c} \ln \left(\frac{x_i}{x_i^*} \right)$$

$$+ \frac{b}{c} \left\{ (y_i - y_i^*) - y_i^* \ln \left(\frac{y_i}{y_i^*} \right) \right\}, i = 1, 2$$

This functions are defined and continuous on $Int(\mathbb{R}^2_+)$. We are interested in constructing lyapunov function for the coupled system (2).

Table 1: Existence of possible steady states of system (2)

Equilibrium point	Conditions of existence
$E_0 = (x_{10}, y_{10}, x_{20}, y_{20}) = (0,0,0,0)$	No conditions
$E_1 = (x_{11}, y_{11}, x_{21}, y_{21}) = (0,0,1,0)$	No conditions
$E_2 = (x_{12}, y_{12}, x_{22}, y_{22}) = (0,0,\frac{d}{c},\frac{a(1-\frac{d}{c})}{b})$	$c > d$
$E_3 = (x_{13}, y_{13}, x_{23}, y_{23}) = (1-\frac{k}{a}, 0, \frac{a+\sqrt{a^2+am}}{2a}, 0)$	$a > k$
$E_4 = (x_{14}, y_{14}, x_{24}, y_{24}) = \left(1-\frac{k}{a}, 0, \frac{d-cm}{c}, \frac{ax_{24}(1-x_{24})+m}{bx_{24}}\right)$	$cm < d < cm + \frac{c}{2a}\left(a+\sqrt{D}\right)$ and $a > k$ where $m = k(1-\frac{k}{a}) > 0$ and $D = a^2 + am > 0$
$E_5 = (x_{15}, y_{15}, x_{25}, y_{25}) = \left(\frac{d}{c}, \frac{a}{b}\left(1-\frac{k}{a}-\frac{d}{c}\right), \frac{a+\sqrt{D_1}}{2a}, 0\right)$	$1 > \frac{k}{a} - \frac{d}{c}$
$E_6 = (x_{16}, y_{16}, x_{26}, y_{26}) = \left(\frac{d}{c}, \frac{a}{b}\left(1-\frac{k}{a}-\frac{d}{c}\right), \frac{d}{c}(1-k), \frac{ax_{26}(1-x_{26})+k\frac{d}{c}}{bx_{26}}\right)$	$k < 1 < \frac{c}{d}\left(a+\frac{\sqrt{D_1}}{2a}\right) + k$ and $1 > \frac{k}{a} - \frac{d}{c}$ where $D_1 = a^2 + 4ak\frac{d}{c} > 0$

Theorem 3.2. *Let*

$$V(x_1, y_1, x_2, y_2) = \sum_{i=1}^{2} V_i(x_i, y_i)$$

For $a > 0$ and k sufficientlly small, the steady state $E_* = (x_1^*, y_1^*, x_2^*, y_2^*)$ is globally asymptotically stable.

References

[1] M. A. Aziz-Alaoui and M. Daher Okiye, Boundedness and global stability for a predator-prey model with modified Leslie-Gower and Holling-type II schemes, Appl. Math. Lett. 16 1069-1075 (2003).

[2] A. F. Nindjin and M. A. Aziz-Alaoui and M. Cadivel, Analysis of a a predator-prey model with modified Leslie-Gower and Holling-type II schemes with time delay, Nonlinear Analysis, Real World Applications, 7(5), pp: 1104-1118, (2006).

[3] Nindjin A.F. and Aziz-Alaoui M.A., Persistence and global stability in a delayed Leslie-Gower type three species food chain, Journal of Mathematical Analysis and Applications, Vol. 340(1), pp: 340-357 (2008)

[4] T. Alligood, T. D. Sauer and J. A. Yorke, Chaos: An Introduction to Dynamical Systems, Springer-Verlag, New York, 1996.

[5] C. Cosner, d. L. DeAngelis, J. S. Ault and D. B. Olson, E?ects of spatial grouping on the function response of predators, Theoretical Population Biology, 56(1999), 65-75.

[6] L. Edelstein-Keshet, Mathematical Models in Biology, McGraw-Hill Inc., New York, 1977.

[7] W. Feng and J. Hinson, Stability and Pattern in Two-Patch Predator-Prey Population Dynamics, Dis. Cont. Dun. Sys. pp. 268-279 (2005).

[8] V. A. A. Jansen, Theoretical Aspects of Metapopulation Dynamcs, Ph. D. thesis, Leiden University, The Netherlands, 1994.

[9] V. A. A. Jansen, Regulation of predator-prey systems through spatial interactions: a possible solution to the paradox of nrichment, Oikos, 74(1995), 384-390.

[10] V. A. A. Jansen and A. M. DeRoos, The Role of space in reducing predator- prey cycles, in "The Geometry of Ecological Interactions Simplifying Spacial Compelxity", Cambridge University Press, (2000), 183-201.

[11] V. A. A. Jansen and A. L. Lloyd, Local stability analysis of spatially ho- mogenous solutions of multi-patch systems, Journal of Mathematical Biology, 41(2000), 232-252.

[12] V. A. A. Jansen, The dynamics of two diffiusively coupled predator-prey populations, Theoretical Population Biology, 59(2001), 119-131.

[13] Y. Kuang and Y. Takeuchi, Predator-Prey Dynamics in Models of Prey Dispersal in Two-Patch Environments, Math. Bisci. 120:77-98 (1994).

[14] J. D. Murray, Lectures on Nonlinear-Differential-Equation Models in Biology, Oxford University Press, Oxford, 1977.

[15] J. D. Murray, Mathematical Biology, Springer-Verlag, Berlin, 1993.

[16] Rosenzweig, M. L., and MacArthur, R. H., Graphical representa- tion and stability conditions of predator-prey interactions, Am. Nat. 97, 209-223 (1963).

[17] G. Quaglia, E. Re, M. Rinaldi and E. Venturino, A Two-Patch Predator-Prey Metapopulation Model, East Asian Journal on Applied Mathematics Vol. 2, No. 3, pp. 238-265 (2012).

[18] R. Yafia, F. El Adnani and H. A. Talibi, Stability of limit cycle in a predator-prey model with modified Leslie-Gower and Holling-type II schemes with time delay, Applied Mathematical Sciences, Vol. 1, 2007, no. 3, 119 - 131.

[19] R. Yafia, F. El Adnani and H. A. Talibi, Hopf bifurcation analysis in a predator-prey model with modified Leslie-Gower and Holling-type II schemes with time delay, Nonlinear Analysis: Real World Applications, Volume 9, Issue 5, (2008), 2055-2067.

Proceedings of ICCSA 2014
Normandie University, Le Havre, France - June 23-26, 2014

QUALITATIVE PROPERTIES AND TURING BIFURCATION IN A TWO SPECIES PREDATOR-PREY SYSTEM WITH DIFFUSION ON A CIRCULAR DOMAIN

Walid Abid* R. Yafia † M. A. Aziz-Alaoui§ H. Bouhafa¶ A. Abichou‖

Abstract. In this paper we consider a predator-prey model given by a system of differential equations with diffusion terms defined on a disc domain $\{(x, y) \in \mathbb{R}^2/x^2+y^2 < R^2\}$. This model incorporates the Holling-type II and a modified Leslie-Gower functional response, we study the local and global stability of the positive equilibrium point of the system. The existence of Hopf and Turing bifurcations and patterns formation are theoretically proved. In the end, we carry out some numerical simulations in order to illustrate how biological processes afect spatio-temporal pattern formation in a spatial domain.

Keywords. Predator-prey model, local and global stability, Hopf and Turing bifurcation, pattern formation, chaos, disc domain.

References

[1] M. A. Aziz-Alaoui, *Study of a Leslie-Gower-type tritrophic population model*, Chaos, Solitons and Fractals, 14 (8), (2002), 1275-1293.

[2] M.A. Aziz-Alaoui and M. Daher Okiye, *Boundedness and global stability for a predator-prey model with modified Leslie-Gower and Holling type II shemes*, Applied Math. Let., 16, (2003), 1069-1075.

[3] A.F. Nindjin, M.A. Aziz-Alaoui and M. Cadivel, *Analysis of a Predator-Prey Model with Modified Leslie-Gower and Holling-Type II Schemes with Time Delay*, Nonlinear Anal. Real World Appl., 7(5), (2006) 1104-1118.

[4] B.I. Camara and M.A. Aziz-Alaoui, Turing and hopf patterns formation in a predator prey model with Leslie- Gower typr functional response, Dynamics of Continuous, Discrete and Impulsive System, series B , 16, (2008) 897-906.

[5] Sze-Bi Hsu, *Constructing Lyapunov Functions for Mathematical Models in Population Biology*, Taiwanese Journal of Math., vol 9, No.2, (2005), 151-173.

[6] A.F. Nindjin and M.A. Aziz-Alaoui, *Persistence and global stability in a delayed Leslie-Gower type three species food chain*, J. Math. Ana. Ap., 340(1), (2008) 340-357.

[7] O. M. Daher and M.A. Aziz-Alaoui, *On the dynamics of a predator-prey model with the Holling-Tanner functional response*, MIRIAM Editions, Editor V. Capasso, Proc. ESMTB conf., (2002) 270-278.

[8] J. D. Murray, *Mathematical biology : II. Spatial Models and Biomedical Applications*, Springer-Verlag Berlin Heidelberg (2003).

[9] R. Yafia and M. A. Aziz Alaoui, *Existence of periodic travelling waves solutions in predator prey model with diffusion*, Applied Mathematical Modelling, Vol. 37(6), 2013, pp: 3635-3644.

*Laboratoire d'ingenierie Mathmatique de l'ecole polytechnique de Tunis, abidwalid007@yahoo.fr

†Corresponding author: R. Yafia.

‡Université Ibn Zohr, Faculté Polydisciplinaire de Ouarzazate, B.P:638, Ouarzazate, Morocco. yafia1@yahoo.fr

§Laboratoire de Mathmatiques Appliques du Havre 25 rue Philippe Lebon, 76600 Le Havre, France, aziz.alaoui@univ-lehavre.fr

¶Laboratoire d'ingenierie Mathmatique de l'ecole polytechnique de Tunis, HabibBouhafa@yahoo.fr

‖Laboratoire d'ingenierie Mathmatique de l'ecole polytechnique de Tunis, azgal.abichou@ept.rnu.tn

Proceedings of ICCSA 2014
Normandie University, Le Havre, France - June 23-26, 2014

COMPARISON OF ODE-BASED MODELS FOR REACTIVE OXYGEN SPECIES REGULATION SYSTEM

Andrew Ignatenko*, Alexey Kolodkin†, Nathan Brady‡, Bernhard Peters and Rudi Balling

Abstract. Reactive oxygen species (ROS) play important role in the functioning of any cell and especially in the lifecycle of mitochondria. Since the action of ROS can be both positive and negative then the remarkable role can be played by ROS regulation system. We constructed three different ODE based kinetic models of different complexity for the ROS management system and shown the difference in the dynamics of these systems under different conditions. Using results of numerical simulation we showed that extraction of some subsystems can make the model more unstable. We also introduced the objective function for comparison of the models with structure of different complexity.

Nonlinear system, ODE-based model, reactive oxigen species, biological model simulation.

1 Introduction

Biological systems are typically complex and demonstrate nonlinear behavior. It is a non-trivial task to provide a comprehensive description of such systems because in order to obtain the most complete information we should know and properly describe every object and link inside the system. Even small biological system may contain hundreds of objects and links and can be governed by hundreds of chemical reactions. Another problem is that we can't consider different subsystems of the bigger system as standalone ones since they are tightly connected with each other. However sometimes it's possible to reduce dimension of the task and to develop a model containing the most important subsystems with the greatest impact on the whole system.

Neurodegenerative diseases are highly complex in nature and involve various physiological processes but some evidences require to pay more attention on the activity of reactive oxygen species (ROS) – chemically reactive molecules containing oxygen (e.g. oxygen ions, peroxide, hydroxyl ions, etc.). ROS are formed as a natural byproduct of the normal metabolism of oxygen and play important role in exchange of the signals inside the cell and homeostasis [1, 2]. During the normal conditions there is always some concentration of ROS inside the cell controlled by the complex ROS management system. However because of various external and internal impacts (e.g. UV-radiation, heat exposure, diseases) the concentration of ROS may increase dramatically and result in significant damage to cell structures and in particular to mithochondria (which provides the energy for the normal cell functioning). This effect is known as oxidative stress and thought to be involved in the development of different diseases. Indeed, it has been shown that mitochondrial dysfunction and excessive ROS generation play an important role in the neurons death e.g. in the death of dopaminergic neurons in Parkinsons disease [3, 4, 5, 6], high concentrations of ROS can damage DNA and proteins and induce cancerogenic mutations [7, 8], ROS also plays important role in the aging process [9]. Very high concentrations of ROS may lead to the cell death. That's why the functioning of ROS regulation system is extremely important.

In the current article we compared several models of the ROS management system of different complexity. The development of models was carried out using diagram editor CellDesigner (www.celldesigner.org) and software application for simulation and analysis of biochemical networks COPASI (www.copasi.org). All simulations were performed with MATLAB.

2 Models of ROS management system

Real ROS management system contains a huge number of subsystems playing their own role and influencing the overall dynamic of the management system. We built the model using only main subsystems which are supposed to have the greatest impact on the ROS management (see Figure 1). We assumed that the main source of ROS generation are damaged mitochondria. The more mitochondria are damaged the more ROS can be produced. We also considered several cell protection mechanisms suppressing ROS level:

- mitophagy – process of programmable death of dam-

*Andrew Ignatenko and Bernhard Peters are with Faculty of Science, Technology and Communication, University of Luxembourg, Luxembourg. E-mail: andrew.ignatenko@uni.lu

†Alexey Kolodkin and Rudi Balling are with Luxembourg Centre for Systems Biomedicine, University of Luxembourg, Luxembourg. E-mails: alexey.kolodkin@uni.lu

‡Nathan Brady is with German Cancer Research Center, Heidelberg, Germany

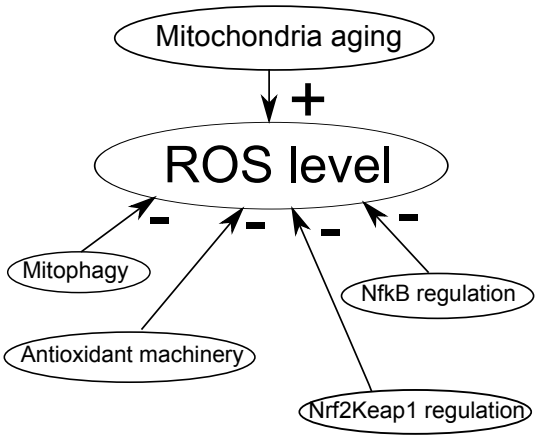

Figure 1: Scheme of the ROS management system. There is one main source of increasing ROS-concentration in normal conditions: aging (damaging) of mitochondria (sign "+"). There are several main mechanisms suppressing ROS level: mitophagy, antioxidant machinery, NFkB regulation and Nrf2Keap regulation (signs "−").

aged mitochondria and as a result, the elimination of the source of ROS production [10];

- antioxidant machinery – mechanisms that inhibit oxidation of other molecules therefore decreasing concentration of ROS [11];
- Nrf2Keap regulation – key oxidative stress response mechanism which regulates the expression of several antioxidants, activated by increasing the ROS level [12, 13];
- NfkB regulation – process, tunes the expression of genes which play an important role in ROS level control [14].

In normal situation when the ROS level is not changed all subsystems are in the equilibrium but if for some reasons ROS level rises the above mentioned mechanisms are switched on and try to suppress rising of the ROS concentration. If protection subsystem manages to stabilize the increasing of ROS concentration then the cell stays alive. If the rate of ROS generation is too high and can't be stopped by protection mechanisms then the cell dies.

3 Mathematical description of the model of ROS management system

Using special software every subsystem of ROS management system can be presented as a set of reactions (see Figure 2) and the reaction laws and parameters can be defined.

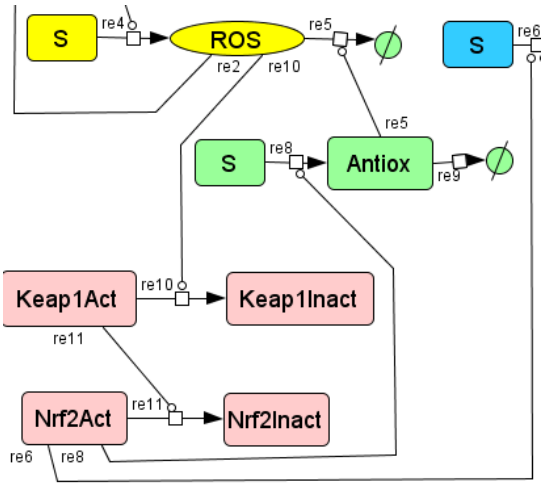

Figure 2: Example of the block describing Nrf2Keap regulation subsystem. Done in CellDesigner and COPASI.

ROS regulation system can be described by the system of nonlinear ODEs:

$$\dot{x}_i(t) = f_i(x_1(t)...x_i(t)...x_m(t), p_i), x_i(0) = x_{0i}, \quad (1)$$

where x_i - corresponds to concentration of certain species in the system (e.g. ROS concentration, proteins concentrations), p_i are the parameters of the reactions between different species, $x_i(0)$ is an initial state of the system.

The above ODE system has several features. Firstly it's autonomous system, i.e. there's no explicit dependency on t so it makes the analysis easier. Secondly as a rule this ODE system contains only polynomial equations or, at the worst case, can contain some rational functions. This feature is defined by the laws of used reactions. Typical equation has the following form:

$$\dot{x}_i(t) = \sum_m \sum_n a_{mn} x_m^\alpha x_n^\beta, \quad (2)$$

where α and β are integer numbers, a_{nm} - are real coefficients. Typically most of the coefficients a_{mn} are equal to zero, i.e. system can be considered as "sparsed".

Another important characteristic of the model is the steady state. The system is assumed to be in a steady state if it is unchanging in time. Steady state can be calculated by solving the system of algebraic equations

$$\dot{x}_i(t) = 0. \quad (3)$$

Since we are considering a real biological system not any solution of Eq. (3) can be suitable for analysis as $x_i(t)$ correspond to the concentrations of certain species and therefore $x_i(t) \geq 0$ for any moment t. Those solutions of Eq. (3) which satisfy the above mentioned condition can be considered and might present either stable or unstable steady state [15].

If we disturb the system in the stable steady state then there is always a certain area of disturbance which allows

to the system go back into the steady state. Sometimes "sparseness" and polynomial nature of equations of considered ODE system allow to obtain even analytical or quasianalytical solutions for the steady state. Usually considered systems have two steady states: one stable and one unstable. During further analysis we will discard steady states sets containing negative values which are meaningless from the biological point of view (species concentrations $x_i(t)$ can't be negative). Also we'll discard oscillatory steady states.

4 Comparison of the different designs of the ROS management system models

ROS management system can use different mechanisms for regulation of ROS level. The very important question is how to estimate the effectiveness of different mechanisms. Should we construct our model using the maximal possible number of regulation subsystems or we can choose only couple of them? To answer this question we constructed three models of different complexity for ROS management system. The only difference between these models is a number of used ROS regulation subsystems (see Table 1).

Table 1: Subsystems included in different models of ROS-management system (see also Fig. 1)

	Model 1	Model 2	Model 3
Mithoh. aging	+	+	+
Mitophagy	+	+	+
Antioxidants	+	+	+
Nfr2Keap	-	+	+
NfkB	-	-	+
ODE-system dim.	3	8	10

According to the table Model 1 has a very basic design including only main ROS-regulating subsystems (mitophagy and antioxidants). Models 2 and 3 have step by step increasing complexity with adding new regulating subsystem (Nrf2Keap and NfkB correspondingly). Models 1, 2 and 3 are described by ODE-systems with dimensions 3, 8 and 10 correspondingly.

The main problem in defining better design is to construct a criteria allowing us to compare the models including different number of blocks, equations and even species. To do that we developed the following criteria.

First of them would be a fraction of healthy mitochondria in the total mitochondria number (or the fraction healthy/damaged mitochondria). Indeed the main source of ROS-generation is the pool of damaged mitochondria so we expect the better characteristics from the system containing more healthy mitochondria than damaged ones. But this criterion doesn't include ROS concentration. So we suggest to use improved version of this criterion, specific ROS concentration R_{sp}:

$$R_{sp} = \frac{R}{D+H}, \tag{4}$$

where H - number of healthy mitochondria, D - number of damaged mitochondria, R - current ROS concentration.

Second criteria is some kind of objective function: the less value it has the better the model is. We constructed it in the following way:

$$F = \frac{1}{H} + \frac{D}{H} + \frac{R}{D+H}. \tag{5}$$

In the best situation when D and R are relatively small and H is very high then F should be very close zero and corresponds to the "good" system with large fraction of healthy mitochondria and low ROS concentration.

Since the ODE-systems describing different models have different number of equations, parameters and variables then we should choose some common characteristic to use during the following comparison. According to our two criteria of comparison the following characteristics should be considered for all three models: specific ROS concentration R_{sp} and objective function F. Also we choose set of important reaction parameters P which is common for all three models: rate of new mitochondria generation (low ROS production), mitophagy level (the rate of "killing" of damaged mitochondria) and ROS production rate.

Now to compare three models we can disturb every model in respect to parameter set P and to analyse models' response to this disturbance. To do this we constructed 250000 different combinations of parameters from the set P, simulated three models with these parameters combinations and compared the results.

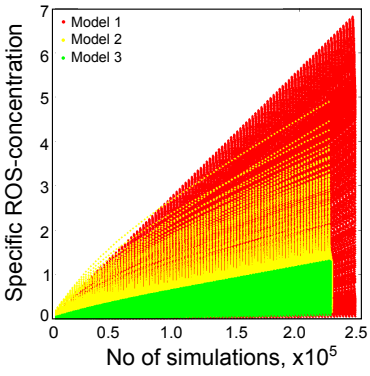

Figure 3: Specific ROS concentration R_{sp}. There are 250000 simulations for every model using different combinations of parameters from the set P. Only simulations with reaching the steady state are taken into account. All values (R, H, D) are measured in steady state.

During the first simulation we analyzed the changing of the steady state specific ROS concentration. Of course not every set of parameters P allows to reach the steady state so we put into consideration only those ones which allow to do that.

It's easy to see that the most complex Model 3 demonstrates higher level of stability in respect to parameters variation. At the same time Model 1 with the same parameters variation shows changing of specific ROS-level in up to 7 times. Model 2 takes an intermediate position between Models 1 and 2.

Very similar behavior of the models is demonstrated on the Figure 4. Model 3 again demonstrates great stability

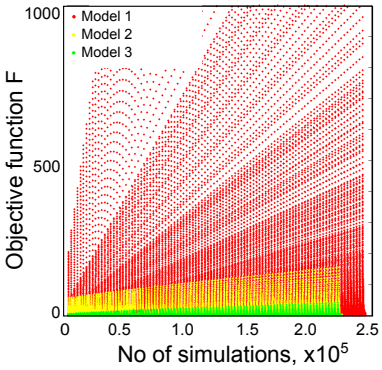

Figure 4: Objective function F for three models and 250000 simulations using different combinations of parameters from the set P. Only simulations with reaching the steady state are taken into account. All values (R, H, D) are measured in steady state.

in respect to variation of the parameters set. Model 2 gives a little bit worse but acceptable results. The simplest Model 1 demonstrates very bad results as objective function is changed in very large range in respect to parameters variation. So these two simulations show that Model 3 is the most stable one with changes in common parameters from the set P.

We also estimated the quality of developed models using another approach: we start the simulation of the models with one given set of parameters (which gives the good results for values of R_{sp} and F for all three models) and then in predefined moments of time we increased the rate of ROS-generation and monitored the model response. The results are given on Figure 5. Model 3 demonstrates the great ability to overcome the increasing of ROS generation rate. Even step-by-step increasing of ROS generation rate could not unbalance the Model 3. Surprisingly Model 1 acts better than Model 2 which demonstrates very unstable response to ROS generation rate increasing.

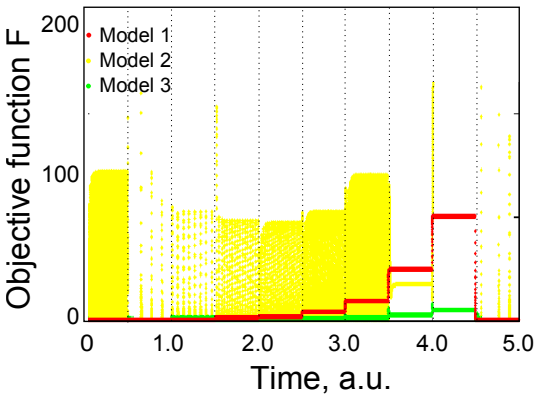

Figure 5: Changing the objective function F for three models with increasing of the ROS generation rate in predefined moments of time (dotted line). All values (R, H, D) are measured in steady state.

5 Conclusion

During this investigation we developed three models of different complexity for the ROS management system. These models have different combinations of mechanisms for decreasing ROS concentration.

We made some analysis to compare developed models and to answer a question about the importance of different protection mechanisms against ROS concentration increasing. We showed that the simplest Model 1 using one most general combined mechanism of both mitophagy and antioxidants machinery has only one advantage – simplicity that allows us to get very general ideas about functioning of ROS management system. Unfortunately this model can't demonstrate stable behavior when some important reaction parameters are changed.

Model 2 has an additional block of Nrf2Keap regulation mechanism and demonstrates better results but sometimes (when ROS generation rate is increased step-by-step in predefined moments of time as on Figure 5) it also becomes unstable demonstrating even worse results than Model 1.

Model 3 is the most complex one and in addition to the mechanisms of Models 1 and 2 has NfkB-mechanism. Stability of Model 3 in comparison with Model 2 can be explained by necessity of using both Nrf2Keap- and NfkB-mechanisms together as they complement each other and omitting only one of them may lead to unpredictable instability (Figure 5).

The above results will be used in further investigation of ROS management system. In particular to answer the question about model optimisation with respect to steady state region of stability, to find an effect of adding other secondary protection mechanisms against ROS increasing and to adapt developed models to the cases of different diseases (neurodegenerative diseases, cancer, etc.). Also developed models could be investigated using optimal control approach for seeking the ways of switching

between given states of the model (for example, "healthy" and "diseased" ones).

Acknowledgements

This work was supported, in part, by the Fonds National de la Recherche Luxembourg.

References

[1] J. T. Hancock, R. Desikan and S. J. Neill, "Role of Reactive Oxygen Species in Cell Signaling Pathways", *Biochemical and Biomedical Aspects of Oxidative Modification*, vol. 29(2), pp. 345-350, 2001.

[2] W. Burhans and N. Heintz, "The Cell Cycle is a Redox Cycle: Linking phase-specific targets to cell fate", *Free Radical Biology and Medicine*, vol. 47, pp. 1282-1294, 2009.

[3] M. Valko, D. Leibfritz, J. Moncol, M. Cronin, M. Mazur, J. Telser. "Free radicals and antioxidants in normal physiological functions and human disease", *International Journal of Biochemistry & Cell Biology*, vol. 39(1), pp. 4484, 2007.

[4] D.-H. Choi, A. C. Cristovao, S. Guhathakutra, T. Joh, F. Beal and Y. S. Kim, "NADPH oxidase 1-mediated oxidative stress leads to dopamine neuron death in Parkinson's disease", *Antioxid Redox Signal*, vol. 16(10), pp. 1033-45, 2012.

[5] V. A. Selivanov, T. V. Votyatkova, V. N. Pivtoraiko, J. Zeak, T. Sukhomlin. M. Trucco, J. Roca and M. Cascante, "Reactive oxygen species production by forward and reverse electron fluxes in the mitochondrial respiratory chain", *PLoS Comput Biol*, vol. 7(3), pp. e1001115, 2011.

[6] M. K. Maccoy and M. R. Cookson, "Mitochondrial Quality Control and Dynamics in Parkinson's Disease", *Antioxid Redox Signal*, vol. 16(9), pp. 869-82, 2012.

[7] B. D'Autreaux and M. B. Toledano, "ROS as signalling molecules: mechanisms that generate specificity in ROS homeostasis", *Nat Rev Mol Cell Biol*, vol. 8(10), pp. 813-24, 2007.

[8] S. Magder, "Reactive oxygen species: toxic molecules or spark of life?" *Crit Care*, vol. 10(1), p. 208, 2006.

[9] B. F. Oliveira, J. A. Nogueira-Machado and M. M. Chaves, "The role of oxidative stress in the aging process", *Scientific World Journal*, vol. 10, pp. 1121-8, 2010.

[10] D. A. Kubli and A. B. Gustafsson "Mitochondria and Mitophagy.The Yin and Yang of Cell Death Control", *Circulation Research*, vol. 111, pp. 1208-1221, 2012.

[11] H. Sies, "Oxidative stress: Oxidants and antioxidants", *Experimental physiology*, vol. 82(2), pp. 291-5, 1997.

[12] T. W. Kensler, N. Wakabayashi and S. Biswal, "Cell survival responses to environmental stresses via the Keap1-Nrf2-ARE pathway", *Annu Rev Pharmacol Toxicol*, vol. 48(2), pp. 89-116, 2007.

[13] W. Li and A. N. Kong, "Molecular mechanisms of Nrf2-mediated antioxidant response", *Mol Carcinog*, vol. 48(2), pp. 91-104, 2009.

[14] M. J. Morgan and Z. Liu, "Crosstalk of reactive oxygen species and NF-B signaling", *Cell Res.*, vol. 21(1), pp. 103-115, 2011.

[15] R. H. Enns, *It's a Nonlinear World*, Springer Undergraduate Texts in Mathematics and Technology, pp. 29-45, 2011.

Proceedings of ICCSA 2014
Normandie University, Le Havre, France - June 23-26, 2014

IDENTIFICATION OF DYNAMICAL BEHAVIORS IN EPILEPTIC DISCHARGES USING A NEURAL MASS MODEL WITH DOUBLE EXCITATORY FEEDBACKS

A. Garnier*, C. Huneau*†, A. Vidal‡, F. Wendling§ and H. Benali*

Abstract. Neural mass modeling is a field of computational neuroscience that aims at studying the activity of neuronal populations without explicit representation of single neurons. This type of mesoscopic model is able to generate output signals that can be compared with experimental data such as stereo-electroencephalograms. Classically, neural mass models consider two interconnected populations: excitatory pyramidal cells and inhibitory interneurons. Regarding the excitatory feedbacks on the pyramidal cell population, two distinct approaches have been proposed. A "direct feedback" on the main pyramidal cell population or an "indirect feedback" via a secondary pyramidal cell population. In this article, we propose a new neural mass model that couples both these approaches. We analyze the model bifurcations in two specific cases and describe the corresponding time series. We then explain the typical features of experimental records in epileptic mice. Finally, we show that the model is able to reproduce two different regimes identified in experimental data. Our study also reveals the similarity in the proper 4Hz frequency of epileptic discharges in experimental data and generated time series.

Keywords. Neural Mass Model, Local Field Potential, Bifurcation, MTLE Mouse Model, Hippocampal Discharge

1 Introduction

Computational neurosciences aim at developing new models and methods to improve our comprehension of complex relations between structure and function in human brain and nervous system in general. Specifically, mathematical models have been developed to reproduce the complexity of neuronal population activities as accurately as possible and analyzed to identify underlying dynamical mechanisms. Such results offer new approaches for experimental data processing based on predictive analysis and improve our knowledge about normal brain functions (cognitive processes) and brain disorders.

At a mesoscopic scale, models based on cellular interaction organization allow us to study the global behavior of neuronal population activities and interaction mechanisms. The neural mass approach was first introduced by Wilson and Cowan [18, 19] who modeled the neuronal activities averaged over small populations (voxels). Neural Mass Models (NMM) have the advantage of producing output signals such as Local Field Potentials (LFP), which are comparable with experimental data, such as electroencephalogram (EEG) outputs [9]. Initially, NMM considered the interactions between two populations: one main population of excitatory pyramidal cells and a population of inhibitory interneurons. These models are useful to understand the impact of the balance between excitation and inhibition on the genesis of cortical rhythms.

These models have been further improved by including an excitatory feedback on the pyramidal population in two different ways: either using a direct feedback of the pyramidal population on itself [10, 6] or through a secondary pyramidal population [9, 8, 16]. Models of the first type produce time series that are potentially faster than those obtained with an indirect excitatory feedback. On the other hand, models of the second type are able to reproduce LFP of the alpha band activity intercut with epileptic-like oscillations. From the viewpoint of global modeling, we cannot privilege one of these excitatory feedbacks over the other since both are biologically relevant. However, to our knowledge, no model considering both feedbacks together has ever been built or analyzed.

In the field of epilepsy, NMM have long been used to simulate the generation and propagation of ictal activity, i.e. seizure [16, 14]. Moreover, recent works have also shown the relevance of computational modeling to produce robust hypotheses about mechanisms underlying ictal and interictal activities in animal models [17, 6, 2]. In comparison with human data, the use of animal models enables better recording conditions associated with a high reproducibility of pathological patterns, and thus a more robust model-based interpretation of the data. Despite their different nature, animal models of epilepsy may present numerous similarities with human epileptic syn-

*Sorbonne Universités, UPMC Univ Paris 06, CNRS UMR 7371, INSERM U1146, Laboratoire d'Imagerie Biomédicale (LIB), F-75013, Paris, France

†Université Paris Diderot, Sorbonne Paris Cité, INSERM UMR_S1161, Génétique et physiopathologie des maladies cérébrovasculaires, F-75010, Paris, France

‡Université d'Évry-Val-d'Essonne, CNRS UMR 8071, Laboratoire de Mathématiques et Modélisation d'Évry (LaMME), F-91000, Évry, Paris, France

§Université de Rennes, INSERM U1099, Laboratoire du Traitement du Signal et de l'Image (LTSI), F-35000, Rennes, France

dromes [13]. Therefore, they constitute a relevant framework for inferring on human pathology.

In this article, we introduce a model involving both direct and indirect feedback weighted by coupling gain parameters. Relying on bifurcation analysis, we show how typical dynamical properties of the model can be used to reproduce identified profiles from experimental time series. We compare model outputs with experimental data recorded from intracerebral electrodes in epileptic mice. Finally, we discuss a typical feature of frequency stability shared by the experimental time series and the model outputs.

2 Materials and methods

2.1 Experimental protocol

In order to confront simulated LFP to real Hippocampal Discharges (HD), we used the Mesial Temporal Lobe Epilepsy (MTLE) mouse model [13]. Experiments were conducted in accordance with the European Communities Council Directive of November 24, 1986 (86/609/EEC). Four epileptic mice were produced by an initial intrahippocampal injection of kainic acid as described in [6]. Mice were also implanted with a bipolar depth electrode in the ipsilateral hippocampus and with monopolar surface electrodes over the cerebellum (electrical reference) and both the right and left cortices. Once animals reach the chronic epileptic stage (around 30 days after the initial kainic acid injection), LFP signals were recorded at a 2048 Hz sampling frequency. Each recording session was preceded by an injection of picrotoxin (2 mg/kg, intraperitoneal).

2.2 Model

Our model includes both direct and indirect feedbacks weighted by two coupling gain parameters. It is built on three feedback loops of the pyramidal population activity. The first loop is inhibitory and involves the excitatory action of pyramidal cells on the interneuron population which, in turn, inhibits the pyramidal activity. The second loop, called "indirect excitation", implies the excitatory action of pyramidal cells on a secondary pyramidal subpopulation, which excites the main pyramidal population. The well-known Jansen-Rit model [8, 7] is built on these two feedbacks. Our model involves a third feedback loop, called "direct excitation" in the following, which represents the excitatory action of the main pyramidal population on itself (Figure 1).

In our model as in the Jansen-Rit model, the state variables are the excitatory (y_1) and inhibitory (y_2) inputs and the output (y_0) of the main pyramidal population. This output acts on the inhibitory interneurons, the secondary excitatory pyramidal population and participates in the direct excitatory feedback. Classically, NMM receive an input representative of the external action of neuronal population activities from other cortical

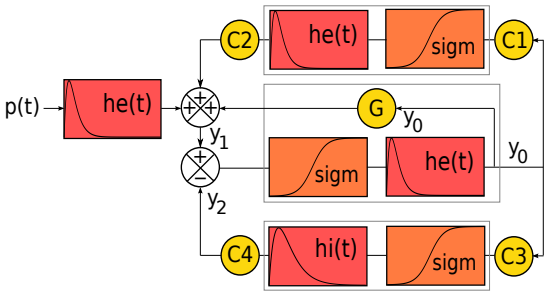

Figure 1: Diagram of the neural mass model with double excitatory feedback. $h_e(t)$ (resp. $h_i(t)$) box: transformation of action potential into excitatory (resp. inhibitory) post-synaptic potential introduced by [15]. sigm box: transformation of average membrane potential into average action potential density, introduced by [4]. C_i box ($i \in [\![1,4]\!]$): coupling gains according to the maximal number of synaptic connections between two populations. G: direct feedback coupling gain. $p(t)$: excitatory input from neighboring and distant neuronal populations. Arrows: excitatory (+) and inhibitory (-) actions from one population on another one.

(or subcortical units) on the main pyramidal population. This input can be stochastic to represent a non-specific background activity [7, 9, 16], or deterministic to represent a specific activity from an other cortical unit [6, 8].

Following the synaptic connection model introduced by Van Rotterdam [15], we obtain the following dynamics associated with the diagram shown in Figure 1:

$$y_0'' = A\,a\,\mathrm{sigm}(y_1 - y_2) - 2\,a\,y_0' - a^2\,y_0 \tag{1a}$$

$$y_1'' = A\,a\,C_2\,\mathrm{sigm}(C_1\,y_0) + A\,a\,G\,\mathrm{sigm}(y_1 - y_2) - 2\,a\,y_1' - a^2\,y_1 + A\,a\,p(t) \tag{1b}$$

$$y_2'' = B\,b\,C_4\,\mathrm{sigm}(C_3\,y_0) - 2\,b\,y_2' - b^2\,y_2 \tag{1c}$$

Parameters C_i, $i \in [\![1,4]\!]$, represent the averaged number of synaptic connections between two populations defined as a proportion α_i of C, the maximum number of synaptic connections between populations [1]:

$$\forall i \in [\![1,4]\!] \qquad C_i = \alpha_i\,C$$

Parameter G represents the average number of synaptic connections in the main pyramidal population. In other words, G is the coupling gain of the direct excitation. Function $p(t)$ represents the excitatory input on pyramidal cells, from neighboring and distant neuronal populations.

Parameter A (resp. B) fits the amplitude of the excitatory (resp. inhibitory) post-synaptic potentials. On the other hand, $\frac{1}{a}$ (resp. $\frac{1}{b}$) is the time constant of excitatory (resp. inhibitory) post-synaptic potentials representative of the kinetics of synaptic transmission and the averaged distributed delays in the dendritic tree [4, 8, 15]. The sigmoid function $\mathrm{sigm}(v) = \frac{2e_0}{1+\exp(r(v_0-v))}$ is used to infer the population activity (mean firing rate) from the

average membrane potential through a smooth threshold process: $2\,e_0$ represents the maximum discharge rate and v_0 the post-synaptic potential threshold.

2.3 Bifurcation analysis and generated time series

We computed bifurcation diagrams of system (1) according to the input $p = p(t)$ considered as a parameter, with different values for parameters α_2 and G. Dedicated codes based on direct calculation of the singular points and on pseudo-arclength continuation methods [3] for the limit cycles were implemented in Matlab® (The Mathworks, Inc.).

In this article, we focus on two specific situations among the various bifurcation diagrams according to p that the system may admit for different balances between direct and indirect excitatory feedbacks. In each case, the geometric invariants of the dynamics and their bifurcations according to p allow us to understand the specific features of the time series generated by system (1) with input $p(t)$ a Gaussian variable.

2.4 Power Spectral Analysis

Spectral analyses were performed using Matlab®. Time-frequency maps were obtained using the short-time Fourier transform (`spectrogram function`). The periodograms were calculated using Welch's method (`p.welch function`).

3 Results

3.1 Epileptic discharges in experimental LFP

The experimental protocol enables to record numerous HD, a classical epileptic event for the MTLE mouse model [13, 5]. According to literature, HD usually start with high amplitude sharp waves followed by a lower amplitude rhythmic discharge (Figure 3(a)). Time-frequency analysis shows that the rhythmic part of HD has an almost constant frequency of 4 Hz. Conversely to this synchronous discharge, the initial sharp waves remain asynchronous as they do not present any specific rhythm.

3.2 Characterization of two bifurcation structures

Figure 2 displays two types of bifurcation diagram of system (1) according to p (bottom panels) and associated LFP time series for a Gaussian input $p(t)$ (top panels). These two situations are characteristic of different balances between direct and indirect excitatory feedbacks. From the main features of the generated time series, we call the case on the left-hand side in Figure 2 Noise Induced Spiking (NIS) and the case on the right-hand side Noise Induced Spiking with Sub-Threshold Oscillations (NIS-STO). In the following, we describe the bifurcation diagrams and detail how they explain the features of the generated time series.

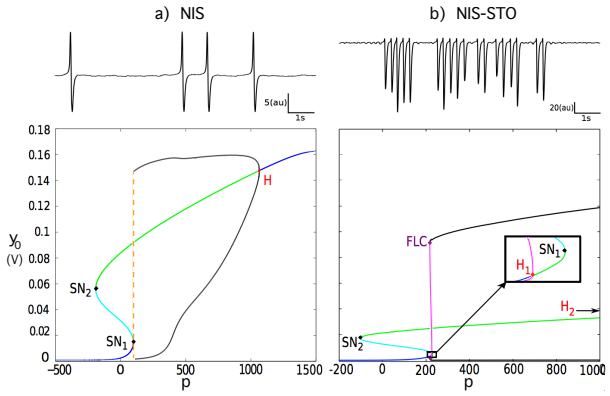

Figure 2: LFP time series (top) and bifurcation diagrams according to p (bottom) associated with the NIS and NIS/STO cases. Blue curve: stable singular points. Cyan (resp. green) curve: singular points with five (resp. four) eigenvalues with negative real parts. Red point: Hopf bifurcations (H and H_2 supercritical and H_1 subcritical). Black points: saddle-node bifurcations SN_1 and SN_2. Purple point: saddle-node bifurcation of limit cycles (FLC). Orange dashed curve: Saddle-Node on Invariant Cycle (SNIC) bifurcation. Black curves: maxima and minima of stable limit cycles. Magenta curves: unstable limit cycle maxima and minima.

In both bifurcation diagrams of Figure 2, the curve of system (1) singular points is S-shaped, admitting two knees SN_1 and SN_2 corresponding to saddle-node bifurcations according to p. These points split the curve of singular points into three branches: the "lower branch" below SN_1, the "middle branch" between SN_1 and SN_2, and the "upper branch" above SN_2. The points on the middle branch are unstable (shown in cyan) in both cases. The singular points on the upper branch are stable (shown in blue) for $p > p_{\mathrm{H}}$ in the NIS case and $p > p_{\mathrm{H}_2}$ in the NIS-STO case, and unstable (shown in green) otherwise. Values $p = p_{\mathrm{H}}$ for NIS and $p = p_{\mathrm{H}_2}$ for NIS-STO correspond to a supercritical Hopf bifurcation giving birth to a family of stable limit cycles for lower values of p (black curves in diagrams of Figure (2) represent the maximal and minimal y_0 values along the cycle for each value of p).

In the NIS case, considering decreasing values for p, the stable limit cycle disappears at $p = p_{\mathrm{SN}_1}$ through a Saddle-Node on Invariant Circle (SNIC) also known as saddle homoclinic bifurcation (dashed orange line). The lower branch is formed by stable singular points. On the other hand, in the NIS-STO case, the lower singular point undergoes a subcritical Hopf bifurcation for $p = p_{\mathrm{H}_1}$, which gives birth to an unstable limit cycle for lower values of p. The families of stable and unstable limit cycles

connect for $p = p_{\mathrm{FLC}}$, which corresponds to a saddle-node bifurcation of limit cycles. In other words, a family of limit cycles connects H_1 and H_2, and for p fixed between p_{FLC} and p_{H_1}, a stable limit cycle of great amplitude coexists with an unstable limit cycle of smaller amplitude.

Note that, in the NIS case, the period of the limit cycle tends to $+\infty$ when p tends to p_{SN_1} from above. On the other hand, in the NIS-STO case, the period of the limit cycle varies smoothly for p around p_{SN_1}. The transition from NIS to NIS/STO bifurcation diagram is a special case of codimension 2 subcritical Bogdanov-Takens bifurcation occurring when a SNIC exists. In this case, the SNIC bifurcation takes the role of the homoclinic bifurcation that emerges from a classical Bogdanov-Takens bifurcation.

Now, let input $p(t)$ be a Gaussian variable with mean value around p_{SN_1}. In the NIS case, the generated time series displays quiescent phases while the current point along the flow is attracted by the lower stable branch. Spikes occur when the current point starts following the family of stable limit cycles. Due to the presence of the SNIC and the great period of the limit cycle for p close to p_{SN_1}, the global return of the current point takes a long time, which explains the long interspike interval in NIS time series. On the contrary, in the NIS-STO case, the spike frequency in the bursts is higher than in the NIS case and remains quite constant. Moreover, the presence of an unstable focus for $p \in]p_{\mathrm{H}_1}, p_{\mathrm{SN}_1}[$ induces small oscillations during the quiescent phases. We call them subthreshold oscillations since they correspond to the transient phenomenon occurring when destabilization is not strong enough to produce a large amplitude oscillation.

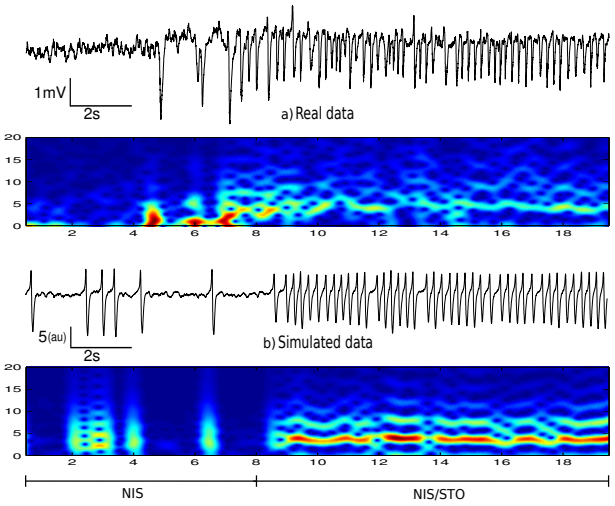

Figure 3: (a) Experimental time series and associated spectrogram. (b) Model output and associated spectrogram: $\alpha_2 = 0.4$ (NIS case) for $t < 8s$ and $\alpha_2 = 0.35$ (NIS-STO case) for $t > 8s$. In the spectrograms, the colors correspond to the number of spikes with a given frequency: the red color indicates the main frequency at time t.

3.3 NIS to NIS-STO switch and transition towards epileptic discharges

The two different regimes identified in the experimental time series share common features with the model outputs in the two cases described above: the NIS case produces isolated large amplitude spikes comparable with preictal spikes and the NIS-STO case produces higher frequency bursts like HD. We have reproduced the transition between the two regimes corresponding to the transition towards HD by a slight change in a parameter value, which induces a switch of the model from the NIS case into the NIS-STO case.

Figure 3 shows an experimental time series and the model output obtained with a change in α_2 value (from 0.4 to 0.35) at time $t = 8s$, which corresponds to reducing the impact of the indirect excitatory feedback. Since a change of activity in a given cortical area impacts the activity in the other areas, their feedback action on the considered population also changed. For sake of consistency in the modeling, the average value of the Gaussian input $p(t)$ is also changed after $t = 8s$ and fixed close to the updated excitability value p_{SN_1}.

The model output is similar to the experimental time series, first displaying long interspike interval then bursts of spikes with higher frequency. Comparing the spectrograms of the experimental time series and the model outputs shows that the oscillation frequencies are similar in each regime.

3.4 Proper frequency in NIS-STO and hippocampal discharges

In the MTLE mouse model, HD have been described to be very reproducible with a mean frequency of 3-7 Hz during the synchronous phase [5]. In this paper, we produced time-frequency map in Figure 3(a) showing that this frequency is about 4 Hz in our data. Moreover we have estimated the Power Spectral Density (PSD) in five HD and find out a high reproducibility of this frequency during the synchronous phase (Figure 4(a)). This result supports the hypothesis that HD have a proper frequency that seems to be intrinsic of the recorded neural circuit. We explained in section 3.2 that, in the NIS-STO case, the spike frequency in each burst is linked with the period of the stable limit cycle, which remains almost the same for any p value close to the mean of the Gaussian input. We performed a simulation trial with various sets of values for parameters C, α_2 and G still corresponding to the NIS-STO case (Figure 4(b)). The PSD in those simulated data also have a proper frequency of about 4 Hz. Relying on this comparison, we hypothesized that NIS-STO structure can be the dynamical mechanism underlying experimental HD.

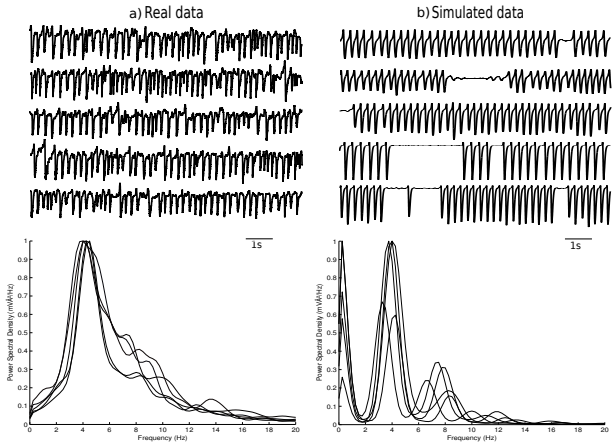

Figure 4: Time series (top) and associated PSD (bottom) from experimental data (a) and NIS-STO type model outputs (b). The experimental time series were extracted from different records. Model outputs were obtained with different values of (C, G, α_2): from top to bottom, $(245\,, 20\,, 0.35)$, $(300\,, 0\,, 0.3)$, $(340\,, 60\,, 0.3)$, $(800\,, 55\,, 0.5)$, and $(900\,, 0\,, 0.3)$.

4 Conclusion and Perspectives

In this article, we have proposed a neural mass model including two existing ways for the excitatory feedbacks: on the one hand, the direct excitatory feedback of pyramidal cell population on itself [6, 10] and, on the other hand, the indirect excitatory feedback through a secondary pyramidal cell population [9, 7, 16]. We have carried out a bifurcation analysis of the model in two specific cases and provided the associated time series NIS and NIS-STO. The SNIC bifurcation in the NIS case explains the long-period spikes in the associated time series. On the other hand, for the second behavior the limit cycle period remains almost constant. For a fixed set of parameter values, this phenomenon can be explained by the small interval of p values allowing to generate NIS-STO. Both these behaviors are physiologically relevant and we have shown that our model is able to reproduce experimental LFP signals from epileptic mice. Computing a PSD analysis on both *in vivo* and *in silico* data, we have shown that the NIS-STO large oscillations and experimental time series frequency remain stable and close to 4Hz even when varying parameters C, α_2 and G in simulations. Finally, arguments detailed in this paper sustain the hypothesis that HD is the manifestation of NIS-STO dynamical behavior of the underlying neural circuit.

In the hippocampal formation, subregions are connected whitin a loop circuit that makes this structure prompt to produce pathological rhythmic activity [12, 11]. This characteristic may be a reason for the occurrence of HD in the LFP signals recorded in epileptic mice. Nevertheless, our results argue for a different hypothesis. Indeed, we have shown that HD can be simulated within a simple NMM. Hence, we assume that HD may be generated intrinsically, and therefore do not necessarily involve a large network activity. With this consideration, it could be interesting to find out which model parameters influence the value of the aforementioned proper frequency. Two ways are possible to answer this question 1) an analytic relation between the proper frequency and parameters or 2) a parameter sensitivity analysis on the proper frequency. Finally, the knowledge of such parameters is a first step to an experimental validation of the hypothesis we put forward in this conclusion.

Acknowledgements

This work was performed within the Labex SMART (ANR-11-LABX-65) supported by French state funds managed by the ANR within the Investissements d'Avenir programme under reference ANR-11-IDEX-0004-02. Clément Huneau holds a grant from "Fondation Leducq Transatlantic Network of Excellence on pathogenesis of small vessel disease of the brain". We thank Mélanie Pelegreni-Issac for her manuscript revision.

References

[1] V. Braitenberg and A. Schüz. *Cortex: Statistics and Geometry of Neuronal Connectivity*. Springer, 2nd edition, 1998.

[2] S. Demont-Guignard, P. Benquet, U. Gerber, A. Biraben, B. Martin and F. Wendling. Distinct hyperexcitability mechanisms underlie fast ripples and epileptic spikes. *Annals of neurology*, 71(3):342–352, 2012.

[3] E.J. Doedel, W. Govaerts and Yu.A. Kuznetsov. Computation of Periodic Solution Bifurcations in ODEs Using Bordered Systems. *SIAM J. Numer. Anal.*, 41(2):401–435, 2003.

[4] W. Freeman. *Mass action in the nervous system*. Academic Press, New York, 1975.

[5] C. Heinrich, S. Lähteinen, F. Suzuki, L. Anne-Marie, S. Huber, U. Häussler, C. Haas, Y. Larmet, E. Castren and A. Depaulis. Increase in BDNF-mediated TrkB signaling promotes epileptogenesis in a mouse model of mesial temporal lobe epilepsy *Neurobiology of disease*, 42(1):35–47, 2011.

[6] C. Huneau, P. Benquet, G. Dieuset, A. Biraben, B. Martin, and F. Wendling. Shape features of epileptic spikes are a marker of epileptogenesis in mice. *Epilepsia*, 54(12):2219–2227, 2013.

[7] B. H. Jansen and V. G. Rit. Electroencephalogram and visual evoked potential generation in a mathematical model of coupled cortical columns. *Biological Cybernetics*, 73(4):357–366, 1995.

[8] B. H. Jansen, G. Zouridakis, and M. E. Brandt. A neurophysiologically-based mathematical model of flash visual evoked potentials. *Biological Cybernetics*, 68(3):275–283, 1993.

[9] F. Lopes da Silva, A. Hoeks, H. Smits, and L. Zetterberg. Model of brain rythmic activity. *Kybernetik*, 15(1):27–37, 1974.

[10] B. Molaee-Ardekani, P. Benquet, F. Bartolomei, and F. Wendling. Computational modeling of high-frequency oscillations at the onset of neocortical partial seizures: From 'altered structure' to 'dysfunction'. *NeuroImage*, 52(3):1109–1122, 2010.

[11] T. Nagao, A. Alonso and M. Avoli Epileptiform activity induced by pilocarpine in the rat hippocampal-entorhinal slice preparation. *Neuroscience*, 72(2):399–408, 1996

[12] D. Paré, M. de Curtis and R. Llinás Role of the hippocampal-entorhinal loop in temporal lobe epilepsy: extra- and intracellular study in the isolated guinea pig brain in vitro. *The Journal*

of neuroscience: the official journal of the Society for Neuroscience, 12(5):1867–1881, 1992.

[13] V. Riban, V. Bouilleret, B.T. Pham-Lê, J.-M. Fritschy, C. Marescaux and A. Depaulis. Evolution of hippocampal epileptic activity during the development of hippocampal sclerosis in a mouse model of temporal lobe epilepsy. *Neuroscience*, 112(1):101–111, 2002.

[14] J. Touboul, F. Wendling, P. Chauvel, and O. Faugeras. Neural mass activity, bifurcations, and epilepsy. *Neural computation*, 23(12):3232–3286, 2011.

[15] A. Van Rotterdam, F. H. Lopes da Silva, J. van den Ende, M. Viergever, and A. Hermans. A model of the spatial-temporal characteristics of the alpha rhythm. *Bulletin of mathematical biology*, 44(2):283–305, 1982.

[16] F. Wendling, F. Bartolomei, J.-J. Bellanger, and P. Chauvel. Epileptic fast activity can be explained by a model of impaired gabaergic dendritic inhibition. *European Journal of Neuroscience*, 15(9):1499–1508, 2002.

[17] F. Wendling, F. Bartolomei, F. Mina, C. Huneau, and P. Benquet. Interictal spikes, fast ripples and seizures in partial epilepsies–combining multi-level computational models with experimental data. *European Journal of Neuroscience*, 36(2):2164–2177, 2012.

[18] H. R. Wilson and J. D. Cowan. Excitatory and inhibitory interactions in localized populations of model neurons. *Biophysical journal*, 12(1):1–24, 1972.

[19] H. R. Wilson and J. D. Cowan. A mathematical theory of the functional dynamics of cortical and thalamic nervous tissue. *Kibernetik*, 13(2):55–80, 1973.

Proceedings of ICCSA 2014
Normandie University, Le Havre, France - June 23-26, 2014

NEW PARADIGM IN DELAY DYNAMICS: VIRTUAL CHIMERA STATES AND BRAIN-INSPIRED PROCESSING

Laurent Larger, Bogdan Penkovsky, Antonio Baylòn Fuentes, Maxime Jacquot, Yanne K. Chembo, and Yuri Maistrenko *†‡

Abstract. Delays systems are well known to provide chaotic solutions in infinite dimensional phase space, though being purely temporal dynamics. They have been explored both fundamentally and experimentally in various context, from living system to photonic oscillators through control theory. We will report on recent further investigations and applications of the complexity underlying nonlinear delay differential equations: first the emergence of virtual Chimera states in autonomous operation, revealing incongruent cluster patterns under some specific parameter conditions; and second, similar delay systems when driven non-autonomously by signal or information, are found as an efficient and elegant way to demonstrate physically the implementation of a novel brain-inspired computing principle, which is making use of nonlinear transient expansion triggered by the information to be processed. Both issues are representing novel attractive paradigm for delay dynamical systems, and can be connected through the space-time analogy for delay dynamics emulating them as a network of virtual dynamical nodes.

Keywords. Delay dynamics, dynamical complexity, Chimera states, Nonlinear transient computing, optoelectronic nonlinear delayed oscillator, Reservoir Computing.

References

[1] Y. Kuramoto and D. Battogtokh, "Coexistence of Coherence and Incoherence in Nonlocally Coupled Phase Oscillators," *Nonlinear phenomena in complex systems*, vol.5, No.4, pp. 380–385, 2002.

[2] D.M. Abrams and S.H. Strogatz, "Chimera States for Coupled Oscillators," *Physical Review Letters*, vol.93, No.17, 174102, 2004.

[3] A.M. Hagerstrom, T.E. Murphy, R. Roy, P. Hövel, I. Omelchenko and E. Schöll, "Experimental observation of chimeras in coupled-map lattices," *Nature Physics*, vol.8, pp. 658-661, 2012.

[4] M.R. Tinsley, S. Nkomo and K. Showalter, "Chimera and phase-cluster states in populations of coupled chemical oscillators," *Nature Physics*, vol.8, p. 662, 2012.

[5] L. Larger, B. Penkovskyi and Y. Maistrenko, "Virtual Chimera States for Delayed-Feedback Systems," *Physical Review Letters*, vol.111, 054103, 2013.

[6] H. Jaeger, and H. Haas, "Harnessing nonlinearity: predicting chaotic systems and saving energy in wireless communication," *Science*, vol.304, pp.78-80, 2004.

[7] L. Appeltant, M.C. Soriano, G. Van der Sande, J. Danckaert, S. Massar, J. Dambre, B. Schrauwen, C.R. Mirasso and I. Fischer, "Information processing using a single dynamical node as complex system," *Nature Communications*, vol.2, No.468, pp. 1-6, 2011.

[8] L. Larger, M.C. Soriano, D. Brunner, L. Appeltant, J.M. Gutierrez, L. Pesquera, C.R. Mirasso and I. Fischer, "Photonic information processing beyond Turing: an optoelectronic implementation of reservoir computing," *Optics Express*, vol.20, No.3, pp 3241–3249, 2012.

*All authors are with FEMTO-ST / Optics Dept., UMR CNRS 6174, University of Franche-Comté, 16 Route de Gray, 25030 Besançon Cedex, France. E-mail: llarger@univ-fcomte.fr

†Maistrenko is also with Ukrainian Academy of Science, Mathematical Institute of Kiev, Ukrain

‡Manuscript received April 19, 2014; revised ???, 2014.

Proceedings of ICCSA 2014
Normandie University, Le Havre, France - June 23-26, 2014

MATHEMATICAL ANALYSIS OF A COMPLEX NETWORK OF NEURONAL REACTION-DIFFUSION SYSTEMS

V.L.E. Phan, B. Ambrosio and M.A. Aziz-Alaoui *

Abstract. We focus on a complex system consisting of a network of n neurons. Each neuron is represented by a PDE system of FitzHugh-Nagumo type (FHN) obtained by a simplification of the famous Hodgkin-Huxley model (HH). After recalling the physiological basis of the model and the assumptions allowing to pass from HH to FHN model, we present some mathematical results on the network. First, we deal with the existence of the global attractor of the complex system in a general mathematical framework. Then, we show some results of synchronization, by establishing sufficient conditions, valid for different topologies, in the case of bidirectional and unidirectional couplings. We finally illustrate the asymptotic behaviors by numerical simulations. These allow to highlight the relationship between the number of neurons and the synchronization threshold according to the network topology.

Keywords. Synchronization, attractor, coupling strength, complex networks, connection graph stability.

1 Introduction

Neuroscience is of fundamental interest in a better scientific knowing of the spirit. As it concerns the nervous system in general, and particularly the brain, it is a branch of biology and physiology. But with the fast development of science, it now relies on physics, chemistry, informatics and... mathematics. In this paper we will propose a general network of n neurons. Each neuron is modeled by a PDE system of d equations. The paradigmatic model of mathematical neuroscience is the Hodgkin-Huxley model (1952):

$$\begin{cases} -C\dfrac{dV}{dt} = m^3 h\overline{g}_{Na}(V - E_{Na}) + n^4\overline{g}_K(V - E_K) \\ \qquad\qquad +\overline{g}_L(V - E_L) - I \\ \dfrac{dn}{dt} = \alpha_n(1-n) - \beta_n n = \dfrac{n_\infty - n}{\tau_n} \\ \dfrac{dm}{dt} = \alpha_m(1-m) - \beta_m m = \dfrac{m_\infty - m}{\tau_m} \\ \dfrac{dh}{dt} = \alpha_h(1-h) - \beta_h h = \dfrac{h_\infty - h}{\tau_h} \end{cases} \tag{1}$$

It describes the evolution of the transmembrane voltage. It is obtained by considering the cellular membrane as a capacitance, and by subsequently writing the Kirkoff law, with the potassium, sodium, leakage, capacitance and input currents. The main idea of Hodgkin and Huxley was to consider potassium and sodium currents as voltage variable dependent currents. The key of their work was to precisely evaluate by experiments the α's and β's functions. It is usual to write the three last equations like in the right and side of equation (1), where:

$$n_\infty = \frac{\alpha_n}{\alpha_n + \beta_n}, \tau_n = \frac{1}{\alpha_n + \beta_n},$$
$$m_\infty = \frac{\alpha_m}{\alpha_m + \beta_m}, \tau_m = \frac{1}{\alpha_m + \beta_m},$$
$$h_\infty = \frac{\alpha_h}{\alpha_h + \beta_h}, \tau_h = \frac{1}{\alpha_h + \beta_h}.$$

Later (1961), R. FitzHugh proposed a $2d$ model, reproducing excitable and oscillatory properties of the Hodgkin-Huxley model, while in 1962 Nagumo proposed the analog equivalent circuit. The FitzHugh-Nagumo model reads as:

$$\begin{cases} \dot{V} = V(V-\alpha)(1-V) - w + I \\ \dot{w} = \epsilon(V - \gamma w) \end{cases} \tag{2}$$

In the last section of this work we will show numerical simulations of networks of PDE FitzHugh-Nagumo systems of the form:

$$\begin{cases} \epsilon u_t = f(u) - v + d\Delta u \\ v_t = au - bv + c \end{cases} \tag{3}$$

where $f(u) = -u^3 + 3u$, $u = u(t,x)$ with initial conditions and Neumann zero flux boundary conditions. As already proposed by Hodgkin and Huxley, we can describe the propagation of action potential along a neuron by adding a diffusive term in the first equation. In the second and third section we will consider general networks of Reaction Diffusion systems that encompass systems of type (3). More precisely, in the second section, we will enunciate the existence of the global attractor in the functional space $(L^2(\Omega))^{nd}$. By using techniques of [3, 4], we generalize some parts of the works [1, 2]. Then we will focus on

*V.L.E. Phan, B. Ambrosio, M.A. Aziz-Alaoui are with Department of Applied Mathematics, University of Le Havre, France. E-mails: pvlem6a2@gmail.com, benjamin.ambrosio@univ-lehavre.fr, aziz.alaoui@univ-lehavre.fr

synchronization. By using the *connection graph stability* method, we establish, in section 3, under linear coupling, the complete synchronization of the whole network. In section 4, we illustrate numerically the results of section 3, when each neuron is modelled by a FitzHugh-Nagumo PDE and the topology is complete or an oriented ring.

2 Existence of the global attractor

We suppose that Ω is an open bounded set of $\mathbb{R}^N$ with boundary $\partial\Omega$. We consider the following initial boundary value problem (a network) involving a vector $U_{n\times 1} = (U_1, U_2, ..., U_n)^T$ from $\Omega \times \mathbb{R}^+$ into $\mathbb{R}^{nd}$; $U_i, 1 \leq i \leq n$ satisfies,

$$U_{it} = F(U_i) + Q\Delta U_i + PH_i(U), \tag{4}$$

where $F(U_i) = (F^1(U_i), ..., F^d(U_i))^T$ is a nonlinear vector function defining the dynamics of the individual oscillator, $U_i = (U_i^1, ..., U_i^d)^T$ is the d-vector containing the coordinates of the ith oscillator, and $H_i(U) = (H_i^1(U), ..., H_i^d(U))^T$ determines the coupling function. The non-zero elements of the $d \times d$ matrix P determine which variables couple the oscillators. It is a diagonal matrix and verify,

$$p_{ll} = \begin{cases} 1 & \text{for } l = 1, ..., s, \\ 0 & \text{for } l = s+1, ..., d. \end{cases}$$

In a analogue way, Q is a diagonal matrix and $q_{ll} > 0$ for $l = 1, ..., s$; $q_{ll} = 0$ for $l = s+1, ..., d$.

In order to separate the equations with diffusive terms and the others we rewrite (4) in the following form,

$$\begin{cases} PU_{it} = PF(U_i) + Q\Delta U_i + PH_i(U), \\ LU_{it} = -L\sigma(x)U_i - L\Phi(x, PU_i). \end{cases}$$

where $\sigma(x) = \text{diag}(\sigma_1(x), \sigma_2(x), ..., \sigma_d(x))$, $\sigma_i(x) \geq \delta > 0, i = \overline{s+1, d}, \sigma_i(x) = 0, i = \overline{1, s}$; and $\Phi = (\Phi_1, \Phi_2, ..., \Phi_d)^T$, where $\Phi_l = 0, l = 1, ..., s$; $\Phi_l = \Phi_l(x, PU_i), l = s+1, ..., d$, depends on x and on PU_i.

The functions F, H_i, σ and Φ are assumed to be twice continuously differentiable in all variables and to satisfy,

$$\sum_{l=1}^{s} \overline{\delta}_1^l |U_i^l|^p + \sum_{m=s+1}^{d} \overline{\delta}_1^m |U_i^m|^2 - \overline{\delta}_3 \leq -U_i^j F^j(U_i) \leq \sum_{l=1}^{s} \overline{\delta}_2^l |U_i^l|^p + \sum_{m=s+1}^{d} \overline{\delta}_2^m |U_i^m|^2 + \overline{\delta}_3, \tag{5}$$

for all $j = 1, ..., s$, $p > 2$, and

$$|PH_i(U)| \leq \delta_4 (P\mathbf{1}_{d\times 1} + \sum_{j=1}^{n} P|U_j|^{p_1}), \quad 0 < p_1 < p - 1, \tag{6}$$

where $\mathbf{1}_{d\times 1} = \underbrace{\begin{pmatrix} 1 & 1 & ... & 1 \end{pmatrix}^T}_{d}$ and $\mathbf{1}_{1\times d} = \mathbf{1}_{d\times 1}^T$.

$$\frac{\partial F^j}{\partial U_i^j} \leq l_1, \quad \frac{\partial H_i^j}{\partial U_i^j} \leq l_2, \quad |\frac{\partial \Phi_l}{\partial U_i^j}| \leq l_3, \tag{7}$$

for $i = \overline{1, n}, j = \overline{1, d}, l = \overline{s+1, d}$.

$$\left|\Phi'_{x_j}(x, PU_i)\right| \leq \delta_5 (\mathbf{1}_{d\times 1} + MP|U_i|), \quad j = \overline{1, n}, \tag{8}$$

$$|\Psi(x, PU_i)| \leq \delta_5 M. \tag{9}$$

where $\overline{\delta}_i^j, i = 1, 2, j = \overline{1, d}$, δ_3, δ_4, δ_5, $\overline{\delta}_3$ and k_1 are positives constants;

$$M_{d\times d} = \begin{pmatrix} 1 & ... & 1 \\ ... & ... & ... \\ 1 & ... & 1 \end{pmatrix}$$

and

$$\Psi(x, PU_i) = \begin{pmatrix} \Phi'_{1U_i^1} & ... & \Phi'_{1U_i^d} \\ ... & ... & ... \\ \Phi'_{dU_i^1} & ... & \Phi'_{dU_i^d} \end{pmatrix}.$$

We used the following notations, for $v = (v_1, ..., v_d)^T, a = (a_1, ..., a_d)^T$, $|v|^k = (|v_1|^k, ..., |v_d|^k)^T; v^k = (v_1^k, ..., v_d^k)^T$, $\forall k \geq 1$, and $v \leq a$ means that $v_i \leq a_i, i = 1, 2, ..., d$ (this notation is also used for the square matrix).

Let $H = ((L^2(\Omega))^d)^n$ and $V = ((H^1(\Omega))^d)^n$. Under the previous assumptions, we have the following theorem,

Theorem 2.1. *The semi-group $S(t)$ associated with the system (4) has a global connected attractor in H.*

3 Synchronization

Definition 3.1. Let us denote by $S(t) = (U_1(t), U_2(t), ..., U_n(t)), i = \overline{1, n}$ a network. We say that S synchronizes if,

$$\lim_{t\to+\infty} \sum_{i=1}^{n-1} \sum_{j=1}^{d} \left(\left\| U_i^j(t) - U_{i+1}^j(t) \right\|_{L^2(\Omega)} \right) = 0.$$

3.1 Symmetrically coupled networks

We consider the following network,

$$U_{it} = F(U_i) + Q\Delta U_i + \sum_{j=1}^{n} \epsilon_{ij}(t) PU_j, \quad i = \overline{1, n}, \tag{10}$$

where $G = (\epsilon_{ij}(t))$ is a symmetric matrix $n \times n$ with vanishing row-sums and non-negative off-diagonal elements. To get further, we have to make some assumptions and introduce the auxiliary system,

$$X_{ijt} = \left[\int_0^1 DF(\sigma U_j + (1-\sigma)U_i) d\sigma - A \right] X_{ij}, \ i, j = \overline{1, n}. \tag{11}$$

where $A = \text{diag}(a_1, a_2, ..., a_d), a_l = 0$ for $l = 1, ..., s, a_l = 0$ for $l = s+1, ..., d$, is a matrix to determine in such a way that there exists Lyapunov function of the form,

$$W_{ij} = \frac{1}{2} X_{ij}^T H X_{ij}, \qquad i, j = \overline{1, n}, \tag{12}$$

where the matrix H is symmetrical and positive definite. This is a crucial requirement for the method. It implies that the auxiliary system can be globally stabilized, provided the negative linear parts parameters $a_1, a_2, ..., a_s$ are sufficiently large. We set $a = \max(a_1, ..., a_s)$. We have the following theorem.

Theorem 3.1. *We suppose that*

$$\epsilon_k(t) > \frac{a}{n} b_k(n,m) \quad for\ k = 1, 2, ..., m \ \ and\ for\ all\ t, \tag{13}$$

where $b_k(n,m) = \sum_{j>i; k \in P_{ij}} z(P_{ij})$ *is the sum of the lengths of all chosen paths* P_{ij} *which pass through a given edge* k *that belongs to the coupling configuration,* m *is the total number of edges in the graph. Then the network* (10) *synchronizes in the sense of definition 3.1.*

Example 3.1. For a complete network, if

$$\epsilon(t) > \frac{a}{t},$$

then the network synchronizes.

3.2 Asymmetrically coupled networks

We consider the following network,

$$U_{it} = F(U_i) + Q\Delta U_i + \sum_{j=1}^{n} c_{ij}(t) P U_j, \quad i = \overline{1,n}, \tag{14}$$

where the G matrix is supposed to be asymmetric. We can represent it by a graph $\mathbf{G}$ with n vertexes and m edges. There is an edge between the vertex i and the vertex j if c_{ij} or c_{ji} differ from zero. We suppose the graph connected. When (c_{ij} or c_{ji}) is different from zero, we define:

$$\frac{c_{ij}(t) + c_{ji}(t)}{2} = \epsilon_{ij}(t) = \epsilon_k(t).$$

The coefficients ϵ_{ij} define a non-oriented graph $\mathbf{E}$ and an associated symmetric matrix E. We denote by $b_k(n,m)$ the sum of all the (minimal) ways P_{ij} passing trough a given edge k of the non-oriented graph $\mathbf{E}$. The following result holds:

Theorem 3.2. *We suppose that*

$$\frac{c_{ij}(t) + c_{ji}(t)}{2} = \epsilon_{ij}(t) = \epsilon_k(t) > \frac{a}{n} b_k(n,m), \tag{15}$$

then the network (14) *synchronizes in the sense of definition 3.1.*

Example 3.2. If we suppose that the graph is a not oriented ring, then if

$$\frac{c}{2} = \epsilon^* > \begin{cases} a\left(\frac{n^2}{24} - \frac{1}{24}\right) & \text{for } n \text{ odd}, \\ a\left(\frac{n^2}{24} + \frac{1}{12}\right) & \text{for } n \text{ even}, \end{cases}$$

the network synchronizes.

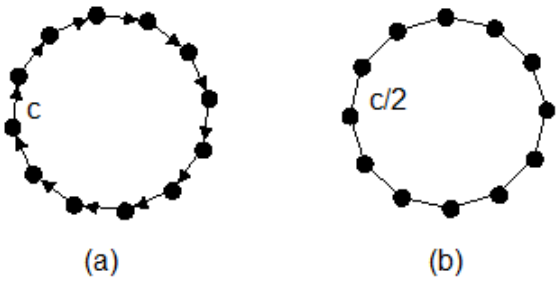

Figure 1: Ring network.

4 Numerical simulations

We proceeded to numerical simulations of system (10) and (14) with the following parameter values: $\epsilon = 0.1, a = 1, b = 0.001, c = 0, d = 0.05$ and $f(u) = -u^3 + 3u$. Our simulations show that both systems synchronize when the coupling strength increase. Furthermore, we approximated the minimal numerical strength coupling needed for synchronization by functions, relatively to the number of edges in the graph. For example, in the case of a complete network, the minimal strength coupling seems to follow an inverse law. This is shown in figure 2. In the case of an oriented ring, the minimal strength coupling seems to follow a square law. This is shown in figure 3.

5 Conclusion

In this work, we studied a neuron network of reaction diffusion systems in a general mathematical framework. We proved the existence of the global attractor of the network, under some conditions on topologies, coupling function and reaction terms. We also showed the synchronization phenomenon in symmetrically and in asymmetrically networks with linear coupling. We have used for this the connection graph stability method, and illustrated the results on some particular networks. Finally, we proceeded to numerical simulations in complete and unidirectionally coupled ring networks of FitzHugh-Nagumo Reaction Diffusion systems with linear coupling. We found theoretically and numerically that the network synchronizes when the coupling strength exceed a critical value. This critical value depends of the number of nodes in the graph and also of the graph topology. Thus, in complete network the critical coupling strength value follows a inverse law of the number of nodes in the graph. In unidirectionally coupled ring network, the critical coupling strength value follows a square law of the number of nodes in the graph. In future work, we aim to apply these results to more realistic neuron networks.

Acknowledgements

We would like to thank: Rgion Haute Normandie and - FEDER (RISC project) for financial support.

References

[1] B. Ambrosio and M.A. Aziz-Alaoui, *Synchronization and control of coupled reaction-diffusion systems of the fitzhugh-Nagumo type*, Computer and Mathematics with application, 64:934-943, september 2012.

[2] B. Ambrosio and J-P Françoise, *Propagation of bursting oscillations*, Phil. Trans. R. Soc. A, 367:4863-4875, 2009.

[3] M. Marion, *Finite-dimensionnal attractors associated with partly dissipative reaction-diffusion systems*, SIAM J. Math. Anal., 20:816-844, 1989.

[4] R. Temam, *Infinite Dynamical Systems in Mechanics and Physics*, Springer, 1988.

[5] V.N. Belykh, N.N. Verichev, L.J. Kocarev, L.O. Chua, in: R. N Madan (Ed.), *Chua's circuit: A Paradigm for Chaos*, World Scientific, Singapore, 1993, 325.

[6] V.N. Belykh, I.V. Belykh, M. Hasler, Phys. Rev. E 62 (2000) 6332.

[7] I.V. Belykh, V.N. Belykh, K.V. Nevedin, M. Hasler, Chaos 13 (2003) 165.

[8] V.N. Belykh, I. Belykh, M. Hasler, *Connection graph stability method for synchronized coupled chaotic systems*, Physica D 195 (2004) 159-187.

[9] I. Belykh, V.N Belykh, M. Hasler, *Sychronization in asymmetrically coupled networks with node balance*, Chaos 16, 015102 (2006).

[10] I. Belykh, E. De Lange, M. Hasler, *Synchronization of bursting neurons: What matters in the network topology*, Phys. Rev. Lett. 188101, 2005.

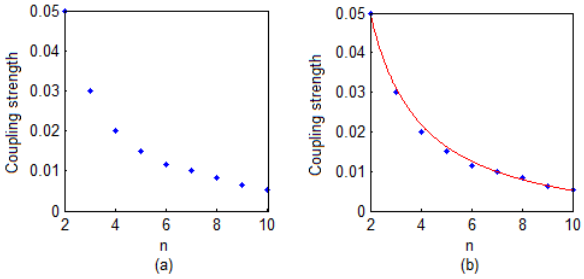

Figure 2: (a) This figure represents the evolution of the critical value of the coupling strength for synchronization as a function of the number of nodes on the network. (b) We have also represented the function $g_n = \dfrac{0.112}{n} - 0.006$, which approximates the numerical data.

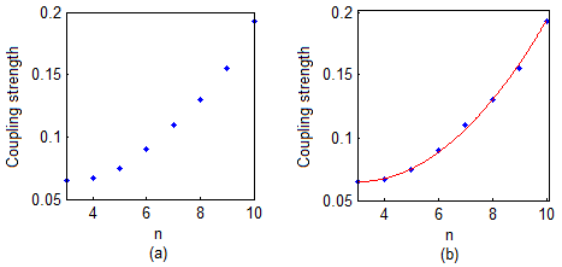

Figure 3: (a) This figure represents the evolution of the critical value of the coupling strength for synchronization as a function of the number of nodes on the network. (b) We have also represented the function $g_n = \dfrac{1}{375}n^2 - \dfrac{49}{3000}n + 0.09$, which approximates the numerical data.

Proceedings of ICCSA 2014
Normandie University, Le Havre, France – June 23-26, 2014

ApiNATOMY: the generation of interactive circuitboard views of complex physiology knowledge

Bernard de Bono[1,2], Pierre Grenon[1], Michiel Helvenstijn[3], Natallia Kokash[3], S. Randall Thomas[4]

Abstract. Physiology experts deal with complex biophysical relationships, across multiple spatial and temporal scales. Automating the discovery of such relationships, in terms of physiological meaning, is a key goal to the physiology community. ApiNATOMY is an effort to provide an interface between the physiology expert's knowledge and all ranges of data relevant to physiology. It does this through an intuitive graphical interface for managing semantic metadata and ontologies relevant to physiology. In this paper, we present a web-based ApiNATOMY environment, allowing physiology experts to navigate through circuitboard visualizations of body components, and their cardiovascular and neural connections, across different scales.

Keywords. Anatomy, Physiology, Knowledge Management, Visualisation, Ontologies.

1 Introduction

An ontology consists of a set of terms and their relations that represent a specific domain of knowledge. Ontologies are created and maintained by knowledge domain experts, and are used as computer-readable taxonomies by software tools intended to support knowledge management activities in that domain.

The complexity of some of the ontologies in current use, as well as the complexity of handling semantic metadata that annotate related resources with ontology terms (*e.g.* as described in (1)), has generated considerable demand for effective visualization in the design, authoring, navigation and management of (i) ontology-based knowledge and (ii) semantic metadata that make use of ontologies.

In response to the above demand, a number of generic ontology visualization tools have been developed to assist knowledge acquisition, browsing and maintenance of ontologies (2). Such tools, however, put a considerable and unrealistic demand on the users' familiarity and expertise in both (i) semantic web technologies and (ii) the design principles of ontologies. It is unlikely that a user with expertise in the domain of an ontology also has expertise in the technologies managing ontologies.

2 Problem statement

The domain of biomedical physiology is a case in point. Physiology experts deal with complex biophysical operations, across multiple spatial and temporal scales, which they represent in terms of the transfer of energy from one form to another and/or from one anatomical location to another. Different kinds of descriptions of these biophysical operations are produced by different disciplines in biomedicine. For instance, (i) a medical doctor may describe the mechanism by which a stone in the ureter causes damage in the kidney; (ii) a pharmacologist may depict the process by which a drug absorbed from gut transits to the hip joints where it reduces inflammation; (iii) a molecular geneticist may trace the anatomical distribution of the expression of particular gene to understand the cause of a skeletal malformation; and, (iv) a bioengineer may build a mathematical model to quantify the effect of hormone production by the small intestine on the production of bile by the liver. These descriptions take diverse forms, ranging from images and free text (*e.g.* for a paper in a journal) to XML documents bearing well-defined data or sets of variables and related equations (*e.g.* as input into a simulation tool).

Automating the discovery of relationships, in terms of physiological meaning, between the above types of description is a key goal to the physiology community. To that end, this community is investing considerable effort in building ontologies for the annotation and semantic management of resources describing physiology. A number of reference ontologies have been created to represent the various entities required to describe physiology, including gene products (3), chemical entities (4) cells (5) and gross anatomy (6). Cumulatively, these reference ontologies consist of hundreds of thousands of terms such that the volume of semantic metadata arising from annotation of resources with these terms is consid-

[1] University College London
[2] Correspondence: b.bono@ucl.ac.uk
[3] University of Leiden
[4] IR4M UMR8081 CNRS Université Paris-Sud,, Orsay

erable. However, conventional technology for the management of ontologies and metadata is not accessible to physiology experts.

3 Main results

The ApiNATOMY effort has emerged to provide intuitive graphical means to manage ontologies and semantic metadata relevant to physiology. In this presentation, we demonstrate a web-based ApiNATOMY environment for physiology experts to navigate through circuitboard visualizations of body components and their connections across scales. In particular, we present a tool prototype that visualizes (i) schematics of ontology-based knowledge about body parts, cardiovascular and neural connections, over which (ii) graphical renderings of semantic metadata linking to gene products and mathematical model of processes are overlaid.

In this presentation, we briefly discuss a core use case for the application ApiNATOMY schematics in support of genomics and drug discovery studies. In so doing, we introduce (i) some of the key ontological and data resources required in this case, as well as (ii) early-stage results of this effort.

The domains of genomics and drug discovery are dependent on physiology knowledge, as both domains take into account the manufacture of gene products in different parts of the body and the regulated long-distance transport of molecules that interact with these products. The location of gene product manufacture (*i.e.* gene expression data, such as (7)), as well as routes associated with pharmacokinetic modeling of molecular interactors (drawn from resources such as (8)) may be usefully depicted in the form of a physiology circuitboard.
In ApiNATOMY, a physiology circuitboard schematic consists of a combination of (i) an anatomical treemap and (ii) an overlay of process graphs. In our earlier prototypes (described in (9)), templates were applied to constrain the layout of tiles in treemaps of the Foundational Model of Anatomy (6) ontology, such that nesting of one tile inside another indicates that the child tile is either a part of a subclass of the parent tile. The Graphical User Interface (GUI) providing the interaction with the circuitboard allows point-and-click navigation of the treemap content. This type of interaction extends to also involve process graphs – in this paper we report on the graphical projection of routes of (i) blood flow processes linking different regions of the human body (using data generated in (10) – illustrated in Figure 1), as well as (ii) transport processes along neurons of the central nervous system (*i.e.* brain and spinal cord) with data obtained via the Neuroscience Information Framework (11).

The ApiNATOMY Graphical User Interface is built from inception as a three dimensional (3D) environment. This feature facilitates interaction not only with 3D renderings of the circuit boards themselves, but also with a wide range of geometry/mesh formats for volumetric models of biological structure across scales. For instance, it is already possible to overlay Wavefront .obj data from BodyParts3D (12) as well as SWC data supported by the neuromorpho.org (13) resource.

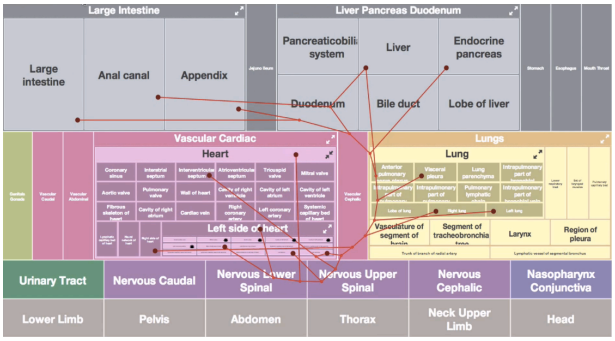

Figure 1: Screenshot depicting the topology of blood vessel connectivity in the ApiNATOMY tool

4 Conclusion

In particular, our presentation will focus on:

- the constraining of treemap layout to generate stable anatomical treemaps,
- the design and overlay of routes of communication for the cardiovascular and neural systems, and
- the querying and 3D depiction of protein architecture schematics for the anatomical overview of gene expression data.

ApiNATOMY is emerging as a potential solution to the management of multiscale knowledge, in support of integrative modeling and simulation interoperability by the Virtual Physiological Human community (14).

Acknowledgment

B.d.B. gratefully acknowledges grants from the Innovative Medicines Initiative (IMI) grants 115156–2 (DDMoRe) and 115568 (AETIONOMY), as well as European Union FP7 grant agreement 600841 (CHIC).

References

1. De Bono B, Hoehndorf R, Wimalaratne S, Gkoutos G, Grenon P. The RICORDO approach to semantic interoperability for biomedical data and models: strategy, standards and solutions. BMC Res Notes. 2011;4:313.

2. Katifori A, Halatsis C, Lepouras G, Vassilakis C, Giannopoulou E. Ontology Visualization Methods&Mdash;a Survey. ACM Comput Surv [Internet].

2007 Nov;39(4). Available from: http://doi.acm.org/10.1145/1287620.1287621

3. Gene Ontology Consortium, Blake JA, Dolan M, Drabkin H, Hill DP, Li N, et al. Gene Ontology annotations and resources. Nucleic Acids Res. 2013 Jan;41(Database issue):D530–535.

4. Hastings J, de Matos P, Dekker A, Ennis M, Harsha B, Kale N, et al. The ChEBI reference database and ontology for biologically relevant chemistry: enhancements for 2013. Nucleic Acids Res. 2013 Jan 1;41(D1):D456–463.

5. Bard J, Rhee SY, Ashburner M. An ontology for cell types. Genome Biol. 2005;6(2):R21.

6. Rosse C, Mejino JLV Jr. A reference ontology for biomedical informatics: the Foundational Model of Anatomy. J Biomed Inform. 2003 Dec;36(6):478–500.

7. ArrayExpress Home | EBI [Internet].. Available from: http://www.ebi.ac.uk/arrayexpress/

8. Harnisch L, Matthews I, Chard J, Karlsson MO. Drug and disease model resources: a consortium to create standards and tools to enhance model-based drug development. CPT Pharmacomet Syst Pharmacol. 2013;2:e34.

9. De Bono B, Grenon P, Sammut SJ. ApiNATOMY: a novel toolkit for visualizing multiscale anatomy schematics with phenotype-related information. Hum Mutat. 2012 May;33(5):837–48.

10. B. de Bono. Achieving Semantic Interoperability between Physiology Models and Clinical Data. In: S.J. Sammut, P. Grenon, editors. 2011. p. 135–42. Available from: http://doi.ieeecomputersociety.org/10.1109/eScienceW.2011.29

11. Gardner D, Akil H, Ascoli GA, Bowden DM, Bug W, Donohue DE, et al. The Neuroscience Information Framework: A Data and Knowledge Environment for Neuroscience. Neuroinformatics. 2008 Sep;6(3):149–60.

12. Mitsuhashi N, Fujieda K, Tamura T, Kawamoto S, Takagi T, Okubo K. BodyParts3D: 3D structure database for anatomical concepts. Nucleic Acids Res. 2009 Jan;37(Database issue):D782–D785.

13. Ascoli GA. Mobilizing the base of neuroscience data: the case of neuronal morphologies. Nat Rev Neurosci. 2006 Apr;7(4):318–24.

14. Hunter P, Chapman T, Coveney PV, de Bono B, Diaz V, Fenner J, et al. A vision and strategy for the virtual physiological human: 2012 update. Interface Focus. 2013 Apr 6;3(2):20130004.

General Session 6
General Dynamical Systems

Proceedings of ICCSA 2014
Normandie University, Le Havre, France – June 23-26, 2014

INSTABILITY IN MAGNETOGRAVITY SHER WAVES

S. Nasraoui

Abstract. We study analytically the instability of the subharmonic resonances in magnetogravity waves excited by a time-periodic shear for an inviscid and nondiffusive unbounded conducting fluid.Due to the fact that the magnetic potential induction is a Lagrangian invariant for magnetohydrodynamic Euler-Boussinesq equations, we show that plane-wave disturbances are governed by a four-dimensional Floquet system. We determine the width and the maximal growth rate of the instability bands associated with subharmonic resonances. This instability persists in the presence of magnetic fields, but its growth rate decreases as the magnetic strength increases.
We also elucidate the similarity between the effect of a magnetic field and the effect of a Coriolis force on the gravity shear waves considering axisymmetric disturbances.

Keywords. Instability, magnetohydrodynamic, resonances

References

[1] R. Lebovitz and E. Zweibell, Astrophys. J **609**, 301 (2004).
[2] A. Salhi, T. Lehner, F. Godeferd, and C. Cambon, Phys. Rev. E **85**, 026301 (2012).
[3] S. A. Balbus and J. F. Hawley, Astrophys. J. **376**, 214 (1991).
[4] A. Salhi and S. Nasraoui, Phys.Rev. E **88**, 063016 (2013).

Department of Physics, Faculty of Sciences of Tunis, University Tunis El MANAR, Tunisia. E-mail: nasraouisaber@yahoo.fr

Proceedings of ICCSA 2014
Normandie University, Le Havre, France - June 23-26, 2014

MULTISCALE METRICS TO ASSESS COMPLEX SYSTEM RESILIENCE

I. Tchiguirinskaia, D. Schertzer, A. Giangola-Murzyn [†]and T. C. Hoang [‡]

Abstract. In this paper, we first argue the need for well defined resilience metrics to better evaluate the resilience of complex systems such as urban flood management systems. We review both the successes and limitations of resilience metrics in the framework of dynamical systems and their generalization in the framework of the viability theory. We then point out that the most important step to achieve is to define resilience across scales instead of doing it at a given scale. We conclude on current developments along this direction.

Keywords. Complex Systems, Urban Floods, Across Scale Approach, Resilience Metrics, Universal Multifractals.

1 Introduction

An important goal of the EU FP7 SMARTesT and INTERREG IVB RainGain projects is to evaluate the effectiveness of urban resilience systems in the framework of scenarios, respectively with and without these systems, simulated with the help of the distributed hydrological model Multi-Hydro [12, 14]. This assessment could not be achieved, like for other systems (e.g. in ecology [6]), without operational definitions of resilience. Unfortunately, whereas the term resilience has become extremely fashionable, a corresponding mathematical definition has remained rather elusive. More precisely, scenario analyses require mathematically defined resilience metrics based on a given conceptual definition. The SMARTesT conceptual definition of the flood resilience system - "The ability to cope with flooding and the ability to recover from flooding" [19]- is rather close to that of "ecological resilience" [16]: "the capacity of a system to absorb disturbance and reorganize while undergoing change so as to still retain essentially the same function, structure, identity, and feedbacks". We briefly review the state-of the-art, which mainly corresponds to resilience metrics based on dynamical system theory and some extensions to the framework of the viability theory [2, 3]. The latter not only enables us to consider more general subsets of constraints, but also feedbacks. However, the question of space-time complexity remains rather untouched and we finally discuss how to answer to it with the help of multifractals.

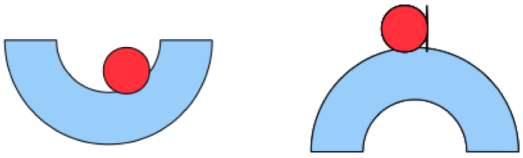

Figure 1: Classical illustration of a ball respectively in a stable and unstable equilibrium (corresponding respectively to a potential well and hill). The vertical barrier symbolises a measure intended to protect against the instability.

2 Dynamical system based resilience metrics

Let us recall that a dynamical system (e.g. [1]) is defined with the help of state variables x, which belong to a given state spaces (generally a real d-dimensional vector space) and a differential system that defines their evolution from a given initial condition x_0. This system is generally supposed to be autonomous (no explicit time dependence), of first order and to depend on a given set of parameters μ:

$$dx(t)/dt = f_\mu(x(t));\ x(t_0) = x_0 \tag{1}$$

In the dynamical system approach, instead of trying to compute the detailed trajectory $x(t)$, one tries to figure out its qualitative features from the very characteristics of the differential system, e.g. the characteristic values of the parameters μ that lead to qualitative change of trajectories, i.e. bifurcations or turning points. In particular, one is interested by the equilibrium states x_e that are invariants for the dynamics:

$$f_\mu(x_e) \quad = 0 \tag{2}$$

*Manuscript received April 17, 2014; revised April 17, 2014.

[†]I. Tchiguirinskaia, D. Schertzer and A. Giangola-Murzyn are with LEESU, University Paris-Est, Ecole des Ponts ParisTech, France. E-mails: Ioulia.Tchiguirinskaia@enpc.fr, Daniel.Schertzer@enpc.fr, giangola@leesu.enpc.fr,

[‡]T. C. Hoang is with Faculty of Energy Engineering, Vietnam Water Resources University, Viet Nam. E-mail: tuanhc@wru.vn

An equilibrium states x_e is stable if it attracts all the states in its vicinity, unstable if some of them are rejected (see figure 1 for the classical illustration of a ball in a potential landscape). More generally, an attractor is a set of states invariant under the dynamics, with a unique attraction basin formed by the neighbouring states that are attracted by it. The dynamics of the system might therefore be qualitatively understood with the help of its attractors, because the state variables $x(t)$ will wander in a given (stable) attraction basin until a strong enough perturbation will drive it to another basin, and so on. This attractor phenomenology is very appealing to define a resilience metric: some attraction basins correspond to a suitable functioning of the system, whereas others should be avoided as much as possible. Because the time spent by the system in the suitable basins should be maximized, the inverse return time to these basins and/or the basin size can be used as resilience metrics. Thanks to the fact that the Multiplicative Ergodic Theorem [20] applies on mild conditions to differential systems, this inverse return time merely corresponds to the Lyapunov exponent, i.e. the largest real part of the spectrum of the tangent transform of the map that defines the differential system (f_μ in eq. 1). This metric was used for ecological problems [8, 24]. The estimate of a attraction basin size is less straightforward, but has been used for low dimensional population dynamics [7, 33].

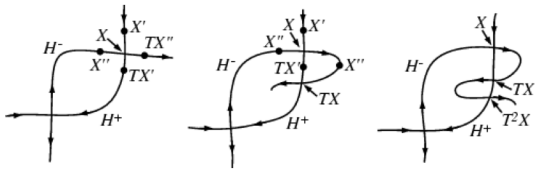

Figure 2: Illustration of the complex topology of an attractor, here of the homoclinic tangle pointed out by [25]: the unstable manifold loops back and becomes part of the stable manifold. This yields a more and more convoluted topology by iteration of the tangent transform T.

3 Limitations of the system dynamical approach

In spite of its mathematical elegance and apparent rigor, there is a series of limitations in the dynamical system approach (e.g. [13, 21]). This includes:

(a) Attraction basins can lead to rather complex behaviours, ranging from limit cycles to chaotic attractors with a quite complex topology. A classical example is the homoclinic tangle, already pointed out by [25] and illustrated in figure 2: the unstable manifold loops back and becomes part of the stable manifold (e.g. [34]).

(b) Although the dynamical system approach seems to be quite general, there are many technical difficulties to go beyond ordinary differential systems: there are indeed fundamental differences between systems complex in time (ordinary differential systems) and those that are complex both in time and space (partial differential systems). The key-point is the emergence with the latter of space scales and the related dependency of state variables, as well as the interplay between space and time scales [22, 24]. This is particularly sensitive for the estimate of inverse return times, because they will depend on the spatial scale of observation and the Multiplicative Ergodic Theorem no longer applies [29, 30].

(c) Although the system dynamics modeling permits to take into account the system feedback as the interactions between different variables, no social feedback is taken into account. This is particularly damageable for the choice of structural resilient measures. Indeed, the lasting problem is to evaluate two different flood management strategies that will at a given time implement distinct (possibly non structural) resilient measures in agreement with public acceptability.

(d) Whereas there might be already some important difficulties with the idea that the desired functioning of a natural hydrological basin will correspond to a dynamical attraction basin, this can be drastically put into question for a highly anthropised hydrological basin.

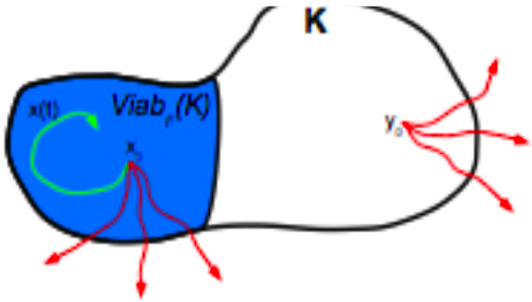

Figure 3: Scheme of the viability constraint space K (the set of suitable system states) and the viability kernel $Viab_{f_\mu}(K)$ (the subset of initial states whose at least one trajectory remains in K). Note that due to control actions there is not a unique trajectory originating from an initial state.

3.1 Viability based resilience metrics

The latest mentioned difficulty (d) is resolved by considering more general subsets of the phase space that would correspond to a suitable functioning of the system. In the

framework of the viability theory, one defines without reference to dynamics a viability constraint set K that corresponds to a suitable functioning of the system, in short: suitable states. In the original perspective of the theory, it corresponded to the set of viable states, but the mathematic concept does not depend on it. However, there is price to be paid for this generalization: the return times are no longer easy to estimate. To take into account a possible management action $u(t)$ (valued on $U(x(t))$, which is generally a vector subspace) at time t in feedback to the state $x(t)$, the latter is included in the map f, which is no longer a simple function of the current state. The differential system (eq. 1) becomes:

$$dx(t)/dt = f_\mu(x(t), u(t)); x(t_0) = x_0; u(t) \in U(x(t)) \quad (3)$$

An important consequence of the action $u(t)$ is that there are no longer a unique trajectory originating from a given initial state x_0 . The viability kernel corresponds to the subset of states that could be managed to obtain an infinite resilience, i.e. they are initial states of trajectories that remain in the viability constraint set K (see figure 3 for illustration):

$$Viab_{f_\mu}(K) = \{x_0 \in K | \exists x(t) : x(0) = x_0, \\ \forall t > 0 : x(t) \in K\} \quad (4)$$

This can be slightly generalized to states having a finite resilience with the help of the concept of the capture basin $Cap_{f_\mu}(C)$ of any given target subset C. The latter is defined as the subset of states that will reach C in a finite time:

$$Cap_{f_\mu}(C) = \{x_0 | \exists x(t) : x(0) = x_0, \\ \exists t, \infty > t > 0 : x(t) \in C\} \quad (5)$$

Therefore, the subset $R_{f_\mu}(K) = Cap_{f_\mu}(Viab_{f_\mu}(K))$ corresponds to the subset of states that will reach K and remain there. As a consequence, $R_{f_\mu}(K)$ can be called the resilient basin [10]. To generalize what was done for attractors, the resilience metric of a given state can be defined [4, 21] by the inverse of the (least) time to reach the viability kernel. Powerful algorithms have been developed to numerically estimate viability kernels for differential systems [9].

4 Ovecoming the space-time complexity: across scale resilience

As argued by [21] the viability theory enables to overcome the limitations (c)-(d) of the system dynamical approach, but not the limitation (b), i.e. the space-time complexity. Indeed, all the environmental case studies that have been investigated with a viability approach have been essentially done with the help of simplified models that were complex only in time and involving only global variables, e.g. species populations, average concentration of phosphate in a lake. There is a huge gap with respect to simulations performed with the help of a distributed model. More generally, as clearly stated by [13]:"multiscale resilience is fundamental for understanding the interplay between persistence and change, adaptability and transformability. Without the scale dimension, resilience and transformation may seem to be in stark contrast or even conflict". An operational definition of multiscale resilience should be therefore achieved to bridge up this gap. In what follows, we show that this is doable as soon as scale symmetries can be considered, because they considerably reduce the space-time complexity by defining scale independent observables from the original fields that are on the contrary sensitively scale dependent. The locally implemented (possibly non structural) resilient measures should not break the overall scale symmetries of the system, but rather to optimise them to make the system flood resilient. If so, the multifractal approach should be integrated in the process of searching for the best flood management strategies.

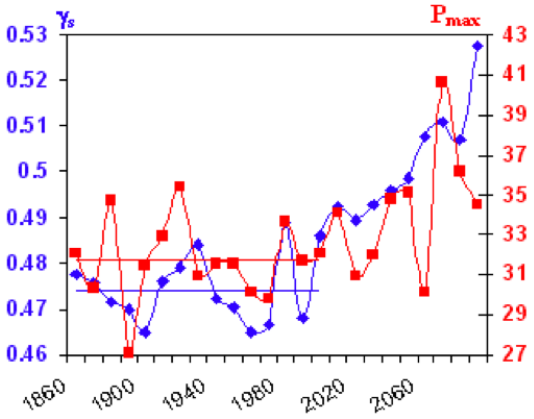

Figure 4: Time evolution of the probable maximum singularity γ_s (blue curves) in the framework of the climate scenario $A2$ obtained with the help of the coupled model CNRM-CM3 over the period 1860-2100, on may note that this singularity γ_s, which is a statical observable, is much more stable that the effective maximumrainfall P_{max} (red curve) and shows a rather clear increase of precipitation extremes, which is hidden in the large fluctuations of P_{max}.

4.1 Multifractal framework

To take into account a hierarchy of structures and their nonlinear interactions over a wide range of space-time scales, the stochastic multifractal approach has been developed [27, 28]. Let us recall that a multifractal field can be loosely understood as defined by an infinite hierarchy of embedded fractal sets [5, 23]. In fact, the physi-

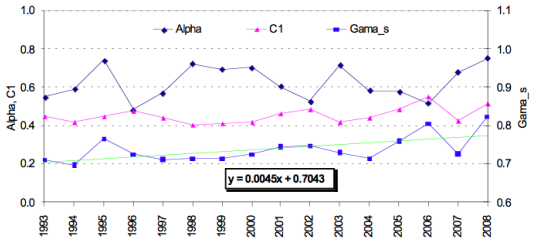

Figure 5: Time evolution of the probable maximum singularity γ_s (light blue squares) estimated from the rainfall in the Paris region over the period 1993-2008. It displays a slightly increasing trend (green straight line), whereas the two other mulitfractal exponents α (dark blue diamonds) and C_1 (pink triangles) have rather contradictory evolutions.

cal basis of multifractality corresponds to dynamical cascade processes that constraint various conserved fluxes to be concentrated in smaller and smaller fractions of space and/or time, thus to be more and more intermittent at smaller and smaller scales. Such cascade processes operate through scale-invariant generators acting from the largest (space-time) scale L down to at least to the observation scale of the system l, in fact down to the inner scale. Equations that describe the whole system remains invariant under the contractions $x \to x/\lambda$ for any resolution $\lambda = L/l$. The probability that a multifractal flux ϵ_λ exceeds a given threshold λ^γ, satisfies the following scaling law:

$$Prob(\epsilon_\lambda \geq \lambda^\gamma \epsilon_1) \propto \lambda^{-c(\gamma)} \quad (6)$$

where $c(\gamma) \neq constant$ is the (statistical) codimension function of the singularities of order γ. This merely means that by taking the log-log plots (in base of the resolution λ) of the probability versus for various resolutions collapse together, whereas this is not the case for the linear-linear plots. In the case of universal multifractals [27], three parameters fully define the codimension function:

$$c(\gamma - H) = C_1(\gamma/(C_1\alpha\prime) + 1/\alpha)^{\alpha\prime};\ 1/\alpha + 1/\alpha\prime = 1 \quad (7)$$

where H measures the degree of non-conservativeness of the mean field ($H = 0$ for a conservative fluxes, such as the energy flux). The parameter α measures how multifractal is the process ($\alpha = 0$ for a fractal field, $\alpha = 2$ for the lognormal case), and it determines the variation of the codimensions around the mean field, while the heterogeneity of the mean field corresponds to the fractal codimension C_1 ($C_1 = 0$ for a homogeneous field). Furthermore, the probable maximum singularity γ_s on a unique sample of dimension D satisfies the equality:

$$c(\gamma_s) = D \quad (8)$$

Equations 7-8 together yield an analytical expression of the probable maximum singularity γ_s and therefore a semi-analytical estimate of γ_s with the help of empirical estimates of the universal exponents H, C_1 and α.

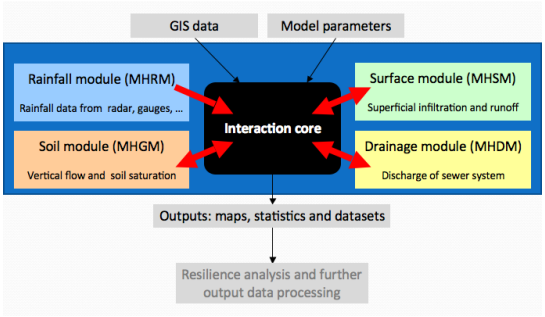

Figure 6: Schematic illustration of linkages between different modules/processes that constitute Multi-Hydro.

4.2 Towards a singularity based resilience metrics

To be scale independent and therefore defined across scales instead of being defined at a given scale, the resilient metric should be defined with the help of these new variables that are the singularities of the involved fields, i.e. the exponent of the (algebraic) divergence of the fields observed at smaller and smaller scales. Concretely, it will correspond to measure qualitative changes of the distribution of these singularities, in fact of their scale independent codimension (eq. 6). This can be equivalently done with the scaling moment function, because both are related by the involutive Legendre transform. This is fundamentally due to the respective analogies of codimensions and scaling moment functions to local entropies and thermodynamic potentials. These scale independent quantifiers have been recently used to analyse hydrological extremes [32], in particular with the help of the probable maximum singularity (eq. 8)[17, 11, 31]. For instance, it has been used to quantify the multiscale evolution of hydrological extremes in climate scenarios [26], see figure 4 for illustration. Time evolution of the maximum probable singularity γ_s, estimated from the raingauge time series of Orly (in Paris region) over the period 1993-2008 [15], displays a similar increasing trend on figure 5, although somewhat weak due to the short length of the series. The two other mulitfractal exponents α and C_1 have rather contradictory evolutions. More recently, the concept of the probable maximum singularity γ_s was applied to the radar data forecasts in the Paris region [18].

5 Scenario evaluation of flood resilience systems

A radical point of view would correspond to define the theoretical analogues of the scale independent viability constraint set, viability kernel and resilient basin for the

singularities. In this paper we rather intend to analyse the flood resilience scenarios simulated with the help of Multi-Hydro along theses ideas and to assess in a scale independent manner the effective multiscale resilience of flood resilience systems. As demonstrated on figure MH, Multi-Hydro is a multi module hydrological model that is not per say any better than other hydrological models, but what makes it *smart* and of interest to users is:

- It is web based, open access, and free of charge.

- It has the potential to demonstrate the local as well as the up and downstream impacts of interventions with flood resilience technologies.

- It can potentially be linked to new modules to provide both a tool able to assess the physical consequences of interventions but also the cost/benefit of interventions - thus potentially a very powerful and unique decision support tool.

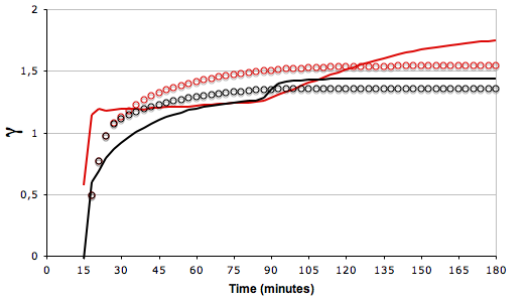

Figure 7: Time evolution of the maximum singularity γ_{Max} (open dotes) in comparison with the probable maximum singularity γ_s (continuous lines) during a (theoretical) constant rainfall. The minimum value of hydraulic conductivity is of the order of: 10^{-6} m/s (red) and 10^{-4} m/s (black). The distributions of simulated water depths were normalised by the mean of the field. This re-normalisation shifts the curves of the effective maximum singularity γ_{Max} towards the ones of the probable maximum singularity γ_s.

Multi-Hydro is complex and thus complicated. Whilst working on 10 m grid mesh seemed to be the most sensible in assessing a $5 - 10$ km^2 urban area. The grid mesh can be reduced to as low as 20 cm, if necessary. This ability to adjust to high resolution will be helpful when considering interventions at building scales. Multi-Hydro already takes into account several types of measures in order to assess the resilience of urban system. Of course 'measures' means flood resilience (FRe) technologies. For example, the model shows the effect of installing barriers in some sensitive areas, under the assumption that these barriers work and that water does not pass through them. When particular FRe technologies have differing impacts on how flood waters react on

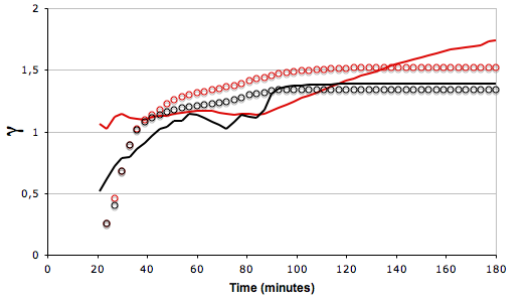

Figure 8: Time evolution of the effective maximum singularity γ_{Max} (open dotes) in comparison with the probable maximum singularity γ_s (continuous lines) during a variable rainfall. The minimum value of hydraulic conductivity is of the order of: 10^{-6} m/s (red) and 10^{-4} m/s (black). The distributions of simulated water depths were normalised by the mean of the field. This re-normalisation shifts the curves of the effective maximum singularity γ_{Max} towards the ones of the probable maximum singularity γ_s.

the nearby streets and the other areas, the FRe technology differences need to be reflected by Multi-Hydro. At this stage, their implementation requires advanced GIS skills to make it work, - it is a tool for experts. However, Multi-Hydro is still under development and must be considered as 'work in progress' ($http://leesu.univ-paris-est.fr/multifractals/MultiHydro/En/garde_en.php$) . As indicated earlier, Multi-Hydro can be linked to new modules to assess economic facets of the resilience of urban system exposed to natural hazards. The public opinion can be used to condition the choice of the flood management strategies. This choice should be reflected in MultiHydro measures, socially predefining what information MultiHydro need to give you in making a decision on which particular type of FRe technology to use.

To assess the physical consequences of (potential) interventions according to several flood resilience scenarios, the users indeed need a multiscale resilience metrics to weigh up flood resilience systems. In this paper we focalise the analysis on a time evolution of the critical singularities γ_s that is estimated by inverting the eq. 8 as a function of D with the help of the eq. 7, using the empirical estimates of the universal multifractal parameters from the $2D$ water depth distributions, simulated by Multi-Hydro. Let us remind that under the assumption that the distributions of simulated water depths will be consistent with the universal multifractal scaling, the critical singularity γ_s is expected to be proportional to the maximal singularity γ_{Max}. This singularity is defined from the water depth maximum, h_{Max}, as follows:

$$\gamma_{Max} = \log_\lambda(h_{Max}) \tag{9}$$

The time evolution of the effective maximum singularity γ_{Max} is exhibited on figures 7 and 8 in comparison

with the probable maximum singularity γ_s (continuous lines). The distributions of simulated water depths were first normalised by the mean of the field to estimate the maximum water depth h_{Max} (see eq. 9).To test the above ideas, we first use a very low value of the minimum hydraulic conductivity (10^{-6} m/s) to reduce the infiltration process. We observe that during the rainfall episode (from about 20 to 90 minutes), the probable maximum singularity γ_s largely underestimates the effective maximum singularity γ_{Max}. Furthermore, γ_s tends to be a constant during this period. By the end of the rainfall episode and up to the end of the Multi-Hydro simulation, the probable maximum singularity strongly increases and, 30 min later, it overestimates the effective maximum singularity. In overall (see figures 7 and 8, red curves), the probable maximum singularity is not at all representative of the effective maximum singularity for the case of low hydraulic conductivity, independently from the type of rainfall. The observed behaviour of the effective maximum singularity is directly related to the non-scaling of water depth distributions and hence the non-stationarity of multifractal parameter estimates [14]. When increasing the minimum value of hydraulic conductivity up to 10^{-4} m/s, the process of infiltration takes place and the Multi-Hydro simulations of water depth distributions becomes much more compatible with the universal multifractal fields. Then the time evolution of probable maximum singularity γ_s, which is entirely statistical indicator, remains in a fairly good agreement with the time evolution of the maximum singularity γ_{Max} being the direct result of a fully distributed physically-based modelling (see figures 7 and 8, black curves). With the help of virtual scenarios of flood resilience measures, the Multi-Hydro users could evaluate the most efficient resilience systems. For example, the topography data can be modified to assumptions re height (of interventions), land use, etc. This means that a Multi-Hydro scenario can reflect changes in elevation created by interventions and asses how these interventions will impact the water flow heights. Figure 9 illustrates an example when due to a re height of the road network, the probable maximum singularity γ_s becomes more stable up to the end of the Multi-Hydro simulation, and this is independently on the rainfall type. The underlined coherence in time evolution of statistical indicators and physical quantities, not only opens new perspectives for an overall evaluation of hydrological model functioning, but could be also used for a more appropriate choice of parameters, e.g., for different land use hydraulic conductivities with respect to the Multi-Hydro resolution.

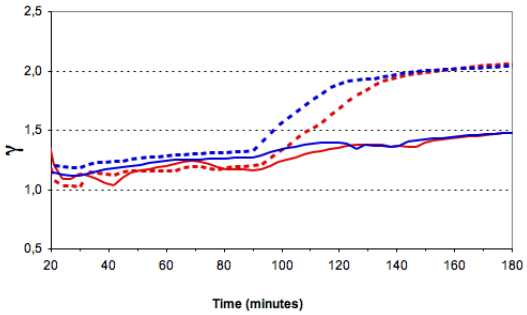

Figure 9: Time evolution of the probable maximum singularity γ_s for the case of either initial land use data (blue) or modified topography (red) during variable rainfall (continuous lines) and constant one (dotted lines).

6 Summary and concluding remarks

Our preliminary, critical analysis of the series of attempts to define an operational resilience metrics led us to consider a scale invariant metrics based on the scale independent codimension of extreme singularities. Multifractal downscaling of climate scenarios can be considered as a first illustration. We focussed on a flood scenario evaluation method with the help of two singularities γ_s and γ_{Max}, corresponding respectively to an effective and a probable maximum singularity, that yield an innovative framework to address the issues of flood resilience systems in a scale independent manner. Indeed, the stationarity of the universal multifractal parameters would result into a rather stable value of probable maximum singularity γ_s. By fixing the limit of acceptability for a maximum flood water depth at a given scale, with a corresponding singularity, we effectively fix the threshold of the probable maximum singularity γ_s as a criterion of the flood resilience we accept. Then various scenarios of flood resilient measures could be simulated with the help of Multi-Hydro. The scenarios that result in estimates of either γ_{Max} or γ_s below the pre-selected γ_s value will assure the effective flood resilience of the whole modeled system across scales.

Acknowledgements

The research for this work was supported, in part, by the EU FP7 SMARTesT and INTERREG IVB RainGain projects. The authors particularly thank Prof. Nigel Lawson and Dr. Stephen Garvin for many constructive discussions during the SMARTesT project. The authors acknowledge very useful comments from anonymous referees.

References

[1] D K Arrowsmith and C M Place. *An introduction to dynamical systems*. Cambridge University Press, 1990.

[2] J P Aubin. *Viability Theory*. Birkhauser, Basel, 1991.

[3] J P Aubin, A Bayen, and P Saint-Pierre. *Viability Theory. New Directions*. Springer, Berlin, 2011.

[4] D Bene, L Doyen, and D Gabay. A viability analysis for a bio-economic model. *Ecol Econ.*, 36(3):385–396, 2001.

[5] R Benzi, G Paladin, G Parisi, and A Vulpiani. On the multifractal nature of fully developped turbulence. *Journal of Physics A*, 17:3521–3531, 1984.

[6] S Carpenter, B Walker, J M Anderies, and N Abel. From Metaphor to Measurement: Resilience of What to What? *Ecosystems*, 4:765–781, 2001.

[7] J B Collings and D J Wollkind. A global analysis of a temperature-dependent model system for a mite predator-prey interaction. *Ecology*, 61(4764–771), 1990.

[8] D L DeAngelis. EEnergy flow, nutrient cycling, and ecosystem resilience. *Ecology*, 61(4):764–771, 1980.

[9] G Deffuant, L Chapel, and S Martin. Approximating viability kernels with Support VectorMachines. *IEEE Trans Automat Contr.*, 52(5):933–937, 2007.

[10] G Deffuant and N Gilbert. Viability and Resilience of Complex Systems, 2011.

[11] M Douglas and P Barros. Probable Maximum Precipitation Estimation Using Multifractals: Application in the Eastern United States. *Journal of Hydrometeorology*, 4:1012–1024, 2003.

[12] E El-Tabach, I Tchiguirinskaia, O Mahmood, and D Schertzer. Multi-Hydro: a spatially distributed numerical model to assess and manage runoff processes in peri-urban watersheds. In E Pasche and C Zevenbergen, editors, *Road Map Towards a Flood Resilient Urban Environment*. Hamburger Wasserbau-Schriftien, Hamburg, 2009.

[13] C Folke, S R Carpenter, B Walker, M Sheffer, T Chapin, and J Rockstroem. Resilience thinking: integrating resilience, adaptability and transformability. *Ecology and Society*, 14(4):20, 2010.

[14] A Giangola-Murzyn, A Gires, C T Hoang, I Tchiguirinskaia, and D Schertzer. Multi-Hydro modelling to assess flood resilience across scales, case study in the Paris Region. In C Maksimovic, editor, *9th International Conference Urban Drainage Modelling*, 2011.

[15] C T Hoang, I Tchiguirinskaia, D Schertzer, P Arnaud, P Laveau, and S Lovejoy. Assessing the high frequency quality of long rainfall series. *Journal of Hydrology*, 2012.

[16] C S Hollings. Resilience and stability of ecological systems. *Annu Rev Ecol Syst.*, 4:1–24, 1973.

[17] P Hubert, Y Tessier, Ph. Ladoy, S Lovejoy, D Schertzer, J P Carbonnel, S Violette, I Desurosne, and F Schmitt. Multifractals and extreme rainfall events. *Geophys. Res. Lett.*, 20(10):931–934, 1993.

[18] A Ichiba, A Gires, I Tchiguirinskaia, D Schertzer, and P Bompard. Mulifractal comparison of two operaional radar rainfall products. In *Proceeding of WRaH 2014*, page 10, Reston, VA, 2014. ASCE.

[19] N Lawson and Al. SMArTesT Glossary, 2011.

[20] M A Lyapunov. Problème général de la stabilité du mouvement. *Annales Fac. Siences Toulouse*, 9, 1907.

[21] S Martin, G Deffuant, and J M Calabrese. Defining Resilience Mathematically: From Attractors To Viability. In *Understanding Complex Systems*. Springer-Verlag, Berlin Heidelberg, 2011.

[22] R M May. *Stability and complexity in model ecosystems*. Princetion University Press, Princetion, NJ, 1973.

[23] G Parisi and U Frisch. On the singularity structure of fully developed turbulence. In M Ghil, R Benzi, and G Parisi, editors, *Turbulence and predictability in geophysical fluid dynamics and climate dynamics*, pages 84–88. North Holland, Amsterdam, 1985.

[24] S L Pimm. The complexity and stability of ecosystems. *Nature*, 307:321–326, 1984.

[25] H Poincare. *Les Méthodes Nouvelles de la Méchanique Céleste,*, volume 1. Gautier-Villars, Paris, 1892.

[26] J F Royer, A Biaou, F Chauvin, D Schertzer, and S Lovejoy. Multifractal analysis of the evolution of simulated precipitation over France in a climate scenario. *C.R. Geoscience*, 340(431-440), 2008.

[27] D Schertzer and S Lovejoy. Physical modeling and Analysis of Rain and Clouds by Anisotropic Scaling Multiplicative Processes. *Journal of Geophysical Research*, D 8(8):9693–9714, 1987.

[28] D Schertzer and S Lovejoy. Non-Linear Variability in Geophysics, Scaling and Fractals, 1991.

[29] D Schertzer and S Lovejoy. Space-time Complexity and Multifractal Predictability. *Physica A*, 338(1-2):173–186, 2004.

[30] D Schertzer and S Lovejoy. Multifractals, generalized scale invariance and complexity in geophysics. *International Journal of Bifurcation and Chaos*, 21(12):3417–3456, 2011.

[31] I Tchiguirinskaia, D Schertzer, C T Hoang, and S Lovejoy. Multifractal study of three storms with different dynamics over the Paris region . In R Moore, editor, *Weather Radar and Hydrology*, pages 421–426. IHAS Press, Wallinford, 2012.

[32] I Tchiguirinskaia, K N Thein, and P Hubert, editors. *Frontiers in Flood Research*, volume 305. IAHS Press, Wallinford, 2006.

[33] L van Coller. Automated techniques for the qualitative analysis of ecological models :Continuous models. *Conserv. Ecol.*, 1(1):5, 1997.

[34] S Wiggins. *Introduction to Applied Nonlinear Dynamical Systems and Chaos*. Springer, 2nd edition, 2000.

Proceedings of ICCSA 2014
Normandie University, Le Havre, France - June 23-26, 2014

ABSOLUTE STABILITY OF A CLASS OF STOCHASTIC SWITCHED SYSTEMS

Yuyun Zhao, Yi Zhang, Mengyi Shi and Chujun Liu *

Abstract. This paper concerns with the absolute stability of stochastic switched system. It is the Itô type stochastic Lurie's system with Markovian switching more precisely to speak. A new definition of stochastic absolute stability will be presented. And we will obtain the algebraic criteria under different hypotheses. An example is given to illustrate our main result.

Keywords. Absolute stability; Stochastic; switched systems; Stochastic differential equation; Markovian switching.

1 Introduction

Absolute stability of Lurie's system was a very important problem in automatic control. It was first proposed by Lurie and Postnikov [6]. The well known frequency-domain criteria was given by Popov [11]. Itô type stochastic Lurie's system was researched around 1970s and 1980s by many mathematicians. We here mention Mahalanabis and Purkayastha [7] who gave the frequency-domain criteria for absolute stability in the sense of asymptotically stable with probility 1, Brusin and Ugrinovskii [2] who discussed the globally asymptotically stable in the mean square, and Korenevskii [3] who obtained the algebraic criteria in the approach of non-quadratic form Lyapunov function. In real life, the system usually consists of finite subsystems, which is called the switched system. At some time points or time intervals, there is only a subsystem working, and it will arrive another along with the switching law. For example, financial system in bear and bull markets is a switched system, while transportation system in sunny and rainy days.

In recent years, stochastic switched systems are well studied by more and more authors because of its wide use in many areas like engineering, traffic and finance. Especially the stochastic differential equation with Markovian switching and stabilities receive a lot of attention, [1], [8], [9], [10], etc. However, there are few papers to discuss the absolute stability of stochastic switched system, even the definition was given by nobody. The gap will be filled by this paper.

In this article, we will study absolute stability of stochastic switched (Markovian switching) system, give its definition and algebraic criteria. An example is given to illustrate our main result.

The remainder of this paper is organized as follows. Section 2 introduces some notations, definitions and lemmas. In section 3, we will give the definition of stochastic absolute stability and its algebraic criteria under different assumptions. An examples is given in section 4.

2 Problem statement and preliminaries

Consider the stochastic switched system

$$\begin{cases} \mathrm{d}x = \big[A\big(r(t)\big)x + bu\big]\,\mathrm{d}t + D\big(x, r(t)\big)\,\mathrm{d}B, \\ y = c^T x, \\ u = -\varphi(y), \\ r : \mathbb{R}_+ \times \Omega \to \mathbb{S} = \{1, 2, \cdots, N\}, \end{cases} \tag{1}$$

where $x \in \mathbb{R}^n$ is the state, $A(i) \in \mathbb{R}^{n\times n}$ is the plant matrix, $D(x,i) \in \mathbb{R}^{n\times m}$ is the noise matrix, $B(t)$ is an m-dimensional Brownian motion, $y \in \mathbb{R}$ is the output, $b, c \in \mathbb{R}^n$, $\varphi \in F_{(0,k)}$ is a controller, where

$$F_{(0,k)} := \big\{\varphi : \varphi(0) = 0,\ 0 < y\varphi(y) < ky^2,\ \forall y \neq 0,$$
$$\text{and } \varphi \text{ satisfies the Lipschitz condition}\big\},$$

$r(t)$ is a Markov process taking values in $\mathbb{S} = \{1, 2, \cdots, N\}$ with generator $\Gamma = (\gamma_{ij})_{N\times N}$ given by

$$P\{r(t+\Delta) = j | r(t) = i\} = \begin{cases} \gamma_{ij}\Delta + o(\Delta), & j \neq i, \\ 1 + \gamma_{ii}\Delta + o(\Delta), & j = i, \end{cases}$$

where $\Delta > 0$, $\gamma_{ij} \geq 0$ is the transition rate from state i to j when $j \neq i$, and

$$\gamma_{ii} = -\sum_{j\neq i} \gamma_{ij} \leq 0.$$

In this paper, we always assume that $r(t)$ is independent of $B(t)$.

If we choose a fixed φ, then we can obtain the Itô type stochastic differential equation with Markovian switching

$$\mathrm{d}x(t) = \big[A\big(r(t)\big)x(t) - b\varphi\big(c^T x(t)\big)\big]\,\mathrm{d}t + D\big(x(t), r(t)\big)\,\mathrm{d}B(t), \tag{2}$$

*Yuyun Zhao, Yi Zhang, Mengyi Shi and Chujun Liu are with Department of Mathematics, Science of College, China University of Petroleum, Beijing. E-mails: z_y11@126.com

or

$$\mathrm{d}x(t) = f\big(x(t),t,r(t)\big)\,\mathrm{d}t + g\big(x(t),t,r(t)\big)\,\mathrm{d}B(t), \quad (3)$$

where $f:\mathbb{R}^n\times\mathbb{R}_+\times\mathbb{S}\to\mathbb{R}^n$ and $g:\mathbb{R}^n\times\mathbb{R}_+\times\mathbb{S}\to\mathbb{R}^{n\times m}$ are defined by

$$\begin{cases} f(x,t,i) = A(i)x - b\varphi(c^Tx), \\ g(x,t,i) = D(x,i). \end{cases} \quad (4)$$

We shall impose some hypotheses:

(**H1**) $D(x,i)$ satisfies the Lipschitz condition: $\exists K>0$ such that

$$|D(x,i)-D(y,i)| \le K|x-y|, \quad \forall x,y\in\mathbb{R}^n, \forall i\in\mathbb{S}. \quad (5)$$

(**H2**) There exists a constant $\lambda>0$, such that $\forall i\in\mathbb{S}$, for any symmetric positive-definite matrix $P\in\mathbb{R}^{n\times n}$,

$$\mathrm{trace}\big(D^T(x,i)PD(x,i)\big) \le \lambda x^TPx, \quad \forall x\in\mathbb{R}^n. \quad (6)$$

(**H3**) $\forall i\in\mathbb{S}$, $D(0,i)=0$.

Throughout this paper, we will use the trace norm for matrix $A=(a_{ij})_{m\times n}$ given by

$$|A| := \sqrt{\mathrm{trace}(A^TA)} = \Big(\sum_{i=1}^m\sum_{j=1}^n a_{ij}^2\Big)^{\frac{1}{2}}. \quad (7)$$

From (6) we have

$$|D(x,i)| = \sqrt{\mathrm{trace}\big(D^T(x,i)D(x,i)\big)} \le \sqrt{\lambda}|x|, \quad \forall x\in\mathbb{R}^n, \quad (8)$$

so hypothesis (H2) contains (H3). Substitute $y=0$ into (5), then by (H3) we have

$$|D(x,i)| \le K|x| \le K\big(1+|x|\big), \quad \forall x\in\mathbb{R}^n, \forall i\in\mathbb{S},$$

which is the linear growth condition. So there exists a unique solution to equation (2) or (3), and $x(t)=0$ is the trivial solution under hypotheses (H1) and (H2) or under hypotheses (H1) and (H3).

In this paper, we always let $\mathbb{R}_+$ denote the interval $[0,+\infty)$, and I denote the identity matrix. We now present some definitions and useful lemmas.

Definition 2.1. The set of $\mathcal{K}$-class functions is defined by

$$\mathcal{K} := \big\{\mu\in C(\mathbb{R}_+;\mathbb{R}_+) : \mu \text{ is monotonically strictly increasing, and } \mu(0)=0\big\}.$$

Definition 2.2. The set of $\mathcal{K}_\infty$-class functions is defined by

$$\mathcal{K}_\infty := \big\{\mu\in\mathcal{K} : \mu(s)\to\infty \text{ when } s\to\infty\big\}.$$

Lemma 2.1. *Let $P\in\mathbb{R}^{n\times n}$ be a symmetric positive-definite matrix, $D(x)$ is a $\mathbb{R}^{n\times m}$-valued function matrix satisfying (H1) and (H3), then we have*

$$\mathrm{trace}\big(D^T(x)PD(x)\big) \le \mathrm{trace}(P)K^2|x|^2. \quad (9)$$

Lemma 2.2. *Let $H\in\mathbb{R}^{n\times n}$ be a $n\times n$ real matrix, $P\in\mathbb{R}^{n\times n}$ be a symmetric positive-definite matrix. If*

$$-PH - H^TP > 0, \quad (10)$$

then $\mathrm{Re}\lambda(H)<0$, which means that all eigenvalues of H have negative real parts.

Lemma 2.3. *$A_i\in\mathbb{R}^{n\times n}$, $b,c\in\mathbb{R}^n$, $\Gamma=(\gamma_{ij})_{N\times N}$, and $k>0$ are given in the system (1). $\lambda>0$ is given by hypothesis (H2). If there exist $\alpha_i>0$ and symmetric positive-definite matrices $P_i\in\mathbb{R}^{n\times n}$, $i\in\mathbb{S}$, such that*

$$R_i - \frac{k}{\alpha_i}d_id_i^T > 0, \quad \forall i\in\mathbb{S}, \quad (11)$$

where

$$\begin{cases} -R_i = P_iA_i + A_i^TP_i + \lambda P_i + \sum_{j=1}^N \gamma_{ij}P_j, \\ d_i = P_ib - \frac{1}{2}\alpha_ic, \end{cases} \quad (12)$$

then $\forall i\in\mathbb{S}$, we have

$$\mathrm{Re}\lambda\Big(A_i+\frac{\lambda+\gamma_{ii}}{2}I\Big)<0, \mathrm{Re}\lambda\Big(A_i-\frac{k}{2}bc^T+\frac{\lambda+\gamma_{ii}}{2}I\Big)<0, \quad (13)$$

which means that all eigenvalues of the matrix

$$G_i := A_i + \frac{\lambda+\gamma_{ii}}{2}I \quad \text{and} \quad H_i := A_i - \frac{k}{2}bc^T + \frac{\lambda+\gamma_{ii}}{2}I \quad (14)$$

have negative real parts.

Lemma 2.4. *$A_i\in\mathbb{R}^{n\times n}$, $b,c\in\mathbb{R}^n$, $\Gamma=(\gamma_{ij})_{N\times N}$, and $k>0$ are given in the system (1). $K>0$ is given by hypothesis (H1). If there exist $\alpha_i>0$ and symmetric positive-definite matrices $P_i\in\mathbb{R}^{n\times n}$, $i\in\mathbb{S}$, such that*

$$R_i - \frac{k}{\alpha_i}d_id_i^T > 0, \quad \forall i\in\mathbb{S}, \quad (15)$$

where

$$\begin{cases} -R_i = P_iA_i + A_i^TP_i + \mathrm{trace}(P_i)K^2I + \sum_{j=1}^N \gamma_{ij}P_j, \\ d_i = P_ib - \frac{1}{2}\alpha_ic, \end{cases} \quad (16)$$

then $\forall i\in\mathbb{S}$, we have

$$\mathrm{Re}\lambda\Big(A_i+\frac{\gamma_{ii}}{2}I\Big)<0 \quad \text{and} \quad \mathrm{Re}\lambda\Big(A_i-\frac{k}{2}bc^T+\frac{\gamma_{ii}}{2}I\Big)<0, \quad (17)$$

which means that all eigenvalues of the matrix

$$G_i := A_i + \frac{\gamma_{ii}}{2}I \quad \text{and} \quad H_i := A_i - \frac{k}{2}bc^T + \frac{\gamma_{ii}}{2}I \quad (18)$$

have negative real parts.

Lemma 2.5. *Let H be a $n \times n$ matrix whose eigenvalues all have negative real parts, i.e.* $\mathrm{Re}\lambda(H) < 0$. *Then for all $Q \in \mathbb{R}^{n\times n}$, equation*

$$PH + H^T P = -Q$$

has a unique solution

$$P = \int_0^\infty \mathrm{e}^{H^T t} Q \mathrm{e}^{Ht}\,\mathrm{d}t.$$

Moreover, if Q is symmetric positive-definite, then so is P.

This lemma can be found in any books on automatic control, like [12].

At last, we introduce an operator $LV : \mathbb{R}^n \times \mathbb{R}_+ \times \mathbb{S} \to \mathbb{R}$ corresponding to $V \in C^{2,1}\big(\mathbb{R}^n \times \mathbb{R}_+ \times \mathbb{S}; \mathbb{R}\big)$ and SDE (3) given by

$$\begin{aligned} LV(x,t,i) &= V_t(x,t,i) + V_x(x,t,i)f(x,t,i) \\ &+ \frac{1}{2}\mathrm{trace}\big[g^T(x,t,i)V_{xx}(x,t,i)g(x,t,i)\big] \\ &+ \sum_{j=1}^N \gamma_{ij} V(x,t,j). \end{aligned}$$

3 Main results

Definition 3.1. System (1) is said to be stochastically absolutely stable with respect to (w.r.t.) $F_{(0,k)}$ if $\forall \varphi \in F_{(0,k)}$, the trivial solution of equation (2) or (3) is stochastically asymptotically stable in the large, which means that
(i) $\forall \varepsilon \in (0,1)$ and $\forall r > 0$, $\exists \delta = \delta(\varepsilon, r, t_0)$ such that

$$P\{|x(t;t_0,x_0,i)| < r, \forall t \geq t_0\} \geq 1 - \varepsilon$$

whenever $(x_0, i) \in S_\delta \times \mathbb{S}$;
(ii) $\forall (t_0, x_0, i) \in \mathbb{R}_+ \times \mathbb{R}^n \times \mathbb{S}$,

$$P\big\{\lim_{t\to\infty} x(t;t_0,x_0,i) = 0\big\} = 1.$$

Theorem 3.1. *Assume that the system* (1) *satisfies hypotheses (H1), (H2) and* (13). *If there exist $\alpha_i > 0$ and symmetric positive-definite matrices $P_i \in \mathbb{R}^{n\times n}$, $i \in \mathbb{S}$, such that*

$$R_i - \frac{k}{\alpha_i} d_i d_i^T > 0, \quad \forall i \in \mathbb{S},$$

where

$$\begin{cases} -R_i = P_i A_i + A_i^T P_i + \lambda P_i + \sum_{j=1}^N \gamma_{ij} P_j, \\ d_i = P_i b - \frac{1}{2}\alpha_i c, \end{cases} \tag{19}$$

then system (1) *is stochastically absolutely stable w.r.t. $F_{(0,k)}$.*

Proof. Let $V(x,t,i) = x^T P_i x, i = 1, 2, \cdots, N$, then

$$V_t(x,t,i) = 0, \quad V_x(x,t,i) = 2x^T P_i, \quad V_{xx}(x,t,i) = 2P_i.$$

It's easy to know that

$$\lambda_{\min}(P_i)|x|^2 \leq V(x,t,i) \leq \lambda_{\max}(P_i)|x|^2.$$

Let

$$\lambda_1 = \min_{i\in\mathbb{S}} \lambda_{\min}(P_i), \quad \lambda_2 = \max_{i\in\mathbb{S}} \lambda_{\max}(P_i).$$

Define $\mu_1, \mu_2 : \mathbb{R}_+ \to \mathbb{R}_+$ by $\mu_1(s) := \lambda_1 s^2$ and $\mu_2(s) := \lambda_2 s^2$, then we have $\mu_1, \mu_2 \in \mathcal{K}_\infty$ and

$$\mu_1(|x|) \leq V(x,t,i) \leq \mu_2(|x|), \forall (x,t,i) \in \mathbb{R}^n \times \mathbb{R}_+ \times \mathbb{S}.$$

According to the criteria of stochastically asymptotically stable in the large for the SDE with Markovian switching ([10, Theorem 5.37]), we just need to show that there exists $\mu_3 \in \mathcal{K}$ such that

$$LV(x,t,i) \leq -\mu_3(|x|), \forall (x,t,i) \in \mathbb{R}^n \times \mathbb{R}_+ \times \mathbb{S}, \forall \varphi \in F_{(0,k)}.$$

From the definition of $F_{(0,k)}$ we know that

$$\alpha_i \varphi(y)\Big(y - \frac{1}{k}\varphi(y)\Big) \geq 0, \quad \forall \alpha_i \geq 0.$$

Then by (H2), $\forall x \neq 0$, $\forall t \geq t_0$, $\forall i \in \mathbb{S}$, $\forall \varphi \in F_{(0,k)}$,

$$\begin{aligned} &LV(x,t,i) \\ &= 2x^T P_i\big[A(i)x - b\varphi(y)\big] + \mathrm{trace}\big[D^T(x,i)P_i D(x,i)\big] \\ &+ \sum_{j=1}^N \gamma_{ij} x^T P_j x \\ &\leq x^T P_i A_i x + x^T A_i^T P_i x - 2b^T P_i x \varphi(y) + \lambda x^T P_i x \\ &+ \sum_{j=1}^N \gamma_{ij} x^T P_j x + \alpha_i \varphi(y)\Big(c^T x - \frac{1}{k}\varphi(y)\Big) \\ &- \alpha_i \varphi(y)\Big(y - \frac{1}{k}\varphi(y)\Big) \\ &\leq x^T \Big(P_i A_i + A_i^T P_i + \lambda P_i + \sum_{j=1}^N \gamma_{ij} P_j\Big) x \\ &- 2\Big(P_i b - \frac{1}{2}\alpha_i c\Big)^T x\varphi(y) - \frac{\alpha_i}{k}\varphi^2(y) \\ &= -\big(x^T, \varphi(y)\big) \begin{bmatrix} R_i & d_i \\ d_i^T & \alpha_i/k \end{bmatrix} \begin{bmatrix} x \\ \varphi(y) \end{bmatrix}. \end{aligned}$$

It's easy to know that if

$$M_i := \begin{bmatrix} R_i & d_i \\ d_i^T & \alpha_i/k \end{bmatrix} > 0,$$

then

$$W_i(x) := -\big(x^T, \varphi(c^T x)\big) M_i \begin{bmatrix} x \\ \varphi(c^T x) \end{bmatrix}$$

is negative-definite, then there exists a function $\mu_3 \in \mathcal{K}$ such that $LV(x,t,i) \le W_i(x) \le -\mu_3(|x|)$ ([5, Theorem 1.3.3]). We know that

$$\begin{bmatrix} I & -kd_i/\alpha_i \\ 0 & 1 \end{bmatrix} \begin{bmatrix} R_i & d_i \\ d_i^T & \alpha_i/k \end{bmatrix} \begin{bmatrix} I & 0 \\ -kd_i^T/\alpha_i & 1 \end{bmatrix} = \begin{bmatrix} R_i - kd_id_i^T/\alpha_i & 0 \\ 0 & \alpha_i/k \end{bmatrix},$$

so $M_i > 0$ if and only if

$$R_i - \frac{k}{\alpha_i} d_i d_i^T > 0 \text{ and } \frac{\alpha_i}{k} > 0.$$

□

Consider the matrix equations

$$-P_iG_i - G_i^TP_i = Q_i \quad \text{and} \quad -P_iH_i - H_i^TP_i = \tilde{Q}_i, \quad i \in \mathbb{S},$$

where G_i and H_i are given by (14), by Lemma 2.5, we can obtain the following corollary.

Corollary 3.1. *Assume that the system* (1) *satisfies hypotheses (H1), (H2) and* (13). *If there exist* $\alpha_i > 0$ *and symmetric positive-definite matrices* $Q_i \in \mathbb{R}^{n\times n}$ *(or* $\tilde{Q}_i \in \mathbb{R}^{n\times n}$*),* $i \in \mathbb{S}$*, such that*

$$E_i := Q_i - \sum_{j\neq i} \gamma_{ij} \left[\int_0^\infty \mathrm{e}^{G_j^T t} Q_j \mathrm{e}^{G_j t}\, \mathrm{d}t \right] - \frac{k}{\alpha_i} \left(\left[\int_0^\infty \mathrm{e}^{G_i^T t} Q_i \mathrm{e}^{G_i t}\, \mathrm{d}t \right] b - \frac{1}{2}\alpha_i c \right) \times \left(\left[\int_0^\infty \mathrm{e}^{G_i^T t} Q_i \mathrm{e}^{G_i t}\, \mathrm{d}t \right] b - \frac{1}{2}\alpha_i c \right)^T > 0, \quad \forall i \in \mathbb{S},$$

(or

$$\tilde{E}_i := \tilde{Q}_i - \sum_{j\neq i} \gamma_{ij} \left[\int_0^\infty \mathrm{e}^{H_j^T t} \tilde{Q}_j \mathrm{e}^{H_j t}\, \mathrm{d}t \right] - \frac{k}{\alpha_i} \left[\int_0^\infty \mathrm{e}^{H_i^T t} \tilde{Q}_i \mathrm{e}^{H_i t}\, \mathrm{d}t \right] bb^T \left[\int_0^\infty \mathrm{e}^{H_i^T t} \tilde{Q}_i \mathrm{e}^{H_i t}\, \mathrm{d}t \right] - \frac{k}{4}\alpha_i cc^T > 0, \quad \forall i \in \mathbb{S}, \ )$$

then system (1) *is stochastically absolutely stable w.r.t.* $F_{(0,k)}$.

In previous, we assume that the diffusion coefficient satisfies (H2) following [7]. However, this is too strong. Next, we will give another result under a weaker assumption.

Theorem 3.2. *Assume that the system* (1) *satisfies hypotheses (H1), (H3) and* (17). *If there exist* $\alpha_i > 0$ *and symmetric positive-definite matrices* $P_i \in \mathbb{R}^{n\times n}$, $i \in \mathbb{S}$, *such that*

$$R_i - \frac{k}{\alpha_i} d_i d_i^T > 0, \quad \forall i \in \mathbb{S},$$

where

$$\begin{cases} -R_i = P_iA_i + A_i^TP_i + \mathrm{trace}(P_i)K^2I + \sum_{j=1}^N \gamma_{ij}P_j, \\ d_i = P_ib - \frac{1}{2}\alpha_i c, \end{cases} \tag{20}$$

then system (1) *is stochastically absolutely stable w.r.t.* $F_{(0,k)}$.

Proof. Let $V(x,t,i) = x^TP_ix, i = 1,2,\cdots,N$. The left of the proof is similar to previous, noting that

$$\mathrm{trace}\big[D^T(x,i)P_iD(x,i)\big] \le \mathrm{trace}(P_i)K^2x^Tx.$$

□

4 Examples

In this section, we use an example to illustrate our main result.

Example 4.1. Let $B(t)$ be a 1-dimensional Brownian motion, $S = \{1,2,3\}$, $r(t)$ be a right-continuous Markov chain with generator

$$\Gamma = \begin{bmatrix} -1 & 0.5 & 0.5 \\ 1 & -2 & 1 \\ 1 & 2 & -3 \end{bmatrix}.$$

Let

$$A_1 = \begin{bmatrix} -1 & 0 & 1 \\ 1 & -2 & 0 \\ -1 & 0 & -3 \end{bmatrix}, \quad A_2 = \begin{bmatrix} -4 & 1 & 2 \\ 0 & -5 & 0 \\ -1 & 0 & -6 \end{bmatrix},$$

$$A_3 = \begin{bmatrix} -7 & 0 & 3 \\ 0 & -8 & 0 \\ 1 & 0 & -9 \end{bmatrix},$$

where $A_i = A(i)$, $i = 1,2,3$, $b = (1,1,1)^T$, $c = (1,1,1)^T$, $k = 5$. Let

$$D(x,i) = \frac{i}{3}x, \quad i = 1,2,3,$$

then $\lambda = 1$.

It's easy to know that hypotheses (H1) and (H2) are satisfied. And we get

$$\max \mathrm{Re}\lambda(G_i) = -2 < 0, \quad \max \mathrm{Re}\lambda(H_i) = -2.1248 < 0,$$

then (13) is satisfied, so we can use Theorem 3.1.

Let $\alpha_1 = 1$, $\alpha_2 = 1$, $\alpha_3 = 1$, $Q_0 = I$, $M = 1$, using the M-method, we can obtain

$$\tilde{P}_1 = \begin{bmatrix} 0.5404 & 0.0458 & 0.0561 \\ 0.0458 & 0.2753 & 0.0364 \\ 0.0561 & 0.0364 & 0.2159 \end{bmatrix}, \quad \begin{matrix} \lambda_{\min}(\tilde{P}_1) = 0.1954, \\ \lambda_{\max}(\tilde{P}_1) = 0.5592, \end{matrix}$$

$$\tilde{P}_2 = \begin{bmatrix} 0.2312 & 0.0400 & 0.0446 \\ 0.0400 & 0.2106 & 0.0317 \\ 0.0446 & 0.0317 & 0.1888 \end{bmatrix}, \quad \begin{matrix} \lambda_{\min}(\tilde{P}_2) = 0.1595, \\ \lambda_{\max}(\tilde{P}_2) = 0.2913, \end{matrix}$$

$$\tilde{P}_3 = \begin{bmatrix} 0.2091 & 0.0184 & 0.0591 \\ 0.0184 & 0.1875 & 0.0201 \\ 0.0591 & 0.0201 & 0.1820 \end{bmatrix}, \quad \begin{aligned} \lambda_{\min}(\tilde{P}_3) &= 0.1345, \\ \lambda_{\max}(\tilde{P}_3) &= 0.2655. \end{aligned}$$

And it's obvious that $MQ_0 - \tilde{P}_i > 0$, $\forall i \in \mathbb{S}$, so we can choose $P_i = \tilde{P}_i$, then by Theorem 3.1, this system is stochastically absolutely stable w.r.t. $F_{(0,5)}$. Actually, we have

$$R_1 - \frac{k}{\alpha_1} d_1 d_1^T = \begin{bmatrix} 0.7798 & -0.0292 & -0.0518 \\ -0.0292 & 0.8009 & -0.0259 \\ -0.0518 & -0.0259 & 0.8146 \end{bmatrix},$$

$$\lambda_{\min}\left(R_1 - \frac{k}{\alpha_1} d_1 d_1^T\right) = 0.7231,$$

$$R_2 - \frac{k}{\alpha_2} d_2 d_2^T = \begin{bmatrix} 1.2505 & -0.0642 & -0.1153 \\ -0.0642 & 1.5371 & -0.0566 \\ -0.1153 & -0.0566 & 1.6021 \end{bmatrix},$$

$$\lambda_{\min}\left(R_2 - \frac{k}{\alpha_2} d_2 d_2^T\right) = 1.1981,$$

$$R_3 - \frac{k}{\alpha_3} d_3 d_3^T = \begin{bmatrix} 1.9972 & -0.1259 & -0.1452 \\ -0.1259 & 2.3034 & -0.0998 \\ -0.1452 & -0.0998 & 2.4065 \end{bmatrix},$$

$$\lambda_{\min}\left(R_3 - \frac{k}{\alpha_3} d_3 d_3^T\right) = 1.8949.$$

Acknowledgements

The research for this work was supported, in part, by the Natural Sciences of China(11371371).

References

[1] G. K. Basak, A.Bisi, and M. K.Ghosh, "Stability of a random diffusion with linear drift," *Journal of Mathematical Analysis and Applications*, vol. 202(2), pp. 604-622, 1996.

[2] V. A.Brusin, and V. A. Ugrinovskii, "Stochastic stability of a class of nonlinear differential equations of Ito type", *Siberian Mathematical Journal,* vol.28(3), pp.381-393, 1987.

[3] D. G. Korenevskii, " Algebraic criteria for absolute (relative to nonlinearity) stability of stochastic automatic control systems with nonlinear feedback", *Ukrainian Mathematical Journal,* vol. 40(6), 616-621, 1988.

[4] H. J.Kushner, *Stochastic stability and control, ser.Mathematics in Science and Engineering,* New York: Academic Press, 1967.

[5] X.Liao, L. Q. Wang, and P. Yu, *Stability of dynamical systems* (Vol. 5), Elsevier, 2007.

[6] A. I.Lurie, and V. N. Postnikov, "On the theory of stability of control systems," *Applied mathematics and mechanics,* vol.8(3), pp. 246-248, 1944.

[7] A. K. Mahalanabis, and S. Purkayastha, "Frequency-domain criteria for stability of a class of nonlinear stochastic systems," *Automatic Control, IEEE Transactions on,* vol, 18(3), pp. 266-270, 1973.

[8] X. Mao, "Stability of stochastic differential equations with Markovian switching," *Stochastic Processes and Their Applications,* vol. 79(1), pp. 45-67, 1999.

[9] X. Mao, "Asymptotic stability for stochastic differential equations with Markovian switching," *WSEAS Trans. Circuits,* vol.(1), pp.68-73, 2002.

[10] X. Mao, and C.Yuan,*Stochastic differential equations with Markovian switching.* London: Imperial College Press, 2006.

[11] V. M. Popov, "Absolute stability of nonlinear systems of automatic control," *Automation and Remote Control,*vol.22(8), pp. 857-875 (1961).

[12] H. M. Xie,*Theory and Application of Absolute stability,* Beijing: Science Press, 1986.

Proceedings of ICCSA 2014
Normandie University, Le Havre, France - June 23-26, 2014

GLOBAL EXPONENTIAL STABILITY OF DISCRETE-TIME DELAY SYSTEMS SUBJECT TO IMPULSIVE PERTURBATIONS

Kexue Zhang, Xinzhi Liu and Wei-Chau Xie *†

Abstract. This paper considers the discrete-time delay systems subject to impulsive perturbations. Global exponential stability results are established, by employing Razumikhin technique and Lyapunov functions. It is shown that a stable discrete-time delay system can successfully tolerate impulsive perturbations to a certain extent. Corresponding results for linear discrete-time delay systems are also derived. A numerical example is provided to demonstrate the main results.

Keywords. Discrete-time system, Impulsive perturbation, Time delay, Exponential stability, Razumikhin technique

1 Introduction

Due to the wide existence of time-delay and the importance of discrete-time systems in mathematical modelling and numerical simulations, the stability of discrete-time delay systems has been investigated extensively over the past few decades (see, e.g., [1], [2], [3], [4], [5]). On the other hand, impulsive effect is a real-world phenomenon that arises in many applied fields, such as secure communications [6], disease infections [7], spacecraft maneuvers [8], dynamical networks [9]. Recently, the impulsive discrete-time systems have been received considerable attentions and various stability results have been established (see, [10], [11], [12], [13]).

In terms of time-delay, two commonly used approaches for stability analysis are Razumikhin technique and Lyapunov functional method. Among these two methods, Razumikhin technique has its advantages in two aspects: it's easier to construct suitable Lyapunov function than a appropriate Lyapunov functional; it does not require the Lyapunov function to vary uniformly on the whole state space. Moreover, when dealing with impulses, it's straightforward for the impulse to alter the value of a Lyapunov function at each impulsive instants. Based on Razumikhin technique, numerous stability results have been reported in literatures (see, e.g., [14], [15], [16], [17], [18]). In [14], stability and asymptotic stability of impulsive discrete-time systems with time-delay were studied, then Liu and Zhang improved these results in [15]. Exponential stability was investigated in [16] and [17]. It is worth noting from these results that impulses can successfully stabilize an unstable system. However, the impulse is a double-edge sword, i.e., it could also destroy the stability of a system or lead to a poor system performance. Impulsive perturbations to discrete-time delay systems have been studied in [18]. By Razumikhin technique, sufficient conditions have been obtained to guarantee the impulsive perturbed system can stay exponentially stable.

In this paper, we will study the exponential stability of discrete-time systems subject to impulsive perturbations which are different from the ones studied in [18] (see Remark 3.1 for more details). The rest of the paper is organized as follows. In Section 2, preliminaries about the system model are introduced. Then in Section 3, Razumikhin-type stability results are addressed. A numerical example is provided in Section 4 to illustrate and interpret the theoretical results. Finally, the paper is concluded by Section 5.

2 Preliminaries

Let $\mathbb{R}$ be the real numbers, $\mathbb{R}^+$ the nonnegative real numbers, $\mathbb{Z}$ the integers, $\mathbb{Z}^+$ the nonnegative integers, $\mathbb{N}$ the natural numbers, i.e., $\mathbb{N} = \{1, 2, ...\}$, and for some positive integer τ, let $\mathbb{N}_{-\tau} = \{-\tau, -\tau+1, ..., -1, 0\}$. Let $\mathbb{R}^N$ denote the $N-$dimensional real space equipped with the Euclidean norm. Let $||A||$ denote the spectral norm of matrix A induced by the Euclidean vector norm. For a given integer τ, let $C = \{\phi : \mathbb{N}_{-\tau} \to \mathbb{R}^N\}$. For any $\phi \in C$, we define $||\phi||_\tau = \max_{\theta \in \mathbb{N}_{-\tau}} \{||\phi(\theta)||\}$.

Consider the following impulsive discrete system with time-delay:

$$\begin{cases} x(n+1) = f(n, \overline{x}_n), & n \geq n_0, \\ \overline{x}(n) = \begin{cases} x(n), & n \neq n_k, \\ x(n) + I_k(n, x(n)), & n = n_k,\ k \in \mathbb{N}, \end{cases} \\ x_{n_0} = \phi, \end{cases} \tag{1}$$

where $x \in \mathbb{R}^N$, $n_0 \in \mathbb{Z}^+$, $f : \mathbb{Z}^+ \times C \to \mathbb{R}^N$, $\phi \in C$, and $\overline{x}_n \in C$ is defined by $\overline{x}_n(s) = \overline{x}(n+s)$ for any $s \in \mathbb{N}_{-\tau}$, with $\tau \in \mathbb{N}$ representing the delay in system (1);

*Kexue Zhang and Xinzhi Liu are with Department of Applied Mathematics, University of Waterloo, Ontario, Canada. E-mails: k57zhang@uwaterloo.ca, xzliu@uwaterloo.ca

†Wei-Chau Xie is with Department of Civil and Environmental Engineering, University of Waterloo, Ontario, Canada. E-mail: xie@uwaterloo.ca

$I_k : \mathbb{N} \times \mathbb{R}^N \to \mathbb{R}^N$ for $k \in \mathbb{N}$, and $0 \le n_0 < n_1 < ... < n_k < ...$ with $\lim_{k\to\infty} n_k = \infty$. It can be seen that $\overline{x}(n_k)$ denotes the state x at n_k with the impulse, and $x(n_k)$ denotes the state x at n_k without the impulse. Hence, if we set, by analogy to the impulsive continuous-time system, $x(n_k^+) = \overline{x}(n_k)$, then system (1) can be rewritten in the following form:

$$\begin{cases} x(n+1) = f(n, x_n), & n_{k-1}^+ \le n < n_k, \\ \Delta x(n) = I_k(n, x(n)), & n = n_k,\ k \in \mathbb{N}, \\ x_{n_0} = \phi, \end{cases} \tag{2}$$

where $\Delta x(n_k) = x(n_k^+) - x(n_k)$, and $x_{n_k^+}(s) = x((n_k + s)^+)$ for $s \in \mathbb{N}_{-\tau}$, $k \in \mathbb{N}$, which have also been considered in [9], [11], [19]. Without loss of generality, we shall investigate system (2) instead of system (1) as the equivalence of the two forms of systems. For more detailed discussions of system models (1) and (2), please refer to [16] and [18].

We assume $f(n, 0) \equiv 0$ and $I_k(n, 0) \equiv 0$ $(k \in \mathbb{N})$ so that system (2) admits the trivial solution. The solution of system (2) is denoted by $x(n) = x(n; n_0, \phi)$ for any given initial condition: $n_0 \in \mathbb{Z}^+$ and $\phi \in C$.

Definition 2.1. *The trivial solution of system* (2) *is said to be globally exponentially stable (GES), if, for any initial condition $x_{n_0} = \phi$, there exist constant $\alpha > 0$ and $M \ge 1$ such that*

$$||x(n; n_0, \phi)|| \le M\|\phi\|_\tau e^{-\alpha(n-n_0)}, \quad \textit{for all } n \ge n_0.$$

3 Razumikhin-Type Theorems

In this section, we first investigate the global exponential stability of system (2).

Theorem 3.1. *Assume that there exist $V : \mathbb{Z} \times \mathbb{R}^N \to \mathbb{R}^+$, and positive constants c_1, c_2, p, γ and $c < 1$ such that the following conditions hold:*

(i) $c_1||x||^p \le V(n, x) \le c_2||x||^p$ *for* $n \ge n_0 - \tau$ *and* $x \in \mathbb{R}^N$;

(ii) *for* $n_{k-1}^+ \le n < n_k$ $(k \in \mathbb{N})$, *if* $qV(n+1, x(n+1)) \ge V(n+s, x(n+s))$ *for all* $s \in \mathbb{N}_{-\tau}$, *then*

$$V(n+1, x(n+1)) - V(n, x(n)) \le -cV(n, x(n)),$$

where $q \ge \frac{1}{1-c}$ *is a constant;*

(iii) *for each* $k \in \mathbb{N}$,

$$V(n_k^+, x(n_k) + I_k(n_k, x(n_k))) \le \gamma V(n_k, x(n_k));$$

(iv) $q > \gamma \ge 1$ *and* $\ln(1-c) < \frac{\ln(1/\gamma)}{\rho}$, *where* $\rho = \inf_{k\in\mathbb{N}}\{n_k - n_{k-1}\}$.

Then the trivial solution of system (2) *is GES.*

Proof: Let $x(n) = x(n; n_0, \phi)$ denote the solution of system (2) with any given initial time n_0 and initial data $\phi \in C$. Without loss of generality, one assume that ϕ is not trivial so that $x(n)$ is a nontrivial solution. It follows from condition (iv) that there exist positive numbers μ and h such that

$$q \ge (\gamma + h)e^{\mu(\tau+1)} > \gamma, \tag{3}$$

and

$$\mu + \ln(1-c) \le \frac{\ln(\frac{1}{\gamma+h})}{\rho}. \tag{4}$$

Let $w(n) = e^{\mu(n-n_0)}V(n, x(n))$ for $n \ge n_0 - \tau$. We shall show that

$$w(n) \le c_1 M||\phi||_\tau^p, \text{ for } n \ge n_0,$$

where $M > \bar{q}\frac{c_2}{c_1}$ with $\bar{q} = \gamma + h$.

First, we will show that

$$w(n) \le c_1 M||\phi||_\tau^p, \text{ for } n_0 \le n \le n_1. \tag{5}$$

Suppose (5) is not true and observe that

$$w(n) \le V(n, x(n)) \le c_2||\phi||_\tau^p < \frac{1}{\bar{q}}c_1 M||\phi||_\tau^p < c_1 M||\phi||_\tau^p$$

for $n_0 - \tau \le n \le n_0$, which implies

$$w(n_0) < \frac{1}{\bar{q}}c_1 M||\phi||_\tau^p < c_1 M||\phi||_\tau^p. \tag{6}$$

Define

$$n^* = \inf\{n_0 \le n \le n_1 \mid w(n) > c_1 M||\phi||_\tau^p\},$$

then $n^* \ge n_0 + 1$, $w(n^*) > c_1 M||\phi||_\tau^p$, and $w(n) \le c_1 M||\phi||_\tau^p$ for $n \le n^* - 1$. In view of (6), define

$$\bar{n} = \sup\{n_0 \le n \le n^* \mid w(n) < \frac{1}{\bar{q}}c_1 M||\phi||_\tau^p\},$$

then, $\bar{n} \le n^* - 1$, $w(\bar{n}) < \frac{1}{\bar{q}}c_1 M||\phi||_\tau^p$, and $w(n) \ge \frac{1}{\bar{q}}c_1 M||\phi||_\tau^p$ for $\bar{n} < n \le n^*$. Thus, for $\bar{n} \le n < n^*$, one has $\bar{n} < n + 1 \le n^*$ and

$$w(n+1) \ge \frac{1}{\bar{q}}c_1 M||\phi||_\tau^p \ge \frac{1}{\bar{q}}w(n+s), \text{ for } s \in \mathbb{N}_{-\tau},$$

then $\bar{q}w(n+1) \ge w(n+s)$. It follows that, for any $s \in \mathbb{N}_{-\tau}$,

$$\begin{aligned} \bar{q}w(n+1) &= \bar{q}e^{\mu(n-n_0)}e^{\mu}V(n+1, x(n+1)) \\ &\ge w(n+s) \\ &= e^{\mu(n-n_0)}e^{\mu s}V(n+s, x(n+s)) \\ &\ge e^{\mu(n-n_0)}e^{-\mu\tau}V(n+s, x(n+s)), \end{aligned}$$

which implies that

$$qV(n+1, x(n+1)) \ge \frac{q}{\bar{q}e^{\mu(\tau+1)}}V(n+s, x(n+s))$$

$$\geq \quad V(n+s, x(n+s)).$$

By Razumikhin-type condition (ii), one obtains that

$$V(n+1, x(n+1)) \leq (1-c)V(n, x(n)), \text{ for } \bar{n} \leq n < n^*.$$

Then, for $\bar{n} \leq n < n^*$,

$$\begin{aligned} w(n+1) &= e^{\mu(n+1-n_0)}V(n+1, x(n+1)) \\ &\leq e^{\mu(n+1-n_0)}(1-c)V(n, x(n)) \\ &= e^{\mu}(1-c)w(n) \\ &\leq w(n). \end{aligned}$$

It follows that $w(n^*) \leq w(\bar{n})$, which is a contradiction. Hence, (5) is true.

Next, assume that

$$w(n) \leq c_1 M||\phi||_\tau^p, \text{ for } n_{k-1}^+ \leq n \leq n_k, \tag{7}$$

for all $k \leq m$. We proceed to show that

$$w(n) \leq c_1 M||\phi||_\tau^p, \text{ for } n_m^+ \leq n \leq n_{m+1}. \tag{8}$$

In order to do this, we first claim that

$$w(n_m) \leq \frac{1}{\bar{q}} c_1 M||\phi||_\tau^p. \tag{9}$$

Suppose (9) is not true, then $w(n_m) > \frac{1}{\bar{q}} c_1 M||\phi||_\tau^p$. In order to derive the contradiction, one considers the following two cases:

Case 1. $w(n) > \frac{1}{\bar{q}} c_1 M||\phi||_\tau^p$ for all $n_{m-1}^+ \leq n \leq n_m$.

Case 2. There exists some n $(n_{m-1}^+ \leq n < n_m)$ such that $w(n) \leq \frac{1}{\bar{q}} c_1 M||\phi||_\tau^p$.

It follows from Case 1 that, for $n_{m-1}^+ \leq n < n_m$,

$$w(n+1) > \frac{1}{\bar{q}} c_1 M||\phi||_\tau^p \geq \frac{1}{\bar{q}} w(n+s), \text{ for all } s \in \mathbb{N}_{-\tau},$$

which, together with condition (ii), implies

$$w(n+1) \leq e^{\mu}(1-c)w(n), \text{ for } n_{m-1}^+ \leq n < n_m.$$

Then,

$$\begin{aligned} w(n_m) &\leq (e^{\mu}(1-c))^{n_m - n_{m-1}} w(n_{m-1}^+) \\ &\leq (e^{\mu}(1-c))^{\rho} w(n_{m-1}^+) \\ &\leq (e^{\mu}(1-c))^{\rho} c_1 M||\phi||_\tau^p \\ &\leq \frac{1}{\bar{q}} c_1 M||\phi||_\tau^p, \end{aligned}$$

which is a contradiction.

For Case 2, define $\bar{n} = \sup\{n_{m-1}^+ \leq n < n_m \mid w(n) \leq \frac{1}{\bar{q}} c_1 M||\phi||_\tau^p\}$. Then, $w(\bar{n}) \leq \frac{1}{\bar{q}} c_1 M||\phi||_\tau^p$ and $w(n) > \frac{1}{\bar{q}} c_1 M||\phi||_\tau^p$ for $\bar{n} < n \leq n_m$. Thus, for $\bar{n} \leq n < n_m$, one has $\bar{n} < n+1 \leq n_m$ and

$$w(n+1) > \frac{1}{\bar{q}} c_1 M||\phi||_\tau^p \geq \frac{1}{\bar{q}} w(n+s), \ \forall \ s \in \mathbb{N}_{-\tau}. \tag{10}$$

From condition (ii) and (10), one can get that

$$w(n+1) \leq e^{\mu}(1-c)w(n) \leq w(n), \text{ for } \bar{n} \leq n < n_m.$$

Then, $w(n_m) \leq w(\bar{n}) \leq \frac{1}{\bar{q}} c_1 M||\phi||_\tau^p$, which also is a contradiction. Hence, the claim (9) is true. By condition (iii), one obtains that

$$w(n_m^+) \leq \gamma w(n_m) \leq \frac{\gamma}{\bar{q}} c_1 M||\phi||_\tau^p < c_1 M||\phi||_\tau^p.$$

Suppose (8) is not true, and define $n^* = \inf\{n_m^+ \leq n \leq n_{m+1} \mid w(n) > c_1 M||\phi||_\tau^p\}$. Then, $n^* \geq n_m + 1$, $w(n^*) > c_1 M||\phi||_\tau^p$, and $w(n) \leq c_1 M||\phi||_\tau^p$ for $n_m^+ \leq n < n^*$. Define $\bar{n} = \sup\{n_m^+ \leq n < n^* \mid w(n) \leq \frac{\gamma}{\bar{q}} c_1 M||\phi||_\tau^p\}$, then $w(\bar{n}) \leq \frac{\gamma}{\bar{q}} c_1 M||\phi||_\tau^p$ and $w(n) > \frac{\gamma}{\bar{q}} c_1 M||\phi||_\tau^p$ for $\bar{n} < n \leq n^*$.

For $\bar{n} \leq n < n^*$, one can see that $\bar{n} < n+1 \leq n^*$ and

$$w(n+1) > \frac{\gamma}{\bar{q}} c_1 M||\phi||_\tau^p \geq \frac{1}{\bar{q}} c_1 M||\phi||_\tau^p \geq \frac{1}{\bar{q}} w(n+s)$$

for $s \in \mathbb{N}_{-\tau}$, which implies $w(n+1) \leq e^{\mu}(1-c)w(n) \leq w(n)$ for $\bar{n} \leq n < n^*$. Then

$$w(n^*) \leq w(\bar{n}) \leq \frac{\gamma}{\bar{q}} c_1 M||\phi||_\tau^p < c_1 M||\phi||_\tau^p,$$

which leads to a contradiction. Therefore, (8) must be true.

By mathematical induction on m, one can conclude that

$$w(n) \leq c_1 M||\phi||_\tau^p, \quad \forall n \geq n_0,$$

i.e.,

$$V(n, x(n)) \leq c_1 M||\phi||_\tau^p e^{-\mu(n-n_0)}, \quad \forall n \geq n_0.$$

By condition (i), we actually have shown that

$$||x(n)|| \leq M^{1/p}||\phi||_\tau e^{-\frac{\mu}{p}(n-n_0)}, \quad \forall n \geq n_0,$$

which shows that the trivial solution of system (2) is GES. □

If $I_k \equiv 0$ in system (2), then system (2) reduces to the following nonlinear discrete-time system with delays:

$$\begin{cases} x(n+1) = f(n, x_n), & n \geq n_0, \\ x_{n_0} = \phi, \end{cases} \tag{11}$$

where f, ϕ, x_n and x_{n_0} are defined the same as those for system (2). It can be seen that conditions (iii) and (iv) of Theorem 3.1 is satisfied for system (11) with $\gamma = 1$. Then we have the following stability result for system (11).

Corollary 3.1. *Assume that there exist $V : \mathbb{Z} \times \mathbb{R}^N \to \mathbb{R}^+$, and positive constants c_1, c_2, p and $c < 1$ such that conditions (i) and (ii) of Theorem 3.1 hold, then the trivial solution of system* (11) *is GES.*

Some remarks about Theorem 3.1 and Corollary 3.1 are discussed as follows.

Remark 3.1. *To apply the Razumikhin-type condition (ii) of Theorem 3.1, we have to compare $V(n+1,x(n+1))$ with $V(n,x(n))$ after comparing $V(n+1,x(n+1))$ with $V(n,x(n))$, $V(n-1,x(n-1))$, ..., $V(n-\tau,x(n-\tau))$, i.e., we need to compare $V(n+1,x(n+1))$ with $V(n,x(n))$ twice to make the following two inequalities hold: $qV(n+1,x(n+1)) \geq V(n,x(n))$ and $V(n+1,x(n+1)) \leq (1-c)V(n,x(n))$. Hence, the condition $q \geq \frac{1}{1-c}$ is written explicitly in Theorem 3.1 to avoid the self-contradiction in condition (ii).*

Remark 3.2. *Corollary 3.1 shows that under conditions (i) and (ii) the impulsive free system is GES, and Theorem 3.1 gives sufficient conditions to guarantee that the system with impulsive perturbations can still attain the GES property. Condition (iv) of Theorem 3.1 shows that impulsive perturbations can not happen frequently, i.e., there is a lower bound for the time difference of two successive impulsive perturbations. The GES property of system (11) subject to impulsive perturbations has been investigated in [18]. However, condition (iii) of Theorem 3.1 shows that the impulsive strength must be bounded, but the total energy $\sum_{k=1}^{\infty}(\gamma-1)$ of the impulses can be unbounded. Therefore, the result in [18] is not applicable to analyze the stability of system (11) subject to this kind of impulsive perturbations.*

Remark 3.3. *From the proof of Theorem 3.1, one can see that constants μ and M are independent on the initial time n_0. Then GES in Definition 2.1 is called globally uniformly exponentially stable (GUES). The GUES property of system (11) has been studied in [20] by Razumikhin technique. It's worth noting that there are two Razumikhin-type conditions in the GUES result in [20]. In Corollary 3.1, only one Razumikhin-type condition is needed, which makes our result easier to verify. Furthermore, the convergence speed is estimated in the proof of Theorem 3.1, which is μ/p. It can be seen from (3) and (4) that μ is closely related to the destabilizing impulsive strength γ, the delay size τ, and the constant q in the Razumikhin-type condition (ii). When τ becomes larger, μ has to be sufficient small to guarantee that (3) is satisfied, i.e., large delay in system (2) leads to slow convergence speed of the system response.*

Next, consider the linear impulsive discrete-time delay system in the form of

$$\begin{cases} x(n+1) = Ax(n) + Bx(n+h(n)), \quad n_{k-1}^{+} \leq n < n_k, \\ \Delta x(n_k) = C_k x(n_k), \quad k \in \mathbb{N}, \\ x_{n_0} = \phi, \end{cases} \tag{12}$$

where $x \in \mathbb{R}^N$, $A, B \in \mathbb{R}^{N\times N}$, $\phi \in C$ and $h : \mathbb{Z}^+ \to \mathbb{N}_{-\tau}$. We have the following result.

Theorem 3.2. *Suppose that there exist constants $\gamma \geq 1$ and $q > \gamma$ such that*

(i) $\gamma \geq ||E + C_k||$, $k \in \mathbb{N}$;

(ii) $||A|| + ||B|| \geq \frac{1}{q}$ *and* $\gamma^{1/\rho}||A|| + q||B|| < 1$, *where* $\rho = \inf_{k\in\mathbb{N}}\{n_k - n_{k-1}\}$.

Then the trivial solution of system (12) is GES.

Proof: Let $V(x) = ||x||$, then condition (i) of Theorem 3.1 is satisfied with $c_1 = c_2 = p = 1$. If $qV(x(n+1)) \geq V(x(n+s))$ for $s \in \mathbb{N}_{-\tau}$, then

$$\begin{aligned} V(x(n+1)) &\leq ||A||V(x(n)) + ||B||V(x(n+h(n))) \\ &\leq ||A||V(x(n)) + q||B||V(x(n+1)), \end{aligned}$$

i.e., $V(x(n+1)) - V(x(n)) \leq -cV(x(n))$ with $c = 1 - \frac{||A||}{1-q||B||}$. Condition (ii) implies that $0 < c < 1$ and $q(1-c) \geq 1$, which shows that condition (ii) of Theorem 3.1 holds. Also, conditions (i) and (ii) demonstrate that condition (iii) and condition (iv) of Theorem 3.1 are satisfied, respectively. Therefore, we can conclude from Theorem 3.1 that the trivial solution of system (12) is GES. □

As discussed for the nonlinear system, if $C_k \equiv 0$ ($k \in \mathbb{N}$), then we have the following linear discrete-time system with time-varying delays

$$\begin{cases} x(n+1) = Ax(n) + Bx(n+h(n)), \quad n \geq n_0, \\ x_{n_0} = \phi. \end{cases} \tag{13}$$

Clearly, condition (i) of Theorem 3.2 is satisfied with $\gamma = 1$. Furthermore, if we choose $q = (||A|| + ||B||)^{-1} > 1$, then $||A|| + q||B|| < 1$ for $||A|| \neq 0$ and $||A|| + ||B|| < 1$. Hence, condition (ii) of Theorem 3.2 holds. We conclude the above discussion with the following result.

Corollary 3.2. *If $||A|| > 0$ and $||A|| + ||B|| < 1$, then the trivial solution of system (13) is GES.*

Remark 3.4. *Based on the proof of Theorem 3.1, we can see from Corollary 3.2 and Theorem 3.2 that the larger $||A|| + ||B||$ becomes with $||A|| + ||B|| < 1$, the slower convergence speed system (13) will have and less impulsive perturbations system (13) can tolerate. Furthermore, Theorem 3.2 and Corollary 3.2 are delay-independent stability results, which are very important for stability analysis of systems with large or even unknown bounded delays. However, as discussed in Remark 3.3, the system convergence speed depends on the system delays. See Example 4.1 for illustrations.*

4 An Example

Example 4.1. *Consider the linear impulsive discrete delay system*

$$\begin{cases} x(n+1) = Ax(n) + Bx(n-\tau), \quad n_{k-1}^{+} \leq n < n_k, \\ \Delta x(n_k) = C_k x(n_k), \quad k \in \mathbb{N}, \\ x_{n_0} = \phi, \end{cases} \tag{14}$$

where $x = (x_1, x_2)^T$, $n_0 = 0$, $\tau = 5$, $n_k = 5k (k \in \mathbb{N})$, $\phi(s) = (0.9, 1.5)^T$ for $s \in \mathbb{N}_{-\tau}$, and

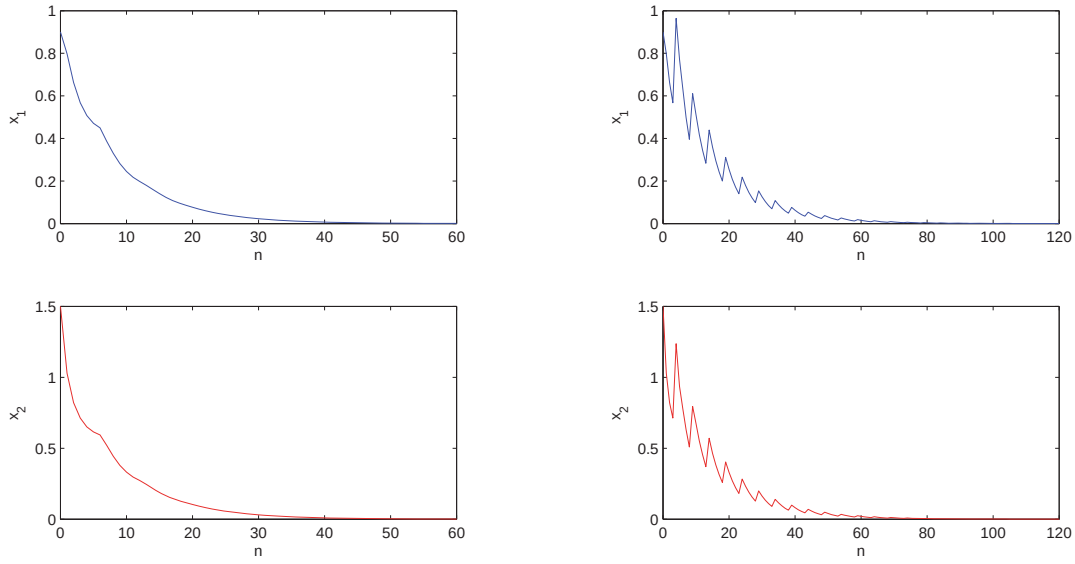

(a)Impulsive free (b)Impulsive perturbations

Figure 1: Simulation results for Example 4.1: (a) system response without impulses; (b) system response with impulsive perturbations.

$$A = \begin{bmatrix} 0.4 & 0.2 \\ 0.19 & 0.4 \end{bmatrix}, \quad B = \begin{bmatrix} -0.03 & 0.11 \\ 0.12 & 0.1 \end{bmatrix},$$

$$C_k = \begin{bmatrix} 0.9 & 0 \\ 0 & 0.9 \end{bmatrix} (k \in \mathbb{N}).$$

Then, $\gamma = ||E + C_k|| = 1.9$ and $\rho = \inf_{k\in\mathbb{N}}\{n_k - n_{k-1}\} = 5$. If we further choose $q = 1.91 \geq \gamma$, then

$$1 > ||A|| + ||B|| = 0.7625 > \frac{1}{q} = 0.5263,$$

and

$$\gamma^{1/\rho}||A|| + q||B|| = 0.9964 < 1.$$

Therefore, all the conditions of Theorem 3.2 are satisfied, which implies that the trivial solution of system (14) with the given parameters is GES. Numerical simulations for this example are shown in Figure 1. It is clearly demonstrated that a GES discrete delay system can successfully tolerate impulsive perturbations.

Next, we increase the delay size in system (14) to $\tau = 10$, and replace B by $B = diag\{-0.4, -0.4\}$, then $||A|| + ||B|| = 0.9950 < 1$. Thus, Corollary 3.2 says that the trivial solution of the impulsive free system is GES. Due to the increase of time-delay τ and the value of $||A|| + ||B||$, the convergence speed of the impulsive free system will drop (see Figure 2(a) for an illustration), which verifies our analysis in Remark 3.3 and 3.4. However, the system subject to the same impulsive perturbations can not maintain the GES property. Numerical simulations for this is shown in Figure 2(b).

5 Conclusions

In this paper, we have considered the discrete-time delay systems subject to a class of impulsive perturbations, which, to our best knowledge, has not been investigated. By Lyapunov-Razumikhin technique, sufficient conditions have been established to guarantee the global exponential stability of the impulsive perturbed systems. It can be seen that the result can be utilized to analyze the stability of impulsive free discrete-time systems with time-delay, and the result is easier to verify than the existing results in literatures. The impact of the impulsive perturbation strength and the size of time-delay on the convergence speed of the system has been discussed in details. Then the results obtained for nonlinear systems has been applied to stability analysis of linear discrete-time delay systems with and without impulsive perturbations, respectively. Finally, an example has been provided with numerical simulations to illustrate out theoretical results.

References

[1] C.E. de Souza, D. Coutinho, "Robust stability and control of uncertain linear discrete-time periodic systems with time-delay", *Automatica*, 50(2) (2014) 431-441.

[2] K. Ramakrishnan, G. Ray, "Robust stability criteria for a class of uncertain discrete-time systems with time-varying delay", *Applied Mathematical Modelling*, 37(3) (2013) 1468-1479.

[3] G. Rajchakit, "Stability of discrete-time systems with time-varying delay: delay decomposition approach", *International Journal of Computers, Communications & Control*, 7(4) (2012) 775-783.

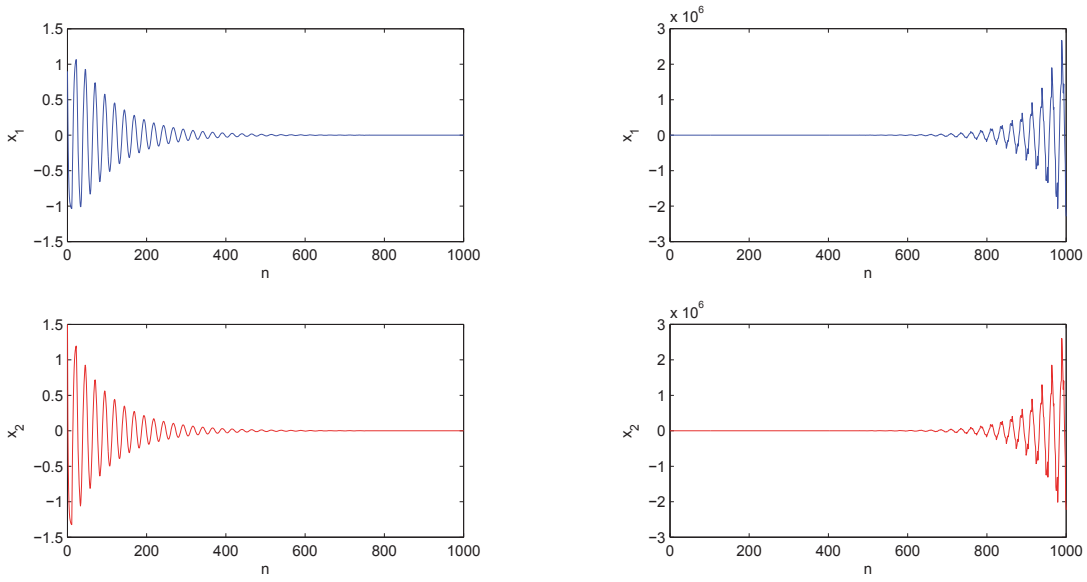

(a)Impulsive free (b)Impulsive perturbations

Figure 2: Simulation results for Example 4.1 with $\tau = 10$ and $B = diag\{-0.4, -0.4\}$.

[4] R. Medina, "Absolute stability of discrete-time systems with delay", *Advances in Difference Equations*, 2008, Article Number 396504.

[5] H. Gao, T. Chen, "New results on stability of discrete-time systems with time-varying state delay", *IEEE Transactions on Automatic Control*, 52(2) (2007) 328-334.

[6] A. Khadra, X. Liu, X. Shen, "Impulsively synchronizing chaotic systems with delay and applications to secure communication", *Automatica*, 41(9) (2005) 1491-1502.

[7] X. Liu, P. Stechlinski, "SIS models with switching and pulse control", *Applied Mathematics and Computation*, 232(2) (2014) 727-742.

[8] T.E. Carter, "Optimal impulsive space trajectories based on linear equations", *Journal of Optimization Theory and Applications*, 72(2) (1991) 277-297.

[9] E. Kaslik, S. Sivasundaram, "Impulsive hybrid discrete-time Hopfield neural networks with delays and multistability analysis", *Neural Networks*, 24(4) (2011) 370-377.

[10] R. Raja, R. Sakthivel, M.S. Anthoni, "Stability analysis for discrete-time stochastic neural networks with mixed time delays and impulsive effects", *Canadian Journal of Physics*, 88(12) (2010) 885-898.

[11] Z. Zhang, X. Liu, "Robust stability of uncertain discrete impulsive switching systems", *Computers & Mathematics with Applications*, 58(2) (2009) 380-389.

[12] B. Liu, D.J. Hill, "Uniform stability and ISS of discrete-time impulsive hybrid systems", *Nonlinear Analysis: Hybrid Systems*, 4(2) (2010) 319-333.

[13] B. Liu, D.J. Hill, "Comparison principle and stability of discrete-time impulsive hybrid systems", *IEEE Transactions on Circuits and Systems I-Regular Papers*, 56(1) (2009) 233-245.

[14] Y. Zhang, J. Sun, G. Feng, "Impulsive control of discrete systems with time delay", *IEEE Transactions on Automatic Control*, 54(4) (2009) 830-834.

[15] X. Liu, Z. Zhang, "Uniform asymptotic stability of impulsive discrete systems with time delay", *Nonlinear Analysis: Theory, Methods & Applications*, 74(15) (2011) 4941-4950.

[16] X. Liu, K. Zhang, "Impulsive control for stabilisation of discrete delay systems and synchronisation of discrete delay dynamical networks", *IET Control Theory and Applications*, doi: 10.1049/iet-cta.2013.0806

[17] S. Wu, C. Li, X. Liao, S. Duan, "Exponential stability of impulsive discrete systems with time delay and applications in stochastic neural networks: a Razumikhin approach", *Neurocomputing*, 82(1) (2012) 29-36.

[18] K. Zhang, X. Liu, "Global exponential stability of nonlinear impulsive discrete systems with time delay", *Proceedings of the 25th CCDC*, Guiyang, China, May 2013, 148-153.

[19] Z. Zhang, "Rubost H_∞ control of a class of discrete impulsive switched systems", *Nonlinear Analysis: Theory, Methods & Applications*, 71(12) (2009) e2790-e2796.

[20] B. Liu, H.J. Marquez, "Razumikhin-type stability theorems for discrete delay systems", *Automatica*, 43(7) (2007) 1219-1225.

Proceedings of ICCSA 2014
Normandie University, Le Havre, France – June 23-26, 2014

CHAOS IN TROPOSPHERIC OZONE CONCENTRATION TIME SERIES

Radko Kříž and Petr Hainc[1]

Abstract. The goal of this paper is to analyze the Tropospheric Ozone (O_3) concentration time series and to find chaos in this time series. This study was based on daily averaged tropospheric ozone (O_3) data from Pardubice in Czech Republic. At first we estimated the time delay and the embedding dimension, which is needed for the Lyapunov exponent estimation and for the phase space reconstruction. Subsequently we computed the largest Lyapunov exponent, which is one of the important indicators of chaos. Then we calculated the 0-1 test for chaos, the correlation dimension and the Kolmogorov-Sinai entropy. The results indicated that chaotic behaviors obviously exist in the Tropospheric Ozone concentration time series. Finally we computed predictions using a radial basis function and polynomials to fit global nonlinear functions to the data.
Keywords. Chaos theory, Tropospheric ozone, Time series analysis, Phase space reconstruction, Prediction.

1 Introduction

Tropospheric ozone (O_3) is one of the major air pollutants. The formation of ozone in the troposphere is a complex system involving the reactions of hundreds of precursors depending on the physical conditions. Photochemical pollution is formed from emissions of nitrogen oxides (NO_x, where $NO_x = NO + NO_2$) and of volatile organic compounds (VOCs) and carbon monoxide (CO) in the presence of sunlight [1]. The most prominent sources of NO_2 are internal combustion engines, thermal power stations and, to a lesser extent, pulp mills. The burning of biomass also creates additional pollutants including NO_x [2].

Exposure to O_3 induces effects on health and the environment, causing respiratory difficulties in sensitive people and possible damage to vegetation and ecosystems. There is evidence from controlled human and animal exposure studies of the potential for O_3 to cause adverse health effects. There is a great deal of evidence to show that ground level ozone can harm lung function and irritate the respiratory system. Exposure to ozone and the pollutants that produce it is linked to premature death, asthma, bronchitis, heart attack, and other cardiopulmonary problems. [3]

Recent advances in the modeling of air pollutants have led to the application of concepts including nonlinear modeling techniques. Numerous new methods of time series analysis have been developed for dealing with nonlinear data e.g. Abarnabel [4], Kantz et Schreiber [5], Mikšovský et Raidl [6]. The concepts from chaos theory reveals that, if the knowledge of a system in terms of its present and past states is available, then it is possible to make predictions of system's future behavior. The approaches based on chaos theory are widely acceptable due to the assumption that, it is possible to predict the future state of the system based on the single scalar time series assuming that, all the information regarding the external forcing factors is contained in that single time series [7]. Chaos theory allows for the reconstruction of phase space from time series, which can be used for specifying the system states. Thus, the dynamics of the system can be investigated by studying the dynamics of the movement of the phase space points [8].

The modeling of O_3 concentration has been studied in several works based on different unconventional approaches such as neural networks [9, 10, 11] and chaos approach [12,13, 14, 15,16].

The main idea in nonlinear time series modeling is that if the exact mathematical description of a dynamic system is unknown, the state space can be reconstructed from single variable time series. [17]. Takens' theorem [17] transforms the prediction problem from time extrapolation to phase space interpolation. We investigate dynamical systems that define the time evolution of underlying dynamics in a phase space.

2 Problem statement and preliminaries

2.1 Input data

This study was based on daily averaged tropospheric ozone (O3) data from Pardubice-Rosice from 1.1.2005 to 31.12.2011. We used the mean of this data set to fill in several missing values. The data were provided by the Czech Hydrometeorological Institute for a related di-

[1] Radko Kříž and Petr Hainc are with University of Pardubice, Czech Republic. E-mail: Radko.Kriz@upce.cz

ploma thesis that is aimed at nonlinear and chaotic behavior of air pollutants time series. Pardubice is the capital of the Pardubice Region and lies on the river Elbe, 100 km east of Prague (Fig. 1).

Figure 1: Map of Czech Republic

Peaks of O_3 concentration are located in the middle of the year when temperatures are highest (Fig. 2).

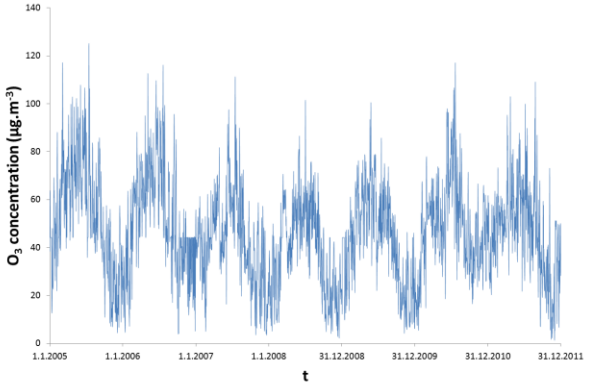

Figure 2: Daily averaged O_3 concentration data from Pardubice

2.2 Phase space reconstruction

Let there be given a time series $x_1, x_2, \ldots, x_N$ which is embedded into the m-dimensional phase space by the time delay vectors. A point in the phase space is given as:

$$Y_n = x_n, x_{n-\tau}, \ldots, x_{n-(m-1)\tau} \quad n = 1,2,\ldots,N-(m-1)\tau \tag{1}$$

where τ is the time delay and m is the embedding dimension. Different choices of τ and m yield different reconstructed trajectories. Kodba et al. [18] discuss How we can determine optimal τ and m. Fraser and Swinney [19] introduced the mutual information between x_n and $x_{n+\tau}$ as a suitable quantity for determining τ. The mutual information between x_n and $x_{n+\tau}$ quantifies the amount of information we have about the state $x_{n+\tau}$ presuming we know the state x_n. Now we can define mutual information function:

$$I(\tau) = -\sum_{h=1}^{j}\sum_{k=1}^{j} P_{h,k}(\tau) \ln \frac{P_{h,k}(\tau)}{P_h P_k} \tag{2}$$

where P_h and P_k denote the probabilities that the variable assumes a value inside the h^{th} and k^{th} bins, respectively, and $P_{h,k}(\tau)$ is the joint probability that x_n is in bin h and $x_{n+\tau}$ is in bin k. The first minimum of $I(\tau)$ then marks the optimal choice for the time delay.

The embedding dimension m can be chosen using the "false nearest neighbors'" method. In order to calculate the fraction of false nearest neighbors the following algorithm is used according to Kennel et al. [20]. Given a point $p(i)$ in the m-dimensional embedding space, one first has to find a neighbor $p(j)$, so that

$$\|p(i) - p(j)\| \le \mu \tag{3}$$

We then calculate the normalized distance R_i between the $(m+1)th$ embedding coordinate of points $p(i)$ and $p(j)$ according to the equation:

$$R_i = \frac{|x_{i+m\tau} - x_{j+m\tau}|}{\|p(i) - p(j)\|} \tag{4}$$

If R_i is larger than a given threshold R_{tr}, then $p(i)$ is marked as having a false nearest neighbor. Equation (4) has to be applied for the whole time series and for various $m = 1, 2, \ldots$ until the fraction of points for which $R_i > R_{tr}$ is negligible [18].

The values of τ and m are used to transform the univariate time series into the phase space vectors Y_n stacked as

$$Y_n = \begin{pmatrix} y_0 \\ y_1 \\ y_2 \\ \vdots \end{pmatrix} = \begin{pmatrix} x_0 & x_\tau & \cdots & x_{(m-1)\tau} \\ x_1 & x_{1-\tau} & \cdots & x_{1-(m-1)\tau} \\ x_2 & x_{2-\tau} & \cdots & x_{2-(m-1)\tau} \\ \vdots & \vdots & \vdots & \vdots \end{pmatrix} \tag{5}$$

Note that each observed scalar value is repeated several time in this matrix. The sequence of the rows in this embedding matrix is important as it generates a trajectory in the phase space. [21]

2.3 The largest Lyapunov exponent

Lyapunov exponent λ of a dynamical system is a quantity that characterizes the rate of separation of infinitesimally close trajectories. Quantitatively, two trajectories in phase space with initial separation δZ_0 diverge.

$$\delta Z(t) \approx e^{\lambda t} |\delta Z_0| \tag{6}$$

The largest Lyapunov exponent can be defined as follows:

$$\lambda = \lim_{\substack{\delta Z_0 \to 0 \\ t \to \infty}} \frac{1}{t} \ln \frac{|\delta Z(t)|}{|\delta Z_0|} \tag{7}$$

The limit $\delta Z_0 \to 0$ ensures the validity of the linear approximation at any time. Largest Lyapunov exponent determines a notion of predictability for a dynamical system. A positive largest Lyapunov exponent is usually taken as an indication that the system is chaotic [22].

We have used the Rosenstein algorithm [23], which counts the largest Lyapunov exponent as follows:

$$\lambda_1(i) = \frac{1}{i\Delta t} \cdot \frac{1}{(M-i)} \sum_{j=1}^{M-i} \ln \frac{d_j(i)}{d_j(0)} \quad (8)$$

where $d_j(i)$ is distance from the j point to its nearest neighbor after i time steps and M is the number of reconstructed points. For more information see [23].

2.4 Correlation dimension

There are many specific definitions of fractal dimension and correlation dimension is used in this paper. The method is based on the concept of correlation dimension D_C suggested by Grassberger et Procaccia [24]. D_C describes the dimensionality of the underlying process in relation to its geometrical reconstruction in phase space. D_C quantifies the "strangeness" of an attractor [25]. D_C is calculated using the fundamental definition. Define the correlation integral $C(\varepsilon)$ for set of M data:

$$C(\varepsilon) = \frac{1}{M(M-1)} \sum_{\substack{i,j=1 \\ i \neq j}}^{M} \Theta(\varepsilon - \|x_i - x_j\|) \quad (9)$$

where Θ is the Heaviside step function.
When a lower limit exists, the correlation dimension is then defined according power law as

$$D_C = \lim_{\substack{\varepsilon \to 0 \\ M \to \infty}} \frac{\partial \ln(C(\varepsilon))}{\partial \ln(\varepsilon)} \quad (10)$$

The resulting Gaussian kernel correlation integral $C_G(\varepsilon)$ has the same scaling properties as the usual $C(\varepsilon)$ [26]. Gaussian kernel correlation integral $C_G(\varepsilon)$ can be obtained from usual $C(\varepsilon)$ via

$$C_G(\varepsilon) = \frac{1}{2\varepsilon^2} \int_0^{\infty} d\tilde{\varepsilon} e^{-\frac{\tilde{\varepsilon}^2}{4\varepsilon^2}} \tilde{\varepsilon} C(\tilde{\varepsilon}) \quad (11)$$

If $C(\varepsilon)$ is given at discrete values of ε, the Gaussian kernel correlation integral $C_G(\varepsilon)$ can be carried out numerically by interpolating $C(\varepsilon)$ with pure power laws [25].

2.5 Entropies

Entropies are an information theoretical concept to characterize the amount of information needed to predict the next measurement with a certain precision. The most popular one is the Kolmogorov-Sinai entropy. When analyzing time series we are usually dealing with distributions of delay vectors with delay τ in an m-dimensional reconstructed phase space. The m dependence of correlation integral C_q in the limit of large m can then be expressed as

$$C_q(m,\varepsilon) \underset{\substack{\varepsilon \to 0 \\ m \to \infty}}{=} \alpha m e^{-(q-1)h_q \tau m} \varepsilon^{(q-1)D_q} \quad (12)$$

which defines the order q entropy h_q. [25] Second order entropy is called Kolmogorov entropy. An algorithm for the determination of the Kolmogorov entropy is given in Cohen et Procaccia [27].

2.6 The 0-1 test for chaos

A new test for the presence of deterministic chaos was developed by Gottwald et Melbourne [28]. Their '0 - 1' test for chaos takes as input a time series of measurements, and returns a single scalar value usually in the range 0 - 1. The '0 - ' test does not depend on phase space reconstruction but rather works directly with the time series given. The input is the time-series data and the output is 0 or 1, depending on whether the dynamics is non-chaotic or chaotic.
Briefly, the 0-1 test takes as input a scalar time series of observations $\varphi_1, \ldots, \varphi_N$. According Dawes et Freeland [29], first we must fix a real parameter c and construct the Fourier transformed series:

$$z_n = \sum_{j=1}^{n} \phi_j e^{ijc}, \quad n = 1,\ldots,N \quad (13)$$

Then we compute the smoothed mean square displacement:

$$M_c(n) = \frac{1}{N-p} \sum_{j=1}^{N-p} |z_{j+n} - z_j|^2 - \left(\sum_{k=1}^{N} \frac{\phi_k}{N} \right)^2 \frac{1-\cos nc}{1-\cos c} \quad (14)$$

Finally we estimate correlation coefficient to evaluate the strength of the linear growth

$$r_c = \frac{\mathrm{cov}(n, M_c(n))}{\sqrt{\mathrm{cov}(n,n)\,\mathrm{cov}(M_c(n), M_c(n))}} \quad (15)$$

2.7 Hurst exponent

Hurst exponent (*H)* is widely used to characterize some processes. Hurst exponent is used to evaluate the presence or absence of long-range dependence and its degree in a time-series. For more information see [24, 30, 31]. The Hurst exponent is a measure that has been widely used to evaluate the self-similarity and correlation properties of fractional Brownian noise, the time-series produced by a fractional Gaussian process [32]. We can describe self-similarity process following equation:

$$X(at) = a^H X(t) \quad (16)$$

where a is a positive constant, and H is the self-similarity parameter, for $0 < H < 1$.
We have used a methodology known as Rescaled Range analysis or R/S analysis. To calculate the Hurst exponent, one must estimate the dependence of the rescaled range on the time span n of observation. The Hurst exponent is defined in terms of the asymptotic behavior of the rescaled range as a function of the time span of a time series as follows:

$$E\left[\frac{R(n)}{S(n)}\right] = Cn^H \text{ as } n \to \infty \quad (17)$$

Where *[R(n)/S(n)]* is the rescaled range; *E[y]* is expected value; n is number of data points in a time series, C is a constant. For more information see [13].

2.8 Prediction

Most properties of chaotic systems are much more easily determined from the governing equations than from a time series. Unfortunately, the governing equations are usually not known, except for well controlled laboratory experiments. Analyzing an empirical model, and maybe synthetic time series data generated from it, can provide a valuable consistency test for the results of time series analysis. The best we can hope for when fitting a model to data is that the result comes close to the real underlying dynamics. Nevertheless, chaotic dynamical systems generically show the phenomenon of structural instability. This means that models with very similar characteristics may exhibit qualitatively different global dynamics, such as near to an attractor crisis. [6]

According [8], using the reconstructed phase space for m and τ, a functional relationship *f* between the current state *Y(t)* and future state *Y(t + T)* can be given as

$$Y(t+T) = f(Y(t)) \tag{18}$$

where *T* represents the number of time steps ahead that one wishes to perform the prediction. Function *f* represents the approximation to unknown dynamical system. It is shown that for sufficiently large values of the embedding dimension and if some additional conditions are satisfied, the reconstructed trajectory has the same topological and geometrical properties as the system's phase space trajectory [16]. This means that, if the conditions of Takens embedding theorem are met, this mapping captures some of the properties of the unknown dynamical system. The predictive mapping can be expressed as

$$Y(t+T) = f_p(Y(t)) \tag{19}$$

The aim is to find the predictor f_p, so that $y(t + T)$ can be predicted based on the reconstructed time series. If the time series is chaotic, then f_p is necessarily nonlinear. Several local and global approaches are available in the literature to find the function f_p [33].

The local linear fits are very flexible, but can go wrong on parts of the phase space where the points do not span the available space dimensions and where the inverse of the matrix involved in the solution of the minimization does not exist. Moreover, very often a large set of different linear maps is unsatisfying. Therefore many authors suggested fitting global nonlinear functions to the data, i.e. to solve

$$\sigma^2 = \sum_n (s_{n+1} - f_p(s_n))^2 \tag{20}$$

where f_p is now a nonlinear function in closed form with parameters *p*, with respect to which the minimization is done. The results depend on how far the chosen ansatz f_p is suited to model the unknown nonlinear function, and on how well the data are deterministic at all. [26]

Experiment 1. RBF model where f_p is modeled by radial basis functions. A radial basis function (RBF) is a real-valued function whose value depends only on the distance from the origin, or alternatively on the distance from some other point y_i, called a center, so that

$$\Phi(y, y_i) = \Phi(\|y - y_i\|) \tag{21}$$

Gaussian kernel is used in this analysis.

$$\Phi(y, y_i) = e^{-c^2\|y-y_i\|^2} \tag{22}$$

Hence the prediction made is:

$$x_{t+1} = a_0 + \sum_{i=1}^{n} a_i e^{-(c\|y-y_i\|)^2} \tag{23}$$

Experiment 2. Polynomial model where f_p is modeled by polynomial

$$P(x) = \sum_{i=0}^{n} a_i x^i \tag{24}$$

where *n* is a natural number, the coefficients $a_0, \ldots, a_n$ are elements of *R*, and *X* is a formal symbol, whose powers X^i are just placeholders for the corresponding coefficients a_i, so that the given formal expression is just a way to encode the sequence $(a_0, a_1, \ldots)$, where there is an *n* such that $a_i = 0$ for all $i > n$. *n* is called order of polynomial.

3 Main results

We will use the mutual information approach to determine the time delay τ and the false nearest neighbor method to determine the minimal sufficient embedding dimension *m*. This approach is described in chapter 2.1. τ is estimated from the graph in Fig. 3. The first minimum of the mutual information function $I(\tau)$ (2) marks the optimal choice for the time delay. Thus, the time delay τ is 5.

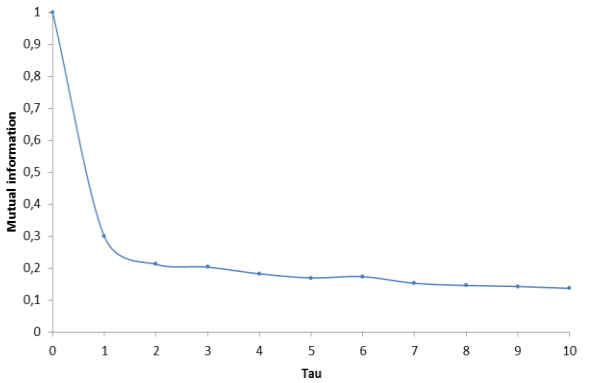

Figure 3: Mutual average information for the O_3 series

The embedding dimension *m* is chosen using the "false nearest neighbors'" method, estimated from the graph in Fig. 4. The minimum embedding dimension capable of containing the reconstructed attractor is that for which the percentage of false nearest neighbors drops to zero for a given tolerance level μ. Thus, the embedding dimension *m* is 6.

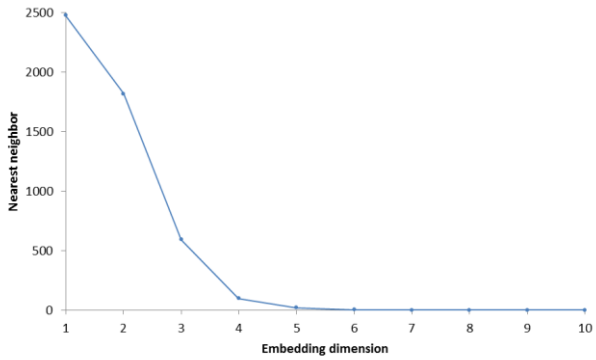

Figure 4: Fraction of false nearest neighbors for the O3 series

We used the Rosenstein algorithm for calculation the largest Lyapunov exponent. The calculation of the largest Lyapunov exponent depends on the estimation of the embedding dimension. The value of the largest Lyapunov exponent was estimated at 0,0014 for embedding dimension 6 and time delay 5. A positive largest Lyapunov exponent is one of the necessary conditions for chaotic behavior. Notice that the largest Lyapunov exponent is relatively small. Consequently, the rate of O_3 concentration evolution is rather slow, showing that it is possible to accurately make a short-term forecast.

Estimation of the correlation dimension is based on relationship between the Gaussian kernel correlation integral $C_G(\varepsilon)$ and radius ε on ln-ln scale with embedding dimensions m from 1 to 6 is shown in Fig 5. The saturation value of the correlation dimension for O_3 concentration time series is 5,24. The value of the Kolmogorov entropy nitrogen dioxide concentration time series was calculated at 8,13 for embedding dimension 6.

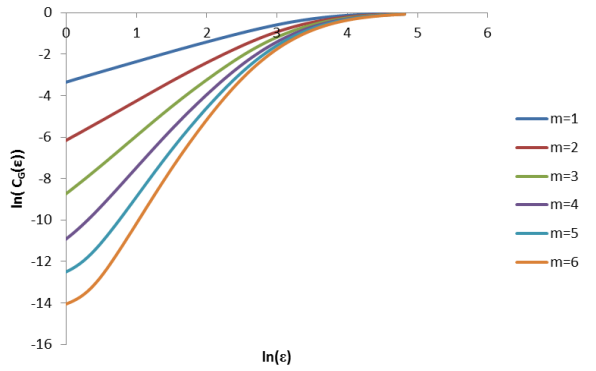

Figure 5: Ln $C_G(\varepsilon)$ versus ln(ε) plots for ozone concentration time series

Then we calculated the correlation coefficient for the 0-1 Test for Chaos. The value of the correlation coefficient was computed at 0,96. The correlation coefficient is near to 0 for non-chaotic data and near 1 for chaotic data. The value of correlation coefficient 0,96 is closer to 1. Hence we can assume to chaotic behavior in the O_3 concentration time series.

The Rescaled Range analysis gave us the value of the Hurst exponent 0,87. The value indicates the present of long memory in O_3 time series and it is in accordance with our expectation. We know that the value of H is between 0 and 1, whilst real time series are usually higher than 0,5. If the exponent value is close to 0 or 1, it means that the time-series has long-range dependence. We can assume that the true value lies somewhere between those values. We think that those values are sufficient for a credible prediction. Now we also know that the fractal dimension $D_F = 2\text{-}H$. We have estimated the value of the fractal dimension 1,13.

PREDICTION

Finally we have computed predictions using a Gaussian radial basis function and polynomials to fit global nonlinear functions to the data. Forecasts are displayed in Fig. 6.

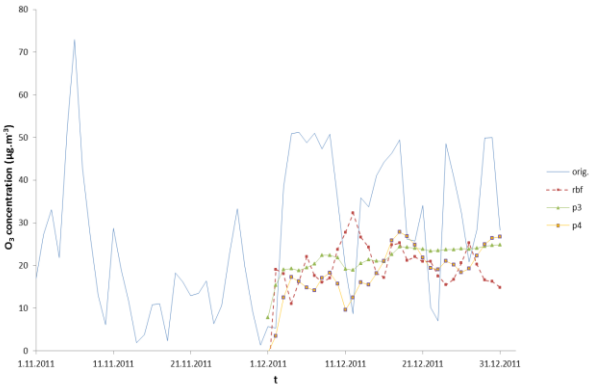

Figure 6: Prediction of ozone concentration time series using RBF and polynomials

Forecast error of Gaussian radial basis function fit is 0,654 and forecast error of polynomial fit is 0,598 for order 3 and 0,617 for order 4.

4 Conclusion

We have shown in this paper that the nitrogen dioxide concentration time series is chaotic and contains long memory. First, we computed the values of the time delay $\tau = 5$ and the embedding dimension $m = 6$. The estimated largest Lyapunov exponent is 0,0014. If the correlation dimension is low, the largest Lyapunov exponent is positive and the Kolmogorov entropy has a finite positive value, chaos is probably present. The application of 0-1 test suggests the presence of chaos as well. From these estimations it can be concluded that O_3 concentration time series is chaotic. Finally we have computed predictions using a Gaussian radial basis function and polynomials to fit global nonlinear functions to the data.

References

[1] Tropospheric ozone in the European Union, The consolidated Report, Luxembourg, 1999

[2] Baťa, R.; Půlkrábková, P. The importance of Modelling the Environmental Impacts of a Biomass Based Electric Power Generation for public safety. WSEAS Transactions on Environment & Development, 9(4), 2013

[3] Health Aspects of Air Pollution with Particulate Matter, Ozone and Nitrogen Dioxide. WHO-Europe report, Bonn, 2003

[4] Abarbanel, H. D. I.: Analysis of Observed Chaotic Data. Springer, New York, 272 pp., 1996.

[5] Kantz, H. and Schreiber, T.: Nonlinear time series analysis. Cambridge University Press, Cambridge, 304 pp., 1997.

[6] Miksovsky, J.; Raidl, A. Testing the performance of three nonlinear methods of time series analysis for prediction and downscaling of European daily temperatures. Nonlinear Processes in Geophysics, 2005, 12.6: 979-991.

[7] Chelani, A., B.; Singh, R., N.; Devotta, S. Nonlinear dynamical characterization and prediction of ambient nitrogen dioxide concentration. Water, air, and soil pollution, 2005, 166.1-4: 121-138.

[8] Abarbanel, H. D., Brown, R., Sidorowich, J. J., & Tsimring, L. S. The analysis of observed chaotic data in physical systems. Reviews of modern physics, 1993, 65.4: 1331.

[9] Abdul-Wahab, Sabah A., and Saleh M. Al-Alawi. "Assessment and prediction of tropospheric ozone concentration levels using artificial neural networks." Environmental Modelling & Software 17.3 (2002): 219-228.

[10] Sousa, S. I. V., Martins, F. G., Alvim-Ferraz, M. C. M., & Pereira, M. C. (2007). Multiple linear regression and artificial neural networks based on principal components to predict ozone concentrations. Environmental Modelling & Software, 22(1), 97-103.

[11] Bandyopadhyay, G., & Chattopadhyay, S. (2007). Single hidden layer artificial neural network models versus multiple linear regression model in forecasting the time series of total ozone. International Journal of Environmental Science & Technology, 4, 141-149.

[12] Chen, J. L., Islam, S., & Biswas, P. (1998). Nonlinear dynamics of hourly ozone concentrations: nonparametric short term prediction. Atmospheric environment, 32(11), 1839-1848.

[13] Koçak, K., Şaylan, L., & Şen, O. (2000). Nonlinear time series prediction of O_3 concentration in Istanbul. Atmospheric Environment, 34(8), 1267-1271.

[14] Chattopadhyay, G., & Chattopadhyay, S. (2008). A probe into the chaotic nature of total ozone time series by correlation dimension method. Soft Computing, 12(10), 1007-1012.

[15] Kříž, R.; Kratochvíl, Š. Analyses of the Chaotic Behavior of the Electricity Price Series. In: ISCS 2013: Interdisciplinary Symposium on Complex Systems. Springer Berlin Heidelberg, 2014. p. 215-226.

[16] Weng, Y. C., Chang, N. B., & Lee, T. Y. (2008). Nonlinear time series analysis of ground-level ozone dynamics in Southern Taiwan. Journal of environmental management, 87(3), 405-414.

[17] Takens, F. Detecting strange attractors in turbulence. In: Dynamical systems and turbulence, Warwick 1980. Springer Berlin Heidelberg, 1981. p. 366-381.

[18] Kodba, S., Perc, M., Marhl, M. Detecting chaos from a time series. European journal of physics, 2005, 26.1: 205.

[19] Fraser, A. M., Swinney, H. L. Independent coordinates for strange attractors from mutual information. Physical review A, 1986, 33.2: 1134.

[20] Kennel, M., B., Brown, R., Abarbanel, H., D. Determining embedding dimension for phase-space reconstruction using a geometrical construction. Physical review A, 1992, 45.6: 3403.

[21] M. Casdagli, Nonlinear prediction of chaotic time series, Physica D 35, 335 (1989)

[22] Lorenz, H. W. Nonlinear dynamical economics and chaotic motion. Berlin: Springer-Verlag, 1993.

[23] Rosenstein, M., T., Collins, J., J., De Luca, C., J. A practical method for calculating largest Lyapunov exponents from small data sets. Physica D: Nonlinear Phenomena, 1993, 65.1: 117-134.

[24] Grassberger, P., Procaccia, I. Characterization of strange attractors. Physical review letters, 1983, 50.5: 346-349.

[25] Schreiber, T. Interdisciplinary application of nonlinear time series methods (1999) Physics Report, 308 (1), pp. 1-64

[26] Hegger, R., Kantz, H., Schreiber, T. Practical implementation of nonlinear time series methods: The TISEAN package (1999) Chaos, 9 (2), pp. 413-435.

[27] Cohen, A., Procaccia, I. Computing the Kolmogorov entropy from time signals of dissipative and conservative dynamical systems, Phys. Rev. A 31 (1985) 1872.

[28] Gottwald, G., A., Melbourne, I. A new test for chaos in deterministic systems. Proceedings of the Royal Society of London. Series A: Mathematical, Physical and Engineering Sciences, 2004, 460.2042: 603-611.

[29] Dawes, J., H., P.; Freeland, M., C. The '0–1 test for chaos' and strange nonchaotic attractors. preprint, 2008.

[30] HURST, H., E.,: "Long term storage capacity of reservoirs". Trans. Am. Soc. Eng. 116: 770–799, 1951.

[31] Kříž, R., Chaotic Analysis of the GDP Time Series. In: Nostradamus 2013: Prediction, Modeling and Analysis of Complex Systems. Springer International Publishing, 2013. p. 353-362.

[32] MANDELBROT, B., B., NESS VAN, J., W.,: Fractional Brownian motions, fractional noises and applications. SIAM Rev. 10, pp. 422, 1968.

[33] Farmer, D., J., Sidorowich, J., J. 1987, 'Predicting chaotic time series', Phys. Rev. Lett. 59, 85–848.

Proceedings of ICCSA 2014
Normandie University, Le Havre, France - June 23-26, 2014

ON THE STUDY OF PERIODIC SOLUTIONS IN THE HODGKIN-HUXLEY MODEL

A. Balti, V. Lanza and M. Aziz-Alaoui *

Abstract. The Hodgkin-Huxley equations are the most accepted and one of the most complete neuronal model in literature. It is well known that, depending on the value of the external stimuli current, it exhibits periodic solutions, both stable and unstable.
Our aim is to detect and characterize such periodic solutions, exploiting a robust and manageable collocation method.
Keywords. Hodgkin-Huxley model, periodic solutions, collocation method.

1 Introduction

In Neuroscience, several mathematical models for describing the neurons activity have been proposed. However, the 1952 paper by Hodgkin ans Huxley [1] on the physiology of the giant axon of the squid remains a milestone in the science of nervous system and at present many of its properties still have to be disclosed.

It is known [6, 2, 10] that, depending on the value of the external current stimuli I, the Hodgkin-Huxley (HH) model exhibit periodic solutions. Moreover, for a certain range of I, it shows hard oscillations, that is a coexistence of a stable equilibrium and a stable limit cycle. Thus, this implies the existence of unstable periodic solutions in order to separate the two basins of attraction. Few authors have been able to characterize these periodic solutions [6, 2, 10], how they emerge and disappear depending on the parameter I.

In general, it is not an easy task to detect a periodic solution of a nonlinear dynamical system. Several methods are exploited to predict the existence of limit cycles and to study their stability, both in time and frequency domain [8, 7, 9]. In particular, for the HH model, this is even more difficult due to the high nonlinear structure of the system.

Our aim is to characterize the periodic solutions of the HH model, exploiting a collocation method that have been revealed to be numerically very robust and really handy.

The paper is structured as follows: in section 2 we present the equations of the Hodgkin-Huxley model and its dynamical properties, depending on the value of the external current I. In section 3 the collocation method we have exploited is briefly explained. In Section 4 we show how it is possible to detect and characterize the periodic solutions of the HH model.

*A. Balti, V. Lanza and M. Aziz-Alaoui are with Laboratoire de Mathématiques Appliquées du Havre, Université du Havre, France. E-mails: aymen.balti@univ-lehavre.fr, valentina.lanza@univ-lehavre.fr, aziz.alaoui@univ-lehavre.fr

2 The Hodgkin-Huxley model

The Hodgkin-Huxley model for a neuron consists in a set of four nonlinear ordinary differential equations in the four variables $X = (V, m, h, n)$, where V is the membrane potential, m and h are the activation and inactivation variables of the sodium channel and n is the activation variable of the potassium current. The corresponding equations are the following [5, 4]:

$$\begin{aligned}
C\frac{dV}{dt} &= I - (120m^3h(V-50) + 36n^4(V+77) + 0.3(V-54.4)) \\
\frac{dn}{dt} &= \frac{1}{10}(1-n)\mathrm{expc}\left(\frac{-55-V}{10}\right) - \frac{1}{8}n\,\exp\left(\frac{-V-65}{80}\right) \\
\frac{dh}{dt} &= (1-h)\mathrm{exp}\left(\frac{-V-65}{20}\right) - \frac{h}{1+\exp\left(\frac{-V-35}{10}\right)} \\
\frac{dm}{dt} &= (1-m)\mathrm{expc}\left(\frac{-40-V}{10}\right) - 4m\,\exp\left(\frac{-V-65}{18}\right),
\end{aligned} \tag{1}$$

where I is the external current stimulus and

$$\mathrm{expc}(x) = \begin{cases} \dfrac{1-x}{\exp(x)} & \text{if} \quad x \neq 0 \\ 1 & \text{if} \quad x = 0. \end{cases}$$

It is worth noting that the numerical values of the different parameters in (1) are not the common ones found in literature [2, 6]. This set of parameters has been provided in the original HH paper [1], but then the Authors decided to shift the membrane potential in order to have the resting potential at $V \approx 0$ mV. According to [4], we have chosen the parameters such that the membrane potential is back to its natural value, that is $V \approx -65$ mV. It is possible to see that this choice does not change the dynamical behaviors of the model.

For small values of the current stimulus I the system exhibits a stable equilibrium point. If I is increased, then a stable large amplitude periodic solution appears, while

the equilibrium point remains stable. This means that necessarily unstable solutions are present, in order to separate the two basins of attraction. In [2], the Author shows that, depending on the value of I the HH model presents from one to three unstable limit cycles. Moreover, in a certain range of values of I the equilibrium point becomes unstable, but finally the stable periodic solution disappears through an Hopf bifurcation and the equilibrium point regains its stability.

At present, few works about the periodic solution of the HH model are present in literature [2, 6, 10], since due to the high dimension of the system and to its high nonlinearity it is not an easy task. They approached it exploiting different methods (finite differences, collocation or shooting methods), that are not so simple to handle. Moreover, in all these papers only the "old" version of the HH model [1] has been considered.

Our aim is to characterize and numerically approximate all the periodic solutions exhibited by the HH model 1. We exploit a collocation method that is numerically very robust and extremely handy.

3 A collocation method for the detection of periodic solutions

Let us consider a dynamical autonomous system

$$\dot{x} = f(x) \tag{2}$$

where f is a vector field defined on $\mathbb{R}^n$, $n \geq 1$, and $x \in \mathbb{R}^n$. A solution $x = X$ of a continuous-time system is periodic with least period T if $X(t+T) = X(t)$ and $X(t+\tau) \neq X(t)$ for $0 < \tau < T$. This periodic solution X of least finite period $T > 0$ of the system corresponds to a closed orbit Γ in $\mathbb{R}^n$ and is such that by specifying the initial time t_0, one specifies a location $x = x_0$ on the orbit.

It is interesting to notice that searching a periodic solution of an ODE is equivalent to the resolution of a boundary-value problem (BVP). In fact, if $x = X$ is a T- periodic solution of (2), then it is solution of the following problem:

$$\begin{cases} \dot{X} = f(X) \\ X(0) = X(T). \end{cases} \tag{3}$$

This problem belongs to the general class of nonlinear boundary value problems and several methods have been proposed in literature to solve it [8]. The more intuitive one is probably the shooting method. The idea is to find an initial condition X_0 and a period T such that $X(0) = X_0 = X(T)$, where the unknown is the couple (X_0, T), with $X_0 \in \mathbb{R}^n$ and $T \in \mathbb{R}+$. If we define the functional G as

$$G(X_0, T) = \varphi(X_0, T) - X_0,$$

where $\varphi(X_0, T)$ is the solution of the Cauchy problem $\dot{X} = F(X)$ with the initial condition $X(0) = X_0$, then it is straightforward to see that a periodic solution of (3) is a zero of G. Unfortunately, this methods fails when the limit cycle under study is unstable, due to the errors of the numerical integration of the equations.

Since our purpose is to detect all the periodic solution of the HH model, both the stable and the unstable ones, we have decided to exploit a collocation method, that is independent on the stability of the periodic solutions under consideration. We briefly recall the main properties of this method.

First of all, since T is usually unknown, with a simple translation of the time scale, it is possible to transform (3) into an equivalent BVP on the interval $[0, 1]$:

$$\begin{cases} \dfrac{du}{d\tau} = Tf(u) \\ u(0) = u(1), \end{cases} \tag{4}$$

where τ is the new time variable. Clearly, a solution $u(\tau)$ of (4) corresponds to a T-periodic solution of (3). However, the boundary condition in (4) does not define the periodic solution uniquely. Indeed, any time shift of a solution to the periodic BVP (4) is another solution. Thus, an additional condition has to be appended to problem (4) in order to select a solution among all those corresponding to the cycle.

Our aim is to find a 1-periodic solution of (4). Moreover, we are interested in finding a function $u \in \mathcal{C}^1[0, 1]$, verifying the condition $u(0) = u(1)$. Let us introduce a partition of the interval $[0, 1]$ by $N + 1$ points:

$$0 = t_0 < t_1 < \cdots < t_N = 1,$$

with $h_i = t_i - t_{i-1}$. The collocation method consists in approximate the solution u by a piecewise-differentiable continuous function, that is a polynomial u_h of maximal degree m within each subinterval $[t_{j-1}, t_j]$, $j = 1, 1, \ldots, N$. Thus $u_h \in \mathbf{P}_h^m = \{u_h \in C[0, 1] : u_{h|_{[t_{i-1}, t_i]}} \in \mathbf{P}^m\}$, where $\mathbf{P}^m$ is the space of polynomials with degree less than or equal to m.

Furthermore, it is possible to represent the polynomial u_h exploiting the Lagrange interpolation

$$\forall\, \tau \in [t_{i-1}, t_i] \qquad u_h(\tau) = \sum_{j=0}^{m} u_h(\tau_{i,j}) l_{i,j}(\tau),$$

where $t_{i-1} = \tau_{i,0} < \tau_{i,1} < \cdots < \tau_{i,m} = t_i$ is a $m + 1$ points mesh of the subinterval $[t_{i-1}, t_i]$, and $l_{i,j}(x)$ are the Lagrange basis polynomials.

Finally, we require the approximate solution to satisfy exactly system (4) at the collocation points within each subinterval:

$$\frac{1}{T}\dot{u}_h(\tau_{i,j}) = f(u_h(\tau_{i,j})), \qquad i = 0, \ldots, N, j = 1, \ldots, m, \tag{5}$$

where T is the unknown period and $u_h(0) = u_h(1)$.

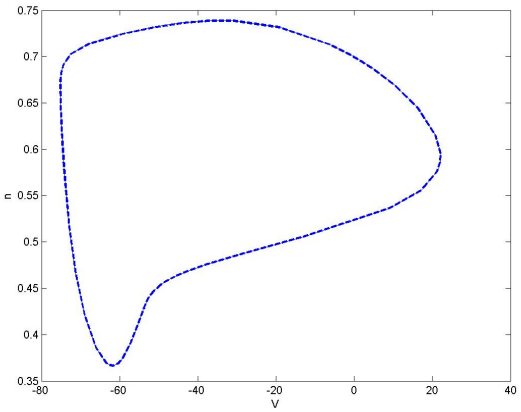

Figure 1: Stable and unstable periodic orbits of the HH model for $I = 6.320$.

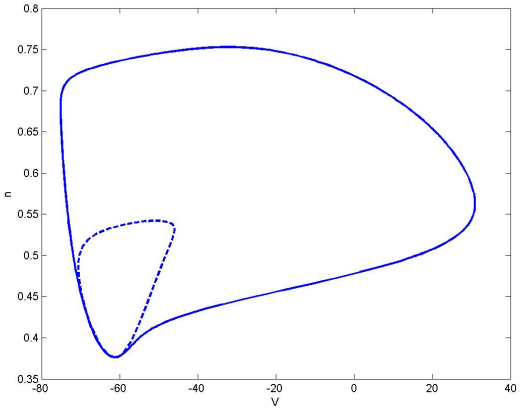

Figure 2: Unstable and stable periodic orbits of the HH model for $I = 7.820$.

4 Numerical detection of the HH periodic solutions

We recall that system (5) is undetermined, since we have the supplementary unknown T. In order to have a system with the same number of equations and unknowns, an additional condition is needed. In [10] the constraint $u_h(0) = U_0$ has been chosen, but unfortunately it is not adapted to follow bifurcation branches to fixed point. In this work, in order to select a solution among all those corresponding to the cycle, we have added as a constraint $\dot{u_h}(0) = 0$. It is worth noting that our constraint is verified whatever the solution is, either a periodic solution or an equilibrium point.

Moreover, in [6] the Authors exploited a collocation method implemented in the program AUTO [3], that is a collocation at equally spaced Gauss points. In this work, we have preferred to use the Matlab routine `bvp4c` [11], that can adapt the mesh by minimizing the residual $r(t) = u(t) - u_h(t)$. Since the HH model in a range of values of I exhibits a slow-fast dynamics, this permits to automatically refine the mesh only where it is necessary. We have remarked that this routine is numerically really robust and very manageable.

Table 1: Variation of the amplitude and period of both stable and unstable orbits for different values of I. Here, Am_{stable} and $Am_{unstable}$ are the amplitudes of the potential for the stable and unstable limit cycles, respectively. T_{stable} and $T_{unstable}$ are the periods of the stable and unstable limit cycles, respectively.

I	Am_{stable}	$Am_{unstable}$	T_{stable}	$T_{unstable}$
6.320	103.8842	97.3027	18.9646	21.2264
6.420	104.7232	91.5178	18.4484	22.3958
6.520	105.1503	85.7421	18.1155	23.2433
6.620	105.4244	80.7009	17.8558	23.8839
6.720	105.6148	75.0726	17.6377	24.3748
6.820	105.7550	69.7699	17.4471	24.7466
6.920	105.8639	64.8818	17.2762	25.0208
7.020	105.9430	59.8255	17.1205	25.2095
7.120	106.0028	55.3818	16.9768	25.3175
7.220	106.0504	50.9684	16.8429	25.3430
7.320	106.0824	47.0067	16.7173	25.2809
7.420	106.1030	43.4585	16.5987	25.1249
7.520	106.1186	40.1920	16.4861	24.8665
7.620	106.1248	37.1229	16.3790	24.4894
7.7200	106.1248	34.1702	16.2766	23.9542
7.8200	106.1193	30.8899	16.1784	23.1437

In this paper, we concentrate on the study of the HH model for low values of the input current stimuli I. In Figures 1 and 2 the detected stable and unstable periodic solutions for different values of I are shown. In Figure 1, we notice that the two solutions are very close. It is possible to see that this is due to the occurrence of a global bifurcation: for $I < 6.320$ the HH model exhibits only a stable equilibrium point, then by increasing I two limit cycles (one stable and one unstable, respectively) arise. Thus, for a certain range of I, the HH model behaves as an hard oscillator [4].

In Table 1 for different values of I the period and the amplitude for the stable and unstable limit cycles, respectively, are shown. As it is easy to notice, the period $T_{unstable}$ of the unstable limit cycle increases until the value of $I = 7.220$, while its amplitude is always decreasing. On the contrary, for the stable solution the period decreases with the increase of I, and this phenomenon is due to the slow-fast behavior of vector fields of the HH model.

Moreover, it is worth noting that the period of the un-

stable orbit is always greater than that of the stable one. It means that the unstable solution is always slower than the stable one. This information is important for the implementation of the numerical method. In fact, we start from the stable periodic solution and we increase the period of the guess for the routine `bvp4c`, in order to converge to the unstable one.

5 Conclusions

In 1952 Hodgkin and Huxley developed the pioneer and still up-to-date mathematical model for describing the activity of the giant squid axon. Depending on the value of the external current stimuli, this fourth-order nonlinear dynamical system exhibits many complex behaviors, such as multiple periodic solutions (both stable and unstable) and chaos. In this paper, we have characterized the periodic solutions that arise in the HH model through an extremely handy collocation method. In future works we envisage to detect the periodic solutions of the HH model for all the values of I, in order to obtain the corresponding bifurcation diagram.

References

[1] A. L. Hodgkin, A. F. Huxley, "A quantitative description of membrane current and its application to conduction and excitation in nerve", *J. Theor. Biol.*, vol. 71, pp. 401-420, 1978.

[2] B. Hassard, "Bifurcation of periodic solutions of the Hodgkin-Huxley model for the squid giant axon", *The Journal of physiology*, vol. 117(4), pp. 500-544, 1952.

[3] E. Doedel, H. B. Keller, and J. P. Kernevez, "Numerical analysis and control of bifurcation problems I", *Internat. J. Bifur. Chaos Appl. Sci. Engrg.*, vol. 1, pp. 493-520, 1991.

[4] E. Izichevich, *Dynamical systems in neuroscience*, MIT Press, 2007.

[5] G. B. Ermentrout, D. H. Terman *Mathematical Foundations of Neuroscience*, Springer, 2010.

[6] J. Guckenheimer, R. A. Oliva, "Chaos in the Hodgkin-Huxley model," *SIAM J. Applied Dynamical Systems*, vol. 1, no.1, pp. 105-114, 2002.

[7] K. S. Kundert, K. J. White, A. Sangiovanni-Vincentelli, *Steady-state methods for simulating analog and microwave circuits*, Kluwer Academic Publishers, Boston, 1990.

[8] Y. A. Kuznetsov, *Elements of applied bifurcation theory*, Springer, New York, 1998.

[9] R. E. Mickens, *Truly nonlinear oscillations: harmonic balance, parameter expansions, iteration, and averaging methods*, World Scientific, 2010.

[10] J. Rinzel, R.N. Miller, "Numerical calculation of stable and unstable periodic solutions to the Hodgkin-Huxley equation", *Mathematical Biosciences*, vol. 49, pp. 27-59, 1980.

[11] L.F. Shampine, J. Kierzenka, M. W. Reichelt, "Solving boundary value problems for ordinary differential equations in MATLAB with bvp4c", *Tutorial Notes - Mathworks.com*, 2000.

Proceedings of ICCSA 2014
Normandie University, Le Havre, France – June 23-26, 2014

LOGISTIC MODEL FOR CUSTOMER DYNAMICS IN THE MOBILE TELECOMMUNICATION SECTOR.

Juan Carlos Pascual Medina[1]

Abstract. Starting from the last decade of the 90`s mobile phone makes its appearance in the world markets, in Mexico it`s also on that date that the first companies are formed, today there are only four mobile companies that compete strongly for the Mexican market, In this article we use the logistic model (S – shaped logistic curve), which describes competitive environments, especially for the popularization of new technologies, to describe the dynamics of the telecommunications sector in Mexico and the probability of the companies to fail and disappear in the market. In economic articles, we see more attention to the dynamics of monopolistic competition and power companies, but it is less used the study of the sales dynamics of the sector and the curves that represent it. The proposed model uses as data the total number of subscribers to mobile phone lines to generate the logistic curves of each company and the total market, in search of main points singularities and stability conditions as predictors of the extinction of technologies and the shot-down of companies in the sector.

Keywords. Complexity, Logistics, Telecommunications, Stochastic, Dynamics, Economy

1 Introduction

The mobile phone sector has been one of the major revolutions of the past 20 years, greatly facilitating communication among the entire population of the planet. The dynamism of growth in this sector is essential in many economies with growth of 2 to 4 times the country´s GDP growth. In Mexico, this sector has had close to 8% annual growth rates and now accounts for 3.2% of the GDP. Therefore, it represents a good case study of the adoption of new technologies in highly competitive environments and how the systems of competition and consumption in highly complex environments are.

In Mexico, the market is dominated by four large companies, Telcel, Movistar, Iusacell and Nextel, founded in the 90´s and has, 70%, 20%, 7% and 3% of the market respectively, the percentage of penetration of mobile telephony is near the 87 lines per 100 habitants, being a medium development country, compared to countries of high penetration such as Finland which has 172 lines per 100 habitants.

In this article we analyze the growth of the demand for telephones in Mexico and competition between companies; not only because of its great economic and financial relevance but for the interest it represents its practical application for companies competing and their actions to stay on the market. The model that we use for the study is the logistic curve in the S form, which is a mathematical function that appears in different models of population growth, spread of epidemic diseases and broadcast in social networks. This model is a refinement of the exponential model for one magnitude growth. Logistic growth is related to the exponential growth for small initial values of the magnitude, the logistic growth is very similar to exponential growth; however, from a certain point the growth is diminished and is tending to grow and reach a point of minimal growth. This makes the curve can adequately represent different systems such as population growth, the spread of rumors, the spread of social networks, epidemics or spread of diseases and in our case study on the extension of a technological innovation; at first innovation is a novelty of difficult access for

[1] Author is with the Centro Universitario Incarnate Word, México DF, México. E-mail:jcpascual@ciw.edu.mx

consumers, but as there is a cost decrease it spreads rapidly for each new user and innovation is likely to influence another individual having contact with him, but as the number of users grows it is more difficult to find a person who has not previously been in contact with innovation.

The model presented in this study uses public information of users of mobile telephony in Mexico and other countries as we compare, available from several sources of statistical information and of the telecommunications sector as well as the public reports of the company listed above.

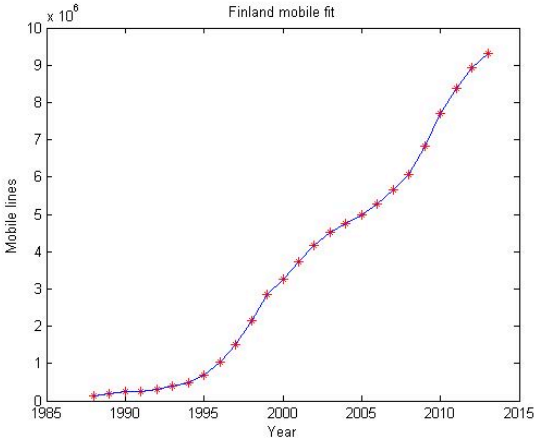

Figure 1: Finland mobile lines

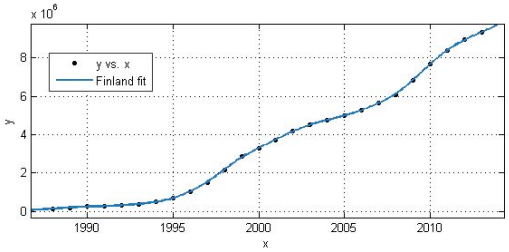

Figure 1a: Finland smoothed spine fit curve, R-square = 1

2 Problem statement and preliminaries

2.1 Model

The classical model of the logistic equation was developed by Pierre Francoise Verhulst, combining the hypothesis of exponential growth with the mechanical hypothesis, raised in 1838 the differential equation:

$$dP(t) = hP(t) - k[P(t)]^2\, dt \qquad \textbf{(1)}$$

Whose analytical solution is:

$$P(t) = \frac{a}{1+ be^{-ht}} \qquad (2)$$

In practice it is convenient to use the population at the beginning of each period, which is indicated by $P0$ by which it has finally the traditional form of the logistic equation:

$$P(t) = P_0 + \frac{K}{1+ e^{-ht}} \qquad (3)$$

$$\lim_{t\to\infty} P = K$$

Equation 3 shows that the rate of change in a population increases exponentially in time, but having a inflexion point midway through its symmetry which begin to reduce its growth until you reach a limit at K, the maximum capacity of the system or superior limit, the dynamic is driven by h, the growth rate of the system.

The logistic model can be adapted to the process of assimilation of new technology easy and clearly, since from a starting point of zero, in our case will be the moment of the first mobile phone that go to the public, begins the adoption of few users who are willing to buy them because of its high price, then as the demand increase and the understanding of the use of this technology, production volumes increase and the lower prices are seen in the market, resulting in the high exponential growth phase. As the technology reaches ma-

turity the baste majority of the population are users, and only a small fraction of the population is left, the growth is diminishing and approaching to its upper limit where the growth stops.

2.2 Methods

The system dynamics in the adoption of a new technology by various manufacturers and a population bounded by social and economic factors can be think as a self organizing complex system, in which we mainly propose an analysis by visualization of dynamic patterns, since the data plotted, show curves with very little statistical noise.

In addition, in order to find the best fit curve and the parameters which characterize each of the companies we use Matlab Curve fitting tools.

For the information of mobile lines we use the paid numbers in the market; we use primarily country data for Mexico and Finland, since we believe that Finland is the best example of adoption of mobile technology and one of the first in which has developed, they have Nokia as mobile phone manufacturer and is highly developed country. The information was obtained from data bases from the World Bank, and Finland statistics, and in Mexico´s from INEGI (National Institute of Statistics), since 1988 until 2013.

For each company the public financial reports and data from the National Institute of telecommunications were consulted, from 2001 up to date.

3 Main results

To validate the use of the proposed model, we will first consider the graph of each case interpretation. The case of Finland is especially useful since it was one of the first countries to adopt the new technology in a country manufacturer of mobile phones, having a very well educated population and concentrated in cities as well as being up-to-date with technological changes.

As shown in Figure 1. From 1988 to 2005 the data line is smooth fitted, without statistical noise and clearly looks a sigmoid shape which refers without doubt an implicit logistic model, from 2005-2013 again appearing further sigmoid movement suggests a new logistic model. When we see this type of paths, there is a clear cluster addition of two groups, in this represents the adoption of a new technology or use associated with the purchase of another line, this effect can have several causes such as, the use of tracking devices in vehicles, PDA`s, and more recently the appearance of tablets. Adjustment of the curve using Smoothing spline method is shown in Figure 1a, in which we have a value for adjusted data with R-square equal 1.

Figure 2 shows the results for the Mexico case, it can be seen that the entry into the mobile phone takes time to achieve affordable prices, this around the year 2000 when begins its exponential growth, this effect of slow boot shadows the appearance of the effect that was seen in Finland in 2005 of new growth stage and is not visible in graphic form rather than as a very high slope of growth. For the year 2013 already we can see that rapid growth has stopped and begins to approach its maximum limit which will be close to 100 lines per 100 inhabitants, since Mexico is a country with 30% in extreme poverty, represents a high population that without improving their conditions ever will be a user of the service. The smooth adjustment, fig 2a, shows an R-square value of 0.9999 that confirm the good fit of this model in the country accumulated statistics.

From Figure 3 shows the data for each of the four mobile companies that are in Mexico.

Telcel, Figure 3, is the dominant competitor and as it was expected due to having 70% of the market, is almost the same as the shape of the country`s curve, however this curve can be seen more smoothed and with less noise, so it resembles more to the behavior of Finland and the perfect logistic model. R-square value of 0.9998, fig 3a, is the result of the smooth curve

for the company, as expected a high and close value to the country data.

Figure 4 belongs to the smaller competitor, Iusacell, recently this company has been immersed in negotiations with various companies shareholders and which maintains a policy of low rates to find the low population segment, up to now its curve is clearly in expansion and in exponential form, without being able to say when will be in a turning point to take the expected sigmoidal behavior, but that it should be in a maximum of two years more because the country is already reaching its maximum penetration level. The smooth curve, fig 4a, had a value for R-square of 0.9998, logic to be as there is almost a perfect exponential curve.

The case of Movistar, Figure 5, is in direct competition with Telcel but entered late to market by way of purchase of other companies with bad coverage service and reflects a slow growth curve. It is very significant that it has reached in 2010 a maximum, decrease in 2011 & 2012 and slight recovery to 2013. This behavior in recent years move them away from a smooth sigmoidal curve and requires more detailed studies to understand the reason of their diversion to the observed logistic model. R-square value of 0.9988, fig 5a, remains as a good fit for the logistic model that take in consideration the flat part of the last 2 year as noise to be filtered.

Finally the most interesting case is presented with Nextel, Figure 6; Nextel is the only competitor that uses a different connection from the standard CDAM and GSM technology, IDEN technology to provide trucking services. Its target market was more for the business users and as you can see from the beginning they have good growth according to the logistic model, however, the entry of 3G and 4G platform systems as well as Smartphone's began to give warning signs to the company. Nextel began to have coverage problems and service quality that made the company think that the way forward to restore growth should be changing standard connection and migrate into 4G platform. The logistic model, however, can be confused in its initial stage with models of growth extinction, such as the epidemic, that present a strong demand fall, that can generate a massive departure of costumers and the disappearance of this technology or the company. This case which was predictable in the year 2011 is confirmed with the recent data from 2013, is seen clearly that it is the only company with a net loss of lines in the order of 5.3%, which is above the 2% on average, seen as "churn" effect in the mobile market. The result for the smooth curve, fig 6a, R-square value of 0.9979, is the lowest of all but remains as a good fit for the logistic model, only that is the fall down in users continue in 2014 we will be in the case of a Poisson model indeed.

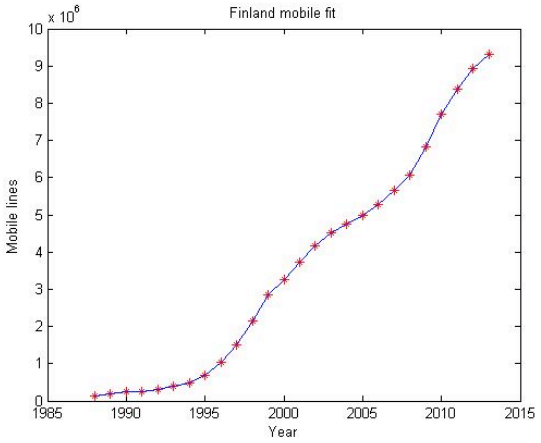

Figure 1: Finland mobile lines

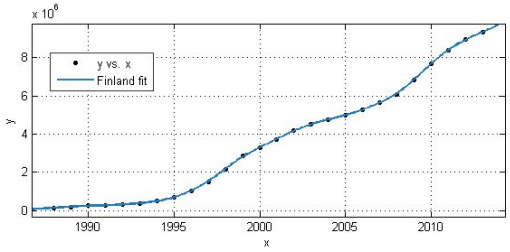

Figure 1a: Finland smoothed spine fit curve, R-square = 1

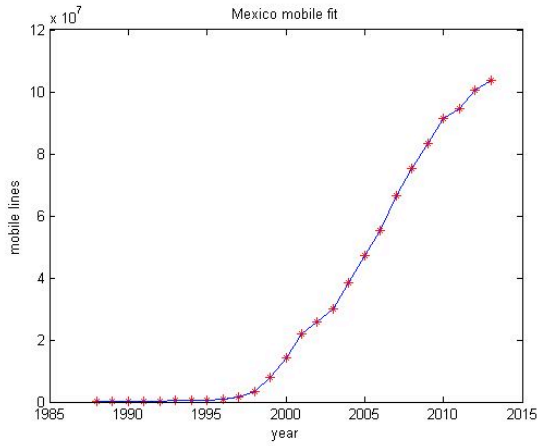

Figure 2: México mobile lines

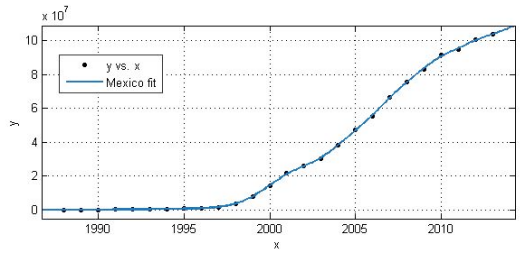

Figure 2a: Fig 2a: México smoothed spine fit curve, R-square = 0.9999

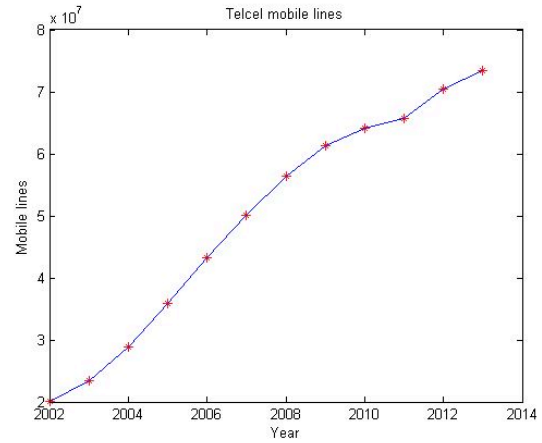

Figure 3: Telcel mobile lines in México

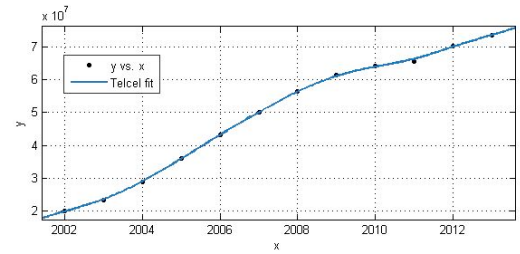

Figure 3a: Telcel smoothed spine fit curve, R-square = 0.9998

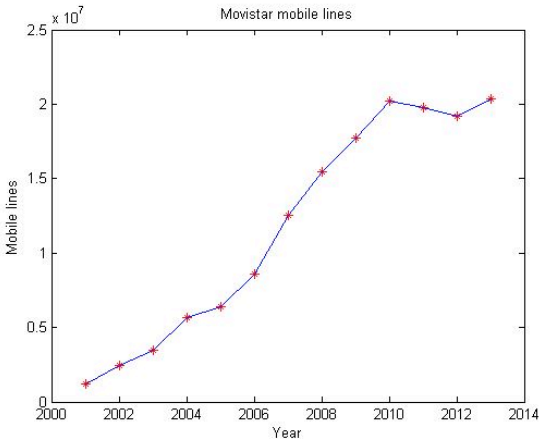

Figure 4: Movistar mobile lines in México

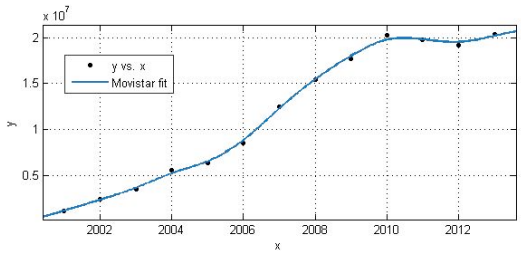

Figure 4a: 4a: Movistar smoothed spine fit curve, R-square = 0.9988

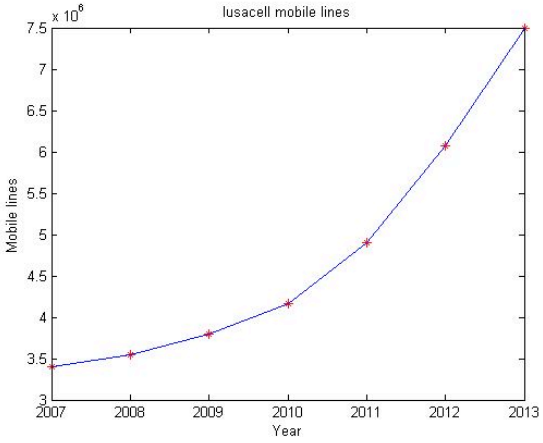

Figure 5: Iusacell mobile lines in México

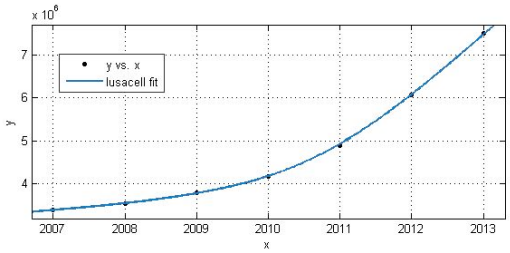

Figure 5a: sacell smoothed spine fit curve, R-square = 0.9998

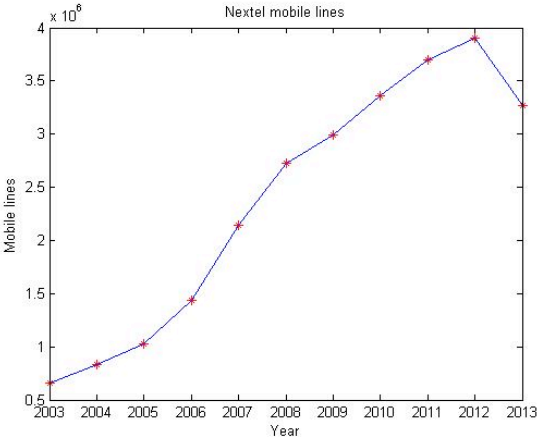

Figure 6: Nextel mobile lines in México

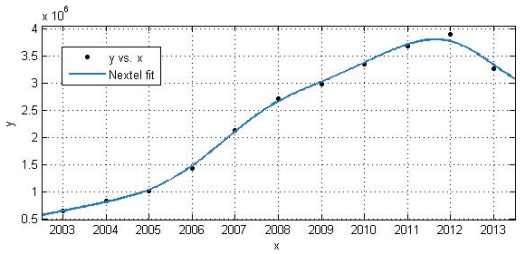

Figure 6a: Nextel smoothed spine fit curve, R-square = 0.9979

4 Application

The emphasis of this analysis becomes not in building and running a new model, but interpreting the logistic model as predictor of the dynamics of a system. In this study, we have applied the logistic model to explain the market behavior of mobile telephony in Mexico, Using public data market and companies; we have considered that to be a complex system we should use a graphic method to search for the validation to the model logistic use as a predictor of the system behavior. Both graphically and using curve deviation, the adjustment error is very low and we can conclude that the logistic model is useful to describe the behavior of new technologies present on the market. Extrapolation of this model into the future is a valuable element to be considered in the companies from these sectors to change the growth strategy to one of consolidation and maintenance of achieved customer base, but even more important is the ability of this model, to generate warning signals that prevent for a rapid and massive customer departure and the likely disappearance of the company..

The speed on which new emerging technologies arrive, will allow that in 2 more years this study confirms the need and validly to use the logistic model.

References

[1] L. Arnold, Stochastic Differential Equations: Theory and Applications, John Wiley and Sons, 1974.

[2] S. Boyd, L. E. Ghaoui, E. Feron, and V. Balakrishnan, Linear Matrix Inequalities in System and Control Theory, SIAM,Philadephia, 1994.

[3] Y. Y. Cao, Y. X. Sun, and C. Cheng, "Delay-dependent robust stabilization of uncertain systems with multiple state delays," IEEE Transactions on Automat. Control, vol. 43, pp. 1608- 1612, 1998.

[4] W.-H. Chen, Z. H. Guan, X. Lu, "Delay-dependent exponential stability of uncertain stochastic systems with multiple delays: an LMI approach," Systems Control Lett., vol. 54, pp. 547-555, 2005.

[5] D. Cheng, "Stabilization of planar switched systems", Systems Control Lett. vol. 51, pp. 79-88, 2004.

[6] J. Daafouz, P. Riedinger, C. Iung, "Stability analysis and con- trol synthesis for switched systems: a switched Lyapunov func- tion approach", IEEE Trans. Automat. Control, vol. 47, pp. 1883-1887, 2002.

General Session 7
Game Theory

Proceedings of ICCSA 2014
Normandie University, Le Havre, France - June 23-26, 2014

MIXED STRATEGIES AND ω-RATIONAL LANGUAGES PROBABILITY COMPUTATION

Mustapha Arfi and Carla Selmi *†

Abstract. We deal in this paper with the notion of mixed strategy on a finite alphabet A, which models probabilistic games. We show that a mixed strategy allows to define a probability measure on the family of Borelian sets in the topological space of infinite words on A. Finally, we give an explicit expression in order to compute effectively the probability of each rational language belonging to this family.

Keywords. Words, infinite words, formal languages, game theory, strategy, mixed strategy, probability, topology

1 Introduction

We propose in this article some mathematical tools allowing to analyze games in a probabilistic view. This work represents a logical continuation of references [1, 2]. We consider infinitely repeated games with a perfect knowledge of the past, involving players whose actions are supposed simultaneous. We model this kind of games by using infinite words on the alphabet of moves. Our study concerns cooperative games as well as non-cooperative ones, since we establish that the latter category represents in fact a particular case of the first one. To optimize their benefits in such games, the players must develop a suitable strategy. In [1], we have proceeded to a specific study of the notion of quasi-strategy, which is a relation that describes the behaviour of the players during the game. We have proved that a language is generated by a quasi-strategy if and only if it is closed in the topological space of infinite words. Our pourpose now is to attach the concept of probability to a strategy, which leads us to define the notion of mixed strategy, with which we associate a probability law on the set of finite words on the alphabet of moves. Then we make use of Kolmogorov extension theorem to the space of infinite words [3] to prove that such a law determines a unique probability measure on the class of Borelian ω-languages. Several examples are given in order to illustrate these new notions, among which the famous Prisonner's Dilemma. The most important result of this paper consists in giving an effective method which enables to compute the probability of a ω-rational language when the probability law is computable, as in the case of probability law defined by an automaton.

Our paper is organized in the following way: In Section 2, we recall the basic notions and properties on finite and infinite words, on the topological space of infinite words, on Borelian sets and on measures. We state, in Section 3, the Kolmogorov extension theorem to the space of infinite words. Section 4 is devoted to the mathematical model for games, which will be used in the sequel. Sections 5 and 6 deal respectively with global and individual mixed strategies. In Section 7, we show how to obtain the probability of open and closed sets when the probability law is computable, then we apply these results, in Section 8, to compute the probability of any Borelian language. Finally, in Section 9, we give an effective method to obtain the probability of ω-rational languages.

*Mustapha Arfi is with LITIS EA 4018, Université du Havre, UFR Sciences et Techniques, France, E-mails: mustapha.arfi@univ-lehavre.fr

†Carla Selmi is with LITIS EA 4018, Université de Rouen, France, E-mail: carla.selmi@univ-rouen.fr

2 Preliminaries

We recall in this section the basic notions and properties on finite and infinite words, on topological space of infinite words, on Borelian sets and on measures.

2.1 Finite and infinite words

A *word* is a finite sequence of elements of an alphabet A. We denote by A^* the set of all words on A. The *length* of a word $w \in A^*$, denoted by $|w|$, is the number of letters of A composing w. The empty word ε is the only word of length zero. We denote by A^k the set of all words in A^* of length k. Given two words $u, v \in A^*$, we say that u is a prefix of v iff $v \in uA^*$

An infinite word on A is an infinite sequence h of elements of A, which we will write $h = h_0h_1 \cdots h_t \cdots$. We denote by A^ω the set of all infinite words on A. Given a word $w \in A^*$ and an infinite word $h \in A^\omega$, we say that w is a *prefix* of h if there exists an infinite word $h' \in A^\omega$ such that $h = wh'$.

If L is a subset of A^ω, we denote by $Pref_k(L)$ the set of all words that are prefixes of length k of words of L. We set $Pref(L) = \bigcup_{i \geq 0} Pref_i(L)$. In the sequel, all the alphabets are supposed to be finite.

2.2 Topology of A^ω

We consider on the set A^ω the distance d defined as follows:

$$d(x,y) = (1+max\{|w| \mid w \in Pref(\{x\}) \bigcap Pref(\{y\})\})^{-1}$$

with the convention $1/\infty = 0$. Equipped with this distance, A^ω is a compact and complete metric space, since A is finite. The reader is referred to [7] for more topological basic definitions. In this reference, a new operator is introduced as follows: for each subset $L \subset A^*$, let

$$\overrightarrow{L} = \{u \in A^\omega |\ u \text{ has infinitely many prefixes in } L\}.$$

Example 2.1. *If $X = (a+b)^*b$ then $\overrightarrow{X} = (a^*b)^\omega$.*

In the same reference, it is shown the following proposition, which we will use in the sequel.

Proposition 2.2. *Let L be a subset of A^ω*

1. *L is a closed set iff $L = \overrightarrow{Pref(L)}$.*
2. *L is an open set iff it is of the form $L = XA^\omega$, $X \subset A^*$. Furthermore, $L = (X \setminus XA^+)A^\omega$ where $X \setminus XA^+$ is a prefix set.*
3. *L is a clopen set iff it is of the form $L = XA^\omega$ where X is a finite subset of A^*.*

2.3 Borelian sets

Let E be a set. We denote by X^c the complement of a subset X of E. A family $\mathcal{F}$ of subsets of E is said a σ-algebra if it satisfies the following conditions:

- $\emptyset \in \mathcal{F}$,
- $X^c \in \mathcal{F}$, $\forall X \in \mathcal{F}$,
- $\bigcup_{n\geq 0} X_n \in \mathcal{F}$, for all sequence $(X_n)_{n\geq 0}$ of elements of $\mathcal{F}$.

In a topological space E, the σ-algebra generated by open subsets of E, which we denote by $\mathcal{B}(E)$, is called the Borelian σ-algebra of E. Its elements constitute the Borelian sets of E. In the case of a metric space E, $\mathcal{B}(E)$ is generated by the family clopen subsets of E.

2.4 Measures

Let E be a set and $\mathcal{F}$ be a σ-algebra of subsets of E. We will say that $(E,\mathcal{F})$ is a measureable space. One defines a measure on $(E,\mathcal{F})$ as a map $\mu : \mathcal{F} \longrightarrow \mathbb{R}_+ \bigcup\{+\infty\}$ such that :

- $\mu(\emptyset) = 0$,
- $\mu(\bigcup_{n\geq 0} X_n) = \sum_{n\geq 0} \mu(X_n)$, for every pairwise disjoint sequence $(X_n)_{n\geq 0}$ of elements of $\mathcal{F}$.

The second condition is called σ-additivity.
A probability measure on $(E,\mathcal{F})$ is a measure $\mu : \mathcal{F} \longrightarrow [0,1]$ such that $\mu(E) = 1$.

3 Kolmogorov extension theorem

Let A be a finite alphabet. A probability law on A^* is a map $\pi : A^* \longrightarrow [0,1]$ such that:

- $\pi(\varepsilon) = 1$,
- $\sum_{a\in A} \pi(wa) = \pi(w),\ \forall w \in A^*$.

The second part of the definition is called coherence condition.

Example 3.1. *Let $A = \{a,b\}$ and $\alpha \in [0,1]$. Consider the morphism $\pi : A^* \longrightarrow [0,1]$ given by $\pi(a) = \alpha$ and $\pi(b) = 1-\alpha$ The morphism π determines a probability law on A^*, called Bernoulli probability law.*

Example 3.2. *This example can be found in [4]. A probability law on words can be given by a finite automaton in the following way. Let $\mathcal{A} = \langle Q, A\rangle$ be a finite deterministic automaton on the alphabet A. Let π_s be a probability distribution on Q. For each state $q \in Q$, we define a probability distribution π_q on the set of edges starting in q. Thus we have:*

$$\sum_{q\in Q} \pi_s(q) = 1 \text{ and } \sum_{a\in A} \pi_q(q,a) = 1,\ \forall q \in Q.$$

This allows to define a probability law π_γ on the set of paths in $\mathcal{A}$. Let

$$c = (q_0,a_0,q_1)(q_1,a_1,q_2)\dots(q_n,a_n,q_{n+1}),$$

$a_i \in A, \forall\ 0 \leq i \leq n, q_j \in Q,\ \forall\ 0 \leq j \leq n+1$, be a path in $\mathcal{A}$. We set:

$$\pi_\gamma(c) = \pi_s(q_0)\pi_{q_0}(q_0,a_0)\pi_{q_1}(q_1,a_1)\dots\pi_{q_n}(q_n,a_n).$$

The probability of empty path is one. We define a probability law π on the set of words on A by:

for each $w \in A^*$, $\pi(w)$ is the sum of $\pi_\gamma(c)$ on all paths c in $\mathcal{A}$ with label w.

The probability law given by a finite automaton is effectively computable.

Remark 3.3. *The Bernoulli law of the Example 3.1 is given by the automaton $\mathcal{A} = \langle\{1\},\{(1,a,1),(1,b,1)\}\rangle$ with $\pi_s(1) = 1, \pi_1(1,a) = \alpha$ and $\pi_1(1,b) = 1-\alpha$.*

In the sequel, all probability laws will be supposed computable.

Let now μ be a probability measure on $\mathcal{B}(A^\omega)$. Consider the map $\pi : A^* \longrightarrow [0,1]$ given by $\pi(w) = \mu(wA^\omega)$ for $w \in A^*$. Then we have $\pi(\varepsilon) = \mu(A^\omega) = 1$. Moreover, π satisfies the coherence condition, since:

$$\begin{array}{rcl} \sum_{a\in A} \pi(wa) & = & \sum_{a\in A} \mu(waA^\omega) \\ & = & \mu(\bigcup_{a\in A} waA^\omega) \\ & = & \mu(wA^\omega) = \pi(w), \forall w \in A. \end{array}$$

Hence, π is a probability law on A^*, as defined at the beginning of this section. The converse statement, known as the Kolmogorov extension theorem [3], is given by

Theorem 3.4. *For each probability law π on A^*, there exists one and only one probability measure P_π on the family of Borelian subsets of A^ω such that $P_\pi(wA^\omega) = \pi(w)$, $\forall w \in A^*$.*

4 Mathematical model for games

We propose, in this section, a mathematical model allowing to analyze infinitely repeated games with a perfect knowledge of the past in a probabilistic view. The reader is referred to [6] for further details of game theory.
A game is a tuple $G = (P, A, \pi, u)$ where :

- $P = \{1, \cdots, n\}$, $n \in \mathbb{N}$, is the set of players.
- A_i is the set of the actions for player i.
- $A = A_1 \times \ldots \times A_n$ is the alphabet of moves.
- $u_i : A \longrightarrow \mathbb{R}$ is the utility function for player i.
- $u = (u_1, \ldots, u_n) : A \longrightarrow \mathbb{R}^n$ is the utility vector.

The values of the utility functions define the expected amount paid to the players.
We consider in this paper the game consisting in infinite repetions of a base game G. In such a game, we model a match h as an infinite sequence of moves which can be represented by an infinite word on the alphabet A: $h = h_0 h_1 \cdots h_t \cdots \in A^\omega$.

Example 4.1. *In game theory, the distinction between cooperative and non-coperative game is crucial. The Prisoner's Dilemma [5] is an interesting example to explain these notions. This game involves two players, $P = \{1, 2\}$, where each one has two possible actions: cooperate (c) or defect (d), $A_1 = A_2 = \{c, d\}$, $A = \{c, d\} \times \{c, d\}$ The game consists of simultaneous actions, called moves, of both players. The utility functions for the players are defined by the matrix:*

u	c	d
c	(4,4)	(0, 5)
d	(5, 0)	(1, 1)

It is clear that if they could play cooperatively and make a binding agreement, they would both play c. If the game is non-cooperative, the best action for each player is d. The infinite word $h = (c, c)^\omega$ is an example of a match in which the two players cooperate infinitely.

5 Global mixed strategies and cooperative games

In [1] and [2], the authors have defined and analyzed the notion of quasi-strategy. A quasi-strategy σ is a relation from A^* into A. We can associate with each quasi-strategy σ a language L of infinite words on A, which is the set of all the matches that may be played if the players follow σ. Suppose now the players should choose, at any step of the match, a probability distribution on the alphabet of moves. This kind of strategy is called a mixed strategy. It allows us to study the general frame where the game is supposed to be cooperative. We will see in the next section that a non-cooperative game is in fact a particular case of a cooperative one.

Definition 5.1. *A mixed global strategy σ on the alphabet A is a map $\sigma : A^* \times A \longrightarrow [0, 1]$ verifying:*

$$\sum_{a \in A} \sigma(w, a) = 1, \forall w \in A^*.$$

Example 5.2. *In the Prisoner's Dilemma, let σ be the mixed global strategy given by:*

$$\begin{array}{rcccl} \sigma(w, (c, c)) & = & \sigma(w(d, d)) & = & 1/2, \\ \sigma(w, (c, d)) & = & \sigma(w(d, c)) & = & 0, \end{array}$$

for each $w \in A^*$.

Given a mixed global strategy σ on the set A, we define the function $\pi_\sigma : A^* \longrightarrow [0, 1]$ by setting:

(i) $\pi_\sigma(\varepsilon) = 1$,

(ii) $\pi_\sigma(wa) = \pi_\sigma(w)\sigma(w, a)$, $\forall w \in A^*$, $\forall a \in A$.

The real number $\pi_\sigma(w)$ denotes the probability to play the move a at the step $|w|$ of the game. We claim:

Proposition 5.3. *For each mixed global strategy $\sigma : A^* \times A \longrightarrow [0, 1]$, π_σ is a probability law on A^*.*

Proof. It suffices only to verify the coherence condition. Indeed,

$$\begin{array}{rcl} \sum_{a \in A} \pi_\sigma(wa) & = & \sum_{a \in A} \pi_\sigma(w)\sigma(w, a) \\ & = & \pi_\sigma(w) \sum_{a \in A} \sigma(w, a) \\ & = & \pi_\sigma(w), \end{array}$$

for each word $w \in A^*$. ∎

By Kolmogorov extension theorem, there exists a unique probability measure P_{π_σ} associated to the probability law π_σ. In the sequel, this measure will be denoted by P_σ.

6 Individual mixed strategies and non-cooperative games

This section is devoted to the case of non-cooperative games in which the global mixed strategy is given by individual mixed strategies. We will show that we can gather all these strategies in a vector, which allows us to proceed to a global study.

Definition 6.1. *A mixed individual strategy σ_i for player i, $1 \leq i \leq n$, is a map $\sigma_i : A^* \times A_i \longrightarrow [0,1]$ verifying:*

$$\sum_{a \in A_i} \sigma_i(w,a) = 1, \ \forall w \in A^*.$$

Definition 6.2. *A mixed strategy vector σ is the tuple $\sigma = (\sigma_1, \ldots, \sigma_n)$ corresponding to the map from $A^* \times A$ into $[0,1]$ given by:*

$$\sigma(w,a) = \prod_{i=1}^{n} \sigma_i(w,a_i).$$

Example 6.3. *The uniform mixed strategy vector for n players is the strategy vector $\sigma = (\sigma_1, \ldots, \sigma_n)$ where each map $\sigma_i : A^* \times A_i \longrightarrow [0,1]$ is defined by $\sigma_i(w,a) = 1/|A_i|$, $\forall i$ such that $1 \leq i \leq n$.*

The following proposition states that each mixed strategy vector $\sigma = (\sigma_1, \ldots, \sigma_n)$ defines a mixed global strategy on the alphabet A in the sense of the previous section.

Proposition 6.4. $\sum_{a \in A} \sigma(w,a) = 1, \forall w \in A^*$.

Proof. We make it by induction on the number n of players. The case $n = 1$ results directly from the definition of a mixed strategy. Suppose now that the property holds at the rank n. Let $A = A_1 \times \ldots \times A_{n+1}$ and $B = A_1 \times \ldots \times A_n$ and let $\sigma = (\sigma_1, \ldots, \sigma_{n+1})$ and $\overline{\sigma} = (\sigma_1, \ldots, \sigma_n)$. We have by definition at the step $n+1$: $\sum_{a \in A} \sigma(w,a) = \sum_{a \in A} \prod_{i=1}^{n+1} \sigma_i(w,a_i)$. Then we obtain:

$$\begin{array}{ll} \sum_{a \in A} \prod_{i=1}^{n+1} \sigma_i(w,a_i) & = \\ \sum_{a_{n+1} \in A_{n+1}} \sum_{b \in B} \sigma_{n+1}(w,a_{n+1}) \prod_{i=1}^{n} \sigma_i(w,b_i) & = \\ \sum_{a_{n+1} \in A_{n+1}} \sigma_{n+1}(w,a_{n+1}) \sum_{b \in B} \prod_{i=1}^{n} \sigma_i(w,b_i). & \end{array}$$

We have by the induction hypothesis:
$\sum_{b \in B} \prod_{i=1}^{n} \sigma_i(w,b_i) = \sum_{b \in B} \overline{\sigma}(w,b) = 1$.
So,

$$\begin{array}{rcl} \sum_{a \in A} \sigma(w,a) & = & \sum_{a \in A} \prod_{i=1}^{n+1} \sigma_i(w,a_i) \\ & = & \sum_{a \in A_{n+1}} \sigma_{n+1}(w,a_{n+1}), \end{array}$$

which returns us to the case $n = 1$ seen at the beginning. Hence, $\sum_{a \in A} \prod_{i=1}^{n+1} \sigma_i(w,a_i) = 1$.

∎

Example 6.5. *The mixed global strategy σ given in the Example 5.2 models a strictly cooperative game. Infact, if $\sigma = (\sigma_1, \sigma_2)$ then we have for each $w \in A^*$:*

$$\sigma_1(w,c) = \sigma(w,(c,c)) + \sigma(w,(c,d)) = 1/2,$$
$$\sigma_2(w,d) = \sigma(w,(d,d)) + \sigma(w,(d,c)) = 1/2.$$

It follows that $\sigma(w,(c,d)) = \sigma_1(w,c)\sigma_2(w,d) = 1/4$. This is at variance with the definition of σ.

As in the case of mixed global strategies, each mixed strategy vector $\sigma = (\sigma_1, \ldots, \sigma_n)$ determines a unique probability measure on A^ω satisfying the conditions of Kolmogorov extension theorem. We will show in the next sections how to compute the probability of rational Borelian languages.

7 Computing probability of open and closed sets of A^ω

First, we show how to compute the probability of open and closed sets. We begin with the following proposition.

Proposition 7.1. *Let π be a probability law on A^* and let $L = XA^\omega, X \subset A^*$, be a an open set of A^ω. Then we have:*

$$P_\pi(L) = \pi(X \setminus XA^+).$$

Proof. Proposition 2.2 implies $L = XA^\omega = \bigcup_{x \in (X \setminus XA^+)} xA^\omega$ where the union is disjoint since $X \setminus XA^+$ is a prefix set. So, we have $P_\pi(L) = \sum_{w \in X \setminus XA^+} P_\pi(wA^\omega)$. By Theorem 3.4, $P_\pi(wA^\omega) = \pi(w)$ for all $w \in A^\omega$. We obtain, $P_\pi(L) = \sum_{w \in X \setminus XA^+} \pi(w) = \pi(X \setminus XA^+)$.

∎

We obtain as a corollary the following statement:

Corollary 7.2. *Let $L = XA^\omega, X \subset A^*$, be a an open set of A^ω where $X \subset A^*$ is a prefix set. Then we have:*

$$P_\pi(L) = \pi(X).$$

We remark that the probability of a clopen set $L = XA^\omega$ is effectively computable since the set $X \subset A^*$ is finite. In Proposition 7.1 we proved that $P_\pi(XA^\omega) = \pi(X \setminus XA^+)$. In the following proposition we show how to compute $\pi(X \setminus XA^+)$ for each $X \subset A^*$. We denote by $X^{(n)} = X \bigcap A^n$ for each $X \subset A^*$ and for each $n \geq 0$.

Proposition 7.3. *Let $L = XA^\omega, X \subset A^*$, be an open set of A^ω. Then we have:*

$$P_\pi(L) = \lim_{n \to \infty} \pi(\bigcup_{k=0}^{n} X^{(k)} A^{n-k}).$$

Proof. We can write

$$XA^\omega = \bigcup_{n \geq 0} X^{(n)} A^\omega = \bigcup_{n \geq 0} (\bigcup_{k=0}^{n} X^{(k)} A^\omega).$$

Since the first union is increasing, we obtain

$$P_\pi(XA^\omega) = \lim_{n \to \infty} P_\pi(\bigcup_{k=0}^{n} X^{(k)} A^\omega).$$

Now, we have

$$\bigcup_{k=0}^{n} X^{(k)} A^\omega = \bigcup_{k=0}^{n} (X^{(k)} A^{n-k}) A^\omega = (\bigcup_{k=0}^{n} X^{(k)} A^{n-k}) A^\omega.$$

So, we obtain

$$P_\pi(XA^\omega) = \lim_{n \to \infty} P_\pi((\bigcup_{k=0}^{n} X^{(k)} A^{n-k}) A^\omega).$$

Since $(\bigcup_{k=0}^{n} X^{(k)} A^{n-k})$ is a prefix set, Corollary 7.2 implies that $P_\pi(XA^\omega) = \lim_{n \to \infty} \pi(\bigcup_{k=0}^{n} (X^{(k)} A^{n-k}))$.

∎

We will use the following result in the sequel to compute the probability of rational ω-languages.

Proposition 7.4. *Let $L_1 = XA^\omega, L_2 = YA^\omega, X, Y \subset A^*$ be open sets of A^ω. Set $R = P_\pi(L_1 \bigcap L_2)$. Then we have:*

$$R = \lim_{n\to\infty} \pi(\bigcup_{p+q\leq n} (X^{(p)}A^q \bigcap Y^{(q)}A^p)A^{n-p-q})).$$

Proof. We can write:

$$\begin{array}{rcl} XA^\omega \bigcap YA^\omega & = & (\bigcup_{p\geq 0} X^{(p)}A^\omega) \bigcap (\bigcup_{q\geq 0} Y^{(q)}A^\omega) \\ & = & \bigcup_{p,q\geq 0}(X^{(p)}A^\omega \bigcap Y^{(q)}A^\omega) \\ & = & \bigcup_{p,q\geq 0}(X^{(p)}A^qA^\omega \bigcap Y^{(q)}A^pA^\omega) \\ & = & \bigcup_{p,q\geq 0}(X^{(p)}A^q \bigcap Y^{(q)}A^p)A^\omega \\ & = & (\bigcup_{p,q\geq 0} X^{(p)}A^q \bigcap Y^{(q)}A^p)A^\omega \\ & = & TA^\omega \end{array}$$

It follows by Proposition 7.3 that

$$P_\pi(XA^\omega \bigcap YA^\omega) = \lim_{n\to\infty} \pi(\bigcup_{k=0}^{n} (T^{(k)}A^{n-k}))$$

Let $S = \bigcup_{k=0}^{n} T^{(k)}A^{n-k}$. Since

$$T^{(k)} = \bigcup_{p+q=k} (X^{(p)}A^q \bigcap Y^{(q)}A^p),$$

we have successively:

$$\begin{array}{rcl} S & = & \bigcup_{k=0}^{n}(\bigcup_{p+q=k}(X^{(p)}A^q \bigcap Y^{(q)}A^p))A^{n-k} \\ & = & \bigcup_{k=0}^{n}\bigcup_{p+q=k}(X^{(p)}A^q \bigcap Y^{(q)}A^p)A^{n-k} \\ & = & \bigcup_{k=0}^{n}\bigcup_{p+q=k}(X^{(p)}A^q \bigcap Y^{(q)}A^p)A^{n-p-q} \\ & = & \bigcup_{p+q\leq n}(X^{(p)}A^q \bigcap Y^{(q)}A^p)A^{n-p-q} \end{array}$$

We obtain

$$R = \lim_{n\to\infty} \pi(\bigcup_{p+q\leq n} ((X^{(p)}A^q \bigcap Y^{(q)}A^p)A^{n-p-q})).$$

∎

The following statements, which proof is given in [1], show how to calcule the probability of closed sets.

Lemma 7.5. *Let F be a closed set of A^ω. Then we have:*

$$F = \bigcap_{t\geq 0} Pref_t(F)A^\omega,$$

where $F_t = Pref_t(F)$.

This lemma leads to the next result:

Proposition 7.6. *Let F be closed set of A^ω. Then we have:*

$$P_\pi(F) = \lim_{t\to\infty} \pi(Pref_t(F)).$$

Proof. By applying the previous lemma, we can write $F = \bigcap_{t\geq 0} Pref_t(F)A^\omega$. Since this intersection is a decreasing one, it implies: $\pi(F) = lim_{t\to\infty} P_\pi(Pref_t(F)A^\omega)$. Remark now that $Pref_t(F)A^\omega$ is a clopen set and that $Pref_t(F)$ is a prefix set, for each $t \geq 0$. So $P_\pi(Pref_t(F)A^\omega) = \pi(Pref_t(F))$. Finally, we obtain: $\pi(F) = \lim_{t\to\infty} \pi(Pref_t(F))$.

∎

Example 7.7. *Given a real number $\alpha \in [0, 1]$, consider the probability law π on $A = \{a, b\}$ defined by: $\pi(\varepsilon) = 1, \pi(wa) = \alpha, \pi(wb) = 1 - \alpha, \ \forall w \in A^*$. Let $L = a^*b^\omega + a^\omega \subset A^\omega$. Since $L = \overrightarrow{Pref(L)}$, L is a closed set. The computation of the languages $L_t = Pref_t(L)$, for $t \geq 0$, leads to the relation: $L_0 = \{\varepsilon\}$ and $L_{t+1} = aL_t + b^{t+1}$ (the proof is left to the reader). So, we obtain on the probability side: $\pi(L_0) = 1$ and $\pi(L_{t+1}) = \alpha\pi(L_t) + (1-\alpha)^{t+1}$. A simple proof by induction gives immediately $\pi(L_t) = \sum_{i=0}^{t} \alpha^{t-i}(1-\alpha)^i = \sum_{i=0}^{t} \alpha^i(1-\alpha)^{t-i}$. Suppose now $\alpha \leq (1-\alpha)$, the other case is symetric. It implies that $\alpha^i \leq (1-\alpha)^i$ for all $i \geq 0$. So, $\sum_{i=0}^{t} \alpha^i(1-\alpha)^{t-i} \leq \sum_{i=0}^{t}(1-\alpha)^t = (t+1)(1-\alpha)^t$. Thus, we have $0 \leq \pi(L_t) \leq (t+1)(1-\alpha)^t$, which allows us to conclude that $\pi(L) = \lim_{t\to\infty} \pi(L_t) = 0$, except for $\alpha = 1$ where this probability is equal to one.*

8 Computing probabilities on $\mathcal{B}(A^\omega)$

The Borelian sets of A^ω, as those of any metric space, are organized in the Borel hierarchy defined as follows:

$\Delta_0 = \Pi_0 = \Sigma_0 = \{L \subset A^\omega \mid L \ clopen\}, \Delta_0 = \Sigma_0$ and for all $n \geq 0$:

$$\begin{array}{rcl} \Sigma_{n+1} & = & \{\bigcup_{i\geq 0} L_i \mid L_i \in \Pi_n\} \\ \Pi_{n+1} & = & \{\bigcap_{i\geq 0} L_i \mid L_i \in \Sigma_n\} \\ \Delta_{n+1} & = & \Sigma_{n+1} \bigcap \Pi_{n+1}. \end{array}$$

Moreover, we have for all $n \geq 0$

$$\Pi_n = \{L^c \mid L \in \Sigma_n\}.$$

We remark that Σ_1 is the family of open sets and Π_1 that of closed ones. In the particular case of metric spaces, the Borel hierarchy verifies the following property:

Proposition 8.1. *In a metric space, the following inclusions hold:*

$$\Delta_1 \subset \Sigma_1 \subset \Delta_2 \subset \Sigma_2 \subset \ldots$$
$$\Delta_1 \subset \Pi_1 \subset \Delta_2 \subset \Pi_2 \subset \ldots$$

We have already seen how to compute the probability of a language belonging to the levels 0 and 1 of this hierarchy, To proceed to the computation of the probability for the upper hierarchy levels, we need to establish the following proposition.

Proposition 8.2. *For any $n \geq 0$, Π_n (resp. Σ_n) is closed under finite union (resp. finite intersection).*

Proof. We will make it by induction on n only for Π_n, the case of Σ_n is the same if one considers the intersection. We know that any finite union of closed sets is a closed one. Thus, the property holds for $n = 0$. Suppose now that the property is true at the rank n, Let $L, K \in \Pi_n$. By definition, we obtain: $L = \bigcap_{i\geq 0} L_i$ and $K = \bigcap_{j\geq 0} K_j$ with $L_i, K_j \in \Pi_n$, then

$$L \bigcup K = (\bigcap_{i\geq 0} L_i) \bigcup (\bigcap_{j\geq 0} L_j) = \bigcap_{i,j\geq 0}(L_i \bigcup K_j), L_i, K_j \in \Pi_n.$$

Since, by induction hypothesis, Π_n is closed by finite union, it follows that $L_i \bigcup K_j \in \Pi_n$. So, $L \bigcup K \in \Pi_{n+1}$. ∎

The following statement represents an immediate consequence of the previous proposition.

Corollary 8.3. *Every Borelian language L of level $n > 0$ can be written as increasing countable union or as a decreasing countable intersection of Borelian sets all belonging to the previous level. That is*

$$L = \bigcup_{i\geq 0} L_i \text{ or } L = \bigcap_{i\geq 0} L_i,$$

where L_i is a Borelian language of level $n-1$, $\forall i \geq 0$. In both cases, we obtain,

$$P_\pi(L) = \lim_{i\to\infty} P_\pi(L_i).$$

We give in the following two examples of computation of the probability of sets belonging to Σ_2 and to Π_2.

Example 8.4. *Consider on the alphabet $A = \{a, b\}$, the language $L = A^*a^\omega$. Notice that this language is not closed for the usual topology on A^ω because $b^\omega \in \overrightarrow{Pref(A^*a)} \setminus A^*a^\omega$. The language L is exactly the set of infinite words having a finite number of b. The language L belongs to Σ_2, since we can write $L = \bigcup_{n\geq 0} A^n a^\omega$, where $A^n a^\omega$ is closed. So: $P_\pi(L) = \lim_{n\to\infty} P_\pi(A^n a^\omega)$. The real numbers $P_\pi(A^n a^\omega) = \lim_{t\to\infty} \pi(Pref_t(A^n a^\omega))$, for each $n \geq 0$, depend on the chosen probability law.*

We denote by $X_{(n)} = \bigcup_{p\geq n} X^{(p)}$ for each $X \subset A^*$ and for each $n \geq 0$. Let $X \subset A^*$. We have $\overrightarrow{X} \in \Pi_2$ since X can be written as an intersection of open sets,

$$\overrightarrow{X} = \bigcap_{n\geq 0} X_{(n)} A^\omega.$$

Using Proposition 7.3, we are able to compute the probability of a set of the form $\overrightarrow{X}, X \subset A^*$.

Proposition 8.5. *Let $\overrightarrow{X} \subset A^\omega$, $X \subset A^*$. Then we have:*

$$P_\pi(\overrightarrow{X}) = \lim_{p\to\infty} \lim_{q\to\infty} \pi(\bigcup_{k=p}^{q} (X^{(k)} A^{q-k})).$$

Proof. We can write $\overrightarrow{X} = \bigcap_{p\geq 0} X_{(p)} A^\omega$ and since this intersection is decreasing, we have $P_\pi(\overrightarrow{X}) = \lim_{p\to\infty} P_\pi(X_{(p)} A^\omega)$. By Proposition 7.3, we obtain:

$$\begin{aligned} P_\pi(\overrightarrow{X}) &= \lim_{p\to\infty} \lim_{q\to\infty} \pi(\bigcup_{k=0}^{q} (X_{(p)}^{(k)} A^{q-k})) \\ &= \lim_{p\to\infty} \lim_{q\to\infty} \pi(\bigcup_{k=p}^{q} (X^{(k)} A^{q-k})), \end{aligned}$$

car $X_{(p)}^{(k)} = X^k$ if $k \geq p$ and $X_{(p)}^{(k)} = \emptyset$ otherwise. ∎

9 Case of rational Borelian languages

On obtain, as a consequence of the theorem of MacNaughton [7], the following proposition:

Proposition 9.1. *Any ω-rational subset L of A^ω is a disjoint union of the form*

$$L = \bigcup_{1\leq i\leq n} (\overrightarrow{X_i} \setminus \overrightarrow{Y_i}),$$

where $X_i, Y_i \subset A^*$ for any $1 \leq i \leq n$.

We computed, in Proposition 8.5, the probability of a set in A^ω of the form $\overrightarrow{X}$ with $X \subset A^*$. The following proposition shows how to compute the probability of a set in A^ω of the form $\overrightarrow{X} \setminus \overrightarrow{Y}$ with $X, Y \subset A^*$. So the probability of any ω-rational subset $L = \bigcup_{1\leq i\leq n} (\overrightarrow{X_i} \setminus \overrightarrow{Y_i})$ is given by $\sum_{i=1}^{n} P_\pi(\overrightarrow{X_i} \setminus \overrightarrow{Y_i})$.

Proposition 9.2. *Let $X, Y \subset A^*$ Then we have:*

$$P_\pi(\overrightarrow{X} \setminus \overrightarrow{Y}) = \lim_{p\to\infty} \lim_{q\to\infty} (\pi(\bigcup_{k=p}^{q} X^{(k)} A^{q-k})) - \lim_{p\to\infty} \lim_{q\to\infty} (\bigcup_{s,t\geq p, s+t\leq q} (X^{(s)} A^t \bigcap Y^{(t)} A^s) A^{q-s-t})).$$

Proof. We can write $\overrightarrow{X} = (\overrightarrow{X} \setminus \overrightarrow{Y}) \bigcup (\overrightarrow{X} \bigcap \overrightarrow{Y})$ and, since this union is disjoint, the probability of $\overrightarrow{X}$ is given by $P_\pi(\overrightarrow{X}) = P_\pi(\overrightarrow{X} \setminus \overrightarrow{Y}) + P_\pi(\overrightarrow{X} \bigcap \overrightarrow{Y})$. We set: $U = P_\pi(\overrightarrow{X} \setminus \overrightarrow{Y})$ and $V = P_\pi(\overrightarrow{X} \bigcap \overrightarrow{Y})$ By Proposition 8.5, we obtain:

$$U = \lim_{p\to\infty} \lim_{q\to\infty} \pi(\bigcup_{k=p}^{q} X^{(k)} A^{q-k}) - V$$

Now, we write:

$$\begin{aligned} \overrightarrow{X} \bigcap \overrightarrow{Y} &= (\bigcap_{t\geq 0} X_{(t)} A^\omega) \bigcap (\bigcap_{t\geq 0} Y_{(t)} A^\omega) \\ &= \bigcap_{p\geq 0} (X_{(p)} A^\omega \bigcap Y_{(p)} A^\omega). \end{aligned}$$

Since the intersection on p is decreasing, we obtain:

$$V = \lim_{p\to\infty} P_\pi(X_{(p)} A^\omega \bigcap Y_{(p)} A^\omega).$$

Applying Proposition 7.4, we have:

$$V = \lim_{p\to\infty} \lim_{q\to\infty} \pi(\bigcup_{s,t\geq p, s+t\leq q} (X^{(s)} A^t \bigcap Y^{(t)} A^s) A^{q-s-t}).$$

Previous computations give:

$$U = \lim_{p\to\infty} \lim_{q\to\infty} ((\pi(\bigcup_{k=p}^{q} X^{(k)} A^{q-k})) - \lim_{p\to\infty} \lim_{q\to\infty} (\pi(\bigcup_{s,t\geq p, s+t\leq q} (X^{(s)} A^t \bigcap Y^{(t)} A^s) A^{q-s-t}))).$$

∎

References

[1] M. Arfi, B. Ould M. Lemine, C. Selmi, "Strategical languages of infinite words," *Information Processing Letters*, vol. 109, pp. 749-753, 2009.

[2] M. Arfi, B. Ould M. Lemine, C. Selmi, "Mixed strategies and closed sets of infinite words," *Proceedings of the Conference Words 2009*, 14-18 Septembre 2009, Salerne, Italy.

[3] J. Berstel, D. Perrin and C. Reutenauer, *Codes and Automata*, Cambridge University Press, 2010.

[4] M. Lothaire, *Applied Combinatorics on Words*, Encyclopedia of Mathematics and its Applications, vol. 105, Cambridge University Press, 2005.

[5] J. F. Nash, "Non-cooperative games", *Annals of Mathematics*, vol. 54, 2, pp. 286-295, 1951.

[6] J. Osborne, and A. Rubistein, *A course in game theory*, MIT Press, 1994.

[7] D. Perrin, and J. É. Pin, *Infinite words, Automata, Semigroups, Logic and Games*, Elsevier, Academic Press, 2004.

Proceedings of ICCSA 2014
Normandie University, Le Havre, France - June 23-26, 2014

LOCAL NASH EQUILIBRIUM

Yichao Zhang, M. A. Aziz-Alaoui and Cyrille Bertelle *†

Abstract. Nash equilibrium is widely present in various social disputes. As of now, in structured static populations, such as social networks, regular, and random graphs, the discussions on the equilibrium between strategies are quite limited. In such a relatively stable gaming network, a rational individual has to comprehensively consider all his/her opponents' strategies before they adopt a unified strategy. In this scenario, a new strategy equilibrium emerges in the system. We define this equilibrium as a local Nash equilibrium. In this paper, we present an explicit definition of the local Nash equilibrium for the two-strategy games in structured populations. Based on the definition, we investigate the condition that a system reaches the evolutionary stable state when the individuals play the Prisoner's dilemma and snow-drift game. The local Nash equilibrium provides a way to judge whether a gaming structured population reaches the evolutionary stable state on one hand. On the other hand, it can be used to predict whether cooperators can survive in a system long before the system reaches its evolutionary stable state for the Prisoner's dilemma. Our work therefore provides a theoretical framework for understanding the evolutionary stable state in the gaming populations with certain structures.

Keywords. ecology and evolution, game theory, Self-organization complex systems

1 Introduction

In the past half century, the concept of Nash equilibrium is widely accepted and applied to analyze the possible outcomes in game theory if several strategists are making decisions at the same time. Their applications on arms races [1], currency crises, environmental regulations [2], auctions, even football matches [3] are well known. In the evolutionary game theory [4, 5, 6], Nash equilibrium [5, 6, 7] actually is a pair of mixed strategies. The mixed strategy denotes that a pure strategy is chosen stochastically with a fixed probability. Instead, in the classical two-player games, the Nash equilibrium is interpreted as that once two individuals are in this equilibrium, they can not gain more payoff by adjusting their own pure strategy unilaterally. In an evolutionary game in a unstructured population, the mixed strategy is allowed, since the opponent at the next round is uncertain. An individual can only adjust his/her strategy according to the distribution of the frequency of the pure strategies in the previous round. Indeed, in such a setting, the Nash equilibrium is composed of all the individuals' strategies. In a structured population as social networks, individuals can't meet each other randomly. In each round of game, an individual has to play with a set of relatively fixed opponents, which are called neighbors in complex networks. In this scenario, a new strategy equilibrium emerges in the system, which unevenly exists in two connected individuals with neighbors. We define this class of strategy equilibrium as a local Nash equilibrium. In this paper, we present an explicit definition of the local Nash equilibrium in networks for the two-strategy games [8, 9]. We investigate the condition that a system reaches the evolutionary stable state. For the Prisoner's dilemma [10, 11, 12, 13, 14, 15, 16] and snow-drift game (also known as the hawk-dove or chicken game) [4, 5, 17, 18], we will show that the Local Nash equilibrium is a typical feature of the evolutionary games in structured populations.

In a structured population, the equilibrium between two strategies is actually determined by the two strategists and all their connected neighbors' strategies. The change on the strategy equilibrium leads to a completely different evolutionary stable state [4]. An evolutionary stable state is composed by a set of strategies with different frequencies. The frequencies of the strategies in this state must be statistically relatively stable. In the evolutionary stable state of the games with cooperators and defectors, the frequency of cooperators in the structured populations has attracted a lot of attention [8, 9, 17, 19, 20, 21]. Researchers are interested in how the cooperators can survive in a circumstance with a large temptation to defect. To clarify this point, one has to understand the generation of the evolutionary stable state at first.

In the evolutionary game theory, previous studies discussed the evolutionary stable state in the unstructured populations from a replicator dynamics perspective [6, 22, 23, 24]. In the structured populations, for example, spatial [17, 19] and social [8, 9, 20, 21] networks, because of the difficulty of formulating the replicator dynamics, the discussions are highly restricted. In the structured populations except the fully connected population, the folk theorem of evolutionary game theory does not stand [6], since the strategy equilibrium only exists locally. To get the evolutionary stable state, there is no need to get all the connected individuals in the local Nash

*

†Manuscript received April 10, 2014; revised June 10, 2014.

equilibrium. A certain number of the local Nash equilibria are sufficient to lead the system into the stable state, since they are enough to balance the payoff distance between different strategies.

2 Summary

In a nutshell, the self-organization of Nash pairs forms the final dynamical complex patterns of evolutionary games in structured populations. The concept of the local Nash equilibrium provides us a way to judge whether a gaming structured population reaches the evolutionary stable state. For the prisoner's dilemma, the concept can also be used to predict whether cooperation can exist in a system long before the system reaches its evolutionary stable state. Our observations may reveal a common reason why cooperators can survive in a structured population where defectors always obtain a higher payoff. The reason is that the local Nash equilibrium defined in this paper limits the payoff of defectors. The restriction effectively protects the cooperators in the system.

Acknowledgements

Y. Z., M. A. A., and C. B. are supported by the region Haute Normandie and the ERDF RISC.

References

[1] T. C. Schelling, *The Strategy of Conflict*, Harvard University Press, Cambridge, 1980.

[2] H. Ward, "Game Theory and the Politics of Global Warming: the State of Play and Beyond", *Political Studies*, vol. 44 pp. 850C871, 1996.

[3] P. Chiappori, S. Levitt, T. Groseclose, "Testing Mixed-Strategy Equilibria When Players Are Heterogeneous: The Case of Penalty Kicks in Soccer", *American Economic Review*, vol. 92 pp. 1138-1151, 2002.

[4] J. M. Smith, "Evolution and the theory of games", *American Scientist*, vol. 64 pp. 41-45, 1976.

[5] H. Gintis, "Game theory evolving: A Problem-Centered Introduction to Modeling Strategic Interaction", *Journal of Economic Literature*, vol. 39 pp. 572-573, 2001.

[6] J. Hofbauer, K. Sigmund, "Evolutionary game dynamics", *Bulletin. (new series) of the american mathematical society*, vol. 40 pp. 479-519, 2003.

[7] J. F. Nash, "Equilibrium points in n-person games", *Proc. Natl. Acad. Sci. USA*, vol. 36, pp. 48-49, 1950.

[8] E. Lieberman, C. Hauert, M. A. Nowak, "Evolutionary dynamics on graphs", *Nature*, vol. 433, pp. 312-316, 2005.

[9] H. Ohtsuki, C. Hauert, E. Lieberman, M. A. Nowak, "A simple rule for the evolution of cooperation on graphs and social networks", *Nature*, vol. 441, pp. 502-505, 2006.

[10] R. Axelrod, W. D. Hamilton, "The Evolution of Cooperation", *Science*, vol. 211 pp. 1390-1396, 1981.

[11] R. Axelrod, "More Effective Choices in the Prisoner's Dilemma", *J. Conflict Resolut.*, vol. 24, pp. 379-403, 1980.

[12] P. Hammerstein, *Genetic and Cultural Evolution of Cooperation [Hammerstein, P. (ed.)]* MIT, Cambridge, MA, 2003.

[13] R. Axelrod, W. D. Hamilton, "The Evolution of Cooperation", *Science (London)*, vol. 211, pp. 1390-1396, 1981.

[14] P. E. Turner, L. Chao, "Prisoner's dilemma in an RNA virus", *Nature (London)*, vol. 398, pp. 441-443, 1999.

[15] C. Gracia-Lázaro C, A. Ferrer, G. Ruiza, A. Tarancón, J. A. Cuesta, A. Sánchez, Y. Moreno, "Heterogeneous networks do not promote cooperation when humans play a Prisoner's Dilemma", *Proc. Natl. Acad. Sci. USA*, vol. 109, pp. 12922C12926, 2012.

[16] D. Semmann, "Conditional cooperation can hinder network reciprocity", *Proc. Natl. Acad. Sci. USA*, vol. 109, pp. 12846-12847, 2012.

[17] C. Hauert, M. Doebeli, "Spatial structure often inhibits the evolution of cooperation in the snowdrift game", *Nature*, vol. 428, pp. 643-646, 2004.

[18] M. Doebeli, C. Hauert, "Models of cooperation based on the Prisoners Dilemma and the Snowdrift game", *Ecol. Lett.*, vol. 8, pp. 748-766, 2005.

[19] M. A. Nowak, R. M. May, "Evolutionary game and spatial chaos", *Nature*, vol. 359, pp. 826-829, 1992.

[20] F. C. Santos, J. M. Pacheco, "Scale-free networks provide a unifying framework for the emergence of cooperation", *Phys. Rev. Lett.*, vol. 95, pp. 098104, 2005.

[21] J. Góez-Gardeñs, M. Campillo, L. M. Floría, Y. Moreno, "Dynamical organization of cooperation in complex topologies", *Phys. Rev. Lett.*, vol. 98, pp. 108103, 2007.

[22] P. D. Taylor, L. Jonker, "Evolutionarily stable strategies and game dynamics" *Math Biosciences* vol. 40, pp. 145-156, 1978.

[23] P. Schuster, K. Sigmund, "Replicator dynamics", *J. Theor. Biology*, vol. 100, pp. 533-538, 1983.

[24] C. Hofbauer, M. Holmes, D. Michael, "Evolutionary Games and Population Dynamics: Maintenance of Cooperation in Public Goods Games", *Proceedings: Biological Sciences*, vol. 273, pp. 2565-2570, 2006.

Satellite Workshop 1
Complex Systems Digital Campus (CS-DC)
Unesco UniTwin Kickoff

Satellite Workshop 1
Complex System Digital Campus UNESCO UniTwin Kickoff

Organizers

- Paul Bourgine (Ecole Polytechnique & CNRS, Paris, France), President of the CS-DC UNESCO UniTwin, paul.bourgine@polytechnique.edu
- Cyrille Bertelle (LITIS FR-CNRS 3638, Le Havre, France), Coordinator of the CS-DC UNESCO UniTwin, cyrille.bertelle@univ-lehavre.fr
- Pierre Collet (ICUBE UMR-CNRS 7357, Strasbourg, France), Coordinator of the CS-DC UNESCO UniTwin , pierre.collet@unistra.fr
- Carlos Gershenson (Universidat National Autonoma, Mexico), cgg@unam.mx
- Jeffrey Johnson (Open University, UK), Jeff.Johnson@open.ac.uk
- Jorge Louçã (ISCTE, Lisbon University Institute, Portugal), Jorge.L@iscte.pt
- Yasmin Merali (University of Hull, UK), Y.Merali@hull.ac.uk
- Carla Taramasco Toro (Universidad de Valparaison, Chile), Carla.Taramasco@polytechnique.edu

Description

The Complex Systems Digital Campus federates the Research and Educational Institutions worldwide addressing the challenges of complex systems science. It coordinates an evolving international network of scientists to identify the scientific challenges though 'living complex systems roadmaps', facilitating the sharing of research and educative resources to address these challenges. The Digital Campus has virtual departments federating the e-community addressing each challenge. The Digital Campus is opened to all citizens of the world to participate in solving the local and global challenges that lie ahead.
The kickoff meeting will allow to share all the research and teaching programmes proposed by each of the 98 Research and EDucational Institutions that become members of the Unitwin over 24 countries and 4 continents. This kickoff will allow to start an efficient sharing of all resources for boosting the creation of e-laboratories in the perspective the pluri-annual Programme of cooperation**,**

Programme

Monday

Multi-level Modeling:

Research & Teaching Programme

Jörg Lehnert (MPI-MiS, Germany) : « Mathematics in the sciences »
Keywords are:
- Education program: Graduate courses mathematical different mathematical aspects of complex systems, video-recorded, online available Topics include: dynamical systems, probability theory, discrete structures
- Research program: Mathematical Foundations of Complex Systems, Mulitlevel Systems, Complexity Measures, Information Theory, Complex Time-Delay Systems, Computational Neurosciences, machine learning

Hector Zenil (Algorithmic Nature Group, LABORES, France/UK/Spain/Sweden) : "The Online Algorithmic Complexity Calculator (OACC): From Sequence Complexity to Graph Complexity"

Keywords: Kolmogorov complexity, Solomonoff Algorithmic Probability, alternative to lossless compression.
Abstract: The Online Algorithmic Complexity Calculator (OACC) is an on-going long-term project of the Algorithmic Nature Group to develop an online tool implementing semi-computable measures of complexity through various numerical methods and algorithms for potential applications in a very wide range of disciplines, from bioinformatics to psychometrics, from linguistics to economics.
It currently retrieves numerical approximations (upper bounds) of Kolmogorv complexity for binary strings of short length by means of algorithmic probability (notably by using the algorithmic Coding theorem relating frequency and complexity), for string length which lossless compression algorithms fail to deal with, hence providing an alternative/complementary method to compression algorithms (in the future the calculator will smoothly make the transition between the algorithmic probability and the lossless compression methods using a technique that the group has developed called the Block Decomposition Method.
More algorithmic information measures, more data and more techniques will be incorporated gradually in the future, covering a wider range of objects such as longer binary strings, non-binary strings and n-dimensional objects, such as images and networks.
Additional material can be found at the Algorithmic Nature Group website at http://www.algorithmicnature.org. An Online Algorithmic Complexity Calculator implementing this technique and making the data available to the research community is accessible at http://www.complexitycalculator.com.

Educational Program :

Oscar Gordon (University Granada, Spain): «*University of Granada interdisciplinary Education Program on Complex Systems*»

Integrative social science :

Research & Teaching Programme :

Maria-Eunice Gonzales (UNESP, UFABC, Brazil ; Social self-organization e-lab) : « title to be defined »

Béatrice Galinon-Melenec (Le Havre University, France ; Human Trace-DC e-lab)

Flavia Mori Sarti (USP, Brazil): «Opportunities to the consolidation of Complex Systems in Brazil: The Center for Interdisciplinary Research in Complex Systems and the Graduate Program in Complex Systems Modelling at University of Sao Paulo»
Keywords: complex systems, social sciences modeling, environmental modeling, networks, agent based modeling.
Abstract: In Brazil, the research in Complex Systems have been a domain within the natural sciences until the last decade. The successful creation of graduate programs that deal with complexity modeling applied to environmental and social subjects in the last few years in Brazil indicates the existence of an interdisciplinary research field in Complex Systems that offers with high innovative potential to several areas of knowledge. Nowadays, there are five Brazilian graduate programs explicitly defined to be directed towards computational modeling of environmental and social problems, amidst 16 graduate programs that indicate “computational modeling” as research scope.

Nevertheless, there is only one program that directly mentions the subject of Complex Systems in its denomination and offers the possibility to join both environmental and social modeling to computational modeling and physics, the Graduate Program in Complex Systems Modelling at University of Sao Paulo. In its core, the program proposes to apply tools from computation and physics for Complex Systems Modeling in economics, management, politics, biology, environmental sciences and theoretical physics, among other. During the last few years since its creation in 2010, there were 15 graduate students who presented Master thesis successfully, and other 11 graduate students are expected to present thesis in 2014, including various themes from analysis of social networks to agent based modeling applied to economics, environmental sustainability, and health systems management. In 2012, the program extended activities to the creation of the Center for Interdisciplinary Research in Complex Systems. The presentation includes the main achievements and research themes of the Complex Systems group from the University of Sao Paulo, in order to seek for potential research collaborations and partnerships.

Keywords: complex systems, social sciences modeling, environmental modeling, networks, agent based modeling.

Tuesday

Integrative Biology :

Research & Teaching Programme :

Karol Mikula (STUBA, Slovaquie) : « Mathematical methods for multiscale 3D+t imaging in integrative biology »

Andres Santos (Universidad Politecnica Madrid, Spain) : « Computational methods for multiscale 3D+t imaging in integrative biology »

Nadine Peyriéras (Embryome-DC e-lab) : « the Embryome challenges »

Territorial intelligence

Research Programme :

Thierry Saint-Gérand (Remgarev e-lab): Remgarev

Sylvie Occelli (IRES, Italy ; Collective situated intelligence e-lab)

Educational Programme :

Céline Rozenblat (Lausanne University, Switzerland) : «Master Geographical Modeling»

Solange Ghernaouti (Lausanne University, Switzerland) : « title »

Wednesday

Integrative science of education :

Research Programme

Jeff Johnson (Open University, UK) "Robust peer assessment for scalable massive CS-DC education"

José Aguilar (Universidad de Los Andes, Venezuela) : « Proposal of an educational model for careers in the area of Computer Sciences »

Chenyun Chang (NTNU, Taiwan) : « NTNU research and teaching programme on complex systems »
Summary: National Taiwan Normal University (NTNU) provides a diversified learning and academic research environment integrating science, education, fine arts, and cultures to engage in knowledge innovation and holistic education. It consists of 10 colleges that include 59 departments and 54 graduate institutes. The teachers and educators prepared by NTNU has been the backbone force for the development of secondary school education in Taiwan. For decades, NTNU has devoted to the research and development of educational policy and teaching practice. According to the recent World University Rankings conducted by the QS Intelligence Unit, NTNU is ranked one of the top 500 world's elite universities and ranked 42th in the education field.
Science education is a major field at NTNU with world's top level research capacity as over the past 10 years, Taiwan has been ranked 7th in number of publication in science education. Moreover, the Science Education Center (SEC) of NTNU has made remarkable contributions to the national development of science education and educational assessment, including: (a) hosting Trends in International Mathematics and Science Study (TIMMS) in Taiwan, in which Taiwan's achievement in science education was demonstrated internationally; (b) hosting International Science Olympiads (ISO) and training students to participate in Olympiads to educate future science elites; and (c) executing national standardized tests such as the high school entrance Basic Competence Test (BCTEST) and developing a unique system of testing and examination affairs.
As the director of SEC, Dr. Chang has lead numerous nationally funded projects, sponsored by the Taiwanese National Science Council and the Ministry of Education, such as: building "The e-Learning Research Teams for Excellence", "The Center for excellence in e-Learning Sciences (CeeLS): i4 future learning environment" as well as the ongoing "Aim for the Top University Project" of establishing the "Center for Research Excellence in Science Education". With these nationally funded projects, Dr. Chang has established and incorporated several innovative Smart Classroom technologies into SEC to facilitate science teaching and learning. The Smart Classroom integrates modern technologies with the aims to create an intelligent classroom embedded with individualized and interactive learning materials. The systems comprised in the Smart Classroom include the following: (1) technology-enhanced interaction system, (2) automatic speech recognition, (3) multiple screen projection, (4) 3D virtual reality learning environment, (5) instant message deliverer, (6) interactive whiteboard system, (7) automatic online assessment, and (8) digital archive of course content.

Manuel Pélissié (IREIS) : « title »

Educational Program :

Klaus Jaffe (Universidad Simon Bolivar, Venezuela) : «Complex Systems Group at the Interdisciplinary Science Doctoral Program»
Keywords: evolution, networks, economy, sex, ants, sociodynamics, bioeconomy

Thursday

Integrative management of complex systems:

Research & Teaching Programme :

Pierre Parrend (ECAM Strasbourg Europe, France) : « Complex systems for industry »
Keywords: industry, evolutionary algorithms, risk management, security, simulation, multi-physical systems, organisation management

Zhangang Han (Beijing Normal University, China): «Systems Science @ BNU»

Charles S. Tapiero (NYU, USA) : « The extreme risk initiative »

Pierre Collet (UNISTRA, France) : « E-lab on Complex Computational Ecosystems (ECCE) »

Integrative cognitive science

Research & Teaching Programme :

Jean-Marc Meunier (Université Paris 8, France) : « Creativity as a way to understand complexity : from Arts to Sciences »

Charles Tijus (Université Paris 8, France) : «a new e-lab on cognition science »

Integrative ecology :

Research & Teaching Programme :

Salima Taïbi (ETSIPA, France) : « Statistical approach for soil monitoring, risk assessment and soil characterization»

Masa Funabashi (Sony CSL, Japan) « Research and Education Program of CS-DC e-laboratory "Open System Exploration for Ecosystems Leveraging" »

Satellite Workshop 2
Modeling and Simulation Platforms

Satellite Workshop 2
Modeling and Simulation Platforms

Organizers

- Nicolas Marilleau, UMI 209 UMMISCO, IRD, Bondy, France, nicolas.marilleau@ird.fr
- Romain Reuillon, ISC-PIF, Paris, France, romain.reuillon@iscpif.fr
- Patrick Taillandier, IDEES UMR-CNRS 6266, Rouen, France, patrick.taillandier@univ-rouen.fr

Description

These last years have seen the development of many high-level computer tools and platforms to study complex-systems through graphs, models, simulations, data analysis, machine learning, model exploration… These tools integrate well known and novel methods in ergonomic interfaces to render them usable by domain experts and complex-system scientists.

This satellite workshop intends to advise various tools covering different aspect of complex systems studying. It workshop will propose tutorials on several FOSS (Free and Open-Source Software) platforms and libraries that focus on the ease-of-use, scalability, collaborative aspects to enable complex-system study for scientists. During these tutorials, platform developers will present their tools, help new users to begin with it and advanced user to improve their skills. Scientist and software developers are welcome to propose tutorials. The format of these tutorials can be either 1.5h or 3h. The main part of the tutorial session should consist in a practical use of the software by the audience.

Proceedings of ICCSA 2014
Normandie University, Le Havre, France - June 23-26, 2014

WS2: MODELING AND SIMULATION PLATFORMS

Organizers: Nicolas Marilleau[*], Romain Reuillon[†] and Patrick Taillandier[‡]

1 Goal of the workshop

These last years have seen the development of many high-level computer tools and platforms to study complex-systems through graphs, models, simulations, data analysis, machine learning, model exploration These tools integrate well known and novel methods in ergonomic interfaces to render them usable by domain experts and complex-system scientists.

This satellite workshop intends to advise various tools covering different aspect of complex systems studying. It workshop will propose tutorials on several FOSS (Free and Open-Source Software) platforms and libraries that focus on the ease-of-use, scalability, collaborative aspects to enable complex-system study for scientists. During these tutorials, platform developers will present their tools, help new users to begin with it and advanced user to improve their skills.

2 Timetable

1. **GAMA** : *Monday June 23, 2014 - 16h-19h*
   Patrick Taillandier (UMR IDEES, University of Rouen) and Nicolas Marilleau (UMI UMMISCO, IRD)
2. **MGS** : *Tuesday June 24, 2014 - 14h-15h* :
   Martin Potier (LACL, University of Paris Est)
3. **Graphstream** : *Tuesday June 24, 2014 - 15h-16h30*
   Yoann Pign, Stefan Balev, Antoine Dutot (UMR LITIS, University of Le Havre)
4. **OpenMole** : *Tuesday June 24, 2014 - 17h-19h*
   Mathieu Leclaire, Romain Reuillon (ISC-PIF)

3 Tutorials abstracts

3.1 GAMA

This open-source GAMA platform is dedicated to the definition and simulation of agent-based models. It offers many powerful features such as an integrated development environment with a dedicated modeling language, a native integration of GIS data, powerful spatial and graph operators, 3D visualization, multi-level modeling.... Most of these features will be presented through a tutorial where participants will be invited to build a model concerning the propagation of a disease in a small city.

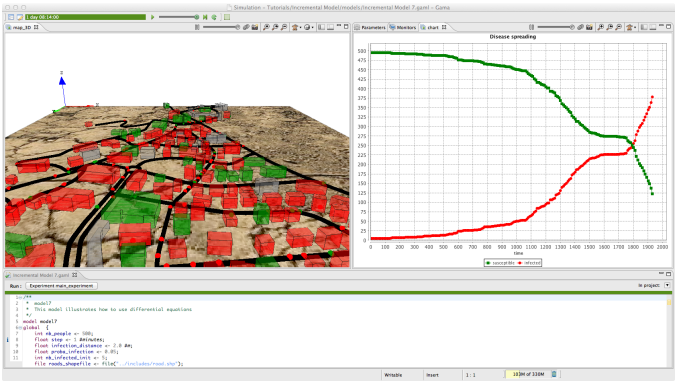

Figure 1: GAMA screenshot

website: https://code.google.com/p/gama-platform

3.2 MGS

The project aims at investigating the concepts and tools (especially programming languages) needed for the modeling and the simulation of dynamical systems exhibiting a dynamical structure. The results are validated by the design and development of an experimental programming language and of various applications (mainly in the area of biological systems modeling). Our approach is based on the use of topological notions to extend the idea of rewriting systems. In this tutorial, we will show different implementations in MGS of a toy example including space, ODE, PDE, Gillespie while giving a tour of MGS topological collections.

website: http://www.spatial-computing.org/mgs/start

3.3 Graphstream

GraphStream is a Java library for the modeling and analysis of dynamic graphs. You can generate, import, export, measure, layout and visualize them. The tool will

[*]UMI 209 UMMISCO, IRD/UPMC, Bondy–France. E-mails:nicolas.marilleau@ird.fr
[†]ISC-PIF, Paris–France. E-mails:romain.reuillon@iscpif.fr
[‡]IDEES UMR-CNRS 6266, Rouen– France E-mail: patrick.taillandier@univ-rouen.fr

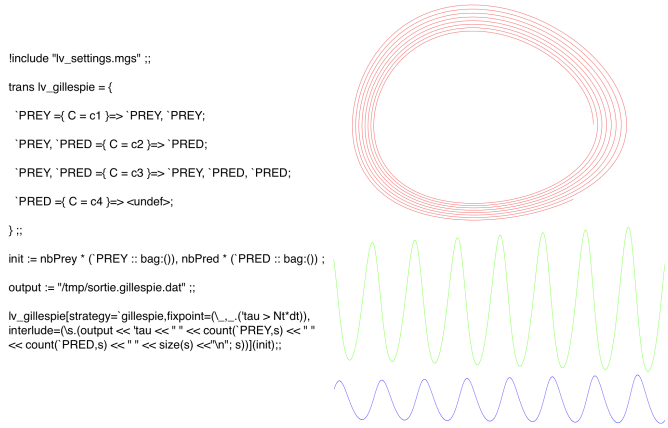

Figure 2: MGS sample of code and results.

be presented with some demos followed by a tutorial on the basic usage of the main parts provided by GraphStream.

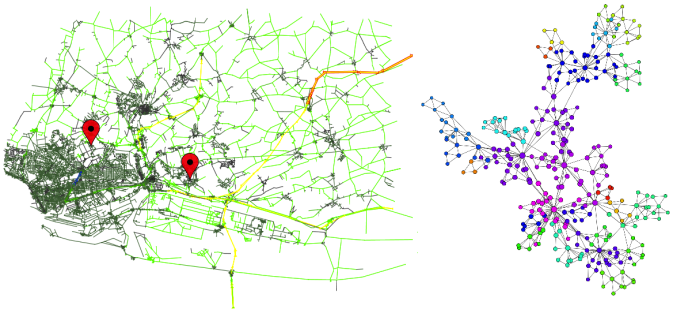

Figure 3: Example of graphs visualized with Graphstream

website: http://graphstream-project.org

3.4 OpenMole

This tutorial presents an introduction to the OpenMOLE platform. OpenMOLE is designed to leverage the power of massively parallel execution environments (servers, clusters, grids) for model exploration. During the session, the basic functionalities of OpenMOLE will be demonstrated through practical exercises during which the attendees will learn how to encapsulate their models into the framework and explore them intensively using various distributed execution environments.

website: http://www.openmole.org

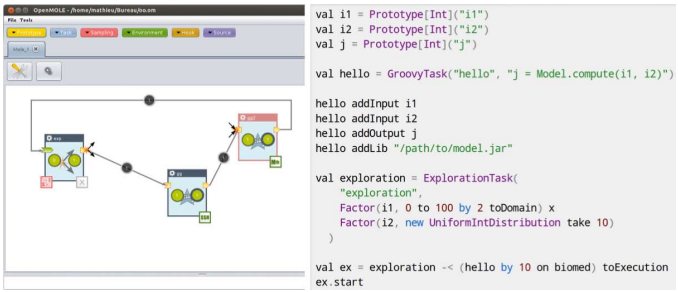

```
val i1 = Prototype[Int]("i1")
val i2 = Prototype[Int]("i2")
val j = Prototype[Int]("j")

val hello = GroovyTask("hello", "j = Model.compute(i1, i2)")

hello addInput i1
hello addInput i2
hello addOutput j
hello addLib "/path/to/model.jar"

val exploration = ExplorationTask(
    "exploration",
    Factor(i1, 0 to 100 by 2 toDomain) x
    Factor(i2, new UniformIntDistribution take 10)
  )

val ex = exploration -< (hello by 10 on biomed) toExecution
ex.start
```

Figure 4: OpenMole screenshot and sample of code.

3.5 Aknowledgement

This workshop is organized by the Simtools Network and is supported by the "Réseau National des Systèmes Complexes (RNSC)" and the "Grands Réseaux de Recherche de Haute-Normandie (GRRHN)".

Satellite Workshop 3
Complex Networks and Dynamics

Satellite Workshop 3
Complex Networks and Dynamics

Organizers

- Benjamin Amor, Imperial College London, b.amor11@imperial.ac.uk
- Mariano Beguerisse Dıaz, Imperial College London, m.beguerisse@imperial.ac.uk
- Jean-Charles Delvenne, jean-charles.delvenne@uclouvain.be
- Till Hoffmann, Imperial College London, t.hoffman13@imperial.ac.uk
- Michael Schaub, Imperial College London, michael.schaub09@imperial.ac.uk

Description

This workshop aims to provide an interdisciplinary forum for researcher working on dynamics on networks and the analysis of temporal networks, i.e. networks that change over time. Areas of interest include, but are not limited to

- statistics to monitor and predict changes in temporal networks,
- centrality measures for temporal networks,
- generative and evolution models for temporal networks,
- community detection in temporal networks,
- visualisation of temporal networks,
- random walks and efficient searching on temporal networks,
- epidemic spreading on temporal networks,
- dynamical and structural robustness and stability of temporal networks,
- agent-based modelling for temporal networks,
- control of dynamics on temporal networks,
- opinion dynamics and consensus formation,
- protein interaction networks and chemical reaction networks,
- inferring network structure from time series data,
- distributed detection in sensor networks,
- data collection from social media and data quality tests.

Scientific Committee

- Mauricio Barahona (Imperial College)
- Tim Evans (Imperial College)
- Petter Holme (Umeå)
- Nick Jones (Imperial College)
- Jukka-Pekka Onella (Harvard)
- Luis Rocha (University of Namur & Karolinska Institutet)
- Martin Rosvall (Umeå)
- Jari Saramäki (Aalto)
- Giovanni Petri (ISI Torino)
- Renaud Lambiotte (Namur)
- Marton Karsai (ENS de Lyon)

Programme

Invited talk
Controlling Contagion Processes in Activity Driven Networks.
Márton Karsai (ENS de Lyon)
The vast majority of strategies aimed at controlling contagion processes on networks consider the connectivity pattern of the system either quenched or annealed. However, in the real world, many networks are highly dynamical and evolve, in time, concurrently to the contagion process. Here [1], we derive an analytical framework for the study of control strategies specifically devised for a class of time-varying networks, namely activity-driven networks. We develop a block variable mean-field approach that allows the derivation of the equations describing the co-evolution of the contagion process and the network dynamic. We derive the critical immunisation threshold and assess the effectiveness of three different control strategies. Finally, we validate the theoretical picture by simulating numerically the spreading process and control strategies in both synthetic networks and a large-scale, real-world, mobile telephone call dataset.
[1] S. Liu, et.al. Phys. Rev. Lett. 112, 118702 (2014)

Contributed talk
Resilience and cascading failures in large-scale systems
Wilbert Samuel Rossi (Politecnico di Torino)
Several cascading phenomena in networks can be studied with epidemic models. Examples are the spread of innovation, default contagion in financial institutions and cascade of re-tweets. While literature has studied the asymptotic spread of the epidemics, we are interested in the transient behavior and dynamic of the process, and in control policies, whenever acting on network parameter is allowed. We consider a threshold model process: given the network topology and the initial infected agents, the infection propagates in synchronous deterministic rounds, where each node become infected if at least a specific threshold number of its out-neighbor were already infected. Our analysis is on large random network: we exploit the tree-like local structure to write recursive equations that approximate the evolution of the expected fraction of infected agents. This equation are exact on infinite networks. However, when the size n of the network is large but finite, the dynamic of the fraction of infected agents concentrates around the approximated expectation, and, for time horizons of order log n the approximation is very good.
Keywords. Bootstrap percolation, Configuration model random graph, cascade, diffusion, threshold.

Contributed talk
Emergence of social Structures via preferential selection
Adam Lipowski (Adam Mickiewicz University)
We examine a weighted-network model of the formation of social structures. The model is based on preferential selection where individuals choose partners with the probability p(w), where w is the number of their past selections. When p(w) increases sub-linearly with the number of past selections (p(w) ~ w\alpha, \alpha < 1), agents develop a uniform preference for all other agents. For a superlinear increase (\alpha > 1), strong heterogeneities emerge and agents make selections mainly within small clusters. Formation of such clusters can be considered as a spontaneous symmetry break- ing and might take place even in a few-agents case. Such (zero-dimensional!)

transitions are analysed within a mean-field approx-imation and Monte Carlo simulations. At \alpha = 1 (linear increase), most of the links virtually vanish and the model undergoes a dra- matic change of the community structure.
Keywords. Social structures, evolving weighted network, preferential selection, community structure

Invited talk
TempoRank: A random walk centrality for temporal networks
Luis Rocha (Karolinska Institutet & University of Namur)
Ranking algorithms based on random walks are particularly useful because they connect topological and diffusive properties of the network. Previous methods based on random walks, as for example the PageRank, have focused on static structures. Several realistic networks are however dynamic, meaning that their structure varies in time. We propose a centrality measure for temporal networks based on random walks that we call TempoRank. TempoRank is the average stationary density of a random walker in a sequence of snapshots under periodic boundaries. While in a static network, the stationary density of the random walk is proportional to the degree or the strength of a node, we find that in temporal networks, the stationary density is proportional to the in-strength of the so-called effective network, a weighted and directed network derived from the original transition matrix. The stationary density also depends on the sojourn probability that regulates the tendency of the walker to stay in the node. We apply our method to human interaction networks and show that although it is important for a node to connect to another node with many random walkers at the right moment (one of the principles of the PageRank), this effect is negligible in practice when the time order of link activation is included.

Contributed talk
Navigating Internet with group and degree information
Alok Kumar (Univeristé catholique de Louvain)
In this work, we present a new navigation scheme for the Internet. It exploits the degree and group of nodes for searching the path between the source and destination. The simulation results show that the scheme can successfully navigate information in a near-optimal manner.
Keywords. Navigation, routing, Internet, degree, group.

Contributed talk
Citation networks and their time constraint
James Clough (Imperial College London)
In many complex networks the vertices are ordered in time and edges represent causal connections. Citation networks have this causal structure because documents can only cite something that was written in the past. Such `temporal vertex networks' therefore form a directed acyclic graph. We argue that analysis methods for such networks must take the temporal constraint into account. We illustrate our approach by using Transitive Reduction on three very different examples and their appropriate null models: arXiv academic papers, US patents, and US Supreme Court verdicts. Transitive Reduction removes all edges which are unnecessary for the causal structure and so highlights connections essential for information transfer in the network.
We find that Transitive Reduction reveals significant differences between citation patterns in these networks, and between individual documents within them. For

instance, we find one academic paper which has 1641 citations only has 3 after TR, while another is only reduced from 806 to 77 citations. On average we find that only 20% of the citations between academic papers are required to maintain their causal structure, matching estimates made elsewhere with other techniques (e.g. Simkin and Roychowdhury, 2005). On the other hand around 90% of citations between patents are needed to maintain the causal structure there, revealing fundamental structural differences between citation networks in different contexts. We also find that in all cases Transitive Reduction is a powerful tool to tackle the effect that the age of a document has on its citation count.

We also show that Transitive Reduction reveals that null models of citations networks which generate networks with similar degree distributions to real networks often do not have the same degree distributions after Transitive Reduction, and so actually have significantly different causal structure.

Just as citation networks can only cite older documents, the causal sets approach to quantum gravity starts from a set of discrete space-time points, related only by their causal relationship. In both cases we have 'temporal vertex networks' which are examples of directed acyclic graphs. In the quantum gravity context the discrete structure is sufficient to fix the properties of the large scale continuous space-time we experience. In particular the space-time dimension can be estimated using just the causal relationships between the discrete points. We will show how to adapt these estimates of manifold dimension in order to characterise the structure of different citation networks.

We apply our dimension measures to the same three examples of citation network: academic papers on arXiv, US patents, and US Supreme Court judgements. We find that independent estimates of dimension converge on a consistent value for a given citation network. However, again we find that networks that otherwise appear very similar in structure turn out to have significantly different dimensions. We will show that by using network analysis methods that take the causal constraints into account, our approach reveals interesting distinctions in the structure of these temporal networks.

Note that most work on temporal networks is on data where the natural representation gives the edges a time (e.g. phone call networks). Such `temporal edge networks' are not directed acyclic graphs and the constraint of time appears in a different way in such cases.

Invited talk

How Basin Stability Complements the Linear-Stability Paradigm

Jürgen Kurths (Potsdam Institute for Climate Impact Research and Humboldt University Berlin)

The human brain, power grids, arrays of coupled lasers and the Amazon rainforest are all characterized by multistability. The likelihood that these systems will remain in the most desirable of their many stable states depends on their stability against significant perturbations, particularly in a state space populated by undesirable states. Here we claim that the traditional linearization-based approach to stability is too local to adequately assess how stable a state is. Instead, we quantify it in terms of basin stability, a new measure related to the volume of the basin of attraction. Basin stability is non-local, nonlinear and easily applicable, even to high-dimensional systems. It provides a long-sought-after explanation for the surprisingly regular topologies of neural networks and power grids, which have eluded theoretical description based solely on linear

stability. We anticipate that basin stability will provide a powerful tool for complex systems studies, including the assessment of multistable climatic tipping elements.
Specifically, we employ a novel component-wise version of basin stability, a nonlinear inspection scheme, to investigate how a grid's degree of stability is influenced by certain patterns in the wiring topology. Various statistics from our ensemble simulations all support one main finding: The widespread and cheapest of all connection schemes, namely dead ends and dead trees, strongly diminish stability. For the Northern European power system we demonstrate that the inverse is also true: `Healing' dead ends by addition of transmission lines substantially enhances stability. This indicates a crucial smart-design principle for tomorrow's sustainable power grids: add just a few more lines to avoid dead ends.
References:
P. Menck, J. Heitzig, N. Marwan, and J. Kurths, Nature Physics 9, 89 (2013)
P. Menck, J. Heitzig, J. Kurths, and H. Schellnhuber, Nature Communication (2014)

Contributed talk
Stochastic Optimal Control in Cooperative Multi-Agent Systems
Dimitri Papadimitriou (Bell Labs)
In this paper, we consider multi-agent systems where agents perform a joint task to satisfy time-varying and uncertain demands modeled by a stochastic process. Agents operate in a cooperative mode with partial knowledge/visibility of the global state of the system. In this context, Stochastic Optimal Control (SOC) enables to formulate agents best response as an infinite horizon discounted cost minimization problem and derive the optimal control law that agents have to apply to optimize their value function. The performance of agents is valued by a global cost function which is an integral of running costs plus an intervention cost, modeling an impulse control.

Contributed talk
Wave propagation in nonlinear networks
J.-G. Caputo (INSA de Rouen)
The propagation of localized waves in nonlinear networks is an ubiquitous problem. Examples are fluxon motion in arrays of Josephson junctions, pulse propagation in the circulatory system.. Modeling such problems is difficult and it is helpful to simplify the equation and the geometry. We will illustrate these issues with the analysis of the propagation of sine-Gordon waves through Y junctions. This is joint work with Denys Dutykh.

Invited talk
Real-world spreading phenomena: experiments on a large-scale P2P system
Fabien Tarissan (Université Pierre et Marie Curie)
Understanding the spread of information on complex networks is a key issue from a theoretical and applied perspective. Despite the effort in developing theoretical models for this phenomenon, gauging them with large-scale real-world data remains an important challenge due to the scarcity of open, extensive and detailed data. In this talk, we explain how traces of peer-to-peer file sharing may be used to this goal. We reconstruct the underlying social network of peers sharing content and perform simulations on it in order to assess the relevance of the standard SIR model to mimic key properties of real spreading cascades. The results show that it is insufficient to mimic real spreading cascades, thus raising an alert against the careless, widespread use of this

model. However, we also show that using the available temporal data in the trace and integrating it into an heterogeneous version for the spreading model enables to improve its relevance in this context.
Back to program.

Contributed talk
Dynamics of media attention
V.A. Traag (KITLV, Leiden)
Studies of human attention dynamics analyses how attention is focused on specific topics, issues or people. In online social media, there are clear signs of exogenous shocks, bursty dynamics, and an exponential or powerlaw lifetime distribution. We here analyse the attention dynamics of traditional media, focussing on co-occurrence of people in newspaper articles. The results are quite different from online social networks and attention. Different regimes seem to be operating at two different time scales. At short time scales we see evidence of bursty dynamics and fast decaying edge lifetimes and attention. This behaviour disappears for longer time scales, and in that regime we find Poissonian dynamics and slower decaying lifetimes. This suggests that a cascading Poisson process may take place, with issues arising at a constant rate over a long time scale, and faster dynamics at a smaller time scale.
Keywords: Co-occurrence network, media attention, attention dynamics, lifetime, Poisson process.

Invited talk
Community structure in multilayer networks
Marya Bazzi (University of Oxford)
An important feature in many networks is the existence of "communities", sets of nodes that are `more strongly' connected to each other than to nodes in the rest of a network. We investigate the detection of communities in multilayer networks using modularity maximization. "Modularity" is a function that measures the quality of a partition of nodes in a network by comparing edge weights within sets in the observed network to edge weights within sets in a "null network", generated from a specified "null model". We illustrate using financial asset correlation networks that the choice of null model should depend on the problem being studied.
To represent the temporal dimension of a network explicitly in the multilayer framework, one can adopt a choice of inter-layer connection that is uniform and "ordinal". We investigate this choice of representation in a generalization of modularity maximization to multilayer networks. We introduce a diagnostic to measure "persistence" in a multilayer partition, an indication of change in community structure through time. We prove some results to show how multilayer modularity maximization reflects the trade-off between static community structure within layers and higher values of persistence across layers. We discuss some issues that the popular Louvain algorithm faces when applied to multilayer networks with uniform and ordinal inter-layer connections, and we suggest ways to mitigate them. Our results extend to maximization problems where the quality function is not the modularity quality function, provided the resulting maximization problem has the same form.

Contributed talk
Driving forces of researchers' mobility
Floriana Gargiulo (University of Namur)

Using methods from network theory and complex systems analysis we study the researchers mobility in the framework of the research job market. Our aim is to understand which are the driving forces responsible for the choice of an academic position. Starting from the large corpus of papers published on the journals of the American Physical Society during the period 1955-2009, we reconstruct the individual researchers careers, namely the sequence of the consecutive affiliations for each scholar.

Contributed talk
Are power grids scale invariant?
Nicolas Retiere (Université de Grenoble)
Power grids are complex systems resulting from the interconnection of power sources and loads. A major source of their increasingly complexity comes from the large-scale implementation of intermittent generation and storage elements. Others factors of complexity are the development of new active loads such as electric vehicles and and the liberalization of the energy market. Hence, power grids analysis and design should benefit from the approaches adopted in various scientific fields to investigate complexity. In our case, we propose to establish whether power grids are scale invariant or not, meaning that there is power-law relations between the scale of observation and characteristic properties. If this assertion is proved to be true, the power-law relations could offer a comprehensive understanding of the emergence of grid properties (e.g. dynamic behavior, cascade resilience) without requiring time-consuming numerical simulations. For that purpose, scale invariance of model networks built from fractals will be first investigated. A particular attention will be paid to the dynamic properties of such networks and to the links with their self-similar topology. Then, we will study if realistic power grids exhibit the same features of scale invariance.

Contributed talk
Oscillations of networks: the role of soft nodes
A. Knippel (INSA de Rouen)
To describe the flow of a miscible quantity on a network, we consider the graph wave equation where the standard continuous Laplacian is replaced by the graph Laplacian. The structure of the graph influences strongly the dynamics. Assuming the graph is forced and damped at specific nodes, we derive the amplitude equations using a basis of eigenvectors of the graph Laplacian. These lead us to introduce the notion of soft nodes. We give sufficient conditions for their existence in general graphs. They can cause several effects as we show on small graphs, for example the ineffectiveness of damping applied to them. Soft nodes may be of critical importance for complex physical networks and engineering networks like power grids. This is joint work with Jean-Guy Caputo and Elie Simo.

Invited talk
Temporal patterns in mobile call networks
Jari Saramäki (Aalto University)
The temporal network framework is directly based on the activation timelines of links - in other words, contact sequences between nodes. This makes it especially suitable for studies of social networks and processes taking place on them. Instead of focusing on who knows who, much can be learned from studying in detail when individuals interact and the temporal patterns formed by their interaction events. I will present some findings on such patterns in mobile telephone communication, from temporal

inhomogeneities beyond burstiness to temporal motifs describing group-level communication patterns.

Contributed talk
Cluster Explosive Synchronization in Complex Networks
Peng Ji (Potsdam Institute for Climate Impact Research)
The emergence of explosive synchronization has been reported as an abrupt transition in complex networks of first-order Kuramoto oscillators. In this Letter we demonstrate that the nodes in a second-order Kuramoto model, perform a cascade of transitions toward a synchronous macroscopic state, which is a novel phenomenon that we call cluster explosive synchronization. We provide a rigorous analytical treatment using a mean-field analysis in uncorrelated networks. Our findings are in good agreement with numerical simulations and fundamentally deepen the understanding of microscopic mechanisms toward synchronization.
Keywords: Cluster explosive synchronization, Second-order Kuramoto model, Complex networks, Hysteresis, degree-frequency correlation

Contributed talk
Diffusion on atomistic, network models of proteins identifies allosteric sites and allosteric pathways
Ben Amor (Imperial College London)
Regulation of proteins at binding sites other than the active-site is central to many biochemical processes and such `allosteric' sites are currently major drug targets. However, classical models of allostery are phenomenological and cannot identify allosteric sites or predict how perturbations propagate through proteins. In this talk, we present a novel network-based method for identifying perturbation pathways in proteins which offers a number of advantages over previous approaches. Firstly, we start from an atomistic description where the edge weights in our network are based on the actual interaction energy between atoms. Secondly, since allosteric communication is transmitted through changes in weak interactions, we focus on long-range coupling between bonds (edges) in the network. Through the behaviour of a diffusive process on this network representation of the protein we derive a matrix in which the entries describe the coupling between weak interactions. We use this to determine which distant bonds are most closely coupled to the active site. We apply our method to three well-studied allosteric proteins, demonstrating in each case that we are able to correctly predict the allosteric site and important allosteric pathways. Furthermore, by analysing NMR ensembles and including water molecules in our network, we uncover information about pathways that would otherwise be missed; demonstrating the importance of dynamics and interaction with the solvent for allosteric behaviour.

Contributed talk
Semi-Formal Methodology for the modeling of high-dimensional and uncertain dynamical systems: Application to the Iron Homeostasis Network.
E. Fanchon (Univ. Grenoble Alpes)
Understanding the biological mechanisms at work within cells is a fundamental issue for improved diagnosis and the development of new therapeutic strategies (e.g. combinatorial therapies). The agents of biological processes at the molecular level are metabolites, proteins and other macromolecules interacting one with the other. The concept of network is thus central in Systems Biology, and networks of different types

are studied (biochemical network, genetic network, signaling network). Such systems have complex dynamics due to the nonlinearity of the basic kinetic laws, and the presence of numerous feedback loops. It is well recognized that two main features make the building and analysis of models of biological networks very difficult: (i) the state and parameter spaces are high-dimensional; (ii) the numerical values of many model parameters are poorly known, and biological data on behavior are often of a qualitative nature, and heterogeneous.

Proceedings of ICCSA 2014
Normandie University, Le Havre, France - June 23-26, 2014

EMERGENCE OF SOCIAL STRUCTURES VIA PREFERENTIAL SELECTION

Adam Lipowski and Dorota Lipowska *†‡

Abstract. We examine a weighted-network model of the formation of social structures. The model is based on preferential selection where individuals choose partners with the probability $p(w)$, where w is the number of their past selections. When $p(w)$ increases sublinearly with the number of past selections ($p(w) \sim w^\alpha$, $\alpha < 1$), agents develop a uniform preference for all other agents. For a superlinear increase ($\alpha > 1$), strong heterogeneities emerge and agents make selections mainly within small clusters. Formation of such clusters can be considered as a spontaneous symmetry breaking and might take place even in a few-agents case. Such (zero-dimensional!) transitions are analysed within a mean-field approximation and Monte Carlo simulations. At $\alpha = 1$ (linear increase), most of the links virtually vanish and the model undergoes a dramatic change of the community structure.

Keywords. Social structures, evolving weighted network, preferential selection, community structure

1 Introduction

Analysis of social networks is a rapidly growing research field, which draws an interdisciplinary interest of sociologists, psychologists but also statisticians, computer scientists, and many others [1]. Such networks reflect the nature of social interactions that are in fact responsible for many aspects of our life and political sentiments, disease spreading, business or friendship are just a handful of examples. To understand formation, structure and functioning of these intricate networks it is tempting to use statistical mechanics approaches where the global behaviour could be inferred from the behaviour of some basic building elements.

Taking into account that social links are of various nature or strength, and moreover, they often vary in time, one might expect that an adequate description of social structures should be provided within the framework of evolving weighted networks. However, substantial complexity of such models hampers their analysis and their understanding is still rather poor [3]. Let us notice that since social networks are examples of complex networks [2], progress in this area mihgt have a wider significance.

The motivation of the present work is to examine a model of the emergence of a social structure in a population of agents. In our model, interactions between agents constitute an evolving weighted network, the behaviour of which is analysed within some analytical as well as numerical approaches.

2 Model and Results

In our model, we consider N agents and we assign a (time-dependent) weight $w_{i,j}$ to each link connecting agents i and j ($i, j = 1, 2, \ldots, N$). The dynamics of the model is defined by the following rules: In each step, one selects an agent with the probability $1/N$. The selected agent, using the roulette-wheel selection [4], chooses one of its neighbours with the probability proportional to $w_{i,j}^\alpha$ (where $\alpha > 0$ is a preference exponent) and the weight of the corresponding link increases by one ($w_{i,j} \to w_{i,j} + 1$).

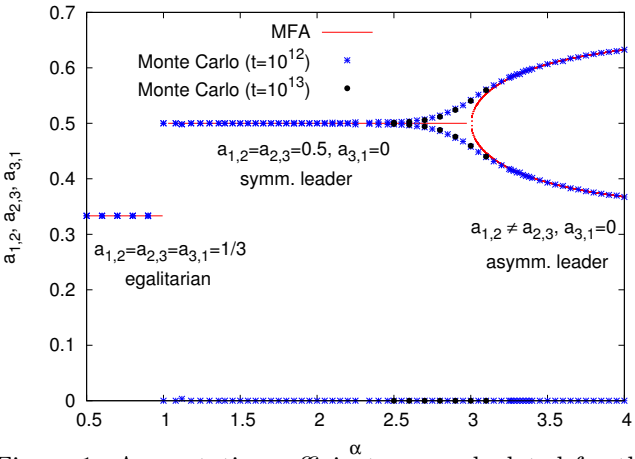

Figure 1: Asymptotic coefficients $a_{i,j}$ calculated for the $N = 3$ system using the mean-field approximation (2) and Monte Carlo simulations

Some analytical insight into the behaviour of our model can be obtained using mean-field arguments. In particular, from the dynamical rules one can deduce that an average evolution of weights should approximately obey

*Adam Lipowski is with Faculty of Physics, Adam Mickiewicz University in Poznań, Poland. E-mail: lipowski@amu.edu.pl
†Dorota Lipowska is with Institute of Linguistics, Adam Mickiewicz University in Poznań, Poland. E-mail: lipowska@amu.edu.pl
‡Manuscript received April 21, 2014

the following set of $N(N-1)/2$ equations:

$$\langle w_{i,j}\rangle_{t+1} = \langle w_{i,j}\rangle_t + \frac{1}{N}\langle w_{i,j}\rangle_t^{\alpha}\left(\frac{1}{z_i}+\frac{1}{z_j}\right) \qquad (1)$$

where t is the number of steps and $z_i = \sum_{k\neq i}\langle w_{i,k}\rangle^{\alpha}$. In general, it is difficult to solve Eqs. (1). However, it is plausible to assume that asymptotically (i.e., for large t) $\langle w_{i,j}\rangle_t = a_{i,j}t$ and this transforms Eqs. (1) into a set of nonlinear equations. To examine the validity of the above equations, we have also analysed the behaviour of our model using Monte Carlo simulations, which implement the dynamical rules of the model. First, let us analyse the smallest N of a nontrivial behaviour, namely $N = 3$. In this case coefficients $a_{i,j}$ obey equations of the following form:

$$\begin{aligned} a_{1,2} &= \frac{1}{3}\left(\frac{a_{1,2}^{\alpha}}{a_{1,2}^{\alpha}+a_{2,3}^{\alpha}}+\frac{a_{1,2}^{\alpha}}{a_{1,2}^{\alpha}+a_{3,1}^{\alpha}}\right) \\ a_{2,3} &= \frac{1}{3}\left(\frac{a_{2,3}^{\alpha}}{a_{2,3}^{\alpha}+a_{3,1}^{\alpha}}+\frac{a_{2,3}^{\alpha}}{a_{2,3}^{\alpha}+a_{1,2}^{\alpha}}\right) \qquad (2) \\ a_{3,1} &= \frac{1}{3}\left(\frac{a_{3,1}^{\alpha}}{a_{3,1}^{\alpha}+a_{1,2}^{\alpha}}+\frac{a_{3,1}^{\alpha}}{a_{3,1}^{\alpha}+a_{2,3}^{\alpha}}\right) \end{aligned}$$

From the solution of Eqs. (2) and from Monte Carlo simulations, one finds that for $\alpha < 1$ the only stable solution is the egalitarian one with $a_{1,2} = a_{2,3} = a_{3,1} = 1/3$, in which case agents develop equal preferences for each other (Fig. 1). For $1 < \alpha < 2.5$, the solutions are of the form $a_{1,2} = a_{2,3} = 1/2$, $a_{3,1} = 0$ (and all permutations). It means that the spontaneous symmetry in the three-agent system gets broken and two agents never select each other. As a result, the third agent becomes a symmetric leader, which is being selected much more often (2/3) than the remaining two agents (1/6). For $\alpha > 2.5$, the symmetry between those agents breaks even more and an asymmetric leader appears with a larger preference for one of the two agents.

Let us notice that despite being only approximate, Eqs. (2) provide quite an accurate description of the model. Some discrepancy with Monte Carlo simulations exists in the vicinity of $\alpha = 2.5$ ('the critical point'; see Fig. 1). We performed similar analyses for a larger number of agents N. Our results show that in this case even richer structures are formed and the parameter α plays an important role in determining their stability. In general, for $\alpha < 1$ egalitarian solutions were found to be stable and for $\alpha > 1$ various clusters of agents emerge. A certain insight into the behaviour of the model for large N can be obtained by determining the community structure of our weighted network (we used a modularity maximization method [5]). As shown in Fig. 2, the average size of a giant community drastically changes at $\alpha = 1$ too. The decomposition into rather small communities at $\alpha = 1$ is also accompanied by vanishing of a substantial proportion of weights. A small fraction of non-vanishing

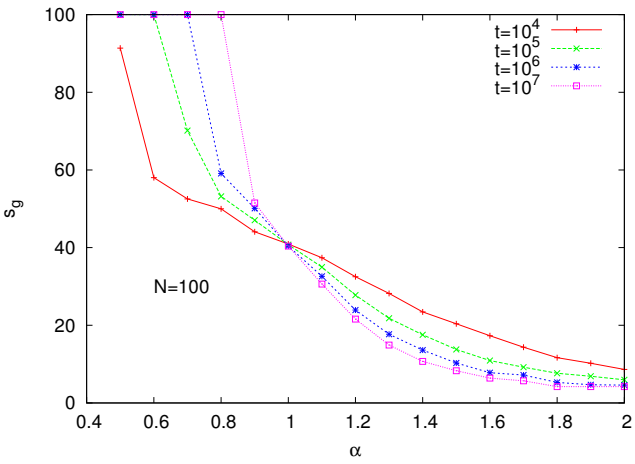

Figure 2: The average size of the giant community s_g as a function of α for $N = 100$ agents.

weights (at $\alpha > 1$) is apparently not able to sustain large (global) clusters, which suggests that the transition at $\alpha = 1$ might be a kind of a percolation transition.

3 Conclusions

In the present paper we introduced a simple model of formation of social structures via a preferential selection mechanism. Our model predicts the transition between two phases: (i) the egalitarian one, where agents select each other with an equal probability and (ii) the phase, where agents select each other only within small clusters. Some of the clusters are asymmetric, which suggests that the model might describe formation of more complex social structures. The largest and most complex clusters are particularly likely at the transition point between the two phases ($\alpha = 1$). Does it suggest that complex societies operate in the linear regime?

Acknowledgements

The research for this work was supported by NCN grants 2013/09/B/ST6/02277 (A.L.) and 2011/01/B/HS2/01293 (D.L.).

References

[1] S. Wasserman and K. Faust, "Social Network Analysis", Cambridge University Press (1994).

[2] R. Albert and A.-L. Barabasi, "Statistical mechanics of complex networks", Rev. Mod. Phys. vol. 74, 47 (2002).

[3] S. H. Yook, H. Jeong, and A.-L. Barabási,"Weighted Evolving Networks", Phys. Rev. Lett. **86**, 5835-5838 (2001). A. Barrat, M. Barthélemy, and A. Vespignani, "Weighted Evolving Networks: Coupling Topology and Weight Dynamics", Phys. Rev. Lett. **92**, 228701 (2004)

[4] For a fast and simple implementation of the roulette selection, see, e.g.: A. Lipowski and D. Lipowska, "Roulette-wheel selection via stochastic acceptance", Physica A **391**, 2193 (2012).

[5] M. E. J. Newman, Phys. Rev. E **69**, 066133 (2004).

Proceedings of ICCSA 2014
Normandie University, Le Havre, France - June 23-26, 2014

DYNAMICS OF MEDIA ATTENTION

V.A. Traag*, R. Reinanda, J. Hicks, G. Van Klinken †‡§

Abstract. Studies of human attention dynamics analyses how attention is focused on specific topics, issues or people. In online social media, there are clear signs of exogenous shocks, bursty dynamics, and an exponential or powerlaw lifetime distribution. We here analyse the attention dynamics of traditional media, focussing on co-occurrence of people in newspaper articles. The results are quite different from online social networks and attention. Different regimes seem to be operating at two different time scales. At short time scales we see evidence of bursty dynamics and fast decaying edge lifetimes and attention. This behaviour disappears for longer time scales, and in that regime we find Poissonian dynamics and slower decaying lifetimes. This suggests that a cascading Poisson process may take place, with issues arising at a constant rate over a long time scale, and faster dynamics at a smaller time scale.

Keywords. co-occurrence network • media attention • attention dynamics • lifetime • Poisson process.

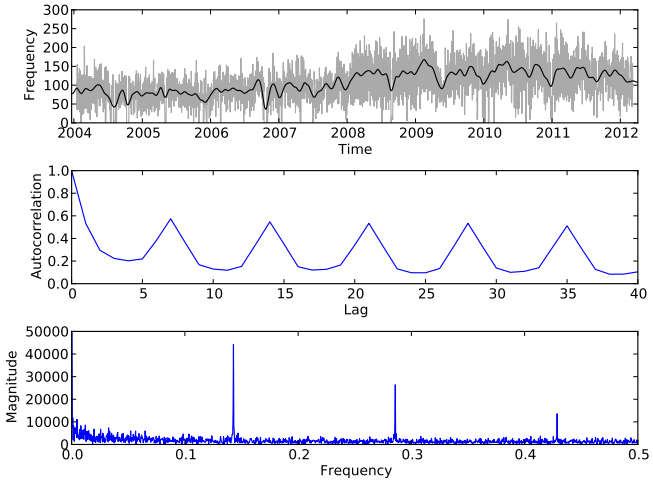

Figure 1: Daily node frequency. The first panel contains the number of nodes in the newspaper (that have at least one co-occurrence) per day (in gray), with the solid black line representing a smoothing (using convolution with a Hann window of 8 weeks) of this daily frequency. The second panel shows the autocorrelation function, which shows a clear peak at a lag of 7 days, indicating there is a weekly pattern in the data. This is also confirmed by Fourier analysis in the third panel, which shows a clear peak at a frequency of $1/7 \approx 0.14$.

1 Introduction

With the arrival of large scale data sets, interest in quantifying human attention rose. It became possible to measure quite precisely how attention grew and decayed [1]. Moreover, it appeared that many human dynamics showed signs of bursty behaviour: short windows of intense activity with long intermittent time spans of inactivity [2]. The duration a person is active—the time between its first and last occurrence, i.e. its lifetime—seems to decay as an exponential, while the edge lifetime seems to follow a powerlaw distribution [3, 4].

We analyse a large dataset of newspaper articles from traditional printed media. We show that the dynamics of this dataset are quite different from social media. Our data consist of 140 263 newspaper articles from Indonesia from roughly 2004 to 2012, gathered by a news service called *Joyo*, mainly focussing on political news. We automatically identify entities by using a technique known as named entity recognition, and only retain person names (we discard organisations and locations) [5]. We then construct a network by creating a node for every person and an edge for each co-occurrence between two persons, and we record the date of the co-occurrence. We only take into account co-occurrences of people in the same sentence, and only about 3.2% of the sentences contain more than one person, so this is quite restrictive. All time is measured in days.

2 Results

In total, there are $n = 9\,467$ nodes and they have about $\langle k_i \rangle \approx 12$ neighbours on average. Two people co-occur on average about 3 times. Let us first simply look at how these quantities vary over time. Let E_t be the number of co-occurrences at time t, and N_t the number of nodes that have a co-occurrence at time t. The dynamics of N_t follow a distinctive weekly pattern (Fig. 1). This is confirmed by the autocorrelation function, which shows a clear peak at a lag of 7 days with a correlation of about 0.57, while the Fourier transform shows clear peaks at a frequency of about $1/7 \approx 0.14$. Results for E_t follow a similar pat-

*Corresponding author: vincent@traag.net
†All authors are with the KITLV, Leiden, the Netherlands
‡R. Reinanda is associated to Faculty of Sciences, University of Amsterdam, the Netherlands
§Manuscript received April 19, 2009; revised January 11, 2010.

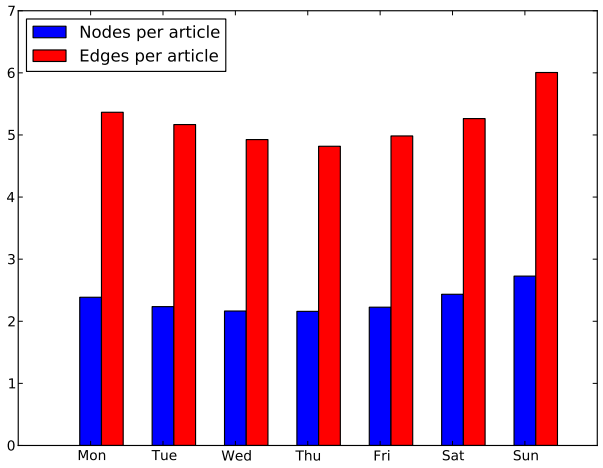

Figure 2: Number of nodes and edges per article per day of the week. Although the largest part of the cyclical behaviour is due to the weekly newscycle (weekend vs. weekday), there still remains some cyclical patterns after normalisation.

tern. Although this largely follows the weekly cycle of the number of articles, some cyclic pattern remains if the node frequencies are normalised by the article frequencies (Fig. 2). For the nodes this pattern is quite weak, but for the edges more noticeable. Surprisingly, the cycle seems to be at its high point at the end/beginning of the week, while its low point is attained in the middle of the week.

Let us denote by $N_t(i)$ the number of co-occurrences of node i with any other node at time t. Neighbours tend to show quite similar patterns of attention, much more than compared to the overall trend. This suggests that attention for people rises and falls together, hinting at some underlying commonality. One possible explanation is that issues arise in which people play a role together, so that they tend to show similar patterns of attention.

Let $t_p(i) = \arg\max_t N_t(i)$ be the peak of the number of co-occurrences of node i with any other node (if there are multiple such times the first is used). We then normalise the time series, such that the peak is centred at 0 with a value of 1, and denote the average of these time series by $\tilde{N}_t$ (see Fig. 3a). Hence $\tilde{N}_0 = 1$, and we are interested in how $\tilde{N}_t$ grows for $t < 0$ and decays for $t > 0$. It was suggested that $\tilde{N}_t \sim |t|^{-\beta}$, where different exponents β would correspond to different universal classes [1]. However, it was also suggested that $\tilde{N}_t \sim -\beta \log |t|$, which is unrealistic for large times since $-\log |t| < 0$ for sufficiently large t. Alternatively, an exponential growth and decay $\tilde{N}_t \sim e^{-\beta|t|}$ is a common phenomena, suggesting the rate of growth/decay is constant throughout time.

However, we find that none of these satisfactorily model the growth and decay of attention. The logarithmic and exponential grow/decay too slowly at a small time (around 10–30 days), while the powerlaw poorly fits the dynamics for larger times. This suggests that $\tilde{N}_t \sim e^{-\beta|t|}|t|^{-\gamma}$ might be a better fit. Indeed, this functional form quite accurately captures the growth and decay in our data, and comparing AIC values, clearly points to this model (see Table 1 for results). This suggests that at a short timescale there is a very fast (powerlaw) decay, but that at longer timescales the exponential decay dominates. In fact, it suggest that the attention essentially diverges for $|t| \to 0$.

Although there is a large degree of symmetry, which would suggest an endogenous pattern following [1], we do find different exponents for the growth and decay (see Table 1). In particular, the decay seems slightly slower than the growth at short time scales, and nodes tend to occur more frequently after their peak than before their peak on longer time scales, contrary to [6].

Let $t_s(i,j)$ be the time of the s^{th} co-occurrence between node i and j. The inter-event time can then be denoted by $\delta_s(i,j) = t_{s+1}(i,j) - t_s(i,j)$, which can possibly be 0 if two (or more) co-occurrences happened at the same day. Similarly for nodes, we denote by $t_s(i)$ the s^{th} co-occurrence of i with another node, and by $\delta_s(i) = t_{s+1}(i) - t_s(i)$ the inter-event time. If events happen at a constant rate, we would expect an exponential distribution of inter-event times. If events follow a bursty patter however, we expect to find a powerlaw inter-event time distribution, often observed in other settings [2]. We find that although the inter-event times decay quite fast at a relatively short time scale, the inter-event times for a larger time scale follow an exponential distribution (Fig. 3b). Altogether, a powerlaw with exponential cutoff $p(x) \sim x^{-\alpha}e^{-\beta x}$ provides the better fit , compared to a pure powerlaw or pure exponential distribution (log-likelihood ratios $6.3 \cdot 10^4$ and $3 \cdot 10^4$). For the edges, using MLE we find coefficients $\alpha \approx 1.003 \pm 2.6 \cdot 10^{-3}$ and $\beta \approx 0.00151 \pm 1.1 \cdot 10^{-5}$, while for the nodes the distribution is slightly less skewed, but decays slightly faster, with $\alpha = 1.045 \pm 3.7 \cdot 10^{-3}$ and $\beta = 0.00244 \pm 2.3 \cdot 10^{-5}$, both using $x_{\min} = 10$. Indeed, for even shorter time intervals, the decay is very fast, and using lower $x_{\min}$ gives poorer fits.

One possible explanation is that if somebody is involved in an issue, his co-occurrence will show a bursty pattern at this shorter time scale, but that the rate at which somebody is involved in an issue follows a Poisson process over a longer time scale, suggesting something like a cascading Poisson process [2].

If the processes would be stationary, then the expected first time we observe a node would be $\langle t_0(i) \rangle = \frac{\langle \delta_s(i)^2 \rangle}{2\langle \delta_s(i) \rangle}$ (and similarly so for edges). Of course there is some censoring in the data, and for those nodes (and edges) we would expect to find $t_0(i) \approx \langle t_0(i) \rangle$. However, if the actual first time a node appears in the paper $t_0(i)$ is much larger than this expected value $\langle t_0(i) \rangle$, it suggest this really is the first time this person appears in the media. We call the difference $\Delta t_0(i) = t_0(i) - \langle t_0(i) \rangle$ the "first time delay", and the distribution is plotted in Fig. 3c. First,

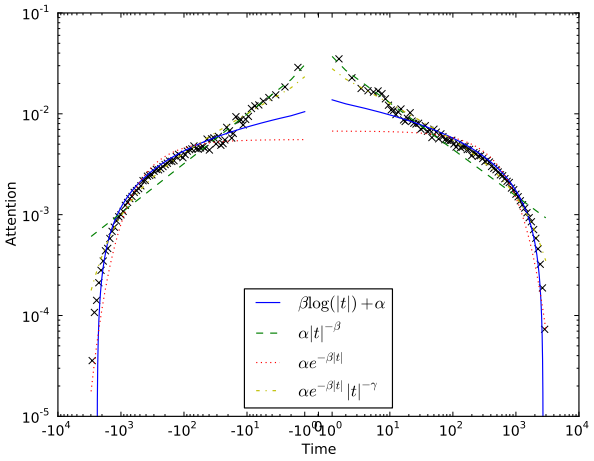

(a) Peak attention

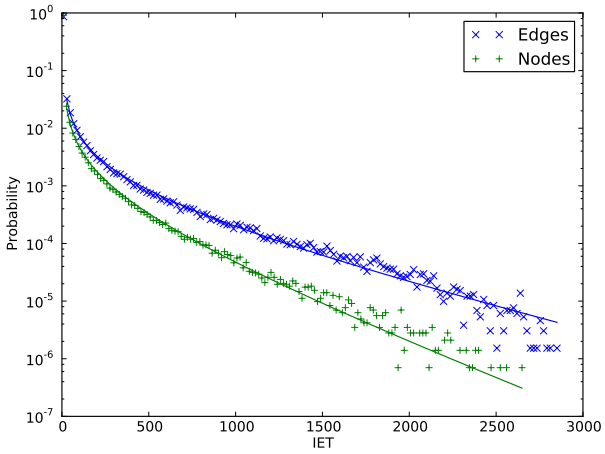

(b) Inter event time

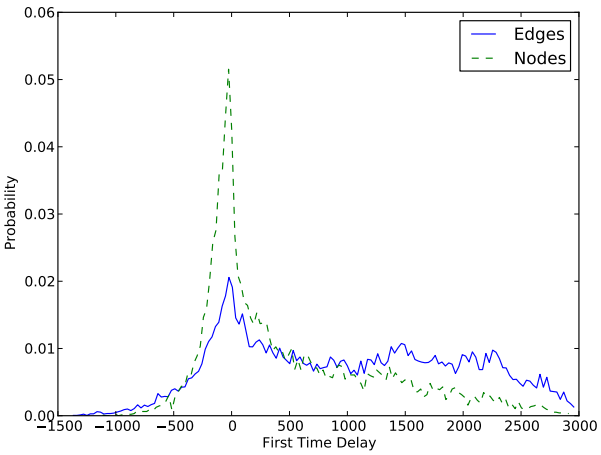

(c) First time delay

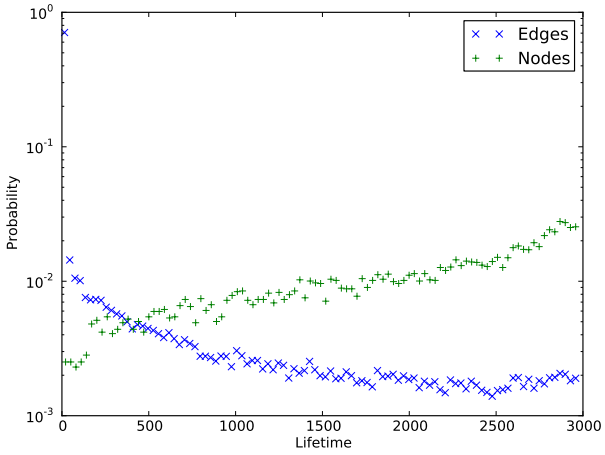

(d) Life time

Figure 3: Attention statistics. Panel (a) shows how attention—as in the frequency of occurring—grows and decays with the peak attention centred at zero. Panel (b) shows the inter-event time distribution, which has a clear exponential tail, suggesting a Poisson process. Panel (c) shows the distribution of the first time delay. This delay represents the difference between the time at which we would expect to first observe a node (or edge) and the time at which we actually observed it in the dataset. This suggests that new nodes and edges are continuously being observed. Finally, in panel (d) the lifetime—the amount of time between the first and last time of observing that node or edge—follows a very peculiar distribution. The edge lifetime decays very fast for the first few days, but then only decays very slowly. The node lifetime actually shows an increasing distribution, suggesting they can have a very long lifetime.

there is a clear peak around $\Delta t_0(i) = 0$, suggesting that censoring played a role in observing these nodes for the first time. The fast decay that is visible on the negative part, does not show at the positive part. This implies that many nodes and edges are first observed much later than expected. This suggests that these nodes and edges are only introduced at a later time. Hence, there are continuously new edges and nodes appearing in the news. This seems especially prominent for the edges, which show an almost uniform distribution between 250–2 000 days of difference, whereas the distribution for the nodes decays more continuously.

We denote by $\Delta(i,j) = \max t_s(i,j) - \min t_s(i,j)$ the lifetime of an edge, and similarly by $\Delta(i)$ the lifetime of a node (Fig. 3d). Most edges have a very low lifetime of only a single day, and the probability to have a larger lifetime quickly decreases. Nonetheless, after an initial rapid decay, the probability decays much slower. This

	Model	$\alpha - \beta \log \lvert t \rvert$	$\alpha \lvert t \rvert^{-\beta}$	$\alpha e^{-\beta t}$	$\alpha e^{-\beta \lvert t \rvert} \lvert t \rvert^{-\gamma}$
Growth	α	$0.011 \pm 6.9 \cdot 10^{-5}$	$0.031 \pm 3.2 \cdot 10^{-4}$	$0.0056 \pm 6.3 \cdot 10^{-5}$	$0.0233 \pm 1.9 \cdot 10^{-4}$
	β	$0.0013 \pm 9.8 \cdot 10^{-6}$	$0.49 \pm 2.3 \cdot 10^{-3}$	$0.0019 \pm 3.1 \cdot 10^{-5}$	$6.6 \cdot 10^{-4} \pm 1.2 \cdot 10^{-5}$
	γ	–	–	–	$0.36 \pm \cdot 2.3 \cdot 10^{-3}$
	ΔAIC	3 117	3 045	4 883	–
Decay	α	$0.014 \pm 8.1 \cdot 10^{-5}$	$0.037 \pm 3.8 \cdot 10^{-4}$	$0.0067 \pm 7.1 \cdot 10^{-5}$	$0.028 \pm 2.3 \cdot 10^{-4}$
	β	$0.0017 \pm 1.1 \cdot 10^{-5}$	$0.46 \pm 2.1 \cdot 10^{-3}$	$0.0015 \pm 2.3 \cdot 10^{-5}$	$5.5 \cdot 10^{-4} \pm 9.8 \cdot 10^{-6}$
	γ	–	–	–	$0.34 \pm 2.2 \cdot 10^{-3}$
	ΔAIC	2 559	2 986	4 820	–

Table 1: Growth and decay estimates and model performance. The AIC differences are quite high, and suggest that $\alpha e^{-\beta|t|}|t|^{-\gamma}$ is the best model.

suggests that besides the more volatile short term links, there are quite some long term stable links. The node lifetimes show a quite unexpected behaviour. Although there are nodes that have a lifetime that is quite short, nodes tend to have a longer lifetime, only cutoff by the duration of the dataset. This suggests that the lifetime of nodes can be extremely long, and can easily run in the decades.

3 Conclusion

Online social media show signs of exogenous shocks, bursty dynamics and exponential lifetime distributions. We have shown here that traditional media seems to operate differently. The current results suggest the media operates at two different time scales. There is a short time scale which operates at the level of issues: links have short lifetime, attention decays quickly and there are indications of burstiness. However, at a longer time scale, these issues seem to occur at a uniform rate, and often involve similar actors: nodes and links have a relatively long lifetime, attention decays slower, and inter-event times decay exponentially. We aim to further analyse this idea in future research, following the cascading Poisson model [2].

References

[1] R. Crane, D. Sornette, *Proc. Natl. Acad. Sci. USA* **105**, 15649 (2008).

[2] R. D. Malmgren, D. B. Stouffer, A. E. Motter, L. A. N. Amaral, *Proc. Natl. Acad. Sci. USA* **105**, 18153 (2008).

[3] C. A. Hidalgo, C. Rodriguez-Sickert, *Physica A* **387**, 3017 (2008).

[4] J. Leskovec, L. Backstrom, R. Kumar, A. Tomkins, *Proceedings of the 14th ACM SIGKDD International Conference on Knowledge Discovery and Data Mining*, KDD '08 (ACM, New York, NY, USA, 2008), p. 462470.

[5] J. R. Finkel, T. Grenager, C. Manning, *Proceedings of the 43rd Annual Meeting on Association for Computational Linguistics*, ACL '05 (Association for Computational Linguistics, Stroudsburg, PA, USA, 2005), p. 363370.

[6] J. Leskovec, L. Backstrom, J. Kleinberg, *Proceedings of the 15th ACM SIGKDD International Conference on Knowledge Discovery and Data Mining*, KDD '09 (ACM, New York, NY, USA, 2009), p. 497506.

Satellite Workshop 4
Space, Topology, Diffusion and Language (STDL): Models, Simulation and Visualization

Satellite Workshop 4
Space, Topology, Diffusion & Language (STDL): Models, Simulation and Visualization

Organizers

- Jean Léo Léonard, IUF & Paris 3, jeanleoleonard@yahoo.fr
- Gérard H. E. Duchamp, LIPN, Paris 13, gheduchamp@gmail.com

Description

The STDL satellite workshop will survey and deepen recent aspects of the application of Complexity Theory (henceforth, CT) to linguistic data or to issues related to spatial and social diffusion of language (dialects or standard languages, "dominant" versus "minority" languages: see Massip-Bonet & Bastardas-Boada, 2013; Patriarca & al. 2012). A focus on geolinguistics (dialect variation in space and time), and the study of dialect or sociolinguistic networks (cf. Milroy, 1980, 2002, Milroy & Gordon, 2008; Mercklé, 2004) is strongly encouraged. The quantitative turn in linguistics, especially in geolinguistics (dialectometry, see Goebl, 1981, 2002; Levensthein algorithm, see Bolognesi & Heeringa, 2002, Beijering, Gooskens & Heeringa 2008; Brown, Holman, Wichmann & Velupillai, 2008, etc.), make linguistic data more available than ever to CT applications. Modeling and simulation is easier on quantitative values, e.g. on interlinguistic distance or similarity, than on phonemes and morphemes. In sociolinguistics, even the co-variationist method, initially contrived by William Labov (1972, 1994, 2001), is being applied to endangered languages, or languages scarcely described up to now (Stanford & Preston, 2009). CT enters the field of quantitative linguistics, especially in fields connected to linguistic ecology (Mufwene, 2013, 2001), beyond the bit complexity approach (Miestamo, Sinnemaki & Karlsson, 2008). The STDL satellite workshop calls for participants from various background, such as mathematics, physics, taxonomy, biology, linguistics, to analyse geolinguistic or sociolinguistic data, from a CT standpoint (Gribbin, 2004; Weisburch & Swirn, 2010). It will explore three strands:
Evolution & diffusion of language(s) in space and time: modeling and visualization.
Competition models and Geolinguistic Spaciality
Game theory (naming game, toy-models, etc.), Geospatiality and Topology.
A focus not only on modeling of language diffusion processes, but also on simulation (Patriarca & Heinsalu, 2009) and visualization (Doan & Lebbah, 2013; Lima, 2013) is expected. In these domains, CT turns out to be a seminal and challenging approach, due to the long tradition and, to a certain extent, the overload of empirical research in geolinguistics, sociolinguistics and language diffusion studies.

References

- Beijering, K. Gooskens C. & Heeringa W. 2008. "Predicting intelligibility and perceived linguistic distance by means of the Levenshtein algorithm", Amsterdam, Linguistics in the Netherlands, 2008,), 13-24.
- Bolognesi, R. and W. Heeringa, 2002. "De invloed van dominante talen op het lexicon en de fonologie van Sardische dialecten". In: D. Bakker, T. Sanders, R. Schoonen and Per van der Wijst (eds.). Gramma/TTT: tijdschrift voor taalwetenschap, Nijmegen University Press, Nijmegen, 9 (1): 45-84.

- Brown, Cecil H., Holman, Eric W., Wichmann, Søren and Velupillai, Viveka. 2008. "Automated classification of the world's languages: a description of the method and preliminary results". STUF Language Typology and Universals 61, 285-308.
- Doan Nhat-Quang, Hanane Azzag & Mustapha Lebbah, 2013. « Growing Self-organizing Trees for Autonomous Hierarchical Clustering », Neural Networks. Special Issue on Autonomous Learning, 41: 85–95.
- Gribbin, John, 2004. Deep Simplicity, Chaos, Complexity and the Emergence of Life, London, Penguin.
- Goebl, Hans 1981. « Eléments d'analyse dialectométrique (avec application à l'AIS) », Revue de Linguistique romane, 45 : 349-420.
- Goebl, Hans 2002. « Analyse dialectométrique des structures de profondeur de l'ALF », Revue de Linguistique Romane, 66 : 5-63.
- Labov, William, 1972. Sociolinguistic Patterns, Philadelphia, University of Pennnsylva nia Press.
- Labov, William, 1994. Principles of Linguistic Change. Vol. I: Internal Factors, Oxford, Blackwell.
- Labov, William, 2001. Principles of Linguistic Change. Vol. II: Social Factors, Oxford, Blackwell.
- Lima, Manuel, 2013. Cartographie des réseaux : l'art de représenter la complexité, Paris, Eyrolles.
- Massip-Bonet, Àngels & Albert Bastardas-Boada (eds.), 2013. Complexity Perspectives on Language, Communication and Society, Springler.
- Mercklé, Pierre, 2004. Sociologie des réseaux, Paris, La Découverte.
- Miestamo, Matti, Kaius Sinnemaki & Fred Karlsson (eds.), 2008. Language Complexity: Typology, Contact, Change. Amsterdam, John Benjamins.
- Milroy, Lesley, 1980. Language and Social Networks, Oxford, Blackwell.
- Milroy, Lesley, 2002. « Social Networks », in The Handbook of Language Variation and Change, Oxford, Blackwell: 549-572.
- Milroy, Leslie & Matthew Gordon, 2008. « The Concept of Social Network », Sociolinguistics: Method and Interpretation, Oxford, John Wiley & Sons: 116-133.
- Mufwene, Salikoko, 2013. Complexity perspectives on language, communication, and society, in Ángels Massip-Bonet & Albert Bastardas-Boada, Springer Verlag: 197-218.
- Mufwene, Salikoko, 2001. The Ecology of Language Evolution, Cambridge Approaches to Language Contact, Cambridge, CUP.
- Patriarca, M., X.Castello, Uriarte, J., Eguiluz, V. & Miguel, M. S., 2012. « Modeling two language competition dynamics », Advances in Complex Systems, 15: 125-48.
- Patriarca, M. & Heinsalu, E., 2009. "Influence of geography on language competition", Physica A 388, 174.
- Stanford, James & Preston Dennis, 2009, Quantitative Sociolinguistic Studies of Indigenous Minority Languages, John Benjamins Publishing Company, series « IMPACT: Studies in Language and Society ».
- Weisbuch, Gérard & Zwirn, André (eds.), 2010. Qu'appelle-t-on aujourd'hui les sciences de la complexité ? Langages, réseaux, marchés, territoires, Paris, Vuibert.

Programme

Salikoko S. Mufwene (University of Chicago)
Title : What Makes Language Evolution So Complex and Difficult to Model Accurately?
Scheduled : Monday June 23, 2014, 16:00-17:30
Abstract: Like any other kind of evolutionary process, language evolution is unplanned. It is the outcome of how adaptively individuals interacting with each other both reproduce and innovate ways of communicating information successfully, a process marked by successive changes between time t1 and tn (t1, t2, t3… tn). While it is convenient and relatively easier to describe changing norms or communal patterns within a population, it is more difficult to account for the actuation of the changes. In the latter case, there are several ecological factors that bear on the evolutionary process, including: 1) the error-prone process of spreading innovations by learning and instantiating them (unlike in the inheritance of genetic traits); 2) variation in innovations, which generates competition between/among variants (during the convergence towards communal norms); 3) the periodization following from differences between the times of particular innovations (and their consequences); and 4) population structure (which constrains how innovations spread and how far). Perhaps more difficult is the fact that evolutionary theories have focused on documenting population-level outcomes of behaviors that are actually specific to and centered around individual agents, none of whom is aware of the full extant system at the time they innovate or borrow an innovation (and thereby contribute to spreading it). Often, they are not even aware of alternatives that already exist or are being innovated by others, though not exactly in the same way, at the time of their behavior. This is when the distinction between internally- and externally-motivated change (articulated inaccurately in traditional historical linguistics!) becomes significant to whoever in concerned with the actuation of change. Self-organization is of course part of the big picture, to the extent that it explains (or does it?) how everything comes together in the emergent system, but we do face the challenge of explaining the nature of the complexity inherent in language evolution. I submit an account that applies not only to structural changes but also to language vitality.

Léo Léonard (IUF & Paris 3, UMR 7018) & Vittorio dell'Aquila (CELE, Milan & Vaasa) Avec la collaboration da Antonella Gaillard-Corvaglia (Postdoc, Inalco)
Title : Algorithmic complexity applied to geolinguistic networks
Scheduled : Monday June 23, 2014, 17:30-18:00
Abstract: Dialectology has long been considered as a marginal field in linguistics, mainly concerned with the recollection of empirical facts, with low theoretical expectations. Nevertheless, thanks to quantification of dialectical data (dialectometry, see Goebl, 1981, 1982, 2002)), geolinguistics in particular turns out to be one of the most promising horizon for Complexity Theory (CT) - as much as CT opens new horizons for dialectology. We'll apply various methods to a Mazatec database from Paul L. Kirk (1966), providing 9000 tokens (750 cognates x 12 locolects): patristic distances (cladistics, see Hennig, 1950, 1966), Levenshtein algorithm (Beijering & al. 2008, Bolognesi & Heeringa, 2002) and dialect intelligibility tests (Kirk, 1970), in order to show multiplicity of prospects on a geolinguistic space. Mazatec as a case study for testing algorithmic complexity has been chosen on several grounds: i) it once provided the empirical base for a landmark study by Sarah Gudschinsky (1958) on the

reconstruction of dialect diversification process (1958), ii) Kirk's data, with less than 10 000 tokens is easier to process than bigger data available on European languages, iii) we have thoroughly checked and revisited Kirk's data through fieldwork within the framework of an empirical research project (IUF, MAmP, 2009-14, see Léonard & al. 2012), iv) phonology and grammar of Mazatec dialects have been formalized within the same project (with declarative phonology and Paradigm Function Morphology). Conditions for a survey of algorithmic complexity are therefore met, allowing a multiplex modeling of Mazatec geolinguistics.

Bibliography :

- Beijering K. Gooskens C. & Heeringa W. "Predicting intelligibility and perceived linguistic distance by means of the Levenshtein algorithm" , Amsterdam, Linguistics in the Netherlands, 2008,), 2008, p. 13-24.
- Bolognesi, R. & W. Heeringa, "De invloed van dominante talen op het lexicon en de fonologie van Sardische dialecten", in D. Bakker, T. Sanders, R. Schoonen and Per van der Wijst (eds.). Gramma/TTT, Tijdschrift voor taalwetenschap, Nijmegen University Press, Nijmegen, 9 (1), 2002, p. 45-84.
- Goebl Hans, "Eléments d'analyse dialectométrique (avec application à l'AIS)", Revue de Linguistique romane, 45, 1981, p. 349-420.
- Goebl Hans, Dialektometrie. Prinzipien und Methoden des Einsatzes der numerischen Taxonomie im Bereich der Dialektgeographie, Vienne, Verlag der Öst. Akademie der Wissenschaften, 1982.
- Goebl Hans, "Analyse dialectométrique des structures de profondeur de l'ALF" , Revue de Linguistique Romane, 66, 2002, p. 5-63.
- Gudschinsky Sarah, "Mazatec dialect history", Language 34, 1958, p. 469-481.
- Gribbin, John, Deep Simplicity, Chaos, Complexity and the Emergence of Life, London, Penguin, 2004.
- Hennig Willi, Grundzüge einer theorie der Phylogenetischen systematik, Berlin, Deutscher Zentralverlag, 1950.
- Hennig Willi, Phylogenetic Systematics. Urbana, University of Illinois Press, 1966.
- Kirk Paul L., Proto-Mazatec phonology. PhD dissertation, University of Washington, 1966.
- Kirk Paul L., "Dialect Intelligibility Testing: The Mazatec Study", International Journal of American Linguistics, 36-3, 1970, p. 205-211.
- Léonard Jean Léo ; dell'Aquila, Vittorio & Gaillard-Corvaglia, Antonella "The ALMaz (Atlas Linguistico Mazateco): from geolinguistic data processing to typological traits", STUF, Akademie Verlag, 6, 2012, p. 78 -94.

Stefan Balev (ISCN, Le Havre), Gérard H.E. Duchamp (LIPN, Paris 13) & Jean Léo Léonard (IUF & Paris 3)

Title : Visualizing and Revisiting Dialect Intelligibility Networks: Mazatec as a case study

Scheduled : Monday June 23, 2014, 18:00-18:30

Abstract: Dialect Intelligibility Testing (DIT) has long been the focus of attention in Native American linguistics (Hockett, 1958: 321-30), as an alternative standpoint to taxonomies based on comparative or quantitative linguistics. It has contributed to enhance the heuristic value of continuous chain models, over discontinuous tree-like models in dialectology. DIT also highlights epigenetic trends over phylogenetic and ontogenetic assessments on dialect variation. In this talk, we'll revisit Kirk's and Casad's

data on Mazatec mutual intelligibility patterns (Kirk, 1970; Casad, 1974: 46-51, 167-79) with visualizing tools such as GraphStream (http://graphstream-project.org/), and we'll question relevant thresholds in Mutual Intelligibility Networks (MIN). We'll suggest a finer-grained grid than the one initially used by Kirk & Casad, in the seventies, and we'll show how previously unobserved communal clusters may emerge from algorithmic complexity, out of raw MIN data, through visualization devices now currently used in processing complex systems.

Àngels Massip i Bonet (Departament de Filologia Catalana, Universitat de Barcelona)
Title : Complexity as a framework for understanding transdisciplinarity
Scheduled : Monday June 23, 2014, 18:30-19:00
Abstract: The goal of this talk is, on the one hand, to introduce the results of the work we have undertaken in recent years in the group Complexity, Sociolinguistics and Communication (http://www.sociocomplexitat.ub.edu/grup-de-complexitat-comunicacio-i-sociolingueistica) at the University of Barcelona and, on the other hand, to provide some prospects on how the modeling of sociocomplexity can be improved and further developed.
We will first highlight the importance of current epistemological agreement, in order to work from a transdisciplinary standpoint. We also wish to review which languages and which tools are appropriate for modeling sociocomplexity.
In order to ground the theory on relevant linguistic and sociolinguistic topics, we will point at a complexic vision of linguistic change, exemplified with data from Catalan and French. We will also provide insight on language shift, comparable to other ones about the issue at stake in the STDL (Space, Topology, Diffusion & Language) workshop.
Bibliography :

- Bastardas-Boada, Albert (2013), "Language policy and planning as an interdisciplinary field: towards a complexity approach", Current Issues in Language Planning, DOI: 10.1080/14664208.2013.829276.
- Bastardas i Boada, A., & Àngels Massip i Bonet (2013), "Llengua i complexitat. Presentació", LSC – Llengua, Societat i Comunicació 11, pp. 1-4. (Monogràfic dedicat a 'Llengua i Complexitat').
- Durand, Daniel (1979), La Systémique. PUF

Marco Patriarca (National Institute of Chemical Physics and Biophysics, Tallinn, Estonia)
Title : Models of language competition
Scheduled : Tuesday June 24, 2014, 14:00-15:00
Abstract: This contribution presents an overview of language competition models that have been introduced and studied for many years by now in different fields such as mathematics, physics, and linguistics. The overview covers some relevant models which resemble the classical mathematical models of competition between biological species. A first aspect that we try to clarify is the statistical interpretation of the models and their corresponding meaning, in particular concerning the role of bilinguals in the competition between two languages. We begin with the Baggs-Freedman models, proceed through the Abrams-Strogatz and Minett-Wang models, and then turn to more recent models. Also the spatial side of language spreading is considered, by illustrating various ways in which the spreading of language (features) through space and time has

been modeled so far in order to take into account geographical, cultural, and social factors.

Adam Lipowski (Faculty of Physics, Adam Mickiewicz University, Poznan, Poland)
Title : Dynamics of Naming Games: Why is it slow and how to make it faster?
Scheduled : Tuesday June 24, 2014, 15:00-15:30
Abstract: Naming Game is an important model of agreement dynamics. It might be used to describe emergence of a common vocabulary but it was also used to describe an opinion formation in a large scale sensor network, simple grammar or leader formation mechanism. Since the time to reach consensus is an important characteristics of Naming Game, its dynamics has been intensively studied. We show that some previous results on the Naming Game needs to be modified. It turns out that due to the formation of stripe structures dynamics of this model is much slower than expected. We also show that one can construct a Naming Game that does not suffer from the formation of such structures and has a much faster dynamics. We suggest the relation of the dynamics of this model with some percolation problems as well as with some other statistical mechanics models.
Bibliography :

- Lipowska Dorota & Adam Lipowski, 2013. "Phase transition and fast agreement in Naming Game with preference for multi-word agents", eprint: http://arxiv.org/abs/1308.3781

Didier Demolin (Gipsa-lab, Université de Grenoble, Alpes, Fr)
Title : Evaluating the complexity of phonological systems
Scheduled : Tuesday June 24, 2014, 15:30-16:00
Abstract: Phonological complexity has been the subject of many discussions for a century, e.g. Zipf and more recently Pellegrino et al. (2009). However, even though there is an agreement in seeing phonological systems as complex adaptive systems, we are still far from able to measure phonological complexity. Factors typically considered are the inherent phonetic complexity of elements in a phonological inventory, the role of combinatorial possibilities and the combination of frequency of occurrences of different elements (Maddieson 2009). Coupé¡¥t al. (2009) emphasize that a system is said to be complex if it is structured in different levels; if the properties of the global level differs from those of the elements of the basic level and if the systemic properties cannot be derived linearly from the basic ones. Phonetic and phonological systems reflect various types of constraints (biological, cognitive, linguistic and social) but the understanding of their interactions and integration is still quite limited. Taking into account the various levels of phonological systems together, gestures, features, vowels, consonants, syllable, suprasegments) is a possible way to start evaluating their complexity.
Complexity in phonology also focuses on the relation between the number of phonemes in a language and the number of allophones. Do we find more allophones where there are fewer phonemes? Do we have fewer allophones when there are more phonemes? Even if phonological descriptions are not always comparable and have been made at different times, we believe that this is an important study to be undertaken and this will be discussed in this presentation.
Bibliography :

- Coupé C., Marsico, E. & Pellegrino, F. (2009). Structural complexity in phonological systems. In Pellegrino, F. Marsico, E., Chitoran, I. Coupé (Eds.). Approaches to phonological complexity. Berlin, Mouton de Gruyter. 141-169.

- Maddieson, I. (2009). Calculating phonological complexity. In Pellegrino, F. Marsico, E., Chitoran, I. Coupé (Eds.). Approaches to phonological complexity. Berlin, Mouton de Gruyter. 85-109.
- Pellegrino, F. Marsico, E., Chitoran, I. Coupé (Eds.). (2009). Approaches to phonological copmplexity. Berlin, Mouton de Gruyter.
- Zipf, G.K. (1949). Human behavior and the principle of least effort. Cambridge (MA), Addison-Wesley.

SW4: Round table/discussion - Space, Topology, Diffusion & Language : prospects for future research
Scheduled : Tuesday June 24, 2014, 16:00-16:30

Satellite Workshop 5
Combinatorial Physics and Complexity

Satellite Workshop 5
Combinatorial Physics and Complexity

Organizers

- Gérard H.E. Duchamp, LIPN, University of Paris XIII, France, gheduchamp@gmail.com
- Hoang Ngoc Minh, LIPN, University of Paris XIII, France, hoang.ngocminh@lipn.univ-paris13.fr

Description

The science of Complex Systems likes to consider the notion of "level of description". On the other hand, the unfolding of new ideas in physics is often tied to the development of new combinatorial methods, and conversely some problems in combinatorics have been successfully attacked using methods inspired by statistical physics or quantum field theory. This Satellite Workshop is dedicated to research announcements and surveys in which combinatorics, physics and complexity interact in all directions. The list of specific subject areas awaited here includes:

- Mathematical and Combinatorial local rules
- Combinatorics of renormalization
- Theoretical Computer Science for Complex Systems
- Statistical Physics
- Exactly solved models
- Combinatorial models for and of emergence
- Graph polynomials and families of polynomials indexed by discrete structures
- Noncommutative differential and difference equations
- Explicit schemes for analysis of dynamical systems: finite (combinatorial) and infinite (based on functional analysis)

Programme

Cyril Banderier
Dirichlet series, Mellin transform, number theory and physics.
Scheduled : Wednesday June 25, 11:00-11:30
Numerous problems in combinatorics and number theory are related to some integer sequences having some "multiplicative properties". For such sequences, we will illustrate how Dirichlet series and Mellin transforms are a powerful tool to get formulas and their asymptotics. We will also give recent applications to the number of residues in Z/nZ, integer factorization, and to problems in physics (in quantum tomography).

Bui van Chiên
Algebra on words with q-deformed stuffle product and expressing polyzetas
Scheduled : Tuesday June 24, 17:30-18:00
From an infinite alphabet $\{y_s: s\in \mathbb{N} ^* \}$, we construct a completed Hopf algebraic structure with bases in duality thanks to concatenation product and q-deformed stuffle product. We also establish structures of polyzetas by expressing on these bases.

Gérard H. E. Duchamp and Hoang Ngoc Minh
An interface between physics and number theory via an analytic version of Cartier-Quillen-Milnor-Moore theorem
Scheduled : Tuesday June 24, 17:00-17:30
The functional expansions were common in physics as well as in engineering and have been developped to represent the evolution systems in QED. The main difficulty is the divergence of these expansions at 0 or at $+\infty$ and leads to the problems of {\it regularization} and {\it renormalization} which can be solved by combinatorial technics. Recently, the combinatorial aspects of noncommutative formal power series (monoidal factorization, transcendence bases, PBW bases, CQMM, \ldots) were intensively amplified for the asymptotic expansions, the computation of the monodromy and of the Galois differential groups of the KZ equation, \ldots facilitating mainly the renormalization and the computation of the associators via polylogarithms and their special values. In this work, we show how a fine study of convolution allows to understand the meaning of the nilpotence of this operator and we focus on this approach to study the renormalization at the singularities in $\{0,1,+\infty\}$ of the solutions of nonlinear differential equations involved in QED

Hoan Quoc Ngo
A scheme of noncommutative Combinatorial Number Theory and Physics
Scheduled : Tuesday June 24, 18:00-18:30
In this talk, we say about a result of the polylogarithm and the harmonic sum. We wil talk about an analytic presentation of the harmonic sums and the polylogarithms. By this way, we define the polylogarithm on the negative points. And so we will study about the values of zetafunction at negative points. On the other hand, we also give some applications of Bernoulli’s numbers in the study. Finally, we consider the polylogarithm and harmonic sums in a relation with words on an alphabet.

Ladji Kane
Combinatoire et algorithmique des factorisations tangentes à l'identité.
Scheduled : Wednesday June 25, 12:00-12:30
Dans cet exposé, nous présenterons un résumé des résultats les plus importants et de nos apports sur l'étude des factorisations tangentes à l'identité grâce à l'ulisation d'outils combinatoires et algorithmiques. L'écriture des factorisations tangentes à l'identité passe par la construction effective d'une paire de bases en dualité et permet l'écriture d'un produit infini. Ce produit ne donne exactement l'identité que sous des conditions très restrictives que nous préciserons. Dans bien des cas, la construction d'une paire de bases en dualité passe par celle d'une base duale à partir d'une base dont on connaît certaines propriétés. Nous nous proposons donc de déterminer les conditions requises que doivent satisfaire la base dont nous partons de sorte que la base duale permette l'écriture des factorisations.

Christian Lavault
On Miki-Gessel Bernoulli identities
Scheduled : Wednesday June 25, 11:30-12:00
The Miki-Gessel (MG) and the Faber-Pandharipande-Zagier (FPZ) Bernoulli numbers identities can be proved and expressed under several forms (e.g. Matiyasevich's). Generalizations may be investigated in plenty directions, such as Bernoulli, Euler and Gennochi polynomials, "mixed" MG and FPZ identities extended Bernoulli convolution

identities, etc. They also provide interesting new proofs using various tools, such as digamma and polygamma function, and methods, e.g. Dunne and Schubert's approach from quantum field theory and topological string theory.

Nguyên Hoàng Nghia
A combinatorial non-commutative Hopf algebra of graphs
Scheduled : Tuesday June 24, 2014 18:30-19:00
A non-commutative, planar, Hopf algebra of planar rooted trees was defined independently by one of the authors in Foissy (2002) and by R. Holtkamp in Holtkamp (2003). In this paper we propose such a non-commutative Hopf algebra for graphs. In order to define a non-commutative product we use a quantum field theoretical (QFT) idea, namely the one of introducing discrete scales on each edge of the graph (which, within the QFT framework, corresponds to energy scales of the associated propagators).

Benoit Cagnard
Sarkovski et les Automates
Scheduled : Wednesday June 25, 12:30-13:00
Le théorème de Sarkovski porte sur la cardinalité des orbites périodiques des fonctions continues de la variable réelle. Il existe un ordre, $\triangleright$, dit ordre de Sarkovski sur les entiers non nuls tel que si une fonction f continue a une orbite périodique de cardinalité n et $n \triangleright m$ alors f possède une orbite périodique de cardinalité m. Nous remarquons tout d'abord que l'ordre de Sarkovski est réalisable par automate si l'on écrit les entiers en base 2. Nous faisons ensuite le lien avec les fonctions dont le graphe est définissable par automate de mots infinis synchrone . Lorsque la numération est en base Pisot, on sait que pour de telles fonctions on peut décider si elles définissent des fonctions continues sur les réels. Si tel est le cas, on peut aussi décider si elles admettent des orbites périodiques de cardinalité n pour tout n. En particulier, on peut décider si elles ont des orbites de toutes cardinalités. De plus, ces fonctions permettent de construire des exemples de fonctions ayant une orbite périodique de cardinalité m fixé et aucune orbite périodique de cardinalité $n \triangleright m$ dans l'ordre de Sarkovski.

Satellite Workshop 6
Dynamical systems applied to population dynamics in ecology and in epidemiology

Satellite Workshop 6
Dynamical systems applied to population dynamics in ecology and in epidemiology

Organizers

- Pierre Auger, UMI 209, IRD & UPMC UMMISCO, Bondy, France, pierre.auger@ird.fr
- Rachid Mchich, ERMEG, ENCGT, Abdelmalek Essaâdi University, Tangier, Morocco, racmchich@yahoo.com
- Jean Jules Tewa, UMI 209, IRD & UPMC UMMISCO, University of Yaounde, Cameroon, tewajules@yahoo.fr
- Tri Nguyen-Huu, UMI 209 UMMISCO, Bondy, France, tri.nguyen-huu@ird.fr

Description

Ecosystems, communities, populations and individuals are exposed to important changes at local and global scales. The session is devoted to the presentation of original works in population dynamics. Population dynamics here is intended in a broad sense, including the study of molecule, cell, animal, plant populations. Hence, topics of the « satellite workshop » include modelling in cellular biology, ecology, epidemiology as well as management of fisheries. This session will focus on modelling using field data, model calibration, model analysis and decision making.

List of papers/presentations

R. Mchich, P. Auger and N. Charouki
"Analysis of the equilibrium stability of a Moroccan fishery management model"

Abstract: Mathematical models in ecology are usually nonlinear dynamical systems including a large number of coupled variables (6). These models are then difficult to study analytically. Aggregation of variables, which is based on time separation methods, permits to build, from a complete model involving many variables, a reduced one which governs a few global variables in the long term. In this work, we analyze the stability of a Moroccan multi fishery management model. Interpretations of our results can be used by the authority responsible of fishery management, the Moroccan government, as general recommendations for a better management of Moroccan fisheries.

Hbid M.L, Ben Miled S., Ramzi A., Khaladi M.A
"Mathematical model for larvae fish recruitment : effects of temperature fluctuations"

Abstract: Mathematical model of population of fish in the larval stage is presented. The model discuss the influence of temperature fluctuations on the recruitment of larvae in juvenile stage. The temperature is a key factor influencing the larval survival and development. It is also considered to be a good indicator of most forcing processes (seasons, winds, upwellings,...etc). We also present and discuss the recruitment rate formula both theoretically and by numerical simulation.

Fechichi A., Jerry M., Ben Miled S.
"Fishing Policy for a Global Hermaphrodite Model"
Abstract: In this work, we study a structured fishing model displaying the three stages of life cycle of a hermaphrodite population, which are juvenile, female and male. We associate to this model the maximization of the total discounted net revenues derived by the exploitation of the stock.

Chakib Jerry (jechakib@yahoo.fr), Nadia Raissi
"Management of salt water in irrigation"
Abstract: Let us consider a field where the water of irrigation (the water of the aquifer) contains some soluble salt of concentration c (positive constant) and the ground also contains some soluble salt of concentration s which is a function of water irrigation x. The dynamical model applied to a field of culture is based on one hand of the salinity evolution in the ground (inspired by the work of Plessner Y. and Feinerman E. :On the Economics of Irrigation with Saline Water: A Dynamic Analysis, Natural Resource Modeling), the water of aquifer dynamics and the quantity of water regenerated after a while in the groundwater. In this work we try to suggest an irrigation policy to maximize the yield of the field using optimal control theory.

M. Jerry (jemounir@yahoo.fr) and C. Jerry (jechakib@yahoo.fr)
"A viability analysis for structured model of fishing problem"
Abstract: In this work we study a structured fishing model, basically displaying the two stages of the ages of a fish population, which are in our case juvenile, and adults. We associate to this model two constraints: one of ecological type ensuring a minimum stock level, the other one of economic type ensuring a minimum income for fishermen. The analytical study focuses on the compatibility between the state constraints and the controlled dynamics. Using the mathematical concept of viability kernel, we define a set of constraints combining the guarantee of consumption and a stock of resources to be preserved at all times.

Ali Moussaoui
"Global dynamics of a predator-prey system and its applications to biological control"
Abstract: A predator-prey model is considered in which both predator and prey are subjected to harvesting. The existence of its steady states and their stability (local and global) are studied using Eigenvalue analysis. The problem of determining the optimal harvesting policy is then solved by using Pontryagin's maximum principle.

N.Raïssi(nraissi@fsr.ac.ma), C.Sanogo(csanogo@yahoo.com), M.Serhani(mserhani@hotmail.com)
"Multi-fishery Management: Differential games approach"
Abstract: The need of planning fishery motivate the development of multi fishery models. Halieutic resources in Morocco are important enough to allow foreign fleet to operate in its Excusive Economic Area (EEA). Neverthelessit is necessary to define terms and conditions of foreign fleet access to fishery, in order to avoid to bankrupt domestic fleet which operate in the same fishery area. In a previous work N.Raissi [4] suggests a fishery model analyzed in the framework of bilevel optimization theory. The result leads to collapse of less efficient fleet. In order to avoid this undesirable situation we usedifferential game theory and the adapted concept of Nash equilibrium. This analysis

will guaranteeto both fleet to harvest and share the same resource. In [1] Colin Clark found the optimal effort in the competitive case. He shows that the less efficient fleethas to quit fishery and only the more efficient still harvest. He also determine Pareto front in cooperative case. C.Mullon et P.Fréonin [3] show in a discrete context, the existence of Nash equilibrium corresponding to fishery model involving several fishery areas as well as several fleets. L.DoyenetJ.C.Perreau in [2] use both viability approach and game theory in order to analyze the impact of bioeconomic constraints onresource dynamic. They show that some kind of stability could be obtained only if the initial values of resource stocks are enough high. Otherwise, forweak levels, the more efficient fleet force the less efficient to leave the fishery. In this present work, we identify a competitive Nash equilibrium candidate assuring fleet cohabitation. We also proof the trajectory optimality leading to the equilibrium, using marginal analysisofHamilton-Jacobi equation.

Bibliography

- [1] C.W.Clark, (1990), Mathematical Bioeconomics : the Optimal Management of Renewable Resources, 2nded., John Wiley and Sons, New York.
- [2] L.DoyenJ.C.Pereau, Sustainable coalitions in the commons, Cahiers du GREThA n°2009-15.
- [3] C. Mullon P. Fréon, (2005), Prototype of an integrated model of the worldwide system of small pelagic fisheries. In R.Hannesson, M.Barange and S.F.Herrick.Climate Change and the Economics of the World's Fisheries : Examples of Small Pelagic Stocks. Edward Elgar Publi- shing, NewHorizons in Environmental Economics, Cheltenham, UK.pp. 262-295.
- [4] N.Raissi, (2001), Features of bioeconomic models for the optimal management of a fishery exploited by two fleets, Natural resources modelling, volume 14, number 2, 287-310 .

Jean Jules TEWA

"Global and local bifurcations in a ratio-dependent predator-prey model with SIS infectious disease"

Abstract: Two ratio-dependent predator-prey models with disease only in prey population and in both populations are proposed. For these models, we investigate the existence of local and global bifurcations trough the qualitative properties of solutions. The existence of homoclinic and heteroclinic bifurcations for the model without disease is established in a di erent and simplest manner to what has been done by Kuang and beretta. The existence of homoclinic and heteroclinic bifurcations for the model with disease only in prey and with disease in both populations is established. The existence of a saddle-node bifurcation is also established for the two models. A discussion on the existence of a H opf bifurcation is carried out for the model without desease. Finally, we use non-standards numerical schemes to illustrate our results.

Mansal F., Nguyen-Huu T., Auger P., Baldé M.

"Mathematical model of a fishery with demand/supply dynamics"

Abstract: we present a mathematical bioeconomic model of a fishery with a variable price. The model describes the time evolution of the resource, the fishing effort and the price which is assumed to vary with respect to supply and demand. The supply is the instantaneous catch while the demand function is assumed to be a monotone decreasing function of price. We show that a generic Market Price Equation (MPE) can be derived and has to be solved to calculate non trivial equilibria of the model. This Market Price

Equation (MPE) can have 1, 2 or 3 equilibria. We perform local and global stability of equilibria. The MPE is extended to two cases: an age-structured fish population and a fishery with storage of the resource.

Ly S., Auger P., Baldé M.
"A bioeconomic model of a multi-site fishery with non linear demand function: number of sites optimizing the total catch."
Abstract: We present a mathematical model of a fishery which takes into account the evolution of the resource, fish and boat movement between different sites, fishing effort and price that varies with respect to supply and demand. Movements of the boats and resource as well as the variation of the price occur at a fast time scale, which allows using methods of aggregation of variables to derive an approximate model governing a reduced number of global variables. We analytically determine the asymptotic behavior and show that the system may end either in a sustainable state or in an over-exploitation state.

Nguyen-Huu T., Mose V., Auger P.
"Modelling dynamics of ungulates populations in Amboseli National Park, Kenya"
Abstract: We present a mathematical model of ungulates populations in Amboseli National Park area. The model explicitly considers the spatial dimension, including habitat fragmentation and evolution of resources such as vegetation density and quality. The model is based on an energy budget demographic model which consists of Ordinary Differential Equations. The dispersal of animals inside the area is based on a statistical study of the distribution of animals, which is a function of several factors such as vegetation quantity and quality.

Nathalie Corson (LMAH, Le Havre), Nicolas Marilleau (UMI 209 UMMISCO, Bondy) , Jonathan Pascalie (LACL, ISC-PIF, Paris), Martin Potier (LACL, Créteil), Antoine Spicher (LACL, Créteil)
"Managing the Interoperability Between Models of a Complex System - Application to Prey-Predator Multi-Modeling"
Abstract: The richness of tools and methodologies available for the study of a complex system often leads to the elaboration of different independent models. The development of these models faces its limits since each model only focuses on some aspects (points of view) of the system. In order to enrich the description of the studied system, an emergent tendency consists in taking advantage of simple models by interfacing them instead of complexifying a unique model (often at the expense of the results). This paper tackles interoperability of models based on various paradigms (e.g. ODE, Stochastic laws or agent). We first propose an original classification of models (compared to the more usual comparison of paradigms) based on their relations to space and time. This classification is then used to establish relations between models and to transpose some results from one model to another. We exemplify our proposition on different toy models of a Prey-Predator system.

Gustavo Cruz
"Dynamics of a cancerous tumor growth under the effect of therapy"
Abstract: Recently there has been several attempts to develop different ways of immunotherapies for cancer including certain types of vaccines to activate an specific immuno response. In this work we present a population type model for the growth of a

tumor under the effect of different types of therapies. First we present a model for the growth of a tumor couple to the immune system. We present the effect on its dynamics of two types of immuno-therapy, passive and active. It will be shown that in this regime immunotherapy either finish with the tumor or stop its growth keeping it under the threshhold of vascularization. We then study the effect of these terapies for a vascularized tumor. In this case most of the times immunotherapy cannot stop the growth of the tumor and chemotherapy must be used. If time allows, we will show the effect of two styles of chemotherapy on the tumor, the traditional chemotherapy and a more recent way of administration known as metronomic chemotherapy.

Proceedings of ICCSA 2014
Normandie University, Le Havre, France - June 23-26, 2014

GLOBAL DYNAMICS OF A PREDATOR-PREY SYSTEM AND ITS APPLICATIONS TO BIOLOGICAL CONTROL

B. Belkhodja and A. Moussaoui *†

Abstract. In this paper, a new predator-prey model is considered in which both predator and prey are subjected to harvesting. Boundedness of the exploited system is examined. The existence of its steady states and their stability (local and global) are studied using Eigenvalue analysis. The possibility of existence of bionomic equilibria has been considered and the optimal harvesting policy is obtained by using the Pontryagin's maximal principle.

Keywords. Predator-prey model, Predator-dependent response, Global stability, Bionomic equilibrium, Optimal harvest, Maximum principles.

1 Introduction

The dynamics of predator-prey systems are often described by differential equations, which represent time continuously. A common framework for such a model is:

$$\begin{cases} \dfrac{dx}{dt} = aF(x) - g(x,y)y, \\ \dfrac{dy}{dt} = eg(x,y)y - cy, \end{cases} \tag{1}$$

where x and y are the prey and predator density, respectively, $F(x)$ is the growth rate of the prey population in the absence of predation. The functional response $g(x,y)$ represents the instantaneous rate of prey depletion per predation. The constant e describes the efficiency of the predator in converting consumed prey into predator offspring, while c denotes the food independent predator mortality rate.

In predator-prey models, functional responses of the predator to the prey density play a critical role, which is defined as the amount of prey catch per predator per unit of time. In general, the functional response g is usually assumed to increase with prey density, x, and decrease (or not change) with predator density, y. However, exceptions exist to both of these rules. This can be classified as: (1) prey dependent, when prey density alone determines the response; (2) predator dependent, when both predator and prey populations affect the response; and (3) multispecies dependent, when species other than the focal predator and its prey species influence the functional response. A historical account of biological relevance of the prey-dependent model and the functional response is available in [1, 8]. In this paper and under suitable conditions, the functional response $g(x,y)$ can accommodate interference among predators. The predator needs a quantity γy for his food, but he has access to a quantity

$$g(x,y) = \frac{bxy}{y+D}$$

where b is the encounter rate with prey by a searching predator and D measures the other causes of mortality outside the metabolism and predation. It gives the extent to which environment provides protection to the prey.
If

$$g(x,y) = \frac{bx}{y+D} \geq \gamma$$

then the predators will be satisfied with the quantity

$$\gamma y$$

for his food. Otherwise, that is, if

$$g(x,y) = \frac{bx}{y+D} \leq \gamma$$

the predators will content himself with

$$g(x,y) = \frac{bxy}{y+D}$$

Consequently, the quantity of food received by the predators is

$$\min\left(\frac{bx(t)}{y(t)+D}, \gamma\right) y(t)$$

(see [4, 7] for more details)
In the present paper, we assume that both species are subjected to harvesting efforts E_1 and E_2 respectively, with the catchability coefficient of the two species $q_1, q_2 (> 0)$. The subject of harvesting in predator-prey systems has been of interest to economists and ecologists for some time now. Most research has focused attention on optimal exploitation, guided entirely by profits from

*Department of Mathematics, Faculty of Sciences, University of Tlemcen, 13000. Algeria E-mails: moussaoui.ali@gmail.com
†Manuscript received April 19, 2009; revised January 11, 2010.

harvesting (see [5, 6, 9, 11, 12, 13] and reference therein).

Thus, with the above assumption, our model takes the form

$$\begin{cases} \dfrac{dx}{dt} = ax(1-\dfrac{x}{K}) - \min\left(\dfrac{bx(t)}{y(t)+D}, \gamma\right) y(t) - q_1E_1x, \\ \dfrac{dy}{dt} = e\min\left(\dfrac{bx(t)}{y(t)+D}, \gamma\right) y(t) - cy - q_2E_2y, \end{cases} \tag{2}$$

where a is the intrinsic growth rate of prey, K is the environmental carrying capacity of the prey.
Here we observe that, if "$E_1 > \frac{a}{q_1}$" then $\dot{x} < 0$, Hence, throughout our analysis, we assume that "$E_1 < \frac{a}{q_1}$".
This paper is arranged as follow: At first, using some assumptions, we reduce our system (2) to a simple form, we present also positivity and boundedness of the solutions, in turn, implies that the system is biologically well behaved. Local and global stability analysis of equilibria is established in Sections 3 and 4, respectively. In Section 5, we prove the existence of the bioeconomic equilibrium. In Section 6 the optimal control policy is established. At last, concluding remarks are given.

2 Some preliminary results

In this section, we shall present some preliminary results. Observing that $lim_{(x,y)\to(0,0)}F_1(x,y) = lim_{(x,y)\to(0,0)}F_2(x,y) = 0$, we may define that $F_1(0,0) = F_2(0,0) = 0$. Clearly, with this extended definition, both F_1 and F_2 are continuous functions on R^2_+. It is easy to see that a solution with non-negative initial value exists and is unique. Moreover, it stays non-negative. Our next task is to show the boundedness of solutions which may be interpreted as a natural restriction to growth as a consequence of limited resources.

Before starting, let $x(0) = x_0$, $y(0) = y_0$ be respectively the initial density of the prey and predator with $x_0 > 0$ and $y_0 > 0$. We suppose that:

$$b < \frac{\gamma(y_0+D)}{x_0}, \qquad (H_1)$$

$$b < \frac{4a\gamma D(c+q_2E_2)}{K(a+c+q_2E_2)^2}, \qquad (H_2)$$

Then we have the following proposition

Proposition 2.1. *For all $t \geq 0$*

$$bx(t) < \gamma(y(t)+D).$$

Proof
Let

$$u(t) = bx(t) - \gamma(y(t)+D)$$

Note that $u(0) < 0$ by condition (H_1). It is claimed that $u(t) < 0$ for all t. If this were not the case, there exists $t_0 > 0$ such that:

$$u(t_0) = 0 \quad \text{and} \quad \frac{du}{dt}(t_0) \geq 0.$$

The condition $u(t_0) = 0$ implies that

$$y(t_0) = \frac{bx(t_0)}{\gamma} - D.$$

From (H_1), we get

$$\begin{aligned} \frac{du}{dt}(t_0) &= b\frac{dx}{dt}(t_0) - \gamma\frac{dy}{dt}(t_0) \\ &= -b(b+e\gamma)\frac{y(t_0)}{y(t_0)+D}x(t_0) + b(a-q_1E_1+c+q_2E_2)x(t_0) \\ &\quad -\gamma(c+q_2E_2)D - \frac{ba}{K}(x(t_0))^2, \end{aligned}$$

It follows that

$$\frac{du}{dt}(t_0) \leq b(a+c+q_2E_2)x(t_0) - \gamma(c+q_2E_2)D - \frac{ba}{K}(x(t_0))^2$$

Condition (H_2) implies that

$$\frac{du}{dt}(t_0) < 0$$

and we obtain a contradiction. This implies that $u(t) < 0$ for all $t \geq 0$. □

Consequently system (2) is reduced to the simple form

$$\begin{cases} \dfrac{dx}{dt} = ax(1-\dfrac{x}{K}) - \dfrac{bxy}{y+D} - q_1E_1x, \\ \dfrac{dy}{dt} = -cy + \dfrac{ebxy}{y+D} - q_2E_2y, \end{cases} \tag{3}$$

2.1 Boundedness of the system

Boundedness of a system guarantees its validity. The following theorem ensures the boundedness of the system (3).

Theorem 2.1. *All solutions of the system (3) which starts in R^+_2 are uniformly bounded.*

Proof
Let $w = ex + y$. Then the time derivative of w is

$$\begin{aligned} \frac{dw}{dt} &= e\frac{dx}{dt} + \frac{dy}{dt} = eax(1-\frac{x}{K}) - eq_1E_1x - (c+q_2E_2)y \\ &\leq \mu - vw \end{aligned}$$

where $\mu = e\frac{K}{4a}(a-q_1E_1+c+q_2E_2)^2$, and $v = (c+q_2E_2)$. Therefore,

$$\frac{dw}{dt} + vw \leq \mu$$

Applying a theorem on differential inequality [2], we obtain

$$0 < w(x,y) \leq \frac{\mu}{v} + e^{-vt}\left\{w(x(0),y(0))\right\},$$

and for $t \to \infty$, we have $0 \leq w \leq \frac{\mu}{v}$.

Thus, all the solutions of the system (3) enter into the region

$$B = \left\{(x,y) \in R_+^2 : w = \frac{\mu}{v} + \varepsilon, for\ any\ \varepsilon > 0\right\}.$$

This completes the theorem.

3 Analysis of the equilibria

We now study the existence of equilibrium of system (3). Particularly, we are interested in the interior or positive equilibrium of the system. To begin with we list all possible equilibria:
(i) the trivial equilibrium $P_0 = (0,0)$
(ii) equilibrium in the absence of predator ($y = 0$)
$P_1 = (\bar{x}, 0)$, where $\bar{x} = \frac{K}{a}(a - q_1E_1)$.
(iii) the interior equilibrium $P_2 = (x^*, y^*)$
where

$$x^* = \frac{c + q_2E_2}{eb}(y^* + D)$$

and

$$y^* = \frac{1}{2}\left(B + \sqrt{B^2 - 4C}\right),$$

where

$$B = 2D - \frac{ebK(-b + a - q_1E_1)}{a(c + q_2E_2)},$$

$$C = D^2 - \frac{ebKD(a - q_1E_1)}{a(c + q_2E_2)}.$$

The interior equilibrium point (x^*, y^*) exists if the following condition hold:

$$0 \leq E_1 \leq \frac{a}{q_1}\left(1 - \frac{D(c + q_2E_2)}{ebK}\right). \tag{4}$$

Now we study the nature of each of these equilibrium points. To determine the local stability character, we need to compute the variational matrix J (the Jacobian). The variational matrix of the system of Equations (3) is

$$J(x,y) = \begin{pmatrix} a - q_1E_1 - \frac{2ax}{K} - \frac{by}{y+D} & \frac{-bDx}{(y+D)^2} \\ \frac{eby}{y+D} & -c - q_2E_2 + \frac{ebDx}{(y+D)^2} \end{pmatrix} \tag{5}$$

First we consider the trivial equilibrium point $(0,0)$. The associated Jacobian is given by

$$J(0,0) = \begin{pmatrix} a - q_1E_1 & 0 \\ 0 & -c - q_2E_2 \end{pmatrix}. \tag{6}$$

The eigenvalues of the $J(0,0)$ are nothing but the diagonal elements, then origin is saddle point.

Consider the second equilibrium point $P_1 = (\bar{x}, 0)$. The Jacobian associated with this point is given by

$$J(\bar{x},0) = \begin{pmatrix} -(a - q_1E_1) & -\frac{bK(a - q_1E_1)}{Da} \\ 0 & -(c + q_2E_2) + \frac{ebK(a - q_1E_1)}{Da} \end{pmatrix}. \tag{7}$$

Clearly the eigenvalues of the above matrix are the diagonal elements and the stationary point $P_1 = (\bar{x}, 0)$ is locally stable only if

$$E_1 > \frac{a}{q_1}\left(1 - \frac{D(c + q_2E_2)}{ebK}\right) \geq 0 \tag{8}$$

Similarly we have from (5),

$$J(x^*,y^*) = \begin{pmatrix} -\frac{ax^*}{K} & -\frac{bDx^*}{(y^*+D)^2} \\ \frac{eby^*}{y^*+D} & -\frac{ebx^*y^*}{(y^*+D)^2} \end{pmatrix}. \tag{9}$$

It is easy to see that the trace of $J(x^*, y^*)$ is

$$trJ(x^*,y^*) = -\frac{ax^*}{K} - \frac{dx^*y^*}{(y^* + D)^2} < 0,$$

and its determinant is

$$detJ(x^*,y^*) = \frac{adx^{*2}y^*}{K(y^* + D)^2} + \frac{bdDx^*y^*}{(y^* + D)^3} > 0.$$

Hence (x^*, y^*) is locally asymptotically stable.

4 Global stability

In this section, we consider the global stability of system (3) by constructing a suitable Lyapunov function. We define a Lyapunov function

$$V(x,y) = \left[(x - x^*) - x^*\log(\frac{x}{x^*})\right] + h\left[(y - y^*) - y^*\log\left(\frac{y}{y^*}\right)\right]$$

where h is a positive constant to be chosen suitably in the subsequent steps. It can be easily verified that the function V is zero at the equilibrium (x^*, y^*) and is positive for all other positive values of x, y.

The time derivative of V along the trajectories of (3) is given by

$$\frac{dV}{dt} = \frac{x-x^*}{x}\frac{dx}{dt} + h\frac{y-y^*}{y}\frac{dy}{dt}$$

$$= (x-x^*)\left[(a-q_1E_1) - \frac{a}{K}x - \frac{by}{y+D}\right] \qquad (10)$$

$$+h(y-y^*)\left[-(c+q_2E_2) + \frac{ebx}{y+D}\right].$$

Also we have the set of equilibrium equations corresponding to the steady state $P_2 = (x^*, y^*)$:

$$a(1-\frac{x^*}{K}) - \frac{by^*}{y^*+D} - q_1E_1 = 0$$

and

$$-c + \frac{ebx^*}{y^*+D} - q_2E_2 = 0.$$

We can write the equation (10) together with the above two equations in the form:

$$\frac{dV}{dt} = (x-x^*)\left[(a-q_1E_1) - \frac{a}{K}x - \frac{by}{y+D} - (a-q_1E_1) + \frac{a}{K}x^* + \frac{by^*}{y^*+D}\right]$$

$$+h(y-y^*)\left[-(c+q_2E_2) + \frac{ebx}{y+D} + (c+q_2E_2) - \frac{ebx^*}{y^*+D}\right]$$

By choosing

$$h = \frac{bD}{eb(y^*+D)},$$

The above equation can be written as

$$\frac{dV}{dt} = -\left[\frac{a}{K}(x-x^*)^2 + \frac{ebhx^*}{(y+D)(y^*+D)}(y-y^*)^2\right].$$

Obviously, $(\frac{dV}{dt}) < 0$ strictly for all $x, y > 0$ except the interior equilibrium point (x^*, y^*) where $(\frac{dV}{dt}) = 0$. Thus $V(x, y)$ satisfies Lyapunov's asymptotic stability theorem, and the interior equilibrium point (x^*, y^*) of system (3) is globally asymptotically stable.

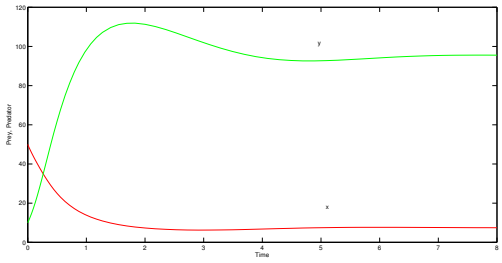

Figure 1: Both the prey and predator population converge to their equilibrium values. $a = 7$; $b = 10$; $c = 7.5$; $d = 12$; $K = 50$; $D = 70$; $q_1 = 1.3$; $q_2 = 0.37$; $E_1 = 0.15$; $E_2 = 1.25$

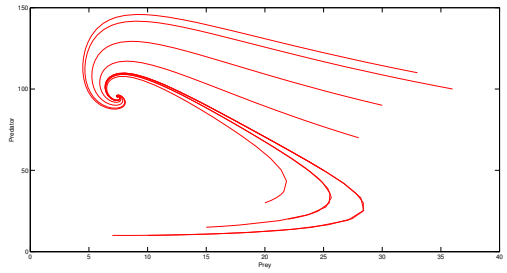

Figure 2: phase space trajectories corresponding to different initial levels.

5 Bionomic equilibrium

Having verified the existence of a positive equilibrium point and proved that conditions exist in order that this point is an attractor, we will show the existence of a bioeconomic or bionomic equilibrium. This term is an amalgamation of the concepts of 'biological equilibrium' and economic equilibrium [3]. As we know, a biological equilibrium is given by $\dot{x} = 0 = \dot{y}$. The economic equilibrium is said to be attained whenTR (total revenue earned by selling the harvested biomass) equals TC (the total cost for the effort employed to harvesting).

Let c_1 and c_2 be the harvesting cost per unit effort, p_1 and p_2 the constant price per unit landed biomass of the prey and predator, respectively. The economic rent (net revenue at any time) is given by:

by

$$\pi = (p_1q_1x - c_1)E_1 + (p_2q_2y - c_2)E_2$$

$$= \pi_1 + \pi_2,$$

where $\pi_1 = (p_1q_1x - c_1)E_1$, $\pi_2 = (p_2q_2y - c_2)E_2$ i.e., π_1 and π_2 represent the net revenues for the prey and predator species, respectively.

The economic parameters p_1, p_1, c_1, c_2 are not in general constants, since they may depend on the stock-levels, type of fishing gears used, market demand, etc. For the sake of simplicity, we take them to be constants.

Thus the bionomic equilibrium $[x_\infty, y_\infty, E_{1\infty}, E_{2\infty}]$ is the solution of the following simultaneous equations:

$$a(1-\frac{x}{K}) - \frac{by}{y+D} - q_1E_1 = 0 \qquad (11)$$

$$-c + \frac{ebx}{y+D} - q_2E_2 = 0, \qquad (12)$$

$$\pi = (p_1q_1x - c_1)E_1 + (p_2q_2y - c_2)E_2 = 0. \qquad (13)$$

In order to determine the bionomic equilibrium, we now

consider the following cases:

Case1: If $c_2 > p_2q_2y$, i.e. the cost is greater than the revenue for the predator, then the predator fishing will be stopped ($E_2 = 0$). Only the prey fishery remains operational (i.e. $c_1 < p_1q_1x$).
We then have $x_\infty = \frac{c_1}{p_1q_1}$ (from(13)). Hence $c_1 < p_1q_1x < p_1q_1K$, then $(y_\infty, E_{1\infty})$ will be any point on the line

$$a\Big(1 - \frac{c_1}{p_1q_1K}\Big) = \frac{by_\infty}{y_\infty + D} + q_1E_{1\infty}.$$

in the first quadrant of the yE_1-plane.

Case2: If $c_1 > p_1q_1x$ i.e. the cost is greater than the revenue in the prey fishery, then prey fishery will be closed ($E_1 = 0$). Only predator fishery remains operational (i.e. $c_2 < p_2q_2y$).

We then have $y_\infty = \frac{c_2}{p_2q_2}$ (from (13)). Now substituting y_∞ into ((11)) we get

$$x_\infty = \frac{K}{a}\Big(a - \frac{by_\infty}{y_\infty + D}\Big)$$

$x_\infty > 0$ provided $\quad a > \frac{by_\infty}{y_\infty + D}$

Substituting x_∞ into 12 we get

$$E_{2\infty} = \frac{1}{q_2}\Big(- c_2 + \frac{ebx_\infty}{y_\infty + D}\Big)$$

$E_{2\infty} > 0$ provided $\quad \frac{ebx_\infty}{y_\infty + D} > c_2$

Case3: If $c_1 > p_1q_1x$, $c_2 > p_2q_2y$. In this case, the cost is greater than revenues for both species and the whole fishery will be closed.

Case4: If $c_1 < p_1q_1x$, $c_2 < p_2q_2y$. In this case, the revenues for both the species being positive, then the whole fishery will be in operation.
In this case, $x_\infty = \frac{c_1}{p_1q_1}$ and $y_\infty = \frac{c_2}{p_2q_2}$ (from (13)).

Now substituting x_∞ and y_∞ into (11) and (12) we get

$$E_{1\infty} = \frac{1}{q_1}\Big(a(1 - \frac{c_1}{p_1q_1K}) - \frac{bc_2}{c_2 + p_2q_2D}\Big),$$

and

$$E_{2\infty} = \frac{1}{q_2}\Big(\frac{ebc_1p_2q_2}{p_1q_1(c_2 + p_2q_2D)} - c\Big).$$

Now

$$E_{1\infty} > 0 \quad \text{if} \quad a(1 - \frac{c_1}{p_1q_1K}) > \frac{bc_2}{c_2 + p_2q_2D}, \tag{14}$$

$$E_{2\infty} > 0 \quad \text{if} \quad c < \frac{ebc_1p_2q_2}{p_1q_1(c_2 + p_2q_2D)}. \tag{15}$$

Thus the nontrivial bionomic equilibrium point $[x_\infty, y_\infty, E_{1\infty}, E_{2\infty}]$ exists if and only if the conditions (14) and (15) hold together.

6 Optimal harvesting policy

In this section, our objective is to maximize, the objective functional form of the harvesting model, with the instantaneous annual rate of discount δ is as follows:

$$J(E_1, E2) = \int_0^\infty e^{-\delta t}\Big\{(p_1q_1x - c_1)E_1(t) + (p_2q_2y - c_2)E_2(t)\Big\}dt \tag{16}$$

subject to the state constraints (3) and the control constraints

$$0 \le E_i(t) \le E_i^{max}, \quad i = 1, 2$$

The present value Hamiltonian

$$H = H(x, y, \lambda_1, \lambda_2, E_1, E_2)$$

for this control problem is

$$\begin{aligned} H = {} & e^{-\delta t}\left\{(p_1q_1x - c_1)E_1 + (p_2q_2y - c_2)\,E_2\right\} \\ & + \lambda_1\left(ax(1 - \frac{x}{K}) - \frac{bxy}{y + D} - q_1E_1x\right) \\ & + \lambda_2\left(-cy + \frac{ebxy}{y + D} - q_2E_2y\right), \end{aligned} \tag{17}$$

where $\lambda_1(t)$ and $\lambda_2(t)$ are the adjoint variables.
We have

$$\frac{\partial H}{\partial E_1} = e^{-\delta t}(p_1q_1x - c_1) - \lambda_1q_1x = \sigma_1(t), \tag{18}$$

$$\frac{\partial H}{\partial E_2} = e^{-\delta t}(p_2q_2y - c_2) - \lambda_2q_2y = \sigma_2(t) \tag{19}$$

The optimal control $E_i(t)$ $(i = 1, 2)$ must clearly satisfy the conditions

$$E_i(t) = \begin{cases} E_i^{max} & \text{if} \quad \sigma_i(t) > 0 \\ \\ 0 & \text{if} \quad \sigma_i(t) < 0. \end{cases}$$

Since $\sigma_i(t)$ causes $E_i(t)$ $(i = 1, 2)$ to switch between level 0 and E_i^{max}, $\sigma_i(t)$ $(i = 1, 2)$ are called switching function. Depending on the sign of the switching function $\sigma_i(t)$, the optimal control $E_i(t)$ is a bang-bang switching from one extreme point to other one.
Obviously, the control variables $E_i(t)$ $(i = 1, 2)$ appear linearly in the Hamiltonian function H. So, the condition $\sigma_i(t) = 0 \quad (i = 1, 2)$ is necessary for the singular control

$E_i^*(t),\ 0 < E_i^*(t) < E_i^{max}$ to be optimal.
Hence the optimal harvesting policy is

$$E_i(t) = \begin{cases} E_i^{max} & \text{if} \quad \sigma_i(t) > 0 \\ 0 & \text{if} \quad \sigma_i(t) < 0. \\ E_i^* & \text{if} \quad \sigma_i(t) = 0 \end{cases}$$

for $i = 1, 2$.
For singular control $\sigma_i(t) = 0$ $(i = 1, 2)$. Assuming that the control constraints are not binding i.e., the optimal solution does not occur at 0 or E_i^{max}. From (18) and (19) we have

$$\lambda_1 = e^{-\delta t}(p_1 - \frac{c_1}{q_1 x}), \tag{20}$$

$$\lambda_2 = e^{-\delta t}(p_2 - \frac{c_2}{q_2 y}). \tag{21}$$

Thus the shadow prices $e^{\delta t}\lambda_i(t), (i = 1, 2)$ do not vary with time in optimal equilibrium. Hence they satisfy the transversality condition at ∞ , i.e. they remain bounded as $t \to \infty$.

We intend to derive here an optimal equilibrium solution of the problem. Since we are considering an equilibrium solution, x, y and E are to be treated as constants in the subsequent steps.

By the maximal principle [10], the adjoint variables satisfy

$$\dot{\lambda}_1 = -\frac{\partial H}{\partial x} = -\Big[e^{-\delta t}p_1 q_1 E_1 + \lambda_1\Big(a - \frac{2ax}{K} - \frac{by}{y+D} - q_1 E_1\Big) + \lambda_2\left(\frac{eby}{y+D}\right)\Big] \tag{22}$$

Using equilibrium conditions, (22) becomes

$$\dot{\lambda}_1 = -e^{-\delta t}p_1 q_1 E_1 + \lambda_1\left(\frac{ax}{K}\right) - \lambda_2\left(\frac{eby}{y+D}\right) \tag{23}$$

From (20), (21) and (23) we have

$$\dot{\lambda}_1 = e^{-\delta t}\Big[-p_1 q_1 E_1 + \Big(p_1 - \frac{c_1}{q_1 x}\Big)\frac{ax}{K} - \Big(p_2 - \frac{c_2}{q_2 y}\Big)\Big(\frac{eby}{y+D}\Big)\Big] \tag{24}$$

Similarly we get,

$$\dot{\lambda}_2 = -\frac{\partial H}{\partial y} = -\Big[e^{-\delta t}(p_2 q_2 E_2) - \lambda_1\Big(\frac{bDx}{(y+D)^2}\Big) + \lambda_2\Big(-c - q_2 E_2 + \frac{ebDx}{(y+D)^2}\Big)\Big] \tag{25}$$

By equilibrium conditions, (25) becomes

$$\dot{\lambda}_2 = -e^{-\delta t}(p_2 q_2 E_2) + \lambda_1\Big(\frac{bDx}{(y+D)^2}\Big) + \lambda_2\Big(\frac{ebxy}{(y+D)^2}\Big) \tag{26}$$

Similarly we get

$$\dot{\lambda}_2 = e^{-\delta t}\Big[-p_2 q_2 E_2 + \Big(p_1 - \frac{c_1}{q_1 x}\Big)\Big(\frac{bDx}{(y+D)^2}\Big) + \Big(p_2 - \frac{c_2}{q_2 y}\Big)\Big(\frac{ebxy}{(y+D)^2}\Big)\Big] \tag{27}$$

Integrating (24) and (27) we get

$$\lambda_1 = \frac{1}{\delta}e^{-\delta t}\left[p_1 q_1 E_1 - \Big(p_1 - \frac{c_1}{q_1 x}\Big)\frac{ax}{K} + \Big(p_2 - \frac{c_2}{q_2 y}\Big)\Big(\frac{eby}{y+D}\Big)\right] \tag{28}$$

$$\lambda_2 = \frac{1}{\delta}e^{-\delta t}\Big[p_2 q_2 E_2 - \Big(p_1 - \frac{c_1}{q_1 x}\Big)\Big(\frac{bDx}{(y+D)^2}\Big) - \Big(p_2 - \frac{c_2}{q_2 y}\Big)\Big(\frac{ebxy}{(y+D)^2}\Big)\Big] \tag{29}$$

We neglect the constant of integration in order to shadow prices $\lambda_i e^{\delta t}$ $(i = 1, 2)$ of the two species are bounded. From (20) and (28) we get,

$$e^{-\delta t}\Big(p_1 - \frac{c_1}{q_1 x}\Big) = \frac{1}{\delta}e^{-\delta t}\Big[p_1 q_1 E_1 - \Big(p_1 - \frac{c_1}{q_1 x}\Big)\Big(\frac{ax}{K}\Big) + \Big(p_2 - \frac{c_2}{q_2 y}\Big)\Big(\frac{eby}{y+D}\Big)\Big]$$

$$\Rightarrow p_1 q_1 E_1 = \delta\Big(p_1 - \frac{c_1}{q_1 x}\Big) + \Big(p_1 - \frac{c_1}{q_1 x}\Big)\Big(\frac{ax}{K}\Big) - \Big(p_2 - \frac{c_2}{q_2 y}\Big)\Big(\frac{eby}{y+D}\Big) \tag{30}$$

And from (21) and (29) we get,

$$e^{-\delta t}\Big(p_2 - \frac{c_2}{q_2 y}\Big) = \frac{1}{\delta}e^{-\delta t}\Big[p_2 q_2 E_2 - \Big(p_1 - \frac{c_1}{q_1 x}\Big)\Big(\frac{bDx}{(y+D)^2}\Big) - \Big(p_2 - \frac{c_2}{q_2 y}\Big)\Big(\frac{ebxy}{(y+D)^2}\Big)\Big]$$

$$\Rightarrow p_2 q_2 E_2 = \delta\Big(p_2 - \frac{c_2}{q_2 y}\Big) + \Big(p_1 - \frac{c_1}{q_1 x}\Big)\Big(\frac{bDx}{(y+D)^2}\Big) + \Big(p_2 - \frac{c_2}{q_2 y}\Big)\Big(\frac{ebxy}{(y+D)^2}\Big) \tag{31}$$

Eqs. (30) and (31) give the optimal harvesting efforts as

$$E_1 = \frac{\delta(p_1 - \frac{c_1}{q_1 x}) + (p_1 - \frac{c_1}{q_1 x})(\frac{ax}{K}) - (p_2 - \frac{c_2}{q_2 y})(\frac{eby}{y+D})}{p_1 q_1}, \tag{32}$$

and

$$E_2 = \frac{\delta(p_2 - \frac{c_2}{q_2 y}) + (p_1 - \frac{c_1}{q_1 x})(\frac{bDx}{(y+D)^2}) + (p_2 - \frac{c_2}{q_2 y})(\frac{ebxy}{(y+D)^2})}{p_2 q_2}. \quad (33)$$

Hence solving steady state equations together with (32) and (33) we get the optimal solution (x_δ, y_δ) and optimal harvesting efforts $E_{1\delta}$ and $E_{2\delta}$.
The optimal harvesting policy means the economic rent for harvesting will be the maximal in the future time, with the populations of the system are permanent.

7 Concluding remarks

In this paper, a harvested predator-prey system with novel functional response is considered. By making some hypotheses on the biological parameters, we have reduced our model to a simple form. Boundedness of the system is established, which, in turn, implies that the system is biologically well-behaved. The local and global stabilities of the equilibria are addressed. It was also found that it is possible to control the system is such a way that the system approaches a required state, using the efforts E_1 and E_2 as controls. We then examine the possibilities of existence of bionomic (biological as well as economic) equilibria of the system. Next the optimal harvesting policy is discussed using Pontryagin's maximal principle.

References

[1] Bazykin, A.D., 1998. Nonlinear Dynamics of Interacting Populations. Series on Nonlinear Science. Ser. A, vol. 11. World Scientific, Singapore. Chua, L.O. (Ed.), Original Russian version: Bazykin, A.D. Nauka, Moscow 1985.

[2] G. Birkoff, G.C. Rota. *Ordinary differential equations*. Ginn, Boston 1982.

[3] C.W. Clark. Mathematical bioeconomics, the Optimal management of renewable resources, second ed., Wiley, New York 1990.

[4] N. C. Fellah, S.M. Bouguima, A. Moussaoui. The effect of water level in a prey-predator interactions: A nonlinear analysis study, Chaos, Solitons & Fractals. 45 205-212, 2012

[5] T. K. Kar. Modelling and analysis of a harvested preypredator system incorporating a prey refuge. Journal of Computational and Applied Mathematics 185 1933, 2006.

[6] A.Maiti, B.Patra and G.P. Samanta. Bionomic exploitation of a ratio-dependent predator-prey system, international journal of mathematical education in science and technology, Vol. 39, No. 8, 15 December 1061-1076, 2008.

[7] A. Moussaoui, SM. Bouguima. A prey-predator interaction under fluctuating level water. Math. Meth. Appl. Sci. 2014. In press.

[8] JD. Murray. Mathematical biology. Berlin: Springer-Verlag 1993.

[9] D. Pal a, G.S. Mahaptra b, G.P. Samanta. Optimal harvesting of preypredator system with interval biological parameters: A bioeconomic model. Mathematical Biosciences 241 181187, 2013.

[10] L.S. Pontryagin, V.G. Boltyonskii, R.V. Gamkrelidre, E.F. Mishchenko. The mathematical theory of optimal processes, Wiley, NewYork 1962.

[11] T. Pradhan, K.S. Chaudhuri, Bioeconomic modeling of selective harvesting in an inshore-offshore fishery, Differential Equations and Dynamic Systems 7 (3), 305320, 1999.

[12] Yunfei. Lv, R. Yuan, Y. Pei. A prey-predator model with harvesting for fishery resource with reserve area, Applied Mathematical Modelling 1-15, 2012

[13] N.Zhang, F.Chen, Q.Su, and T.Wu. Dynamic Behaviors of a Harvesting Leslie-Gower Predator-Prey Model. Discrete Dynamics in Nature and Society. doi:10.1155/2011/473949. 2011.

Satellite Workshop 7
Memristor and Complex Networks: Theory and Applications

Satellite Workshop 7
Memristor and Complex Networks: Theory and Applications

Organizers

- Valentina LANZA, LMAH, FR-CNRS 3335, Le Havre, France, valentina.lanza@univ-lehavre.fr
- Fernando CORINTO, Politecnico di Torino, Italia, fernando.corinto@polito.it

Description

This special session aims to provide a broad survey on recent trends on complex networks with adaptive interactions, including recent advances of memristor technology for dynamic couplings. The special session includes contributed papers that will deal with the key research topics on memristor technology in nonlinear network arrays, the emergence of synchronized patterns and the applications in neuromorphic networks.

List of papers/presentations

- Miroslav MIRCHEV and Ljupco KOCAREV (Ss. Cyril and Methodius University)
- Ronald Tetzlaff and Alon ASCOLI (TUD)
- Michel BONNIN and Fernando CORINTO (Politecnico di Torino)
- Keyong-Sik MIN (Kookmin University)

Proceedings of ICCSA 2014
Normandie University, Le Havre, France - June 23-26, 2014

THE ROLE OF NOISE ON THE SYNCHRONIZATION OF OSCILLATORS

Michele Bonnin, Valentina Lanza and Fernando Corinto *†

Abstract. Synchronization of coupled oscillators is a paradigm for complexity in many areas of science and engineering. Any realistic network model should include noise effects. For long time, noise has been considered a nuisance for synchronization, but recent developments, e.g. stochastic resonance, reveals that noise can play an active role to enhance self organization. Traditionally, phase noise has been described as a diffusion process, i.e. noise is responsible for phase diffusion, leaving the oscillation frequency unchanged. We show that phase noise in oscillator is best described as a convection diffusion problem, i.e. noise is responsible for both phase diffusion and frequency drift. We derive a simplified model to study the influence if noise on the oscillation frequency, and we discuss the implication to the synchronization of coupled and periodically driven oscillators.

Keywords. Synchronization, nonlinear oscillators, phase noise, stochastic differential equations, Itô calculus.

1 Introduction

Periodically driven oscillators and coupled oscillators are classical problems in nonlinear dynamics, with many relevant applications in physics, chemistry, biology and engineering [1, 2, 3]. To make the models more realistic, external inputs can be included, to represent the unavoidable random fluctuations that occur in real world systems, due to the physical properties of the oscillators or induced by the environment. Such disturbances can be modeled by stochastic forces applied to the oscillators, which are then described by stochastic differential equations [4].

Corrupting noise can dramatically affect the performance of oscillators. This is of particular relevance, for instance, in the field of modern electronic devices. Phase noise in oscillators can produce distortion or complete loss of incoming information in traditional receivers, and high bit error rates in phase modulated applications. Traditionally, the action of noise on electronic oscillators has been described as purely diffusive process [5, 6]. It is commonly assumed that the effect of white noise on the spectrum of an oscillator is to produce a broadening of the oscillator's spectrum without affecting the positions of the peaks. Recently, this assumption has been questioned by the analysis of some simple solvable models, and by the development of improved mathematical techniques [7, 8]. These works have shown that the phase noise problem is best described as a convection–diffusion process. That is, white noise may also be responsible for a shift in the oscillator's angular frequency.

On the one hand, that an external disturbance may modify the oscillation frequency should not come as a surprise. In fact, synchronization is commonly defined as a frequency adjustment in response to an external signal. On the other hand, it may sound surprising that a random perturbation can produce some kind of coherent modification to the oscillator's frequency. In fact one may expect that, as a result of their random nature, fluctuations have a null net effect and leave the oscillation frequency and amplitude unaffected. However we must keep in mind that we are dealing with systems that are not only stochastic, but also nonlinear in nature. Some directions are preferred to others, so that perturbations along some directions are amplified, while others are attenuated. The result is that coherent behavior can emerge from random excitations.

In this paper we present a novel derivation of the amplitude–phase equations for nonlinear oscillators driven by white Gaussian noise. The amplitude–phase equations are derived within the framework of Itô stochastic calculus, this allows a natural evaluation of the expected angular frequency which, in turn, is instrumental for synchronization analysis. The main advantage of this novel derivation is that the influence of noise on the oscillation frequency is made transparent and arises through Itô formula naturally. The relationship with Statonovich interpretation is also discussed.

2 Noisy oscillators

Noisy oscillators can be conveniently described by the stochastic differential equation (SDE) (see [4])

$$d\boldsymbol{X}(t) = \boldsymbol{a}(\boldsymbol{X}(t))\,dt + \varepsilon\,\boldsymbol{B}(\boldsymbol{X}(t))\,d\boldsymbol{W}(t) \qquad (1)$$

*M. Bonnin and F. Corinto are with Department of Electronics and Telecommunications, Politecnico di Torino, Turin, Italy. E-mails: michele.bonnin@polito.it, fernando.corinto@polito.it

†V. Lanza is with Laboratoire de Mathématiques Appliquées du Havre, Université du Havre, Le Havre, France, E-mail: valentina.lanza@univ-lehavre.fr

where $\boldsymbol{X} : \mathbb{R} \mapsto \mathbb{R}^n$, $\boldsymbol{a} : \mathbb{R}^n \mapsto \mathbb{R}^n$, and $\boldsymbol{B} : \mathbb{R}^n \mapsto \mathbb{R}^{n,m}$. $\varepsilon \in \mathbb{R}$ is a parameter, non necessarily small, and $\boldsymbol{W} : \mathbb{R} \mapsto \mathbb{R}^m$ is a Brownian motion, i.e. a Gaussian distributed stochastic process characterized by zero expectation value, uncorrelated increments and representing the integral of a white noise [4]. The Brownian motion describes the unavoidable noise sources that are always present in real world systems.

Eq. (1) can be interpreted following two main schemes: Stratonovich or Itô [4]. Both interpretations are completely rigorous, and both have their own advantages and disadvantages. Roughly speaking, in Stratonovich view the Brownian motion is interpreted as the limit of a correlated process for correlation time approaching zero. The main advantage of Stratonovich interpretation is that traditional calculus rules applies. The drawback is that stochastic variables and noise increments are not statistically independent (a consequence of the "look in the future property" of Stratonovich stochastic integral), making the calculation of expectation values difficult. By contrast in Itô interpretation Brownian motion is a truly uncorrelated process. The pros are that Itô integrals are adapted processes, they do not suffer of the "look in the future property", and stochastic variables and noise increments are statistically independent, making calculation of expectation values easier. The cons is that a new set of calculus rules, known as Itô calculus, are required. However, any Stratonovich (respectively Itô) SDE can be transformed into an equivalent Itô (respectively Stratonovich) SDE. By equivalent we mean a different SDE, interpreted with different rules, but that has the same solution. This equivalence opens the possibility to switch from one interpretation to the other taking advantage of the pros of both the definitions.

In this paper we shall interpret (1) as an Itô SDE, to take advantage of the non anticipating nature of Itô stochastic integral, and we shall use the notation $\boldsymbol{B}(\boldsymbol{X}) \circ d\boldsymbol{W}$ to denote the Stratonovich stochastic integral used in Stratonovich SDE.

3 Amplitude and phase description of noisy oscillators

For $\varepsilon = 0$ the SDE (1) reduces to the ordinary differential equation

$$\dot{\boldsymbol{x}}(t) = \boldsymbol{a}(\boldsymbol{x}(t)) \tag{2}$$

In absence of noise an oscillator exhibits a perfectly periodic solution. The periodic solution is represented by an asymptotically stable limit cycle $\boldsymbol{x}_0(t)$ in the oscillator's state space defined by

$$\left\{ \begin{array}{rcl} \dot{\boldsymbol{x}}_0(t) & = & \boldsymbol{a}(\boldsymbol{x}_0(t)) \\ \boldsymbol{x}_0(t) & = & \boldsymbol{x}_0(t+T). \end{array} \right. \tag{3}$$

where T is the period od the oscillation. We denote by $\omega_0 = 2\pi/T$ the oscillator's free running frequency.

The synchronization of nonlinear oscillators is best studied by looking to the phase relations between the oscillators. To this scope, we introduce a phase function $\phi : \mathbb{R}^n \mapsto [0, T), \mod T$, and an amplitude function $\boldsymbol{R} : \mathbb{R}^n \mapsto \mathbb{R}^{n-1}$, with $\phi, \boldsymbol{R} \in \mathcal{C}^m(\mathbb{R}^n)$, $m \geq 2$. The phase function is interpreted as an elapsed time from an initial reference point. Let us take a reference initial point $\boldsymbol{x}_0(0)$ on the limit cycle, and let us assign phase zero to this point, i.e. $\phi(\boldsymbol{x}_0(0)) = 0$. The phase of the point $\boldsymbol{x}_0(t)$ is $\phi(\boldsymbol{x}_0(t)) = t$. Thus, the phase represent a new parametrization of the limit cycle. The amplitude function $\boldsymbol{R}(\boldsymbol{x})$ is the Euclidean distance from the limit cycle. For our purposes we introduce the tangent unit vector

$$\boldsymbol{u}_1(t) = \frac{\boldsymbol{a}(\boldsymbol{x}_0(t))}{|\boldsymbol{a}(\boldsymbol{x}_0(t))|} \tag{4}$$

Together with $\boldsymbol{u}_1$ we consider other $n-1$ linear independent unit vectors $\boldsymbol{u}_2(t), \ldots, \boldsymbol{u}_n(t)$, such that the set $\{\boldsymbol{u}_1(t), \ldots, \boldsymbol{u}_n(t)\}$ is a basis for $\mathbb{R}^n$. We also consider another basis of $\mathbb{R}^n$, $\{\boldsymbol{v}_1(t), \ldots, \boldsymbol{v}_n(t)\}$ constructed as follows. Given the matrix $\boldsymbol{U}(t) = [\boldsymbol{u}_1(t), \ldots, \boldsymbol{u}_n(t)]$, we take its inverse

$$\boldsymbol{V}(t) = \boldsymbol{U}^{-1}(t) = \left[\begin{array}{c} \boldsymbol{v}_1^T(t) \\ \vdots \\ \boldsymbol{v}_n^T(t) \end{array} \right] \tag{5}$$

It follows the bi–orthogonality condition $\boldsymbol{v}_i^T \boldsymbol{u}_j = \delta_{ij}$. To simplify notation we also introduce $r(\phi) = |\boldsymbol{a}(\boldsymbol{x}_0(\phi))|$.

The following theorem establishes the amplitude–phase model corresponding to the SDE (1).

Theorem 3.1. *Consider the Itô diffusion* (1)*, and a coordinate transformation* $\boldsymbol{x} = \boldsymbol{h}(\phi, \boldsymbol{R})$*. Let* $\boldsymbol{h}$ *be invertible, at least locally in a neighborhood of the limit cycle* $I(\boldsymbol{x}_0)$*, and let the inverse* $\boldsymbol{h}^{-1} \in \mathcal{C}^m(I(\boldsymbol{x}_0))$*,* $m \geq 2$*. Let* $\boldsymbol{Y}(\phi) = [\boldsymbol{u}_2(\phi), \ldots, \boldsymbol{u}_n(\phi)]$ *and* $\boldsymbol{Z}(\phi) = [\boldsymbol{v}_2(\phi, \ldots, \boldsymbol{v}_n(\phi)]$*. Then the amplitude and phase are Itô processes given by*

$$d\phi = \big(1 + a_1(\phi, \boldsymbol{R})\big) dt + \varepsilon \boldsymbol{B}_1(\phi, \boldsymbol{R})\, d\boldsymbol{W}_t \tag{6}$$

$$d\boldsymbol{R} = \big(\boldsymbol{A}(\phi) + \boldsymbol{a}_2(\phi, \boldsymbol{R})\big) dt + \varepsilon \boldsymbol{B}_2(\phi, \boldsymbol{R})\, d\boldsymbol{W}_t \tag{7}$$

where

$$\begin{aligned} a_1 &= \left(r + \boldsymbol{v}_1^T \frac{\partial \boldsymbol{Y}}{\partial \phi} \boldsymbol{R}\right)^{-1} \boldsymbol{v}_1^T \Big(\boldsymbol{a}(\boldsymbol{x}_0 + \boldsymbol{Y}\boldsymbol{R}) - \boldsymbol{a}(\boldsymbol{x}_0) - \frac{\partial \boldsymbol{Y}}{\partial \phi} \boldsymbol{R} \\ &\quad - \frac{\varepsilon^2}{2} \Big(\frac{\partial \boldsymbol{a}(\boldsymbol{x}_0)}{\partial \phi} + \frac{\partial^2 \boldsymbol{Y}}{\partial \phi^2} \boldsymbol{R} \Big) \boldsymbol{B}_1^T \boldsymbol{B}_1 - \varepsilon^2 \frac{\partial \boldsymbol{Y}}{\partial \phi} \boldsymbol{B}_2^T \boldsymbol{B}_1 \Big) \end{aligned} \tag{8}$$

$$\boldsymbol{B}_1 = \left(r + \boldsymbol{v}_1^T \frac{\partial \boldsymbol{Y}}{\partial \phi} \boldsymbol{R}\right)^{-1} \boldsymbol{v}_1^T \boldsymbol{B}(\boldsymbol{x}_0 + \boldsymbol{Y}\boldsymbol{R}) \tag{9}$$

$$\boldsymbol{A} = -\boldsymbol{Z}^T \frac{\partial \boldsymbol{Y}}{\partial \phi} \tag{10}$$

$$\boldsymbol{a}_2 = \boldsymbol{Z}^T \Big(- \frac{\partial \boldsymbol{Y}}{\partial \phi} \boldsymbol{R}\, a_1 + \boldsymbol{a}(\boldsymbol{x}_0 + \boldsymbol{Y}\boldsymbol{R}) \tag{11}$$

$$- \frac{\varepsilon^2}{2} \Big(\frac{\partial \boldsymbol{a}(\boldsymbol{x}_0)}{\partial \phi} + \frac{\partial^2 \boldsymbol{Y}}{\partial \phi^2} \boldsymbol{R} \Big) \boldsymbol{B}_1^T \boldsymbol{B}_1 - \varepsilon^2 \frac{\partial \boldsymbol{Y}}{\partial \phi} \boldsymbol{B}_2^T \boldsymbol{B}_1 \Big) \tag{12}$$

$$\boldsymbol{B}_2 = \boldsymbol{Z}^T \boldsymbol{B}(\boldsymbol{x}_0 + \boldsymbol{Y}\boldsymbol{R}) - \boldsymbol{Z}^T \frac{\partial \boldsymbol{Y}}{\partial \phi} \boldsymbol{R} \boldsymbol{B}_1(\boldsymbol{x}_0 + \boldsymbol{Y}\boldsymbol{R}) \tag{13}$$

Proof: That ϕ and $\boldsymbol{R}$ are Itô processes is a direct consequence of the hypothesis that $\boldsymbol{h}$ is invertible with inverse of class at least $\mathcal{C}^2(I(\boldsymbol{x}_0))$. Then we can find $\phi = \phi(\boldsymbol{x})$ and $\boldsymbol{R} = \boldsymbol{R}(\boldsymbol{x})$. It follows from Itô formula that ϕ and $\boldsymbol{R}$ are Itô processes. If $\boldsymbol{X}(t)$ is a solution of (1), then using Itô formula ϕ and $\boldsymbol{R}$ satisfy equations of type

$$d\phi = \alpha\, dt + \boldsymbol{\beta}\, d\boldsymbol{W} \quad (14)$$

$$d\boldsymbol{R} = \gamma\, dt + \boldsymbol{\sigma}\, d\boldsymbol{W} \quad (15)$$

that using Itô lemma gives

$$d\phi^2 = \boldsymbol{\beta}\boldsymbol{\beta}^T\, dt \quad (16)$$

$$d\phi\, d\boldsymbol{R} = \boldsymbol{\sigma}\boldsymbol{\beta}^T\, dt \quad (17)$$

From $\boldsymbol{x} = \boldsymbol{h}(\phi, \boldsymbol{R})$ we have, using Itô formula and (1)

$$\frac{\partial \boldsymbol{h}}{\partial \phi}\, d\phi + \frac{\partial \boldsymbol{h}}{\partial \boldsymbol{R}}\, d\boldsymbol{R} + \frac{1}{2}\frac{\partial^2 \boldsymbol{h}}{\partial \phi^2} d\phi^2 + \frac{1}{2}\frac{\partial^2 \boldsymbol{h}}{\partial \boldsymbol{R}\partial\phi} d\boldsymbol{R} d\phi$$

$$+\frac{1}{2} d\boldsymbol{R}^T \frac{\partial^2 \boldsymbol{h}}{\partial \boldsymbol{R}^2} d\boldsymbol{R} = \boldsymbol{a}(\boldsymbol{h}(\phi, \boldsymbol{R}))dt + \varepsilon \boldsymbol{B}(\boldsymbol{h}(\phi, \boldsymbol{R}))d\boldsymbol{W} \quad (18)$$

We look for a change of coordinates in the form

$$\boldsymbol{h}(\phi, \boldsymbol{R}) = \boldsymbol{x}_0(\phi) + \boldsymbol{Y}(\phi)\boldsymbol{R}(t)$$

Introducing this ansatz in (18) yields

$$\left(\boldsymbol{a}(\boldsymbol{x}_0) + \frac{\partial \boldsymbol{Y}}{\partial \phi}\,\boldsymbol{R}\right) d\phi + \boldsymbol{Y}\, d\boldsymbol{R} + \frac{1}{2}\left(\frac{\partial \boldsymbol{a}(\boldsymbol{x}_0)}{\partial \phi} + \frac{\partial^2 \boldsymbol{Y}}{\partial \phi^2}\boldsymbol{R}\right) d\phi^2$$

$$+\frac{\partial \boldsymbol{Y}}{\partial \phi}\, d\phi\, d\boldsymbol{R} = \boldsymbol{a}(\boldsymbol{x}_0 + \boldsymbol{Y}\boldsymbol{R})dt + \varepsilon \boldsymbol{B}(\boldsymbol{x}_0 + \boldsymbol{Y}\boldsymbol{R}) \quad (19)$$

Multiplying to the left by $\boldsymbol{v}_1^T$ and using the bi–orthogonality condition we get

$$\left(r + \boldsymbol{v}_1^T \frac{\partial \boldsymbol{Y}}{\partial \phi}\,\boldsymbol{R}\right) d\phi + \frac{1}{2}\boldsymbol{v}_1^T \left(\frac{\partial \boldsymbol{a}(\boldsymbol{x}_0)}{\partial \phi} + \frac{\partial^2 \boldsymbol{Y}}{\partial \phi^2}\boldsymbol{R}\right) d\phi^2$$

$$+\boldsymbol{v}_1^T \frac{\partial \boldsymbol{Y}}{\partial \phi}\, d\phi\, d\boldsymbol{R} = \boldsymbol{v}_1^T \boldsymbol{a}(\boldsymbol{x}_0 + \boldsymbol{Y}\boldsymbol{R})dt + \varepsilon \boldsymbol{v}_1^T \boldsymbol{B}(\boldsymbol{x}_0 + \boldsymbol{Y}\boldsymbol{R})d\boldsymbol{W} \quad (20)$$

Multiplying (17) to the left by $\boldsymbol{Z}^T$ we get

$$\boldsymbol{Z}^T \frac{\partial \boldsymbol{Y}}{\partial \phi}\boldsymbol{R}\, d\phi + d\boldsymbol{R} + \frac{1}{2}\boldsymbol{Z}^T \left(\frac{\partial \boldsymbol{a}(\boldsymbol{x}_0)}{\partial \phi} + \frac{\partial^2 \boldsymbol{Y}}{\partial \phi^2}\boldsymbol{R}\right) d\phi^2$$

$$+\boldsymbol{Z}^T \frac{\partial \boldsymbol{Y}}{\partial \phi}\, d\phi\, d\boldsymbol{R} = \boldsymbol{Z}^T \boldsymbol{a}(\boldsymbol{x}_0 + \boldsymbol{Y}\boldsymbol{R})dt + \varepsilon \boldsymbol{Z}^T \boldsymbol{B}(\boldsymbol{x}_0 + \boldsymbol{Y}\boldsymbol{R})d\boldsymbol{W} \quad (21)$$

Introducing (14)–(17) into (20)–(21) and equating term in $d\boldsymbol{W}$ yields

$$\boldsymbol{\beta} = \varepsilon\left(r + \boldsymbol{v}_1^T \frac{\partial \boldsymbol{Y}}{\partial \phi}\boldsymbol{R}\right)^{-1} \boldsymbol{v}_1^T \boldsymbol{B}(\boldsymbol{x}_0 + \boldsymbol{Y}\boldsymbol{R}) \quad (22)$$

$$\boldsymbol{\sigma} = \varepsilon \boldsymbol{Z}^T \boldsymbol{B}(\boldsymbol{x}_0 + \boldsymbol{Y}\boldsymbol{R}) - \boldsymbol{Z}^T \frac{\partial \boldsymbol{Y}}{\partial \phi}\boldsymbol{R}\boldsymbol{\beta} \quad (23)$$

Finally introducing (16)–(17) and (22)–(23) into (20)–(21) and rearranging the terms we get the thesis. □

The amplitude–phase equations (6)–(7) crucially depends on the choice of the basis vectors $\boldsymbol{u}_2, \ldots, \boldsymbol{u}_n$. Two special sets of vectors look particularly suitable. The first is an orthonormal set. This choice allows to take advantage of Frenet formulas for moving orthonormal coordinate systems. The second choice is related to Floquet's basis [6, 7, 9].

Corollary 3.1. *If the basis vectors* $\{\boldsymbol{u}_2(\phi), \ldots, \boldsymbol{u}_n(\phi)\}$ *are such that*

$$\frac{\partial \boldsymbol{Y}}{\partial \phi} = \frac{\partial \boldsymbol{a}(\boldsymbol{x}_0)}{\partial \boldsymbol{x}}\, \boldsymbol{Y} \quad (24)$$

then, up to the first perturbative order, the Itô processes for the phase and amplitude reduce to

$$d\phi = \big(1 + \varepsilon^2 \hat{a}_1(\phi, \boldsymbol{R})\big)dt + \varepsilon \boldsymbol{B}_1(\phi, \boldsymbol{R})\, d\boldsymbol{W}_t \quad (25)$$

$$d\boldsymbol{R} = \varepsilon^2 \hat{\boldsymbol{a}}_2(\phi, \boldsymbol{R}) d\, t + \varepsilon \boldsymbol{B}_2(\phi, \boldsymbol{R})\, d\boldsymbol{W}_t \quad (26)$$

where

$$\hat{a}_1 = -\left(r + \boldsymbol{v}_1^T \frac{\partial \boldsymbol{Y}}{\partial \phi}\boldsymbol{R}\right)^{-1} \boldsymbol{v}_1^T \left(\frac{1}{2}\left(\frac{\partial \boldsymbol{a}(\boldsymbol{x}_0)}{\partial \phi} + \frac{\partial^2 \boldsymbol{Y}}{\partial \phi^2}\,\boldsymbol{R}\right)\boldsymbol{B}_1^T \boldsymbol{B}_1 + \frac{\partial \boldsymbol{Y}}{\partial \phi}\boldsymbol{B}_2^T \boldsymbol{B}_1\right) \quad (27)$$

$$\hat{\boldsymbol{a}}_2 = -\boldsymbol{Z}^T \left(\frac{\partial \boldsymbol{Y}}{\partial \phi}\boldsymbol{R}\,\hat{a}_1 + \frac{1}{2}\left(\frac{\partial \boldsymbol{a}(\boldsymbol{x}_0)}{\partial \phi} + \frac{\partial^2 \boldsymbol{Y}}{\partial \phi^2}\,\boldsymbol{R}\right)\boldsymbol{B}_1^T \boldsymbol{B}_1 + \frac{\partial \boldsymbol{Y}}{\partial \phi}\boldsymbol{B}_2^T \boldsymbol{B}_1\right) \quad (28)$$

Proof: It is sufficient to substitute in the previous equations the truncated Taylor expansion

$$\boldsymbol{a}(\boldsymbol{x}_0 + \boldsymbol{Y}\boldsymbol{R}) = \boldsymbol{a}(\boldsymbol{x}_0) + \frac{\partial \boldsymbol{a}(\boldsymbol{x}_0)}{\partial \boldsymbol{x}}\boldsymbol{Y}$$

and consider that $\boldsymbol{Z}^T \boldsymbol{a}(\boldsymbol{x}_0) = 0$. □

It can be shown that $\boldsymbol{v}_1$ is locally tangent on the limit cycle to the manifold on which the phase is most sensitive to perturbations. By contrast $\boldsymbol{v}_2, \ldots, \boldsymbol{v}_n$ span the direction tangent to the manifold where the phase is insensitive to perturbations [7, 9]. The projection of the noise along these linear spaces allows a partial decoupling of the amplitude and phase dynamics. In absence of noise ($\varepsilon = 0$) the system evolves with constant amplitude and constant angular frequency, similarly to the popular action-angle variables formalism of classical mechanics. In the limit $\varepsilon \ll 1$, the amplitude dynamics is one order of magnitude slower than the phase dynamics. This observation suggests the ida to neglect the amplitude fluctuations, and substitute $\boldsymbol{R} = 0$ in (25). This approximation leads to the phase reduced model

$$d\phi = \big(1 + \varepsilon^2 \hat{a}_1(\phi)\big)dt + \varepsilon \boldsymbol{B}_1(\phi)\, d\boldsymbol{W} \quad (29)$$

We remark that the assumptions leading to (25)–(26) and (29) are often made more for mathematical convenience than being physically plausible. In fact, (25)–(26) rely on linear approximation of manifolds, and nonlinear effects will become stronger the further we move away

from the limit cycle. Moreover, (29) is based on the assumption that any perturbation is instantaneously adsorbed and trajectories immediately relaxes back to the limit cycle. However, the presence of nearby invariant structures such as equilibrium points and invariant manifolds may result in trajectories spending long periods of time away from the limit cycle.

4 Influence of noise on the frequency of an oscillator

The phase reduced model (29) shows that the drift effect due to $\varepsilon^2\hat{a}_1$ becomes negligible in the limit of vanishing small noise ($\varepsilon \to 0$). The phase model in this limit has been extensively studied both at the single oscillator and network level [5, 6, 10]. However, for small but finite values of ε, the drift effect may become significant if $\hat{a}_1$ becomes large enough. That the drift effect should not be neglected even for small values of ε can also be seen as follows. Let $h(\phi)$ be an arbitrary function of the phase, and let $u(t,\phi) = E[h(\phi)]$ be the expected value of this function, with $u(0,\phi) = h(\phi)$ then the time evolution of $u(t,\phi)$ is governed by the Kolmogorov backward equation [4]

$$\frac{\partial u}{\partial t} = Au \tag{30}$$

where A is the generator of the Itô diffusion

$$Ah(\phi) = \left(\omega_0+\varepsilon^2 a_1(\phi)\right)\frac{\partial h(\phi)}{\partial \phi}+\frac{\varepsilon^2}{2}\left(\boldsymbol{B}_1(\phi)\boldsymbol{B}1(\phi)^T\right)\frac{\partial^2 h(\phi)}{\partial \phi^2} \tag{31}$$

Equations (30) and (31) show that both the $\mathcal{O}(\varepsilon^2)$ drift coefficient and the $\mathcal{O}(\varepsilon)$ diffusion coefficient contribute for ε^2 terms to the evolution of expected quantities, and therefore we are not allowed to neglect one term with respect to the other.

It is possible to determine the expected mean angular frequency directly from the reduced phase model (28) without solving the Kolmogorov backward equation. The mean angular frequency can be defined as $\omega = 1/T\int_0^T d\phi$. The expected mean angular frequency is computed using the following property of Itô stochastic integral: for any non anticipating function (adapted process) $h(\boldsymbol{X}_t)$

$$E\left[\int_{t_0}^{t} h(\boldsymbol{X}_t)\, d\boldsymbol{W}_t\right] = 0 \tag{32}$$

as a consequence of the fact that $E[\boldsymbol{W}_t] = 0$. Thus from (28) we have

$$E[\omega] = 1 + \frac{\varepsilon^2}{T}E\left[\int_0^T \hat{a}_1(\phi)\, dt\right] \tag{33}$$

One may argue that the drift term is an artifact due to Itô interpretation. However, it turns out that the frequency drift is also present if Stratonovich interpretation is used [7]. To clarify the point, consider the Stratonovich SDE

$$d\boldsymbol{X} = \boldsymbol{a}^{(S)}(\boldsymbol{X})\, dt + \varepsilon \boldsymbol{B}(\boldsymbol{X}) \circ d\boldsymbol{W} \tag{34}$$

where the index (S) means "Stratonovich". Taking into account that in Stratonovich interpretation traditional calculus rules apply, repeating the procedure used in the previous section we arrive to the reduced phase model

$$d\phi = dt + \varepsilon \boldsymbol{B}_1(\phi) \circ d\boldsymbol{W} \tag{35}$$

However, deriving the expected mean angular frequency from (35) is not trivial, because in Stratonovich interpretation $E[\int_{t_0}^{t} h(\boldsymbol{X}) \circ d\boldsymbol{W}] \neq 0$. This is a consequence of the anticipating nature or "look in the future" property of Stratonovich stochastic integral. Because of its anticipating nature, in Stratonovich view stochastic processes and noise increments are correlated. To resolve the statistical dependence, a Stratonovich SDE has to be transformed into its equivalent Itô SDE by the addition of the drift correction term [4, 11]. Here is where the drift coefficient, that arises naturally from the quadratic terms in Itô formula, comes into play.

5 Discussion

Synchronization of oscillators is commonly defined as an adjustment of frequencies in response to an external stimulus. Usually, the external stimulus is taken in the form of either a coherent signal, e.g. a periodic function, or as couplings among oscillators. The synchronization is the result of different competing mechanisms. On the one hand, the application of a periodic input, and/or couplings between the oscillators play a constructive role, and favor the formation of common rhythms. On the other hand, differences between the oscillators natural frequencies are destructive to synchronization. In the traditional picture, noise is added as a nuisance to synchronization. The negative effect produced by phase diffusion and the resulting occurrence of phase slips has been extensively studied and is rather well understood [1, 2]. However it has been recently discovered that noise can play a constructive role in information transmission and processing, and in the emergence of coherent structures in complex systems [12, 13].

Here we limit ourselves to discuss the role of noise in synchronization through its action on the frequency of an oscillator. It is well known that an oscillator will synchronize with a periodic external signal, provided that the strength of the signal exceeds a thresholds determined by the frequency mismatch between the oscillator and the input. The situation is analogous for coupled oscillators. Because of the dependence of the frequency on the noise intensity, noise can both favor synchronization if it reduces the frequency mismatch, or it can contrast the formation of rhythms if the mismatch is increased. It is worth noting that this mechanism is different from

stochastic resonance, although they bear some resemblance. In stochastic resonance the role of noise is to enhance the signal level at a certain frequency. By contrast, the present mechanism is based on the modification of the oscillator frequency.

In figure 1 we show the expected angular frequency $E[\omega]$ versus the noise intensity for a van der Pol oscillator with additive noise described by the SDE

$$\begin{aligned} dx &= y\,dt + \varepsilon\,dB_1 \\ dy &= \big(-x + \mu(1-x^2)y\big)dt + \varepsilon\,dB_2 \end{aligned} \tag{36}$$

The expected angular frequency has been obtained through Monte Carlo simulations. For each value of the noise intensity we have run simulations for one thousand different realizations of the noise process. For each realization, the mean frequency has been evaluated as $\omega = (\phi(t_2) - \phi(t_1))/(t_2 - t_1)$ for $t_2 \gg t_1$. The expected values has been computed as the mean of the ω values. Since the noise is additive, there is no difference between Itô and Stratonovich interpretation. The quadratic dependence of the frequency drift on the noise intensity is well reproduced by numerical data.

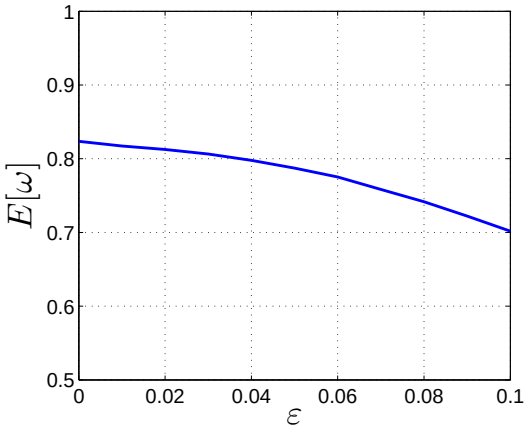

Figure 1: Expected mean angular frequency vs noise intensity for a van der Pol oscillator with additive noise. The parameter is set to $\mu = 2$.

Figure 2 shows the time evolution of the phase difference between two uncoupled Stuart–Landau oscillators. In polar coordinates the Stuart–Landau oscillator is described by the SDE

$$\begin{aligned} dr &= \big(r - r^3\big)dt + \varepsilon dB_r \\ d\theta &= \big(\alpha - \beta r^2\big)\,dt + \varepsilon dB_\theta \end{aligned} \tag{37}$$

It is easy to see that the oscillator admits an asymptotically stable limit cycle of amplitude $r = 1$ and angular frequency $\omega_0 = \alpha - \beta$. This example is instructive because, introducing the new phase function $\phi = \theta - \beta \log r$, we obtain the Itô SDE

$$\begin{aligned} dr &= \big(r - r^3\big)dt + \varepsilon dB_r \\ d\phi &= \left(\omega_0 + \frac{\varepsilon^2}{2}\frac{\beta}{r^2}\right)dt + \varepsilon\left(dB_\theta - \frac{\beta}{r}dB_r\right) \end{aligned} \tag{38}$$

Thus, in absence of noise, the system admits a solution representing oscillations of constant amplitude and constant angular frequency, in complete analogy with (25)–(26). If amplitude fluctuations are neglected, we have the expected angular frequency $E[\omega] = \alpha - \beta + \varepsilon^2\beta/2$. Figure 2 shows the result for two oscillators with free running angular frequencies $\omega_1 = 4$ and $\omega_2 = 3.995$, respectively. The two oscillators are expected to have the same mean angular frequency for $\varepsilon \simeq 0.25$. The figure shows that, in absence of noise the phase difference would grow linearly in time, while for the proper noise intensity it remains bounded, as expected. The large fluctuations in the phase difference are due to the relatively high noise intensity required to achieve the same mean angularfrequency.

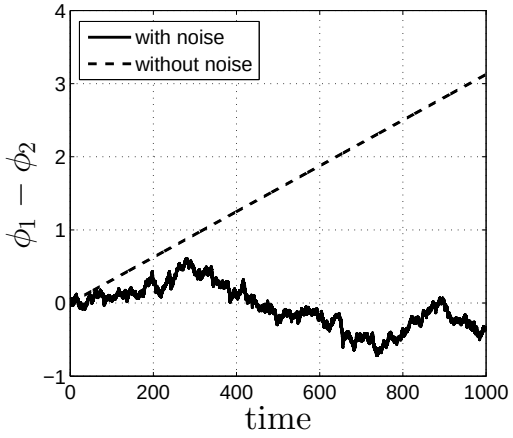

Figure 2: Phase difference for two uncoupled Stuart–Landau oscillator with slightly different frequencies both in presence of noise (solid line) and without noise. Noise intensity is $\varepsilon = 0.25$

6 Conclusions

We have discussed the role of noise on nonlinear oscillators subject to white Gaussian noise. Noisy oscillators can be conveniently described by stochastic differential equations. Using projection techniques and Itô calculus a set of stochastic differential equations describing the evolution of the phase and the amplitude of the oscillator can be derived.

The resulting amplitude–phase equations describe the phase noise problem as a convection–diffusion process. White noise is responsible for both phase diffusion and a drift in the frequency of oscillations. We have discussed the condition under which an approximate phase reduced model can be derived. The phase reduced model is a simplified model, that describe the behavior of the noisy oscillator in terms of the sole phase variable. We have shown how the frequency drift emerges if the Stratonovich interpretation is used instead of Itô view.

We discussed the implication of the frequency drift to

the synchronization of coupled and forced oscillators. Oscillators adjust their frequency in response to noise intensity, and as a consequence noise can actively contribute to the synchronization by decreasing the frequency mismatch between an oscillator and a periodic driving signal. Thus noise can favor the emergence of coherent behavior, through a mechanism similar to stochastic resonance.

Acknowledgements

This work was partially supported by the Ministry of Foreign Affairs (Italy) "*Con il contributo del Ministero degli Affari Esteri, Direzione Generale per la Promozione del Sistema Paese*".

References

[1] Y. Kuramoto, *Chemical Oscillations, Waves and Turbulence*, Springer–Verlag, Berlin, 2003.

[2] A. Pikovsky, M. Rosenblum and J. Kurths, *Synchronization A universal concept in nonlinear sciences*, Cambridge Univesity Press, 2001.

[3] E. Izhikevich, *Dynamical Systems in Neuroscience: The Geometry of Excitability and Bursting* MIT Press, 2006.

[4] B. Øksendal, *Stochastic Differential Equations*, Springer, New York, 2003.

[5] F. X. Kaertner, "Analysis of white and $f^{-\alpha}$ noise in oscillators," *International Journal of Circuit Theory and Applications*, vol. 18, pp. 485–519, 1990.

[6] A. Demir, A. Mehrotra and J. Roychowdhury, "Phase noise in oscillators: A unifying theory and numerical methods for characterization," *IEEE Transactions on Circuits and Systems I: Regular Papers*, vol. 47, no. 5, pp. 655–674, May 2000.

[7] M. Bonnin and F. Corinto, "Phase noise and noise induced frequency shift in stochastic nonlinear oscillators," *IEEE Transactions on Circuits and Systems I: Regular Papers*, vol. 60, no. 8, pp. 2104–2115, August 2013.

[8] M. Bonnin and F. Corinto, "Influence of noise on the phase and amplitude of second order oscillators," *IEEE Transactions on Circuits and Systems II: Express Briefs*, vol. 61, no. 3, pp. 158–162, March 2014.

[9] M. Bonnin, F. Corinto and M. Gilli, "Phase space decomposition for phase noise and synchronization analysis of planar nonlinear oscillators," *IEEE Transactions on Circuits and SystemsII: Express Briefs*, vol. 59, no. 10, pp. 638–642, October 2012.

[10] G. S. Medvedev, "Synchronization of coupled stochastic limit cycle oscillators," *Physics Letters A*, vol. 374, pp. 1712–1720, 2010.

[11] C. W. Gardiner, *Handbook of Stochastic Methods*, Springer, Berlin, 1985.

[12] K. Wiesenfeld, and F. Moss, "Stochastic resonance and the benefits of noise: from ice ages to crayfish and SQUIDs" *Nature*, vol. 373, pp. 33–36, 1995.

[13] L. Gammaitoni *et al*, "Stochastic resonance" *Reviews of Modern Physics*, vol. 70, no. 10, pp. 223–287, 1998.

Proceedings of ICCSA 2014
Normandie University, Le Havre, France - June 23-26, 2014

ANALYTICAL CONDITIONS FOR SYNCHRONIZATION FOR A SIMPLE MEMRISTIVE NEURAL NETWORK

Alon Ascoli, Valentina Lanza, Fernando Corinto, and Ronald Tetzlaff *†‡

Abstract. The memristor manifests qualities and behaviors naturally observed in biological synapses. It exists at the nanoscale, consumes very little power, is ideally suited for parallel processing, may process and store information, and exhibits a flux-dependent conductivity. Further, the memristor may reproduce rules governing the process of neural learning, including the Hebbian rule, Spike-Time-Dependent-Plasticity and Spike-Rate-Dependent-Plasticity. Hence memristive nano-structures are suitable candidates for the design of core elements of novel neuromorphic systems. It is then of interest to investigate models of memristive neural networks in order to gain some insight into the mechanisms underlying the complex dynamics emerging in biological systems. This manuscript presents an analytical treatment, based on the contraction mapping theorem, which allows the derivation of analytical expressions for the conditions of synchronization in a simple memristive neural network consisting of two Hindmarsh-Rose neurons interacting through a unidirectional memristive coupling arrangement. The results of the study confirm the conclusions from recent numerical investigations which revealed the strong impact of the dynamics occurring on the memristive coupling path on the emergence of synchrononization among the neuron oscillators.

Keywords. Memristor, synapse, Hindmarsh-Rose, neuron, synchronization

1 Introduction

Networks of nonlinear and dynamical cells constitute a suitable framework for the model of various natural phenomena. Interestingly, the architecture of neuromorphic circuits [1] is based upon networks of nonlinear and dynamical cells. The mathematical models describing such artificial neural networks are, in the simplest form, large sets of nonlinear functional differential equations [2], therefore most of the investigations of the dynamics emerging in them has traditionally been based on numerical simulations. However, it is of great interest to develop analytical methodologies which may support the predictions of the models. Most of the studies on the steady-state dynamics developing in artificial neural networks has been devoted to non-stationary behaviors, since these may be used to model spatio-temporal patterns in neural recognition processes [3]. Another important aspect of the research endeavors concerns synchronization [4] (a scenario where all the cells of a network act in unison), since synchronous behaviors of neuron oscillators are at the basis of neural learning processes [5]. The plastic behavior of biological synapses plays a central role in the mechanisms lying under the emergence of synchronization in neural networks. Unfortunately the dynamics of conventional electronic implementations of synapses in artificial neural networks may not exhibit the same level of adaptability. The advent of the memristor, theoretically envisioned by Prof. L. O. Chua back in 1971 [6], in the realm of circuit elements available to the designer [7] is deemed to change dramatically the course of history. In fact, it was recently proved [8] that the memristor may closely match the behavior of a synapse. This is the reason why so much research is currently under way to unfold the full potential of memristors as synapses in artificial neural networks [9]. The aim of this work is to present an analytical methodology, inspired from the contraction mapping theory [10], to derive conditions for synchronization in a simple network of Hindmarsh-Rose HR neurons [11]. The results of the analytical treatment confirm the conclusions drawn recently on the basis of numerical investigations of a similar artificial neural network [12], which revealed the strong influence of the nonlinear behavior of memristive synapses on the development of synchronization in the network.

2 Theoretical study of the synchronization between two HR cells unidirectionally coupled through non-ideal memristors

The following analytical description intends to confirm the main conclusion [12] resulting from recent numerical

*A. Ascoli and R. Tetzlaff are with the Faculty of Electronics and Electrotechnics, Technische Universität Dresden, Dresden, Germany, emails: alon.ascoli@tu-dresden.de,ronald.tetzlaff@tu-dresden.de

†V. Lanza is with the Laboratoire de Mathématiques Appliquées du Havre, Université du Havre, 25 rue Philippe Lebon, 76058 Le Havre cedex, France, email: valentina.lanza@univ-lehavre.fr

‡F. Corinto is with the Department of Electronics and Telecommunications, Politecnico di Torino, Torino, Italy, e-mail: fernando.corinto@polito.it

investigations on the mechanisms behind the occurrence of synchronization between two memristively-coupled HR neurons. These investigations revealed the key role which the memristor plays in the development of synchrony in the simple neural network.

2.1 System under study

In this section we shall first describe the memristive network under study (named as original system) and then apply the methodology proposed in [10] to derive the virtual system associated with it.

2.1.1 Original system equations

In this work we take inspiration from [10] to derive the conditions under which two HR oscillators interacting through a unidirectional memristive coupling arrangement lock into synchronization. First of all, application of the contraction algorithm [10] requires to recast the classical equations describing two uncoupled HR oscillators [11] as follows:

$$\frac{dx_i}{d\tau} = y_i - ax_i^3 + bx_i^2 - z_i + I_i \quad (1)$$
$$\frac{dy_i}{d\tau} = c - dx_i^2 - y_i \quad (2)$$
$$\frac{dz_i}{d\tau} = r\left(s(x_i - x_{i0}) - z_i\right) \quad (3)$$
$$\frac{dw_i}{d\tau} = -x_i - w_i, \qquad (i,j) \in \{(1,2),(2,1)\} \quad (4)$$

The first three equations correspond to the classical model of an HR neuron. The fourth equation does not influence the other three and its significance will be now explained in the context of the network description. The two HR oscillators described in (1)-(4) are coupled through the following memristive circuit. The following explanation applies for each $(i,j) \in \{(1,2),(2,1)\}$. First of all each cell i involves the use of a grounded memristor m_i tied to the node at voltage x_i. The state of the grounded memristor is w_i, whose time evolution is governed by differential equation (4). Further, the dimensionless normalized memductance function of memristor m_i is denoted as $\hat{W}(\tilde{w}_i)$, while, letting ε denote the coupling strength coefficient, $C(\tilde{w}_i) = \varepsilon\hat{W}(\tilde{w}_i)$ represents the effective coupling strength coefficient. The polarity of the memristor is such that it sinks current from the node at voltage x_i when $x_i < 0\,V$. The current through memristor m_i is then mirrored and sign reversed and loads unidirectionally the node at voltage x_j of the cell j (sinking current from this node when $x_j > 0\,V$). Such a memristor coupling arrangement leads to the following model for the network:

$$\frac{dx_i}{d\tau} = y_i - ax_i^3 + bx_i^2 - z_i + I_i + C(w_i)x_i - C(w_j)x_j \quad (5)$$
$$\frac{dy_i}{d\tau} = c - dx_i^2 - y_i \quad (6)$$
$$\frac{dz_i}{d\tau} = r\left(s(x_i - x_{i0}) - z_i\right) \quad (7)$$
$$\frac{dw_i}{d\tau} = -x_i - w_i, \qquad (i,j) \in \{(1,2),(2,1)\} \quad (8)$$

where we further assumed $x_{i0} = x_0$ for $i = 1, 2$.

2.1.2 Virtual system equations

The network equations (5)-(8) fall into the following class [10]:

$$\dot{\mathbf{z}} = \mathbf{f}(\mathbf{z}) + \mathbf{h}(\mathbf{w}) - \mathbf{h}(\mathbf{z}) \quad (9)$$
$$\dot{\mathbf{w}} = \mathbf{f}(\mathbf{w}) + \mathbf{h}(\mathbf{z}) - \mathbf{h}(\mathbf{w}) \quad (10)$$
$$(11)$$

where $\mathbf{z} = [x_1 y_1 z_1 w_1]' \in \mathbb{R}^m$ ($m = 4$ is the order of the virtual system), $\mathbf{w} = [x_2 y_2 z_2 w_2]' \in \mathbb{R}^m$, while $\mathbf{f}(\mathbf{z}) \in \mathbb{R}^m \to \mathbb{R}^m$ and $\mathbf{h}(z) \in \mathbb{R}^m \to \mathbb{R}^m$ are expressed as

$$\mathbf{f}(\mathbf{z}) = \begin{pmatrix} y_1 - ax_1^3 + bx_1^2 - z_1 + I_1 \\ c - dx_1^2 - y_1 \\ r\left(s(x_1 - x_0) - z_1\right) \\ -x_1 - w_1 \end{pmatrix} \quad (12)$$

$$\mathbf{h}(\mathbf{z}) = \begin{pmatrix} -C(w_1)x_1 \\ 0 \\ 0 \\ 0 \end{pmatrix} \quad (13)$$

$$(14)$$

For dynamical systems falling into the class (9)-(10) [10], a possible choice for the virtual system is

$$\dot{\mathbf{y}} = \mathbf{f}(\mathbf{y}) - 2\mathbf{h}(\mathbf{y}) + \mathbf{h}(\mathbf{z}) + \mathbf{h}(\mathbf{w}) \quad (15)$$

Adapting (15) to our case, use of equations (12) and (13) into (15) leads to

$$\frac{d\tilde{x}}{d\tau} = \tilde{y} - a\tilde{x}^3 + b\tilde{x}^2 - \tilde{z} + \tilde{I} + 2C(\tilde{w})\tilde{x} - C(w_1)x_1 - C(w_2)x_2 \quad (16)$$
$$\frac{d\tilde{y}}{d\tau} = c - d\tilde{x}^2 - \tilde{y} \quad (17)$$
$$\frac{d\tilde{z}}{d\tau} = r\left(s(\tilde{x} - \tilde{x_0}) - \tilde{z}\right) \quad (18)$$
$$\frac{d\tilde{w}}{d\tau} = -\tilde{x} - \tilde{w} \quad (19)$$

where the variables $\tilde{x}$, $\tilde{y}$, $\tilde{z}$, and $\tilde{w}$ denote the states of the virtual oscillator. Particularly, $\tilde{w}$ stands for the state of the virtual grounded memristor.

According to the contraction mapping theorem [10], the virtual system (15) is contracting and thus the original system (9)-(10) locks into synchronization if the Jacobian of (15), i.e. the matrix $\frac{\partial \mathbf{f}(\mathbf{y})}{\partial \mathbf{y}} - 2\frac{\partial \mathbf{h}(\mathbf{y})}{\partial \mathbf{y}}$ is uniformly negative. The Jacobian of our virtual system (16)-(19) is expressed as

$$\mathbf{J} = \begin{pmatrix} -3a\tilde{x}^2 + 2b\tilde{x} + 2C(\tilde{w}) & 1 & -1 & 2\tilde{x}\frac{dC(\tilde{w})}{d\tilde{w}} \\ -2d\tilde{x} & -1 & 0 & 0 \\ rs & 0 & -r & 0 \\ -1 & 0 & 0 & -1 \end{pmatrix} \quad (20)$$

Let us denote as $J_{i,j}$ the element of the Jacobian at position (i, j). Before proceeding in the derivation of the synchronization conditions, let us assume that $a, b, c, d, r, s \in \mathbb{R}_+$, and that, in particular, $s = 1$ holds.

In the next section we shall analyze the contraction properties of the virtual system to gain a deep insight into the synchronization mechanisms of the original one.

2.2 Analysis of the virtual system

Let us first derive the partially-directed graph associated to the Jacobian matrix (20).

2.2.1 Partially-directed graph

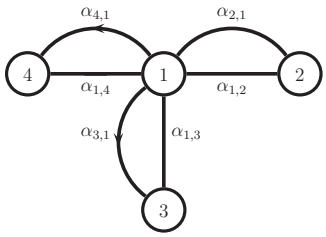

Figure 1: Partially-directed graph $\mathcal{G}(\mathbf{A})$ associated with matrix $\mathbf{A}$ in (21).

Following the algorithm defined in [10], the adjacency matrix $\mathbf{A}$ is then constructed as follows. It has ones at positions (i, j) and (j, i) provided either $J_{i,j}$ or $J_{j,i}$ is non-null. In all other cases it has zeros.

Inspecting (20), matrix $\mathbf{A}$ is thus expressed as

$$\mathbf{A} = \begin{pmatrix} 1 & 1 & 1 & 1 \\ 1 & 1 & 0 & 0 \\ 1 & 0 & 1 & 0 \\ 1 & 0 & 0 & 1 \end{pmatrix} \quad (21)$$

The partially-directed graph $\mathcal{G}(\mathbf{A})$ associated with this matrix is shown in Fig. 1. There are m nodes (as many as the order of the virtual system). The edge from node i to node j ($i, j \in \{1, 2, 3, 4\}$, $i \neq j$) is present if the element $A_{i,j}$ of the $\mathbf{A}$ is non-null. To each edge the following quantity is associated:

$$\alpha_{i,j} = \frac{|J_{i,j}|}{|J_{i,i}|}(m - n_{0i} - 1) \quad (22)$$

where n_{0i} are the zeros on the i^{th} row of $\mathbf{A}$. The quantities $\alpha_{i,j}$, computed from (22), determine the directions of the edges in the partially-directed graph $\mathcal{G}(\mathbf{A})$. Once these directions shall be specified, a directed graph $\mathcal{G}_d(\mathbf{A})$ will be drawn. Using (20) into (22), these quantities [10] are reported in Table 1.

Table 1: Expression for $\alpha_{i,j}$ ($i, j \in \{1, 2, 3, 4\}$, $i \neq j$) for the virtual system (16)-(19).

$\alpha_{1,2}$	$\alpha_{2,1}$	$\alpha_{1,3}$
$\frac{3}{\lvert J_{1,1}\rvert}$	$2d\lvert\tilde{x}\rvert$	$\frac{3}{\lvert J_{1,1}\rvert}$
$\alpha_{3,1}$	$\alpha_{1,4}$	$\alpha_{4,1}$
s	$\frac{6\lvert\tilde{x}\rvert\lvert\frac{dC(\tilde{w})}{d\tilde{w}}\rvert}{\lvert J_{1,1}\rvert}$	1

where $J_{1,1}$ denotes the element of the Jacobian at position $(i = 1, j = 1)$.

In the next section the conditions for contraction of the virtual system, which also ensure the occurrence of synchronization in the original system, shall be analytically derived.

2.2.2 Conditions for contraction of the virtual system

Two are the essential requirements for our virtual system (16)-(19) to manifest the contraction property [10] which implies synchronization for the original system (5)-(8):

1. The elements $J_{i,i}$ of the Jacobian $\mathbf{J}$ in (20) need to be strictly negative for all $i \in \{1, 2, 3, 4\}$.

2. no loop is allowed to exist in the directed graph $\mathcal{G}_d(\mathbf{A})$ and for all $i \neq j$ we require that $\alpha_{i,j}\alpha_{j,i} \leq 1$.

In order to ensure that $\mathcal{G}_d(\mathbf{A})$ contains no loop, we need to study the directions of the edges in the partially-directed graph of Fig. 1.

According to the contraction algorithm [10], the direction of the edge connecting node i to node j is from node i to node j if $\alpha_{i,j} < 1$, while it is from node j to node i if $\alpha_{i,j} \geq 1$.

Before proceeding in the analysis, let us point out a few important aspects. First, from Table 1 it is clear that only $\alpha_{3,1} = s = 1$ (since $s = 1$ by hypothesis) and $\alpha_{4,1} = 1$ have time-invariant absolute values. Consequently, the edge between node 3 and node 1 (node 4 and node 1) is directed from 1 to 3 (from 1 to 4), as shown in Fig. 1. The directions of all other edges in $\mathcal{G}(\mathbf{A})$ may not be specified yet. In general, they may vary with time, since the quantities $\alpha_{i,j}$ associated with them depend on the

states of the virtual system (see Table (1)). Similarly, the sign of $J_{1,1}$ may depend on time (see 20).

However, the above requirements 1) and 2) for the contraction of our virtual system need to hold for any time. Thus the dynamical behavior of the virtual system shall have to comply with a number of constraints, which are derived in the lines to follow.

From requirement 1) we need to ensure that $J_{1,1}$ is negative. From (20) it follows that this occurs if

$$J_{1,1} = -3a\tilde{x}^2 + 2b\tilde{x} + 2C(\tilde{w}) < 0. \tag{23}$$

Note that (23) implies that our virtual system is dissipative.

All other elements on the diagonal of $\mathbf{J}$ are negative, therefore condition (23) allows the first requirement 1) to be fulfilled. Moving on, let us unfold the second requirement 2).

We already pointed out that $\alpha_{3,1} = s = 1$ by hypothesis. As a result, in order to avoid the presence of a closed loop in the directed graph $\mathcal{G}_d(\mathbf{A})$ we need to impose that $\alpha_{1,3} < 1$. Note that, should this hold, the other condition $\alpha_{1,3}\alpha_{3,1} \leq 1$ would automatically hold with the $<$ inequality sign. With reference to Table 1, enforcing $\alpha_{1,3} < 1$ with the assumption that condition (23) holds, leads to the following constraint:

$$J_{1,1} = -3a\tilde{x}^2 + 2b\tilde{x} + 2C(\tilde{w}) < -3 \tag{24}$$

Since condition (24) is more stringent than condition (23) (i.e. it includes it), we do not need to consider the latter any further.

Let us now consider the quantities $\alpha_{1,2}$ and $\alpha_{2,1}$ associated with the edges connecting nodes 1 and 2 in the partially-directed graph $\mathcal{G}(\mathbf{A})$ of Fig. 1. With reference to Table 1, since $\alpha_{1,2} = \alpha_{1,3}$, requirement 2) imposes that

$$\alpha_{2,1} \geq 1 \tag{25}$$

$$\alpha_{1,2}\alpha_{2,1} \leq 1 \tag{26}$$

hold at all times. Inequality (25) yields

$$|\tilde{x}| \geq \frac{1}{2d} \tag{27}$$

Using condition (23) into (26), we get:

$$-J_{1,1} \geq 6d|\tilde{x}| \geq 3 \tag{28}$$

where the last inequality holds as long as (27) applies. Conditions (24) and (28) may be combined as

$$J_{11} < -6d|\tilde{x}| \leq -3 \tag{29}$$

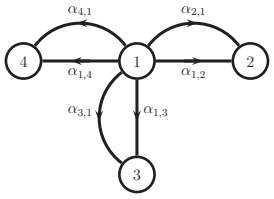

Figure 2: Directed graph $\mathcal{G}_d(\mathbf{A})$ associated with matrix $\mathbf{A}$ in (21).

Therefore so far two are the conditions constraining the dynamics of our virtual system for contraction to occur, i.e. conditions (27) and (29).

Finally, from Table 1, since $\alpha_{4,1} = 1$, the quantity $\alpha_{1,4}$ needs to be smaller than unity at all times so that requirement 2) applies. Should this hold, the other condition $\alpha_{1,4}\alpha_{4,1} \leq 1$ would be automatically verified with the $<$ inequality sign.

Using (23) and (29), $\alpha_{1,4}$ may upper limited through

$$\alpha_{1,4} < \left|\frac{dC(\tilde{w})}{d\tilde{w}}\right| \frac{1}{d} < 1 \tag{30}$$

where the last inequality is enforced to ensure that $\alpha_{1,4}$ is smaller than unity.

This is the third condition to be taken into account besides (27) and (29). In summary the analytical expressions for the conditions for contraction of the virtual system are:

$$|\tilde{x}| \geq \frac{1}{2d} \tag{31}$$

$$-3a\tilde{x}^2 + 2b\tilde{x} + 2C(\tilde{w}) < -6d|\tilde{x}| \tag{32}$$

$$\left|\frac{dC(\tilde{w})}{d\tilde{w}}\right| < d \tag{33}$$

The directed graph $\mathcal{G}_d(\mathbf{A})$ originating from them is reported in Fig. 2.

The satisfaction of constraints (31)-(33) crucially depends on the choice of the parameter values in equations (16)-(19), on the input $\tilde{I}$, and on the initial conditions of the states $\tilde{x}$, $\tilde{y}$, $\tilde{z}$, and $\tilde{w}$ of the virtual system. A major role in the mechanisms behind the contraction of the virtual system (and, consequently, in the process leading to the synchronization between the HR oscillators of the original system) is played by the dynamics in the memristive coupling path, as it is evident from the structure of two of the three constraints, i.e. (32) and (33).

3 Conclusions

Memristive dynamics may efficiently and accurately model synaptic behavior.Therefore the investigation of the dynamics developing in memristor-based artificial neural networks is a hot topic of research presently. This

work presents a theoretical analysis which leads to determine a simple set of analytical conditions for the synchronization of two Hindmarsh-Rose neurons interacting through a unidirectional coupling arrangement involving a pair of memristive systems. The study confirms the predictions of recent numerical investigation of a similar artificial neural network, where the dynamics in the memristive coupling path were found to play a key role in the development of synchronous behaviors in the Hindmarsh-Rose oscillators.

References

[1] L. S. Smith, "Neuromorphic systems: past, present and future," *Adv. in Exp. Med. and Bio.*, vol. 657, pp. 167-182, 2010

[2] N. V. Azbelev, V. P. Maksimov, L. F. Rakhmatullina, *Introduction to the theory of functional differential equations: methods and applications*, Hindawi Publishing Corporation, New York, USA, 2007

[3] F. Corinto, V. Lanza, M. Gilli, "Design of bio-inspired network models for spatio-temporal pattern identification," *Proc. European Conference on Circuit Theory and Design (ECCTD)*, pp. 292-295, 2007

[4] C. W. Wu, *Synchronization in complex networks of nonlinear dynamical systems*, Word Scientific, Singapore, 2007, ISBN: 978-981-270-973-8

[5] A. A. Ponomarenko, J.S. Li, T. M. Korotkova, J. P. Huston, and H. L. Haas, "Frequency of network synchronization in the hippocampus marks learning," *Eur. J. Neurosci*, vol. 27, no. 11, pp. 3035-3042, 2008

[6] L. O. Chua, "Memristor: the missing circuit element," *IEEE Trans. on Circuit Theory*, vol. 18, no. 5, pp. 507-519, 1971

[7] D. B. Strukov, G. S. Snider, D. R. Stewart, and R. S. Williams, "The missing memristor found," *Nature*, vol. 453, no. 7191, pp. 80-83, 2008

[8] S. H. Jo, T. Chang, I. Ebong, B. B. Bhadviya, P. Mazumder, and W. Lu, "Nanoscale memristor device as synapse in neuromorphic systems," *Nano Lett.*, vol. 10, pp. 1297-1301, 2010

[9] F. Corinto, A. Ascoli, M. Gilli, "Nonlinear dynamics of memristor oscillators," *IEEE Trans. on Circuits and Systems – I*, vol. 58, no. 6, pp. 1323–1336, 2011

[10] G. Russo, M. di Bernardo, and J.-J. E. Slotine, "A graphical approach to prove contraction of nonlinear circuits and systems," *IEEE Trans. on Circuits and Systems–I*, vol. 58, no. 2, pp. 336-348, 2011

[11] J. L. Hindmarsh and R. M. Rose, "A model of neuronal bursting using three coupled first order differential equations," *Proc. Royal Society of London, Series B, Biol. Sci.*, vol. 221, no. 1222, pp. 87–102, 1984

[12] A. Ascoli, V. Lanza, F. Corinto, and R. Tetzlaff, "Emergence of synchronization in bio-inspired memristor-coupled oscillatory cells," *Journal NOn-Linear Theory and Its Applications (NOLTA), IEICE*, 2014

Proceedings of ICCSA 2014
Normandie University, Le Havre, France - June 23-26, 2014

MEMRISTIVE NETWORKS OF CHUA'S CIRCUITS

Miroslav Mirchev, Igor Mishkovski, and Ljupco Kocarev *†

Abstract. Although envisioned in 1971 by L. Chua, memristors have attracted the attention of the research community recently by the promotion of their feasibility and a vast number of possible applications in non-volatile computer memory, pattern recognition and modelling neural networks. Synchronization is widely studied as a phenomenon in neural networks. This work provides synchronization analyses of two kinds of memristive networks of oscillators. First, we numerically examine networks of Chua's circuits coupled by memristors that adapt according to the local state disagreements. As second, we employ the Master stability function (MSF) approach to study synchronization in networks of memristive Chua's circuits coupled through simple resistors.

Keywords. memristors, nonlinear oscillators, synchronization, stability, Chua's circuit.

1 Introduction

The three basic passive electrical elements, the inductor, the capacitor and the resistor, are well known long time ago and have been thoroughly studied in the literature. In a paper [1] from 1971, Chua logically predicted the existence of a fourth basic element named 'memristor' that relates flux with charge, which was a missing link at that time. Basically, the resistiveness of the memristor is dependent on the history of the voltage across it or the current that has flown through it. Recently, experimental analysis in the laboratories at HP have revealed that such materials with memristive properties actually exist [2].

Even though memristors are still mostly used in research, they could have technological impacts. The possible applications include non-volatile memory, low power circuits, analog computation, circuits mimicking biological systems, programmable logic, and many more.

The electrical elements are often used to design oscillating circuits with certain characteristics either mimicking some natural phenomena or implementing some desired function. One widely studied phenomenon is chaotic behavior and the simplest electronic circuit with such properties is the Chua's circuit [3]. This circuit exhibits different types of behaviors and it can be used for studying various problems including synchronization of electronic oscillators [4]. In a recent paper [5], we studied synchronization in network of Chua's oscillators with and without parameter disturbances using the Master Stability Function (MSF) approach. Several memristive oscillators have been given in [6], derived from the Chua's circuit, while some dynamical behaviors of memristive oscillatory networks have been studied in [7].

In this work we numerically study how memristive coupling affects synchronization of networks of Chua's circuits. Furthermore, we show that this kind of coupling could be used to find the appropriate weights between the Chua's circuits in order to achieve synchronization. The second approach, used in this work, using the MSF approach examines the local stability of resistively coupled memristive Chua's circuit.

In Section 2, we present the Chua's circuit and the basic concept of memristors. Synchronization in networks of Chua's circuits coupled through memristive interactions is numerically studied in Section 3. The local stability of network of memristive Chua's circuits is investigated in Section 4, while concluding words are given in Section 5.

2 Preliminaries on the Chua's circuit and memristors

2.1 The Chua's circuit

The dynamics of the Chua's circuit, shown in Fig. 1, is defined as [3]:

$$\begin{aligned} \frac{dv_1}{dt} &= \frac{1}{C_1}\left(\frac{v_2 - v_1}{R} - f(v_1)\right) \\ \frac{dv_2}{dt} &= \frac{1}{C_2}\left(\frac{v_1 - v_2}{R} - i_3\right) \\ \frac{di_3}{dt} &= \frac{v_2}{L} \end{aligned} \tag{1}$$

where the characteristic of the nonlinear resistor is

$$f(v_1) = G_b v_1 + 0.5(G_a - G_b)(|v_1 + E| - |v_1 - E|) \tag{2}$$

The voltage E is used to switch between the two slopes G_a and G_b.

*Miroslav Mirchev, Igor Mishkovski and Ljupco Kocarev are with the Faculty of Computer Science and Engineering, Ss. Cyril and Methodius University in Skopje, Macedonia. E-mails: miroslav.mirchev@finki.ukim.mk and igor.mishkovski@finki.ukim.mk

†Ljupco Kocarev is also with the Macedonian Academy of Sciences and Arts, Macedonia and the BioCircuits Institute, University of California San Diego, CA, USA. E-mail: l.kocarev@ucsd.edu

It is often more convenient to work with dimensionless form of the circuit, which after a set of transformations can be rewritten as [3, 8]

$$\begin{aligned}\dot{x} &= \alpha[y - x - h(x)] \\ \dot{y} &= x - y + z \\ \dot{z} &= -\beta y\end{aligned} \tag{3}$$

where

$$h(x) = m_b x + 0.5(m_a - m_b)(|x+1| - |x-1|), \tag{4}$$

$\mathbf{x} = [x, y, z] = (1/E)[v_1, v_2, i_3 R]$ is a state vector, $\alpha = C_2/C_1$, $\beta = C_2 R^2/L$, $m_a = RG_a$, $m_b = RG_b$ and $t = \tau|RC_2|$.

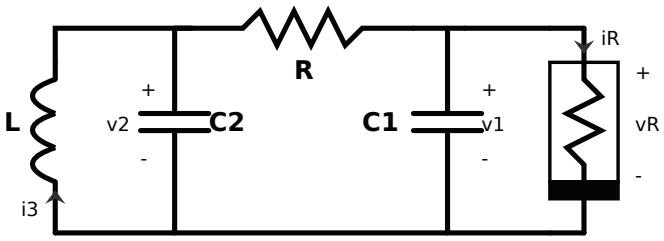

Figure 1: The Chua's circuit

The Chua's circuit can exhibit various types of behavior for different parameter sets, from chaotic attractors to limit cycles.

A network of N symmetrically coupled Chua's circuits can be constructed where the network dynamics can be described using the network's Laplacian matrix $\mathbf{L} = [L_{ij}]_{N\times N}$

$$\dot{\mathbf{x}}_i = F(\mathbf{x}_i) - g\sum_{j=1}^{N} L_{ij} H(\mathbf{x}_j), \tag{5}$$

$F(\cdot)$ is a function defining the dynamics of a single oscillator, $g > 0$ is coupling strength, $H : R^D \to R^D$ is a coupling function and $D = 3$ is the dimension of the oscillators. Standardly, a network Laplacian matrix is denoted as $\mathbf{L} = \mathbf{D} - \mathbf{A}$, with $\mathbf{D}$ being a diagonal node degree matrix and $\mathbf{A}$ being the nodes adjacency matrix.

2.2 Memristors

As in [1], a memristor is typically represented as in Fig. 2 and its dynamics is described as charge controlled

$$v = M(q)i, \tag{6}$$

or flux controlled

$$i = W(\varphi)v, \tag{7}$$

where v is the voltage across the memristor, i is the current through the memristor, q is charge, φ is flux linkage, M is its memristance and W its memductance.

A typical characteristic of memristors is the pinched hysteresis form of their voltage-current curve. As Chua initially described "if it's pinched it is a memristor" and later he expanded this statement to consider an element as memristor if and only if it has a pinched voltage-current curve. The memristor's current-voltage curve is frequency dependent and as the frequency ω increases the pinched hysteresis gets narrower [9], and as $\omega \to \infty$ the curve becomes straight line and the memristor shows properties as a regular resistor. One initial memristor implementation proposed by Chua relied on active circuits [1], while recently memristors have been constructed using nanotechnology, as for example the memrsistor from HP [2].

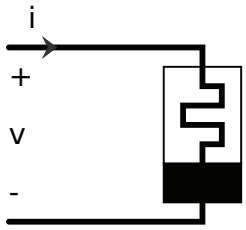

Figure 2: Memristor symbol proposed in [1]

One definition of the memductance, given in [6], is

$$W_{PWL}(\varphi) = \begin{cases} r, & |\varphi| \le 1 \\ s, & |\varphi| > 1 \end{cases} \tag{8}$$

where

$$\frac{d\varphi}{dt} = v \tag{9}$$

is the dynamics of the internal memristor state and v is the voltage across the memristor.

Another definition given in [10] with a cubic function

$$q(\varphi) = l\varphi + m\varphi^3 \tag{10}$$

provides a memductance function

$$W_Q(\varphi) = \frac{dq}{d\varphi} = l + 3m\varphi^2 \tag{11}$$

where again $d\varphi/dt$ changes as in Eq. (9).

3 Networks of Chua's circuits with memristive interactions

In this section we study synchronization in networks of Chua's oscillators coupled through the first state variable using memristors. The dynamics of each oscillators is given as

$$\dot{\mathbf{x}}_i = F(\mathbf{x}_i) + g\sum_{j\neq i} W_{PWL}(\varphi_{ij})(x_j - x_i), \tag{12}$$

where each memristor state φ_{ij} develops as

$$\frac{d\varphi_{ij}}{dt} = x_i - x_j, \tag{13}$$

and the memductance function $W_{PWL}(\varphi_{ij})$ follows Eq. (8) with $r = 0.1$ and $s = 1$.

Networks with memristive interactions are in a certain way realization of the concept of local adaptive coupling, studied in [11, 12]. In those papers the authors show asymptotic stability of the synchronized state with examples like synchronization in network of Chua's circuits and the network consensus problem.

In this section we simulate networks of four completely connected oscillators with the following two types of behavior

- Periodic Limit Cycle (LC) obtained with $\alpha = 10.2$, $\beta = 21.89$, $m_a = -1.5$, $m_b = -0.81$, and
- Chaotic Double Scroll (DS) obtained with $\alpha = 10.2$, $\beta = 20.27$, $m_a = -1.44$, $m_b = -0.78$.

If the coupling strength g is large enough the network synchronizes and in order to measure the level of synchronization the following error function is used

$$\langle e \rangle = \frac{1}{t_f - t_t} \int_{t_t}^{t_f} \sum_{k=1}^{D} \mathrm{Var}(\mathbf{x}^{(k)}(t)) dt, \tag{14}$$

where $\mathbf{x}^{(k)}(t) = [x_i^{(k)}(t), \ldots, x_N^{(k)}(t)]$, with $x_i^{(k)}(t)$ denoting the k-th state variable of the i-th oscillator, the variance function $\mathrm{Var}(\cdot)$ indicates how much dispersed are the node's states, t_t is a time moment after the transient period and t_f is a sufficiently distant moment that provides accurate calculation of the error function.

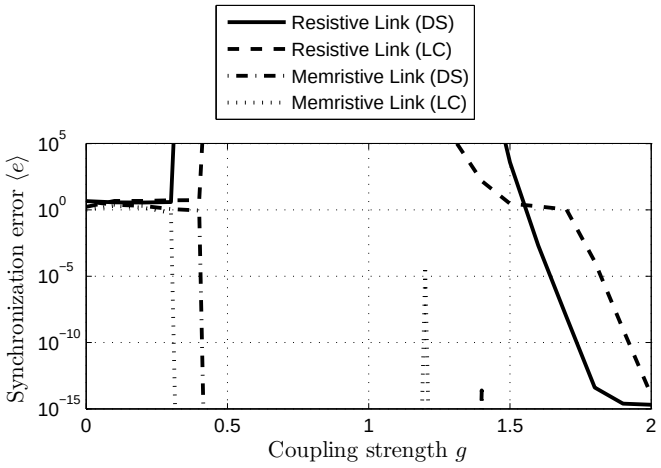

Figure 3: The synchronization error in networks of Chua's circuit with resistive and memristive coupling exhibiting double scroll (DS) and limit cycle (LC) for different coupling strength (g).

It can be seen in Fig. 3 that synchronization occurs in networks with memristive interactions for significantly lower coupling strength. As the maximum possible memductance is $s = 1$ it can be concluded that synchronization is improved only by the adaptability of the interactions, not by increasing the coupling strength. It should be noted that the network synchronization in networks with memristive interactions can result in lower final effective conductance of the links in the synchronized network. Therefore, to further characterize the synchronization properties of memristive networks we calculate the overall memductance W_o in the network as the sum from the memductance function at the last moment of the simulation (finite time)

$$W_o = \sum_i \sum_{j<i} W_{PWL}(\varphi_{ij}) \tag{15}$$

and in Fig. 4 it can be seen that the W_o required for synchronization decreases with the increase of the coupling strength g. In the presented numerical results the required W_o is slightly lower for the limit cycle behavior compared to double scroll.

The analysis of the change of W_o for different coupling strength revealed that for very small coupling strength all the memductances remain high. As the coupling strength increases some of the memductances decrease leading to a kind of star network that is known to have good synchronization properties. Eventually, for large coupling strength all memductances start to take low values. If the memductance function was continuous this transition would be smoother. These observations could be potentially used for designing networks with specified desired synchronization properties.

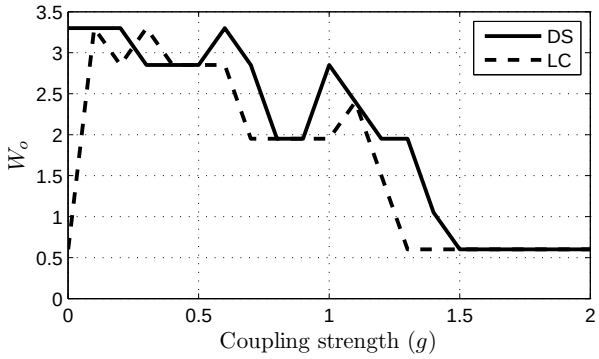

Figure 4: The overall memductance W_o after sufficiently long simulation time in memristively coupled networks of Chua's oscillators exhibiting double scroll (DS) and limit cycle (LC) for different coupling strength (g).

4 Networks of memristive Chua's circuits

In order to build a network of memristive Chua's circuits we have used the Chua circuit from Fig. 1 and we have

replaced the Chua diode with a flux-controlled memristor in Fig. 5 [13]. The equations for the memristive version

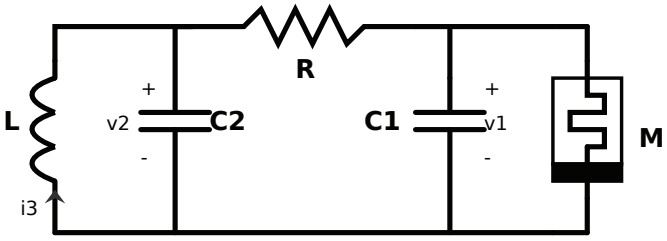

Figure 5: A memristive Chua's circuit

of the Chua circuit, similar to the ones presented in [10], are as follows:

$$\begin{aligned}
\frac{d\varphi}{dt} &= v_1(t) \\
\frac{dv_1(t)}{dt} &= \frac{1}{C_1}\left(\frac{v_2(t)-v_1(t)}{R} - i(t)\right) \\
\frac{dv_2(t)}{dt} &= \frac{1}{C_2}\left(\frac{v_1(t)-v_2(t)}{R} - i_3(t)\right) \\
\frac{di_3(t)}{dt} &= \frac{v_2(t)}{L}
\end{aligned} \tag{16}$$

where $i = l + 3m\varphi^2$, obtained from Eqs. (7), (9) and the cubic nonlinearity for the $q - \varphi$ function, from Eq. (10). For the circuit parameters we have used: $L = 18mH, C_1 = 6.8nF, C_2 = 68nF$ and to obtain chaotic attractor we have set $R = 2000\Omega$ [14].

By substituting $u = \varphi$, $x = v_1$, $y = v_2$, $z = i_3$ and time-scaling the ODEs for numerical stability with $t = \tau c$ where $c = \sqrt{LC_2}$, the following state variables are obtained for the memristive Chua's circuit [10]:

$$\begin{aligned}
\frac{du}{d\tau} &= cx \\
\frac{dx}{d\tau} &= \frac{c}{C_1}\left(\frac{y-x}{R} - W(u)\cdot x\right) \\
\frac{dy}{d\tau} &= \frac{c}{C_2}\left(\frac{x-y}{R} - z\right) \\
\frac{dz}{d\tau} &= \frac{cy}{L}
\end{aligned} \tag{17}$$

In addition to this, because of the unrealistic voltage, the author in [10] rescales the set of variable by a rescaling factor $\zeta = 8200\Omega \cdot 47 * 10^{-9} nF$. However, this rescaling was not necessary for our synchronization analysis in this section.

In the following we analyze the synchronization of a network of N identical memristive Chua's circuits coupled symmetrically with resistive elements. For this purpose we are using Eq. (5), where now $F(\cdot)$ is the dynamics of an isolated memristive Chua circuit (see Eq. (16)), the dimension of the oscillators is $D = 4$ and the new state vector is $\mathbf{x} = [u, x, y, z]$.

One systematic approach for estimating local stability of the synchronized state in oscillatory networks was given in [15, 16]. This approach uses the eigenvalues of the network Laplacian matrix to express the dynamics and at the synchronous manifold $\mathbf{x}_1 = \mathbf{x}_2 = \ldots = \mathbf{x}_N = \bar{\mathbf{x}}$, all oscillators evolve according to

$$\dot{\bar{x}} = F(\bar{\mathbf{x}}). \tag{18}$$

In this approach the variational equations of Eq. (5) are expressed using transversed modes of the form

$$\dot{\delta} = [DF(\bar{\mathbf{x}}) - \sigma DH(\bar{\mathbf{x}})]\delta \tag{19}$$

where $DF(\bar{\mathbf{x}})$ and $DH(\bar{\mathbf{x}})$ are Jacobians calculated at $\bar{\mathbf{x}}$, having equal values for all modes; $\sigma_n = g\lambda_n, n \in \{2, \ldots, N\}$ are coupling eigenvalues, and $\lambda_1 = 0 < \lambda_2 \leq ... \leq \lambda_N$ are eigenvalues of L (all real for a symmetric L).

The master stability function (MSF) $\Lambda(\sigma)$ is the maximum Lyapunov exponent of Eqs. (18) and (19) [15] and it indicates whether the synchronized state is stable (if negative for all transverse modes $\Lambda(g\lambda_n) < 0$) or unstable (if it is nonnegative for any mode).

The linear system, i.e. the Jacobian DF, around the synchronization manifold for the memristor version of the Chua's circuit is as follows:

$$DF = \begin{matrix} 0 & c & 0 & 0 \\ -\frac{c}{C_1}xW'_{PWL}(u) & -\frac{c}{RC_1} - \frac{W_{PWL}(u)}{C1} & \frac{c}{RC_1} & 0 \\ 0 & \frac{c}{RC_2} & -\frac{c}{RC_2} & -\frac{c}{C_2} \\ 0 & 0 & \frac{c}{L1} & 0 \end{matrix}$$

where for the memductance function $W_{PWL}(u)$ we have chosen $l = -0.66710^{-3}$, $m = 0.02910^{-3}$ and $W'_{PWL}(u)$ is the first derivative of the memductance function.

When the memristor Chua's oscillators are coupled only on the x state variable, i.e. $DH = [0000; 0100; 0000; 0000]$ our MSF analysis show that the synchronization manifold is never locally stable no matter how big is the coupling eigenvalue σ, i.e. MSF tends to 0 as $\sigma \to \infty$.

In Fig. 6, we show the MSF for $DH = [1000; 0100; 0000; 0000]$, that is the memristor Chua's circuits are coupled on the w and the x state variable. Using this coupling the synchronization manifold is locally stable only if the coupling eigenvalue, i.e. the product of the smallest non-zero eigenvalue of L and the coupling strength, is larger than 1.25.

Thus, by using simple resistive link between the memristor Chua's circuits the synchronization manifold is never locally stable, this comes from the fact that the memristor is dependent on the history of the voltage across it. However, if the memristances between the circuits are coupled the network synchronization manifold could be stable when $\sigma > 1.25$.

In order to numerically check the MSF approach we simulated in time a network of four fully connected oscillators with network Laplacian matrix

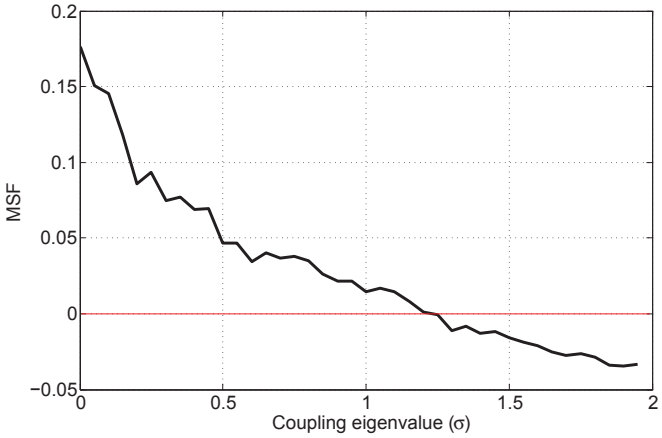

Figure 6: MSF of a network of memristive Chua's circuits exhibiting chaotic behavior coupled on w and x state variables as a function of σ.

$$\mathbf{L} = \begin{bmatrix} -3 & 1 & 1 & 1 \\ 1 & -3 & 1 & 1 \\ 1 & 1 & -3 & 1 \\ 1 & 1 & 1 & -3 \end{bmatrix}.$$

The threshold coupling strength at which synchronization occur in the network was well matched with the threshold obtained with MSF.

5 Conclusion

In this paper we have analyzed: i) synchronization in network of Chua's circuits coupled using memristive elements and ii) the local stability of the synchronous state of memristive Chua's circuits coupled with resistors. The numerical simulations for the first analysis showed that in networks with memristive interactions the synchronization occurs for significantly lower coupling values. Moreover, the results showed that the final effective memductance in synchronized networks is quite low. This approach actually provides a network of adaptively coupled Chua's circuits, by using memristive interactions in order to enhance synchronization. Thus, it can be used as a network design method providing optimal network configurations. In the second part, using MSF approach, we showed under which conditions the synchronized state of the network of memristive Chua's circuits with resistive interaction is locally stable.

Acknowledgements

The authors thank the Faculty of computer science and engineering at the Ss. Cyril and Methodius University in Skopje, for the support under the project MultiNets (Modelling and Analysis of Dynamical Processes in Composite and Multiplex Networks). The authors would particularly like to thank Fernando Corinto for his useful comments.

References

[1] L.O. Chua, Memristor: the missing circuit element, *IEEE Transactions on Circuit Theory*, vol. 18, no. 5, pp. 507–519, 1971.

[2] D.B. Strukov, G.S. Snider, D.R. Stewart, and R.S. Williams", The missing memristor found, *Nature*, vol. 453, pp. 80–83, 2008.

[3] L.O. Chua, C.W. Wu, A. Huang, G.-Q. Zhong, A universal circuit for studying and generating chaos. I. Routes to chaos, *IEEE Transactions on Circuits and Systems I: Fundamental theory and Applications*, vol. 40, no. 10, pp. 732–744, 1993.

[4] C.W. Wu and L.O. Chua, Synchronization in an array of linearly coupled dynamical systems, *IEEE Transactions on Circuits and Systems I: Fundamental Theory and Applications*, vol. 42, no. 8, pp. 430–447, 1995.

[5] I. Mishkovski, M. Mirchev, F. Corinto, and M. Biey, Synchronization analysis of networks of identical and nearly identical Chua's oscillators, *IEEE International Symposium on Circuits and Systems (ISCAS)*, pp. 2115–2118, 2012.

[6] M. Itoh and L.O. Chua, Memristor oscillators, International Journal of Bifurcation and Chaos, vol. 18, no. 11, 3183–3206, 2008.

[7] F. Corinto, A. Ascoli, and M. Gilli, Nonlinear Dynamics of Memristor Oscillators, *IEEE Transactions on Circuits and Systems I: Regular Papers*, vol. 58, no. 6, pp. 1323–1336, 2011.

[8] R.N. Madan (Guest Editor), *Journal of Circuits Systems and Computers*, Special Issue on Chua's Circuit: A Paradigm for Chaos, 1993, vol. 3, Mar. 1993 (Part I) and June 1993 (Part II).

[9] L.O. Chua and S.M. Kang, Memristive devices and systems, *Proceeding of the IEEE*, vol. 64, no. 2, pp. 1976.

[10] B. Muthuswamy, Implementing memristor based chaotic circuits, International Journal of Bifurcation and Chaos, vol. 20, no. 5, 1335–1350, 2010.

[11] P. De Lellis, M. di Bernardo and F. Garofalo, "Synchronization of complex networks through local adaptive coupling," *Chaos*, vol. 18, pp. 037110, 2008.

[12] P. De Lellis, M. di Bernardo and F. Garofalo, "Novel decentralized adaptive strategies for the synchronization of complex networks," *Automatica*, vol. 45, pp. 1312–1318, 2009.

[13] B. Muthuswamy and P. P. Kokate, "Memristor based chaotic circuits," *IETE Technical Review* Vol. 26, pp. 415–426, 2009.

[14] G. Zhong,"Implementation of Chua's circuit with a cubic nonlinearity," *IEEE Transactions on Circuits and Systems I: Fundamental Theory and Applications*, vol. 41, no. 12, pp. 934–941, 1994.

[15] L.M. Pecora and T.L. Carroll, "Master Stability Functions for Synchronized Coupled Systems," *Physical Review Letters*, vol. 80, pp. 2109–2112, 1998.

[16] M. Barahona and L.M. Pecora, "Synchronization in Small-World Systems," *Physical Review Letters*, vol. 89, no.5, p. 054101, 2002.

Satellite Workshop 8
Ecological Dynamics in Sport

Satellite Workshop 8
Ecological dynamics in sport

Organizers

- Ludovic SEIFERT, CETAPS, Rouen, France, ludovic.seifert@univ-rouen.fr

Description

Ecological dynamics framework advocates that there is an intertwined relationship between the specific intentions, perceptions and actions of individual, which constrains this relationship between coordination pattern stability and variability in each individual performer. This workshop will attempt to emphasise the key theoretical and methodological issues to investigate coordination pattern variability and stability in relation to interacting constraints (task, environment and organismic) that performer may encounter, in order to highlight how athletes individually adapt their behaviour in a functional way. This new approach of the problem (movement and coordination variability in sport) invite to re-think the training and teaching process by manipulating key constraints to make emerge adaptive pattern of coordination instead of teaching and training 'ideal' pattern of coordination.

List of papers/presentations

- K. Davids: Introduction to Ecological dynamics framework
- J. Komar: Dynamics of learning in swimming
- R. Charrier & N. Corson: Arm and leg oscillation modelling in swimming
- D. Orth: Representative learning design in climbing
- L. Seifert (Chairman): Movement variability and affordance detection in ice climbing
- Renshaw: Affective learning design
- R. Thouvarecq: Stochasticity and determinism of postural coordination during standing task

Proceedings of ICCSA 2014
Normandie University, Le Havre, France - June 23-26, 2014

ARM AND LEG OSCILLATION MODELLING IN SWIMMING

R. Charrier, N. Corson, L. Seifert, J. Komar *†‡

Abstract. This paper addresses the modelling of the dynamics of the knee and elbow evolution during a swimming cycle. Our final aim is to compare beginner strokes to expert strokes so as to characterize and to understand their dynamics. From data collected in a sport lab, the aim is to construct an oscillator model which reproduces experimental data. To achieve this goal, we have identified the parameters of a hybrid theoretical model of Rayleigh-Van der Pol with experimental data in order to exhibit the same dynamical behaviour. We have applied an algorithm using a swarm intelligence metaheuristics as well, to identify parameters. Results are convincing in a certain extent, showing that the chosen theoretical model has to be enhanced to recover all data.

Keywords. Swimming Modelling, Nonlinear oscillators, Parameter identification, PSO Algorithm.

1 Introduction

Mathematical and Computer science models can contribute to the search of performance and training of high level athletes. Beyond new technologies we can use, especially in terms of sensors and images analysis, it remains very important to understand and analyse the movement coordination according to the environment (air, water,...), taking into account the movement complexity. This coordination can be either intuitive or controled.
Learning methods leading to expert movements remains open problems in research. But to be efficient, these methods have to be based on experimental data and theoretical modelling. The work described in this paper has focused on the swimming skills and specifically on the study of oscillations of the knee and the elbow movements.
From experimental data, the goal has been to design a theoretical dynamical system which could reproduce and follow the series of data. The chosen model is an hybrid of a Van der Pol and a Rayleigh oscillator. For example, in other sports such as ski, it has been shown through the study of Hooke portraits, giving the acceleration according to the speed, that an expert behavior was quite well represented with a Van der Pol oscillator whereas a beginner behavior could be quite well represented with a Rayleigh oscillator [Teulier et al., 2006, Nourrit et al., 2003]. The aquatic environment of swimmer may change this observation in the swimming case.
To identify the set of parameters for a Van der Pol - Rayleigh oscillator, we have used an optimization algorithm from the swarm intelligence field. This procedure consumes a lot of computation ressources and time. The difficulty to tackle the problem in an analytical way has led us to select among the best approximation algorithms to achieve the parameter identification.
The first part of this paper consists in explaining firstly how data have been captured from real swimmers wearing sensors, then how the model has been designed and finally how the identification has been achieved.
The second part is devoted to analyze results and to discuss on limitations in our approach and model design.

2 Model design and Parameter identification

2.1 Collecting data

Breaststroke: In breaststroke swimming, achieving high performance requires a particular management of both arm and leg movements, in order to maximise propulsion and optimise the glide and recovery times. Therefore, expertise in breaststroke is defined by adopting a precise coordination pattern between arms and legs (i.e. a specific spatial and temporal relationship between elbow and knee oscillations). Indeed, when knees are flexing, elbows should be fully extended (180), whereas knees should be fully extended (180) when elbows are flexing, in order to ensure a hydrodynamic position of the non-propulsive limbs when the first pair of limbs is actually propulsive.

Data: Participant performed 10 trials of 25-m swim during each session, with 1 x 25-m consisting approximatively in 8 recorded cycles (one cycle correspond to the period between two successive maximal knee flexion). Coordination between elbow and knee was defined by the

*R. Charrier is with LITIS, University of Le Havre, E-mail: rodolphe.charrier@univ-lehavre.fr
†N. Corson is with LMAH, university of Le Havre, E-mail: nathalie.corson@univ-lehavre.fr
‡L. Seifert and J. Komar are with CETAPS, University of Rouen, E-mail: ludovic.seifert@univ-rouen.fr

continuous relative phase between these two oscillators, considering elbows and knees as acting like individual pendulums. A value of relative phase close to -180 or 180 defined an anti-phase relationship (i.e. opposite movements of knee and elbow) while a value close to 0 defined an in-phase mode of coordination (i.e. identical movements of knee and elbow). Each cycle performed during the learning process was therefore defined by time series of continuous relative phase (normalised to a 100 values) describing the relationship between the knee and the elbow during all the swimming cycle.

Sensors: During every learning session, all learners were equipped with small motion sensors on both arms and legs including a data logger and recording elbow and knee angle at a frequency of 200 Hz. Four small inertial centrals were fixed on the right leg and right thigh to record knee angle and on the right foream and right arm to assess the elbow angle. These sensors combines 3D gyroscope (1600 /s), 3D accelerometer (+/-8G) and 3D magnetometer (MotionLog, Movea©, Grenoble, France). These sensors used North magnetic and gravity references. The advantage of using sensor is that all the cycles performed by each swimmer were recorded during the entire learning process and available for the analysis (i.e. 8 cycles x 10 trials x 16 sessions = approximatively 1280 cycles per learners).

2.2 Plotting data

In this section, we analyse experimental data collected during beginner sessions. Thanks to litterature, we have the idea that a hybrid Van der Pol - Rayleigh oscillator model could fit data.
Experimental data are given as time series of knee and elbow angle. The sampling frequence is $f = 200Hz$.
In the case of the elbow, data of three swimming sessions are used : 3, 10 et 17. Each session is itself divided into ten swimming sequences. The speed and acceleration are computed using a polynomial interpolation. This method prevents us from numerous computation artefacts because of noise in data. To go through these drawbacks, we interpolate a sample of 50 points before and after the current point with a polynom of a sufficiently high degree (degree 10 in our case) so that we can compute proper derivatives on each point.
This way, we can obtain phase portraits and hooke portraits from time series. Figure 1(a) shows the knee datas for three sessions. Figure 1(b) shows the phase portraits (angular speed according to angle), and figure 1(c) shows Hooke portraits, meaning the angular acceleration according to the angle.

This first visualisation allows to have an idea of the model which could be used to obtain the same behavior. Indeed, we can see that during sessions 3 and 17, cycles of the attractor (cf. figure 1(b)) are not symmetric and that

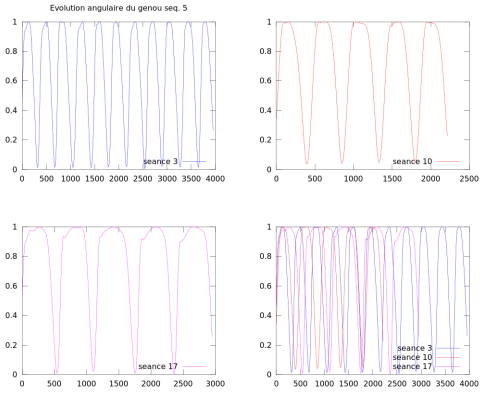

(a) Angle time series

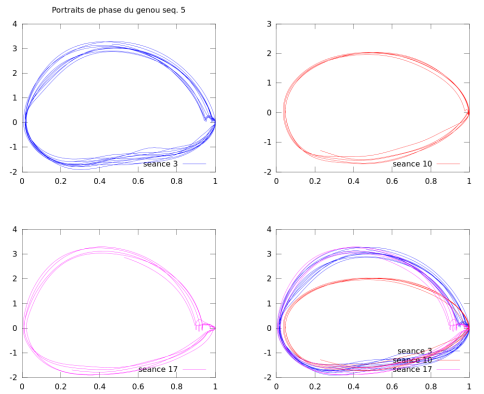

(b) Phase portraits

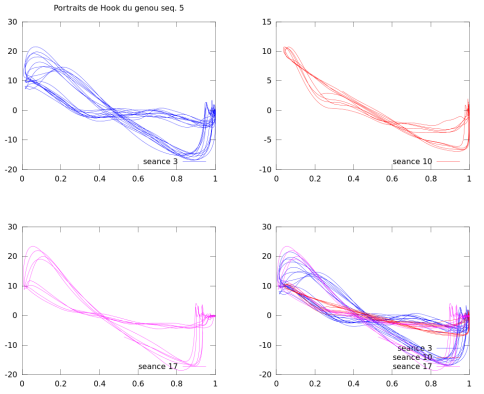

(c) Hook Portraits

Figure 1: Normalized data of knees and elbows during the same cycle of a swimming cycle.

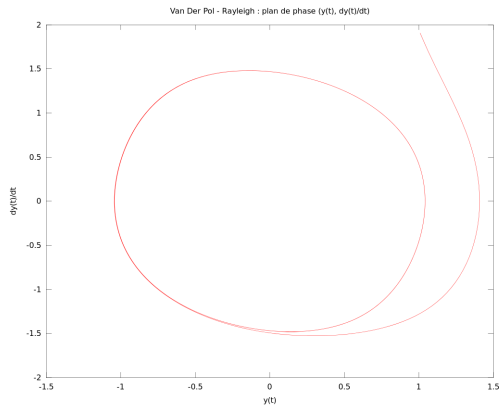

Figure 2: Phase porttrait of a hybrid Rayleigh - Van der Pol model, with : $t_0, \gamma = 2.0$, $\epsilon = 1.2$, $\delta = 1.0$, $\omega = 1.5$

the speed remains zero for a while (cf. time series). This introduces a delay in the data cycles. This asymetric behavior will make the parameter identification of the Van der Pol - Rayleigh model much more complicated as we will see later.

2.3 Hybrid Rayleigh - Van der Pol model

In this field of research, periodic behavior of human movements are often studied using Van der Pol or Rayleigh oscillatoors [Beek et al., 1995, Beek et al., 2002, Delignières et al., 1999]. This model is described by the following differential equations :

$$\ddot{x} - (\gamma - \epsilon x^2 - \delta \dot{x}^2)\dot{x} + \omega^2 x = 0$$

where $x(t)$ is the variable, $\dot{x}$ et $\ddot{x}$ are its two first time derivatives [Huys and Jirsa, 2011]. All parameters are positive, and this model can be rewritten as a two dimensional differential system as follows:

$$\begin{cases} \dot{x} = y \\ \dot{y} = (\gamma - \epsilon x^2 - \delta y^2)\ y - \omega^2 x \end{cases}$$

The trajectories of such a differential system can be visualized for example on figure 2.

We aim at identifying as well as possible (i.e. in the mean of least squares) solutions of this differential model to experimental data.
Let $\tilde{x}(t)$ the time series corresponding to experimental data. This problem consists of finding the parameter set $(\gamma, \epsilon, \delta, \omega)$ which minimizes the following objective function:

$$F = \frac{1}{N} \sum_{i=0}^{N-1} (x(t_i) - \tilde{x}(t_i))^2$$

N is the number of considered sampling.
The following section presents an algorithm to realize this optimization.

2.4 Chaotic PSO for parameter identification

This optimization problem is a difficult one since it is a nonlinear identification problem in a multi-dimensional continuous space. The parameter space is large enough so that classical methods such as Levensberg-Marquardt cannot be used [Ljung, 2010].

In this case, alternatives are said "soft computing" approaches using metaheuristics for optimization. One of these metaheuristics is inspired by the collective behavior of social insects and is very famous for fetching a zero point in a continuous search space. This class of swarm intelligence algorithm is known as "Particle Swarm Optimization". The design of these algorithm consists of a swarm of particles –each one representing a possible solution– moving in the search space for finding the best position, which corresponds also to the best solution. On each explored point, the particle computes the objective function and shares this information with the rest of the swarm, to improve the search. This method can be summarized by the following dynamical system, governing particle i:

$$\begin{cases} \mathbf{v}_i(t+1) = w\ \mathbf{v}_i(t) + c_1(\mathbf{x}_b(i) - \mathbf{x}_i(t)) + c_2(\mathbf{x}_g - \mathbf{x}_i(t)) \\ \mathbf{x}_i(t+1) = \mathbf{x}_i(t) + \mathbf{v}_i(t+1) \end{cases}$$

where $\mathbf{x}_b(i)$ and $\mathbf{x}_g$ are respectively the best position of the current particle through its own history and the best position within the group at time t only. Parameters w, c_1 and c_2 are random coefficients in a certain range, representing respectively an inertia coefficient (controling the importance of the exploration phase in the search space) and two coefficients of balance between individual and collective performance.

For this study, we used a derived algorithm that adds a random local search on the best position of the group at time t by using a chaotic map for exploration. It appears that these applications are more efficient than a classical random uniform local search. This is due to the particular probability density of chaotic maps that gives more chance to extrem and central values of the search range than uniform [Yang et al., 2012]. The chaotic map we used for the local research here is the following one:

$$x_{n+1} = \frac{sin(4\pi\ x_n) + 1}{2}$$

This kind of algorithm, named Chaotic PSO in many papers, is used since about ten years. Results presented in the next section are obtained with this method.

3 Results

Results presented here concern training sessions named $E3$, $E10$, $E17$ and the parameter values found are listed

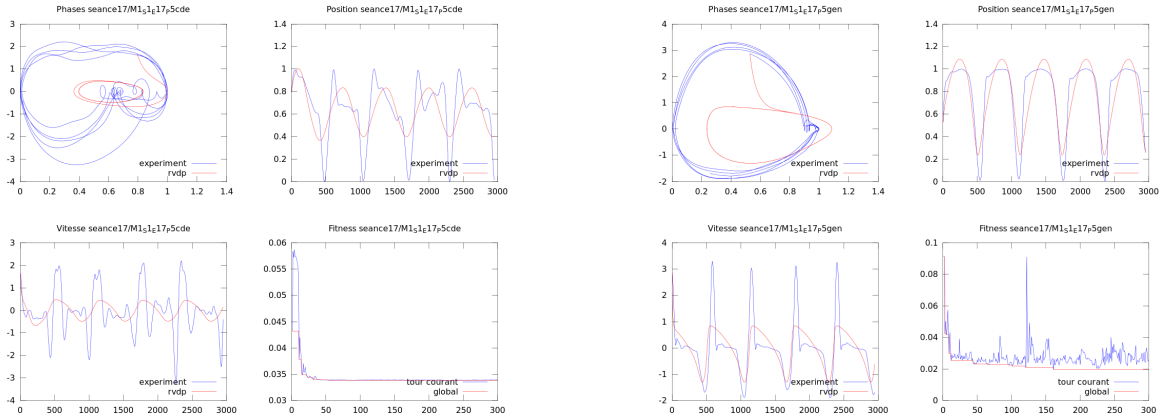

(a) E17 P5 coude

(b) E17 P5 genou

Figure 3: Identifications in session $E17$.

in the table of appendix A. The Session 10 gives the better parameter identification, in particular concerning the elbow angle. We show the corresponding result charts in appendix B. The two other series have been studied but have given less convincing results as examples of session $E17$ in figure 3 show the fact. This can be explained by the presence of little loops in trajectories which reveals a higher dimension in the dynamics. We will discuss this in the next section.

We can also oberve a real variability of exploration according to the best performance. The best fitness function gives from 0.2% to 0.5% average quadratic error and the obtained attractors follow the experimental trajectories for the session $E10$ of the elbow, despite noise in measures.
In the table of parameter values in appendix A, one can try to follow the evolution of the parameter values to see if a behavior corresponds whether to a Rayleigh or a Van der Pol one, looking at the two specific parameters ϵ and δ. The first one corresponds to the nonlinear effect of the angle variable, that is a Van der Pol dynamics, while the second one corresponds to the nonlinear effect of the velocity variable, that is a Rayleigh dynamics. From the litterature review, we expected that the dynamics would have evolved from a Van der Pol dynamics for a beginner, to a Rayleigh dynamics for the experts. This is not what we may observe here, except for the knee series in session $E10$, but the identification process has not been good enough to trust these reconstructed data.

3.1 Discussion

Results of identification allow to conclude that, unlike the skiing case, a swimmer behavior can not be easily assimilated to a Rayleigh or Van der Pol oscillator if we study real data. Indeed, identification fits quite well in the case of sessions 3 and 10 for the elbow. In these cases, it could be very interesting to study the evolution of the parameter values to check if they are signiticative in terms of learning. We look indeed for a trajectory in the parameter space which could characterize the swimmer. We have not obtained this result yet.
However, the hypothesis of a Rayleigh - Van der Pol dynamic concerning the knee is almost never verified using this identification method. This might be due to the complexity of particular trajectories in the phase space, notably in the session $E17$.

The complexity of some trajectories is confirmed by the close returns plots showed in appendix C. These plots reveal the recurrence rate of time series, that is the presence of some periodicity in them. A close returns diagram is computed as follows for a x series of discrete time values:

$$R_{ij} = \theta(\alpha - |x_i - x_{i+j}|) \quad (1)$$

where the function θ is the Heaviside step function. So R_{ij} equals 1 if the difference of the two delayed points (by a delay of j samples) is less than the threshold α (which is 10^{-2} in our case), then we plot a black dot, else R_{ij} equals 0 and there is no dot plotted.
Through these diagram we can see that close returns plots for session $E17$ are much less regular than those for sessions $E3$ and $E10$. We explain this complexity by the fact that the dynamics evolves no more in a 2-dimensional space, but in a minimum of 3-dimensional space because notably of loops occuring in trajectories. This result shows already something interesting: the dynamics of a swimming beginner is less complicated than the dynamics of an expert because the dimension of his dynamics evolves in a lower dimensional space...

4 Conclusion

Hypothesis on the hybrid de Van der Pol-Rayleigh model are validated on most of the experimental data in the case

of elbow angles. The interest of using this model is that it requires a low number of parameters and allows a simplified representation of the trajectories in the parameter space. However, this model does not fit well in most of the knee data and as soon as the swimming stroke becomes an expert one. The dynamical model of Van der Pol and Rayleigh is not appropriate anymore and needs to be enhanced, in particular by increasing the dimension of the dynamical system. The difficulty lies in the design of this more complicated dynamical system and then in the consequently difficult identification process.

Acknowledgements

The research for this work was supported, in part, by project RISC within GRR TL-TI.

References

[Beek et al., 1995] Beek, P., Schmidt, R., and Morris, A. (1995). Linear and nonlinear stiffness and friction in biological rhythmic movements. *Biological ....*

[Beek et al., 2002] Beek, P. J., Peper, C. E., and a Daffertshofer (2002). Modeling rhythmic interlimb coordination: beyond the Haken-Kelso-Bunz model. *Brain and cognition*, 48(1):149–65.

[Delignières et al., 1999] Delignières, D., Nourrit, D., and Deschamps, T. (1999). Effects of practice and task constraints on stiffness and friction functions in biological movements. *Human movement ...*, 18.

[Huys and Jirsa, 2011] Huys, R. and Jirsa, V. K., editors (2011). *Nonlinear Dynamics in Human Behavior*, pages 27–33. Studies in Computational Intelligence. Springer.

[Ljung, 2010] Ljung, L. (2010). Perspectives on system identification. *Annual Reviews in Control*, 34(1):1–12.

[Nourrit et al., 2003] Nourrit, D., Delignières, D., Caillou, N., Deschamps, T., and Lauriot, B. (2003). On discontinuities in motor learning: A longitudinal study of complex skill acquisition on a ski-simulator. *Journal of motor behavior*, 35(2):151–170.

[Teulier et al., 2006] Teulier, C., Nourrit, D., and Delignières, D. (2006). The Evolution of Oscillatory Behavior During Learning on a Ski Simulator. *Research quarterly for exercise ....*

[Yang et al., 2012] Yang, C.-H., Tsai, S.-W., Chuang, L.-Y., and Yang, C.-H. (2012). An improved particle swarm optimization with double-bottom chaotic maps for numerical optimization. *Applied Mathematics and Computation*, 219(1):260–279.

Appendix A Identified equations identification

Parameters given in this table correpond to the best approximation obtained with the swarm chaotic particle algorithm. These simulations have been perfomed only once.

series	γ	ϵ	δ	ω
E3 P1 elb	3.70	5.95	1.36	4.07
E3 P3 elb	8.45	10.00	3.52	4.39
E3 P5 elb	6.93	8.05	3.10	4.05
E3 P7 elb	6.01	5.10	2.47	4.28
E3 P9 elb	1.87	9.94	0.51	3.88
E10 P1 elb	8.65	3.25	3.62	4.50
E10 P3 elb	5.25	7.46	1.89	3.91
E10 P5 elb	5.53	9.65	2.42	3.66
E10 P7 elb	4.22	0.04	1.85	3.61
E10 P9 elb	4.00	6.17	1.19	3.63
E17 P1 elb	3.53	8.07	9.86	2.29
E17 P3 elb	3.20	9.15	9.58	2.44
E17 P5 elb	1.31	0.03	7.12	2.24
E17 P7 elb	4.67	8.99	9.72	2.96
E17 P9 elb	3.51	9.55	9.97	2.76
E3 P1 knee	4.62	4.69	1.11	4.41
E3 P3 knee	2.27	0.15	0.82	3.99
E3 P5 knee	6.96	4.34	3.22	4.06
E3 P7 knee	9.17	3.43	4.44	4.61
E3 P9 knee	8.95	8.64	3.41	4.58
E10 P1 knee	3.39	2.88	0.65	3.62
E10 P3 knee	4.48	0.69	0.76	3.88
E10 P5 knee	3.58	1.29	0.92	3.53
E10 P7 knee	3.30	1.09	1.22	3.49
E10 P9 knee	2.58	0.29	1.30	3.38
E17 P1 knee	4.40	1.74	3.19	2.96
E17 P3 knee	5.61	1.99	3.25	3.37
E17 P5 knee	6.30	3.77	3.83	3.48
E17 P7 knee	9.56	0.00	4.57	4.45
E17 P9 knee	9.86	3.15	6.50	4.55

Appendix B Identification results

The following results have been obtained using Octave software within a single execution, involving 100 particles, on the 10th session of training.

Appendix C Close returns plots

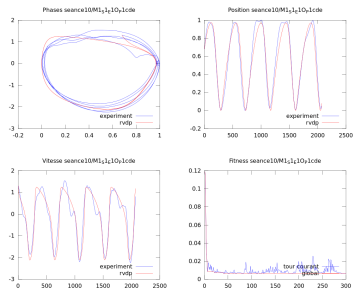

(a) Elbow stage 1

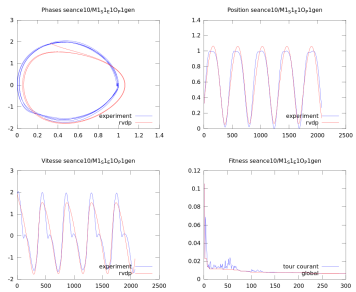

(b) Knee stage 1

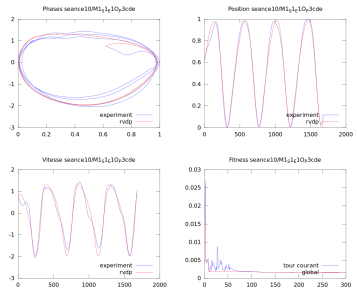

(c) Elbow stage 3

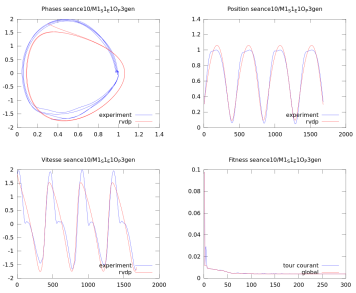

(d) Knee stage 3

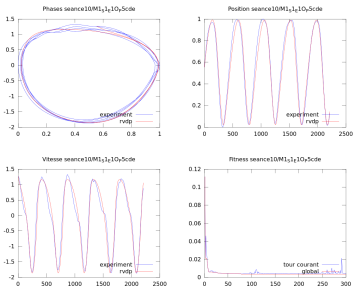

(e) Elbow stage 5

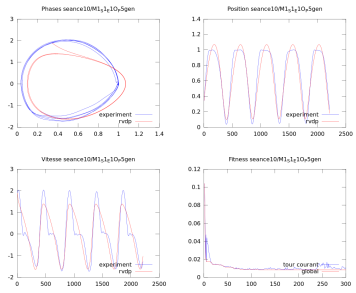

(f) Knee stage 5

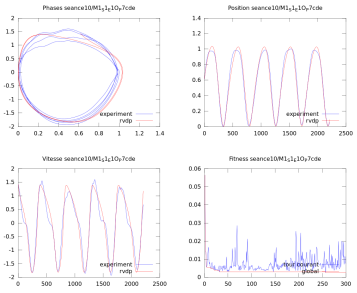

(g) Elbow stage 7

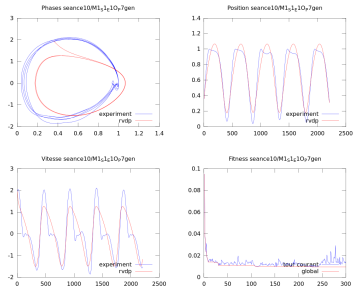

(h) Knee stage 7

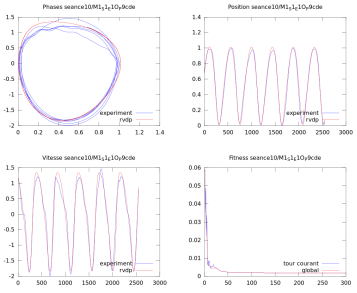

(i) Elbow stage 9

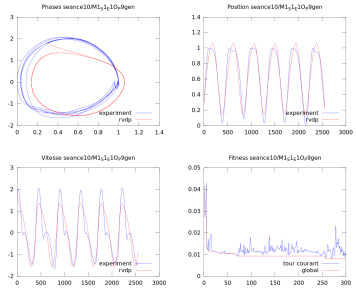

(j) Knee stage 9

Figure 4: Identification Results for the training session 10 obtained by a chaotic PSO involving 100 particles. For each chart, from up left to bottom right, phase portrait, angle, velocity, fitness values.

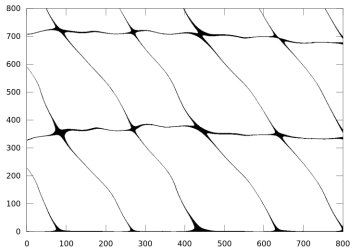

(a) Elbow session 1 stage 3

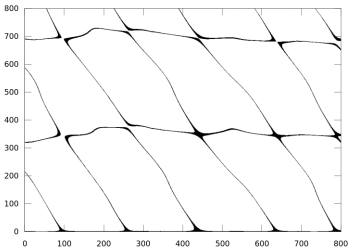

(b) Elbow session 1 stage 7

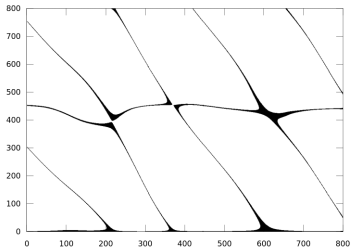

(c) Elbow session 2 stage 3

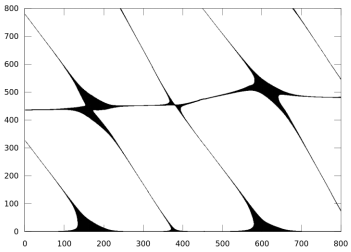

(d) Elbow session 2 stage 7

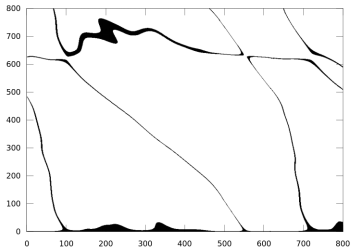

(e) Elbow session 3 stage 3

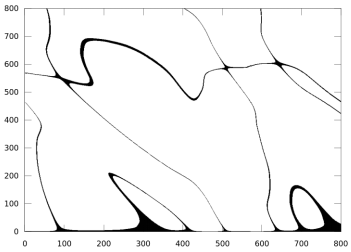

(f) Elbow session 3 stage 7

Figure 5: Evolution of close returns plots between each session of elbow series computed with a threshold of 10^{-2}. We may notice that the dynamics tends to be more and more complicated.

Proceedings of ICCSA 2014
Normandie University, Le Havre, France – June 23-26, 2014

ECOLOGICAL DYNAMICS AND COMPLEXITY IN SPORT

Keith Davids1

Abstract. Application of concepts and principles of the complexity sciences to the domain of sport performance has grown in popularity over the past decades. This paper discusses ecological dynamics as a theoretical framework for capturing how the intertwined relations between cognition, perception and action underpin performance and learning in athletes and sports teams considered as complex systems. Key ideas from ecological psychology and dynamical systems theory propose that coordination tendencies within and between individual athletes emerge as a function of interacting constraints on performance. The emergent coordination tendencies in individuals and teams are continuously regulated by information from a performance environment, inviting a re-consideration of traditional pedagogical practice in sport and specifying a pedagogy for nonlinear dynamical movement systems.
Keywords. Sport performance; perception and action; affordances; neurobiological degeneracy; adaptive movement variability; representative design.

1 Introduction

The emphasis in the complexity sciences, accorded to understanding how systems spontaneously change their organizational states as a function of the constraints acting on them, has provided an innovative rationale for studying performance and learning in sport[1]. The inherent complexity of individual athletes and sports teams has highlighted them as self-organising phenomena. During the past decades the important theoretical framework of ecological dynamics has emerged to develop insights to support an extensive empirical programme of research into complex systems in sport. This innovative modelling has provided new theoretical insights into performance and learning in sport and fresh perspectives on the organization of practical programmes for training, understanding performance behaviours and the development of expertise and talent [1].

The impact of ecological dynamics in sport science is timely, given concerns over traditional views on the acquisition of expertise in domains like sport. Traditionally, theories of the acquisition of skill and expertise have been dominated by models
emphasizing the importance of 10,000 hrs of deliberate practice. It has been proposed that deliberate practice provides a special kind of focus on practice of a putative optimal technique which is intense, unenjoyable and repetitive in order to inhibit deviations from an internalized model of an action [2]. However, the data behind these ideas have profound weaknesses mainly due to large reported variations in trajectories of experts. Taking chess as an example, reported practice time ranges from 832 to 24,284 hrs to reach masters level. The consequence is that deliberate practice has a relatively low level of variance explained (34%) [3].

Ecological dynamics is a theory of skill acquisition and expertise which captures athletes and sports teams as complex systems in which coordination tendencies, amongst component parts, emerge under various interacting constraints. These constraints are oriented towards each individual, the task being learned or performed, and the social and physical environment [4]. It is a conceptually rich theoretical framework and this paper addresses how functional actions emerge from dynamic patterns capturing intra-individual and inter-individual coordination tendencies of interacting athletes within the constraints of the performance environment. Key insights are provided by ecological psychology which emphasizes the continuous cyclical relationship that exists between information present in a performance environment and the dynamical movement patterns that emerge under constraints for each individual. In contrast to traditional accounts of how skill and expertise is acquired, the emphasis is on the quality of experiences undertaken during practice which shape these information-movement couplings formed during interactions of athletes with ecological constraints of a performance environment in Figure 1.

1 Keith Davids is with the Centre for Sports Engineering Research at Sheffield Hallam University and FiDiPro at the University of Jyväskylä, Finland

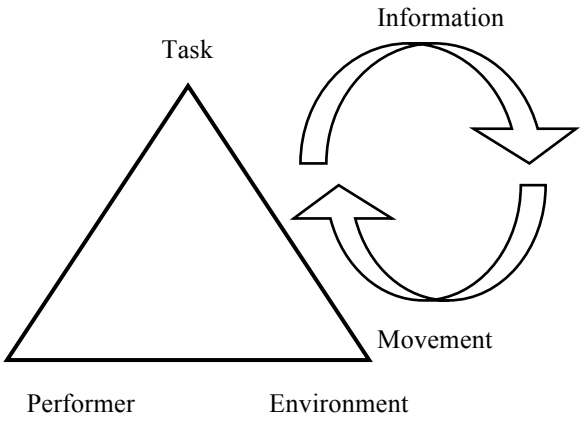

Figure 1: A coupling of information and movement emerges from each individual to satisfy interacting constraints of the performer, task and environment

In ecological dynamics, two key ideas are prominent in complex systems analyses of performance and learning in sport: (i) the role of pattern-forming dynamics in inducing qualitative changes in behaviour due to learning and development; and (ii), how affordances for action emerge from informational constraints of performance and practice environments.

2 Pattern Forming dynamics and behavioural change in sport

The inherent complexity of athletes and teams in sport is predicated on the spontaneous emergence of dynamically patterned relations, from their many interacting components. The numerous structural components of an athlete's body (e.g., muscles, joints, limb segments) and of a sports team (cooperating teammates) provide an abundance of system degrees of freedom which can regulate behaviours to achieve performance outcomes. These systems in sport have complexity and inherent tendencies for couplings or synergies to emerge between system components, predicated on neurobiological degeneracy[1].

Neurobiological system degeneracy provides flexibility in achieving performance outcomes and is a feature of the large number of available motor system degrees of freedom that can be harnessed to achieve similar performance outcomes. Despite the abundance of motor system degrees of freedom, and their potential for interactions, the presence of inherent feedback loops continuously constrains component interactions [5], providing a neurobiological system with temporary stability and the capacity to exploit emergent coordinated relations between system components. In individual athletes these components include, for example, muscles, joints, limb segments, and in sports teams (considered as social neurobiological systems) degrees of freedom are teammates. Thus, intra-personal and inter-personal coordination tendencies in complex systems in sport are predicated on the formation of temporarily stable, couplings formed between micro-components in assembling goal-directed actions. The important role of degeneracy in providing a platform for emergent coordination tendencies in sport was identified by Davids and Glazier[6].

In neurobiology, research on coordination in neuro-musculo-skeletal systems has revealed that degeneracy supports system components, that are structurally different, to be harnessed in producing similar or different functions, or similar or different outputs, depending on context. Degeneracy provides a functional way for athletes to exhibit their behavioural adaptability to satisfy interacting task and environmental constraints during performance and learning. According to Mason [7], degeneracy supports the emergence of richer functional behaviours in human activity than system redundancy which corresponds to the presence of isomorphic and isofunctional components. In contrast, degenerate elements correspond to the presence of heteromorphic variants that are isofunctional. In sport, degeneracy may be expressed through the assembly of a coordinative structure (a task-specific movement pattern) that achieves a function by combining relevant system components.

Skill performance is the assembly of unique and adaptable coordinative structures. Such neurobiological system synergies provide a highly adaptive capacity since two or more independent system structures may converge upon the same function. Since fluctuations probe system stability in each athlete and between team players coordinating their actions during performance, a functionally adaptive system is able to exploit these inherent instabilities to achieve a successful performance outcome under different interacting task and environmental constraints. During practice, under well designed conditions that *represent* the task constraints of a performance environment, learners will become skillful in harnessing system pattern-forming dynamics to achieve consistent performance outcomes, through exploiting adaptive movement variability. Thus, representative learning design is an important feature of practice task simulation in sport to encourage performers to adaptively vary their movement patterns.

3 The Role of Affordances in Sport

The adaptive power of neurobiological system degeneracy can be harnessed in conjunction with the context-sensitivity of human behaviour. Skilled athletic

performance is characterised by elegant context-sensitivity and adaptive flexibility and both aspects of functional behaviour in sport are dependent on the coupling of information and movement. The concept of affordances is a powerful constraint on coupling of information and movement in sport, since "within the theory of affordances, perception is an invitation to act, and action is an essential component of perception" by Gibson[8]. In order to establish functional couplings between complex system components, to successfully regulate their actions, athletes need to become perceptually attuned to key informational constraints of the performance environment. Affordances are specific invitations for each individual to act in a performance environment, picked up through task-specific experience and learning. Affordances are perceived in relation to relevant properties of each individual including the scale of key body dimensions (e.g., limb dimensions), or action capabilities (e.g., flexibility, speed, strength). With increasing expertise in sport, informational constraints designed into practice environments should progressively lead an individual to *specifyin*g information sources that invite the organisation of *specific actions* and enhance their capacity to adapt to the dynamical constraints of a competitive performance environment.

Research in ecological dynamics has shown that expert athletes display a greater *dependence* on specifying properties of performance environments compared to less skilled individuals [9]. Movement patterns can be subtly adapted as experts perceive variations in key environmental properties which they can exploit to regulate their actions. The perception of different affordances by expert athletes is supported by their ability to explore greater levels of performance variability. Their coordination tendencies can vary greatly as they explore different aspects of a performance environment which supports their movements. In contrast, less skilled athletes tend to display higher levels of movement pattern stability and fewer exploratory activities. They only tend to rely on a small number of movement patterns because their intentions are fewer: their inherent system complexity is not harnessed and their performance is predicated on simplicity because they cannot detect the affordances to regulate their actions offered by different properties of a performance environment.

4 A Nonlinear Pedagogy for athletes as complex systems

These key ideas have been harnessed in adoption of a pedagogical approach for athletes considered as nonlinear dynamical systems [9]. In such a nonlinear pedagogy, an important task is to design representative performance environments which allow athletes to explore and harness movement pattern variability in achieving consistent performance outcomes. Practice tasks should place an athlete in a region of a performance landscape which is far from equilibrium so that they can exploit these inherent tendencies for change over time. Representative design, introduced earlier, is an aspect of ecological psychology emphasised by Egon Brunswik. He proposed that for the study of organism-environment interactions, 'cues' (or perceptual variables) should be sampled from a specific organism's typical environment so as to be *representative* of the environmental stimuli from which they have been adapted, and to which behaviour is intended to be generalized [10]. In sport, this definition of representative design implies the need to ensure that practice and training task constraints are designed to provide an accurate simulation, that is a faithful representation of the task constraints of a specific performance environment e.g., team sports or rock climbing. In particular, research needs to identify the key informational constraints of a performance environment so that they can be sampled and faithfully simulated in practice tasks. Representative design in learning helps athletes to form functional synergetic couplings to underpin their actions (see Fig. 1).

Ecological dynamics research suggests that traditional theories of skill acquisition have tended to over-value the importance of repeating a putative ideal movement template in sport pedagogy [e.g., 2]. There is a prevalent belief in many sports that skill acquisition underpins expert performance through constant rehearsal of an idealised movement pattern (e.g, a classical technique). For example, this assumption is exemplified by the erroneous obsession that some coaches have with the acquisition of a specific set of mechanics for 'the golf swing', to be perfected through hours of practice under the constant conditions of a golf driving range. It is also instantiated in practice of multi-articular actions in elite sport programmes, when initial preparatory movements, considered less than ideal, are often terminated, preventing athletes from learning how to adapt their ongoing movement patterns for performance of ensuing phases of action [for an example in springboard diving see 11]. In a nonlinear pedagogy, skill acquisition is conceptualised as a search for *functional coordination solutions* that emerge from the dynamical interaction of key constraints on each individual athlete (categorised as individual, task-oriented and environmental in nature [12]. Expert performance in sport is defined by an *increasingly more functional athlete-environment relationship acquired over time with task experience* [13].

This view of skill and expertise, as a *more functional relationship,* is distinct from traditional theories which emphasize the repetition of a particular movement pat-

tern or coordination mode through constant practice. It recognizes the need for each individual learner to adapt to, and satisfy, the unique array of interacting constraints impinging on him/her at a specific stage of development and level of experience. Through the process of co-adaptation, expert performance in sport can evolve as skilled individuals acquire the capacity (and subtly) *re-invent themselves* in response to changing constraints, for example due to tactical changes in team sports, as new opponents set unique challenges, as rules change, as equipment evolves, and as maturation and ageing affects the systems of each athlete's body.

5 Conclusions

In sport, the cognition, perception and action of athletes function in an intertwined manner, expressed in expert performance as a continuous switching between *dependence on* and *independence of* environmental information sources in performance. In complex systems in sport, coordination tendencies are harnessed during performance, but skilled athletes and successful teams are not locked into rigid behaviours by specific constraints of a performance environment (so that they *react* to situations that arise). Their actions are emergent and can be guided by a combination of intentions and the perception of specific information sources to adapt movement activities in a particular way to achieve specific performance goals. An important aspect of expertise in sport is the capacity to *perceive affordances* by learning to detect key sources of environmental information which support successful task performance. Nonlinear pedagogy is predicated on the inherent and ubiquitous complexity within the performance domain of sport. Expertise can be enhanced by sport pedagogists who understand how to design affordances into learning programmes for complex systems (athletes and teams). This strategy will strengthen the synergetic couplings that emerge in skilled athletes, and between teammates, as they seek to exploit inherent properties of neurobiological degeneracy and context sensitivity to consistently achieve their performance goals.

References

[1] Davids K, Hristovski R, Araújo, D., et al. (Eds.) Complex Systems in Sport. London: Routledge, 2014.
[2] Ericsson KA, Krampe RT, Tesch-Römer C. The role of deliberate practice in the acquisition of expert performance. Psychol. Rev. 1993;100: 363–406.
[3] Hambrick, DZ, Oswald, F, Altman, EM et al. Deliberate practice: is that all it takes to become an expert? Intell.; in press.
[4] Davids K, Araújo D, Hristovski R., et al. Ecological dynamics and motor learning design in sport; 2012; London: Routledge; In Skill Acquisition in Sport: Research, Theory & Practice, 2nd edition (Edited by A. M. Williams & N. Hodges); pp112-130.
[5] Riley, M., Shockley, K, van Orden, G. Learning from the body about the mind. Top. in Cog Sci. 2012; 4:21-34.
[6] Davids K, Glazier, P. Deconstructing neurobiological coordination: the role of the biomechanics-motor control nexus. Ex. Sp. Sci. Rev. 2010;38:86–90.
[7] Mason, P. Degeneracy at multiple levels of complexity. Biol.Theory 2010; 5: 277–88.
[8] Gibson JJ. The ecological approach to visual perception. Boston (MA): Houghton Mifflin; 1979.
[9] Button C. Chow J.-Y., Travassos, B., et al. A nonlinear pedagogy for sports teams as social neurobiological systems: How teams can harness self-organization tendencies. In: Ovens, A. Hopper, T. & Butler, J. (Eds.), Complexity in Physical Education: Reframing Curriculum, Pedagogy and Research, pp.135-150; Routledge: London; 2013.
[10] Brunswik E. Perception and the representative design of psychological experiments. Berkeley (CA): University of California Press; 1956.
[11] Barris S, Farrow D, Davids K. Increasing Functional Variability in the Preparatory Phase of the Takeoff Improves Elite Springboard Diving Performance. Res. Quart. for Ex. and Sp.; 85: 97-106.
[12] Newell, KM. Constraints on the development of coordination. In MG Wade & HTA Whiting (Eds.), Motor development in children. Aspects of coordination and control, pp. 341-360. Dordrecht, Netherlands: Martinus Nijhoff, 1986.
[13] Davids, K, Button, C, Bennett, S. Dynamics of skill acquisition: A constraints-led approach. Champaign, IL: Human Kinetics, 2008.

Proceedings of ICCSA 2014
Normandie University, Le Havre, France – June 23-26, 2014

AFFECTIVE LEARNING DESIGN: BUILDING EMOTIONS INTO REPRESENTATIVE LEARNING DESIGN

Ian Renshaw[1], Jonathan Headrick[2] and Keith Davids[34]

Abstract. The role of emotions during skill acquisition and the development of expertise in sport has often been neglected or overlooked. Traditional cognitive approaches have commonly attempted to decompose or remove emotion from learning due to the perceived detrimental effect it may have on performance. This paper will discuss why emotion, and affect overall, should be included and considered in learning tasks by adopting an ecological dynamics approach. Key areas of discussion include the role of the Amygdala in affective attention and creating emotion-laden memories, and the interaction between emotions, cognitions, perceptions, and actions in metastable periods. Based on these underpinnings, practical considerations will be identified focussing on the enhancement of representative (learning) design concepts to include the influence emotion on learning. To bring these ideas together the concept of Affective Learning Design (ALD) will be introduced as a potential framework for effectively incorporating the influence of emotions in the acquisition and development of skill in sport. Key considerations of ALD include (i) adopting individualised approaches, (ii) catering for beginners through to expert performers, (iii) creating scenarios or vignettes to provide context in learning environments, and (iv) distinguishing clear performance goals for learning

Keywords: representative design, affect, emotion, learning, ecological dynamics

1 Introduction

Despite the inter-dependent relationship between skill acquisition and emotions in learning and performing in sport, so far very little attention has been paid to the role that emotions play in this interaction. In sport, performers need to be able to adapt to task constraints while performing under potentially high emotional states induced in competitive performance that might influence their cognitions, perceptions and actions [1, 2]. In fact, emotions have generally been viewed as detrimental to skill acquisition and attempts have been made to remove them from the process until the skill is established [3]. This reductionist approach is in line with traditional thinking in skill learning where tasks are decomposed to reduce the cognitive load and make it easier for beginners.

The neglect of emotion in the study of sporting expertise can be seen in current thinking on visual perception, for example, the focus on the two visual system model [4, 5]. However, an overlooked aspect of visual perception in sport is the mediating role of a 3rd pathway via the Amygdala. Given the key role of the amygdala in affective (emotion-laden) attention [6], this omission is somewhat surprising. The Amygdala is involved in shaping perception when *affectively* significant visual information is encountered in an environment. The intensity of the emotions generated reflects the significance of the stimuli to the individual and the strength of the response on the visual cortex [6]. An event is thought to be affectively relevant for an organism if it can significantly influence (positively or negatively) the attainment of his or her goals, the satisfaction of his or her needs, or the maintenance of his or her well-being [7]. Consequently, greater engagement is seen in unpredictable situations that are viewed as "threatening", for example in sport, where failure can result in career termination. In summary, emotional engagement in learning and performance influences how performers perceive the world, specifically, emotions experienced during learning influence the perceptions, actions and intentions of performers. The intensity of an emotional experience also acts to positively or negatively strengthen memories. Importantly, for those designing learning tasks, the amygdale pathway is 'preferentially

[1] Ian Renshaw and Jonathan Headrick are with School of Exercise and Nutrition Sciences, Queensland University of Technology, Victoria Park Road, Kelvin Grove, QLD 4059, Australia E-mails: i.renshaw@qut.edu.au; jj.headrick@qut.edu.au
[34] Keith Davids with FiDiPro Programme, University of Jyväskylä, Finland & Centre for Sports Engineering Research, Sheffield Hallam University, UK E-mail: k.davids@shu.ac.uk

invoked' in ambiguous learning situations [6]. For example, increased affective attention is thought to increase signal-to-noise ratios (see [8]) and as such could enhance those decision-making tasks that require attunement to key information sources to differentiate different movement patterns of opponents [9].

2 Representative Learning Design: Embedding emotion in learning design

Given the previous discussion, an issue of concern is how to support individuals in the task of learning to perform in emotional situations such as competition. For learners, desirable stable states represent periods of system organisation that are functional in terms of 'what works' and 'what feels right'(see [10]). Learning is often accompanied by increased intensity and range of emotions as individuals' transit from the 'known' to the 'unknown' requiring adoption of novel and functional states of system organisation [2]. For example, selection for the first time in a higher standard of competition can be a threat to self-efficacy for many players who do not know if there intrinsic dynamics are matched to the new unique task demands. These periods of uncertainty, where the intrinsic dynamics of the learner may not match the task demands, are referred to as metastable periods where the system (learner) attempts to function whilst transitioning between stable attractor states [11]. During periods of metastability it is expected that the emotions, thoughts, and actions of learners will be highly variable as they attempt to explore the task environment for opportunities to fulfil their goals or intentions [2]. How then can sport scientists and pedagogues support the performer in these delicate and challenging situations?

We propose that one approach which may be of some use is the concept of representative design, a term that captures the idea of sampling perceptual variables from an individual's 'natural' environment [12]. More recent work has applied the concept of representative design to the study of sport performance and developed an approach called Representative Learning Design (RLD) [13]. RLD proposes that the inclusion of situation-specific information sampled from the performance environment can lead to a simulation of the demands of a competitive performance environment {13]. So far, the focus of RLD has been on sampling information from the *external* environment, but given the previous discussions it is clear that information from *within* the individual (i.e., cognitive-emotional interpretations – see [2]) can also shape actions as they interact with the world and therefore there is a need to sample the affective impact of task constraints. In recent work, we have proposed to fill this void by introducing the concept of Affective learning Design {14]). Key aspects of ALD include (i) adopting individualised approaches, (ii) catering for beginners through to expert performers, (iii) creating scenarios or vignettes to provide context in learning environments, and (iv) distinguishing clear performance goals for learning, performance and competitive environments [14]. Implementing ALD requires practitioners to sample, predict and plan for the potential emotional and cognitive circumstances of competition, and adequately sample them in learning simulations with the aim of developing effective movement behaviours (actions). In order to achieve this, practitioners and pedagogues should identify key control parameters that can be manipulated or scaled to induce metastability.

3 Conclusion

Incorporating ALD into learning design acknowledges the need to create emotion-laden learning experiences that effectively simulate the constraints of performance environments in sport. Considering the effects of emotion on learning experiences means that practitioners must design tasks that meet skill acquisition *and* basic psychological needs [15]. Given that emotions continuously interact with intentions, cognitions, perception and actions to constrain the acquisition of perceptual-motor skills, task demands and the dynamic psychological state of each individual learner should be seen as interacting constraints that influence behavioural, cognitive, and emotional tendencies [15]. By incorporating affective constraints into RLD we propose that simulating the task demands of performance can result in more effective learning and enhanced adaptability to novel performance environments.

References

1] Jones, M. V. (2003). Controlling emotions in sport. The Sport Psychologist, 17, 471-486.

[2] Lewis, M. D. (2004). The emergence of mind in the emotional brain. In A. Demetriou & A. Raftopoulos (Eds.), *Cognitive developmental change*. New York Cambridge University Press.

[3] Hutto, D. D. (2012). Truly enactive emotion. *Emotion Review, 4*(2), 176-181.

[4] Milner, A. D., & Goodale, M. A. (1995). The visual brain in action. Oxford: Oxford University Press.

[5] van der Kamp, J., Rivas, F., van Doorn, H., & Savelsbergh, G. (2008). Ventral and dorsal contributions in visual anticipation in fast ball

sports. *International Journal of Sport Psychology*, 39(2), 100-130.

[6] Pessoa, L. (2011). Reprint of: Emotion and cognition and the amygdala: From "what is it?" to "what's to be done?" *Neuropsychologia, 49*(4), 681-694.

[7] Sander, D. (2013). Models of emotion: The affective neuroscience approach. In J. Armony & P. Vuilleumier (Eds.), *The Cambridge Handbook of Human Affective Neuroscience* (pp. 5-53). New York, NY: Cambridge University Press.

[8] Davids, K., Shuttleworth, R., Button, C., Renshaw, I., & Glazier, P. (2004). "Essential noise"-enhancing variability of informational constraints benefits movement control: a comment on Waddington and Adams. British Journal of Sports Medicine. 38(5), 597-600.

[9] Gibson, E. J. & Pick, A. D. (2000). *An Ecological Approach to Perceptual Learning and Development*. Oxford: Oxford University Press.

[10] Thelen, E., & Smith, L. B. (1994). *A Dynamic Systems Approach to the Development of Cognition and Action*. Cambridge, MA: The MIT Press. \

[11] Kelso, J. A. S. (1995). *Dynamic Patterns: The Self-Organization of Brain and Behavior*. Cambridge: MIT press.

[12] Brunswik, E. (1956). *Perception and the representative design of psychological experiements* (2nd ed.). Berkeley: University of California Press.

[13] Pinder, R. A., Davids, K., Renshaw, I., & Araújo, D. (2011). Representative learning design and functionality of research and practice in sport. *Journal of Sport & Exercise Psychology, 33*, 146-155.

[14] Headrick, J.J., Renshaw, I., Davids, K, Araujo, D., & Pinder, R. (in press). The Dynamics of Expertise Acquisition in Sport: A Conceptual Model of Affective Learning Design. *Pyschology of Sport & Exercise*.

[15] Renshaw, I., Oldham, A. R. H., & Bawden, M. (2012). Nonlinear pedagogy underpins intrinsic motivation in sports coaching. *The Open Sports Sciences Journal, 5*(Suppl 1), 88-99.

Satellite Workshop 9
Dynamics of complex living systems

Satellite Workshop 9
Dynamics of complex living systems

Organizers

- Christophe Letellier, CORIA, University of Rouen, France, christophe.letellier@univ-rouen.fr

Description

Living systems are complex in the sense that they result from a collective behavior of a huge number of elements (as cells for instance) or are made of very few elements affected by many external factors (as the heart or two interacting peoples). This satellite workshop is intended for stimulating interactions between different peoples working in various field as biological networks, biomedicine, cognition, learning processes, etc.

List of papers/presentations

Irene Sendina-Nadal (King Juan carlos University),
Longitudinal network analysis of neuronal cultures
Abstract: The issue of why and how an assembly of isolated (cultured) neurons self-organizes to form a complex neural network is a fundamental problem. Despite their more limited, and yet laboratory-controllable, repertoire of responses, the understanding of such cultures' organization is, indeed, a basis for the comprehension of the mechanisms involved in their in vivo counterparts, and provide a useful framework for the investigation of neuronal network development in real biological systems. In vitro primary cultures of dissociated invertebrate neurons from locust ganglia are used to experimentally investigate the morphological and topological evolution of assemblies of living neurons, as they self-organize from collections of separated cells into elaborated, clustered, networks. At all the different stages of the culture's development, identification of neurons' and neurites' location by means of a dedicated software allows to ultimately extract an adjacency matrix from each image of the culture. In turn, a systematic statistical analysis of a group of topological observables grants us the possibility of quantifying and tracking the progression of the main network's characteristics during the self-organization process of the culture. Our results point to the existence of a particular state corresponding to a small-world network configuration, in which several relevant graph's micro- and meso-scale properties emerge. Finally, we identify the main physical processes ruling the culture's morphological transformations, and embed them into a simplified growth model qualitatively reproducing the overall set of experimental observations.

L. Viger, F. Denis, M. Rosalie & C. Letellier (CORIA - Université de Rouen)
A cancer model for the angiogenic switch
Abstract: The occurrence of metastasis is an important feature in cancer development. In order to have a one-site model taking into account the interactions between host, effector immune and tumor cells which is not only valid for the early stages of tumor growth but also for vascular tumor growth, we developed a new model where are incorporated interactions of these three cell populations with endothelial cells. These

latter cells are responsible for the neo-vascularization of the tumor site which allows migration of tumor cells to distant sites. It is thus shown that, for some parameter values, the resulting model for the four cell populations reproduces the angiogenic switch, that is, the transition from avascular to vascular tumor.

Massimo Di Felice (ENSEA, Cergy Pontoise),
Controllability and stabilizability analysis of a cancer chaotic system
Abstract: A four-dimensional cancer model describing interactions between host, immune, tumor and endothelial cells was investigated via a stability analysis exibiting the key parameter for controlling the dynamics toward a tumor-free site. Such a result was also supported by a less local approach based on a Lyapunov function. A treatment based on an impulsive control technique was proposed: the effect of the delay with which the action (killing a certain amount of the tumor cells) is applied was also investigated.

Emeline Fresnel (CORIA - Université de Rouen)
Characterization of cardiodynamics from first-return maps on Delta-RR intervals. Application to different pathological groups
Abstract: Heart rate variability analysis using 24-hour Holter monitoring is frequently performed to assess the cardiovascular status of a patient. The studies are typically based on the beat-to-beat intervals (RR) and time or frequency-dependent domain indicators. In the present study, we started from the beat-to-beat interval variations or ΔRR which offer a better view of the underlying structures ruling the cardiodynamics. Using first-return maps built on the ΔRR, we observed different patterns of cardiodynamics which are investigated via a symbolic dynamics using an age-dependant partition. We computed a Shannon entropy, quantifying the complexity underlying the cardiac variability, and an asymmetry coefficient, here introduced to quantify the balance between accelerations and decelerations in the rhythm. A map spanned by the Shannon entropy and the asymmetry coefficient allowed to distinguish three different types of dynamics, "clustering" first-return maps with similar structures in given domains of the map. We applied this method to i) 45 adults from Physionet databases, ii) 14 vulnerable infants routinely monitored at the Rouen University Hospital and iii) 10 patients with respiratory failure and mechanically ventilated during sleep.

Aurélie Vallée (PSY.NCA - Université de Rouen)
Characterization of the dynamics underlying mediated interactions of visually impaired and normal teenagers

Binbin Xu, Sabir Jacquir, Stéphane Binczak, Jean-Marie Bilbault (LE21 CNRS UMR 6306, Univ. Bourgogne, Dijon, France),
Phase Space Reconstruction of an Experimental Cardiac Electrical Signal
Abstract: Cardiac arrhythmias are very common pathologies which can be treated either by medications, invasive ablation procedures or device implantations. In order to improve theses treatments, clinical and experimental models are used to test new drugs. In this context, in vitro cultures of cardiac cells represent valuable models to study the mechanism of the arrhythmias at the cellular level. In this paper, we investigate the stability and robustness of an experimental model in normal and under external stimulation conditions. Phase space reconstructions of attractors in normal and

arrhythmic cases are performed after characterizing the nonlinearity of the model, computing the embedding dimension and the time lag. Our results show that the electrical stimulation modifies slightly the embedding dimension. The parameter time lag τ increases when arrhythmia happens. The shape of attractors remains globally similar, although more disturbed in case of arrhythmia than in normal conditions. The correlation dimension qualifies the attractors as strange.

Proceedings of ICCSA 2014
Normandie University, Le Havre, France - June 23-26, 2014

AN EASY-TO-USE TECHNIQUE TO CHARACTERIZE CARDIODYNAMICS FROM FIRST-RETURN MAPS ON ΔRR

Emeline Fresnel*†† Valérie Messager* Jean-François Muir‡ Christophe Letellier*†

Abstract. Heart rate variability analysis using 24-hour Holter monitoring is frequently performed to assess the cardiovascular status of a patient. Rather than using the common beat-to-beat intervals (RR) present study is based on the beat-to-beat interval variations, the so-designated ΔRR, which offer a better view of the underlying structures ruling the cardiodynamics. The different structures observed in the first-return maps (also called Poincaré maps) built on the ΔRR are analyzed using a symbolic dynamics built with an an age-dependent partition. We computed a Shannon entropy, quantifying the complexity underlying the cardiac variability, and an asymmetry coefficient here introduced to quantify the balance between accelerations and decelerations in the cardiac rhythm. A map spanned by the Shannon entropy and the asymmetry coefficient allowed us to distinguish three different types of dynamics, grouping first-return maps with similar structures in given domains of the map. We applied this method to i) 45 adults from Physionet databases, ii) 14 vulnerable infants routinely monitored at the Rouen University Hospital and iii) 10 patients with respiratory failure and mechanically ventilated during sleep. It was thus possible to show that the different patterns of cardiac dynamics are observed in various cohorts of patients.

Keywords. cardiodynamics, first-return map, Shannon entropy, vulnerable infants, mechanical ventilation

1 Introduction

Variability of the beat-to-beat interval is a physiological feature depending on different levels of regulation whose main component is the autonomic nervous system. Investigating RR interval variability allows to assess these control mechanisms and can be used as an indicator of cardiovascular health in any population. Modifications in heart rate variability reveal pathophysiological disorders and can be associated with a range of severe diseases [1]. A decreased variability was thus found in patients with congestive heart failure [2, 3], left ventricular dysfunction [4] or diabetic neuropathy [5]. In particular, reduced variability has been shown to be a predictor of mortality in patients who underwent a myocardial infection [6].

In all these works, heart rate variability has been studied using traditional time or frequency-dependent domain indicators. However, it has been shown that nonlinear analysis could better characterize the cardiodynamics [7, 8, 9]. The application of nonlinear dynamics methods to biomedical data already provided valuable information, and a prognostic value was given, for instance, using symbolic dynamics [8]. Our objective is not to determine whether cardiac dynamics is chaotic or not, mostly because we do not have yet a conclusive answer concerning a possible underlying determinism [10, 11] as it was pointed out in the challenge posed by Glass [12]. Nevertheless, such a lack of proof for a chaotic cardiodynamics do not prevent us to apply tools borrowed from the nonlinear dynamical systems theory.

Our objective is thus to develop an easy-to-use technique to analyze heart rate variability using 24-hour Holter monitoring and to discriminate various classes of patients as investigated in the challenge proposed by Glass [12]. Once validated using a cohort of 45 patients from the Physionet database, our technique will be used to investigate the cardiodynamics of 14 vulnerable infants who were routinely monitored at the Rouen University Hospital, and then to analyze the cardiodynamics of 10 patients with respiratory failure and mechanically ventilated during sleep.

2 Methods

2.1 Heart rate variability mechanisms

Cardiodynamics is largely under the control of the autonomic nervous system [1, 13] which is classically divided into two subsystems. The parasympathetic system which slows the heart rate via the vagus nerve and the sympathetic system which accelerates the pace via β-adrenegic receptors [14]. Acceleration and deceleration in the heart rhythm thus result from two opposite physiological processes which can be modulated by external oscillators inducing short or long-term variations in the heart period [15].

Gender and age are also known to affect the heart rate variability. Many studies showed that heart rate variability is reduced when age is increased. The intrinsic heart rate was proposed by Jose and Collison in 1970 [16] as a

*CORIA UMR 6614, Normandie Université, Saint-Etienne du Rouvray, France. E-mail: fresnele@coria.fr
†ADIR Association, Bois-Guillaume Hospital, Rouen, France.
‡GRHV EA 3830, Rouen University Hospital, France.

function of the age a (in years) as

$$\mathrm{HR}_i = 118.1 - 0.57a \ (r = 0.64)\,, \tag{1}$$

where HR_i is the intrinsic heart rate in bpm.

Ageing effects in heart rate variability have been evaluated in various studies [17, 18, 19, 20]. In all studies, a significant reduction of the heart rate variability in older people as assessed by time and frequency-dependent indicators was observed.

Cardiodynamics was much more investigated in adults than in newborns and infants. During infancy, a progressive maturation of the autonomic nervous system is observed, with developmental changes of vagal and sympathetic mediation of heart rate. Time and frequency domain indices were found to be correlated to age in infants and children aged 3 days to 14 years [21]. As we previously mentioned, these indices were found anti-correlated to the age of adults.

To sum up, the autonomic nervous system is mostly responsible for the heart rate variability which evolves during the whole life. In infancy and in older adults, there is a prevalence of the sympathetic activity over a weak vagal activity. In younger adults, the parasympathetic activity is prevailing, combined with a moderate to a high level of sympathetic activity [22]. The heart rate variability is thus at a low level in the early life, increases during childhood until young adulthood, and then decreases until the end of life. These features will be later used to define an age-dependent partition for building a symbolic dynamics.

2.2 Nonlinear tools

Cardiodynamics is here investigated using the differences between successive RR intervals, that is, using

$$\Delta\mathrm{RR}_n = \mathrm{RR}_{n+1} - \mathrm{RR}_n\,. \tag{2}$$

Working with ΔRR allows to analyze the variations in the heart rate and to overcome any long-term drift due to the sinus activity [11]. We built first-return maps (or Poincaré maps) for the whole data set (at least many hours in each case).

For healthy adults, these maps present a circular cloud of points centered around zero and associated with a low variability which is typically associated with the sinus variability. Isolated points distant from the first bisecting line are representative of large beat-to-beat variations in the heart rate, thus corresponding to arrhythmias.

The heart dynamics is investigated using a symbolic dynamics based on a partition of first-return maps into domains mainly built for distinguishing normal variability from arrhythmias. As we discussed earlier, the heart rate variability is related to age and so the size of the central disk associated with sinus variability. Thus, the range visited by $\Delta\mathrm{RR}_n$ is split in three domains according to the partition

$$\sigma_n = \left| \begin{array}{lll} 0 & & \Delta\mathrm{RR}_n \leq -\tau \\ 1 & \text{if} & -\tau < \Delta\mathrm{RR}_n < +\tau \\ 2 & & \Delta\mathrm{RR}_n \geq +\tau\,, \end{array} \right. \tag{3}$$

where symbol 1 represents small variations due to the sinus rhythm, symbol 0 is associated with fast decreasing of RR intervals and, symbol 2 corresponds to fast increasing in RR intervals. Such a symbolic dynamics thus transforms a series of real numbers into symbol sequences that are easier to treat and interpret.

In order to better distinguish different groups of patients with the same age but with different diseases, the partition should be only age dependent. Such a dependency should be related to the fact that the global heart rate variability thus starts at a low level, increases during childhood until young adulthood, and then decreases until the end of life. We chose to make a linear dependency for adults as

$$\tau = 89 - 0.60a\,, \tag{4}$$

where a is the patient age in years and τ is the "radius" of the central disk in ms. Such a partition was found to provide a good discrimination between patients with various diseases. Based on a preliminary investigation of the heart dynamics recorded in newborns (see below), we found that the threshold should be around 20 ms for few month newborns. The maximal variability and, consequently, the maximal threshold τ, being assumed to observe at about 20 years, we thus obtained a dependency of τ versus the age a according to a sixth-degree polynomial

$$\begin{array}{ll} \tau(a) & = 17.7 + 9.1a - 5.16a^2 + 0.014a^3 \\ & \quad -0.0002a^4 + 0.0000015a^5 - 4.4.10^{-9}a^6\,. \end{array} \tag{5}$$

When only adults are considered, the linear regression (4) would be sufficient to determine the threshold τ.

Once the symbolic dynamics is built according to partition (3), the heart variability is investigated in terms of sub-sequences of a given number N_q of symbols. We used $N_q = 6$ consecutive symbols, taken among the $N_p = 3$ different symbols {0,1,2}. This leads to $N_p^{N_q} = 3^6 = 729$ possible sequences. Our statistics is thus correctly defined since a 24-hour Holter contains about 100,000 RR intervals. From these symbolic sequences, we choose to characterize the cardiodynamics by computing a Shannon entropy which was introduced to measure the information production rate of a process [23]. We are here using such an entropy as a measure of the "complexity" of the dynamics, a small entropy being associated with a simple (periodic) solution and a large one with a complex (aperiodic) solution. Typically, the entropy for a period 1 regime is equal to zero since there is no information produced from an event to the next one. Contrary to this, the entropy is maximum when all possible sequences (distinguished states) are equiprobable. The Shannon entropy

is defined as

$$\tilde{S}_h = -\sum_{n=0}^{N_p^{N_q}-1} P_n \log P_n \,, \tag{6}$$

where P_n is the realization probability of the nth symbolic sequence among the 729 possible ones where n corresponds to the integer of the 6-symbol sequence read in base 3. The Shannon entropy is normalized by the largest entropy which is obtained when all sequences are equiprobable, that is, with a probability equal to 6.59. The relative Shannon entropy $S_h = \frac{\tilde{S}_h}{S_{\max}}$ is thus within the unit interval $[0,1]$. A relative Shannon entropy S_h close to 1 implies a very complex dynamics for which arrhythmias are frequent. By definition, sinus rhythm is mostly associated with small variations (symbols "1") and characterized by an entropy close to 0. As we will see in next section, the entropy for subjects with a normal sinus rhythm is roughly 0.3.

The symbolic dynamics defined by the partition (3) splits the first-return map in 9 panels (Fig. 1), each of them being characterized by a probability of visits η_{ij}. The central domain designated by "11" therefore corresponds to a cardiac dynamics ruled by the sinus node. Domains 00, 10, 20 and 21 correspond to a fast decreasing between two consecutive RR intervals (acceleration in the heart rate), whereas domains 01, 02, 12 and 22 correspond to a fast increasing between two consecutive RR intervals (deceleration in the heart rate).

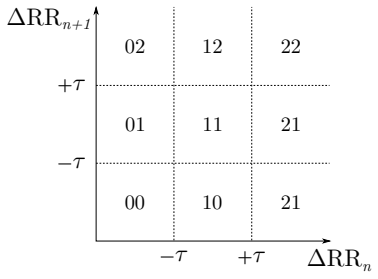

Figure 1: Partition of the first-return map in 9 panels, according to partition (3) used to define the symbolic dynamics.

Asymmetry in the sinus heart rate was already investigated using different measures from the RR intervals [24, 25, 26]. In the present study, we choose to use the differences ΔRR between successive RR intervals; we therefore did not perform our analysis from the same variable. Moreover, we did not filter the data to remove arrhythmias (such as VPC), contrary to what is commonly done in other studies. Our objective was thus to define an index being representative of the asymmetry of the entire cardiac dynamics, including arrhythmias if there are any. We defined our asymmetry coefficient as

$$\alpha = \frac{1}{4}\left[\frac{\eta_{00}}{\eta_{22}} + \frac{\eta_{01}}{\eta_{21}} + \frac{\eta_{02}}{\eta_{20}} + \frac{\eta_{10}}{\eta_{12}}\right] \tag{7}$$

where each term is the ratio between the probability of visits of a domain corresponding to fast accelerations and its symmetric under an inversion symmetry (in the plane of the first-return map on ΔRR). Consequently, an α coefficient roughly equal to 1 is representative of a balance between fast accelerations and decelerations in the rhythm. $\alpha < 1$ represents a tendency to fast decelerations and $\alpha > 1$ represents a tendency to fast accelerations in the cardiac rhythm.

Using the normalized Shannon entropy S_h and the asymmetry coefficient α, we constructed a map in order to distinguish the different types of dynamics, grouping the first-return maps with similar structures in given domains of the map S_h-α. The Shannon entropy allows to discriminate wide from reduced variabilities, whereas extreme values of the asymmetry coefficient α indicate an imbalance between accelerations and decelerations in the heart dynamics.

3 Validation protocol

3.1 PHYSIONET data

In order to test the discriminating power of our technique, we selected three different groups of patients from the PHYSIONET database [27]. For each of them, a long-term ECGs (24 hours) containing around 100,000 RR intervals was downloaded. The first group included 15 healthy subjects with normal sinus rhythm (NSR) and no significant arrhythmias, aged 33 ± 7 years (range 20 to 45). According to Eq. (4), the corresponding threshold τ_{NSR} required for constructing the symbolic dynamics was thus 69 ms. The second group was made of 15 patients with severe congestive heart failure (CHF) (NYHA class 3-4), aged 59 ± 6 years (range 48 to 71). The corresponding threshold τ_{CHF} was thus 54 ms. The third group contained 15 patients with sustained atrial fibrillation (AF) (one or more episodes during at least 20 hours of the recordings), aged 66 ± 12 years (range 39 to 87). The corresponding threshold τ_{AF} for the symbolic dynamics was thus 50 ms.

3.2 Structures of the first-return maps

Firstly, we plotted the first-return maps from the ΔRR variable for all patients from the three groups. First-return maps of healthy subjects are characterized by a central cloud of points whose size depends on the considered patient. Some points can be out of the central cloud but their repartition is rather homogeneous.

Patients affected by congestive heart failure are characterized by a central cloud (abnormally smaller than in healthy subjects) and four well-defined segments whose orientations do not depend on the patients. Atypical angular distribution shows that the four segments are oriented at $\frac{2\pi}{3}$, π, $\frac{3\pi}{2}$ and at about $\frac{11\pi}{6}$ (Fig 3). These segments correspond to ventricular premature contractions (VPC) consisting in a premature contraction which is not

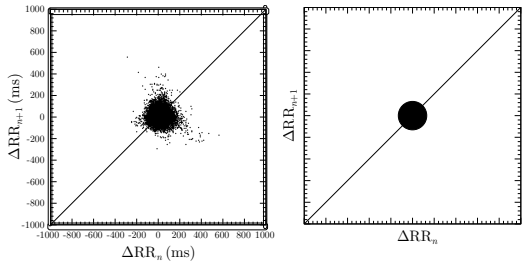

(a) NSR$_{13}$ patient (b) Healthy model

Figure 2: First-return map built on ΔRR for a PHYSIONET patient from the group NSR and the corresponding schematic model.

triggered by the sinus node but by an ectopic centre: they occur randomly. The premature beat is always followed by a prolonged beat that offsets the anticipation in order to synchronize cardiac contraction with the sinus node activity [28]. The structure of the first-return maps of patients with congestive heart failure thus suggests that they are subject to VPCs. A relation between heart failure and VPCs had been established but the underlying mechanism remains poorly understood [29].

When bursts of successive VPCs occur, two additional segments can be distinguished in the first-return map at $\theta = \frac{3\pi}{4}$ and $\theta = \frac{7\pi}{4}$, respectively.

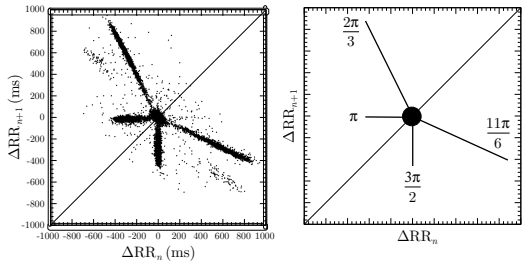

(a) CHF$_7$ patient (b) CHF model

Figure 3: First-return map built on ΔRR for a PHYSIONET patient from the group CHF and its schematic model.

Patients affected by atrial fibrillation present a very wide and dense first-return map, with a characteristic triangular shape (Fig. 4). This triangular shape is highlighted by the angular distribution which presents three main orientations located at $\frac{\pi}{2}$, π and $\frac{7\pi}{4}$, respectively. The central disk cannot be distinguished: the cardiac rhythm is not governed by the sinus node. By investigating the three heights of the triangle, they mostly correspond to fast isolated decelerations in the heart rate. When a deceleration event occurs with an elongated RR interval, the heart returns to its normal activity by a resynchronization to the sinus node during the following beat. Consequently, short irregular heart beats (tachycardia) frequently occurs in ECG. Such an acceleration of the heart rate is balanced according to a property of the atrioventricular node which presents a decremental conduction, that is, the more frequently the node is stimulated, the slower it conducts [30]. This prevents rapid conduction to the ventricles in the case of rapid atrial rhythms as encountered in atrial fibrillation. These patients suffering of atrial fibrillation are thus subject to an interplay between very frequent fast accelerations and decelerations in the heart rhythm, decelerations structuring the triangular shape of the first-return maps.

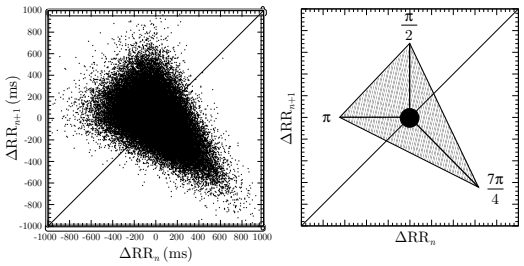

(a) AF$_{13}$ patient (b) AF model

Figure 4: First-return map built on ΔRR for a PHYSIONET patient from the group AF and its schematic corresponding model.

3.3 Results

The very different dynamical properties presented by the three groups of patients were clearly evidenced by our computations (Tab. 1). The relative Shannon entropy was rather small for the CHF group, slightly greater for healthy patients, and substantially greater for the AF group. The asymmetry coefficient α was close to 1 for healthy subjects and patients with AF, and significantly greater for the CHF group. The realization probability P_{111111} (using the three-symbol dynamics) was large for patients with CHF, smaller in healthy patients and the smallest for the AF group.

The $S_h - \alpha$ map allows to discriminate the different types of cardiac dynamics by grouping the first-return maps with similar structures in given domains (Fig. 5). CHF patients whose first-return maps present characteristic segments due to the occurrence of VPCs are located in the upper left corner of the map. This area corresponds to large asymmetry coefficient α and to small Shannon entropy. Structures in the right part of the map correspond to the largest Shannon entropies, thus revealing complex dynamics. Moreover, the first-return maps are located in the neighbourhood of the line $\alpha = 1$, thus clustering patients affected by atrial fibrillation (whose first-return maps have a triangular shape) at the extreme right of this line. Healthy subjects are in the middle part of the map with a Shannon entropy distributed around $S_h = 0.3$ and with an asymmetry coefficient close to 1. Their first-return maps have a mostly circular shape of variable size. Thus, the association between the shape of first-return maps and the computed characteristics allows to clearly

Table 1: Mean and standard deviation of the relative Shannon entropy S_h, of the realization probability of sequence "111111" encoded with the 3-symbol dynamics and of the asymmetry coefficient α, for each group of the PHYSIONET patients. p-values between each group are also reported (Wilcoxon rank-sum test).

Patients	$\overline{S_h}$	p-value	
NSR_i	0.304 ± 0.172	$]p < 0.01$	$]p < 0.01$
CHF_i	0.150 ± 0.159	$]p < 0.01$	
AF_i	0.893 ± 0.035		
Patients	$\overline{\alpha}$	p-value	
NSR_i	0.952 ± 0.268	$]p < 0.01$	$]p = 0.54$ n.s.
CHF_i	3.386 ± 2.798	$]p < 0.01$	
AF_i	1.068 ± 0.106		
Patients	$\overline{111111}$	p-value	
NSR_i	68.44 ± 18.02 %	$]p < 0.01$	$]p < 0.01$
CHF_i	83.33 ± 21.05 %	$]p < 0.01$	
AF_i	1.52 ± 4.95 %		

discriminate the three groups of patients (Tab. 2). The S_h-α map provides an overview of the results allowing to visually identify the group to which a patient belongs.

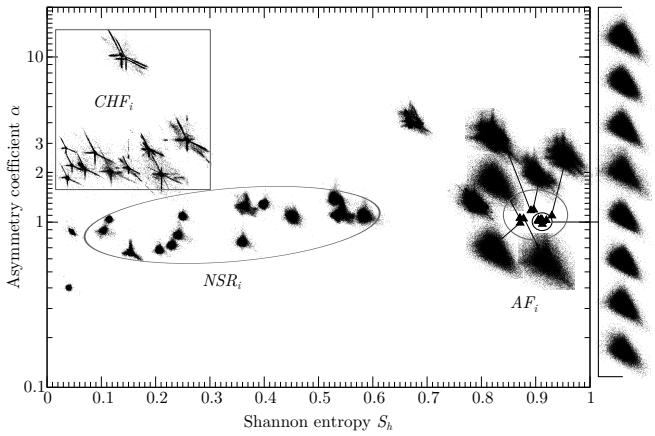

Figure 5: Map spanned by the relative Shannon entropy S_h and the asymmetry coefficient α. The 15 patients of each group are reported. A logarithmic scale is used in the abscissa to improve the clarity of the map.

4 Cardiac dynamics from vulnerable infants

4.1 Data

A routine monitoring was performed in fourteen infants who were hospitalized for cardio-respiratory alerts at the Rouen University Hospital. These infants are among the quite rare infants hospitalized with such events during the two years of our protocol. The electrocardiograms — recorded with a monitor PHILIPS MP 70 — were converted into tachograms using the PHYSIONET software (free access online). All the infants were followed up after an acute event: mostly after a bronchiolitis with or without respiratory syncytial virus (RSV), or after a gastro-oesophageal reflux, discomfort, vomiting or alarms during home monitoring.

Table 2: Main tendencies of the Shannon entropy and the asymmetry coefficient α for each group of patients. The shape of first-return maps is also reported.

Group	S_h	α	Structure
NSR	medium	around 1	circular
CHF	low to medium	greater than 1	segments
AF	high	around 1	triangular

4.2 Results

Since the infants are between 0 and 1 year old, the symbolic dynamics is constructed using a threshold τ equal to 26 ms according to equation (5). Heart rate variability among the infants is quite important, as shown by the average relative Shannon entropy ($\overline{S_h} = 0.42 \pm 0.19$) which is greater than the value ($S_h = 0.30$) for which the variability is considered as being "normal" for adults. The average asymmetry coefficient is slightly greater than 1 ($\overline{\alpha} = 1.25 \pm 0.68$). All the results are reported in Tab. 3.

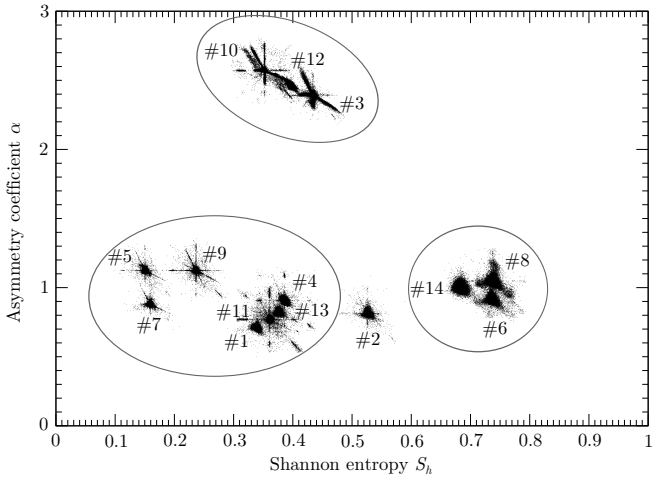

Figure 6: Map spanned by the relative Shannon entropy S_h and the asymmetry coefficient α, in which are reported the first-return maps for the 14 infants of our protocol.

At least five infants among the fourteen monitored presented severe cardiodynamical troubles. The relative Shannon entropy reveals the presence of many arrhythmias in infants 6 ($S_h = 0.74$), 8 ($S_h = 0.74$) and 14 ($S_h = 0.68$); in these three infants, there is low realization probability P_{111111}. Numerous ΔRR have been therefore encoded with symbols 0 and 2, meaning that many large variations were detected and that these infants have complex cardiac dynamics. The asymmetry coefficient α for these patients are close to 1, resulting from arrhythmias

such as accelerations which are balanced by decelerations. First-return maps of these infants present a triangular shape. For these reasons, infants 6, 8 and 14 are identified as being similar to the group with atrial fibrillation. In the map spanned by the relative Shannon entropy and the asymmetry coefficient, infant 2 is at an intermediary location between the three infants with atrial fibrillation and those with a more normal heart variability. His asymmetry coefficient is slightly less than 1, more or less as encountered in healthy people but his relative Shannon entropy is an intermediate value ($S_h = 0.53$). The corresponding return map has a triangular shape as most of the maps (see the maps for infants 1, 4, 13 or even infant 7) but with a greater size. The first-return map computed for infant 7 has a small triangular shape and small segments very rarely visited which are different from the four segments characteristic of PVCs. These cardiodynamics of these infants present the same dynamical feature as observed in patients with atrial fibrillation.

Table 3: Relative Shannon entropy S_h, asymmetry coefficient α and realization probability P_{111111} computed from RR intervals recorded in the 14 infants of our protocol.

	S_h	α	P_{111111}
1	0.34	0.72	64.9%
2	0.53	0.80	40.9%
3	0.43	**2.40**	43.2%
4	0.38	0.90	60.9%
5	0.15	1.13	86.6%
6	**0.74**	0.92	19.4%
7	0.16	0.88	85.0%
8	**0.74**	0.92	19.4%
9	0.24	1.13	77.0%
10	0.35	**2.58**	57.4%
11	0.36	0.76	65.4%
12	0.40	**2.47**	59.6%
13	0.38	0.84	61.1%
14	**0.68**	1.00	31.3%

The asymmetry coefficient α reveals that infants 3, 10 and 12 present many fast accelerations of the heart rate: according to the shape of their first-return maps, there are isolated extrasystoles (case of infant 3, $\alpha = 2.40$) or bursts of successive extrasystoles (case of infant 10, $\alpha = 2.58$). Infant 12 has an atypical first-return map in which points are located along the second bisecting line, implying a tendency to bigeminy, that is, a period-2 regime, alternating fast accelerations and decelerations in the heart rate. For these three infants, the associated Shannon entropies are quite large, contrary to what was found in the adults previously investigated. These three first-return maps are associated with entropies revealing complex dynamics. Infants 3, 10 and 12 have characteristics corresponding to a congestive heart failure.

Infants 1, 4, 11 and 13 have Shannon entropies between 0.30 and 0.40, and asymmetry coefficients less than 1. The percentage of realized sequence "111111" is greater than 60% and the first-return maps are made of a central cloud with a shape roughly suggesting a triangle (infants 1, 4 and 13); perhaps this is a signature of the immaturity of the regulation mechanisms. According to the Shannon entropy and the asymmetry coefficient, these infants should be identified as having a sinus rhythm supposed to be normal for an infant. The lack of available data does not allow us to compare these dynamics with those measured in infants without cardio-respiratory alerts.

Lastly, infants 5, 7 and 9 have the smallest Shannon entropies, suggesting reduced variabilities. We can distinguish small segments (although not so often visited) as typically encountered in patients with congestive heart failure). Very likely, arrhythmias are not significant in these infants.

As for adults, the S_h-α map provides a visual classification of the fourteen cardiodynamics as previously explained (Fig. 6). Infants 3, 10 and 12 are in the upper part of the map and would be associated with CHF. Infants 6, 8 and 14 are in the right part of the map, thus suggesting an AF. The remaining infants (1, 4, 5, 7, 9, 11, 13) are in the middle part of the map, a feature that would most likely correspond to a NSR; the triangular shape of the central cloud could be a signature of the immaturity of the cardiodynamics. Infant 2 had a very atypical map which should deserve further investigations.

5 Cardiac dynamics from patients with respiratory failure

5.1 Data

Fourteen patients with chronic respiratory failure were monitored during three nights at the Rouen University Hospital [**?**]. The first night consisted in a polysomnography recorded during spontaneous breathing in order to have a reference night without mechanical ventilation. The following night was recorded under noninvasive mechanical ventilation. Ventilator settings were adjusted during the week in order to improve the synchronization between patient's ventilatory cycle and the pressure cycle delivered by the ventilator. Each patient was then recorded two weeks after the first night under mechanical ventilation. Data were recorded using a CID102-L8D (CIDELEC SA, France).

Six patients (1, 2, 4, 5, 8 and 9) suffered from an obesity hyperventilation syndrome (OHS), often associated with sleep apneas. Three patients (3, 7 and 10) suffered from amyotrophic lateral sclerosis with sleep apneas for the first two. Patient 6 suffered from kyphoscoliosis with sleep apneas.

5.2 Results

Since the mean age for these ten patients was 65 ± 12, the dynamics was constructed using a time threshold τ set at 50 ms according to equation (5). Shannon entropy and asymmetry coefficient for these ten patients are reported in Tab 4. Heart rate variability is quite large in these patients as evidenced by the mean relative Shannon entropy ($\overline{S}_h = 0.50 \pm 0.34$) which is greater than the "normal" value computed for healthy adults ($S_h = 0.30$). It has been shown that obesity can predispose to or is associated with numerous cardiac complications such as coronary heart disease, heart failure, and sudden death [31]. Moreover, weight-stable obese subjects have an increased risk of arrhythmias and sudden death, even in the absence of cardiac dysfunction [32, 33], a risk observed in both genders [34]. More than half of our patients suffering from OHS, they are good candidates for complex cardiac dynamics. The average asymmetry coefficient is greater than 1 ($\overline{\alpha} = 1.63 \pm 0.86$): this can be explained by the fact that the autonomic nervous system can be disturbed in chronic respiratory failure via an activation of the sympathetic system known for increasing the rate and the contraction force of the heart [35].

Table 4: Relative Shannon entropy S_h, asymmetry coefficient α and realization probability P_{111111} computed from ΔRR recorded in our 10 patients with chronic respiratory failure in spontaneous breathing.

	S_h	α	P_{111111}
1	0.07	1.08	95.0%
2	0.73	**2.86**	13.7%
3	**0.90**	1.14	1.6%
4	**0.80**	1.26	0.8%
5	0.05	1.11	96.3%
6	0.65	**3.55**	8.5%
7	0.49	**1.62**	39.1%
8	0.24	1.29	77.5%
9	**0.88**	1.17	7.2%
10	0.18	1.25	84.6%

At least five patients in spontaneous breathing presented cardiodynamics troubles. The relative Shannon entropy reveals the presence of many arrhythmias in patients 3 ($S_h = 0.90$), 4 ($S_h = 0.80$) and 9 ($S_h = 0.88$); the realization probability P_{111111} of normal beats is very low in these patients. Contrary to what was observed with previous patients with high Shannon entropies, these ten patients present an asymmetry coefficient α which is greater than 1 (it was close to 1 in patients with AF and in the infants). These α values may result from the sympathetic activation due to chronic respiratory failure. First-return maps of patients 3 and 4 present a triangular shape, whereas the first-return map for patient 9 presents the three oriented segments and is more restricted to a central disk than the two previous ones. These three patients present characteristics similar to those observed in patients suffering from AF.

The asymmetry coefficient α reveals that patients 2 and 6 present many fast accelerations of the heart rate: according to the shape of their first-return maps, they have isolated extrasystoles (patient 2, $\alpha = 2.86$) or bursts of successive extrasystoles (patient 6, $\alpha = 3.55$). These two patients have characteristics corresponding to those presented by patient suffering from CHF. Contrary to the PHYSIONET patients with CHF, these patients are characterized by large Shannon entropies. Patient 2 is suffering from an obesity hypoventilation syndrome which may induce cardiac arrhythmia; patient 6 is affected with kyphoscoliosis which may induce respiratory and cardiac failure [36]. Patient 7 presents large asymmetry coefficient and Shannon entropy. Its first-return map does not have segments and is located in the S_h-α map between those associated with healthy adults and those for patients suffering from CHF.

Patients 8 and 10 have Shannon entropies around 0.20 and a percentage of sequence 111111 greater than 75%. Asymmetry coefficient α is slightly greater than 1. These patients could be considered as being healthy from the cardiac point of view. Patients 1 and 5 are characterized by the smallest Shannon entropies, thus suggesting reduced variabilities.

As for the PHYSIONET patients, the S_h-α map (Fig. 7) provides a classification of the ten cardiodynamics as previously explained. Patients 2 and 5 are in the upper part of the map where first-return maps on ΔRR associated with patient suffering from CHF are located. Patients 3, 4 and 9 are in the right part of the map, where those corresponding to patient suffering from AF are observed. The remaining patients (1, 5, 8, 10) are in the middle left part of the map where patients with NSR are located. Patient 7 has atypical characteristics and is isolated from the other groups.

The recordings during the first and the fourteenth nights of mechanical ventilation were made for investigating the impact of such ventilatory assistance on cardiodynamics. During the first night of mechanical ventilation, there are some clear indications that the cardiodynamics is affected. Although the mean Shannon entropy ($\overline{S}_h = 0.47 \pm 0.30$) is not significantly changed compared to the value under spontaneous breathing ($\overline{S}_h = 0.50 \pm 0.34$) and, consequently, remains rather large, the mean asymmetry coefficient ($\overline{\alpha} = 1.23 \pm 0.19$) is significantly decreased ($p = 0.037$, Wilcoxon rank-sum test) under mechanical ventilation compared to those under spontaneous breathing ($\overline{\alpha} = 1.63 \pm 0.86$). The imbalance between fast acceleration and fast deceleration is strongly reduced, particularly for the two patients 2 and 6 who presented a large number of extrasystoles (compare the location in the S_h-α map under spontaneous breathing shown in Fig. 7a and in the corresponding map under mechanical ventilation (Figs. 7b and 7c): as a consequence, the probability p_{111111} for observing a sequence of normals beats

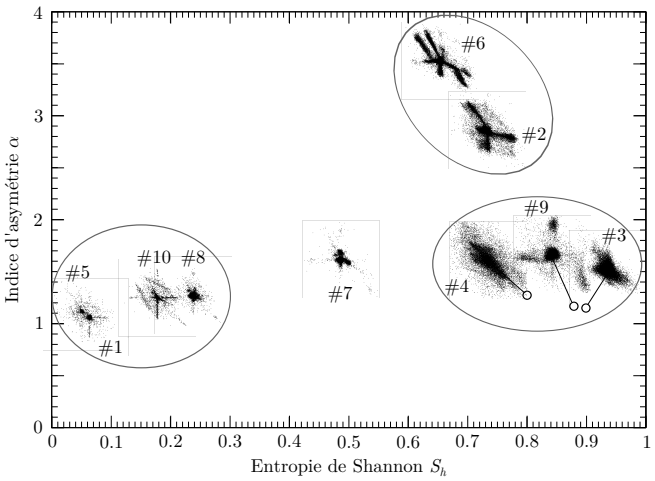

(a) Under spontaneaous breathing

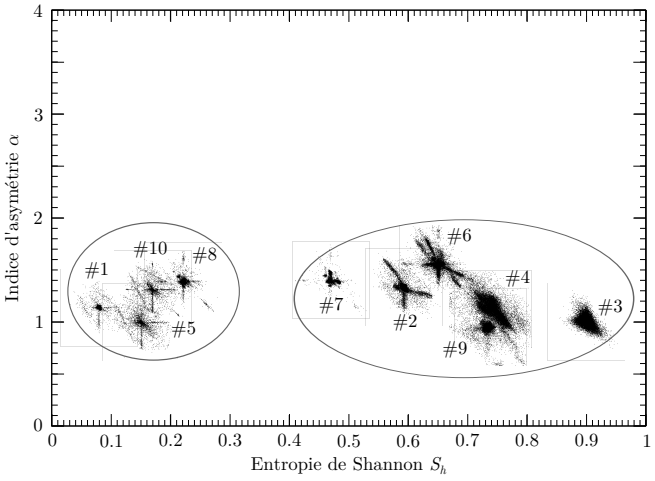

(b) First night under mechanical ventilation

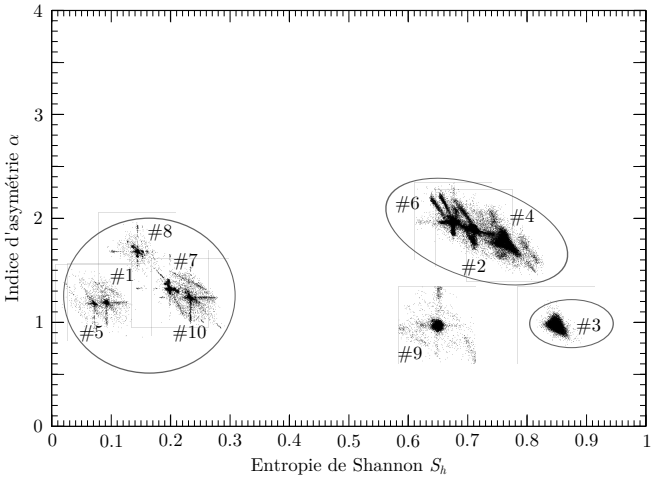

(c) 14th night under mechanical ventilation

Figure 7: Map spanned by the relative Shannon entropy S_h and the asymmetry coefficient α, in which are reported the first-return maps for the 10 patients of our protocol.

increased.

After two weeks under mechanical ventilation, the mean Shannon entropy ($\overline{S}_h = 0.44 \pm 0.32$) is still slightly smaller than the one under spontaneous breathing but the difference remains non significant: this is certainly due too few patients who received a ventilation with ventilator settings perhaps non optimal. Indeed, some patients presented a Shannon entropy which was clearly reduced, for instance from $S_h = 0.54$ under spontaneous breathing to 0.36 during the 14th night under mechanical ventilation (case of patient 4). Concerning the asymmetry coefficient α, there is a rebond effect since, after two weeks, it increases to become non significantly different ($\overline{\alpha} = 1.42 \pm 0.38$) compared to the value under spontaneous breathing. In particular the number of of extrasystoles increases as evidenced in the map S_h-α (Fig. 7c). A larger cohort should be investigated to confirm these features.

6 Conclusion

We discriminated three different characteristic patterns of cardiac dynamics in three groups of adults with clearly identified status as reported in the PHYSIONET database. First-return maps built on the ΔRR recorded in adults with normal sinus variability are mostly structured around a central disk; those associated with patients suffering from atrial fibrillation presented a quite large triangular shape and those for patients with congestive heart failure evidenced clear segments characteristics of extrasystoles. The map spanned by the Shannon entropy and the asymmetry coefficient provided an efficient tool for discriminating the cardiodynamics, clustering the first-return maps on ΔRR according to their structures. This was confirmed on various cohort as newborns with cardiorespiratory alerts or ventilated patients suffering from chronic respiratory failure. These three main patterns could therefore serve as references for analyzing cardiodynamics in a general way, thus suggesting than using first-return maps on ΔRR is a powerful tool for distinguishing patients with different cardiac pathologies, from the newborn to the adults.

Acknowledgements

The data used for this work were measured by Emad Yacoub and Roomila Naeck during their respective Ph.D. thesis.

References

[1] Task Force of the European Society of Cardiology and the North American Society of Pacing and Electrophysiology, "Heart rate variability: standards of measurement, physiological interpretation, and clinical use", *Circulation*, vol. 93, pp. 1043-1065, 1996.

[2] J.P. Saul, Y. Arai, R.D. Berger, L.S. Lilly, W.S. Colucci, R.J. Cohen, "Assessment of autonomic regulation in chronic congestive heart failure by heart rate spectral analysis", *American Journal of Cardiology*, vol. 61, pp. 1292-1299, 1988.

[3] B.M. Szabò, D.J. van Veldhuisen, J. Brouwer, J. Haaksma, K.I. Lie, "Relation between severity of disease and impairment of heart rate variability parameters in patients with chronic congestive heart failure secondary to coronary artery disease", *American Journal of Cardiology*, vol. 76, pp. 713-716, 1995.

[4] J. Nolan, A.D. Flapan, S. Capewell, T.M. MacDonald, J.M. Neilson, D.J. Ewing, "Decreased cardiac parasympathetic activity in chronic heart failure and its relation to left ventricular function", *British Heart Journal*, vol. 67, pp. 482-485, 1992.

[5] D.J. Ewing, I.W. Campbell, B.F. Clarke, "Assessment of cardiovascular effects in diabetic neuropathy and prognostic implications", *Annals of Internal Medicine*, vol. 92, pp. 308-311, 1980.

[6] R.E. Kleiger, J.P. Miller, J.T. Bigger, A.J. Moss, "Decreased heart rate variability and its association with increased mortality after acute myocardial infarction", *American Journal of Cardiology*, vol. 59, pp. 256-262, 1987.

[7] A. Babloyantz, A. Destexhe, "Is the normal heart a periodic oscillator?", *Biological Cybernetics*, vol. 58, pp. 203-211, 1988.

[8] A. Voss, J. Kurths, H.J. Kleiner, A. Witt, N. Wessel, P. Saparin, K.J. Osterziel, R. Schurath, R. Dietz, "The application of methods of non-linear dynamics for the improved and predictive recognition of patients threatened by sudden cardiac death", *Cardiovascular Research*, vol. 31, pp. 419-433, 1996.

[9] N. Wessel, C. Ziehmann, J. Kurths, U. Meyerfeldt, A. Schirdewan, A. Voss, "Short-term forecasting of life-threatening cardiac arrhythmias based on symbolic dynamics and finite-time growth rates", *Physical Review E*, vol. 61, pp. 733-739, 2000.

[10] N. Wessel, M. Riedl, J. Kurths, "Is the normal heart rate " chaotic" due to respiration", *Chaos*, vol. 19, pp. 028508, 2009.

[11] U. S. Freitas, E. Roulin, J.-F. Muir, C. Letellier, "Identifying chaos from heart rate: the right task?", *Chaos*, vol. 19, pp. 028505, 2009.

[12] L. Glass, "Introduction to controversial topics in nonlinear science: Is the normal heart rate chaotic?" *Chaos*, vol. 19, pp. 028501 (2009).

[13] J.P. Saul, R.F. Rea, D.L. Eckberg, R.J. Cohen, "Heart rate and muscle sympathetic nerve variability during reflex changes of autonomic activity", *American Journal of Cardiology*, vol. 258, pp. H713-721, 1990.

[14] A. Malliani, "Cardiovascular sympathetic afferent fibers", *Reviews of Physiology, Biochemistry and Pharmacology*, vol. 94, pp. 11-74, 1982.

[15] A. Malliani, M. Pagani, F. Lombardi, S. Cerutti, "Cardiovascular neural regulation explored in the frequency domain", *Circulation*, vol. 84, pp. 482-492, 1991.

[16] A.D. Jose, D. Collison, "The normal range and determinants of the intrinsic heart rate in man", *Cardiovascular Research*, vol. 4, pp. 160-167, 1970.

[17] K. Jensen-Urstad, N. Storck, F. Bouvier, M. Ericson, L.E. Lindblad, M. Jensen-Urstad, "Heart rate variability in healthy subjects is related to age and gender", *Acta Physiologica Scandinavica*, vol. 160, pp. 235-241, 1997.

[18] P.K. Stein, R.E. Kleiger, J.N. Rottman, "Differing effects of age on heart rate variability in men and women", *American Journal of Cardiology*, vol. 80, pp. 302-305, 1997.

[19] K. Umetani, D.H. Singer, R. McCraty, M. Atkinson, "Twenty-four hour time domain heart rate variability and heart rate: relations to age and gender over nine decades", *Journal of the American College of Cardiology*, vol. 31, pp. 593-601, 1998.

[20] D. Ramaekers, H. Ector, A.E. Aubert, A. Rubens, F. Van de Werf, "Heart rate variability and heart rate in healthy volunteers", *European Heart Journal*, vol. 19, pp. 1334-1341, 1998.

[21] M. Massin, G. von Bernuth, "Normal ranges of heart rate variability during infancy and childhood", *Pediatric Cardiology*, vol. 18, pp. 297-302, 1997.

[22] O.V. Korkushko, V.B. Shatilo, Yu.I. Plachinda, T.V. Shatilo, "Autonomic control of cardiac chronotropic function in man as a function of age: assessment by power spectral analysis of heart rate variability", *Journal of the Autonomic Nervous System*, vol. 32, pp. 191-198, 1991.

[23] C. E. Shannon, "A mathematical theory of communication", *Bell System Technical Journal*, vol. 27, pp. 379-423 & 623-656, 1948.

[24] P. Guzik, J. Piskorski, T. Krauze, A. Wykretowicz, H. Wysocki, "Heart rate asymmetry by Poincaré plots of RR intervals", *Biomedizinische Technik*, vol. 51 (4), pp. 272-275, 2006.

[25] J. Piskorski, P. Guzik, "Geometry of the Poincaré plot of RR intervals and its asymmetry in healthy adults", *Physiological Measurements*, vol. 28, pp. 287-300, 2007.

[26] J. Piskorski, P. Guzik, "The structure of heart rate asymmetry: deceleration and acceleration runs", *Physiological Measurements*, vol. 32, pp. 1011-1023, 2011.

[27] A.L. Goldberger, L.A.N. Amaral, L. Glass, J.M. Hausdorff, P.Ch. Ivanov, R.G. Mark, J.E. Mietus, G.B. Moody, C.-K. Peng, H.E. Stanley, "PhysioBank, PhysioToolkit, and PhysioNet: Components of a New Research Resource for Complex Physiologic Signals", *Circulation*, vol. 101, pp. e215-220, 2000.

[28] R. Langendorf, "Ventricular premature systoles with postponed compensatory pause", *American Heart Journal*, vol. 46, pp. 401-404, 1953.

[29] S.K. Agarwal, R.J. Simpson, P. Rautaharju, A. Alfonso, E. Shahar, M Massing, S. Saba, G. Heiss, "Relation of Ventricular Premature Complexes to Heart Failure", *American Journal of Cardiology*, vol. 190, pp. 105-109, 2012.

[30] E. Patterson, B.J. Scherlag, "Decremental conduction in the posterior and anterior AV nodal inputs", *Journal of Interventional Cardiac Electrophysiology*, vol. 7, pp. 137-148, 2002.

[31] P. Poirier, T.D. Giles, G.A. Bray, Y. Hong, J.S. Stern, F.X. Pi-Sunyer, R.H. Eckel, "Obesity and Cardiovascular Disease: Pathophysiology, Evaluation, and Effect of Weight Loss", *Arteriosclerosis, Thrombosis, and Vascular Biology*, vol. 26, pp. 968-976, 2006.

[32] F.H. Messerli, B.D. Nunez, H.O. Ventura, D.W. Snyder, "Overweight and sudden death: increased ventricular ectopy in cardiopathy of obesity", *Archives of Internal Medicine*, vol. 147, pp. 1725-1728, 1987.

[33] W.B. Kannel, J.F. Plehn, L.A. Cupples, "Cardiac failure and sudden death in the Framingham Study", *American Heart Journal*, vol. 115, pp. 869-875, 1988.

[34] S.W. Rabkin, F.A Mathewson, P.H. Hsu, "Relation of body weight to development of ischemic heart disease in a cohort of young North American men after a 26 observation period: the Manitoba Study", *American Journal of Cardiology*, vol. 39, pp. 452-458, 1977.

[35] S. Heindl, M. Lehnert, C.P. Criée, G. Hasenfuss, S. Andreas, "Marked sympathetic activation in patients with chronic respiratory failure", *American Journal of Respiratory and Critical Care Medicine*, vol. 164, pp. 597-601, 2001.

[36] E.R. Kafer, "Respiratory and cardiovascular functions in scoliosis and the principles of anesthetic management", *Anesthesiology*, vol. 52, pp. 339-351, 1980.

Proceedings of ICCSA 2014
Normandie University, Le Havre, France - June 23-26, 2014

A CANCER MODEL FOR THE ANGIOGENIC SWITCH

L. Viger *, F. Denis †, M. Rosalie ‡ & C. Letellier §

Abstract. The occurrence of metastasis is an important feature in cancer development. In order to have a one-site model taking into account the interactions between host, effector immune and tumor cells which is not only valid for the early stages of tumor growth but also for vascular tumor growth, we developed a new model where are incorporated interactions of these three cell populations with endothelial cells. These latter cells are responsible for the neo-vascularization of the tumor site which allows migration of tumor cells to distant sites. It is thus shown that, for some parameter values, the resulting model for the four cell populations reproduces the angiogenic switch, that is, the transition from avascular to vascular tumor.

Keywords. Cancer model, angiogenic switch, endothelial cells, Chaos

1 Introduction

Tumor growth is a complex process depending on various cell types as mutant (tumor) cells, host (normal-tissue) cells, immune cells (lymphocytes, macrophages), endothelial cells... In order to get real insights into key parameters that control system dynamics, theoretical models are required [1]. They can also be used for designing new effective treatments without an extensive experimentation [2]. Most of the models used for investigating tumor growth are at the tissue level as reviewed in [3, 4]: at this level of description unavoidable simplifications are made, focusing on some detailed mechanisms depending on the objectives. In the present, we would like to develop a generic model (not specific to a given type of cancer) at the tissue level for a single tumor site. Our aim is to include the micro-environment (host or healthy cells) of the tumor cells as considered in [5, 6]. To overcome the limitation of these latter models which are only for avascular tumor growth, we introduced interactions between tumor, immune, host and endothelial cells as recommended by Merlo and co-workers [7]. Since we limit our model to a single tumor site, cell migration by diffusion or by circulating through the blood vessels is not considered in this paper. Nevertheless, we would like to have a model for which the presence (or not) of angiogenesis depends in a simple way on some parameters since angiogenesis is a necessary process for reproducing the emergence of multiple solid tumors [8]. Thus by introducing endothelial cells in the model initially proposed by de Pillis and Radunskaya [9, 10] we constructed a one-site cancer model which is also valid for vascular tumor growth. Indeed, as a prerequisite step, before considering spatio-temporal models for tumor growth, it is relevant to have a model which reproduces the angiogenic switch, an important feature inducing metastasis during tumor growth.

2 A four-dimensional model with endothelial cells

In most of cancers, tissue invasion and the occurrence of metastasis is a key step in tumor growth associated with a bad prognostic. Tumor cells become thus more aggressive once tumor hypoxia triggered neo-vessels. Indeed, beyond a given size, numerous tumor cells become in a state of hypoxia and therefore trigger the tumor neo-angiogenesis, that is, induces the production of new vessels issued from the existing ones. Fed with supplementary resources, tumor cells proliferate with an increased growth rate and neo-vascularization opens new routes for tissue invasion and metastasis. This is the so-called angiogenic switch corresponding to the switch from an avascular to a vascular tumor. Such an angiogenic switch cannot exist without endothelial cells that are responsible for the production of vessels.

Our objective is thus to build a four-dimensional model able to reproduce the angiogenic switch by the means of endothelial cells. Three main interactions have to be considered. The first type of interactions are between tumor cells and endothelial cells. When the tumor diameter is less than 1 or 2 mm, tumor cell needs in oxygen and nutriments are satisfied by blood vessels at a distance not exceeding 50-100 μm, that is, within the oxygen diffusion distance. When the tumor size increases beyond this threshold, tumor needs become too important and can no longer be satisfied by these pre-existing blood vessels.

*CORIA-UMR 6614 — Normandie Université, CNRS-Université et INSA de Rouen Campus Universitaire du Madrillet, 76800 Saint-Etienne du Rouvray, France. E-mail: vigerl.@coria.fr

†Centre Jean Bernard, 9 rue Beauverger, 72000 Le Mans, France

‡CORIA-UMR 6614 — Normandie Université, CNRS-Université et INSA de Rouen Campus Universitaire du Madrillet, 76800 Saint-Etienne du Rouvray, France.

§CORIA-UMR 6614 — Normandie Université, CNRS-Université et INSA de Rouen Campus Universitaire du Madrillet, 76800 Saint-Etienne du Rouvray, France.

Tumor cells must therefore drain oxygen and nutriments from more distant locations, being beyond the oxygen diffusion limit. Pushed to cellular hypoxia [11], tumor cells produce Hypoxia Inducible Factor (HIF) proteins which stimulate in turn transcription of Vascular Endothelial Growth Factor genes. The newly produced VEGF protein binds to VEGF receptors on endothelial cells producing vessels. Such a bind induces a signal stimulating a proliferation of endothelial cells. It corresponds to arrow 1 drawn in the flow graph of our four-dimensional model (Fig. 1).

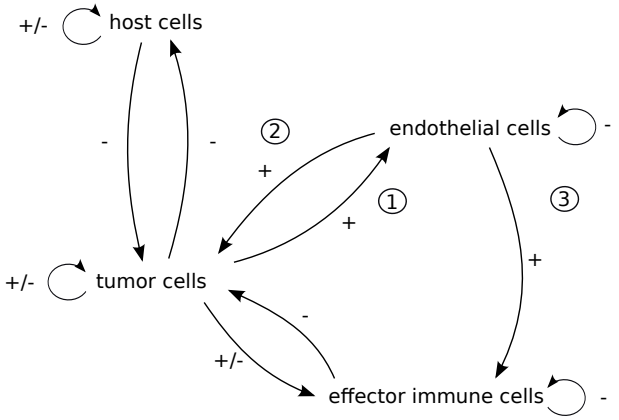

Figure 1: Flow graph of our four-dimensional model describing interactions between host, effector immune, tumor and endothelial cells.

The second type of interactions involving the endothelial cells concerns those with tumor cells. Once their growth is stimulated and that their migration is triggered, endothelial cells structure new blood vessels. New vessels thus reach the neighborhood of tumor cells and, consequently, increase the proliferation of the latter. In principle, new vasculature would not be selective in the types of cells it provides nourishment and, consequently, it should also benefit to host cells. Nevertheless, tumor cells have the ability to migrate through neo-vessels and to proliferate more importantly than host cells without saturating the considered tumor site. For this reason, tumor cells are more dependent on endothelial cells than host cells; we therefore neglected interactions between endothelial cells and host cells.

The third type of interactions considered in our model is between endothelial cells and effector immune cells. Once cancerogenesis is initiated, effector immune cells become the main actors of the organism reaction against tumor cells. To reach tumor cells, immune cells travel in blood vessels. Thus, the vascular development in the neighborhood of the tumor also increases the ability of immune cells to interact with tumor cells and, consequently, to improve the response of the immune system against the cancer. Endothelial cells secrete chemoattractant molecules attracting immune cells; thus an increase of chemoattractant concentration induced by a growth of endothelial cells induces an additional influx of immune cells to the tumor site [1, 2, 12, 13]. By the same time, endothelial cells may have a negative effect on immune cells [12], a feature taken into account in our model by the indirect effect endothelial cells have on immune cells via interactions these two populations of cells have with tumor cells. In turn, a decrease of immune cells provokes an increase of the tumor cell population.

Since our main objective is to obtain a cancer model reproducing the tumor neo-angiogenesis, we focused our attention on the previous three types of interactions. Other interactions between endothelial cells and host cells or effector immune cells are not relevant in the context of the present model. For instance, we assumed that immune cells have no (or a very limited) impact on the development of endothelial cells as done in [14]. More importantly, there is no positive feedback loop of endothelial cells to themselves because their development essentially results from the interactions they have with tumor cells. Consequently, proliferation of endothelial cells is due, in our model, to a coupling between tumor cells and endothelial cells associated with a small natural death rate represented by a negative feedback loop.

3 The equations and a stability analysis of singular points

According to the flow graph, and based on the three-dimensional model [9, 10], we built a set of four differential equations describing the tumor growth taking into account endothelial cells. The 4D model reads

$$\begin{cases} \dot{x} = \rho_1 x(1-x) - \alpha_{13} xz \\ \dot{y} = \dfrac{\rho_2 yz}{1+z} - \alpha_{23} yz - \delta_2 y + \alpha_{24} yw \\ \dot{z} = \rho_3 z(1-z) - \alpha_{31} zx - \alpha_{32} zy + \dfrac{\alpha_{34} zw}{1+w} \\ \dot{w} = \dfrac{\rho_4 wz}{1+z} - \delta_4 w \end{cases} \tag{1}$$

where x represents the population of host cells, y is associated with the population of effector immune cells, z with tumor cells and w corresponds to endothelial cells. Positive interaction between immune and endothelial cells is represented by the sole term $\alpha_{24} yw$ in the second equation of model (1).

When an immune response is triggered, effector lymphocytes reach the pathogen site (the tumor) via the blood flow ; they use vessels for their migration. Consequently, immune cells are thus promoted by endothelial cells contributing to new vessels through which they can reach the tumor [12]. If immune cells do not require endothelial cells to proliferate, the immune response is obviously stronger when they are present.

Tumor cells interact with endothelial cells in a reciprocal manner, that is, both types of cells receive benefits from their interactions. At the cellular level, the presence of tumor cells in the environment triggers the endothelial

cell proliferation. At the tissue level, such a feature can be described by a Michaelis-Menten term such as $\frac{\rho_4 wz}{1+z}$ in the fourth equation of model (1); the population of endothelial cells thus saturates at the maximal value ρ_4. When new vessels are formed, tumor cells are no longer in hypoxia and their proliferation is increased: this is the so-called angiogenic switch leading to the vascular phase. A term reflecting the proliferation of tumor cells due to the presence of endothelial cells is thus added to the logistic term modelling the tumor cell growth. In the third equation of model (1) we choose to represent this additional term by $\frac{\alpha_{34} zw}{1+w}$ as done for describing the proliferation of endothelial cells.

The two terms for describing interactions between tumor and endothelial cells are type II Holling response functions whose saturation effects are more adequate to model these interactions than a type I Holling response function. To complete this cancer model, the term $-\delta_4 w$ in the fourth equation describes the natural death rate of endothelial cells.

Our 4D model (1) is investigated with parameter values as

$\alpha_{24} = 0.3$	stimulation of effector cells by endothelial cells;
$\alpha_{34} = 0.75$	tumor cell growth rate due to neo-angiogenesis;
$\rho_4 = 0.86$	endothelial cell growth rate;
$\delta_4 = \frac{1}{11}$	endothelial cell natural death rate,

the other parameters being kept as for the 3D model [9, 15] whose solution is a chaotic attractor, that is,

$\rho_1 = 0.518$	host cell growth rate;
$\alpha_{13} = 1.5$	host cell killing rate by tumor cells;
$\rho_2 = 4.5$	effector immune cell growth rate;
$\alpha_{23} = 0.2$	effector immune cell inhibition rate by tumor cells;
$\delta_2 = 0.5$	effector immune cell natural death rate;
$\rho_3 = 1$	tumor growth rate;
$\alpha_{31} = 1$	tumor killing rate by host cells;
$\alpha_{32} = 2.5$	tumor cell killing rate by effector immune cells.

As for most mathematical models at tissue level, biological meaning of these values is rather uncertain.

With these parameter values, the 4D model (1) has seven fixed points with positive coordinates, namely

$$S_0 = \begin{vmatrix} 0 \\ 0 \\ 0 \\ 0 \end{vmatrix}, \quad S_1 = \begin{vmatrix} 1 \\ 0 \\ 0 \\ 0 \end{vmatrix}, \quad S_2 = \begin{vmatrix} 0 \\ 0 \\ 1 \\ 0 \end{vmatrix}, \quad S_3 = \begin{vmatrix} 0 \\ 0.394 \\ 0.118 \\ 0.160 \end{vmatrix},$$

$$S_4 = \begin{vmatrix} 0 \\ 0.347 \\ 0.133 \\ 0 \end{vmatrix}, \quad S_5 = \begin{vmatrix} 0.616 \\ 0.101 \\ 0.133 \\ 0 \end{vmatrix}, \text{ and } \quad S_6 = \begin{vmatrix} 0.658 \\ 0.131 \\ 0.118 \\ 0.160 \end{vmatrix}.$$

There are also four singular points which have at least one negative coordinates; they do not contribute to the dynamics since they are not located in the positive domain of the phase space (a population cannot be negative). Point S_0 (saddle point), located at the origin of the phase space, corresponds to an empty site. This point must be unstable (since it has not biological meaning, it should not be possible to observe it). Point S_1 (nearly a stable node) is associated with a site only inhabited by host cells whose growth is governed by the logistic function $\rho_1 x(1-x)$: it should be stable, at least for healthy patients. Point S_2 (saddle point) corresponds to a site where only tumor cells are observed with the growth according to $\rho_3 z(1-z)$. This is thus a pathological state for which tumor cells are at hypoxia: it must be unstable by definition. Contrary to this, point S_3 (saddle-focus SF_-) corresponds to a site where tumor cells are at equilibrium with effector immune and endothelial cells: it can be stable, a property which would be of a worse prognostic for the patient than point S_2 since tumor cells can migrate to other sites due to new blood vessels produced by endothelial cells. Point S_4 (saddle-focus SF_-) is associated with a site inhabited by immune and tumor cells: *a priori*, this point corresponds to an avascular tumor which cannot induce metastasis since there is no endothelial cell involved. The tumor should remain localized and, consequently, could be quite well-treated by a radiotherapy, for instance. Point S_5 (saddle-focus SF_+) corresponds to a site where host, immune and tumor cells co-exist: such a state could be associated with a tumor before the angiogenic switch occurs. Host cells are still dominant. The existence of such a point reveals that, in certain cases, rare if this point is unstable, a tumor does not necessarily increase its size up to the angiogenic switch. Point S_6 (saddle-focus SF_+) represents a site in which the four populations co-exist, meaning that the angiogenic switch already occurred: this is therefore a vascular tumor. At such a point, the prognostic for the patient would be uncertain since metastasis are very likely expected.

4 Dynamical analysis

In order to perform the dynamical analysis, we choose to use the differential embeddings induced by each variable of our four-dimensional model. Let us designate by s the "measured" variable. The corresponding differential embedding is thus spanned by $(X, Y, Z, W) = (s, \dot{s}, \ddot{s}, \dddot{s})$. As for the 3D model (see a detailed discussion in [15]), the differential embedding induced by variable x is the single one which does not present a domain of the phase space where the trajectories are strongly confined, meaning that host cells should still provide the best observability of the dynamics.

In order to browse various patient conditions, we choose to vary parameter values, namely the growth rate ρ_1 of host cells since we observed that it allows to switch from

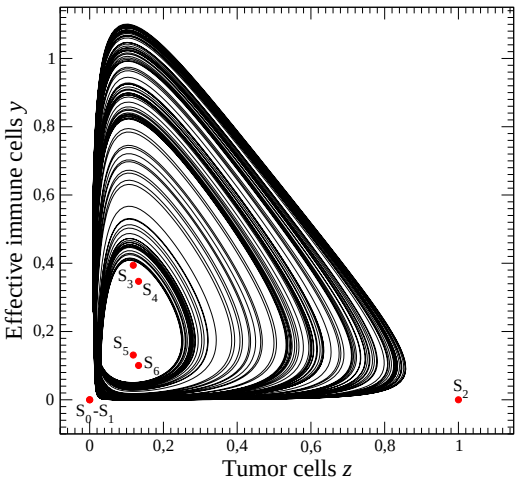

Figure 2: Chaotic attractor solution to the four-dimensional model (1). Singular points structuring the attractor are also shown. Parameter values as in the main text and $\rho_1 = 0.518$, $\alpha_{13} = 1.5$, $\rho_2 = 4.5$, $\alpha_{23} = 0.2$, $\delta_2 = 0.5$, $\alpha_{32} = 2.5$, $\alpha_{31} = 1.0$.

common to dormant cancer [15], and parameters ρ_2 and ρ_4. Bifurcation diagrams versus one of these parameters are computed as introduced in [15], that is, using minima and maxima of a given variable to obtain its range of variability. This is easily done in a differentiable embedding by defining the two-componentsPoincaré section as

$$\mathcal{P}_D \equiv \left\{(X_n, Z_n, W_n) \in \mathbb{R}^3 \mid Y_n = 0, Z_n \gtrless 0\right\} \qquad (2)$$

where $Z_n > 0$ corresponds to minima and $Z_n < 0$ to maxima of the "measured" variable. The bifurcation diagrams versus the endothelial cell growth rate ρ_4 are shown in Figs. 3a-c: they are ended at $\rho_4 = \rho_\infty \approx 0.92$, when the trajectory is ejected to infinity. The most remarkable feature is that there is a threshold value $\overline{\rho}_4 = 0.777$ under which there is no bifurcation, thus meaning that this growth rate does not affect the dynamics (the tumor growth) when $\rho_4 < \overline{\rho}_4$: there is thus a range of "patient conditions" for which the tumor growth does not depend on the endothelial cell growth rate, and which corresponds to non metastatic patients. Beyond the threshold value $\overline{\rho}_4$, the population of endothelial cells starts to be significantly different from zero and presents chaotic oscillations as the others (Fig. 3c). A patient with an endothelial cell growth rate greater than $\overline{\rho}_4$ could present a neo-vascularized tumor as discussed below. To this bifurcation corresponds a threshold value $\overline{\rho}_4$ beyond which the angiogenic switch we wanted to describe with our model can be observed. As a consequence, the tumor site can be considered as being avascular when $\rho_4 < \overline{\rho}_4$ and vascular otherwise. This means that when the vascularization is large enough ($\rho_4 \geq 0.9$), tumor cells saturate the site and start to migrate toward other sites leading to metastasis which are therefore strongly governed by the endothelial cell growth rate. If other parameter values are kept constant, there are thus two different groups of patients, one with a growth rate ρ_4 less than the threshold value and for which patients do not present vascular tumor, and one with a growth rate greater than the threshold value, leading to vascular tumor. It is clear that this threshold value depends on the other parameter values, that is, on other patient conditions.

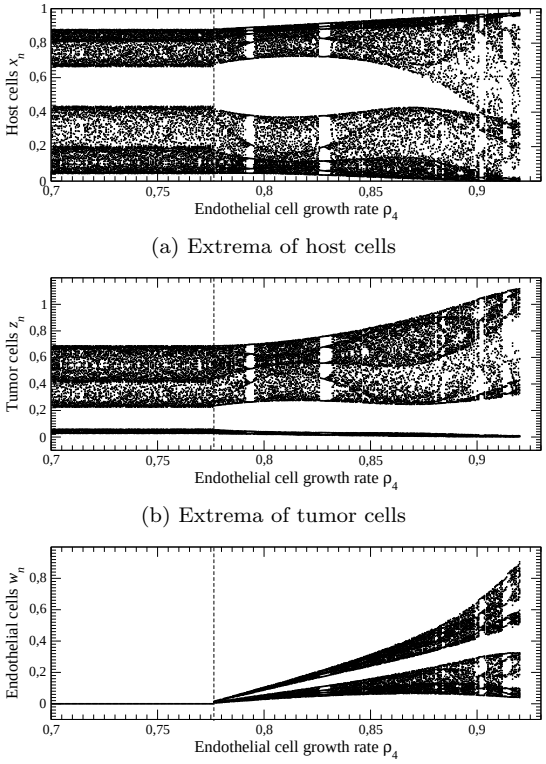

(a) Extrema of host cells

(b) Extrema of tumor cells

(c) Extrema of endothelial cells

Figure 3: Bifurcation diagrams versus the endothelial cell growth rate ρ_4 ($\rho_2 = 4.5$). Other parameter values as in Fig. 2.

From a dynamical point of view, this means that for $\rho_4 < \overline{\rho}_4$, the chaotic attractor can be embedded in the three-dimensional sub-space $\mathbb{R}^3(x, y, z)$ since $w = 0$. The first-return map to a Poincaré section built from the minima of variable x is a smooth unimodal map exactly as observed in the 3D model for the same parameters value. Consequently, this attractor is topologically equivalent to the attractor solution to the 3D model.

Similar conclusions can be adressed when the immune cell growth rate ρ_2 is decreased (Figs. 4). For values larger than $\overline{\rho}_2 = 4,9536$, the population of endothelial cells remains very small. Below this threshold value, this population of cells start to grow and vascular tumor can be observed. When $\rho_2 \leq 4.21$, the population of tumor cells becomes too large to remain in the same tumor site and necessarily starts to migrate toward other sites. When the growth of endothelial cells (immune cells) is too large (small), metastatic cancer can be most likely expected.

Clinically speaking, let us consider one patient characterized, from our model point of view, by a given set of parameter values. It seems reasonable to assume that a

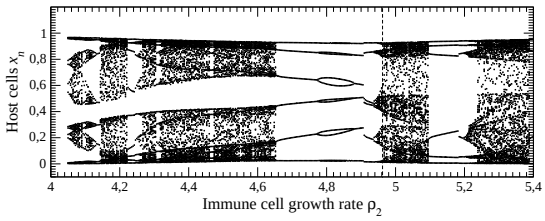

(a) Extrema of host cells

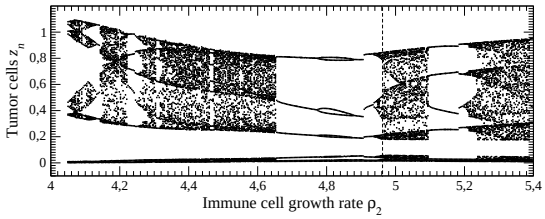

b) Extrema of tumor cells

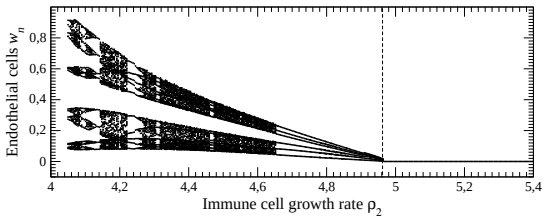

(c) Extrema of endothelial cells

Figure 4: Bifurcation diagrams versus the immune cell growth rate ρ_2 ($\rho_4 = 0.86$). Other parameter values as in Fig. 2.

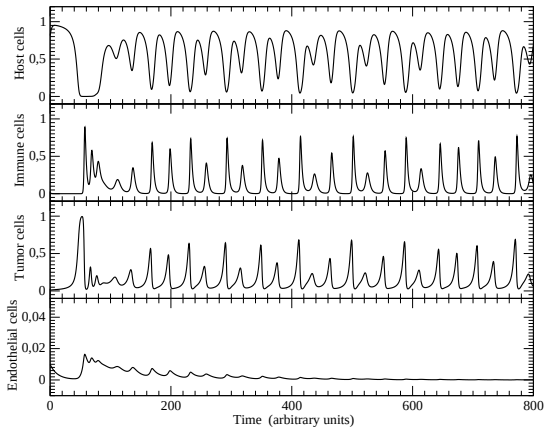

(a) $\rho_4 = 0.72$: avascular tumor

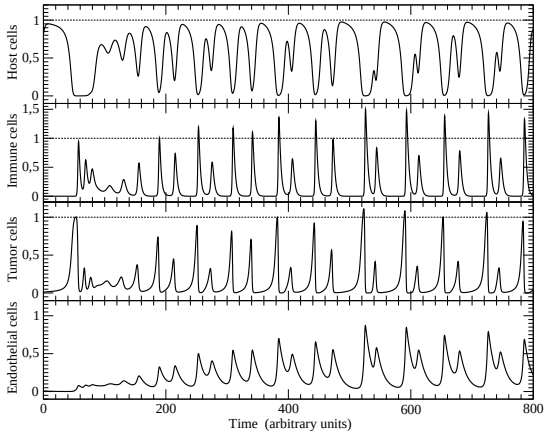

(b) $\rho_4 = 0.92$: vascular tumor

Figure 5: Time series of the four populations of cells produced by model (1). Initial conditions $x_0 = 1$, $y_0 = 0.01$, $z_0 = 0.01$ and $w_0 = 0.01$.

patient in stable conditions would present parameter values constant in time. It is thus possible to imagine various scenarios, only depending on patient conditions, that is, on its parameter values. Let us first consider a patient with an endothelial growth rate $\rho_4 = 0.72 < \overline{\rho}_4$, the other parameter values being those used in Fig. 2. Assume that he has a tumor site with very few tumor cells, thus corresponding to initial conditions as $x_0 = 1$, $y_0 = 0.01$, $z_0 = 0.01$ and, $w_0 = 0.01$. Time series of cell populations are shown in Fig. 5a. First, tumor cells quickly proliferate, shortly followed by a rapid growth of the population of effector immune cells, in reaction against the cancer progression. At the beginning of the evolution, the population of host cells decreases near zero, and there is a very light increase of endothelial cells. Then, all these populations start to oscillate, with the exception of the population of endothelial cells which vanishes. A patient with such a tumor site would never have metastasis as long as none of his parameters change in such a way that the previously discussed bifurcation occurs. In the absence of any therapy, all these parameters should not change significantly over the duration commonly clinically considered for a tumor growth, that is, over a few years.

Let us now take a second case for which the endothelial growth rate $\rho_4 = 0.92 > \overline{\rho}_4$ (Fig. 5b). From the same initial conditions as used in the previous case, the time series during the early growth ($t < 200$ arbitrary units of time) presented by the populations of host, immune and tumor cells are quite similar to those observed for $\rho_4 = 0.72$: consequently, clinically speaking, the early tumor progression ($t < 200$ arbitrary units of time) would not be distinguished from the previous one. In fact, the main departure is in the evolution of endothelial cells which are progressively increasing their population up to be significant (the angiogenic switch already occurred) and, then to mainly affect the dynamics of immune and tumor cells. The populations of immune and endothelial cells present nearly synchronous oscillations in response to those of tumor cells. Endothelial cells are now able to build new blood vessels to drain supplementary resources, mostly for tumor cells, in this site. As already mentioned, since our model kept the site isolated from a larger environment, populations of immune and tumor cells become greater than those allowed by the carrying capacity.

In this second case, the patient would have metastasis for $t > 380$ arbitrary units of time. From the clinical point of view, what would help to predict the occurrence of metastasis would be to investigate the ability of the patient to produce new endothelial cells in response to the

demand of tumor cells, a parameter which is not clinically assessed and thus leaving the impression that cancer progression is only governed by stochastic laws.

5 Conclusion

The 3D model proposed by de Pillis and Radunskaya is very interesting because it takes into account interactions of immune and tumor cells (two very often considered populations in cancer models) with host cells (very rarely considered). Its study led us to observe behaviors which are consistent to some clinical observations [16, 17, 15] as, for instance, the fact that some fast growing tumor after dormant cancer can be observed for some parameter values. Nevertheless, this was a single tumor site model which was therefore not able to reproduce relevant phenomena as the occurrence of metastasis. In order to overcome such a limitation, we introduced in this 3D model the population of endothelial cells. Our 4D resulting model reproduces the angiogenic switch, a key phenomenon for tissue invasion and the production of metastasis. This model must be considered as a prerequisite before considering a spatial model for tumor growth.

Contrary to de Pillis and Radunskaya's model which was limited to early stage of tumor growth, our model thus spontaneously reproduces the angiogenic switch which characterizes some developed cancers. In the present one tumor-site version, the population of tumor cells increases beyond the carrying capacity: when it will be connected to other sites, this will be transformed into a tumor-cell migration. Such a migration would thus result from interactions between tumor cells and their microenvironment [18, 19]. Our model does not take into account the biological complexity of cancer (genomic instability, expression of a given inhibition factor, etc.) but focuses on generic interactions between the different cell populations. It thus allows to reproduce situations observed *in vivo* or in clinics, as for instance, more or less long latence phases without metastasis as well as strongly invasive tumors providing very quickly metastasis [20, 21]. Our 4D model helped us to understand that metastasis strongly depends on patient conditions.

Acknowledgements

Louise Viger's Ph.D. thesis is supported by the company Hypérion in collaboration with the companies Takeda and Chugai, and with Roche Group. It is associated with a Cifre agreement.

References

[1] R. A. Gatenby & P. M. Maini, "Mathematical oncology," *Nature*, vol. 421, pp. 321, 2003.

[2] H. M. Byrne, "Using mathematics to study solid tumour growth," in *Proceedings of the 9th General Meetings of European Women in Mathematics*, pp. 81-107, 1999.

[3] R. P. Araujo & D. L. S. McElwain, "A history of the study of solid tumour growth: the contribution of mathematical modelling," *Bulletin of Mathematical Biology*, vol. 66, pp. 1039-1091, 2004.

[4] R. Eftimie, J. L. Bramson & D. J. D. Earn, "Interactions between the immune system and cancer: a brief review of non-spatial mathematical models," *Bulletin of Mathematical Biology*, vol. 73, pp. 2-32, 2011.

[5] M. R. Owen & J. A. Sherratt, "Modelling the macrophage invasion of tumours: effects on growth and composition," *IMA Journal of Mathematics Applied in Medicine & Biology*, vol. 15, pp. 165-185, 1998.

[6] L. G. De Pillis, W. Gu & A. E. Radunskaya, "Mixed immunotherapy and chemotherapy of tumor: modeling, applications and biological interpretations," *Journal of Theoretical Biology*, vol. 238, pp. 841-862, 2006.

[7] L. M. Merlo, J. W. Pepper, B. J. Reid & C. C. Maley, "Cancer as an evolutionary and ecological process," *Nature Review Cancer*, vol. 6, pp. 924-935, 2006.

[8] J. Folkman, "What is the evidence that tumors are angiogenesis-dependent?," *Journal of the National Cancer Institute*, vol. 82, pp. 4-6, 1989.

[9] L. G. De Pillis & A. Radunskaya, "A mathematical tumor model with immune resistance and drug therapy: an optimal control approach," *Journal of Theoretical Medicine*, vol. 3, pp. 79-100, 2001.

[10] L. G. De Pillis & A. Radunskaya, "The dynamics of an optimally controlled tumor model: a case study," *Mathematical and Computer Modelling*, vol. 37, pp. 1221-1244, 2003.

[11] F. Hillen, A. W. Griffioen, "Tumour vascularization : sprouting angiogenesis and beyond," *Cancer Metastasis Review*, vol. 26, pp. 489-502, 2007.

[12] M. R. Young, "Endothelial cells in the eyes of an immunologist," *Cancer Immunology and Immunotherapy*, vol. 61 (10), pp. 1609-1616, 2012.

[13] V. S. Salsman et al., "Crosstalk between medulloblastoma cells and endothelium triggers a strong chemotactic signal recruiting T lymphocytes to the tumor microenvironment," *PLoS ONE*, vol. 6 (5), e20267, 2012.

[14] I. Brazzoli, E. De Angelis & P.-E. Jabin, "A mathematical model of immune competition related to cancer dynamics," *Mathematical Methods in the Applied Sciences*, vol. 33, pp. 733-750, 2010.

[15] C. Letellier, F. Denis & L. A. Aguirre, "What can be learned from a chaotic cancer model?" *Journal of Theoretical Biology*, vol. 322, pp. 7-16, 2013.

[16] F. Denis, C. Letellier, "Chaos Theory and radiotherapy: the tit and the butterfly," *Cancer Radiotherapy*, vol. 16 (5-6), pp. 404-409, 2012.

[17] F. Denis, C. Letellier, "Chaos theory: a fascinating concept for oncologist," *Cancer Radiotherapy*, vol. 16 (4), pp. 230-236, 2012.

[18] D. Liao, Y. Luo, D. Markowitz, R. Xiang, R. A. Reisfeld, "Cancer associated fibroblasts promote tumor growth and metastasis by modulating the tumor immune microenvironment in a 4T1 murine breast cancer model," *PLoS ONE*, vol. 4 (11), e7965, 2009.

[19] Y. Raz, N. Erez, "An inflammatory vicious cycle: Fibroblasts and immune cell recruitment in cancer," *Experimental Cell Research*, vol. 319, pp. 1596-1603, 2013.

[20] G. N. Naumov, L. A. Akslen, J. Folkman, "Role of angiogenesis in human tumor dormancy: animal models of the angiogenic switch," *Cell Cycle*, vol. 5 (16), pp. 1779-1787, 2006.

[21] G. N. Naumov, J. Folkman, O. Straume & L. A. Akslen, "Tumor-vascular interactions and tumor dormancy," *Acta Pathologica, Microbiologica et Immunologica Scandinavica*, vol. 116 (7-8), pp. 569-585, 2008.

Proceedings of ICCSA 2014
Normandie University, Le Havre, France - June 23-26, 2014

STABILIZABILITY AND IMPULSIVE CONTROL OF A FOUR–DIMENSIONAL CANCER MODEL

M. Di Felice [*], E. Pihan [†], S. Attioui [‡], L. Viger [§], J.-P. Barbot [¶],
S. Di Gennaro [‖], F. Denis [*&], C. Letellier [††]

Abstract. A four-dimensional cancer model describing interactions between host, immune, tumor and endothelial cells was investigated via a stability analysis exibiting the key parameter for controlling the dynamics toward a tumor-free site. Such a result was also supported by a less local approach based on a Lyapunov function. A treatment based on an impulsive control technique was proposed: the effect of the delay with which the action (killing a certain amount of the tumor cells) is applied was also investigated.

Keywords. Tumoral Growth, Positive Systems, Chaotic Behavior, Lyapunov Analysis, Impulsive Systems.

1 Introduction

Understanding tumor dynamics is essential for developing treatments specific to a given cancer and, if possible, to a given patient [1, 2, 3, 4]. From this point of view, the mathematical modelling by differential equations of tumor growth and their study in the paradigm of the nonlinear dynamical systems theory are particularly suitable for explaining clinical observations [5, 6]. When interactions between tumor cells, immune cells and host cells are considered, the tumor growth can present some characteristics of a chaotic behavior [7]. Moreover, one of the most relevant properties of cancer dynamics is the so-called "angiogenic switch" associated with the transition from an avascular to a vascular tumor, that is, when neovessels are mobilized for providing dioxygen and nutriments to the tumor site [8]. The model here investigated therefore takes into account endothelial cells interacting with the three other populations and, consequently, reproduces the angiogenic switch [6].

In order to develop specific treatments, it is necessary to identify the most relevant parameter for controlling the dynamics toward a tumor-free site, more or less as it is expected from a hormonotherapy. Our aim is thus to force the solution of the considered cancer model to reach an healthy (tumor-free) singular state by acting on this key parameter which was selected using the control theory and, in particular, by investigating the controllability and the stabilizability of the cancer model. An (idealized) impulsive control technique was also developed for controlling the tumor growth.

2 A 4–Dimensional Cancer Model

In this work we consider the four-dimensional tumor growth model [6]

$$\begin{aligned}
\dot{X} &= \rho_1 X(1-X) - \alpha_{13} X z \\
\dot{y} &= \rho_2 y \frac{z}{1+z} - \alpha_{23} y z - \delta_2 y + \alpha_{24} y w \\
\dot{z} &= \rho_3 z(1-z) - \alpha_{31} X z - \alpha_{32} y z + \alpha_{34} z \frac{w}{1+w} \\
\dot{w} &= \rho_4 w \frac{z}{1+z} - \delta_4 w
\end{aligned} \tag{1}$$

describing the interactions between populations of host cells X, immune cells y, tumor cells z and endothelial cells w. The parameter values (Tab. 1) of system (1) are chosen in such a way that the asymptotic solution is a chaotic attractor $\mathcal{A}$. Two projections in three–dimensional subspaces of the chaotic attractor $\mathcal{A}$ issued from the initial state $(X(0), y(0), z(0), w(0))^T = (0.8, 0.1, 0.3, 0.2)^T$ are shown in Figs. 1.

[*]Department of Information Engineering, Computer Science and Mathematics — Center of Excellence DEWS, University of L'Aquila, Italy.
[†]ECS-lab EA 3649 ENSEA 6 Avenue du Ponceau, 95014 Cergy-Pontoise, France.
[‡]ECS-lab EA 3649 ENSEA 6 Avenue du Ponceau, 95014 Cergy-Pontoise, France.
[§]CORIA-UMR 6614 — Normandie Université, CNRS-Université et INSA de Rouen Campus Universitaire du Madrillet 76800 Saint-Etienne du Rouvray, France.
[¶]ECS-lab EA 3649 ENSEA 6 Avenue du Ponceau, 95014 Cergy-Pontoise, France and EPI Non–A, INRIA, Lille Nord–Europe, France.
[‖]Department of Information Engineering, Computer Science and Mathematics — Center of Excellence DEWS, University of L'Aquila, Italy.
[**]Centre Jean Bernard, 9 rue Beauverger, 72000 Le Mans, France
[††]CORIA-UMR 6614 — Normandie Université, CNRS-Université et INSA de Rouen Campus Universitaire du Madrillet 76800 Saint-Etienne du Rouvray, France.

Table 1: Parameter values of system (1) leading to a chaotic attractor $\mathcal{A}$ corresponding to an avascular tumor.

$\rho_1 = 0.518$	$\alpha_{13} = 1.5$	$\rho_2 = 4.5$	$\alpha_{23} = 0.2$
$\delta_2 = 0.5$	$\alpha_{31} = 1$	$\alpha_{32} = 2.5$	$\alpha_{24} = 0.3$
$\alpha_{34} = 0.75$	$\delta_4 = 0.0909$	$\rho_4 = 0.86$	

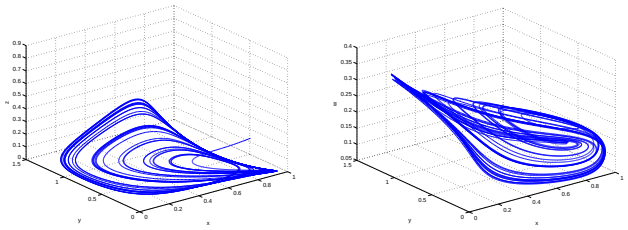

(a) Subspace $\mathbb{R}^3(X, y, z)$ (b) Subspace $\mathbb{R}^3(X, y, w)$

Figure 1: State space of system (1) for parameter values as reported in Table 1.

Any trajectory in this attractor is associated with positive state variables. Indeed, the chaotic attractor $\mathcal{A}$ is located in the positive domain

$$\bar{D} = \{X, y, z, w \mid X \geq 0, y \geq 0, z \geq 0, \text{ and } w \geq 0\}.$$

Among the singular points of system (1), there is the point $\mathcal{S} \equiv (1, 0, 0, 0)^T$ corresponding to a site where only host cells are present: this singular point thus corresponds to a tumor-free site. We would like to impose to any trajectory initially in the attractor $\mathcal{A}$ to converge toward $\mathcal{S}$ by using small parameter variations and the smallest number of state measurements. Such a task will be investigated with the stability analysis around $\mathcal{S}$ in the next section.

3 Stability Analysis

We first consider the change of variable $x = 1 - X$ (the other variables are unchanged) in order to displace the singular point $\mathcal{S}$ at the origin of the state space. System (1) is thus transformed into

$$\begin{aligned}
\dot{x} &= -\rho_1 x(1-x) + \alpha_{13}(1-x)z \\
\dot{y} &= \rho_2 y\frac{z}{1+z} - \alpha_{23}yz - \delta_2 y + \alpha_{24}yw \\
\dot{z} &= \rho_3 z(1-z) - \alpha_{31}(1-x)z - \alpha_{32}yz + \alpha_{34}z\frac{w}{1+w} \\
\dot{w} &= \rho_4 w\frac{z}{1+z} - \delta_4 w\,.
\end{aligned} \tag{2}$$

The singular point $\mathcal{S}$ is located at $(0, 0, 0, 0)$ in the corresponding state space $\mathbb{R}^4(x, y, z, w)$. Let us start by defining the conditions under which the domain

$$D = \{x, y, z, w \mid x, y, z, w \in [0, 1]\}$$

remains invariant, that is, any trajectory issued from domain D remains in D.

Remark 3.1. This coordinate change is only considered for $X \in [0, 1]$ in order to preserve the system positivity. $\diamond$

3.1 Using linear form

The linear system associated with system (2) is

$$\begin{aligned}
\dot{x} &= -\rho_1 x + \alpha_{13} z \\
\dot{y} &= -\delta_2 y \\
\dot{z} &= -(\alpha_{31} - 1)z \\
\dot{w} &= -\delta_4 w.
\end{aligned} \tag{3}$$

The stability of system (3) at the origin depends on the eigenvalues of the matrix

$$A = \begin{bmatrix} -\rho_1 & 0 & \alpha_{13} & 0 \\ 0 & -\delta_2 & 0 & 0 \\ 0 & 0 & -(\alpha_{31}-1) & 0 \\ 0 & 0 & 0 & -\delta_4 \end{bmatrix}. \tag{4}$$

According to the structure of matrix A, the four eigenvalues are real and negative if and only if $\alpha_{31} > 1$, since the system parameters are positive. The global asymptotic stability of system (3) at the origin induces, at least locally, the asymptotic stability of nonlinear system (2) at the origin. The singular point $\mathcal{S}$ is thus a stable node under a single condition on parameter α_{31} which is therefore the most important parameter for stabilizing this point. According to this, the most important interactions are between host and tumor cells.

Normal form was introduced by Poincaré to study the stability at a bifurcation point (here corresponding to α_{31}, and each form characterizes an equivalent class via a diffeomorphism [9]. Kang and Krener introduced a new normal form for studying the controllability [10] at a singular controllability point which was later extended to the observability context [11]. It is therefore natural to use Poincaré's normal form for studying the stability of system (2) at the origin.

In order to do this, a new state variables transformation is considered in such a way that matrix (4) is rewritten as a diagonal one. This is obtained with the transformation

$$T = \begin{bmatrix} 1 & 0 & -\dfrac{\alpha_{13}}{\rho_1 + 1 - \alpha_{31}} & 0 \\ 0 & 1 & 0 & 0 \\ 0 & 0 & 1 & 0 \\ 0 & 0 & 0 & 1 \end{bmatrix}$$

whose inverse is

$$T^{-1} = \begin{bmatrix} 1 & 0 & \dfrac{\alpha_{13}}{\rho_1 + 1 - \alpha_{31}} & 0 \\ 0 & 1 & 0 & 0 \\ 0 & 0 & 1 & 0 \\ 0 & 0 & 0 & 1 \end{bmatrix}.$$

Consequently, the change of variables $z_e = Tx_e$ with $x_e = (x, y, z, w)^T$ is

$$z_e = \left(x - \frac{\alpha_{13}}{\rho_1 + 1 - \alpha_{31}}z,\ y,\ z,\ w\right)^T. \tag{5}$$

We thus obtained the diagonal matrix

$$\Lambda = TAT^{-1} = \begin{bmatrix} -\rho_1 & 0 & 0 & 0 \\ 0 & -\delta_2 & 0 & 0 \\ 0 & 0 & -(\alpha_{31}-1) & 0 \\ 0 & 0 & 0 & -\delta_4 \end{bmatrix}$$

which is the first term of the Poincaré normal form. The classical analysis using Poincaré's normal form ends at this point since transformation (5) removes the positivity of the state variables, a property required for performing a rather global analysis. Moreover, the analysis by using normal form would remain valid for values of parameter $\alpha_{31} \approx 1$, that is, near the bifurcation point, a condition not necessarily verified for any specific case of tumor growth.

3.2 Using a Lyapunov Approach

From system (2), and using a Taylor expansion of the terms $\frac{z}{1+z}$ and $\frac{w}{1+w}$, we obtained

$$\begin{aligned} \dot{x} &= -\rho_1 x(1-x) + \alpha_{13}(1-x)z \\ \dot{y} &= \rho_2 yz\big(1 - z + \mathcal{O}(z^2)\big) - \alpha_{23}yz - \delta_2 y + \alpha_{24}yw \\ \dot{z} &= z(1-z) - \alpha_{31}(1-x)z - \alpha_{32}yz \\ &\quad + \alpha_{34}zw\big(1 - w + \mathcal{O}(w^2)\big) \\ \dot{w} &= \rho_4 wz\big(1 - z + \mathcal{O}(z^2)\big) - \delta_4 w\,. \end{aligned} \tag{6}$$

Using the new restricted domain

$$D' = \big\{x, y, z, w \mid x, y, z, w \in [0, 1)\big\}\,, \tag{7}$$

we thus established the theorem as follows.

Theorem 3.1. *If the state vector $(x, y, z, w)^T$ of system (6) remains in D', it is possible to compute a Lyapunov function*

$$V = V^{[2]} + V^{[3]} + \cdots + V^{[g]}$$

at any order $2 \leq g \in \mathbb{N}$, such that V is positive definite, and $\dot{V}$ is negative definite. ◇

Proof: System (6) can be written as

$$\dot{x}_e = F = \sum_{j=1}^{\infty} F^{[j]}$$

where, for instance, the first two terms are

$$F^{[1]} = \begin{bmatrix} -\rho_1 x + \alpha_{13} z \\ -\delta_2 y \\ -(\alpha_{31}-1)z \\ -\delta_4 w \end{bmatrix} = Ax_e$$

and

$$F^{[2]} = \begin{bmatrix} \rho_1 x^2 - \alpha_{13} xz \\ \rho_2 yz - \alpha_{23} yz + \alpha_{24} yw \\ z^2 - \alpha_{31} xz - \alpha_{32} yz + \alpha_{34} zw \\ \rho_4 zw \end{bmatrix},$$

respectively. One can compute the desired Lyapunov function by considering, for a generic $k \geq 2$, the derivative of the Lyapunov candidate

$$\mathcal{V}_k = \sum_{i=2}^{k} V^{[i]}.$$

Deriving this Lyapunov candidate, one gets

$$\begin{aligned} \dot{\mathcal{V}}_k &= \sum_{i=2}^{k} \frac{dV^{[i]}}{dx_e}\left(F^{[1]} + F^{[2]} + \cdots + F^{[k-1]} + \cdots\right) \\ &= \left[\frac{dV^{[2]}}{dx_e}\left(F^{[1]} + F^{[2]} + \cdots + F^{[k-1]}\right) + \right. \\ &\quad + \frac{dV^{[3]}}{dx_e}\left(F^{[1]} + F^{[2]} + \cdots + F^{[k-2]}\right) + \cdots \\ &\quad \left. + \frac{dV^{[k]}}{dx_e}F^{[1]}\right] + \cdots \end{aligned}$$

where the member between brackets (made of elements up to order k) is assumed to be negative definite. The order-2 term ($k = 2$) is indeed negative definite since

$$\mathcal{V}_2 = V^{[2]} = \frac{\left(x - \frac{\alpha_{13}}{\rho_1 + 1 - \alpha_{31}} z\right)^2}{2} + \frac{y^2}{2} + \frac{z^2}{2} + \frac{w^2}{2} = \frac{1}{2} z_e^T z_e$$

with

$$\begin{aligned} \dot{\mathcal{V}}_2 = \dot{V}^{[2]} &= z_e^T \sum_{k=1}^{\infty} TF^{[k]} \\ &= \frac{dV^{[2]}}{dz_e} T\left(F^{[1]} + F^{[2]} + \cdots\right) \\ &= -z_e^T \Lambda z_e + \frac{dV^{[2]}}{dx_e}\left(F^{[2]} + \cdots\right) \end{aligned}$$

and $F^{[1]} = A_e T^{-1} z_e$, we have thus

$$\frac{dV^{[2]}}{dx_e} = x_e^T T^T T = \frac{dV^{[2]}}{dz_e} T, \qquad \frac{dV^{[2]}}{dz_e} = z_e^T = x_e^T T^T$$

and

$$\begin{aligned} \frac{dV^{[2]}}{dz_e} TF^{[1]} &= -z_e^T \Lambda z_e \\ &= -\rho_1 \left(x - \frac{\alpha_{13}}{\rho_1 + 1 - \alpha_{31}} z\right)^2 \\ &\quad - \delta_2 y^2 - (\alpha_{31} - 1) z^2 - \delta_4 w^2 < 0. \end{aligned}$$

The derivation of $V^{[2]}$ produces also third-order terms

$$p_3 = \frac{dV^{[2]}}{dx_e} F^{[2]} = p_3^- + p_3^+\,,$$

some of them being negative (designated by polynomial p_3^-) and some others being positive (designated by polynomial p_3^+). Considering as a new Lyapunov candidate

$$V^{[2]} + V^{[3]}$$

where $V^{[3]}$ is a third order positive definite function appropriately chosen; terms p_3^+ can be eliminated by terms of the $V^{[3]}$ derivative, that is, by terms of

$$\frac{dV^{[3]}}{dx_e}F^{[1]}\,.$$

Nevertheless, there are order-$(k+1)$ terms

$$\begin{aligned} p_{k+1} &= \sum_{i=2}^{k}\frac{dV^{[i]}}{dx_e}F^{[k+2-i]} = \frac{dV^{[2]}}{dx_e}F^{[k]} + \cdots + \frac{dV^{[k]}}{dx_e}F^{[2]} \\ &= p_{k+1}^- + p_{k+1}^+ \end{aligned}$$

which are also induced by this derivation. In the previous equation, we distinguished positive terms p_{k+1}^+ from negative ones p_{k+1}^-. For $k=2$, these terms are

$$p_3 = \frac{dV^{[2]}}{dx_e}F^{[2]} = p_3^- + p_3^+\,.$$

The objective is thus to design a Lyapunov candidate

$$\mathcal{V}_{k+1} = \sum_{i=2}^{k+1} V^{[i]} = \mathcal{V}_k + V^{[k+1]}$$

and, in particular, a positive definite function $V^{[k+1]}$ of order $k+1$ allowing to vanish p_{k+1}^+, and to aggregate simultaneously a negative definite term in such a way that

$$\frac{dV^{[k+1]}}{dx_e}F^{[1]} = -p_{k+1}^+ - \phi(x,y,z,w)$$

with $\phi(x,y,z,w) \geq 0$. Let us now distinguish the term $\bar{p}_{k+1}^+(x,y,z,w)$ depending on x from the term $\bar{\bar{p}}_{k+1}^+(y,z,w)$ which does not dependent on x; we thus have

$$p_{k+1}^+ = \bar{p}_{k+1}^+(x,y,z,w) + \bar{\bar{p}}_{k+1}^+(y,z,w)\,.$$

Correspondingly, let us decompose $V^{[k+1]}$ as

$$V^{[k+1]} = \bar{V}^{[k+1]}(x,y,z,w) + \bar{\bar{V}}^{[k+1]}(y,z,w).$$

The term $\bar{V}^{[k+1]}(x,y,z,w)$ is determined using $k+1$ steps as follows. It is possible to rewrite $\bar{p}_{k+1}^+(x,y,z,w)$ as a sum of polynomial terms, that is, as

$$\bar{p}_{k+1}^+(x,y,z,w) = \sum_{\substack{i,j,m,n=0\\ i+j+m+n=k+1}}^{k+1} c_{i,j,m,n}x^i y^j z^m w^n$$

where $c_{i,j,m,n}$ are non negative constant coefficients. It is also always possible to choose $\bar{V}_0^{[k+1]}(x,y,z,w)$ in such a way that

$$\begin{aligned} \frac{d\bar{V}_0^{[k+1]}}{dx}(-\rho_1 x) &= -\bar{p}_{k+1}^+(x,y,z,w) \\ &= -\sum_{\substack{i,j,m,n=0\\ i+j+m+n=k+1}}^{k+1} c_{i,j,m,n}x^i y^j z^m w^n. \end{aligned}$$

Integrating this equation, one obtains

$$\bar{V}_0^{[k+1]} = \frac{1}{\rho_1}\sum_{\substack{i,j,m,n=0\\ i+j+m+n=k+1}}^{k+1} c_{i,j,m,n}\frac{x^i}{i}y^j z^m w^n.$$

Nevertheless, with the choice of positive terms as introduced in $\dot{V}^{[k+1]}$, that is,

$$\frac{d\bar{V}_0^{[k+1]}}{dx}\dot{x} = \frac{d\bar{V}_0^{[k+1]}}{dx}(-\rho_1 x) + \frac{d\bar{V}_0^{[k+1]}}{dx}\alpha_{13}z$$

where

$$\begin{aligned} \frac{d\bar{V}_0^{[k+1]}}{dx}\alpha_{13}z &= \frac{\alpha_{13}}{\rho_1}\sum_{\substack{i,j,m,n=0\\ i+j+m+n=k+1}}^{k+1} c_{i,j,m,n}\frac{x^{i-1}}{i}y^j z^{m+1}w^n \\ &= \bar{p}_{1,k+1}^+(x,y,z,w) + \bar{\bar{p}}_{1,k+1}^+(y,z,w)\,, \end{aligned}$$

the order of x is decreased by one. Similarly to what was done for $V_0^{[k+1]}$, it is possible to choose $V_1^{[k+1]}$ such as

$$\frac{d\bar{V}_1^{[k+1]}}{dx}(-\rho_1 x) = -\bar{p}_{1,k+1}^+(x,y,z,w)\,.$$

This expression introduces in $\dot{V}^{[k+1]}$ a new positive term as

$$\frac{d\bar{V}_1^{[k+1]}}{dx}\alpha_{13}z = \bar{p}_{2,k+1}^+(x,y,z,w) + \bar{\bar{p}}_{2,k+1}^+(y,z,w).$$

Again, the order of x is decreased by one. Hence, using $g \leq k+1$ steps it is possible to remove x from $\dot{V}^{[k+1]}$ with $g = \max i$ such that $c_{i,j,m,n} \neq 0$ and $x^i y^j z^m w^n$ is of order $k+1$. At the end of this iterative process,

$$\dot{V}^{[k+1]} = \bar{\bar{p}}_{k+1}^+(y,z,w) + \sum_{i=1}^{g}\bar{\bar{p}}_{j,k+1}^+(y,z,w)\,.$$

is only a function of variables y, z, and w. Checking that $\dot{V}^{[k+1]}$ is positive is then immediate since, for instance, if

$$\begin{aligned} \bar{\bar{V}}^{[k+1]}(x,y,z,w) = &\left(\bar{\bar{p}}_{k+1}^+(y,z,w) + \sum_{j=1}^{g}\bar{\bar{p}}_{j,k+1}^+(y,z,w)\right)\times \\ &\times\left(\frac{y}{\delta_2} + \frac{z}{(1-\alpha_{31})} + \frac{w}{\delta_4}\right) \end{aligned}$$

is derived with respect to y, z or w, there are only negative terms of order $k+1$. Therefore,

$$V^{[k+1]} = \sum_{i=0}^{g-1}\bar{V}_i^{[k+1]}(x,y,z,w) + \bar{\bar{V}}^{[k+1]}(x,y,z,w).$$

This ends the proof. □

Lemma 3.1. *Let us consider the order-($g = 3$) approximation*

$$\mathcal{V}_a = V^{[2]} + V^{[3]} = \frac{x^2}{2} + \frac{y^2}{2} + \frac{z^2}{2} + \frac{w^2}{2} + \frac{\alpha_{13}xz}{(\alpha_{31}-1)} + \frac{\alpha_{13}z^2}{2(\alpha_{31}-1)} + \frac{x^3}{3} + \frac{\alpha_{13}x^2z}{\rho_2 2} + \frac{\alpha_{13}xz^2}{\rho_1} + \frac{\alpha_{31}xz^2}{\rho_1} + \frac{\rho_2 y^2 z}{(\alpha_{31}-1)} + \frac{\alpha_{24}y^2w}{\delta_4} + \frac{\alpha_{34}z^2w}{\delta_4} + \frac{\rho_4 z w^2}{(\alpha_{31}-1)} + \frac{\alpha_{13}^2 z^3}{3\rho_1(\alpha_{31}-1)} + \frac{\alpha_{31}^2 z^3}{3\rho_1(\alpha_{31}-1)}$$

of the Lyapunov candidate. If the initial state $(x(0), y(0), z(0), w(0))$ is in the domain

$$D_0 = \left\{ (x_0, y_0, z_0, w_0) \mid V(x_0, y_0, z_0, w_0) < \frac{1}{2} \right\} \quad (8)$$

then the initial state is in D' given by (7). ◇

Proof: The proof is a direct consequence of the worst case. □

Proposition 3.1. *Let system (1) be approximated at order 3 and the initial state be in D_0 given by (8). Then the trajectory remains in D', as defined in (7), at any time and converges to the origin $(0, 0, 0, 0)^T$.* ◇

Proof: The proof results from Theorem 3.1 and the definition given for D_0. □

Simulations using two different values of α_{31} confirms the strong dependence of the solution to system (1) on the value of this parameter: in both cases, the initial state is $(0.8, 0.1, 0.3, 0.2)$. With $\alpha_{31} = 1$, the solution is chaotic (Figs. 2); it converges to the singular point $\mathcal{S}$ with $\alpha_{31} = 1.1$ (Figs. 3). Making the host cells slightly more agressive against tumor cells is therefore sufficient to retrieve a tumor-free site.

From the biological point of view, modifying the value of α_{31} could be done in two ways: i) the population of host cells is stimulated to be more aggressive against tumor cells, or ii) tumor cells can be weakened. In the first case, molecules (proteins such as enzymes) must be identified for only acting positively on host cells via adequate receptors. When injected in patient, these molecules would bind to their receptors expressed by host cells for activating the molecule function which can produce, for instance, an increase of host cell proliferation. In the second case, molecules having a negative effect on tumor cells must be found. Such molecules would stimulate the growth of inhibitors only recognizing tumor cells or molecules with a very selective action as those used in hormonotherapy [12]. The resulting binding blocks the link between the hormone and the receptor, thus inducing a lack of intratumoral growth signal and an absence of tumor cell proliferation. Today, strategies acting on tumor cells exists. Selective action on host cells is more complicated because receptors specific to host cells are not yet identified, despite the obvious interest in acting on host cells to fight againt tumor growth.

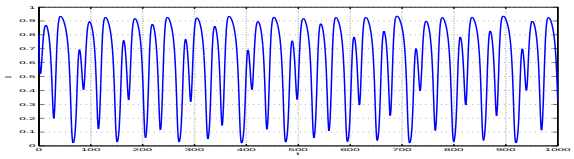

(a) variable x: host cells

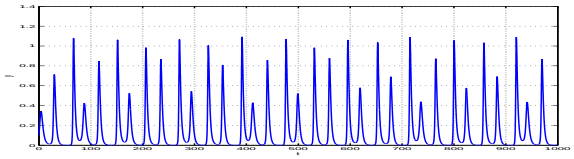

(b) variable y: immune cells

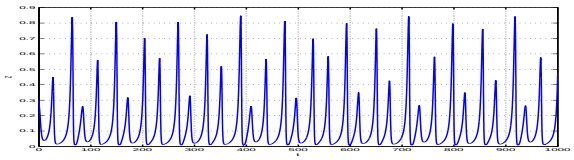

(c) variable z: tumor cells

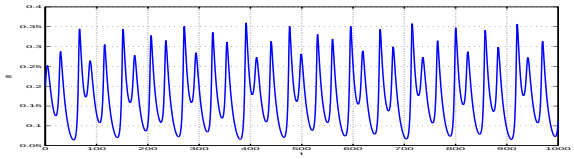

(d) variable w: endothelial cells

Figure 2: Chaotic solution to system (1) with $\alpha_{31} = 1$.

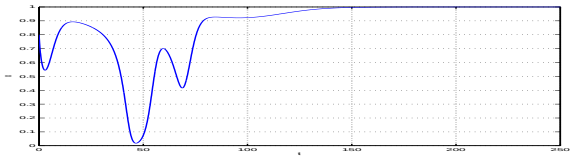

(a) variable x: host cells

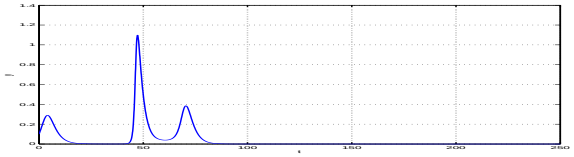

(b) variable y: immune cells

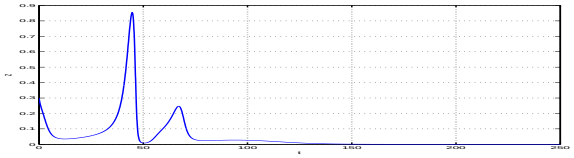

(c) variable z: tumor cells

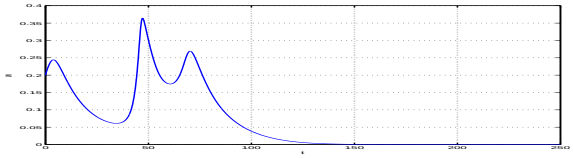

(d) variable w: endothelial cells

Figure 3: Transient regime toward the singular point $\mathcal{S}$ issued from the initial state $(0.8, 0.1, 0.3, 0.2)$ with $\alpha_{31} = 1.1$ Other parameter values as reported in Tab. 1.

4 Impulse control of tumor growth

Although it has been proved that increasing α_{31} beyond 1.0 led to a convergence toward the singular point $\mathcal{S}$, that is, toward a tumor-free site, we are still looking for a feasible biological procedure; we therefore investigated another technique for controlling the tumor growth.

4.1 Numerical evidences

When a surgery for removing the whole tumor is not possible, common treatments in cancer are based on killing a certain amount μ of tumor cells by i) chemiotherapy applied at one to three weeks of intervals during 3 to 6 months, ii) daily radiotherapy (5 days a week) for 6 to 7 weeks [13] or, iii) both combined [14, 15, 16]. As a first step in our investigations, we considered that such a treatment was ideally selective and thus able to only affect tumor cells. While common clinical treatments are applied at constant interval of time, it was noticed during our simulations that a much more effective strategy consists in using a threshold value $z_{\rm th}$ on the population of tumor cells to trigger the action. Considering that an oscillation of the cell populations as shown in Figs. 2 lasts for about one month and that there is always a delay δ between detecting the threshold value $z_{\rm th}$ and triggering the treatment, we investigated different threshold values $z_{\rm th}$ and different delays δ (expressed in days). At each treatment, we considered that a ratio μ of tumor cells (in % of the actual value z) was killed. By default, the initial state was $(X(0), y(0), z(0), z(0)) = (0.8, 0.1, 0.3, 0.2)$. Depending on the treatment parameters $z_{\rm th}$, δ and μ, we distinguished five main scenarios, three of them leading to a tumor-free site and two others with sustained chaotic oscillations in the populations of cells. These scenarios are as follows.

1. Type-I efficient treatment: after a few (or even none) oscillations, the trajectory converges monotonously toward the singular point $\mathcal{S}$ (Figs. 4);

2. Type-II efficient treatment: the transient regime presents some oscillations before the monotonous convergence toward the singular point $\mathcal{S}$ (Figs. 5);

3. Type-III efficient treatment: the trajectory converges toward the singular point $\mathcal{S}$ only after a rather long transient regime during which there are long — deleterous — durations corresponding to a very small population of host cells (Figs. 6);

4. Type-I inefficient treatment: the trajectory remains on a chaotic attractor with a population of tumor cells always less than 1, there is therefore no vascularization of the tumor but, globally, the treatment is inefficient (Figs. 7);

5. Type-II inefficient treatment: the trajectory remains on a chaotic attractor with a population of tumor cells which can be greater than 1, thus inducing a vascularization of the tumor; the treatment is deleterous since it contributes to develop the tumor (Figs. 8).

Type-II efficient treatment may be characterized by pretty fast convergence toward a tumor-free site (singular point $\mathcal{S}$) although after some oscillations: these cases are designated as type-II* efficient treatment.

Table 2: Efficiency of the treatment depending on the threshold value $z_{\rm th}$, the delay δ (in days) with which it is applied and, the amount μ of killed tumor cells.

δ	$z_{\rm th}$	μ	Treatment
1	$[0.1, 0.9]$	10% or 20%	Type-I efficient**
2	≤ 0.11	10%	Type-III efficient
	0.12		Type-II efficient
	0.15		Type-II efficient
	0.2		Type-II efficient
	0.3		Type-II* efficient
	≥ 0.4		Type-III efficient
	≤ 0.29	20%	Type-I efficient
	0.3		Type-II efficient
	≥ 0.31		Type-I efficient
3	≤ 0.1	10%	Type-I inefficient
	> 0.1		Type-II inefficient
	0.1	20%	Type-III efficient
	0.2		Type-II efficient
	0.3		Type-II* efficient
	0.4		Type-II efficient
	0.5		Type-II efficient
	0.6		Type-III efficient
	≥ 0.7		Type-II efficient
4	any	10%	Type-I efficient **
	≤ 0.4	20%	Type-III efficient
	0.5		Type-II efficient
	0.6		Type-II inefficient
	0.7		Type-III efficient
	≥ 0.8		Type-II inefficient

**Verified for different initial conditions.

4.2 Mathematical Proof of the Stability Properties

In this subsection a stability analysis with respect to δ and μ is performed in order to justify mathematically the proposed treatment. From system (1), the dynamics governing the tumor cell population z is

$$\begin{aligned}\dot{z} &= \rho_3 z(1-z) - \alpha_{31} X z - \alpha_{32} y z + \alpha_{34} z \frac{w}{1+w} \\ &\leq z - z^2 + \frac{\alpha_{34}}{2} z = \alpha z - z^2\end{aligned}$$

where $\alpha = 1 + \frac{\alpha_{34}}{2}$ corresponds to the worst scenario with respect to x, y and w by setting $X = 0$, $y = 0$, $w = 1$. We here considered $\rho_3 = 1$ as in all numerical simulations performed in this paper. This allows to obtain a conservative but guaranteed stability condition which only depends on

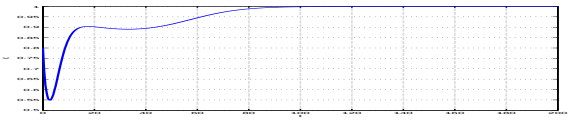

(a) Variable X: host cells

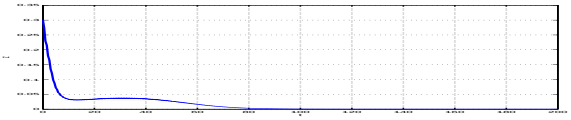

(b) Variable z: tumor cells

Figure 4: Type-I efficient treatment: the tumor is removed after a very few actions. Treatment parameter values: $\delta = 1$, $z_{\text{th}} = 0.3$ and μ=10%.

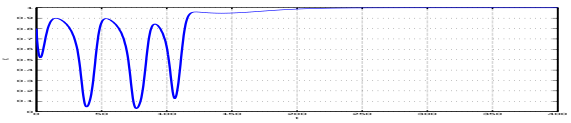

(a) Variable X: host cells

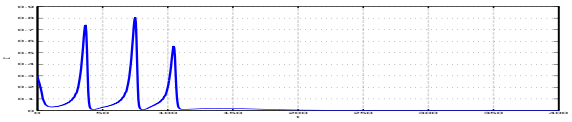

(b) Variable z: tumor cells

Figure 5: Type-II efficient treatment: three actions were here required for removing the tumor. Treatment parameter values: $\delta = 1$, $z_{\text{th}} = 0.2$ and μ=10%.

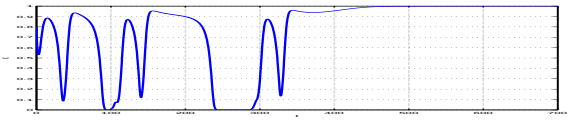

(a) Variable X: host cells

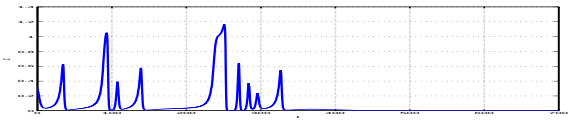

(b) Variable z: tumor cells

Figure 6: Type-III efficient treatment: six actions were here necessary for removing the tumor after a long duration with a very small population of host cells. Treatment parameter values: $\delta = 2$, $z_{\text{th}} = 0.5$ and μ=10%.

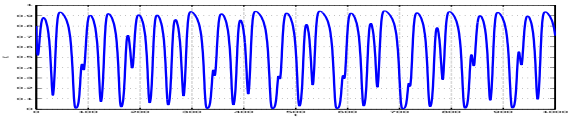

(a) Variable X: host cells

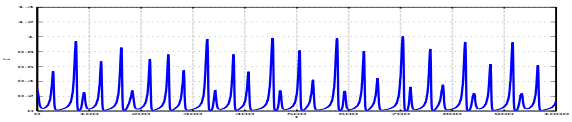

(b) Variable z: tumor cells

Figure 7: Type-I inefficient treatment: the populations present sustained chaotic oscillations but there are always less than 1, meaning that there is no angiogenesis. Treatment parameter values: $\delta = 4$, $z_{\text{th}} = 0.5$ and μ=10%.

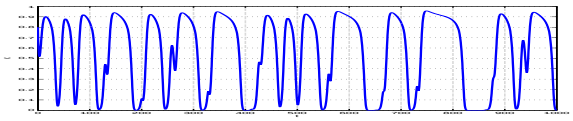

(a) Variable X: host cells

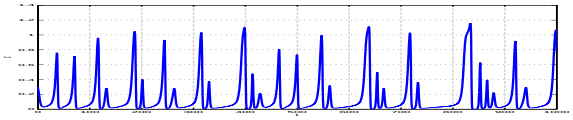

(b) Variable z: tumor cells

Figure 8: Type-II inefficient treatment: despite the actions, the populations present sustained chaotic oscillations and some of them can greater than 1, meaning that the angiogenic switch occured. Treatment parameter values: $\delta = 4$, $z_{\text{th}} = 0.9$ and μ=10%.

z. By setting $\zeta = z^{-1}$, the resulting Bernoulli differential equation

$$\dot{\zeta} = -z^{-2}\dot{z} \geq -\alpha\frac{1}{z} + 1 = -\alpha\zeta + 1$$

can be easily solved analytically, thus leading to the solution

$$\zeta(t) \geq \frac{\alpha\zeta(t_i) - 1}{\alpha} e^{-\alpha(t-t_i)} + \frac{1}{\alpha}$$

for t in the time interval $[t_i, t_{i+1})$. This solution can be also expressed using variable z as

$$z(t) \leq \frac{1}{\zeta(t)} = \frac{\alpha}{1 - \left(1 - \dfrac{\alpha}{z(t_i)}\right) e^{-\alpha(t-t_i)}}, \quad t \in [t_i, t_{i+1})$$

with $i \in \mathbb{N}$. The aim is now to compute the time t_i at which the action is applied for ensuring the convergence of z towards zero. Hence, μ must satisfy the inequality

$$|\mu z(t_{i+1})| < |z(t_i)|\,.$$

Since system (1) has only positive solutions, this inequality is equivalent to $\mu z(t_{i+1}) < z(t_i)$, or

$$\mu\frac{z(t_{i+1})}{z(t_i)} < 1$$

which can be rewritten as

$$\mu\frac{z(t_{i+1})}{z(t_i)} = \mu\frac{\alpha}{z(t_i) - (z(t_i) - \alpha)e^{-\alpha(t_{i+1}-t_i)}} < 1\,.$$

For the sake of simplicity, we simply considered a constant delay $\delta = t_{i+1} - t_i$ (more complicated procedure can be imagined) and we choose the initial time as $t_0 = 0$; one thus gets the condition on the killing rate of tumor cells

$$\mu < \frac{1 - e^{-\alpha\delta}}{\alpha} z(0) + e^{-\alpha\delta}\,.$$

This condition on the killing rate is obviously based on the assumption (at least conservative) that the population of

tumor cells at the initial time is known. When this is not the case, it is possible to consider the more conservative condition

$$\mu < \mu_{\min} = e^{-\alpha\delta} .$$

In such a case, one can choose $\mu = \mu_{\min}$ and starts the first action at $t = 0$, thus ensuring that z never reaches 1.

5 Conclusions

In this paper, a stability analysis of a four dimensional cancer model was performed: the key parameter controlling the tumor growth is the one defining interactions between host and tumor cells. It can be shown that it is efficient to kill a rather small amount of tumor cells when this population just starts to grow; tumor cells can be removed from a given tumor site after very few oscillations (if not none) when the delay of the action is not too large (typically one day). It was shown that larger the delay, less efficient the treatment. These numerical evidences were supported by a proof for the stability of the tumor-free site under the proposed treatment. In the present work, the treatment was supposed to be ideally selective (only tumor cells were killed) and its action was immediate, two properties chemiotherapy and radiotherapy do not have. For instance, in radiotherapy, the amount of tumor cells killed by each session can be from 0.5 to 5% (and cells actually die between 1 to 3 months after the session) [17]. In chemiotherapy, the amount of cells is between 10 and 20% [18]. The delay with which the treatment is actually effective will therefore be considered in future works as well as a lack of selectivity in the cells affected.

References

[1] H. Byrne, Using mathematics to study solid tumour growth, in *Proceedings of the 9th General Meetings of European Women in Mathematics*, pp. 81-107, 1999.

[2] R. A. Gatenby & P. M. Maini, Mathematical oncology: Cancer summed up, *Nature*, vol. 421, p. 321, 2003.

[3] H. Byrne, Dissecting cancer through mathematics: from the cell to the animal model, *Nature Review Cancer*, vol. 10, pp. 221-230, 2010.

[4] A. H. Chauviere, H. Hatzikirou, J. S. Lowengrub, H. B. Frieboes, A. M. Thompson & V. Cristini, Mathematical oncology: How are the mathematical and physical sciences contributing to the war on breast cancer? *Current Breast Cancer Reports*, vol. 2, pp. 121-129, 2010.

[5] C. Letellier, F. Denis & L. A. Aguirre, What can be learned from a chaotic cancer model? *Journal of Theoretical Biology*, vol. 322, pp. 7-16, 2013.

[6] L. Viger, F. Denis, M. Rosalie & C. Letellier, A cancer model for the angiogenic switch, *Journal of Theoretical Biology*, submitted.

[7] M. Itik & S. P. Banks, Chaos in three-dimensional cancer model, *International Journal of Bifuraction and Chaos*, vol. 20, pp. 71-73, 2010.

[8] L. M. Merlo, J. W. Pepper, B. J. Reid & C. C. Maley, Cancer as an evolutionary and ecological process, *Nature Review Cancer*, vol. 6, pp. 924-935, 2006.

[9] H. Poincaré, Solutions périodiques dans le voisinage d'un point d'équilibre — Lunes sans quadrature, *Les Méthodes Nouvelles de la Mécanique Céleste*, Gauthier–Villars, pp. 156–161, 1892.

[10] W. Kang & A. J. Krener, Extended quadratic controller normal form and dynamic state feedback linearization of nonlinear systems, *SIAM Journal on Control and Optimization*, Vol. 30, pp. 1319–1337, 1992.

[11] G. Zheng, D. Boutat & J.-P. Barbot, Single output–dependent observability normal form, *SIAM Journal on Control and Optimization*, Vol. 46, pp. 2242–2255, 2007.

[12] J. Abraham & J. Staffurth, Hormonal therapy for cancer, *Medicine*, vol. 39, pp. 723-727, 2011.

Certain of these molecules bind to the hormone dependant receptor on the tumor cell surface.

[13] J. M. Michalski, Y. Yan, D. Watkins-Bruner, W. R. Bosch, K. Winter, J. M. Galvin, J. P. Bahary, G. C. Morton, M. B. Parliament & H. M. Sandler, Preliminary toxicity analysis of 3-dimensional conformal radiation therapy versus intensity modulated radiation therapy on the high-dose arm of the Radiation Therapy Oncology Group 0126 prostate cancer trial, *International Journal of Radiation Oncology Biology Physics*, vol. 87, pp. 932-938, 2013.

[14] M. Al-Sarraf, M. LeBlanc, P. G. Giri, K. K. FuK, J. Cooper, T. Vuong, A. A. Forastiere, G. Adams, W. A. Sakr, D. E. Schuller & J. F. Ensley, Chemoradiotherapy versus radiotherapy in patients with advanced nasopharyngeal cancer: phase III randomized Intergroup study 0099, *Journal of Clinical Oncology*, vol. 16, pp. 1310-1317, 1998.

[15] A. Herskovic, K. Martz, M. al-Sarraf, L. Leichman, J. Brindle, V. Vaitkevicius, J. Cooper, R. Byhardt, L. Davis & B. Emami, Combined chemotherapy and radiotherapy compared with radiotherapy alone in patients with cancer of the esophagus, *New England Journal of Medicine*, vol. 326, no. 24, pp. 1593-1598, 1992.

[16] Y. J. Beijer, M. Koopman, C. H. J. Terhaard, W. W. Braunius, R. J. J. van Es & A. de Graeff, Outcome and toxicity of radiotherapy combined with chemotherapy or cetuximab for head and neck cancer: Our experience in one hundred and twenty-five patients, *Clinical Otolaryngology*, vol. 38, pp. 69-74, 2013.

[17] T. Waldman, Y. Zhang, L. Dillehay, J. Yu, K. Kinzler, B. Vogelstein & J. Williams, Cell cycle arrest versus cell death in cancer therapy, *Nature Medicine*, vol. 3, pp. 10341036, 1997.

[18] S. Gwe Ahn, S. Ah Lee, H. Woo Lee, H. Min Lee & J. Jeong, In vitro chemoresponse assay based on the intrinsic subtypes in breast cancer, *Japanese Journal of Clinical Oncology*, online, 2014.

Proceedings of ICCSA 2014
Normandie University, Le Havre, France - June 23-26, 2014

CHARACTERIZATION OF THE DYNAMICS UNDERLYING COMPUTER MEDIATED COMMUNICATION OF VISUALLY IMPAIRED AND NORMAL TEENAGERS

Aurélie Vallée *, Katia Rovira*, Monica N. Toba* & Christophe Letellier †

Abstract. In order to investigate whether visually impaired and sighted teenagers interact in a similar way via mediated communication, we designed a protocol in which two participants interact via two connected perceptual supplementation devices. The two participants were asked to cooperate for locating a public object. We compared the probability for correct joint location and the dynamics of their spatial explorations.

Keywords. Joint action, interaction dynamics, visually impaired teenagers

1 Introduction

According to De Jaegher *et al.* [1], interactions are defined as "mutually engaged co-regulated coupling between at least two autonomous agents where the co-regulation and the coupling mutually affect each other, and constitute a self-sustaining organization in the domain of relational dynamics". Such a co-regulation is possible through verbal as well as non verbal interactions. Indeed, nonverbal interactions can be developed by the perception of movements of eyes, faces, hands and body of other individuals thus providing information about their action and intention [2]. Such behaviors are involved in a complex form of social interactions, the so-called joint action defined as "any form of social interaction whereby two or more individuals coordinate their actions in space and time to bring about a change in the environment" [3]. So, one needs to see the other individuals to coordinate their actions with his own ones for achieving a common task. An important problem arises when someone does not have access to visual modality. Without vision, the smooth development of interactions is strongly compromised. Several authors asserted that children with visual impairment present various types of deficits in social interactions [4, 5, 6], leading to social isolation, mainly due to quite difficult exchanges with sighted peers.

But today social interactions between teenagers have changed. They are over using social network (90% of young Europeans aged from 12 to 18 years, according to IPSOS, 2013) and are interacting through game online like MMORPG (Massively Multiplayer Online Role Playing Game): this is the so-called *mediated communication*. We can expected that, throught this new type of communication, the interaction between sighted teenagers and visually impaired teenagers takes place without difficulties. However, Lefebvre, Perron & Pauchet [7], who studied non-verbal behaviour while using a collaborative virtual storytelling device (VIRSTORY), found that the vision of partners' communicative behavior (through their avatars) is as important as during non-mediated communication. It is therefore expected that visually impaired teenagers would have difficulties for interacting with sighted teenagers through mediated communication.

Several sensory substitution devices have been created for allowing visually impaired persons to access to mediated communication taking advantage of their haptic compentence. For instance, "Tactos" is a perceptual supplementation device allowing to explore and to read digital shapes appearing in a computer screen by the means of tactile stimulation induced by controlling the activation of piezoelectric Braill cells depending on the cursor movements in the two-dimensional space of the screen [8]. Two peripheral elements, an effector (the pointer of the mouse) and a tactile stimulator are connected to the computer; when the latter crosses at least one black pixel of the screen, a tactile stimulator is activated. Several studies showed that visually impaired adolescents are thus able to locate, recognize, categorize and identify digital shapes more or less complex [9, 10].

When several "Tactos" systems are connected in a network, this constitutes a new device named "Intertact". Each user, by the means of his effector, controls i) the movements of a matrix of receptor fields, that is, a perceiving body that is coupled to the same number of tactils stimulators and, ii) the movements of an avatar, that is, a body-image that the other users can perceive with their own receptor fields. By this way, when one user touches the other, he is also touched by him. This latter device allows to investigate interaction processes involved in computer mediated communication, like joint activities. A

*UPRES PSY-NCA - EA 4306 — Normandie Université, Rue Lavoisier 76821 Mont Saint Aignan, France. E-mail: valleaur@gmail.com

†CORIA-UMR 6614 — Normandie Université, CNRS-Université et INSA de Rouen Campus Universitaire du Madrillet 76800 Saint Etienne du Rouvray, France.

recent study with sighted adults [11] has been conducted to investigate the posibility for interactions to perform a cooperative task. Participants enter into contact, either with objects existing in the shared environment, or with the body-image of the other user. The final goal is that each participant must locate the object shared with the other. There is three conditions governning interactions according to the type of tactile stimulation :

1. Differentiated : the 4 top pins are activated when a subject encounters the other and the 4 down pins are activated when he encounters an object;
2. Mono : all the pins are activated when the participant encounters the other or an object;
3. Parallelism: pins are activated one by one, thus providing access to the other participant.

Deschamps' results show that participants actually interact and coordinate their perceptual activities mainly with "Differentiated" tactile simulation. So, unlike the conclusion provided by the study VIRSTORY, an individual seems to be able to interact and to joint act without vision. We thus propose to use a similar experimental configuration to those conducted by Deschamps [11] for determining whether visually impaired teenagers and sighted teenagers interact and jointly act within "Intertact" in the same way as sighted teenagers.

2 Experimental Protocol

Similarly to the study conducted by Deschamps [11] with adults, 12 visually impaired teenagers and 10 sighted teenagers (MA : 13 years old and 6 month) were invited to interact and cooperate via the "Intertact" setup. We created a "Plateform game" scenario for stimulating teenagers' interactions. Participants were grouped by pairs (matched age and visual status). Each subject moves along a shared one-dimensional space of 400 pixels by the means of a mouse. In the virtual space at their disposal, participants can encounter two types of object: the "public object" perceived by both participants and the "private" object only perceived by one of the two participants. Participant receives a tactile stimulation when his cursor encounters the cursor of his partner or an object. We used two of the three conditions governing interactions via tactile simulation for our experimental protocol: there are the two conditions retained in the study conducted by Deschamps [11], that is, "Differentiated" and "Parallelism". The condition "Mono" was judged irrelevant according to previous results.

Each participant is asked to practice for 16 sessions of one minute each (eight sessions by condition). There were five training sessions (not recorded) for each condition. In each session, the participant had to interact with the other participant to locate the public object. At the end of each session, participants were asked to click at the location where they think the public object was. At the end of the experiment, we made a debriefing with the two participants.

3 State Space Reconstruction

Our aim is to investigate the dynamics underlying interactions between our teenagers using some concepts borrowed from the nonlinear dynamical systems theory. In order to do that, the first step is to reconstruct from the available measurements an adequate state space [12]. The measured data consist in the successive locations of the pointer in a segment of 400 pixels. The particularity is that when the pointer is at the right (left) end of the segment, it automatically switches to the other end, thus introducing a discontinuity in the data which must be removed (the analysis of a trajectory in the state space is always performed in the paradigm of determinism). The pointer motion is therefore mapped into a plane, along a circle with a 400 pixel perimeter, that is, with a radius $R = \frac{400}{2\pi}$. The location is thus determined by the angle

$$\theta = \frac{X}{R}\,, \tag{1}$$

or, equivalently, by the two coordinates

$$\left| \begin{array}{l} x = R\cos\theta \\ y = R\sin\theta\,. \end{array} \right. \tag{2}$$

The set of locations actually visited by each teenager thus forms an arc of a circle (or a circle in certain cases) as shown in Fig. 1. The portion of the space explored can be quantified using the "angular aperture" $\Delta\theta = \theta_{\max} - \theta_{\min}$.

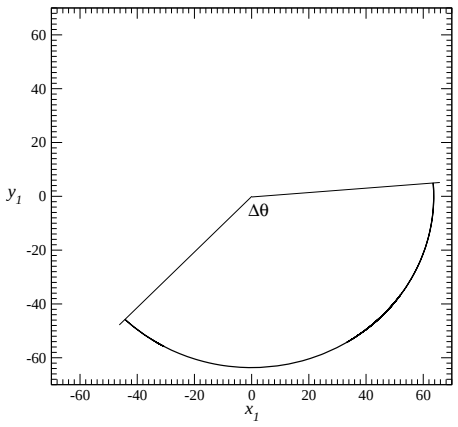

Figure 1: Projection of the evolution of the pointer driven by a teenager. Case of subject 1 from the pair 1 of normal teenargers interacting using condition 1.

The dynamics underlying interactions between teenagers could be investigated from the relative locations (x, y). Nevertheless, since the cooperative task proposed to these teenagers was to locate the public object using their mediated interactions, it was convenient

to investigate individual dynamics for checking how each participant was able to locate the public object, the relative motion being saved for investigating joint action. Individual dynamics was therefore investigated using location (x_i, y_i) of the ith participant. It appeared that interactions between participants strongly depends on the velocities with which each pointer was moved (see next section). The pointer motion of each teenager can be investigated using a representation focused on the ith subject and using the location of his pointer $\vec{x}_i = (x_i, y_i)$ from which the velocity $\vec{V}_i = (V_x, V_y)$ was computed according to the technique detailed in [13]. The location of the pointer driven by the second subject is analyzed in a similar way. In order to unfold the information contained in the velocity, we choose to rotate by $\frac{\pi}{4}$ the velocity vector (which, by definition, is tangent to the trajectory). In order to save a shape globally circular to the resulting state portrait, we applied a coefficient reducing by 10 the norm of the velocity vector. The trajectory representative of the pointer dynamics driven by each subject is thus obtained using the coordinates

$$\left| \begin{array}{l} u_i = x_i + 0.1\, V_{i,y} \\ v_i = y_i - 0.1\, V_{i,x}\,. \end{array} \right. \tag{3}$$

Four examples of these representations are shown in Figs. 2: when the velocity is small, the trajectory presents a global circular shape (Fig. 2a). Larger the velocity is, more different from a circle the state portrait is (Fig. 2b). These two examples therefore correspond to very different velocities although the angular apertures are nearly the same ($\Delta\theta = 0,99$ in Fig. 2a and $\Delta\theta = 0,94$ in Fig. 2b). In the third case, the subject explores much more the available space ($\Delta\theta = 1,91$) with a velocity presenting moderate fluctuations thus inducing a state portrait with a "ring" shape. Contrary to this, the fourth case (Fig. 2d) presents a trajectory visiting a relatively large part of the available space with a greatly fluctuating velocity, thus blurring the annular shape of the state portrait. Our state portraits are thus representative of the individual dynamics.

The trajectories often end at the location of one of the objects (private or public) (Figs. 2a, 2b and 2d); these objects thus structure the state portrait more or less as singular points are structuring chaotic attractors: they are relevant for the organization of the trajectories in the state space, at least when the teenagers successfully locate one of the objects. The two teenagers of a given pair are said to be "jointly acting" when the distance

$$d = \sqrt{(u_1 - u_2)^2 + (v_1 - v_2)^2} \tag{4}$$

is less than $\epsilon = 5,09$, this threshold corresponding to the retained precision (16 pixels) for correctly locating an object.

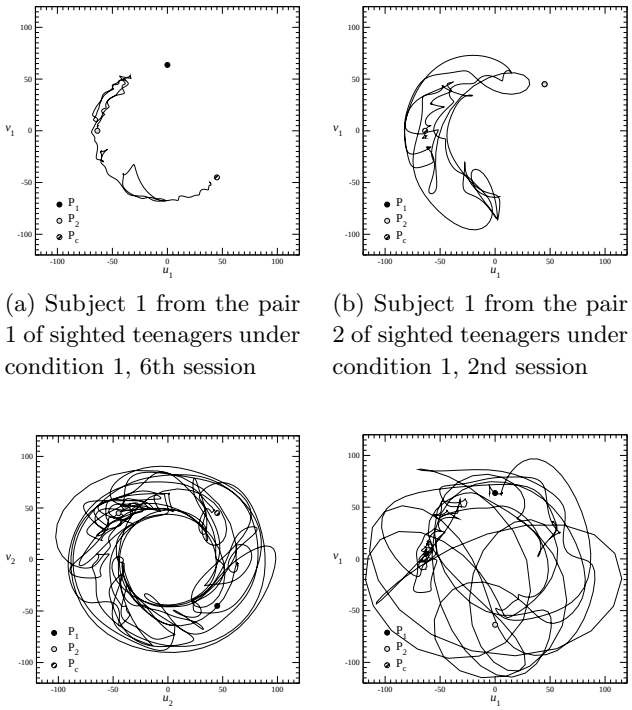

(a) Subject 1 from the pair 1 of sighted teenagers under condition 1, 6th session

(b) Subject 1 from the pair 2 of sighted teenagers under condition 1, 2nd session

(c) Subject 2 from the pair 2 of visually impaired teenagers under condition 1, 5th session

(d) Subject 1 from the pair 2 of visually impaired teenagers under condition 2, 6th session

Figure 2: Examples of state portraits for different subjects and different coupling condition.

4 Results

4.1 Locating the public object

Participants were asked to click at the location where they identified the public object. They had to do this at the very end of each session. We thus investigated the probability P_{cjl} with which both participants correctly located the public object and compare these probabilities obtained with the pairs of visually impaired teenagers to those computed for sighted participants (Fig. 3). However, oral exchanges with participants at the end of the session reveal that visually impaired teenagers actually try to collaborate to locate the public object; they claimed for designing a strategy to achieve their task. Contrary to this, sighted teenagers, although there were placed in situation in which cooperation was strongly suggested, remain in a competing attitude, still trying to better perform than the other. They were more focused on the pin simulations than the corresponding meaning in terms of interaction with the other participants.

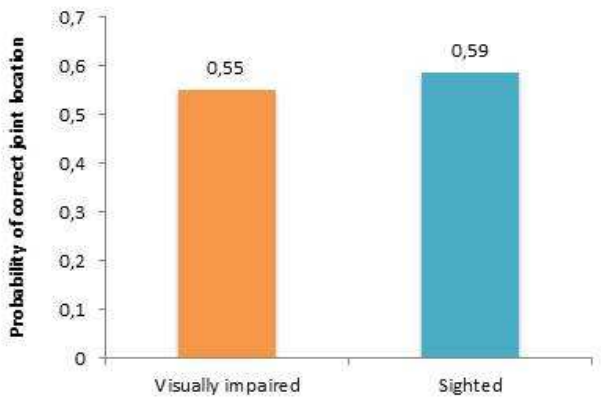

Figure 3: Probability of correct joint location P_{cjl} of the public object by pairs of visually impaired and sighted teenagers.

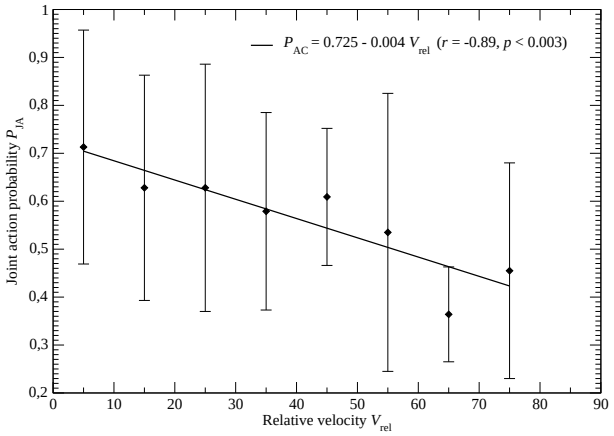

Figure 4: Mean probability for joint action P_{JA} (for each subinterval of $\overline{V}_{\mathrm{rel}}$ versus the mean relative velocity $\overline{V}_{\mathrm{rel}}$. All pairs for all conditions are taken into account.

4.2 Joint action

We started our dynamical analysis by computing the relative velocity

$$V_{\mathrm{rel}} = \sqrt{(V_{1,x} - V_{2,x})^2 + (V_{1,y} - V_{2,y})^2} \qquad (5)$$

between the two participants. We then computed the mean relative velocity $\overline{V}_{\mathrm{rel}}$ of a session; the probability for joint action P_{JA}, defined as the duration for which $d < \epsilon$ related to the duration of the session, was plotted versus $\overline{V}_{\mathrm{rel}}$ (not shown). The interval over which the main relative velocity was found was divided by intervals of 10 pixel.s^{-1}: over each interval the mean probability for joint action was computed with its standard deviation; both were then plotted versus the mean relative velocity $\overline{V}_{\mathrm{rel}}$ as shown in Fig. 4. Normal and visually impaired teenagers were here considered for the two types of conditions. The probability for joint action P_{JA} was significantly auto-correlated ($r = -0.89$, $p < 0.003$) to the mean relative velocity $\overline{V}_{\mathrm{rel}}$. It thus appears that smaller the mean relative velocity, greater the probability for joint action. Nevertheless, we should not miss the large standard deviation observed in most of the interval $\overline{V}_{\mathrm{rel}}$.

In a similar way, we investigated the correlation between the minimal mean velocity $\overline{V}_{\mathrm{min}}$ presented among the pointers of the two participants ($\mathrm{Min}(V_1, V_2)$, during each session): the probability for joint action P_{AJ} is also significantly anti-correlated ($r = -0.84$, $p < 0.01$) to the minimal mean velocity $\overline{V}_{\mathrm{min}}$ (Fig. 5). It is therefore relevant to have at least one of the two participants who drives slowly his pointer: this increases the probability for the two participants to follow each other, and so to have a joint action.

There is a significant departure in these correlations between the normal and visually impaired teenagers (Fig. 6): the probability for joint action is significantly anti-correlated to the minimal velocity V_{min} for the normal teenargers ($r = -0.82$, $p < 0.02$) but not for the visually

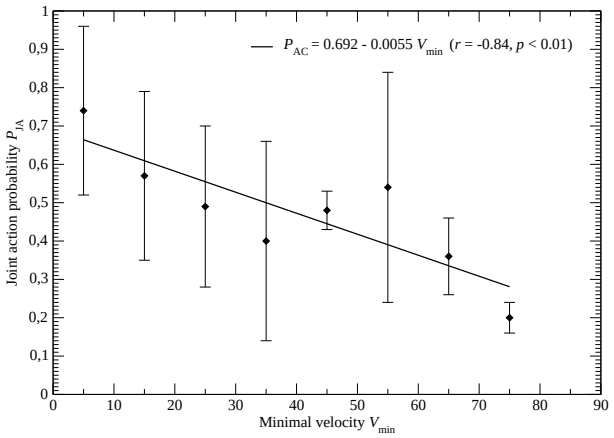

Figure 5: Mean probability for joint action P_{JA} (for each subinterval of $\overline{V}_{\mathrm{min}}$ versus the mean minimum velocity $\overline{V}_{\mathrm{min}}$. All pairs for all conditions are taken into account.

impaired teenagers ($r = -0.49$, NS). This would mean that the visually impaired teenagers are more able to develop joint action with high speed than the normal ones.

5 Conclusions

The present dynamical analysis reveals that, although there is no significant difference for completing the initial task (locating the public object), the dynamical analysis and oral exchanges with participants at the end of the recording sessions evidenced different strategies used by visually impaired and sighted teenargers. Thus, sighted teenagers used velocities less than those used by visually impaired teenagers; moreover; the formers need to focused on the shared object while the latters do not present an equally large duration of joint action. This feature suggests that visually impaired teenagers are able to explore more quickly the environment, interact and locate the shared object.

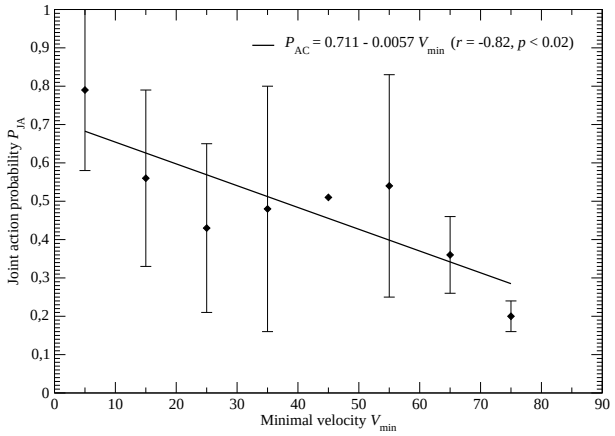

(a) Normal teenagers

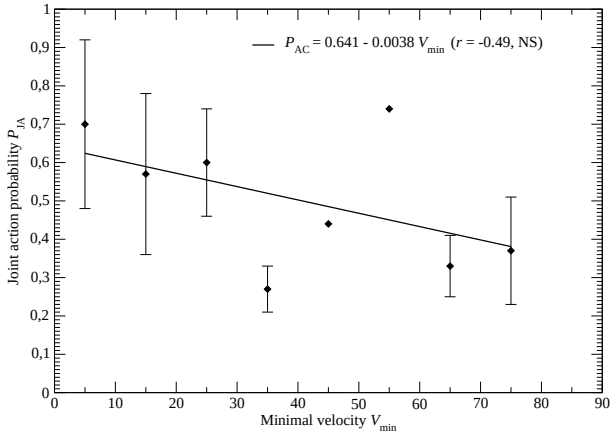

(b) Visually impaired teenagers

Figure 6: Mean probability for joint action P_{JA} (foe each subinterval of $\overline{V}_{\mathrm{min}}$) versus the mean minimum velocity $\overline{V}_{\mathrm{min}}$. Normal (a) and visually impaired (b) teenagers for both conditions are taken into account.

According to answers by sighted teenagers, this reduction in the velocities could be due to the fact they focused their attention to explore the digital space more on tactile simulations than on the interactions with the other participant. In other words, they needed their full attention to detect pin simulations and were unable to interpret them as the presence of the other. Contrary to this, visually impaired teenagers have a very good haptic competence leaving them to easily access to the meaning of pin simulations and, consequently, they were able to interact with the other participants. Such a variability in haptic competence was already evidenced in previous studies as those conducted by one of us [14] between blind and sighted adolescents: they found that sighted subjects spent twice as long as the blind subjects in order to explore the shape of an object. These results are thus consistent with the fact that touch can provide as much information as sight [15] and that, consequently, visually impaired teenagers develop haptic competence for compensatinig the lack of visual experience. If there is no difference in completing the final task (identifying the location of the public object), this is because sighted teenagers can learn to explore space by tactile simulation: nevertheless, their strategy differ from those presented by visually impaired teenagers mostly due to a weaker capacity for memorizing location without visual reference points. Regarding this latter aspect, visually impaired teenagers seem to present a better ability for memorizing location than the sighted subjects. This feature is currently under investigation from the present data.

Acknowledgements

This study was partly supported by the project ITOIP (Région Picardie) and large research network (GRR) from Haute-Normandie "*Personnes en situation de handicap : aides techniques et accompagnement humain*". We wish to thank the center Normandie Lorraine and the school "Le Roumois" from Routot for their reception.

References

[1] H. de Jaegher, E. Di Paolo & S. Gallagher, Can social interaction constitute social cognition?, *Trends in Cognitive Sciences*, vol. 14, pp. 441-447, 2010.

[2] T. Allison, A. Puce & C. McCarthy, Social perception from visual cues: role of the STS region, *Trends in Cognitive Sciences*, vol. 4, pp. 267-278, 2000.

[3] N. Sebanz, H. Bekkering & G. Knoblich, Joint action: bodies and minds moving together, *Trends in Cognitive Sciences*, vol. 10, pp. 70-76, 2006.

[4] R. C. Mulford, Referential development in blind children, In A. E. Mills (Ed.), *Language acquisition in the blind child: Normal and deficient* (London: Groom Helm), 1983.

[5] C. Tinti, Spontaneous facial expressions in congenitally blind and sighted children aged 811, *Journal of Visual Impairment & Blindness*, vol. 97, pp. 418428, 2003.

[6] M. Celeste & D. K. Grum, Social integration of children with visual impairment: A developmental model, *Elementary Education Online*, vol. 9, pp. 1122, 2010.

[7] L. Lefebvre, L. Perron & A. Pauchet, (2007). Animations d'avatars dans les EVC: choix des indices non verbaux pour l'interaction, Paper presented at the 2$^{\text{émes}}$ journées de l'AFRV (Association Française de Réalité Virtuelle), Marseille, France.

[8] S. Hanneton, O. Gapenne, C. Genoulle, C. Lenay & C. Marque, (1999), Dynamics of shape recognition through a minimal visuo-tactile sensory substitution interface, *Third International Conference on Cognitive and Neural Systems*, pp. 26-29, Boston, May 1999.

[9] O. Gapenne, K. Rovira, A. Ali Ammar & C. Lenay, TACTOS: A special computer interface for the reading and writing of 2D forms in blind people, In: C. Stephanidis, (eds.) *Universal Access in HCI, Inclusive Design in the Information Society*, Lawrence Erlbaum Associates, London, pp. 1270-1274, 2003.

[10] K. Rovira & O. Gapenne, Tactile classification on traditional and computerized media in three adolescents who are blind, *Journal of Visual Impairment and Blindness*, vol. 103, pp. 430-435, 2009.

[11] L. Deschamps, *Suppléance perceptive et cognition sociale : étude des interactions tactiles minimalistes*, Ph.D. Thesis, Université de Technologie de Compiègne, 2013.

[12] C. Letellier, *Chaos in Nature*, World Scientific Publishing, 2013.

[13] C. Letellier, L. A. Aguirre & U. S. Freitas, Frequently Asked Questions about global modelling, *Chaos*, vol. 19, n^{o}023103, 2009.

[14] K. Rovira, L. Deschamps & D. Baena-Gomez, Mental rotation in blind and sighted adolescents: The effects of haptic strategies, *Revue Européenne de Psychologie Appliquée*, vol. 61, pp. 153-160, 2011.

[15] J. M. Kennedy, *Drawing and the blind*, Yale University Press, New Haven, CT, 1993.

Proceedings of ICCSA 2014
Normandie University, Le Havre, France - June 23-26, 2014

SINGULARITY ANALYSIS: A METHOD FOR PROPERLY CHARACTERIZING COMPLEXITY IN CARDIODYNAMICS

Oriol Pont *

Abstract. Characterization of arrhythmia complexity requires defining well behaved measures that respect the known signal symmetries. Multifractal analysis methods take into account the intermittency of the fluctuations observed in the cardiac electric potential. We present how singularity analysis provides a measure to robustly characterize complexity at a local level. This method is essentially nonlinear and it minimizes the effect of common artefacts on empirical signals such as finite size, noise and aliasing. The presented method aims at improving the understanding of arrhythmia mechanisms with minimal base hypotheses. In that sense, it highlights arrhythmogenic areas on electrocardiographic potential maps of the epicardium. From it, key descriptors could help in determining the prognosis of the arrhythmia, to forecast the outcome of ablation and resynchronization procedures, and to guide the surgical action in these operations.

Keywords. singularity analysis, excitable systems, multifractal dynamics, multiresolution analysis, electrocardiographic mapping

1 Introduction and State of the Art

The usual approach to electrocardiography (ECG) consists of qualitatively characterizing typical shapes of potential signals, often labeled as *waves*. Some characteristic signatures of such shapes are specific to certain arrhythmias and this is principally what makes them a standard diagnostic tool. Alternatively, but in a quite similar way, the statistical approach tries to highlight specificities that are not evident in the electrical signals themselves but in their distribution functions or some measure derived from them. Statistical methods for processing cardiac signals have had a notable success in several areas, e.g., providing measures of complexity of a certain arrhythmia. Additionally, they output quantitative measures, they provide confidence intervals and, sometimes, we know robust implementations for them.

Standard statistical methods do not always respect the signal invariances. This fact motivates looking for fractal [16] or multifractal [11, 10] approaches to heart rate variability, which do capture the multiscale structure of the process. More interestingly, multifractal analysis reconnects the statistical features of the signal with a geometrical interpretation linked to the effective macroscopic transfer of information in the signal [19, 20, 17, 18, 23].

Taking a different path, embedding methods can also reconstruct the effective attractor of the system that produced the signal. This effect reinforces the possibilities for cross-validating the obtained parameters as well as obtaining their physical interpretation [25, 24]. This makes an interesting duality of approaches, with the one based on a multiscale hierarchy and the other on reconstructing a chaotic dynamics. Since the analysis is done at the effective level (i.e., independently of the microscopic descriptors), it is unclear whether the assumption of chaos is correct or not [3, 31]. Actually, *chaotic* cardiac electrophysiological models coexist with *stochastic* ones.

Atrial fibrillation (AF), the most common form of cardiac arrhythmia, consists in the chaotic operation, electrical activation and pumping of the atria. In some circumstances, it can induce life-threatening complications such as inducing a heart failure or forming blood clots that lead to stroke. In cases where medication is impossible or ineffective, a successful treatment consists in radiofrequency ablation of the endocardial tissue to ease an appropriate electrical conduction. In case of paroxysmal AF, Haïssaguerre et al. have shown [6] that for 80 % of patients, electrical insulation of the pulmonary veins allows the patient to regain a normal heart rhythm, but in persistent or permanent AF, the location of problematic areas remains difficult and is still an open problem [2, 27, 29, 8, 9, 7, 4]. In persistent AF, the arrhythmogenic foci can be anywhere in the atria and so need a well focused ablation.

Specific nonlinear analysis methods are required to properly tackle the dynamics of the electrical activity of the human heart. Complex synchronization processes between pacemaker cells, conduction inhomogeneities and chaotic nonlinear amplification of fluctuations challenge descriptional efforts, especially those of forecasting value [10, 12, 14, 15].

This is particularly crucial in complex arrhythmic regimes or at any level where linearizations deviate significantly from the described phenomena. In a context of

*Team GeoStat - INRIA Bordeaux Sud-Ouest, F-33405 Talence, France & L'Institut de rythmologie et modélisation cardiaque LIRYC, Université de Bordeaux, F-33000 Bordeaux, France

noninvasive mapping of the epicardial potential, singularity analysis becomes an appropriate processing methodology that can provide robust and accurate characterizations of dynamical transition fronts [19, 30, 17].

In this work, we derive from first principles an effective cardiodynamical description where singularity exponents sift a simple fast dynamics from its slow modulation [22, 23]. We characterize singularity transitions in epicardial potential maps from patients with atrial flutter and atrial fibrillation.

Such local transition analysis could eventually be incorporated to the inverse-problem regularization and improve information on anomalous activity areas to e.g., support diagnosis or guide catheter ablation procedures.

The paper is structured as follows: section 2 introduces the basic methods used for processing the cardiac electrical signals. In section 3 we show our results in the identification of dynamical regimes. Finally, in section 4 we discuss the results and present the conclusions of our study.

2 Statistical methods based on nonlinear dynamics

The electrical activity of the heart is often described as a complex system. Complexity can have multiple interpretations varying in both nature and extent. Nevertheless, the effect in all cases is that the behaviour of the system as a whole is an emergent behaviour, which could not be derived from separately considering the microscopic mechanisms (be them at cell level or even at molecular level). This non-separability of the different scales involved is a consequence of nonlinear interactions or, in other words, expressing the effect at a given level requires more than just the sum of effects at lower levels. This is what makes global synchronization possible, also can amplify microscopic fluctuations to perturb the whole regime [10].

Emergence of chaos becomes even more important in complex arrhythmic regimes, where linearized descriptors fail to provide meaningful parameterizations except only possibly for very short time windows, or microscopic space or parametric scales. In this context, any appropriate processing methodology must be nonlinear in nature. Singularity analysis provides a robust framework that identifies dynamical transition fronts and information content [19, 21, 17] which is useful for cardiac electric potential signals [23, 25].

2.1 Singularity analysis

The degree of singularity or regularity of a given point in a signal tells how rare is the signal at this point and therefore how much information it contains. A local expansion of the signal around this point has a leading order that dominates at the local neighbourhood (short distances, or small perturbations of the position). This leading order is the scale parameter raised to an exponent, which is not necessarily integer. A signal $s(\mathbf{x})$ has a (fractional) singularity exponent $h(\mathbf{x})$ at point $\mathbf{x}$ if

$$\mathcal{T}_\Psi \mu(\mathbf{x}, r) \;=\; \alpha_\Psi(\mathbf{x})\, r^{h(\mathbf{x})} \;+\; o\left(r^{h(\mathbf{x})}\right) \qquad (r \to 0), \quad (1)$$

with $\mathcal{T}_\Psi \mu(\mathbf{x}, r) = \int_{\mathbb{R}^d} \mathrm{d}\mu(\mathbf{x}')\, \Psi\left((\mathbf{x} - \mathbf{x}')/r\right)$ as the wavelet-projected measure μ at scale r and Ψ as a certain wavelet kernel. The measure is differentially defined: $\mathrm{d}\mu(\mathbf{x}) = \|\nabla s\|(\mathbf{x})\, \mathrm{d}\mathbf{x}$.

2.2 Source field (SF)

Now, the sole requirements of being deterministic, linear, isotropic and translational invariant permit to define a local reconstruction kernel [30, 18, 21]. Its form implies locally evaluated singularities and thus no need to assume any kind of stationarity. Actually, this minimal-assumption reconstruction identifies a *reduced* signal which is reconstructed only from the orientation of the signal on its most singular points [22, 23]. As reported in these references, the orientation of singularities defines a fast and simple dynamics which, for the case of heartbeat, is statistically compatible with a stochastic process without memory. The key manifold of the signal driving its dynamics is called the *oriented* most-singular component. The *reduced signal* follows the same behaviour (1) with the same exponents but different prefactor $\alpha(\mathbf{x})$ and secondary terms. The original signal s and its reduced counterpart r are related through a complex but slow-changing modulation called *source field* (SF) [23], which is defined as the Radon-Nykodym derivative between their respective measures:

$$\mu_s(\mathcal{A}) = \int_{\mathcal{A}} \mathrm{d}\mu_r(\vec{x}, t)\; SF(\vec{x}, t), \qquad (2)$$

where r refers to the reduced signal. This allows defining the SF as the Radon-Nikodym derivative between the measure on the signal and that on the reduced signal,

$$SF(\vec{x}, t) = \frac{\mathrm{d}\mu_s}{\mathrm{d}\mu_r}(\vec{x}, t). \qquad (3)$$

Singularity analysis gives a geometric perspective to the system dynamics, which is only partially observed from electrographic variables. When applicable, it provides an accurate measure of complexity. All the structural complexity of the system is abstractly represented as means of effective dynamics: the dynamical changes implied from singularity analysis also highlight atrial fibrillation in a local way, as described in [23] and presented as well in [25, 24].

3 Empirical singularity exponents on a case of atrial flutter

To show the presented methods in practice, we present the analyses made on electrocardiographic maps from Bordeaux Haut-Leveque Hospital. Prior to the measurments, heart geometry is extracted from a tomographic scan. A 252-electrode vest measures the electric potential around the torso and these measures are mapped on the epicardial surface [26, 13, 1]. The recordings correspond to differences of electric potential between the vest electrodes. This way, potential maps are reconstructed from inverting the body surface maps (ecVue, CardioInsight, Cleveland OH) [26]. In any case, we have canceled the QRS complexes as detected on the body surface ECGs, since the ventricular activity blinds a proper mapping on the atria; we have used an algorithm based on that in [28], improved and adapted to our case.This inverse problem is essentially ill-posed and requires extensive regularization. Therefore, it is important that the analysis methods are robust to perturbations and regularization artefacts [5].

The robust and compact framework provided by the singularity exponents and source field can give a proper description while filtering spurious effects, in a model-agnostic way that stays as close to the empirical data as possible. The first step has been to validate that eq. (1) is verified in both space and time for our signals [25, 24]. This means that calculating singularity exponents makes sense in that case. Additionally, the approach had already been validated for endocardial potentials too [23], though only for time series.

The singularity analysis approach here presented is equivalent to the calculation of the source field that we have presented at [25] for a setting similar to the one presented here. While time-evolving, the mapping series are too short to extract a tachogram from them and so we processed the potential signal itself, whose fluctuations dynamically evolve – an effect usually related to *fractionation*.

In the space domain, the estimation is done by considering the relative positions and orientations of the nearest neighbours. In other words, we can compute the exponents in time domain (treating each point as an independent time series), in space domain, or in space-time domain, with the typical propagation speed regularizing the time coordinate. The spatial processing requires interpolating the varying directions of each triangle, as well as their unequal distances and curvatures. The result for a case of atrial flutter (Fig. 1) shows how singularities concentrate in a small zone next to the tricuspid valve, consistent with the focus of that case of regular flutter. Interestingly enough, space-only and time-only exponents appear as missing a part of the picture, i.e., showing less information than the spatiotemporal case.

As the next step, and following a procedure analogue to the one at [23], singularity exponents define in a natural way a separation between a fast-simple dynamics

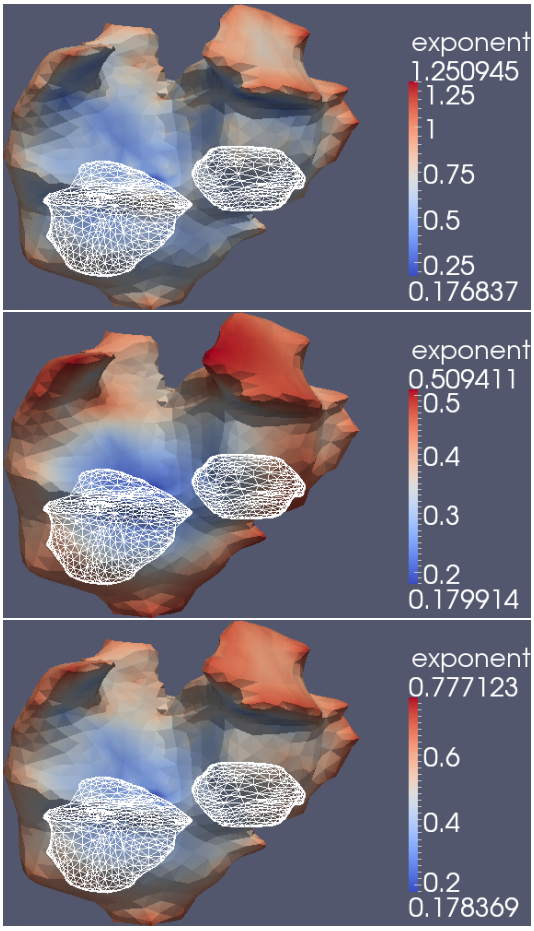

Figure 1: Median singularity exponent of the epicardial electric potential in a case of atrial flutter, calculated on space (top), time (middle) and space-time (bottom) domains. We show the mapping on the atria and indicate the position of the valves for reference. We observe a concentration of less regular exponents in the key area around the tricuspid valve. Error propagations in the algorithms indicate a sigma around 0.03 for the exponents.

from a slow-complex one. As presented there, singularity-exponent orientation over the most singular component defines a 3-state chain process that lacks memory, and so it can be reduced to a transitional matrix characterized by its eigenvalues (2nd and 3rd, as the 1st one is always equal to one). The slow modulation counterpart is the aforementioned SF, and we can see them in practice in Fig. 2. Extreme values of source field highlight areas specifically related to the arrhythmias. The reentry around the valve is traduced in less regular exponents and higher value of SF, meaning larger modulation factor. The SF field changes more abruptly in the reentry region, showing more specifically the problem area. The sharper transitions characterized as smaller singularity exponents indicate the reentry area. Consistently, the SF behaves more specifically in the edges of the areas, and relatively smaller SF values indicate a larger influence of the orientational dynamics [23] in them. In general, extreme values indicate an arrhythmogenic point in the tissue.

4 Discussion and conclusions

Nonlinear analysis provides methods for characterizing cardiac dynamics. Singularity analysis and phase-space reconstruction are physically meaningful complexity measures with minimal assumptions on the underlying interactions. They are based on effective descriptions derived from first principles, and as a consequence, parameters are robustly estimated. We have validated this approach on ECGs and electrocardiographic maps.

A noninvasive map sequence of epicardial potential allows evaluation of spatio-temporal singularity exponents in that signal. While the regular low-variation areas are more prone to be affected by masking artefacts of the inverse projections, the most singular points describing the transitions are expected to be comparatively less perturbed. This way spurious effects can be filtered out and working on the singularity field can be more robust than on the potential signal itself, while staying close to the physical data and without imposing any model or unreasonable hypothesis.

Moreover, singularity orientation provides a sharp and specific descriptor of transitional dynamics. We have processed maps under atrial flutter, showing exponent and SF transitions connected to problem areas on the anomalous atrial cardiac dynamics. Key parameters vary infrequently and exhibit sharp transitions, which show where information concentrates and correspond to actual dynamical regime changes. Singularity exponents sift a simple fast dynamics from its slow modulation. In space domain, extreme values highlight arrhythmogenic areas. This characterization of information transitions could be used in the regularization of inverse-problem mapping of electrocardiographic epicardial maps. Furthermore, this opens the way for improved model-independent complexity descriptors to be used in non-invasive, automatic diag-

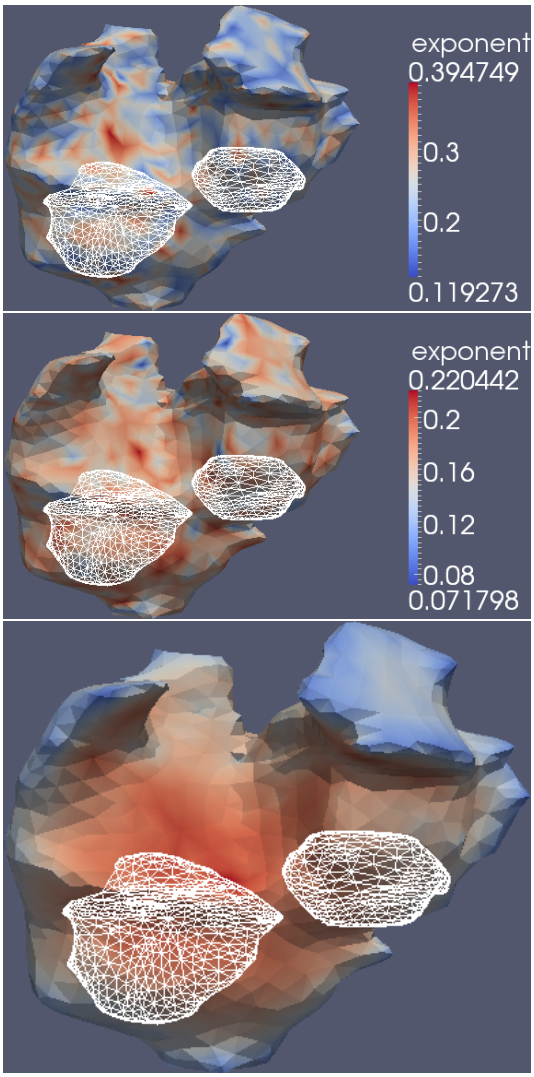

Figure 2: Average 2nd (top) and 3rd (middle) eigenvalues, and average normalized SF value (bottom) of the epicardial electric potential in a case of atrial flutter. We show the mapping on the atria and indicate the position of the valves for reference. We observe a larger source field in the key area around the tricuspid valve. The source field is sharp on the flutter area. Error propagations in the algorithms indicate a sigma around 0.1 for the SF.

nosis support and ablation guide for electrical insulation therapy, in cases of arrhythmias such as atrial flutter and fibrillation.

These results open the way for improved model-independent complexity descriptors to be used as non-invasive diagnosis support or operation guide in cases of cardiac arrhythmias, particularly atrial fibrillation.

Acknowledgements

We thank CHU Bordeaux - Haut-Leveque hospital, IHU LIRYC and CardioInsight Technologies for the epicardial electrocardiographic maps.

References

[1] Phillip S. Cuculich, Yong Wang, Bruce D. Lindsay, Mitchell N. Faddis, Richard B. Schuessler, Ralph J. Damiano, Li Li, and Yoram Rudy. Noninvasive characterization of epicardial activation in humans with diverse atrial fibrillation patterns / clinical perspective. *Circulation*, 122(14):1364–1372, 2010.

[2] R. Dubois, P. Roussel, M. Hocini, F. Sacher, M. Haissaguerre, and G. Dreyfus. A wavelet transform for atrial fibrillation cycle length measurements. In *Computers in Cardiology, 2009*, pages 501 –504, sept. 2009.

[3] R. B. Govindan, K. Narayanan, and M. S. Gopinathan. On the evidence of deterministic chaos in ecg: Surrogate and predictability analysis. *Chaos*, 8(2):495–502, Jun 1998.

[4] Michel Haissaguerre, Fabrice Extramiana, Meleze Hocini, Bruno Cauchemez, Pierre Jais, Jose Angel Cabrera, Geronimo Farre, Antoine Leenhardt, Prashanthan Sanders, Christophe Scavee, Li-Fern Hsu, Rukshen Weerasooriya, Dipen C. Shah, Robert Frank, Philippe Maury, Marc Delay, Stephane Garrigue, and Jacques Clementy. Mapping and ablation of ventricular fibrillation associated with long-qt and brugada syndromes. *Circulation*, 108(8):925–928, 2003.

[5] Michel Haissaguerre, Meleze Hocini, Ashok J. Shah, Nicolas Derval, Frederic Sacher, Pierre Jais, and Remi Dubois. Noninvasive panoramic mapping of human atrial fibrillation mechanisms: a feasibility report. *J Cardiovasc Electrophysiol*, 24(6):711–717, Jun 2013.

[6] Michel Haïssaguerre, Pierre Jaïs, Dipen C. Shah, Atsushi Takahashi, Mélèze Hocini, Gilles Quiniou, Stéphane Garrigue, Alain Le Mouroux, Philippe Le Métayer, and Jacques Clémenty. Spontaneous initiation of atrial fibrillation by ectopic beats originating in the pulmonary veins. *New England Journal of Medicine*, 339(10):659–666, September 1998.

[7] M Hocini, P Jais, F Sacher, S Reuter, J Clementy, and M Haissaguerre. Mapping and ablation of malignant ventricular arrhythmias. *Arch Mal Coeur Vaiss*, 98(5):34–41, Dec 2005.

[8] Meleze Hocini, Pierre Jais, Prashanthan Sanders, Yoshihide Takahashi, Martin Rotter, Thomas Rostock, Li-Fern Hsu, Frederic Sacher, Sylvain Reuter, Jacques Clementy, and Michel Haissaguerre. Techniques, evaluation, and consequences of linear block at the left atrial roof in paroxysmal atrial fibrillation: a prospective randomized study. *Circulation*, 112(24):3688–3696, Dec 2005.

[9] Mélèze Hocini, Prashanthan Sanders, Pierre Jaïs, Li-Fern Hsu, Rukshen Weerasoriya, Christophe Scavée, Yoshihide Takahashi, Martin Rotter, Florence Raybaud, Laurent Macle, Jacques Clémenty, and Michel Haïssaguerre. Prevalence of pulmonary vein disconnection after anatomical ablation for atrial fibrillation: consequences of wide atrial encircling of the pulmonary veins. *European Heart Journal*, 26(7):696–704, 2005.

[10] P. Ivanov, L. Amaral, A. Goldberger, S. Havlin, M. Rosenblum, Z. Struzik, and H. Stanley. Multifractality in human heartbeat dynamics. *Nature*, 399:461–465, 1999.

[11] P. Ivanov, M. Rosenblum, C.-K. Peng, J. Mietus, S. Havlin, H. Stanley, and A. Goldberger. Scaling behaviour of heartbet intervals obtained by wavelet-based time-series analysis. *Nature*, 383:323–327, 1996.

[12] Plamen Ivanov. Long-range dependence in heartbeat dynamics. In Govindan Rangarajan and Mingzhou Ding, editors, *Processes with Long-Range Correlations*, volume 621 of *Lecture Notes in Physics*, pages 339–372. Springer Berlin / Heidelberg, 2003. 10.1007/3-540-44832-2.

[13] Ping Jia, Charulatha Ramanathan, Raja N. Ghanem, Kyungmoo Ryu, Niraj Varma, and Yoram Rudy. Electrocardiographic imaging of cardiac resynchronization therapy in heart failure: Observation of variable electrophysiologic responses. *Heart Rhythm*, 3(3):296–310, March 2006.

[14] Samuel P Kozaitis. Improved feature detection in ecg signals through denoising. *International Journal of Signal and Imaging Systems Engineering*, 1(2):108–114, 2008.

[15] M. Martinelli, D. Moroni, O. Salvetti, and M. Tampucci. A knowledge-based infrastructure for the management of diagnostic imaging procedures in the heart failure domain. *Transactions on Mass-Data Analysis of Images and Signals*, 2(1):3–18, Sep 2010.

[16] C.-K. Peng, J. Mietus, J. M. Hausdorff, S. Havlin, H. E. Stanley, and A. L. Goldberger. Long-range anticorrelations and non-gaussian behavior of the heartbeat. *Phys. Rev. Lett.*, 70(9):1343–1346, Mar 1993.

[17] O. Pont, A. Turiel, and C. Perez-Vicente. Empirical evidences of a common multifractal signature in economic, biological and physical systems. *Physica A*, 388(10):2025–2035, February 2009.

[18] O. Pont, A. Turiel, and C. Perez-Vicente. On optimal wavelet bases for the realization of microcanonical cascade processes. *Int. J. Wavelets Multi., IJWMIP*, 9(1):35–61, January 2011.

[19] O. Pont, A. Turiel, and C. J. Perez-Vicente. Application of the microcanonical multifractal formalism to monofractal systems. *Physical Review E*, 74:061110–061123, 2006.

[20] O. Pont, A. Turiel, and C. J. Perez-Vicente. Description, modeling and forecasting of data with optimal wavelets. *Journal of Economic Interaction and Coordination*, 4(1):39–54, June 2009.

[21] O. Pont, A. Turiel, and H. Yahia. Singularity analysis of digital signals through the evaluation of their unpredictable point manifold. *International Journal of Computer Mathematics*, 90(8):1693–1707, 2013.

[22] Oriol Pont, Michel Haissaguerre, Hussein Yahia, Nicolas Derval, and Mélèze Hocini. Heartbeat dynamics from a microcanonical multifractal approach. In *Computing in Cardiology*, volume 38, 2011.

[23] Oriol Pont, Michel Haissaguerre, Hussein Yahia, Nicolas Derval, and Mélèze Hocini. Microcanonical processing methodology for ECG and intracardial potential: application to atrial fibrillation. *Transactions on Mass-Data Analysis of Images and Signals*, 3(1):15–34, 2011.

[24] Oriol Pont and Binbin Xu. Characterizing Complexity of Atrial Arrhythmias through Effective Dynamics from Electric Potential Measures. In *Computing in Cardiology, CinC 2013*, Saragossa, Spain, 2013.

[25] Oriol Pont, Hussein Yahia, and Binbin Xu. Arrhythmic dynamics from singularity analysis of electrocardiographic maps. In *EMBC 2013. 35th Annual International Conference of the IEEE Engineering in Medicine and Biology Society*, Osaka, Japan, 2013. IEEE EMBS.

[26] Charulatha Ramanathan, Raja N Ghanem, Ping Jia, Kyungmoo Ryu, and Yoram Rudy. Noninvasive electrocardiographic imaging for cardiac electrophysiology and arrhythmia. *Nat Med*, 10(4):422–428, April 2004.

[27] Prashanthan Sanders, Chrishan J. Nalliah, Rémi Dubois, Yoshihide Takahashi, Mélèze Hocini, Martin Rotter, Thomas Rostock, Frédéric Sacher, Lifern Hsu, Anders Jönsson, Mark D. O'neill, Pierre Jaïs, and Michel Haïssaguerre. Frequency mapping of the pulmonary veins in paroxysmal versus permanent atrial fibrillation. *Journal of Cardiovascular Electrophysiology*, 17(9):965–972, 2006.

[28] M Stridh and L Sornmo. Spatiotemporal qrst cancellation techniques for analysis of atrial fibrillation. *IEEE Trans Biomed Eng*, 48(1):105–111, Jan 2001. 0018-9294 (Linking).

[29] Yoshihide Takahashi, Prashanthan Sanders, Pierre Jaïs, Mélèze Hocini, Rémi Dubois, Martin Rotter, Thomas Rostock, Chrishan J. Nalliah, Frédéric Sacher, Jacques Clémenty, and Michel Haïssaguerre. Organization of frequency spectra of atrial fibrillation: Relevance to radiofrequency catheter ablation. *Journal of Cardiovascular Electrophysiology*, 17(4):382–388, 2006.

[30] A. Turiel, H. Yahia, and C. Pérez-Vicente. Microcanonical multifractal formalism: a geometrical approach to multifractal systems. Part I: Singularity analysis. *Journal of Physics A*, 41:015501, 2008.

[31] Charlotte Werndl. Are deterministic descriptions and indeterministic descriptions observationally equivalent? *Studies in History and Philosophy of Science Part B: Studies in History and Philosophy of Modern Physics*, 40(3):232 – 242, 2009.

Satellite Workshop 10
Logistics

Satellite Workshop 10
Logistics

Organizers

- Adnan YASSINE, LMAH EA 3821, Université du Havre, France, adnan.yassine@univ-lehavre.fr
- Abdelkader SBIHI, Laboratoire METIS, Ecole de Management de Normandie, France, a.sbihi@em-normandie.fr

Description

Logistics is the activity which aims to manage the physical flows of an organization between the point of origin and the point of consumption in order to meet customer requirements and with the objective of ensuring the resources corresponding to determined needs. With many actors and activities involved in the supply chain, logistics represent mainly a complex system. The arising problems are generally hard to solve, due to their inherent complexity, and in most of the time the stakeholders are seeking a quick response for act accordingly.
The main goal of this session is to investigate the recent state-of-the art by contributing to solve logistical problems in term of developing new approaches and modern algorithms. These problems include, but not limited to:

- Modeling and Simulation of Logistics
- Advances in Optimization Models, Algorithms and Resolution methods
- Supply Chain Optimization
- Optimization under Uncertainty
- Planning, Storage and Scheduling
- Transportation, Logistics and Distribution Networks
- Lot-sizing Problem
- Green Logistics: a new Paradigm in Transportation
- Integrated Supply Chain
- Reverse Logistics and Remanufacturing Models

Proceedings of ICCSA 2014
Normandie University, Le Havre, France - June 23-26, 2014

OPTIMIZATION ALGORITHMS FOR SOLVING MULTI-OBJECTIVE VEHICLE ROUTING PROBLEMS WITH FUZZY DEMANDS

Bahri Oumayma[1], Ben Amor Nahla[1] and El-Ghazali Talbi[2] *†

1 Abstract

Vehicle routing problems (VRPs) are very difficult and complex combinatorial optimization problems for which various techniques and methods have been used. Yet, in real-world applications, these problems are naturally multi-objective since they usually involve the simultaneous satisfaction of multiple conflicting objectives. Besides, they are often subject to significant uncertainties which must be taken into account such as the most common uncertainty of customer demands. Therefore, the widely studied problem that has gained more and more attention in recent years is the multi-objective version under uncertainty because of its wide applicability in many real-life situations.

The aim of our study is to deal with a bi-objective variant of VRP with uncertain demands, in which the uncertainty is expressed by means of triangular fuzzy numbers (TFNs): the Multi-objective Vehicle Routing Problems with Time Windows and Fuzzy demands (MO-VRPTW-FD henceforth). As a consequence in this fuzzy context, the classical methods of VRP cannot be applied to obtain optimal solutions and so a need for special optimization methods capable to handle such problems is evident. However, almost all of existing approaches have been devoted to solve this problem in the mono-objective context, while only few studies have been performed in the multi-objective setting. To this end, we propose a fuzzy extension of two well-known multi-objective evolutionary algorithms: SPEA2 and NSGAII, in order to enable them working in uncertainty space (i.e. fuzzy context) and consequently handling the MO-VRPTW-FD problem. The proposed algorithms, based mainly on the use of new Pareto approach over triangular fuzzy numbers, are implemented with the version 2.0 of ParadisEO-MOEO under Linux.

In order to verify the performance of our both algorithms, we test them on few instances of Solomons benchmark and finally we evaluate the obtained solutions using some experimental tests based on multi-objective quality indicators such as, Hypervolume and Epsilon indicators.

As a future work, we intend to extend the multi-objective performance metrics to uncertain context and to apply the proposed approach on a multi-objective VRP having more than one uncertain data (ex. uncertainty in demand and travel time).

Keywords. Vehicle Routing Problem, Multi-objective, Uncertainty, Triangular fuzzy numbers, SPEA2, NSGA2, Solomon's benchmark.

*B. Oumayma and B.A. Nahla are from LARODEC Lab, Université de Tunis, Tunisie. E-mails: oumayma.b@gmail.com, nahla.benamor@gmx.fr

†E-G. Talbi is from both INRIA-Lille and CNRS/LIFL Labs, Université de Lille1, France. E-mail: el-ghazali.talbi@lifl.fr

References

[1] P. Toth and D. Vigo, *The Vehicle Routing Problem*, SIAM, 2002.

[2] E-G. Talbi, N. Jozefowiez and F. Semet, *Multi-objective vehicle routing problems*, European Journal of Operational Research, 2007.

[3] D. Sulieman, L. Jourdan and E.-G. Talbi, *Using multiobjective metaheuristics to solve VRP with uncertain demands*, Evolutionary Computation, pp. 1-8, 2010.

[4] L.A. Zadeh, *Fuzzy sets as a basis for a theory of possibility*, Fuzzy sets and systems, 3-28, 1987.

[5] S. Asma, E-G. Talbi, M. Ader and A. Liefooghe, *Multi-Objective Local Search with epistemic uncertainty: Application to Multi-Objective Vehicle Routing Problem with uncertain demands*, ISOR'11, 2011.

[6] G. Goncalves, T. Hsu and J. Xu, *Vehicle routing problem with time windows and fuzzy demands: an approach based on the possibility theory*, Int. Journal of Advanced Operational Management, vol. 1.4, Inderscience, pp. 312-330, 2009.

[7] B. Oumayma, B.A. Nahla and E.G. Talbi, *A Possibilistic Framework for Solving Multi-objective Problems under Uncertainty*, IPDPSW, 405-414, 2013.

[8] K. Deb, et al. , *A Fast Elitist Non-Dominated Sorting Genetic Algorithm for Multi-objective Optimization: NSGAII*, Lecture Notes in Computer Science, vol. 1917, 849-858, 2000.

[9] E. Zitzler, M. Laumans and L. Thiele, *SPEA2: Improving the strength Pareto evolutionary algorithm*, Proc. EUROGEN 2001 Evolutionary Methods for Design, Optimization and Control With Applications to Industrial Problems, 2001.

[10] M.M. Solomon, *Algorithms for the vehicle Routing and Scheduling Problem with Time Window Constraints*, Operations Research, vol. 35.2, Informs, pp. 254-265, 1987.

Proceedings of ICCSA 2014
Normandie University, Le Havre, France – June 23-26, 2014

Computing Dynamic Routes in Maritime Logistic Networks

Jean-Yves COLIN[1], Moustafa NAKECHBANDI[2],

and Hervé MATHIEU[3]

Abstract. In this paper, we study the problem of finding the most interesting path (the one that maximizes the gain) toward one of several destination ports subject to uncertain information on the expected gain in each port.
Although the cost of a ship trip between two points is usually predictable, some events may happen, thus impacting the cost. However, in most cases, only the final part of the trip is subject to changes. The price of goods to be delivered may fluctuate during the trip (thus impacting the gain), or the price to pay at the destination point can be higher as expected (in case of a strike for example). Besides, during the ship trip, the destination port can turn to be unavailable (conflicts in the country, bombings etc.). All of this has important economical consequences for the shipowner and for the port on a long term basis. In this context, it is important for a shipowner to be able to react quickly when a destination port is no longer available. When a port terminal is on strike for example, ships are rerouted to other ports to be loaded and unloaded.
We propose in this paper a simple and yet efficient algorithm to recompute the path of the ship, when she is on the way, based on the computation of the longest path in a weakly dynamic graphs, in order to maximize the global gain of the trip. Parametric routing tables are precomputed, and critical values are deduced.
Keywords: Dynamic Graph; Longest Path Problem; Maritime Network; Route Planning; Time and Cost Factors.

1 Introduction

Static graphs have a long history of being used to efficiently represent static problems. In these problems, all the data are known from the start. The real world is not static, however, and the solutions to static problems may not always be used [2]. Some data may change, or be unknown in advance. For example, the traversal duration of a location may depend on traffic density, the presence or not of traffic jams, work in progress, etc. that are all time dependent and usually hard to predict. Thus several approaches have been proposed to study parametric graphs [1] and dynamic graphs [6].

Fully dynamic algorithms, for example, are applied to problems that can be solved in polynomial time. They start with a computed optimal solution, and then try to maintain them when changes occur in the problem. They often propose sophisticated data structures to reach this goal [8].

When the delay between a change and the moment a new solution is needed is very small, or when the problem itself is NP-hard, faster algorithms are needed. These reoptimizing algorithms usually start from an initial solution that is not optimal but is expected to be of good quality, if possible. As soon as a change is detected, they compute a new solution, trying to do it faster than classical algorithms. Or they compute a new solution as quickly as the classical algorithms but this resulting solution is better than the ones found by classical algorithms. These algorithms include meta-heuristics such as ants colony algorithms [5], or swarm algorithms [3].

Another approach used is probabilistic. Probabilities are associated to some variables in the graph, such as the value of a weight, or the presence of a node or of a constraint, for example. The algorithms used in these problems usually compute a solution and then do some robustness analysis in the probability space [9]. Or they do a quick re-optimization of the solution once the parameters of the problem are perfectly known [4, 10].

In this paper, we study route planning in maritime network [11]. More specifically, we study the problem of finding the most interesting path toward one of several destination ports subject to uncertain information on the expected gain in each port. Although the cost of a ship trip between two points is usually predictable, some events may happen, thus impacting the cost. However, in most cases, only the final part of the trip is subject to change. The price of goods to be delivered may locally fluctuate during the trip (thus impacting the gain), or the price to pay at the destination point can be higher than expected. For example, it may happen that the dockers of a maritime port are on strike (examples of strikes include

[1] LITIS, Le Havre University, 5 rue Ph. Lebon, BP 540, 76058, Le Havre, France, moustafa.nakechbandi@univ-lehavre.fr.
[2] LITIS, Le Havre University, 5 rue Ph. Lebon, BP 540, 76058, Le Havre, France, jean-yves.colin@univ-lehavre.fr.
[3] ISEL, Le Havre University, Quai Frissard - BP 1137 - Le Havre Cedex France, herve.mathieu@univ-lehavre.fr

Le Havre-Rouen-Marseille 2008, Liverpool between 1995 and 1998 also known as Liverpool's Dockers' strike, Rotterdam 2013....). Actually, the strike phenomenon in maritime ports happens on a regular basis all over the world. To have an idea of the strike impact on maritime traffic, we can quote the example of the Greek port of Pireus: Piraeus' volume peaked at 1.6 million TEU (Twenty feet Equivalent Unit) in 2003, but strikes and unrest led to a throughput of only 433,000 TEU in 2008 [14]. Moreover, "exceptional" events can make a destination port unavailable: bombing, blockade because of economical sanctions etc... It is then necessary to reroute a ship when its destination port is unavailable as soon as possible [15]. All of this has important economical consequences for the ship-owner and for the port on a long term basis. Thus, when a merchandise ship has to stay docked in a port without being taking care of, it implies a money loss that can be important for the ship-owner: sailors' wages, ship rental, blocked merchandise, disrespect of deadlines for merchandise delivery (penalties), and extra fuel consumption. In this context, it is important for a ship-owner to be able to react quickly when a destination port is no longer available.

2 Problem statement

Maritime Shipping Graph (MSG): To study this problem, we will consider a graph $G = (V, E)$. V is the set of nodes, $V = S \cup P \cup \{D\}$, $S = \{1, 2, .. s\}$ is the set of stable nodes, $P=\{X_1, X_2,... Xp\}$ is the set of non-stable nodes (representing destination ports) and D is the destination node. E is the set of edges, and to each edge is associated a weight $w \in R$. All the edges between a node of S and any other node are stable and their negative weights, that represent costs, never change. There is no edge between a stable node and D. However all edges leading to the final destination D in the graph are not stable and their weights may change at any time. The Xi nodes indicate the various ports available for delivery, and D is an added node indicating the abstract delivery of the load. Each edge between a node Xi and node D is non stable and has a value xi, representing the current expected profit for delivering the load in port Xi. We call this graph a MSG, Maritime Shipping Graph:

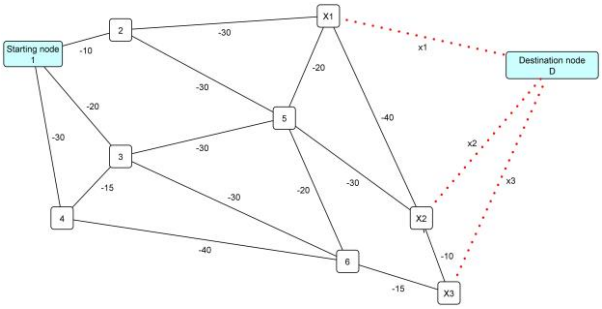

Fig. 1 – Example of Maritime Shipping Graph with 3 variable edges ($x1$, $x2$, $x3$) to the destination D (dashed lines on the graph).{1,2,3,4,5,6} is the set S of stable nodes and {$X1$, $X2$, $X3$} is the set P of non-stable nodes.

The length of a path is the sum of the weights of its edges. Longest paths that do not include any variable edge may be computed with the Bellman algorithm.

For example, taking the simplistic example of a wheat cargo, starting from Argentina to Europe, it may pass through several points (such as the Horn Cap or the Panama Canal). The price to pay, in oil, time, fees and such is usually known and may be represented by a simple static graph. Once the ship is close to Europe, each possible port will have different and possibly changing profit due the local conditions (port disponibilities, adding the cost of train or road transports, strikes...). The profit earned we will consider is:
Selling price at final destination - local fees and expenses at final destination - travel costs to Europe.

For example on the graph of Fig. 1, starting from node 1, we intend to reach one of the final ports X_1, X_2 or X_3. The profit expected from port X_i will be the price received for the cargo minus the cost to deliver it, minus the cost to go to the port. We aggregate the price received there for the cargo with the cost to deliver there in a non-stable value xi that is represented on the graph as an edge between node Xi and a virtual node D.

We are interested in the "One-to-All" Longest path problem (LPP), that is, finding the longest paths from one node to all other nodes of this graph. This must be done considering the weights of the non-stable edges. Preliminary results on the Shortest Path Problem (SPP) on weakly dynamic graphs with one variable edge were presented in [7]. In [13] this result is extended to two variable arcs. In both results, alternative shortest paths or parametric routing tables are pre-computed for all possible values of the non-stable weights. Thus when the non-stable weights change, new optimal paths may directly and immediately be deduced and used without any further recomputations.

The LPP we study will use the model illustrated on Fig. 1. Each stable value is a negative value representing its cost, and the non-stable value of this kind of weakly dynamic graph is the price received for the cargo minus the mis-

cellaneous local costs (including the effects of strikes, if any.).

3 Main results

3.1 The proposed algorithm

We present now the following algorithm to solve this problem:

Algorithm

Input: $G=(V, E)$ is a MSG, with P being the subset of non-stable nodes, and D being the destination
Output: longest paths $LP(j, D)$ from any node j of G to D

For each non stable node X_i of P do

Compute $LPS(X_i)$ = set of longest paths that do not use a variable edge, from

all nodes j, $j \in V-\{D\}$ to node X_i using Bellman algorithm.

Let $dX_i[j]$ = the length of the path in $LPS(X_i)$ that starts from $j \in V-\{D\}$ of the graph.
EndFor

The longest path $LP(j, D)$ from j to D is the path such that length $(LP(j, D))$ = max $(dX_i[j] + x_i , X_i \in P)$

3.2 Example: we now apply this algorithm on the graph of Fig. 1.

The least costly distance from each stable node to each non stable node is presented in Table 1.

Table 1: distances from all stable nodes to all non-stable nodes

Stable node to non-stable node	X_1	X_2	X_3
1	-40	-70	-65
2	-30	-60	-65
3	**-50**	**-55**	**-45**
4	-65	-65	-55
5	-20	-30	-35
6	-40	-25	-15

For example, the value of the least costly path from node 3 to go to node X_1 is -50, to go to node X_2 is -55 and to go to node X_3 is -45.
We now suppose that the current expected profits at the possible delivery ports are (x_1, x_2, x_3) = (1000, 1100, 1200).

The length of the longest path (that is the one with the highest total profit) from node 3 to D is max (1000 – 50, 1100 – 55, 1200 – 45) = 1155. From node 3, the longest path will go to port X_3 for delivery in the current conditions.

Now, if x_3 falls to 1050 and the other values do not change, then the length of the longest path from node 3 to node D is max (1000 – 50, 1100 – 55, 1050 – 45) = 1045. From node 3, the longest path will go to port X_2 for delivery in these new conditions.

3.3 Some proprieties of the algorithm

Theorem 1: Let $G=(V, E)$ a Maritime Shipping Graph, $\{xi$, with $X_i \in P\}$ be the values of the non-stable edges. Let $dX_i[j]$ the longest path without non stable edges from a stable node j to X_i, $X_i \in P$. Then the length of the longest path from a node j to node D is max $\{dX_i[j] + x_i$, with $X_i \in P\}$

Theorem 2: The complexity of the algorithm is O(pnm). n is the number nodes and p is number of non-stable nodes and m is the number of edges.

One interesting use of this result is in the building of pre-computed parametric routing tables. These parametric routing tables include critical conditions that can easily be used to instantly establish a new destination if the expected profit in any possible final destination crosses a computed threshold value.

We call critical conditions of a given node, the set of length functions associated to the longest paths to this given node computed by the algorithm. Because the functions of this set are constants, or very simple linear functions of the non-stable weights, they can be computed and compared very easily. Thus for each target node, the set of alternative paths can be stored along with the associated set of critical conditions. As soon as any variable weight changes, the critical conditions of the target node just need to be recomputed and compared. Then the new longest path may be chosen among the alternative paths stored for this node. No recomputation of longest paths is needed, no data beside the current values of the variable edges need to be exchanged, and all decisions may be taken locally.

The result found by the proposed algorithm can then be used to build alternative routing tables for each ship starting from any location of the graph. The same tables can then be used to route these ships to the most profitable destination at any time during its journey.

We develop the above ideas in the next part, using the example of Figure 1.

4 Developed example

We now again use the example of Figure 1 with the current values (x_1, x_2, x_3) = (1000, 1100, 1200) for the current non-stable weights. Applying the algorithm gives the distances, from all nodes to D, presented in the right part of Table 2:

Table 2: distances from all stable nodes to all non-stable nodes, and to *D* with (x_1, x_2, x_3) = (1000, 1100, 1200).

	X_1	X_2	X_3	Distance to D using (X_1, D)	Distance to D using (X_2, D)	Distance to D using (X_3, D)	Best distance to D if (x_1,x_2,x_3) = (1000,1100,1200)
1	−40	−70	−65	x_1−40	x_2−70	x_3−65	1135
2	−30	−60	−65	x_1−30	x_2−60	x_3−65	1135
3	−50	−55	−45	x_1−50	x_2−55	x_3−45	1155
4	−65	−65	−55	x_1−65	x_2−65	x_3−55	1145
5	−20	−30	−35	x_1−20	x_2−30	x_3−35	1165
6	−40	−25	−15	x_1−40	x_2−25	x_3−15	1185
X_1	0	−40	−50	x_1	x_2−40	x_3−50	1150
X_2	−40	0	−10	x_1−40	x_2	x_3−10	1190
X_3	−50	−10	0	x_1−50	x_2−10	x_3	1200

Now, for any node, the length of its longest distance depends on the values of the non-stable edges. The possible lengths are summarized in Table 3.

Table 3: Parameterized longest distance to go to D

Node	Parameterized longest distance to go to *D*
1	Max(x_1−40, x_2−70, x_3−65)
2	Max(x_1−30, x_2−60, x_3−65)
3	Max(x_1−50, x_2−55, x_3−45)
4	Max (x_1−65, x_2−65, x_3−55)
5	Max(x_1−20, x_2−30, x_3−35)
6	Max(x_1−40, x_2−25, x_3−15)
X_1	Max(x_1, x_2−40, x_3−50)
X_2	Max(x_1−40, x_2, x_3−10)
X_3	Max(x_1−50, x_2−10, x_3)

Next, it is now possible to build *a parameterized routing table* in each node to go to *D*. In the parameterized routing table of a given node, which neighbor to use depends on which part of the max formula gives the highest result using the current values of the non-stables edges. Table 4 presents the parameterized routing tables of nodes 3 and 4 if we have (x_1, x_2, x_3) = (1000, 1100, 1200). With these values, x_3–55 in Table 4.b at node 4 gives the highest result of 1145, so a ship at node 4 with the above conditions will go next to node 6.

Table 4: Parameterized routing tables of nodes 3 and 4, to go to node D, (x_1, x_2, x_3) = (1000, 1100, 1200)

Table 4.a

If current highest critical condition at node 3 is	Then go to neighbor node:
x_1 – 50	5
x_2 – 55	6
x_3 – 45	6

Table 4.b

If current highest critical condition at node 4 is	Then go to neighbor node:
x_1 – 65	3
x_2 – 65	6
x_3 – 55	6

We now start to compute the sensitivity of the result in each node, stable or not.
At node 1 for example, the best path to D has a length of 1135, and uses edge (X_3, *D*) to *D*. The second best destination port is X_2, using edge (X_2, *D*) to *D*, and has a length of 1030. The remaining possible destination is X_1, using edge (X_1, *D*) to *D*, and has a length of 960.

Now, for a different path to be chosen if only one non-stable value changes, two cases are possible. Either the profit at the best destination port falls so much that the second best becomes better, or the profit at one destination port that is not the best one climbs so much that it becomes the best one.

Comparing the values found in Table 2, and using the computed distance formula to go from any stable node to any non-stable node, we can deduce that, at node 1 for example, the second best destination port becomes the best one if $x_3 - 65 < 1030$, that is if $x_3 < 1095$. We can also deduce that, at node 1, destination port X_1 will becomes the best destination port if $x_1 - 40 > 1135$, that is if $x_1 > 1175$. And that, at node 1, destination port X_2 will becomes the best destination port if $x_2 - 70 > 1135$, that is if $x_2 > 1205$.

We call these values (1175, 1205, 1095) at node 1 the *critical values* of node 1 for the prices at destination ports (X_1, X_2, X_3) if (x_1, x_2, x_3) = (1000, 1100, 1200). If any single profit change occurs from the initial conditions (x_1, x_2, x_3) = (1000, 1100, 1200), then there will be no path change to consider if the new price is not above its critical value for a non-best destination port, or is not below its critical value for the best destination port. Furthermore, if the local profit that changed changes again many times and the other non-stable profits do not change, than there is no recomputation needed of any path and values.

5 Conclusions

In this paper, we studied the problem of finding the most interesting path (the one that maximizes the gain) toward one of several destination ports subject to uncertain information on the expected gain in each port and rerouting a ship when needed.
We proposed a simple and yet efficient algorithm to recompute the path of the ship, when she is on the way, based on the computation of the longest path in a weakly dynamic graphs, in order to maximize the global gain of the trip. Parametric routing tables are precomputed, and critical values are deduced.

As a final remark, one can note that a particular pathological classical situation that may arise in this kind of problem is that the expected values between two possible final destinations may change several times such that the ship must alternatively follow a path along and edge from a to b, then back from b to a, several time. It is a

well-known problem of sensitivity in dynamic problems. One idea of heuristic may be that the ship is not allowed to come back toward another destination port unless the total expected profit there is superior to the total expected profit before the last change. With this heuristic, it is not possible for a ship to travel forever between two ports, because the prices will not increase forever.

In the future, we intend to study the problem of finding longest paths in weakly dynamic graphs when some non-stables edges are not close to the destination node (passing through the Suez Canal for example).

We also intend to work on extending this result to the problem of arbitraging multi-deliveries when several destinations must be reached by a ship at one time or another.

References

[1] R. K. Ahuja, T. L. Magnanti, J. B. Orlin, "Network Flows: Theory, Algorithms, and Applications", PP.164−165, Prentice Hall 1993.

[2] M. Alivand, A.A. Alesheikh, M.R. Malek, "New method for finding optimal path in dynamic networks". World Applied Sci. J.,2008, 3: 25−33, 2008.

[3] H.R. Bajgan, R.Z. Farahani. "Using colony system and neighborhood search for dynamic vehicle routing problem". American Journal of Operational Research, vol. 2, no.4, pp. 31−44, 2012.

[4] D.J. Bertsimas. "Probabilistic combinatorial optimization problems". PhD thesis, Massachusetts, Institute of Technology, 1988.

[5] S. Balev, F. Guinand, Y. Pigné, "Maintaining Shortest Paths in Dynamic Graphs". In proceedings of the International Conference on Non−Convex Programming: Local and Global Approaches Theory, Algorithms and Applications (NCP'O7). 2007, December 17−21, Rouen, 2007.

[6] Nicolas Boria, Vangelis Th. Paschos, "Optimization in dynamic environments", CAHIER DU LAMSADE 314, Université Paris−Dauphine, 2011.

[7] J−Y Colin, A. S. Ould Cheikh, M. Nakechbandi, "Route Planning in a Weakly Dynamic Undirected Graph" 1st International IEEE Conference on Advanced Logistics and Transport (ICALT'2013), May 29−31, 2013 in Sousse, Tunisia (2013).

[8] C. Demetrescu and G.F. Italiano, "A new approach to dynamic all pairs shortest paths", J. ACM, 2004, 51(6):968–992, 2004.

[9] D. Fulkerson, "Expected critical path lengths in PERT networks". Operations Research 10 808 − 817, 1962.

[10] P. Jaillet. "Probabilistic traveling salesman problems". PhD thesis, Massachusetts Institute of Technology, 1985.

[11] O. Joly, "La Structuration des Réseaux de Circulation Maritime", PhD thesis, Le Havre University, 1999.

[12] O. Merk, et al., "The Competitiveness of Global Port−Cities: the Case of the Seine Axis (Le Havre, Rouen, Paris, Caen) − France", OECD Regional Development Working Papers, 2011/07, OECD Publishing, 2011.

[13] M. Nakechbandi, J−Y Colin, A. S. Ould Cheikh, "Routing and Rerouting in Territorial Systems Modeled by Weakly Dynamics Graphs" M. Nakechbandi, J−Y Colin, A. S. Ould Cheikh, ECCS'13, September 16−20, 2013, Barcelona, Spain(2013).

[14] T. Notteboom, "Recent traffic dynamics in the European container port system". Port Technology International, Issue 58, 2013.

[15] source : http://www.hamburgsud−line.com/hsdg/media/hamburgsd/documents_1/regionalinformation/northamerica/usa/news/2013/JR−101713_Rotterdam.pdf

Proceedings of ICCSA 2014
Normandie University, Le Havre, France – June 23-26, 2014

Multi-Objective Optimization of the Integrated Problem of Location Assignment and Vehicle Scheduling at Automated Container Terminals

Hamdi Dkhil, Adnan Yassine, Habib Chabchoub

Abstract. A new generation of terminals using automated container handling equipment needs efficient solutions to optimize task scheduling and operating costs. In this work we propose a new multi-objective approach to optimize the operating times, the storage space organization and the number of equipment used.

Keywords. Vehicle Scheduling, AGV (Automated Guided Vehicle), ALV (Automated Lifting Vehicle), Location assignment, Storage Location, Storage Bay, Transfer Crane, Multi-Objective Optimization, NP-Completeness, Operating Cost Evaluation, Makespan, Location Assignment Cost, Multi-Objective Optimization, Multi-Objective Evolutionary Algorithms.

1 Introduction

Considering the phenomenal evolution of world container traffic and particularly the increasing of container ship capacity, maritime terminals need more and more efficiency in their handling operations. In this work we propose a new integrated modeling considering the import case in maritime automated container terminal. We consider combination between two known problems, the first is the storage location assignment problem and the second is the vehicle scheduling problem. In fact, we

study the Multi-Objective Integrated Problem of Location Assignment and Vehicle Scheduling (IPLAVS) in automated container terminal at import. This approach which combines two chronologically successive problems prefers the use of multi-objective optimization (MOO). Three kinds of automated container terminal are studied. We identify these kinds of terminal considering their vehicles: Auto-Straddle-Carrier, AGV or ALV.

Yassine Adnan and Dkhil Hamdi are in Laboratory of Applied Mathematics of Le Havre, University of Le Havre, France.
Chabchoub Habib and Dkhil Hamdi are in department of Enginery of Computing Systems in National School of Sfax, Tunisia.
hamdi.dkhil@doct.univ-lehavre.fr
yassine.adnan@univ-lehavre.fr
habib.chabchoub@fsegs.rnu.tn

2 Reviews of literature

As we know, this work is the second study of this specific problem (IPLAVS) considering automated container terminals.

The first study of the integrated problem of storage space allocation and vehicle scheduling, in the specific context of automated container terminals, was the study of Bish et al [1] which treats the problem for AGV handling system. In that work, the vehicle schedule and location assignment are optimized in order to minimize one objective which is the handling time. However, the waiting-times in bay entry (AGV wait for stacking crane in bay entry), which is a crucial constraint of the real problem, is not considered. In other studies, the optimization of storage location assignment, in the general context of container terminal, considers total vehicle routing distance. However, vehicle scheduling, waiting time in bay entries, as well as the interaction between the different equipment and others parameters are not considered.

Golias and al. [2] formulated and solved the discrete space and dynamic vessels arrival time (DDBSP). For the first time, the multi-criteria aspect of the problem is considered. Two objectives are maximized: the customer satisfaction and the reliability of the berth schedule. Authors used a multi-objective genetic algorithm to solve the problem.

Giallombardo et all [3] studied the integrated problem of berth allocation and QC scheduling. Two objectives are considered, the first is to maximize the total value of chosen QC profiles and the second is to minimize the housekeeping costs of the transshipment flow.

3 Operating cost evaluation and multi-objective optimization at automated container terminal

The objective is to minimize the operating cost which we evaluate considering eight components: the date of last task “makespan”, the total vehicle operating time, the total transfer crane operating time (or the total storage bay occupation time for terminals with straddle carriers), the number of vehicles used, the number of transfer cranes used (or the number of storage bays used for terminal with straddle carriers), the number of storage locations used, and two different average costs of storage location assignment. The first average cost of storage location assignment is evaluated in order to favor the feasibility of next storage operations at import. The second average cost of storage location assignment is evaluated in order to facilitate containers transfer for deliveries. We assume that the operating cost is a function of these components and that the influence of each component is variable and dependent on different parameters. These parameters are essentially: the number of quays in the terminal; the vehicle traffic layout; the number of container ships to serve in the terminal; the influence of concurrent operations in the terminal; the storage space configuration; the number of free transfer cranes (the number of free storage bays for terminals with straddle carriers), the number of free vehicles, the number of free quay cranes, the mobility of quay cranes; etc.
Considering our approach, in one hand, the integration of two optimization problems is theoretical guaranty of higher optimality. In the other hand, our solution proposes an 8-objective optimization process. It is also a new and efficient approach considering the real-world significance of the optimized objectives.
We proved that the problem is NP-Complete using polynomial reductions of IPLAVS to the parallel machine problem (PMP) and the Traveling Salesman Problem (TSP). We studied the numerical aspect of the total routing path variation considering a chosen layout.

4 Resolution

We developed a Multi-Objective genetic algorithm adapted to the studied problem. The algorithm use different populations, we associate to each population a specific
k-levels selection process. A central population is used and the best individuals of the others populations migrate to it periodically. The efficiency of the algorithm is proved by numerical results considering a large real instance of 1000 containers and a total storage space capacity of 10 000 containers.

5 Conclusion and perspective

In this study, we treated the multi-objective optimization of the different kinds of automated container terminal. We optimized the operating cost of the handling systems considering different components. Real instances are used to prove the efficiency of our optimization approach. IPLAVS is solved effectively for large instances up to 1000 containers and a storage space of 10 000 containers capacity.
In future works, we will develop other multi-objective meta-heuristics to determine efficiently the approaches adapted to the studied problem. A comparative study of the productivity of the different kind of terminals will be introduced also.

References

[1] Bish, E.K. Leong, T. Li, C. Ng, J.W.C. Simchi-Levi, D. , Analysis of a new Vehicle Scheduling and Location Problem, Naval Research Logistics, vol 48, 363-385. 2001.
[2] Golias, M.N. Theofanis, S. Boile, M. , A bi-level formulation of the berth scheduling problem with variable vessel release dates to reduce port emissions, Proceeding of 2009 International Conference on Shipping, Ports, Logistics Management, Inha University, korea, ISLC, Incheon. 2009.
[3] Giallombardo, G. Moccia, L. Salani, M. Vacca, I. , The tactical berth allocation problem with quay crane assignment and transshipment-related quadratic yard costs, Proceedings of the European Transport Conference (ETC), 1-27. 2008.

Proceedings of ICCSA 2014
Normandie University, Le Havre, France – June 23-26, 2014

GAME THEORY TO STUDY THE BEHAVIORAL PROBABILITIES IN THE SUPPLY CHAIN

Ilham SLIMANI[1] and Said ACHCHAB[1]

Abstract. In this paper, we reviewed a game theoretic approach to analyze an inventory and transportation optimization problem in a basic supply chain. We focus on a single channel, two-echelon supply chain with a single retailer and a single supplier of a one-product with the objective of modeling interactions among players. Careful attention is given to information flow, more precisely demand forecasting, and its impacts on the supply chain's performance since the retailer is closer to the market and has a better view of demand forecasts.
Keywords. Game theory, Supply chain management, Inventory and Transportation costs, Asymmetric information, Probabilistic demand.

1 Introduction

When it comes to applying mathematics to analyze or evaluate strategic decisions among at least two rational actors, called players, we are in the realm of game theory; with sometimes cooperative and sometimes conflicting interests. Behaving rationally, for one player, means acting to maximize his own payoff, knowing that the final outcome of each player depends not only on his own action or on chance events, but also on the actions of other players.

Since the ultimate goal of any effective supply chain management system is to reduce its total relevant cost with the assumption that products are available when needed; this paper uses a game theoretic approach to analyze an inventory and transportation optimization problem in a basic supply chain. We start by presenting game theory through examples: basic concepts…in order to explain how supply chain behavior can be predicted and optimized under a set of given objectives. Followed by demonstrating the importance of demand forecasting among the supply chain's members. Then we define the studied system with a mathematical modeling of inventory and transportation costs: we consider a two-echelon supply chain composed of one retailer facing a random demand of a final product, and his supplier, we focus on information sharing and its impact on the payoff of each player. As a solution concept, we choose to find the equilibrium that guaranties the maximum profit for all players. Different games are employed throughout this work to demonstrate the application of game theory's tools.

[1] Al-Qualsadi Research & Development Team, National Higher School for Computer Science and System analysis (ENSIAS), Mohammed Vth University Souissi Rabat, Mohammed Ben Abdallah Regragui avenue, Madinat Al Irfane, BP 713, Agdal, Morocco.
E-mails: slimani.ilham@gmail.com, s.achchab@um5s.net.ma

2 Game theory through examples

2.1 Literature background

Game theory is a mathematical tool that deals with interdependence decisions (cooperation/competition) among multiple agents (players); It has proved its success in many areas (politics, economy,).This theory was first introduced by Von Neumann and Morgenstern [1], then by John Nash [2], [3], [4], and [5] who developed the solution concepts for these games, more precisely the concept of equilibrium. Kuhn [6] focuses in his work on the concept of imperfect information.

Cachon and Zipkin [7] studied a single channel, two-stage supply chain with stationary stochastic demand considering that inventory holding costs and backorder penalty cost are charged at each echelon of the supply chain. Two games are considered where inventory cost is charged by the two independent stage separately (competition) and then by choosing the same local inventory with shared costs (cooperation). The author demonstrate that the games have a unique equilibrium that differs from the optimal solution.

Hongwei et al. [8] Analyzes a non-cooperative mechanism in a two-echelon decentralized supply chain composed of one supplier and n retailers under two conditions: sufficient and insufficient supply. Several Nash Equilibrium contracts are used both in echelon inventory games and local inventory games with the omission of the con-

cept of asymmetric information.

In Esmaeili et al. [9], several seller-buyer supply chain models are studied using non-cooperative and cooperative games with the Stackelberg strategy as a solution concept for the non-cooperative game and Pareto efficient solutions for the cooperative game.

Tetsuo and Zipkin [10] studied the benefits of sharing demand forecasts information of a stochastic demand in both cooperative and competition settings on a simple supply chain of a single supplier and a single retailer. Different modes of decision making are studied: centralized mode, cooperative case, competitive case with centralized demand forecasts and competitive case with decentralized demand forecasts.

In its general form, a game is defined by three parameters [11] $< N, X_i, \pi_i >$:

- N: set of i players where N ={1,2…,n};
- X_i: set of possible strategies of player i; called pure strategies of players
- Payoff function of player i denoted $\pi_i(x_i, x_{-i})$ choosing to play the strategy x_i given the strategies adopted by the other players denoted x_{-i}.

The main objective of each player i is to maximize his individual profit by finding the optimal strategy $x_i^* \in X_i$; where:

$$x_i^*(x_{-i}) = \arg\max \pi_i(x_i, x_{-i}) \quad (1)$$

A mixed strategy for player is distribution on his pure strategies with given probabilities that determines the player's decision. Note that not every game has a pure strategy equilibrium. However, every game has a mixed strategy Nash equilibrium. The idea is that each action is assigned a probability of play and given these probabilities, a player who is adopting a mixed strategy is indifferent between his actions. The example bellow (see example 2) explain how optimizing payoff might require a randomized strategy.

2.2 Examples of game theory

In order for game theory to apply, two assumptions must be made:

- The players are rational which means that each player is acting in his self-interest
- Each player (choice made) has only partial control of the game's outcome

We can describe a game by listing the players participating in the game as well as listing the alternative actions for each player. The simple form game is a two-player game, in this case the game is modeled in a matrix where the rows are the actions of the first player, and the columns represent those of the second. In this matrix, the utilities of players are represented by two numbers: (First player's payoff, Second player's payoff). Note that higher numbers are better (more utility).

Example 1. Prisoner's dilemma game (Pure strategy)

The prisoner's dilemma game is one of the famous games, where two players are partners in a crime. Each prisoner is placed in a separate cell, and offered the opportunity to confess or not. The game can be represented by the following matrix of payoffs:

		Prisoner 2	
		Not confess	Confess
Prisoner 1	Not confess	(3,3)	(0,5)
	Confess	(5,0)	(1,1)

In this example, (Not confess-Not confess) is a dominant strategy equilibrium. However, it is not Pareto optimal. Both players could be made better off if neither defected against the other.

Example 2. Mixed strategy

		Wife	
		Football	Shopping
Husband	Football	(2,1)	(0,0)
	Shopping	(0,0)	(1,2)

In pure strategies, the probability of each action is $1/2$:
Husband's payoff:

$$\pi_H(\text{Football}) = 1/2 * 2 + 1/2 * 0 = 1$$
$$\pi_H(\text{Shopping}) = 1/2 * 0 + 1/2 * 1 = 1/2$$

Wife's payoff:

$$\pi_W(\text{Football}) = 1/2$$
$$\pi_W(\text{Shopping}) = 1$$

We conclude that if we limit to pure strategy players will not coordinate therefore the best solution for players is being indifferent to their choices by associating a probability to each action:

- α: probability of choosing football for husband
- β: probability of choosing shopping for wife

Since payoffs must be equal for both players:
Husband:
$\alpha * 2 = (1 - \alpha) * 1$ Meaning that $\alpha = 1/3$
Wife:
$(1 - \beta) * 1 = \beta * 2$ Meaning that $\beta = 1/3$

In both cases the expected payoff of each player is $2/3$

3 Demand forecasting techniques

In the industrial world, firms cannot risk waiting for the

actual demand to occur so they can react and determine the quantities to purchase, produce and deliver; knowing that each one of these operations takes time and for a supply chain manager time is money. Demand forecasts are important and necessary to any member of the supply chain as they gave them the advantage of planning and anticipating for future needs (Just in Time delivery policy to costumer orders).

The result of better demand forecasts leads to reducing stock, giving the opportunity of planning production, reducing logistic costs, and improving customer service. There are three commonly used techniques of modeling demand forecasts:

- Qualitative techniques: based on opinion and intuition, used with limited or unavailable costumer demand data.
- Quantitative techniques: based on mathematical models and historical data to make forecasts.
- Time series techniques: this technique is the most frequently used method in the literature, we
  - *Simple Moving Average Forecasting Model* that uses historical data to generate a forecast:

$$F_{t+1} = \frac{\sum_{t-n+1}^{t} A_i}{n} \quad (2)$$

Where
F_{t+1}: Forecasts for period t+1
n: Number of period used to calculate moving average
A_i: Actual demand in period i

  - *Weighted Moving Average Forecasting Model that is* based on an n-period weighted moving average:

$$F_{t+1} = \sum_{t-n+1}^{t} w_i A_i \quad (3)$$

Where
F_{t+1}: Forecasts for period t+1
n: Number of period used to calculate moving average
A_i: Actual demand in period i
w_i: Weight assigned to period i with $\sum_{t-n+1}^{t} w_i = 1$

4 Problem statement: Two-echelon supply chain

The first study of this work (Figure 1) examines a single product in a two-echelon supply chain composed of a single retailer (buyer) and a single supplier (vendor).

The proposed models in this paper are based on assuming that transportation cost is paid by the supplier. Demand D is a random variable with distribution function F_D and density function f_D. It is defined by (m, σ) mean and standard deviation. Our goal is to apply game theory on a basic supply chain by modeling interactions among players in order to optimize both inventory and transportation costs of the whole system.

The decision making process of this model is presented in figure 1.

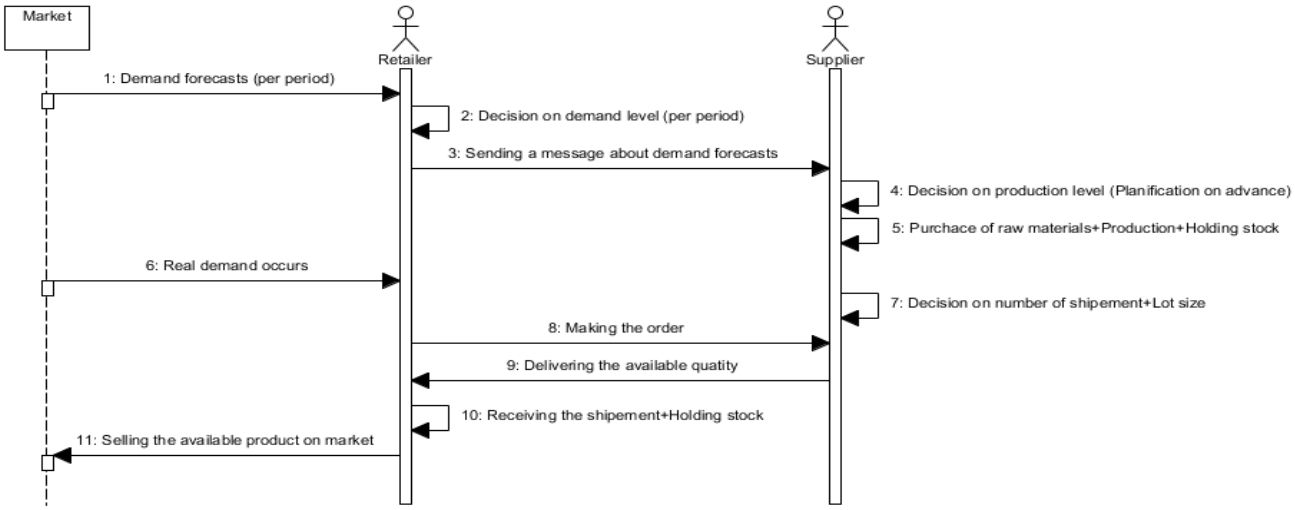

Figure 1: Sequence diagram of the two-echelon supply chain with demand information

4.1 Notations

The following notations are used:

C: Capacity of vehicle;

d: Distance (per Km) between the retailer and the supplier;

C_f : Transportation fixed cost of the vehicle per Km, it is considered constant in each period (for example: parking fare or rewards to the driver…);

C_V: Transportation variable cost of the vehicle per, it depends mainly on the fuel consumed that is related directly to the distance travelled;

D: Market demand of the product during the current period;

T: Length of each period;

Q: Ordered quantity to the supplier per period T;

r: Unit price with which the retailer buys the product from the supplier;

p: Unit selling price of the product on the market by the retailer;

c_r : Unit production cost of the retailer;

b_r : Unit breakdown cost of the retailer;

c_s : Unit production cost of the supplier;

b_s : Unit breakdown cost of the supplier;

N: Supplier's replenishment level, it is the quantity in stock at the end of each period before demand arrives;

h_s: Cost of unsold unit paid by the supplier;

π_r : Retailer's profit

π_s : Supplier's profit;

4.2 The retailer's model formulation

The retailer's objective is to maximize his net profit: Max [retailer's profit = Sales revenue – Purchasing cost – Shortage cost – Production cost];

$$\text{Max}\{\pi_r\} = \text{Max}\ \{E[(p - r - C_r)\min(N, D) - b_r\,(D - N)^+]\} \quad (4)$$

With

$$(x)^+ = \max(0, x) \quad (5)$$

Where:

$$Sales\ revenue = p\min(N, D) \quad (6)$$
$$Purchasing\ cost = r\min(N, D) \quad (7)$$
$$Shortage\ cost = b_r\,(D - N)^+ \quad (8)$$
$$Production\ cost = C_r\min(N, D) \quad (9)$$

4.3 The supplier's model formulation

Since the players are rational, the supplier is also in search of his optimal net profit, supplier's profit = Sales revenue – Production cost – Shortage cost – Cost related to unsold product – Transportation cost;

$$\text{Max}\{\pi_s\} = \text{Max}\ \{E[r\min(N, D) - C_s.N - b_s\,(D - N)^+ - h_s\,(D - N)^+ - C_T]\} \quad (10)$$

Where:

$$Production\ cost = C_s.N \quad (11)$$
$$Shortage\ cost = b_s\,(D - N)^+ \quad (12)$$
$$Cost\ unsold\ product = h_s(N - D)^+ \quad (13)$$

Using the model proposed by Martel [12], including both the fixed cost C_f : and the variable cost C_V ; Transportation cost is modeled as follows:

$$C_T = C_f + C_V.\text{Q} \quad (14)$$

Where:

$$C_f = C_a + C_d.d \quad (15)$$

C_a: Stopping cost;

C_d: Cost related directly to the distance travelled

4.4 Game's matrix

We suppose that each player has two choices: "Cooperate" or "Not cooperate", as explained in the table 1.

Table 1: Players strategies in the proposed model

	Retailer	Supplier
Cooperate	Send exact (trust worthy) demand forecasts to supplier	Trust demand forecasts sent by retailer and plan production level based on it
Not cooperate	Send wrong demand forecasts to supplier	Not Trust demand forecasts sent by retailer and use mixed strategy

		Supplier	
		Cooperate	Not cooperate
Retailer	Cooperate	(π_r^*, π_s^*)	(π_r^o, π_s^o)
	Not cooperate	(π_r', π_s')	(π_r^o, π_s^o)

5 Conclusion

Several works studying two-echelon supply chains using a game-theoretic mechanism were presented in this paper. Our goal is to use this theory to find the optimal situation for a decentralized retailer-supplier system with the objective of finding the equilibrium that guaranties maximum profit for both players and demonstrating how

payoffs depend on the two actions.

It is true that our work is still unfinished, and since we are still validating our results by numerical examples we chose, for now, not to present these results. Next, as future work we propose the introduction of a third player (the distributor) to this problem.

References

[1] V. N. Morgenstern, Theory of Games and Economic Behavior, Princeton, 1944.

[2] J. Nash, "Equilibrium points in N-Person Games," 1950.

[3] J. Nash, "The Bargaining Problem," *Econometrica,* 1950.

[4] J. Nash, "Non-Cooperative Games," *Annals of Mathematics,* 1951.

[5] J. Nash, "Two-Person Cooperative Games," *Econometrica,* 1953.

[6] H. W. Kuhn, "Extensive Games and the Problem of Information.," 1953.

[7] C. G. a. Z. Paul, "Competition and cooperation inventory policies in a two-stage supply chain," *Management science ,* 1999.

[8] W. Hongwei, M. Guo and J. Efstathiou, "A game-theoretical cooperative mechanism design for two-echelon decentralized supply chain," *Elsevier,* 2003.

[9] M. Esmaeili, Mir-Bahador and Zeephongsekul, "A game theory approach in seller-buyer supply chain," *Elsevier,* 2008.

[10] L. T. a. P. Zipkin, "Competition and cooperation in a two-stage supply chain with demand forecasts," *Informs,* 2010.

[11] S. a. C. G. Netessine, "Game theory in supply chain analysis," *Handbook of Quantitative Supply Chain Analysis: Modeling in the eBusiness Era, Kluwer,* 2004.

[12] M. A, "Coûts logistiques et création de valeur. Cours MBA gestion manufacturière et logistique : conception et Gestion de chaînes logistiques," *Quebec, Canada,* pp. chapitre 2, : pp 51-94, 2001.

[13] G. Cachon and S. Netessine, "Game theory in supply chain analysis. Handbook of Quantitative Supply Chain Analysis: Modeling in the eBusiness Era," *Kluwer,* 2004.

[14] W. Hongwei, M. Guo and J. Efstathiou, "A game-theoretical cooperative mechanism design for two-echelon decentralized supply chain," *Elsevier,* 2003.

[15] M. Esmaeili, Mir-Bahador and Zeephongsekul, "A game theory approach in seller-buyer supply chain," *Elsevier,* 2008.

[16] L. Tetsuo and P. Zipkin, "Competition and cooperation in a two-stage supply chain with demand forecasts," *Informs,* 2010.

[17] M. A., S. M. and S. M, "The newsvendor game has a nonempty core," *Games and Economic Behavior, ,* pp. 38, pp. 118-126, 2002.

Proceedings of ICCSA 2014
Normandie University, Le Havre, France - June 23-26, 2014

ROUTING PARALLEL HETEROGENEOUS MACHINES IN MAINTENANCE PLANNING: A HYPER-HEURISTIC APPROACH

Kassem Danach, Wissam Khalil, Francisco C. Lima Junior and Shahin Gelareh *†‡

Abstract. We consider a parallel heterogenous machine scheduling problem arising in maintenance planning of heterogeneous fixed installations[1][2][5][7][9][11]. A set of mobile maintenance machines are responsible to accomplish some tasks that are located at certain locations. Each task needs a given level of maintenance which is only offered by certain mobile maintenance machines. Each task at a discrete location point is a production machine which is broken. Given the distance between the discrete locations, the required service level and the production of every installation, the problem is to route the mobile maintenance machine in order to minimize the overall loss of production[4]. We propose a time-arc indexed mathematical formulation as well as a hyper-heuristic method based on a set of constructive, improvement, perturbation, and others types of heuristic[3][8]. Our computational results demonstrate the efficiency and quality of our hyper-heuristic against the exact methods (our branch, price and cut) in terms of quality and time[6][10].

Keywords. Routing problem, Hyper-heuristic, Self-adaptive, Artificial intelligence, branch price and cut.

References

[1] Aloise, D. J., Aloise, D., Rocha, C. T., Ribeiro, C. C., Filho, J. C. R., Moura, L. S., 2006. Scheduling workover rigs for onshore oil production. Discrete Applied Mathematics 154 (5), 695 – 702.

[2] Barnes, J. W., Brennan, J. J., Knap, R. M., 1977. Scheduling a backlog of oil well workovers. Journal of Petroleum Technology 29(12), 16511653.

[3] Burke, E. K., Misir, M., Ochoa, G., Ozcan, E., 2008. Learning heuristic selection in hyperheuristics for examination timetabling. In: Proceedings of 7th International Conference of Practice and Theory of Automated Timetabling (PATAT08), Montreal, Canada.

[4] Carlier, J., Pinson, E., 1989. An algorithm for solving the job-shop problem. Management science 35 (2), 164–176.

[5] Duhamel, C., Cynthia Santos, A., Moreira Guedes, L., 2012. Models and hybrid methods for the onshore wells maintenance problem. Computers & Operations Research 39 (12), 2944–2953.

[6] Mattos Ribeiro, G., Desaulniers, G., Desrosiers, J., 2012. A branch-price-and-cut algorithm for the workover rig routing problem. Computers & Operations Research 39 (12), 3305–3315.

[7] Mattos Ribeiro, G., Regis Mauri, G., Antonio Nogueira Lorena, L., 2011. A simple and robust simulated annealing algorithm for scheduling workover rigs on onshore oil fields. Computers & Industrial Engineering 60 (4), 519–526.

[8] Misir, M., 2012. Intelligent hyper-heuristics: a tool for solving generic optimisation problems. status: published.

[9] Noronha T. F., Lima F. C. J., A. D. J., 2001. Um algoritmo heurístico guloso aplicado ao problema do gerenciamento das intervenções em poços petrolíferos por sondas de produção terrestre. in proceedings of the xxxiii brazilian symposium on operations research. p. 135.

[10] Pessoa, A., Uchoa, E., de Aragão, M. P., Rodrigues, R., 2010. Exact algorithm over an arc-time-indexed formulation for parallel machine scheduling problems. Mathematical Programming Computation 2 (3-4), 259–290.

[11] Ribeiro, G. M., Laporte, G., Mauri, G. R., 2012. A comparison of three metaheuristics for the workover rig routing problem. European Journal of Operational Research 220 (1), 28–36.

*Kassem Danach,Wissam Khalil and Shahin Gelareh are with Universite D'Artois, LGI2A, F-62400, Bethune, France. E-mails: kassem_danach@live.com, wissam.khalil@univ-artois.fr, shahin.gelareh@univ-artois.fr

†Francisco C. Lima Junior is with DUERN, DI State University of Rio Grande do Norte, 596000, Mossoro, Brazil. E-mail: fclimajr@gmail.com

‡Manuscript received April 15, 2014.

Satellite Workshop 11
Chaos theory and applications

Satellite Workshop 11
Chaos theory and applications

Organizer

- Christophe Letellier, CORIA, University of Rouen, France, christophe.letellier@univ-rouen.fr

Description

This session is supposed to bring together peoples developping tools for characterizing chaos, its existence as well as its nature by using a qualitative (topological) or a quantitative approach. These techniques can be also used in some applications in physics, chemistry, engineering, etc.

List of papers/presentations

Bob Gilmore (Drexel University)
"Tale of Two Maps"
Abstract: The logistic map has been used to enrich our understanding of a large class of highly dissipative dynamical systems, especially those contained in a genus-one torus. A different unimodal map can be used to enrich our understanding of highly dissipative dynamical systems contained in tori of genus $g>1$. The two maps are dual in a precise topological sense. The two maps are described and their properties and predictions compared.

Jean-Marc Malasoma (ENTPE))
"Simplest time-reversible chaotic flow"
Abstract: Temperature control in molecular dynamics numerical simulations is an essential task. Nosé resolve this problem during the eighty years by using time-reversible integral feedback to control the kinetic energy [Mol. Phys. 52, 255-268 (1984)]. The dynamics of the so-called Nosé-Hoover oscillator is governed by a set three autonomous ordinary differential equations which exhibit both regular (periodic and quasiperiodic) and chaotic solutions. So far, the Nosé-Hoover system was considered the most elegant and algebraically simplest time-reversible conservative flow with deterministic chaos. Quite recently, the minimal algebraic structure which is necessary to allow chaos in three-dimensional quadratic flows was identified. Unfortunately, this interesting property is based on the strong assumption (not verified by the Nosé-Hoover oscillator) that the divergence of the flow is constant. New theoretical developments, leaving aside this assumption, have uncovered what appears to be the algebraically simplest example of time-reversible chaotic system.

Laurent Larger, Roman Lavrov, Antonio Baylon Fuentes, Maxime Jacquot, Yanne K. Chembo, V.S. Udaltsov
"Dual Delay Electro-optic Phase Oscillators: a Nonlinear Non-local Dynamics for High Performance Secure Optical Chaos Communications"
Abstract: From the early beginning of chaos communications, delay dynamics have been considered as an attractive solution for obtaining a robust, as well as a highly complex chaotic motion for carrying the data to be hidden within chaos. This infinite dimensional

temporal dynamics are moreover popular and relatively easy to design in photonics, in which fiber optics communications are obviously a relevant field of application for novel physical layer encryption approaches. Some of the challenges in this original application of chaos theory are the wide bandwidth provided in the Fourier spectrum by the chaotic motion (for the ability to encode high bit rate digital data), and its non- discernibility from a purely random noise signal (security is related to the inability to extract any deterministic feature from the chaotic motion). In our last attempt to design such a chaotic transmission system, a particular dual delay electro-optic phase oscillator was proposed, successfully addressing these two requirements, additionally to the capability to allow for a robust and accurate experimental chaos synchronization between two distant emitter and receiver. State of the art speed and distance optical secure communications have been obtained, moreover with field experiments over installed commercial fiber optic networks.

Christophe Letellier, Gustavo H. Oliveira Salgado & Luis A. Aguirre
"Fractional-order systems: Does the derivative order differ from a bifurcation parameter?"

Abstract: Fractional-order systems have been investigated in the context of control theory since the early 1990's. They have attracted recent attention to the researchers developing techniques for controlling chaotic behaviours. Nevertheless, many fundamental questions about dynamical properties of chaotic fractional-order systems are still left open. We propose to address a few such questions as, for instance: does the derivative order differ from a bifurcation parameter ? How is the dissipation rate of the dynamics affected by the derivative fractional-order? What is the dimension of the phase space of a fractional-order system? Numerical simulations of known bench systems are used to provide (sometimes partial) answers to such questions.

Adrien Kerfourn
"Phase synchronisation in a ring of Rössler systems"

Luc Pastur, Charles Pivot, François Lusseyran & Christophe Letellier
"Time-delayed feedback control for phase coherent and phase noncoherent chaotic regimes"

Proceedings of ICCSA 2014
Normandie University, Le Havre, France - June 23-26, 2014

A TALE OF TWO MAPS

Robert Gilmore *†

Abstract. The logistic map has been used to enrich our understanding of a large class of highly dissipative dynamical systems, especially those contained in a genus-one torus. A different unimodal map can be used to enrich our understanding of highly dissipative dynamical systems contained in tori of genus $g > 1$. The two maps are dual in a precise topological sense. They are described and their properties and predictions compared.

Keywords. Logistic map, symbolic dynamics, fold map, cusp map, explosion, chaotic attractor.

1 Introduction

Many strange attractors are organized around a single unstable focus. The Rössler attractor [1] is a typical example. In such cases the departure of a trajectory from the unstable focus decelerates and eventually the trajectory returns to the neighborhood of the focus and the process is repeated. The chaos-generating mechanism is of "stretch and fold" type and the return map has a characteristic fold or parabolic shape. Strange attractors of this type are typically contained in genus-one bounding tori [2].

Other strange attractors are organized around two or more unstable foci. The Lorenz attractor is a typical example [3]. In such cases the departure of a trajectory from the unstable focus accelerates and eventually the trajectory departs from the neighborhood of one unstable focus and enters the neighborhood of another. The chaos-generating mechanism in such cases is of "tear and squeeze" type and a suitable form of the return map has a characteristic cusp shape (See: Fig. 4 in [3] and Fig. 3.8 in [4].). Strange attractors of this type are typically contained in bounding tori of genus $g > 1$ [2, 5].

2 Two Maps

The dynamics in the highly dissipative limit can be represented by fold and cusp maps [6]. The fold and cusp maps can be given similar forms:

$$\begin{array}{lccccc} \text{Fold} & x' & = & f(x,a) & = & a - |x|^k \\ \text{Cusp} & y' & = & g(y,b) & = & b - |y|^{1/k} \end{array} \qquad (1)$$

It is useful to choose $k = 2$ [7]. Both are unimodal maps of the interval. As a result, kneading theory results are directly applicable to both [8]. For the fold map both branches are concave (down). For the cusp both branches are convex. This difference in topological type reverses the order in which interesting bifurcations occur in the two maps. The return map for the Lorenz equations [3] with $(R, \sigma, b) = (28.0, 10.0, 8/3)$ is well-approximated, after suitable rescaling, by the map $z' = 0.282 - |z|^{0.48}$.

3 Bifurcation Diagrams

The bifurcation diagram for the fold map $x' = f(x, a)$ has been well-studied [5, 9]. A pair of period-one orbits is created via saddle-node bifurcation at $a = -1/4, x = -1/2$. A period-doubling cascade begins with a pitchfork bifurcation at $a = 3/4, x = 1/2$ and continues until the accumulation point is reached at $a_\infty = 1.401155$. Beyond the accumulation point there is a series of noisy period-halving bifurcations [10]. In this region, extending from the accumulation point a_∞ to $a = 1.543689$, there is an admixture of chaotic behavior and stable windows based on orbits of even period created by saddle-node bifurcations. When $a > 1.543689$ orbits of both even and odd period exist. The last stable window is created at $a = 2 - \epsilon$. The boundaries of the strange attractor are $x_{\text{upper}} = f(0, a) = a > x_{\text{lower}} = f^2(0, a) = f\,[f(0, a), a] = a - a^2$. There is a global attractor at $x = -\infty$ and it is the only attractor outside the range $-1/4 < a < 2$. At $a = 2$ the lower bound x_{lower} intersects the period-one orbit that was unstable when created in the saddle-node bifurcation at $a = -1/4$. This creates a crisis [11] that destroys the strange attractor, leaving behind a set of unstable periodic orbits that continue to exist for all $a > 2$. Almost all initial conditions escape to the global attractor at $-\infty$.

The bifurcation diagram for the cusp map $y' = g(y, b)$ is not so well known [6]. There are three period-one orbits in the range $0 < b < 1/4$ and one outside this range. They are organized together as a singular snake [5]. At $b = 1/4$ an inverse regular saddle-node bifurcation destroys the stable period-one orbit that exists for

*Department of Physics, Drexel University, Philadelphia, PA, USA E-mails: robert.gilmore@drexel.edu, bob@bach.physics.drexel.edu

†Manuscript received May 2, 2014; revised May 2, 2014.

$b < 1/4$ and one of the two unstable period-one orbits created in the first explosion at $b = 0$. In the range $1/4 < b < 3/4$ there is a strange attractor that exists in the range $y_{\rm upper} = g(0,b) = b > y_{\rm lower} = g^2(0,b) = b - \sqrt{b}$. In this parameter range there is a countable infinity of explosions, none of which is visible as there are no stable windows. They follow the inverse order of orbit creation in the fold map. At $b = 3/4$ the unstable period-one orbit undergoes a pitchfork bifurcation, becoming stable. The unstable periodic orbits that remain undergo some additional explosions, and are eventually all annihilated at $b = 1$. For all b there is a global repellor at $y = -\infty$ and a global attractor at finite values of y. The global attractor is a chaotic attracter in the range $1/4 < b < 3/4$ and a stable period one orbit outside this range. For $b < 0$ and $b > 1$ the *only* periodic orbit is a stable period one orbit.

4 Caustics and Anticaustics

Caustics are the forward images of the critical point $x = 0$ of $f(x,a)$. Caustics appear in the bifurcation diagram as traces with anomalously large density. The intersections of the $p^{\rm th}$ caustic with the critical line $x = 0$ identifies parameter values a at which period p orbits become superstable. The interleaving of the various caustics identifies the order in which orbits of corresponding periods are created as the control parameter a increases. Five caustics $f^p(0,a)$, $p = 3 \cdots 7$ are shown in Fig. 1.

The caustics $f^1(0,a)$ and $f^2(0,a)$ are the upper and lower bounds on the attractor. All caustics with $p \geq 3$ intersect at $a_{\rm xing} = 1.543689, x = 0.839286$. For $a > a_{\rm xing}$ orbits of both even and odd period are created; for $a_\infty < a < a_{\rm xing}$ (the noisy period-halving region [10]) only even period orbits are created. In this region the second and third caustics $f^p(0,a)$, $p = 2,3$ form the first interior boundaries of the attractor; then $f^p(0)$, $p = 4,5,6,7$ form additional interior boundaries, and so on back to the first accumulation point at a_∞.

Anticaustics are forward images of the critical point $y = 0$ of $g(y,b)$. They are invisible on the bifurcation diagram of the cusp map. Zero crossings of the anticaustics identify points at which explosions take place. The first explosion occurs at $b = 0$. It creates every trajectory that can be composed of the two symbols $0, 1$. All are unstable. The interleaving of the anticaustics identifies how explosions of orbits of corresponding periods are ordered. Eight anticaustics $g^p(0,b)$, $p = 1 \cdots 8$ are shown in Fig. 2. The anticaustics $g^1(0,b)$ and $g^2(0,b)$ are the right- and left- boundaries of the strange attractor.

All anticaustics cross at $(b,y) = (1/4, -1/4)$ and at $(0.595743, 0.176100)$. To the left of the first crossing point $(0 < b < 1/4)$ no bifurcations of any kind take place. In the intermediate range $1/4 < b < 0.595743$ explosions involving both even and odd period orbits take place. For $b > 0.595743$ explosions involving only even period orbits occur. These cease when $b = 0.782598$.

Table 1: For the cusp map $y' = b - |y|^{1/2}$ different processes take place in different ranges of the control parameter value b, as described below. $b_b = 0.575974, b_c = 0.782598$.

Left	Right	What goes on
$-\infty$	$1/4$	Stable period one orbit exists.
0	0	Explosion at $b = 0$ creates all orbits based on symbols 0, 1.
0	$1/4$	No bifurcations in this range.
$1/4$	$1/4$	Stable period-one orbit destroyed in inverse saddle-node bifurcation.
$1/4$	b_b	Explosions remove all odd- and most even-period orbits.
b_b	b_c	Explosions remove even period orbits
$3/4$	$3/4$	Unstable period-one orbit undergoes pitchfork bifurcation, becomes stable.
$3/4$	$+\infty$	Stable period-one orbit exists.
b_c	1	No further bifurcations in this range.
1	1	Explosion at $b = 1$ removes remaining even-period orbits.

At this point all even anticaustics with $p > 2$ cross at $y_{\rm even} = 0.1020047$ and all odd anticaustics with $p > 2$ cross at $y_{\rm odd} = 0.463150$.

The anticaustics $g^2(0,b)$ and $g^3(0,b)$ form interior boundaries of the bifurcation diagram of the cusp map just as the caustics $f^2(0,a)$ and $f^3(0,a)$ form interior boundaries of the fold's bifurcation diagram. Other interior boundaries of $g(y,b)$ cannot be seen because the period-one orbit becomes stable for $b > 3/4$. For $0.782598 < b < 1$ there are no explosions of any type. The explosion at $b = 1$ removes all remaining unstable even period orbits. These results are summarized in Table 1.

5 Explosions

The period-one explosion as b increases through $b = 0$ is the prototype for all explosions. For $b = 0 - \epsilon$ the cusp tip at $y = 0$ fails to contact the diagonal $y' = y$ through the origin. So also do all forward iterates $g^p(y,b)$. At $b = 0$ the cusp tip makes contact with the diagonal, as do all forward iterates. As the tip pushes through the diagonal, $g(y,b)$ intersects the diagonal twice near the origin, $g^2(y,b)$ four $(= 2^2)$ times, and $g^p(y,b)$ 2^p times. Periodic orbits of all possible periods exist. Their symbolic dynamics correspond to all possible sequences of the two symbols 0 and 1. In the parameter range $0 < b < 1/4$ the $p^{\rm th}$ iterate $g^p(y,b)$ continues to have 2^p intersections with the diagonal.

Following the explosion at $b = 0$ that creates all possible periodic orbits there is a refractory interval $0 < b < 1/4$ in which no explosions take place.

As b increases above $b = 1/4$ a series of inverse explosions remove periodic orbits. For example, at the period-

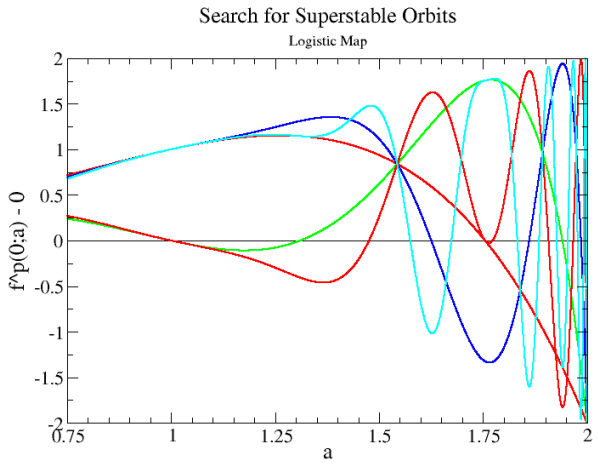

Figure 1: Caustics of the fold map $f^p(x=0,a)$ are shown for $p = 3 \cdots 7$. Their zero crossings identify control parameter values at which period-p orbits become superstable.

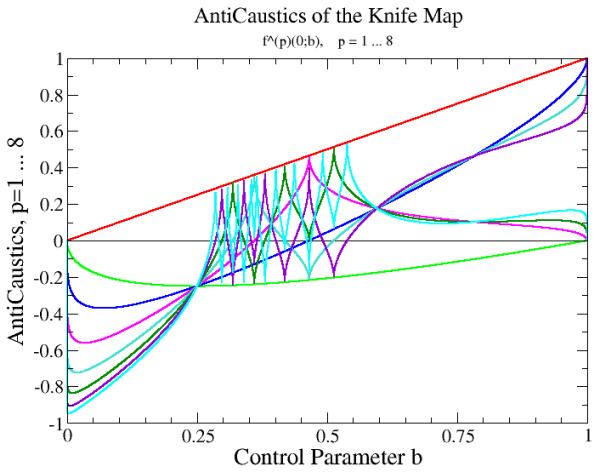

Figure 2: Anticaustics of the cusp map $g^p(y=0,b)$ are shown for $p = 1 \cdots 8$. Their zero crossings identify control parameter values at which period-p explosions occur. The order of superstable orbit formation with a increasing (Fig. 1) is the same as the order of orbit explosions with b decreasing (above). Corresponding zero crossings describe orbits with the same symbol set.

three explosion, which occurs as b decreases through b_3, all possible periodic orbits built from the two symbols $K10$ with $K = 0, 1$ are created. In the reverse direction, as b increases through b_3 this set of orbits is removed from the set of orbits created in the period-one explosion at $b = 0$. Other inverse explosions remove all the remaining orbits created in the first explosion by the time $b = 1$, with the single exception of one of the two period-one orbits created in the initial explosion at $b = 0$.

As a function of b decreasing from $b = 1$ to $b = 0$ the symbolic dynamics of the explosions follows the symbolic dynamics of orbit and periodic window creation in the fold map $f(x, a)$ as a increases in the range $-1/4 < a < 2$. The refractory intervals following explosions in the cusp map correspond to windows following saddle-node bifurcations in the fold map.

6 Renormalization

The b values at which explosions occur are identified by the crossings of the anticaustics with the critical point. The procedure will be illustrated for the period-three explosion. The idea is to expand

$$g^3(y;b) = b - \sqrt{|b - \sqrt{|b - \sqrt{|y|}|}|} \to \Delta(b - b_3) + \alpha\sqrt{|y|} \tag{2}$$

in the neighborhood of an intersection with the anticaustic $g^3(y = 0, b)$ with the critical point $y = 0$. The two fundamental period-three orbits created at this explosion have symbol set $K\sigma_1\sigma_2 = K10$, with $K = 0, 1$. The recursive expression in Eq. (2) is replaced by [12]

$$g^3(y;b) = b - \sqrt{s_2(b - \sqrt{s_1(b - \sqrt{|y|})})} \tag{3}$$
$$s_i = +1 \quad \text{if} \quad \sigma_i = 1$$
$$s_i = -1 \quad \text{if} \quad \sigma_i = 0$$

The resulting expression is Taylor expanded about b_3 to terms linear in $b - b_3$ and $\sqrt{|y|}$. The result is

$$g^3(y, b_3 + \epsilon) \to \left(b_3 - \sqrt{\sqrt{b_3} - b_3}\right) + \left(1 + \frac{2\sqrt{b_3} - 1}{4\sqrt{\sqrt{b_3} - b_3}\sqrt{b_3}}\right)(b - b_3) + \left(\frac{1}{4\sqrt{\sqrt{b_3} - b_3}\sqrt{b_3}}\right)\sqrt{|y|} \tag{4}$$

Zeroing out the constant term determines the value of b_3 (=0.465571) at which the explosion takes place. The coefficients of Δ of $(b - b_3)$ and α of $\sqrt{|y|}$ determine the scales of the renormalization in the the state variable direction (α^2, where $\alpha = 0.786974$). and in the control parameter direction (Δ/α^2, where $\Delta = 1.286974$). The extent of the refractory interval after the period-three explosion is determined as for the period-one explosion.

The values of the parameters b_*, Δ, α for low period orbits up to $p = 6$ are collected in Table 2.

Table 2: Values of the parameters b_{K1*}, Δ, α that are involved in the renormalization of explosions of orbits of the cusp map up to period six. Explosions occur in the direction of increasing b when the signs of Δ and α are opposite, *i.e.* , only the period-one orbit.

Orbit	Symbolics	b_c	Δ	α
1	K	0	1	-1
2	$K1$	1	1/2	1/2
3_1	$K10$	0.465571	1.286974	0.786974
4_2	$K100$	0.360157	2.624703	1.180563
5_3	$K1000$	0.318897	4.647225	1.664335
5_2	$K1001$	0.418656	-3.231180	-1.983690
5_1	$K1011$	0.513175	2.628970	1.509712
6_5	$K10000$	0.297846	7.481728	2.233184
6_4	$K10001$	0.340328	-8.535145	-3.639587
6_3	$K10011$	0.380540	7.596535	3.574548

7 Summary

A great deal of what we know about the development of strange attractors that are contained in genus-one bounding tori has been learned by studying the first return map. This has the form of a parabola, or a folded curve. By contrast, fewer systematics are known for flows that can be contained in bounding tori of genus greater than one, for instance the Lorenz flow. The return map, in such cases, has singularities like the cusp map. These two maps (c.f., Eq. (1)) have similarities and differences. Briefly put: both are unimodal, one is concave, the other convex. One has zero or two period-one orbits; the other has one or three. For one, regular saddle-node bifurcations create stable orbits that then period double; for the other singular saddle-node bifurcations create explosions. Windows for one correspond to refractory intervals with no bifurcations for the other. For one there is a global attractor at $x = -\infty$, for the other there is a global repellor at $y = -\infty$. For one the strange attractor is locally stable; for the other it is globally stable. Superstable orbits are located by the zero crossings of caustics; explosions by the zero crossings of anticaustics. For one there is a renormalization theory within a period doubling cascade *and* from window to window; for the other there is a renormalization theory from explosion to explosion. The zero crossings of caustics and anticaustics occur in the same order with a increasing for one map and b decreasing for the other. There are regions in which orbits of only even period are created in both maps and other regions in which both even and odd period orbits are created. Caustic crossings and anticaustic crossings separate the control parameter space into regions in which related processes occur. Topological entropy increases from 0 to $\log 2$ as a increases to $a = 2$ and decreases from $\log 2$ to 0 as b increases from $b = 0$ to $b = 1$.

References

[1] O. E. Rossler, "An equation for continuous chaos", *Physics Letters* **57A**, pp. 397-398, 1976.

[2] T. D. Tsankov and R. Gilmore, "Strange attractors are classified by bounding tori", *Phys. Rev. Lett.* **91**(13), 134104, 2003.

[3] E. N. Lorenz, "Deterministic Nonperiodic Behavior", *J. Atmos. Sci.* **20**, pp. 130-141, 1963.

[4] R. Gilmore and C. Letellier, *The Symmetry of Chaos*, Oxford: Oxford University Press, 2008.

[5] R. Gilmore and M. Lefranc, *The Topology of Chaos*, 2nd Edition, N.Y.: Wiley, 2011.

[6] R. Gilmore, "The knife map", (unpublished).

[7] The cusp of Catastrophe Theory has $1/k = 2/3$.

[8] John Milnor and William Thurston, "On Iterated Maps of the Interval. Dynamical Systems" (College Park, MD, 1986-1987), *Lecture Notes in Mathematics*, **1332**, pp. 465-563, Berlin: Springer, 1988.

[9] Pierre Collet and Jean-Pierre Eckmann, *Iterated Maps on the Interval as Dynamical Systems*, Boston: Birkhäuser, 1980.

[10] E. N. Lorenz, "Noisy periodicity and reverse bifurcation", *Ann. NY Acad. Sci.* **357**, pp. 282-291, 1980.

[11] C. Grebogi, E. Ott and J. A. Yorke, "Crises, sudden changes in chaotic attractors and transient chaos", *Physica* **D7**, pp. 181-200, 1983.

[12] Hao Bai-lin, *Elementary Symbolic Dynamics and Chaos in Dissipative Systems*, Singapore: World Scientific, 1989.

Proceedings of ICCSA 2014
Normandie University, Le Havre, France - June 23-26, 2014

TEMPLATES OF TWO FOLIATED ATTRACTORS — LORENZ AND CHEN SYSTEMS

M. Rosalie*

Abstract. A chaotic attractor solution of the Lorenz system [1] with foliated structure is topologically characterized. Its template permits to both summarize the organization of its periodic orbits and detail the topology of the solution as a branched manifold. A template of an attractor solution of the Chen system [2] with a similar foliated structure is also established.

Keywords. Chaotic attractor, topological characterization, template

1 Introduction

The Lorenz system has been introduced with a set of parameters [1] for which the solution is a chaotic attractor. The topology of this solution has been established by Birman & Williams [3] considering the periodic orbits of the solution as knots evolving in a branched manifold, currently called template. From experimental or numerical data, the idea of using periodic orbits to characterize chaotic attractors comes from Auerbach *et al.* [4] and has been developed since [5]. This topological analysis of a chaotic attractor permits to obtain a template that synthesises the relative organisation of its periodic orbits.

In 2003, Tsankov & Gilmore [6] introduced the theory of toroidal boundary of a chaotic attractor as a way to organize the branched manifold of the attractor as template do for periodic orbits. In their second paper [7] they explained how the Lorenz template can be rewritten in order to fit its genus-3 toroidal boundary. Recently, the general method has been extended in order to obtain the template of chaotic attractors bounded by higher genus torus [8]. Using this method, the topological characterization of two foliated attractors is performed, one is a solution of the Lorenz system, and the other attractor is solution of the Chen system [2] with more foliations.

This paper is organized as follows. Firstly, the template of a foliated attractor solution of the Lorenz system is obtained. Secondly, the topological analysis is performed on an attractor solution of the Chen system.

*CORIA-UMR 6614 - Normandie Université, CNRS-Université et INSA de Rouen Campus Universitaire du Madrillet 76800 Saint Etienne du Rouvray, France. E-mail: martin.rosalie@coria.fr

2 A foliated attractor solution of the Lorenz system

The procedure of topological characterisation of attractors is presented for a solution of the Sprott system [9]. Recently [8], it is also presented and applied on an attractor solution of the Rössler system [10] and of the Lorenz system [1]. To remind the major steps of this procedure, firstly we summarize the topological characterization of a Rössler attractor, already studied by Letellier *et al.* [11]. Secondly, the topological characterization of a foliated attractor solution of the Lorenz system is detailed.

2.1 Topological characterisation of a Rössler attractor

First, using the toroidal boundary theory [6], the bounding torus of the solution is established and gives the structure of the Poincaré section. This attractor is bounded by a genus-1 torus, thus a one component Poincaré section is required to analyse the dynamics of the solution by a discretization of trajectories. Secondly, a unique variable is build to represent the section from which a first return map is built and reveals an unimodal shape. Periodic points of this map are used to identify orbits. Also from this unimodal map, a symbolic dynamic is constructed in order to obtain a partition of the map where trajectories have the same behaviour over a period. Finally, the linking numbers between pair of orbits are computed and a template is proposed to summarized the relative organization of these orbits by providing the theoretical linking number (see [11, 8] for details).

2.2 Topological characterisation of a Lorenz attractor

Poincaré section and return map For the set of parameters $R = 192$, $\beta = \frac{8}{3}$ and $\sigma = 10$, the solution of Lorenz system

$$\begin{cases} \dot{x} = \sigma(y - x) \\ \dot{y} = Rx - y - xz \\ \dot{z} = -\beta z + xy \ , \end{cases} \tag{1}$$

is a chaotic attractor denoted $\mathcal{L}$ (Fig. 1). This system (1) is symmetric by rotation and has three singular points

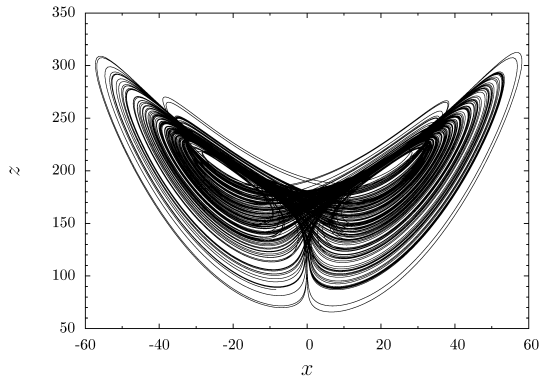

Figure 1: Chaotic attractor $\mathcal{L}$ solution of the Lorenz system (1) for the parameters $R = 192$, $\beta = \frac{8}{3}$ and $\sigma = 10$.

that structure the phase space: the origin and two symmetric singular points S_+ and S_- that are respectively a saddle point and two symmetric foci.

$\mathcal{L}$ is bounded by a genus-3 torus with aligned holes, as singular points are. The theory of toroidal boundary introduced by Tsankov & Gilmore [6] indicates that a two components Poincaré section is required to get a discretization of trajectories. As previously done for this system [8], a Poincaré section is defined using two symmetric components

$$\begin{aligned}\mathcal{P} \equiv A \cup B \equiv &\left\{(y_n, z_n) \in \mathbb{R}^2 \ | x_n = x_+, \ \dot{x}_n < 0\right\} \\ &\cup \left\{(y_n, z_n) \in \mathbb{R}^2 \ | x_n = x_-, \ \dot{x}_n > 0\right\},\end{aligned} \tag{2}$$

where the x_+ and x_- are the x coordinate of the singular points S_- and S_+. Fig. 2a is a representation of $\mathcal{L}$ in the projection (x, y) with the Poincaré section (2) where the flow evolves clockwise around the foci. We remain that the origin is a saddle point, thus it ensures that a genus-3 torus bound the attractor. This projection emphasises the rotational symmetry of the system onto the flow and the Poincaré section. In order to use the rules about partitioning a first return map with distinguishing increasing and decreasing branches [11], we choose to build a unique variable to represent the Poincaré section with y_n as already done for the other attractor of the Lorenz system even if it is not in bijection with the flow (Fig. 2b).

The use of a first return map built on a unique variable from the inside to the outside permits to distinguish parts of a chaotic attractor where trajectories have the same behaviour. Thus, ρ_n is built to represent the n^{th} passage through the Poincaré section

$$\rho_n = \mathbb{1}_A \cdot \rho_{A,n} + \mathbb{1}_B \cdot (1 + \rho_{B,n}) \tag{3}$$

where $\rho_{A,n}$ and $\rho_{B,n}$ are normalised in $]0; 1[$ and represent a component from the inside to the outside of the flow for each focus [8]; the indicator function of a component is a value, it is 1 if the trajectory is in the component and 0 else.

Fig. 3a is the return map on ρ_n to the Poincaré section (2). A partition of the return map, and also a partition

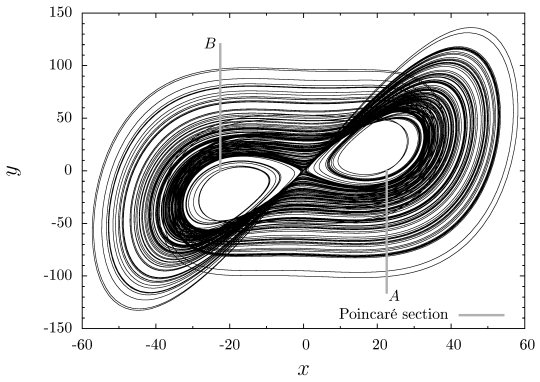

(a) Attractor $\mathcal{L}$.

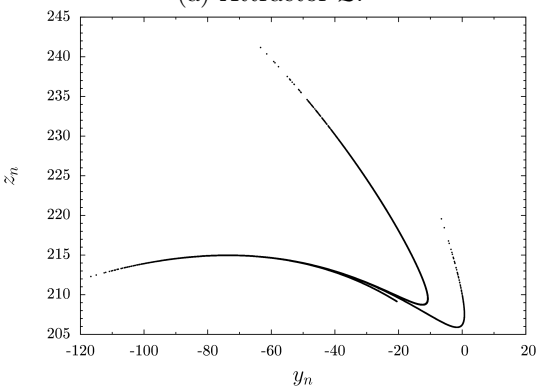

(b) Cross section of the flow with the A component.

Figure 2: (a) Attractor $\mathcal{L}$ with a two components Poincaré section (2). (b) Cross section of the flow with the A component of the Poincaré section (2) that is symmetric to the B component.

of the Poincaré section, permits to distinguish periodic points that represent a portion of trajectories that will have the same behaviour until the next Poincaré section component. For a component, there are five points where the slope of the application changes, three of them are non differentiable points as displayed Fig. 3b. The two other points are the extrema of the two unimodal parts of the application in a component (Fig. 3b). These ten points, five for each component, are chosen to split the first return map. Thus, six branches with monotonous slope are distinguished on each component. We chose to label them with symbols 0, 2, 3, 4, 5 and 6 for the component A and $\overline{0}$, $\overline{2}$, $\overline{3}$, $\overline{4}$, $\overline{5}$ and $\overline{6}$ for the component B. We intentionally do not make any distinction between the two increasing parts of the branch 0, or 2 for the A component, respectively $\overline{0}$ and $\overline{2}$ of B because the left and right parts of such branches are increasing and there is a differentiable point that indicates a continuity between these two parts. These parts are the consequence of the projection choice that repeats twice the same branch of the first return map. We consider that two consecutive increasing branches are in fact only one increasing branch. This is due to the variable chosen to represent the Poincaré section. In the case of unimodal return map, the natural order [12] permits to organize periodic points. Thus, we

consider that the two branches are a unique branch for which the natural order reorganizes its periodic points.

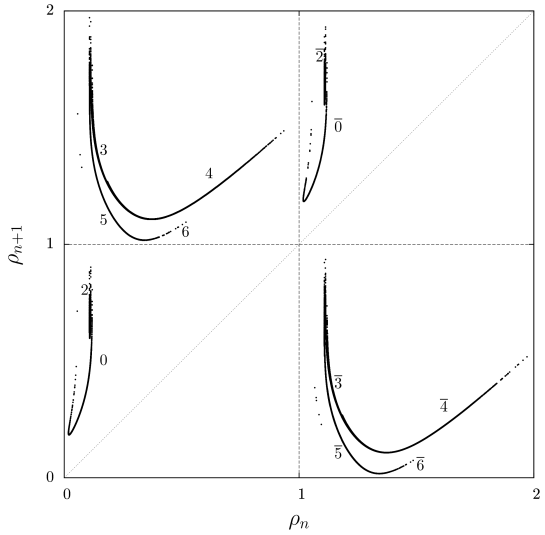

(a) First return map

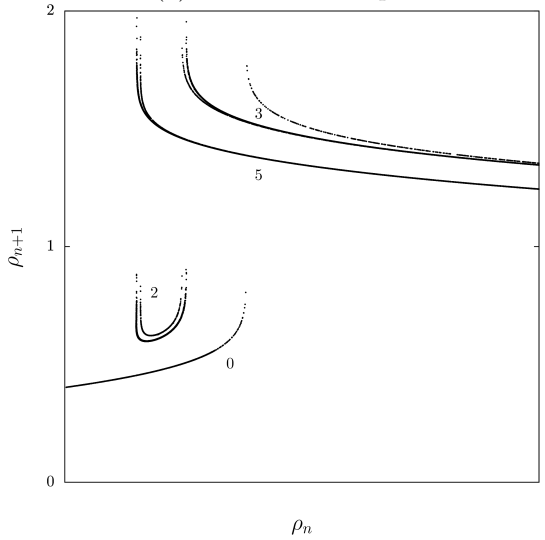

(b) Detail of the first return map

Figure 3: (a) First return map to ρ_n that represents the Poincaré section (2). (b) Details of component A.

From the return map, we can extract a transition matrix T between symbols that details which transitions are allowed for a given sequence of symbols

$$T = \begin{array}{c} \\ 0 \\ 2 \\ 3 \\ 4 \\ 5 \\ 6 \\ \overline{0} \\ \overline{2} \\ \overline{3} \\ \overline{4} \\ \overline{5} \\ \overline{6} \end{array} \begin{array}{c} \begin{array}{cccccccccccc} 0 & 0 & 1 & 1 & 1 & 1 & 0 & 0 & 0 & 0 & 0 & 0 \end{array} \\ \left[\begin{array}{cccccccccccc} 0 & 0 & 0 & 1 & 0 & 0 & 0 & 0 & 0 & 0 & 0 & 0 \\ 0 & 0 & 0 & 0 & 0 & 0 & 0 & 1 & 1 & 1 & 0 & 0 \\ 0 & 0 & 0 & 0 & 0 & 0 & 0 & 1 & 1 & 1 & 1 & 1 \\ 0 & 0 & 0 & 0 & 0 & 0 & 1 & 0 & 1 & 1 & 1 & 1 \\ 0 & 0 & 0 & 0 & 0 & 0 & 1 & 0 & 0 & 0 & 0 & 0 \\ 0 & 0 & 0 & 0 & 0 & 0 & 0 & 0 & 1 & 1 & 1 & 1 \\ 0 & 0 & 0 & 0 & 0 & 0 & 0 & 0 & 0 & 1 & 0 & 0 \\ 0 & 1 & 1 & 1 & 0 & 0 & 0 & 0 & 0 & 0 & 0 & 0 \\ 0 & 1 & 1 & 1 & 1 & 1 & 0 & 0 & 0 & 0 & 0 & 0 \\ 1 & 0 & 1 & 1 & 1 & 1 & 0 & 0 & 0 & 0 & 0 & 0 \\ 1 & 0 & 0 & 0 & 0 & 0 & 0 & 0 & 0 & 0 & 0 & 0 \end{array}\right] \end{array} . \quad (4)$$

For instance, this transition matrix between symbols indicates that a sequence that contains symbol 2 must be followed by a symbol 4. Due to the non bijection of ρ_n with the flow, this transition matrix is exhaustive because it might allow transitions that do not occur.

Orbits and template To extract periodic orbits, a Poincaré section and a trajectory from any initial conditions in the basin of attraction of the attractor are sufficient because periodic orbits are dense in the solution. The method consists in looking for points in the section that the trajectory will reach after n passages through the Poincaré section. This method also works in the first return map and directly permits to give a symbol to each periodic point of the orbits extracted. Fourteen orbits of period lower than six have been extracted from $\mathcal{L}$. Orbits are considered as knots and we compute pair by pair their linking numbers in order to obtain a numerical invariant that is an integer (Tab. 1). All orbits extracted are symmetric, except $(\overline{4}00\overline{3}5)$ for which it symmetric orbit exists but was unsuccessfully detected in our numerical data.

A template is validated when the linking numbers theoretically computed correspond to those numerically computed [5, 15]. In order to have periodic orbits with symbols 2 and $\overline{2}$, we also compute linking numbers between higher periodic orbits

$$lk(\overline{4}50\overline{3}24\overline{5}03\overline{3}4\overline{5}3\overline{2}, 3\overline{3}24\overline{5}04\overline{5}3\overline{3}) = 24 , \quad (5)$$

$$lk(\overline{4}50\overline{3}24\overline{5}03\overline{3}4\overline{5}3\overline{2}, \overline{4}50\overline{4}5\overline{3}3\overline{3}3\overline{3}2) = 30 . \quad (6)$$

Up to this point, the parity of twists that occur over each strip of the template is given by the parity of the associated symbol. The second point is that there is only positive linking numbers. In the paper [13], a first return map of another Lorenz attractor looks like the return map built on $\mathcal{L}$ with only three branches for each component; the template of this attractor is given. Using the terminology of mixers [8], we can rewrite this template with two identical mixers defined by the linking matrix

$$\left|\begin{bmatrix} 0 & 0 & 0 \\ 0 & 1 & 0 \\ 0 & 0 & 0 \end{bmatrix}\right| . \quad (7)$$

For the attractor $\mathcal{L}$, the first-return map reveals that there are couples of branches $(3, 4)$, $(5, 6)$, $(\overline{3}, \overline{4})$ and $(\overline{5}, \overline{6})$ with unimodal shapes that means their associated strips stretch, fold and squeeze. This first-return map also reveals three non differentiable points meaning that there are three tearing mechanisms occurring to separate the flow after each component. Compared with the template whose linking matrix is (7), there is after each component a tearing chart and a stretching and folding mechanism. We suppose that a tearing mechanism occurs before this first tearing. Thus, we obtain three tearing mechanisms and two stretching and folding mechanisms as the return map shows. It implies that all the mechanisms of (7) are

Table 1: Linking numbers between pairs of periodic orbits of the attractor $\mathcal{L}$.

	$(\overline{5}4)$	$(\overline{4}5)$	$(\overline{3}3)$	$(\overline{6}5\overline{0})$	$(\overline{5}06)$	$(\overline{5}3\overline{3}4)$	$(\overline{4}5\overline{3}3)$	$(\overline{6}03\overline{3}4)$	$(\overline{5}03\overline{3}4)$	$(\overline{5}04\overline{5}4)$	$(\overline{4}6\overline{0}35)$	$(\overline{4}6\overline{0}33)$	$(\overline{4}5\overline{0}33)$
$(\overline{4}5)$	1												
$(\overline{3}3)$	1	1											
$(\overline{6}5\overline{0})$	1	1	1										
$(\overline{5}06)$	1	1	1	1									
$(\overline{5}3\overline{3}4)$	1	2	2	2	2								
$(\overline{4}5\overline{3}3)$	2	1	2	2	2	4							
$(\overline{6}03\overline{3}4)$	1	2	2	2	2	3	4						
$(\overline{5}03\overline{3}4)$	1	2	2	2	2	3	4	3					
$(\overline{5}04\overline{5}4)$	1	2	2	2	2	3	4	3	3				
$(\overline{4}6\overline{0}35)$	2	1	2	2	2	4	3	4	4	4			
$(\overline{4}6\overline{0}33)$	2	1	2	2	2	4	3	4	4	4	3		
$(\overline{4}5\overline{0}33)$	2	1	2	2	2	4	3	4	4	4	3	3	
$(\overline{4}5\overline{0}\overline{4}5)$	2	1	2	2	2	4	3	4	4	4	3	3	3

repeated twice for the mixer of each component. To explain the fact that mechanisms are doubled, we suppose that the squeezing mechanism that unified the strips does not occur entirely. Consequently, at the end of the mixer, there are two distinguishable strips that will undergo the mechanisms of (7). To overcome the fact that strips do not entirely squeeze and are still one over the other, we propose to use the convention of standard insertion [5] that gives that upper strips are located to the leftest side and lower strips are on the rightest side. As a consequence, at the end of the mixer, the tearing mechanism separates the flow in order to organize the strips with this convention.

Finally, Fig. 4 is proposed as the template of $\mathcal{L}$. In this template, the squeezing mechanism of each mixer considers that all strips are unified in a branch line, but thereafter the tearing mechanism reorganizes parts of strips that not squeeze according to the standard convention. Consequently, the linking matrices of this proposed template (Fig. 4) are

$$M_A = \begin{array}{c|cccccc||c} 0 & 0 & 0 & 0 & 0 & 0 & 0 & 0 \\ 2 & 0 & 0 & 0 & 0 & 0 & 0 & 2 \\ \overline{3} & 0 & 0 & 1 & 0 & 1 & 0 & 3 \\ \overline{4} & 0 & 0 & 0 & 0 & 1 & 0 & 4 \\ \overline{5} & 0 & 0 & 1 & 1 & 1 & 0 & 5 \\ \overline{6} & 0 & 0 & 0 & 0 & 0 & 0 & 6 \end{array}$$

$$M_B = \begin{array}{c|cccccc||c} \overline{0} & 0 & 0 & 0 & 0 & 0 & 0 & \overline{0} \\ \overline{2} & 0 & 0 & 0 & 0 & 0 & 0 & \overline{2} \\ 3 & 0 & 0 & 1 & 0 & 1 & 0 & \overline{3} \\ 4 & 0 & 0 & 0 & 0 & 1 & 0 & \overline{4} \\ 5 & 0 & 0 & 1 & 1 & 1 & 0 & \overline{5} \\ 6 & 0 & 0 & 0 & 0 & 0 & 0 & \overline{6} \end{array} . \qquad (8)$$

The cross-section Fig. 2b illustrates the end of the mixer after the squeezing and before the tearing, it corresponds to the structure of the proposed template. With the method introduced by Le Sceller *et al.* [14], and extended in [8], all linking numbers computed theoretically correspond to those computed numerically. In appendix A, the theoretical computation of the linking number of (6) is detailed. These calculations permit to ensure the validity [15] of the template of $\mathcal{L}$ (Fig. 4). The template proposed permits to compute all linking numbers between pairs of orbits but it also contains a subtemplate that is a more precise description of this attractor. Up to this point we obtain a template of another attractor with a foliated structure that is a solution of the Lorenz system.

3 A foliated attractor solution of the Chen system

Introduced by Chen & Ueta [2] the system

$$\begin{cases} \dot{x} = a(y - x) \\ \dot{y} = (c - a)x + cy - xz \\ \dot{z} = -bz + xy \ , \end{cases} \qquad (9)$$

of three differential equations can exhibit a chaotic attractor as a solution. This system is a Lorenz-like system because of its equations; see Tab. II of [13] for relations between various symmetric systems with same quadratic terms. For the set of parameters $a = 35$, $b = 3$ and $c = 28$, this system has an attractor solution denoted $\mathcal{C}$ (Fig. 5). There are three singular points, O the origin, $S_+ = (3\sqrt{7}, 3\sqrt{7}, 21)$ and $S_- = (-3\sqrt{7}, -3\sqrt{7}, 21)$; their respective eigenvalues

$$\Lambda_O = \begin{vmatrix} -23.8 \\ -30.8 \\ -3 \end{vmatrix} , \Lambda_{S_+} = \Lambda_{S_-} = \begin{vmatrix} -18.43 \\ -4.21 + 14.88\mathrm{i} \\ -4.21 - 14.88\mathrm{i} \end{vmatrix} \qquad (10)$$

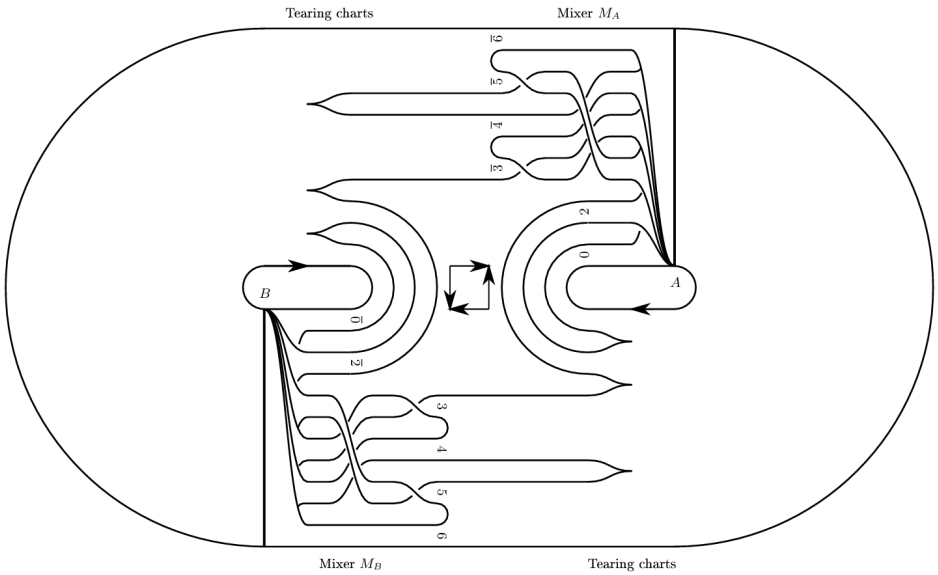

Figure 4: Template of the attractor $\mathcal{L}$ with the two mixers M_A and M_B.

give that the origin is a saddle point and that the symmetric singular points are foci.

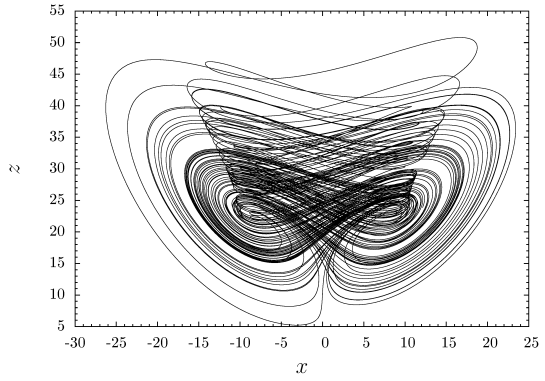

Figure 5: Chaotic attractor $\mathcal{C}$ solution of the Chen system (9) for the parameters $a = 35$, $b = 3$ and $c = 28$.

In the (x, y) plan projection, the flow of $\mathcal{C}$ evolves clockwise around the foci (Fig. 6a). $\mathcal{C}$ is bounded by a genus-3 torus. According to the toroidal boundary theory [6] the Poincaré section is made of two components

$$\begin{aligned} \mathcal{Q} \equiv A \cup B \equiv \left\{(y_n, z_n) \in \mathbb{R}^2 \ | x_n = 7, \ \dot{x}_n < 0\right\} \\ \cup \left\{(y_n, z_n) \in \mathbb{R}^2 \ | x_n = -7, \ \dot{x}_n > 0\right\}, \end{aligned} \tag{11}$$

The cross-section of the attractor $\mathcal{C}$ is similar to the cross-section of the attractor $\mathcal{L}$ with more foliations; it seems that there are four strips. ρ_n is built as previously to obtain a variable that represents the Poincaré section (11) from the inside to the outside. A first-return map to this Poincar section is built (Fig. 7).

Again, the same structure appears with the foliation in the first-return map. As previously done for the attractor $\mathcal{L}$, a partition is made and symbols are associated to each

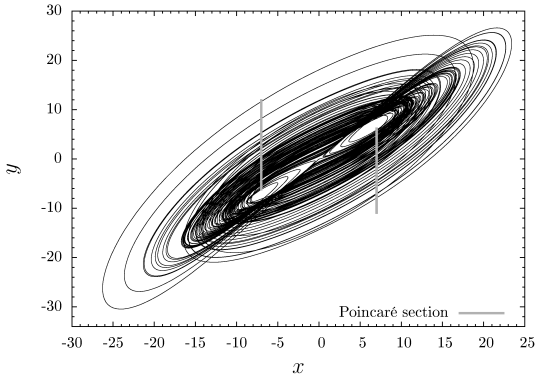

(a) Attractor $\mathcal{C}$.

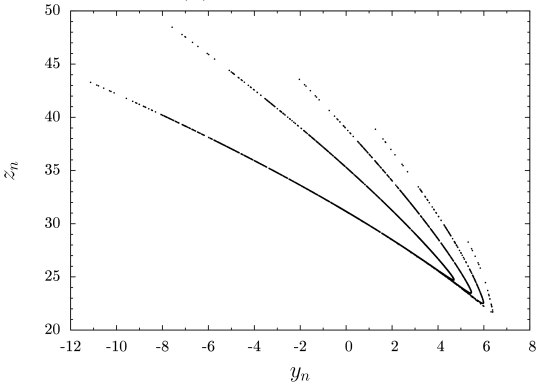

(b) Cross section of the flow with the A component.

Figure 6: (a) Attractor $\mathcal{C}$ with a two components Poincaré section (11). (b) Cross section of the flow with the A component of the Poincaré section (11) that is symmetric to the B component.

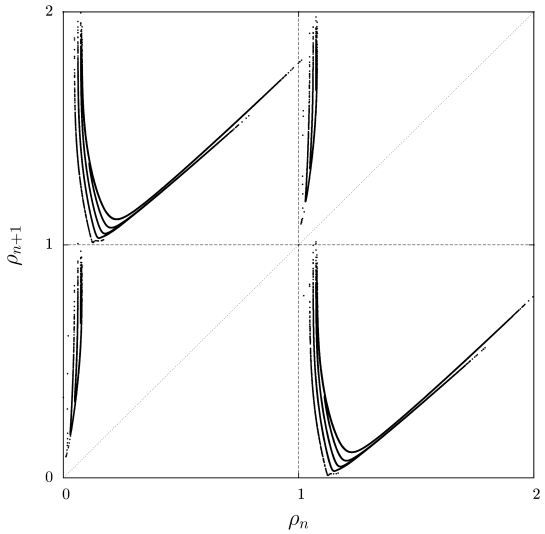

(a) First return map

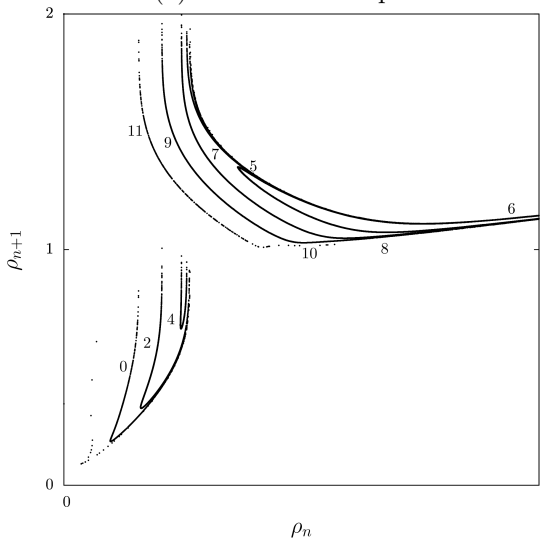

(b) Detail of the first return map

Figure 7: (a) First return map to ρ_n that represents the Poincaré section (11). (b) Details of component A.

distinguishable branches 0, 2, 4, 5, 6, 7, 8, 9, 10 and 11 for the component A and respectively the same symbols with an overline for the component B. As previously done for branch 0 for the return map of $\mathcal{L}$, the branch 5 is a double decreasing branch considered as a unique decreasing branch, the same applies for branch 6. Thus, the structure is similar with more foliations.

From this first-return map, several periodic orbits are extracted and, pair by pair, their linking numbers are numerically computed (Tab. 2). In order to obtain informations on strips with missing symbols we compute numerically linking numbers between hight periodic orbits, for instance

$$lk(\overline{6}66\overline{8}\overline{11}5\overline{6}6\overline{4}, \overline{6}5\overline{5}6\overline{6}7\overline{2}) = 6\ , \tag{12}$$

$$lk(\overline{6}5\overline{5}6\overline{6}7\overline{2}, \overline{6}5\overline{5}6\overline{6}8\overline{2}) = 6\ , \tag{13}$$

$$lk(\overline{6}8\overline{9}6\overline{6}7\overline{6}6\overline{7}6, \overline{6}66\overline{8}\overline{11}5\overline{6}6\overline{4}) = 9\ . \tag{14}$$

Table 2: Linking numbers between pairs of periodic orbits of the attractor $\mathcal{C}$.

	$(\overline{6}5)$	$(\overline{5}5)$	$(\overline{5}6)$	$(\overline{6}8\overline{9}6)$	$(\overline{6}7\overline{5}6)$	$(\overline{6}6\overline{8}9)$	$(\overline{6}6\overline{7}5)$	$(\overline{6}5\overline{5}5)$
$(\overline{5}5)$	1							
$(\overline{5}6)$	1	1						
$(\overline{6}8\overline{9}6)$	1	1	1					
$(\overline{6}7\overline{5}6)$	1	1	1	2				
$(\overline{6}6\overline{8}9)$	1	1	1	2	2			
$(\overline{6}6\overline{7}5)$	1	1	1	2	2	2		
$(\overline{6}5\overline{5}5)$	1	2	2	2	2	2	2	
$(\overline{5}5\overline{5}6)$	2	2	1	2	2	2	2	4

To propose the template Fig. 8 of $\mathcal{C}$, we use the same chaotic mechanism of stretching and folding repeated four times. The foliated structure of these chaotic mechanisms is translated in the mixer where the structure of (8) is also repeated to obtain the linking matrices

$$N_A = \begin{array}{c|cccccccccc||c} 0 & 0&0&0&0&0&0&0&0&0&0 & 0 \\ 2 & 0&0&0&0&0&0&0&0&0&0 & 2 \\ 4 & 0&0&0&0&0&0&0&0&0&0 & 4 \\ \overline{5} & 0&0&0&1&0&1&0&1&0&1 & 5 \\ \overline{6} & 0&0&0&0&0&1&0&1&0&1 & 6 \\ \overline{7} & 0&0&0&1&1&1&0&1&0&1 & 7 \\ \overline{8} & 0&0&0&0&0&0&0&1&0&1 & 8 \\ \overline{9} & 0&0&0&1&1&1&1&1&0&1 & 9 \\ \overline{10} & 0&0&0&0&0&0&0&0&0&1 & 10 \\ \overline{11} & 0&0&0&1&1&1&1&1&1&1 & 11 \end{array} \tag{15}$$

$$N_B = \begin{array}{c|cccccccccc||c} \overline{0} & 0&0&0&0&0&0&0&0&0&0 & \overline{0} \\ \overline{2} & 0&0&0&0&0&0&0&0&0&0 & \overline{2} \\ \overline{4} & 0&0&0&0&0&0&0&0&0&0 & \overline{4} \\ 5 & 0&0&0&1&0&1&0&1&0&1 & \overline{5} \\ 6 & 0&0&0&0&0&1&0&1&0&1 & \overline{6} \\ 7 & 0&0&0&1&1&1&0&1&0&1 & \overline{7} \\ 8 & 0&0&0&0&0&0&0&1&0&1 & \overline{8} \\ 9 & 0&0&0&1&1&1&1&1&0&1 & \overline{9} \\ 10 & 0&0&0&0&0&0&0&0&0&1 & \overline{10} \\ 11 & 0&0&0&1&1&1&1&1&1&1 & \overline{11} \end{array} .$$

that algebraically describe the proposed template of the attractor $\mathcal{C}$. To validate this template, we also compute theoretically linking numbers using the procedure detailed in appendix A for the attractor $\mathcal{L}$. All the theoretical linking numbers computed correspond with those numerically computed, thus the template (Fig. 8) is validated.

4 Conclusion

This paper is the topological characterization of two foliated attractors solution of two systems of differential equations of different kind. Their templates give the relative organization of their periodic orbits, more precisely, from their linking matrices that algebraically describe these templates, it is possible to obtain the linking

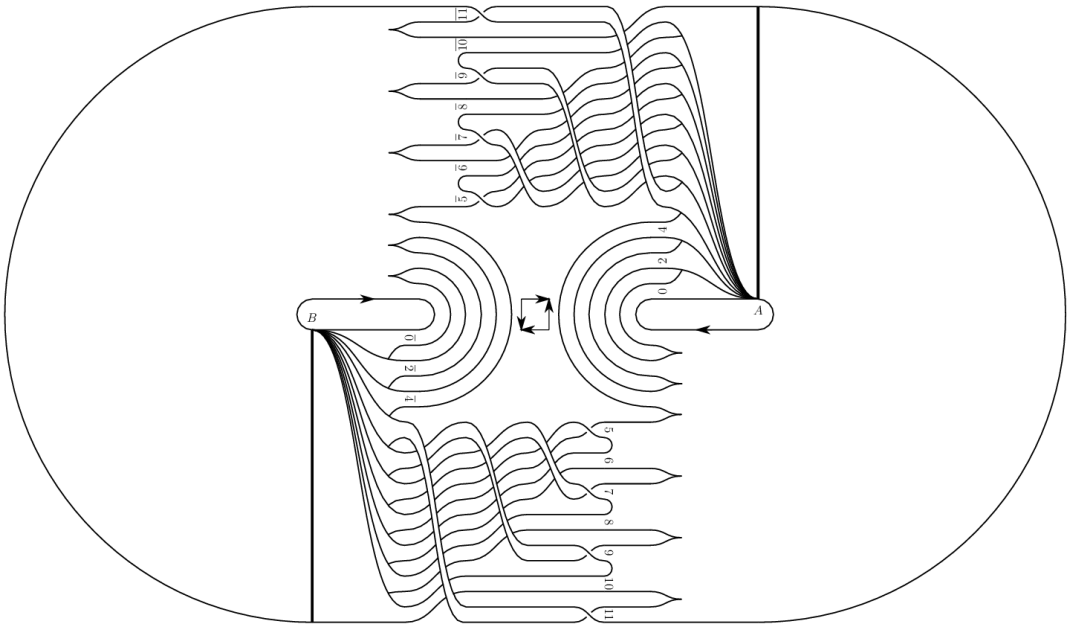

Figure 8: Template of the attractor $\mathcal{C}$.

number between two orbits of these solutions. These attractors are symmetric, then their linking matrices are identical for each symmetric part. These attractors have a foliated structure that is visible in their linking matrix with the repetition of a pattern. This pattern reminds the work on the Rössler system when a parameter is varied. In fact, this variation adds strips rolled up in the chaotic mechanism with a spiraling process; the explicit linking matrix with a pattern is given Eq. (12) of [11]. Here we face a similar structure between these two systems that have a solution with foliations. The attractor of the Chen system is more foliated and consequently it exhibits more complicated dynamics. On the other hand, the attractor of the Lorenz system contains only two foliations that enable us to establish these templates.

A Example of theoretical computation of a linking number

The method used consists in numerically computing linking numbers and finding a template that can predict theoretically these linking numbers. Numerically, the linking number between two orbits of $\mathcal{L}$ is computed (Fig. 10)

$$lk(\overline{4}50\overline{3}24\overline{5}03\overline{3}4\overline{5}3\overline{2}, \overline{4}50\overline{4}53\overline{3}33\overline{3}3\overline{2}) = 30\ . \qquad (16)$$

In this section, we present the details of the theoretical computation of this linking number.

The first step is to distinguish periodic points that represent trajectory in mixer M_A from mixer M_B. Only the first three symbols of a periodic point are used to label it. The second step is to organize periodic points in strips using the unimodal order, or natural order [12].

M_A	M_B
$03\overline{3}$	$\overline{0}\overline{3}2 \lhd \overline{04}5$
$24\overline{5}$	$\overline{2}4\overline{5} \lhd \overline{2}4\overline{5}$
$\overline{3}4\overline{5} \lhd \overline{3}3\overline{2} \lhd \overline{3}3\overline{3} \lhd \overline{3}3\overline{3} \lhd \overline{3}24$	$3\overline{3}3 \lhd 3\overline{3}3 \lhd 3\overline{3}4 \lhd 3\overline{24} \lhd 3\overline{24}$
$\overline{4}5\overline{3} \lhd \overline{4}5\overline{0} \lhd \overline{4}5\overline{0}$	$4\overline{5}3 \lhd 4\overline{5}0$
$\overline{5}32 \lhd \overline{5}03$	$5\overline{3}3 \lhd 5\overline{0}4 \lhd 5\overline{03}$

(17)

Then, we use formula given by Le Sceller *et al.* [14] for two orbits $\mathcal{O}$ and $\mathcal{O}'$, respectively of period p and p', with σ_i is the i^{th} symbol

$$lk(\mathcal{O}, \mathcal{O}') = \frac{1}{2}\left(\sum_{i=1}^{p}\sum_{j=1}^{p'} L(\sigma_i, \sigma_j) + N_{\text{joining}}(\mathcal{O}, \mathcal{O}')\right)\ . \qquad (18)$$

L are the crossings due to mixers (except from the insertion mechanism) and N_{joining} are the crossings due to the insertion mechanism. There are two joining charts, one for each mixer. The initial procedure introduce by Le Sceller does not consider that periodic points can come from various Poincaré section components; we adapt the procedure with the following rules. First, the periodic points are ordered with the strip order at the beginning of the mixer. Then, torsions and permutations are applied. Finally, the shift is operated. Positive crossings occur if there are permutations between the two final ordered set of periodic points. These crossings are underlined with the circles of Fig. 9 (N_{joining}); crossings between the two orbits and not self crossing.

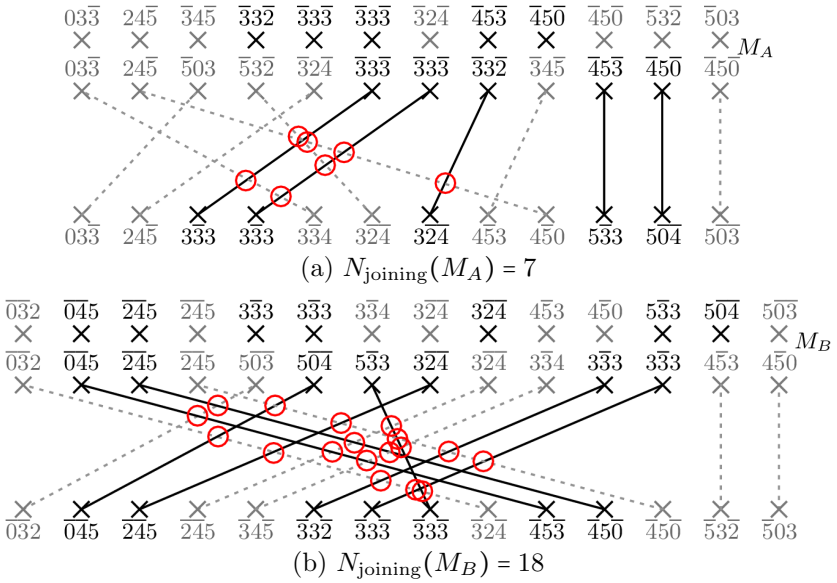

(a) $N_{\text{joining}}(M_A) = 7$

(b) $N_{\text{joining}}(M_B) = 18$

Figure 9: Joining charts indicating the number of positive crossing that occur at the end of mixers M_A and M_B.

Thus, we can theoretically compute the linking number

$$\begin{aligned} &lk(\overline{4}\overline{5}\overline{0}\overline{3}\overline{2}\overline{4}\overline{5}\overline{0}\overline{3}\overline{3}\overline{4}\overline{5}\overline{3}\overline{2}, \overline{4}\overline{5}\overline{0}\overline{4}\overline{5}\overline{3}\overline{3}\overline{3}\overline{3}\overline{3}\overline{2}) \\ &= \tfrac{1}{2}\big(3M_A(0,\overline{3}) + 2M_A(0,\overline{4}) + 3M_A(2,\overline{3}) + 2M_A(2,\overline{4}) \\ &+8M_A(\overline{3},\overline{3}) + 5M_A(\overline{3},\overline{4}) + 6M_A(\overline{3},\overline{5}) + 2M_A(\overline{4},\overline{4}) \\ &+4M_A(\overline{4},\overline{5}) + M_B(\overline{0},\overline{0}) + 2M_B(\overline{0},\overline{2}) + 5M_B(\overline{0},3) \\ &+2M_B(\overline{0},4) + 3M_B(\overline{0},5) + M_B(\overline{2},\overline{2}) + 5M_B(\overline{2},3) \\ &+2M_B(\overline{2},4) + 3M_B(\overline{2},5) + 6M_B(3,3) + 6M_B(3,4) \\ &+7M_(3,5) + 4M_B(4,5) + 2M_B(5,5) \\ &+ N_{\text{joining}}(M_A) + N_{\text{joining}}(M_B)\big) \\ &= \tfrac{1}{2}(35 + 7 + 18) = 30\ , \end{aligned} \tag{19}$$

that corresponds to the numerical linking number.

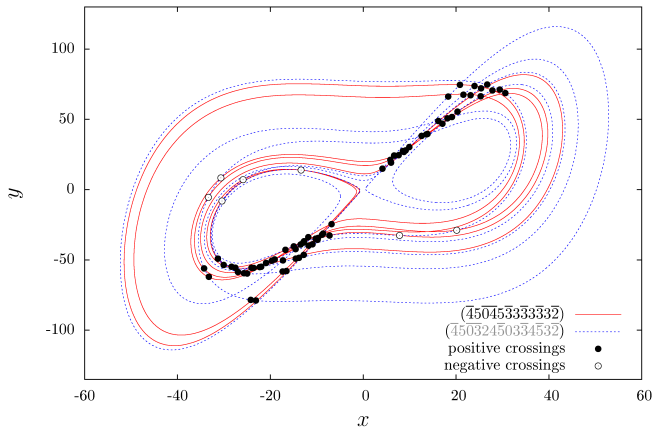

Figure 10: (Color online) Numerical oriented crossings computed in the plane (x, y) giving the linking number $lk(\overline{4}\overline{5}\overline{0}\overline{3}\overline{2}\overline{4}\overline{5}\overline{0}\overline{3}\overline{3}\overline{4}\overline{5}\overline{3}\overline{2}, \overline{4}\overline{5}\overline{0}\overline{4}\overline{5}\overline{3}\overline{3}\overline{3}\overline{3}\overline{3}\overline{2}) = \frac{1}{2}(68 - 8) = 30$.

References

[1] E. N. Lorenz, "Deterministic nonperiodic flow," *Journal of the Atmospheric Sciences*, vol. 20, pp. 130-141, 1963.

[2] G. Chen & T. Ueta, "Yet another chaotic attractor," *International Journal of Bifurcation and Chaos*, vol. 9, pp. 1465-1466, 1999.

[3] J. Birman & R. F. Williams, "Knotted periodic orbits in dynamical systems -I: Lorenz's equations," *Topology*, vol. 22, pp. 47-82, 1983.

[4] D. Auerbach, C. Cvitanović, J.-P. Eckmann, G.Gunaratne & I. Procaccia, "Exploring chaotic motion through periodic orbits," *Physical Review Letters*, vol. 58, pp. 2387-2389, 1987.

[5] N. B. Tufillaro, T. Abbott & J. Reilly, *An experimental approach to nonlinear dynamics and chaos*, Addison-Wesley Redwood City, 1992.

[6] T. D. Tsankov & R. Gilmore, "Strange attractors are classified by bounding tori," *Physical Review Letters*, vol. 91, pp. 134104, 2003.

[7] T. D. Tsankov & R. Gilmore, "Topological aspects of the structure of chaotic attractors in $\mathbb{R}^3$," *Physical Review E*, vol. 69, pp. 056206, 2004.

[8] M. Rosalie & C. Letellier, "Toward a general procedure for extracting templates from chaotic attractors bounded by high genus torus," *International Journal of Bifurcation and Chaos*, in press.

[9] C. Letellier & L. A. Aguirre, "Required criteria for recognizing new types of chaos: application to the "Cord" attractor," *Physical Review E*, vol. 85, pp. 036204, 2012.

[10] O. E. Rössler, "An equation for continuous chaos," *Physics Letters A*, vol. 57, pp. 397-398, 1976.

[11] C. Letellier, P. Dutertre & B. Maheu, "Unstable periodic orbits and templates of the Rössler system: toward a systematic topological characterization," *Chaos*, vol. 5, pp. 271-282, 1995.

[12] B.-L. Hao, *Elementary symbolic dynamics and chaos in dissipative systems*, World Scientific Publishing, Singapore, 1989.

[13] C. Letellier, T. D. Tsankov, G. Byrne & R. Gilmore, "Large-scale structural reorganization of strange attractors," *Physical Review E*, vol. 72, pp. 026212, 2005.

[14] L. Le Sceller, C. Letellier & G. Gouesbet, "Algebraic evaluation of linking numbers of unstable periodic orbits in chaotic attractors," *Physical Review E*, vol. 49, pp. 4693-4695, 1994.

[15] R. Gilmore & M. Lefranc, *The topology of chaos*, Wiley, 2002.

Proceedings of ICCSA 2014
Normandie University, Le Havre, France - June 23-26, 2014

FRACTIONAL-ORDER SYSTEMS: DOES THE DERIVATIVE ORDER DIFFER FROM A BIFURCATION PARAMETER?

Christophe Letellier, Gustavo H. Oliveira Salgado & Luis A. Aguirre *

Abstract. Fractional-order systems have been investigated in the context of control theory since the early 1990's. They have attracted recent attention to the researchers developing techniques for controlling chaotic behaviours. Nevertheless, many fundamental questions about dynamical properties of chaotic fractional-order systems are still left open. We propose to address a few such questions as, for instance: does the derivative order differ from a bifurcation parameter ? How is the dissipation rate of the dynamics affected by the derivative fractional-order? What is the dimension of the phase space of a fractional-order system? Numerical simulations of known bench systems are used to provide (sometimes partial) answers to such questions.

Keywords. Fractional-order systems, chaotic attractor, topological characterization, bifurcation diagram

1 Introduction

Fractional calculus is a topic as old as integer calculus since it was mentioned in a letter from Gottfried Leibniz to Guillaume de l'Hospital in 1695 (Leibniz, 1962). Its application was considered in various fields as in viscoelasticity, acoustics, rheology, polimeric and chemistry have been considered useful (Oldham, 1974). In control theory, a fractional control was introduced with CRONE control (Oustaloup, 1990) and a generalization for PID-controller, called $\mathrm{PI}^{\lambda}\mathrm{D}^{\mu}$-controller, by replacing the integer-order integral and derivatives by fractional orders, shows better performance in comparison with the classical one, when used in fractional order systems (Podlubny, 1997). The concept of fractional-order modeling in biological systems has been observed in signal processing (Eke, 2002; West, 2006). These applications result from some behaviors which cannot be fully reproduced by an integer calculus modeling, but can be better explained by fractional one (Westerlund, 1991).

Chaotic attractors can also be produced by fractional-order systems by replacing the integer-order derivatives with fractional-order ones (Hartley, 1995). It was shown that chaotic behaviours can be produced by fractional-order systems with a total order q_T, defined as the sum of the order of each equation, less than three (Hartley, 1995; Petráš, 2011). Such a result leads to the necessity to distinguish the total order of a set of fractional-order differential equations from the dimension of its associated phase space. For integer order systems, the total order q_T, which is necessarily an integer, is equal to the dimension of the associated phase space. For fractional-order systems, the total order q_T is most often a non-integer (a real) number and cannot be equal to the dimension of the phase space, the dimension of a vectorial space being, by definition, an integer. Thus, the phase space dimension must be $\mathrm{Int}(q_T)+1$. Consequently, fractional-order chaotic systems must present a total order q_T such as $\mathrm{Int}(q_T)+1 \geq 3$. The Poincaré-Bendixson theorem that requires a phase space with a dimension at least equal to three for having chaos thus remains valid for fractional-order systems.

One of the aims of this paper is to address quite fundamental issues related to fractional-order systems, with a special attention paid to the role played by the fractional-order q and, for instance, how it is related to a bifurcation parameter. This paper is organized as follows. Section 2 provides some definitions for the fractional-order derivatives. In Section 3, fractional-order derivatives of time series are used to reconstruct some phase portraits. The analogy which can be made between the fractional-order and a bifurcation parameter is investigated in Section 4. Section 5 gives some conclusions.

2 Definitions of fractional derivatives

There are more than one definitions for fractional derivative. We present and discuss some of them in what follows. Fractional calculus is an extention of integer calculus and the most commonly used definitions are Riemann-Liouville (RL), Caputo and Grünwald-Letinikov (GL) (Oldham, 1974). Basically, these definitions are based on iterate processes involving n-fold integrals and superior orders derivatives.

The RL integral of a function $f(x)$, $x \in [a,b]$, is defined by

$$J_a^q f(x) := \frac{1}{\Gamma(q)} \int_a^x (x-t)^{q-1} f(t)\,\mathrm{d}t\,, \qquad (1)$$

*CORIA-UMR 6614 — Normandie Université, CNRS-Université et INSA de Rouen Campus Universitaire du Madrillet 76800 Saint Etienne du Rouvray, France. E-mail: Christophe.Letellier@coria.fr

for $q > 0$ and $x \leq b$ and where $\Gamma(q) = \int_0^\infty e^{-t}\, t^{q-1} \mathrm{d}t$, is an Euler's Γ-funtion defined for all $q \in \mathbb{R} - \mathbb{Z}_-^*$. The RL derivative of a function $f(x)$ is defined by

$$D_a^q f(x) = D^n J_a^{n-q} f(x), \tag{2}$$

such that $n = \lceil q \rceil$, that is, $n - 1 < q \leq n$ and D^n represents the derivative of order n. The Caputo derivative of a function $f(x)$ is defined by

$${}^C D_a^q f(x) = J_a^{n-q} D^n f(x), \tag{3}$$

such that $n = \lceil q \rceil$. The GL derivative of a function $f(x)$, $x \in (a, b]$ is defined by

$${}^{GL} D_a^q f(x) = \lim_{N \to \infty} \frac{1}{h_N^q} \sum_{k=0}^{N} \frac{(-1)^k \Gamma(q+1)}{\Gamma(q-k+1)\Gamma(k+1)} f(x - k h_N), \tag{4}$$

such that $h_N = \dfrac{(x-a)}{N}$. The RL and GL derivatives are equivalent for functions defined in $f \in C^{\lceil q \rceil}[a, b]$ (Diethelm, 2010). Although the RL and the Caputo derivatives are very similar, these definitions are not equivalent. The relation between them is expressed as

$${}^C D_a^q f(x) = D_a^q \left(f(x) - T_{n-1}[f; a] \right), \tag{5}$$

where $T_{n-1}[f; a]$ denotes the Taylor polynomial of degree $n-1$ of f around $x = a$ (Diethelm, 2010). The numerical evaluation for fractional calculus is based on the GL definition.

From equation (4) and equivalence between RL and GL definitions, the RL derivative can be approximated by

$$D_a^q y(t) \approx h^{-q} \sum_{k=0}^{N} \frac{(-1)^k \Gamma(q+1)}{\Gamma(q-k+1)\Gamma(k+1)} y(t - kh), \tag{6}$$

for N large. For a discrete grid within $[a, b]$ with $\frac{t-a}{N+1}$ points $D_a^q y_i \approx h^{-q} \sum_{k=0}^{i} c_k^q\, y_{i-k}$, where $y_{i-k} = y(t_i - kh)$ for $i = 1, \cdots, N$, $h = \frac{t-a}{N}$, $c_0^q = 1$, and $c_k^q = \left(1 - \dfrac{1+q}{k}\right) c_{k-1}^q$ for $k > 1$.

3 Fractional derivatives for phase portrait reconstruction

A well-known result from the nonlinear dynamical system theory is the possibility to reconstruct the dynamics from a single time series (Takens, 1981). A possible reconstructed space is spanned by the (integer) derivative coordinates. We now investigate the role played by fractional-order derivatives in reconstructing a phase portrait from a single time series.

Consider a scalar time series $x(t) = \sin \omega t$ and the 2D reconstructed space spanned by

$$\left| \begin{array}{l} X = x(t) = \sin \omega t \\ Y = D^q X = D^q \sin \omega t\,. \end{array} \right. \tag{7}$$

Depending on the fractional-order q used, the circle is more or less deformed into an ellipse which is, along the first bisecting line ($q < 1$) or along the second bisecting line ($q > 1$) (Fig. 1a-c). These reconstructions should be compared to those obtained with delay coordinates (Figs. 1d-f). It appears that the fractional-order q plays more or less the same role as the delay τ when delay coordinates are used.

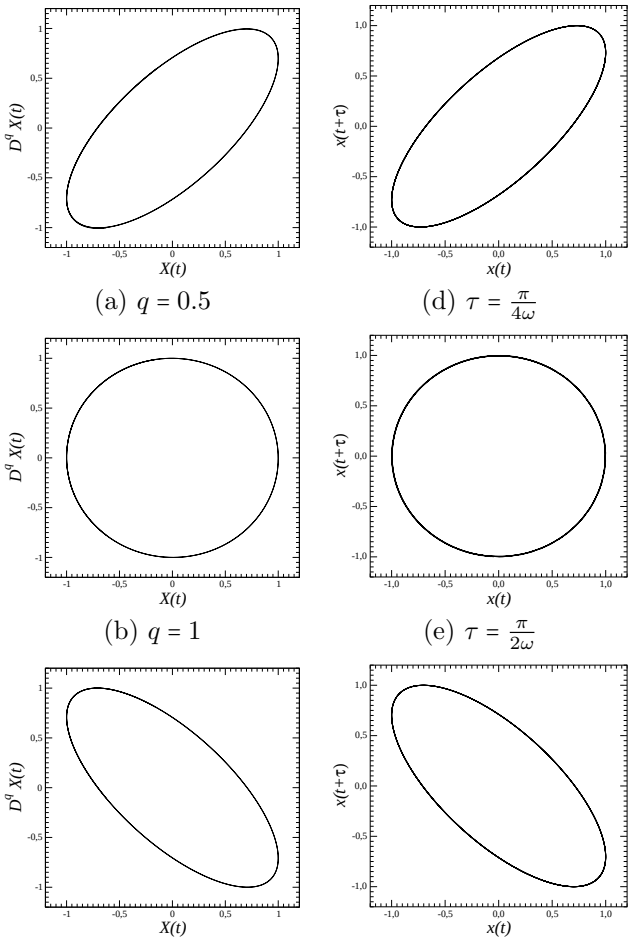

(a) $q = 0.5$ (d) $\tau = \frac{\pi}{4\omega}$

(b) $q = 1$ (e) $\tau = \frac{\pi}{2\omega}$

(c) $q = 1.5$ (f) $\tau = \frac{3\pi}{4\omega}$

Figure 1: Reconstructed phase portraits using fractional derivatives (a-c) and delay coordinates (d-e). Parameter value: $\omega = 1$.

A similar investigation is now performed using the Rössler system

$$\left\{ \begin{array}{l} \dot{x} = -y - z \\ \dot{y} = x + ay \\ \dot{z} = b + z(x - c) \end{array} \right. \tag{8}$$

with $a = 0.43295$, $b = 2$ and $c = 4$. For small q-value, the phase portrait spanned by fractional-order derivatives is in the neighborhood of the first bisecting line (Fig. 2a) as observed when using delay coordinates (Fig. 2d) with a delay commonly considered as being too small. For $q = 1$, the phase portrait spanned by fractional order derivatives (Fig. 2b) is topologically equivalent to the portrait

spanned by the delay coordinates (Fig. 2e) with an optimal delay τ_0 (here equal to a quarter of the pseudo-period of the Rössler system). The most interesting case is obtained with q greater than one. For instance, for $q = 1.5$, the attractor (Fig. 2c) starts to be structured along the second bisecting line and additional structures are easily identified in the right lower part of the attractor. As observed with delay coordinates, the obtained attractor remains topologically equivalent to the original Rössler attractor (as shown in Figs. 2b and 2e, for instance). We would thus conclude that the reconstructed portrait was reconstructed with a too large fractional-order, as we concluded for the portrait reconstructed using delay coordinate and shown in Fig. 2f. Fractional-order derivative coordinates are thus another possible set of coordinates quite similar to delay coordinates, for which the free parameter is q and τ, respectively.

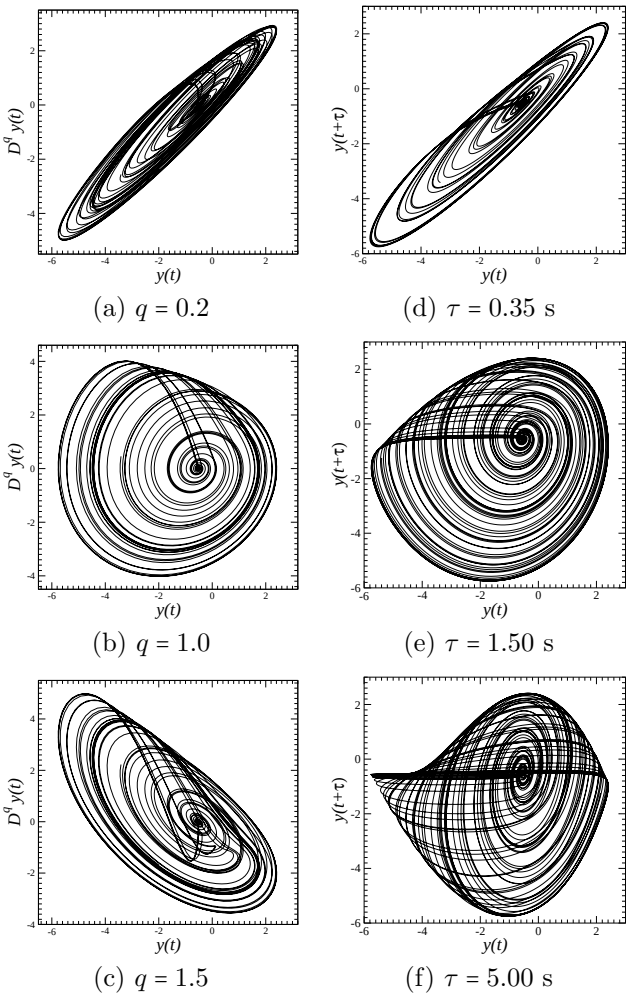

(a) $q = 0.2$ (d) $\tau = 0.35$ s

(b) $q = 1.0$ (e) $\tau = 1.50$ s

(c) $q = 1.5$ (f) $\tau = 5.00$ s

Figure 2: Reconstructed phase portraits using fractional derivatives (a-c) and delay coordinates (d-f) from the measurements of variable y of the Rössler system. Parameter values: $a = 0.432$, $b = 2$, and $c = 4$.

Delay coordinates and fractional-order derivative coordinates are not fully equivalent ; both tend to "simplify" (linearize) the dynamics when the free parameter (τ for the delay coordinates and q for the fractional-order derivatives) is too small, compared to the "optimal" value (τ_0 and $q = 1$, respectively) and tend to add spurious foldings, although not affecting the resulting topology of the reconstructed attractor, when the free parameter is too large compared to the optimal value. The way in which these parameters affect the original dynamics only differs in the nature of the additional foldings.

4 The fractional order q as a bifurcation parameter

4.1 Two conservative systems

An ideal (frictionless and linearized) pendulum can be described by

$$\begin{cases} \dot{u} = v \\ \dot{v} = -\omega^2 u\,. \end{cases} \tag{9}$$

This system has a single singular point at the origin of the phase space $\mathbb{R}^2(u, v)$ which is characterized by $\lambda_\pm = \pm i\omega$: it is thus a center point. Varying the single parameter (ω) of system (9) just changes the pulsation, that is, the time period of the periodic orbit. For all parameter values ($\omega \in \mathbb{R}^+$), the system (9) is conservative and the singular point remains a center.

The corresponding fractional order system reads

$$\begin{cases} D^{q_1} u = v \\ D^{q_2} v = -\omega^2 u\,. \end{cases} \tag{10}$$

When $q_1 = q_2$, this system is said to be commensurate (Petráš, 2011). According to the stability condition $|\mathrm{Arg}(\lambda)| > \frac{q\pi}{2}$ (Petráš, 2011 and Abdelouahab, 2012), the singular point at the origin has two complex conjugated eigenvalues with a negative real part for $q < 1$ and with a positive real part for $q > 1$. For the integer system, the bifurcation observed at $\omega = 1$, transforms the stable focus point ($\omega < 1$) into an unstable focus point ($\omega > 1$). The system being linear, there is no limit cycle resulting from this bifurcation and the trajectory is ejected to infinity. The fractional-order counterpart of the ideal pendulum (9) is no longer conservative for $q \neq 1$: it is dissipative for $q < 1$ and expansive for $q > 1$ (Figs. 3).

We now investigate the case of the Nosé-Hoover system (Posch, 1986) also known as the Sprott A system (Sprott, 1994)

$$\begin{cases} \dot{x} = y \\ \dot{y} = -x + yz \\ \dot{z} = 1 - y^2\,. \end{cases} \tag{11}$$

This system has no singular point and is conservative (Posch, 1986). Depending on the initial conditions, this system produces periodic orbits, quasi-periodic solutions or chaotic regimes. We choose initial conditions such as the resulting behavior is quasi-periodic (Fig. 4a) and whose Poincaré section has an annular structure (Fig. 4b).

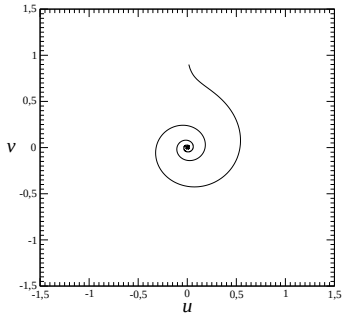

(a) $q = 0.9$

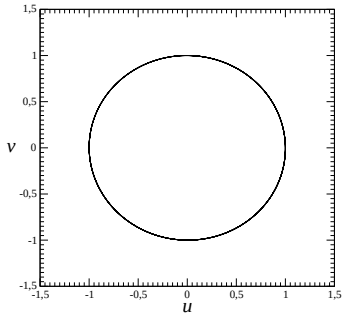

(b) $q = 1.0$

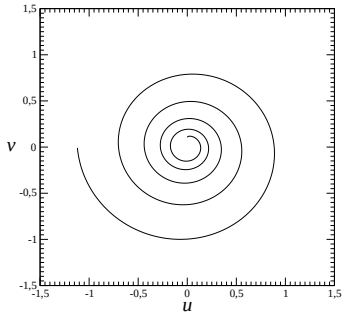

(c) $q = 1.05$

Figure 3: Phase portrait of the ideal pendulum. Parameter value: $\omega = 1$ rad.s^{-1}.

The fractional counterpart of the Nosé-Hoover systems is integrated with $q = 1$. Our algorithms, which was validated with the Rössler system (Letellier, 2013), is unable to produce a quasi-periodic solution with an annular Poincaré section. The phase portrait (Fig. 4c) looks quite similar to the portrait produced by the integer system (Fig. 4a) but the Poincaré section is characterized by an annular structure whose radius slowly decreases, ending after a long transient regime — depending on the time step — in a limit cycle. Such a feature thus suggests that the main characteristics of integer conservative systems are not recovered in the fractional counterpart, at least using our algorithm. Conservative systems thus require specific integration algorithms as the sympletic scheme developed for integer conservative systems to ensure that the energy is actually conserved.

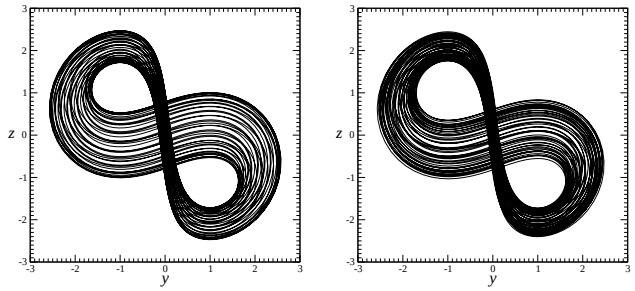

Phase portraits

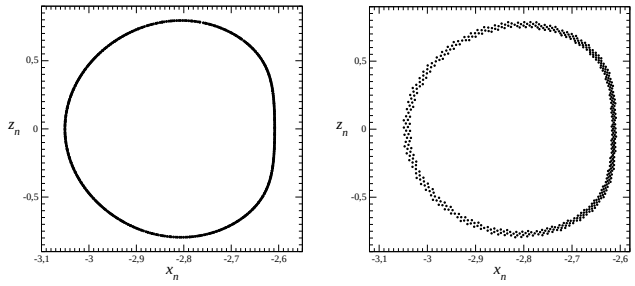

Poincaré sections

(a) Integer order (c) Fractional order

Figure 4: The Nosé-Hoover system in its integer version (a) and in its "fractional" ($q = 1$) counterpart (b). Initial conditions: $x_0 = 0.2$, $y_0 = z_0 = 0$.

4.2 Nonlinear damped pendulum

We now investigate the van der Pol equation, which is a nonlinear damped pendulum (van der Pol, 1926)

$$\ddot{x} - \mu(1 - x^2)\dot{x} + x = 0 \tag{12}$$

which can be rewritten as a set of two differential equations

$$\begin{cases} \dot{x} = y \\ \dot{y} = \mu(1 - x^2)y - x\,. \end{cases} \tag{13}$$

It has a single singular point at the origin of the phase space whose eigenvalues are $\lambda_\pm = \frac{\mu \pm \sqrt{\mu^2 - 4}}{2}$. A Hopf bifurcation is observed for $\mu = 0$ in the integer system (13).

The fractional-order van der Pol counterpart is obtained by changing the integer-order derivatives in (13) by fractional-order derivatives, thus getting

$$\begin{cases} D^{q_1} x = y \\ D^{q_2} y = \mu(1 - x^2)y - x\,. \end{cases} \tag{14}$$

We will consider the commensurate case for which $q_1 = q_2$. According to the stability condition for fractional order systems, a Hopf bifurcation must occur for

$$q_{\text{Hopf}} = \frac{2}{\pi}\left|\arctan\frac{\sqrt{\mu^2 - 4}}{\mu}\right|, \tag{15}$$

that is, for $q = q_{\text{Hopf}} = 0.667$ with $\mu = 1$. The bifurcation diagram computed for the commensurate fractional order van der Pol system *versus* q (Fig. 5) allows to numerically

check that the Hopf bifurcation is actually observed for $q \approx 0.667$ (a longer transient would provide a better agreement).

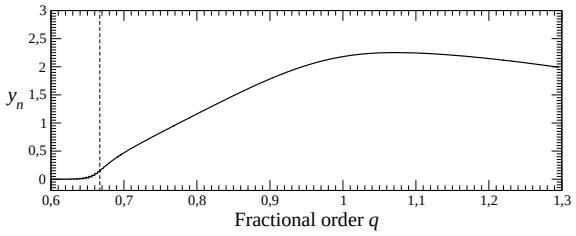

Figure 5: Bifurcation diagram of system (14) with $q_1 = q_2 = q$.

The nonlinearity of the solution increases with q (Figs. 6). For $q = 1.3 > 1.161$, the trajectory presents self-intersections in the plane $\mathbb{R}^2(x_q, y_q)$ where x_q and y_q are the x and y coordinates of the fractional-order system. Here increasing q induced a type of solution that is *not* observed for the integer-order counterpart. Such a result confirms the fact that the order of a fractional-order system must be distinguished from the dimension of the corresponding phase space. Self-intersections of the solution clearly indicate that the dimension of the reconstruction space $\mathbb{R}^2(x_q, y_q)$ is inadequate. With $q = 1.3$, the total order q_T of system (14) equals to 2.6. For integer-order systems, the dimension of the associated phase space is the number of phase variables. Since the dimension of a *vectorial space* cannot be fractal, it clearly appears that the total order q_T of a fractional system is *not* equal to the dimension of the associated phase space, an important difference compared to integer-order systems. Hence, the dimension of the phase space for the fractional van der Pol system (14) must be greater than 2.

In order to introduce a new variable, let us start from the integer van der Pol system (14) and rewrite it with three variables as

$$\begin{cases} D^q u_1 = u_2 \\ D^q u_2 = u_3 \\ D^q u_3 = \mu(1-u_1^2)u_2 - u_1, \end{cases} \tag{16}$$

with $q = \frac{2.6}{3} = 0.87$ to preserve the total order q_T of the system. Such a system diverges to infinity. In fact, system (16) can be rewritten as

$$D^{3q}u_1 = \mu(1-u_1^2)D^q u_1 - u_1, \tag{17}$$

which is not equal to (12), that is, $u_2 = D^q u_1 \neq y$. A limit cyle can be obtained when the third equation is replaced with

$$D^q u_3 = \mu(1-u_1^2)u_3 - u_1 \tag{18}$$

but the nonlinear aspect of the limit cycle is not recovered (Fig. 7a). This second 3D fractional van der Pol system is not yet equivalent to the 2D fractional system (14).

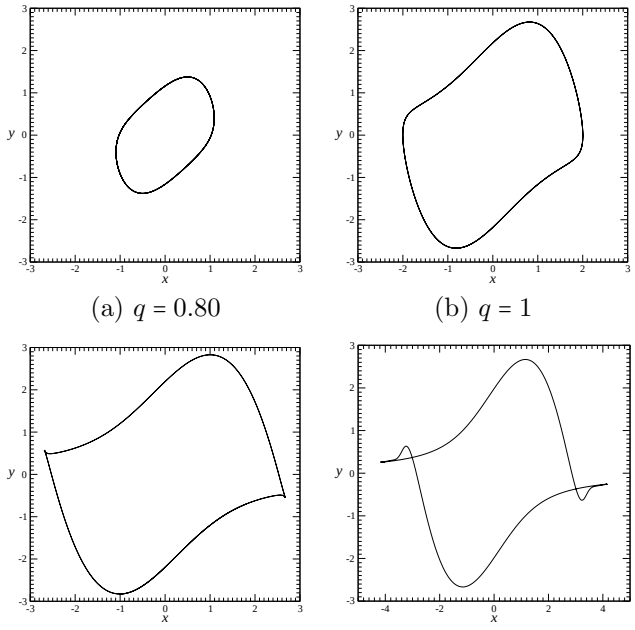

(a) $q = 0.80$ (b) $q = 1$

(c) $q = 1.161$ (d) $q = 1.3$

Figure 6: Phase portraits of system (14) with $q_1 = q_2 = q$.

A fractional van der Pol equation equivalent to (12) can be obtained with

$$D^{4q}\, u_1 = \mu(1-u_1^2)D^{2q}u_1 - u_1\,, \tag{19}$$

that is, with the 4D fractional van der Pol system

$$\begin{cases} D^q\, v_1 = v_2 \\ D^q\, v_2 = v_3 \\ D^q\, v_3 = v_4 \\ D^q\, v_4 = \mu(1-v_1^2)v_3 - v_1\,, \end{cases} \tag{20}$$

where $q = \frac{2.6}{4} = 0.65$ to preserve the total order q_T of system (14). A nearly equivalent solution to those observed in Fig. 6d is obtained, thus validating this 4D system. This indicates that the dynamics results from a system whose phase space dimension is most likely four. We have thus a four-dimensional system with total order $q_T = 2.6$. In a general way, the phase space dimension d must obey $d \geq \mathrm{Int}(q_T) + 1$. Consequently, for $q < 1$, fractional systems are associated with a d_i-dimensional phase space where d_i is the dimension of the phase space associated with its integer counterpart. For $1 < q < 2$, fractional systems should be rewritten as $2d_i$-dimensional systems with $1 < q < 2 \mapsto 0 < \tilde{q} < 1$ where $\tilde{q}$ is its fractional order.

4.3 Rössler system

We will now investigate the fractional Rössler system

$$\begin{cases} \mathrm{D}^{q_x} x = -y - z \\ \mathrm{d}^{q_y} y = x + ay \\ \mathrm{d}^{q_z} z = b + z(x-c) \end{cases} \tag{21}$$

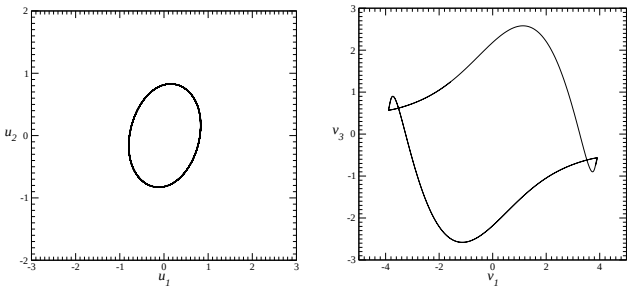

(a) 3D case: $q = 0.87$ (b) 4D case: $q = 0.65$

Figure 7: Solution to the three-dimensional (a) and the four-dimensional (b) fractional commensurate van der Pol system. Both have the same total order $q_T = 2.6$.

with $b = 2$, $c = 4$ and $q_x = q_y = q_z = q$. The dynamics of (21) will be compared to those of the original Rössler system from a topological standpoint as detailed in (Letellier, 1995). With $q = 1$ and $a = 0.43295$, the Rössler system settles to a chaotic attractor characterized by a smooth unimodal map. The increasing branch should touch the first bisecting line, thus corresponding to a nearly complete symbolic dynamics (any symbolic sequences on the two symbols $\{0, 1\}$ are realized as unstable periodic orbits).

Increasing parameter a of the Rössler from 0.3 system leads to a period-doubling cascade as a route to chaos. Unimodal chaos observed after the accumulation point is characterized by a first-return map made of two monotonic branches splitted by a critical point located at the differentiable maximum. When a period-doubling cascade is observed, the maximum is necessarily differentiable. For any system characterized by a smooth unimodal map, the periodic orbits are created according to the so-called unimodal order which can be determined from the symbolic sequences (Collet, 1980). Thus, the whole population is determined by identifying the last created orbit, that is the so-called kneading orbit.

Figure 8a shows a bifurcation diagram for the fractional Rössler system using q as a bifurcation parameter. When q is increased, a period-doubling cascade is the route to chaos as observed in the original Rössler system. Consequently, increasing the fractional-order q develops the underlying dynamics. Conversely, decreasing the fractional-order q in the commensurate fractional system (21) reduces the underlying dynamics to the point that, for $q \lesssim 0.965$, the dynamics is reduced to a limit cycle or even to a stable singular point. In this case, the fractional-order q can be considered as a bifurcation parameter.

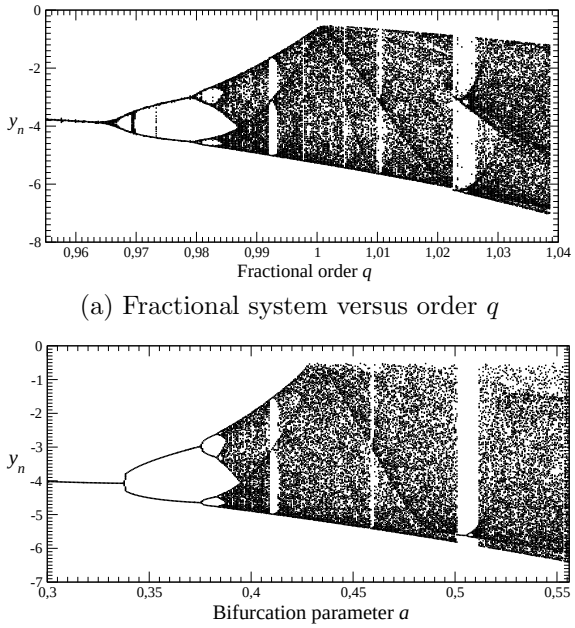

(a) Fractional system versus order q

(b) Integer system versus parameter a

Figure 8: Bifurcation diagrams for the fractional system (21) and the integer Rössler system with $a = 0.43295$. Other parameter values: $b = 2$ and $c = 4$.

5 Conclusions

Various fractional systems were investigated. The results discussed in this paper helped us to better understand the role played by the total order q_T. In particular, it was clearly shown that *the total order of a system should not be confused with the dimension of the associated phase space*. In certain cases, increasing the fractional-order beyond one induces a dynamics which can no longer be embedded within a space with dimension equal to the dimension of the phase space to the corresponding integer system. In other cases, the fractional-order q plays the role of a bifurcation parameter and a higher-dimensional phase space is not required, as seen in the case of the Rössler system. An interesting remark is that we were unable to obtain (in a general way) solutions characteristic of conservative system by simulating the fractional-order counterpart. This was only achieved in the very special case of a very simple linear system with $q = 1$. It thus seems that the algorithm used to simulate fractional-order systems might need adaptation when used with conservative systems.

Acknowledgements

LAA gratefully acknowledges financial support by CNPq.

References

[1] M.-S. Abdelouahab, N.-E. Hamri & J. Wang Hopf bifurcation and chaos in fractional-order modified hybrid optical system, *Nonlinear Dynamics*, vol. 69, pp. 275-284, 2012.

[2] P. Collet & J. P. Eckmann, *Iterated maps on the interval as dynamical systems*, Birkhäuser, 1980.

[3] K. Diethelm, *The Analysis of Fractional Differential Equations*, Spring-Verlag Berlin Heidelberg, 2010.

[4] A. Eke, P. Herman, L. Kocsis, & L. Kozak, Fractal characterization of complexity in temporal physiological signals, *Physiological Measurements*, vol. 23, pp. R1-R38, 2002.

[5] T. T. Hartley, C. F. Lorenzo & H. K. Qammer, Chaos in a fractional order Chua's system, *IEEE Transactions on Circuits and Systems*, vol. 42 (8), pp. 485-490, 1995.

[6] G. W. Leibniz, *Leibnizens mathematische Schriften*, Georg Ohns Verlagsbuch Handlung Hildesheim, 1962.

[7] C. Letellier, P. Dutertre & B. Maheu, Unstable periodic orbits and templates of the Rssler system: toward a systematic topological characterization, *Chaos*, vol. 5 (1), pp. 272-281, 1995.

[8] C. Letellier & L. A. Aguirre, Dynamical analysis of fractional-order Rssler and modified Lorenz systems, *Physics Letters A*, vol. 377 (28-30), pp. 1707-1719, 2013.

[9] K. B. Oldham & J. Spanier, *The Fractional Calculus*, Academic Press, New York and London, 1974.

[10] A. Oustaloup, CRONE Control: Principle, synthesis, performances with non-linearities and robustness-input immunity dilemma, *Lecture Notes in Control and Information Sciences*, vol. 144, pp. 767-777, 1990.

[11] I. Petráš, *Fractional-Order Nonlinear Systems*, Spring-Verlag, Nonlinear Physical Science, 2011.

[12] I. Podlubny, Numerical solution of ordinary fractional differential equations by the fractional difference method in *Advances in Difference Equations*, S. Elaydi, I. Gyori, G. Ladas (eds), Gordon and Breach Scientific Publications, Amsterdam, 1997.

[13] H. A. Posch, W. G. Hoover & F. J. Vesely, Canonical dynamics of the Nosé oscillator: stability, order and chaos, *Physical Review A*, vol. 33 (6), pp. 4253-4267, 1986.

[14] A. Razminia, V. J. Majd & D. Baleanu, Chaotic incommensurate fractional-order Rössler system: active control and synchronization, *Advances in Difference Equations*, vol. 15, n^o 2011, 2011.

[15] J. C. Sprott, Some simple chaotic flows, *Physical Review E*, vol. 50 (2), pp. 647-650, 1994.

[16] K. Sun, X. Wang & J. C. Sprott, Bifurcations and chaos in fractional-order simplified Lorenz system, *International Journal of Bifurcation & Chaos*, vol. 20 (4), pp. 1209-1219, 2010.

[17] F. Takens, Detecting strange attractors in turbulence, *Lecture Notes in Mathematics*, vol. 898, pp. 366-381, 1981.

[18] B. van der Pol, On "relaxation-oscillations", *Philosophical Magazine*, vol. 7, pp. 978-992, 1926.

[19] B. West, Fractal physiology and the fractional calculus: a perspective, *Frontiers in Fractal Physiology*, vol. 1 (12), pp. 1-17, 2010.

[20] S. Westerlund, Dead matter has memory!, *Physica Scripta*, vol. 43, pp. 174-179, 1991.

Proceedings of ICCSA 2014
Normandie University, Le Havre, France - June 23-26, 2014

PHASE SYNCHRONISATION IN A RING OF RÖSSLER SYSTEMS

Adrien Kerfourn*† Laurent Laval ‡ Christophe Letellier*†

Abstract. We investigated the dynamics of a ring of coupled Rössler systems with some parameter mismatch. We focused our attention on the cases in which local systems are phase synchronized and how the "collective" dynamics depends on the parameter mismatch and the number of local oscillators. The role of the observability of the original phase space provided by the coupling variable is also investigated. We found that under certain conditions, the collective dynamics is equivalent to the dynamics of a single isolated Rössler system.

Keywords. Ring of Rössler systems, observability, phase synchronization, parameter mismatch.

1 Introduction

Spatio-temporal dynamics are typically produced by partial differential equations in which the spatial derivative induces an infinite-dimensional state space. Sometimes, spatio-temporal dynamics are investigated by the means of a ring of coupled oscillators [1, 2, 3]. Under certain conditions, spatiotemporal chaos can be produced [4, 5, 6, 7]. In such a case, the dimension of the state space is no longer infinite but remains large enough for inducing difficulties in the characterization of the resulting dynamics. Nevertheless, in particular situations, that is, when the local oscillators are phase synchronized, the resulting dynamics may be embedded in a "low dimensional" state space where it can be investigated with common tools used for characterizing temporal chaos [7]. Despite of this, these systems are mostly studied by using spatio-temporal diagrams [8] and no link was established with the structure of the chaotic attractor associated with such a collective behavior. Perhaps this link was not searched due to the lack of a "Takens-like" theorem for this kind of systems: we have therefore no guarantee that there is a possibility for reconstructing from a single time series a phase portrait diffeomorphically equivalent to the portrait in the original state space [7]. When these oscillators are phase synchronized and since they only differ by a rather limited parameter mismatch, it seems possible to assume that all oscillators produce an equivalent dynamics and, consequently, that the collective dynamics can be embedded within a low-dimensional state space, if not in a space whose dimension is equal to the dimension of the state space associated with a single isolated oscillator.

From the seminal paper by Pecora and Carrol [9] on synchronization, it is known that the quality of synchronization depends on the variable chosen for coupling the systems. In most of the papers, the results are presented using one variable chosen *a priori* without any justification. Very frequently, systems are empirically coupled using the variable providing the best observability: for instance, Rössler systems are coupled using variable y [10] which is the best variable since there is a global diffeomorphism between the original state space of the Rössler system and the differential embedding induced by variable y and its first two derivatives [11]. Since a diffeomorphism represents the best map between the original state space and a reconstructed space, one may consider that all the relevant information is retrieved in the reconstructed space [11]. Variable y is the best one for synchronizing Rössler systems [12]. In the other hand, Lorenz systems are often coupled using variable x as done in [9]. Although there is no global diffeomorphism between the state space of the Lorenz system and the x-induced differential embedding, variable x provides the best observability [13]. A variable is associated with a lack of observability when there is a domain — the observability singular manifold defined by $\mathrm{Det}\ \mathcal{J}_{\Phi_s} = 0$ where $\mathcal{J}_{\Phi_s}$ is the jacobian matrix of the coordinate transformation Φ between the original state space and the differential embedding induced by the "measured" variable s — in the state space which cannot be properly reconstructed using the chosen variable. Obviously the location of the observability singular manifold related to the chaotic attractor has an impact on the quality of the variable [14].

The interplay between observability and synchronization was shown for bidirectional coupling between two nearly identical systems [12]: the range of values of the coupling parameter for which complete and/or phase synchronization can be obtained is the largest when the systems are coupled *via* a variable providing a good observability as shown, for instance, in the case of two Rössler systems bidirectionally coupled (Fig. 1).

After a description of the architecture of the ring of Rössler oscillators we studied, we defined how phase syn-

*CORIA UMR 6614, Normandie Université, Saint-Etienne du Rouvray, France. E-mail: adrien.kerfourn@coria.fr, christophe.letellier@coria.fr
†GRHV EA 3830, Rouen University Hospital, France.
‡ECS-Lab, ENSEA, 6 avenue du Ponceau, 95014 Cergy-Pontoise cedex, France

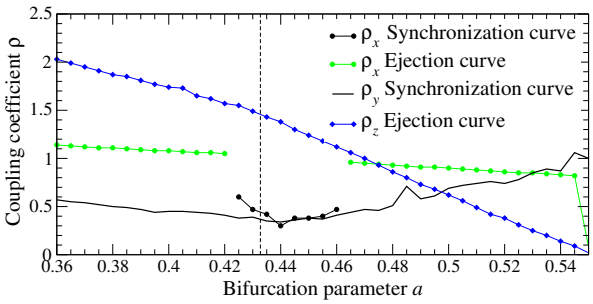

Figure 1: Critical coupling curves that correspond to the onset of synchronization (synchronization curve) and the ejection of the trajectory to infinity (ejection curve), respectively. Below the synchronization curve, the average distance between points and the first bisecting line of plane y_1-y_2 is greater than 0.1. Case of two Rössler systems, $b = 2$, $c = 4$.

chronization was determined and a measure of the departure from phase synchronization is introduced. Some numerical simulations show how the dynamics of a local oscillator is affected by the ring architecture and how it can be sometimes considered as equivalent to the behavior of a single isolated system. This paper ends by some conclusions.

2 Architecture of the Ring of Oscillators

The ring of oscillators here investigated is characterized by a closed chain of dynamical systems S_i $(i = 1, \ldots, N)$ in the form

$$\dot{\boldsymbol{X}}_i = \boldsymbol{f}_i(\boldsymbol{X}_i) + \boldsymbol{U}_i \tag{1}$$

where $\boldsymbol{f}_i(\boldsymbol{X}_i)$ are the governing equations of the ith isolated oscillator and $\boldsymbol{U}_i$ the coupling command. The elements of the ring are coupled in a bidirectional and symmetrical way according to

$$\boldsymbol{U}_i = \boldsymbol{U}_{i,i-1} + \boldsymbol{U}_{i,i+1} \tag{2}$$

where $\boldsymbol{U}_{i,j}$ is the coupling of S_j on S_i. In order to close the chain, we have $\boldsymbol{U}_{1,0} = \boldsymbol{U}_{1,N}$ and $\boldsymbol{U}_{N,N+1} = \boldsymbol{U}_{N,1}$. To impose the symmetry of coupling terms, we must have $\boldsymbol{U}_{i,i-1} = -\boldsymbol{U}_{i-1,i}$.

In this study each node is a Rössler system [15] defined (without the coupling command) as

$$S_i \equiv \begin{cases} \dot{x}_i &= -y_i - z_i \\ \dot{y}_i &= x_i + a_i y_i \\ \dot{z}_i &= b + z_i(x_i - c) \end{cases} \tag{3}$$

where $b = 2$ and $c = 4$. Parameters a_i is specific to the ith oscillator S_i. The Rössler system was chosen as a "local oscillator" for three reasons: i) it is not equivariant (this is important since symmetry properties induce quite complex dynamics and tend to reduce the quality of the synchronization [12]), ii) the dynamics of the Rössler system is well known [16], and iii) there is one variable (y) providing a full observability and one variable (z) providing a very bad observability [17, 18]. Each Rössler system is then slightly "perturbed" by varying the value of parameter a using parameter mismatch δa as shown in Fig. 2. Thus we have a ring of different systems (from the parameter point of view) and we will investigate how the behavior of each local oscillator is modified by the other oscillators.

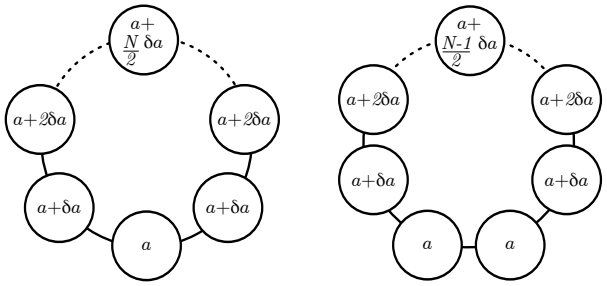

(a) Even number (b) Odd number

Figure 2: Distribution of the parameter mismatch δa for a ring with an even (a) and an odd (b) number of bidirectionally coupled Rössler systems. From the parameter point of view, the ring has a reflection symmetry.

We thus used the couplings

$$\begin{aligned} \boldsymbol{U}_{i,i-1} &= \boldsymbol{K}_p(\boldsymbol{X}_{i-1} - \boldsymbol{X}_i) \\ \boldsymbol{U}_{i,i+1} &= \boldsymbol{K}_s(\boldsymbol{X}_{i+1} - \boldsymbol{X}_i) \end{aligned} \tag{4}$$

where $\boldsymbol{X}_i = [x_i \ y_i \ z_i]^T \in \mathbb{R}^3$. $\boldsymbol{K}_p \in \mathbb{R}^3$ and $\boldsymbol{K}_s \in \mathbb{R}^3$ are two coupling parameters. To have a symmetrical coupling, we impose $\boldsymbol{K} = \boldsymbol{K}_s = \boldsymbol{K}_p$ with a single non-null component (to choose the coupling variable), that is, $\boldsymbol{K} = [K \ 0 \ 0]^T$ for a coupling *via* variable x and $\boldsymbol{K} = [0 \ K \ 0]^T$ for a coupling *via* variable y.

3 Analytical Study

Since the existence of a complete synchronization is rather difficult to prove for N systems, we here investigated a simplest form of synchronization, that is, phase synchronization. In this case, we are only looking for having the oscillators with a nearly constant phase between them. Nevertheless, we are facing with the sometimes difficult problem to define the phase of a system. For example, the Rössler system here used as local oscillator can produce — for certain parameter values — solutions for which a phase is rather tricky to determine (this kind of behavior is said to be "phase non coherent") [19, 16]. Indeed, defining a phase for some solutions to the Rössler system is not a trivial task since they are governed by two rotation axes (each one is associated with the real eigenvalue for each of the two singular points): these phase

non coherent solutions are characterized by two different pulsations.

Since, according to the bounding tori as introduced by Tsankov and Gilmore [20], phase non coherent solution is bounded by genus-one torus as phase coherent solution, the phase should be defined in the same way for the two types of solutions. The single "hole" in the middle of the attractor can thus be used as a reference for defining a phase. The simplest way to do this is thus to use the one-component Poincaré section as a reference and to consider that the phase is increased by 2π between two successive crossings of the trajectory with the Poincaré section. Hereafter, the duration T_k between these two successive intersections is associated with the increment by 2π and the linear interpolation

$$\phi(t) = 2\pi k + 2\pi \frac{t - T_k}{T_{k+1} - T_k} \text{ (rad)}. \quad (5)$$

allows to have the phase for any arbitrary time $T_k < t < T_{k+1}$ [12]. There is a slight approximation here in the sense that the linear interpolation would have been rigorous only if the velocity would have been constant during a revolution, a property which is not verified in the Rössler system. Nevertheless, the departure with the actual phase remains limited since it is vanished at every crossing with the Poincaré section, by definition. With such a definition, we avoid the problem of the choice of the rotation axis required for defining a phase. Despite all these advantages, this procedure can only be used in numerical simulation. It is therefore not possible to develop an analytical proof for the existence of a phase synchronization between a given number N of Rössler systems. It is not possible to determine the conditions under which (from the parameter values point of view, for instance) phase synchronization can be obtained.

In the simulations discussed in the subsequent part of this paper, we computed the bifurcation diagrams for each local system of the ring. For each parameter value, systems are integrated for at least 1000 crossings with the Poincaré section. When systems are phase synchronized, the number of crossings with the Poincaré section is the same for each system. But, and this is particularly true when solutions are phase non coherent, different systems may present different number of crossings with the Poincaré section: this is thus a direct evidence for a lack of phase synchronization. For the sake of simplicity and because we can expect that these numbers will differ the most for the more distant systems, that is, for oscillators with the largest mismatch according to the architecture of our ring, we only reported the bifurcation diagrams for these two local oscillators.

Moreover, the lack of phase synchronization is assessed by computing the relative difference

$$\eta_{\mathrm{a}} = \frac{|L_1 - L_2|}{\min(L_1, L_2)} \quad (6)$$

between the number of crossings with the Poincaré section counted for these two distant oscillators, that is, L_1 and L_2, respectively. η_{a} will be named the "asynchrony rate" in the subsequent part of this paper. In Eq. (6), the function $\min(L_1, L_2)$ returns the smallest value among L_1 and L_2.

4 Dynamical Analysis

In our rings of Rössler systems, there is parameter a_i that is specific to the ith oscillator. As previously explained, the ring is constructed with a constant parameter mismatch δa (Fig. 2) between two consecutive systems (with the exception of ring with an odd number N of oscillators for which there are two systems with the same parameter value, that is, a null mismatch). It is thus possible to investigate how local dynamics depends on the nominal parameter value a and for a given mismatch δa the ith parameter value being $a_i = a + g(i)\delta a$ where $g(i)$ depends on the ring architecture, see Fig. 2).

The parameter mismatch δa affects the intrinsic parameter value a of each local Rössler system and so its dynamics according to Fig. 3. We are now investigating how are affected the dynamics of the coupled Rössler systems differing by the parameter mismatch δa. Let us start with a ring of $N = 4$ Rössler systems coupled by variable y with a gain $K = 25.0$ and for various values of the parameter mismatch δa. For any value of δa for which the trajectory remained in a chaotic attractor, we always observed that the four oscillators were phase synchronized. The dynamics of each oscillator was strongly dependent on the mismatch δa as shown in Fig. 4: in fact, δa plays the role of a bifurcation parameter (similar to the role played by parameter a in the present case) and a bifurcation diagram equivalent to the reference diagram (Fig. 3) is obtained. The fact that all the systems are phase synchronized, as evidenced by the asynchrony rate which remains null for any δa-value as well as by the feature that every bifurcation occurs at the same δa-value for any oscillator, indicates that the ring of four oscillators behaves as a single isolated Rössler system with a parameter value affected by the mismatch δa.

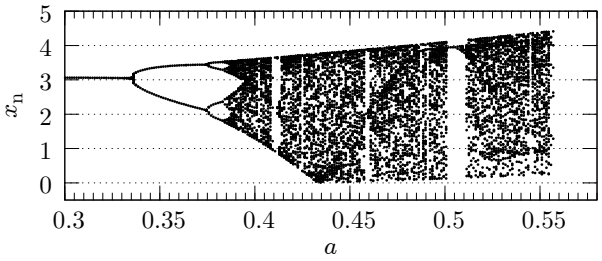

Figure 3: Bifurcation diagram versus parameter a of a single isolated Rössler system. This bifurcation diagram served as a reference for many comparisons with diagrams computed for coupled Rössler systems.

In order to investigate how the observability provided by the variable used for coupling the oscillators affects the

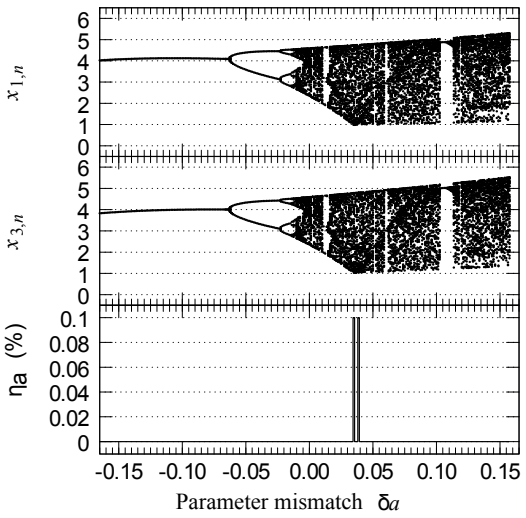

(a) $N = 4$

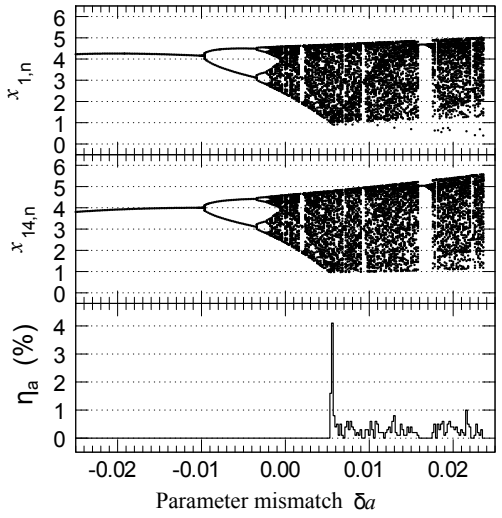

(b) $N = 26$

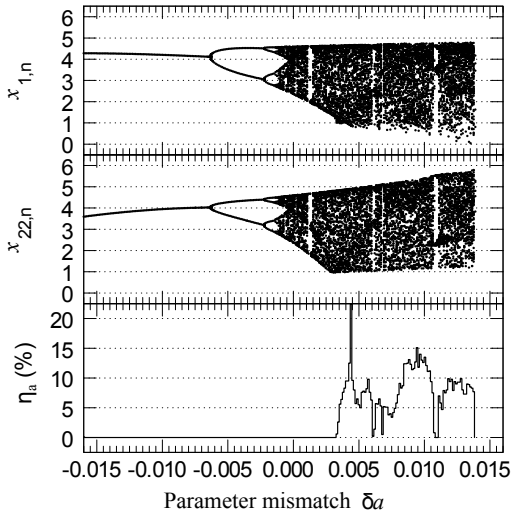

(c) $N = 42$

Figure 4: Bifurcation diagrams for the most distant local oscillators in a ring made of $N = 42$ Rössler systems coupled *via* variable y. Parameter values: $a = 0.398$, $b = 2$, $c = 4$ and $K = 25$.

local dynamics, we used the three state variables, from the best (variable y) to the worst (variable z). We also investigated how the "size" of the ring, that is, the number N of oscillators, influences the local dynamics. The best observability is provided by variable y and, obviously, this is the variable that allowed phase synchronization for the largest range of values for the parameter mismatch δa. As already mentioned, the collective dynamics is equivalent to the dynamics of a single isolated oscillator. When δa is decreased from 0, the chaotic attractor is progressively reduced by pruning the population of unstable periodic orbits up to a simple period-1 limit cycle. When δa is increased, the chaotic behavior is developed as the Rössler system is when parameter a is increased [16]. Around $\delta a = 0.16$, the trajectory is ejected to infinity due to a boundary crisis between the attractor and the boundary of the attraction basin as observed in an isolated Rössler system [16]. We never observed some behaviors which were not solution to the original Rössler system.

When we changed the nominal value of parameter a, we did not observe any change in the collective dynamics and the bifurcation diagram was only shifted in a-values. This property was verified for any number N of local oscillators in the ring (but not for any coupling variable). We can thus limit our study by always using the same nominal parameter value (say, for instance, $a = 0.398$). When the number N of oscillators in the ring was increased, the bifurcation diagram versus the parameter mismatch δa remained qualitatively the same; the attractor was reduced when we decreased δa from 0 and developed when δa was increased. Only the δa-values at which the bifurcations occur were changed in such a way that the δa-value beyond which the trajectory is ejected to infinity was reduced from $\delta a \approx 0.16$ with $N = 4$ systems (Fig. 4a) to $\delta a \approx 0.014$ with $N = 42$ systems (Fig. 4c).

The asynchrony rate η_a is related to the number N of systems in the ring. Pecora and Carroll showed that there is a limit in the number of Rössler systems which can be coupled with a complete synchronization [21]: this limit was 42 for Rössler systems coupled via variable y. We here observed that when the number of systems in the ring is small enough (Fig. 4a) the asynchrony rate is always zero. When this number is increased (Fig. 4b), the asynchrony rate becomes nonzero for the largest parameter mismatch, that is, when the dynamics of each local oscillator is strongly phase non coherent. When the number N of systems is increased again, the asynchrony rate becomes larger and is nonzero as soon as the dynamics of the local oscillators are phase non coherent ($\delta a \approx 0.005$), that is, when a third branch occurs in the first-return map [16] (Fig. 4c). When the asynchrony rate is computed versus the number N of oscillators in the ring (Fig. 5), we observed that it becomes nonzero when $N \approx 24$ and increases as N was increased. It returns to zero for $N = 36$ because the collective dynamics was a period-2 limit cycle and all oscillators were thus phase synchronized. The increase of η_a versus N (when

the collective dynamics was not a limit cycle) means that the number N of oscillators plays more or less the role of a bifurcation parameter. Moreover, there is an upper limit ($N_{\text{lim}} \approx 24$) beyond which phase synchronization is no longer observed. Such a limit also depends on the mismatch δa, the nominal value a and the coupling variable as discussed below.

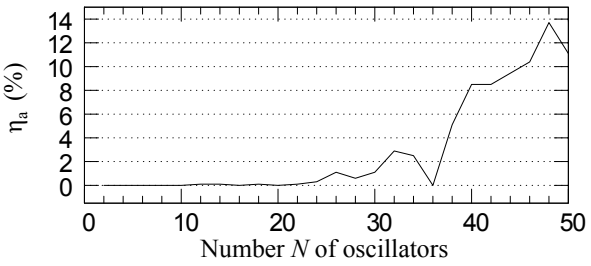

Figure 5: Asynchrony rate η_a versus the number N of local oscillators in a ring of Rössler systems coupled by variable y. The parameter mismatch δa is chosen in such a way that $< a >_N = 0.528$ (see below). Other parameter values: $a = O.398$, $b = 2$, $c = 4$ and, $K = 25$.

Consequently phase synchronization strongly depends on i) the phase coherence of the dynamics underlying each local oscillator and ii) the number N of oscillators which are in the ring. Roughly speaking, we can say that phase synchronization is more difficult to obtain when the complexity of the ring increases. It is interesting to remark that the asynchrony rate is zero when local oscillators produce limit cycle (Fig. 4c): see for instance, the period-1 window located at $\delta a \approx 0.012$.

The results obtained with a coupling *via* variable y evidence that the global behavior of the ring can be associated with the behavior of a single isolated Rössler system. In fact all oscillators have the same behavior and then can be viewed as isolated Rössler systems for which parameter a would take the mean value

$$< a >_N = a + \frac{N}{4}\delta a \tag{7}$$

when there are an even number N of oscillators and the mean value

$$< a >_N = a + \frac{(N-1)^2}{4N}\delta a \tag{8}$$

when N is odd,

In order to check this assertion, we compared the first-return map of a local Rössler system from different ring configurations to the map computed for an isolated Rössler system with $a =< a >_N$. The simplest case is when the parameter mismatch $\delta a = 0$ (Fig. 6): in this case $< a >_N = a = 0.398$ for any $N \in \mathbb{N}^+$: all systems are phase synchronized and the resulting first-return maps are identical to the map of the isolated Rössler system. The collective dynamics is therefore equivalent to the dynamics produced by a single Rössler system. When the

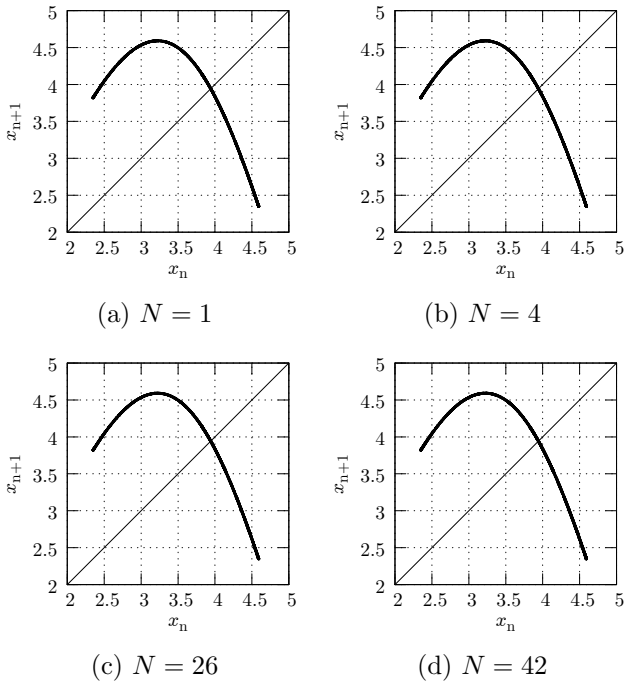

(a) $N = 1$ (b) $N = 4$

(c) $N = 26$ (d) $N = 42$

Figure 6: First-return maps of a local Rössler system from different ring configurations. Parameter values: $a_0 = 0.398$, $\delta a = 0$, $b = 2$, $c = 4$ and $K = 25$.

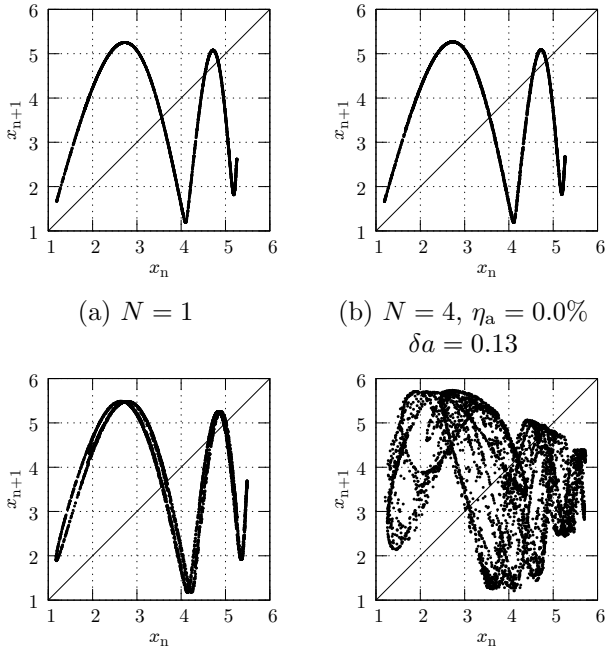

(a) $N = 1$ (b) $N = 4$, $\eta_a = 0.0\%$ $\delta a = 0.13$

(c) $N = 26$, $\eta_a = 1.1\%$ $\delta a = 0.02$ (d) $N = 42$, $\eta_a = 8.5\%$ $\delta a = 0.012380952$

Figure 7: First-return maps of a local Rössler system from different ring configurations. In each case $< a >_N = 0.528$. Parameter values: $b = 2$, $c = 4$ and $K = 25$.

parameter mismatch δa is non zero, the mean parameter $< a >_N$ is increased. We choose the case where $< a >_N = 0.528$ for various N-values (Fig. 7): the first-return map has now four branches and the dynamics is phase non coherent. When N is not too large ($N \leq 26$), the number of monotonous branches is still four even if they are slightly foliated for $N = 26$ (Fig. 7c). Within a good level of approximation, the collective dynamics can still be considered as resulting from a single isolated Rössler system, mainly because local oscillators are nearly phase synchronized. This is no longer the case with $N = 42$: local oscillators are not phase synchronized ($\eta_{\rm a} = 8.5\%$) and the collective dynamics is no longer equivalent to the dynamics produced by a single isolated Rössler system as evidenced by the multi-layered first-return map (Fig. 7d). A first consequence of this lack of synchronization is that the embedding dimension increases (the attractor can no longer be embedded within a 3D subspace of the $3N$-dimensional state space). Consequently, there exists an upper limit $N_{\rm lim}$ for the number N of oscillators for which phase synchronization can be obtained with good enough approximation, that is, with $\eta_{\rm a} = 0$.

Unfortunately, if using a variable with a full observability for coupling the systems allows to get a formula for the value of parameter a to use in an isolated Rössler system for reproducing the collective dynamics when oscillators are phase synchronized, this is not the case when the coupling variable does not provide a full observability of the original state space is used: we observed such a feature when variable x was used as the coupling variable. Nevertheless we obtained a phase synchronization when N was not too large and we thus investigated the differences with a coupling via variable y. The main departure is that the bifurcation diagrams are not complete and a rigorous comparison with a single Rössler system is no longer possible.

For instance with a ring made of four oscillators, decreasing the parameter mismatch δa induces a simplification of the resulting chaotic attractor as observed with a coupling via variable y (compare the left part ($\delta a < 0$) of the bifurcation diagram shown in Fig. 8 with the corresponding part of the bifurcation diagram shown in Fig. 4). It was nearly impossible to use a positive parameter mismatch δa with a gain $K = 0.5$: the trajectory was quickly ejected to infinity. When the gain is reduced to $K = 0.1$, phase synchronization was retrieved even for positive mismatch δa (Fig. 8b). Nevertheless, a period-4 window occurs with a relative length which is not common (if ever observed) in the Rössler system: at this end of this period-4 window, the local oscillators are no longer phase synchronized ($\eta_{\rm a} \neq 0$) and the collective dynamics can no longer be embedded within a three-dimensional subspace. When the coupling variable does not provide a full observability, the collective dynamics becomes very sensitive to the gain K (a feature not observed using the coupling variable y over a large range of K-value). When

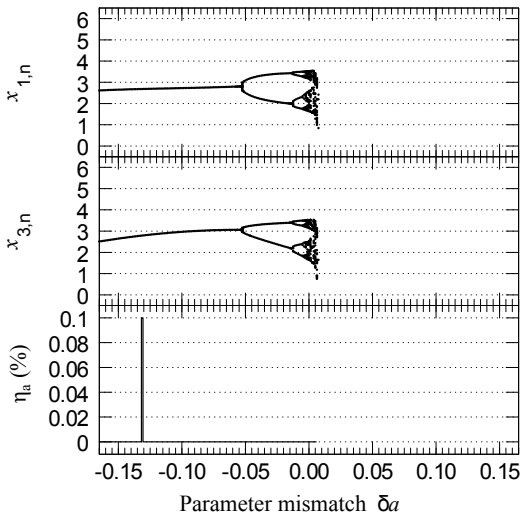

(a) $N = 4$, $K = 0.5$

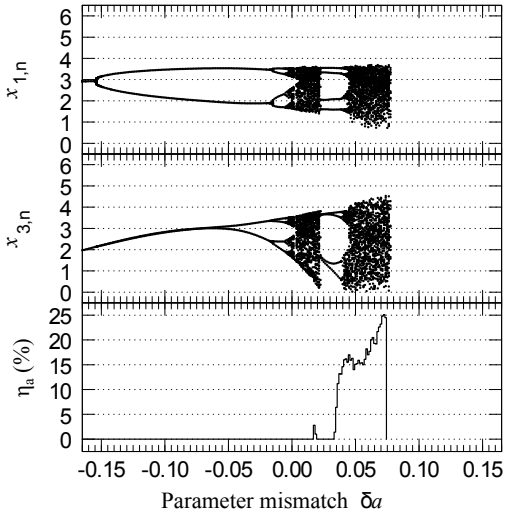

(b) $N = 4$, $K = 0.1$

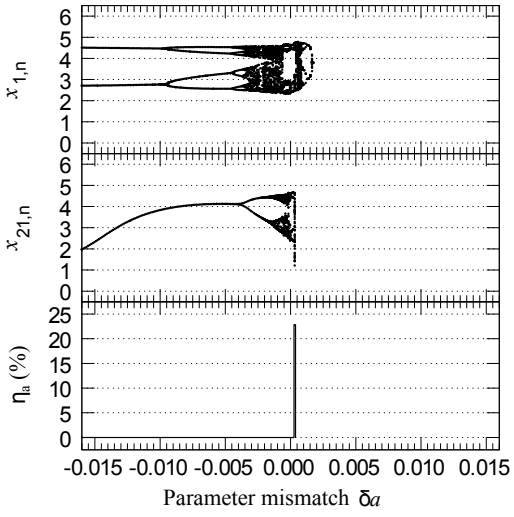

(c) $N = 42$, $K = 0.5$

Figure 8: Bifurcation diagrams for the most distant local oscillators in a ring made of N Rössler systems coupled *via* variable x. Parameters : $a_0 = 0.398$, $b = 2$, and $c = 4$.

K was left equal to 0.5 but N increased to 42, the dynamics was still reduced for negative δa-values but the development was not observed for positive δa-values: contrary to this, a cascade of inverse period-doubling bifurcations is observed, leading to a period-1 cycle. Hereafter, the trajectory was ejected to infinity. Consequently, the collective dynamics strongly depends on the coupling variable due to the different observability of the state space it may provide. As shown in [12], using variable z as a coupling variable does not allow to get easily phase synchronization and we did not investigate this acid case.

5 Conclusion

In this study we investigated how the value of parameter a and of the parameter mismatch δa in a ring of coupled Rössler systems affects the collective behavior. We thus showed that when the coupling is realized using variable y — a variable providing a full observability —, the collective dynamics can be compared to an isolated Rössler system. In this situation, the oscillators are phase synchronized for a large range of values of the parameter mismatch δa, the gain K or the number of oscillators. When phase synchronization is observed, we showed that oscillators have the same dynamics which is equivalent to the dynamics produced by a single isolated Rössler system with a parameter a-value provided by an analytical formula only depending on the number N of oscillators. Nevertheless, when the number of oscillators becomes too large, phase synchronization can no longer be observed, perhaps due to the delay with which "information" was propagated from one oscillator to any others.

When the observability of the original state space provided by the coupling variable decreases, the range of parameter values for which local oscillators are phase synchronized is significantly reduced compared to what is observed with a coupling variable with a full observability. The dual aspect of such a feature is that the collective dynamics is much more sensitive to parameter values. In that case, even when local systems are phase synchronized, it is not always possible to determine whether the dynamics can be produced by a single isolated Rössler system and for which parameter values. The collective dynamics of a ring of oscillators therefore strongly depends on the observability provided by the coupling variable. When this observability is not global, the gain of the coupling term, the number of oscillators, the mismatch between local oscillator strongly affect the collective dynamics. These results are specific to the Rössler system in the sense that its controllability does not depend on the coupling variable.

References

[1] N. Akamatsu, Period-doubling phenomena and chaos generated in the GaAs ring-oscillator, *Electronics and Communications in Japan* III, vol. 72, pp. 1028-1035, 1989.

[2] S. J. Lee, B. Kim & K. Lee, A novel high-speed ring oscillator for multiphase clock generation using negative skewed delay scheme, *IEEE Journal of Solid-State Circuits*, vol. 32, pp. 289-291, 1997.

[3] Y. Hosokawa & Y. Nishio, Simple chaotic circuit using CMOS ring oscillators, *International Journal of Bifurcation & Chaos*, vol. 14, pp. 2513-2524, 2004.

[4] G. dAlessandro, Spatiotemporal dynamics of a unidirectional ring oscillator with photorefractive gain, *Physical Review A*, vol. 46, pp. 2791-2802, 1992.

[5] H. G. Enjieu Kadji, J. B. Chabi Orou & P. Woafo, Spatiotemporal dynamics in a ring of N mutually coupled self-sustained systems *Chaos*, vol. 17, 033109, 2007.

[6] H. Daido, Suppression and recovery of spatiotemporal chaos in a ring of coupled oscillators with a single inactive site, *European Physics Letters*, vol. 87, 40001, 2009.

[7] D. Amroun-Aliane, L. Pastur & C. Letellier, "Defects in spatiotemporal diagrams and their relations to phase coherence and lack of observability," *Physical Review*, vol. 83, pp. 056212, 2011.

[8] M. Dolnik, A. M. Zhabotinsky, A. B. Rovinsky & I. R. Epstein, Spatio-temporal patterns in a reaction-diffusion system with wave instability, *Chemical Engineering Science*, vol. 55, pp. 223-231, 2000.

[9] L. M. Pecora & T. L. Carroll, "Synchronization in chaotic systems," *Physical Review Letters*, vol. 64, pp. 821-824, 1990.

[10] G. V. Osipov, B. Hu, C. Zhou, M. V. Ivanchenko & J. Kurths, "Three types of transitions to phase synchronization in coupled chaotic oscillators," *Physical Review Letters*, vol. 91, pp. 024101, 2003.

[11] C. Letellier, L. A. Aguirre & J. Maquet, "Relation between observability and differential embeddings for nonlinear dynamics," *Physical Review E*, vol. 71, pp. 066213, 2005.

[12] C. Letellier & L. A. Aguirre, "On the interplay among synchronization, observability and dynamics," *Physical Review E*, vol. 82, pp. 016204, 2010.

[13] C. Letellier & L. A. Aguirre, "A graphical interpretation of observability in terms of feedback circuits," *Physical Review E*, vol. 72, pp. 056202, 2005.

[14] M. Frunzete, J.-P. Barbot & C. Letellier, Influence of the singular manifold of nonobservable states in reconstructing chaotic attractors, *Physical Review E*, vol. 86, 026205, 2012.

[15] O. E. Rössler, "An equation for continuous chaos," *Physics Letters A*, vol. 57, pp. 397-398, 1976.

[16] C. Letellier, P. Dutertre & B. Maheu, "Unstable periodic orbits and templates of the Rössler system: toward a systematic topological characterization," *Chaos*, vol. 5, pp. 271-282, 1995.

[17] C. Letellier, J. Maquet, L. Le Sceller, G. Gouesbet & L. A. Aguirre, "On the non-equivalence of observables in phase space reconstructions from recorded time series," *Journal of Physics A*, vol. 31, pp. 7913-7927, 1998.

[18] C. Letellier & L. A. Aguirre, "Investigating nonlinear dynamics from time series: the influence of symmetries and the choice of observables," *Chaos*, vol. 12, pp. 549-558, 2002.

[19] J. D. Farmer, J. P. Crutchfield, H. Frœling, N. H. Packard & R. S. Shaw, Power spectra and mixing properties of strange attractors, *Annals of the New York Academy of Sciences*, vol. 357, pp. 453-472, 1980.

[20] T. D. Tsankov & R. Gilmore, Topological aspects of the structure of chaotic attractors in $\mathbb{R}^3$, *Physical Review E*, vol. 69, 056206, 2004.

[21] L. M. Pecora & T. L. Carroll, "Master Stability Function for Synchronized Coupled System" *Physical Review Letters*, vol. 80, pp. 2109-2112, 1998.

Proceedings of ICCSA 2014
Normandie University, Le Havre, France - June 23-26, 2014

TOPOLOGICALLY INEQUIVALENT CHAOTIC ATTRACTORS SOLUTION TO THE CHUA CIRCUIT

Martin Rosalie & Christophe Letellier*

Abstract. We investigated topologically inequivalent chaotic attractors solutions to a variant of the Chua circuit. We thus showed that the circuit can produce spiral and funnel Rössler attractors, attractors equivalent to those produced by Lorenz-like systems, and the double-scroll attractor. Very few other types are also mentioned. The Chua circuit is thus a system with a great richness of dynamics but the number of topologically different attractors is not as large as sometimes claimed.

Keywords. Chaotic attractor, topological characterization, template

1 Introduction

Among the most studied chaotic attractors there are the Lorenz attractor [1], the Rössler attractor [2] and the double-scroll attractor known to be solution to the Chua circuit [3]. The best way to evidence differences between these three types of chaotic attractors is to perform a topological characterization as developed by Gilmore and co-workers [4, 5]. The first level of description of an attractor is to consider a closed surface bounding the domain of the state space containing the attractor considered [6, 7]. The genus g of this so-called bounding torus determines the $(g-1)$-components the Poincaré section is made of. Thus the Rössler attractor is bounded by a genus-1 torus [8], the Lorenz attractor by a genus-3 torus and the double-scroll attractor by a genus-5 torus [9]: these three attractors must be therefore investigated using a one-, two- and four-component Poincaré section. Since bounded by tori of different genus, these three attractors are topologically inequivalent.

The second level of description which can be used for describing the topological structure of attractors is made in terms of branched manifolds (or templates). Branched manifold was implictely used by Lorenz who computed the "isopleths" [1] and by Rössler who draw "paper models" for distinguishing normal from Möbius bands [10]. It was more explicitly defined by Williams [11] and clearly introduced as knot holder by Birman & Williams [12], the knots corresponding to the unstable periodic orbits constituting the skeleton of the attractor [13, 14]. A branched manifold is characterized by the number of branches it contains, the torsion each branch presents and their relative organization [15, 4]. From the branch manifold point of view, the spiral Rössler attractor has two branches [10, 16], the Lorenz attractor has four [17] and the double-scroll attractor, as observed in the Chua circuit, has eight [9], or more as seen below.

The third level of description is related to the first-return map to a $(g-1)$-component Poincaré section. The spiral Rössler attractor is characterized by a unimodal smooth map [16], the Lorenz attractor by a three-modal (or cubic) map with three non-differentiable critical points [18] and the double-scroll attractor by a seven-modal map with four differentiable and three non-differentiable critical points (see Fig. 2 in [9]). Differentiable critical points (between monotonous branches whose slopes are of opposite signs) are associated with folding mechanisms while non-differentiable critical points correspond to tearing mechanisms [19]. There are deep implications resulting from the differences between differentiable and non-differentiable critical points (or, equivalently, between folding and tearing mechanisms): for instance, a period-doubling cascade is necessarily associated with a differentiable critical point.

Topological characterization is therefore a very refined technique for distinguishing (classifying) chaotic attractors and it should not be claimed that a given attractor is "new" before checking that its topology is inequivalent to the topology of any other attractor [20]. The Chua circuit is known to produce various types of chaotic attractors [21]. Some authors even claimed that it can produce nearly nine hundred of different attractors, but they only showed pictures of the attractors and no topological characterization was performed [22]. Our aim is here to start from the "zoo" of attractors as described in [21] and to investigate whether these attractors are actually topologically inequivalent or not.

*M. Rosalie and C. Letellier are with Normandie Université, CORIA-UMR 6614 — CNRS-Université et INSA de Rouen Campus Universitaire du Madrillet 76800 Saint-Etienne du Rouvray, France. E-mail: martin.rosalie@coria.fr

2 The Chua circuit and the double-scroll attractor

Chaotic attractors were noted in electronic circuits by van der Pol and van der Mark in their investigations of the now so-called van der Pol equation driven by a periodic term [23]; this was later confirmed by Levinson who investigated the "bad" solutions which were qualified by Cartwright and Littlewood as being "very difficult to rule out" [24]; Levinson thus showed that some of the solutions are aperiodic (today we would have said "chaotic") [25]. In the late 1970s, few electronic circuits were identified as producing chaotic attractors (see [26] and [27] for a review). Today one of the most popular electronic circuit was proposed by Leon Chua during a stay at Waseda University (Tokyo) from October 1983 to January 1984. Chua visited Takashi Matsumoto with whom he already published few papers [28, 29, 30]. With the know-how Chua had in the use of piecewise-linear electronic elements, Chua suggested a new circuit with a piecewise-linear resistor; Chua was convinced that the use of a piecewise-linear function is convenient for realizing electronic circuits producing rich dynamics as well as facilitating analysis and programming. This is true for designing circuits, true for some type of analysis but has no deep consequence for computing. Very quickly, Matsumoto was able to produce a double-scroll attractor by using numerical integrations. Thus, the double-scroll attractor was observed in this electronic circuit on October 1983 [31], that is, at the beginning of Chua's stay at Waseda University.

We here investigated a variant of the Chua circuit in the form as [21]

$$\begin{cases} \dot{x} = \kappa\alpha(y - x - \phi) \\ \dot{y} = \kappa(x - y + z) \\ \dot{z} = -\kappa(\beta y + \gamma z) \end{cases} \tag{1}$$

with the piecewise linear function

$$\phi = bx + \frac{(a-b)(|x+1| - |x-1|)}{2}\,.$$

For certain parameter values, this system can produce a chaotic attractor now designated as the double-scroll attractor (Fig. 1a). This attractor is bounded by a genus-5 torus [9]. It is structured around three singular points, one being located at the origin of the state space $\mathbb{R}^3(x, y, z)$, the two others being located at

$$S_\pm = \left| \begin{array}{l} x_\pm = \pm 1.7333 \\ y_\pm = \pm 0.0651 \\ z_\pm = \mp 1.6682\,. \end{array} \right. \tag{2}$$

This system is equivariant under an inversion symmetry: the two singular points $S_\pm$ are thus symmetry-related. For the sake of simplicity, this attractor is investigated using a two-component Poincaré section defined as

$$\begin{array}{rl} \mathcal{P} \equiv & \left\{(y_n, z_n) \in \mathbb{R}^2 \mid x_n = +1.35, \dot{x}_n < 0\right\} \cup \\ & \left\{(y_n, z_n) \in \mathbb{R}^2 \mid x_n = -1.35, \dot{x}_n > 0\right\}\,; \end{array} \tag{3}$$

such a simplification results from the fact that the two components which should be added for characterizing this dynamics as imposed by the genus-5 bounding torus are

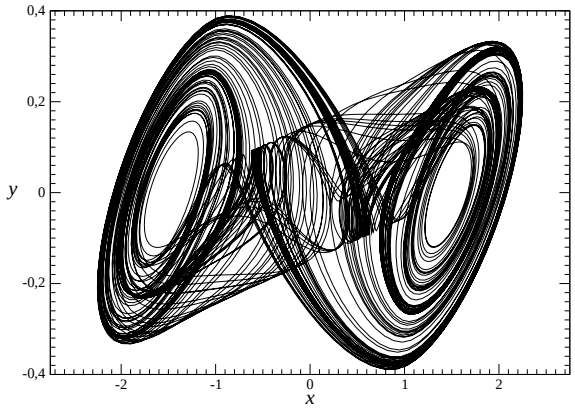

(a) Double-scroll chaotic attractor

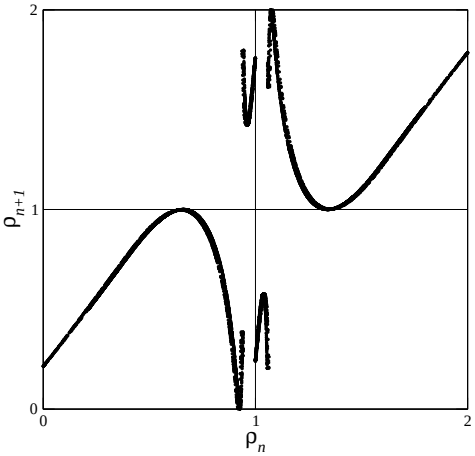

(b) First-return map

Figure 1: The double-scroll attractor solution to the Chua circuit (1). Parameter values: $\alpha = 9.3515908493$, $\beta = 14.7903198054$, $\gamma = 0.0160739649$, $a = -1.1384111956$, $b = -0.7224511209$, and $\kappa = +1$.

very complicated to define. The Poincaré section is therefore made of two components in relation to the order-2 symmetry (an inversion is an order-2 symmetry [18]) as used in [32] for the double-scroll attractor. The first-return map to the two-component Poincaré section $\mathcal{P}$ is made of ten monotonous branches (Fig. 1b). Compared to the double-scroll attractor investigated in [9], there are two additional branches (the third in the lower left panel and the first in the upper right panel). The relative organization of the eight others is equivalent to the organization of branches of the double-scroll attractor investigated in [9]. Since the template for the latter double-scroll attractor was shown to be topologically equivalent to the unimodal template proposed by Ghrist [33], the present double-scroll attractor (Fig. 1a), which is more developed, also contains all types of knots (by the means of its unstable periodic orbits).

Table 1: Parameter values used for producing the different types of attractors observed in the Chua circuit (1).

Fig.	α	β	γ	a	b	κ
2a	6.5792294	10.8976626	-0.0447440	-1.1819730	-0.6523354	+1
2b	-1.3635256	-0.0874054	-0.3114345	1.292150	-0.49717	-1
2c	-1.5590535	0.0156453	0.1374556	-0.24385532	-0.0425189	-1
2d	8.4562218	12.0732335	0.0051631	-0.7056296	-1.1467573	-1
2e	-75.6	31.25	-3.125	-2.4	-0.98	-1
2f	-4.08685	-2.0	0	-1.142837	-0.7142858	+1
2g	-5.053	-3.624135	-0.00118088	-2.501256	-0.9297201	+1
2h	143.1037	207.34198	-3.8767721	-0.855372	-1.09956	-1
2i	-1.458906	-0.0930819	-0.3214346	1.218416	-0.5128436	-1
2j	-1.5590535	0.0156453	0.1574556	-0.2438532	-0.0425189	-1
2k	3.7091002	24.0799705	-0.8592556	-2.7647222	0.1805569	+1
2l	-1.3184010	0.0125741	0.1328593	-0.2241328	-0.0281101	-1

3 A zoo of chaotic attractors

Chua and co-workers obtained various other chaotic attractors [34]. The most typical examples are shown in Figs 2 where we selected attractors which were actually different from the topological point of view, that is, discarding attractors only differing by a rotation and a rescaling which were considered as equivalent. Parameter values used for producing the retained attractors are reported in Tab. 1. For each case the most suggestive plane projection was shown according to the orientation of the attractor in the state space $\mathbb{R}^3(x, y, z)$.

The different attractors are ordered by increasing the genus of tori bounding them, thus from the simplest (Fig. 2a) to the most complicated (Fig. 2l). The simplest attractor is a genus-1 mono-folded chaotic attractor (Fig. 2a): the first-return map is thus unimodal and smooth. The attractor is therefore observed after a period-doubling cascade. It is topologically equivalent to a spiral Rössler attractor. There are in fact two coexisting attractors, one being the symmetric of the other under the inversion symmetry. The attractor shown in Fig. 2b is also observed after a period-doubling cascade but it encircles the two symmetry-related singular points $S_{\pm}$ while the previous attractor was only encircling one of them. Such differences have great implication in the attractor resulting from the merging attractor crisis encountered when one of the parameter is varied.

The third attractor (Fig. 2c) has also a symmetric companion under the inversion symmetry; it differs from the first two by the fact that it is multi-folded, being thus characterized by a first-return map with many monotonous branches as the funnel Rössler attractor [16]. We qualified this attractor as being multi-folded because there are many differentiable critical points, each of them corresponding to a folding.

The fourth and the fifth attractors are globally left invariant under the inversion symmetry. There are typically observed after a merging attractor crisis unifying two genus-1 mono-folded attractors: there are topologically equivalent. They can be viewed as the two-fold cover by an inversion symmetry of a genus-1 mono-folded attractor (like a spiral Rössler attractor): they differ from the order-2 rotation cover of a spiral Rössler attractor as produced in [35] by the fact that the two foldings are of opposite signs in the formers but of the same sign in the latter. According to [20], these two attractors cannot be considered as "new" since they are resulting from covering an attractor already identified (the spiral Rössler attractor).

The attractor shown in Fig. 2f is a genus-1 inversion cover of a two-folded attractor. This attractor looks like a Burke and Shaw attractor [36, 37]: a detailed topological characterization (see Section 4b) reveals that it has two additional branches in the first-return map compared to the attractor investigated in [37].

The attractor shown in Fig. 2g is a genus-3 inversion cover of a teared-and-folded attractor: this means that the first-return map presents differentiable and non-differentiable critical points as observed in the Lorenz system for certain parameter values (for instance, $R = 91$ as investigated in [17]). The most significant departure from the teared-and-folded attractor solution to the Lorenz system which is globally invariant under a $\mathcal{R}_z(\pi)$-rotation symmetry is that the attractor shown in Fig. 2g is invariant under an inversion symmetry. This attractor is fully characterized in Section 4c. The attractor shown in Fig. 2h is a variant of the attractor shown in Fig. 2g. This is also a genus-3 inversion cover of a teared-and-folded attractor but the monotonous branches of the first-return

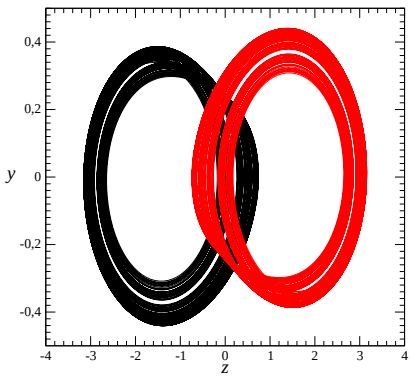

(a) Genus-1 mono-folded

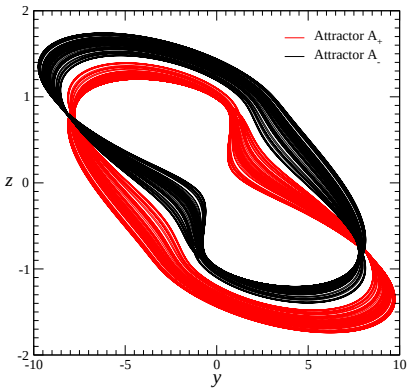

(b) Genus-1 mono-folded

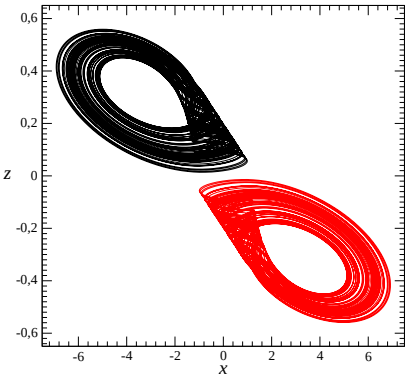

(c) Genus-1 multi-folded

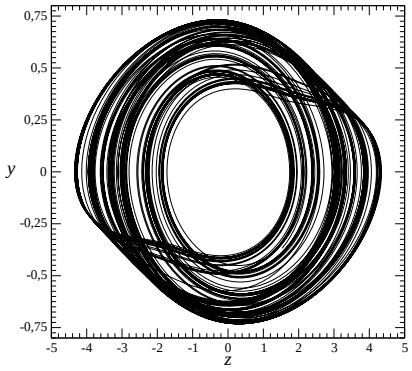

(d) Genus-1 inversion cover of a mono-folded

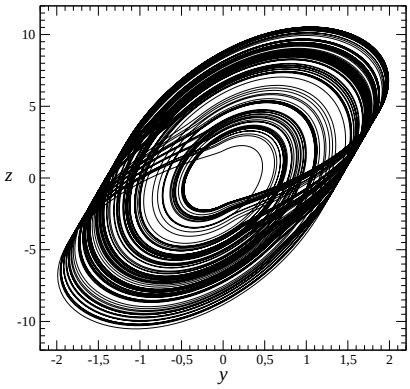

(e) Genus-1 inversion cover of a mono-folded

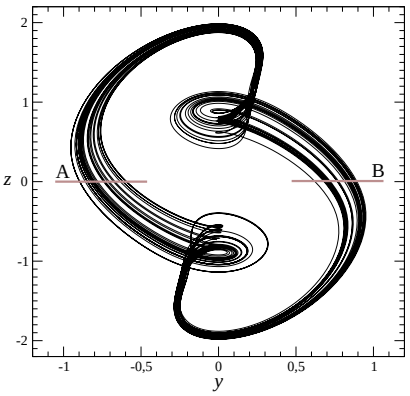

(f) Genus-3 inversion cover of a multi-folded

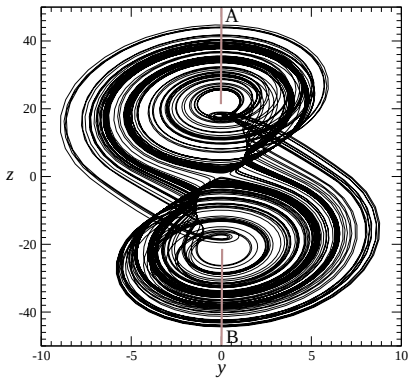

(g) Genus-3 inversion cover of a teared-and-folded

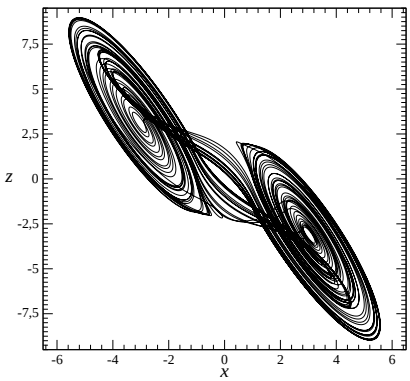

(h) Genus-3 inversion cover of a teared-and-folded

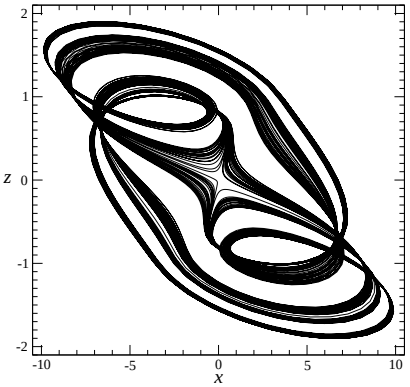

(i) Genus-3 inversion cover of a teared-and-folded

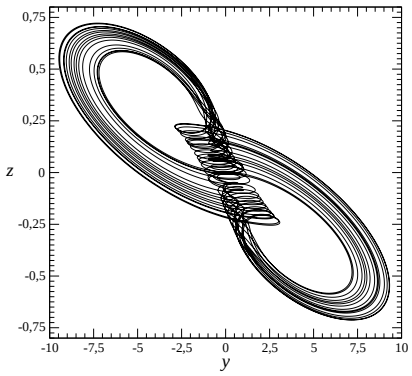

(j) Genus-5 inversion cover of a multi-folded

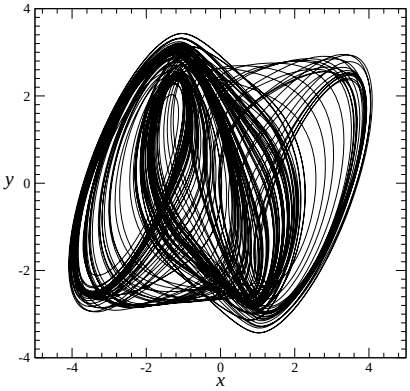

(k) Layered cylinder

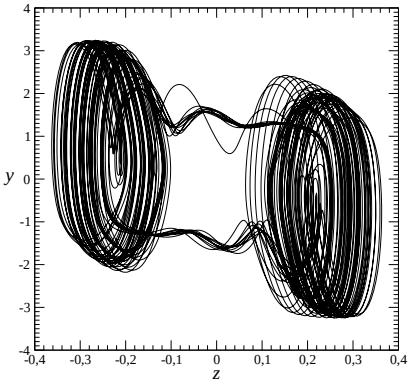

(l) "Cord" attractor

Figure 2: Zoology of chaotic attractors solution to the Chua circuit (1). Parameter values are reported in Tab. 1.

map are distributed in different manner as it will be detailed in Section 4c. The attractor shown in Fig. 2i is a "banded" version of the two previous attractors.

The attractor shown in Fig. 2j is obtained from the genus-1 multi-folded attractor (Fig. 2c) by increasing parameter γ to observe a merging attractor crisis. After such a crisis, the attractor is bounded by a genus-5 torus. It is multi-folded. If parameter γ is increased up to $\gamma = 0.165$, it becomes an attractor topologically equivalent to the genus-1 inversion cover of a multi-folded attractor as shown in Fig. 2f. This route to a Burke and Shaw attractor was never observed in Lorenz-like systems and seems to be quite specific to the Chua circuit.

The last two attractors are much more complicated to characterize because they have either a multi-foliated structure (case of the attractor shown in Fig. 2k) or a "cord" shape (Fig. 2l) as observed in [20]. A detailed topological analysis is postponed for future works. We focused our attention on cases 2b, 2f, and 2g as discussed in the next section.

4 Topological analysis of some attractors

4.1 Genus-1 mono-folded attractor

We focused our attention on case 2b for which there are two chaotic attractors co-existing in the state space. Let us designate by $\mathcal{A}_-$, the attractor resulting from initial conditions $(x_0, y_0, z_0) = (10, 6, -1)$ and $\mathcal{A}_+$ the attractor issued from initial conditions $(x_0, y_0, z_0) = (-10, -6, +1)$. These two attractors are structured around the three singular points, S_0 and

$$S_\pm = \begin{vmatrix} x_\pm = \pm 6.435 \\ y_\pm = \pm 5.025 \\ z_\pm = \mp 1.410\,. \end{vmatrix} \tag{4}$$

The singular point S_0 located at the origin of the state space $\mathbb{R}^3(x, y, z)$ is characterized by the eigenvalues

$$\Lambda_0 = \begin{vmatrix} 0.7303 \\ -4.4079 \\ -2.7592\,: \end{vmatrix} \tag{5}$$

this is a saddle point. The two symmetry-related points $S_\pm$ are associated with the eigenvalues

$$\Lambda_\pm = \begin{vmatrix} 0.1353 \pm 0.7394\,i \\ -0.2676 \end{vmatrix} \tag{6}$$

and, consequently, are saddle-foci with a two-dimensional unstable manifold.

We used the y-z plane projection of the state space where the flow is clockwise as recommended in [38]. Since bounded by a genus-1 torus, a one-component Poincaré

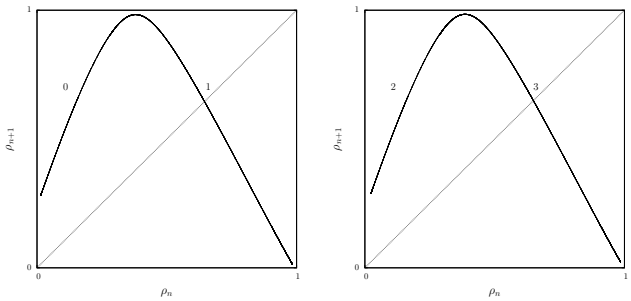

(a) For attractor $\mathcal{A}_+$ (b) For attractor $\mathcal{A}_-$

Figure 3: First-return maps to the one-component Poincaré section built on variable ρ_n for attractors $\mathcal{A}_+$ and $\mathcal{A}_-$ corresponding to case 2b. Parameter values are reported in Tab. 1.

section is required for performing the topological analysis of each attractor. The section is defined as

$$\mathcal{P}_{\mathcal{A}_+} \equiv \left\{(x_n, z_n) \in \mathbb{R}^2 \;|y_n = y_-,\; \dot{y}_n > 0\right\} \tag{7}$$

for attractor $\mathcal{A}_-$ and as

$$\mathcal{P}_{\mathcal{A}_-} \equiv \left\{(x_n, z_n) \in \mathbb{R}^2 \;|y_n = y_+,\; \dot{y}_n < 0\right\} \tag{8}$$

for attractor $\mathcal{A}_+$. As introduced in [18] and generalized in [38], a variable ρ_n is built from inside to outside of the attractor and rescaled to be in the unit interval. These first-return maps are unimodal and smooth (Figs. 3). Periodic orbits are extracted from the two attractors and linking numbers between pairs of orbits are computed and reported in Tab. 2.

Table 2: Linking numbers between pairs of periodic orbits extracted from attractors $\mathcal{A}_-$ and $\mathcal{A}_+$, respectively.

$\mathcal{A}_-$	(1)	(10)	(100)
(10)	-1		
(100)	-1	-2	
(1011)	-2	-3	-4

$\mathcal{A}_+$	(3)	(32)	(322)
(32)	1		
(322)	1	2	
(3233)	2	3	4

Linking numbers are all negative for $\mathcal{A}_-$ and all positive for $\mathcal{A}_+$. Due to the inversion symmetry, linking numbers are such as

$$\mathcal{L}(\mathcal{O}_{\mathcal{A}_-}, \mathcal{O}'_{\mathcal{A}_-}) = -\mathcal{L}(\mathcal{O}_{\mathcal{A}_+}, \mathcal{O}'_{\mathcal{A}_+}) \tag{9}$$

where $\mathcal{O}_{\mathcal{A}_-}$ ($\mathcal{O}'_{\mathcal{A}_-}$) designates an orbit from $\mathcal{A}_-$ which is the symmetric of the orbit $\mathcal{O}_{\mathcal{A}_+}$ ($\mathcal{O}'_{\mathcal{A}_+}$) from $\mathcal{A}_+$ under

the inversion symmetry. The linking matrix defining the templates of these two attractors are

$$M_{\mathcal{A}_-} = \begin{bmatrix} 0 & -1 \\ -1 & -1 \end{bmatrix} \tag{10}$$

with the natural order $0 \lhd 1$ and

$$M_{\mathcal{A}_+} = \begin{bmatrix} 0 & 0 \\ 0 & 1 \end{bmatrix} \tag{11}$$

with the natural order $2 \lhd 3$ (see [38] for details). It can be shown that $M_{\mathcal{A}_-}$ is the symmetric of $M_{\mathcal{A}_+}$ under the inversion symmetry. We checked that linking numbers reported in Tab. 2 are correctly predicted from these linking matrices using

$$\mathrm{lk}(\mathcal{O},\mathcal{O}') = \frac{1}{2}\left(\sum_{i=1}^{p}\sum_{j=1}^{p'} L(\sigma_i,\sigma_j) + N_{\text{joining}}(\mathcal{O},\mathcal{O}')\right) \tag{12}$$

as introduced by Le Sceller *et al* [39] for a period-p orbit $\mathcal{O}$ and a period-p' $\mathcal{O}'$; in this equation, σ_i represents the ith symbol of the orbital sequence of the considered orbit. Elements $M(\sigma_i,\sigma_i)$ correspond to the local torsion of the ith branch and elements $M(\sigma_i,\sigma_j)$ to the number of permutations between the ith and the jth branches [40]. Term N_{joining} designates crossings due to the insertion mechanism as introduced in [39]. These two attractors are thus topologically equivalent to the spiral Rössler attractor (modulo the sign of the folding mechanism).

4.2 Genus-1 inversion cover of a multi-folded attractor

The attractor shown in Fig. 2f is now investigated. This is a genus-1 inversion cover of a multi-folded attractor as detailed below. This attractor is structured around the origin of the state space and the two symmetry-related singular points

$$S_\pm = \begin{vmatrix} x_\pm = \mp 1.499 \\ y_\pm = 0 \\ z_\pm = \pm 1.499\,. \end{vmatrix} \tag{13}$$

These singular points are associated with the eigenvalues

$$\Lambda_0 = \begin{vmatrix} -0.966 \pm 1.553\mathrm{i} \\ 0.349 \end{vmatrix} \text{ and } \Lambda_\pm = \begin{vmatrix} 0.613 \pm 1.355\mathrm{i} \\ -1.056 \end{vmatrix}, \tag{14}$$

respectively. Point S_0 is thus a saddle-focus point with a two-dimensional stable manifold and points $S_\pm$ are saddle-focus points with a two-dimensional unstable manifold.

Attractor $\mathcal{C}$ (Fig. 2f) is bounded by a genus-1 torus and it is globally invariant under the inversion symmetry. We choose to use a two-component Poincaré section in order to take into account the symmetry property. The Poincaré section is defined as

$$\begin{aligned} \mathcal{P}_\mathcal{C} \equiv &\left\{(x_n,y_n)\in\mathbb{R}^2 \,|z_n = z_0,\ \dot{z}_n < 0\right\} \\ &\cup \left\{(x_n,z_n)\in\mathbb{R}^2 \,|z_n = z_0,\ \dot{z}_n > 0\right\}, \end{aligned} \tag{15}$$

and the first-return map is built on

$$\rho_n = \mathbb{1}_A \cdot \rho_{A,n} + \mathbb{1}_B \cdot (1 + \rho_{B,n}) \tag{16}$$

(see [40] for details). The first-return map (Fig. 4) to this Poincaré reveals the symmetric structure of the attractor.

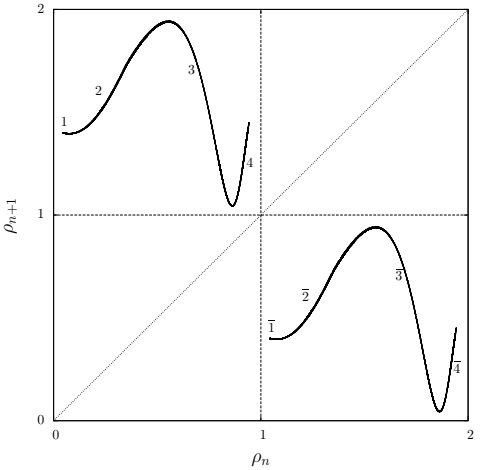

Figure 4: First-return map built on variable ρ_n for attractor $\mathcal{C}$ shown in Fig. 2f.

There are four branches for each components; they are labeled 1, 2, 3 and 4 for component A and $\overline{1}$, $\overline{2}$, $\overline{3}$ and $\overline{4}$ for component B. A branch labeled by symbol σ is the symmetric of the branch associated with symbol $\overline{\sigma}$. Any branch from component A is sent to component B, and *vice versa*: a signature of this feature is that the return map only visits the upper left and the bottom right panels (not the on-diagonal ones). The inversion symmetry implies that any oriented crossing has its symmetric with the opposite sign. Consequently, we have for instance

$$lk(4\overline{2}3\overline{2},4\overline{2}3\overline{3}) = -lk(2\overline{4}2\overline{3},3\overline{4}2\overline{3}) \tag{17}$$

where orbit $(4\overline{2}3\overline{2})$ is the symmetric of orbit $(2\overline{4}2\overline{3})$ under the inversion symmetry. Linking numbers of orbits extracted from attractor $\mathcal{C}$ are reported in Tab. 3.

As developed in [38] the foldings evidenced by the differentiable critical points of the first-return map can be grouped into two sets, each of them being associated with one of the two components of the Poincaré section. There are therefore two mixers which can be investigated independently as explained in [38]. Since one mixer is the symmetric of the other under the inversion symmetry, it is sufficient to characterize one of them, that is, to provide its linking matrix and to write the linking matrix of the symmetric mixer using the formula [38]

$$\overline{M}_L = -M_L - \begin{vmatrix} 0 & +1 & +1 & +1 \\ +1 & 0 & +1 & +1 \\ +1 & +1 & 0 & +1 \\ +1 & +1 & +1 & 0 \end{vmatrix}. \tag{18}$$

Let us start with mixer $\mathcal{M}_\mathrm{A}$ associated with component

Table 3: Linking numbers between pairs of periodic orbits extracted from attractor $\mathcal{C}$.

$\mathcal{C}$	$(3\overline{2})$	$(3\overline{3})$	$(2\overline{3})$	$(4\overline{2}3\overline{2})$	$(4\overline{2}3\overline{3})$	$(3\overline{2}3\overline{3})$	$(3\overline{3}2\overline{3})$	$(3\overline{4}2\overline{3})$
$(3\overline{3})$	0							
$(2\overline{3})$	0	0						
$(4\overline{2}3\overline{2})$	-1	0	0					
$(4\overline{2}3\overline{3})$	-1	0	0	-2				
$(3\overline{2}3\overline{3})$	-1	0	0	-2	-2			
$(3\overline{3}2\overline{3})$	0	0	1	0	0	0		
$(3\overline{4}2\overline{3})$	0	0	1	0	0	0	2	
$(2\overline{4}2\overline{3})$	0	0	1	0	0	0	2	2

A. Its linking matrix

$$M_{\mathrm{A}} = \begin{bmatrix} 1 & 0 & 0 & 1 \\ 0 & 0 & 0 & 1 \\ 0 & 0 & 1 & 1 \\ 1 & 1 & 1 & 2 \end{bmatrix} \tag{19}$$

is written between component B using the natural order $\overline{1} \lhd \overline{2} \lhd \overline{3} \lhd \overline{4}$ and component A using the natural order $1 \lhd 2 \lhd 3 \lhd 4$. Using the relationship (18), we thus obtained

$$\begin{aligned} M_{\mathrm{B}} &= -\begin{bmatrix} 1 & 0 & 0 & 1 \\ 0 & 0 & 0 & 1 \\ 0 & 0 & 1 & 1 \\ 1 & 1 & 1 & 2 \end{bmatrix} - \begin{vmatrix} 0 & +1 & +1 & +1 \\ +1 & 0 & +1 & +1 \\ +1 & +1 & 0 & +1 \\ +1 & +1 & +1 & 0 \end{vmatrix} \\ &= \begin{bmatrix} -1 & -1 & -1 & -2 \\ -1 & 0 & -1 & -2 \\ -1 & -1 & -1 & -2 \\ -2 & -2 & -2 & -2 \end{bmatrix} \end{aligned} \tag{20}$$

between component A and B. These two linking matrices determine univocally the template of attractor $\mathcal{C}$ (Fig. 6).

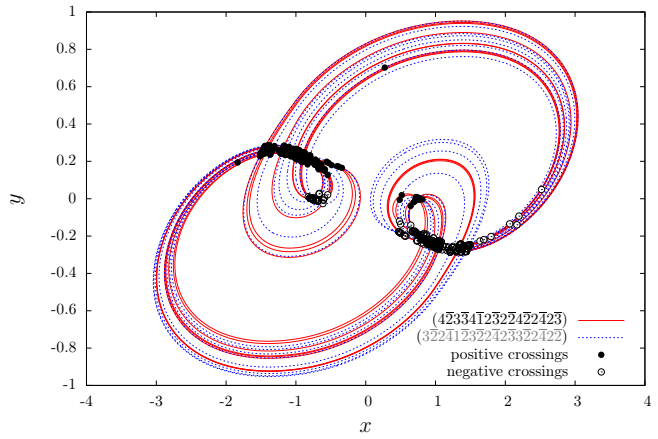

Figure 5: (Color online) Oriented crossings located in the x-y plane for computing the linking number $lk(3\overline{2}2\overline{4}1\overline{2}3\overline{2}2\overline{4}2\overline{3}3\overline{2}2\overline{4}2\overline{2}, 4\overline{2}3\overline{3}4\overline{1}2\overline{3}2\overline{2}4\overline{2}2\overline{4}2\overline{3}) = \frac{1}{2}(239 - 247) = -4$

Linking matrices M_{A} and M_{B} are validated using long periodic orbits visiting all branches as for instance with the linking number

$$\begin{aligned} &lk(3\overline{2}2\overline{4}1\overline{2}3\overline{2}2\overline{4}2\overline{3}3\overline{2}2\overline{4}2\overline{2}, 4\overline{2}3\overline{3}4\overline{1}2\overline{3}2\overline{2}4\overline{2}2\overline{4}2\overline{3}) \\ &\quad = \frac{1}{2}(-43 + N^{A}_{\text{joining}} + N^{B}_{\text{joining}}) \\ &\quad = \frac{1}{2}(-43 + 29 + 7) = -4\,. \end{aligned} \tag{21}$$

which is found to be equal to the linking number counted in a regular plane projection of these two periodic orbits (Fig. 5). Our template is thus validated.

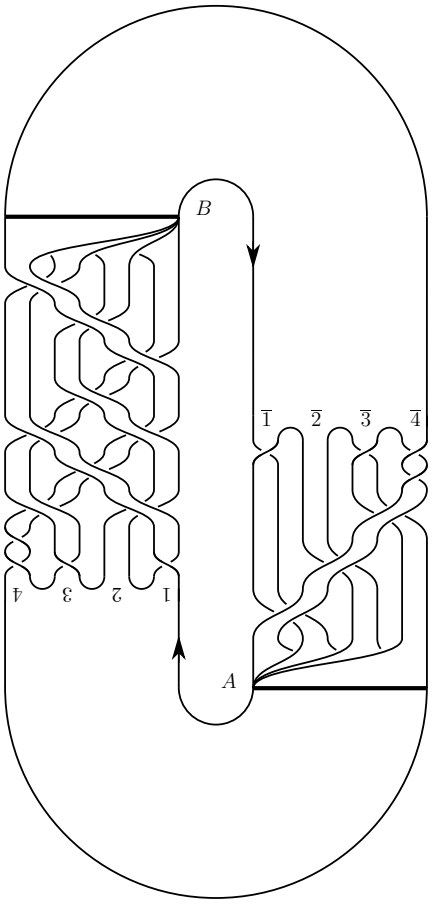

Figure 6: Template of the attractor $\mathcal{C}$.

4.3 Genus-3 inversion cover of a teared-and-folded attractor

The case of the attractor shown in Fig. 2g is now considered. This is a genus-3 inversion cover of a teared-and-folded attractor. This attractor is structured around the origin which is a saddle point according to its eigenvalues

$$\Lambda_0 = \begin{vmatrix} 1.275 \\ -2.378 \\ -6.581 \end{vmatrix} \tag{22}$$

and the two symmetry-related singular points

$$S_\pm = \begin{vmatrix} x_\pm = \mp 22.465 \\ y_\pm = 0.007 \\ z_\pm = \pm 22.465 \end{vmatrix} \tag{23}$$

whose eigenvalues are

$$\Lambda_\pm = \begin{vmatrix} 0.150 \pm 1.155\mathrm{i} \\ -1.056 \end{vmatrix}, \tag{24}$$

and which correspond to saddle-focus points with a two-dimensional unstable manifold. Compared to the previous attractor, this one visits the neighborhood of the origin directly responsible for the tearing mechanism. As observed in the Lorenz system for which genus-1 inversion cover of a folded attractor is observed around the z-axis with a transverse stability of a focus type and a genus-3 inversion cover of a teared-and-folded attractor is observed around the z-axis with a transverse stability partly of a focus type and partly of a saddle type, the Chua circuit presents various types of attractors depending on the type of the singular point S_0 located at the origin of the state space.

This genus-3 attractor is investigated using the Poincaré section defined according to

$$\begin{aligned} \mathcal{P}_\mathcal{C} \equiv & \left\{ (x_n, z_n) \in \mathbb{R}^2 \ | y_n = y_+, \ \dot{y}_n < 0, \ z_n > z_+ \right\} \\ & \cup \left\{ (x_n, z_n) \in \mathbb{R}^2 \ | y_n = y_-, \ \dot{y}_n > 0, \ z_n < z_- \right\}. \end{aligned} \tag{25}$$

A first-return map to this Poincaré section (Fig. 7a) reveals a teared-and-folded structure since differentiable and non-differentiable critical points are observed. Monotonous branches inserted in component A are labeled 0, 1, 5 and 6, and those inserted in component B are labeled $\overline{0}$, $\overline{1}$, $\overline{5}$ and $\overline{6}$. Contrary to what was observed in attractor $\mathcal{C}$, there are some branches which are reinjected in the component from which they are issued: this is the case of branch 0 and 1 ($\overline{0}$ and $\overline{1}$) which connect component A (B) to itself; the others transit from one component to the other.

Several linking numbers were computed between orbits extracted from attractor $\mathcal{D}$; all of them are equal to zero. As attractor $\mathcal{C}$, attractor $\mathcal{D}$ is made of two mixers, one being the symmetric of the other. There are described by

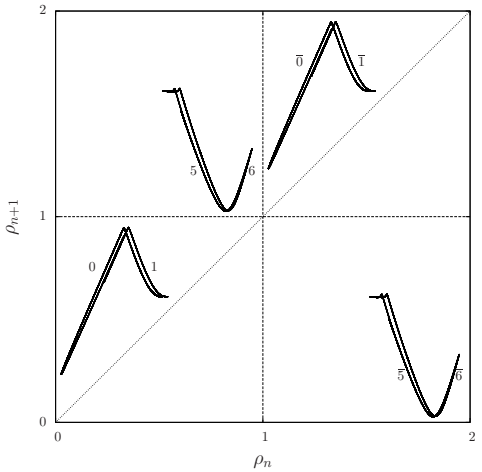

(a) From the attractor shown in Fig. 2g

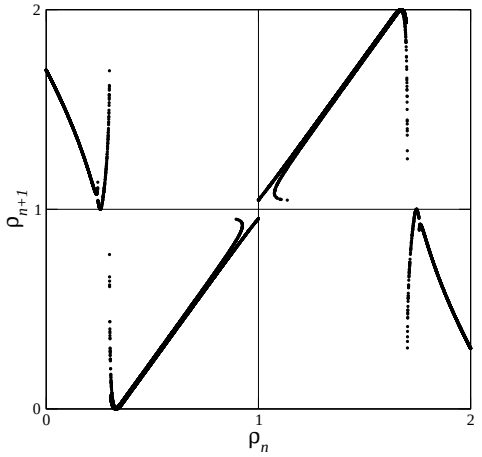

(b) From the attractor shown in Fig. 2h

Figure 7: First-return maps built on variable ρ_n for two genus-3 inversion covers of a teared-and-folded attractor.

the linking matrix

$$M_\mathrm{A} = \begin{bmatrix} 0 & -1 & 0 & 0 \\ -1 & -1 & 0 & 0 \\ 0 & 0 & 1 & 0 \\ 0 & 0 & 0 & 0 \end{bmatrix} \tag{26}$$

between the natural orders $0 \lhd 1 \lhd \overline{5} \lhd \overline{6}$ and $0 \lhd 1 \lhd 5 \lhd 6$, and the linking matrix

$$M_\mathrm{B} = \begin{bmatrix} 0 & 0 & -1 & -1 \\ 0 & 1 & -1 & -1 \\ -1 & -1 & -1 & -1 \\ -1 & -1 & -1 & 0 \end{bmatrix} \tag{27}$$

between $\overline{0} \lhd \overline{1} \lhd 5 \lhd 6$ and $\overline{0} \lhd \overline{1} \lhd \overline{5} \lhd \overline{6}$, respectively. It can be checked that M_A is the symmetric of M_B using the formula (18). As an example, the linking number

$$\begin{aligned} & lk(15\overline{05}5\overline{15}, 015\overline{15}) \\ & = \frac{1}{2}(-5 + N^A_\mathrm{joining} + N^B_\mathrm{joining}) \\ & = \frac{1}{2}(-5 + 5 + 0) = 0 \end{aligned} \tag{28}$$

predicted by the template (determined by these two linking matrices and drawn in Fig. 8) is equal to the linking number counted in a regular plane projection. Attractor $\mathcal{D}$ is thus topologically equivalent to teared-and-folded attractors observed in the Lorenz-like systems [41].

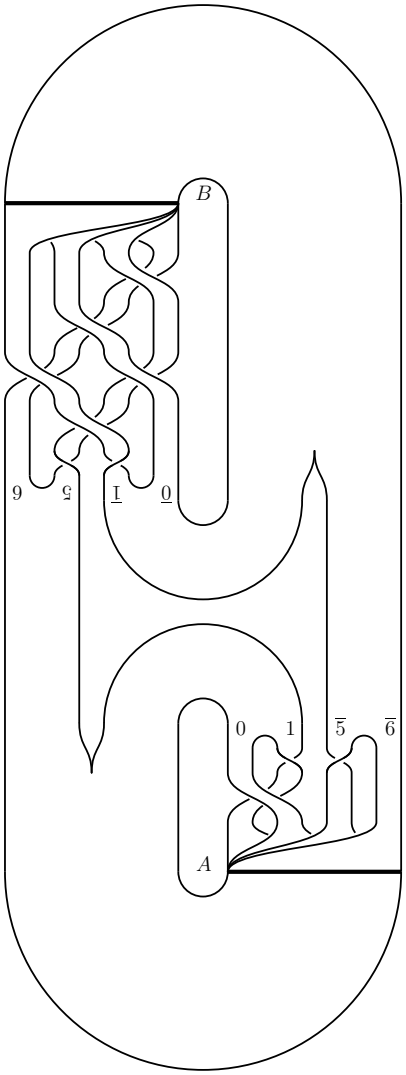

Figure 8: Template of attractor $\mathcal{D}$.

5 Conclusion

The Chua circuit produces various types of attractors including those produced by Rössler-like systems (spiral and funnel attractors, here designated as genus-one mono-folded and genus-one multi-folded attractors) and by Lorenz-like systems with the difference that the symmetry involved is an inversion symmetry rather than a rotation symmetry. Thus, genus-3 inversion cover of teared-and-folded attractors are observed (the corresponding attractors in Lorenz-like systems are genus-3 order-2 rotation cover of teared-and-folded attractors). In addition to these two classes of attractors, there are the double-scroll attractors bounded by genus-5 tori. Double-scroll attractors seem to require an inversion symmetry to be produced. We left for future works two attractors whose structures were, to the best of our knowledge, never observed in other systems. The Chua circuit can therefore produce a large set of topologically inequivalent chaotic attractors but the number of different attractors is far less than nine hundreds...

Acknowledgements

This work was stimulated by master projects performed by Marion Bliard, Emeline Fresnel, Sabrina Liénafa, Céline Marré, Léa Moreau, and Louise Viger.

References

[1] E. N. Lorenz, "Deterministic nonperiodic flow," *Journal of the Atmospheric Sciences*, vol. 20, pp. 130-141, 1963.

[2] O. E. Rössler, "An equation for continuous chaos," *Physics Letters A*, vol. 57, pp. 397-398, 1976.

[3] T. Matsumoto, L. O. Chua & M. Komuro, "The Double Scroll," *IEEE Transactions on Circuits and Systems*, vol. 32, pp. 798-818 (1985).

[4] R. Gilmore, "Topological analysis of chaotic dynamical systems," *Reviews of Modern Physics*, vol. 70, 1455-1529, 1998.

[5] R. Gilmore & M. Lefranc, *The topology of chaos*, Wiley, 2002.

[6] T. D. Tsankov & R. Gilmore, "Strange attractors are classified by bounding tori," *Physical Review Letters*, vol. 91, pp. 134104, 2003.

[7] T. D. Tsankov & R. Gilmore, "Topological aspects of the structure of chaotic attractors in $\mathbb{R}^3$," *Physical Review E*, vol. 69, pp. 056206, 2004.

[8] C. Letellier, E. Roulin & O. E. Rssler, "Inequivalent topologies of chaos in simple equations," *Chaos, Solitons & Fractals*, vol. 28, 337-360, 2006.

[9] C. Letellier & R. Gilmore, "The universal template is a subtemplate of the double-scroll template," *Journal of Physics A*, vol. 46, 065102, 2013.

[10] O. E. Rössler, "Chaotic behavior in simple reaction system," *Zeitschrift für Naturforschung A*, vol. 31, pp. 259-264, 1976.

[11] R. Williams, "The Lorenz Attractor," *Lecture Notes in Mathematics*, vol. 615, pp. 94-112, 1977.

[12] J. S. Birman & R. F. Williams, "Knotted periodic orbits in dynamical systems I: Lorenz's equations," *Topology*, vol. 22, pp. 47-82, 1983.

[13] H. Poincaré, "Sur le problème des trois corps et les équations de la dynamique, " *Acta Mathematica*, vol. 13, pp. 1-270, 1890.

[14] D. Auerbach, C. Cvitanović, J.-P. Eckmann, G. Gunaratne & I. Procaccia, "Exploring chaotic motion through periodic orbits," *Physical Review Letters*, vol. 58, pp. 2387-2389, 1987.

[15] G. B. Mindlin & R. Gilmore, "Topological analysis and synthesis of chaotic time series," *Physica D*, vol. 58, pp. 229-242, 1992.

[16] C. Letellier, P. Dutertre & B. Maheu, "Unstable periodic orbits and templates of the Rössler system: toward a systematic topological characterization," *Chaos*, vol. 5, pp. 271-282, 1995.

[17] C. Letellier, P. Dutertre & G. Gouesbet, "Characterization of the Lorenz system taking into account the equivariance of the vector field," *Physical Review E*, vol. 49, pp. 3492-3495, 1994.

[18] R. Gilmore & C. Letellier, *The symmetry of chaos*, Oxford University Press, 2007.

[19] G. Byrne, R. Gilmore & C. Letellier, "Distinguishing between folding and tearing mechanisms in strange attractors," *Physical Review E*, vol. 70, 056214, 2004.

[20] C. Letellier & L. A. Aguirre, "Required criteria for recognizing new types of chaos: Application to the "cord" attractor," *Physical Review E*, vol. 85, 036204, 2012.

[21] L. Chua, K. Komuro & T. Matsumoto, "A universal circuit for studying and generating chaos – Part II: Strange attractor," *IEEE Transactions on circuit and systems*, vol. 40, pp. 745-761, 1993.

[22] E. Bilotta & P. Pantano, *A gallery of Chua attractors*, World Scientific Publishing, 2008.

[23] B. van der Pol & J. van der Mark, "Frequency demultiplication, " *Nature*, vol. 120, pp. 363-364, 1927.

[24] M. L. Cartwright & J. E. Littlewood, "On non-linear differential equations of the second order: I The equation $y - k(l - y^2)\dot{y} + y = b\lambda k\cos(\lambda t + a)$, k large," *Journal of the London Mathematical Society*, vol. s1-20, pp. 180-189, 1945.

[25] N. Levinson, "Second-order differential equation with singular solutions, " *The Annals of Mathematics*, II, vol. 50, pp. 127-153, 1949.

[26] C. Letellier & J.-M. Ginoux, "Development of the nonlinear dynamical systems theory from radio engineering to electronics," *International Journal of Bifurcation & Chaos*, vol. 19, pp. 2131-2163, 2009.

[27] C. Letellier, "Chaos in electronic circuits: Chua's contribution (1980-2000)," *Chaos, CNN, Memristors and Beyond: A Festschrift for Leon Chua*, World Scientific Publishing, pp. 211-235, 2013.

[28] L. 0. Chua, "Dynamic Nonlinear Networks: State-of-the-Art," *IEEE Transactions on Circuit and Systems*, vol. 27, pp. 1059-1087, 1980.

[29] T. Matsumoto, L. O. Chua, H. Kawakami & S. Ichiraku, "Geometric-properties of dynamic non-linear networks — Transversality, local-solvability and eventual passivity," *IEEE Transactions on Circuits & Systems*, vol. 28, pp. 406-428, 1981.

[30] T. Matsumoto, G. Ikegami & L. O. Chua, "Strong structural stability of resistive nonlinear n-ports," *IEEE Transactions on Circuits & Systems*, vol. 30, pp. 197-222, 1983.

[31] T. Matsumoto, "A Chaotic Attractor from Chua's Circuit," *IEEE Transactions on Circuits and Systems*, vol. 31, pp. 1055-1058, 1984.

[32] C. Letellier, G. Gouesbet & N. Rulkov, "Topological analysis of chaos in equivariant electronic circuits," *International Journal of Bifurcation & Chaos*, vol. 6, pp. 2531-2555, 1996.

[33] R. W. Ghrist, "Branched two-manifolds supporting all links," *Topology*, vol. 36, pp. 423-448, 1997.

[34] L. 0. Chua, M. Komuro & T. Matsumoto, "A Universal Circuit for Studying and Generating Chaos — Part II: Strange Attractors," *IEEE Transactions on Circuit and Systems*, vol. 40, pp. 745-761, 1993.

[35] C. Letellier & R. Gilmore, "Covering dynamical systems: Two-fold covers," *Physical Review E*, vol. 63, n^o 16206, 2001.

[36] R. Shaw, "Strange attractor, chaotic behavior and information flow," *Zeitschrift für Naturforschung A*, vol. 36, 80-112, 1981.

[37] C. Letellier, P. Dutertre, J. Reizner & G. Gouesbet, "Evolution of multimodal map induced by an equivariant vector field," *Journal of Physics A*, vol. 29, pp. 5359-5373, 1996.

[38] M. Rosalie & C. Letellier, "Systematic template extraction from chaotic attractors : I. Genus-one attractors with an inversion symmetry," *Journal of Physics A*, vol. 46, n^o 375101, 2013.

[39] L. Le Sceller, C. Letellier & G. Gouesbet, "Algebraic evaluation of linking numbers of unstable periodic orbits in chaotic attractors," *Physical Review E*, vol. 49, pp. 4693-4695, 1994.

[40] M. Rosalie & C. Letellier, "Toward a general procedure for extracting templates from chaotic attractors bounded by high genus torus," *International Journal of Bifurcation and Chaos*, vol. 24, n^o 1450045, 2014.

[41] C. Letellier, G. F. V. Amaral & L. A. Aguirre "Insights into the algebraic structure of Lorenz-like systems using feedback circuit analysis and piecewise affine models," *Chaos*, vol. 17, n^o 023104, 2007.

Satellite Workshop 12
Slow-fast dynamics: theory and application

Satellite Workshop 12
Slow-fast dynamics: theory and application

Organizers

- Nikola Popovic (University of Edinburgh, United Kingdom), Nikola.Popovic@ed.ac.uk

Description

Mathematical models in which processes occur on multiple (spatial or temporal) scales are ubiquitous in the physical and biological sciences, and are known to give rise to complex and frequently unexpected dynamics; examples include mixed-mode oscillatory firing in the brain, protein synthesis in bursts during gene expression, and spontaneous wave generation in the Earth's atmosphere, among many others. The underlying models are oftentimes formulated in terms of nonlinear slow-fast differential equations. While their study can hence rely on analytical, asymptotic, and computational techniques from the well-developed theory of dynamical systems, many challenges remain. In this session, we will report on recent progress in the theory and application of slow-fast dynamics, and we will provide a forum for the discussion of current trends, questions, and opinions in the field.

List of papers/presentations

B. Ambrosio (University of Le Havre, France)
Weakly coupled two slow-two fast systems, folded singularities and mixed mode oscillations
Abstract: In this talk, we will focus on the emergence of Mixed Mode Oscillations (MMOs) in systems of two weakly coupled slow/fast oscillators. We will particularly study the existence and properties of a folded singularity called FSN II that allows the emergence of MMOs in the presence of a suitable global return mechanism. After a background on the 3d case, we will present how the theory can be extented to some 4d systems. As FSN II corresponds to a transcritical bifurcation for a desingularized reduced system, we prove that, under certain non-degeneracy conditions, such a transcritical bifurcation exists. We then apply this result to the case of two coupled systems of FitzHugh-Nagumo type. This leads to a non trivial condition on the coupling that enables the existence of MMOs.
(Joint work with M. Krupa and M.A. Aziz-Alaoui.)

E. Benoit (University of la Rochelle, France)
Slow fast vector fields of dimension 2+2
Abstract: The slow fast vector fields are now well known in dimension 1+1 (van der Pol equation is the typical example). The canards are generic in one-parameter family. In dimension 2+1 the folded nodes are the most interesting points. In dimension 2+1 it is the delayed Hopf bifurcation. I will present a complete classification of the generic points in dimension 2+2. Some points give canards as in pseudo-singular points of dimension 3, others give delayed Hopf bifurcation, and some problems appear when these two problems occur simultaneously. I will present a method to visualize the

trajectories of such systems in R4. The method gives a new point of view for the system of two coupled van der Pol equations.

S. Fernandez-Garcia (INRIA Paris-Rocquencourt, France)
Canards in planar piecewise linear systems
Abstract: Piecewise linear (PWL) systems are well-known to model faithfully, inter alia, the behavior of electronic circuits. Also, they are proven to reproduce all aspects of nonlinear dynamics and they can even show new behaviors, impossible to obtain under differentiability hypothesis. The fact that one has access to explicit solutions in every linearity zone offers, in principle, better mathematical tractability than their smooth counterpart. However, the lack of differentiability of the system in separations between linearity zones prevents us to obtain a general solution and the classical theory of differential systems cannot be applied. This forces to tacklePWL systems in a different way.PWL systems have also been used to model biological systems, given thatelectronic circuits provide a first approach of the behavior of neurons. Moreover, the existence of canards in smooth models of neurons has been largely investigated.In this talk, we analyze the existence and stablity of canards in a class ofplanar PWL slow-fast systems with three zones, using a singular perturbationtheory approach. Similarities and differences between this non-smooth case and the smooth one are highlighted.
(Joint work with M. Desroches, M. Krupa and A.E. Teruel.)

J.M. Ginoux (University of Toulon, France)
Canards Existence in R^2+2
Abstract: In a previous paper we have proposed a new method for proving the existence of "canard solutions" for three and four-dimensional singularly perturbed systems with only one fast variable. The aim of this work is to extend this method to the case of four-dimensional singularly perturbed systems with two slow and two fast variables. Contrary to previous works, this method does not require a center manifold reduction nor a blow-up technique i.e. a desingularization procedure for pseudo singular points but uses the normalized slow dynamics and not the projection of the desingularized vector field. This method enables to state a unique generic condition for the existence of "canard solutions" for such four-dimensional singularly perturbed systems which is based on the stability of pseudo singular points of the normalized slow dynamics and not of the projection of the desingularized vector field. Applications of this method to the famous coupled FitzHugh-Nagumo equations and to the Hodgkin-Huxley model will enable to prove as many previous works the existence of "canard solutions" in such system.

I. Kosiuk (Max Planck Institute for Mathematics in the Sciences, Leipzig, Germany)
Mathematical analysis of complex networks of protein interactions
Abstract: Understanding the process of cell division is a central issue in cell biology. A molecular description and the basic mechanisms of the cell cycle oscillator have been defined through experiments over the past three decades. Due to the complexity of the process, mathematical modelling and simulation are commonly used to gain better understanding of the functioning and dynamics of the cell cycle.In this talk I will present a geometric analysis of a minimal model developed by A. Goldbeter describing the embryonic cell division cycle. It is known from numerical simulations that for certain parameter values and Michaelis constants small in the model interesting oscillatory behaviour emerges. Our geometric analysis provides the explanation and full

understanding of the mathematical mechanisms leading to the oscillatory behaviour of proteins related to mitosis of the cell division cycle. I will demonstrate that geometric singular perturbation theory and geometric desingularization based on the blow-up method are well-suited for the analysis of this and related problems.

E. Kutafina (Hasselt University, Belgium)
Complex periodic oscillation patterns in a prototypical three time scale model
Abstract: We consider a simple prototypical three-dimensional model with a folded singularity of saddle-node type and return mechanism. Additionally this model has a three different time scales. We extend the known case with the scales (1,\epsilon,\epsilon^2) to more general (1,\epsilon,\epsilon^\alpha) and show that a change of time scales rates may essentially influence the behavior of periodic solutions. We will present some numerical results on the mixed mode oscillations with SAOs based on two different mechanisms – sector and delayed Hopf bifurcation.
(Joint work with N. Popovic and P. De Maesschalck.)

A. Kuznetsov (Indiana University Purdue University Indianapolis, U.S.A.)
Can a delay differential equation produce relaxation oscillations?
Abstract: One application of delay differential equations (DDEs) is modeling of oscillations in genetic regulatory networks. The delay simplifies modeling because it replaces many unknown reaction steps in the feedback loop that sustains oscillations. However, mathematical analysis of DDEs is difficult because they are infinitely-dimensional by construction and cannot be analyzed by methods common for finite systems of ordinary differential equations (ODEs). We simulate dynamics in a single delay differential equation and find that the oscillations remain periodic for growing delay if the equation includes only monotonic functions of the variable. Under this condition, we reduce the DDE to a three-dimensional system of ODEs. The resulting system is equivalent to a standard relaxation oscillator. We discuss implications of the similarity of the delay-induced oscillations and hysteresis-based relaxation oscillations.

J. Starke (Technical University of Denmark, Copenhagen)
Analysis of particle models by implicit equation-free methods
Abstract: An implicit method for equation-free analysis of slow-fast systems is presented and applied to analyze particle models. It can be shown, that the implicitly defined coarse-level time stepper converges to the true dynamics on the slow manifold. The method is applied to perform a coarse bifurcation analysis of a microscopic particle model describing car traffic on single lane highways. The standard deviation is chosen as a macroscopic measure to investigate traveling wave solutions (traffic jam waves) and is continued on the macroscopic level in the equation-free setup. The collapse of the traffic jam to the free flow solution corresponds in the relevant parameter region at the macroscopic level to a saddle-node bifurcation of the traveling wave. We continue this bifurcation point in two parameters using equation-free analysis. An extension to particle models in two space dimensions leads to pedestrian models. We consider situations where the pedestrian flow shows the emergence of an oscillatory pattern for two crowds passing a narrow door in opposite directions. The oscillatory solutions appear due to a Hopf bifurcation. This is detected numerically by an equation-free continuation of a stationary state of the system. Furthermore, an equation-free two-parameter continuation of the Hopf point has been performed to investigate the

oscillatory behaviour in detail using the door width and ratio of velocities of the two pedestrian crowds as parameters.
(Joint work with R. Berkemer, O. Corradi, P. Hjorth, A. Kawamoto, C. Marschler and J. Sieber.)

F. Veerman (University of Oxford, United Kingdom)
Pulse patterns in singularly perturbed reaction-diffusion systems
Abstract: Using geometric singular perturbation theory, we construct homoclinic pulse solutions in a general class of singularly perturbed reaction-diffusion systems. Using the same techniques, we extend the construction to incorporate periodic pulse patterns. The stability of the both homoclinic pulses and pulse patterns is analysed using Evans function techniques. Again, the slow-fast structure of the stationary patterns plays a crucial role, and allows us to obtain explicit expressions for the Evans function. The general context in which these techniques are applied leads to new, previously unobserved phenomena.

N. Popovic (University of Edinburgh, United Kingdom)
A geometric analysis of fast-slow models for stochastic gene expression
Abstract: Stochastic models for gene expression frequently exhibit dynamics on different time-scales. One potential scale separation is due to significant differences in the lifetimes of mRNA and the protein it synthesises, which allows for the application of perturbation techniques. Here, we develop a dynamical systems framework for the analysis of a family of "fast-slow" models for gene expression that is based on geometric singular perturbation theory. We illustrate our approach by giving a complete characterisation of a standard two-stage model which assumes transcription, translation, and degradation to be birth-and-death processes of first order. In particular, we develop a systematic expansion procedure for the resulting propagator probabilities that can in principle be taken to any order in the perturbation parameter. Finally, we verify our asymptotics by numerical simulation, and we explore its practical applicability, as well as the effects of a variation in the system parameters and the scale separation.
(Joint work with C. Marr and P.S. Swain.)

Additional Paper

Proceedings of ICCSA 2014
Normandie University, Le Havre, France - June 23-26, 2014

LOGISTICS OPTIMIZATION USING ONTOLOGIES

Hayder I. Hendi, Adeel Ahmad, Mourad Bouneffa, and Cyril Fonlupt *†

Abstract. Logistics processes involve complex physical flows and integration of different elements. It is widely observed that the uncontrolled processes can decline the state of logistics. The optimization of logistic processes can support the desired growth and consistent continuity of logistics. In this paper, we present a software framework for logistic processes optimization. It primarily defines logistic ontologies and then optimize them. It intends to assist the design of a computational knowledge-base tool for better utilisation of the logistic resources. The defined ontologies share the knowledge domain of logistics and optimization. The knowledge-base incorporates the standard optimization techniques, along with the definition of ontologies to resolve logistic problems. It can help to better understand the inherent complexities of logistic problems.
Keywords. Logistics, Ontologies, Classification of logistic problems, Optimization methods, Protégé

1 Introduction

The logistics connect vast amounts of events, activities, and actors. The involved complexity can generate difficult situations to be analyzed for process improvement [Rushton et al., 2014]. We believe ontologies can help in this matter. It potentially contributed in solving integration problems in information systems [Kayikci and Zsifkovits, 2013]. It can extend the research work for the harmonization of heterogeneous information and resources for knowledge discovery [Fensel, 2001, Kalfoglou and Schorlemmer, 2003]. Many individual ontologies have been adapted for logistics [Anand et al., 2012, Moussas et al., 2013]. Ontologies in logistics are mostly focused on supply chain management, and often, these didn't consider the complex logistic problems, like the logistic optimization [Leukel and Kirn, 2008]. However, the current logistic ontologies have not yet achieved a consensual acceptance and maturity.

In this paper, we define and specialize logistic ontologies for optimization purpose. These are further extended to cope with the logistic problems, encountered due to the heterogeneity of involved elements. It assists the end users, in this case the developers, in exchanging semantic information to share the domain knowledge and the instance knowledge for optimization. It requires, formerly, to investigate the optimization related knowledge and artifacts, while laterly, to establish common vocabularies, nomenclatures, and taxonomies, among them. An artifact, in our study, represents an activity, event, actor, resource,or any document that can influence the other related elements. A relation is a dependence transient that signifies the strength of influence among involved elements, although it evaluates the nature of dependence. We further define the interoperability, integration, and reuse of artifacts, and their optimization with the help of ontologies. It may support the development of algorithms, models, libraries, and simulation tools to minimize the logistics problems.

The rest of the paper is organized as follows; In the section 2, we discuss the context of our approach. The section 3 provides a brief overview of the ontology based approach. The section 4 presents a detailed analysis of logistics ontologies. In section 5, we describe optimization problems which basically exploits the concerned logistic problem. We discuss in detail, the design of optimization ontologies, in section 6. The section 7, provides a brief note on application of defined ontologies, along with an insight on their implementation. Later, in section 8, we conclude the contents of this paper.

2 Related work

In the literature, we find numerous work regarding logistic ontologies. The authors, in [Leukel and Kirn, 2008], propose an approach, regarding the supply-chain management. They devise the core elements of logistic ontologies where the top level ontologies are *process* class having the subclasses *plan*, *source*, *make*, *deliver*, *return*, and the *metrics*. We also find the ontologies defined in [Scheuermann and Hoxha, 2012, Hoxha et al., 2010], where the authors presents an approach to achieve flexibility and decentralization in supply chain configuration and management. They define the top level ontologies for *process*, *service*, *resource*, and *service level parameter*. The logistics resource concept is further specialized into more specific concepts. The *transportation mean*, *warehouse* and *human resources* are derived as the subclasses. Logistics KPI are specialized, among others, into

*Université Lille Nord de France, Laboratoire d'Informatique Signal et Image de la Côte d'Opale, 50, rue Ferdinand Buisson BP 719 62228 Calais Cedex France. E-mails: {hendi, ahmad, bouneffa, fonlupt}@lisic.univ-littoral.fr
†Manuscript received May 21, 2014; revised Month DD, YYYY.

sub concepts of Delivery Flexibility and Delivery Reliability. These are in general insufficient to address the logistic issues.

The currently available optimization ontologies focus on the problem field (e.g. design, simulation, and modeling) and they include an optimization part for the solution [Miller et al., 2004]. SoPT [Han et al., 2011], ONTOP [Witherell et al., 2006] and GOO [Moussas et al., 2013] are the closest to our work. General Optimization Ontology (GOO) is designed and structured with the main focus on the optimization. The authors developed the basic concepts common to all optimization problems that are required by the core part of the ontology. The first aim has been to support automatic selection of the appropriate optimization tool for a given optimization problem. ONTOP (Ontology for Optimization) has been developed to facilitate engineering problems. The preliminary work began with the development of a Finite Element Model (FEM) knowledge-capturing tool. ONTOP's structure provides the means to identify feasible optimization techniques, for a given design optimization problem. Likewise, SoPT, the ontology for Simulation OPTimization includes concepts from both conventional/mathematical programming and simulation optimization. SoPT aims to describe simulation optimization methods and help detect the correct tool for each specific case. It facilitates component reuse, especially in systems where simulators and optimizers are loosely-coupled.

To create flexible optimization ontologies, it is necessary to decompose it in two parts, the core or common part of and the domain or application specific part of the ontologies. The major goal of the optimization ontology remains to provide a formalization of a generic design improvement cycle so that the iterative nature of the product design process can be effectively captured and described for both human and simulation workflows.

3 Architecture of logistics ontologies framework

Although, we restrain our focus on the conceptualization of logistic ontologies but the main objective of this research work remains to develop a software suite to better exploit the logistic resources. It is therefore, we first define the logistic ontologies and later on, the optimization ontologies, to simplify the task. The global architecture of our framework is shown in the figure 1. It attempts to develop an environment that receives the user queries through an interface of query search engine. Which then exploits our knowledge-base with the help of generalized rules. The rules actually represents the generalized dependencies among different related elements of the system in consideration. The knowledge-base contains the facts in form of logistic and optimization ontologies, which are subsequently integrated with software suite ontologies, as per user requirements.

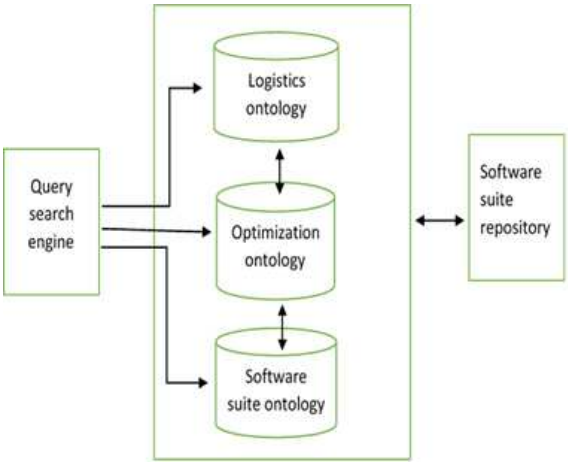

Figure 1: Global architecture of logistics ontologies framework

4 Logistics ontologies

The objective of the logistics ontologies is to capture the essence of the logistic domain. Typically, it contains the concepts, relations, axioms, individuals and assertions. The proposed logistic ontologies define the top level classes as "*process*, *service*, *resource*, *performance*, *supply chain*, *activity*, and *logistic problem*", as shown in figure 2. These are further extended into subsidiary classes e.g. logistic process is a sub-class of process and supply-chain. Likewise, the logistic service is a sub-class of service and vice-versa.

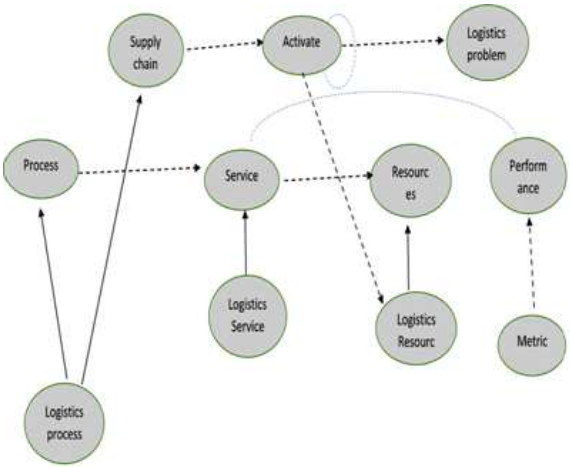

Figure 2: Top level ontologies for logistics

5 Logistics optimization problems

The logistic systems have many resources that provide services for customers and suppliers. It essentially requires optimization methods for resource management and services provision, in order to perform activities in

an optimized way; respecting the minimum cost and time. Among others, the major logistic problems can be categorized as transport problem and airline schedule problem. These further integrates the resource management problems, such as supply-chain management and people management, etc. Similarly, we classify the logistics optimization problems into three major categories depending on the type of problem, which are [Onsel, 2009] :

- Supply-chain management problems
- Airline optimizations problems
- People management problems

As summarised in figure 3, the supply-chain management problems are, in general, the aggravations of issues arising from transportation, location, and inventory management. Whereas the airline optimization problems are mostly contributed from the issues arising from revenue, schedule planning, and aircraft load planning.

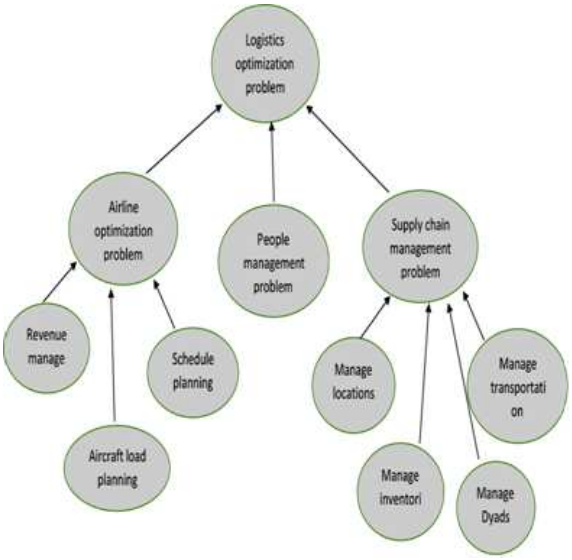

Figure 3: Classification of logistic optimization problems

6 Conceptualization of optimization ontologies

The core optimization ontologies must include the definitions for typical optimization problems along with the descriptions of the methods applied to solve an optimization task. The basic structure of these ontologies should support optimization processes. It should also focus on how to select and apply a suitable solution for the encountered optimization problem. It reflects that the ontology classes must eventually cover all entities that concur in an optimization task. Accordingly, we categorise optimization as follows :

- optimization problem model
- optimization method model
- optimization component

The figure 4 explains dependencies among the top level optimization ontologies. The *Optimization* class basically extended by the *optimization component*, *optimization problem*, and *optimization method* classes, whereas the *logistic problem* class is addressed by *optimization method* class, in this regard.

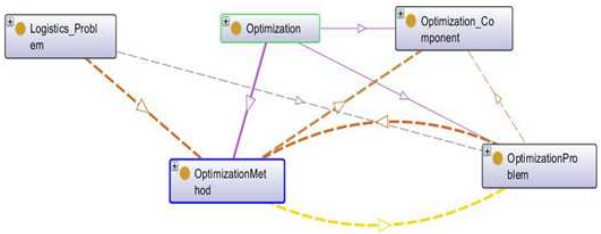

Figure 4: The top level optimization ontologies

In the following sections, we briefly narrate the optimization components, optimization problems, and optimization methods.

6.1 Optimization components

The optimization problem is generally encompassed around multiple components. These components actually describe the nature of optimization problem, depending on the component type. These components are notified as artifacts in our knowledge-base whereas, specifically their classification is as follows (also shown in figure 5) :

- Data
- Objective function
- Constraints
- Parameter

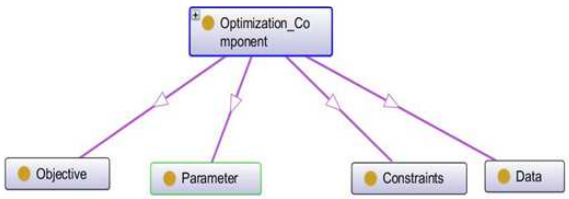

Figure 5: Optimization components

6.2 Optimization problems

The optimization problem basically depends on the nature of involved components. These can be addressed by one of the following problems [Hillier and Lieberman, 2001]:

- Continuous optimization versus discrete optimization
- Unconstrained versus constrained
- Non, one, or many objectives
- Deterministic optimization versus stochastic optimization

Likewise, as shown in figure 6, the type of optimization problem depends on the problematic component such as objective function or constrained, etc. These are further extended into subsequent classes for better understanding, as given below:

- Linear object function
  - integer problem
  - parametric linear problem
- Nonlinear object function
  - convex function problem
  - fractional object function problem
  - geometric object function problem
  - linearly constrained problem
  - multi-variable unconstrained problem
  - non-convex problem
  - quadratic problem
  - separable problem
  - unconstrained problem
- Stochastic
- Dynamic
- Network
  - maximum flow problem
  - minimum spanning tree problem
  - shortest path problem

6.3 Optimization methods

The applied optimization method depends on the type of problem and the component involved. Respective to the problem, these can be as follows (figure 7):

- Nonlinear programming method
  - gradient search method

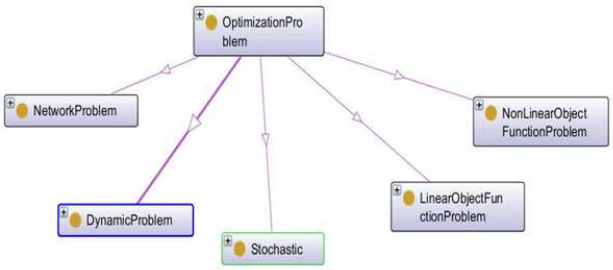

Figure 6: Optimization problems

  - karush-kuhu-tucker
  - key property of separable programming
  - modified simplex method
  - one dimensional search method
  - sequential linear approximation
  - sequential unconstrained minimum
- Linear programming method
  - interior point method
  - simplex method
  - upper bound technique
- Network programming method
  - network simplex method
- Approximate method
  - Heuristic method
  - Meta heuristic method
    - Tabu search
    - Genetic algorithms
    - Ant colony algorithms
    - Simulated annealing method

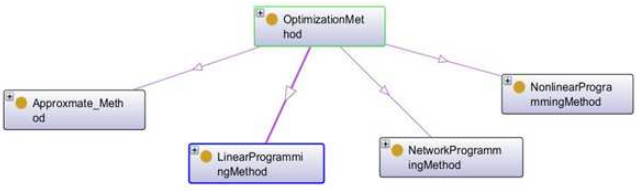

Figure 7: Optimization methods

Currently, we are focussing more on the Meta-heuristic methods for experimentation purposes. The inherent ontologies of meta-heuristic optimization methods are shown in figure 8.

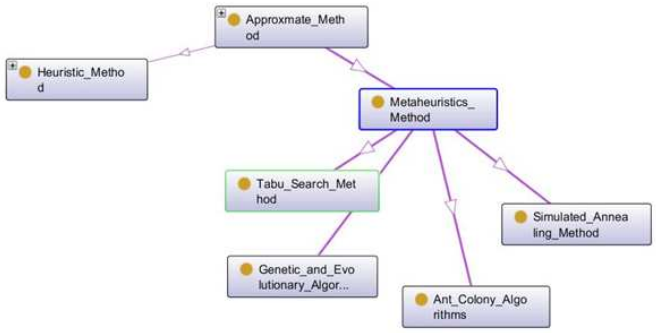

Figure 8: Meta heuristic methods

7 Ontologies application design

We have been experimenting with the logistic ontologies and the consequent query analysis with the help of Protégé framework[1]. It is one of the most widely used, open-source ontological engineering tool developed, by a group of researchers at Stanford university. We followed protégé 4.2 as an implementation mechanism and computational environment to conceptualize our logistic and optimization ontologies. The top level classes of logistic and optimization, along with their sub-classes are shown in figure 9.

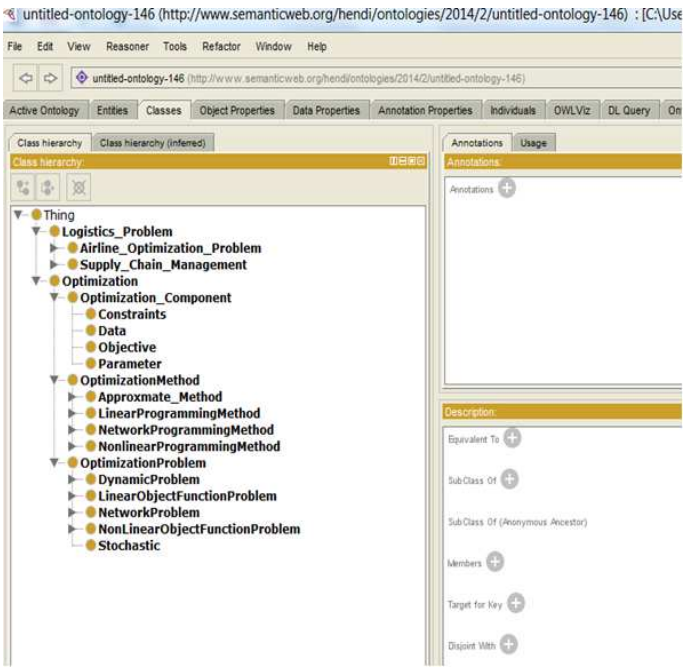

Figure 9: Top level classes of optimization ontologies in protégé

The top level roles of ontologies, as shown in figure 10, are the followings:

- *hasComponent* is a role, its domain is *optimization problem* and range is *optimization component*

[1]http://protege.stanford.edu/

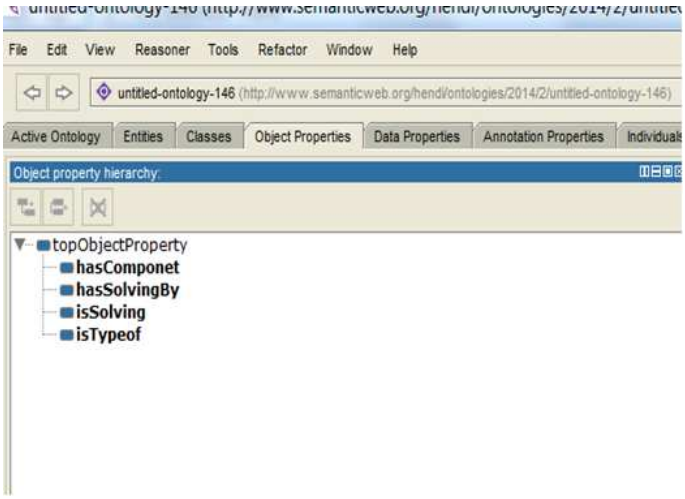

Figure 10: Roles of optimization ontologies in protégé

- *hasSolvingBy* is a role, its domain is *optimization problem* and range is *optimization method* and its inverse role *isSolving*

- *istypeof* is a role, its domain is *logistics optimization problem* and range is *optimization problem*

For instance, lets consider a routing problem, which can be a specialised class of transportation management in supply-chain management of logistic, as explained in section 5. In particular, this role can be used to retrieve results of a query related to the vehicle routing. In our ontologies *Vehicle routing problem* is a subset of *Transportation Management* class, as shown in figure 11. It has a role *hasTypeOf* with *Travelling Sales Person* is an *Integer Problem* which is actually a subset of *Linear Objective Function problem*, as depending on the problem component. The *Travelling Sales Person problem* has role *hasSolvingBy* to *Methods* class.

8 Conclusion

We devise ontologies for logistic and further extends them for optimization of logistic resources. These ontologies are intended to design a knowledge-base system, capable to support users in a general purpose software suite development. The conceptualization of optimization ontologies contributes in the identification of optimization components, optimization problem and exploitation of a significant optimization method for the logistic problem resolution.

We extend the currently available ontologies to adapt them specifically for logistics and optimization problems, but the application problem are different. We classify the problems and the corresponding optimization methods along with the ontologies definition. GOO (for instance) contains the top level of ontology problems, methods and algorithms; its application remains limited. The opti-

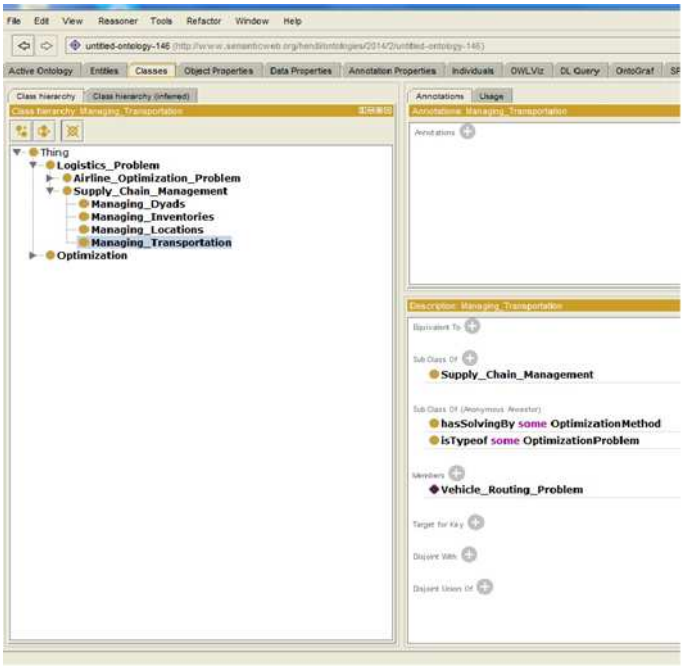

Figure 11: The ontologies for Vehicle Routing Problem

mization methods in GOO are similar to the optimization algorithms. While considering the ONTOP ontologies, where the authors, classifies the optimization types either as continuous problem or as discrete programming. Moreover, the continuous programming is classified as constrained and unconstrained, where the linear programming is sub-class of constrained programming. It conflicts the classification concept of integer programming, where it is sub-class of linear progrmming which, in turn, is a sub-class of discrete programming. Also the non-linear programming is classified as two sub-classes of both unconstrained and constrained programming, in ONTOP. In the current work, we exploit the inherent relationship between the optimization problem and the problematic component (i.e components involved in the problem) to classify the optimization problem. Furthermore, we classify the optimization methods into classical methods and approximate methods.

In the future we intend to develop an exhaustive framework to support users in the development of logistic software applications.

Acknowledgements

The research for this work has been supported, in part, by the CAMPUS France, Thi Qar Univeristy, Iraq, and the Le Laboratoire d'Informatique Signal et Image de la Côte d'Opale, Calais, France.

References

[Anand et al., 2012] Anand, N., Yang, M., Van Duin, J. H. R., and Tavasszy, L. (2012). Genclon: An ontology for city logistics. *Expert Syst. Appl.*, 39(15):11944–11960.

[Fensel, 2001] Fensel, D. (2001). Ontologies. In *Ontologies*, pages 11–18. Springer Berlin Heidelberg.

[Han et al., 2011] Han, J., Miller, J. A., and Silver, G. A. (2011). Sopt: Ontology for simulation optimization for scientific experiments. In *Proceedings of the Winter Simulation Conference*, WSC '11, pages 2914–2925. Winter Simulation Conference.

[Hillier and Lieberman, 2001] Hillier, F. S. and Lieberman, G. J. (2001). *Introduction to Operations Research, 7th Ed.* McGraw-Hill, New York.

[Hoxha et al., 2010] Hoxha, J., Scheuerman, A., and Bloehdorn, S. (2010). An approach to formal and semantic representation of logistics services. In Schill, K., Scholz-Reiter, B., and Frommberger, L., editors, *Proceedings of the Workshop on Artificial Intelligence and Logistics (AILog) at the 19th European Conference on Artificial Intelligence (ECAI 2010), Lisbon, Portugal*, pages 73–78. published online.

[Kalfoglou and Schorlemmer, 2003] Kalfoglou, Y. and Schorlemmer, M. (2003). Ontology mapping: the state of the art. *The Knowledge Engineering Review*, 18:1–31.

[Kayikci and Zsifkovits, 2013] Kayikci, Y. and Zsifkovits, H. (2013). Successful ict integration in transport collaboration. *Pioneering solutions in supply chain performance management : concepts, technology and applications*, pages 201–220.

[Leukel and Kirn, 2008] Leukel, J. and Kirn, S. (2008). A supply chain management approach to logistics ontologies in information systems. In Abramowicz, W. and Fensel, D., editors, *Business Information Systems*, volume 7 of *Lecture Notes in Business Information Processing*, pages 95–105. Springer Berlin Heidelberg.

[Miller et al., 2004] Miller, J., Baramidze, G., Sheth, A., and Fishwick, P. (2004). Investigating ontologies for simulation modeling. In *Simulation Symposium, 2004. Proceedings. 37th Annual*, pages 55–63.

[Moussas et al., 2013] Moussas, V., J, T., and Tsahalis, H.-T. (2013). Design of an ontology for simulation workflow optimization. *5th International Conference on Experiments/Process/System Modeling/Simulation/Optimization.*

[Onsel, 2009] Onsel, u. (2009). Operations researchapplications, edited by a. ravi ravindran. *International Journal of Production Research*, 47(23):6781–6782.

[Rushton et al., 2014] Rushton, A., Croucher, P., and Baker, P. (2014). Kogan Page, fifth edition edition.

[Scheuermann and Hoxha, 2012] Scheuermann, A. and Hoxha, J. (2012). Ontologies for intelligent provision of logistics services. *The Seventh International Conference on Internet and Web Applications and Services.*

[Witherell et al., 2006] Witherell, P., Krishnamurty, S., and Grosse, I. R. (2006). Ontologies for supporting engineering design optimization. *Journal of Computing and Information Science in Engineering.*


Normandie Université
UNIVERSITÉ
LE HAVRE
litis
LMAH
cnrs
RNSC
Réseau National des Systèmes Complexes
ISCN
risc
Liberté • Égalité • Fraternité
RÉPUBLIQUE FRANÇAISE
MINISTÈRE
DE L'ENSEIGNEMENT SUPÉRIEUR
ET DE LA RECHERCHE
l'Europe
s'engage en
Haute-Normandie
REGION
HAUTE
NORMANDIE
CODAH
Communauté de
l'Agglomération Havraise